

# Bulletin of Materials Science

Volume 8, January–December 1986

## CONTENTS

Kinetics of electrophoretic deposition of  $\beta$ -alumina

*D U Krishna Rao, A B Malage, D Baral and E C Subbarao*

Microstructural and dielectric behaviour of glass ceramics in the system

$\text{PbO-BaO-TiO}_2\text{-B}_2\text{O}_3\text{-SiO}_2$

*Om Parkash, Devendra Kumar and R Rajagopalan*

Dielectric properties of the system  $\text{Pb}_{2-x}\text{Nd}_x\text{Li}_{0.5}\text{Nb}_{1.5}\text{O}_{6+\delta}$

*S G Phadnis, M Subramanian and R Rajan*

Surface morphology and properties of GaAs epilayers controlled by temperature difference method of liquid phase epitaxy

*Y K Su, C C Wei, S C Lu and C C Chang*

Magnetic and Mössbauer studies on ductile Fe-Cr-Co permanent magnet alloys

*V Chandrasekaran, Ch Sreerama Murthy, P Subramaniam and G Venkateswarlu*

Tunnelling of electrons from deep traps of MgO

*M N Bapat and S Sivaraman*

Thermal expansion studies on As-Sb-Se glasses

*A Giridhar, Sudha Mahadevan and A K Singh*

X-ray line profile analysis of silver base Ag-Cd-In alloys

*S Venkat Reddy and S V Suryanarayana*

Phase relations and activities in the Co-Ni-O system at 1373 K

*K T Jacob, S Srikanth and G N K Iyengar*

Effect of texture and grain size on the mechanical properties of warm-worked cadmium, zinc and zinc-0.35% aluminium alloy

*K Ratnaji Rao, S Ranganathan and D H Sastry*

**Proceedings of the symposium on Computer Modelling and Applications in Metallurgical Research and Industry**

Foreword

Computer models for fuel element behaviour

*J R Matthews*

Computer calculations of phase diagrams

*A K Mallik*

Computer-aided design of rolling mills

*K G Pandey*

Computer modelling application in life prediction of high temperature components

*V M Radhakrishnan* 1

Computer applications in the field of furnace design

*V S Pakala* 1

Computer simulation of defects and radiation damage	
	<i>K Krishan, B Purniah and S Srinivasan</i> 14
Some fundamental considerations to precede image analysis	<i>Dieter Vollath</i> 16
Computer-aided roll pass design for continuous billet mill	
	<i>Ashok Kumar, Sudhaker Jha and V Ramaswamy</i> 18
Computer-aided composition-treatment-structure-property correlation studies in steels	
	<i>K Vijayaraju and E S Dwarakadasa</i> 19
Computer simulation of pressure sintering	
	<i>N Ramakrishnan, T Balakrishna Bhat and V S Arunachalam</i> 1
Computer simulation of serrated yielding	<i>K Neelakantan</i> 2
An absolute method for the determination of surface tension of liquids using pendent drop profiles	<i>S Ramesh Babu</i> 2
Personal computer-based CAMAC system for data acquisition	
	<i>S K Kataria, V S Ramamurthy, V G Gaonkar and Surendra Kumar</i> 2
Image analysis system for quantitative metallography	
	<i>V K Chadda, D G Joshi, S N Murthy, S V Kulgod, C Baburao, D K Bhattacharya and Baldev Raj</i> 3
Modern computer assisted methods in metallurgy	
	<i>G W Jenkinson and T Kelly</i> 3
Computer simulation of dislocation-carbon interaction in nickel	
	<i>B Purniah and S Srinivasan</i>
Water reactor fuel performance code PROFESS and its application for predicting the behaviour of the fuel elements of D-Com blind problem	
	<i>D N Sah, D Venkatesh and E Ramadasan</i>
<b>Proceedings of the symposium on Thin Film Science and Technology</b>	
<b>Foreword</b>	
Electrical and optical properties of $\mu\text{c-SiH}$ films	
	<i>G C Dubey, R A Singh, S N Mukherjee, Surendra Pal and M G Rao</i>
Thin film $\text{CdZnS/CuInSe}_2$ solar cells by spray pyrolysis	
	<i>P Raja Ram, R Thangaraj and O P Agnihotri</i>
a-Si:H/CuInS <sub>2</sub> heterojunctions for photovoltaic conversion	
	<i>Satyendra Kumar, A N Tiwari, O S Sastry, D K Pandya and K L Chopra</i>
Flash-evaporated thin films of $\text{CuInSe}_2$	
	<i>R D Pachori, A Banerjee and K L Chopra</i>
Growth of polysilicon and silicide films for MOS-VLSI application	
	<i>S K Aggarwal, M Bal, G D Sharda, Mahavir Singh and K K Laroia</i>
Electrical and structural characteristics of oxides grown from polycrystalline silicon	
	<i>B B Dixit, P D Vyas, W S Khokle, K Mahadevan and H N Acharya</i>

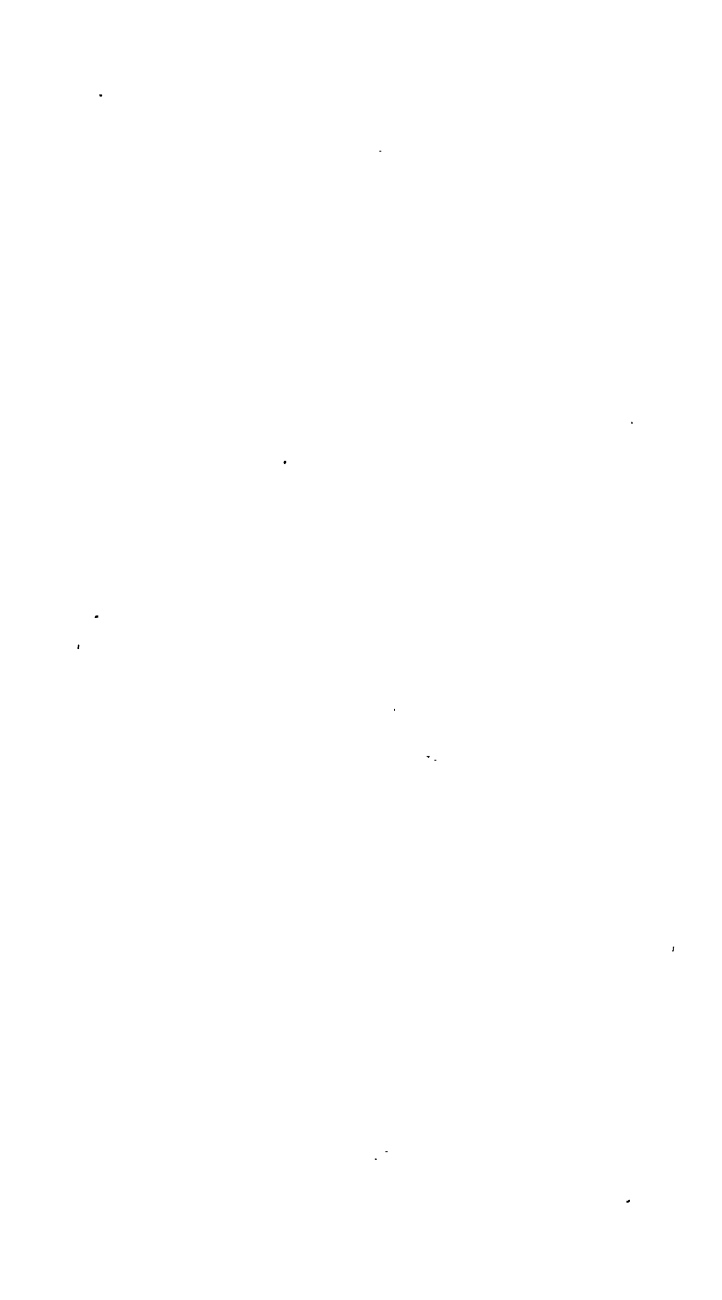


## Contents

SnO <sub>2</sub> :F films synthesized by chemical vapour deposition technique using hydrofluoric acid as doping material	
	<i>A K Saxena, R Thangaraj, S P Singh and O P Agnihotri</i>
Preparation and characterization of flash-evaporated CuInSe <sub>2</sub> thin films	
	<i>D Sridevi, J J B Prasad and K V Reddy</i>
Deposition and assessment of thin dielectric films on photocathode substrate made of Kodial glass	
	<i>V R Katti and L M Rangarajan</i>
Development of high resolution thin film patterns on curved photocathode substrates of image tubes	
	<i>L M Rangarajan and V R Katti</i>
Dielectric mirrors for high power laser applications	
	<i>K V S R Apparao</i>
Design and development of a thin film dielectric beam combiner	
	<i>K V S R Apparao and N K Sahoo</i>
Optical constants in the ultraviolet region of evaporated high index thin films	
	<i>K V S R Apparao and T C Bagchi</i>
Quality and reliability of optical coatings	
	<i>C L Nagendra and G K M Thutupalli</i>
Optical and electrical properties of SnO <sub>2</sub> films prepared by chemical vapour deposition	
	<i>S Raghunath Reddy, A K Mallik and S R Jawalekar</i>
Pyroelectric polymer films for infrared detection	
	<i>P Jayarama Reddy and M Sirajuddin</i>
Photoresponsive measurements of InAs <sub>0.8</sub> Sb <sub>0.7</sub> infrared detector	
	<i>M Raja Reddy, B Srinivasulu Naidu and P Jayarama Reddy</i>
R.F. magnetron sputtered tungsten carbide thin films	
	<i>P K Srivastava, V D Vankar and K L Chopra</i>
Cobalt oxide-iron oxide selective coatings for high temperature applications	
	<i>C S Uma, L K Malhotra and K L Chopra</i>
Transistors made in laser recrystallized polysilicon on insulator films	
	<i>S Chandrasekhar, P R Apte and S K Roy</i>
Effect of bulk and thin film dielectric overlay on the characteristics of micro-strip rejection filter and simple microstriplines	
	<i>K Vijaya, M L Jadhav, S A Gangal and R N Karekar</i>
Thermoluminescence in thin films of zinc and copper phthalocyanines	
	<i>L N Tripathi and Y Misra</i>
Characterization of Pb <sub>3</sub> O <sub>4</sub> films by electrochemical techniques	
	<i>M Sharon, Sudhir Kumar and S R Jawalekar</i>
Electrochemical bath deposition technique: Deposition of CdS thin films	
	<i>S H Pawar, C H Bhosale and L P Deshmukh</i>
Spray pyrolytic deposition of CuBiS <sub>2</sub> thin films	
	<i>S H Pawar, A J Pawar and P N Bhosale</i>

Preparation and properties of $\text{Bi}_{2-x}\text{As}_x\text{S}_3$ thin films by solution-gas interface technique	<i>S H Pawar and P N Bhosale</i>	427
Electron microscopy study of chemically deposited Ni-P films	<i>S V S Tyagi, V K Tandon and S Ray</i>	433
Liquid phase epitaxy growth of GaAs:Si by temperature difference method	<i>C C Wei, Y K Su, C C Chang and S C Lu</i>	439
X-ray diffraction study on epitaxial zinc and cadmium films prepared by hot-wall technique	<i>A V Kulkarni and R Pratap</i>	449
Concept of thermodynamic capacity	<i>R Akila, K T Jacob and A K Shukla</i>	453
Growth of low dislocation density single crystals of nickel	<i>S K Khanna and K Govinda Rajan</i>	467
Emission spectrographic technique for the quantitative determination of trace elements in granitic rocks	<i>A El Bialy, M Rasmy, L A Guirguis and W Moussa</i>	471
Determination of oxygen to metal ratio of U-Pu mixed oxides by x-ray diffraction	<i>Ravi Verma and P R Roy</i>	479
Kinetics of calcium molybdate crystallization	<i>N M Batra and S K Arora</i>	489
Thermal transformation in a chrysotile asbestos	<i>A K Datta, B K Samantaray and S Bhattacharjee</i>	497
Effect of $\text{H}^+$ ion irradiation on surface morphology of $\text{Fe}_{40}\text{Ni}_{40}\text{B}_{20}$ metallic glass	<i>A J K Prasad and Vakil Singh</i>	505
Periodic crystallization of barium oxalate in silica hydrogel	<i>S M Dharma Prakash and P Mohan Rao</i>	511
Studies on etching of gel-grown barium oxalate dihydrate crystals	<i>S M Dharmaprakash and P Mohan Rao</i>	519
Determination of molecular weight distribution of polyethylene terephthalate by gelpermeation chromatography	<i>K Sreenivasan and Prabha D Nair</i>	527
Space charge limited currents in chlorazole black E dye	<i>J P S Chauhan, D C Dube and S C Mathur</i>	531
Microstrip losses with $\text{Al}_2\text{O}_3$ overlay	<i>K K Joshi, C Dhanavantri, S A Gangal and R N Karekar</i>	535
<b>Comments</b>		
Thermoluminescence of alkali halides doped with alkaline earth impurities	<i>A R Lakshmanan and S V Moharil</i>	541
A simple hydrothermal cell for synthesis at moderate temperatures and pressures	<i>J A K Tareen, B Basavalingu, M A Shankara and Ali Reza Fazeli</i>	543
Characterization and thermal behaviour of lanthanum tartrate crystals grown from silica gels	<i>P N Kotru, N K Gupta, K K Raina and M L Koul</i>	547

Glass ceramics containing ferroelectric phases	
<i>Om Parkash, Devendra Kumar and Lakshman Pandey</i>	557
Magnetic hysteresis and crystallization studies on metallic glass alloy $\text{Fe}_{67}\text{Co}_{18}\text{B}_{14}\text{Si}_1$	
<i>A M Varaprasad and C Radhakrishnamurthy</i>	567
Influence of eutectic addition on the electrical conductivity of $\text{Li}_2\text{O}:\text{B}_2\text{O}_3$ system	
<i>V K Deshpande and K Singh</i>	577
Optical black coatings for space applications	
<i>K Ramaseshan, M Viswanathan and G K M Thutupalli</i>	581
Dislocation density in electrolytically coloured KCl crystals	
<i>N L Bhole and B T Deshmukh</i>	587
A low-temperature attachment for a four-circle neutron diffractometer	
<i>A Sequeira, Sandhya Bhakay-Tamhane and S R Sawani</i>	591
<b>Subject index</b>	597
<b>Author index</b>	606



## Kinetics of electrophoretic deposition of $\beta$ -alumina

D U KRISHNA RAO\*, A B MALAGE\*\*, D BARAL\*\*\* and  
E C SUBBARAO\*\*\*\*

Department of Metallurgical Engineering, Indian Institute of Technology, Kanpur 208 016, India

Present Address: \*Bharat Electronics Limited, Materials Development Dept., Bangalore 560 013, India

\*\*Widia (India) Limited, Tumkur Road, Bangalore 560 073, India

\*\*\*Memorex Corp., Sanata Clara, CA, USA

\*\*\*\*Tata Research Development & Design Centre 1, Mangaldas Road, Pune 411 001, India

MS received 8 October 1984; revised 2 November 1985

**Abstract.** The equations describing electrophoretic deposition, proposed by Hamaker Avgustinik and coworkers, have been verified in the case of  $\beta$ -alumina suspended in isoamyl alcohol. The variation of electrophoretic yield with (i) concentration of suspension, (ii) extent of grinding the suspension, (iii) temperature of the suspension, and (iv) electrode separation was studied. The effect of addition of glycol monoethyl ether was also investigated. The effect of various parameters on the electrical conductivity of the suspension, which in turn influences the yield, was noted.

**Keywords.** Electrophoretic kinetics; electrophoretic deposition; beta alumina; concentration; temperature; electrode separation.

### 1. Introduction

The energy crisis has accelerated the pace of research on unconventional modes of energy generation and storage. Among the high energy density batteries, sodium-sulphur battery is a strong candidate (Robinson 1976). In this, liquid sodium and sulphur are separated by a solid-electrolyte, namely  $\beta$ -alumina ( $\text{Na}_2\text{O} \cdot x\text{Al}_2\text{O}_3$ ) ceramic. Most of the cost and failures of these batteries are attributed to this electrolyte. Therefore, production of dense, mechanically sound, electrically conducting  $\beta$ -alumina in desired shapes (mostly one end closed tubes) is receiving active attention. Slip casting (Byckalo *et al* 1976), extrusion (Ford Annual Report 1975-76), isostatic pressing (Youngblood *et al* 1977) and electrophoresis (Fally *et al* 1973; Powers 1975; Kennedy and Foissy 1975; Powers *et al* 1981) are being explored for fabrication of these tubes, followed by sintering. Alternately, hot pressing may be employed.

#### 1.1 Electrophoresis

Electrophoresis is an electrokinetic phenomenon in which the suspended charged particles move under the influence of an electric field. An electrical double layer is formed at the boundary between the solid and the surrounding liquid, since both the phases are electrically charged.

1.1a *Kinetics of electrophoretic deposition.* Hamaker (1940) showed that yield or amount of electrophoretic deposition,  $Y$ , in g,

$$Y = a \int \mu F C A \, dt. \quad (1)$$

Here,  $\mu$  is the electrophoretic mobility, the velocity of a particle in a unit field of 1 V/cm;  $F$  is the electric field;  $C$  is the concentration of particles in g/cc;  $A$  is the electrode area, over which deposition is taking place; and  $t$  is the time. The coefficient  $a$  takes into account the possibility that not all particles which migrate to the electrode may deposit.

Avgustinik *et al* (1962) derived an expression for the electrophoretic yield,  $v_t$ , in g/cm,

$$v_t = \frac{F \zeta C l \epsilon}{3 \ln \frac{r_1}{r_2} \eta} \quad (2)$$

where  $\zeta$  is the zeta potential;  $\epsilon$  the dielectric constant of the medium;  $l$  the length of the cylinder;  $r_1, r_2$  are the radii of inner and outer electrodes respectively;  $\eta$  is the viscosity of the medium; and  $F, C$ , and  $t$  are as defined in (1).

1.1b *Electrophoretic forming of  $\beta$ -alumina:* Tubes of  $\beta$ -alumina have been successfully fabricated by this technique by Fally *et al* (1973), Powers (1975), Kennedy and Foissy (1975, 1977) and Foissy and Robert (1982). Fally *et al* (1973) used polar and organic liquids such as nitromethane or trichloromethane as the vehicle for suspension. Their tubes were quite thick (200–2000  $\mu\text{m}$ ) and they needed isostatic pressing for removal from the electrode. Kennedy and Foissy (1975, 1977) and Foissy and Robert (1982) used dichloromethane as the medium with trichloro-acetic acid as additive. Kennedy and Foissy (1975) formed the tubes (3–4 cm long, 0.03 to 0.1 cm thick) on carbon electrodes and the tubes were removed by burning off the carbon rod. Powers (1975) evaluated various vehicles and found that vehicles which have dielectric constants in the range of 12 to 25 and specific conductance of  $10^{-7}$  to  $10^{-4}$  ( $\text{ohm cm}$ ) $^{-1}$  are suitable. He used very smooth stainless steel electrodes and reported that the tubes came off easily from the mandrel after drying the deposits.

From the above, it may be noted that some of the variables governing the kinetics of electrophoretic deposition of beta alumina have been examined qualitatively, but there was hardly any quantitative data even in the case of the variables explored. The purpose of the present work is, therefore, to study the effect of various parameters on the rate of electrophoretic deposition of beta alumina in non-aqueous media in quantitative terms. The variables chosen are:

- (i) selection of vehicle (benzyl vs iso-amyl alcohol) on the basis of yield rate, conductivity, viscosity, and boiling point;
- (ii) effect of concentration, grinding (particle size) and temperature on viscosity, conductivity and specific yield;
- (iii) effect of addition of ethylene glycol on conductivity and yield;
- (iv) role of electrode separation and mandrel material (graphite and stainless steel) in electrophoretic deposition.

## 2. Experimental

The three major steps involved in this work are (1) preparation of  $\beta$ -alumina powder; (2) preparation of suspension; and (3) electrophoretic deposition.

### 2.1 Powder preparation

Alumina (Alcoa A-2) was heated to 1000°C and preserved in an oven at 110°C. Sodium carbonate (BDH), which is hygroscopic, was also stored in the oven at 110°C. 1:5 mol of  $\text{Na}_2\text{O}$  and  $\text{Al}_2\text{O}_3$  were mixed in acetone in an alumina ball jar. The liquid was dried and the cake was calcined in platinum crucibles at 1250°C for 4 to 5 hours. Then the furnace was cooled to 800°C in 2 hrs and the crucibles were taken out of the furnace, air-cooled (Baral 1977) and stored till usage in an oven at 350°C to prevent rehydration (Foissy and Robert 1982; Powers *et al* 1981).

The calcine contains  $\beta$  and  $\beta''$  alumina, the latter being preferable to  $\beta$ -alumina as a solid electrolyte. The relative amount of  $\beta$ -alumina is given by a factor (Youngblood *et al* 1977)

$$f(\beta) = \frac{I_{(\beta)}}{I_{(\beta)} + I_{(\beta'')}}, \quad (3)$$

which was calculated by using the integrated intensities of the x-ray diffraction characteristic lines at  $2\theta = 44.3^\circ$  and  $46^\circ$  of  $\beta$  and  $\beta''$ -alumina, respectively.

The  $f(\beta)$  of the calcine in the present work was found to be 0.33, showing more of  $\beta''$  alumina. However, for convenience, the powder is referred as  $\beta$ -alumina here.

A small amount of powder was stirred well in dichloromethane with two drops of trichloroacetic acid to increase stability (Kennedy and Foissy 1975, 1977). It was dispersed on a glass slide and dried before studying under NU2 Carl Zeiss-Jena microscope for particle size distribution. The particles of the calcined powder were 0.8 to 6  $\mu\text{m}$  in size with an average of 2  $\mu\text{m}$ . The powder density was 3.19  $\text{g/cm}^3$ , whereas the theoretical density of  $\beta$  and  $\beta''$  are 3.24 and 3.27  $\text{g/cm}^3$ , respectively.

### 2.2 Preparation of suspension

Generally, 100 g of powder and 200 cc of vehicle were taken in an alumina ball jar, ground for 5½ hrs and transferred to the electrophoretic cell.

### 2.3 Electrophoretic deposition

Two types of cells were used (figure 1). To prevent settling, the beaker was rotated for 1 minute before every deposition. The perforations in the tubular counter electrode (figure 1a) and its off-centre position in the beaker enhanced the stirring action. In the second case, figure 1b, the counter electrode itself was the container for the suspension, which was stirred before pouring into the container.

### 2.4 Computation of concentration and conductivity of the suspension and area of coated mandrel

A method was devised to calculate the concentration of the suspension for each deposition (Krishna Rao 1978). It was computed on the basis of geometry of the cell (figure 2), which is self-explanatory. The volume of the suspension in the can

$$V = \pi \frac{D^2}{4} (H + h + p - L) - \pi \frac{D_x^2}{4} H. \quad (4)$$

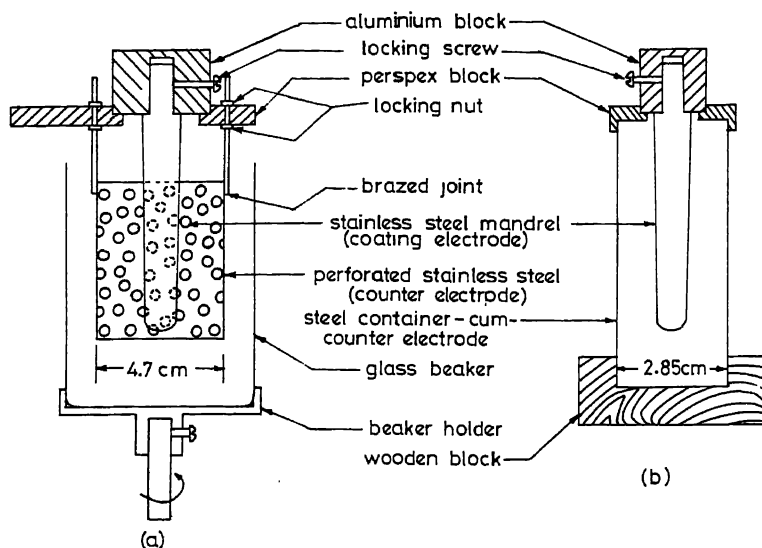


Figure 1. Cells for electrophoresis.

Concentration of the suspension (g of powder per 100 cc suspension) =

$$\frac{\text{amount of solid in the suspension}}{\text{volume of the suspension}} \times 100 \quad (5)$$

The amount of solid in the suspension was calculated as follows. The amount deposited in each deposition stage was measured, and after all the depositions, the remaining suspension in the can was dried at 350°C and weighed. The total amount of solid in the suspension was computed by adding the weight of the dried suspension and amount deposited. Thus, the amount of powder in the suspension at any stage of deposition could be computed and, thereby, the concentration of suspension as well.

The area of deposition ( $A$ ) of the electrode (figure 2) is calculated as follows:

$$\tan \theta = \frac{H/2}{(D_x - d_e)/2} = \frac{L}{(d_s - d_e)/2}, \quad (6)$$

$$D_x = \frac{(d_s - d_e) H}{2L} + d_e, \quad (7)$$

$$A = \pi D_x H + \frac{\pi}{4} d_e^2. \quad (8)$$

The conductivity of the suspension ( $\sigma$ ) was measured using the  $I$ - $V$  characteristics using the equation

$$\sigma = (\text{current} \times \text{electrode separation}) / (\text{voltage} \times \text{surface area of the mandrel, } A, \text{ dipped in the suspension}). \quad (9)$$

These results were in good accordance with the value measured with a General Radio impedance bridge (GR 1608) at a frequency of 1 kHz.



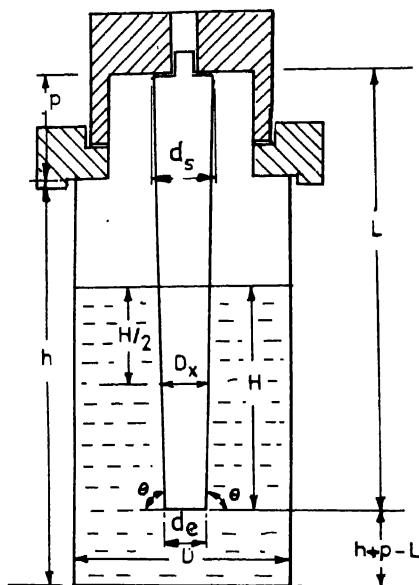


Figure 2. Geometry of the cell and the mandrel.

Table 1. Characteristics of  $\beta$ -alumina suspensions

Vehicle and (boiling point)	Viscosity millipoise	Dielectric constant	pH	Conductivity	Specific yield rate ( $\times 10^4$ g/cm <sup>2</sup> min V)
Benzyl alcohol (205)	(55.82) at 20°C	(13.0)	(5.25) 9.0	(0.926) 20.46	4.6
Iso-amyl alcohol (130)	(4.811) at 15°C	(14.7)	(6.0) 8.0	(2.256) 9.09	4.25

The charge on particles was positive; the numbers in brackets refer to the properties of the vehicle.

### 3. Results and discussion

#### 3.1 Evaluation of vehicles

Powers (1975) has shown that satisfactory deposits of  $\beta$ -alumina can be obtained only with vehicles in a limited range of dielectric constants (12–25). Lower zeta potential liquids (Kennedy and Foissy 1977) and higher voltage (Powers 1975) were suggested for good electrophoretic deposition of  $\beta$ -alumina. Higher voltages decrease the time required to get a required thickness of deposit and this minimizes the problem of the suspension stability. Also the amount of dripping from the mandrel decreases. To use higher voltages, low conductivity suspensions have to be used, otherwise bubbling of the deposit occurs. Also, it was reported (Troelstra 1951) that the yield is inversely proportional to conductivity of the suspension. Two types of alcohols viz benzyl and isoamyl alcohols were evaluated. From table 1, it may be noted that, with  $\beta$ -alumina

powder addition to the vehicle, both the pH and conductivity of the suspension increased. Even though the specific yield was almost equal with benzyl and iso-amyl alcohols, the former was not preferred as it has higher viscosity, boiling point (b.p.) and also higher conductivity of the suspension. Because of higher b.p., drying of the deposit was more difficult and because of high viscosity of the vehicle, deformation of the deposit during drying was possible. These results are consistent with the earlier reports on MgO (Krishna Rao and Subbarao 1979). Therefore, iso-amyl alcohol was chosen for further studies.

### 3.2 Concentration

The effect of concentration of the suspension (g of powder/100 cc suspension) on the amount of material sticking to the mandrel ( $\text{g}/\text{cm}^2$ ), conductivity of suspension and specific yield ( $\text{g}/\text{cm}^2$ ) at 100 V/1 min were studied (figure 3).

To start with, higher concentration (about 80 g/100 cc) suspension was prepared. The concentration decreased as successive depositions were made from the same suspension. As the concentration decreased from 76 to 28 g/100 cc suspension, the conductivity increased from 14 to  $24 \mu\text{S cm}^{-1}$ . This may be because of the accumulation of leached out ions in the suspension (Foissy and Robert 1982) with successive depositions. This was not the case with MgO system (Krishna Rao and Subbarao 1979) where there may not be any leaching of ions. The amount of powder (suspension) sticking to the mandrel when it is dipped in the suspension, is a function of viscosity of the suspension and the viscosity increases drastically at higher concentra-

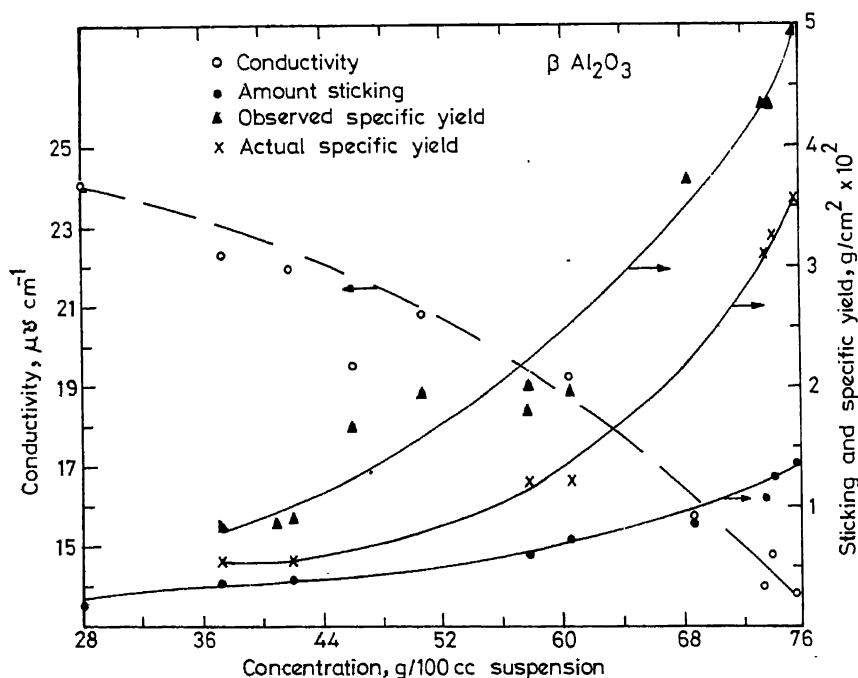


Figure 3. Variation of conductivity of suspension, amount sticking and specific yield with concentration of the suspension.

tions (Krishna Rao and Subbarao 1979). In the present study, the observed and actual (observed minus the amount sticking to mandrel) specific yields increased drastically with concentration (figure 3). Similar type of behaviour was observed by Krishna Rao and Subbarao (1979) and Andrews *et al* (1969). This nonlinear behaviour was not in accordance with equations (1) and (2), and may be due to the following: (1) The coefficient  $a$  in (1) appears to increase with the concentration of the suspension (Hamaker 1940), i.e., all the particles reaching the electrode may not be depositing at low concentrations; (2) The probability that the moving particles may drag other particles with them and thus raise the yield rate, as suggested by Avgustinik *et al* (1962). This dragging effect may be more pronounced at higher concentrations. The linear behaviour observed by Powers (1975) appears to be due to the limited range of concentrations studied.

### 3.3 Grinding

One hundred grams of the powder in 200 cc iso-amyl alcohol was ground for zero,  $1\frac{1}{2}$  and 7 hours successively. Electrophoresis was carried out with cell 1 (figure 1a) at 25 V for different durations of deposition. The results (figure 4) show that (i) the specific yield increases with deposition time in accordance with (1) and (2), (ii) the curves do not

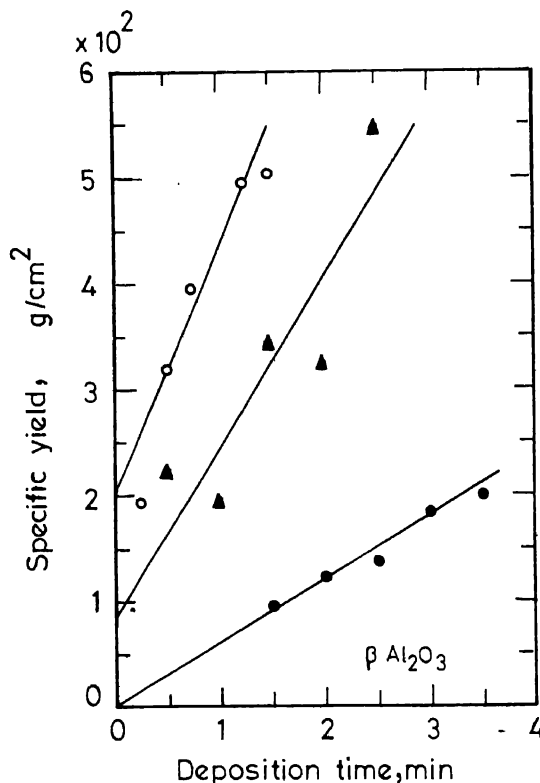


Figure 4. Variation of specific yield with deposition time (voltage = 25 V). The grinding time was 0 (solid circle) 1.5 (solid triangle) and 8.5 hr (circle) and the slopes ( $\times 10^4$  g/cm<sup>2</sup> V<sub>min</sub>) were 2.4, 6.4 and 8.8, respectively.

pass through the origin, confirming the physically observed fact that the amount of material sticking to the mandrel soon after insertion into the suspension (and in the absence of an applied voltage) increases with fineness of particle size (i.e. larger grinding) and greater viscosity (see figure 3 also), and (iii) the change in yield rate is not linear with grinding time. Similar results were obtained at higher applied voltages also. Based on these results, grinding for 5½ hours was employed for further experiments.

Depending on the suspension system (Fally *et al* 1973; Powers 1975; Kennedy and Foissy 1975, 1977), the grinding of the suspension influences the charge, zeta potential and mobility of particles. In the present system, the yield and conductivity of the suspension have gone up. According to Troelstra (1951), higher conductivity should decrease the yield. However, in the present case, the higher conductivity may be due to increased charge on the particles, which can lead to increase of the mobility (Kennedy and Foissy 1977) and therefore the yield.

### 3.4 Temperature

The suspension with the can and mandrel (figure 1b) was heated to 70°C in an oven, stirred and taken out. Before every deposition at 100 V for 1 min, the temperature was noted after stirring. The depositions were carried out as the suspension cooled. The variation in concentration of suspension was not much during this series of experiments.

It was observed that with temperature, the yield increased linearly (figure 5), which is consistent with the behaviour observed in the case of alumina in ethanol (Michaels

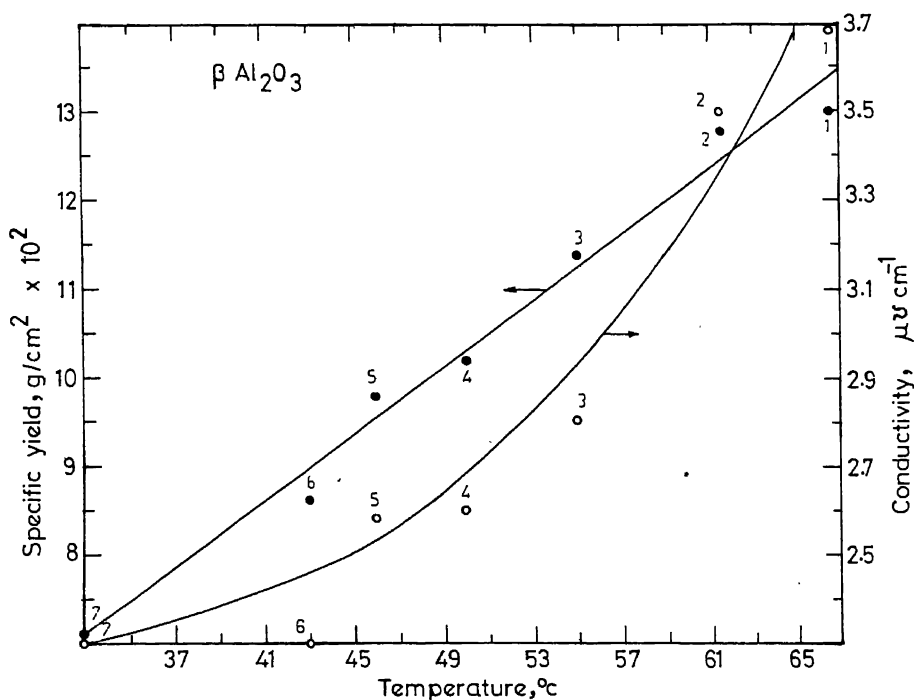


Figure 5. Variation of specific yield and conductivity of the suspension with temperature.

1958). With temperature, the ionic mobility and conductivity increase and the viscosity of the suspension decreases and thereby increases the yield ((1) and (2)).

### 3.5 Additives

The concentration of additives such as water, trichloro-acetic acid, and benzoic acid influences the charge on particle, mobility, stability of suspension (Fally *et al* 1973; Powers 1975; Kennedy and Foissy 1975, 1977; Foissy and Robert 1982; Powers *et al* 1981; Andrews *et al* 1969), depending on the vehicle used for dispersing the powder. A limited study was carried out in the present system with ethyl glycol monoethyl ether additions on electrophoretic yield.

Addition of 0.5 cc of this additive to 50 cc of the ground suspension increased the specific yield by 8.3 times and the conductivity of suspension by about 2.5 times (figure 6). There was no bubbling even at 100 V. The increased conductivity could be due to the increased charge on the particles as is reported in other systems (Fally *et al* 1973; Powers 1975; Kennedy and Foissy 1975, 1977; Foissy and Robert 1982). The specific yield and the conductivity of the suspension varied linearly with the concentration of the suspension, thus verifying (1) and (2) and consistent with the behaviour reported in figure 3. It was observed that adding ethyl glycol to the ground suspension gave more specific yield than making the addition before grinding. This aspect requires further study.

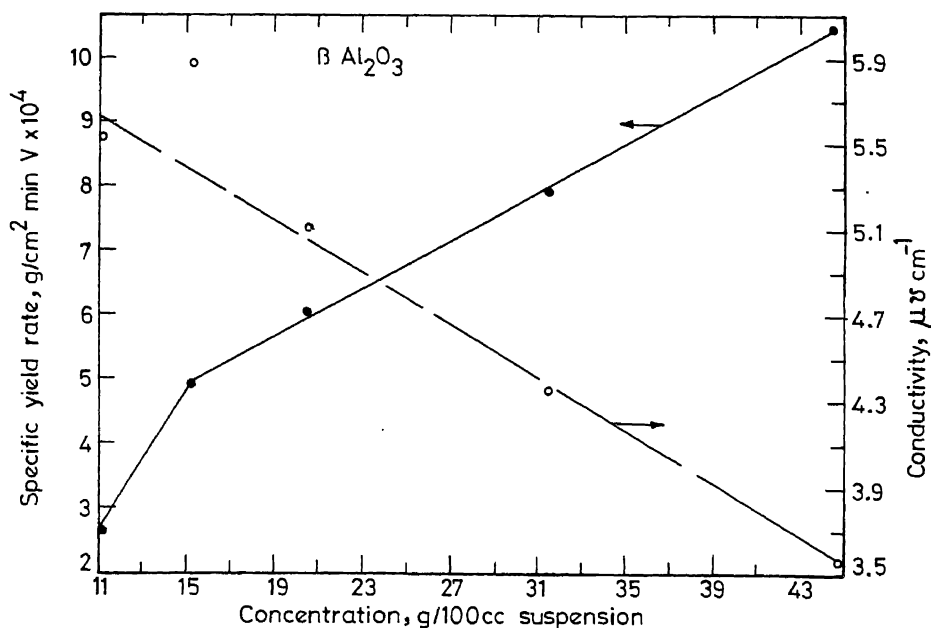


Figure 6. Variation of specific yield rate and conductivity of the suspension with concentration of the suspension containing ethylene glycol.

### 3.6 Electrode separation

The effect of electrode separation on specific yield was studied by using two types of mandrels, viz steel and graphite and steel counter electrodes of different sizes (table 2).

Experimental yield ratio  $M$  and the computed yield ratio  $N$ , from (2) were noted in table 3. The  $M/N$  ratio should be 1, but the experimental values varied from 1.05 to 1.13, which is within the experimental error (Malage 1979; Krishna Rao 1978).  $v_g/v_s$  is also in agreement with (2), which shows that the yield rate is independent of the mandrel material (graphite or steel).

## 4. Conclusion

The experimental results on the electrophoretic yield of  $\beta$ -alumina suspended in iso-amyl alcohol are in quantitative agreement with (1) and (2) in terms of (i) a linear

**Table 2.** Electrophoretic yield with different electrodes

Set	Mandrel		Counter electrode		Yield
	Type	Radius (cm)	Type	Radius (cm)	
(a)	Steel	0.43	Steel can	1.72	$v_x$
	Steel	0.43	Steel can	1.42	$v_y$
	Steel	0.43	Steel can	0.93	$v_z$
(b)	Steel	0.42	Steel can	1.42	$v_c$
	Steel	0.42	Perforated steel can	2.35	$v_p$
(c)	Steel	0.42	Steel can	1.42	$v_s$
	Graphite	0.37	Steel can	1.42	$v_g$

**Table 3.** Effect of electrode separation on electrophoretic yield

Set	Electrophoretic yield ratio			
	Ratio	Expt. $M$	Computed $N$	$M/N$
(a)	$\frac{v_x}{v_y}$	0.93	0.86	1.08
	$\frac{v_y}{v_z}$	0.68	0.65	1.05
	$\frac{v_x}{v_z}$	0.63	0.56	1.13
(b)	$\frac{v_p}{v_c}$	0.75	0.71	1.05
(c)	$\frac{v_g}{v_s}$	0.99	0.92	1.07

variation with time and (ii) inverse dependence of  $\ln(r_1/r_2)$  where  $r_1$  and  $r_2$  are the radii of the inner and outer electrode (irrespective of the electrode material, viz steel or graphite). However, the nonlinear dependence of yield on concentration is not consistent with these equations and may be due to the very wide concentration range (28 to 76 g of solid/100 cc of suspension) covered.

Other interesting results obtained are (i) the yield rate increasing with grinding duration of the suspension, though not proportionately, (ii) the yield increased linearly with temperature in the range 33 to 66°C and (iii) addition of 1% ethyl glycol monoethyl ether increases the yield substantially.

## References

- Andrews J H, Collins A H, Cornish D C and Drass J 1969 *Proc. Br. Ceram. Soc.* **12** 211  
Avgustinik A I, Vigdergamz V S and Zherravlev G I 1962 *Zh. Priklad Khim.* **35** 2175  
Baral D 1977  $\beta$ - $\beta''$  alumina electrolytes preparation, characterization and electrophoretic forming of tubes, M. Tech. Thesis, I.I.T, Kanpur  
Byckalo W, Rosenblath G, Lam J and Nicholson P S 1976 *Am. Ceram. Soc. Bull.* **55** 286  
Fally J, Lasne C, Lazennec Y, Le Cars Y and Margotin P 1973 *J. Electrochem. Soc.* **120** 1296  
Foissy A and Robert G 1982 *Am. Ceram. Soc. Bull.* **61** 251  
Ford Annual Report 1975-76 *Research on electrodes and electrolytes for the Ford sodium-sulphur battery*, under contract No. NSF-C805  
Hamaker H C 1940 *Trans. Faraday Soc.* **36** 279  
Kennedy J H and Foissy A 1975 *J. Electrochem. Soc.* **122** 482  
Kennedy J H and Foissy A 1977 *J. Am. Ceram. Soc.* **60** 33  
Krishna Rao D U 1978 *Electrophoretic deposition of magnesia, and  $\beta$ -alumina*, M. Tech. Thesis, I.I.T, Kanpur  
Krishna Rao D U and Subbarao E C 1979 *Am. Ceram. Soc. Bull.* **58** 467  
Malage A B 1979 *Factors affecting electrophoretic deposition of  $\beta$ - $\beta''$  alumina tubes*, M. Tech Thesis, I.I.T, Kanpur  
Michaels A S 1958 in *Ceramics fabrication processes* (ed.) W D Kingery (New York: John Wiley) p. 24  
Powers R W 1975 *J. Electrochem. Soc.* **112** 490  
Powers R W, Mitoff S P, King R N and Bielawski J C 1981 in *Fast ion transport in solids* (eds) J B Bates and G C Farrington (Amsterdam: North Holland) p. 287  
Robinson A L 1976 *Science* **192** 541  
Troelstra S A 1951 *Phillips Tech. Rev.* **12** 293  
Youngblood G E, Cannon W R, Ramussen J R and Gordon R S 1977 *Am. Ceram. Soc. Bull.* **56** 206

10

11

12

13

14

15

16

17

18

19

20

21

22



## Microstructural and dielectric behaviour of glass ceramics in the system $\text{PbO-BaO-TiO}_2\text{-B}_2\text{O}_3\text{-SiO}_2$

OM PARKASH, DEVENDRA KUMAR\* and R RAJGOPALAN

School of Materials Science and Technology and \*Department of Ceramic Engineering, Institute of Technology, Banaras Hindu University, Varanasi 221 005, India

MS received 25 October 1985

**Abstract.** Glasses in the system  $\text{PbO-BaO-TiO}_2\text{-B}_2\text{O}_3\text{-SiO}_2$  with and without  $\text{P}_2\text{O}_5$  as nucleant have been prepared. The glass samples were ceramized based on DTA studies. The ferroelectric phase crystallizing out has been found to be  $\text{BaTiO}_3$  from XRD. The optical and scanning electron micrographs show the presence of  $\text{BaTiO}_3$  as major phase. In these glass ceramic samples, dielectric constant and dissipation factor are approximately constant with temperature and frequency upto the glass transition temperature  $T_g$  and thereafter increase sharply with temperature and finally level off. The addition of  $\text{P}_2\text{O}_5$  as nucleant and molar ratio of  $(\text{PbO} + \text{BaO})$  to  $\text{TiO}_2$  has marked influence on the dielectric behaviour and composition of ferroelectric phase crystallizing out.

**Keywords.** Microstructure; dielectric behaviour; glass ceramic; differential thermal analysis.

### 1. Introduction

There has been considerable interest in the last two decades to produce ferroelectric crystals in a glassy matrix by glass ceramic process (Bergeron 1961; Herczog 1964; Grossman and Isard 1969a, b; Borrelli and Layton 1971; Kokubo and Tashiro 1973/74; Herczog 1984). This is an efficient way of producing an uniform pore-free and fine-grained microstructure which is highly desirable in ferroelectric materials. Bergeron (1964) was the first to develop  $\text{PbTiO}_3$  crystals from the glasses in the system  $\text{PbO-TiO}_2\text{-B}_2\text{O}_3$ . Various workers have since attempted to produce solid solution crystals for obtaining the desired ferroelectric properties by this process. Herczog (1964) reported that the effect of adding  $\text{CaO}$ ,  $\text{SrO}$ ,  $\text{PbO}$  etc to the glass system  $\text{BaO-TiO}_2\text{-B}_2\text{O}_3\text{-SiO}_2$  on the ferroelectric properties of glass ceramics was the same as that found in the ceramic  $\text{BaTiO}_3$  solid solution. However, no details were reported. Grossman and Isard (1969b) studied the crystallization of glasses in the system  $\text{PbO-BaO-TiO}_2\text{-B}_2\text{O}_3$ . They reported the formation of  $\text{PbTiO}_3$  using the x-ray diffraction technique. Such procedures may not be powerful tools in establishing the formation of solid solutions since shifts in the interplanar spacings resulting from the formation of solid solution may not be distinguished from the shifts arising from the strain effects due to crystal clamping (Grossman and Isard 1969a; Lynch and Shelby 1984).

Hence, Lynch and Shelby (1984) used dilatometric method to determine the ferroelectric-paraelectric transition temperature and thus for identification of ferroelectric phase. They established the formation of  $\text{PbTiO}_3$  only in the system  $\text{PbO-BaO-TiO}_2\text{-B}_2\text{O}_3$ . It is noted that they studied almost the same compositions as studied earlier by Grossman and Isard (1969). Both these groups did not use the requisite

amount of  $\text{TiO}_2$  to crystallize both  $\text{BaTiO}_3$  and  $\text{PbTiO}_3$  either as independent phases in the solid solution form.

It is quite likely that the formation of ferroelectric phase in either of these forms during ceramization process depends on the initial glass composition i.e.,  $\text{BaO}$  to  $\text{PbO}$  ratio and/or  $(\text{BaO} + \text{PbO})$  to  $\text{TiO}_2$  ratio. This paper reports the results of investigation of crystalline phases developed in the glass system  $\text{BaO-PbO-TiO}_2\text{-B}_2\text{O}_3\text{-SiO}_2$  during ceramization process. We have chosen an initial glass composition in which both  $\text{BaO}$  and  $\text{PbO}$  and  $(\text{BaO} + \text{PbO})$  to  $\text{TiO}_2$  ratios are equimolar. The effect of addition of  $\text{P}_2\text{O}_5$  as a nucleant in the glass on the ceramization and dielectric behaviour is also reported.

## Experimental

High purity grade  $\text{PbO}$ ,  $\text{BaCO}_3$ ,  $\text{TiO}_2$ ,  $\text{SiO}_2$ ,  $\text{H}_3\text{BO}_3$  and  $(\text{NH}_4)_2\text{HPO}_4$  were used in the preparation of glasses. Batches weighing 50 g were mixed in an agate mortar using pestle. The mixed powders were melted in alumina crucibles at 1375 K and kept for about 30 minutes with intermittent stirring for homogenization and removal of bubbles. The melts were poured into an aluminium mold quickly and pressed by another aluminium plate to produce transparent glass samples. The cast glasses were immediately annealed by transferring to another preheated furnace kept at 475 K. The composition of the glasses prepared is given in table 1.

The amorphosity of glasses was confirmed by x-ray diffraction. Differential thermal analysis (DTA) of glasses was done using 505 MOM derivatograph to find the glass transition,  $T_g$ , nucleation,  $T_N$  and growth temperature of possible crystalline phases which would form during ceramization. Glasses were given two-stage heat treatments corresponding to nucleation and growth temperatures determined by DTA, following a procedure indicated below. Glass samples were introduced into a furnace preheated to the nucleation temperature and held for 30 minutes following which the temperature was raised quickly to the growth temperature. They were kept at growth temperatures for 3–12 hr and then slowly withdrawn from the furnace and x-ray diffraction patterns of the resulting glass ceramic samples were taken using Rich and Inert Iso-Debye flex 2002 diffractometer employing  $\text{Cu-K}_\alpha$  radiation.

For microstructural studies the samples were polished and etched using warm 10% HF solution. The microstructures were taken using Zeiss optical microscope (model 5) and Phillips scanning electron microscope (model PSEM 500). Dielectric constant and loss tangent were measured in the frequency range 1 kHz to 100 kHz from room temperature to 775 K using General Radio capacitance bridge (Model 1615).

## Results and discussion

DTA plots of glass compositions 1 and 2 are shown in figure 1. Both the glasses showed glass transition around 575 K. There is an endothermic peak around 810 K and two

**Table 1.** Composition of glasses (mol %)

Glass No.	PbO	BaO	TiO <sub>2</sub>	SiO <sub>2</sub>	B <sub>2</sub> O <sub>3</sub>	P <sub>2</sub> O <sub>5</sub>
1	21	21	42	6	10	0
2	21	21	42	4	10	2

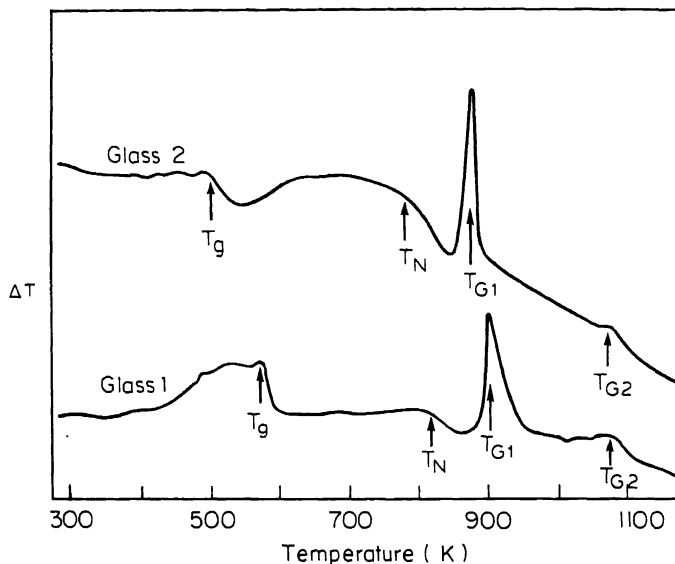
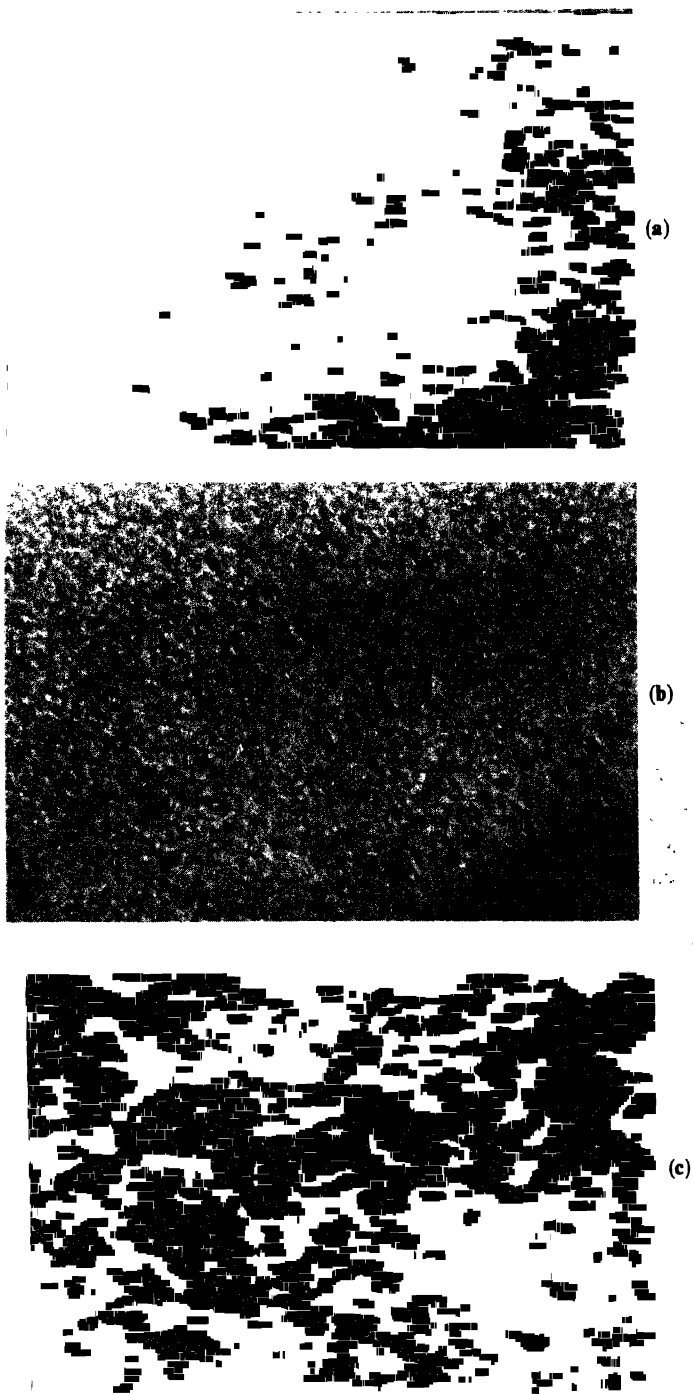


Figure 1. DTA plot of glasses 1 and 2.

exothermic peaks at 900 K and 1075 K in glass no 1. The endothermic peak is assigned to nucleation temperature  $T_N$  and the two exothermic peaks to two growth temperatures,  $T_{G1}$  and  $T_{G2}$  of two crystalline phases which develop during heat treatment. The corresponding temperatures for glass no 2 are 780, 880 and 1060 K respectively. Based on these results, glasses (nos 1 and 2) were subjected to various heat treatments schedules. X-ray diffraction of sample no 1A (heat-treated at  $T_N$  for 30 min and at  $T_{G1}$  for 3 hrs) indicated the formation of only  $\text{BaTiO}_3$  phase during ceramization. However, the sample 2A (heat treated at  $T_N$  for 30 min and at  $T_{G1}$  for 3 hrs) of glass no. 2 indicated the presence of a small amount of another phase besides  $\text{BaTiO}_3$  which is the major constituent. Hence  $T_{G1}$  corresponds to growth of  $\text{BaTiO}_3$  phase, while  $T_{G2}$  represents the growth temperature of a second crystalline phase. The presence of  $\text{BaTiO}_3$  is confirmed by DTA of glass ceramic sample no. 2A. The DTA shows a broad exothermic peak at around 375 K which represents the Curie temperature of  $\text{BaTiO}_3$ .

X-ray diffraction studies of other glass ceramic samples heat-treated at higher temperatures 975K/1075K, show the presence of both  $\text{BaTiO}_3$  as well as a second phase which could not be identified. Grossman and Isard (1969b) and Lynch and Shelby (1984) reported the formation of only  $\text{PbTiO}_3$  in the system  $\text{PbO-BaO-TiO}_2\text{-B}_2\text{O}_3\text{-SiO}_2$  where  $(\text{PbO} + \text{BaO})$  to  $\text{TiO}_2$  ratio was very near to 2 : 1. In the present study the above ratio is 1 : 1 and it is found that the ferroelectric phase formed is  $\text{BaTiO}_3$ . Although XRD alone cannot determine the formation of solid solution, it can definitely distinguish between  $\text{BaTiO}_3$  and  $\text{PbTiO}_3$ . The second strongest line of  $\text{PbTiO}_3$  is missing in  $\text{BaTiO}_3$ . Thus it appears that  $(\text{PbO} + \text{BaO})$  to  $\text{TiO}_2$  ratio in base glass composition influences the composition of ferroelectric phase that forms on crystallization.

Optical micrographs of the sample 1A, 1B and 2A are shown in figure 2. The micrograph of sample 1A (figure 2a) shows that it contains uniform dispersion of fine-



**Figure 2.** Optical micrograph of the glass ceramic sample (a) 1A heat-treated at 810 K for 30 min and 900 K for 3 hrs (b) sample 1B heat-treated at 875 K for 30 min and 1075 K for 3 hr (c) 2A heat-treated at 780 K for 30 min and 880 K for 3 hrs.

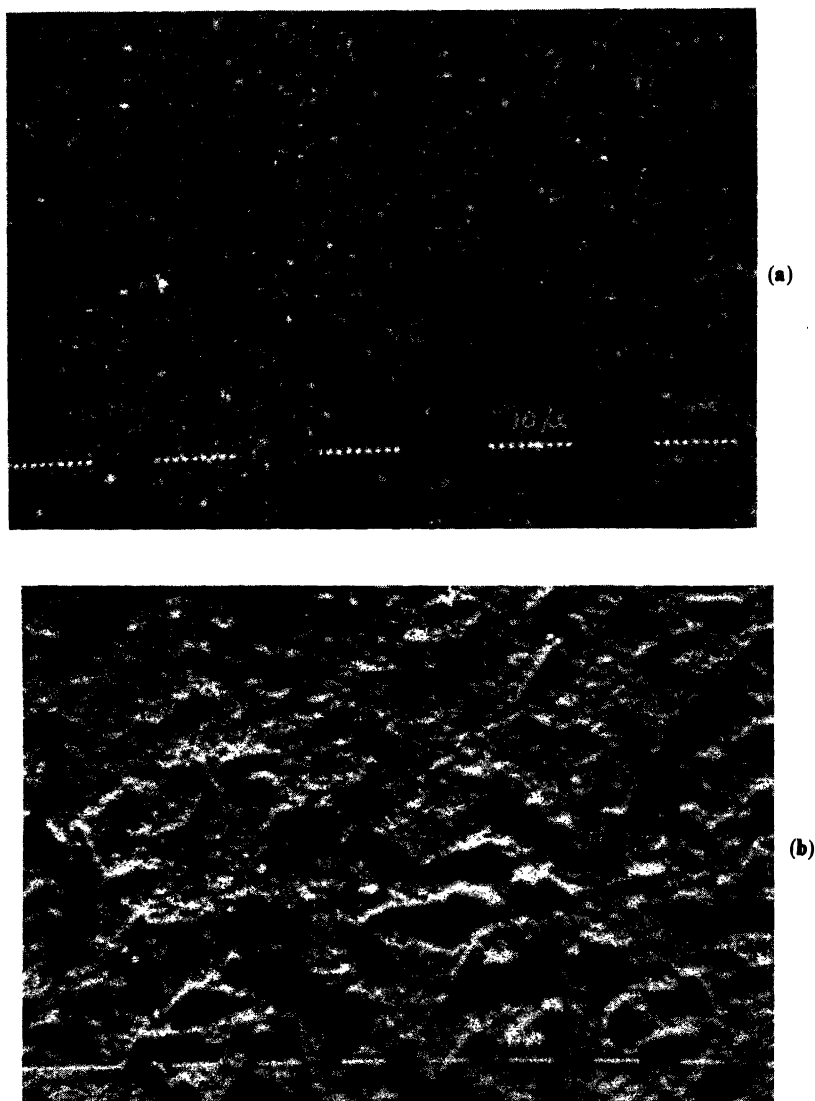


**Figure 3.** Scanning electron micrograph of sample (a) 1A at magnification  $1500\times$  (b) 2B heat-treated at 975 K for 12 hr at magnification  $750\times$ ,  $10\mu\text{m}$ .

grained  $\text{BaTiO}_3$  crystallites having an average size of  $< 1\mu\text{m}$ . On the other hand, sample 1B (figure 2c) which was obtained by heat treatment at higher temperature contains crystallites of second phase having an average particle size of  $30\mu\text{m}$  along with a fine dispersion of  $\text{BaTiO}_3$ . These results are in conformity with the results of x-ray diffraction which indicated the formation of only  $\text{BaTiO}_3$  phase in sample 1A and of  $\text{BaTiO}_3$  and a second phase in 1B. The optical micrograph of sample 2A is similar to that of sample 1A except that the size and particle distribution are different. Figures 3a and 3b show scanning electron micrographs of samples 1A and 2B respectively. As is clear from the micrograph (figure 3a), sample 1A contains a uniform dispersion of fine-

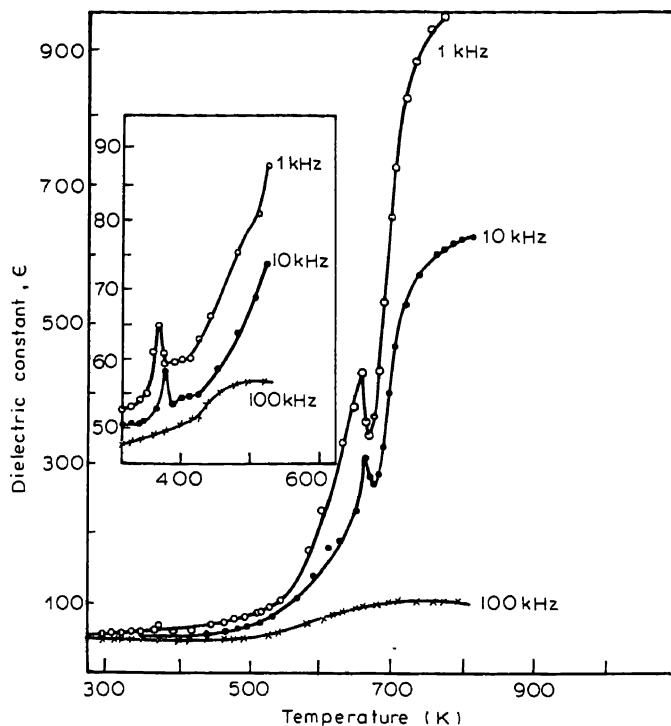


**Figure 4.** Variation of dielectric constant  $\epsilon$  with temperature at 1 kHz, 10 kHz and 100 kHz for sample 1A. The insert shows the same variation on enlarged Y-scale.

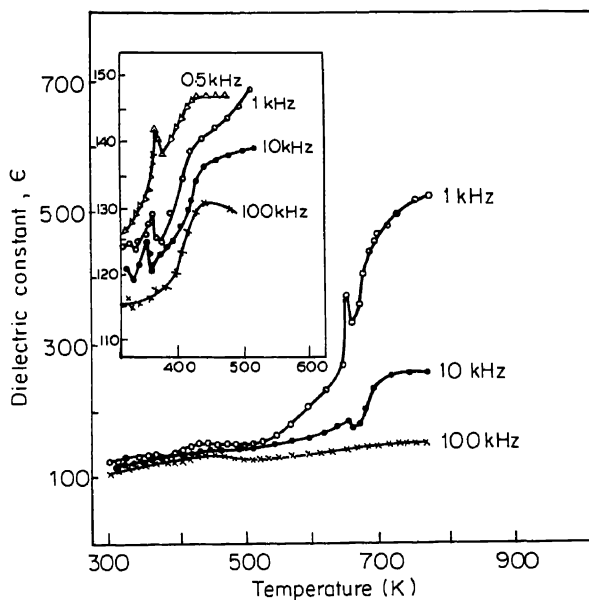


**Figure 5.** Variation of dielectric constant  $\epsilon$  with temperature at different frequencies for sample 2A. Insert shows the same variation on enlarged Y-scale.

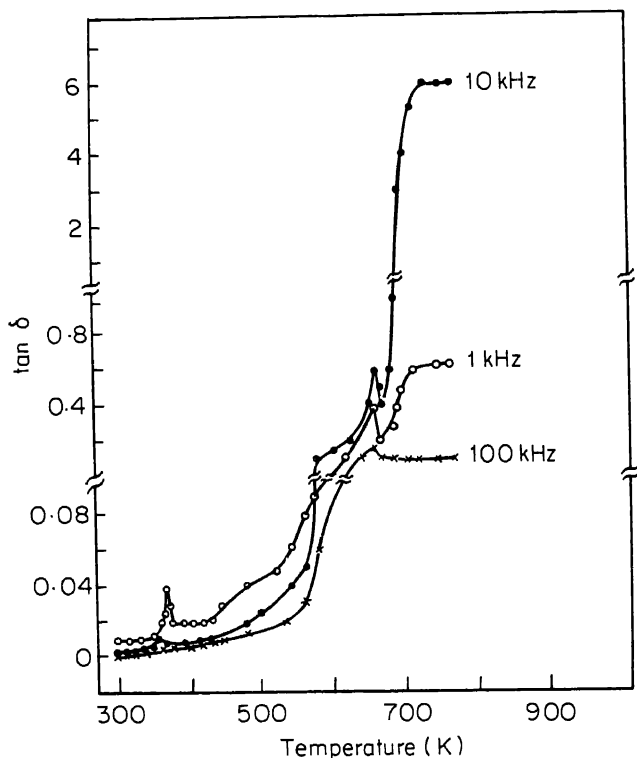
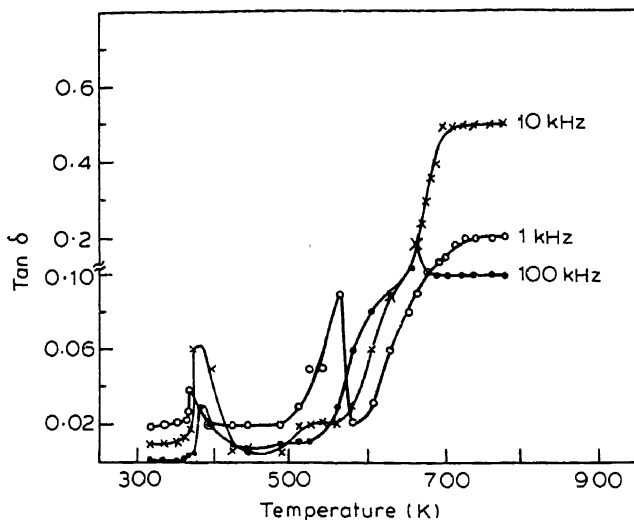


Figure 6. Variation of dissipation factor  $D$  with temperature at different frequencies for 1A.

grained  $\text{BaTiO}_3$  phase. In sample 2B which was given a single-stage heat treatment at 975 K for 12 hr, there are a few big crystals of second phase which grew with well-defined angles and edges having an approximate size of  $20\ \mu\text{m}$  and a very fine dispersion of  $\text{BaTiO}_3$  particles having a size less than  $1\ \mu\text{m}$ .

The variation of dielectric constant of samples 1A and 2A as a function of temperature at 1 kHz, 10 kHz and 100 kHz is shown in figures 4 and 5 respectively. Variation of dissipation factor,  $\tan\delta$ , with temperature at these three frequencies is shown in figures 6 and 7 respectively. There is an anomaly in dielectric constant at around 375–400 K in these samples as is clear from the inserts of figures 4 and 5. Similar anomaly is also noticed in the corresponding dissipation factor at the same temperature. This temperature represents the Curie temperature of  $\text{BaTiO}_3$ . There is another anomaly in the dielectric constant at around 675 K which was also observed in the as-cast glasses. This dielectric behaviour of all the samples is reproducible under repeated heating and cooling cycle. This peak thus does not represent any ferroelectric-paraelectric transition of any crystalline phase. The origin of this anomaly is under investigation.

The dielectric constant and the dissipation factor do not increase significantly with temperature up to 525 K for sample 1A and upto 575 K for sample 2A. Up to this temperature the variation of dielectric constant and dissipation factor with frequency is linear and quite small. Beyond this temperature, the dielectric constant increases sharply and levels off at higher temperatures (figures 4 and 5). This increase in dielectric



**Figure 7.** Variation of dissipation factor  $D$  with temperature of sample 2A at different frequencies.

constant is less at 100 kHz and increases with decreasing frequency. The dissipation factor also increases sharply beyond this temperature. At higher temperatures, the dissipation factor appears to show a maximum between 1 and 100 kHz near 10 kHz. It is observed that this temperature upto which dielectric constant and dissipation factor remain almost constant with frequency and temperature is the same as the glass transition temperature,  $T_g$ , of respective samples determined from DTA. This approximately constant value of dielectric constant below  $T_g$  can be understood in terms of the small grain size of  $\text{BaTiO}_3$  and restraining effect of rigid glassy matrix. Upto  $T_g$ , the polarization remain small as the dipoles cannot respond easily to the external electric field. After the  $T_g$ , the glass matrix softens, whereby the dipoles start responding to external electric field giving a high value of dielectric constant. The maxima in dissipation factor at around 10 kHz can be understood in terms of space charge polarization relaxation phenomena associated with this reorientation of dipoles.

Comparing the dielectric behaviour of samples 1A and 2A (containing  $\text{P}_2\text{O}_5$ ) it is observed that the effect of nucleant  $\text{P}_2\text{O}_5$  is (i) to increase the low temperature dielectric constant and (ii) to decrease the high temperature dielectric constant and dielectric loss. The first may be attributed to the large volume fraction of  $\text{BaTiO}_3$  phase precipitated in sample 2A. The latter may be understood in terms of the presence of the second phase along with the  $\text{BaTiO}_3$ -phase restricting the orientation of dipoles.

#### 4. Conclusions

The present studies indicate that the molar ratios of  $\text{PbO}$  to  $\text{BaO}$  and  $(\text{PbO} + \text{BaO})$  to  $\text{TiO}_2$  in the initial glass composition have a marked influence on the composition of ferroelectric phase and addition of a nucleant such as  $\text{P}_2\text{O}_5$  has profound effect on the microstructural and dielectric behaviour of glass ceramic system.



## **Acknowledgements**

The authors are thankful to Prof. P Ramachandrarao for stimulating discussions and comments and to Advanced Centre for Materials Science, IIT, Kanpur for providing some facilities during the study.

## **References**

- Bergeron C G 1961 *Crystallization of perovskite lead titanate from glass*, Ph.D. Thesis, University of Illinois  
Borrelli N F and Layton M M 1971 *J. Non-Cryst. Solids* **6** 197  
Grossman D G and Isard J O 1969a *J. Mater. Sci.* **4** 1059  
Grossman D G and Isard J O 1969b *J. Am. Ceram. Soc.* **52** 230  
Herczog A 1964 *J. Am. Ceram. Soc.* **47** 107  
Herczog A 1984 *J. Am. Ceram. Soc.* **67** 484  
Kokubo T and Tashiro M 1973/74 *J. Non-Cryst. Solids* **13** 328  
Lynch S M and Shelby J E 1984 *J. Am. Ceram. Soc.* **67** 424

□ □

□

□ □

□ □

□ □

## Dielectric properties of the system $\text{Pb}_{2-x}\text{Nd}_x\text{Li}_{0.5}\text{Nb}_{1.5}\text{O}_{6+\delta}$

S G PHADNIS\*, M SUBRAMANIAN and R RAJAN

Department of Physics, Indian Institute of Technology, Bombay 400 076, India

MS received 3 June 1985; revised 14 October 1985

**Abstract.** The dielectric properties of the ceramic defect pyrochlore-structured system  $\text{Pb}_{2-x}\text{Nd}_x\text{Li}_{0.5}\text{Nb}_{1.5}\text{O}_{6+\delta}$  has been studied as a function of concentration  $x$ , frequency and temperature. The results have been analyzed for relaxation process and conduction mechanism.

**Keywords.** Dielectric properties; ceramics; neodymium doping; pyrochlore-structured system.

### 1. Introduction

The system  $\text{A}_2\text{B}_2\text{O}_6\text{X}$ , where A and B are cations, X is O, OH or F stands for the pyrochlore group having the structure of the mineral  $\text{CaNaNb}_2\text{O}_6\text{F}$  studied by Bystrom (1944). Cadmium niobate  $\text{Cd}_2\text{Nb}_2\text{O}_7$  has been reported to show ferroelectric nature by Cook and Jaffe (1952). In some cases the site X may be vacant or partly vacant as in  $\text{Pb}_{1.5}\text{Nb}_2\text{O}_{6.5}$ . Venevtsev (1970) reported that the composition  $\text{Pb}_{1.9}\text{Ba}_{0.1}\text{Li}_{0.5}\text{Nb}_{1.5}\text{O}_6$  is possibly ferroelectric. The electrical resistivity and the dielectric properties of the system  $\text{Pb}_{2-x}\text{Ba}_x\text{Li}_{0.5}\text{Nb}_{1.5}\text{O}_6$  were studied by Khare and Rajan (1977, 1978). The thermoelectric properties of the system  $\text{Pb}_{2-x}\text{La}_x\text{Li}_{0.5}\text{Nb}_{1.5}\text{O}_6$  have been studied by Phadnis *et al* (1982) and the dielectric properties of the same system by Phadnis *et al* (1983). The present paper reports the dielectric properties as a part of the material characterization of the system  $\text{Pb}_{2-x}\text{Nd}_x\text{Li}_{0.5}\text{Nb}_{1.5}\text{O}_6$ .

### 2. Material preparation

The specimens were prepared by reaction between the mixtures of PbO (BDH) LR,  $\text{Nd}_2\text{O}_3$  (Indian Rare Earths),  $\text{Nb}_2\text{O}_5$  (Fluka) AR and  $\text{Li}_2\text{CO}_3$  (BDH) LR. The compounds were mixed thoroughly in a mortar and presintered at  $800^\circ\text{C}$  for 4–5 hr. The presintered mixture was ground to a fine powder and pressed into circular pellets at 0.5 kbar and were finally sintered at  $1000\text{--}1100^\circ\text{C}$  for 12 hr.

### 3. Method and measurements

X-ray diffraction patterns of the samples of various concentrations were identical, indicating qualitatively the presence of one phase only. The strong peaks gave the

---

\* Now deceased.

following values for the unit cell in the cubic system  $a_0 = 10.53 \pm 0.01$  Å.  $Z = 8$  molecular units, calculated density = 7.3–7.4 space group  $Fd\bar{3}m$  agreeing with published data (Anon 1974) for other pyrochlore-structured systems. The strong peaks were assigned to (222), (440) and (622) planes. The measured value gave the apparent specific gravity 6.6, due to the porosity of the ceramics.

The capacitor system was a compact three-terminal type. Short lengths of fine teflon-coated connecting wires were used as leads to the capacitor. The capacitance with dielectric  $c_d$  was measured with a Hewlett-Packard (4275A) multifrequency model with digital read-out. The frequency range was from 10 kHz to 10 MHz in steps. The capacitance of the air gap  $c_a$  was calculated from sample dimensions. The  $c_d$  was measured as a function of temperature with a capacitance meter (E12-I Russian make) working on the principle of the heterodyne beat. The samples were coated with conducting silver paint (Ladd Co., USA) to increase the ohmic contact. The temperature was measured by copper-constantan thermocouple.

The real part of the dielectric permittivity  $\epsilon'$  and the loss  $\tan \delta$  were obtained experimentally while the imaginary part was evaluated using the relations  $\epsilon''/\epsilon' = \tan \delta$ . The a.c. conductivity was calculated by the formula  $1/\sigma = \rho = 1.8 \times 10^{10}/f\epsilon' \tan \delta$  as shown by Bogoroditsky *et al* (1979).

#### 4. Results and discussion

Table 1 shows the physical dimension of the circular pellet samples, the weight percentage of neodymium and the calculated capacitance of equivalent air gap. A 10 mm die was used in making the pellet. The sintering produced varying contractions for different concentrations, giving changed macroscopic densities. Table 2 gives the experimental  $\tan \delta$  and the approximate calculated values of a.c. resistivity in ohm-meters, for various frequency ranges. Figure 1 shows the plot of  $\epsilon'$  vs  $\ln f$  for varying  $x$ . Figure 2 shows the variation of  $\epsilon'$  vs temperature for varying  $x$ .

The thermoelectric properties of the system studied by Phadnis *et al* (1985) revealed that concentration  $x = 0.0, 0.001, 0.01$  and  $0.05$  show  $n$  type behaviour, whereas  $x = 0.15$  and  $0.2$  show  $p$ -type. Similar results were observed earlier on the system  $Pb_{2-x}La_xLi_{0.5}Nb_{1.5}O_{6+\delta}$  (Phadnis *et al* 1982). The frequency variation of  $\epsilon''$  does not show a step and  $\tan \delta$  does not show any maximum in the frequency range 10 kHz to 10 MHz indicating the absence of well-defined relaxation processes. The conduction mechanism is the only process, going to low values at high frequencies. The temperature

Table 1. Physical dimensions of the samples  $Pb_{2-x}Nd_xLi_{0.5}Nb_{1.5}O_{6+\delta}$

Sample No.	$x$	Weight % Nd	Diameter (d) mm	Thickness (t) mm	$C_{air}$ pf calculated
0	0.00	0	11.68	2.47	0.30
I	0.001	0.033	9.33	1.84	0.33
II	0.010	0.327	8.86	1.66	0.33
III	0.050	1.63	8.98	2.24	0.25
IV	0.150	4.88	9.05	2.77	0.21
V	0.200	6.39	9.19	1.97	0.30

Table 2. Frequency vs loss factor and a.c. resistivity (calculated)

Frequency (kHz)	x = 0		x = 0.001		x = 0.01		x = 0.05		x = 0.15	
	tan $\delta$	$\rho \times 10^{-6}$	tan $\delta$	$\rho \times 10^{-6}$	tan $\delta$	$\rho \times 10^{-6}$	tan $\delta$	$\rho \times 10^{-6}$	tan $\delta$	$\rho \times 10^{-6}$
10	0.081	3.0	0.718	0.072	0.432	0.082	0.559	0.110	0.948	0.052
30	0.033	2.9	0.523	0.045	0.310	0.046	0.391	0.067	0.608	0.036
50	0.023	2.5	0.441	0.036	0.260	0.036	0.322	0.053	0.487	0.031
100	0.014	2.0	0.344	0.026	0.205	0.014	0.244	0.039	0.456	0.023
300	0.006	1.5	0.230	0.015	0.139	0.016	0.157	0.022	0.215	0.015
500	0.005	1.2	0.191	0.011	0.117	0.009	0.128	0.017	0.170	0.012
1000	0.003	0.9	0.147	0.008	0.092	0.006	0.097	0.012	0.124	0.008
3000	0.005	0.6	0.093	0.004	0.062	0.003	0.061	0.006	0.073	0.005
5000	0.000	3.6	0.067	0.003	0.047	0.002	0.043	0.005	0.051	0.004
10000	—	—	0.006	0.019	0.010	0.006			0.0031	

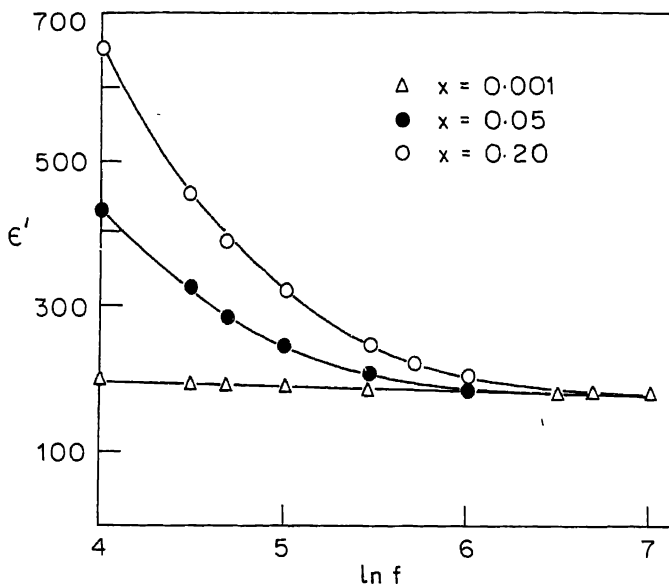


Figure 1.  $\epsilon'$  vs  $\ln f$  (sample with conducting point).

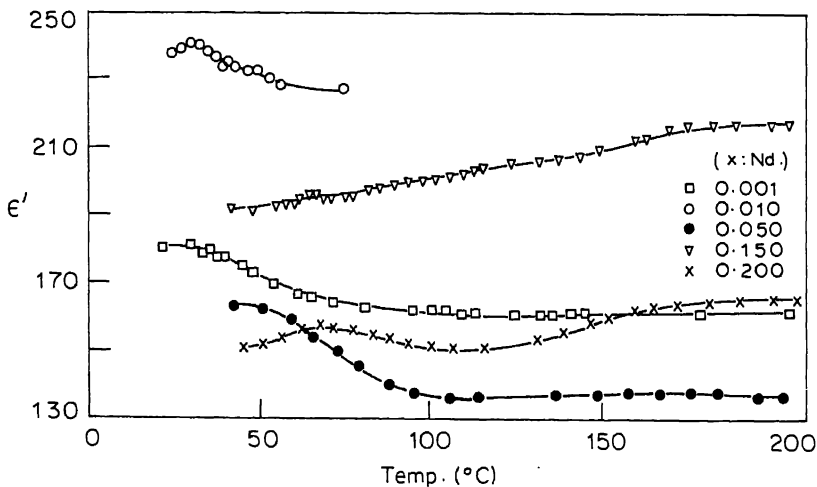


Figure 2.  $\epsilon'$  vs temperature.

variation of  $\epsilon'$  vs temperature shows a peak near room temperature for all concentrations. However, the peak broadens with increasing  $x$  and  $\epsilon'_{\max}$  occurs at different temperatures. The  $\epsilon'$  values decrease slowly in the range 100–300°C for lower concentrations, whereas there is an increase for  $x = 0.15$  and 0.20. The following conclusions are surmised.

- (i) A positive temperature coefficient (PTC) effect is present for lower concentrations which show *n*-type behaviour.
- (ii) Cation vacancies are formed for lower concentrations whereas oxygen anion vacancies are preferred at higher concentrations.
- (iii) The conduction mechanism is predominantly electron-hole type with low activation energies.
- (iv) Non-stoichiometry plays considerable part in the conduction mechanisms.
- (v) Point defects in the lattice are responsible for the complex behaviour of the temperature variation of  $\epsilon'$ .
- (vi) The  $\tan \delta$  values are dependent on the electrodes, being fairly high for samples coated with conducting point than those of unpainted samples. Both bulk conduction and surface conduction are envisaged.
- (vii) Differences in the grain size and losses at the grain boundaries perhaps account for the temperature variation differences.
- (viii) Surface state phenomena suggested by Heywang (1964) occurs on sintering at high temperatures.

### Acknowledgement

The authors thank Prof. C M Srivastava for facilities.

### References

- Anon 1974 Joint Committee on Powder Diffraction Standards: Selected powder diffraction data for minerals  
Bogoroditsky N P, Pasynkov V V and Tareev B M 1979 *Electrical engineering materials* (English Translation) (Moscow: Mir Publishers)  
Bystrom A 1944 *Ark. Kemi. Min. Geol.* **A18** 21  
Cook W R and Jaffe H 1952 *Phys. Rev.* **88** 1426  
Heywang W J 1964 *J. Am. Ceram. Soc.* **47** 384  
Khare R K and Rajan R 1977 *Indian J. Pure Appl. Phys.* **15** 597  
Khare R K and Rajan R 1978 *Indian J. Pure Appl. Phys.* **16** 492  
Phadnis S G, Rajan R and Kulkarni K S 1982 *Bull. Mater. Sci.* **4** 579  
Phadnis S G, Rajan R and Kulkarni K S 1983 *Bull. Mater. Sci.* **5** 139  
Phadnis S G, Subramanian M and Rajan R 1985 (communicated)  
Venetsev Yu N 1970 *J. Phys. Soc. Jpn. (Suppl)* **28** 139





## Surface morphology and properties of GaAs epilayers controlled by temperature difference method of liquid phase epitaxy

Y K SU, C C WEI, S C LU and C C CHANG

Research Institute of Electronic and Electrical Engineering, National Cheng Kung University, Tainan, Taiwan, Republic of China

MS received 25 February 1985; revised 17 September 1985

**Abstract.** Epilayers of gallium arsenide were grown by using the steady-state temperature difference method of liquid phase epitaxy. The surface of grown layers was smooth and shiny. Carrier concentrations of films varying from  $10^{16}$  to  $10^{17} \text{ cm}^{-3}$  could be obtained with good reproducibility. The surface morphology growth rate, carrier concentration and Hall mobility of the epilayers were studied. Several distinct types of surface features were also investigated and explained. A segregation coefficient for the net carrier concentration versus tin concentration in the growth melt was calculated as  $1.84 \times 10^{-4}$  at  $700^\circ\text{C}$  for (100) GaAs substrate. Thickness control for epilayers down to submicron can be obtained reproducibly.

**Keywords.** Liquid phase epitaxy; GaAs thin films; surface morphology.

### 1. Introduction

The use of liquid phase epitaxy to grow GaAs layers onto GaAs substrates was pioneered by Nelson (1963) using a tipping furnace. Subsequently, horizontal sliding (Mlavsky and Weinstein 1963), vertical dipping (Shih *et al* 1962) and rotating methods (Vilms and Garrett 1972) have been used for layer growth along with every variety of boat and slider designs. Multiple-layer structures have wide applications in the fabrication of opto-electronic devices.

Most authors in developing liquid phase epitaxial system used transient system (Su *et al* 1984; Wu *et al* 1985). In this paper, experiments were made by the steady-state LPE method. The advantages of this method are: (1) easier temperature control compared with the transient method; (2) constant growth rate of the thermal gradient and the system temperature are kept constant. The desired thickness of epilayer can be obtained by precisely controlling the growth time; (3) since there is a temperature gradient imposed normal to the growing interface, constitutional supercooling can be inhibited (Wei *et al* 1981). Single and double epilayers were grown onto GaAs substrate. Tin was used as the *n*-type dopant.

The growth apparatus and experimental procedure will be described in §2. Section 3 deals with the experimental results and discussions about the surface morphology, the growth rate, and the properties of epilayers and the conclusions are presented in §4.

### 2. LPE apparatus and experimental procedure

A sliding boat for the growth system was used in our experiment. The experimental set-up consisted of a central quartz reactor tube with 54 mm in O.D. and 48 mm in I.D., a

transparent furnace with a reflecting gold ( $\sim 200 \text{ \AA}$ ) coated on the inner surface. This furnace had a flat temperature zone within  $\pm 1^\circ\text{C}$  over 70% of its length. The graphite boat similar to that used by Dawson (1974) was made of high purity graphite (POCO Co.). It consisted of a sliding part with two wells of size  $10 \times 10 \times 0.4 \text{ mm}^3$  which were used to hold the major substrate and a precursor substrate if necessary during growth. Another part of the graphite boat contained three crucibles for melt. Two tungsten sub-heating wires were wound around the upper side of the melt crucibles to produce temperature difference ( $\Delta T$ ). An additional power of 12 watts produced a temperature difference of about  $10^\circ\text{C}$  in the melt. Two Pt - Pt + 13% Rh thermocouples were used to measure the imposed temperature difference and control the growth temperature respectively.

After cleaning, etching and loading the substrates and sources into the furnace, it was sealed and evacuated, then backfilled with purified  $\text{H}_2$  and kept on purging with a flow rate of 0.5 l/min for 30 min. The furnace was then heated to the growth temperature,  $700^\circ\text{C}$  and stabilized for about 1–2 hr to equilibrate and homogenize the solution. Temperature difference between substrate and sources was established by turning on the power supply. A few minutes later, the substrate was pushed into contact with the first melt, then the second one successively for a given time interval, then pushed away and the growth run terminated. The furnace was then moved away from the boat. The substrate was removed from the furnace after cooling.

The surface morphology of epilayers was examined with a Nomarski phase contrast microscope. Thickness was measured with optical microscope by suitably staining the cleavage with MSO photo-etchant (Wei *et al* 1981). Van der Pauw-Hall measurements were performed to calculate the electrical properties of the epilayers. Doping concentration and uniformity could be deduced from C-V measurements. In order to do this, Al Schottky barriers of  $200 \text{ }\mu\text{m}$  in diameter had been evaporated through a photomask.

### 3. Results and discussion

#### 3.1 Surface morphology

There are several distinct types of surface features: (1) meniscus lines, (2) cusps, (3) island growth, (4) terraces and (5) nearly perfect flat. The meniscus lines are shown in figures 1(a) and (b). It has been proved that these lines are instantaneous trailing edge of the liquid surface at it moved across the crystal during the sliding procedure (Small *et al* 1975). They are roughly parallel and spaced about  $100 + 50 \text{ }\mu\text{m}$  apart with height about  $100 \text{ \AA}$ . Device fabrication is not seriously perturbed if we fabricate them parallel to the meniscus lines.

Figure 1(b) also shows the cusps. The formation of cusps neither corresponds to dislocations in the substrate nor corresponds to contaminating particles on the substrate before growth. The factors governing this surface morphology are still not understood. The density of the cusps is about  $1.1 \times 10^3/\text{cm}^2$ .

Figure 2(a) shows the pattern of growth on a (100) substrate where the solution was about  $20^\circ\text{C}$  below liquidus temperature. The steps or "mesas" appeared to be caused by the spotty contact between the solution and the substrate because of severe supersaturation. The top of the mesa forms a rectangle whose sides are parallel to the

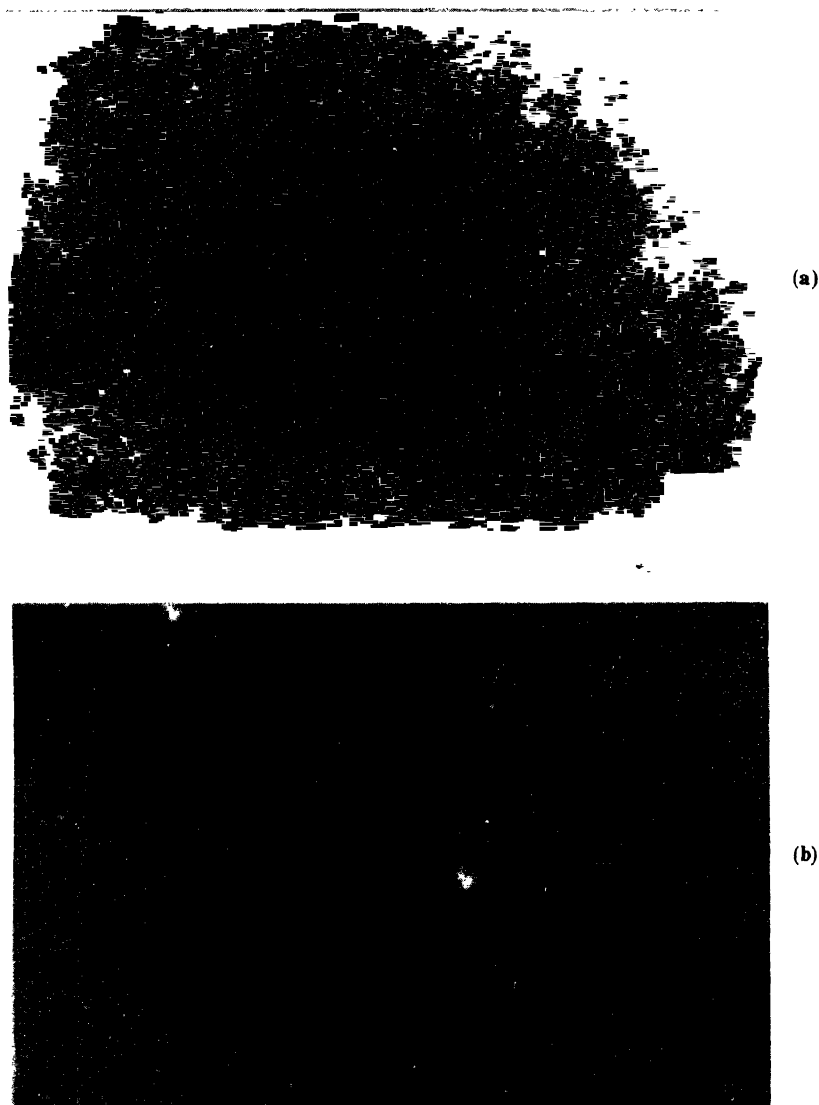
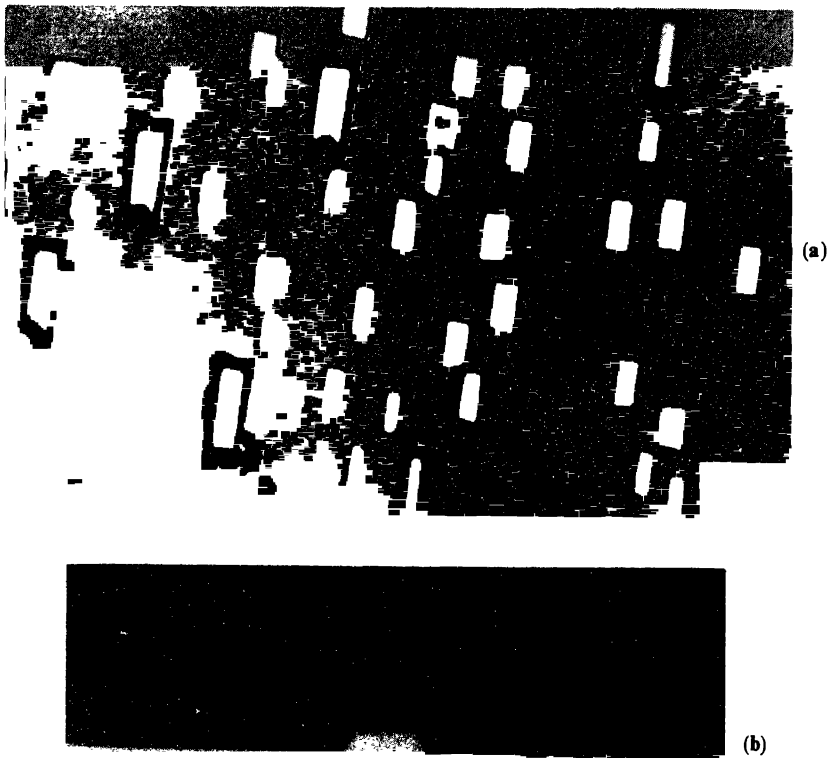


Figure 1. (a) Optical micrograph showing meniscus lines. (b) Nomarski contrast micrograph showing meniscus line and cusps.

[110] axis. The trapezoidal planes which form the sides of the mesa line in the (111) plane can be shown in the cleaved edge view of figures 2(a) and 2(b).

Another kind of surface morphology is terraces as shown in figure 3(a). Mattes and Route (1974) have found that the surface terraces appear to be influenced by the nuclei formations and thermal fluctuations at the liquid-solid interface. Figure 3(b) shows the cleaved and stained edge view of figure 3(a). From this figure we can find that the terraces look like a triangular waveform, the "peak to peak" height is about  $1.2 \mu\text{m}$ , too severe to be used for device fabrication.



**Figure 2.** (a) Island growth of LPE on a (100) substrate. (b) Higher magnification cleaved edge view of (a).

The last type of feature, nearly perfectly flat regions with no structure observable by Nomarski phase contrast microscope is shown in figure 4. This smooth and mirror-like epilayers can be reproducibly obtained for the optimum growth condition.

### 3.2 Growth rate

Thickness control for layer down to submicron is obtained by properly controlling the temperature difference and cooling rate. Any residual Ga melt left on the surface of epilayer will cause an extra growth of 5 to 10  $\mu\text{m}$  during the cooling interval and cannot be used for the fabrication of devices. Removing the growing epilayer from the solution with a rapid and smooth motion helps to minimize the adherence of liquid Ga droplets on the surface of epilayer.

The dependence of epilayer thickness on the growth time for  $\Delta T = 5^\circ\text{C}$  and  $10^\circ\text{C}$  is shown in figure 5. The growth temperature is kept at  $700^\circ\text{C}$  throughout our

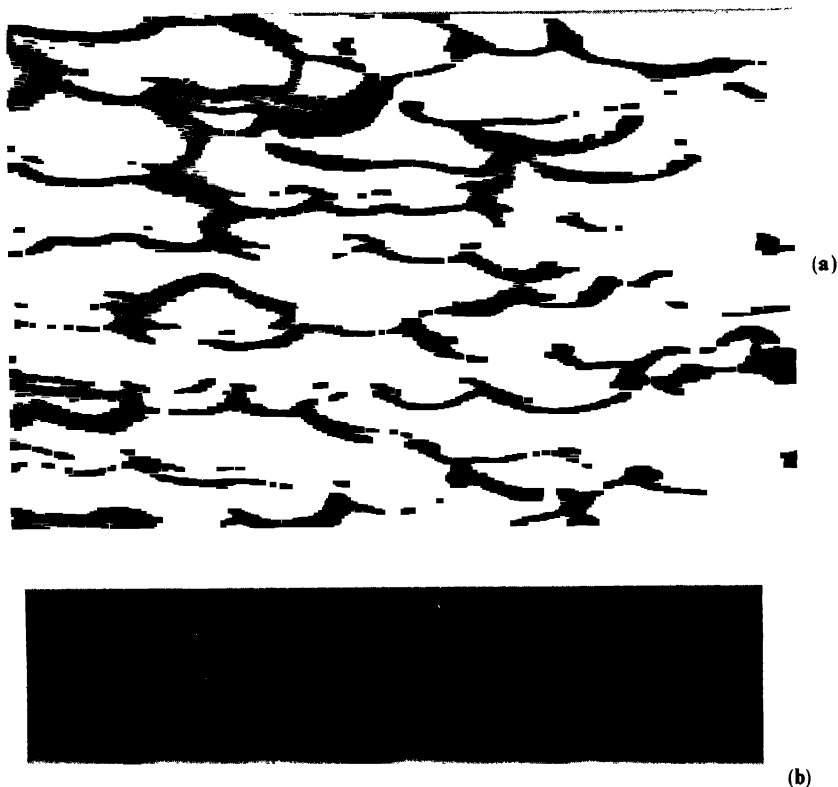


Figure 3. (a) Nomarski contrast micrograph of epilayers showing terraces. (b) The cleaved and stained edge view of (a).

experiments. Temperature control is carried out by the main heater wound on the reaction tube mentioned above, while the substrates are used to impose temperature difference ( $\Delta T$ ). The layer thickness is proportional to the growth time for two different  $\Delta T$ , and these results are similar to those obtained by Nishizawa and Okuno (1978). The growth rates are about  $0.1 \mu\text{m}/\text{min}$  and  $0.22 \mu\text{m}/\text{min}$  for  $\Delta T = 5^\circ\text{C}$  and  $10^\circ\text{C}$  respectively.

All the layer thickness are determined by cleaving (110) surface, then staining and measuring by optical microscope. This measurement results are also illustrated in figure 6 which shows the cross-sectional view of some single and double epilayers.

### 3.3 Doping study with tin

Tin is selected as *n*-type dopant in spite of its amphoteric property because of its extremely low vapour pressure, low segregation coefficient under the epitaxial growth

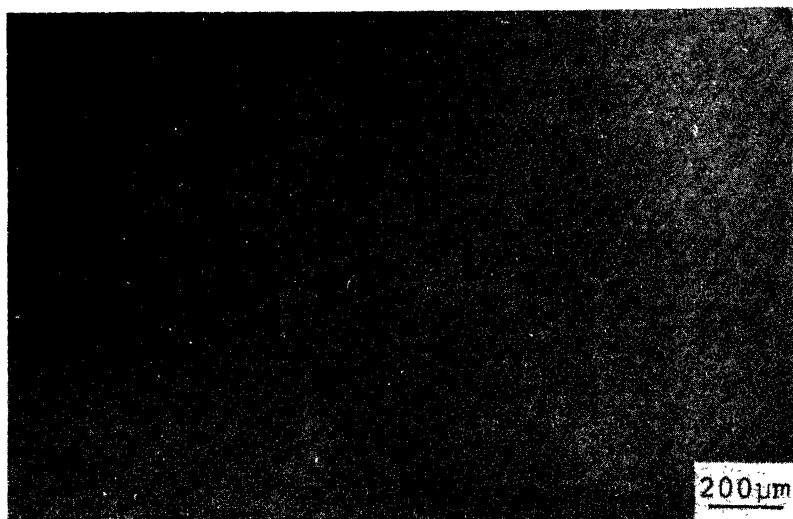


Figure 4. Nomarski contrast micrograph of grown layer showing nearly perfectly flat.

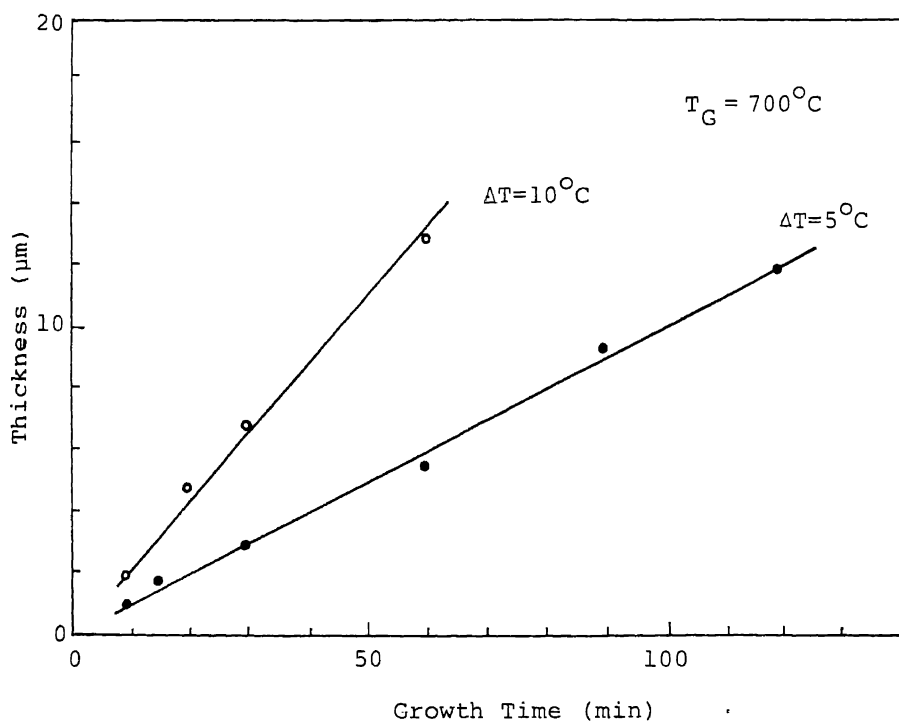
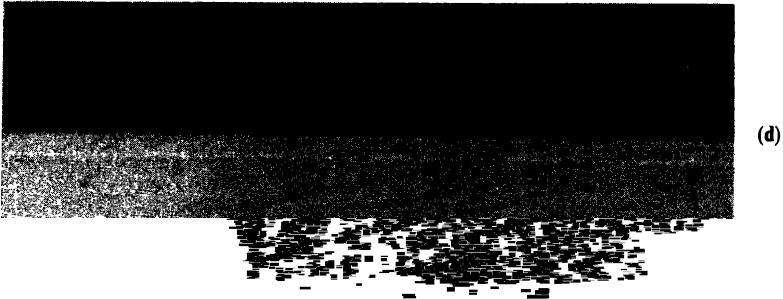
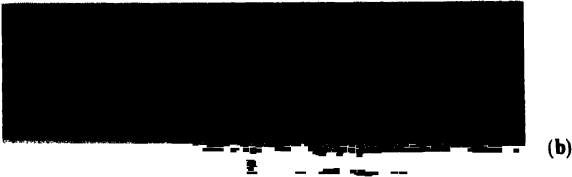
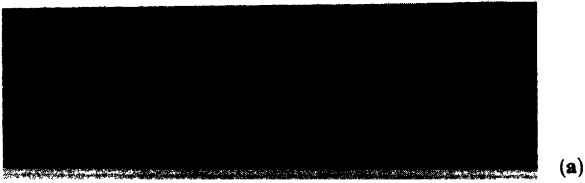
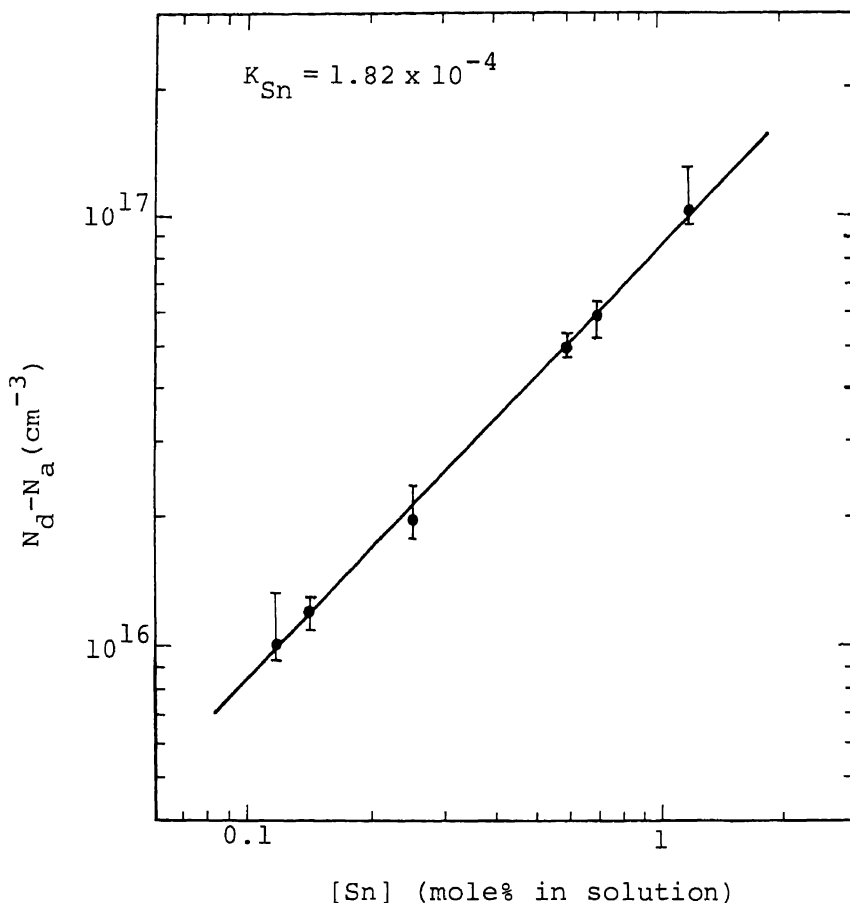


Figure 5. Epilayer thickness as a function of growth time for  $\Delta T = 10^\circ\text{C}$  and  $\Delta T = 5^\circ\text{C}$ .

condition and solubility in gallium (Shunt 1969). Figure 7 shows the carrier concentration of epitaxial films as a function of tin mole percent in the growth solution at  $700^\circ\text{C}$ . Based on our data, the segregation coefficient for GaAs growth from Ga solution at  $700^\circ\text{C}$  is  $1.84 \times 10^{-4}$ . This is in good agreement with the values reported



**Figure 6.** Cleaved and stained cross-sectional view of epilayers. (a) Single layer, 1  $\mu\text{m}$ ; (b) Double layer, 2.5 – 7.5  $\mu\text{m}$ ; (c) Single layer, 0.5  $\mu\text{m}$ ; (d) Double layer, 0.3–2.3  $\mu\text{m}$ .



**Figure 7.** Carrier concentration of grown layers as a function of tin mole percent in growth solution at 700°C.

elsewhere (Harris and Synder 1969; Vilms and Garrett 1972; Rosztochy and Kinoshita 1974; Toyada *et al* 1976).

In order to measure the Hall mobility, a series of epilayers are grown from growth melt with increasing amount of Sn on semi-insulating (100) oriented substrates. The Hall mobility at room temperature as a function of carrier concentration is shown in figure 8.

The C-V measurement is plotted in figure 9, indicating that the doping concentration is extremely uniform and  $N_d$  is equal to  $2.16 \times 10^{16}/\text{cm}^3$ . A built-in voltage of 0.7 volts is obtained from the intercept of the voltage axis.

### 3.4 X-ray diffraction

X-ray diffraction method is utilized to determine the orientation of the GaAs epilayer on the GaAs substrate. The peak of the spectrum represents the (200) reflection of GaAs. This indicates that the epilayer has good crystallinity properties and the orientation of the epilayer is the same as that of the substrate.



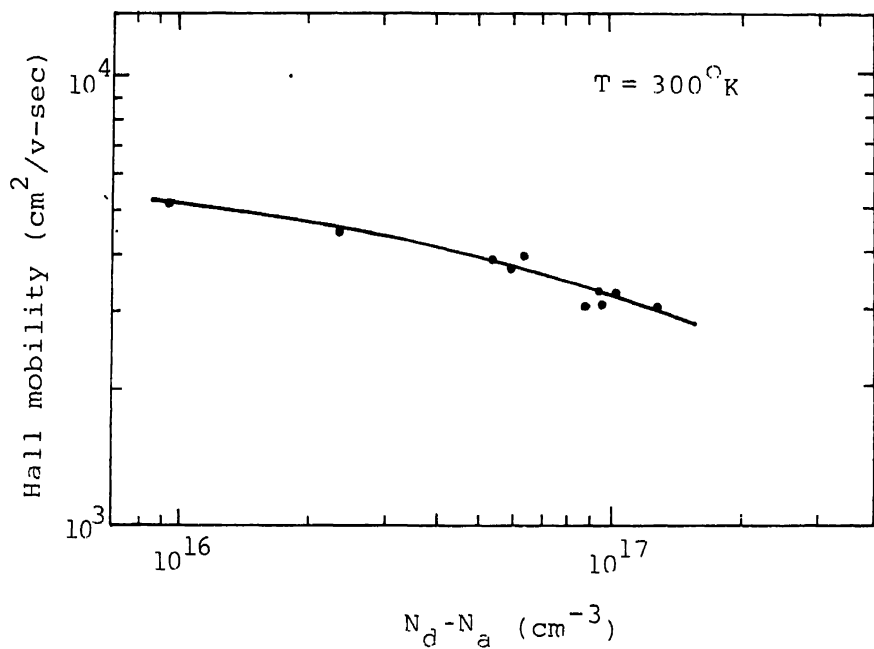


**Figure 8.** Hall mobility of Sn-doped n-type GaAs layer versus carrier concentration at  $300^\circ\text{K}$ .

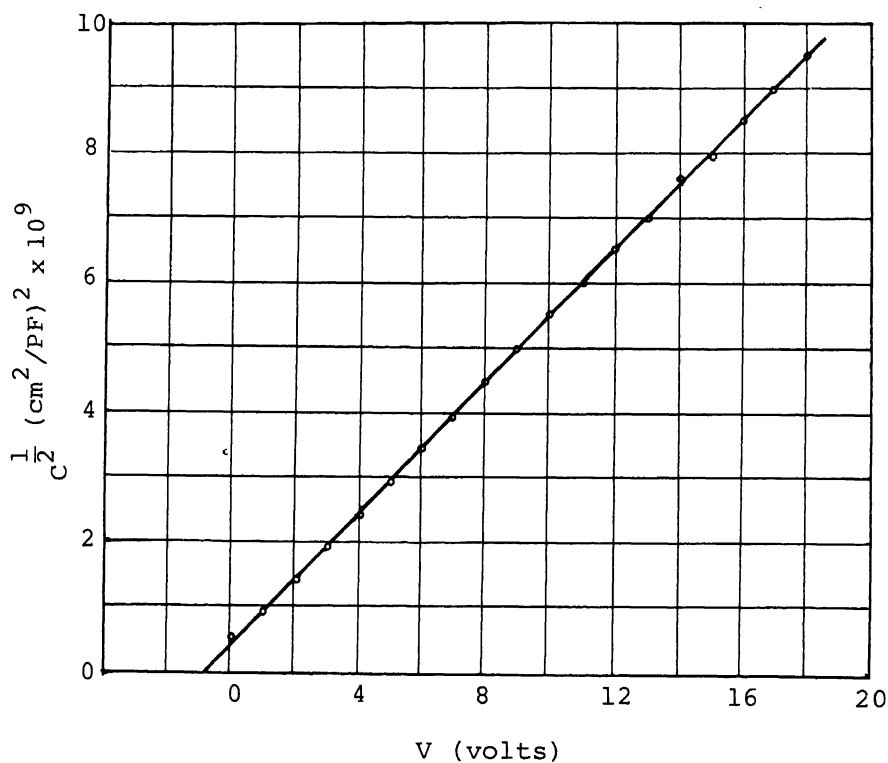


**Figure 9.**  $1/C^2$  versus applied voltage for the Schottky diode indicating  $N_D$  is a constant.

#### 4. Conclusion

Epilayers of gallium arsenide were grown by using the temperature difference method of liquid phase epitaxy. The thickness of thin films can be precisely controlled even down to submicron meter. Also, doping concentration can be varied by the amount of tin added into the growth solution and the results showed that the uniformity of doping is very good. The carrier concentration ranges from  $10^{16}$  to  $10^{17} \text{ cm}^{-3}$ . X-ray diffraction shows that the epilayers have good crystalline properties and have the same orientation as the substrate. Several distinct types of surface features are also investigated. The segregation coefficient for the net carrier concentration versus tin concentration in the melt is calculated as  $1.84 \times 10^{-4}$  at  $700^\circ\text{C}$  for (100) GaAs substrate.

#### Acknowledgements

The authors gratefully acknowledge Dr T S Wu for his fruitful discussions and suggestions. The authors also thank the National Science Council, Republic of China for financial support in this research project (NSC 75-0608-E006-05R).

#### References

- Dawson L R 1974 *J. Cryst. Growth* **27** 86
- Harris J S and Synder W L 1969 *Solid State Electron* **12** 337
- Mattes B L and Route R K 1974 *J. Cryst. Growth* **27** 133
- Malvsky A I and Weinstein M 1963 *J. Appl. Phys.* **34** 2885
- Nelson H 1963 *RCA Rev.* **24** 603
- Nishizawa J and Okuno Y 1978 RIEC Technical Report, TR-41 Apr.
- Rosztoczy F E and Kinoshita J 1974 *J. Electrochem. Soc.* **121** 439
- Shih K K, Woodall J M, Blum S E and Foster L M 1968 *J. Appl. Phys.* **39** 2962
- Shunt F A 1969 *Constitution of binary alloys* (New York: McGraw-Hill) 2nd Suppl.
- Small M B, Blakeslee A E, Shih K K and Potemski R M 1975 *J. Cryst. Growth* **30** 257
- Su Y K, Wu M C, Cheng K Y and Chang C Y 1984 *J. Cryst. Growth* **67** 477
- Toyada N, Mihara M and Hara T 1976 *J. Appl. Phys.* **47** 443
- Vilms J and Garrett J P 1972 *Solid State Electron* **15** 443
- Wei C C, Su Y K, Chang C C, Liu B D and Lu S C 1981 *Chinese J. Mater. Sci.* **13** 56
- Wu M C, Su Y K, Chang C Y and Cheng K Y 1985 *J. Appl. Phys.* (to be published)

## Magnetic and Mössbauer studies on ductile Fe-Cr-Co permanent magnet alloys

V CHANDRASEKARAN, CH SREERAMA MURTHY,  
P SUBRAHMANIAM and G VENKATESWARLU

Defence Metallurgical Research Laboratory, P.O. Kanchanbagh, Hyderabad 500 258, India

MS received 28 October 1985

**Abstract.** Iron-chromium-cobalt alloys possess attractive magnetic properties combined with good formability and hence are identified as technologically important magnetic materials. Alloys with compositions Fe-28.9 Cr-15.6 Co and Fe-28.4 Cr-20.1Co (weight percent) have been studied. Heat-treatment parameters during thermomagnetic treatment viz temperature, time and external magnetic field were optimized with reference to magnetic properties. The fully treated anisotropic alloys develop remanence = 11.5–12.0 kilo Gauss, coercivity = 600–650 Oersted and energy product = 4–4.5 million Gauss Oersted. Electron microscopic and Mössbauer spectroscopic techniques were used to identify the original and transformed phases. During the various stages of the development of the alloy, the changes in mechanical hardness were correlated with magnetic hardness.

**Keywords.** Magnetic properties; heat treatments; phase identification; development of ductile permanent magnet; Mössbauer studies; iron-chromium-cobalt alloys.

### 1. Introduction

Iron-chromium-cobalt magnetic alloys, first reported by Kaneko *et al* (1971) combine excellent permanent magnetic properties with good ductility. The magnetic properties such as remanence ( $B_r$ ), coercivity ( $H_c$ ) and energy product  $(BH)_{\max}$  obtained in these alloys are comparable (Chin 1980) to those of Alnico V, a conventional magnetic material widely used for many applications. The Fe-Cr-Co alloy, completely free from nickel, needs less cobalt than the brittle Alnico V and hence has been identified as technologically important magnetic material (Chin 1978). Due to these superior features, considerable effort has been made for the development and better understanding of these alloys (Belli *et al* 1978; Chin 1978; 1980; Chin *et al* 1978, 1983 a, b; Cremer and Pfeiffer 1975; Gin and Gayle 1980; Green *et al* 1980; Homma 1977; Houghton *et al* 1978; Kaneko *et al* 1972, 1975 a, b, 1976, 1977; Livingston 1981; Mahajan *et al* 1978; Minowa *et al* 1980; Okada *et al* 1978; Sherwood *et al* 1979; Tin 1979; Tin *et al* 1980 a, b; Wang Run *et al* 1984; Zijlstra 1978). Studies carried out in the course of development of two alloys, namely Fe-28.9Cr-15.6Co and Fe-28.4Cr-20.1Co, are presented and discussed in this paper.

### 2. Experimental

Armco iron, electrolytic cobalt and chromium in appropriate quantities were melted in magnesia crucibles under a dynamic vacuum of  $10^{-3}$  torr in a 15 kW, 8000 Hz Stokes vacuum induction furnace. The alloy in each case was poured at 1650°C into preheated

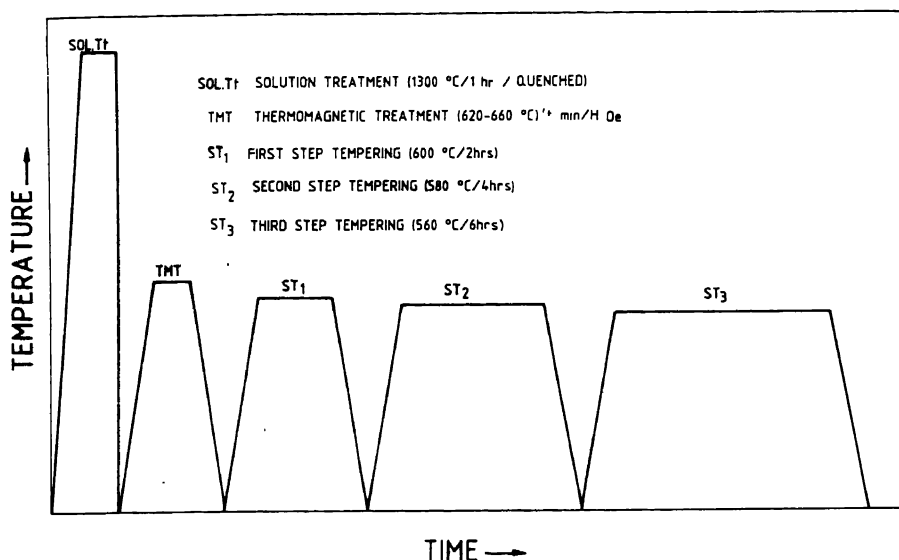


Figure 1. Heat treatment schedule for Fe-Cr-Co magnetic alloys.

25 mm round cast iron moulds. The ingots were processed by hot forging and hot rolling at 1250°C to 12.7 mm dia rods and test samples of the size 10 mm dia  $\times$  15 mm long were prepared. The chemical composition of the two alloys by wt % was as follows: Fe-28.9Cr-15.6Co (alloy-1) and Fe-28.4Cr-20.1Co (alloy-2). The heat-treatment procedure adopted in the present study is schematically given in figure 1. The samples were solution-treated at 1300°C for one hour and quenched in brine water to retain the high temperature single phase (bcc phase) at room temperature. Optical metallography and x-ray diffraction techniques were used to confirm the presence of this single phase. To carry out the critical thermomagnetic treatment (TMT), an isothermal treatment in a magnetic field, a small Kanthal-wire-wound furnace was fabricated and housed between the poles of a heavy duty electromagnet capable of generating a uniform magnetic field of 3750 Oersted. The important parameters controlled during TMT were: (i) the temperature, (ii) soaking time and (iii) the strength of the external magnetic field.

Experiments were carried out to optimize these parameters keeping two of the variables constant at a time and varying the third. The samples were subsequently step-tempered at 600°C/2 hr, 580°C/4 hr and 560°C/6 hr as given in figure 1. After every stage of the heat-treatment, the magnetic properties of the samples were measured using a double yoke ferrotester and the hardness of the alloys was also measured. Electron microscope was used to note the morphology of the phases formed during the treatment. For Mössbauer studies, solution-treated samples of alloy-1, electrochemically thinned to 50  $\mu$ m thickness, were encapsulated in evacuated quartz tube and subjected to all the treatments as shown in figure 1. However, since the samples were thin foils, the duration of the treatments was suitably reduced to avoid overaging and the following schedule was used: 635°C/20'/2000 Oe, 600°C/1 hr, 580°C/2 hr, 560°C/3 hr was followed. The Mössbauer transmission spectrum after each stage of treatment was recorded at room temperature using ECIL Mössbauer spectrometer.

(MBS 35) with 10 milli Curie strength  $^{57}\text{Co}$  radioactive source in palladium matrix in the constant acceleration mode.

### 3. Results and discussion

The magnetic properties ( $B_r$ ,  $H_c$  and  $[\text{BH}]_{\text{max}}$ ) of the two alloys after complete step tempering treatments have been plotted in figures 2 a, b, c for the experimental conditions indicated therein. It can be seen from figure 2a that the magnetic properties, especially coercivity and energy product are sensitive to the changes in the temperature of TMT and the variation is parabolic. In alloy 1,  $B_r$  remains constant throughout the treatment while in alloy 2 a slight decrease in  $B_r$  at high temperature has been observed. The maximum  $H_c$  is obtained at the spinodal decomposition (Homma 1977) temperature  $635^\circ\text{C}$  and  $645^\circ\text{C}$  for alloys 1 and 2 respectively. The observed increase in the decomposition temperature for alloy 2 is due to the increase in cobalt content (Chin 1978).

The spinodal decomposition in Fe-Cr-Co alloy, at temperatures below  $700^\circ\text{C}$ , leading to the high temperature single phase  $\alpha$  decomposing into two isomorphous phases  $\alpha_1$  (rich in Fe and Co) and  $\alpha_2$  (rich in Cr) has been investigated by earlier workers (Homma 1977; Okada *et al* 1978; Wang Run *et al* 1984). Due to the difference in their chemical composition, the two phases possess different values of saturation magnetisation and curie temperature. During the step-tempering treatment, diffusion of Fe and

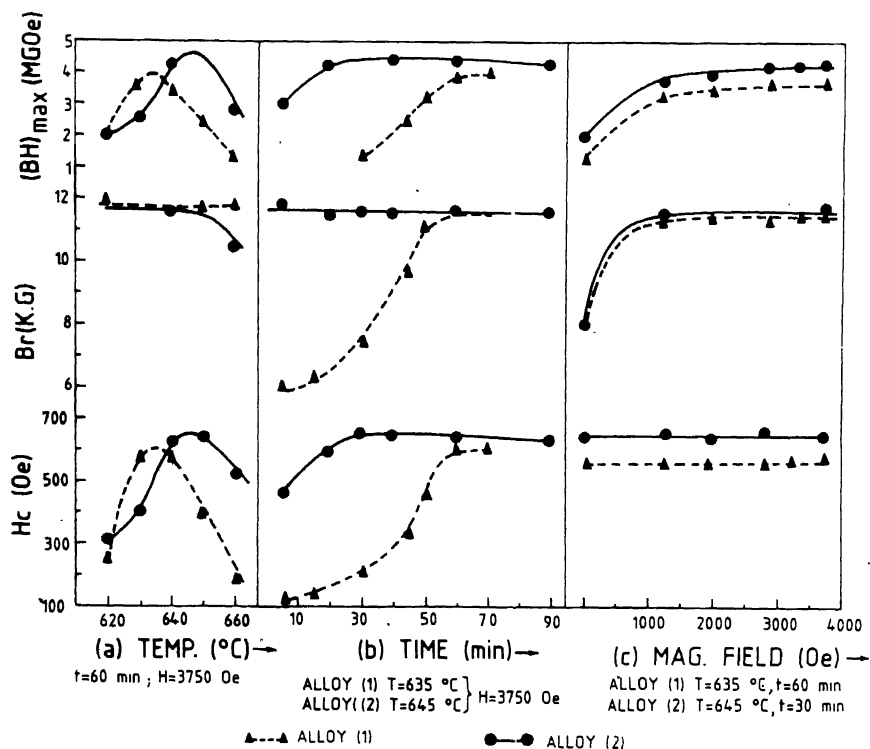


Figure 2. Magnetic properties of fully treated Fe-Cr-Co alloys vs TMT parameters.

Co from  $\alpha_1$  to  $\alpha_2$  occurs (Okada *et al* 1978) thus making  $\alpha_1$  strongly ferromagnetic and  $\alpha_2$  paramagnetic. The presence of magnetic and non-magnetic phases and the complex domain wall interactions account for the high coercivity in these alloys (Mahajan *et al* 1978; Livingston 1981). For a group of oriented ellipsoidal single domain particles in a less magnetic matrix, Stoner and Wohlfarth (1948) derived the following relationship for coercivity:

$$H_c = p(1 - p)(N_2 - N_1)(I_1 - I_2)^2/I_s$$

where  $N_1$  and  $N_2$  are demagnetization factors along major and minor axes respectively;  $I_1$  and  $I_2$ , saturation magnetization of the ellipsoid and the matrix respectively;  $I_s$ , the average saturation magnetization and  $p$ , the volume fraction of the particles.

The demagnetization factors explain the magnetic anisotropy whereas the volume fractions and the saturation magnetization values account for the mechanism of domain wall motion for coercivity. This theory has been widely accepted (Mason *et al* 1970) for Alnico alloys. Since Fe-Cr-Co alloys are akin to Alnicos in achieving high magnetic hardness, the present experimental observations on the coercivity could be understood on the basis of the Stoner and Wohlfarth theory. Due to the asymmetric shape of the miscibility gap in Fe-Cr-Co system (Kaneko *et al* 1977; Minowa *et al* 1980) the volume fractions of the  $\alpha_1$  and  $\alpha_2$  change with TMT temperature. It has been reported (Okada *et al* 1978) that during the step-tempering treatments, the morphology and volume fractions of the phases essentially remain unchanged. Hence the ultimate volume fractions of the phases which control the coercivity through Stoner and Wohlfarth relationship mainly depend on the temperature of TMT, thus explaining the parabolic variation of  $H_c$  and  $(BH)_{\max}$ .

Figure 2b shows that  $H_c$  of the alloys increases with soaking time when treated at optimized temperatures. A minimum period of 60' and 30' are needed for the alloys 1 and 2 respectively to maximize coercivity by imparting magnetic anisotropy and completing the decomposition of  $\alpha$  phase to the required level. The decreasing trend in  $H_c$  due to prolonged treatment can be noted from the curve for alloy 2. The need for more soaking time for the low cobalt alloy is due to slower kinetics at lower temperature. During the initial stages, this alloy exhibits lower values of remanence which may be due to the isotropic nature (Okada *et al* 1978) of products of the decomposition. The improvement in magnetic anisotropy and completion of the decomposition reaction which alter the demagnetization factors and saturation magnetization values of the phases increase the coercivity as expected from the Stoner and Wohlfarth relation.

Figure 2c shows the strong dependence of  $B_r$  on the external magnetic field applied during the treatment. A significant increase from 8000 G to 12000 G in  $B_r$  is observed due to the presence of the field. The purpose of the application of an external field during TMT is to align the phases and elongate them in its direction and this effect can be observed from the electron micrographs (carbon replica) for the alloy 1 presented in figures 3a, b. The coalescence of the spherical phases in the form of ellipsoids elongated in the direction of the field not only improves  $B_r$  but also enhances magnetic anisotropy. A minimum field of 1500–2000 Oe is essential to maximize  $B_r$ . Though from figure 2c no apparent effect of magnetic field on coercivity is seen, figure 4 (Curves 4 and 5) however shows that the magnetic field affects the shape of the demagnetization curves. The 'knee of the demagnetization curve' is absent in samples treated without the

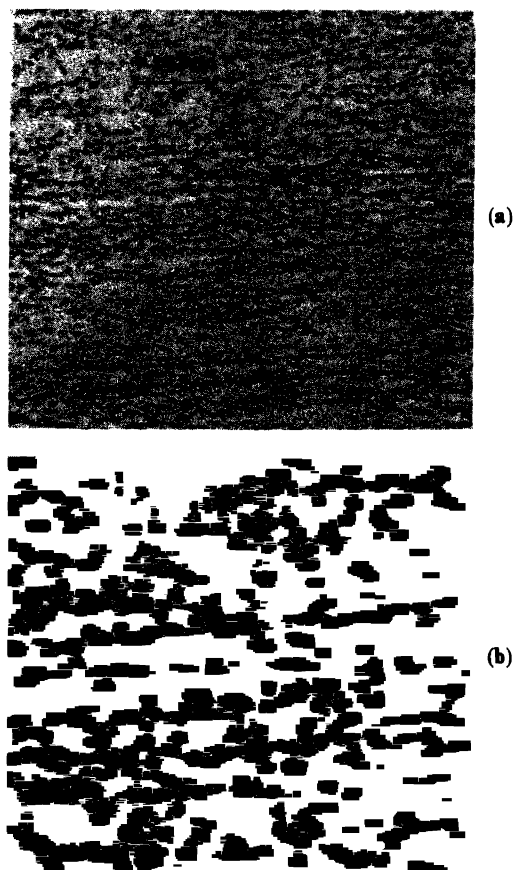


**Figure 3.** Carbon replica micrograph of alloy-1. (a) Spherical morphology of the decomposed phase aligned along the direction of the applied field. (b) Coalescence of the phases to ellipsoid shape.

magnetic field which indicates the absence of strong magnetic anisotropy in these samples.

The gradual improvement in coercivity with step tempering treatments is shown in figure 4. The observed increase in  $H_c$  is associated with the increase in the difference in the saturation magnetization values of  $\alpha_1$  and  $\alpha_2$  phases upon step-tempering through diffusion-controlled composition variations in the phases. Thus thermomagnetic treatment plays the important role of fixing the volume fractions and magnetic anisotropy while the step-tempering treatments help in widening the difference in saturation magnetization values between the phases. Hence the Stoner-Wohlfarth relation for coercivity has been found to fittingly explain the experimental observations in achieving magnetic properties of Fe-Cr-Co alloys. The isotropic and anisotropic magnetic properties of the fully treated alloys are listed in table 1.

The close relationship between mechanical and magnetic hardness is established through figure 5 in which the values are plotted stagewise. In the solution-treated condition, the alloys are mechanically soft and machining operations are possible in

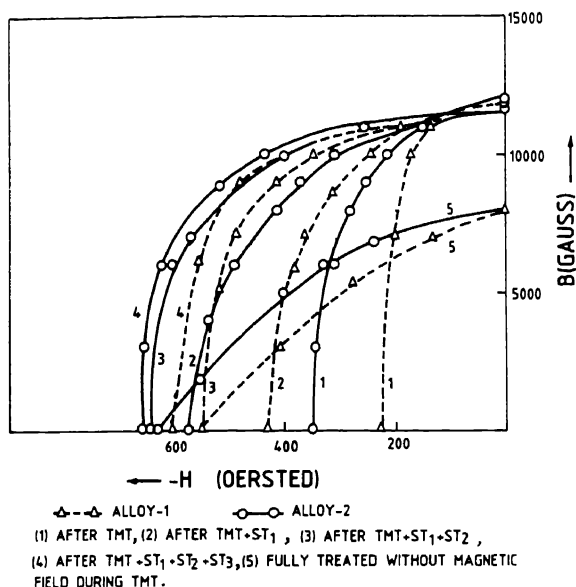


**Figure 4.** Second quadrant demagnetization curves for Fe-Cr-Co alloys. The gradual improvement in coercivity, shape of the curve upon heat treatment (curves 1 to 4) and the absence of 'knee of the demagnetization curve' in isotropic magnets (curve 5) can be observed.

**Table 1.** Permanent magnetic properties of Fe-Cr-Co alloys

Alloy	Remanence $B_r$ (gauss)	Coercivity $H_c$ (Oersted)	Energy product (BH) <sub>max</sub> (MGOe)
Fe-28.9Cr-15.6Co			
(a) Anisotropic	$11750 \pm 250$	$600 \pm 25$	$4.0 \pm 0.2$
(b) Isotropic	$8250 \pm 250$	$500 \pm 25$	$1.5 \pm 0.2$
Fe-28.4Cr-20.1Co			
(a) Anisotropic	$11750 \pm 250$	$650 \pm 25$	$4.5 \pm 0.2$
(b) Isotropic	$8250 \pm 250$	$625 \pm 25$	$2.0 \pm 0.2$

this condition. As a result of the heat treatments, due to the decomposition of  $\alpha$ -phase and enrichment of chromium in  $\alpha_2$  the values of mechanical as well as magnetic hardness increase simultaneously.

### 3.1 Mössbauer studies

In the Fe-Cr-Co system, due to the magnetic phases available after TMT and the constant changes in the magnetic nature of the phases during step-tempering treatments, Mössbauer spectroscopy has been effectively utilised (Houghton *et al* 1978; Chen Ming-Yan *et al* 1982) to understand the decomposition mechanisms.

In figure 6 are presented the Mössbauer spectra of alloy 1 along with the spectrum of  $\alpha$ -Fe for reference and to serve as a calibration standard for the estimation of hyperfine



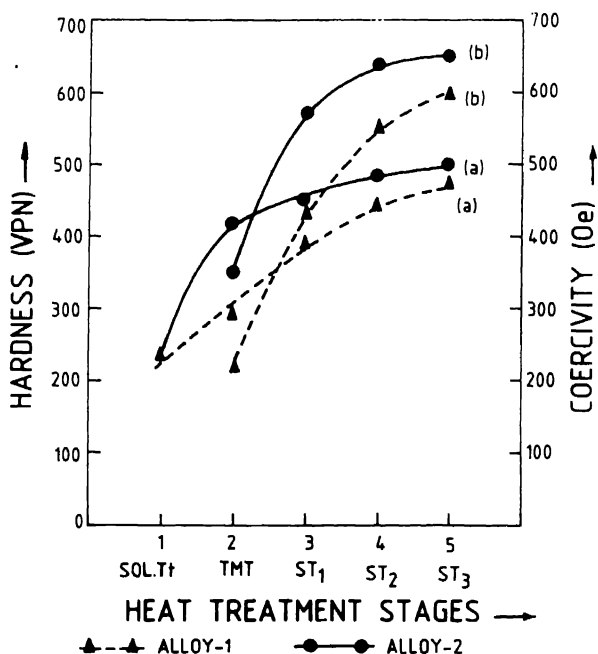
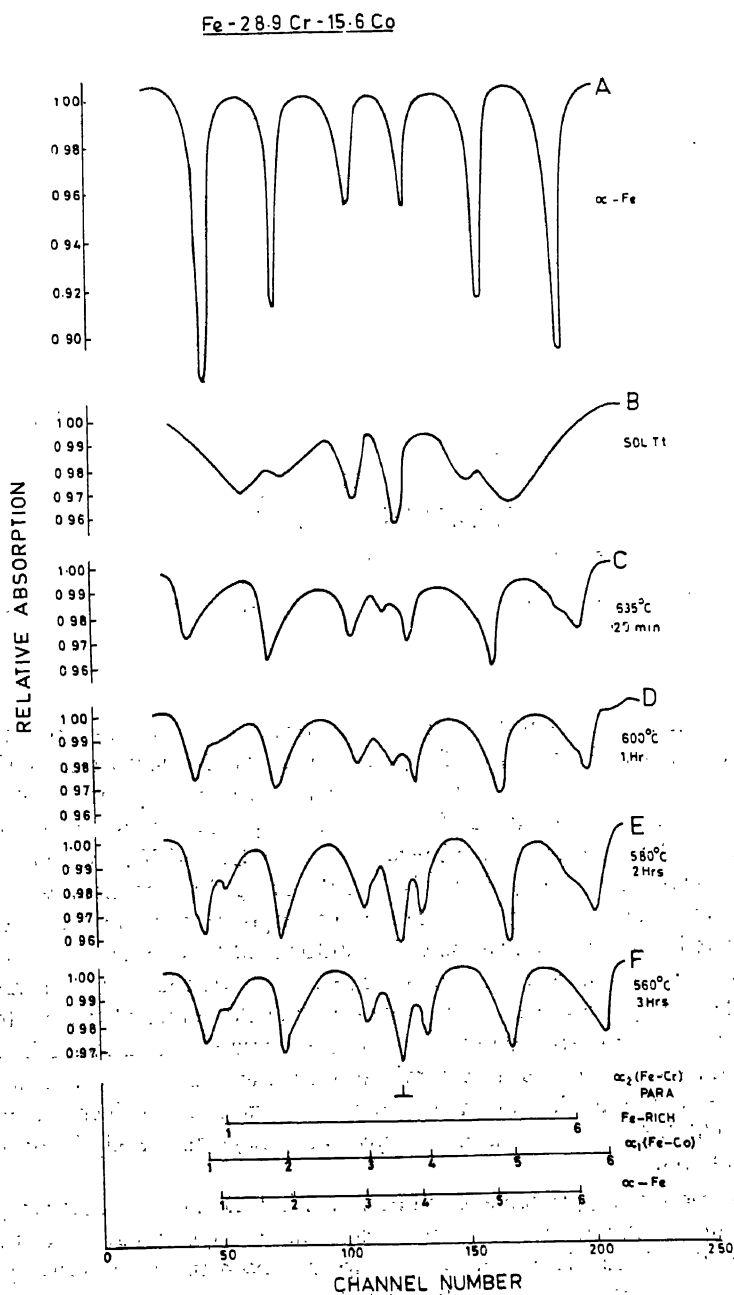


Figure 5. Improvement in mechanical (a) and magnetic (b) hardness in Fe-Cr-Co alloys upon heat treatment.

fields. The spectrum at 6-B of the solution-treated sample shows single phase structure ( $\alpha$ ) of the alloy. Broad distribution of hyperfine fields and the small isomer shift indicate randomized atomic distribution within the single phase. The hyperfine field has been found to be centred near about 250 KOe. From the spectrum at 6-C which pertains to TMT, there is evidence for two hyperfine fields of 355 KOe and 202 KOe corresponding to the two phases  $\alpha_1$  and  $\alpha_2$  respectively both being ferromagnetic with different magnitudes of intensity of magnetization. The corresponding two six-line spectra could not be resolved because of overlapping (Houghton *et al* 1978) of outer lines of smaller field with the second and fifth lines of larger field. The existence of  $\alpha_2$  in paramagnetic state is indicated by the presence of a small peak at the centre of the spectrum. The spectra from 6-D to F correspond to those for step-tempering treatments. The gradual increase in the spectral area of the central paramagnetic peak and the narrowing of the other lines indicate that the volume fraction of paramagnetic  $\alpha_2$  increases with step-tempering. This is due to the progressive conversion of  $\alpha_2$  from weakly ferromagnetic to paramagnetic state.

Under the present experimental conditions, (with thickness of sample being around 50  $\mu\text{m}$ ) it will be difficult to quantitatively correlate the spectral areas to the volume fractions of the phases. However, an attempt has been made to derive qualitative correlations. The relative area of central line of  $\alpha_2$  to the total area of the spectrum has been found to be 0.03, 0.06 and 0.10 for the three step-tempering treatments at 600°, 580° and 560°C respectively indicating the increase in the amount of paramagnetic  $\alpha_2$ . The observed increase in coercivity with these treatments (figure 4) can be explained on this basis.



**Figure 6.** Mössbauer spectra of  $\alpha$ -Fe (for calibration) and alloy 1 at various stages of heat treatment.

The conversion of weakly ferromagnetic  $\alpha_2$  to paramagnetic state occurs by the diffusion of Fe-rich phase from  $\alpha_2$  to  $\alpha_1$ . The migrating Fe-rich phase forms a third intermediate phase whose presence is evidenced by the occurrence of small peaks in the spectrum 6-D to F. The hyperfine field corresponding to this phase has been found to be 320 KOe. During the step-tempering treatments, it can be seen that the spectral area of this phase decreases, which may be attributed to the migration from  $\alpha_2$  to  $\alpha_1$ . However, no corresponding change in the hyperfine field of  $\alpha_1$  due to this addition has been noticed.

#### 4. Conclusions

The following conclusions are drawn from the present studies.

- (i) Fe-28.9Cr-15.6Co and Fe-28.4Cr-20.1Co alloys develop attractive permanent magnetic properties  $B_r = 11.5\text{--}12.0$  K Gauss,  $H_c = 600\text{--}650$  Oe and  $(BH)_{\max} = 4.0\text{--}4.5$  MGOe.
- (ii) The coercivity of the alloys is sensitive to thermomagnetic treatment and improves gradually upon step-tempering treatment. The remanence of the alloys depends on the strength of the external magnetic field applied during TMT and is not altered during step-tempering.
- (iii) TMT parameters such as  $635^\circ\text{C}$ , 60 minutes time and 2000 Oe field are characteristic for alloy 1 while  $645^\circ\text{C}$ , 30 minutes time and 2000 Oe field are so for alloy 2.
- (iv) The widely accepted Stoner and Wohlfarth theory for coercivity in Alnico alloys has been applied to explain qualitatively the experimental observations in Fe-Cr-Co alloys.
- (v) From Mössbauer studies, it has been confirmed that soon after TMT, the alloy develops a strongly ferromagnetic phase  $\alpha_1$  and a second phase  $\alpha_2$  existing in weakly ferromagnetic and paramagnetic states. On step-tempering, ferromagnetic  $\alpha_2$  becomes paramagnetic with the presence of a third intermediate Fe-rich phase.

#### Acknowledgements

The authors gratefully acknowledge the help rendered by their colleagues in Chemical Analysis, Technical Assistance, x-ray, Optical and Electron Microscopy divisions. Thanks are due to Dr P Rama Rao, Director, DMRL for his keen interest.

#### References

- Belli Y, Okada M, Thomas G, Homma M and Kaneko H 1978 *J. Appl. Phys.* **49** 2049  
 Chen Ming Yan, Wang Hui Juan, Yan Yong, Shao Han Ru, Li De Xin, Lin Wen Gui and Liguang Dong 1982 *J. Appl. Phys.* **53** 2377  
 Chin G Y 1978 *J. Magn. Mag. Mat.* **9** 283  
 Chin G Y 1980 *Science* **208** 888  
 Chin G Y, Plewes J T and Wonsiewicz B C 1978 *J. Appl. Phys.* **49** 2046  
 Chin T S, Chang C Y, Wu T S, Hsu T K and Chang Y H 1983a *IEEE Trans. Mag.* **MAG-19** 2035  
 Chin T S, Wu T S, Chang C Y, Hsu T K and Chang Y H 1983b *J. Mater. Sci.* **18** 1681  
 Cremer R and Pfeiffer I 1975 *Physica* **B80** 164  
 Gin S and Gayle N V 1980 *IEEE. Trans. Mag.* **MAG-16** 526

- Green M L, Sherwood R C, Chin G Y, Wernick J H and Bernardini J 1980 *IEEE. Trans. Mag.* **MAG-16** 1053
- Homma M 1977 *Proc. 1st International Seminar on Magnetism, Sebnitz, GDR*, 1
- Houghton M E, Rossitier P L and Clark P E 1978 *J. Mater. Sci.* **13** 155
- Kaneko H, Homma M, Fukunaga T and Okada M 1975a *IEEE. Trans. Mag.* **MAG-11** 1140
- Kaneko H, Homma M and Minowa T 1976 *IEEE. Trans. Mag.* **MAG-12** 977
- Kaneko H, Homma M and Miura M 1972 *IEEE. Trans. Mag.* **MAG-8** 347
- Kaneko H, Homma M and Nakamura N 1971 *AIP Conf. Proc.* **5** 1088
- Kaneko H, Homma M, Nakamura K, Okada M and Thomas G 1977 *IEEE. Trans. Mag.* **MAG-13** 1325
- Kaneko H, Homma M, Okada M, Nakamura S and Ikuta N 1975b *AIP. Conf. Proc.* **29** 620
- Livingston J D 1981 *J. Appl. Phys.* **52** 2544
- Mahajan S, Gyorgy E M, Sherwood R C, Jin S, Makahara S, Brasen D and Eibschutz M 1978 *Appl. Phys. Lett.* **32** 688
- Mason J J, Ashall D W and Dean A V 1970 *Cobalt* **46** 23
- Minowa T, Okada M and Homma M 1980 *IEEE. Trans. Mag.* **MAG-16** 529
- Okada M, Thomas G, Homma M and Kaneko H 1978 *IEEE. Trans. Mag.* **MAG-14** 245
- Sherwood R C, Tin S and Chin G Y 1979 *IEEE. Trans. Mag.* **MAG-15** 1774
- Stoner E C and Wohlfarth E P 1948 *Phil. Trans. R. Soc. A* **240** 599
- Tin S 1979 *IEEE. Trans. Mag.* **MAG-15** 1748
- Tin S, Chin G Y and Wonsiewicz B C 1980a *IEEE. Trans. Mag.* **MAG-16** 139
- Tin S, Mahajan S and Brasen D 1980b *Met. Trans.* **A11** 69
- Wang Run, Chen Jufang and Zhou Shouzeng 1984 *J. Appl. Phys.* **55** 2109
- Zijlstra H 1978 *IEEE. Trans. Mag.* **MAG-14** 661

## Tunnelling of electrons from deep traps of MgO

M N BAPAT and S SIVARAMAN

Department of Physics, Dr Harisingh Gour Vishwavidyalaya, Sagar 470 003, India

MS received 11 September 1985

**Abstract.** A new result on electron tunnelling from the deep traps of MgO, reported recently is discussed. The electrons from the 540 K trapping group are released spontaneously at 480 K. The proposed mechanism for electron tunnelling is discussed in the light of existing theories. The location of the peak in the isothermal decay is found to depend on (i) the extent of population of the source trap group; (ii) the availability of shallow trapping levels to the rushing electrons and (iii) the nature of traps.

The glow curve experiment indicates that the isothermal decay after saturation excitation causes reduction in the thermoluminescence intensity of the 540 K peak.

**Keywords.** Electron tunnelling; isothermal decay; thermoluminescence; trapping groups.

Phosphorescence has been used for studying the shallow traps in the crystal. The emission that persists after cessation of excitation is known as phosphorescence. The rate of decay of emission intensity depends on a variety of factors viz host composition, energy of excitation, concentration of traps, level of population, ambient temperature etc. The rate of decay generally increases as the ambient temperature is raised above the break-even point (Leverenz 1968). Since the isothermal decay at different temperatures yields information regarding the recombination kinetics (Kathuria and Sunta 1982; Takamori and Dove 1983), it has become a useful tool for studying thermoluminescence peaks of a phosphor (May and Partridge 1964; Sathyamoorthy and Luthra 1978).

We have obtained isothermal decay curves for MgO:Li:Ce  $10^{-2}$ :Eu  $10^{-3}$  fired in carbon monoxide (Bapat and Sivaraman 1983) at different temperatures. It was noted that the phosphor behaved differently at 480 K. The decay curve showed a usual decrease in intensity up to 15 sec. After this the intensity showed a reversal. The rise in intensity continued up to 63 sec. Further lapse of time, however, showed a slow decrease in the emission intensity. This feature of the decay viz the rise in intensity to values which should prevail at earlier times, is a surprising result (Bapat and Sivaraman 1985). This result is fairly reproducible within the limits to which the parameters involved i.e. dose of excitation and the temperature can be kept constant.

It is evident that if one takes the phenomenon as a property of the host, one has to account for a large number of electrons in the traps later than the period preceding it. The only source from which electrons could reach the traps emptying at 480 K would be the traps corresponding to temperatures greater than 500 K. Since the result is reproducible in that the peak occurs at the same time under similar conditions, there would be a regular sequence of events. We therefore hypothesize that: (i) the number of electrons tunnelling into the shallower traps depends on the population of electrons in the deeper traps; (ii) the number of rushing electrons depends on the number of shallower levels available; (iii) electrons from deeper traps rush towards shallower traps

only if the traps are of the same kind. If these assumptions are valid, it should be possible to affect the position of the peak by changing the extent to which deep traps are occupied (by changing the dose of excitation) and also altering the population of the shallower group using a different ambient temperature.

To verify the first hypothesis, the sample was annealed at 800 K to empty all the traps up to this temperature. The phosphor was then excited for different times so that the number of deep traps occupied is altered. As envisaged the peak occurs earlier as the excitation dose is increased (figure 1), showing that the tunnelling depends on the number of electrons in deeper traps. The peak intensities were also higher for increased doses of excitation.

If the temperature of decay measurements is raised from 480 to 500 and 520 K it is expected that the shallower traps would empty at a faster rate and the peak would be expected earlier. Figure 2 shows that the decay pattern confirms this view.

It was observed that there was a threshold x-ray dose for observing the peak. If we excite the sample to a lower dose no observable peak is produced. This property helps in identifying the source group of trapped carriers.

Figure 3 shows the thermoluminescence glow runs obtained after a specific dose of excitation at 480 K. The time interval between the cessation of excitation and the start of the glow experiment causes a reduction in the intensity of the TL peak around 540 K of this sample. The sample was then excited for a time sufficient to populate the deep traps and the TL run was started immediately after switching off the excitation without waiting for any decay. This was to ensure that a reasonable number of shallower traps were still occupied. In the following experiment, after the same exposure at 480 K, the excitation was stopped and the sample was allowed to decay for 1 min before recording the TL. The TL peak corresponding to 540 K showed a marked decrease in the latter case indicating that this group had been depopulated. Thus it appears that the TL group at

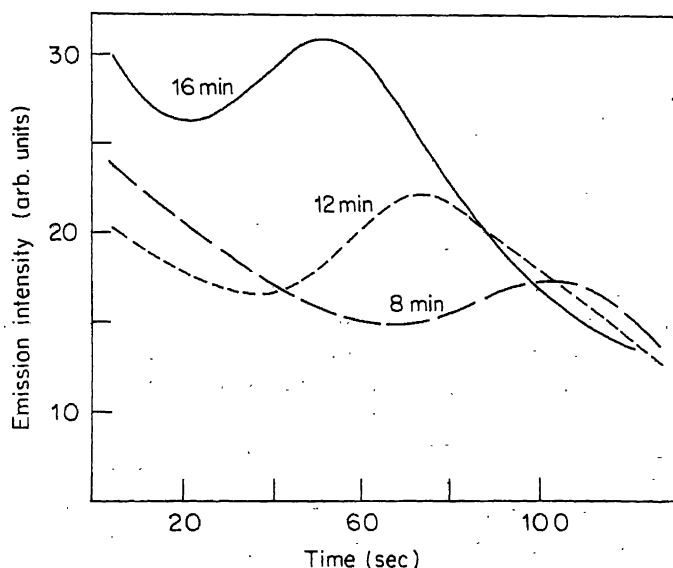
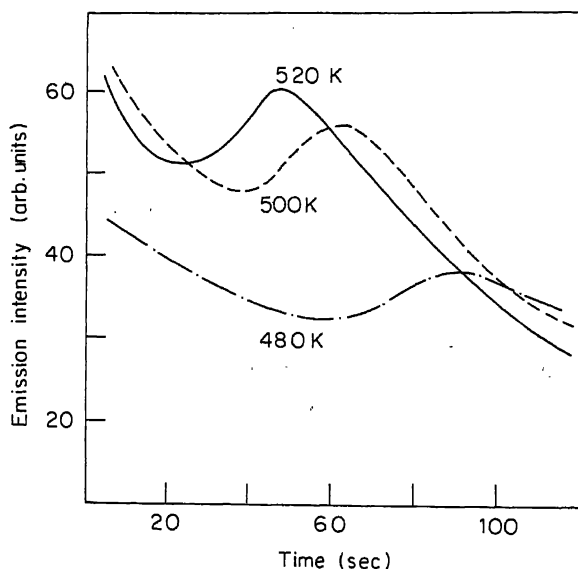
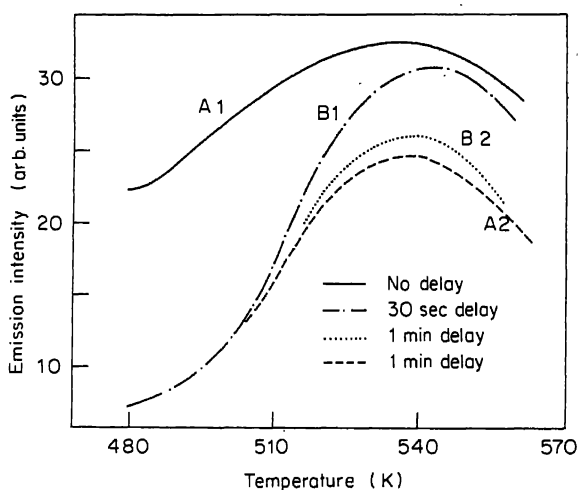


Figure 1. Decay of phosphorescence of  $\text{MgO}:\text{Li}:\text{Ce } 10^{-2}:\text{Eu } 10^{-3}$  fired in CO after different x-ray doses.



**Figure 2.** Decay monitored at different ambient temperatures after 10 min dose of 30 kV, 10 mA x-rays.



**Figure 3.** Thermoluminescence glow curves: A1, A2 after saturation excitation; B1, B2 after 3 min excitation.

540 K is atleast one of the sources for the electrons being received by the shallower group.

We know from the literature (Kirsh *et al* 1977) that the trapping group corresponding to 550 K of MgO is of electron releasing nature. This being so, if we lower the ambient temperature of decay measurements to a value where hole traps are emptied,

no such phenomenon should occur. Experiments performed at or below 430 K give results consistent with the third hypothesis.

This phenomenon was not observed in all our samples. In this connection some general remarks may be in order. One requirement for observing the peak is obviously the condition that at a particular instant the number of carriers tunnelling in must exceed the number being thermally emptied. Another condition would be that apart from the two group of traps being of the same kind, a certain overlap in the wave functions of the carriers at the given temperature should exist. This in turn would depend upon the nature of the two trap groups (potentials) and their actual distribution in the crystal matrix.

Therefore, while this phenomenon is not all too common since certain critical conditions outlined above have to be satisfied, it may not be all that rare. We therefore performed this experiment on a number of systems available to us and found that it occurred in europium-doped MgO and dysprosium-doped strontium silicate as well. What was more rewarding was that all the experiments conducted on them verified the hypotheses presented earlier.

## References

- Bapat M N and Sivaraman S 1983 *Indian J. Pure Appl. Phys.* **21** 247  
Bapat M N and Sivaraman S 1985 *Indian J. Pure Appl. Phys.* (in press)  
Kirsh Y, Kristianpoller N and Chen Y 1977 *Philos. Mag.* **35** 653  
Kathuria S P and Sunta C M 1982 *J. Phys.* **D15** 497  
Leverenz H W 1968 *An introduction to luminescence of solids* (New York: Dover) p. 256  
May C E and Partridge J 1964 *J. Chem. Phys.* **40** 1401  
Sathyamoorthy A and Luthra J M 1978 *J. Mater. Sci.* **13** 2637  
Takamori T and Dove D B 1983 *J. Electrochem. Soc.* **130** 1437



## Thermal expansion studies on As-Sb-Se glasses

A GIRIDHAR, SUDHA MAHADEVAN and A K SINGH

Materials Science Division, National Aeronautical Laboratory, Bangalore 560017, India

MS received 24 September 1985

**Abstract.** The results of measurement of thermal expansion coefficient from 50°C to the softening temperature on eight glass compositions of the As-Sb-Se system are presented. Measurements have been made on  $(\text{As}, \text{Sb})_{40}\text{Se}_{60}$  and  $\text{As}_x\text{Sb}_{15}\text{Se}_{85-x}$  glasses at heating rates of 1°C/min and 5°C/min. The composition and temperature dependence of the thermal expansion coefficient is discussed in the light of results of other chalcogenide glasses.

**Keywords.** As-Sb-Se glasses; thermal expansion coefficient; glass transition region.

### 1. Introduction

The study of thermal expansion coefficient ( $\alpha$ ) of chalcogenide glasses has not received much attention as compared with other properties of these glasses. There are some data on the composition dependence of  $\alpha$  for As-Se (Webber and Savage 1976), As-S (Tsuchihashi and Kawamoto 1970), Ge-As-Se (Webber and Savage 1976) and Ge-Sb-Se (Sudha Mahadevan *et al* 1984) glasses. There is a scatter of about 15% in the reported value of  $\alpha$  for  $\text{As}_2\text{S}_3$  (Tsuchihashi and Kawamoto 1970; Hilton *et al* 1966) and of about 35% for  $\text{As}_2\text{Se}_3$  (Henderson and Ast 1984; Webber and Savage 1976). It is generally known that the temperature dependence of  $\alpha$  of glasses has two regions; an initial low temperature or 'normal' region where  $\alpha$  is independent of temperature, followed by the glass transition region where  $\alpha$  increases with increase of temperature. Measurement of  $\alpha$  of Ge-Sb-Se glasses (Sudha Mahadevan *et al* 1984) using a conventional horizontal thermal dilatometer at a heating rate of 5°C/min indicated that the increase of  $\alpha$  with temperature in the transition region occurred over a temperature range of about 30°C. This is followed by softening of the glasses. Values of  $\alpha$  for  $\text{As}_2\text{Se}_3$  measured using a parallel plate viscometer (Henderson and Ast 1984) indicate an abrupt increase of  $\alpha$  (over a few degree temperature interval) from  $15.5 \times 10^{-6}/^\circ\text{C}$  in the normal region to about  $100 \times 10^{-6}/^\circ\text{C}$  after transition.

The results of measurement of  $\alpha$  on eight glass compositions of the As-Sb-Se system are reported in this communication. The composition of four of these glasses can be represented by  $(\text{As}, \text{Sb})_{40}\text{Se}_{60}$ . These fall along the  $\text{As}_2\text{Se}_3$ – $\text{Sb}_2\text{Se}_3$  pseudo-binary tie line and constitute the so-called 'stoichiometric' glasses of the As-Sb-Se system. The composition of the other four glasses studied can be represented by  $\text{As}_x\text{Sb}_{15}\text{Se}_{85-x}$ ; these four along with the stoichiometric composition with 15 atomic percent of Sb, namely,  $\text{As}_{25}\text{Sb}_{15}\text{Se}_{60}$  form five glasses of the  $\text{As}_x\text{Sb}_{15}\text{Se}_{85-x}$  family of the As-Sb-Se system. The results of measurement of the glass transition temperature ( $T_g$ ), density, electrical conductivity and elastic properties of these glasses have been reported elsewhere (Giridhar and Sudha Mahadevan 1982; Giridhar *et al* 1984).

## 2. Experimental

The elemental components (5N purity, from Koch Light Co.) in appropriate atomic proportions (table 1) were sealed in quartz ampoules (12 mm diameter) under a vacuum of  $10^{-3}$  torr. The contents of the ampoule were melted in a rotary furnace at about  $950^{\circ}\text{C}$  for 24 hr. The charge was then cooled to  $800^{\circ}\text{C}$  and quenched in cold water to obtain glasses. Samples were cut into rectangular sections of 3 mm thick  $\times$  8 mm width and of length about 10 mm to 20 mm depending on the piece available in the glass preparation boule. The end faces normal to the length of the sample were rendered smooth and parallel using a hand polishing jig fabricated for this purpose. Before measurement each sample was annealed in situ by holding it for 30 min at a temperature of about  $5^{\circ}\text{C}$  higher than its  $T_g$  and cooling it slowly.

The expansion measurements were made in a conventional horizontal dilatometer (thermal dilatometric analyser, Harrop Laboratories, USA, model TDA-H1-PP2) which was standardised against an alumina rod supplied with the instrument. The sample temperature was measured using a calibrated chromel-alumel thermocouple in contact with the sample. Using an X-Y recorder (sensitivity 0.2 mV/cm., Watanabe model WX 431) in conjunction with the dilatometer, expansion of the samples were recorded from room temperature upto the respective softening temperature ( $T_s$ ) at heating rates of  $5^{\circ}\text{C}/\text{min}$  and  $1^{\circ}\text{C}/\text{min}$ .

A typical trace showing the change in sample length  $\Delta l_s$  versus temperature is shown in figure 1 for one of the compositions. Also shown in figure 1 is the corresponding  $\alpha$  calculated using the expression  $\alpha = (l/l_s)(\Delta l_s/\Delta T)$ , with a temperature increment of  $10^{\circ}$ .

## 3. Results and discussion

### 3.1 $(\text{As}, \text{Sb})_{40}\text{Se}_{60}$ glasses

The results for these glasses are summarised in figures 2 and 3 and in table 1. Three to four batches of glasses were prepared for each composition to assess the spread in the value of  $\alpha$ . While the samples from different batch preparations gave spread of about

Table 1.  $T_g$ ,  $\alpha$  and  $\Delta\alpha$  data of As-Sb-Se glasses

Composition As:Sb:Se	$T_g(^{\circ}\text{C})$ by DSC		Range of $\alpha$ (in the normal region) $\times 10^6 (^{\circ}\text{C})$	$\Delta\alpha \times 10^6 (^{\circ}\text{C})$	$V_f \times 10^6$ ( $\approx 3\Delta\alpha T_g^*$ )
	1.25 $^{\circ}\text{C}$ /min	5 $^{\circ}\text{C}$ /min			
10:15:75	86	92	24.0–25.4	65	0.072
20:15:65	135	142	21.0–23.0	59	0.073
30:15:55	175.5	183	17.5–18.8	55	0.075
35:15:50	179.5	187.5	18.0–20.7	50	0.069
40:0:60	164	171	19.4–20.7	70	0.093
35:5:60	167.5	175.5	18.6–21.0	53	0.071
30:10:60	171.5	178.5	18.3–20.5	60	0.081
25:15:60	174.5	181.5	17.7–20.0	55	0.075
22:18:60	175	182	17.2–19.0	54	0.074

\*  $T_g$  in  $^{\circ}\text{K}$  has been used

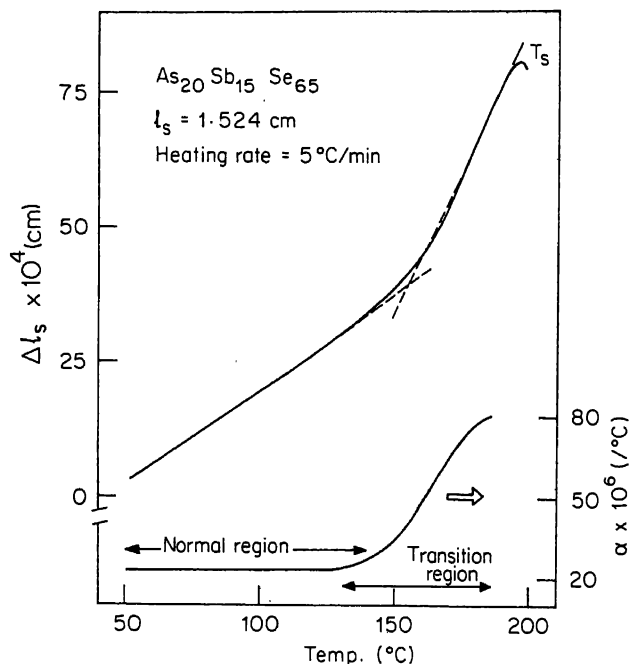


**Figure 1.** A typical data of the change in sample length  $\Delta l_s$  versus temperature for one of the compositions. Also shown is the corresponding  $\alpha$  obtained by  $\alpha = (l/l_s) (\Delta l_s / \Delta T)$ .

6% to 12% depending on the composition, the value of  $\alpha$  of samples from the same batch did not differ much. Because of the wide spread in the reported value of  $\alpha$  for As<sub>2</sub>Se<sub>3</sub>, two batches of As<sub>40</sub>Se<sub>60</sub> glass were prepared and  $\alpha$  was measured for the present study. The results for this composition are also included in figures 2 and 3. The  $T_g$ 's of these glasses obtained at heating rates of 1.25°C/min and 5°C/min using a Perkin Elmer model DSC-2 differential scanning calorimeter are also included in table 1. The temperatures at which  $\alpha$  increases rapidly (figure 2) agree closely with  $T_g$ 's of these glasses.

The variation of  $\alpha$  in the transition region of these glasses at the slow heating rate (1°C/min, dotted line, figure 2) indicates the existence of a relaxation process near  $T_g$ . It was found to be present in all the samples studied, though the magnitude of the effect differed. The origin of this relaxation process is not clear at present. It is probably similar to the relaxation process (Schnaus *et al* 1970) normally encountered in the measurement of heat capacity ( $C_p$ ) of glasses in the transition region. In heat capacity measurements it is attributed as an artifact of the rate dependence of glass properties in the transition region, and is associated with the structural relaxation times involved. However, further work is necessary to trace the origin of the relaxation process observed presently for these glasses.

The composition dependence of  $\alpha$  of these glasses in the normal region is shown in figure 3 with the vertical bars indicating the range of  $\alpha$  measured on samples from different batch preparations. A decrease of  $\alpha$  with increase of Sb content in the glass is seen from the results of figure 3.

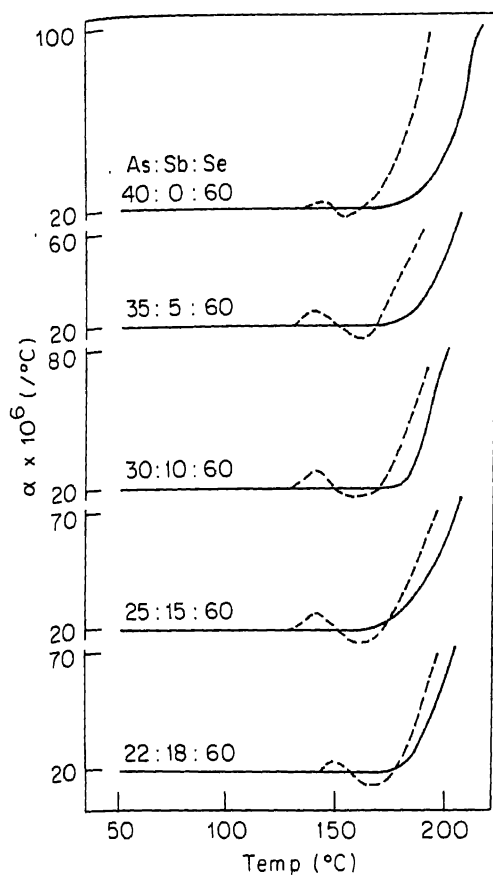


Figure 2.  $\alpha$ -T data for five glasses of  $(\text{As}, \text{Sb})_{40}\text{Se}_{60}$  (with Sb of 0, 5, 10, 15 and 18 atomic percent) at heating rates of  $1^\circ\text{C}/\text{min}$  (broken lines) and  $5^\circ\text{C}/\text{min}$  (continuous lines).

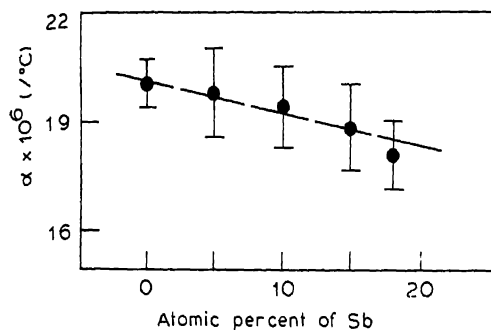


Figure 3.  $\alpha$  in the normal region versus composition for  $(\text{As}, \text{Sb})_{40}\text{Se}_{60}$  glasses. The vertical bars show the spread of  $\alpha$  obtained by measurements on samples from different batch preparations.

3.2  $As_xSb_{15}Se_{85-x}$  glasses

The variation of  $\alpha$  with temperature for glasses of this family was similar to those shown in figure 2 for stoichiometric compositions, with  $\alpha$  being constant upto the corresponding  $T_g$ , and increasing rapidly beyond that. However, the relaxation effect was not as prominent as in the case of stoichiometric glasses. The variation with composition of  $\alpha$  in the normal region for these glasses is shown in figure 4 along with the  $\alpha$ -composition data of  $As_xSe_{100-x}$ ,  $Ge_xAs_{10}Se_{90-x}$  (Webber and Savage 1976),  $Ge_xSb_{15}Se_{85-x}$  (Sudha Mahadevan *et al* 1984) and  $As_xS_{100-x}$  (Tsuchishshai and Kawamoto 1970) glasses. The lower values of  $\alpha$  for the Ge rich glasses of the Ge-chalcogenide glasses (figure 4) can be understood on the basis that As-(S, Se) glasses are basically in the form of layers and chains while Ge-(S, Se) glasses are generally in the form of three-dimensional networks. In the composition dependence of  $\alpha$  for Ge-Se (Feltz 1975), Ge-Sb-Se (figure 4) systems, a change of slope is seen at the respective stoichiometric composition, while for the As-S, As-Se systems (figure 4) a minimum is seen at the corresponding stoichiometric composition. A broad minimum is seen at the stoichiometric composition for the As-Sb-Se system. The variation in  $\alpha$  with composition in  $As_xSb_{15}Se_{85-x}$  is far less compared with those in case of  $As_xSe_{100-x}$  and  $As_xS_{100-x}$

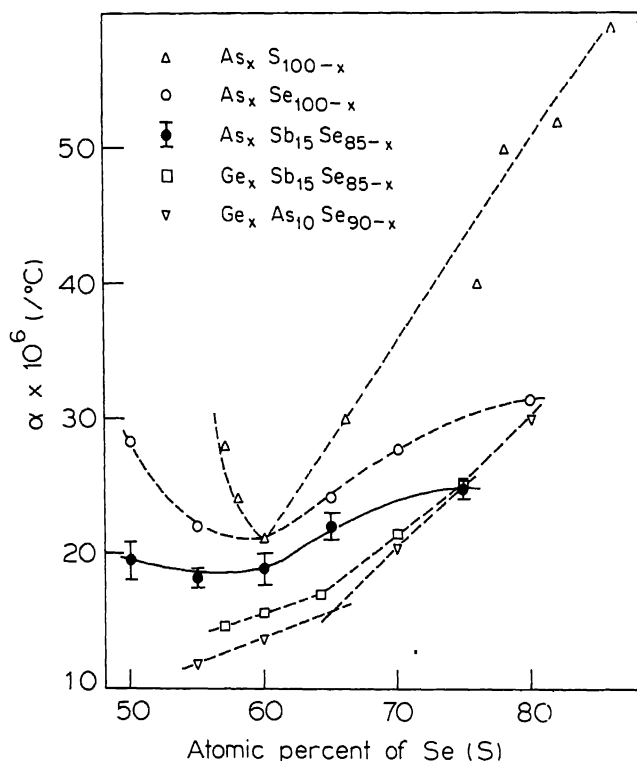


Figure 4.  $\alpha$ -composition data for  $As_xSb_{15}Se_{85-x}$  glasses. Also shown in the graph are the  $\alpha$ - $T$  data from the literature for  $As_xS_{100-x}$  (Tsuchihashi and Kawamoto 1970),  $As_xSe_{100-x}$ ,  $Ge_xAs_{10}Se_{90-x}$  (Webber and Savage 1976) and  $Ge_xSb_{15}Se_{85-x}$  (Sudha Mahadevan *et al* 1984) glasses.

(figure 4) glasses. The addition of Sb seems to suppress the variation of  $\alpha$  with composition.

### 3.3 Variation of $\alpha$ in the transition region

In the normal region, the  $\alpha$  of these glasses is not dependent on the temperature or the heating rate employed for the measurement. In the transition region, a marked dependence of  $\alpha$  is seen both on the temperature and on the heating rate. This behaviour is similar to the behaviour of heat capacity of glasses in the transition region (Schnaus *et al* 1973). The region of rapidly increasing  $\alpha$  is shifted to higher temperature as the heating rate is increased (figure 2), a behaviour similar to that of the heat capacity of glasses.

These measurements, as many others made earlier, indicate that  $\alpha$  increases in the transition region. The present measurements have been made with a dilatometer wherein a probe rod under load makes contact with the sample. The temperature in the set-up has been varied continuously at a chosen heating rate. The results for  $\text{As}_2\text{Se}_3$  at heating rates of  $1^\circ\text{C}/\text{min}$  and  $5^\circ\text{C}/\text{min}$  are shown in figure 5 (traces a and b respectively). In these cases,  $\alpha$  has been calculated from the slope of the  $\Delta l_s$  versus  $T$  trace (similar to that of figure 1) with a  $10^\circ\text{C}$  temperature increment. The increase in  $\alpha$  is spread over a temperature of about  $45^\circ\text{C}$  for  $5^\circ\text{C}/\text{min}$  heating rate, and about  $30^\circ\text{C}$  for  $1.25^\circ\text{C}/\text{min}$  heating rate. It is interesting to note in this context that the expansion data of  $\text{As}_2\text{Se}_3$  and  $\text{As}_2\text{S}_3$ -PbS glasses (Bhat and Bhatia 1978) also indicate an increase in  $\alpha$  taking place over a temperature range of about  $40^\circ\text{C}$  in the transition region. Recent results (Ahmed *et al* 1985) on thermal expansion of mixed alkali borate glasses also indicate an increase in  $\alpha$  occurring over a temperature interval of more than  $75^\circ\text{C}$  around the transition region for some of the compositions. This is to be expected because the transformation to a glass does not take place at one strictly defined temperature, but within a temperature range, representing the transformation region (Maurer 1968; Vacher *et al* 1974; Rehage and Borchard 1973). However, it is a general

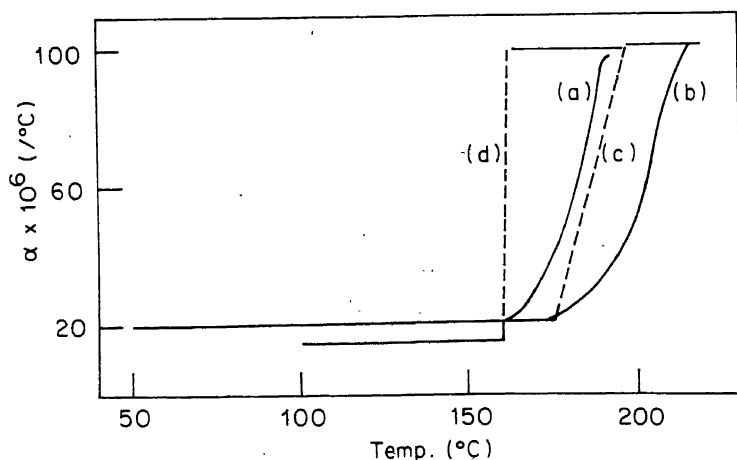


**Figure 5.**  $\alpha$ - $T$  in the transition region for  $\text{As}_2\text{Se}_3$  at the heating rates of  $1^\circ\text{C}/\text{min}$  (trace a) and  $5^\circ\text{C}/\text{min}$  (trace b). Trace c is calculated from the data obtained at the heating rate of  $5^\circ\text{C}/\text{min}$  by approximating the  $\Delta l_s$  vs  $T$  in the transition region to a straight line. The data of Henderson and Ast (1984) obtained from viscometer measurement is shown in trace d.

practice to approximate the variation of  $\Delta l_s$  with  $T$  in the transition region to a straight line (as shown by the dotted line in figure 1) and ascribe a value for  $\alpha$  after transition as inferred from the slope of this line. The result of such a calculation (for the heating rate of  $5^\circ\text{C}/\text{min}$ ) for  $\text{As}_2\text{Se}_3$  is as shown in trace (c) of figure 5. Also shown in figure 5 are the data on  $\alpha$  of  $\text{As}_2\text{Se}_3$  obtained by Henderson and Ast (1984) (trace (d), figure 5). The maximum value of  $\alpha$  of about  $100 \times 10^{-6}/^\circ\text{C}$  obtained presently agrees well with that obtained by Henderson and Ast (1984). However, the manner in which  $\alpha$  increases in the transition region before reaching its maximum value is different in the two measurements. In the set-up used by Henderson and Ast, the sample is placed between the plates of a parallel plate viscometer and the temperature is increased in steps. In this sense, these measurements are under isothermal conditions. Henderson and Ast (1984) also reported that the load used did not cause any deformation of the sample. The  $\alpha$  in this case is seen to increase to its final value in a few degrees range of temperature, whereas the present measurements indicate that the increase is spread over a wider range of temperature. This feature is introduced because of the continuous heating. The increase in  $\alpha$  is spread over a range of  $45^\circ\text{C}$  for  $5^\circ\text{C}/\text{min}$  heating rate and about  $30^\circ\text{C}$  for the  $1.25^\circ\text{C}/\text{min}$  heating rate. Also, by approximating the  $\Delta l_s$  vs  $T$  in the transition to a straight line, the spread of temperature range over which the increase in  $\alpha$  occurs is narrowed down, as can be seen from trace (c) of figure 5. It is to be expected that at still slower heating rates (approaching isothermal conditions) the spread will further decrease and resemble the data of Henderson and Ast (1984). Isothermal measurements were attempted on the dilatometer to check this point. But this could not be checked because the probe rod started indenting the sample when the sample was held for a sufficiently long time at any temperature in the transition region, indicating an apparent decrease in length. Thus while there is an increase of  $\alpha$  in the transition region, the detailed nature of this increase seems to depend on the heating rate employed, the procedure used to evaluate  $\alpha$  (from the  $\Delta l_s$  vs  $T$  data) and the method employed for the measurement of  $\alpha$ .

The free volume  $V_f$  during glass transition is given (Simha and Boyer 1962; Suzuki *et al* 1971) as the product of the difference in cubical expansion coefficient above and below the glass transition temperature and  $T_g \cdot V_f$  is of the order of  $3 \Delta\alpha T_g$  where  $\Delta\alpha$  is the change in linear expansion coefficient above and below  $T_g$ . For oxide glasses, the ratio of free volumes, namely,  $V_{f(\text{B}_2\text{O}_3)}/V_{f(\text{GeO}_2)}$  is found to be equal to eight, while by considering the average free volume changes in As-Se, As-S, Ge-Se and Ge-S systems, it has been found that  $V_{f(\text{As}_2\text{Se}_3)}/V_{f(\text{GeSe}_2)}$  is about 1.2 and  $V_{f(\text{As}_2\text{S}_3)}/V_{f(\text{GeS}_2)}$  is about 1 (Suzuki and Abe 1981). It is therefore concluded (Suzuki and Abe 1981; Suzuki *et al* 1978) that chalcogenide glasses are in a state of isofree volume during glass transition. The average value of  $V_f$  for  $(\text{As}_2\text{Se}_3)(\text{Sb}_2\text{Se}_3)$  glasses (table 1) is seen to be 0.0789. The average value of  $V_f$  from the data of  $\Delta\alpha$  and  $T_g$  for  $(\text{GeSe}_2)(\text{Sb}_2\text{Se}_3)$  glasses (Sudha Mahadevan *et al* 1984) is seen to be 0.0760. The value of 1.04 for the ratio  $V_{f(\text{As}_2\text{Se}_3)(\text{Sb}_2\text{Se}_3)}/V_{f(\text{GeSe}_2)(\text{Sb}_2\text{Se}_3)}$  therefore falls in line with the general observation of isofree volume during glass transition for chalcogenide glasses, despite the difference in structure.

#### 4. Summary and conclusions

Measurements have been made on the dependence of thermal expansion coefficient ( $\alpha$ ) on temperature and composition for eight glass compositions of the As-Sb-Se system at

the heating rates of 1°C/min and 5°C/min. The  $\alpha$ -T data indicate an initial 'normal' region where  $\alpha$  is independent of temperature followed by a 'transition' region where  $\alpha$  increases steeply with temperature. The temperature where  $\alpha$  begins to show a steep increase shifts to higher values as the heating rate is increased. The detailed nature of the increase of  $\alpha$  in the transition region seems to depend on the heating rate employed, the procedure used to evaluate  $\alpha$  and the method employed for the measurement of  $\alpha$ .

The composition dependence of  $\alpha$  of  $\text{As}_x\text{Sb}_{15}\text{Se}_{85-x}$  glasses have been compared with those of  $\text{As}_x\text{S}_{100-x}$  and  $\text{As}_x\text{Se}_{100-x}$  glasses. A broad minimum is seen at the 'stoichiometric' composition  $\text{As}_{25}\text{Sb}_{15}\text{Se}_{60}$  in the  $\alpha$ -composition dependence of these glasses.

The  $\alpha$  in the 'normal' region for  $(\text{As}, \text{Sb})_{40}\text{Se}_{60}$  glasses shows a slight decrease with increasing Sb content in the glasses. At the heating rate of 1°C/min, these glasses exhibit a relaxation process around the transition region. The results on  $\alpha$  and  $T_g$  of these glasses along with those of Ge-Sb-Se glasses fall in line with the general observation of iso-free volume during glass transition for chalcogenide glasses, despite differences in structure.

## References

- Ahmed A A, Abbas A F and Salman S M 1985 *Phys. Chem. Glasses* **26** 17  
 Bhat P K and Bhatia K L 1978 *Phys. Chem. Glasses* **19** 55  
 Feltz A 1975 *Z. Anorg. Allg. Chem.* **412** 20  
 Giridhar A and Sudha Mahadevan 1982 *J. Non-Cryst. Solids* **51** 305  
 Giridhar A, Sudha Mahadevan and Singh A K 1984 *Bull. Mater. Sci.* **6** 1001  
 Henderson W and Ast D G 1984 *J. Non-Cryst. Solids* **64** 43  
 Hilton A R, Jones C E and Brau M 1966 *Phys. Chem. Glasses* **7** 105  
 Kawamoto Y and Tsuchihashi S 1971 *J. Am. Cer. Soc.* **54** 131  
 Maurer J J 1968 in *Analytical chemistry VI* (New York: Plenum Press) pp 107  
 Rehage C and Borchard W 1973 in *The physics of glassy polymers* (London: Applied Science Publications) pp 54  
 Schnaus V E, Moynihan C T, Gammon R W and Macedo P B 1970 *Phys. Chem. Glasses* **11** 213  
 Simha R and Boyer R F 1962 *J. Chem. Phys.* **37** 1003  
 Sudha Mahadevan, Giridhar A, Narasimham P S L and Singh A K 1984 *J. Non-Cryst. Solids* **65** 233  
 Suzuki S and Abe Y 1981 *J. Non-Cryst. Solids* **43** 141  
 Suzuki S, Takahashi M and Kobayoshi T 1978 *Yogyo Kyokai Shi* **86** 428  
 Tsuchihashi S and Kawamoto S 1970 *J. Non-Cryst. Solids* **5** 286  
 Vacher R, Delsanti M, Pelous J, Cecchi L, Winter A and Zarzyki J 1984 *J. Mater. Sci.* **9** 829  
 Webber P J and Savage J A 1976 *J. Non-Cryst. Solids* **20** 271



## X-ray line profile analysis of silver base Ag-Cd-In alloys

S VENKAT REDDY\* and S V SURYANARAYANA

Department of Physics, University College of Science, Osmania University, Hyderabad 500 007, India

\*Sardar Patel College, Secunderabad 500 025, India

MS received 7 November 1983; revised 7 November 1985

**Abstract.** X-ray diffraction line profiles of five silver base ternary alloys in  $\alpha$ -phase with varying atomic percentages of cadmium and indium were recorded in both cold-worked and annealed states of the samples. Detailed studies on the profiles involving peak shift, peak asymmetry and Fourier analysis of line shapes have been carried out to evaluate microstructural parameters such as deformation fault probabilities, RMS strains and dislocation densities. It was found that the addition of indium has a marked effect in producing deformation fault probabilities in comparison to that of adding cadmium in ternary silver base alloys. Compound fault probability was found to be maximum for the alloy Ag-10Cd-15In.

**Keywords.** Microstructure; line profile analysis; cold-worked state; silver base ternary alloys; stacking fault probabilities.

### 1. Introduction

Extensive studies of microstructural analysis of various silver base binary alloys using x-ray methods have been made (Wagner 1966; Anantharaman *et al* 1972; Adler and Wagner 1962; Sen Gupta and Goswami 1967; De 1969; Sen Gupta 1967; Sen Gupta and De 1970; Chatterjee *et al* 1976). These studies have indicated that addition of solutes such as cadmium and indium to pure silver increases the stacking fault probability. According to phase diagram,  $\alpha$ -phase silver base ternary alloys can be prepared with cadmium and indium as solutes up to about 25 at % (Snyder 1966). Krishnan *et al* (1971) evaluated only the intrinsic fault probabilities ( $\alpha'$ ) in some Ag-Cd-In alloys from a measurement of peak shift of (111) and (200) reflections. Recently the present authors reported that in four of the Ag-Cd-In alloys, in which the concentration of one of the constituent metals (indium) was kept constant at 5 at %, the deformation fault probability increases with increasing cadmium content (Reddy and Suryanarayana 1983). The present paper is an extension of our earlier work and the results on microstructural analysis of five more silver base ternary alloys using x-ray diffraction technique are included along with a detailed discussion on the deformation fault probabilities, root mean square (RMS) microstrains, effective domain size and dislocation densities on all the nine alloys.

### 2. Experimental procedure

The desired alloy samples were prepared from high purity silver, cadmium and indium metals. The details of the preparation of the samples and homogenization were

reported earlier (Reddy and Suryanarayana 1983). The x-ray data on annealed and cold-worked samples were collected by point counting method using a Philips goniometer fitted on to a PW 1730 x-ray generator and proportional counter; copper  $K_\alpha$  radiation was used. The line profiles of the (111), (200), (220), (311), (222) and (400) reflections were recorded taking all necessary precautions (Reddy and Suryanarayana 1983).

The faulting parameters  $\alpha (= \alpha' - \alpha'')$  and  $4.5\alpha'' + \beta$  were calculated from peak shift and peak asymmetry measurements of the profiles using well-known relations of Wagner (1966) and Cohen and Wagner (1962). The peak and the centre of gravity of the line profiles were determined by standard methods (Bearden 1933; Halder *et al* 1977).

Observed line profiles for cold-worked state of the alloys were corrected for instrumental broadening using the technique developed by Stokes (1948) and expressed as Fourier series (Warren 1969). The Warren-Averbach method (Warren and Averbach 1950; Warren 1959) was applied to separate the particle size coefficients  $(D_e)_{hkl}$  and RMS strains  $\langle \epsilon^2 \rangle_{hkl}^{1/2}$  in [111] and [100] directions and also to evaluate compound fault probability  $[1.5(\alpha' + \alpha'') + \beta]$ . Subsequent line shape analysis (Adler and Wagner 1962) also provides information about particle size due to faulting ( $D_{SF}$ ) and minimum value of domain size ( $T_{min}$ ) as defined by Warren (1961).

All the numerical calculations were done on Integra/1001 computer adopting a suitable program.

### 3. Results and discussion

#### 3.1 Lattice parameters and peak shift analysis

The lattice parameter of each alloy specimen was calculated from a plot of  $a_{hkl}$  vs  $\cos \theta \cot \theta$ . In table 1 the data on lattice parameters of annealed and cold-worked samples are given and the results are shown in figure 1. It can be seen that for annealed samples all the  $a_{hkl}$  values fall on a straight line but for cold-worked samples the values of  $a_{hkl}$  scatter from the line and this scatter is consistent with Paterson's theory (Paterson 1952). From an analysis of the data on lattice parameters, one can infer that cold working causes contraction of the lattice in all these alloys of Ag-Cd-In system. These results are in agreement with those obtained on binary silver base alloys namely Ag-In, Ag-Cd, Ag-Sn and Ag-Ga (Adler and Wagner 1962; Chatterjee *et al* 1976).

Deformation fault probability ( $\alpha$ ) was evaluated by using the following relation (Adler and Wagner 1962).

$$(\Delta a/a')_{hkl} = G_{hkl} \alpha, \quad (1)$$

where  $G_{hkl}$  is the planar parameter and  $(\Delta a)_{hkl}$  is the difference between the measured cold-worked lattice parameter ( $a_{hkl}$ ) and hypothetical lattice parameter ( $a'_{hkl}$ ). The mean values of stacking fault probability ( $\alpha$ ) as obtained from equation (1) and also obtained from the peak shift of neighbouring pairs of reflections namely (111), (200), (220) and (311) are given in table 1. The results of Krishnan *et al* (1971) are also included in table 1. A general agreement can be seen between the results obtained in the present work and those reported by Krishnan *et al* in respect of the observation that deformation fault probability increases with increasing solute content. However, there is difference between the individual values reported. In this context, it is worth mentioning that while Krishnan *et al* evaluated  $\alpha$  only from one neighbouring pair of reflections, the

Table 1. The values of lattice spacings and stacking fault probabilities  $\alpha'$ ,  $\alpha''$  and  $\beta$  from line profile analysis in Ag-Cd-In alloys

Composition of the alloy		Lattice spacings		$\alpha_1 (\times 10^3)$									
		Present work											
		$(a_0)_{\text{Ann}}$ (Å)	$(a_0)_{\text{CW}}$ (Å)	Krishnan <i>et al</i> (1971)	From peak shift	From lattice parameter	$4.5\alpha'' + \beta$ ( $\times 10^3$ )	$1.5(\alpha' + \alpha'') + \beta$ ( $\times 10^3$ )	$\alpha'$ ( $\times 10^3$ )	$\alpha''$ ( $\times 10^3$ )	$\beta$ ( $\times 10^3$ )		
Sl No.	in at % Ag-Cd-In												
1.	90-5-5	4.1103	4.1064	12.2	13.09	13.17	8.69	36.91	7.38	-5.71	34.41		
2.	85-10-5	4.1220	4.1172	17.0	17.78	19.89	13.94	29.27	25.34	7.56	-20.08		
3.	75-20-5	4.1432	4.1407	29.1	28.14	29.69	12.54	53.88	28.72	0.58	9.93		
4.	70-25-5	4.1594	4.1547	32.4	25.96	27.35	17.24	62.39	21.82	-4.14	35.87		
5.	85-5-10	4.1272	4.1235	31.6	24.89	25.19	24.29	53.25	30.47	5.58	-0.82		
6.	80-10-10	4.1415	4.1375	39.5	25.69	22.68	20.04	36.37	40.49	14.80	-45.56		
7.	75-15-10	4.1468	4.1416	—	34.43	36.70	15.75	51.82	44.81	10.38	-30.96		
8.	80-5-15	4.1431	4.1407	64.7	39.77	42.81	1.40	40.59	53.41	13.64	-59.98		
9.	75-10-15	4.1556	4.1522	70.8	49.19	51.35	8.10	70.40	56.85	7.66	-26.37		
Error limits		$\pm 0.0002$			$\pm 3 \text{ to } \pm 5$		$\pm 4 \text{ to } \pm 10$	$\pm 2 \text{ to } \pm 10$	$\pm 5 \text{ to } \pm 8$	$\pm 2 \text{ to } \pm 3$	$\pm 5 \text{ to } \pm 10$		

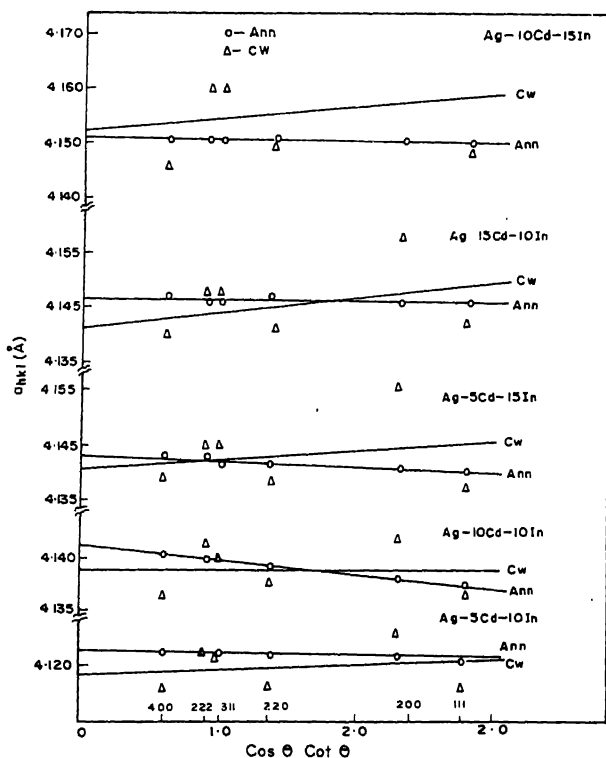


Figure 1. The plots of  $a_{hkl}$  vs extrapolation function  $\cos \theta \cot \theta$  for Ag-Cd-In alloys.

present datum reported in table 1 is an average from three pairs of reflections.

With a view to studying the individual effects of solutes (cadmium and indium) on microstructural parameters of Ag-Cd-In alloys, the nine alloys so far studied and listed in table 1 are divided into four sets where in each set, the concentration of one of the solutes was constant. The data for the alloys at serial numbers 1-4 are taken from Reddy and Suryanarayana (1983). The other three sets of alloys considered now are with constant indium concentration of 10 at. % (Sl. Nos. 5, 6, 7 referred to as 2nd set), with constant cadmium concentration of 5 at. % (Sl. Nos. 1, 5, 8 referred to as 3rd set) and with constant cadmium concentration of 10 at. % (Sl. Nos. 2, 6, 9 referred to as 4th set). The plots of deformation fault probabilities ( $\alpha$ ) vs combined solute (Cd + In) at. % for the four sets of alloys are shown in figure 2. It is observed from these plots that adding either indium or cadmium in the ternary silver base alloys would increase the deformation fault probability. However, it is noteworthy that adding indium has a marked effect in producing deformation fault probability in Ag-Cd-In alloys with constant cadmium (3rd and 4th sets) in comparison to the effect of adding cadmium to the alloys with constant indium concentration (1st and 2nd sets). The present observations agree with those on binary Ag-In, Ag-Cd alloys (Adler and Wagner 1962).

The concept of electron-to-atom (e/a) ratio has been widely used as a normalizing parameter in correlating the changes in  $\alpha$  with composition in most of the binary alloys. However, in the case of the ternary alloys, e/a ratio is not such a useful parameter since

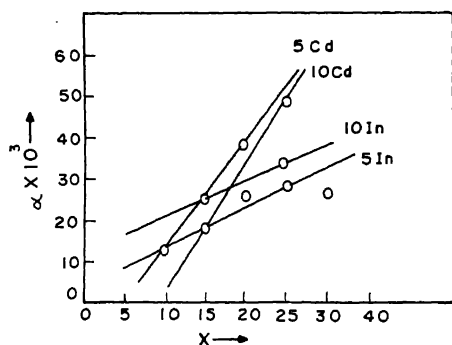


Figure 2. The plots of deformation fault probability ( $\alpha$ ) vs  $X$ , at. % of solute (Cd + In) for some Ag-Cd-In alloys.

one can prepare a number of alloys with the same e/a (Ag-25Cd-5In, Ag-15Cd-10In, Ag-5Cd-15In). So Krishnan *et al* (1971) extended the concept of solvent solute valence difference for ternary alloys which was originally proposed by Delehouzee and Deruyttere (1967) for binary alloys to explain the compositional dependence of  $\alpha$  through the following expression

$$\alpha = \alpha_0 \exp(k|\Delta Z|p), \quad (2)$$

where  $\alpha$  is the deformation fault probability in the alloy containing  $p$  atomic percentage of solute,  $\alpha_0$  is the deformation fault probability in the solvent metal alone,  $|\Delta Z|$  the difference between the solute and solvent valences and  $k$ , a constant for a series of alloys based on particular solvent. The plot of  $\ln \alpha$  versus  $p|\Delta Z|$  for the present data on Ag-Cd-In alloys is shown in figure 3. The values of  $\alpha_0$  and  $k$  are evaluated from intercept and slope of this plot and these values are  $6.8 \times 10^{-3}$  and 0.05 respectively. Liu and Gallagher (1971) reported the value of  $k$  in the case of silver base binary alloys as 0.08.

### 3.2 Peak asymmetry analysis

The asymmetry analysis of (111) and (200) line profiles was made from measurements of the centre of gravity of the line profile and the peak maximum. The values of the parameter  $4.5\alpha'' + \beta$  obtained in this analysis are given in table 1 for calculating individual fault parameters  $\alpha'$ ,  $\alpha''$  and  $\beta$ . It was observed that asymmetry parameter ( $4.5\alpha'' + \beta$ ) in the first set of alloys (with constant indium concentration of 5 at. %) increases with the addition of cadmium while in the second set of alloys a reverse effect was observed. However, no systematic variations of this asymmetry parameter with solute concentration (Cd + In) were observed in 3rd and 4th sets of these alloys.

### 3.3 Line shape analysis

The values of effective particle size  $(D_e)_{hkl}$ , RMS strain  $\{\langle \epsilon_L^2 \rangle_{50\text{\AA}}^{1/2}\}$ , particle size due to faulting  $(D_{SF})_{hkl}$  and minimum value of domain size  $(T_{\min})$  are listed in table 2. The variation of RMS strain  $\{\langle \epsilon_L^2 \rangle^{1/2}\}$  with  $L$  (distance in  $\text{\AA}$  normal to reflecting planes) as shown in figure 4 describes the usual picture of the strain field around the dislocation in deformed lattice and it is found that RMS strain and particle size along  $[100]$  direction

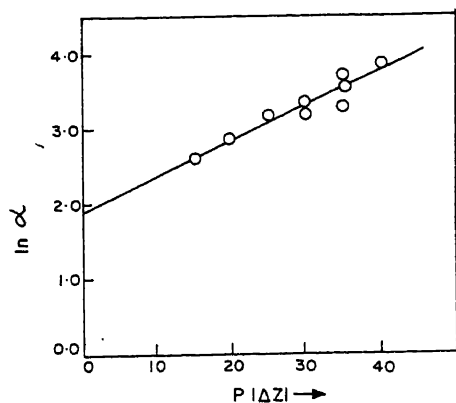


**Figure 3.** Variation of  $\ln \alpha$  with  $p |\Delta Z|$  for Ag-Cd-In alloys.

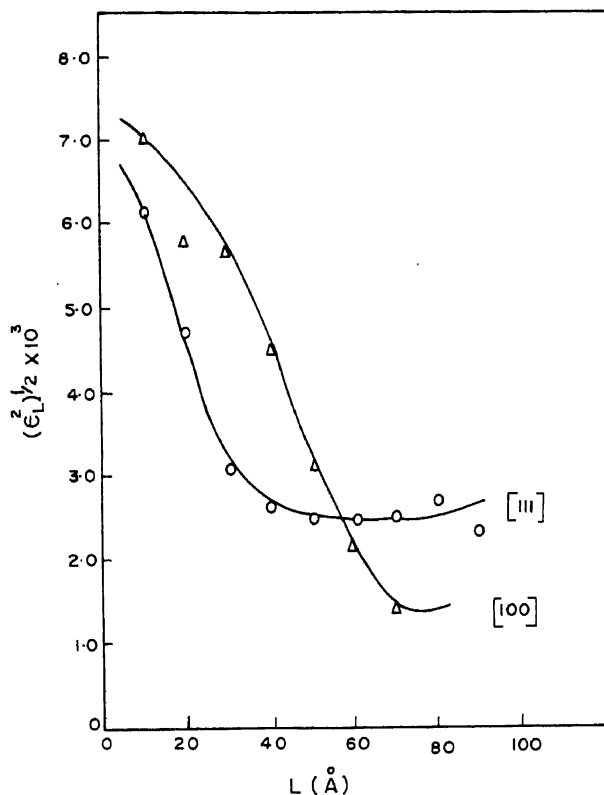


**Figure 4.** The plots of the RMS strains  $\langle \varepsilon_L^2 \rangle^{1/2}$  vs  $L$  (in Å) for Ag-10Cd-15In alloy.

are greater than those along  $[111]$  direction in these alloys (anisotropy in particle size and in RMS microstrains). It is also observed that the values of particle size  $(D_e)_{hkl}$  along  $[111]$  and  $[100]$  directions decrease with increasing sum of the solutes (Cd + In) concentration for all the four sets of alloys. The particle size due to faulting ( $D_{SF}$ ) is

**Table 2.** The values of effective domain sizes, RMS microstrains,  $D_{\text{SF}}$ ,  $T_{\text{min}}$ , dislocation densities  $\rho$  and  $\gamma/\mu$  parameters for Ag-Cd-In alloys

Sl No.	Compositions of the alloy in at %										$\rho$ ( $\times 10^{-11}$ cm/cm <sup>3</sup> )	$\rho_{av}$ ( $\times 10^{-11}$ cm/cm <sup>3</sup> )	$\gamma/\mu$ ( $\times 10^{11}$ cm)
	Ag-Cd-In		$D_e(\text{\AA})$		$\langle \epsilon_L^2 = 50\text{\AA} \rangle^{1/2}$ ( $\times 10^3$ )		$D_{SF}(\text{\AA})$		$T_{min}$ ( $\text{\AA}$ )				
	[111]	[100]	[111]	[100]	[111]	[100]	[111]	[100]	[111]	[100]			
1.	90-5-5	100	73	191	235	354	153	87	495	833	664	270	
2.	85-10-5	118	80	195	390	325	141	116	417	1258	837	252	
3.	75-20-5	87	53	180	295	178	77	107	531	1429	980	189	
4.	70-25-5	87	50	228	290	154	67	125	670	1483	1076	287	
5.	85-5-10	92	55	235	200	179	78	118	658	937	798	173	
6.	80-10-10	72	53	140	293	263	114	62	499	1419	959	247	
7.	75-15-10	52	38	230	290	183	80	67	1134	1957	1546	245	
8.	80-5-15	90	60	203	260	235	102	91	579	1112	846	116	
9.	75-10-15	65	40	254	370	136	59	78	985	2369	1677	187	
Error limits $\pm 5$ to $\pm 10$													

inversely proportional to compound fault probability  $[1.5(\alpha' + \alpha'') + \beta]$  so that the effective particle size decreases with increasing compound fault probability when the solute concentration is more.

The values of compound fault probability  $[1.5(\alpha' + \alpha'') + \beta]$  for all the alloys are given in table 2. This parameter has been found to increase at higher solute concentration and the result of a maximum value ( $70.4 \times 10^{-3}$ ) for Ag-10Cd-15In alloy is noteworthy. In our earlier studies (Reddy and Suryanarayana 1984) on x-ray Debye temperatures of Ag-Cd-In alloys, it was reported that the same alloy shows a maximum value for  $\theta_M$  (317° K).

### 3.4 Stacking fault concentrations

The individual values of  $\alpha'$ ,  $\alpha''$  and  $\beta$  were estimated from all the parameters obtained from peak shift, peak asymmetry and peak broadening (table 1). It is found that the intrinsic faults ( $\alpha'$ ) are greater than the extrinsic faults ( $\alpha''$ ) in these alloys. The twin fault probability ( $\beta$ ) is found to be negative for the alloys with Sl. Nos. 2 and 5–9 indicating total absence of such type of faults in these alloys. However, the twin fault probability ( $\beta$ ) is found to be positive for the alloys with Sl. Nos. 1, 3 and 4. These positive values of  $\beta$  may be attributed to the segregation of solutes at stacking faults in these three alloys. According to Wilson (1962), the asymmetry in profiles may also be produced by the segregation of solutes at stacking faults (Suzuki effect) in addition to the extrinsic and twin faults. However it is difficult to detect Suzuki effect and also to eliminate asymmetry due to extrinsic and twin faults. It may also be mentioned here that the determination of parameter  $4.5\alpha'' + \beta$  involves the accurate determination of peak maximum position and centre of gravity (CG) of profile but the determination of CG suffers from the experimental limitations such as long tails of peak and peak overlap and hence much reliance cannot be placed on the values of  $\beta$ .

Finally it may be concluded that cold working produces appreciable intrinsic faults and to a small extent extrinsic faults, but fails to produce twin faults in most of these Ag-Cd-In alloys. These observations are similar to the results on some binary and ternary alloys namely Cu-Ga, Cu-Sb, Cu-In, Cu-Sn, Ag-Zn, Ag-Sb, Ag-Ga and Cu-Ni-Zn (Chatterjee *et al* 1976, 1977; Halder *et al* 1977; Sen Gupta and De 1970).

### 3.5 Dislocation density ( $\rho$ ) and stacking fault energy ( $\gamma$ )

The values of dislocation density ( $\rho$ )<sub>hkl</sub> are calculated using the method suggested by Williamson and Smallman (1956) and the results are given in table 2. The average values of  $\rho$  and  $\alpha$  were used to determine the parameter  $\gamma/\mu$  for these alloys. It was not possible to calculate the stacking fault energy ( $\gamma$ ) as the values of shear moduli ( $\mu$ ) for these alloys are not available. It is observed that the dislocation density along [100] direction is greater than that along [111] direction for the same alloy and the effect of adding a solute is to increase the dislocation density.

### 3.6 Anomaly in Ag-10Cd-15In alloy

As mentioned in §3.3, the value of compound fault probability of this alloy was found to be maximum. This alloy also had shown an anomalously high value of Debye temperature (317° K) when compared to the value of 244° K in the case of pure silver (Reddy and Suryanarayana 1984) and for the other silver alloys. Another observation from the present work is that due to cold work the lattice parameter of the alloy



decreases causing a contraction of the lattice. Such a behaviour in binary and ternary alloys has earlier been attributed to the Suzuki effect (Halder *et al* 1977). While the Suzuki effect may be present in all the nine alloys studied, in the particular alloy (Ag-10Cd-15In) the anomalous behaviour may also be due to a possible order-disorder phenomenon. To investigate this proposition, the authors have taken another diffractogram to look for any additional low angle peak. No such extra reflection was observed. Since the differences between the atomic scattering factors of Ag, Cd and In are small for x-rays, even if the phenomenon of order-disorder persists, it would be difficult to detect it from x-ray work. Therefore, it may be intuitive to subject the sample for careful resistivity measurements under different heating and cooling cycles to detect the presence of any such behaviour. Presently such a study is being undertaken by the authors.

### Acknowledgements

The authors wish to thank the University Grants Commission, New Delhi for financial assistance. They also wish to thank Dr P Rama Rao, Director, Defence Metallurgical Research Laboratory, Hyderabad for his interest in this work and for providing the samples. They wish to thank Dr S P Sen Gupta, Indian Association for Cultivation of Science, Calcutta, for supplying the necessary computer program.

### References

- Adler R P I and Wagner C N J 1962 *J. Appl. Phys.* **33** 3451
- Anantharaman T R, Rama Rao P and Lele S 1972 Recent developments in metallurgical Science and Technology, Silver Jubilee Symposium, Indian Institute of Metals, New Delhi
- Bearden J A 1933 *Phys. Rev.* **43** 92
- Chatterjee S K, Halder S K and Sen Gupta S P 1976 *J. Appl. Phys.* **47** 411
- Chatterjee S K, Halder S K and Sen Gupta S P 1977 *J. Appl. Phys.* **48** 1442
- Cohen J B and Wagner C N J 1962 *J. Appl. Phys.* **33** 2073
- De M 1969 *J. Appl. Crystallogr.* **2** 82
- Delehouzee L and Deruyttere A 1967 *Act. Metall.* **15** 727
- Halder S K, De M and Sen Gupta S P 1977 *J. Appl. Phys.* **48** 3560
- Krishnan R G, Gupta R K and Rama Rao P 1971 *Metall. Trans.* **2** 3373
- Liu Y C and Gallagher P C J 1971 *J. Appl. Phys.* **42** 3322
- Paterson M S 1952 *J. Appl. Phys.* **23** 805
- Reddy S V and Suryanarayana S V 1983 *J. Appl. Phys.* **54** 6317
- Reddy S V and Suryanarayana S V 1984 *Indian J. Pure Appl. Phys.* **22** 161
- Sen Gupta S P 1967 *Acta. Crystallogr.* **23** 244
- Sen Gupta S P and Goswami K N 1967 *Acta Crystallogr.* **22** 81
- Sen Gupta S P and De M 1970 *J. Appl. Crystallogr.* **3** 410
- Snyder H J 1966 Ph.D. Thesis, University of Pittsburgh, USA
- Stokes A R 1948 *Proc. Phys. Soc. (London)* **61** 382
- Wagner C N J 1966 Local atomic arrangements studied by x-ray diffraction (New York: Gordon and Breach)
- Warren B E 1959 *Progr. Metal Phys.* **8** 147
- Warren B E 1961 *J. Appl. Phys.* **32** 2428
- Warren B E 1969 X-ray diffraction (New York: Addison-Wesley)
- Warren B E and Averbach B L 1950 *J. Appl. Phys.* **21** 595
- Williamson G K and Smallman R E 1956 *Philos. Mag.* **1** 34
- Wilson A J C 1962 *Nature (London)* **193** 568



## Phase relations and activities in the Co-Ni-O system at 1373 K

K T JACOB, S SRIKANTH and G N K IYENGAR

Department of Metallurgy, Indian Institute of Science, Bangalore 560012, India

MS received 26 August 1985

**Abstract.** The tie-lines delineating equilibria between CoO-NiO and Co-Ni solid solutions in the ternary Co-Ni-O system at 1373 K have been determined by electron microprobe and EDAX point count analysis of the oxide phase equilibrated with the alloy. The oxygen potentials corresponding to the tie-line compositions have been measured using a solid oxide galvanic cell with calcia-stabilized zirconia electrolyte and Ni + NiO reference electrode. Activities in the metallic and oxide solid solution have been derived using a new Gibbs–Duhem integration technique. Both phases exhibit small positive deviations from ideality; the values of  $G^E/X_1X_2$  are  $2640 \text{ J mol}^{-1}$  for the metallic phase and  $2870 \text{ J mol}^{-1}$  for the oxide solid solution.

**Keywords.** Free energy of mixing; cobalt-nickel alloys; cobalt oxide-nickel oxide solid solution; oxygen potential; solid state cell; thermodynamic properties; phase diagram; electromotive force.

### 1. Introduction

Cobalt and nickel-based alloys are extensively used in high temperature applications. A knowledge of the oxygen potential and temperature for the oxidation of the alloy and the composition of the oxide phase is important for the design of oxidation-resistant alloys. Complex phase relations for commercial alloys can be projected with useful accuracy from a knowledge of the constituent binary and ternary systems. Phase relations in the ternary Co-Ni-O system have not been reported in the literature. Early literature on the Co-Ni binary system has been compiled by Hultgren *et al* (1973). More recently activities in the Co-Ni solid alloys have been measured by Vrestal and Kucera (1971) by the effusion method using isotopes of Co and Ni in the temperature range 1420 to 1600 K, and by Tomiska *et al* (1979) using Knudsen effusion mass spectrometry in the temperature range 1480 to 1875 K. Their investigations show negative deviations from Raoult's law.

Although a number of measurements have been reported in the literature for liquid Co-Ni alloys (Tomiska *et al* 1979; Maruyama and Ban-ya 1978; Tozaki *et al* 1973; Predel and Mohs 1970; Iguchi *et al* 1977; Tsemakhman *et al* 1971) the results are contradictory. Maruyama and Ban-ya (1978), Tozaki *et al* (1973), Predel and Mohs (1970), Iguchi *et al* (1977) report small positive deviations from Raoult's law, while Tomiska *et al* (1979) and Tsemakhman *et al* (1971) suggest mild negative deviations.

Activities in the system NiO-CoO have been evaluated by Torkar and Schneider (1976) for  $0.34 < X_{\text{CoO}} < 0.87$  with a solid state electrochemical cell at 1000 and 1300 K using an approximate thermodynamic analysis. Their study indicates small positive deviation from Raoult's law.

In the present study, compositions of coexisting alloy and oxide phases in the Co-Ni-O system, and the equilibrium oxygen potentials corresponding to the tie-lines have been measured at 1373 K. A thermodynamic analysis of ( $M_1$ - $M_2$ -O) ternary system is

developed which permits the derivation of activities of components in the alloy phase from tie-line compositions and oxygen potentials.

## 2. Experimental technique

### 2.1 Materials

Powders of Ni, Co, NiO and CoO of 99.99 + purity and particle size of the order of 100  $\mu\text{m}$  were used. The oxide and metallic solid solutions were prepared by heating compacted pellets at 1573 K for 600 ks. The pellets, contained in alumina crucibles, were held under prepurified argon.

### 2.2 Apparatus and procedure

**2.2a Tie-line determination:** Powders of the oxide and metallic solid solution were intimately mixed in equimolar ratios and pelletized. The Co/Ni ratio of the starting solid solutions in each pellet was approximately equal. The pellets were placed in alumina crucibles, sealed under vacuum in silica capsules and heated at 1373 K for 600 ks. After equilibration the capsules were quenched in water. The material was ground, pelletized and heated for another 600 ks under identical conditions. The quenched pellets were then mounted for metallographic examination. The composition of the phases was determined by electron microprobe and energy dispersive x-ray analysis. Pure Co, Ni, NiO and CoO were used as standards. In all cases, atomic absorption and fluorescence effects were eliminated using computer-compensated adjustments. The composition profiles across the grains were found to be uniform and agreement between the two methods of compositional analysis was better than 1 %.

**2.2b Oxygen potential measurements:** The equilibrium oxygen potential over each alloy/oxide pellet at 1373 K was measured using a solid-state electrochemical cell

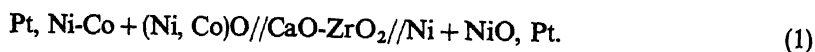


**Table 1.** Equilibrium compositions, EMF, partial pressures and activities at 1373 K for Co-Ni-O System

$X_{\text{Co}}$	$X_{\text{CoO}}$	EMF (mV)	$P_{\text{O}_2} \times 10^{-9}$ (atm)	$a_{\text{Co}}$	$a_{\text{Ni}}$	$a_{\text{CoO}}$	$a_{\text{NiO}}$
0.07	0.313	16.5	0.644	0.084	0.931	0.352	0.704
0.139	0.511	29.9	0.410	0.163	0.865	0.543	0.522
0.181	0.595	36.8	0.324	0.209	0.825	0.620	0.443
0.246	0.688	46.0	0.238	0.278	0.764	0.705	0.351
0.317	0.759	54.4	0.178	0.350	0.698	0.771	0.278
0.401	0.819	62.9	0.134	0.433	0.620	0.826	0.214
0.610	0.910	79.2	0.0773	0.630	0.423	0.912	0.111
0.738	0.946	87.1	0.0590	0.749	0.295	0.947	0.067
0.829	0.967	92.2	0.0496	0.834	0.198	0.967	0.041
0.892	0.980	95.6	0.0443	0.894	0.128	0.980	0.025
1.00	1.00	101.1	0.00396	1.0	0.0	1.0	0.0

The reference electrode consisted of an equimolar mixture of Ni and NiO. The working electrode consisting of metallic solid solution in equilibrium with the oxide solid solution was taken from the set of pellets prepared for tie-line determination. The details of the experimental set-up have been discussed earlier (Petric and Jacob 1982). Prepurified inert gas was passed over each electrode.

The emf of the cell was measured with a digital voltmeter with an internal impedance greater than  $10^{12} \Omega$ . The reversibility of the cell was checked by passing small currents in either direction through the cell. In each case the emf was found to return to the original value. The emf was found to be independent of the flow rate of argon over the electrodes. The time required to reach equilibrium was  $\approx 4$  ks at 1373 K. No attempt was made to measure the emf as a function of temperature since compositions are temperature dependent and compositional changes are diffusion controlled. Hence very long periods are required to obtain a stable emf at other temperatures.

### 3. Results

#### 3.1 Tie-line study

The equilibrium composition of Co-Ni alloy and (Co Ni)O solid solution at 1373 K is given in table 1. Tie-lines representing the exchange reaction;



are shown in figure 1.

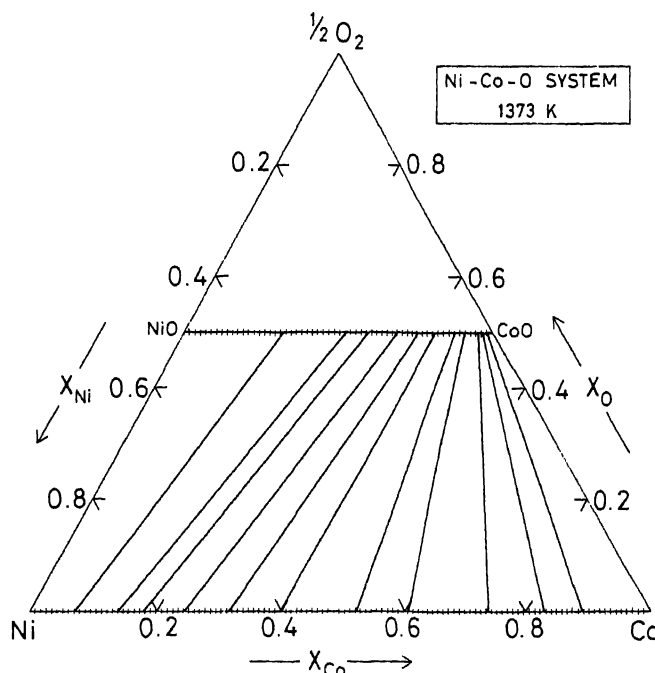


Figure 1. Phase diagram of the Co-Ni-O system showing the tie-lines between the metallic and rocksalt phases at 1373 K.

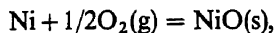
### 3.2 Emf study

The emf of cell 1 is related to the oxygen potential corresponding to the tie-lines. The emf values are summarized in table 1 and plotted in figure 2 as a function of composition of both the oxide and metallic solid solution phases.

The open circuit potential is expressed as

$$E = (RT/2F) \ln [p_{O_2(i)}^{1/2}/p_{O_2(ii)}^{1/2}], \quad (3)$$

where  $p_{O_2(i)}$  and  $p_{O_2(ii)}$  are the oxygen potentials at the right and left hand electrodes respectively,  $T$  the absolute temperature,  $F$  the Faraday constant and  $R$  the gas constant. The oxygen potential of the reference electrode is defined by (Steele 1968);



$$\Delta G^\circ = 1/2\Delta\mu_{\text{O}_2} = -234,160 + 84.89 T \text{ J mol}^{-1}. \quad (4)$$

The oxygen potential over the two phase alloy is deduced from the measured emf values using equation (3). The partial pressures are given in table 1 as a function of composition. The corresponding oxygen potential diagram at 1373 K is shown in figure 2. Topological rules that apply to the more common  $T$ - $X$  phase diagrams are also valid for this chemical potential-composition ( $\Delta\mu$ - $X$ ) diagram. The oxygen potentials for the oxidation of any Co-Ni alloy and the composition of the oxide phase can be readily obtained from this diagram. Similar diagrams at other temperatures can be easily constructed from the thermodynamic information obtained in this study.

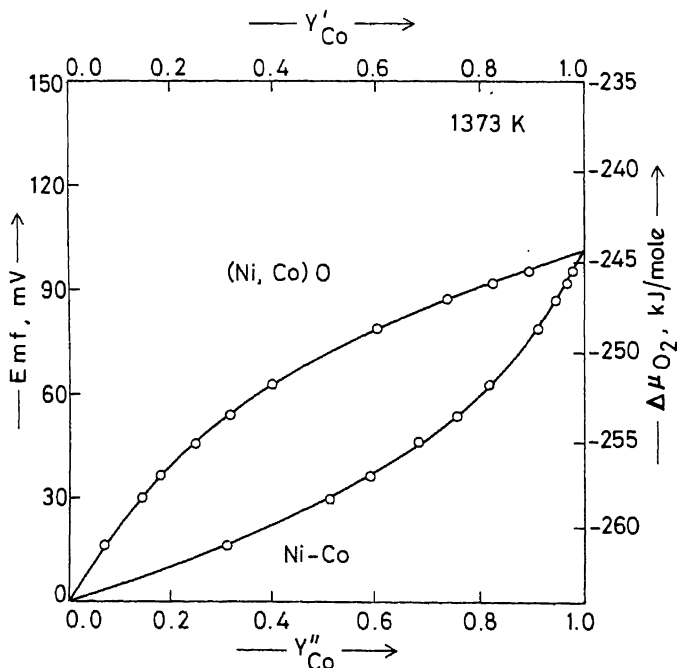


Figure 2. Emf and oxygen potential—composition diagram for the Co-Ni-O system at 1373 K

### 3.3 Thermodynamic analysis

In thermodynamic analysis of ternary systems involving a nonmetallic component, it is convenient to introduce composition variables,  $Y_i$  defined as:

$$Y_{\text{Co}} = n_{\text{Co}}/n_{\text{Ni}} + n_{\text{Co}}; Y_{\text{Ni}} = n_{\text{Ni}}/n_{\text{Ni}} + n_{\text{Co}}; Y_{\text{O}} = n_{\text{O}}/n_{\text{Ni}} + n_{\text{Co}},$$

where  $n_i$  is the number of moles of component  $i$ . It follows from the above that  $Y_{\text{Ni}} = 1 - Y_{\text{Co}}$ . The parameter  $Y_{\text{O}}$  represents the ratio of nonmetallic (anionic) to the metallic (cationic) component in a given phase.

By dividing each term in the general Gibbs–Duhem equation,

$$\sum n_i d \ln a_i = 0 \quad (4)$$

by  $(n_{\text{Ni}} + n_{\text{Co}})$ , one obtains,

$$\sum Y_i d \ln a_i = 0. \quad (5)$$

Since activities are constant along tie-lines, the Gibbs–Duhem relation in the two-phase region of the ternary Co-Ni-O system may be written as,

$$Y'_{\text{Co}} d \ln a_{\text{Co}} + (1 - Y'_{\text{Co}}) d \ln a_{\text{Ni}} + Y'_{\text{O}} d \ln p_{\text{O}_2}^{1/2} = 0, \quad (6)$$

$$Y''_{\text{Co}} d \ln a_{\text{Co}} + (1 - Y''_{\text{Co}}) d \ln a_{\text{Ni}} + Y''_{\text{O}} d \ln p_{\text{O}_2}^{1/2} = 0, \quad (7)$$

where (') denotes the oxide phase and (") represents the alloy. Subtracting (7) from (6),

$$(Y'_{\text{Co}} - Y''_{\text{Co}}) d \ln a_{\text{Co}} + (Y'_{\text{Ni}} - Y''_{\text{Ni}}) d \ln a_{\text{Ni}} + (Y'_{\text{O}} - Y''_{\text{O}}) d \ln p_{\text{O}_2}^{1/2} = 0, \quad (8)$$

or

$$(Y'_{\text{Co}} - Y''_{\text{Co}}) d \ln (a_{\text{Co}}/a_{\text{Ni}}) + (Y'_{\text{O}} - Y''_{\text{O}}) d \ln p_{\text{O}_2}^{1/2} = 0. \quad (9)$$

Therefore,

$$d \ln (a_{\text{Ni}}/a_{\text{Co}}) = \frac{(Y'_{\text{O}} - Y''_{\text{O}})}{(Y'_{\text{Co}} - Y''_{\text{Co}})} d \ln p_{\text{O}_2}^{1/2}. \quad (10)$$

Because of the negligible solid solubility of oxygen in Co-Ni alloys,  $Y''_{\text{O}}$  can be considered to be zero, and  $Y'_{\text{O}}$  is approximately unity for the oxide phase. At an oxygen pressure of 1 atm and 1373 K, the nonstoichiometry parameter  $y$  has values of  $8 \times 10^{-3}$  for  $\text{Co}_{1-y}\text{O}$  and  $2 \times 10^{-3}$  for  $\text{Ni}_{1-y}\text{O}$  (Kofstad 1972). Equation (10) then simplifies to,

$$d \ln (a_{\text{Ni}}/a_{\text{Co}}) = \frac{1}{Y'_{\text{Co}} - Y''_{\text{Co}}} d \ln p_{\text{O}_2}^{1/2}. \quad (11)$$

It has been shown earlier (Jacob and Jeffes 1972) that activity of any component in a binary or pseudobinary system can be deduced from the composition dependence of activity ratio. For the Co-Ni binary this relation is

$$\ln a_{\text{Ni}} = \int_1^{Y'_{\text{Ni}}} Y'_{\text{Co}} d \ln (a_{\text{Ni}}/a_{\text{Co}}). \quad (12)$$

Combining (11) and (12),

$$\ln a_{\text{Ni}} = \int_{p_{\text{O}_2(\text{Ni} + \text{NiO})}}^{p_{\text{O}_2}} \frac{Y'_{\text{Co}}}{2(Y'_{\text{Co}} - Y''_{\text{Co}})} d \ln p_{\text{O}_2}. \quad (13)$$

The same result can also be derived by equating the third term in (7) to zero, and then

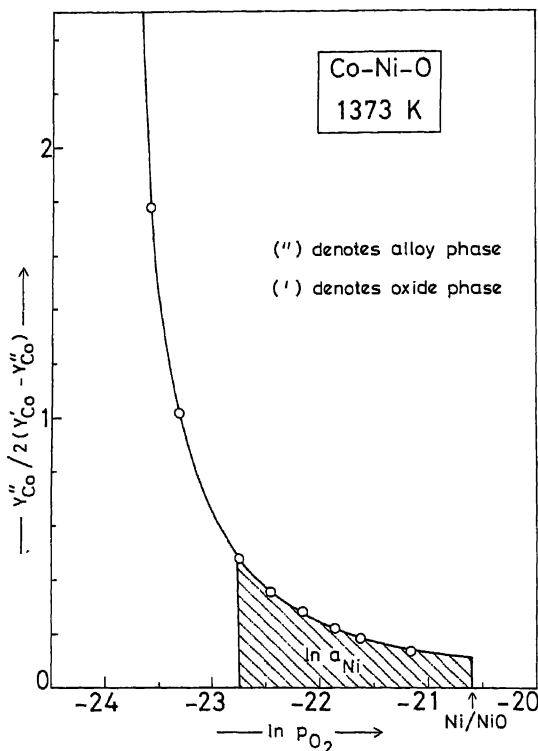


Figure 3. Gibbs-Duhem integration plot for the Co-Ni binary alloy.

combining (6) and (7) with algebraic rearrangement. A similar equation can be written for the activity of cobalt.

$$\ln a_{\text{Co}} = \int_{P_{\text{O}_2(\text{Co} + \text{CoO})}}^{P_{\text{O}_2}} \frac{Y''_{\text{Ni}}}{2(Y'_{\text{Ni}} - Y''_{\text{Ni}})} d \ln P_{\text{O}_2}. \quad (14)$$

### 3.4 Activities in metal and oxide solid solutions

From the partial pressures obtained through emf study, the activity of Ni and Co were deduced using (13) and (14). The integration plot for evaluating the activity of Ni is shown in figure 3. It is important to note that  $Y''_{\text{Co}}/2(Y'_{\text{Co}} - Y''_{\text{Co}})$  does not go to zero at  $Y_{\text{Ni}} \rightarrow 1$ . The corresponding activities of the oxide components were calculated from the activities of Co and Ni, the partial pressure of oxygen and the standard free energies of formation of CoO and NiO available in the literature (Steele 1968; Jacob and Pandit 1985). The activities of the oxide components and the metallic components in the oxide and metallic solid solution phases at the tie-line compositions are listed in table 1.

## 4. Discussion

The thermodynamic properties of Co-Ni and CoO-NiO solid solutions obtained in this



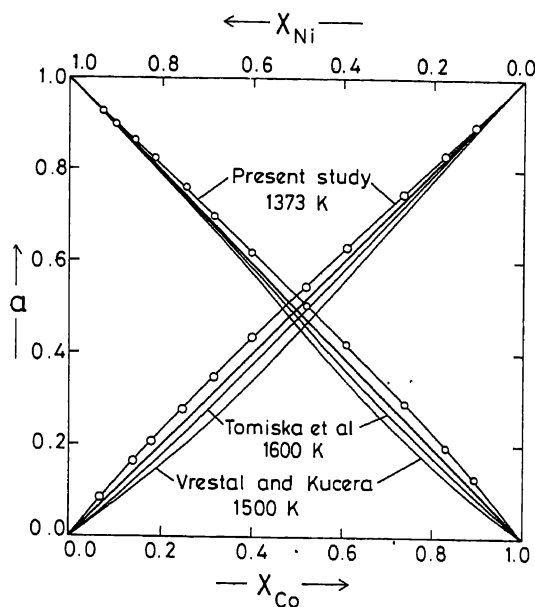


Figure 4. Activity-composition relationship in the Co-Ni binary alloy.

study at 1373 K can be expressed by,

$$G_{\text{Ni-Co}}^E = 2460 X_{\text{Ni}} X_{\text{Co}} \text{ J mol}^{-1}, \quad (15)$$

$$G_{\text{NiO-CoO}}^E = 2870 X_{\text{NiO}} X_{\text{CoO}} \text{ J mol}^{-1}. \quad (16)$$

The activities of components obtained in this study are compared with the data reported by Vrestal and Kucera (1971) and Tomiska *et al* (1979) in figure 4. The present results indicate a slight positive deviation from Raoult's law in contrast to the negative deviation suggested by Vrestal and Kucera (1971) and Tomiska *et al* (1979). The measurements of Vrestal and Kucera (1971) are based on the Knudsen effusion technique using molybdenum cells. Phase diagrams for Co-Mo and Ni-Mo systems show stable intermetallic compounds at the experimental temperature. Formation of these intermetallics by reaction between the vapour species and molybdenum could have interfered with the attainment of equilibrium inside the Knudsen cell. Further Vrestal and Kucera (1971) have not demonstrated the absence of surface depletion in their samples by measuring vapour pressure as a function of orifice diameter. Tomiska *et al* (1979) have used a Knudsen effusion mass spectrometric technique for activity measurements and their results can be approximated by  $G^E/X_{\text{Ni}}X_{\text{Co}} = -2012 \text{ J mol}^{-1}$  at 1600 K. The authors (Tomiska *et al* 1979) have not discussed possible surface depletion of the volatile component during their measurements.

The activity-composition relationship for the rocksalt solid solution is shown in figure 5 along with the data of Torkar and Schneider (1976) who estimated the composition of this alloy phase by making a number of assumptions including unit activity coefficients for the alloy. They have estimated the values of  $G^E/X_{\text{CoO}}X_{\text{NiO}}$  equal to  $4500 (\pm 1200) \text{ J mol}^{-1}$  at 1000 K and  $2300 (\pm 1600) \text{ J mol}^{-1}$  at 1300 K. When extrapolated to 1373 K, results of Torkar and Schneider (1976) yield  $G^E/X_{\text{CoO}}X_{\text{NiO}}$

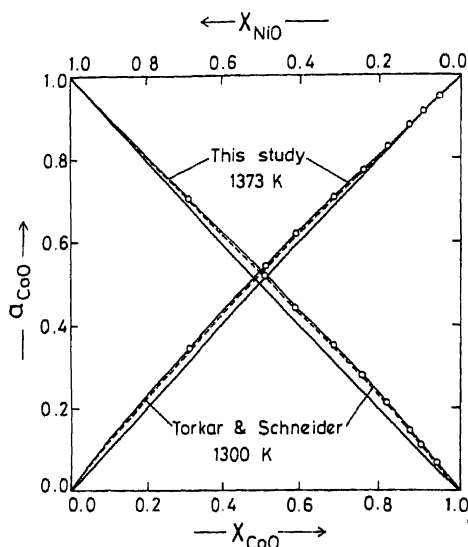


Figure 5. Activities for NiO and CoO in the rocksalt solid solution.

equal to  $1770 \text{ J mol}^{-1}$  which compares with a value of  $2870 (\pm 500) \text{ J mol}^{-1}$  obtained in this study. Since the derivation of thermodynamic data reported in this study is rigorous, and free from simplifying assumptions, the data obtained in this study is considered to be more reliable than that reported earlier. Positive deviations in the oxide solid solution arise from the small size difference between  $\text{Co}^{2+}$  and  $\text{Ni}^{2+}$  ions. The ionic radii of  $\text{Co}^{2+}$  and  $\text{Ni}^{2+}$  in low spin state are 0.79 and 0.84 Å respectively (Shannon and Prewitt 1969, 1970).

### Acknowledgement

Part of this work was done when one of the authors (KTJ) was at the University of Toronto. The authors wish to thank Mr N Venugopal Rao and Mr A V Narayan for assistance in the preparation of the manuscript.

### References

- Hultgren R, Orr R L, Anderson P O and Kelley K K 1973 *Selected values of thermodynamic properties of metals and alloys* (OH: ASM, Metals Park) p. 561
- Iguchi Y, Tozaki Y, Kazikawa M, Ban-ya S and Fuwa T 1977 *Tetsu to Ko* **63** 953
- Jacob K T and Jeffes J H E 1972 *High Temp. High Press.* **4** 177
- Jacob K T and Shashidara Pandit S 1985 *J. Solid State Chem.* **60** 237
- Kofstad P 1972 *Nonstoichiometry, diffusion, and electrical conductivity in binary metal oxides* (New York Wiley-Interscience) p. 238
- Maruyama N and Ban-ya S 1978 *Niken Kinzo ku Gabbaiishi* **42** 994
- Petric A and Jacob K T 1982 *Solid State Ionics* **6** 47
- Predel B and Mohs R 1970 *Archiv Eisenhüttenw* **41** 143
- Shannon R D and Prewitt C T 1969 *Acta Crystallogr.* **B25** 925

- Shannon R D and Prewitt C T 1970 *Acta Crystallogr.* **B26** 1046
- Steele B C H 1968 *Electromotive force measurements in high temperature systems* (ed.) C B Alcock (London: Inst. Min. Met.) p. 3
- Tomiska J, Nowotny H, Erdely L and Neckel A 1979 *Ber. Bunsenges. Phys. Chem.* **83** 1035
- Torkar K and Schneider R 1976 *J. Solid State Chem.* **18** 89
- Tozaki Y, Iguchi Y, Ban-ya S and Fuwa T 1973 *Chemical metallurgy of iron and steel* (London: The Iron and Steel Institute) p. 130
- Tsemakhman D Sh, Vaishurd S E and Shirokova I F 1971 *Zh. Fiz. Khim* **45** 2074
- Vrestal J and Kucera R 1971 *Met. Trans.* **2** 3367



## Effect of texture and grain size on the mechanical properties of warm-worked cadmium, zinc and zinc-0.35% aluminium alloy

K RATNAJI RAO, S RANGANATHAN and D H SASTRY

Department of Metallurgy, Indian Institute of Science, Bangalore 560 012, India

MS received 29 June 1985; revised 13 December 1985

**Abstract.** Changes in the grain size and crystallographic texture during warm working and their influence on the room temperature mechanical properties are investigated on Cd, Zn and a Zn-Al alloy. The yield strength increase in the early stages of working in extruded cadmium is accounted for based on the development of a basal texture while in rolled zinc and zinc alloy, the properties are affected more by the grain size. Cadmium exhibits ductile fracture at all extrusion ratios whereas the fracture mode in zinc and the alloy changes from cleavage at small rolling strains to ductile at higher deformation strains.

**Keywords.** Grain size; texture; warm working; yield stress; fracture.

### 1. Introduction

It is now generally recognized that mechanical processing of materials in the warm working temperature range ( $0.4-0.6 T_m$ , where  $T_m$  is the absolute temperature of melting) results in improved mechanical strength without much loss of ductility (Yegneswaran *et al* 1978). This can be attributed to one or more of the following, namely, grain refinement, development of a stable substructure and development of crystallographic texture. In view of the limited number of available slip systems, strong textures often develop in c.p.h. metals and alloys during deformation processing. Textured materials exhibit anisotropy and both texture strengthening and texture weakening are possible depending on the type of texture present which in turn is determined by the details of processing (Hsu *et al* 1977).

The aim of the present investigation is to study the structural changes that occur during warm working of cadmium, zinc and zinc-0.35% aluminium and their influence on the resulting mechanical properties. These materials are selected since they can easily be worked at room temperature which is in the warm-working range. The Zn-Al alloy is chosen because aluminium refines the grain size and in addition could lower the stacking fault energy of zinc which influences the development of textures. The deformation process selected is extrusion for cadmium and rolling for zinc and the zinc alloy.

### 2. Experimental

Cadmium metal of 99.95% purity was melted and cast into billets. They were extruded at room temperature in a 250 ton vertical hydraulic press. Five extrusion ratios in the range 6–130 were employed.

Anal grade zinc (99.95%) was used in the present work and high purity aluminium (99.98%) was used to prepare the zinc-0.35% aluminium alloy. The as-cast slabs of the metal and the alloy were hot-forged at 573 K and subsequently flat-rolled to 4 mm thickness. The material was then annealed. With the annealed strip as the starting material, different amounts of reduction were given by rolling at room temperature. The deformation produced by sheet rolling is represented as the true thickness strain because no significant lateral spread was observed.

Tensile tests were carried out at room temperature on rod samples of extruded cadmium and rolled sheets of zinc and Zn-Al alloy. Tukon microhardness measurements were done on the transverse section of the extruded samples. On the rolled sheets, measurements were done on the rolling plane. The grain size in the various samples was determined by standard metallographic techniques. The fracture surfaces of the tested specimens were observed in a scanning electron microscope (Cambridge Stereoscan 150).

The crystallographic texture developed during processing was examined by measuring the x-ray line integrated intensities from planes parallel to the exposed surface (rolling plane in the case of sheets, longitudinal as well as transverse sections in the case of rods). Philips x-ray diffractometer with Cu K- $\alpha$  radiation was used for this purpose. For comparison, random samples were prepared from well-annealed powders of cadmium and zinc and the line intensities were recorded under identical conditions.

### 3. Results and discussion

The extruded structure in cadmium showed completely recrystallized equiaxed grains at all strains. Little or no twinning was observed at any strain. Figure 1 shows the variation of the average grain diameter measured on the transverse section with true strain. The grain size shows a continuous increase with deformation—from 14  $\mu\text{m}$  at a thickness strain of  $\epsilon = 1.83$  to about 40  $\mu\text{m}$  at  $\epsilon = 4.15$ . This may be attributed to the lower recrystallization temperatures at higher deformations and also to more heat generated during extrusion.

The variation of the yield stress (0.2% strain offset flow stress) and the UTS at room temperature of the warm extruded cadmium with extrusion strain is recorded in figure 2. Both the quantities increase with true strain, reach a peak value and decrease thereafter with further deformation. The peak strength is reached at an  $\epsilon$  value of about 2.25.

It is obvious that the yield strength variation with extrusion strain cannot be accounted for on the basis of grain size variation. Whereas the grain size continuously increased with strain, the yield stress exhibited a peak. Therefore, a Hall-Petch type grain boundary strengthening relationship is not obeyed in extruded cadmium. The yield stress-extrusion strain relationship in cadmium can however be understood in terms of the strong basal texture developed during extrusion. Figure 3 is a plot of the x-ray line intensity ratio  $I_{0002}/I_{10\bar{1}1}$  with the transverse section exposed to the x-ray beam. It also shows the intensity of the  $(10\bar{1}1)$  reflection in the extruded rod normalized with respect to the random sample. Both variations are a pointer to the development of a strong  $[0001]$  fibre axis at a true extrusion ratio of about 2.25. At large deformations, the ratio  $(I/I_0)$   $(10\bar{1}1)$  reaches unity indicating random texture. Since the basal planes are perpendicular to the extrusion direction, the texture is unfavourable for slip and

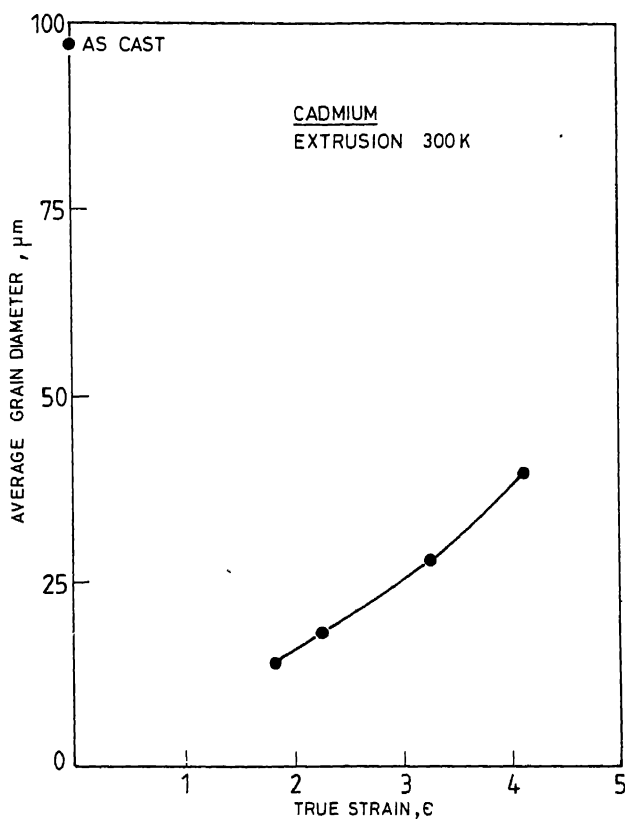


Figure 1. Variation of average grain diameter with true strain.

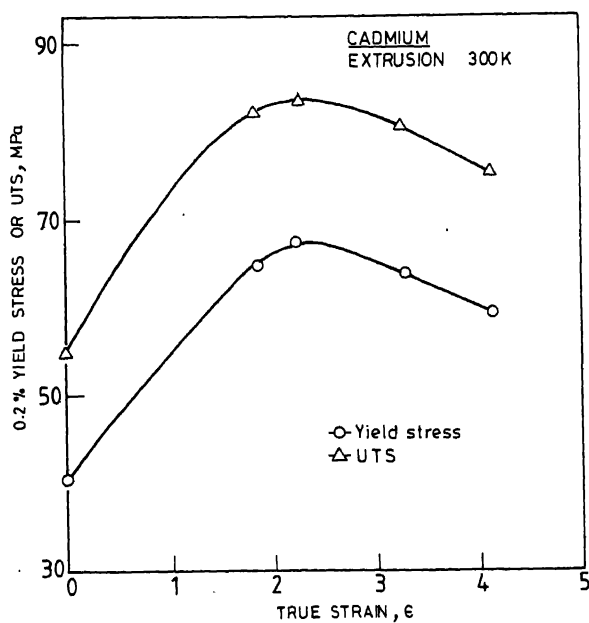


Figure 2. Variation of yield strength and UTS at 300 K with true strain.

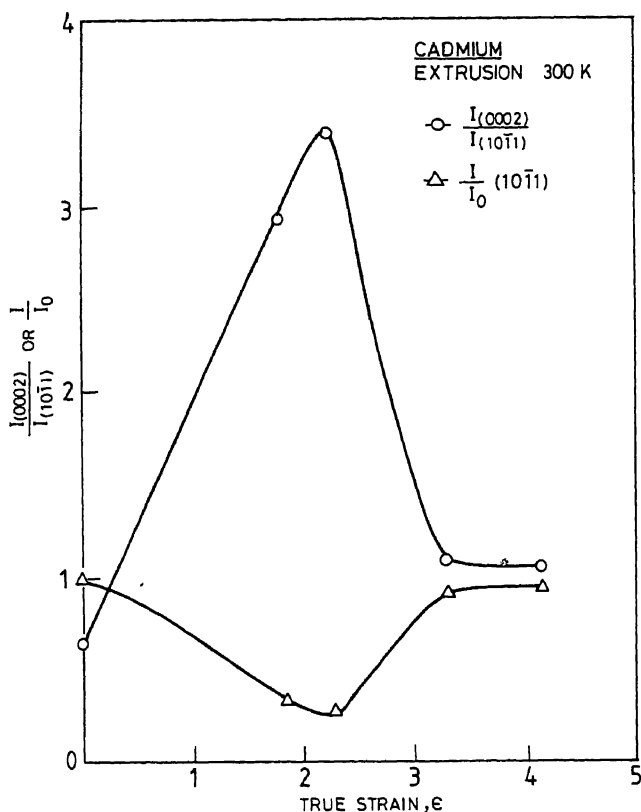


Figure 3. Variation of  $(I_{(0002)}/I_{(10\bar{1}1)})$  or  $(I/I_0) (10\bar{1}1)$  with true strain.

texture hardening is observed upto  $\epsilon = 2.25$ . The decrease in yield strength beyond this strain can be associated with a corresponding decrease in the intensity of basal texture as well as an increase in grain size. Similar texture hardening has been reported on cadmium and zinc by Bly *et al* (1973).

The variation of grain size with true thickness strain in rolled zinc and zinc alloy is shown in figure 4. The measurements were made in the rolling plane. In the early stages of deformation, extensive mechanical twinning has occurred and at large deformations, twins have decreased and the grain size becomes very small. The grain size has been measured without including twin boundaries. In both materials, the grain size continuously decreased with increasing strain. The normalized x-ray line intensity from (0002) planes and the ratio of intensities from (0002) and  $(10\bar{1}1)$  planes in the sheet are plotted against true thickness strain in figure 5. Zinc shows a basal texture i.e., (0001) parallel to the rolling plane, in the initial stages of deformation. However, the texture is weak and above about  $\epsilon = 0.3$ , the intensities are close to that of a random sample. The alloy also has no significant texture especially in the initial stages of deformation.

The variation in the yield stress (0.2% strain offset flow stress) of warm rolled zinc and Zn-Al alloy at 300 K with rolling strain is shown in figure 6. In both materials, the yield stress is slightly higher in the transverse direction than in the longitudinal



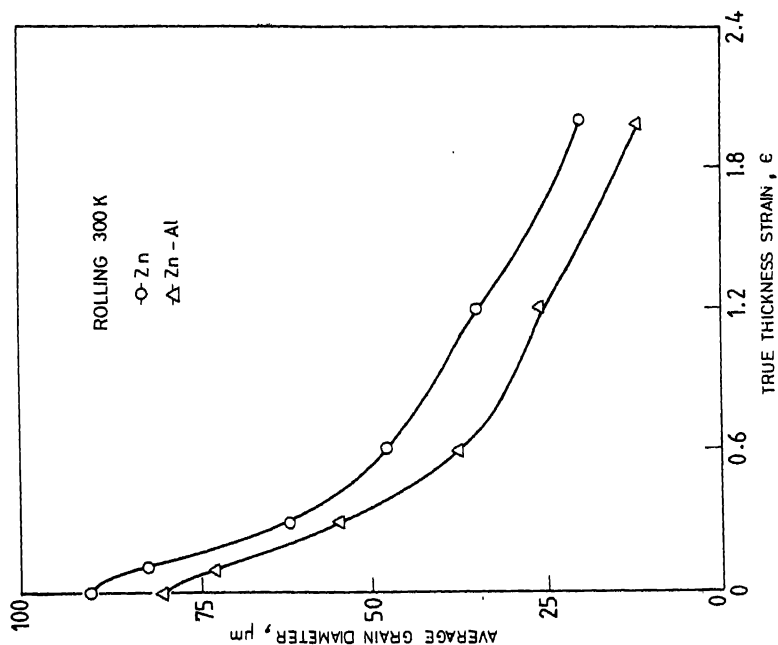


Figure 4. Variation of average grain diameter with true thickness strain.

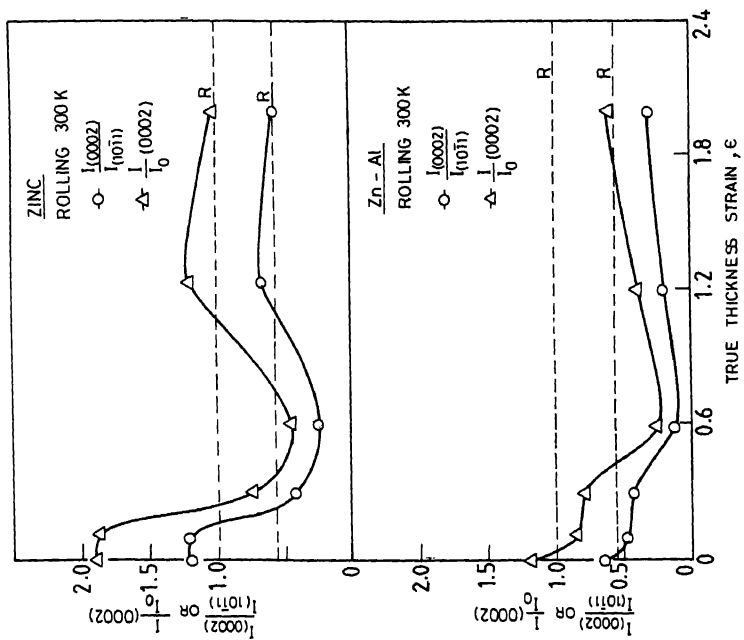


Figure 5. Variation of  $(I_{0002}/I_{10\bar{1}1})$  or  $(I/I_0) (0002)$  with true thickness strain.

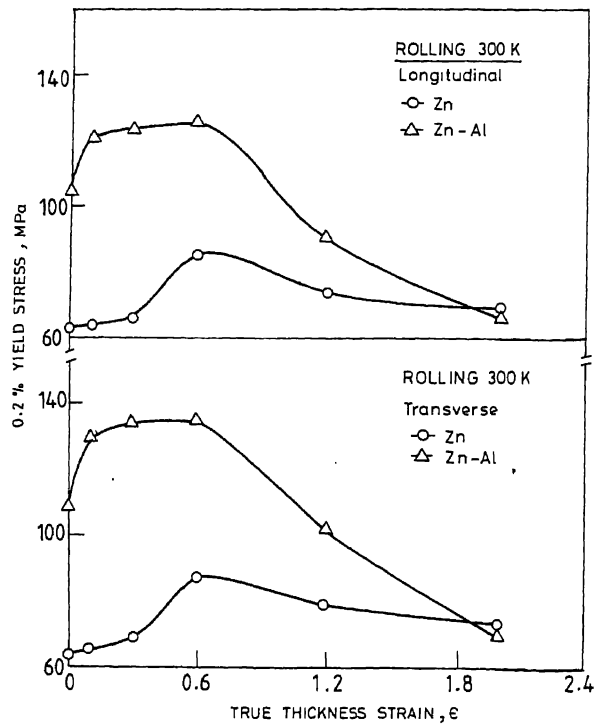


Figure 6. Variation of yield stress with true thickness strain.

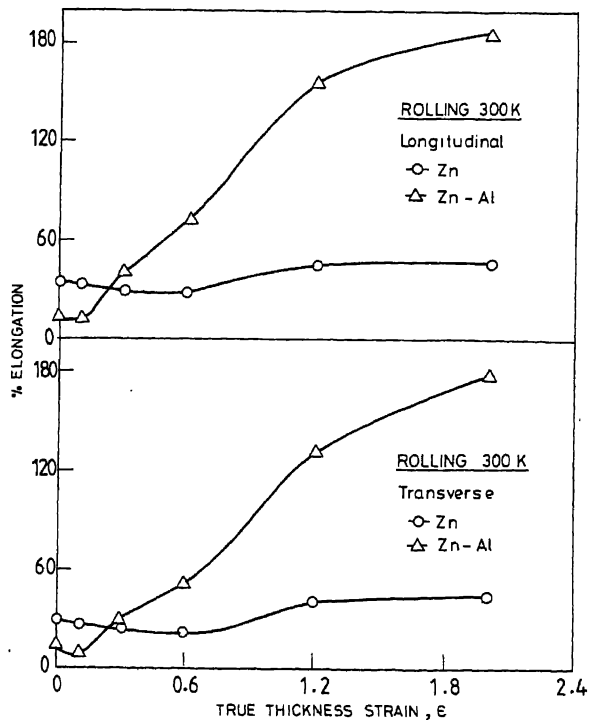


Figure 7. Variation of % elongation with true thickness strain.

direction. In either direction, the yield stress increases with true thickness strain initially and then decreases beyond a certain strain. UTS also shows a similar behaviour. The tensile elongation to fracture is shown in figure 7. In general, whenever there is an increase in yield stress, a decrease in elongation is recorded. Transverse samples show slightly lower elongations at all strains. At large thickness strains, the alloy exhibits high elongation to fracture. The fracture mode in Zn and Zn-Al varies with true thickness strains (figure 8). In the initial stages of deformation, the material exhibits cleavage fracture. With increasing strain, the fracture shows a mixed mode i.e., cleavage and ductile, while at higher deformations only ductile fracture is observed. By contrast, cadmium shows ductile fracture at all strains.

The present data on zinc show an increase in yield strength with deformation without much loss in ductility. This is in conformity with the observation made on different materials in earlier studies (Young and Sherby 1973; Naziri and Pearce 1969). However, in the present work, the yield stress decreased at higher strains and the elongation increased. Since a significant texture is not observed, the grain size effect on the mechanical properties is stronger in both zinc and the alloy. In figure 9, the yield strengths measured on warm-rolled Zn and Zn-Al are tested for the validity of the Hall-Petch equation  $\sigma = \sigma_0 + K \cdot d^{-1/2}$  where  $\sigma$  is the yield strength,  $d$  is the grain diameter and  $\sigma_0$  and  $K$  are constants. The relationship is found to hold only above a certain grain size. The decrease in flow stress and increase in elongation below the critical grain size

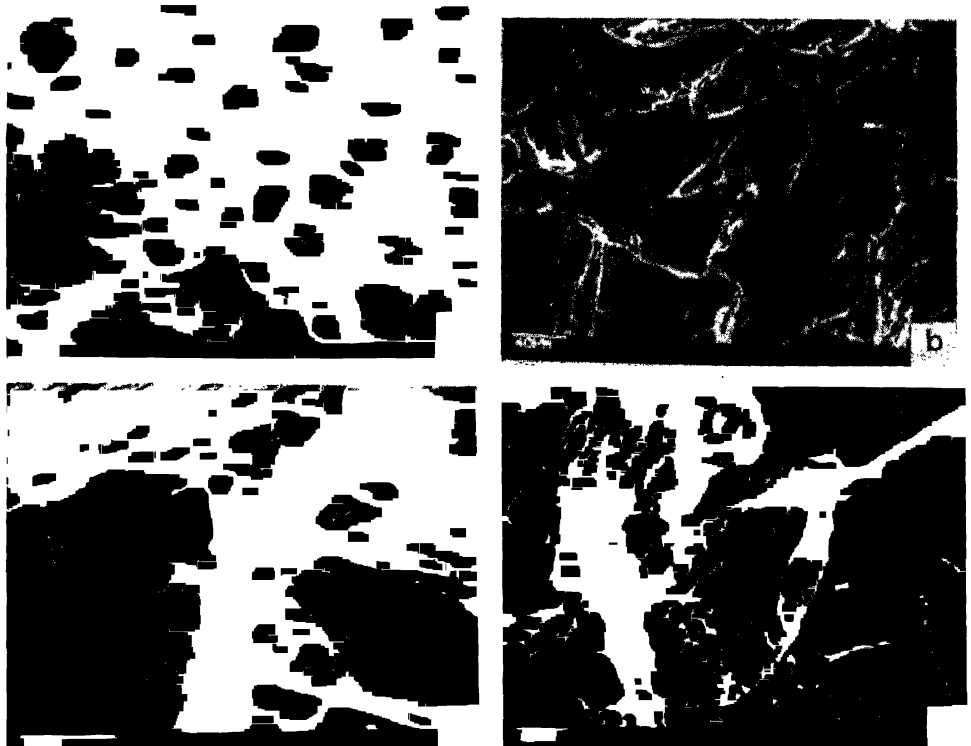


Figure 8. Scanning electron micrographs of fracture surfaces (a) Cd,  $\epsilon = 1.83$  (ductile). (b) Zn-Al,  $\epsilon = 0$  (cleavage). (c) Zn-Al,  $\epsilon = 0.1$  (mixed mode). (d) Zn-Al,  $\epsilon = 0.3$  (mixed mode).

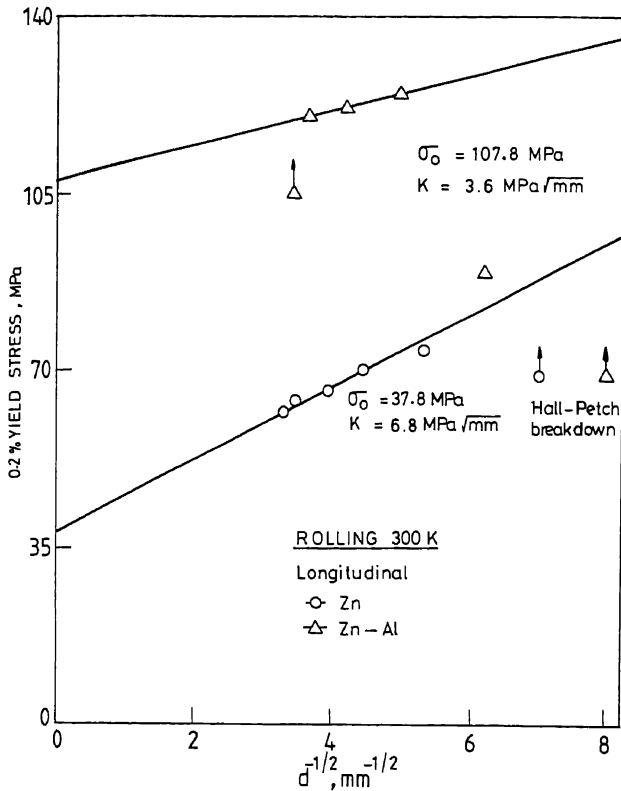


Figure 9. Yield strength-grain size relation.

must involve a change in dominant deformation mechanism and has been attributed in the literature to the onset of superplasticity (Ecob and Ralph 1983). The very small grain sizes produced at larger thickness strains are indeed conducive for superplastic behaviour. In fact, Zn-Al has shown a steep increase in elongation to fracture at higher warm working strains (figure 7). Similar behaviour has been noticed by Ecob and Ralph (1983) in a Zn-0.1 Al-0.05 Mg alloy. The scatter in the experimental results and the small range of grain size make the determination of the Hall-Petch constants difficult. However, the values estimated for zinc,  $\sigma_0 = 37.8 \text{ MPa}$  and  $K = 6.8 \text{ MPa}/\sqrt{\text{mm}}$ , are in good agreement with those from an earlier work on zinc (Prasad *et al* 1974).

#### 4. Conclusions

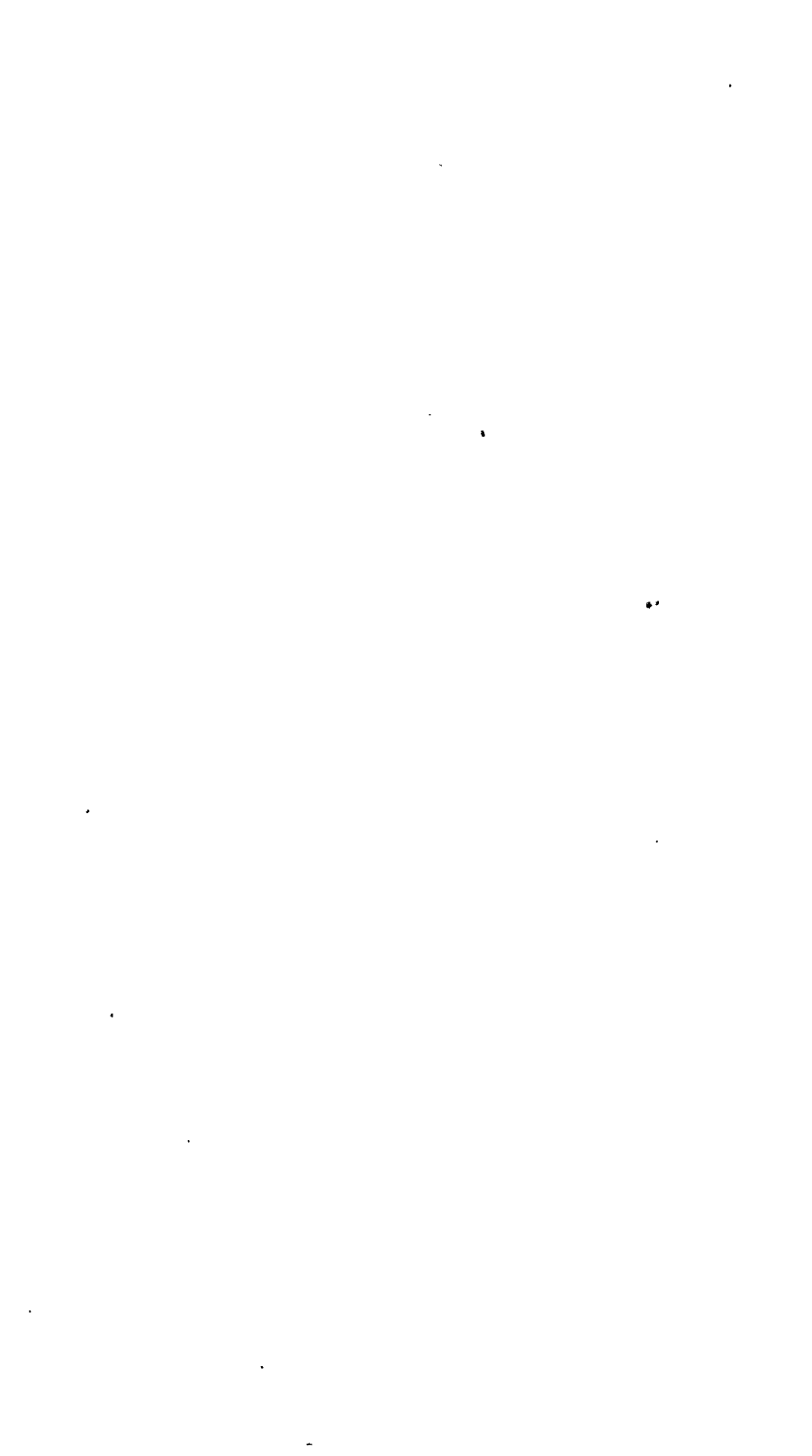
- (i) Warm extrusion enhances the strength of cadmium with no significant loss in ductility. The increase in strength is due to strong unfavourable basal texture i.e., the fibre axis is [0001].
- (ii) In zinc and Zn-0.35 Al alloy, the grain size decreased continuously with increase in true thickness strain in rolling. The grain size in the alloy is smaller than in the metal at all strains.

(iii) Only a weak texture is observed in zinc and Zn-Al and the grain size has a greater effect on the mechanical properties of these materials. The Hall-Petch equation is obeyed above a certain grain size. At finer grain sizes near-superplastic behaviour is observed.

(iv) Cadmium failed in a ductile manner at all extrusion strains. In zinc and zinc alloy, there is a continuous change in fracture mode with thickness strain. The materials failed by cleavage at small deformations, by mixed mode at intermediate deformations and by completely ductile mode at higher strains.

## References

- Bly D L, Sherby O D, Young C M and Mischchenkov 1973 *Met. Sci. Eng.* **12** 41  
Ecob N R and Ralph B 1983 *Metal Sci.* **17** 317  
Hsu S-E, Edwards G R, Shyne J C and Sherby O D 1977 *J. Mater. Sci.* **12** 131  
Naziri H and Pearce R 1969 *Scripta Metall.* **3** 811  
Prasad Y V R K, Madhava N M and Armstrong R W 1974 *Proc. Fourth Bolton Landing Conference on Grain Boundaries in Engineering Materials* (Baton Rouge: Claitor's Publishing Division) p. 67  
Prasad Y V R K 1984 *Trans. Indian Inst. Met.* **37** 399  
Yegneswaran A H, Prasad Y V R K and Raman K S 1978 *Metall. Trans.* **A9** 1311  
Young C M and Sherby O D 1973 *J. Iron Steel Inst.* **211** 640



# Proceedings of the symposium on COMAMRI

## FOREWORD

Computer modelling has many important applications in several areas of metallurgical research and industries, e.g. on-line control of metallurgical processes, design of components, plants and furnaces, prediction of materials behaviour under conditions which are difficult to be simulated by experiment, phase diagram calculations, simulation of radiation damage in materials, on-line data acquisition and data processing etc. Research in these areas has acquired impetus recently in our country by virtue of increased availability of computers and due to a need to modernize the industries by utilizing the potential of digital computers. However, there was no forum where the work done in this area could be presented and discussed. In view of this, a need was felt to organize a symposium to review the state-of-art of the developments made in the field of computer utilization in metallurgy and to provide an opportunity for a close interaction between the scientists and engineers working in this field. Therefore, the Materials Science Committee of the Board of Research in Nuclear Sciences, Department of Atomic Energy organized a two-day National Symposium on "Computer Modelling and Applications in Metallurgical Research and Industry (COMAMRI)" at BARC Bombay on 14-15 March 1985. The symposium was spread over five technical sessions dealing with computer modelling and applications in the areas of nuclear fuel element behaviour, phase diagrams and phase stability, iron and steel industry, design and performance, simulation studies, image analysis and data processing. About 200 delegates from India and abroad participated in the symposium. A panel discussion held at the close of the symposium identified several important areas for future work and made suggestions for better interaction between the scientific workers in this field. Some of the points noted during panel discussion emphasized the need for (a) development of application-oriented computer models for on-line control of chemical and metallurgical processes, (b) development of sensors for high temperature use for the measurement of parameters such as pressure, temperature, flow rate etc. (c) holding short term courses on computer modelling techniques, (d) setting up of a National Code Centre, and (e) assisting the industries in intelligent use of computers.

The National Organising Committee decided to publish the symposium proceedings as a special issue of the Bulletin of Materials Science with a view to provide a wide circulation of the technical information contained in the invited talks and contributed papers presented at the symposium. Out of a total of 25 technical presentations made at the symposium, 17 are included in this volume. These papers cover a wide range of applications of computer modelling in metallurgy and materials science. To our knowledge, this is the first published document in our country containing a collection of papers on this topic and we are confident that it will be very useful to the scientists and engineers working in this field.

We wish to express our thanks to Prof. R. Vijayaraghavan of TIFR and Shri D. N. Sah, the Convener of Symposium on COMAMRI, for their strenuous efforts in reviewing and editing of the papers contained in this volume.

C. N. R. Rao  
Editor of Publications  
Indian Academy of Sciences

P. R. Roy  
Chairman, Materials Science Committee  
B.R.N.S., B.A.R.C.

1

1





## Computer models for fuel element behaviour

J R MATTHEWS

Theoretical Physics Division, AERE Harwell, UK

**Abstract.** Over the past 20 years computer modelling of fuel performance has developed into a well-established procedure, which has been valuable in the understanding and the improvement of fuel rod behaviour. The range of computer models presently applied to cylindrical ceramic fuels is reviewed. A critical appraisal is made of the numerical techniques used for mechanical and thermal analysis. The necessity for benchmark calculations is emphasized and various approaches for model validation are discussed. A number of special topics are chosen for deeper discussion. These include: improved description of cladding deformation and the estimation of failure; the analysis of stress concentrations in the cladding; fission gas analysis; and chemical modelling. Finally some speculation is made on the future of fuel rod modelling.

**Keywords.** Computer modelling; nuclear fuels; oxide fuels; deformation; failure; heat transfer; fission products; fission gases.

### 1. Introduction

This paper will give a very personal view of the subject of fuel element computer modelling. It will look critically at the development of computer programs for the simulation of the behaviour of cylindrical fuel rods containing ceramic fuel under normal and accident conditions. On this basis particulate fuels, metal fuels and cermet fuels will not be considered. To limit the scope somewhat, the behaviour of individual fuel rods will be discussed and the subject of rod-to-rod interactions or fuel rod interactions with other structural components will not be covered.

The development of computer models for fuel performance has its origins in the mid-1960s when, at a number of centres, heat transfer and fuel rod mechanics calculations were coupled for the first time. The best known of these early models is CYGRO, which laid out the structure that future models followed (Freidrich 1965). During the next five years there was an explosion of activity when almost every research centre in the USA, Japan and Western Europe produced its own fuel performance model; for a list of the models of this period see Matthews (1972). Some of the names of the computer codes written at that time are still used, such as SATURN, COMETHE, LIFE and CYGRO, but the methods used within them have in general been greatly improved.

During the 1970s there was a growing interest in reactor safety and many of the codes were extended for use in accident calculations. There was also an interest in producing more detailed codes that permitted the study of microstructural processes within the fuel and its cladding. More recently the decline of nuclear power plant ordering in the USA has limited the number of active centres in that country. Interest has remained strong in Western Europe and Japan and there have also been encouraging developments in Eastern Europe, Latin America and India. For recent reviews of water reactor fuel element modelling for performance and safety studies see Gittus (1982, 1984).

The content of fuel behaviour codes varies enormously and they range from very simple empirical models with the minimum of computational framework to complex detailed calculations including many physical and chemical sub-models. The simpler codes tend to be aimed at the fuel of a single reactor type, or even a single fuel variant within that type. The more physically based codes are often applied to a wide range of fuels. This is not surprising as most power reactors use fuel of similar configuration: i.e. a cylindrical metal cladding tube filled with cylindrical  $\text{UO}_2$  or  $(\text{U}, \text{Pu})\text{O}_2$  pellets. This is the case for fast breeder reactors, the UK advanced gas cooled reactor, the pressurised water reactor, the boiling water reactor and the various heavy water reactors.

## 2. Range of fuel behaviour codes

It would be impossible in this short paper to list all the current fuel codes and not much would be gained without a reasonably detailed assessment of each. However it is worth looking at the range of models and classifying them with a few selected examples. Most models attempt to represent a fuel rod by assembling a series of transverse slices or zones and connecting them loosely by pin pressure, axial loading conditions and the coolant heat transfer (see figure 1). This is often referred to as the  $1\frac{1}{2}$ -dimensional approximation. A number of codes use two-dimensional finite-element analyses to investigate specific aspects of behaviour such as clad interaction with pellet "hour-glassing" or local stress concentrations near cracks, e.g. SAFENR (Chhatre *et al* 1983) or MIPAC (Ichikawa *et al* 1980). The modelling of whole pin behaviour however is wasteful because the local stress concentrations occur on a scale that is too small to be usefully covered. Often such calculations are done by coupling with a  $1\frac{1}{2}$ -dimensional code.

The  $1\frac{1}{2}$ -dimensional codes fall into a number of types. There are simple performance codes that do not have complicated mechanics models, but concentrate on temperature calculation and the development of fuel restructuring and fission gas release, e.g. the US fast reactor code SIEX (Dutt and Baker 1975) and the UK thermal reactor code MINIPAT (Hughes *et al* 1982). Such simple codes are also often used to supply the starting conditions for accident analysis codes, i.e. FRAPCON (Berna *et al* 1980). Then there are detailed performance codes that include descriptions of the deformation of both the fuel and cladding by creep and plastic flow, as well as thermal and restructuring calculations, e.g. the UK code FRUMP (Wilmore and Matthews 1979), the Argentinian code BACO (Harriague *et al* 1980) and the Indian code PROFESS (Sah and Venkatesh 1984). These codes also have some limited transient capability. The most complex are extremely versatile, e.g. URANUS (Preusser and Lassmann 1983) which can be applied to oxide or carbide fuel, water or fast breeder reactors, transient or steady state, and in deterministic or probabilistic modes. Similarly the US LIFE-4 code (Stephen *et al* 1977) has been issued in transient, water reactor and carbide versions in addition to the fast breeder performance form it was originally written in. The COMETHE code (van Vliet and Meulemeester 1980) should also be mentioned as it has been widely used for analysis of performance and mild transients on water reactor and fast breeder fuel both in its country of origin and by EPRI in the USA.

In going to the field of safety analysis the range of codes is bridged by the TRAFIC code (Matthews 1984), which has the complete range fuel performance models, but also special modules for analysis of accident conditions. These include models for sodium boiling, molten fuel motion within the fuel pin, fuel ejection from the pin and a

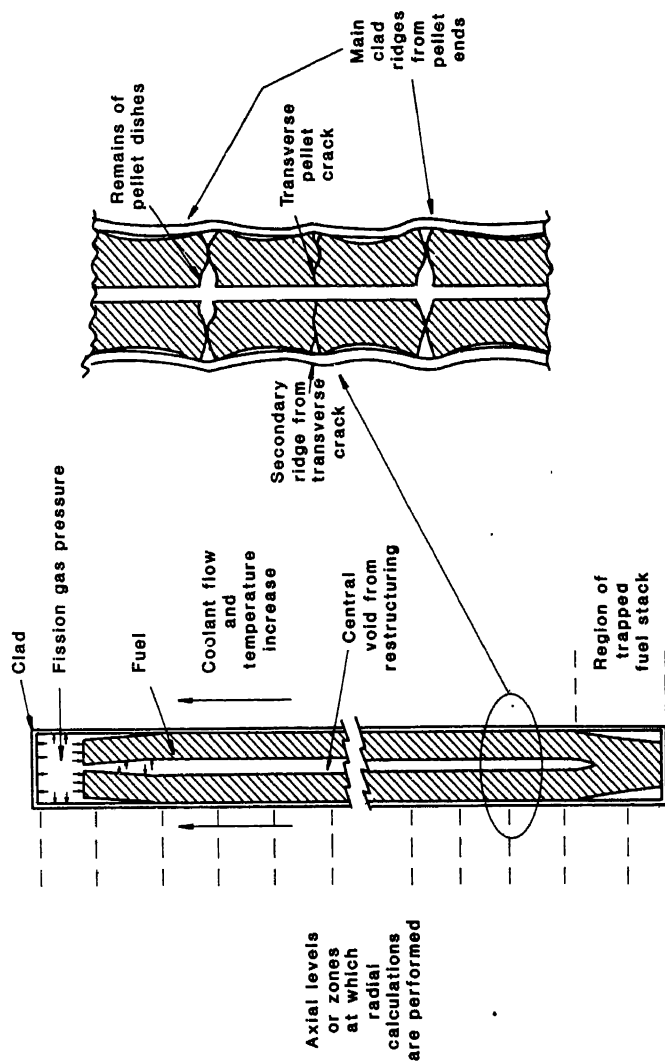


Figure 1. Schematic illustration of how a series of one-dimensional calculations (in the radial direction) are coupled, via coolant heat transfer axial loading and pin internal pressure. Causes of axial stress concentrations are also shown; the stack-trapping effect and clad ridging from pellet hour-glassing.

transient fission gas model (Matthews *et al* 1985). More specific accident models concentrate on the aspects of behaviour which are inherent in the type of fuel being studied. The fuel pin modelling within these codes is often simplified, as the main objective of the calculation is the blockage of coolant channels, the thermo-hydraulic problem and changes in the fuel rod configuration. For water reactors the most comprehensive code is FRAP-T6 (Seifken 1983). On the fast breeder reactor side the French Physura code (Melis 1982) and the US code SAS-4A (Wider *et al* 1982) probably have the widest range of models. Most of the fast reactor models have recently been compared on a common test problem (Cacciabue *et al* 1982).

In addition to the whole pin models there are separate models that deal with a specific aspect of fuel rod behaviour. Many of these models can be coupled to whole pin models, although they are uneconomic for routine use. One example is fission gas behaviour analysis with codes such as GRASS and FASTGRASS (Rest 1979). Another is the detailed deformation analysis of Zircaloy and 316 stainless steel using the MATMOD programs (Schmidt and Miller 1981; Miller and Sherby 1977).

### 3. The philosophy of fuel behaviour modelling

Fuel rod behaviour modelling is one of the first examples of a complex physical system being simulated on the computer. For this reason it is worth examining the philosophy of modelling laying down some general principles to guide more effective future work.

First of all let us consider why such computer codes need to be constructed, rather than simpler calculations on specific aspects of behaviour such as temperature, fission gas release or cladding deformation. The reason is one of self-consistency. All aspects of the fuel behaviour are intimately connected. Take the example of fuel temperature. Fuel temperature is very sensitive to the size and condition of the fuel-cladding interface. Changes in the fuel temperature cause changes in the fuel size from thermal expansion and hence the size of the fuel-cladding gap and its heat transfer coefficient. Similarly release of fission gas from the fuel, which is sensitive to fuel temperature, alters the purity of the rod-filling gas, which changes the gas heat transfer coefficient and hence the fuel temperatures. Such interconnections make some sort of comprehensive fuel-rod model essential to the understanding of its behaviour. On a wider front whole pin models are also required to study the interactions with the coolant thermal and hydraulic behaviour. For the fast breeder reactor this is extended for safety analyses to calculation of the interactions with the reactivity of the reactor core.

The applications of fuel behaviour computer models are varied and it is essential to construct a model with appropriate characteristics. The following guidelines are worth adopting.

- (i) The accuracy of the calculation should be sufficient. Methods should be chosen to give adequate accuracy, but the use of error control which is more stricter than necessary is inefficient.
- (ii) The code should use sub-models which have consistent levels of approximation. It is no use coupling a sophisticated fission gas model or detailed finite-element model to a code which is basically incompatible.
- (iii) No short-cuts should be taken on stability. The adding of extra models without proper coupling to avoid instabilities has led to problems in many codes.

- (iv) The code should be constructed in modular form to make the addition of sub-models easy. This is not a trivial problem when stability is to be maintained.
- (v) The main methods used in the code and all the sub-models should be verified (benchmarked) against standard or closed-form solutions. There has been at least one case of a major fuel-model being found to be at fault after several years of application.
- (vi) All the controlling processes should be identified and included in the code. This is not so easy and is the key to effective modelling.
- (vii) Computer codes should be identified by their materials properties, data-sets as well as their sub-models. Confusion often occurs because the data-set used was not clearly identified.
- (viii) If empirical correlations are used as sub-models care should be taken that the correct assumptions were used when making them. This is an easily forgotten problem, e.g. when correlating gap conductance against fuel relocation the same models for fuel expansion and cracking should be used in making the correlations as in the code in which it is to be used; otherwise the effect could be included twice.

When constructing models, a decision has to be made on the degree of mechanistic detail which should be included in the code. Some codes are phenomenological but the processes identified are described by empirical correlations of the macroscopic processes. In this case the code itself can be calibrated by means of free parameters in the models. In practice this approach has not been very successful. The models can give a good description of the fuel-rod behaviour within the range of the data-base, but outside the deviations can be unsatisfactory. Such codes add little to the understanding of the system. A more satisfactory approach is to restrict empirical correlation to processes that can be evaluated by separate experiment. If the code then gives bad predictions it means that some controlling process or interaction has been omitted. Fuel behaviour codes for design purposes or for use as part of a larger thermo-hydraulics or accident code, do not need detailed physically based sub-models. Codes used for experiment interpretation should be based on sub-models with a sound physical basis. Detailed modelling is very valuable in determining what the controlling processes are, and ensuring that simpler models have identified ranges of application.

#### **4. Methods for thermal and mechanical calculations**

The number of numerical methods for solving the basic heat transfer and fuel rod mechanics problems is almost as many as there are fuel codes. These, however, break down into three basic techniques on closer examination. Numerical approximations are required because most of the properties controlling behaviour are sensitive to temperature and to other physical variables which are functions of position. The three techniques are: (i) the finite difference approximation, where the differential equations for the system are approximated by difference expansions; (ii) the finite element approximation, where trial functions representing the variables being calculated are made to fit the differential equations of the system approximately over limited regions and then the whole system is made self-consistent; and (iii) the use of analytical or semi-analytical solutions to represent the behaviour over rings of the material which are then made self-consistent over the whole system. There are a host of variations on these

methods by taking different orders of difference approximation, integration techniques, orders of trial function and the choice of variables to represent the system. Currently there is a move towards the use of finite element methods because of the ease with which the variation in properties over the system can be accommodated. Finite element methods tend to be simpler to formulate, but care has to be taken when interpolating values from the solutions as the values taken from the trial functions can sometimes be misleading at positions other than integration points.

The heat transfer problem within the fuel pin presents few problems, even taking account of transients, apart from where melting takes place. Care has to be taken to ensure that enthalpy is conserved when fixing the position of the melting front (Matthews 1979).

The description of the mechanical behaviour of the fuel rod is a much more difficult problem. One of the main difficulties arises from the very large variation in creep properties in the fuel, because of the sensitivity of creep to temperature. The creep strength of the fuel can vary typically by 10 orders of magnitude in a highly rated fuel design, in going from the cooler outer fuel regions dominated by irradiation creep to the hot plastic centre. This caused many problems in early models. One standard solution to the problem was to partition the fuel, above a somewhat arbitrary temperature, into a plastic zone where all shear stresses are relaxed. Despite this, the time-steps taken by the codes were often unacceptably small. One method of overcoming this problem was to extrapolate the total strains calculated by the codes to the next time-step and then solve for the stresses at the end of the time-step to enable a better estimate of the creep strain to be obtained (Jankus and Weeks 1970). This method works well for many cases and especially where the strain increment is controlled by a change in temperature or a swelling increment which is a weak function of the stress in the system. The method, however, breaks down in some circumstances and particularly for the case of the creep of the cladding tube by fission gas pressure (Nimo and Ogawra 1980). The only sound solution is to use a method which has a strong implicit component and is guaranteed stable. The Crank-Nicholson or Euler backward approximations are adequate for most applications, but the problem of dealing with nonlinearities in the response of the system has to be faced.

The simplest method of linearising the problem is to use the Newton-Raphson approximation. Many workers have avoided implicit solutions and the use of the Newton-Raphson method because they interfered with the modular nature of the code and were complicated to implement. Recent work has shown that this need not be the case (Matthews 1983) and the TRAFIC code is fully modular and uses a fully implicit method of solution. One aspect to be careful of is the treatment of fuel hot-pressing and stress-dependent fuel swelling. Some codes take care to deal with the problem of fuel creep, but then find there are stability problems when a new fuel densification or swelling model is added to the code. The same criteria should be applied to the calculation of fuel volume changes as those used to implement creep deformation.

There are many other problems associated with the fuel-rods mechanics calculation, and it is worth quickly listing a few. Fuel strains are often large, even if cladding strains are small, and care must be taken to make the deformation account for finite strains. In some cases the plastic strains in the fuel or clad are very large compared with the level of elastic strain in the system. Some finite element techniques become inaccurate in this situation and an additional degree of freedom should be introduced into the solution to avoid this (Hermmann 1965). Fuel cracking is an important factor in determining the

fuel-cladding gap and reducing the fuel-cladding mechanical interaction (FCMI). Some models calculate no FCMI prior to the closure of the cracks. This will underestimate the cladding strains and as will be seen below the cracks play an important role in fuel-rod failure. Some codes neglect transverse cracks, lying normal to the axial direction; in doing so they will underestimate fuel relocation and miss important effects on fuel stack axial-loading (see figure 1).

Finally the interaction between the thermal and mechanical calculations must not be forgotten. In most codes the thermal calculation is performed first for a time-step followed by the mechanics, with iterations if necessary. This can result, when the fuel-cladding gap is small, in an oscillating instability. This problem is only encountered occasionally and can be countered by introducing some form of numerical damping into the calculation. A more rigorous approach would be to couple the thermal and mechanical calculations; a possibility that we will return to in the discussion on future developments.

## 5. Special topics

In this section we discuss recent developments and requirements in a few selected areas of interest.

### 5.1 *Improved models for cladding deformation and failure*

The deformation and rupture of fuel-rod cladding presents perhaps the greatest challenge to fuel behaviour modelling. Up to now cladding deformation has been included in codes by simple correlations on creep and plastic deformation, supplemented by corrections for radiation hardening and empirical representation of irradiation creep, the growth of Zircaloy or void swelling of steels in fast breeder reactors. In fact the dimensional changes that a metal alloy will undergo under an applied stress and a simultaneous exposure to fast neutron damage are extremely complex. Figure 2 illustrates this. Some of the effects have been recently reviewed by Bullough (1984). Irradiation changes the dislocation structure, alters the distribution of both the major and minor constituents of the alloy and produces a range of embrittling effects. Added to this is the effect of the presence of fission products adjacent to the cladding inner surface.

To make sense of these interactions new techniques are required. Simple semi-empirical models can be constructed, which are based on the actual physical processes taking place. In this way several processes like irradiation creep, dislocation structure evolution, growth, void swelling and thermal creep can all be interlinked (Bullough *et al* 1981). The model can then be used as the basis of an empirical correlation, but with the minimum of free variables. This should increase the ability of modelling to reproduce the observed behaviour of fuel-rods and remove some of the present discrepancies.

### 5.2 *Stress concentration and failure*

Failure of thermal reactor fuel rods is often dominated by local stress concentrations. There are two main sources; the ends of pellets (see figure 1) and the regions of cladding

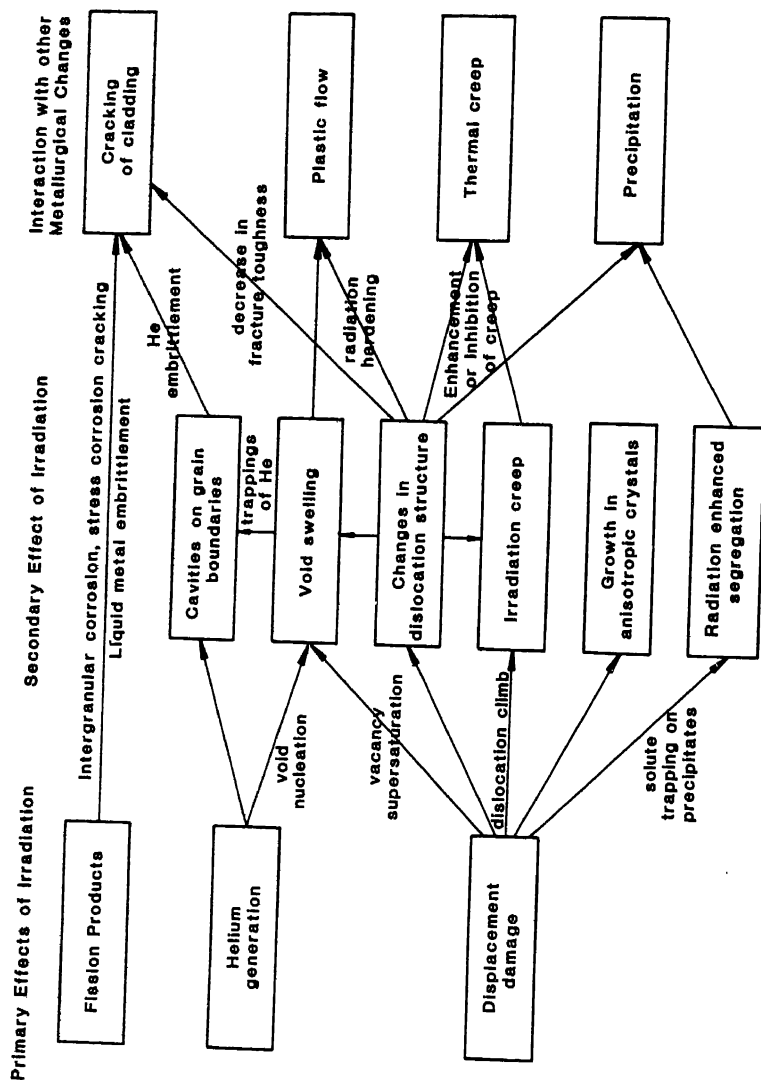


Figure 2. Illustration of the effects of radiation damage and how they interact with the metallurgical characteristics of engineering alloys.



adjacent to radial cracks in fuel pellets (see figure 3). The most widely used model for stress concentrations over cracks is that of Gittus (Gittus *et al* 1970; Gittus 1972). Although found useful in practice this model has several deficiencies. The stress equilibrium conditions in the cladding shell are not soundly based. To do this properly is difficult and complicated and much of the elegance of Gittus' solutions is lost (Tromans and Matthews 1984). The treatment neglects bending moments in the cladding, which are often dominant (Nakatsuka 1981). The solutions to the friction problem should have a stuck region and a sliding region, in order to satisfy cyclic boundary conditions (figure 3). The stress concentration extends only over the region of the cladding over the crack and where sliding takes place (figure 4). The extent of the sliding region is sensitive to the external coolant pressure. The size of the stress concentration on the cladding inner surface is greatly underestimated by the thin shell model, as the through wall stress gradients are large. Only rigorous two-dimensional calculations are able to fix the inner stress accurately. The stress concentration is over-

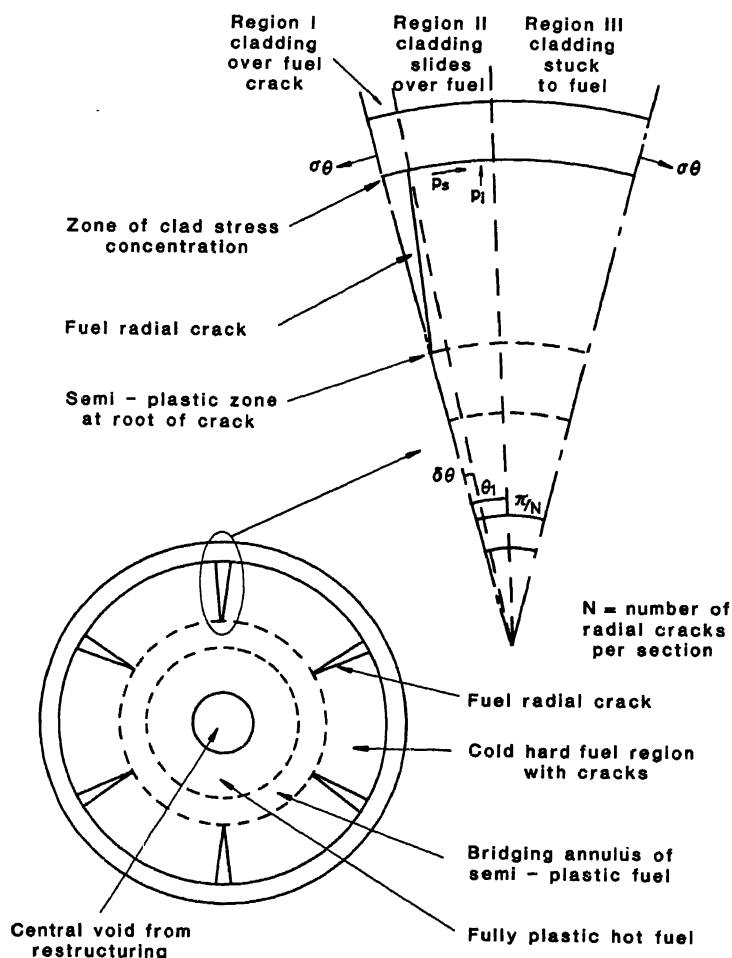


Figure 3. Schematic illustration of the relationship between fuel radial cracking, fuel structural zones and stress concentrations in cladding.

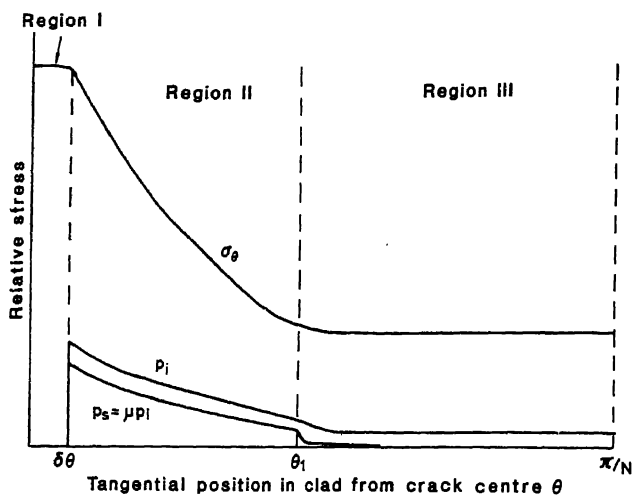


Figure 4. Schematic illustration of clad mean hoop stress, normal pressure and shear traction, vary with angular position, when sliding and sticking occur between fuel and cladding.

estimated, however, because the reaction of the fuel is neglected. Even if the fuel adjacent to the cladding is hard, the fuel at the crack roots may be plastic and reduce the load on the cladding (Stephen *et al* 1979). The stress concentration at the cladding does not arise from the radial displacement of the fuel, but from the relative opening of the cracks, which occurs from thermal expansion on power increases and from differential swelling (Tromans and Matthews 1984). Finally the simple shell model does not include other sources of internal stress in the cladding, such as thermal stresses, which will be important when nonlinear deformation is taking place.

Many of these remarks also apply to simple analyses of cladding interactions with the pellet ends. The lesson is that this is an example where simple one-dimensional calculations are inadequate. Guidelines for the effect of clad-ridging from pellet interactions or stress concentrations over cracks, should be carried out with the appropriate two-dimensional finite-element model of the fuel and clad together.

These aspects of local cladding stress concentrations are not so important in fast reactor fuel because: the coolant pressure is low; the cladding is relatively thick and strong; the fuel is more highly rated and softer with many more radial and transverse cracks; and stress corrosion cracking has not yet been recognized as a problem. The main problem with strain concentrations in fast reactor cladding arises from local temperature perturbations or hot-spots. These occur because of the high surface heat fluxes on fast reactor fuel-rods and because of the problem with fast neutron induced swelling of the cladding causing distortions of the fuel bundle.

### 5.3 Fission gas behaviour

Fission gas swelling and release are important processes in determining fuel pin behaviour both under normal and accident conditions. Swelling is an important factor in FCMI and can also cushion rapid clad loading in overpower transient conditions.

Fission gas release is also important as many fuel designs have limited plenum volumes to accommodate fission gases. Fast reactor fuel normally releases a high proportion of its fission gas inventory during normal high rating operation and many aspects of fuel behaviour in accidents are controlled by the retained gas in the fuel after melting (Wood *et al* 1984).

The processes involved in a complete description of fission gas behaviour are many and their interactions are complex (see figure 5). A recent review describes how these processes are handled in the OGRES and NEFIG models which form part of the TRAFIC code (Matthews and Wood 1984). There are, however, some indications that there may be some deficiencies in our understanding of fission gas behaviour in transients. Experiments both in the laboratory (Zimmermann 1984) and in-pile (Sontheimer *et al* 1984) give higher gas releases than anticipated. This was also evident in the DCOM blind problem that was reviewed at the Bowness-on-Windermere Conference in 1984. Current mechanistic fission gas models predict that on mild temperature transients most of the gas would be trapped in small bubbles and fission gas release would be small. There are several rival explanations of this discrepancy: the bubbles may become over-stuffed with gas and reject gas atoms, leaving a higher concentration in solution (Brearley *et al* 1984); grain boundary sweeping may be more important than previously thought (van Vliet and Billaux 1984); or the amount of gas held on the grain boundaries may be higher than previously thought. All of these explanations have their deficiencies. The observation of the growth of a coarse bubble population after high temperature annealing, suggests that what were previously thought to be small bubbles were in fact vacancy clusters which disappear before they trap gas (Matthews *et al* 1985). Hopefully these questions will be resolved in the next few years, as several experimental programmes are being conducted at present to provide more microstructural information.

#### 5.4 Chemical modelling

Perhaps the most neglected aspect of fuel behaviour modelling has been fuel chemistry. Models so far have at most simple descriptions of oxygen redistribution within the fuel or simple calculations of caesium and plutonium migration. Chemical effects are very important in determining fuel-rod failure and better estimates of the fuel-cladding gap inventory of fission products and their chemical state are required. This is not a trivial problem as the number of chemical species and compounds involved is large. Among the problems are: calculations of the amounts of free iodine and tellurium as a function of linear rating and burn-up; good definition of the oxygen potential to the fuel-cladding interface, which is particularly important for stainless steel clad rods; definition of the location and chemical state of caesium throughout the fuel rod; and good description of oxygen and plutonium redistribution during irradiation.

### 6. Future developments

This paper has looked at a range of important topics in the subject of fuel behaviour modelling, but there are insufficient space to discuss many other aspects that are just as important. For example we have neglected to discuss fuel restructuring processes and the behaviour of fuel rods during extreme accident conditions. To finish the paper it is worth briefly commenting on possible future trends.

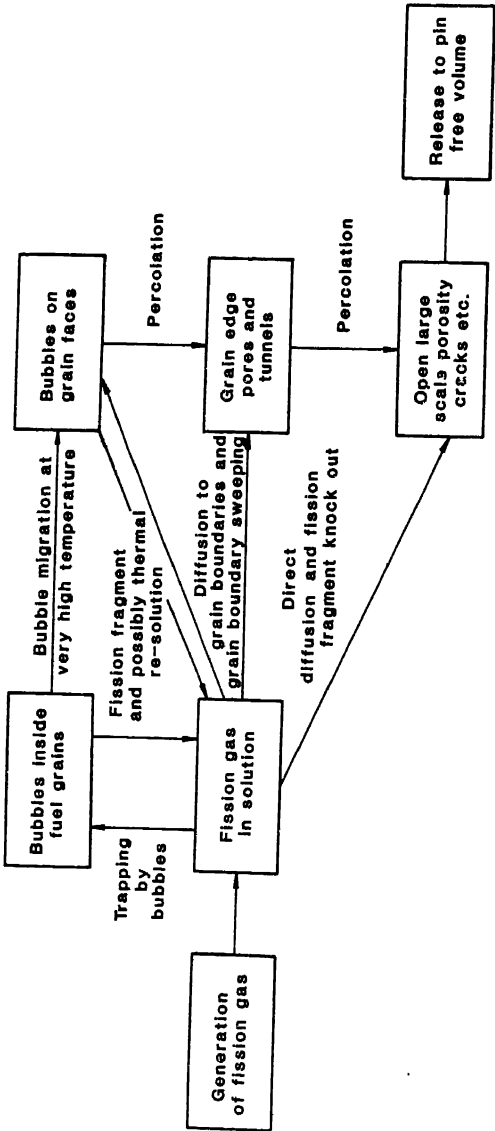


Figure 5. Illustration of the interactions between the various mechanisms governing fission gas release and swelling.

The most important new development is the introduction of the supercomputers (Duff 1984), which have recently increased the computing power available to fuel rod modellers by two orders of magnitude. This will enable calculations that were previously too expensive and long-running to be tackled. Two- and three-dimensional models of fuel behaviour will be introduced in cluster behaviour or even whole-core models. The basic  $1\frac{1}{2}$ -dimensional fuel pin code will still have an important place in modelling, but it will be more frequently supplemented by two-dimensional finite-element calculation to study stress concentrations and non axysymmetric effects. In particular it will be possible to couple the mechanics and thermal calculation directly for the whole fuel rod. This will remove the remaining sources of instability in the code and with proper vectorization of the calculation could be achieved with little cost penalty. It will then be possible to have improved treatments of coolant boiling, molten fuel motion and complex axial loadings coupled to the code. The TRAFIC code is being rewritten in this form at the moment for use on the Harwell CRAY computer.

## References

- Berna G A *et al* 1980 FRAPCON-2. A computer code for the calculation of steady-state thermo-mechanical behaviour of oxide fuel rods NUREG/CR-1845
- Brearley I R *et al* 1984 *Eur. Appl. Rept., Nucl. Sci. Technol.* **5** 1159
- Bullough R 1984 in *Proc. Conf. on dislocations and properties and real materials*, London (Royal Society, Metals Society)
- Bullough R *et al* 1981 *J. Nucl. Mater.* **103**, **104** 1263
- Cacciabue P C *et al* 1982 Comparative analysis of a hypothetical 0.15/sec transient overpower accident in an irradiated LMFBR core using different computer models. Commission of the European Communities Report EUR 8018EN
- Chatre A G 1983 *Trans. 7th Int. Conf. on Structural Mechanics in Reactor Technology, Chicago*, paper C3/6
- Duff I S 1984 in *Proc. Conf. on Vector and Parallel Processors in Computation and Science II*, Oxford, UK
- Dutt D S and Baker R B 1975 SIFEX, A correlation code for the prediction of LMFBR fuel performance, Hanford Report HEDL-TME 74-55
- Freidrich C M 1965 CYGRO Stress analysis of the growth of concentric cylinders, Bettis Atomic Power Labs. Report WAPD-TM-514
- Gittus J H *et al* 1970 *Nucl. Appl. Technol.* **9** 40
- Gittus J H 1972 *Nucl. Eng. Des.* **18** 69
- Gittus J H 1982 International experience and status of fuel element performance and modelling for water reactors, Springfield Nuclear Power Development Labs. Report ND-R 604(S)
- Gittus J H 1984 *Proc. Specialists Meeting on Water Reactor Fuel Element Performance Computer Modelling*, Bowness-on-Windermere, UK, IAEA report IWGFPT/19, p. 15
- Harriague S *et al* 1980 *Nucl. Eng. Des.* **56** 83
- Hermann L R 1965 *A.I.A.A.* July 3, 1896
- Hughes H *et al* 1982 Fuel rod behaviour during transients Part 1. Description of codes, Springfield Report ND-R-702(S)
- Ichikawa M *et al* 1980 *Proc. Specialists Meeting on Fuel Element Performance Computer Modelling*, Blackpool, UK, IAEA Report IWGFPT 7 p. 216
- Jankus V Z and Weeks R W 1970 LIFE 1 - A Fortran IV computer code for the prediction of fast reactor fuel element behaviour. Argonne Report ANL 7736
- Matthews J R 1972 *Adv. Nucl. Sci. Technol.* **6** 67
- Matthews J R 1979 *Trans. 5th Int. Conf. on Structural Mechanics in Reactor Technology, Berlin*, paper D7/1
- Matthews J R 1983 *J. Nucl. Eng. Des.* (to be published)
- Matthews J R 1984 The basis of the TRAFIC fuel performance code, Harwell Report AERE-R. 10818 (rev.)
- Matthews J R *et al* 1985 *The application of the TRAFIC fuel performance code to steady and transient conditions*, BNEW Conf. on Nuclear Fuel performance, Stratford-upon-Avon, UK
- Matthews J R and Wood M H 1984 *Eur. Appl. Res. Rept., Nucl. Sci. Technol.* **5** 1685

- Melis J C et al 1982 *PHYSURA – A code for the interpretation of safety experiments*, Int. Topical Meeting on LMFBR Safety and Related Design and Operational Aspects, Lyon, France p. II-45
- Miller A K and Sherby O D 1977 *Development of the Materials Code MATMOD (constitutive equations for Zircaloy)* EPR NP 567
- Nakatsuka M 1981 *Nucl. Eng. Des.* **65** 197
- Nimo H and Ogawa S 1980 Proc. Specialists Meeting on fuel element performance computer modelling, Blackpool, UK, IAEA Report IWGFPT/7 paper 29
- Preusser T and Lassmann K 1983 *Trans. 7th Int. Conf. on Structural Mechanics in Reactor Technology*, Chicago, paper C4/3
- Rest J 1979 in *Proc. 2nd Int. Seminar on Mathematical/Mechanical Modelling of Reactor Fuel Elements* (Berlin: Bundesanstalt für Materialprüfung)
- Sah D N and Venkatesh D 1984 Proc. Specialists Meeting on Water Reactor Fuel Element Performance Computer Modelling, Bowness-on-Windermere, UK, IAEA Report IWGFPT/19 p. 237
- Schmidt C G and Miller A K 1981 *Res. Mechanica* **3** 109, 175
- Seifken L J 1983 *Trans. 7th Int. Conf. on Structural Mechanics in Reactor Technology*, Chicago paper C3/1.
- Sontheimer F et al 1984 *J. Nucl. Mater.* **124** 33
- Stephen J D et al 1977 *The LIFE code system for analysis of oxide fuel pin thermal/structural behaviour*. *Trans. Advanced LMFBR Fuels Topical Meeting*, Tucson, Arizona
- Stephen J D et al 1979 Proc. Specialists Meeting on Theoretical Modelling of LMFBR Fuel Pin Behaviour, Fontenay-aux-Roses, France, IAEA Report IWGFR/31, p. 139
- Tromans N J and Matthews J R 1984 (unpublished work)
- Van Vliet J and Billaux M 1984 Proc. Specialists Meeting on Water Reactor Fuel Element Performance Computer Modelling, Bowness-on-Windermere UK, IAEA Report IWGFPT/19 p. 151
- Van Vliet J and de Meulemeester E 1980 *Nucl. Eng. Des.* **56** 71
- Wider H U et al 1982 *Status and validation of the SAS4A accident analysis code system*. Int. Topical Meeting on LMFBR Safety and Related Design and Operational Aspects, Lyon, France p. II-13
- Wilmore D and Matthews J R 1979 *FRUMP – A physically based fuel model*. *Proc. Conf. on Fast Breeder Reactor Fuel*, Monterey, California, p. 665
- Wood M H et al 1984 *Eur. Appl. Res. Rept., Nucl. Sci. Technol.* **5** 1515
- Zimmermann H 1984 *Eur. Appl. Res. Rept., Nucl. Sci. Technol.* **5** 1349

## Computer calculations of phase diagrams

A K MALLIK

Indian Institute of Technology, Bombay 400 076, India

**Abstract.** The thermodynamic route of establishing phase diagrams is a relatively recent activity, considering that till about the fifties most phase diagrams were determined by the measurement of certain physical property or quantitative microscopy using light optics or x-ray diffraction. The thermodynamic formalism used by Kaufman and Bernstein is explained and illustrated with examples of the development of hypothetical binary phase diagrams. The calculation of ternary phase diagrams can begin with the binary phase diagram data as a first approximation. However, to calculate a reasonably accurate ternary phase diagram a certain amount of ternary solution data is necessary. Various empirical equations have been proposed in the literature to express ternary thermodynamic data.

Calculation of simple ternary isothermal sections is illustrated with the examples of Mo-V-W and Cd-Sn-Pb systems. The numerical techniques which involve the differentiation of thermodynamic parameters with respect to composition get more involved with the number of components becoming 3 or more. A simpler approach has been applied recently to find the minimum position on the Gibbs free energy surface.

**Keywords.** Phase diagrams; solution models; binary diagrams; lattice stability; ternary diagrams; miscibility gap; hill climbing technique.

### 1. Introduction

A phase diagram represents the domains of stable phases under a given condition of composition and pressure. Till the fifties, phase diagrams were approached mainly through experimental measurements which did not involve thermodynamics, using either direct phase estimation methods or indirect methods. The indirect methods involve measurement of a physical property or rather a change thereof like dilation, resistivity etc or thermal analysis. The thermodynamics of phase equilibria represented, till about the fifties, a parallel activity with few bridges or connections with the former approach. As the stable state of a phase is associated with the minimum of free energy, it should be possible to link up thermodynamics with phase diagram, provided of course that an adequate representation of thermodynamic data is available. The reason why this link-up got going only after the fifties is perhaps due to the lack of communication between the physical chemists and physical metallurgists.

The relatively slow progress of the thermodynamic route to phase diagram has also been caused by the lack of data even for binary systems, not to speak of ternary systems. On the contrary, by the use of a physical property, phase diagrams can be determined directly. A natural consequence has been that "the number of systems for which phase diagrams have been determined is much greater than that for which the thermodynamic properties of solution phases are known" (Ansara 1979).

The situation has changed considerably during the last twenty five years and more and more phase diagrams are being generated from thermodynamic data. Not only does it provide considerable saving of labour but the exercise gives a deeper insight to the systematics of phase diagrams. The calculations have become feasible with the

availability of computers and appropriate numerical methods. Further, with the availability of sophisticated instruments, it has become possible to generate more precise and reliable thermodynamic data. Some of the early usage of thermodynamic data for the calculation of phase diagrams were by Wagner (1954), White *et al* (1977) and Hardy (1953). Extensive contributions have been made subsequently by Kubaschewski and Barin (1974), Kaufman and Bernstein (1970), Hillert (1970), Gaye and Lupis (1975), Chart *et al* (1975) and Pelton and Thompson (1975) on the calculation of phase diagrams. To conserve space, the mathematical formalism used in the present paper will be that of Kaufman and Bernstein, except where mentioned otherwise.

## 2. Phase equilibrium

At a given temperature and pressure, the maximum number of coexisting phases in a system formed by  $m$  components is equal to  $(m + 1)$  phases according to the phase rule. If there are  $j$  phases in the system, the partial free energy of a given component is the same for each phase under equilibrium conditions (figure 1). The condition can be expressed by a set of nonlinear equations such as

$$\bar{G}_i^{(1)} = \bar{G}_i^{(2)} = \bar{G}_i^{(j)}, \quad (1)$$

for  $i = 1$  to  $m$ th element and  $1$  to  $j$ th phase. The equilibrium for a system is represented by the condition that the molar free energy is minimum.

## 3. Solution models

For an alloy system  $A-B$ , in which  $X$  represents the atom fraction of  $B$  and which exhibits two competing phases  $\alpha$  and  $\beta$ , the free energies of each phase may be represented by the following equations

$$G^\alpha = (1 - X)G_A^\alpha + XG_B^\alpha + RT[X \ln X + (1 - X) \ln (1 - X)] + {}^E G^\alpha, \quad (2)$$

$$G^\beta = (1 - X)G_A^\beta + XG_B^\beta + RT[X \ln X + (1 - X) \ln (1 - X)] + {}^E G^\beta. \quad (3)$$

In (2) and (3)  $G_A^\alpha$  and  $G_B^\alpha$  are the free energies of the  $\alpha$  and  $\beta$  modifications of the element  $A$ , while  $G_A^\beta$  and  $G_B^\beta$  are the free energies of the  $\alpha$  and  $\beta$  modifications of the element  $B$ .

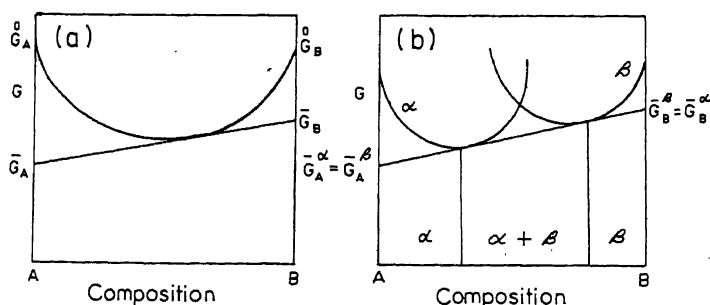


Figure 1. Common tangent construction to define equilibrium between two phases.



The excess free energies of mixing of the  $\alpha$  and  $\beta$  phases are expressed as  ${}^E G^\alpha$  and  ${}^E G^\beta$  and  $X$  is the atom fraction of  $B$ .

The partial molar free energies of  $A$  and  $B$  in an alloy containing  $X$  atom fraction  $B$  are  $G_A$  and  $G_B$  respectively and are defined as

$$\bar{G}_A = G - X \frac{\partial G}{\partial X}, \quad (4)$$

$$\bar{G}_B = G + (1 - X) \frac{\partial G}{\partial X}. \quad (5)$$

By differentiating  $G^\alpha$  and  $G^\beta$  in (2) and (3) with respect to  $X$ , one can obtain the expressions for  $\bar{G}_A^\alpha$ ,  $\bar{G}_B^\alpha$ ,  $\bar{G}_A^\beta$  and  $\bar{G}_B^\beta$  i.e. the partial free energy terms. Further applying the concept of equality of chemical potentials as defined in (1), the following general equations can be obtained.

$$\Delta G_{A \rightarrow B}^\alpha + RT \ln \left( \frac{1 - X_\beta}{1 - X_\alpha} \right) = \left( {}^E G^\alpha - X \frac{\partial {}^E G^\alpha}{\partial X} \right) - \left( {}^E G^\beta - X \frac{\partial {}^E G^\beta}{\partial X} \right), \quad (6)$$

$$\Delta G_{B \rightarrow A}^\beta + RT \ln \frac{X_\beta}{X_\alpha} = \left( {}^E G^\alpha + (1 - X) \frac{\partial {}^E G^\alpha}{\partial X} \right) - \left( {}^E G^\beta + (1 - X) \frac{\partial {}^E G^\beta}{\partial X} \right). \quad (7)$$

When  ${}^E G = 0$ , the solution is said to be ideal and the above equations can be considered simplified. Unfortunately, the ideal solution model is too simplistic and few solutions whether liquid or solid conform to it. A wide range of solution models have been suggested in the literature. However, in the present paper only the regular solution model will be used, which postulates that the  ${}^E G$  term is equal to the enthalpy of mixing  $\Delta H_m$ . For the regular solution model

$${}^E G^\alpha = E_\alpha X(1 - X), \quad (8)$$

$${}^E G^\beta = E_\beta X(1 - X), \quad (9)$$

where  $E_\alpha$  and  $E_\beta$  are the interaction parameters for the  $\alpha$  and  $\beta$  phases respectively. Equations (6) and (7) can now be simplified as

$$\Delta G_{A \rightarrow B}^\alpha + RT \ln \left( \frac{1 - X_\beta}{1 - X_\alpha} \right) = E_\alpha X_\alpha^2 - E_\beta X_\beta^2, \quad (10)$$

$$\Delta G_{B \rightarrow A}^\beta + RT \ln \frac{X_\beta}{X_\alpha} = E_\alpha (1 - X_\alpha)^2 - E_\beta (1 - X_\beta)^2. \quad (11)$$

#### 4. Numerical methods

Once the phase stability parameters  $\Delta G_{A \rightarrow B}^\alpha$ ,  $\Delta G_{B \rightarrow A}^\beta$  and the interaction parameters  $E_\alpha$  and  $E_\beta$  are estimated with some confidence, (10) and (11) can be solved by appropriate iterative procedures to obtain values for  $X_\alpha$  and  $X_\beta$ , which make it possible to locate  $\alpha|\alpha + \beta|\beta$  phase boundaries. Rudman (1969) used a trial and error method by assigning arbitrary values to the unknown  $X_\alpha$  and  $X_\beta$ , so that the whole range of composition is covered. The values are then selected which best fit the equations. Kaufman and Bernstein (1970) used a method based on the Newton-Raphson iteration technique,

which will be briefly described here. This method involves selecting a couple of approximate equilibrium values for  $X_\alpha$  and  $X_\beta$  as a starting point, from which more precise solutions are obtained using approximation computed as under

$$X_{\beta(n+1)} = X_{\beta(n)} - \frac{1}{(X_{\beta n}, X_{\alpha n})} \begin{vmatrix} F(X_{\beta n}, X_{\alpha n}) & F_{X_\alpha}(X_{\beta n}, X_{\alpha n}) \\ G(X_{\beta n}, X_{\alpha n}) & G_{X_\alpha}(X_{\beta n}, X_{\alpha n}) \end{vmatrix} \quad (12)$$

$$= X_{\beta(n)} - \frac{\Delta X_{\beta(n)}}{J(X_{\beta n}, X_{\alpha n})}$$

$$X_{\alpha(n+1)} = X_{\alpha(n)} - \frac{1}{J(X_{\beta n}, X_{\alpha n})} \begin{vmatrix} F_{X_\beta}(X_{\beta n}, X_{\alpha n}) & F(X_{\beta n}, X_{\alpha n}) \\ G_{X_\beta}(X_{\beta n}, X_{\alpha n}) & G(X_{\beta n}, X_{\alpha n}) \end{vmatrix} \\ = X_{\alpha(n)} - \frac{\Delta X_{\alpha(n)}}{J(X_{\beta n}, X_{\alpha n})}, \quad (13)$$

$$\text{where } F(X_\beta, X_\alpha) = 0, G(X_\beta, X_\alpha) = 0, \quad (14)$$

and the Jacobian

$$J(X_\beta, X_\alpha) = \begin{vmatrix} F'_{X_\beta}(X_\beta, X_\alpha) & F'_{X_\alpha}(X_\beta, X_\alpha) \\ G'_{X_\beta}(X_\beta, X_\alpha) & G'_{X_\alpha}(X_\beta, X_\alpha) \end{vmatrix}. \quad (15)$$

It can be seen that differentiation of thermodynamic properties with respect to the atomic fraction is involved and this becomes more difficult and involved as the number of components increases. They also have to be repeated for all expressions relating the free energy and atom fraction.

## 5. Binary diagrams

The utility of the Newton-Raphson iterative technique can be illustrated with the development of hypothetical binary phase diagrams reported by Balakrishna and Mallik (1979, 1980) and which are shown in figure 2. To begin with, simple isomorphous phase diagram is calculated when the solution is considered ideal. As the interaction parameters  $E_L$  and  $E_\alpha$  are increased for the purpose of computation, the solidification range is enlarged and a solid state miscibility gap appears. Between the values of 4250 and 4500 cal/mol for the interaction parameters, an invariant peritectic reaction appears. By further raising the interaction parameter magnitude, a monotectic type reaction can be brought out.

The scope of the calculation can be illustrated further to deal with components exhibiting allotropy. Figure 3 shows the development of phase diagrams involving three phases, liquid ( $L$ ) and solid phases ( $\alpha$ ) and ( $\beta$ ), with varying combinations of the interaction parameters  $E_L$ ,  $E_\alpha$  and  $E_\beta$ . With small positive values of the interaction parameters, the equilibrium between  $L/\beta$  and  $\beta/\alpha$  phases correspond to azeotropic minima. Increase of the value for  $E_\alpha$  leads to the development of a miscibility gap in the  $\alpha$  region. A further increase of  $E_\alpha$  leads to the formation of an eutectoid reaction.

By suitably varying the relative magnitudes of the interaction parameters a wide range of phase diagrams can be generated. In real systems, however, the solid state interaction parameter will be greater than that of the liquid state. Further, by the very

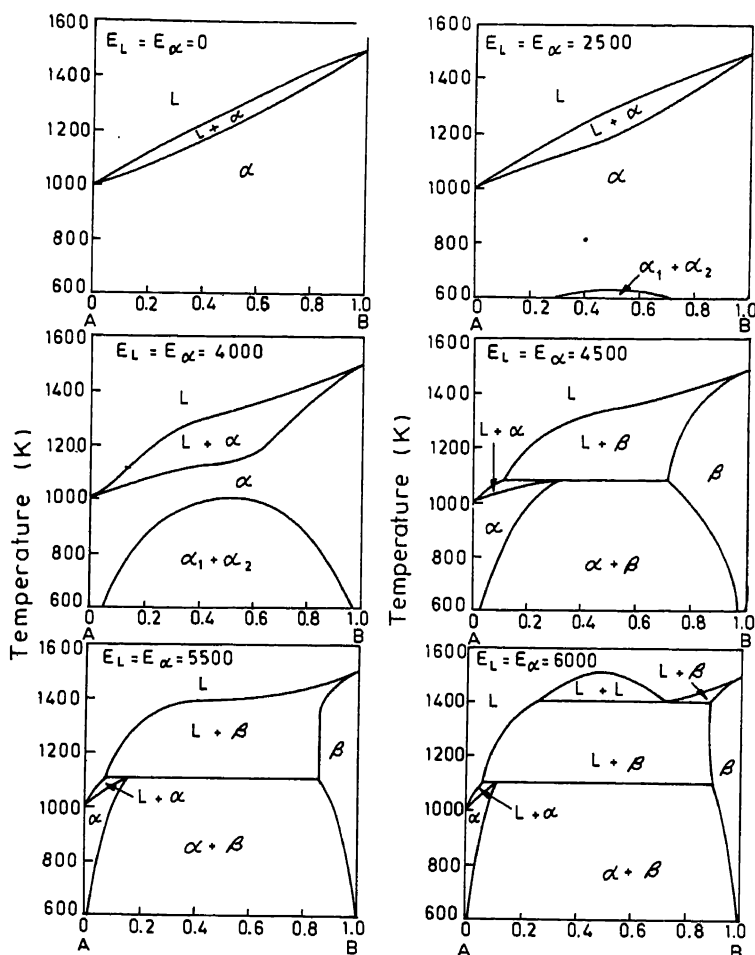


**Figure 2.** Development of peritectic and monotectic reactions with use of highly positive interaction parameters (cal/mol) (Balakrishna and Mallik 1979).

nature of formalism, the miscibility gaps so obtained are symmetrical. To deal with intermediate phases, in addition to the terminal phases, additional data are needed. Since there are many phase diagrams for which limited or very little thermodynamic data are available, it is quite possible to apply (10) and (11) in reverse, wherein the interaction parameters can be calculated using known values of  $X_\alpha$ ,  $X_\beta$  at the phase boundaries. The computed interaction parameters can be compared and averaged with available thermodynamic data to replot the phase diagram with more reliability (Appendix 1).

## 6. Lattice stability

To be able to determine the form of the free energy-composition curves, two important data are needed, which are the lattice stability and the free energy of mixing. While the

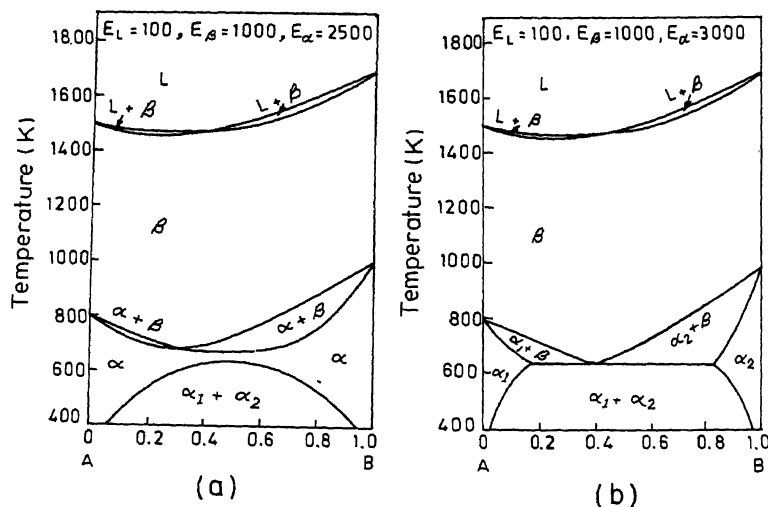


Figure 3. Development of phase diagrams with allotropy of both the components (interaction parameters in cal/mol) (Balakrishna and Mallik 1980).

relative shape of the curves is controlled by the latter, the former i.e. the lattice stability value controls the relative position of the free energy curves. Kaufman and Bernstein (1970) estimated the phase stability values for a number of elements, mainly transition metals, for different structural forms which are liquid, fcc, bcc and cph structures. The regular solution phase diagrams of 72 binary refractory metal systems were computed using the lattice stability values and computed interaction parameters.

While it would be ideal to obtain quantitative information on the lattice stability values from first principle formalism, such calculations are extremely difficult. If a metal exhibits polymorphism at atmospheric pressure, the free energy difference can be estimated from the measurements of the latent heat of transformation, heat of fusion and the volume changes attending the transformations. In cases where no polymorphism is displayed at one atmosphere, phase transformations at high pressures can be studied. The T-P diagram can be used with thermodynamic and volumetric data pertaining to one atmosphere to obtain the lattice stability expressions for various polymorphs. The analysis of phase diagram can enable the estimation of phase stability. For example, the lattice stability of hcp, fcc and bcc forms of Zn has been estimated through individual analysis of Al-Zn, Cu-Zn and Ag-Zn phase diagrams. Kaufman and Nesor (1978) and Kaufman (1978) published an extensive range of lattice stability values for a wide range of elements on coupled phase diagrams and thermochemical data.

## 7. Empirical equations for solutions

For the calculation of phase diagrams it is necessary to express the thermodynamic properties of multicomponent phases as analytical functions of composition. If no ternary data are available, the following representation for the excess integral free

energy may be used (Kohler 1960)

$${}^E G = (1 - X_A)^2 {}^E G(BC) + (1 - X_B)^2 {}^E G(CA) + (1 - X_C)^2 {}^E G(AB) + \sum_{\substack{n \geq 1 \\ m \geq 1 \\ k \geq 1}} \phi_{nmk} X_A^n X_B^m X_C^k. \quad (16)$$

The three binary terms in (16) gives an exact representation of  ${}^E G$  in the ternary system, if the ternary solution as well as all three binary solutions are regular and the ternary terms can be set to zero. An expression for the partial property  ${}^E G_A$  corresponding to (16) may be derived by differentiation. Several other empirical equations have been proposed for expressing the thermodynamic properties of ternary systems which are shown in figure 4. Toop (1965) expressed the excess free energy of mixing for a ternary system by the following equation

$${}^E G = \left[ \frac{X_B}{1 - X_A} {}^E G_{(AB)} + \frac{X_C}{1 - X_A} {}^E G_{(AC)} \right] X_A + [(1 - X_A)^2 {}^E G_{(BC)}] X_B / X_C \quad (17)$$

The equations given by Toop (1965) and Kohler (1960) have also been used with an additional term of the form  $X_A X_B X_C (AX_A + BX_B + CX_C + D)$  to represent experimental data, the coefficients  $A, B, C$  and  $D$  being calculated from a least square analysis. Pelton and Bale (1977) represented the integral molar excess free energy  $E$  at any constant temperature for the ternary system (Bi-Cd-Zn) by a general polynomial expansion as given below

$${}^E G = \sum \phi_{nmk} X_{Zn}^n X_{Cd}^m X_{Bi}^k, \quad (18)$$

where the  $\phi_{nmk}$  are constant coefficients. Any number of terms necessary to adequately represent the system may be included. Expressions for the partial molar excess free

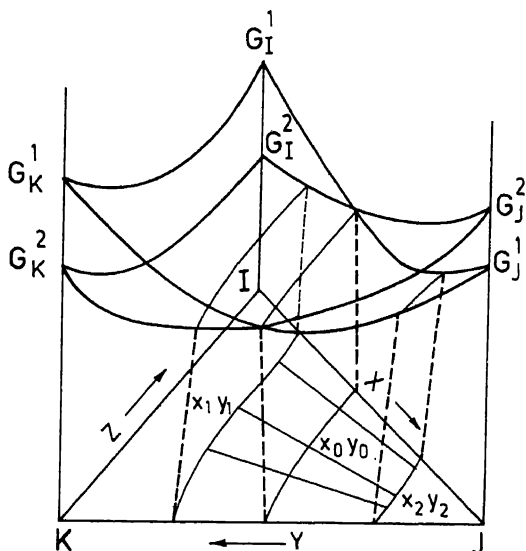


Figure 4. Free energy surfaces of competing phases in ternary system and application of the common tangent principle.

energy may be obtained by differentiation of (18). Using the above formalism Pelton and Bale (1977) calculated the phase diagrams for the Bi-Cd-Zn, Bi-Cd-Sn and Fe-Cr-Ni-O systems.

## 8. Ternary diagrams

The formalism reported for the binary system can be extended to the ternary system. The integral free energy of a single phase solution with 3 components can be expressed as (Kaufman and Bernstein 1970)

$$G[X, Y, T] = ZG_i + XG_j + YG_k + RT(Z \ln Z + X \ln X + Y \ln Y) \\ + XZ E_{ij} + YZ E_{ik} + XY E_{jk}, \quad (19)$$

where  $X, Y, Z$  are atomic fraction of elements  $J, K$  and  $I$  respectively,  $G_i, G_j, G_k$  the free energies of the pure element  $I, J, K$  and  $E_{ij}, E_{ik}$  and  $E_{jk}$  are the binary interaction parameters.

The partial free energies of  $I, J, K$  in a given phase are

$$\bar{G}_i = G - X \frac{\partial G}{\partial X} - Y \frac{\partial G}{\partial Y}, \\ \bar{G}_j = G + (1 - X) \frac{\partial G}{\partial X} - Y \frac{\partial G}{\partial Y}, \\ \bar{G}_k = G - X \frac{\partial G}{\partial X} + (1 - Y) \frac{\partial G}{\partial Y}. \quad (20)$$

The equilibria between two phases, liquid ( $L$ ) and solid ( $S$ ) can be shown schematically by the common tangent plane in figure 4, which shows the locus of points  $(X_1, Y_1)$  and  $(X_2, Y_2)$  corresponding to possible tangent points of a plane tangent to the two free energy surfaces  $G^1[X, Y, T]$  and  $G^2[X, Y, T]$ . As with the binary diagrams and equations (10) and (11), similar equations can be written for the ternary case as

$$A_i = \Delta G_i^{1 \rightarrow 2} + RT \ln (Z_2/Z_1) + (E_{ij}^2 X_2^2 - E_{ij}^1 X_1^2) + (E_{ik}^2 Y_2^2 - E_{ik}^1 Y_1^2) \\ + (\Delta E^2 X_2 Y_2 - \Delta E^1 X_1 Y_1) = 0, \\ A_j = \Delta G_j^{1 \rightarrow 2} + RT \ln (X_2/X_1) + [E_{ij}^2 (1 - X_2)^2 - E_{ij}^1 (1 - X_1)^2] \\ + (E_{ik}^2 Y_2^2 - E_{ik}^1 Y_1^2) - [\Delta E^2 Y_2 (1 - X_2) - \Delta E^1 Y_1 (1 - X_1)] = 0, \\ A_k = \Delta G_k^{1 \rightarrow 2} + RT \ln (Y_2/Y_1) + (E_{ij}^2 X_2^2 - E_{ij}^1 X_1^2) + [E_{ik}^2 (1 - Y_2)^2 \\ - E_{ik}^1 (1 - Y_1)^2] - [\Delta E^2 X_2 (1 - Y_2) - \Delta E^1 X_1 (1 - Y_1)] = 0, \quad (21)$$

$$\text{where} \quad \Delta E = E_{ij} + E_{ik} - E_{jk}. \quad (22)$$

Equation (21) is solved numerically by the Newton-Raphson iteration technique (Appendix 2).

For starting the iteration one has to choose the initial value of  $X_1$  for the independent variable and then choose the starting values of  $X_2^0, Y_1^0, Y_2^0$ . As shown in figure 5 the two binary edges  $IJ$  and  $JK$  define limits of  $X_1, Y_1$  and  $X_2, Y_2$ . The iteration is continued until it converges on a solution of  $X_2, Y_1, Y_2$ . The value of  $X_1$  is then changed slightly and the procedure is repeated using previous solutions found for  $X_1$ . The correctors

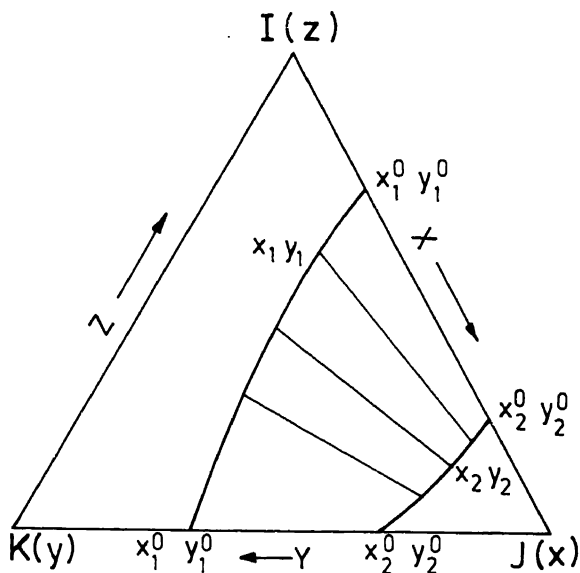


Figure 5. Computation of phase boundaries and tie lines with isothermal ternary sections from  $IJ$  edge to the  $JK$  edge.

$\Delta X_2$ ,  $\Delta Y_1$ ,  $\Delta Y_2$  in the determinant form are

$$J \Delta X_2 = \begin{vmatrix} -A_i \frac{\partial A_i}{\partial Y_1} \frac{\partial A_i}{\partial Y_2} \\ -A_j \frac{\partial A_j}{\partial Y_1} \frac{\partial A_j}{\partial Y_2} \\ -A_k \frac{\partial A_k}{\partial Y_1} \frac{\partial A_k}{\partial Y_2} \end{vmatrix},$$

$$J \Delta Y_1 = \begin{vmatrix} \frac{\partial A_i}{\partial X_2} - A_i \frac{\partial A_i}{\partial Y_2} \\ \frac{\partial A_j}{\partial X_2} - A_j \frac{\partial A_j}{\partial Y_2} \\ \frac{\partial A_k}{\partial X_2} - A_k \frac{\partial A_k}{\partial Y_2} \end{vmatrix},$$

$$J \Delta Y_2 = \begin{vmatrix} \frac{\partial A_i}{\partial X_2} \frac{\partial A_i}{\partial Y_1} - A_i \\ \frac{\partial A_j}{\partial X_2} \frac{\partial A_j}{\partial Y_1} - A_j \\ \frac{\partial A_k}{\partial X_2} \frac{\partial A_k}{\partial Y_1} - A_k \end{vmatrix},$$

where  $J$ , the Jacobian determinant is

$$J = \begin{vmatrix} \frac{\partial A_i}{\partial X_2} & \frac{\partial A_i}{\partial Y_1} & \frac{\partial A_i}{\partial Y_2} \\ \frac{\partial A_j}{\partial X_2} & \frac{\partial A_j}{\partial Y_1} & \frac{\partial A_j}{\partial Y_2} \\ \frac{\partial A_k}{\partial X_2} & \frac{\partial A_k}{\partial Y_1} & \frac{\partial A_k}{\partial Y_2} \end{vmatrix} \quad (24)$$

### 8.1 Calculated phase diagrams

Figure 6 shows the calculated isothermal section for the Mo-V-W system by Bhansali and Mallik (1984) using the above approach, for which experimental diagram is not available. All the binaries are of the isomorphous type with complete solid solubility. Both ideal and regular solution models have been used. It may be noted that while the

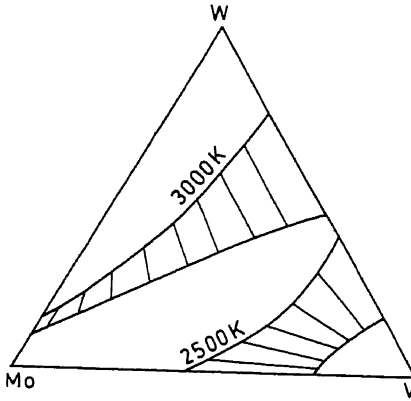


Figure 6. Calculated isothermal sections for the Mo-V-W ternary phase diagram (Bhansali and Mallik 1984).

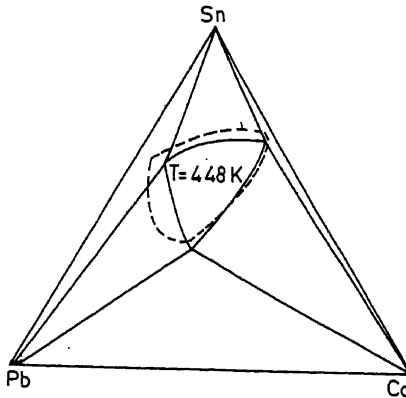


Figure 7. Calculated isothermal sections for the Cd-Pb-Sn ternary phase diagram (Bhansali and Mallik 1984) --- experimental.



ideal solution model produces almost straight liquidus and solidus lines, the regular solution model produces more realistic contours which are naturally curved.

Figure 7 shows the calculated liquidus projections for the ternary system Cd-Pb-Sn, (Bhansali and Mallik 1984) which shows one eutectic reaction at each of the binary edges. The figure also shows experimental lines obtained by thermal analysis and the match between experimental and computed lines is rather satisfactory. This is so considering that only binary phase diagram data have been used in the calculation of this diagram. Two alternatives are available. The first is to use calculated binary interaction parameters. The second is to use interaction parameters which are manipulated to produce the best fit with the binary diagram. In the above ternary phase diagrams the second alternative has been used. It is further possible to introduce ternary interaction parameters. This is where some measurements of thermodynamic data in the ternary region can be extremely useful.

## 8.2 Ternary miscibility gap

The magnitudes of the interaction parameters indicate the extent of solubility or immiscibility. Positive interaction parameter represents repulsive interaction between the two atomic species in solution. If the binary interaction parameter exceeds  $2RT$  a miscibility gap is expected, which may or may not extend to the other binary edge depending on the magnitude of the other binary interaction parameter. The problem of defining the phase boundaries is similar to the two solution phase situation. The schematic free energy surface is shown in figure 8, which shows the occurrence of miscibility gaps on  $IJ$  and  $IK$  binary edges. Equation (21) can be used with the modification that  $\Delta G_i^{1 \rightarrow 2} = 0$ ,  $E_{ij}^1 = E_{ij}^2 = E_{ij}$ . In case only one binary shows the miscibility gap the upward convexity of the free energy surface will gradually disappear as one moves from one binary edge to the other.

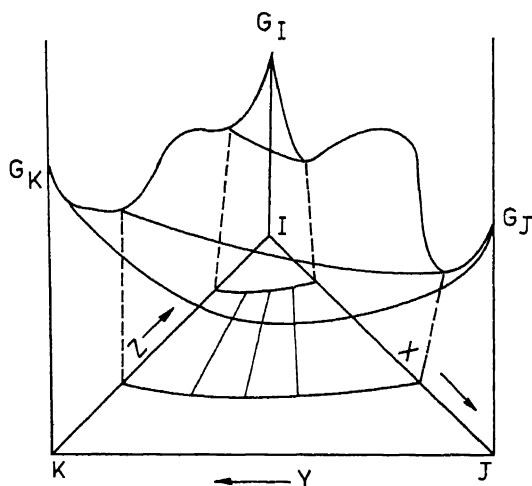


**Figure 8.** Schematic representation of the free energy surface for miscibility gaps at two binary edges.

## 9. Hill climbing technique

It has been pointed out that the differentiation of thermodynamic properties with respect to atomic fraction becomes more difficult and cumbersome as the number of components increases beyond three. The problem becomes even more difficult if there are small erroneous inflexions in the free energy curve determined from experimental observations. Nelder and Mead (1965) suggested a simplex approach which finds the minimum positions on the Gibbs free energy surface by hill climbing computational technique. In this method, the free energy of a multicomponent system is calculated at a certain number of coordinates, usually 10. The point which has the highest value of free energy is replaced by another one. The procedure is iterated until a minimum value is obtained. This technique has been used by Counsell *et al* (1971) to calculate the miscibility gap in the liquid Cd-Pb-Zn and Cd-Pb-Sn-Zn systems. The method can also be used when tables of discrete values of thermodynamic data are used in place of analytical expressions. The minimization of free energy has been tested for two-phase separation in binary, ternary and quaternary mixtures. The procedure can be used to minimize a function of  $m$  variables by comparison of the values of this function at  $m + 1$  points, followed by replacement of the point corresponding to the highest value of the function by another point. The process is continued by reflection, contraction and expansion upto the point when a minimum value is obtained.

## 10. Higher order phase diagrams

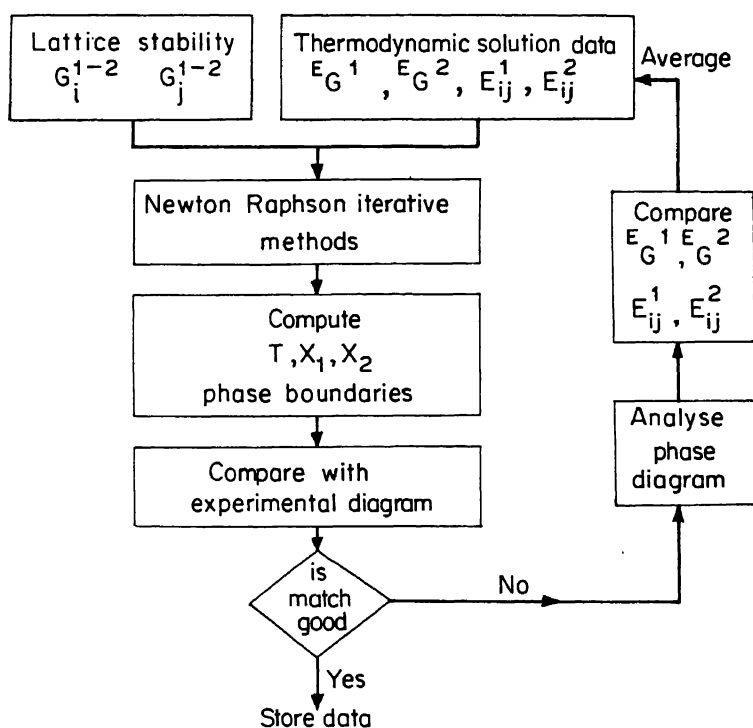
A quaternary phase diagram is usually represented as a regular tetrahedron, where the four equilateral triangular surfaces represent the 4 ternary diagrams and the six edges represent 6 binary diagrams at a given temperature. The lattice simplex method has been used (Ansara 1979) to express mathematically liquidus or solidus volumes in higher order systems. In principle, the method (Scheffe 1958; Gorman and Hinman 1962) involves constructing mathematical models, commonly polynomials, which correlate the property and composition of test alloys. To calculate the coefficients of the equations, the properties are measured according to a definite distribution within a simple lattice. Relatively few quaternary systems have been investigated in detail.

## 11. Conclusions

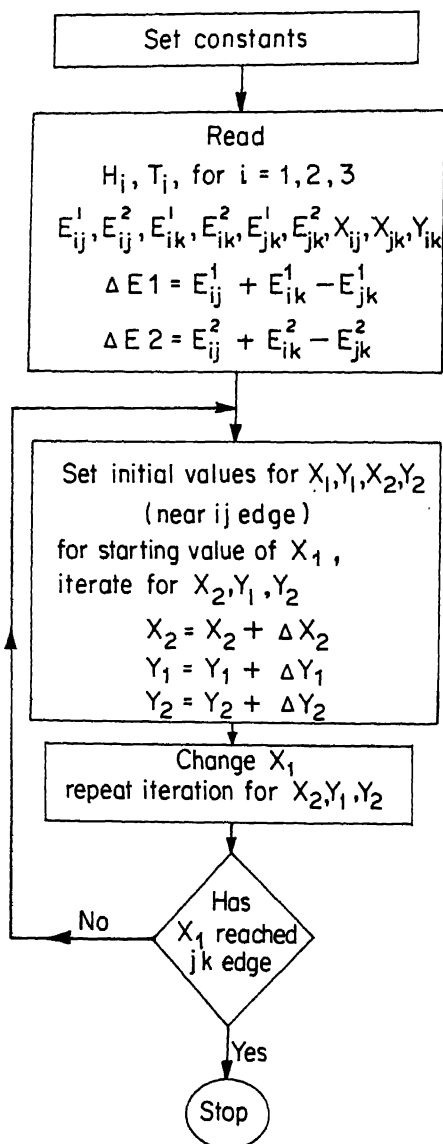
The calculation of binary phase diagrams has been actively pursued in the last 25 years. While adequate description exists for the terminal phases (bcc, fcc and hcp forms), phase diagrams with several intermediate phases can only be attempted with some experimental data about their stability. The regular solution model, notwithstanding its limitations has been used quite extensively.

For the calculation of ternary phase diagrams the starting point can be the binary system data. Analytical series expansions have been developed for representing the thermodynamic data of ternary and higher order solutions as a function of composition. A major uncertainty relates to the extension of the binary intermediate phases into the ternary regions. Asymmetrical miscibility gaps also cannot be determined without some data.

Such computational techniques which use the differentiation of thermodynamic parameters with respect to composition become more difficult beyond ternary diagrams. Thus, use of other minimization techniques, which do not involve differentiation may be more attractive. As yet, the calculation of quaternary phase diagrams has been attempted on a limited scale only.



**Appendix 1.** Flow diagram for coupling of thermodynamic data with phase diagram data for the generation of averaged phase diagram.



**Appendix 2.** Flow diagram for the iterative calculation of phase boundaries in ternary diagram isothermal sections.

## References

- Ansara I 1979 *Int. Metall. Rev.* **238** 20  
 Balakrishna S S and Mallik A K 1979 ICMS-77 Varanasi, Indian Inst. of Met, Varanasi p. 107  
 Balakrishna S S and Mallik A K 1980 *Trans. Indian Inst. Met.* **33** 155  
 Bhansali A and Mallik A K 1985 (Communicated)  
 Counsell J F, Lees E B and Spencer P J 1971 *Met. Sci. J.* **5** 210  
 Chart T G, Counsell J F, Jones G P, Slough W and Spencer J P 1975 *Int. Metall. Rev.* **20** 57

- Gaye H and Lupis C H P 1975 *Metall. Trans.* **4** 685
- Gorman L W and Hinman J E 1962 *Technometrics* **4** 463
- Hardy H K 1953 *Acta Metall.* **1** 202
- Hillert M 1970 *Phase transformations* (Ohio: Am. Soc. for Metals)
- Kohler F 1960 *Monatsh. Chem.* **91** 738
- Kaufman L and Bernstein H 1970 *Computer calculations of phase diagrams* (New York: Academic Press)
- Kubaschewski O and Barin I 1974 *Pure Appl. Chem.* **38** 469
- Kaufman L and Nesor H 1978 CALPHAD (*Computer coupling of phase diagrams and thermochemistry*) **2** 81
- Kaufman L 1978 CALPHAD (*Computer coupling of phase diagrams and thermochemistry*) **2** 117
- Nelder J A and Mead R 1965 *Comput. J.* **7** 308
- Pelton A D and Bale C W 1977 CALPHAD (*Computer coupling of phase diagrams and thermochemistry*) **1** 253
- Pelton A D and Thompson W T 1975 *Prog. Solid State Chem.* **10** 119
- Rudman P S 1969 *Advances in materials research* (New York: Interscience) Vol. 4
- Scheffe H 1958 *J. R. Stat. Soc.* **B20** 344
- Toop G W 1965 *Trans. Metall. Soc. AIME*, **233** 850
- Wagner C 1954 *Acta Metall.* **2** 242
- White J L, Orr R L and Hultgren R 1977 *Acta Metall.* **5** 747



## Computer-aided design of rolling mills

K G PANDEY

MECON (India) Limited, Ranchi 834 002, India

**Abstract.** Computers have been used for design of rolling mills since 1960s. Easy access to high speed digital computers has facilitated use of more accurate rolling theories for design work and comprehensive computer simulations have been developed for all types of mills. These simulations include optimization of roll pass sequence, calculation of roll force, torque and temperature and detailed time studies for productivity calculations. These aspects of mill simulation are examined with specific examples.

In the design of rolling mills equipment, computer-aided design has been widely used. The available software, which covers both steady state and dynamic analysis of items such as mill stands, drive systems, manipulators, cooling beds, roll cooling, and automatic gauge control systems, is reviewed with special reference to the nature of analysis and range of applications.

Computer drafting is being increasingly used by rolling mills designers for both interactive and non-interactive applications. The integration of computer graphics with the design software holds promise for improving the productivity and creativity of designers and is an active area of development in rolling mills design organizations. A specific application where such integration has been achieved is discussed.

**Keywords.** Computer-aided design; rolling mills; computer drafting; computer simulation

### 1. Introduction

Mathematical modelling and computer simulation are being widely used today both for design and control of rolling mills. Many of the complex phenomena involved in the rolling process can be understood and quantified only with the help of computer models. Computer simulation is also used to accurately predict the effect of variations in rolling process on the mill design and for optimization studies.

The earliest attempt to develop a mathematical model of the rolling process dates back to the pioneering works of Siebel (1924) and von Karman (1925). By the end of the 1950s substantial theoretical work had been done and many design methods developed. Much of the impetus for this work came from designers and builders of rolling mills. Before undertaking the detailed design of a mill it is a normal practice to compute rolling schedules to properly size the mill for a specific application. The rolling schedule shows the nature and magnitude of forces, torques and power parameters required to reduce metal of a given stock size to the final finish size. These parameters depend on the size of the mill, the reduction pattern adopted and the other conditions of rolling such as temperature, speed, tension, roll coolant etc. It is usual to evaluate several alternatives in terms of their suitability for customer requirements.

The high volume of work involved together with the complexity of various calculations has led to the widespread use of computer methods in almost every phase of rolling mills design. The present day applications of computer-aided design (CAD) may be broadly grouped into (i) simulation models for specific types of mills and (ii) programs for detailed analysis and design of individual equipment. In most of the

leading design organizations dealing with rolling mills, computer drafting is being gradually integrated with the design software.

## 2. Mill simulation

In the design of a new rolling mill the starting point is a mill simulation program for the specific type of mill i.e. slabbing and blooming mill, billet, bar and section mill, rod mill, plate mill, hot strip mill, single stand reversing and non-reversing cold mill, fully continuous tandem cold mill and skin pass mill. Broadly speaking all mill simulation programs consist of three parts for: (a) calculating the pass sequence (b) computing the roll separating force, torque and power required and (c) a time study for evaluating the productivity. Temperature calculations are also an integral part of (a) and (b) above in the simulation of hot rolling mills. These calculations constitute interacting loops that are intimately related to each other. A straight forward calculation is not possible but for purposes of discussion the four calculations will be treated separately.

### 2.1 Roll pass sequence

The various factors to be considered in the calculation of a roll pass sequence are pass geometry, roll bite, temperature and other rollability conditions, metal spread, technological limitations of reduction per pass and overall reduction, limitations arising out of mill parameters such as roll force limit and torque limit, and the requirements of mill productivity. In general the calculation of a roll pass sequence aims at maximizing the productivity of the mill without violating any of the constraints due to technology or equipment. Clearly the calculations relating to roll force, torque and power, along with temperature and productivity calculations are implicit in any scheme for computing the roll pass sequence. The resultant complexity makes this an ideal situation for the use of CAD. A few illustrative applications are discussed in detail.

**2.1a Single stand cold mill:** A cold reducing mill offers two major simplifications: temperature effects can be largely ignored and the metal spread is also negligible. Programs have been developed in which it is necessary only to define the various constraints of roll-bite angle, permissible reduction per pass and total roll force limit, mill speed, torque and power limit and available tension. The optimal reduction pattern that requires minimum number of passes is then automatically calculated. As a first step the rollability conditions are checked. The maximum draft which does not violate the constraints of bite angle and material reduction limits is then computed. With this value of draft the roll force calculation loop is referenced and the values of roll force and torque obtained are checked against the specified constraints. If any of the constraints is violated the draft is reduced and the calculation repeated. With properly defined gradients, a feasible solution is easily found.

**2.1b Dimensioning of shaped passes:** The need for accurate calculation of roll pass sequence is greater for shaped passes in that the roll grooves have to be cut according to these dimensions and any error in the grooves reflects on the quality of the finished product. The calculations are also more complex because the additional factors of metal spread and temperature assume an important role. As an illustration of the general



approach, the dimensioning of intermediate ovals with the entry and delivery squares defined will be considered. To start the iteration, some reasonable dimensions of the intermediate oval are assumed (table 1). With these assumed dimensions, the various constraints are checked. If any of the conditions is violated a gradient is computed. This gradient is used to calculate the next trial value. The iterative procedure is not prone to oscillation and normally converges within 4 to 6 trials.

## 2.2 Roll force models

The many roll force models available today may be grouped under one of two broad heads: models based on measured field data of specific energy consumption vs elongation and analytical models based on resistance to deformation vs temperature (for hot rolling) or yield strength vs reduction (for cold rolling). Used with care, both approaches give acceptable results.

The analytical models are, however, better in some ways. They can be used to calculate the roll force and torque only from the geometrical and physical data about the rolls and the rolled material. They are thus more general in nature and may be used more readily to examine the effect of extending the existing regimes of rolling practice.

Analytical models of the rolling process are of course extremely complex. The physical phenomenon is essentially one of inhomogenous compression of a material with variable yield stress moving within the roll bite with a frictional drag that varies in nature, magnitude and direction. The associated mathematics is further complicated by the geometry of a rectilinear work piece passing through a roll gap bounded by two curvilinear roll surfaces.

The many analytic models reported in the literature vary widely in terms of level of detail, complexity and accuracy.

The model that one adopts for simulation is dictated by the end use for which the simulation is developed. Three discrete levels of modelling can be identified. When the modelling is aimed at understanding and quantifying the physical phenomenon involved in rolling, a very high level of detail such as is offered by Orowan (1943) is required. At this level, physical assumptions are almost totally avoided and mathematical approximations are also not made. For purposes of day-to-day design, the simulations need to accurately reflect only the main features of the rolling process and they need to consider only the most important factors. Such models may include many physical assumptions valid for specific design regimes. Mathematical approximations may or may not be required depending on the mathematical complexity of individual design loops and the sensitivity of the whole model to the particular design variable.

**Table 1.** Iterations for dimensioning of an oval groove

Iteration no.	Oval width (mm)	Oval height (mm)	Norm of error vector
1	52.5	12.00	15.04
2	30.99	13.92	2.59
3	30.16	15.34	0.16
4	30.48	15.23	0.001

Input square: 21 mm. Delivery square: 16.2 mm

Lastly a model that is to be used for process control has to be sufficiently simple to ensure that the computation time adequately meets the control requirements. Such a model must of necessity include all reasonable physical approximations and many mathematical approximations as well.

As an illustration of the above, one may consider a problem that is of fundamental importance in the simulation of rolling process. In any rolling mill, material of large stock size  $A1$  enters at a low speed  $V1$  and is reduced to a smaller size  $A2$  leaving at a higher speed  $V2$ . The deformation is carried out by rolls rotating with a peripheral speed,  $V$ ,  $V1 < V < V2$ . A basic question that is important for all calculations is the location of the neutral plane where the metal velocity is equal to the peripheral velocity of the rolls. For a precise determination of the neutral plane it is necessary to integrate the rolling equation:

$$df/d\phi = Ds \cos \phi (\tan \phi \pm \mu)$$

where  $f$  is the horizontal force per unit width,  $s$  the normal roll pressure,  $D$  the roll diameter,  $\phi$  the angular coordinate of arc of contact and  $\mu$  the coefficient of friction as shown in Figure 1 below, with full consideration of sticking/slipping friction, roll flattening etc. This requires numerical integration of a nonlinear variable parameter differential equation and the results allow for a precise understanding of metal behaviour in the roll bite.

For most design calculations, however, such complexity is not required and the use of a simplified closed form equation such as that given by Sims (1954) is generally acceptable:

$$\phi_n = \sqrt{\frac{h_2}{R'}} \tan \left[ \left\{ \frac{\pi}{4} \ln(1-r) + (R'/h_2)^{\frac{1}{2}} \arctan \left( \frac{r}{1-r} \right)^{\frac{1}{2}} \right\} / 2(R'/h_2)^{\frac{1}{2}} \right].$$

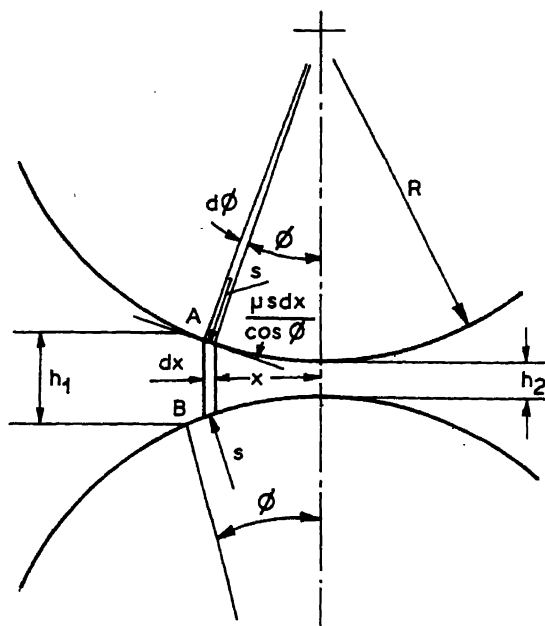


Figure 1. Deformation in roll gap.

For purposes of on-line computer control even the above equation is not acceptable because of the computation time required, and a polynomial approximation of the type

$$\phi_n = a + bx + cx^2; x = \left(\frac{h_1}{R}\right)^{\frac{1}{2}} \left[ \left(\frac{1-r}{r}\right)^{\frac{1}{2}} - \left(\frac{1-r}{\sqrt{r}}\right) \right]; r = 1 - h_2/h_1$$

which is sufficiently accurate may be used.

At the second level, which is of greater interest to design organizations, the calculation of roll force is generally straightforward; a notable exception being the estimation of roll flattening. As expressed by Hitchcock (1935), the extent of roll flattening depends both on the undeformed roll diameter and the roll force:

$$R' = f(r, P)$$

where  $R$  is the deformed roll radius,  $r$ , the undeformed radius and  $P$ , the roll separating force. Since the roll separating force is itself dependent on the contact arc, an iterative solution is called for.

Tension is an important technological parameter, particularly in cold rolling. For the results of simulation to be meaningful, the model used must take proper account of this factor. Further, in the process of optimizing the pass sequence, the iterative process must continually seek to maintain optimum levels of tension.

### 2.3 Temperature calculations

Temperature calculations constitute an essential part of all hot mill simulations. These calculations are required for estimating the force and power parameters of the process because they are mutually related to the temperature. Proper analysis of temperature conditions is also necessary for determining the thermal stresses in the rolls and for designing the roll cooling systems. Additionally, proper control of temperature is important from the viewpoint of the physical and mechanical properties of the metal and dimensional tolerance of the rolled product. Numerous temperature models have been reported in the literature. They are mostly quite detailed in concept but usually involve the "matching" of certain coefficients with experimental data which somewhat limits the predictive value of these models for design purposes.

For temperature calculations it is common practice to divide the roll into different zones as shown in figure 2. Within the roll gap, the heat transfer mechanism consists of heat generation in the strip through plastic deformation and conductive heat transfer between the rolls and the metal. Outside the contact area, both the strip and rolls lose heat through radiation, convection and to the cooling water.

The heat transfer mechanism in the roll gap is perhaps the most complex. In a model proposed by Bryant and Heslton (1982), the roll gap heat transfer to the rolls has been analyzed in terms of multiple line sources. Cernis' solution for line sources is used in conjunction with the method of superposition to calculate the steady state roll temperature distribution with depth at any angle. Similarly, a discrete model of the temperature distribution in the strip is also developed considering unsteady state heat transfer to the rolls. The two equations are solved simultaneously with the boundary condition being that the surface temperatures of roll and strip are equal along the contact arc. The heat transfer mechanism in other zones may be analyzed reasonably well with well-established finite difference methods.

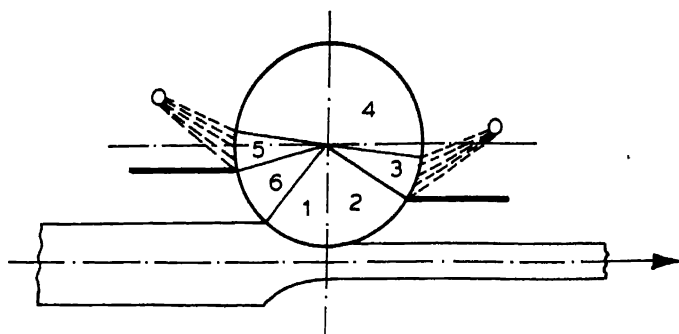


Figure 2. Heat transfer zones of a work roll.

## 2.4 Productivity calculations

In order to obtain an accurate estimate of mill productivity, all mill simulation models incorporate realistic time studies. These time studies include gap time between pieces, material feeding time, acceleration time, run time at top speed, deceleration time, tail-out time and reversal time. Motor heating is always estimated as an integral part of the mill simulation and the motor characteristics of torque vs speed are fully taken into account. As an illustration of the extent to which detailed analysis is undertaken let us consider the acceleration of a tandem cold mill train. A program that is used for this analysis takes into consideration the variation in inertia of the input and delivery coils, the inertia of the drive trains, the rolling power in each stand and the torque vs speed characteristic of all individual motors. If one of the motors is in current limit at any point of time the acceleration rate is accordingly reduced. Similarly in the simulation of primary mills, the torque vs speed characteristic of the main drive motor is fully taken into account. If the motor goes into current limit after having accelerated beyond the base speed, the acceleration ramp is immediately reduced to a level consistent with the available torque and the combined inertia of the drive train and work piece.

## 3. Equipment design program

The mill simulations discussed above are required in order to properly size the rolling mills for specific requirements. For the detailed design of individual equipment they are of immense value as a starting point in that they serve to define the nature and magnitude of forces and stresses acting on the system. A different set of "equipment design" programs is required for the routine analysis and design of individual equipment such as mill housings, screwdown systems, drive systems, manipulators, roller tables, cooling beds and winding/unwinding reels. Both static and dynamic analysis are required. In addition, general purpose packages such as STRUDL II are also used as and when required for specific problems. Some of the more important programs in this category are discussed below.

In the ultimate analysis, the detailed design of individual equipment does influence the nature and magnitude of forces developed. Polukhin (1975) attempted to integrate these effects and obtained some rather interesting results but for most design purposes the prevalent method is to isolate the two. The results obtained are sufficiently accurate.

### 3.1 Analysis of mill stand stresses and deformation

The basic working element in the rolling mill is of course the mill stand which houses the rolls.

The roll separating force required to deform the metal acts on the rolls to cause stresses and deformations in the rolls, bearings, chocks, screws and the housing itself. As a result of elastic deformations in these elements, the effective (active) roll gap varies with the roll separating force.

Large variations in the active roll gap not only result in non-uniform dimensions of the rolled product and variations in interstand tension but they adversely affect the output of the mill and life of rolls. Roll force variations may be as high as 10–15 % of the nominal value and it is therefore important to increase the stand stiffness to as high a value as possible within the constraints of mill size. Proper understanding of mill stand stresses and deformations makes it possible to evaluate the effects of various factors on the stiffness of the stand and optimize the design of the mill housing. The models used for these studies are based on frame analysis and they fully take into account the deflections of the rolls, bearings, chocks, screws and also the compression of the working fluid in case of hydraulic mills.

Dynamic analysis of the mill housing is also required for the design and optimization of automatic gauge control systems as described later. For these purposes it is generally sufficient to use a second order model for the mill housing.

### 3.2 Torque amplification studies

In much the same way that the mill stand serves to exert the forces required for deforming the metal, the mill spindles must be properly designed to transmit the torque from the motor to the rolls. The sharp increase in operating speeds of mills during the 1960s led to several premature failures of the mill drive components which could not be explained by the conventional steady state analysis used in mill design upto that time. This drew attention to the phenomenon of transient torsional vibrations in mill drive systems. Transient oscillations can produce mechanical torques many times greater than the electrical ratings and resonant or near resonant conditions can lead to fatigue failures. Because of the large number of masses and gears in their drive trains the hot strip mills are particularly susceptible to high torque amplifications, and the first attempt at such analysis was with respect to these mills. In most cases these drives are subjected to linearly varying torques only and the drive systems may be modelled as a linear oscillatory system with proper representation of the inertias, torsional stiffness, damping action in the bearings and the applied torques. In the primary (reversing) mills such as the blooming and slabbing mills, nonlinear effects such as backlash become important and linear models no longer suffice.

In either case, for adequately describing the physical system, the mathematical model has to be of high order. The overall drive system consists of two subsystems i.e. the electrical drive and control system and the mechanical system. In earlier studies relating to hot strip mills the mechanical system only was analyzed but for the reversing primary mills, the interactions of the two subsystems become important and a more elaborate model as shown in figure 3, is required.

The solution of the associated differential equations has become possible only after the development of computer programs. In addition to solving the natural frequencies and normal modes, these programs also determine the transient response to several

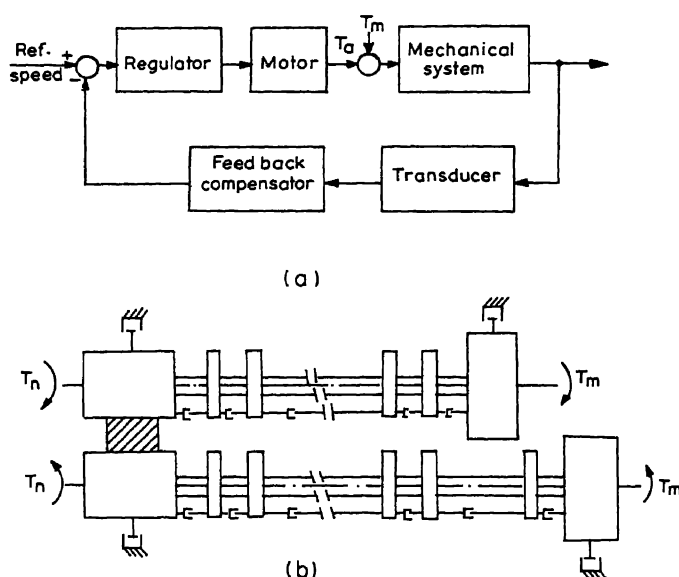


Figure 3. Mathematical models used for dynamic analysis and synthesis. (a) Block diagram of drive system and (b) Lumped parameter model for torque amplification studies.

types of inputs to represent as far as possible all types of disturbances such as ramming of bar, slipping in the roll bite, nonuniform section, nonuniform reduction etc.

Computer studies of the large hot strip mills have occasionally led to changes in the proposed design to limit torque amplification to acceptable values. For the reversing mills the computer studies are reported to have led to substantial improvements in the optimization of the speed regulation compensator.

### 3.3 AGC system response studies

The influence of mill stand rigidity on the dimensional tolerances of the rolled product has been referred to earlier. In order to meet increasingly more stringent demands on dimensional tolerance automatic gauge control (AGC) systems have been developed to compensate for these variations. For proper control these systems are required to have a response time of about 20–30 msec and a frequency response that is flat upto about 10–15 Hz. Except in case of smaller rolling mills these systems are generally controlled by a microprocessor or a computer.

The design and optimization of AGC systems is generally based on detailed computer models that include all parts of the system i.e. the physical plant, the sensors, the controllers and the actuators. For purposes of illustration, a computer model of a single stand hydraulic AGC system will be considered. A schematic of the same is shown in figure 4. The transfer function of each component is carefully determined and the computer simulation is used both for time domain analysis and frequency domain analysis. Such a model makes it possible to analyze the response to a step or other disturbance in incoming strip thickness, material hardness, roll separating force, tension, speed, etc either with or without AGC. For design optimization the general form of the compensator transfer function may be preselected and the different coefficients varied within a specified range. Clearly the validity of these simulations depends on the

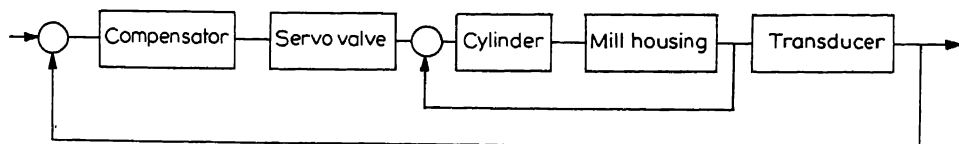


Figure 4. Block diagram of AGC system model.

accurate modelling of individual components such as mill stand, cylinder, load cell and servo valve, and also on the use of an accurate roll force model.

#### 4. Graphics applications

The mathematical models and simulations described so far have played an important role in transforming rolling mills design from the domain of empiricism to an analytical level. Since the engineer works in graphic as well as mathematical terms, the results of analysis needed to be translated into graphic form. Besides the tedium of such work, the likelihood of error and the noncreative expenditure of time required, served as major disincentives for the widespread use of these techniques. New developments in "computer graphics" have finally allowed the design engineers to overcome these problems and communicate with the computer in a truly natural form.

The term computer graphics is very broad and includes numerous peripheral devices such as xy plotters, printers and drafting machines and graphic display screens. The most rudimentary application of computer graphics is for plotting the computed results as graphs, bar charts, etc. Examples of such applications include the plotting of transient response of drive systems, plotting the locus of linkages, plotting the profile of gear teeth, etc.

##### 4.1 Roll groove drawings

At a somewhat more advanced level, computer graphics may be used for generating schematics and mechanical drawings of predefined shape. The graphic display screen is not essential for these applications but it may be used if available.

A popular application at this level is the generation of roll groove drawings. The geometry of these drawings is more or less fixed and all the dimensions may be obtained from the programs that calculate the pass dimensions as discussed earlier. The program developed in the present author's establishment (MECON) consists of the following parts:

- (i) selection of a standard scale factor,
- (ii) calculation of all coordinates for the main drawing and for all dimension lines,
- (iii) selecting a position for the drawing on the plotter and drawing of boundary lines and name plate,
- (iv) plotting the groove drawing,
- (v) plotting the dimension lines and inserting the dimensions and
- (vi) plotting of all textual information.

The data used for generating the groove drawings can also be used for generating roll drawings. This feature has been implemented by some mill builders and is under development at MECON.

## 4.2 Hydraulic schematic circuits

One of the earliest applications requiring the use of an interactive graphics terminal is the generation of schematics made up of items in a predefined menu. An example of such application is the interactive graphics software presently under development at MECON for hydraulic schematic circuits required in rolling mills design. User-defined keys have been associated with all standard element symbols such as tank, pump, filter, accumulator, check valve, servo valve etc. Working on an interactive graphics terminal, the designer can develop a complete schematic consisting of any arbitrary combination of these elements.

The elements can be individually rotated and scaled with conversational commands. Moreover the drawing as a whole can also be scaled for viewing on the screen or drawing on the plotter. Care has been taken to facilitate editing functions such as deletion and insertion of individual elements or complete circuit branches.

## 5. Summary and conclusions

The large number of simulations and design programs being used for rolling mills design have been developed over a period of several years. The mathematical models have been steadily upgraded to include the greatest level of detail possible within the limitations of computer time. Most design organizations have constantly updated the material characteristics to conform to field measurements. The software has generally undergone numerous modifications in order to meet the specific requirements of designers without sacrificing generality. There has also been a persistent effort to make the programs fully automatic as far as possible.

With the availability of interactive graphics facility, the present area of thrust is towards increased use of computer graphics. Wherever possible the calculation programs have been integrated with graphics software as described for the design of roll grooves. Such integration serves to eliminate the tedium of mechanically translating a computer printout into a drawing and allows the rolling mills design engineers to iterate more design concepts and trade-offs in a given time and greatly increase his creativity and productivity.

## References

- Bryant G F and Heselton M O 1982 *Met. Technol.* **9** 469
- Hitchcock J R 1935 Roll neck bearings, Special Report, ASME
- Orowan E 1943 *Proc. Inst. Mech. Eng.* **150** 141
- Polukhin V P 1975 *Mathematical simulation and computer analysis of thin strip rolling mills* (Moscow: Mir Publishers)
- Siebel E 1925 *Berichte des Walzwerksausschusses, Verein deutscher Eisenhüttenleute*, No. 37 (also 1924 *Stahl und Eisen* **45** 1563)
- Sims R B 1954 *Proc. Inst. Mech. Eng.* **168** 191
- von Karman T 1925 *Z. Angew. Math. Mech.* **5** 139



## Computer modelling application in life prediction of high temperature components

V M RADHAKRISHNAN

Indian Institute of Technology, Madras 600 036, India

**Abstract.** Defects introduced in pressure vessel components during fabrication processes act as potential sources for damage accumulation and subsequent catastrophic failure. Cracks nucleate at these stress risers and propagate aided by fatigue type of loading, corrosion and creep. Analysis of crack growth under conditions of 'time-dependent fatigue' is very important for the life prediction of pressure vessel components. In this paper the interaction of creep-hot corrosion and low cycle fatigue is analyzed based on the energy expended for the nucleation of damage at the advancing crack front. The total damage accumulation is divided into that due to (i) fatigue, (ii) corrosion and (iii) creep for modelling purpose. The analysis yields a relation in terms of  $J$ -integral which is applicable to both crack propagation and final failure. A corrosion-creep parameter ( $F_i$ ) has been introduced at the crack propagation stage and raw data from different sources have been analyzed for different types of loading and compared with the theoretical predictions. The total energy in tension which includes the tension going time, appears to be a good parameter for the prediction of time-dependent fatigue life.

**Keywords.** Life prediction; pressure vessel; high temperature components; fatigue life; computer model; crack growth model.

### 1. Introduction

Pressure vessels operating in the creep range include steam chests, loop pipes, HP and IP cylinders, turbine parts, valves and numerous items of pipe works. Many of these components will contain crack-like defects specifically at places where joints are made. As large components involve a high capital investment, maximum service life consistent with safety of operation has to be ensured. Failure of many high temperature pressure vessel components due to crack growth has been reported in the literature (Toft *et al* 1976). A typical example is the failure of a welded joint between IP steam chest and a loop pipe (figure 1a) in a 350 MW unit plant in UK. The material of the steam chest was cast 1 Cr-Mo-V steel and that of the loop pipe was 1/2Cr-1/2Mo-1/4 V steel. The steam was at 35 bar pressure and 560°C. The welded joint between steam chest and the loop pipe failed explosively. Investigations revealed a sub-surface crack of 300 mm length in the heat-affected zone of the weld on the steam chest side. The crack was formed during the post-weld stress relief heat treatment and had grown in service. Another example is the failure of a superheater tube (figure 1b) of a 100 MW plant. The material of the tube was 18Cr-12Ni-1Nb (AISI/347) steel and that of the spacers was 25Cr-20Ni. The superheater tubes are kept in alignment and correctly spaced by the use of interlocking spacers which are welded to the tube, but free to move in the vertical plane to accommodate thermal expansion. Tube failures occurred after 12,000 hours of operation and examination revealed cracking at the fillet weld interface.

The significance of crack nucleation and its growth behaviour under dynamic

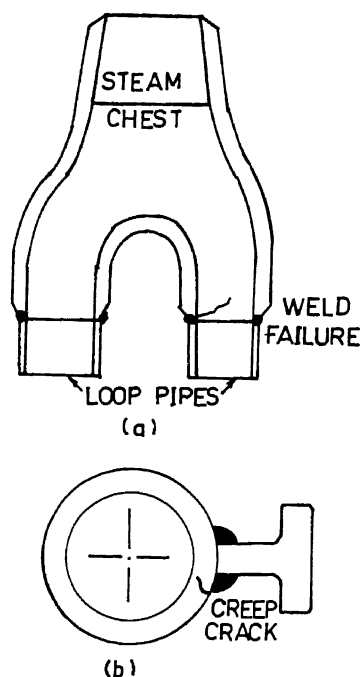


Figure 1. (a) IP steam chest and pipe joint. (b) superheater tube joint.

stresses where creep, corrosion and low cycle fatigue are the main contributing factors to damage processes has started receiving attention only recently. In this paper an analysis is presented to evaluate the time-dependent crack growth and its application in life prediction methods.

## 2. Crack growth model

In time-dependent fatigue, damage nucleation at the tip of the advancing crack could be in the form of micro-cracks or voids contributed by point and line defects. Both the strain energy at the crack tip  $\delta W^*$  and the thermal energy will contribute to the damage nucleation ahead of the crack tip. The damage nucleated per cycle in a unit volume of the material ahead of the crack can be given as a rate equation in the form (Radhakrishnan 1982)

$$dD/dN = A_1 \exp\left(\frac{-Q + m' \log(\delta W^*/W_0)}{kT}\right), \quad (1)$$

where  $Q$  is the activation energy and  $A_1$ ,  $m'$  and  $W_0$  are constants. A similar  $da/dN$  dependence ( $a$  = crack length) of the activation energy had been found to be valid in the case of high temperature fatigue of aluminium (Jeglic *et al* 1973). The above relation can be rewritten as

$$dD/dN = A_1 (\delta W^*/W_0)^m \exp(-Q/kT), \quad (2)$$

where  $m = m'/kT$ .

The damage takes place over a small highly strained volume, represented by its linear dimension  $R_p$ . In the case of elastic field this dimension can be identified as the width of the plastic zone given by

$$R_p = (E/\sigma_{ys}^2) J_e, \quad (3)$$

where  $E$  is the Young's modulus and  $\sigma_{ys}$  the yield stress.  $J_e$  is the  $J$ -integral corresponding to the stress field. In the case of high temperature low cycle fatigue, the width of the highly strained volume can be given by a similar type of relation in the form

$$R_p = (E/\sigma_{ys}^2) \delta J. \quad (4)$$

The total damage in the highly strained zone joins the crack and the crack advances through a small distance  $da$  at time  $dN$ . Hence the crack growth rate can be given as

$$R_p(dD/dN) = A_1(E/\sigma_{ys}^2)(\delta J)(\delta W^*/W_0)^m \exp(-Q/kT). \quad (5)$$

The energy density  $\delta W^*$  at the crack front can be related to the applied energy density  $\delta W$  and the crack length  $a$  by (Radhakrishnan 1980a)

$$\delta W^* = (4/r)(\delta W \cdot a), \quad (6)$$

where  $r$  is the crack tip radius. It can also be shown that the  $J$ -integral range  $\delta J$  is given by a function of the type (Kaisand and Mowbray 1979)

$$\delta J = \text{constant}(\delta W \cdot a), \quad (7)$$

where  $\delta W$  is the work done during the tensile portion of loading. With (6) and (7) we can write the crack propagation rate as

$$da/dN = A_2(\delta W \cdot a)^{m+1} = A_3(\delta J)^{m+1}, \quad (8)$$

where  $A_2$  and  $A_3$  are constants which include all the other constants.

Under certain conditions of loading, as in vacuum, some of these damages nucleated at the crack front may get healed during compressive loading. Under normal conditions of testing with ambient air, such healing may not be possible. In addition, with hold time or with low frequency, the crack front will be subjected to environmental attack. Hofflener and Speidel (1979) reported that the crack propagation rate is twice higher in air than in vacuum for IN 738LC and IN 939 alloys at 850°C. In addition to the fatigue and corrosion effects, if the tensile-going frequency is sufficiently low, then creep effect will also come into the picture which will generate some more defects at the crack front thereby increasing the crack growth rate. The basic model of the contributions to the crack growth due to the three factors, namely, fatigue, corrosion and creep is schematically shown in figure 2. In these components,  $(\delta a)_f$  may be considered to be due to PP type of loading (only due to fatigue). The corrosion component  $(\delta a)_{cor}$  is added when the frequency is low or when there is a hold period. Oxide layers will form and if the scale that forms spalls off, then further corrosion may take place. Or else, the corrosion effect will slow down and hold times beyond a certain value will not add much to the damage accumulation. The corrosion effect may be taken as a log function (or any other suitable function) of the time of exposure of the newly formed surface—in this analysis the tensile going time—and can be given by

$$\delta a_{cor} = A_{cor} \log(t/t_0) \text{ func}(\delta J), \quad (9)$$

where  $A_{cor}$  and  $t_0$  are constants.

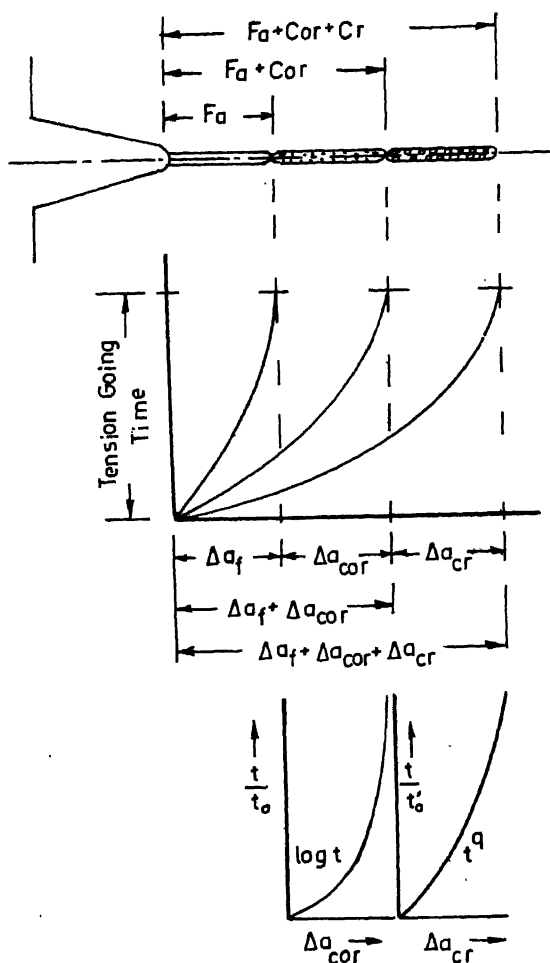


Figure 2. Crack growth model.

When the frequency is very low and the stress generated due to the applied strain range is sufficiently high at the operating temperature to cause creep deformation, then creep damage will also occur at the crack tip during the tensile portion of the cycle. The essential condition is that the creep rate due to that particular stress level must be higher than the imposed strain rate. The creep damage under such a condition can be assumed to be a function of the creep strain. Since during each cycle load is applied afresh, the creep strain will be in the transient stage and so it will follow generally the one third law. So the contribution due to creep for the crack growth, i.e.,  $\delta a_{\text{creep}}$  can be taken as a power function of the tensile going time and can be written as

$$\delta a_{\text{creep}} = A_{\text{cr}} (t/t_0)^q \text{ func}(\delta J), \quad (10)$$

where the value of the exponent  $q = 0.33$ . These growth phenomena are assumed to take place during the tensile going frequency and hence this treatment can be applied to unbalanced hysteresis loops and tensile hold periods.

Now combining the effects of corrosion and creep, the crack growth during each cycle can be given as

$$\delta a = \delta a_f + \delta a_{\text{cor}} + \delta a_{\text{cr}}, \quad (11)$$

which yields the generalized relation in the form (equation (8))

$$da/dN = A_f (1 + \alpha \log(t/t_0) + \beta(t/t'_0)^q) (\delta J)^{m+1}, \quad (12)$$

where  $\alpha = A_{\text{cor}}/A_f$  and  $\beta = A_{\text{cr}}/A_f$ .  $t_0$  and  $t'_0$  are the tensile-going times (the corresponding frequencies being  $v_0$  and  $v'_0$ ) beyond which corrosion and creep will be active respectively.

The above relation is also applicable when there is a hold period in the stress-strain cycling. When there is a stress hold, the creep effect will come into the picture and the term  $\beta(t/t'_0)^q$  will have to be taken in the equation. But when there is a strain hold, then relaxation of stress will take place. Some of the cavities created during the peak stress may collapse. So the effect of stress relaxation will be similar to corrosion and the contribution due to the damage accumulation can be similar to that of corrosion in the form

$$(\delta a)_{\text{relaxation}} = A_r \log(t/t_0) \text{func}(\delta J). \quad (13)$$

### 3. Data analysis

Expressing the  $J$  range ( $\delta J$ ) in terms of LEFM parameter  $\delta K$  in the form  $\delta J = \delta K^2/E$ , relation (12) can be written as

$$da/dN = A_f (F_i) (\delta K)^{2(m+1)}, \quad (14)$$

where  $A_f$  is a constant for a given material and temperature.  $F_i$  is the interaction parameter and is equal to  $1 + \alpha \log(t/t_0) + \beta(t/t'_0)^q$  or  $\alpha' \log(t/t_0)$ . Equation (14) is similar to the Paris-Erdogan law given as

$$da/dN = C(\delta K)^n. \quad (15)$$

Crack growth data (James 1972) obtained on a 304 type stainless steel tested at 538°C over a wide frequency range of 6.67 Hz to 0.0014 Hz were analyzed based on (14) and the relation between  $da/dN$  and  $\delta K$  is shown in figure 3, with the values of the constant  $A_f = 1.7 \times 10^{-8} \text{ mm}/(\text{MPa}\sqrt{\text{m}})^3$ ,  $\alpha = 0.2$  and  $\beta = 0.75$ . As the frequency decreases there is a decrease in the value of the exponent ( $m+1$ ). It has been shown (Radhakrishnan 1980b) that in the Paris equation describing the state II crack growth, the constant  $C$  and the exponent  $n$  are inter-related. As  $C$  increases the value of  $n$  decreases. In a similar manner, in this case also, as frequency is lowered, the interaction factor ( $F_i$ ) in (14) will increase with a consequent decrease in the value of the exponent ( $m+1$ ).

Equation (14) can be rearranged and integrated with crack length  $a$  from initiation  $a_i$  to critical length  $a_f$  and the number of cycles  $N$  from nucleation time  $N_i$  to final fracture  $N_f$ . Assuming the nucleation of the crack to start within a first few cycles and  $a_i \ll a_f$ , it can be shown

$$(F_i) (\delta W_i)^{m+1} N_{\text{fi}} = \text{constant}, \quad (16)$$

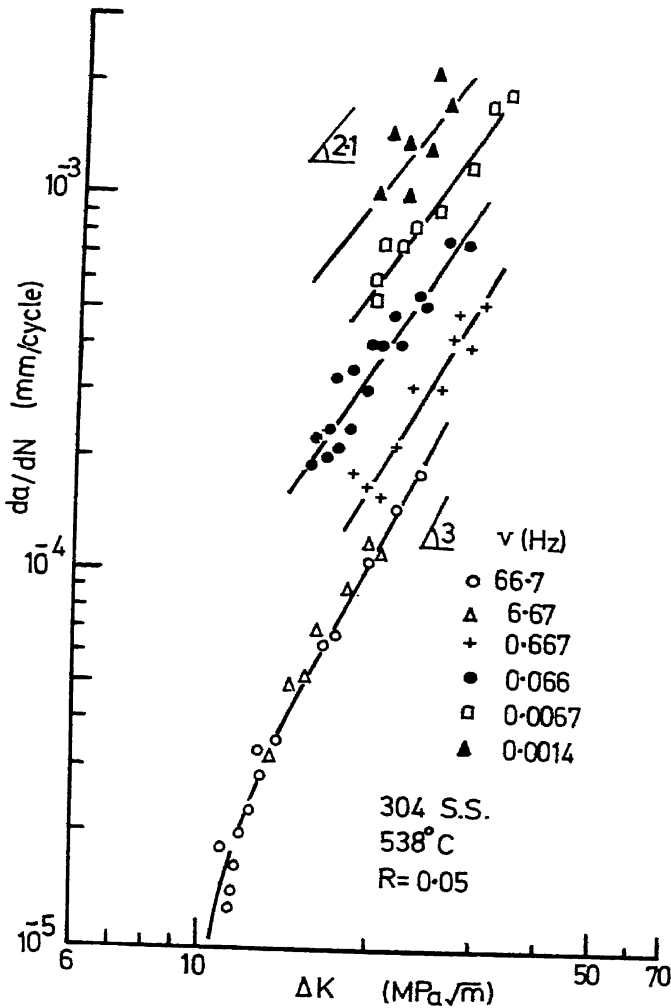


Figure 3. Relation between  $da/dN$  and  $\Delta K$ .

where  $\delta W_t$  is the tensile energy input per cycle per unit volume.  $N_{fi}$  is the number of cycles to failure under interaction conditions. If  $(F_i) = 1$ , the  $N_{fi} = N_f$ . If the cyclic stress-strain relation is known,  $\delta W_t$  can be expressed in terms of  $\delta\epsilon$  or  $\delta\sigma$ . Thus the usual endurance life relation can be established. It can be seen that decreasing the frequency will shift the  $\delta\epsilon - N_{fi}$  relation downwards on the log-log plot. The slope of these lines will be proportional to  $1/(m+1)$  and since the value of  $(m+1)$  decreases with decreasing frequency or increasing tensile hold period, the slope of the lines  $\delta\epsilon - N_{fi}$  on the log-log plot will increase, thereby showing a rotational effect in addition to a downward shift as the frequency is reduced.

The energy associated with the tensile portion of the cycle depends on the wave shape—typical examples of which are shown in figure 4. In the case of a balanced hysteresis loop with no creep effect, the energy associated with the  $J$  integral will be  $\delta W_e$ .

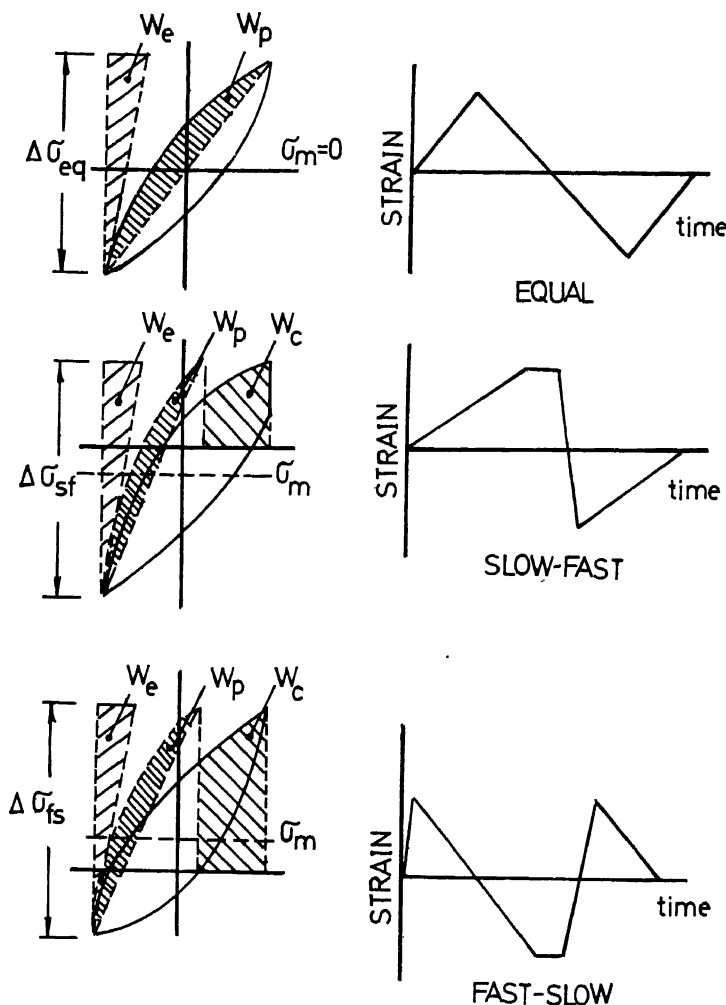


Figure 4. Energy separation method.

and  $\delta W_p$ , the elastic and plastic energy corresponding to  $\delta J_e$  and  $\delta J_p$ . This energy term will be

$$\begin{aligned}\delta W_t &= \delta W_e + \delta W_p, \\ &= \frac{\delta \sigma}{2} \delta \varepsilon_{el} + \frac{(1-n')}{(1+n')} \frac{\delta \sigma}{2} \delta \varepsilon_{pl}.\end{aligned}\quad (17)$$

The second term corresponding to the plastic region depends on the cyclic strain hardening exponent  $n'$  under the PP type of loading. At high temperatures where the hardening of the material drops, the value of the exponent  $n'$  will be small ( $= 0.1$  to  $0.15$ ) and in such a case relation (16) can be written as

$$(F_t)(\sigma_t \delta \varepsilon_t)^{m+1} N_f = \text{constant}.\quad (18)$$

Raw data from Taraneshi and McEvily (1981) have been analysed and typical relations

between the tensile energy  $\delta W_t$  and the cycles to failure  $N_f$  for 800 and 800H nickel alloys are shown in figure 5. Here the cycling was rather continuous and the influence of creep could be negligible.

Even when the stress or strain is held constant for a duration either in tension or in compression, if the temperature is not high enough to cause creep damage or stress corrosion cracking in the small interval of time, the interaction parameter ( $F_i$ ) in (16) will almost be equal to unity and the relation between  $\delta W_t$  and  $N_f$  on log-log scale will be a straight line for continuous cycles, tension hold (SF), compression hold (FS) and tension-compression hold (SS). Such a typical correlation at comparatively low temperature where creep damage effect may be negligible, is shown in figure 6 for Cr-Mo steel.

The need to consider the unbalancing in hysteresis loop comes in at temperatures where corrosion and creep effects will be more pronounced. In the model presented here, the entire tensile energy term is divided into three components,  $W_e$ ,  $W_p$  and  $W_{cr}$ —the last term being due to tensile stress  $\sigma_t$  and the displacement  $\varepsilon_{creep}$ . So  $\delta W_t$  is written as

$$\delta W_t = \frac{\delta \sigma}{2} \delta \varepsilon_e + \frac{(1-n')}{(1+n')} \frac{\delta \sigma}{2} \delta \varepsilon_p + \sigma_t \delta \varepsilon_{cr}, \quad (19)$$

where  $\delta \varepsilon_e + \delta \varepsilon_p + \delta \varepsilon_{cr} = \delta \varepsilon_{total}$ . The third term need not necessarily be due to creep under constant stress hold. When the frequency is very low and the stress developed is high enough to cause a creep rate which is higher than the imposed strain rate, the effect of creep will come in. Since the tensile portion of the energy is considered in the analysis, the type of tests PP (FF) and PC (FS) can be considered to be similar and that of CC (SS) and CP (SF) will be similar excepting for the mean stress effect. Figure 7 shows the relation between the tensile energy and the number of cycles to failure under interaction conditions for a turbine disc alloy tested at 750°C. It can be seen that PP and PC types

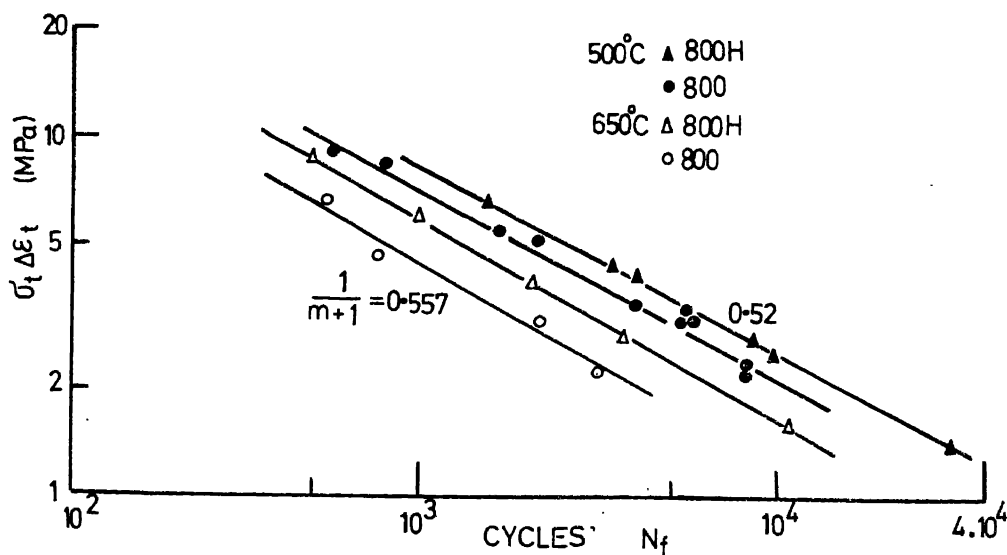
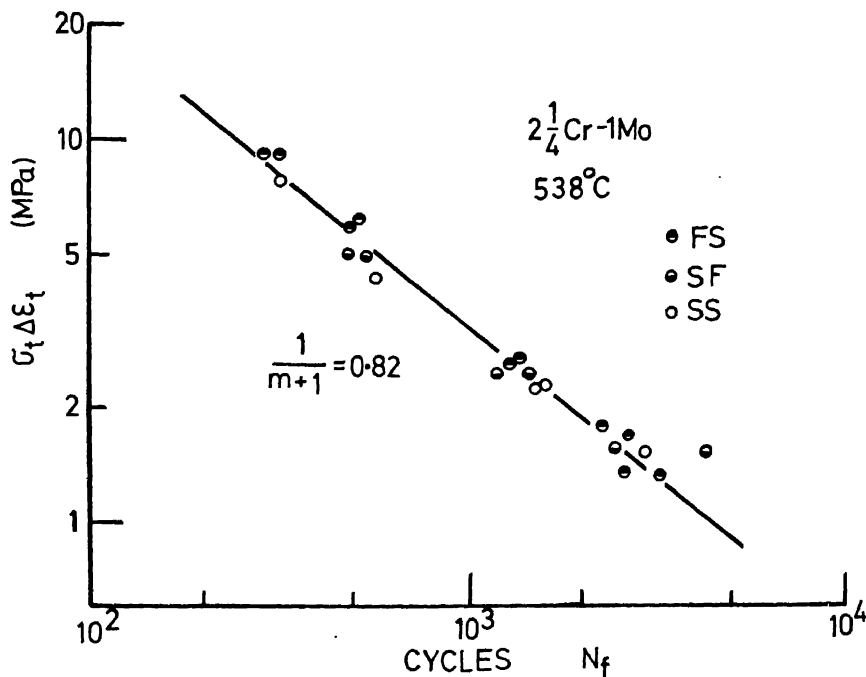
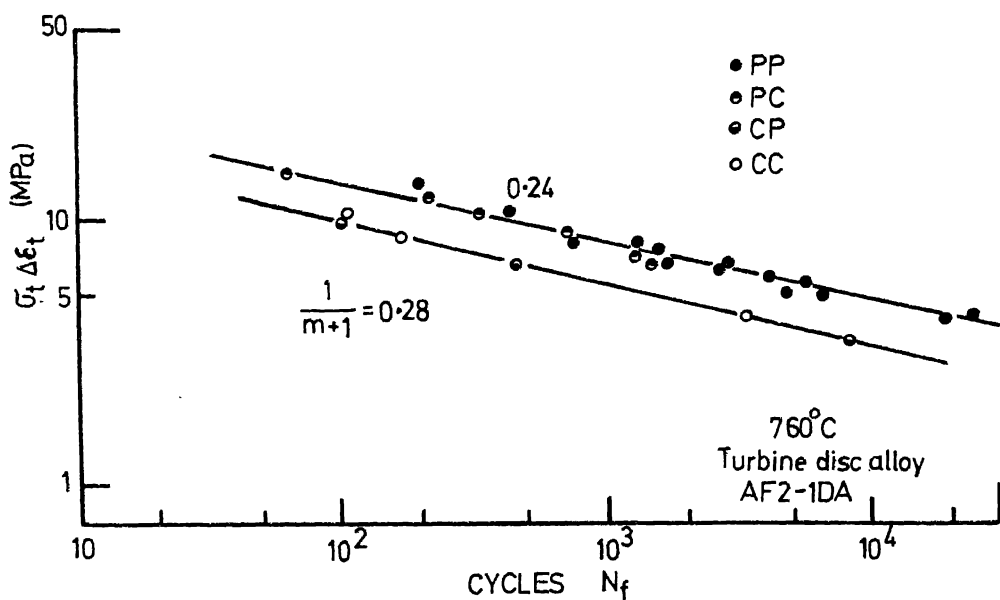


Figure 5. Relation between tensile energy density and cycles to failure.



Figure 6. Relation between  $\delta W_t$  and  $N_f$ .Figure 7. Relation between  $\delta W_t$  and  $N_f$ .

of loading data fall on one line and that of CP and CC on the other. The interaction factor ( $F_i$ ) was not taken into consideration. This has resulted in two separate lines for these two types of loading schemes. Figure 8 shows the relation between tensile energy and the number of cycles to failure under different loading frequencies and tensile hold times for type 304 stainless steel. Tensile strain hold times up to 600 minutes were employed. It can be seen from the results that when there is no hold time and the test is of PP type, (curve corresponding to 4 E-03) the slope of the line is 0.5 ( $= 1/(1+m)$ ). As the hold time is introduced or as the frequency is reduced the slope increases to 0.525 and 0.625 as indicated in the figure and the interaction factor ( $F_i$ ) also increases, because of the corrosion and creep effects.

In (18) which can be written in the form

$$N_{fi} = \text{const.} \frac{(\delta W_t)^{-(m+1)}}{(F_i)}, \quad (20)$$

the exponent ( $m+1$ ) is dependent on the interaction factor ( $F_i$ ), as was discussed earlier, and it decreases as the value of ( $F_i$ ) increases. This relation can be given in the form

$$(m+1) = A - \gamma \log(F_i), \quad (21)$$

where  $A = m+1$  when there is no interaction i.e., ( $F_i$ ) = 1.  $\gamma$  is a constant. As discussed in figure 8, the value of the constant  $\gamma$  is taken as 1.2 for 304 stainless steel at 593°C.

In many situations it is advantageous to represent the failure cycles  $N_{fi}$  as a function of tensile cycle time or tensile hold time. Figure 9 shows the relation between  $N_{fi}$  and the cycle time for cast 316 stainless steel and 304 stainless steel. It can be seen that for lower values of the strain range ( $\delta\epsilon_t = 0.5\%$ ) the reduction in interaction cycle for larger

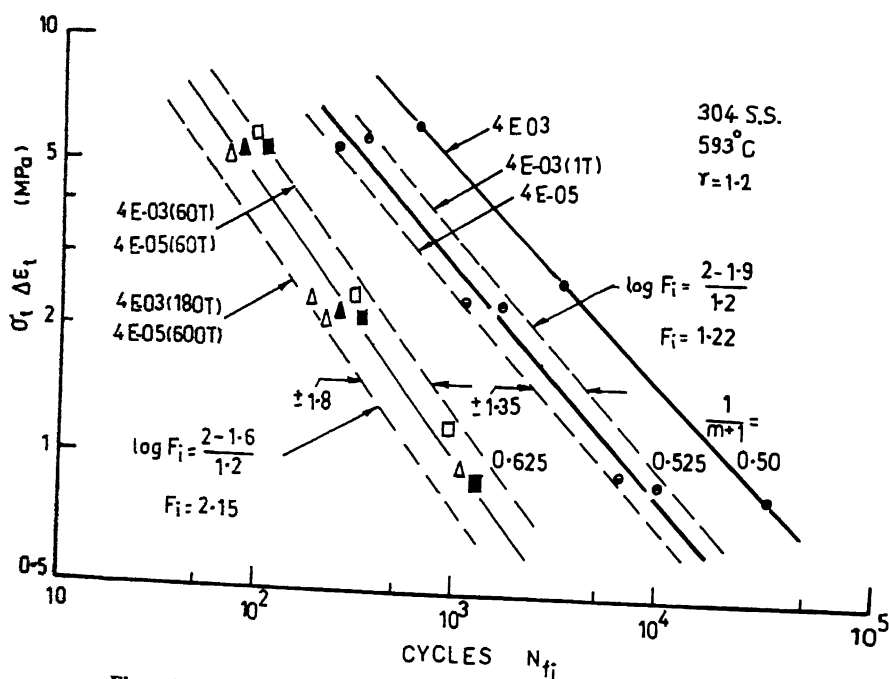


Figure 8. Relation between  $\delta W_t$  and  $N_{fi}$ .

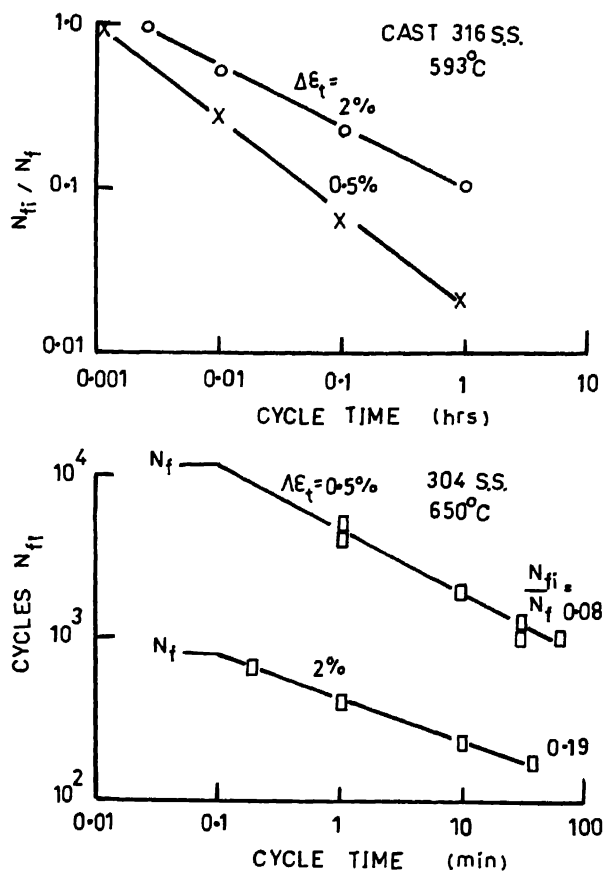


Figure 9. Relation between  $N_{fi}$  and cycle time.

cycle time is much higher than for higher strain ranges ( $\delta\epsilon_t = 2\%$ ). Equation (20) is able to explain such a behaviour that has been observed in many other cases also. Assuming a simple relation between stress and strain in the form  $\delta\sigma = \sigma_0(\delta\epsilon)^n$  so that  $\delta W_t \propto (\delta\epsilon)^{n'+1}$  we get the relation (20) as

$$(\delta\epsilon)^{(n'+1)(m+1)} N_f = \text{constant},$$

for PP type of loading and

$$(F_i)(\delta\epsilon)^{(n'+1)(A-\gamma \log F_i)} N_{fi} = \text{constant}, \quad (22)$$

for interaction conditions. The fatigue life under interaction condition  $N_{fi}$  can thus be written as a function of the normal fatigue life  $N_f$  as

$$\frac{N_{fi}}{N_f} = \frac{(\delta\epsilon)^{(n'+1)\gamma \log F_i}}{(F_i)}. \quad (23)$$

The above relation shows that  $N_{fi}/N_f$  is dependent on the applied strain range—the higher the strain range, the larger is the life ratio. This is what has been observed in the data presented in figure 9 (Wareing 1981).

Equation (23) forms the basis for the construction of the interaction diagram i.e., the relation between the fatigue life under interaction conditions and the tensile going time which can include the stress or strain hold periods. In the case of strain-hold, the interaction factor ( $F_i$ ) becomes

$$\begin{aligned} F_i &= 1 + \alpha \log(t/t_0) + \alpha' \log(t/t_0) \\ &= 1 + (\alpha + \alpha') \log(t/t_0). \end{aligned} \quad (24)$$

In the case of stress hold, it is given as

$$F_i = 1 + \alpha \log(t/t_0) + \beta(t/t_0)^q. \quad (25)$$

Figure 10 shows the interaction diagram for 304 type stainless steel. The full line is obtained with the interaction factor  $F_i$  as given by (24) as this is a case of strain hold and stress relaxation can be expected to occur during the hold period. When the hold is very small, it is the same as normal fatigue without any interaction effect. As the hold time is increased, corrosion comes into the picture. Still further increase in hold time gives rise to corrosion and relaxation to occur. The value of  $(\alpha + \alpha')$  is taken as 0.2. Here again it can be seen that the reduction in fatigue life is much more pronounced when the strain range is small.

Figures 11 and 12 show the relation between  $N_{fi}$  and the tensile hold period under both stress and strain hold conditions for 304 type stainless steel at 650°C and IN597 alloy at 850°C. It can be seen that with stress-hold the relation between  $N_{fi}$  and time on the log-log plot becomes more or less a straight line with a negative slope approximately equal to one at higher hold periods. This means that the life becomes more time-dependent than cycle dependent as the stress hold period is increased. At high tensile

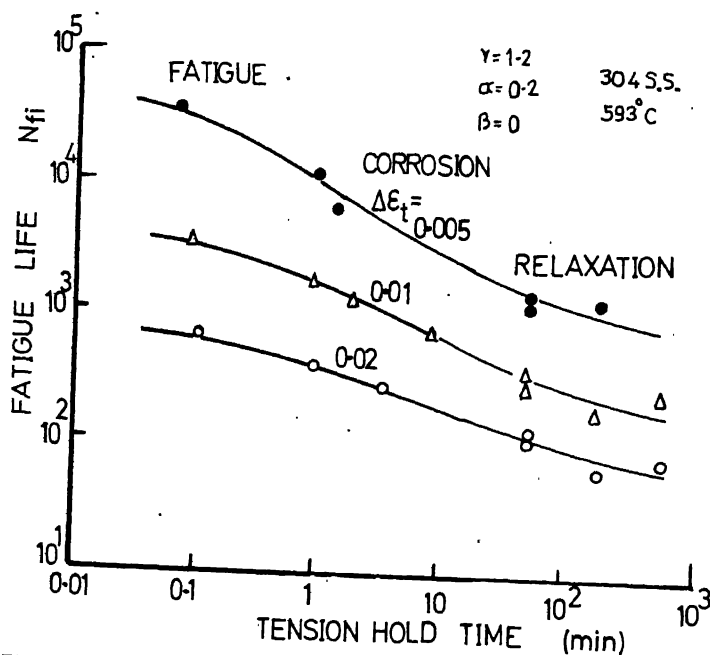


Figure 10. Interaction diagram for 304 stainless steel at 593°C.

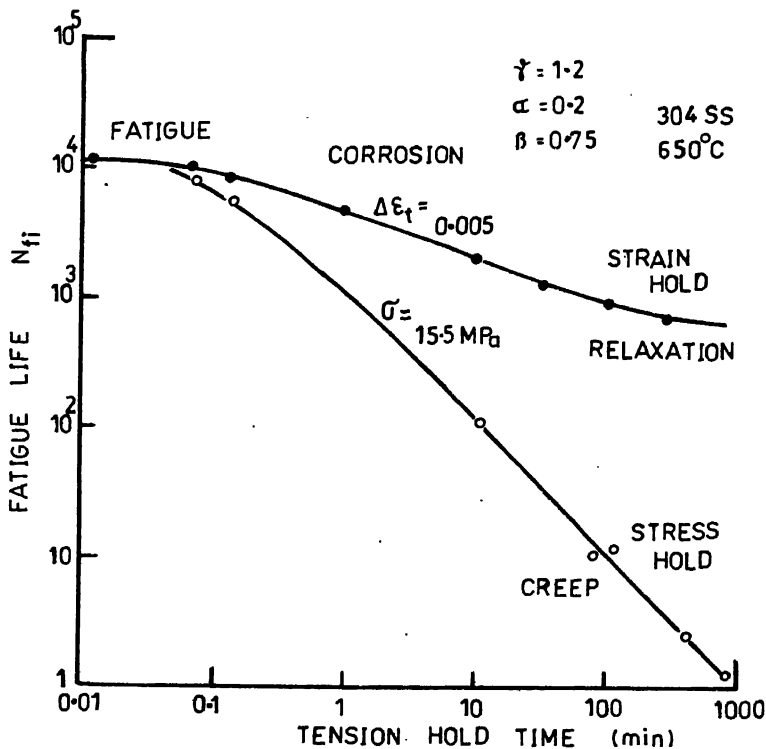


Figure 11. Interaction diagram for 304 stainless steel at 650°C.

hold periods creep plays a dominant role under stress hold conditions. But under strain-hold conditions, a saturation level is reached and the fatigue life appears to be independent of the hold period beyond a certain stage, as relaxation governs the crack tip conditions. The same trend has been observed in all the cases (Radhakrishnan 1983).

The variables involved in the analysis of life prediction of components at high temperature are quite large. Various phenomena like hot corrosion, low cycle fatigue, creep, relaxation and thermal fatigue take place either individually or two or more combinations of them. In addition to these mechanical type of considerations, metallurgical factors such as chemical attack on grain boundaries and general structural degradation are also to be considered. In the model proposed, only the mechanical aspects are considered. This can be improved and extended to metallurgical variables also as more data are analysed.

#### 4. Concluding remarks

In trying to model the damage accumulation and thereby predict the life of the component it is very important to know all the parameters that affect the damage process and their relative weightage. The logic and the governing equations are to be properly evaluated to build the sequence block diagram.

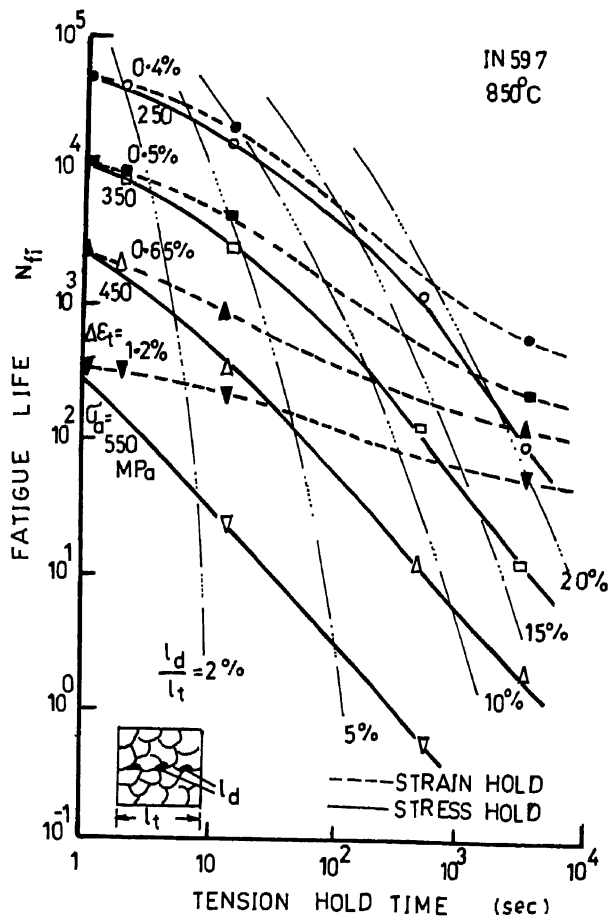


Figure 12. Interaction diagram for IN 597 alloy at 850°C.

## References

- Hofflener W and Speidel M O 1979 *Proc. Int. Conf. on High Temperature Alloys in Aggressive Environments*, Petten, The Netherlands, 993
- James L A 1972 American Society for Testing Materials Special Technical Report 513 218
- Jeglic F, Niesen P and Burns D J 1973 ASTM STP 520 139
- Kaisand L R and Mowbray D F 1979 *J. Test. Eval.* 7 270
- Radhakrishnan V M 1980a *Fatigue Engg. Mater. Struct.* 3 75
- Radhakrishnan V M 1980b *Engg. Fract. Mech.* 13 129
- Radhakrishnan V M 1982 *Damage accumulation and fracture life in low cycle high temperature fatigue*, ASTM STP 770 135
- Radhakrishnan V M 1983 Interaction diagram for time-dependent fatigue 1983 *Trans. A.S.M.E. JEMT* 105 273
- Taraneshi H and McEvily A J 1981 *Proc. ICF-5 Cannes*, 1981
- Toft L H, Yeldham D E and Plastow B A 1976 *Proc. Conf. Failure of Components operating in Creep Range I*, Mech. E., London (1976) p. 107
- Wareing 1981 *J. Fatigue Engg. Mater. Struct.* 4 131

## Computer applications in the field of furnace design

V S PAKALA

Department of Metallurgy, Regional Engineering College, Rourkela 769 008, India

**Abstract.** The development of mathematical models of furnaces is briefly reviewed. The basic processes taking place in furnaces and the problems associated with their mathematical formulation and the necessary assumptions are discussed. The difficulty of determining the process parameters, and the methods of their estimation are included. Applications of mathematical models for the study of cooling of ingots, heating of steel, cowper stoves and for the study of erosion of refractories are also discussed.

**Keywords.** Heating furnaces; mathematical models; process parameters; furnace design

### 1. Introduction

At the beginning of the present century, a Russian scientist, Groume-Grjimailo, placed the transparent model of a furnace upside down and passed water through it so as to study the flow of combustion products through the furnace. He could thus formulate the principles of design of some furnaces. This probably was the first scientific approach to the design of furnaces, and also the beginning of model studies of furnaces.

With the developments in the field of model studies it soon became evident that a clear understanding of the interaction of various parameters, influencing the process under study, is necessary for setting up an appropriate model. These interactions are best expressed in the form of mathematical relationships i.e. mathematical models.

The development of a mathematical model depends on a knowledge of the laws of behaviour of the system being studied, the capacity of expressing these in the form of mathematical equations, and the ability to solve them.

The basic processes, taking place in furnaces, are known for a long time, but the difficulties associated with the solution of the partial differential equations, with the complex boundary conditions involved, restricted the use of mathematical modelling of furnaces. Thring (1952) made some simplifying assumptions to calculate the heat transfer in open hearth furnaces and this probably is the beginning of mathematical modelling of furnaces.

With the developments in the field of digital computers, the interest in mathematical modelling of furnaces has increased significantly.

In this article, models of only heating furnaces i.e. furnaces where the charge does not undergo any chemical changes, are considered.

### 2. Types of models

Mathematical models based on the fundamental laws of behaviour of the system are called process models. These are concerned with the activity between start and finish of

the process and describe, among other things, the cause of the variability of the process time. The activities, in general, are continuous and the model consists of equations relating rates of change of variables, describing the system, to their current values i.e. the model consists of differential equations.

In some cases, e.g. logistics of assembly processes, models generating the time history of process are known as simulations. In these models the matters of interest are the start and finish of the process. The model determines the complete history of events from these events and the logistic laws.

Process models serve many purposes, including our understanding of the process and indicate areas where information is limited and further research desirable. In engineering they facilitate experiments which are otherwise not feasible since practical experiments on full scale iron and steel making units are difficult and expensive. Engineering modifications are also costly and almost impossible to examine experimentally on full scale plants. However, once a mathematical model is formulated and verified by plant measurements, it is in principle comparatively easier to carry out the necessary computer experimentation. Even if full scale experimentation is needed it can be restricted to a minimum number of crucial cases.

It must be recognized that every model is imperfect in one aspect or the other, either due to simplifications of the process mechanism that are necessary to evolve a practical model, or due to inadequate understanding of the mechanisms.

### 3. Formulation of furnace models

For heating furnaces where heating of the charge to a given temperature is the main objective, the model must be able to predict the internal temperature distribution of the charge at any given time. The temperature distribution in a solid charge is given by the conduction equation

$$\frac{1}{\rho c} \frac{\partial t}{\partial \tau} = K \nabla^2 t, \quad (1)$$

where  $K$  is the thermal conductivity of the material,  $\rho$  the density,  $c$  the specific heat,  $t$  the temperature and  $\tau$  the time. This equation has to be solved with the appropriate boundary and initial conditions to obtain the temperature distribution.

The boundary conditions usually give the heat flux to the surface.

$$q = -K \frac{\partial t}{\partial x}, \text{ at the boundary.} \quad (2)$$

For some simple boundary conditions, (1) can be solved by analytical methods if  $K$ ,  $\rho$  and  $c$  are independent of temperature. But in actual practice the boundary conditions are not simple and the values of  $K$  and  $c$  are dependent on temperature. In such cases only numerical solutions of the equation are possible, the method of finite differences being the most common. These methods have been described by Dusinberre (1961). Thomas *et al* (1984) analyzed the different methods and concluded that for simple geometry of the body, finite difference method is the most suitable. Tocher (1970) briefly analyzed the errors involved in these methods.



The value of  $q$  in (2) depends on the rate of heat transfer to the surface of the body from the furnace. This consists of radiation from flame, radiation and convection from the combustion products and radiation from the refractory walls. For precise calculation of the internal temperature of the body, precise formulation of these external heat flows is necessary.

The problems associated with mathematical description of flames were analyzed by Beer (1972). Furnaces usually have turbulent diffusion flames, and it is reasonable to assume that the development of the flame depends only on the mixing of fuel and air. The description of a turbulent flow system, with an exothermic chemical reaction, in terms of spatial distribution of velocity, concentration and temperature requires the simultaneous solution of partial differential equations for mass, momentum and energy transfer. Patankar and Spalding (1970) and Gosman (1969) discussed the solution of these equations. Apart from the complexity of the solution, difficulty arises with the values of the turbulent transport properties, which are not constants for the medium. Added to this is the difficulty to evaluate the development of luminosity in flames.

Most models developed for fuel-fired furnaces use simplifying assumptions for calculation of the external heat flow. Usually the furnace gases are assumed to be non-luminous having uniform temperature within the furnace chamber. In long furnaces, like pusher re-heating type, the furnace may be considered as consisting of a number of isothermal zones. If the temperatures of gas, refractory surfaces and charge surface can be represented by their respective mean temperatures, the heat transfer to the charge can be calculated by standard methods (McAdams 1954; Averin *et al* 1969; Davies *et al* 1970). Salter and Costick (1972) applied experimentally determined flame parameters for modelling a re-heating furnace. Fitzgerald and Sheridan (1970) used measured surface temperature of the charge to calculate the internal temperature distribution.

#### 4. Process parameters

The necessity of considering the variation of physical properties of steel with temperature was mentioned earlier. A fairly comprehensive source of data is a compilation by BISRA (1953). These are experimentally determined values. For temperatures above 1000°C, an error of 8–15% can be expected.

While heating steel, in most of the cases a layer of scale forms on the surface. Reliable data on the properties of scale are not available.

The difficulties involved in calculating the heat flow to the charge were mentioned earlier. In practice either simplifying assumptions have to be made or heat transfer parameters have to be determined from measurements on actual furnace.

The heat flux to the charge can be represented as either

$$q = \sigma F(T_f^4 - T_m^4) + h(T_f - T_m), \quad (3)$$

or 
$$q = H(T_f - T_m), \quad (4)$$

where  $T_f$  and  $T_m$  are the temperatures of furnace and the surface of the metal respectively,  $\sigma$  the Stefan-Boltzman constant,  $F$  is a radiation factor,  $h$  the heat transfer coefficient by convection and  $H$  is the combined heat transfer coefficient. The value of  $T_f$  is usually taken as the temperature indicated by the thermocouple located in the furnace chamber. From the measured temperatures of the metal the values of  $F$  and  $h$  or  $H$  are computed by solving the inverse heat transfer problem.

Lambert and Economopoulos (1970) described a method of using probes for determining the heat transfer coefficients. The heat transfer coefficients by convection can be determined with the help of isothermal physical models by making use of an analogy between heat transfer and mass transfer. From the measured mass transfer coefficients the heat transfer coefficients are computed. Davis *et al* (1970) used evaporation of naphthalene and Choudhury and Mukherjee (1979) used transfer of  $\text{CO}_2$  from the gases to filter papers soaked in NaOH solution to measure mass transfer coefficients.

## 5. Application of mathematical models for furnace design

A few of the applications of mathematical models for design of furnaces are discussed below.

### 5.1 Solidification of ingots

Although solidification of ingots is not a process taking place inside a furnace, the knowledge of internal temperature distribution of hot ingots is necessary for subsequent heating. By optimizing the stripping time and subsequent transit time before charging the ingots into soaking pits, considerable energy can be saved in the soaking pits. This problem was studied by Jackson *et al* (1944) using analogues and by Sargent and Slack (1954) using numerical methods and others.

The peculiarity of the solidification process is the liquid-solid transformation, which is accompanied by the liberation of latent heat. The governing differential equation becomes

$$\rho C \cdot \frac{\partial t}{\partial \tau} = K \nabla^2 t + \rho L \frac{\partial f_s}{\partial \tau} \quad (5)$$

where  $L$  is the latent heat and  $f_s$  the fraction of solid. This equation can be solved by applying the equivalent specific heat method where the specific heat is increased by an amount equivalent to latent heat in the solidification zone. This method is most widely used. Other assumptions made in formulating the model are: (a) the mould is filled instantaneously; (b) initially there is good thermal contact between the metal and the mould, for 2–3 min, when the heat transfer from metal to mould is by conduction; (c) very soon a solid skin is formed on the ingot, which shrinks away from the mould, leaving an air gap. Further heat transfer is by radiation only; (d) heat losses from the outer wall of the mould are uniform.

Sevrin (1970) calculated the solidification time of ingots and showed that mould thickness and mould temperatures, within limits, have no significant effect on the solidification time. Cherapanov and Kalashnikova (1971) claimed significant saving in the mould weight, based on these calculations.

Making use of the above assumptions the solidification of a 21-tonne ingot was earlier carried out by mathematical modelling (Pakala 1975). The calculated surface temperature was compared with values measured on an ingot, after stripping by optical pyrometer. The results showed good agreement, with a difference of about  $10^\circ\text{C}$  just

after stripping. But with further cooling the measured temperatures were lower than the calculated values. This was assumed to be due to scale formation on the ingot which was not considered in the model.

## 5.2 Heating of steel

Models for heating of ingots and billets were developed by Fitzgerald and Sheridan (1970), Collins (1970), Massey and Sheridan (1971), Massey *et al* (1973) etc. In all these models the furnace gas temperature was assumed to be uniform and the external heat transfer parameters were estimated from measurements on furnaces.

One of the factors to be considered in heating of massive steel ingots and billets is the heating rate. Too fast a heating rate results in a large temperature differential in the part with accompanying thermal stresses. In order to develop a satisfactory heating schedule for cold ingots a model was developed by the present author (Pakala 1975). Here the furnace gases were assumed to be at uniform temperature. The furnace walls were assumed to be perfect reflectors of radiation. This assumption was based on the fact that the wall temperature does not vary much with time and the heat conducted away through the walls is of the same order as the heat received by the walls by conduction.

The heat transfer parameters were calculated using equations reported in literature (Averin *et al* 1969). Variation of thermal conductivity and specific heat was accounted for. The mean gas temperature was calculated for every time step by iteration, assuming that

$$\text{Heat input through fuel and preheated air} = \text{Heat transferred to metal} \\ + \text{wall losses} + \text{waste gas losses.}$$

The fuel gases were assumed to leave the furnace at the mean gas temperature. Restrictions were incorporated in the programme, to ensure that the fuel rate does not exceed a given maximum value, and that the temperature difference between the surface and centre of the ingot does not exceed a given limit while the temperature of the ingot is below 500°C at the centre.

The minimum time of heating of 10 tonne ingots was calculated taking into account a two-dimensional heat flow. The heating schedule was adopted for an industrial unit and the ingots were found satisfactory for subsequent rolling. By this a 10% saving in heating time was achieved.

Chopdar *et al* (1980) calculated the heating time for annealing of open coils of steel strip under controlled atmosphere, and Padhy (1982) calculated the same for tight coils using mathematical models. Both these results were used for design calculations of hood annealing furnaces.

Fitzgerald and Sheridan (1970) described design modifications carried out on a reheating furnace based on the results of mathematical models.

## 5.3 Cowper stoves

A detailed model of Cowper stove was described by Hoffman and Kappelmayer (1970). Rakesh Kumar and Sugavanam formulated a simplified model of Cowper stoves, for evaluating the effect of fuel rate, duration of on-blast and on-gas periods etc on the performance of stoves.

#### 5.4 Refractory erosion in blast furnace

Erosion of refractories in the hearth of a blast furnace, giving rise to formation of salamander is of primary importance from the point of view of campaign life. Paschkiss and Mirsipassi (1954) considered this purely from the heat transfer point of view and solved the two-dimensional steady state conduction problem on electrical analogue. They considered that only liquid iron can erode the refractories and that the salamander can penetrate to the level of 1150°C isotherm. Das (1981) calculated the isotherm for blast furnace at Rourkela. Singh *et al* (1982) reported monitoring of B.F. hearths by temperature measurements at TISCO.

Yoshikawa and Szekeley (1981) considered the problem taking into account convection currents in the hearth. Bandak (1973) described a model for estimating the erosion of lining in the bosh and stack regions of blast furnace.

## 6. Conclusions

At the present state of knowledge, the mathematical models of furnaces, particularly those involving combustion of fuel, are far from perfect because of the difficulties involved in modelling the external heat transfer. Hence any model set up requires verification on industrial units. Despite these difficulties, considerable information can be obtained from these models for design and operation of industrial furnaces, and can be considered as a necessary tool for improvement of design and performance of furnaces.

## References

- Averin S I, Goldfarb A M, Kravtsov A F, Radchenko I I, Rosengart U I, Svinolov N P, Semikin I D and Taits N U 1969 *Calculations of heating furnaces (in Russian)* 2 e Kiev, Technica Chapter 6
- Bandak T A 1973 *Mathematical process models in Iron and Steel making*, Metals Society 26
- Beer J M 1972 *Jl. Inst. of Fuel* 370
- BISRA 1953 *Physical Constants of some commercial steels at elevated temperatures* (London: Butterworth)
- Cherapanov K A and Kalashnikova U K 1971 *Steel in USSR* p. 442
- Chopdar A K, Behera R C and Pakala V S 1980 *Trans I.I.M.* 32 384
- Collins R 1970 Mathematical models in metallurgical process development, The Iron & Steel Institute Sp. report, p. 230
- Das B K 1981 *Salamander penetration and its impact on blast furnace relining*, M.Sc (Engg) Thesis, RE College, Rourkela
- Davies R M, Lucas D M, Master J and Toth H E 1970 Mathematical models in metallurgical process development, The Iron & Steel Institute Sp. report, p. 29
- Dusinberre G M 1961 *Heat transfer calculations by finite differences* (Scranton: Int. Text Book Co.)
- Fitzgerald F and Sheridan A T 1970 Mathematical models in metallurgical process development, The Iron & Steel Institute Sp. report, p. 18
- Gosman A D 1969 *Heat and mass transfer in recirculating flows* (London: Academic press)
- Hoffman E E and Kappelmayer A 1970 Mathematical models in metallurgical process development, The Iron & Steel Institute Sp. report, p. 115
- Jackson R 1944 *Jl. of the Iron & Steel Institute* 150 211
- Lambert N and Economopoulos M 1970 Mathematical models in metallurgical process development, The Iron & Steel Institute Sp. report, p. 133
- Massey I D and Sheridan A T 1971 *Jl. of the Iron & Steel Institute* 391
- Massey I D, Robertson A D, Sanders L M and Sheridan A T 1973 *Jl. Inst. of Fuel* 379
- McAdams 1954 *Heat Transmission* (New York: McGraw Hill)

- Padhy A K 1982 *Design of Hood annealing furnace*, M. Tech thesis, RE College, Rourkela
- Pakala V S 1975 *Combined application of physical and mathematical models to heating furnaces*, Ph.D. thesis, Zhdanov Metallurgical Institute, USSR
- Paschkiss V and Mirsipassi T 1954 *Iron Steel Eng.* **31** 54
- Patanakar S V and Spalding D 1970 *Heat and mass transfer in boundary layers* (London: Int. Text Book Co.)
- Rakesh Kumar and Sugavanam R 1981 *Mathematical model of Cowper Stove*, B.Sc (Engg) Project report, RE College, Rourkela
- Salter F M and Costick J A 1974 *Jl. Inst. of Fuel* **47** 3
- Sevrin R 1970 Mathematical models in metallurgical process development, The Iron & Steel Institute Sp. report, p. 147
- Singh B N, Chatterjee L M and Chatterjee A 1982 *Trans. I.I.M.* **35** 475
- Surgent R J and Slack M R 1954 *Jl. of the Iron & Steel Institute* **177** 428
- Thomas B G, Samarasekera I V and Brimacombe J K 1984 *Met. Trans.* **B15**(2) 307
- Thrig M W 1952 *Jl. of the Iron & Steel Institute* **171** 381
- Tocher K D 1970 Mathematical models in metallurgical process development, The Iron & Steel Institute Sp. report, p. 2
- Yoshikawa F and Szekely J 1981 *Ironmaking Steelmaking* **4** 159



## Computer simulation of defects and radiation damage

K KRISHAN, B PURNIAH and S SRINIVASAN

Materials Science Laboratory, Indira Gandhi Centre for Atomic Research, Kalpakkam 603 102, India

**Abstract.** In this paper, we describe the computer simulation technique and its application to the study of radiation damage. Details of two important methods: the static and the dynamic methods have been discussed. Applications to the study of point defect formation and stability, their clusters, diffusion, dislocations and dislocation-point defect interaction are discussed drawing from our own work wherever possible. A short mention is made of the importance of the interatomic potential. Examples for the case of magnesium and other hcp metals, bcc iron and fcc Ni are cited and numbers for various quantities like formation energy, dipole tensor, interaction energy etc are quoted.

**Keywords.** Computer simulation; interatomic potential; static method; dynamic method; point defects; dislocations; displacement damage.

### 1. Introduction

The study of matter in radiation environments has developed into an important area of research due to the technological demand of finding reliable and stable materials for the structural components of nuclear reactor systems. The energetic particles of the radiation displace the atoms in a metal (or alloy) bringing about irreversible changes in the composition and microstructure. These changes at an elementary level involve three processes: the formation of defects, their diffusion and subsequently annihilation. Each of these damage events leaves behind a permanent mark whose cumulative effect results in the changes in alloy properties often referred to as radiation damage. Some examples of these are embrittlement, irradiation creep and swelling. Invariably, these involve the redistribution of radiation-produced defects due to diffusion and are studied with the help of rate equations whose parameters are related to basic 'damage events'. It is in the study of this more basic aspect of radiation damage that computer 'experiments' play a very important role.

The basic damage process occurs over several orders of magnitude in time. In the first  $10^{-17}$  sec an energetic projectile transfers its energy to the nucleus of the metal lattice atom producing a primary knock-on-atom (PKA). In the next  $10^{-13}$  sec the PKA slows down creating a cascade of secondary displacements. The cascade volume dissipates its energy in  $10^{-11}$  sec forming unstable defects which spontaneously rearrange themselves into stable defects. Then begins a long period of several hundreds of seconds when these defects diffuse and eventually annihilate at sinks. This annihilation, or defect annealing, depends on the interaction between the defects and leads to the formation of clusters or complexes depending on their relative stability. The very short times involved and the statistical nature of the events (due to the large number of degrees of freedom) makes it difficult to use analytic methods of investigation or device experiments where each event can be followed. However, the advent of high speed

computers has made it possible to simulate these processes in a way as if they are actually occurring in a solid. It is for this reason that such studies have been termed computer experiments.

Computer experiments deal either with the dynamic aspects of damage like the formation of cascades or with static aspects which concern the formation of stable defect configurations. In §2, we give an account of the computer simulation procedure for both static and dynamic experiments. Section 3 deals with the range of problems which have been studied with typical examples and results drawn from our own work wherever possible. Finally in §4 we give a brief conclusion.

## 2. Computer simulation technique

In general, in all computer simulation methods, a model crystallite of the required material is constructed in which the atoms are allowed to interact via a suitable interatomic potential. The defect is then placed at the centre of this crystallite. The presence of the defect will cause forces to act on the atoms surrounding it. This configuration is allowed to relax using either the static or dynamic method. The number of atoms in this crystallite usually ranges from a few hundred to a few thousand depending on the complexity of the defect under study and the range of interatomic potential. The computation of the various quantities of interest requires that a neighbour set be generated for each atom in the crystallite. While the generation of the crystallite itself is quite simple once the crystal type is known, generation of neighbours calls for greater efforts and will be treated in greater detail below. After a brief discussion on interatomic potentials we discuss the techniques for relaxation. Several techniques used in computer simulation including sample programmes are discussed in a recent book by Beeler (1983a). Towards the end of this section two specific examples viz the simulation of point defects and dislocations is discussed in slightly greater detail.

### 2.1 Generation of neighbours

In the case of cubic crystals the position vector of any atom can be conveniently described by a set of three integers if distances are measured in half lattice units. The neighbour positions in an fcc crystal can be generated by a technique of partitioning the squares of the radial distances  $NR^2$  (which occur in multiples of 2) and thereafter by taking the various possible permutations of these partitioned numbers. Thus we have  $NR^2 = NX^2 + NY^2 + NZ^2$  where the integers  $NX$ ,  $NY$  and  $NZ$  represent the components along the  $x$ ,  $y$  and  $z$  directions respectively (see table 1). A given value of  $NR^2$  denotes a particular shell and the atoms in the shell can be obtained by the permutations of the three numbers as shown in the table.

The generation of neighbours in an hcp lattice is more complicated. Firstly, the radius vector of all the atoms in the crystallite is calculated from a given origin and arranged in an ascending order. Atoms having the same radius are grouped together into one shell. These atom co-ordinates are then normalized to yield integer numbers and these are stored for later use. It may be noted that a further complication arises because of the  $c/a$  ratio. For instance the fourth and sixth neighbour shells of Mg ( $c/a = 1.63$ ) and Zr ( $c/a = 1.86$ ) get interchanged.



**Table 1.** Shell-wise neighbour generation for an fcc crystal

$NR^2$	$NX$	$NY$	$NZ$	$X$	$Y$	$Z$
0	0	0	0	0	0	0
2	0	1	1	0 0	1 1	1 -1
4	0	0	2	0 0	-1 -1	1 -1
6	1	1	2	1 1	0 0	1 -1
8	0	2	2	-1 -1	0 0	1 -1
10	0	1	3	1 1	1 -1	0 0
12	2	2	2	-1 -1	1 -1	0 0
:	:	:	:	:	:	:

While the above discussion holds for the simulation of point defects, in the case of dislocation simulation, it is convenient to choose the co-ordinate axes along the dislocation line and Burgers vector thereby necessitating a transformation in neighbour co-ordinates.

## 2.2 Interatomic potential

A crucial aspect of computer simulation is the choice of an appropriate interatomic potential. A large number of diverse interatomic potentials have been proposed in the literature. These can be broadly classified as empirical and pseudopotentials. Examples of the former are the Morse, Lennard-Jones and several polynomial potentials (Johnson 1973). Pseudopotentials are known to represent the interaction better but these have not made much headway in defect calculations. The most widely used polynomial potentials for defect calculations have been the cubic and the quintic splines where the polynomial coefficients are obtained by least squares spline fitting the potential to the elastic constants of the material. Such potentials for cubic metals have been described by Baskes and Melius (1979) while those for hcp metals have been described by Purniah *et al* (1980).

## 2.3 Relaxation techniques

As already stated, the configuration of the crystallite containing the defect is allowed to relax to a minimum energy configuration. The crystallite is usually divided into two regions to save on computation time. In the inner region I, the atoms are allowed to relax under the influence of the chosen potential. The atoms in the outer region II are constrained to their perfect lattice positions as shown in figure 1. The relaxation of atoms in region I can be done either by the static method or the dynamic method. In the static method, the relaxation is performed by an iterative technique using the Newton-

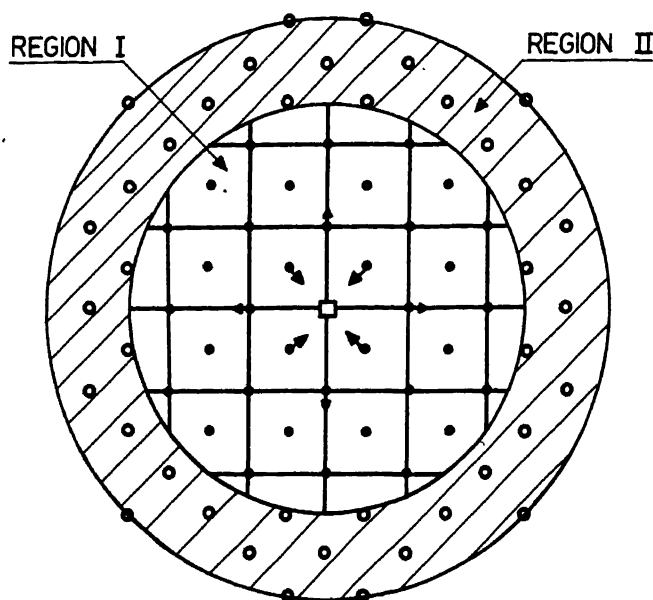


Figure 1. Schematic representation of the two regions in a crystallite used in computer simulation studies. Open circles represent atoms which are fixed while filled circles indicate the atoms which are allowed to move. Also shown by arrows is the displacement of atoms around a vacancy ( $\square$ ) placed at the centre.

Raphson method. Thus the relaxed position of the  $n$ th atom after  $k+1$  iterations is given by

$$X_{k+1}(n) = X_k(n) - \alpha \frac{\partial U}{\partial X(n)} \bigg/ \frac{\partial^2 U}{\partial X^2(n)} \bigg|_{X(n) = X_k(n)},$$

where  $X_k(n)$  is the co-ordinate of the  $n$ th atom after the  $k$ th iteration and  $U$  is the configuration energy. The convergence factor  $\alpha$  ( $0 < \alpha \leq 1$ ) has been introduced to damp out the oscillations which are usually present in the co-ordinates  $X_k$  while applying the Newton-Raphson technique directly. The total number of iterations for reasonable convergence may run into several hundred depending on the problem being considered. From the above discussion it is clear that the simulation work requires a large and fast computer. Typically all the programs operate in double precision, occupying 512 kilobytes of core memory and take upto one hour of CPU time.

In the dynamical method also referred to as "molecular dynamics" method, the movement of individual atoms in an assembly is followed using Newton's equations. Given the initial position and the velocity for each atom in the crystallite, the dynamical history is followed by numerically integrating the  $3N$  simultaneous equations of motion for the co-ordinate components of the  $N$  atoms in the crystallite. In the process, the  $3N$  velocity components for the  $N$  atoms are also determined.

The dynamical method is very useful in describing temperature effects on Frenkel pair production, annihilation and point defect complexes.

The net force  $F(t)$  experienced by an atom at time  $t$  is determined by the relative positions of all the other atoms at time  $t$  and  $a(t) = F(t)/m$ . Given  $a(t)$ , the advanced

time quantities are given by using one of the many schemes available (Gibson *et al* 1960)

$$v(t + \Delta t/2) = v(t - \Delta t/2) + a(t) \Delta t,$$

$$x(t + \Delta t) = x(t) + v(t + \Delta t/2) \Delta t.$$

In these simulations, the value of  $\Delta t$  is in the region of  $10^{-14}$  sec which gives an idea of the time scales which can be probed.

## 2.4 Simulation of point defects and dislocations

In the case of point defect simulation, the inner region I is chosen to be a sphere. Periodic boundary conditions are employed to essentially generate the large size of the assembly needed to remove any surface effects. This is further checked out by varying the size of region I to see the effect of the boundary region. The defect formation energy is calculated by subtracting the energy of the perfect lattice from the energy of the relaxed lattice with either an extra atom (vacancy case) or an atom-less (interstitial case) at the crystal surface. The relaxation energy is obtained by subtracting the energy of the crystallite with the defect in the relaxed condition from that in the unrelaxed condition.

The inner region for the case of dislocation simulation is chosen to be cylindrical to take advantage of the symmetry in the problem. The direction of the dislocation coincides with the cylinder axis and periodicity along the dislocation line is assumed. The 'introduction' of the dislocation is done by imparting elastic displacements to the atoms by considering a dislocation at the centre of the block (Cotterill and Doyama 1967). The core configuration and other parameters can be obtained by the relaxation technique described. There have been several modifications to the methods described above for dislocations. One of these is the 'flexible' boundary condition method (Hoagland *et al* 1976) where the atoms in region II are moved in response to the changes which occur in the inner region. This enables a smaller crystallite size to be chosen thereby reducing the computation time. It may however be noted that in the study of the dislocation point defect interaction the flexible boundary methods cannot be used since the introduction of the point defect destroys the symmetry in the problem.

## 3. Application of computer simulation to radiation damage problems

In this section we briefly discuss some of the areas where computer simulation has been successfully used to investigate the behaviour and properties of defects produced by radiation. The selection has been made to cover a range of problems and to emphasize the nature of information obtained by the technique rather than the detailed results.

### 3.1 Vacancies, interstitials and their clusters and complexes

The study of point defects and their clusters has been one of the important areas where computer simulation experiments have been particularly successful. Here due to the many degrees of freedom available one has to examine from amongst several possibilities, the configurations which would be most stable. For example figure 2 shows three configurations each of di-vacancies and tri-vacancies and the three possible sites for a self-interstitial—namely split, tetrahedral and octahedral for an hcp lattice.

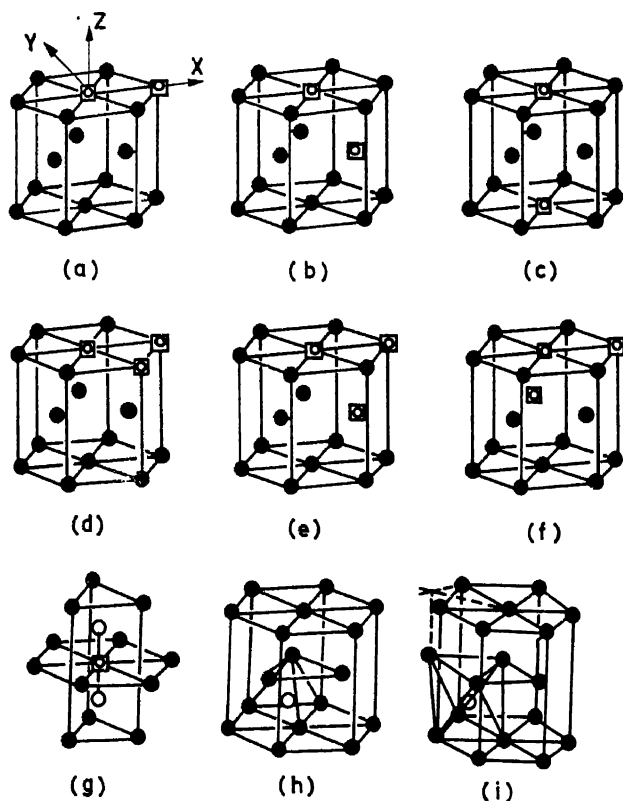


Figure 2. The three possible configurations each of the divacancy (a, b, c) and trivacancy (d, e, f) in hcp magnesium. The three configurations at the bottom are those for the split, tetrahedral and octahedral interstitial.

These are amongst the more favourable ones and further possibilities cannot be ruled out. Computer simulation has shown that for self-interstitials the split configurations along  $\langle 110 \rangle$  for bcc,  $\langle 100 \rangle$  for fcc and  $\langle 0001 \rangle$  for hcp are most favourable on the basis of minimum energy consideration. A comparison of the strain field of a vacancy and a self-interstitial is shown in figure 3 for hcp Mg as a typical example (Sahu *et al* 1980). Table 2 shows the relaxation field around a monovacancy for several hcp metals (Purniah *et al* 1980). Characteristic of this strain field are the positive and negative displacements of the different neighbouring shells; the maximum displacement at the third neighbour for a vacancy in Mg; nearly an order of magnitude higher strain field for self-interstitials as compared to vacancies. Similar features have been seen in bcc iron and fcc nickel which are some of the metals extensively studied. Very similar to these are investigations on over-sized and under-sized substitutional impurities whose strain fields show similar behaviour. For a 10% over-sized impurity in bcc iron, the energy of each of the first-neighbour atoms increases (+0.036 eV) (i.e. high energy atom site) and that of the second neighbours decreases (−0.026 eV) (low energy atom site). A systematic study of this feature leads to a rule for predicting the geometry of an impurity-vacancy complex (Beeler 1983b). If a high-energy atom site in the substitutional impurity atom displacement field is replaced by a vacancy, the resulting

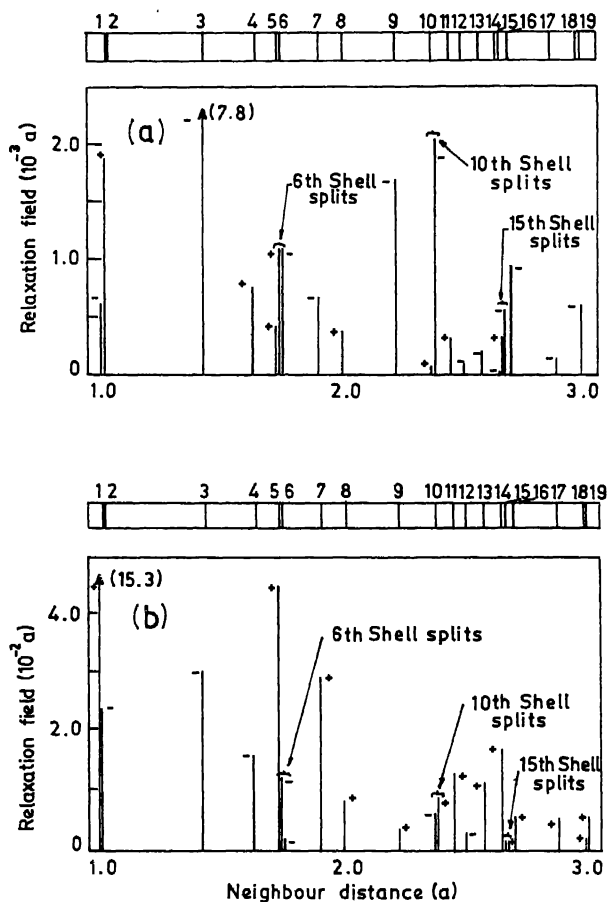


Figure 3. The relaxation field of all shells up to nineteen neighbours around a single vacancy (a) and a split interstitial (b). The bars on top represent the neighbour positions shown separately for clarity. (+ and - signs indicate outward and inward relaxation).

Table 2. Relaxation field around a monovacancy. The numbers 1st, 2nd, 3rd and 4th refer to neighbours. (The + and - signs indicate outward and inward relaxation).

Metal	Relaxation field ( $10^{-2} a$ )				Relaxation volume $\Delta V/V_{at}$	Dipole tensor (eV)	
	1st	2nd	3rd	4th		$P_{11} = P_{22}$	$P_{33}$
Hf	-1.32	-0.65	+0.48	+0.41	-0.18	-4.09	-7.94
Mg	-0.40	-0.34	-0.69	+0.01	-0.09	-0.93	-0.95
Re	-0.80	-0.70	+0.12	+0.19	-0.14	-8.16	-11.24
Y	-2.09	+0.70	+1.36	+0.48	-0.21	-1.57	-6.32
$\alpha$ -Zr	-1.62	-1.80	+0.28	+0.35	-0.31	-6.92	-8.36
Be	+6.15	+2.04	+5.65	+3.72	+0.56	+7.74	+1.73

complex will have a positive binding energy while for a low-energy atom it will result in a negative binding energy. Such features are also found in the stability of some defect complexes. For example in bcc iron a second neighbour arrangement of vacancies has been found to be more stable than first neighbours arrangement. In hcp Mg, of the three configurations (a), (b) and (c) shown in figure 2 for di-vacancies the formation (and binding) energies are 1.377 (0.086), 1.379 (0.084), 1.386 (0.077) eV respectively showing that configurations (a) and (b) are likely to be more stable at lower temperatures (Sahu *et al* 1980). Similarly for the tri-vacancy configurations (d), (e) and (f) have energies 1.939 (0.256), 1.942 (0.252) and 1.972 (0.222) eV which favours the planar configuration (d). Extensions of such simulation experiments have been carried out to very large vacancy clusters ( $\sim 40$ ) to examine how such clusters could develop into vacancy dislocation loops or voids (Beeler and Johnson 1967).

Apart from substitutional impurities, light atoms like C, N and O often occupy interstitial locations. The simulation technique in this case is very similar to that for self-interstitials, the important difference arises from the use of an impurity-host potential. Apart from the defect formation energy  $E_f$  and migration energy  $E_m$ , other important parameters are the defect formation volume and the dipole tensor. Results for some of the calculations are shown in table 3 (Purniah *et al* 1982). The agreement between the estimated  $E_m$  and that obtained from experiments is seen to be very good. Further the dipole tensor values compare very favourably in sign and magnitude from those obtained by anelastic data and x-ray measurements.

Studying the behaviour of He in metals has been a problem of great technological interest where computer experiments have been very valuable. Helium can diffuse interstitially and readily forms complexes with vacancies. Computer simulation studies have revealed that as many as six to seven helium atoms can be accommodated in a single vacancy! These studies give detailed information about helium and vacancy binding to a complex of  $n$  helium atoms and  $m$  vacancies (Wilson *et al* 1976). The structure of some typical complexes is given in figure 4.

The study of diffusion of vacancies, interstitials, clusters and complexes of defects is an area where computer simulation is particularly useful. A defect moving from one equilibrium position to another has to pass through an intermediate unstable saddle point which determines the height for the migration barrier. Computer simulation provides detailed information about these intermediate configurations. As an example figure 5 shows the results of computer simulation of vacancy migration in bcc iron. The nature of the interaction and the positions of the surrounding atoms gives rise to two saddle points SP1 and SP2 as the atom A moves from its site to the vacancy (Beeler 1983c).

Table 3. Simulation results for various quantities for interstitials in  $\alpha$ -Fe, Zr and Hf

Interstitials	$E_f^i$ (eV)	$V_f$ ( $\Omega_0$ )	$E_m$ (eV)	$E_m$ (expt) (eV)	Dipole tensor (eV)	
					$P_{11} = P_{22}$	$P_{33}$
C in $\alpha$ -Fe	1.35	0.055	0.86	0.835	-0.053	4.223
C in Zr	1.38	0.048	1.48	1.48	1.472	1.395
O in Zr	2.98	-0.002	1.94	2.04	-0.049	-0.046
O in Hf	3.30	0.0	2.16	2.26	0.001	0.001

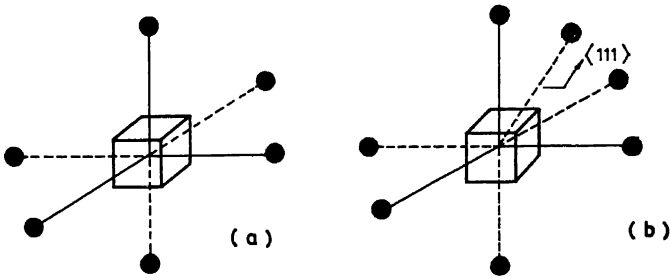


Figure 4. Minimum energy configurations of six and seven helium atoms in a single vacancy in Cu. Helium atoms are described by filled circles and the vacancy by the empty cube.

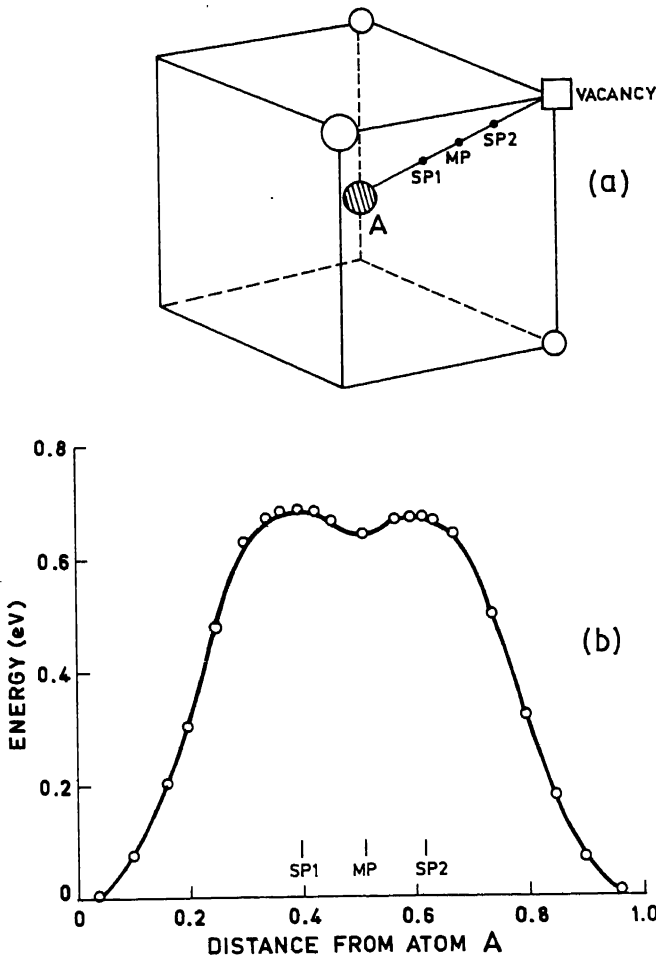


Figure 5. (a) Vacancy migration in bcc iron. The vacancy ( $\square$ ) migrates to the site A (the body centre position) via the two saddle points SP1 and SP2. MP is the mid-point of the path. (b) Crystal configuration energy change for the vacancy migration path shown above.

Computer simulation has also been employed in the study of dislocations and their interaction with point defects. For example the splitting into partials of an edge dislocation in an fcc lattice has been seen by simulation. Quantities like the stacking fault width and the core structure have been evaluated (Perrin *et al* 1972). A most recent review covering the literature of dislocation modelling in various systems can be found in Puls (1980).

The study of dislocation-point defect interaction is very important to understand many metallurgical processes like strain aging etc. Computer simulation has been effectively utilized to obtain information regarding the configuration and energetics of this interaction. The interaction of a carbon atom with an edge dislocation in fcc nickel has been studied by Purniah *et al* (1985). The salient features of these results are the correct prediction that the small-sized interstitial prefers to sit above the slip plane. Further, the dipole tensor which was originally spherical in the absence of the dislocation becomes monoclinic.

### 3.2 Displacement damage simulation

Most of our knowledge about atomic displacements and cascade damage has come from dynamic computer simulation. A projectile with a given energy and appropriate direction with reference to the crystallographic orientations is allowed to move at time  $t = 0$ . The subsequent interactions with the lattice atoms are then observed according to the predetermined force laws. Different structures emerge depending on the kinetic energy of the projectile. At energies less than the displacement energy  $E_d$  (typically 10–50 eV in most metals), the energy loss is mainly by elastic collisions. This energy loss is channelled normally along crystallographic directions called focussons (Silsbee 1957). At energies around  $E_d$  and above, a Frenkel pair is formed. One of the important features of this process is the replacement collision sequence where atoms in a chain exchange positions. The length of such sequences is generally 3 to 10 atomic distances but rather long replacement collision chains (greater than 50 atomic distances) can also exist in certain close packed directions (Lucasson 1975). The minimum displacement energy  $E_d$  depends on the relative direction of the projectile with respect to the crystallographic planes and is often obtained as the displacement energy surface as shown in figure 6a. At higher projectile energies the probability of forming more than one Frenkel defect increases (figure 6b). At still higher energies new features emerge. The initial PKA is able to impart enough kinetic energy to atoms to produce secondary collision cascades which normally branch off at right angles to the primary cascades thus resulting in multiple Frenkel pairs. These subcascades can sometimes overlap reducing somewhat the chances of survival of Frenkel pairs. In all these simulation runs the relaxation of atoms, spontaneous reorganization or recombination of unstable configurations is built into the simulation event. A graphical picture of the process at 5 keV obtained by Beeler (1966) is given in figure 7.

## 4. Conclusions

In this paper we have discussed the computer simulation technique and its application to the study of defects in materials. In particular, we have considered the case of point defects, impurities, dislocations and dislocation-point defect interactions. Several other



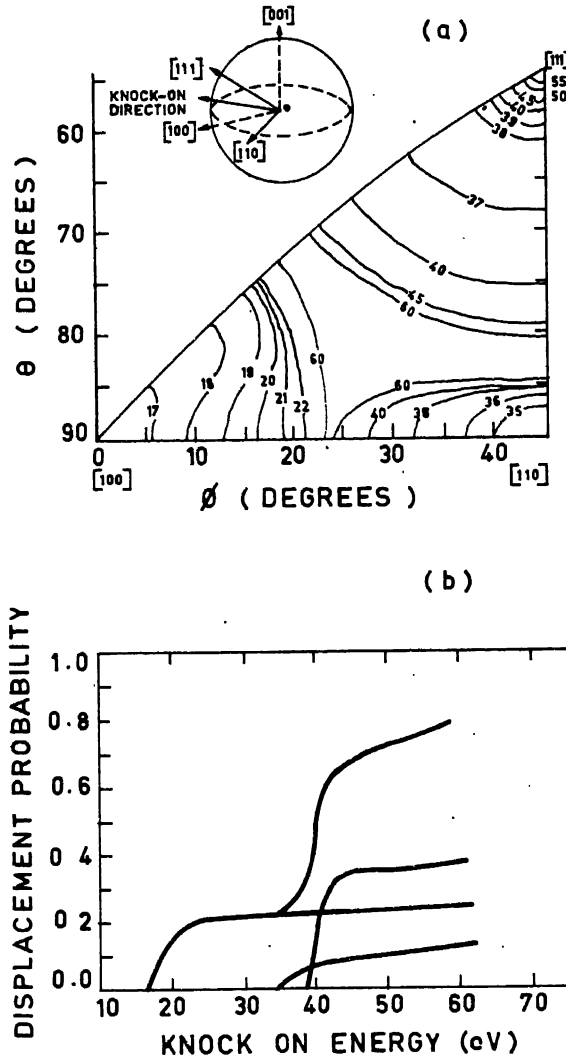


Figure 6. (a) Contours of constant displacement energy threshold (in eV) in bcc Fe. T polar and azimuthal angles define the PKA emission direction (Erginsoy *et al* 1964). Integrated displacement probability  $P_d(t)$  for a PKA of energy  $E$  and random direction in iron. Contributions to the three low-index directions are shown separately.

areas of study have been omitted due to the limitations of space. Notable among the are studies regarding the behaviour of grain boundaries, slip and other deformation related processes. While the results depend very much on the exact interatom potential chosen, the wide applicability of this technique makes it a very useful tool research.

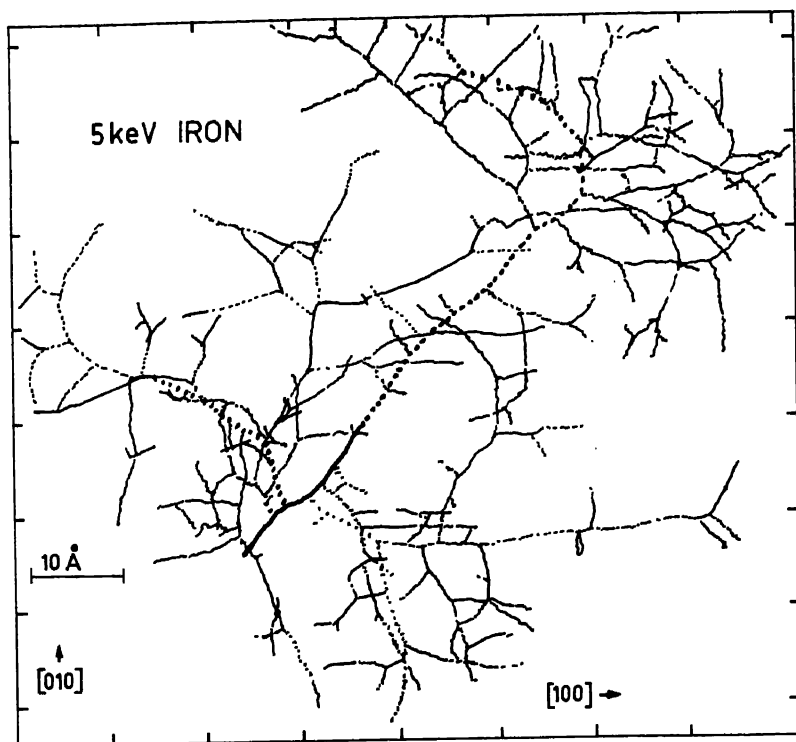


Figure 7. Trajectory map for a 5 keV collision crack in bcc iron. The short thick line represents the PKA trajectory. The 3 main secondary knock on trajectories are represented by heavy dotted lines. For higher order knock on the trajectory lines are alternately solid and dashed lines.

## References

- Baskes M I and Melius C F 1979 *Phys. Rev.* **B20** 3197
- Beeler J R Jr 1966 *Phys. Rev.* **150** 470
- Beeler J R Jr 1983a *Radiation effects computer experiments* (Amsterdam: North-Holland)
- Beeler J R Jr 1983b *Radiation effects computer experiments* (Amsterdam: North-Holland) p. 318
- Beeler J R Jr 1983c *Radiation effects computer experiments* (Amsterdam: North-Holland) p. 428
- Beeler J R Jr and Johnson R A 1967 *Phys. Rev.* **156** 677
- Cotterill R M J and Doyama M 1967 in *Lattice defects and their interactions* (ed.) R R Hasiguti (New York: Gordon and Breach) p. 20
- Erginsoy C, Vineyard G H and Englert A 1964 *Phys. Rev.* **A133** 595
- Gibson J B, Goland A N, Milgrom M and Vineyard G H 1960 *Phys. Rev.* **120** 1229
- Hoagland R G, Hirth J P and Gehlen P C 1976 *Philos. Mag.* **34** 413
- Johnson R A 1973 *J. Phys.* **F3** 295
- Lucasson P 1975 in *Fundamental aspects of radiation in metals* (eds) M T Robinson and F W Young (US Department of Commerce, National Technical Information Service, Springfield, USA, Report Conf. 751006) Vol. 1, p. 42
- Perrin R C, Englert A and Bullough R 1972 in *Interatomic potentials and simulation of lattice defects* (eds) P C Gehlen, J R Beeler Jr. and R I Jaffee (New York: Plenum Press) p. 509
- Puls M P 1980 in *Proc. Int. Conf. on Dislocation Modelling of Physical Systems*, (ed) C S Hartley (UK: Pergamon Press) *Special Acta Met./Scripta Met. Publication*

- Purniah B, Srinivasan S and Krishan K 1980 in *Proc. Nucl. Phys. and Sol. State Phys. Symposium, Delhi* (Department of Atomic Energy) Vol. C23, p. 742
- Purniah B, Srinivasan S and Krishan K 1982 in *Point defects and defect interactions in metals* Proc. Int. Conf., (eds) J Takamura, M Doyama and M Kiritani (Tokyo: Univ. of Tokyo Press) p. 322
- Purniah B and Srinivasan S 1986 *Bull. Mater. Sci.* **8** 247
- Sahu H K, Srinivasan S and Krishnan K 1980 *Pramana (J. Phys.)* **15** 189
- Silsbee R H 1957 *J. Appl. Phys.* **28** 1246
- Wilson W D, Baskes M I and Bisson C L 1976 *Phys. Rev.* **B13** 2470



## Some fundamental considerations to precede image analysis

DIETER VOLLATH

Kernforschungszentrum Karlsruhe GmbH, Institut für Material- und Festkörperforschung III, Postfach 3640, D-7500 Karlsruhe, FRG

**Abstract.** This paper explains the different types of specimens which are of a deterministic or stochastic nature. Especially for stochastic specimens it is pointed out that, before any measurement is done, the problem has to be analyzed as to why we measure. As a size per se does not exist it is shown that particles must be analyzed by size and shape. For this, two methods are indicated, while it is stressed that in materials science the Delfiner approach for description of particle sizes is the most practicable.

Based on Delfiner's concept of size the classification of particles according to their size, shape and orientation is explained. For measuring use of the image transformations *erosion*, *ouverture* is proposed. In addition, a new transformation called "*Template matching*" is explained. This new transformation avoids the disadvantages of erosion and ouverture in case of concave particles. Besides, template matching, in contrast to erosion or ouverture, is able to give true values of area and circumference. The concept of classification is explained by simple examples.

**Keywords.** Image analysis; erosion; ouverture; template matching.

### 1. Introduction

Many instruments for image analysis are presently on the market. Each of these instruments has many characteristic features. With the steady increase of computer performance the image analysers offer a growing number of possibilities. The user of these instruments is confused. It is the aim of this paper to give some hints on how to begin measurements with an image analyser. These considerations are made from the standpoint of a materials scientist. Possibly in life sciences the questions are different and likewise the solutions; but, maybe, the basic ideas are similar.

### 2. Categories of problems

Before a measurement starts the underlying problem must first be defined. This may seem a trivial condition, and it is without any significance as long as there are only limited possibilities of measurement. It becomes relevant only as a result of the fact that the theoretical and technical advances in measurement have made it possible to find answers to a broader range of questions.

When selecting the measuring technique, first of all the character of the sample material must be studied. In this respect, two categories of problems must be distinguished:

- Deterministic problems. They refer to sample material, each detail of which must be analyzed and classified. A typical problem in this category is, e.g., automatic reading of texts in which each and every letter must be identified and classified. Another

example is the automatic quality control of workpieces for perfection. Also in this case, each individual workpiece must be analyzed and faulty workpieces sorted out.

- Stochastic problems arise if parts of a sample are measured which satisfy a distribution function and the sample satisfies conditions of stationarity. In this sample material it is not important to measure each individual element of the particles of interest. It is sufficient to measure a statistically significant fraction of the sample. However, care must be taken to avoid a bias to be introduced into the statistics by the choice of the fraction of the sample measured. Typical applications of this technique are measurements of segregations in alloys or counts of pore size distributions. The automatic examination for cracks in workpieces does not fall under this category of problems, because in this case even a single crack in a workpiece may mean that the respective item must be scrapped. This is a typical deterministic problem, because every potential crack must be found.

Also the measuring techniques to be applied depend on the problem at hand. In the case of deterministic problems, the individual objects must be singularized before measurement; in general, methods of pattern recognition are applied subsequently. In the case of stochastic samples we are not interested in readings obtained from individual particles. In this case we measure field quantities (Nawrath and Serra 1979), it may even be necessary to carry out transformation before measuring within the image. These techniques are based on Minkowski's operations of sets (Hadwiger 1950) or on correlation functions (Vollath 1981). In this connection, especially the field of mathematical morphology has advanced quite far (Matheron 1967; Haas *et al* 1967a,b; Serra 1969). These are the fundamental papers, which have produced an immense amount of literature.

Occasionally, however, also sample material of a stochastic nature may cause problems which cannot be solved by the familiar techniques applied to analysis of such sample materials. In this case, a roundabout way will have to be found, which involves individual analysis of the particles of the sample and further processing by the rules of statistics of the results of such deterministic analysis.

Table 1 is a summary of these problems and the corresponding methods of evaluation. This paper will be limited to the problems of processing samples of a

**Table 1.** Problems and methods of evaluation used in image analysis

	Character of sample	
	Deterministic	Stochastic
Structure of sample	Group of significant shapes	Randomly distributed particles
Application	Pattern recognition, sorting out faulty workpieces	Materials analysis, characterization of powders
Methods	All techniques of pattern recognition	Minkowski operations of sets (mathematical morphology), correlation function
Results	Significance of a symbol, yes-no information about the quality of workpieces	Distribution function with respect to one or more parameters

stochastic nature, although a considerable part of the treatment also applies to sampling of a deterministic analysis.

### 3. What to measure?

Once the type of sample has been defined, a technique of measurement can be found. Any measurement must be based on a clear-cut technical or physical problem. In order to allow the measured result to be interpreted in the sense of such a problem, it is necessary to derive from the problem a behavioural model and develop a measuring technique compatible with it.

If we have understood what we wish to measure the next intuitive question will be: What is the size of the particles? If we look at the particles drawn in figure 1 we will realize that a size per se is not existing. If we wish to make a statement about the size of these particles, we have to give additional information about these shapes. We must realize that any information about size of a particle in principle supposes a dimension adequate to the shape of the particle to be evaluated. Consequently, the new demand for taking into account the shape in classifying particles has much more far reaching consequences. It incorporates the need to break up into subsets a group of particles, the descriptors of these subsets being different shapes simple to describe in terms of geometry. The desired result is not a size distribution function, but several distribution functions, which can be assigned to different shapes describable in geometric terms. Each of these distribution functions describes only that fraction of the particles which can be described by the corresponding shape.

When performing an actual analysis we are usually not solely interested in obtaining just data. So we will never ask, e.g., a question such as "how large are the pores in a sintered body with respect to a certain shape". Instead, the question must be, "how large are the pores with respect to a certain property (e.g., thermal conductivity)." Asking for size per se is not meaningful, because any definition of size will also incorporate the shape, and the shapes by which the pores should be analyzed are a function of the model underlying the description of a property. If, e.g., in our example the property is the thermal conductivity of the sintered material the shapes suited for analyzing this property are more frequently ellipses.

Some examples of such correspondence between a physical problem and its description in a model or by image analysis will be given below. For instance, if the technique of image analysis is to be applied to simulate the measuring process of mercury porosimetry when characterizing sintered specimens, this is best done by using an approximately circular structuring element used for the "ouverture" image transformation (Müller 1973; Vollath 1979b). If area measurements are conducted at

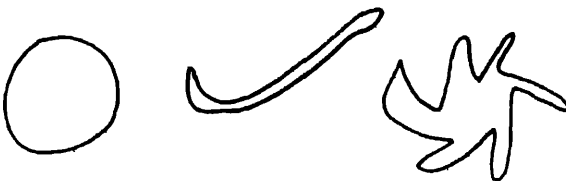


Figure 1. How can we describe these shapes?

these image transformations, comparison with the results of mercury porosimetry will furnish very interesting insights into pore structures (Vollath 1979).

Figure 2 shows a comparison of the principles of mercury porosimetry and image analysis. The fundamental difference that in case of mercury porosimetry pores are filled from outside and in image analysis the pores are filled in a cut plane leads to significant differences of the results giving interesting information of the pore network.

The question about the "size" of particles rich in plutonium in  $\text{UO}_2\text{-PuO}_2$  nuclear fuels can be answered if it is known that the size of these particles is limited because of potential overheating in cases of rapidly rising reactor power. Hence, in a first approximation, the maximum heat conduction pathway is the dimension characteristic of size in this case. The maximum heat conduction pathway is indicated in a first approximation by the radius of the largest spheres inscribable in the particles (Vollath 1979a). Refinement of this model leads to the description of particles by ellipsoids (Vollath 1982).

Depending on the method of fabrication adopted sintered bodies sometimes have pores approximately tetrahedral in shape besides those approximately spherical.

Figure 3 depicts the situation observed in a ceramographically prepared specimen.

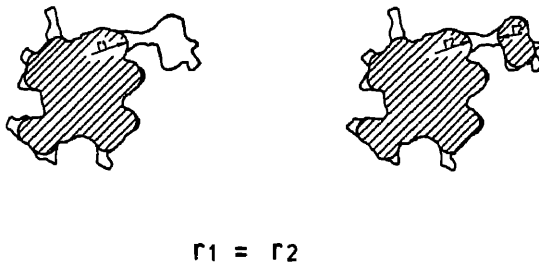


Figure 2. Comparison of measurement: Hg-intrusion porosimetry vs image analysis.

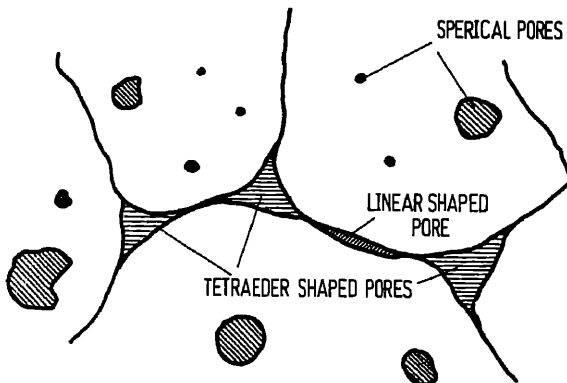


Figure 3. Typical microstructure of a sintered material made of granulated powder.



Some of the physical properties, such as thermal conductivity, strongly depend on different fractions of these two pore shapes. If the sections of rather spherical pores approximated by squares and those of more tetrahedral ones by triangles, the fraction of these two types of pores can be estimated (Vollath 1982).

#### **4. How to measure?**

We have stated now the type of results we would like to obtain and we have shown a few problems and results of measurements. But we have not considered any method of measurement.

For determining shapes of particles we have in general two philosophies which can be applied. The first is to singularize the particles of an image and to determine shape factors for each of these particles. Having done this we collect all the measures for size and shape factors and calculate a new distribution function.

Information about shape factors does not always give the true relationships. For example, if we consider the shape factor given by the ratio of area to circumference of a particle it is maximum for a circular figure. As the circle is deformed to form an ellipse the shape factor decreases as the axis ratio of the ellipse increases. It is thus possible with this shape factor to obtain information about the shape of the particles. This information is not, however, unequivocal. If a circular particle has a wavy or even frayed border, it is certainly possible to take measures in this particular case to obtain usable results but it must be remembered that in some special cases these measures will induce inaccuracies.

Even if there are many disadvantages resulting from the use of shape factors, in the case of complicated patterns such as concave particles there is even now no choice of method.

If we wish to analyze more or less convex particles and if we are satisfied with describing these particles by simple patterns the concept of size proposed by Delfiner (1972) is unequalled today. Delfiner defines the size of a particle  $P$  by the largest template  $T$  ("structuring element") which can be inscribed.

The data obtained by this method can be evaluated by mathematical morphology pioneered by Serra (1969) and Matheron (1967). If we analyze our specimens with templates of different shapes we can obtain a classification of particles by size and shape.

#### **5. Definition of a particle size**

In particles of simple shapes, such as circles, particle size can be defined unequivocally, e.g., through the diameter of the circle. In a similar way it is also possible to describe in simple terms the size of linear particles. However, in most cases much more complicated particle shapes are encountered. In those cases, description by way of maximum chord lengths or maximum dimensions (Feret diameters) are inadequate.

In the light of this problem Delfiner (1972) proposed a generalized concept of particle size. Delfiner assumes a basic pattern of any given shape and establishes a monotonic sequence of elements which are homothetic of the basic pattern selected. The size of a particle is then given by the largest element of this sequence which can be inscribed in this particle.

Let us consider sets (particles)  $G$  which are to be compared with other sets  $T_i$  (templates). The sets  $T_i$  are subsets of the ordered set  $T$ . All subsets of  $T$  are supposed to be homothetic.

$$T_i \subset T_{i+j} \quad j > 0 \quad i, j \in \mathbb{N}.$$

The size of  $G$  with respect to the elements of  $\tau$  is given by

$$G =: G_{T_i} \Leftrightarrow T_i \subset^* \cdot \wedge \cdot T_{i+j} \not\subset^* G \quad i, j \in \mathbb{N} \quad (1)$$

(Vollath 1982) with

$$T_i \subset^* G: \exists \underset{x}{(X(x) \oplus T_i)} \subset G.$$

The set  $X(x)$  shifts  $T_i$  by  $x$  as a result of a connection.  $\oplus$  stands for Minkowski addition (Hadwiger 1950; Matheron 1967; Serra 1982).

If the criterion (1) is met, the particle  $G$  has the size  $i$  relative to the sequence of structuring elements given by  $T$ . Classification in accordance with (1) can be clearly conceived as involving the use of templates of different sizes of the shape  $T$ . Out of the inventory of such templates one selects the largest template particle  $G$  will fit. As a coefficient of size measurement, the particle is assigned the number  $i$  of the largest fitting template.

If the possible sets  $T$  are restricted to the class of convex sets, the size can be determined by means of a Minkowski set operation. The elements of the sequence  $T$  can be determined from a convex unit element  $T_1$  as partial sums of a Minkowski series (Meschkowski and Ahrens 1974),

$$T_i = T_0 \oplus \bigoplus_{k=1}^i T_1 \quad i, k \in \mathbb{N}, \quad (2)$$

where the set  $T_0$  generally only consists of the origin.  $T_i$  can also be represented by means of the recursion formula (Vollath 1982)

$$T_i = T_{i-1} \oplus T_1 \quad i \in \mathbb{N}.$$

The classification of sets  $G$  in accordance with elements of  $T$  now can be arranged by means of Minkowski subtractions in analogy with (1).  $G$  can be assigned to the class  $i$  of a sequence  $T$  (Vollath 1982) if

$$G = G_{T_i} \Leftrightarrow G \ominus T_i \neq \phi \cdot \wedge \cdot G \ominus T_{i+j} = \phi \quad i, j \in \mathbb{N} \quad (3)$$

The particle  $G$  to be classified is the subset of an image  $B$ . In processing an image one proceeds by eroding the image by Minkowski subtractions. A sequence of deformed images is obtained,

$$B_{T_i} = B \ominus T_i.$$

According to Matheron (1967), the two Minkowski set connections can be linked so as to form another operation suitable for classification, the ouverture. A sequence of images is obtained, which were deformed by the ouverture transformation

$$B'_{T_i} = (B \ominus T_i) \oplus T_i. \quad (4)$$

$\oplus$  stands for the Minkowski addition (Hadwiger 1950; Matheron 1967; Serra 1982).

$\ominus$  stands for the Minkowski subtraction (Hadwiger 1950; Matheron 1967; Serra 1982).

In the transformed images  $B_{T_i}$  it is now possible to determine areas, perimeters and particle numbers as coefficients of measure.

The quantities measurable in the images transformed by erosion or ouverture will not always generate the required information. Thus, e.g., dumb-bell shaped particles may disintegrate into two separate particles after erosion or ouverture. This may have a disturbing effect on particle counting. There are also measuring problems when particles are to be classified in accordance with given patterns, but also the coefficients of measure are to be determined in the unchanged particles. In such cases, classification must be carried out by means of a template matching procedure. For the case of a sequence  $T$  of convex templates the following method can be used for image transformation in which, first of all, the particles in the image are classified by erosion,

$$B_{T_i} = B \ominus T_i$$

and the original shape of the particles is then reconstructed by the recursion formula

$$B_{T_i}^*(k+1) = \bigcup_{j=1}^8 (B_{T_i}^*(k) \oplus S_j) \cap B. \quad (5)$$

The first element  $B_{T_i}$  of the sequence of sets produced is

$$B_{T_i}^*(1) = B_{T_i}.$$

The set  $S_j$  always consists of the origin and one of its eight neighbourhood points. The process of iteration must be continued until the condition

$$B_{T_i}^*(k+1) = B_{T_i}^*(k)$$

is met.

In the following sections, which will deal with classification by shape and size, it will be assumed that classification has already been carried out by one of the three methods of classification discussed (erosion, ouverture, or template matching).

## 6. Classification of particles in accordance with several sequences of patterns

Let us now consider the case of particles of a sample being classified in accordance with  $M$  different sequences of convex template  $T^l$ . Each set  $T^l$  consists of  $N^l$  elements of the size  $j$ ,  $T_j^l \in T^l$ . The subset  $T_j^l$  is used to determine in the images such measures as particle numbers or areas. For the sake of simplicity we assume that these measures were determined by means of the template matching technique of classification. When measuring with the templates  $T_j^l$  the cumulative frequencies,  $H^l$  are determined. These cumulative frequencies, result from the class frequencies  $h_j^l$  through the sum of

$$H_j^l = \sum_{k=j}^{N^l} h_k^l \quad l \in \{1, \dots, M\}. \quad (6)$$

From the matrix of measured values ( $H_j^l$ ) a matrix ( $h_j^{*l}$ ) is now to be determined of the class frequencies at which also separation by shapes will be performed. Such separation may be carried out on the basis of two different principles.

### 6.1 Separation by inclusions

For all elements of the sequences of patterns  $T^m$  it holds that

$$T_i^m \subset^* T_{i+j}^m \quad i, j \in \mathbb{N}. \quad (7)$$

If we compare two sequences of patterns, we always find pairs of elements obeying the following relationship:

$$T_l^m \subset^* T_{l(l, m, n)+j} \quad i, j, l, m, n \in \mathbb{N}. \quad (8)$$

The element  $T_{lm}^m(l, m, n) + 1$  is the smallest element of the sequence  $T^m$  containing the element  $T_l^m$  as a subset. Obviously, in determining the class frequencies  $h_j^{*m}$ , corrected by shapes, the numbers and areas, respectively, of all patterns must be subtracted in which  $T_l^m$  is fully contained.

$$h_j^{*m} = H_j^m - \sum_{k=1}^M \sum_{l=1(l, m, k)+1}^N h_l^{*k} \quad (9)$$

Consequently, calculating the class frequencies,  $h_j^{*m}$  presupposes knowledge of the class frequencies  $h_l^{*k}$  of the elements  $T_l^k$  in which  $T_j^m$  is contained. Evaluation of the formula (9) is started with the element  $T_l^k$  for which no further element in the series of measurements contains  $T_l^k$ .

As a simple example, figure 4 shows two ordered sequences of patterns. The sequences  $T^1$  consists of squares, the sequence  $T^2$  consists of right angled isosceles triangles. Below the images those elements are indicated which contain elements  $T_l^k$ .

### 6.2 Separating shapes by given measures

Instead of the inclusions (7) and (8), also a measure,  $\mu(T_l^m)$ , to be assigned to the pattern  $T_l^m$ , can be used to distinguish by different shapes. The only measure to be used for this purpose are areas. We then obtain the following relationships as the basis on which to

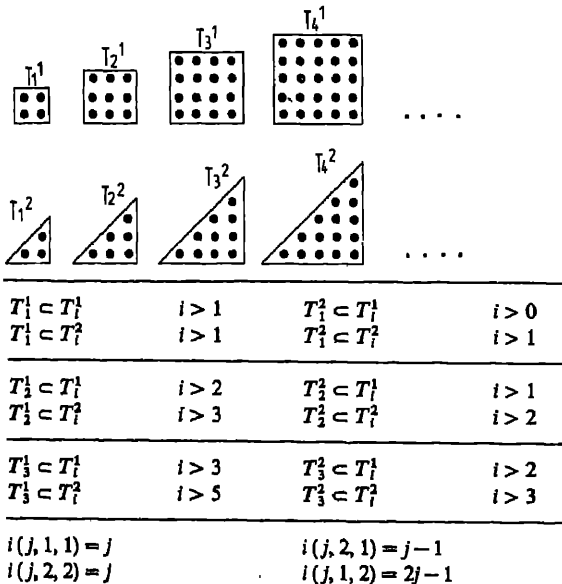


Figure 4. - Separating particle shapes by inclusions.

assign particles to the different patterns:

$$\mu(T_i^m) < \mu(T_{i+j}^m) \quad i, j \in \mathbb{N}.$$

Since we take into account only positive and monotonic measures this condition is identical with (7). For assignment to different sequences of patterns one uses

$$\mu(T_i^m) < \mu(T_{l(i, m, n) + j}^n) \quad i, j, l \in \mathbb{N}.$$

The element  $T_{l(i, m, n) + 1}^n$  is the smallest element in the sequences  $T^n$  whose measure is larger than that of  $T_i^m$ .

The class frequencies corrected by shapes are determined in accordance with (9) in this case.

For the example shown in figure 4 it is outlined in figure 5 which elements have larger areas than an element  $T_i^k$ . The example of classification by squares and triangles indicates another major characteristic of classification by shapes. While for a square of a given size there is only one orientation, the triangle used in principle can be at any of four orientations. Consequently, if it is not known in advance that the triangles in a sample can have only one orientation, all four possible congruent triangles must be used as templates. In the given example this would imply the need to analyze not two, but for five sequences of patterns. However, if one is not interested in additional discrimination of triangles of different orientations, the measures obtained from the four orientations can be combined in the evaluation (Vollath 1984).

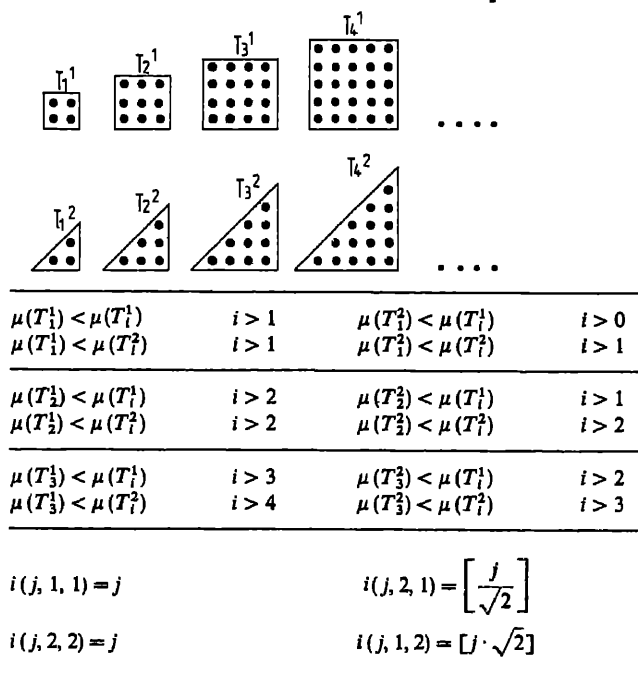


Figure 5. Separating particle shapes by given measures.

### 7. Classification of particles by multi-parameter sequences of patterns

So far we have looked at sequences of patterns  $T$  whose elements depended on only one parameter describing the size. Let us now consider sequences  $T$  whose elements obey the law of formation

$$T_{i,j} = T_{0,0} + T_{i,0} \oplus T_{0,j}. \tag{11}$$

With

$$T_{i,0} = T_{0,0} \oplus \bigoplus_{m=1}^i T_{1,0} \quad i, j, m, n \in N_0$$

$$T_{0,j} = T_{0,0} \oplus \bigoplus_{m=1}^j T_{0,1}.$$

As in (2) also in this case the set  $T_{0,0}$  consists of only one point, normally the origin. The sets  $T_{0,1}$  and  $T_{1,0}$  are the two basic patterns from which the two-parameter sequence of sets considered is built up. Naturally, also multi-parameter sequences of sets can be built up in accordance with scheme (11) or, as in §6, several multi-parameter sequences of sets can be combined with each other. However, it should be avoided that, as a result of the introduction of too many classes, insufficient, i.e., insignificant, coverage in the individual classes is produced.

Figure 6 shows a simple two-parameter sequence of patterns built up of the unit vectors,  $e_1$  as  $T_{1,0}$  and  $e_2$  as  $T_{0,1}$ . In this example one clearly sees the typical structure of such a two-parameter family of structuring elements. Adding the two diagonal vectors  $\begin{bmatrix} 1 \\ 1 \end{bmatrix}$  and  $\begin{bmatrix} 1 \\ -1 \end{bmatrix}$ , one obtains a system of templates which in a first approximation, come close to the size, the axial relationships and the orientations of ellipses approximated by octagons. In a similar way, in a hexagonal grid, one obtains by continued Minkowski additions of the three basic vectors, a system of hexagons to approximate ellipses.

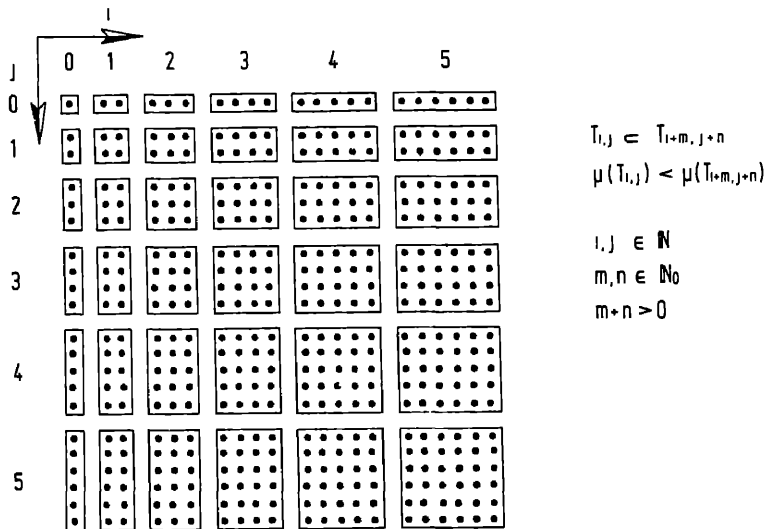


Figure 6. Example of a two-parameter sequence of structural elements.

## Considerations in image analysis

On the basis of the law of formation of patterns  $T_{i,j}$  it is seen that

$$\begin{aligned} T_{i,j} &\subset^* T_{i+m,j+n} \Leftrightarrow \mu(T_{i,j}) < \mu(T_{i+m,j+n}) \\ i, j &\in Nm, n \in N \\ m+n &> 0. \end{aligned}$$

Hence, unlike in the case of classification by several single parameter sequences patterns, one should not distinguish between two criteria of classification. Since in this case the measurement proceeds analogously to that described above, one obtains, using the same argument for the corrected class frequencies,

$$\begin{aligned} h_{i,j} &= H_{i,j} - \sum_{m=i+\delta_1} \sum_{n=j+\delta_2} h_{m,n}^* \quad i, j, m, n \in N \\ \delta_i &\in \{0, 1\} \quad \delta_1 + \delta_2 > 0. \end{aligned}$$

Also in this case, calculation of  $h_{i,j}^*$  must be started with the largest element. To explain this evaluation in more detail, a simple image (figure 7) has been constructed as an example so that the "particles" it contains can be described by the elements shown in figure 6. Table 2 shows the measured frequencies  $H_{i,j}$ , from which the class frequencies  $h_{i,j}^*$ , corrected for shapes and directions were calculated. The  $h_{i,j}^*$  values are summarized in table 3.

Another example is depicted in figures 8 and 9 (Vollath 1982). In this example an analysis of pores into more tetrahedral and more spherical shapes is shown. In figure 8 we see the results obtained for the selected templates (squares and triangles) and in figure 9 depicts these results after separation by inclusion according to (9) (see also figures 3, 4 and 5).

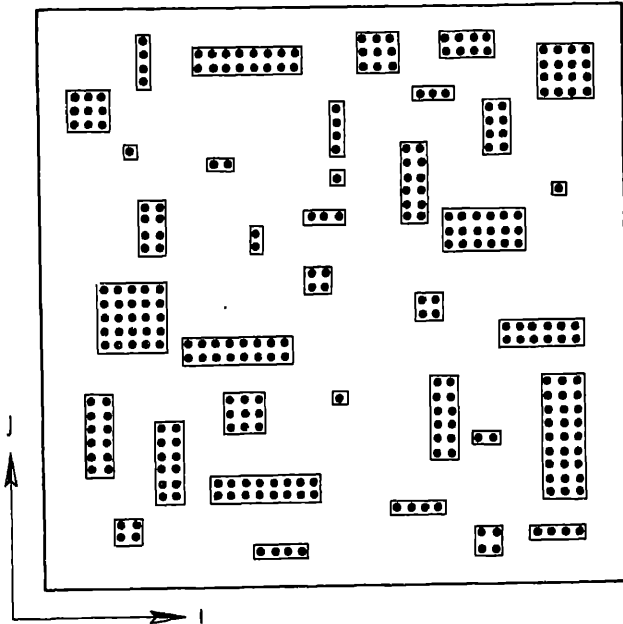


Figure 7. Example of a sample for classifying particles by shape, size and orientation.

**Table 2.** Particle numbers obtained in figure 7 after application of the structural elements in a measurement (e.g., erosion) as represented in figure 6. The subscripts *i* and *j* have the same meaning as in figure 6.

<i>j</i>	<i>i</i>	1	2	3	4	5	6	7	8
1		36	29	17	11	6	5	3	3
2		25	22	11	8	6	5	3	3
3		15	13	7	3	2	1		
4		11	9	3	2	1			
5		6	6	2	1	1			
6		5	5	1					
7		1	1	1					
8		1	1	1					
9		1	1	1					

**Table 3.** Particle numbers of figure 7 corrected for size, shape and orientation. The subscripts *i* and *j* have the same meaning as in figure 6.

<i>j</i>	<i>i</i>	1	2	3	4	5	6	7	8
1		4	2	2	3				
2		1	4		1		1		3
3				3			1		
4		2	2		2				
5						1			
6			4						
7									
8									
9				1					

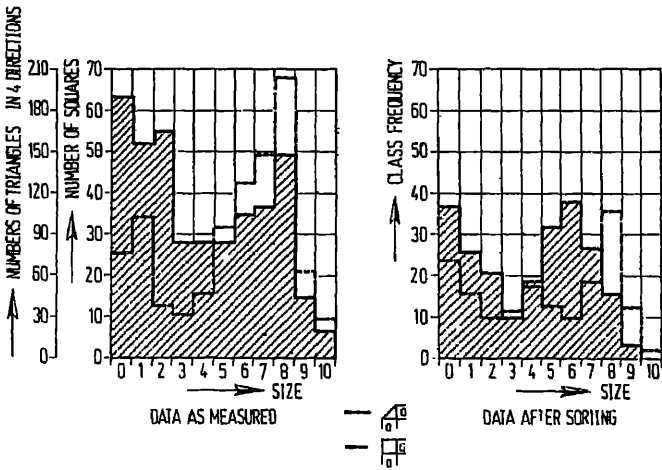


**Figure 8.** Separation of pores in a sintered material due to their shapes (separation by inclusion).



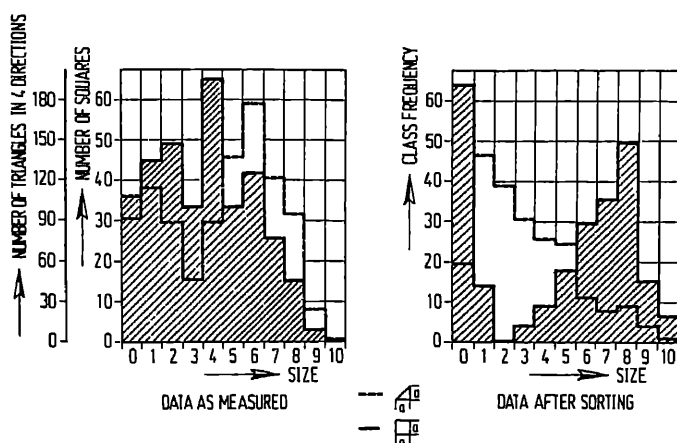


Figure 9. Separation of pores in a sintered material due to their shapes (separation by ar

## 8. Conclusions

In this paper a few basic considerations have been explained which are necessary beginning in image analysis. The major point stressed was that before starting a measurement the physical problem imposing an analysis, e.g., particle sizes, must be examined. From this examination we have to derive a behavioural model and develop a measuring technique compatible with it.

It has been shown in this study how to extract measured values from an image, which characterizes the individual elements of the image in terms of size, shape and orientation. The basis used throughout was a description of the image and of its elements by means of the methods of the theory of sets. Based on Delfiner's concept of shapes a method of particle classification was developed using erosion, ouverture or template matching image transformation for classification. A new transformation, "template matching for particles" is explained.

This transformation avoids the disadvantages of erosion or ouverture in case of concave particles. Nevertheless, template matching is also restricted to applications with convex templates.

## Acknowledgements

Thanks are due to Dr Pecht and Mr Stiller of IMF III/PBE for their critical review of the draft of this paper.

## References

- Delfiner P 1972 *J. Microsc.* **95** 203
- Haas A, Matheron G and Serra J 1967a *Ann. Mines* **XI** 736
- Haas A, Matheron G and Serra J 1967b *Ann. Mines* **XII** 767

Hadwiger H 1950 *Math. Z.* **53** 210

Matheron G 1967 *Elements pour une Theorie des Milieux Poreux* (Paris: Masson)

Müller W 1973 *Leitz Mittlg. Suppl.* **1** 101

Meschkowski H and Ahrens I 1974 *Theorie der Punktmengen*, Bi-Wissenschaftsverlag, Mannheim

Nawrath R and Serra J 1979 *Microsc. Acta* **82** 101

Serra J 1969 *Introduction a la Morphologie Mathematique Cahier du Centre de Morphologie, Mathematique ENSMP No. 3*

Serra J 1982 *Image analysis and mathematical morphology* (New York: Academic Press)

Vollath D 1979a *Leitz-Mitt. Wiss. Tech.* **7** 129

Vollath D 1979b *J. Nucl. Mater.* **81** 115

Vollath D 1981 *J. Microsc.* **122** 35

Vollath D 1982 *J. Nucl. Mat.* **10** 71

Vollath D 1982 *Prakt. Metallogr.* **19** 7, 94

## Computer-aided roll pass design for continuous billet mill

ASHOK KUMAR, SUDHAKER JHA and V RAMASWAMY

Research & Development Centre for Iron and Steel, Steel Authority of India Limited  
India

**Abstract.** A mathematical model has been developed for computing the geometrical dimensions of square-diamond square pass sequence for a continuous billet mill. The model is based on derivation of shape and size factor from the geometry of the pass taking into account pass filling, pass rounding etc. Using these factors and a basic equation of spread rolling, a governing equation incorporating angle of diamond and reduction in consecutive passes has been formulated. Newton's substitution method has been used to solve the equation. With known reduction between consecutive passes, geometrical dimensions of square and diamond passes are computed. A model has been used to calculate pass design for the finishing train of a continuous billet mill producing 60 mm square billet from 120 mm round bloom. The elongation values have been optimized by varying the apex angle of diamond passes. Close agreement between computed and actual values shows the validity of the model.

**Keywords.** Geometrical dimensions; square-diamond pass; computer-aided model; sequence; apex angle; rolling force; torque

### 1. Introduction

Diamond-square pass sequence is used in the finishing group of stands of a continuous billet mill to produce round-cornered squares. Conventionally the sequence is designed (Burtsev 1973) by obtaining elongation coefficient on the principle of having width in any given pass equal to the height of the preceding pass. Form changes in diamond passes have also been studied experimentally (Zaitsev and Anufriev 1966). Nomograms have been prepared for obtaining pass dimensions. However, these methods generally require trial and error to establish roll pass design and at the same time do not effectively utilise available biting ability, mill power etc of different stands. To overcome these shortcomings, a software package was developed at the Research & Development Centre for Iron and Steel, Steel Authority of India Limited for computer-aided pass design for continuous billet mill. This paper outlines the approach adopted and compares the results obtained from the computer model with the actual mill performance.

### 2. Approach

Diamond-square pass sequence can be fully developed if the elongation coefficient between two consecutive passes is known. In the present work the coefficient is obtained by converting the diamond square passes into equivalent rectangles of width equal to their effective width and the Ekelund spread formula (Jha 1980) has been modified and made use of. This offers the advantage of calculating reduction sequence starting from the last finishing pass and is superior in accuracy to other spread factor methods.

(Jha 1980). With the calculated value of  $\lambda$ , for an assumed angle of diamond, the dimension of pass in the next mill stand is obtained. Limitations of permissible angle of bite, mill speed, power force parameters etc have been observed. If needed a change in apex angle of diamond pass is effected and this in turn changes the value of  $\lambda$  and pass dimensions. Computation is repeated for all the mill stands and the dimensions of ingoing bloom entering the finishing mill are figured. If there is a limitation on bloom size as well,  $\lambda$  is readjusted again by changing the apex angle of diamond in passes of different mill stands.

## 2.1 Elongation coefficient

Figure 1 shows a diamond bar going into square pass along with their equivalent rectangles. If

$$\delta = b_1/h_1; n = h_2/b_2 \text{ and } \gamma = h_2/h_1.$$

Elongation coefficients ( $\lambda$ ) for the pair of pass will be

$$\lambda = A_1/A_2 = b_1 h_1 / b_2 h_2 = n \cdot \delta / \gamma^2. \quad (1)$$

The modified Ekelund spread equation is given as

$$\beta = 1 + \frac{2(1-\gamma)}{1+\gamma} \cdot \frac{M}{M+1},$$

where 
$$M = \frac{0.8}{(b_1/ld)^2} \left[ 2 - \frac{3(h_1 - h_2)}{ld} \right].$$

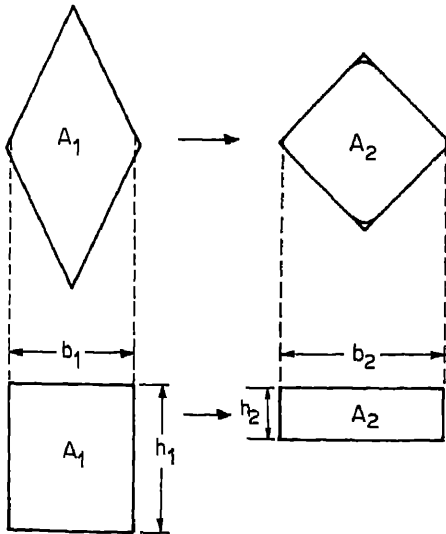


Figure 1. Diamond and square passes with their equivalent rectangles.

The final equation can be written as

$$n = \frac{(\gamma/\delta)}{1 + \frac{2(1-\gamma)}{1+\gamma} \left[ \frac{0.4\gamma(1-\gamma) \left\{ 2 - 3 \left[ \left( \frac{2(1-\gamma)}{\gamma} \right) \left( \frac{h_2}{D} \right) \right]^{1/2} \right\}}{\delta^2 \frac{h_2}{D} + 0.4\gamma(1-\gamma) \left\{ 2 - 3 \left[ \left( \frac{2(1-\gamma)}{\gamma} \right) \left( \frac{h_2}{D} \right) \right]^{1/2} \right\}} \right]}$$

Equations (1) and (2) can be used for determining elongation coefficients ( $\lambda$ ) if  $\delta$ ,  $n$  and  $h_2/D$  are known.

## 2.2 Shape factors

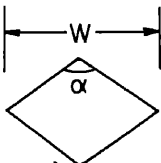
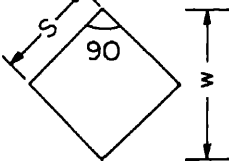
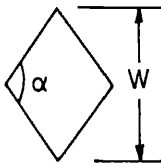
$\delta$  and  $n$  largely depend on the geometrical shape of passes and are therefore termed shape factors. For any pass,  $\delta \cdot n = 1$ . Considering pass filling and apex rounding diamond and square passes, the shape and size factor ( $h_2/D$ ) can be written as shown in figure 2.

## 2.3 Rolling force and torque

Roll separating force and rolling torque were computed using the following equations which are derived from the basic theory of deformation for rolling of square and diamond sections (Jha *et al* 1983).

## 2.4 Roll force

$$F = \sigma \cdot l \cdot n_s \left[ \frac{2W}{3} - \frac{H_1 \cdot W}{10 R} \right]$$

Shape	$\delta$ (in going)	$n$ (out going)	$h_2/D$ (out going)
	$2 \cdot f_h^2 \tan(\alpha/2)$	$\frac{\cot(\alpha/2)}{2 \cdot f_h^2}$	$\frac{\cot(\alpha/2) W}{2 \cdot f_h \cdot D}$
	1.73	0.578	$\frac{W}{1.7 D}$
	$2 \cdot f_v^2 \cdot \cot(\alpha/2)$ $f_h \text{ \& \; } f_v$	$\frac{\tan(\alpha/2)}{2 \cdot f_v^2}$	$\frac{W}{2 \cdot f_v \cdot D}$

$f_h \text{ \& \; } f_v$  Denotes the degree of pass filling

Figure 2. Shape and size factors for diamond and square passes.

Here

$$n_s = \frac{ld \left[ \frac{1 - H_1/4R}{(H_0 + H_1)/W} + \frac{W}{8R} \frac{(H_0 + H_1)}{(H_0 - H_1)} \right]}{2/3 - H_1/10 R}$$

$$\sigma = \frac{K \cdot e^{0.6235} \dot{\epsilon}^{0.087}}{e^{0.0037t}}$$

### 2.5 Rolling torque

$$T = 2 \cdot \sigma \cdot \psi \cdot ld^2 \cdot W \left[ M_1 \left( 0.5 - \frac{H_1}{8R} \right) + \frac{0.25}{M_1} \right]$$

$$M_1 = ld/H_m$$

$$ld = [R(H_0 - H_1)]^{1/2}$$

The terms used in the above mathematical expressions are explained in the list of symbols given at the end of the paper.

## 3. Mathematical model

A mathematical model has been developed for diamond square sequence using the shape and size factor of the pass along with elongation and spread equations. The flow charts of the computer program developed for the above model are shown in figures 3a, b. Figure 3a shows the flow chart of the program taking the limitation of initial square size and optimizing the apex angle. Figure 3b shows how elongation coefficient was optimized at all mill stands by considering the limitation of power force parameter and biting ability etc and compute the geometrical dimensions of the passes. The program (figure 3a) computes the shape and size factor from the initial assumed value of the diamond angle. Using the shape and size factor, the reduction ( $\gamma$ ) was computed from the spread equation given by (2). The spread equation has been solved by employing Newton's substitution iterative method. For this we start with an arbitrary value of  $\gamma$  in the first iteration and a new value of  $\gamma$  is obtained. The process is repeated until convergence (accuracy:  $10^{-3}$ ) is achieved, normally after 6 iterations. After getting the value of  $\gamma$  and taking the finish square size as the starting dimensions, the elongation, bite angle etc were computed using the corresponding subroutine. The process was repeated till the required pass. If the square size so obtained after the last pass is less than the required initial size, the apex angle of last diamond pass is increased by  $2^\circ$  and the initial square size is again computed. If again the computed square size is less than the required size of square, the apex angle of pre-last and subsequent diamond passes are increased by  $2^\circ$  and the square size is computed.

The process is repeated until the calculated square size is greater than the required square size. If the apex angle is given for all the diamond passes then starting with the finish size the program will compute the required initial square size for that finish square size. It is essential to have the following initial data for operation of the computer model: (a) mode of pass sequence; (b) no. of passes; (c) roll diameter at each stand; (d) roll gap at each stand; (e) final rolling speed; (f) final product size; (g) initial

size and (h) apex angle of all the diamond passes. Once this is computed it can be compared with the actual mill parameter.

#### 4. Results and discussion

To ascertain the accuracy of the model developed, a case study was made. In the geometrical dimensions of square-diamond-square pass sequence for a known 4-p

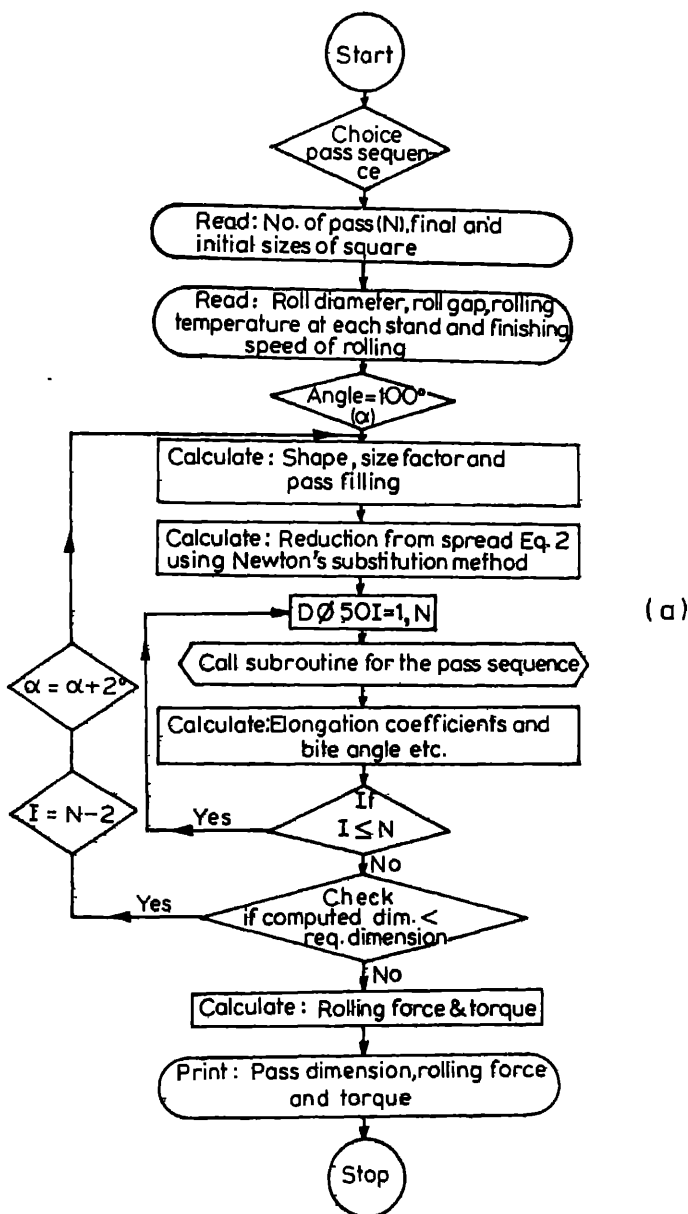
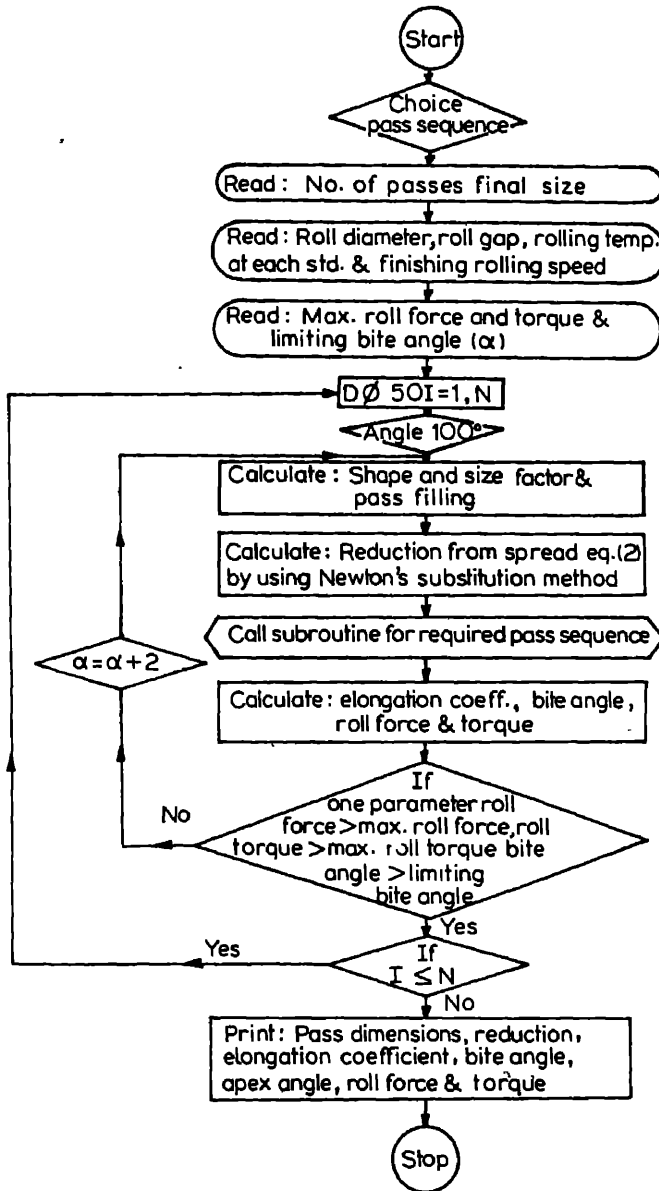


Figure 3a. for caption, see p. 188.



(b)

Figure 3. Flow chart of computer program for calculating roll passes with limitations of a. initial square size. b. Power force and biting angle.

sequence (Bakhtinov and Shternov 1953) are computed using the above model by taking the final square size of 99.7 mm as the starting dimensions. The roll diameter, roll gap and apex angle of diamond used for calculating the geometrical dimensions are given in the table 1 along with the elongation value and reduction in each pass. The



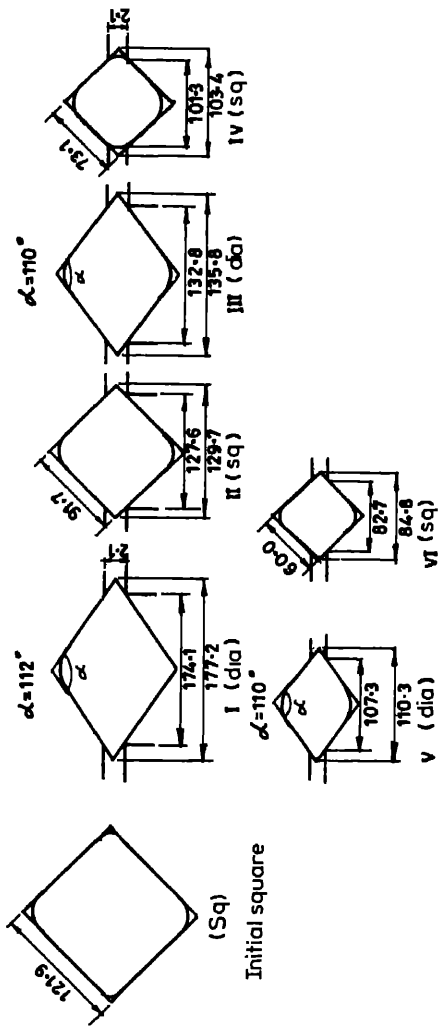


Figure 4. Roll pass design obtained by model for rolling 60 mm billet from 121.9 billet.

calculated square and diamond sizes are compared with the actual data obtained from the mill. This is also shown in table 1. A comparison between these two values shows a close agreement. Discrepancy in the width of the diamond pass may be due to the extent of pass filling and pass rounding which was considered in the above model.

#### 4.1 Roll pass design

A model has been used to design roll passes for the finishing train of a continuous 530 mm billet mill producing 60 mm square billet from input square of 120 mm in six passes. The results are shown in figure 4 with geometrical dimensions of passes. The apex angle of diamond passes has been manipulated in the model to achieve the desired input square. As can be seen in figure 5, with increasing apex angle of diamond, the elongation coefficient increases. With diamond angle of  $110^\circ$  in all the passes, the initial square size permitted according to model is 119.25 mm. This necessitates increasing the apex diamond angle to  $112^\circ$  in the first pass. It can also be observed from figure 5 that

**Table 1.** Comparison between computed and in practice roll pass design (starting size of square(s) 99.7 mm)

Pass No.	Shape	Roll dia (d) (mm)	Roll gap (mm)	Apex angle ( $\alpha$ )	Elongation coefficient ( $\lambda$ )	Reduction (R)	Geometrical pass dimension	
							Computed	In practice
1	Diamond	800	10	108	1.19	0.78	$W = 177.0$	$W = 169.0$
2	Square	800	10	108	1.23	0.77	$S = 118.1$	$S = 119.5$
3	Diamond	780	10	111.2	1.232	0.75	$W = 223.9$	$W = 229.0$
4	Square	780	10	111.2	1.32	0.72	$S = 150.4$	$S = 150.0$

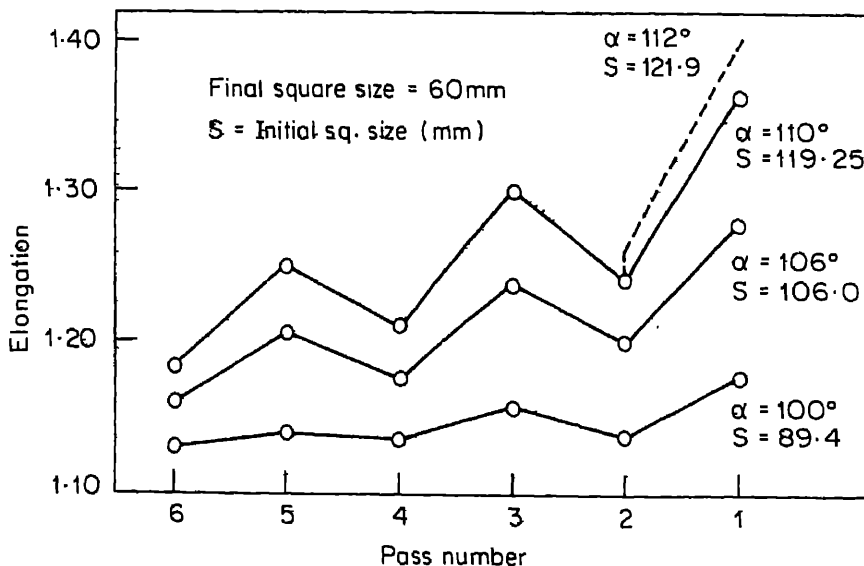


**Figure 5.** Effect of apex angle on elongation for different passes.

## Roll pass design

elongation in square passes is higher compared to those of diamond passes. Uniformity of elongation in diamond and square pass increases with increase in angle of diamond.

Pass design developed above is being implemented in one of our continuous mills.

## 5. Conclusions

A computer-aided roll pass design has been developed for producing a software package accurately calculates the geometrical dimensions of diamond and square passes either under the limitation of rolling force, rolling torque, biting or the input bloom size for different mill stands thus avoiding trial and error normally practised by pass designers. The model has been verified with actual data and it is shown that the calculated and observed size of the passes is in agreement.

## References

- Bakhtinov and Shternov 1953 *Roll pass design* (Moscow: Metallurgia) p. 232  
Burtsev K 1973 *Rolling practice* (Moscow: Mir Publishers) p. 146  
Jha S 1980 *Steel India* 3 1  
Jha S, Acharya N K and Sengupta D 1983 *Investigation into rolling technology of continuous*  
Internal Report, Research and Development Centre for Iron and Steel, Ranchi, 16.02.480.8.  
Zaitsev M L and Anufriev G V 1969 *Stal in English*, 8x Vol. 8, p. 727

## List of symbols

$D$	working diameter of outgoing pass	$R$	collar diameter
$F$	rolling force	$S$	square size (ou
$H_0, H_1$	initial and final height of pass	$t$	rolling tempera
$H_m$	average height	$T$	rolling torque
$h_2/D$	size factor of pass	$W$	width of diamc
$K$	constant	$\gamma$	reduction at pa
$ld$	arc of contact	$\delta, n$	shape factor of
		$\varepsilon, \dot{\varepsilon}$	strain and strai
$M$	$\frac{0.8}{(b_1/ld)^2} \left[ 2 - \frac{3(h_1 - h_2)}{ld} \right]$	$\lambda$	elongation coef
		$\sigma$	yield stress
$n_\sigma$	stress coefficient	$\psi$	lever arm ratio



## Computer-aided composition-treatment-structure-property correlation studies in steels

K VIJAYARAJU and E S DWARAKADASA

Department of Metallurgy, Indian Institute of Science, Bangalore 560012, India

**Abstract.** Internal structure of materials uniquely decides their properties. The structure-property correlation is a complicated function of composition and thermal and/or mechanical treatment. Inter-relation is so complex that a highly generalized correlation is very difficult. Steel is a very good example to illustrate this complexity. Advent of mini- and microcomputers have now paved way for handling such multiparametric problems in a more rational way, with greater ease and increased confidence. This paper is an attempt to develop a computer software which will be useful to the user in three different ways: (a) to determine the treatments that will generate a desired structure, when compositions are known; (b) to determine composition limits within which a desired structure will result having defined the treatments, and (c) to predict structures that can be generated when composition and treatments are limited. This program has immense use in (i) best use of available inventory, (ii) reduction of standards, varieties and inventory and (iii) most importantly to decide the best purchase based on treatment limitations in the steel. A large data bank is being built to support the program.

**Keywords.** Steel; property; structure; correlation; software; computer handling.

### 1. Introduction

Microstructure plays a very important role in deciding the properties of a material. Microstructures can be altered by changing material composition and by imparting suitable thermal and/or mechanical and thermomechanical treatments. The problem of alloy chemistry is complex and treatment variables are many. The case of ferrous materials, steels in short, is a typical example in hand. Investigations over the several centuries have generated innumerable steel compositions and treatments. The result, as we see today, is the huge inventory and list of standards the materials engineer has to cope up with. There is an urgent need to rationalize the picture and many attempts are being made. Structure property correlation studies have been looked into in great detail to derive constitutive but empirical relationships that may be used to predict material properties. However, these studies are of limited application as they are governed by severe restrictions. The advent of mini- and microcomputers has now changed the approach to the problem and further offers tremendous possibilities. It only needs a serious investigation to utilize the data available to fit in meaningful relationships and an objectively built program. To take the specific example of steels, problems may be defined in terms of a few typical goal oriented questions.

- (i) Property limits for a particular application are defined, what would constitute the range of ideal conditions of composition, structure and treatment that will satisfy the situation?
- (ii) A given set of steel varieties are available in the yard. What would be the minimum and maximum properties that can be achieved making use of all applicable treatments? What would be the microstructure in each case?

- (iii) A certain microstructure is to be generated. What are the steel compositions and treatments that will result in this microstructure?

Even with these three goals, the dimension of the problem becomes huge and underlines the need for computer handling of the problem. A long term plan to build a software facility to handle this problem has been initiated (Vijayaraju 1984). This paper describes the first phase of the development of an interactive program in which the composition, microstructure and treatment are interrelated to yield the mechanical properties. The program has been mainly developed based on a number of empirical relationships that relate composition and/or structure with the resulting properties, and hence is applicable only within certain limiting conditions that have been imposed such as medium carbon steels, single continuous cooling, straight forward microstructures, etc. The long term plan is to develop a set of programs in all dimensions to make it applicable to all steels universally.

## 2. Software description

The methodology of the development of the software is shown in figure 1. As a first step, the composition data are fed into the program. Based on this data the program calculates the various transformation temperatures  $M_s$ ,  $AC_1$ ,  $AC_3$  using equations (1)–(3) (Cias 1977).

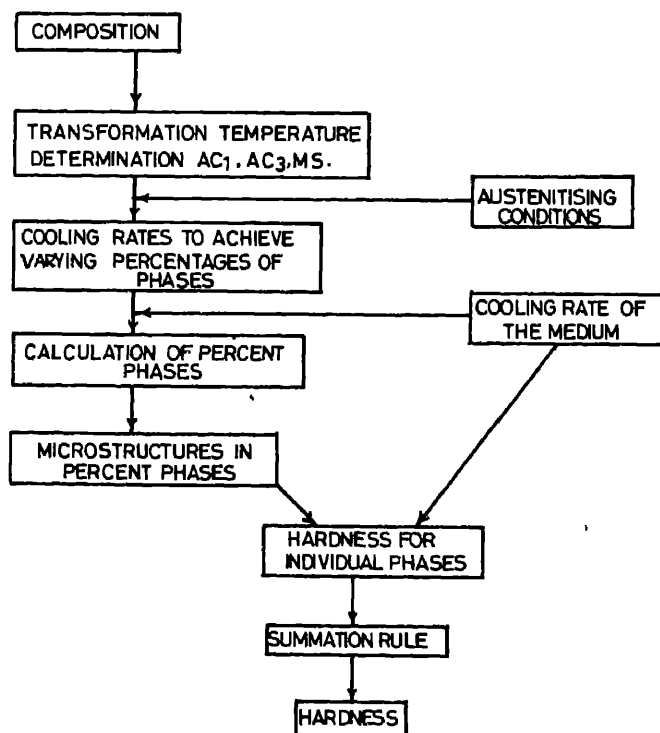


Figure 1. Methodology of the software development.

$$AC_1 = 712 + 20.4 \text{ Si} - 17.8 \text{ Mn} - 9.8 \text{ Mo} + 11.9 \text{ Cr} - 19.1 \text{ Ni} \quad (1)$$

$$AC_3 = 871 - 254.4 \text{ C} + 51.7 \text{ Si} - 14.2 \text{ Ni} \quad (2)$$

$$M_s = 531 - 39.2 \text{ C} - 43.3 \text{ Mn} - 16.2 \text{ Cr} - 21.8 \text{ Ni} \quad (3)$$

Then from these results the user can prefer the austenitization temperature and time of austenitization from the section size and geometry. Now to take care of the grain growth during the austenitization, a parameter called 'austenitization parameter'  $P_A$ , is defined and can be calculated from the equation given below (Maynier *et al* 1978):

$$P_A = \left[ 1/T - \frac{nR}{H} \log(t/t_0) \right]^{-1}, \quad (4)$$

where  $T$  is the austenitization temperature ( $^{\circ}\text{K}$ ),  $R$  is the gas constant,  $H$ , the activation energy for the grain growth and  $t, t_0$  is the time of austenitization and unit time. Using the data on composition and transformation in the following set of equations the cooling rates to obtain a particular combination of percentage phases are calculated (Maynier *et al* 1978)

$$\log V_1 = 9.81 - (4.62 \text{ C} + 1.05 \text{ Mn} + 0.54 \text{ Ni} + 0.50 \text{ Cr} + 0.66 \text{ Mo} + 0.00183 P_A), \quad (5)$$

$$\log V_2 = 10.17 - (3.80 \text{ C} + 1.07 \text{ Mn} + 0.70 \text{ Ni} + 0.57 \text{ Cr} + 1.58 \text{ Mo} + 0.0032 P_A), \quad (6)$$

$$\log V_3 = 6.36 - (0.43 \text{ C} + 0.49 \text{ Mn} + 0.78 \text{ Ni} + 0.27 \text{ Cr} + 0.38 \text{ Mo} + 2\sqrt{\text{Mo}} + 0.0019 P_A) \quad (7)$$

$$\log V_{190} = 8.76 - (4.04 \text{ C} + 0.96 \text{ Mn} + 0.49 \text{ Ni} + 0.58 \text{ Cr} + 0.97 \text{ Mo} + 0.0010 P_A) \quad (8)$$

$$\log V_{290} = 10.55 - (3.65 \text{ C} + 1.08 \text{ Mn} + 6.77 \text{ Ni} + 0.61 \text{ Cr} + 1.60 \text{ Mo} + 0.0032 P_A) \quad (9)$$

$$\log V_{390} = 7.59 - (9.38 \text{ C} + 0.35 \text{ Mn} + 0.93 \text{ Ni} + 0.11 \text{ Cr} + 2.31 \text{ Mo} + 0.0033 P_A) \quad (10)$$

$$\log V_{250} = 8.50 - (4.12 \text{ C} + 0.86 \text{ Mn} + 0.57 \text{ Ni} + 0.41 \text{ Cr} + 0.94 \text{ Mo} + 0.0012 P_A) \quad (11)$$

$$\log V_{250} = 8.74 - (2.23 \text{ C} + 0.86 \text{ Mn} + 0.56 \text{ Ni} + 0.59 \text{ Cr} + 1.60 \text{ Mo} + 0.0032 P_A), \quad (12)$$

where  $V_1$  = minimum quench velocity to attain a complete martensitic structure,  $V_2$  = critical cooling velocity resulting in entirely bainitic structure with small amounts of martensite,  $V_3$  = critical cooling velocity to achieve a completely annealed structure, i.e., ferrite and pearlite,  $V_{190}$  = critical cooling velocity giving 10% bainite and 90% martensite,  $V_{290}$  = critical cooling velocity giving 10% ferrite-pearlite and 90% bainite,  $V_{390}$  = critical cooling velocity giving 90% ferrite-pearlite and 10% bainite,  $V_{150}$  = critical cooling velocity giving 50% martensite and 50% bainite,  $V_{250}$  = critical cooling velocity giving 50% bainite and 50% ferrite-pearlite.

From the various critical cooling rates to attain different discrete combinations of martensite, bainite and ferrite-pearlite, two second order polynomial equations have been fitted. Using this, the intermediate combinations of different phases are calculated.

for any cooling rate. This results in the final microstructures in terms of percentage of martensite, bainite and pearlite. Equations (13)–(15) are taken from the literature (Maynier *et al* 1978) for the determination of hardness values of the individual phases, i.e., 100% martensite or 100% bainite or 100% ferrite-pearlite. The hardness of the final microstructure is calculated using the summation rule:

$$HVM = 127 + 949 C + 27 Si + 11 Mn + 8 Ni + 16 Cr + 21 \log (Cv), \quad (13)$$

$$HVB = 323 + 185 C - 330 Si + 153 Mn + 65 Ni + 144 Cr + 194 Mo - \log Cv (89 + 53 C - 55 Si - 22 Mn - 10 Ni - 20 Cr - 30 Mo) \quad (14)$$

$$HV(F + P) = 42 + 23 C + 53 Si + 30 Mn + 12.6 Ni + 7 Cr + 19 Mo - \log Cv (10 - 19 Si + 4 Ni + 8 Cr + 130 V), \quad (15)$$

$Cv$  = cooling velocity,  $HVM$  = hardness of 100% martensitic structure,  $HVB$  = hardness of entirely bainitic structure,  $HV(F + P)$  = hardness of completely annealed structure, i.e., fully ferrite-pearlitic structure.

A graphical representation of the variation of the percentage of each phase with the cooling rates is shown in figure 2. Similarly the variation of the hardness values ( $VHN$ ) with the cooling rate is shown in figure 3.

### 3. Limitations

The validity of this study is limited to the following ranges of composition and conditions of austenitization and tempering.

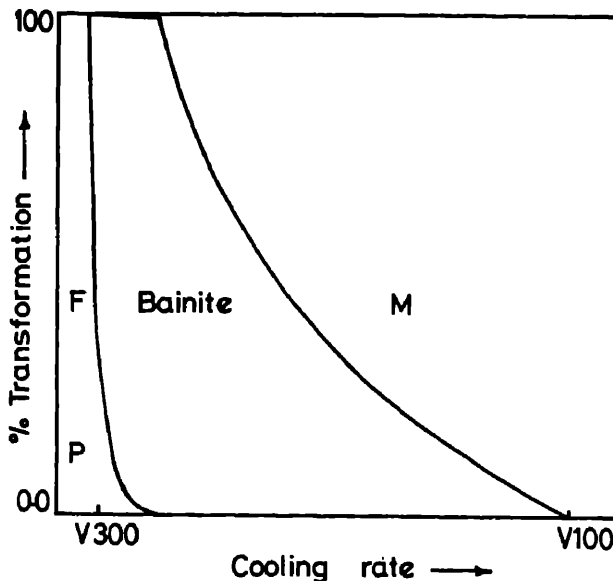


Figure 2. Identification of product as a function of cooling rate.



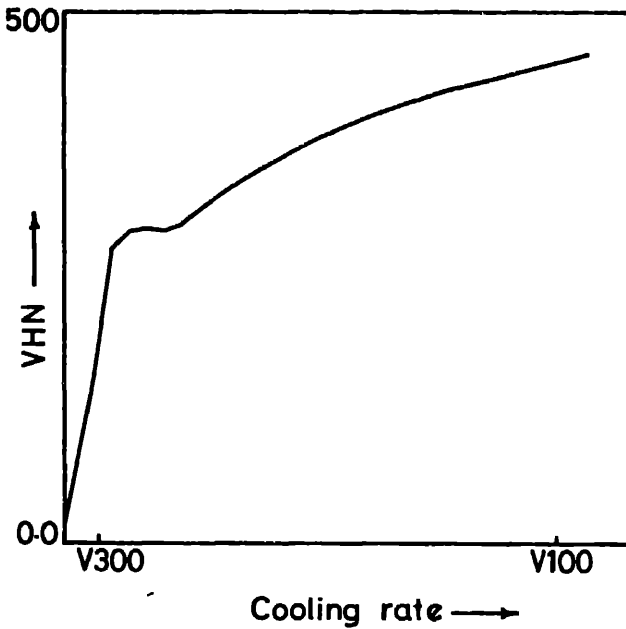


Figure 3. Variation of hardness of steel as a function of cooling rate.

### 3.1 Composition range: (weight %)

$0.1 < C < 0.5$ ;  $Mn < 2$ ;  $Ni < 4$ ;  $Cr < 3$ ;  $Si < 1$ ;  $Mo < 1$ ;  
 $V < 0.2$ ;  $Cu < 0.5$ ;  $Mn + Ni + Cr + Mo < 5$ ;  $0.01 < Al < 0.05$ .

### 3.2 Austenitizing conditions

It should be between  $800^{\circ}\text{C}$  for 1 hr and  $1100^{\circ}\text{C}$  for 1 hr. Tempering conditions should be between  $500^{\circ}\text{C}$  – 1 hr and  $700^{\circ}\text{C}$  – 200 hr. Intercritical treatment is not included. Alloying additions like Nb, Ti, B and Zr are not included in this study.

## 4. Conclusion

The present study opens up many physical and mechanical metallurgical aspects of steels for theoretical predictions. The predicted results are comparable with experimental points within an allowable variation. Although the flow chart shown in figure 1 gives the methodology of the present study, it is possible to trace back the path that will result in the optimization of composition and treatment for a required set of mechanical properties. Presently this work is being projected to cope up with a variety of steels and extending the operating range of composition and treatment conditions, although limited by certain factors. The value of the prediction will be greatly enhanced if the microstructure is simulated on the Visual Display Unit (VDU) for the given set of compositions and treatments.

**References**

- Cias W W 1977 Phase transformation kinetics of selected wrought structural steels, Report, Climax Molybdenum Co., Greenwich, Connecticut, USA
- Maynier Ph, Dollet J and Bastien P 1978 *Proc. Symp. Met. Soc. AIME*, (Philadelphia: AIME) p. 163
- Vijayaraju K 1984 B E Project Report, Department of Metallurgy, Indian Institute of Science, Bangalore

## Computer simulation of pressure sintering

N RAMAKRISHNAN, T BALAKRISHNA BHAT and  
V S ARUNACHALAM\*

Defence Metallurgical Research Laboratory, Hyderabad 500 258, India

\*Scientific Adviser to Defence Minister, New Delhi 110 011, India

**Abstract.** The densification process during pressure sintering has been analyzed using finite element analysis. This analysis uses an iterative solution algorithm. With this the densification process in complex geometries with complex boundary conditions can be analyzed and the technique is particularly suited for tackling material nonlinearity. Evolution of densified structures with gradual closure of pores is described for two typical geometries.

**Keywords.** Computer simulation; pressure sintering; finite element analysis; creep model

### 1. Introduction

Pressure sintering is a technique in which a powder aggregate is subjected to high pressures at high temperatures to achieve simultaneous compaction and sintering. Theoretical analysis of pressure sintering is greatly restricted due to the complexities involved in the geometries and the nonlinear material properties. Usually, powder aggregates are idealized to simple geometries (McKenzie 1948; Coble 1956; Kovalachenko and Samsonov 1961; Wilkinson and Ashby 1975; Notis and Krishnamachary 1975) disregarding the spatial and size distribution of pores or interaction of pores. These problems can be reduced substantially by the use of numerical techniques and we have chosen finite element method (FEM) for analyzing pressure sintering with all its complexities, as it provides a simple and direct approach to handle complex geometries, boundary conditions and material behavior (Ramakrishnan *et al* 1984).

### 2. Simulation of powder aggregates

Two types of two-dimensional configurations have been identified for simulating powder aggregates: (i) randomly packed spheres of log normal size distribution (figure 3a) (ii) randomly distributed spherical pores of log normal size distribution in a homogeneous matrix (figure 4a). To construct the first geometry, a hypothetical arrangement of circular discs of log normal size distribution placed in a rectangular matrix has been considered. The packing is done starting from the bottom row ensuring mechanical stability of the arrangement. This geometry represents the initial stage of compaction of powder aggregates.

The second geometry is formed by randomly placing circular pores of log normal size distribution in a rectangular material matrix. This geometry depicts the final stage of sintering where pores become spherical due to surface tension and the material matrix

becomes nearly continuous. These geometries are subdivided into a number of small rectangular and triangular elements for finite element analysis. As the stress varies rapidly near the pores, a finer discretization is performed there.

### 3. Analysis of densification of powder aggregates

Densification in pressure sintering takes place mainly through creep processes such as diffusion creep, dislocation creep and grain boundary sliding. These processes are driven by the local stresses. Therefore for the analysis of densification it is necessary to compute the stresses at various locations in the material matrix for the applied external pressure and the boundary conditions. These stresses are in turn used to compute the strains and the displacements for a given interval of time at the corresponding locations to obtain the new geometry. Again the new geometry is subjected to similar analysis and this process is continued in an iterative fashion until the porosity reaches the desired low value. The increments in time are decided in such a way that the change in geometry in any particular iteration is small.

### 4. Finite element analysis (FEA) of creep deformation

In FEA of creep deformation, the behaviour of each element is described in terms of force-displacement rate relationship. The governing system of equations for the whole geometry is established by the assembly of elemental behaviour, subject to compatibility and dynamic equilibrium conditions at each node. These equations are solved to yield stresses and displacement rates at various nodes.

#### 4.1 Basic equations

The force-displacement rate relation is given by

$$\{F\}^e = [K]^e \{q\}^e, \quad (1)$$

where  $[K]^e$  represents the stiffness matrix,  $\{q\}$  the displacement rate vector and  $\{F\}^e$  the nodal force vector. On assembly, these equations assume the following global form:

$$\{F\}^g = [K]^g \{q\}^g. \quad (2)$$

The stresses and strain rates in terms of displacement rates are given by the following equations:

$$\{\dot{\epsilon}\} = [B]\{q\}, \quad (3)$$

$$\{\sigma\} = E_c^e [C]\{\dot{\epsilon}\}, \quad (4)$$

where  $[B]$  is the coefficient matrix, purely dependent on the geometry of the element and  $[C]$  is given by (Donea 1978)

$$[C] = \frac{1}{(1-2\gamma)(1+\gamma)} \begin{bmatrix} 1-\gamma & \gamma & 0 \\ \gamma & 1-\gamma & 0 \\ 0 & 0 & 2(1+\gamma) \end{bmatrix}$$

for plain strain condition where  $\gamma$  is the Poisson's ratio.  $E_c^e$  is the elemental creep modulus and for the constant strain elements we define it as

$$E_c^e = \sigma_*^e / \dot{\epsilon}_*^e, \quad (1)$$

where  $\sigma_*$  and  $\dot{\epsilon}_*$  are effective stress and strain rates respectively. The stress-strain rate relationship is nonlinear and is generally represented in the form of power law

$$\dot{\epsilon}_* = A_c \sigma_*^n, \quad (2)$$

where  $A_c$  and  $n$  are creep constants which depend on the material and the temperature.

#### 4.2 Procedure for determining the stiffness matrix

The minimum potential energy condition is used to establish the stiffness matrix. The total potential energy can be represented as

$$\pi = [\iiint \{\sigma\}^T \{\epsilon\} dV - \iint \{P\} \{q\} dS] \Delta t, \quad (3)$$

where  $[P]$  represents forces per unit area and  $\Delta t$  a small interval of time. Using (3) and (4), (7) can be modified to

$$\pi = [\iiint E_c^e \{q\}^T [B]^T [C] [B] \{q\} dv - \iint \{P\} \{q\} dS] \Delta t. \quad (4)$$

For dynamic equilibrium  $\delta\pi/\delta\dot{q} = 0$ . Assuming the displacement rates to be constant in a sufficiently small interval of time, the above criterion can be shown to give,

$$F = 2E_c^e [B]^T [C] [B] \{q\} h S_e, \quad (5)$$

where  $h$  and  $S_e$  are the thickness and the area of the element respectively, within which strain is assumed constant. Hence stiffness matrix for creep is given by

$$[K]^e = 2h S_e [B]^T [C] [B] E_c^e. \quad (6)$$

#### 4.3 Procedure for analyzing densification

To start with, the elemental creep modulus of all the elements are assumed to be identical and an arbitrary  $E_c^e$  is assigned to all the elements. The displacement rates  $\{q\}$  and nodal forces  $[F]$  are obtained by solving (9) for the given boundary conditions.  $\{\sigma\}$  and  $\{\epsilon\}$  are then computed using (3) and (4). These stresses do not correspond to actual stresses and the actual stresses can be calculated only by an iterative procedure that gives a convergent, compatible solution. Effective stresses  $\sigma_*$  and effective strain rate  $\dot{\epsilon}_*$  are calculated using the equations

$$\sigma_*^2 = (\sigma_1 - \sigma_2)^2 + (\sigma_2 - \sigma_3)^2 + (\sigma_3 - \sigma_1)^2, \quad (11)$$

where  $\sigma_1, \sigma_2, \sigma_3$  are the principal stresses

$$\text{and} \quad \dot{\epsilon}_* = A \sigma_*^n.$$

The creep moduli for the subsequent iteration is computed by the equation

$$E_c^e = (1/A)^{1/n} (\dot{\epsilon}_*)^{1/n-1}. \quad (12)$$

Using these creep moduli, new displacement rates are obtained. These calculations are continued until the stresses converge in each element. After the convergence, the nodal

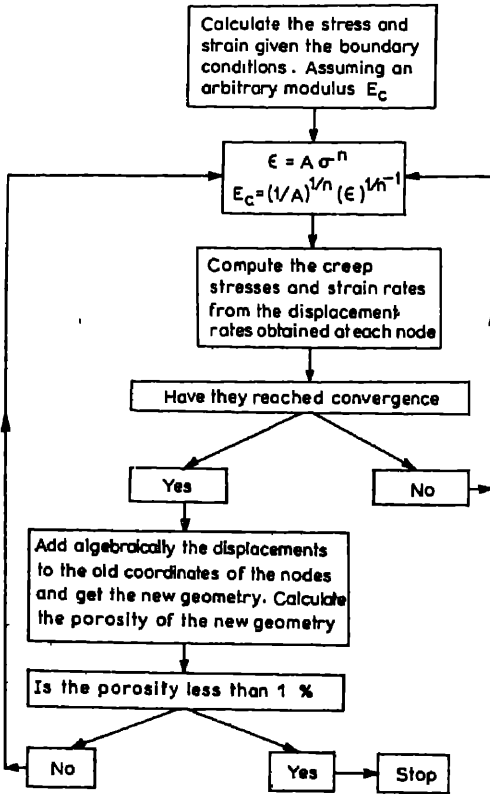


Figure 1. Flow chart for computer simulation of pressure sintering.

co-ordinates are updated using the displacements at each node and the procedure is repeated for the new porosity. In figure 1, the whole procedure is given in the form of a flow chart.

#### 4.4 Boundary conditions

Either force boundary conditions or displacement rate boundary conditions can be thought of for this analysis; the first one appears apparently simple and more relevant as what we know in practice is only the external pressure. But if we impose force boundary conditions, the displacement rates computed for all the boundary nodes may not be perfectly same as we are not dealing with a perfectly random system. The distortions in the geometry introduced by this becomes increasingly pronounced in subsequent iterations. To overcome this problem the following procedure is adopted.

Unit displacement rate is imposed on the boundary nodes ensuring that there are no contradictions, in representing the actual situation. For example in isostatic pressing as in figure 2a, the boundary conditions given are,

- for  $x = l, \{q_x\} = -1$ ; for  $y = l, \{q_y\} = -1$ ;  
 for  $x = 0, y = 0, \{q_x\} = \{q_y\} = 0$ .

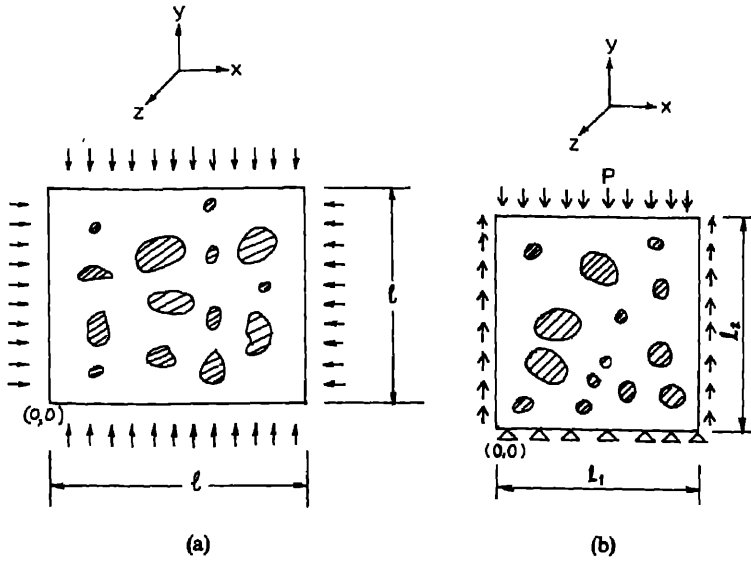


**Figure 2.** Boundary conditions for (a) isostatic pressing (b) uniaxial pressing with boundary wall friction.

Using (2) we can obtain the forces at various nodes needed to produce these displacement rates. These forces can be used to calculate the dummy pressure  $P'$  and if  $P$  is the actual pressure, we normalize all the calculated values using the scaling factor

$$\lambda = P'/P. \quad (13)$$

The relationship between dummy and actual displacement rates is given by

$$\{q'\} = \lambda \{q\}. \quad (14)$$

The actual boundary conditions used in this analysis for (i) isostatic pressing (ii) uniaxial pressing are shown in figures 2a, b respectively.

#### 4.5 Updating the geometry

Once the convergence of stresses is established for any particular porosity, the displacements are calculated at each node for a given time increment and these are algebraically added to the original coordinates of the nodes to get the new geometry. To have a control over the change in the geometry with densification, the incremental boundary displacements are fixed instead of fixing the incremental time intervals and for each step, time increment is actually calculated.

It is often necessary to refine and regenerate the mesh at regular intervals. Otherwise the elements may start overlapping when a particular pore is completely closed. If two nodes come very close, then one of the nodal data is removed from the nodal information directory and correspondingly element directory is modified. If the segments joining the nodes surrounding the pores intersect, a new node is created at the

point of intersection and the nodal and elemental directories are appropriately altered. The resulting node number sequence may increase the bandwidth of the stiffness matrix. Therefore the region of interest is scanned and the nodal and the elemental directories are modified in the whole region to bring down the bandwidth.

## 5. Results of the computer simulation

### 5.1 Evolution of pore geometries

During pressure sintering, the geometry of the powder compact undergoes a variation with time. Figure 3 is a typical sequence depicting this variation in a powder aggregate. It may be seen that the smaller particles and the boundary regions of coarser particles only get deformed significantly and not the interior of a large particle. Figure 4 represents isostatic pressing and figure 5 represents uniaxial pressing with die wall friction taken into account. Figure 5 particularly brings out the density variation at various locations similar to earlier experimental curves obtained for uniaxial pressing (Jones 1960).

### 5.2 Pore size variation

The decrease in pore sizes with densification is depicted in figure 6. It is very clearly seen from the figure that the distribution of pore sizes narrows down with densification. Also

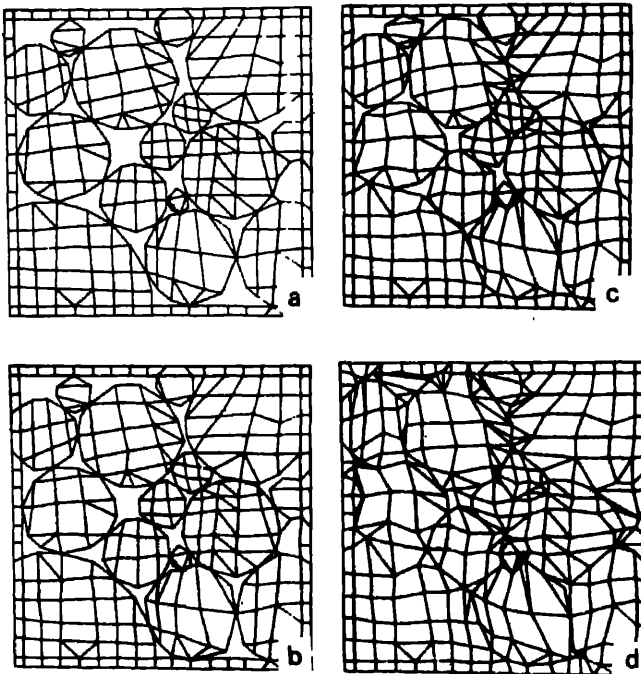


**Figure 3.** Sequence of closure in a powder compact during isostatic pressing.



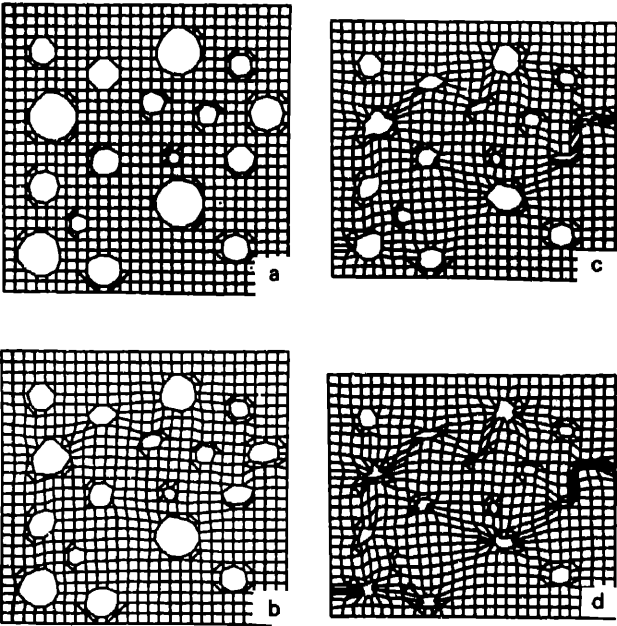


**Figure 4.** Sequence of pore closure in a compact with initially rounded pores during isostatic pressing.

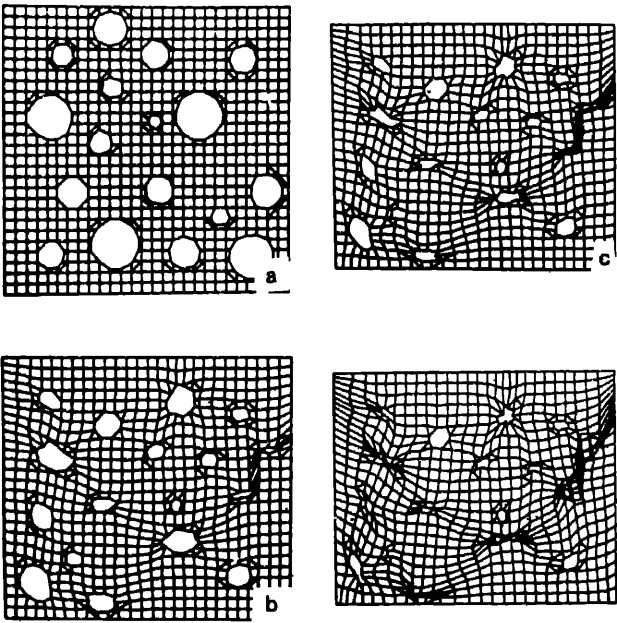


**Figure 5.** Sequence of pore closure in a compact with initially rounded pores during uniaxial pressing with boundary wall friction.

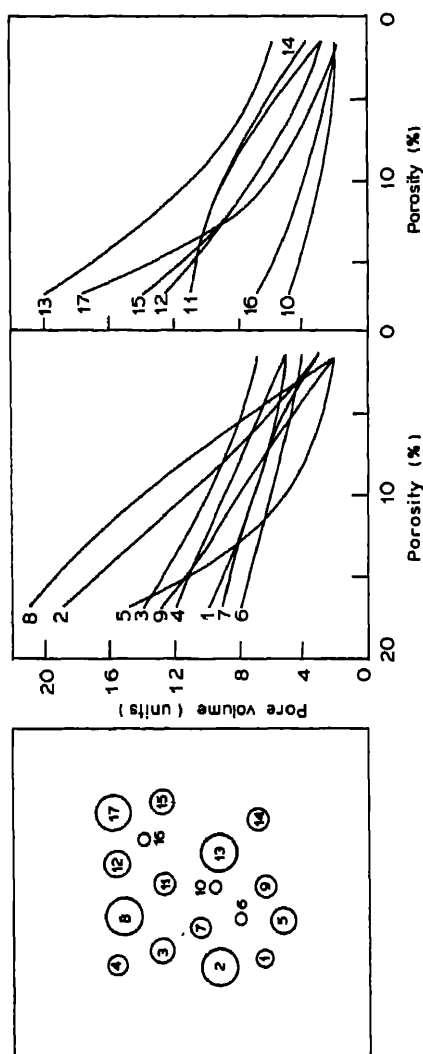


Figure 6. Variation of individual pore size with progressive densification. The curve number corresponds to pore identity.

curves crossing each other suggests that the closure rate not only depends on its size but also on its neighbours.

## 6. Conclusion

Finite element analysis can be used to analyze complex geometries of porous aggregate sintering under pressure. Even nonlinear material flow behaviour can be taken into account using a concept of creep modulus to provide a globally convergent solution. The technique applied to a compact containing a set of pores indicates that the closure of any given pore is governed not only by its own size but also its neighbourhood.

## References

- Coble R L 1970 *J. Appl. Phys.* **41** 4798  
Donea J 1978 *Creep in engineering materials and structures* (eds) G Barnasconi and G Piat (London: Applied Science Publishers) p. 34  
Jones W D 1960 *Fundamental principles of powder metallurgy* (Leeds; Arnold) p. 299  
Kovalachenko M/S and Samsonov G V 1961 *Poroshkov Metall.* **1** 3  
McKenzie J K 1948 *Proc. R. Soc. (London)* **B62** 833  
Notis M R and Krishnamachary V 1975 *Sintering and catalysis* (eds) G C Kuczinsky (New York; Plenum Press) p. 493  
Ramakrishnan N, Balakrishna Bhat T and Arunachalam V S 1984 *Acta Metall.* **32** 357  
Wilkinson D S and Ashby M F 1975 *Acta Metall.* **23** 1277



## Computer simulation of serrated yielding

K NEELAKANTAN

Indira Gandhi Centre for Atomic Research, Kalpakkam 603 102, India

**Abstract.** A model for serrated yielding based on the negative resistance characteristics materials is discussed. An analog computer based on this model is described. The simulated curves show oscillations which are regular and uniform in amplitude. To simulate more realistic tensile test curves, a refined model which includes the effects of fluctuations in dislocation density and velocity is described. Some simulated curves using this refined model are presented. These results are close to observed tensile test curves.

**Keywords.** Serrated yielding; machine equations; electronic analog; noise.

### 1. Introduction

The phenomenon of serrated yielding during tensile test experiments has been widely observed (Keh *et al* 1968; Brindley and Worthington 1970; Hall 1970) and is discussed in the literature under various names such as the Portevin-Le Chatelier effect, jerky flow etc. Experiments have shown that serrated yielding is affected by temperature, strain rate and composition. On the theoretical side the basic idea has been that dynamic strain ageing goes back, in a sense, to Cottrell and Bilby (1949).

While the strain ageing concept no doubt gives an insight into the physical origin of serrated yielding, it does not by itself provide a description of the temporal behaviour observed during experiments. It is interesting to examine the stress oscillations in terms of the interplay between the machine kinematics and the defect kinetics. The crucial point is that the dislocation drag mechanism has a negative resistance characteristic (Cottrell 1953).

In this paper, the temporal behaviour of the stress oscillations is examined in terms of the Cottrell model (which incorporates a negative resistance feature). A simple electronic analog computer (Neelakantan and Venkataraman 1983) to simulate the behaviour of the material during a constant strain rate test is described. It will be seen that the serrations are regular and uniform in amplitude unlike the ones in real tensile test curves. However the circuit describes the observed behaviour in other respects. A refined model (Neelakantan and Venkataraman 1986) which takes into account the fluctuations in dislocation density and velocity is then described. Results from numerical simulation using this refined model are presented.

### 2. The machine equations

The starting point is the machine equation which quantifies the material response during tensile testing. The machine schematic is shown in figure 1a. Figures 1b and 1c show the mechanical and electrical equivalent (to be discussed in §3). The cr

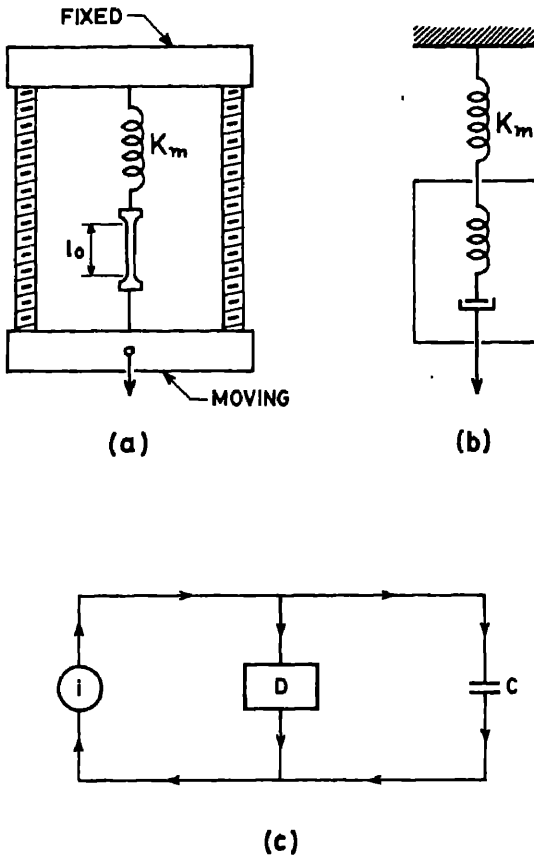


Figure 1. (a) Machine schematic for tensile testing (b) Mechanical equivalent. (c) Electrical equivalent.

head moves with a constant speed  $S$ . If the machine stiffness is  $K_m$  then at time  $t$

$$St = P/K_m + (Pl_0/AE) + \varepsilon_p l_0, \quad (1)$$

where  $A$  is the area of cross-section of the specimen,  $E$  its elastic modulus and  $\varepsilon_p$  the plastic strain. The load  $P$  is given by  $A\sigma$  where  $\sigma$  is the stress developed. Defining an effective stiffness  $K_{\text{eff}}$  as

$$1/K_{\text{eff}} = A/l_0 K_m + 1/E, \quad (2)$$

we get

$$\dot{\varepsilon} = \dot{\sigma}/K_{\text{eff}} + \dot{\varepsilon}_p, \quad (3)$$

where  $\dot{\varepsilon}$  is the applied strain rate.

Now  $\dot{\varepsilon}_p$  is described by Orowan's equation

$$\dot{\varepsilon}_p = gb\rho u, \quad (4)$$

where  $g$  is a parameter,  $b$  is the Burger's vector,  $u$  the velocity and  $\rho$  the density of mobile

dislocations. The dislocation density can be modelled as (Bergstrom and Roberts 1973)

$$\rho = \rho_0 \exp(-\Omega \varepsilon_p) + \rho_f (1 - \exp(-\Omega \varepsilon_p)), \quad (5)$$

where  $\rho_0$  and  $\rho_f$  are the initial and final dislocation densities and  $\Omega$  is a parameter related to the remobilization rate. For low values of plastic strain we can write (5) as:

$$\rho = \rho_0 + B \varepsilon_p. \quad (6)$$

Now the only thing that remains to be specified is the dislocation velocity. This is a highly nonlinear function of the stress. Choosing the Cottrell model which is schematically shown in figure 2 and taking into account the work hardening effect one can write (Nabarro *et al* 1964)

$$u = f(\sigma - \alpha \varepsilon_p^m), \quad (7)$$

where  $\alpha$  is the work hardening coefficient and  $m$  is a parameter.

### 3. The electronic analog

Going back to figure 1c which shows the electrical equivalent of the tensile test, one sees the following correspondences

$$\dot{\varepsilon} \leftrightarrow i \text{ (current) and } \sigma \leftrightarrow v \text{ (voltage).}$$

In the circuit shown, the capacitor represents the compliance and the device D simulates the complex nonlinear behaviour of the plastically deforming material. Maintaining a constant strain rate is equivalent to driving the circuit with a constant current source

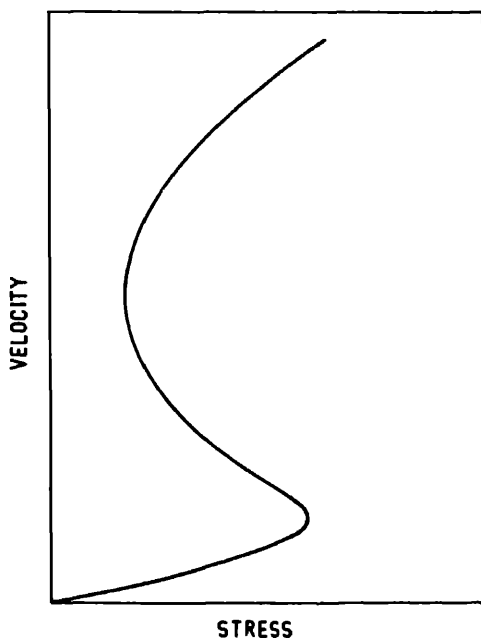
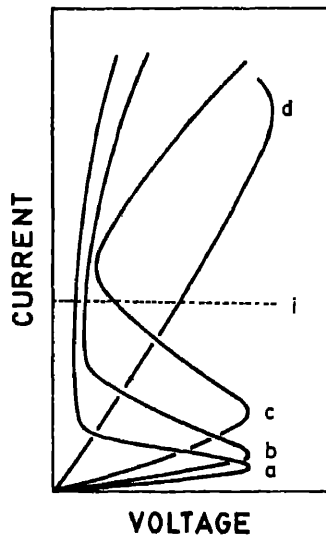


Figure 2. Schematic of dislocation velocity versus stress.

Initially, when the circuit is switched on, both  $i$  and the voltage  $v$  will be zero. After switching on, the system will evolve towards an operating condition where the load line (applied current) intersects the device characteristics. The device characteristics will however, evolve with the plastic charge (plastic strain) as shown in figure 3 which shows that initially the load line intersects the device characteristics in a region where the device exhibits a positive slope (curve a). Hence the circuit will be stable and no oscillations will be seen. As some 'plastic current' flows through the device D, its characteristics evolve through curves b and c. The load line then intersects curve c in a negative slope region and hence the circuit is unstable and shows oscillations. Later, when the characteristics evolve to curve d, the oscillations will cease.

In order to simulate such behaviour, a tunnel diode was used to mimic the negative slope characteristics of the material. The circuit schematic is shown in figure 4. The capacitor C represents the compliance of the specimen. The voltage across the capacitor is buffered by OPAMP A1 and suitably amplified by A2. The output of A2 is applied to a tunnel diode TD. The current drawn by the tunnel diode is sensed by A3 and the output of A3 represents the dislocation velocity. OPAMP A4 acts as an integrator and its output represents the plastic strain. The output of A6 represents the dislocation density. The outputs of A3 and A6 are multiplied by the multiplier M whose output controls the current ('plastic current') through the transistor T. The work hardening effect is incorporated through A5 whose output subtracts from the voltage across the capacitor.

The curve in figure 5 was obtained using the circuit described above. It can be seen that the features of a tensile test curve namely the initial yield drop, the delayed onset of serrations and the serrations themselves are all manifested in the curve. Several different biasing conditions were tried and the results showed that the simulation was faithful



**Figure 3.** Evolution of the material characteristics with plastic strain. The curves a, b, c and d represent the material characteristics as the specimen is strained. The dotted line is the applied strain rate.



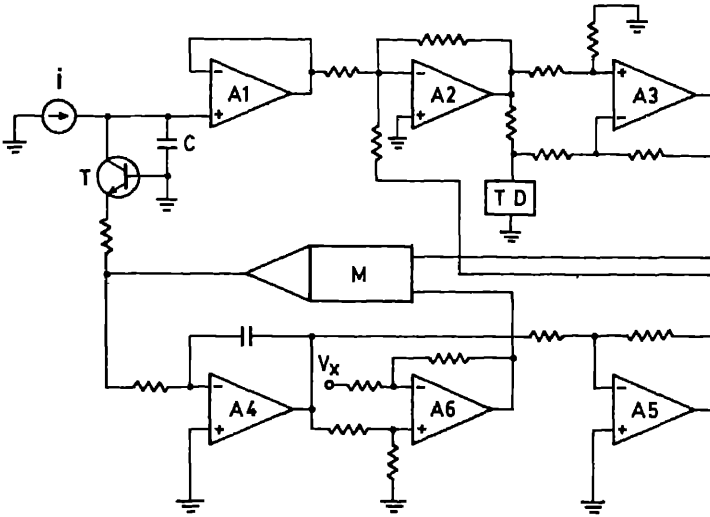


Figure 4. Circuit schematic for the analog computer.

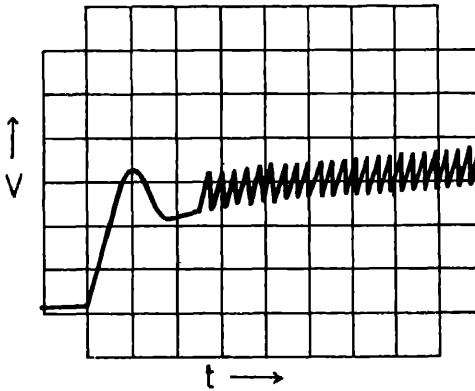


Figure 5. Output of the analog computer when the circuit is biased in the negative resistor region.

except for details of pulse shape, frequency and amplitude. These details cannot be reproduced by a circuit in which some necessary simplifications are made. Two major simplifications are the assumption that the dislocation density follows (6) with a relatively small value of  $B$  (compared to reality) and the assumption that  $m$  is unity in (7).

One major drawback of the above model is that it ignores the effects of fluctuations in the dislocation density and velocity. This is considered in the next section.

#### 4. Role of noise

The few models available for serrated yielding (Malygin 1973; Kubin *et al* 1981; Neelakantan and Venkataraman 1983) all predict regular serrations whereas  $t$

observed ones are usually irregular and occur in various types (Pink and Grinberg 1981). In this section, a realistic simulation of the various types of serrations is described.

We start with equations (3), (4), (5) and (7). Using a three-piece linear approximation to the S-shaped  $\sigma$ - $u$  curve, the system of equations describing the phenomenon was solved numerically. However, during the straining, dislocations are not only born and annihilated but also temporarily immobilized as well as unlocked. The dislocation velocity is also a random variable as it depends on thermal interactions with the lattice etc. To take into account the fluctuations in these quantities, the dislocation density and velocity are made random according to

$$u(\sigma) = \langle u(\sigma) \rangle + \beta(\sigma)\eta, \tag{8}$$

and

$$\rho(\varepsilon_p) = \langle \rho(\varepsilon_p) \rangle + \gamma(\varepsilon_p)\eta, \tag{9}$$

where  $\eta$  is a fluctuating quantity.

A wide variety of tensile test curves have been simulated and figures 6 and 7 offer a selection of the results. The various types of serrations reported in the literature have

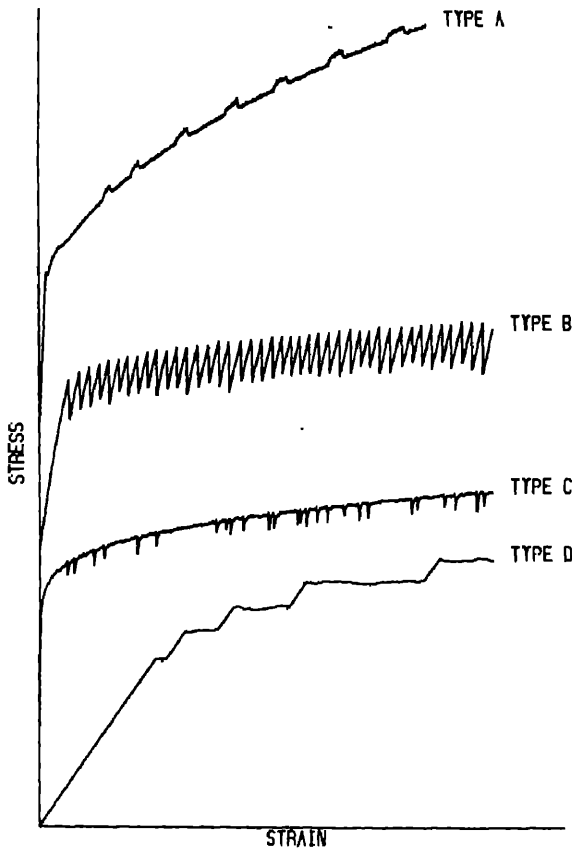


Figure 6. Various types of serrations obtained by numerical simulation.

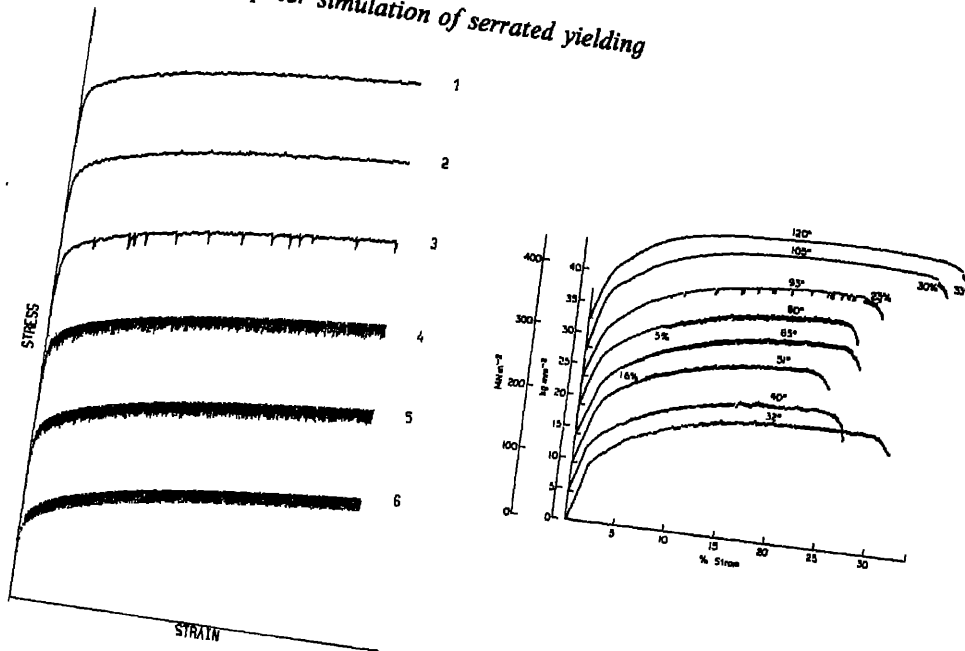


Figure 7. On the left are simulated curves. Curve 6 is for the same conditions as curve 4 but without noise. On the right are the observed curves for an Al-Mg alloy (Hall 1970).

been simulated in figure 6. The shapes depend upon the point of intersection of the load line with the material characteristics (among other factors). If the bias is near the threshold of oscillations, noise triggers random repeated yields (type C in figure 6). Figure 7 shows a family of curves corresponding to a situation where the strain rate is held constant but the temperature is varied. The similarity to observed patterns is striking.

## 5. Conclusions

A model for serrated yielding behaviour has been presented. Simulations on an analogue computer using this model results in serrations which are regular. However, the inclusion of fluctuations in dislocation density and velocity refines the model to the extent that the simulated curves are very close to actual observed tensile test curves. More than mimicking reality, the message is that the random aspects of serration need to be studied and understood. Attention must be paid to spatial inhomogeneity also.

## Acknowledgement

The author wishes to thank Dr G Venkataraman for suggesting the problem and for innumerable discussion and constant encouragement.

## References

- Bergstrom Y and Roberts W 1973 *Acta Metall.* **21** 741  
Brindley B and Worthington P J 1970 *Metall. Rev.* **15** 101  
Cottrell A H 1953 *Dislocations and plastic flow in crystals* (Oxford: Clarendon Press)  
Cottrell A H and Bilby B A 1949 *Proc. Phys. Soc.* **A62** 49  
Hall E O 1970 *Yield point phenomena in metals and alloys* (New York: Plenum)  
Keh A S, Nakada Y and Leslie W C 1968 in *Dislocation dynamics* (eds) A H Rosenfield, G T Hahn, A L Bement and R I Jafec (New York: McGraw Hill) p. 381  
Kubin L P, Ph. Spiesser and Estrin Y 1982 *Acta Metall.* **30** 385  
Malygin G A 1973 *Phys. Status Solidi.* **A15** 51  
Nabarro F R N, Basinski Z S and Holt D B 1964 *Adv. Phys.* **13** 193  
Neelakantan K and Venkataraman G 1983 *Acta. Metall.* **31** 77  
Neelakantan K and Venkataraman G 1986 (to be published)  
Pink E and Grinberg A 1981 *Mat. Sci. Eng.* **51** 1

## An absolute method for the determination of surface tension of liquids using pendent drop profiles

S RAMESH BABU

Department of Metallurgy, Indian Institute of Science, Bangalore 560 012, India

**Abstract.** Drop formation at conical tips which is of relevance to metallurgists is investigated based on the principle of minimization of free energy using the variational approach. The dimensionless governing equations for drop profiles are computer solved using the fourth order Runge-Kutta method. For different cone angles, the theoretical plots of  $X_T$  and  $Z_T$ , their ratio, are statistically analyzed, where  $X_T$  and  $Z_T$  are the dimensionless  $x$  and  $z$  coordinates of the drop profile at a plane at the conical tip, perpendicular to the axis of symmetry. Based on the mathematical description of these curves, an absolute method has been proposed for the determination of surface tension of liquids, which is shown to be preferable in comparison with the earlier pendent-drop profile methods.

**Keywords.** Surface tension; drop profiles; regression analysis; Runge-Kutta method

### 1. Introduction

The importance of the understanding of interfacial phenomena in many metallurgic processes has been rightly recognized (Richardson 1973, 1974; Szekeley 1979). For a study pertaining to interfacial phenomena, a good knowledge of the interfacial tension/surface tension of liquids is indispensable. Therefore, the methods available for the determination of this important physical property warrant considerable attention. While there are a number of methods available for this purpose (Padday 1969), very few methods are applicable for the determination of surface tension of liquid metals. Among these, White (1962) recommends the pendent drop profile method as most suitable. Again, among the various versions of the pendent drop profile method (Hartland and Hartley 1976), the method proposed originally by Andreas *et al* (1973) which has subsequently been refined, particularly with the advent of modern fast and reliable computing facilities (Stauffer 1965; Winkel 1965), is recommended for accurate work. While the pendent drops at capillary tips have been investigated since the time of Rayleigh, excepting a simple dimensional analysis by Brown and McCormick (1947) that lead to a comparative method for the surface tension determination, no other significant work on drop formation at conical tips has appeared in literature. It may be mentioned that the drop formation studies at conical tips can also lead to a better understanding of drop formation at the tip of melting rods, which will be of relevance to metallurgists as in the area of ESR process. The computer-aided analysis of drop formation at conical tips leading to an absolute method for the determination of surface tension of liquids using pendent drop profiles, is discussed in this paper.

## 2. Model

The principle of minimization of free energy has been used to develop a model to predict the pendent drop profiles at conical tips (see figure 1) using the 'variational approach' (Ramesh Babu 1985a). The governing equations, in dimensionless form are given by

$$d\theta/dS = (2/B) - (\sin\theta/X) - Z, \quad (1)$$

$$dX/dS = \cos\theta, \quad (2)$$

$$dZ/dS = \sin\theta, \quad (3)$$

$$dV/dS = \pi X^2 \sin\theta. \quad (4)$$

With the following boundary conditions

$$\text{at } Z = 0, X = 0; dX/dZ = \infty \text{ and } V = 0, \quad (5)$$

$$\text{at } Z = Z_0, dX/dZ = \tan\beta, \quad (6)$$

where,  $X = x C^{1/2}$ ;  $Z = z C^{1/2}$ ;  $S = s C^{1/2}$ ;  $V = v C^{1/2}$ ;  $B = b C^{1/2}$ ;  $C = g(\rho_d - \rho_L)/\gamma$ ;  $b$  = radius of curvature at the drop apex,  $s$  = arc length,  $\rho_d$  = density of the drop, and  $\rho_L$  = density of the surrounding fluid,  $\gamma$  = interfacial tension at the drop-fluid interface and  $v$  = drop volume.

The same governing equations have also been shown to be deducible by an alternate approach using the concept of double buoyancy effect (Ramesh Babu 1984). Choosing a particular value of  $B$ , equations (1) to (4), together with the boundary conditions, equations (5) to (6), were solved simultaneously by the 'fourth order Runge-Kutta procedure', for which a computer program was developed ensuring an accuracy better than a part per million in the computed values (Ramesh Babu 1985b). The method of 'Regula-Falsi' was also incorporated in the program for calculating the interpolated values of interest. The flow chart highlighting the programme logic is given in figure 2.

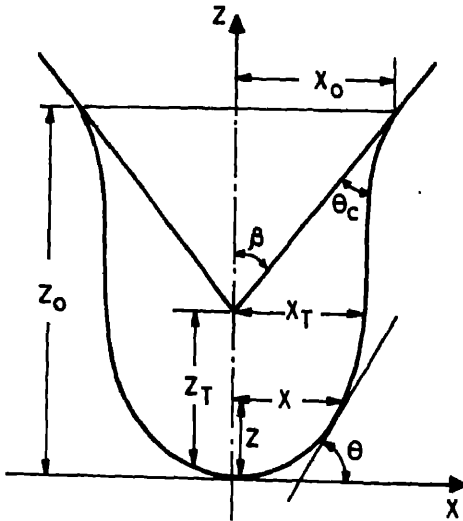


Figure 1. Axisymmetric pendent liquid drop at an infinite conical tip.

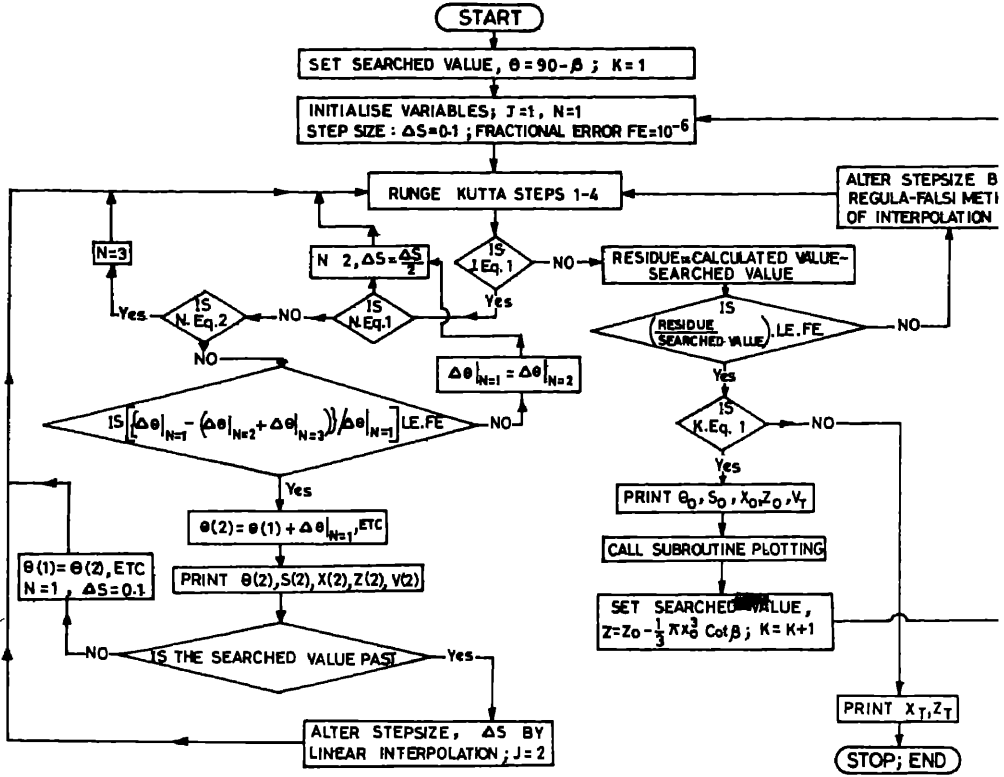


Figure 2. Flow chart highlighting the programme logic for generating pendent drop profiles at conical tips.

The maximum drop volume was obtained numerically. The significance of the numerical results obtained for various cone angles is discussed elsewhere (Ramesh Babu 1985a). The model permits the calculation of drop volume as well as to follow the changing sequence of drop profiles until the onset of instability. The sequence of drop growth at different conical tips is illustrated in figure 3.

### 3. Determination of surface tension

Considering the equilibrium situation of a pendent liquid drop at a conical tip as shown in figure 1, for a specified cone angle, it is possible to theoretically calculate the values of  $X_T$  corresponding to  $Z_T$ , and hence their ratio, during the drop formation until it enters the instability stage, where,

$$X_T = x_T \left( \frac{(\rho_d - \rho_L)}{\gamma} g \right)^{1/2}, \quad (7)$$

and

$$Z_T = z_T \left( \frac{(\rho_d - \rho_L)}{\gamma} g \right)^{1/2}. \quad (8)$$

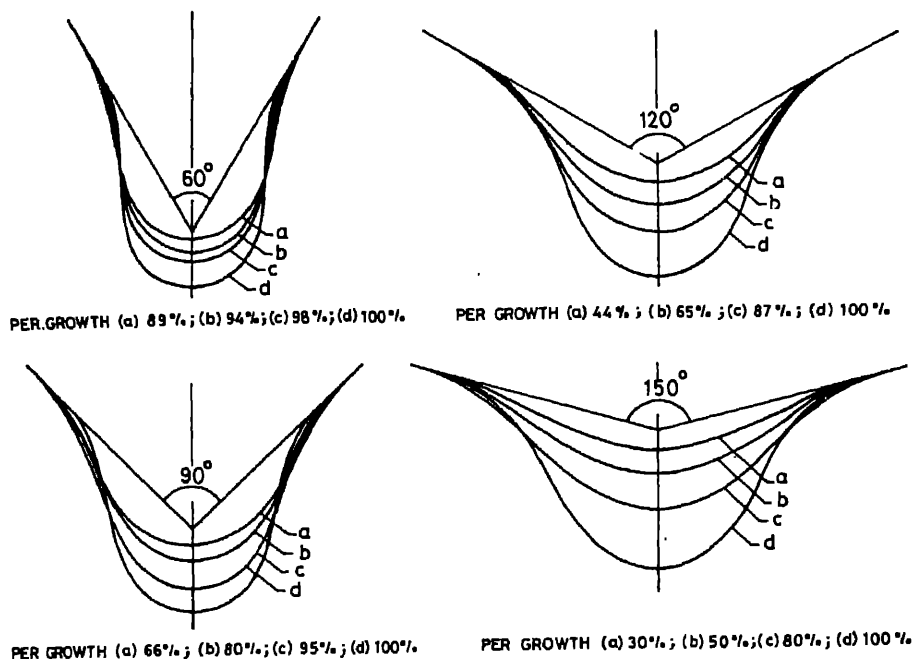


Figure 3. Sequence of drop growth at conical tips.

Dividing (8) by (7), we get

$$Z_T/X_T = z_T/x_T. \quad (9)$$

Therefore, by photographically measuring the values of  $x_T$  and  $z_T$ , in view of (9) the corresponding  $X_T$  and  $Z_T$  can be calculated. The interfacial tension can be calculated using (7) or (8).

#### 4. Regression analysis

To facilitate quick computation of  $\gamma$ , it is desirable to have a relation between  $X_T$  and  $Z_T$  and their ratios. Figures 4–7 illustrate the variation of both  $X_T$  and  $Z_T$  with  $X_T/Z_T$  and  $Z_T/X_T$  in the range  $0 \leq Z_T \leq Z_T^{\max}$ , where,  $Z_T^{\max}$  corresponds to the critical profile enclosing the maximum drop volume, for each of the cone angles 60°, 90°, 120° and 150°. Each of these plots was statistically analyzed using a computer algorithm that has been shown to be superior even to Gauss elimination technique upto fifth order polynomial (Ramesh Babu 1985c). The coefficient of variation defined below was used as the criterion for choosing the best fit polynomial.

$$CV = \frac{SD}{\bar{y}} \times 100; \quad SD = \left( \frac{\sum_{i=1}^n (y_{LF} - y_i)^2}{n - (K + 1)} \right)^{1/2}, \quad (10)$$

where, SD is the standard deviation,  $y_{LF}$  is the least square fitted value of  $y_i$ ,  $\bar{y}$  is the average of  $y_i$  and  $K$  is the degree of the polynomial fitted onto  $n$  data points.



## Surface tension using pendent drop profiles

**Table 1.** Summary of the regression analysis of the curves  $X_T$  vs  $X_T/Z_T$  and  $Z_T$  vs  $X_T$

Curve investigated			$X_T$ vs $X_T/Z_T$			$Z_T$ vs $X_T/Z_T$		
Cone angle	Range of $X_T/Z_T$	$n$	$K$	PEM (%)	CV (%)	$K$	PEM (%)	CV (%)
60°	1.34-6.60	16	2	4.52	1.03	2	87.34	11.992
	1.34-2.88	12	5	0.32	0.239	2	3.59	1.456
90°	0.97-3.48	22	1	2.66	1.387	2	25.31	4.059
	0.97-3.14	21	2	2.48	1.223	2	15.96	3.011
120°	0.90-18.39	27	2	44.91	6.076	2	2402.30	41.84
	1.11-3.61	19	2	2.03	1.046	2	16.79	3.172
150°	0.95-23.16	24	2	30.68	5.575	2	2355.5	49.87
	1.08-5.21	17	2	3.44	2.003	2	41.56	7.52

**Table 2.** Summary of the regression analysis of the curves  $X_T$  vs  $Z_T/X_T$  and  $Z_T$  vs  $Z_T/X_T$

Curve investigated			$X_T$ vs $Z_T/X_T$			$Z_T$ vs $Z_T/X_T$		
Cone angle	Range of $Z_T/X_T$	$n$	$K$	PEM (%)	CV (%)	$K$	PEM (%)	CV (%)
60°	0.15-0.75	16	2	0.27	0.175	2	26.78	1.782
	0.35-0.75	12	2	0.19	0.114	2	1.17	0.371
90°	0.28-1.03	22	2	2.22	0.823	5	6.88	0.785
	0.32-1.03	21	2	1.84	0.727	5	4.11	0.558
120°	0.05-1.12	27	2	26.16	3.567	1	706.65	5.291
	0.28-0.90	19	2	1.80	0.705	5	3.90	0.518
150°	0.04-1.05	24	2	47.58	6.365	5	599.96	5.399
	0.19-0.93	17	2	4.64	1.887	5	5.31	0.668

Since the analysis showed too large values of CV, the analysis was repeated reducing the range. The results are summarized in tables 1 and 2. The significant improvement in the CV value upon reducing the range is obvious. It could also be seen that the descriptions of the plots  $X_T$  vs  $Z_T/X_T$  and  $Z_T$  vs  $Z_T/X_T$  are far more desirable than the other two. The coefficients of the best fit polynomial to these curves are tabulated in tables 3 and 4. Utilizing these results, tables have been prepared in intervals of 0.001 of  $Z_T/X_T$  over a sufficiently wide range of practical utility for each of the 4 cone angles.

## 5. Results and discussion

A common feature of all the curves (see figures 4-7) is that the slope of the curve increases with cone angle, which suggests that a 60° cone is preferable. While the plots of  $Z_T$  vs  $Z_T/X_T$  show a uniform gradient throughout, the plots of  $Z_T$  vs  $X_T/Z_T$  show steep gradients in the range of practical interest. The plots of  $X_T$  vs  $Z_T/X_T$  indicate that

Table 3. Coefficients of the best fit polynomial to the curve  $X_T$  vs  $Z_T/X_T$ 

Cone angle	Range of $Z_T/X_T$	CV (%)	$X_T = A_1 + A_2(Z_T/X_T) + A_3(Z_T/X_T)^2$		
			$A_1$	$A_2$	$A_3$
60°	0.35–0.75	0.114	–0.00054	1.91325	–1.11559
90°	0.32–1.03	0.727	0.11320	2.01519	–1.10914
120°	0.28–0.90	0.705	0.17625	2.73173	–1.67780
150°	0.19–0.93	1.887	0.48231	3.59968	–2.49335

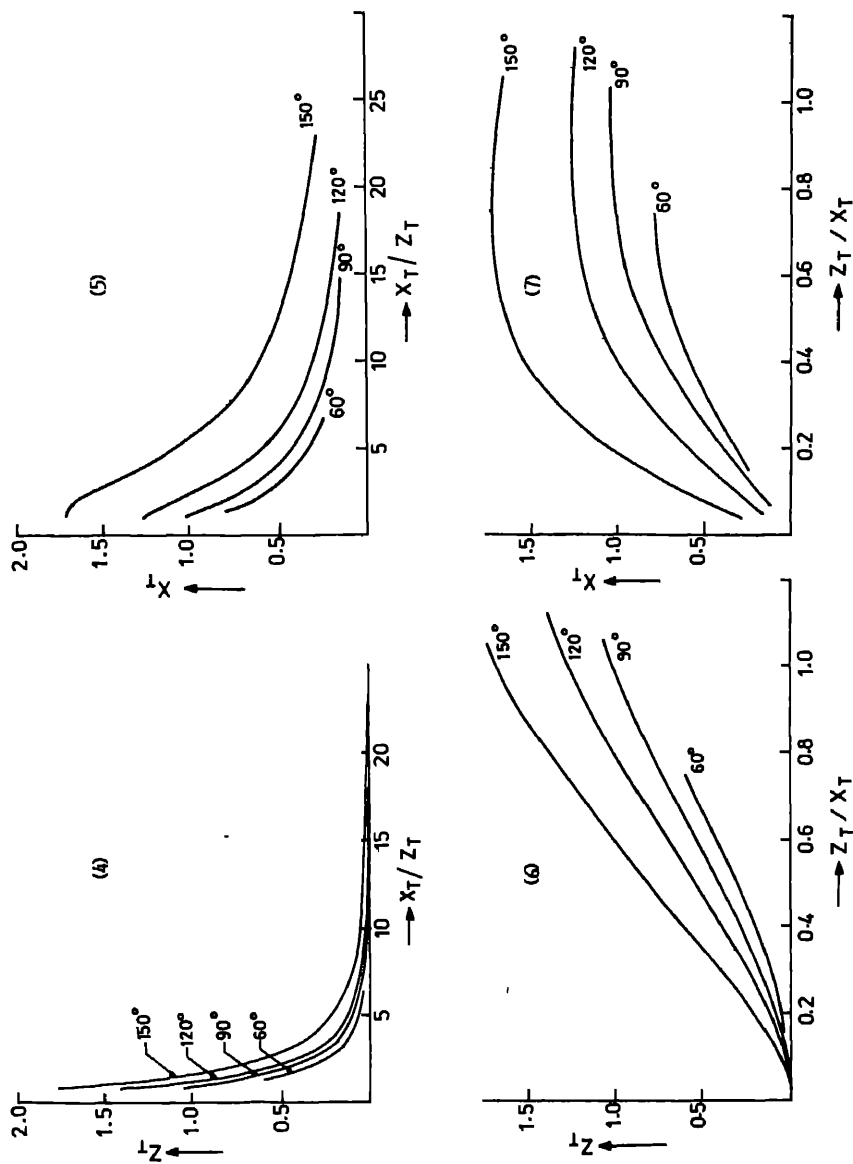
Table 4. Coefficients of the best fit polynomial to the curve  $Z_T$  vs  $Z_T/X_T$ 

Cone angle	Range of $Z_T/X_T$	CV (%)	$Z_T = A_1 + A_2(Z_T/X_T) + A_3(Z_T/X_T)^2 + A_4(Z_T/X_T)^3 + A_5(Z_T/X_T)^4 + A_6(Z_T/X_T)^5$					
			$A_1$	$A_2$	$A_3$	$A_4$	$A_5$	$A_6$
60°	0.35–0.75	0.371	–0.16413	0.96421	0.08756	—	—	—
90°	0.32–1.03	0.558	–0.22483	1.31150	–0.00061	–0.00056	–0.00003	–0.05832
120°	0.28–0.90	0.518	–0.23624	1.61267	–0.00063	–0.00068	–0.00006	–0.09064
150°	0.19–0.93	0.668	–0.21477	2.09723	0.00012	–0.00129	–0.00045	–0.19713

over a wide range of  $Z_T/X_T$  the curves are almost parallel to the x-axis, hence errors in the measured  $Z_T/X_T$  will not significantly affect the accuracy of the corresponding  $X_T$  value.

The proposed method has several distinct advantages over the other methods employing the pendent drop profiles at capillary tips (Padday 1969):

- (i) The method is free from empiricism, as it is based on a sound theory;
- (ii) The well-defined conical tip inside the drop enables accurate measurements of  $x_T$  and  $z_T$ ;
- (iii) The measurement of the linear dimensions being independent of each other, the undesirable cascading error in the method of selected planes (Andreas *et al* 1938) is obviated;
- (iv) A single cone is sufficient to form drops of desirable shapes. This is in sharp contrast to the extra care required in selecting a suitable capillary to obtain a desired drop shape, in all the earlier methods.
- (v) Since different drop shapes could be obtained from a single cone, a number of measurements of  $x_T$  and  $z_T$  could be made, providing as many cross checks for  $\gamma$  as required. In addition, each set of  $x_T$  and  $z_T$  values permits the calculation of  $\gamma$  by two independent methods vide (7) and (8).
- (vi) Formation of drops at conical tips is much simpler and easier compared to any other method of drop formation reported in literature.



Figures 4-7. 4. Variation of  $Z_T$  with  $X_T/Z_T$ . 5. Variation of  $X_T$  with  $X_T/Z_T$ . 6. Variation of  $Z_T$  with  $Z_T/X_T$ . 7. Variation of  $X_T$  with  $Z_T/X_T$ .

The design of a simple experimental set-up to form drops at conical tips under desired controlled flow rates has been described elsewhere (Ramesh Babu 1985b). Drops could also be formed at conical tips by immersing a metal cone in the liquid bath and gradually moving it away from the liquid surface or vice versa. This method of drop formation is particularly suited for liquid metals. In view of the several advantages of the proposed method, application to liquid metals deserves considerable attention.

### Acknowledgement

The financial assistance received from the Department of Atomic Energy, Government of India is gratefully acknowledged.

### References

- Andreas J M *et al* 1938 *J. Phys. Chem.* **42** 1001  
Brown R C and McCormick H 1948 *Philos. Mag.* **39** 420  
Hartland S and Hartley R W 1976 *Axi-symmetric fluid-liquid interfaces* (Amsterdam: Elsevier)  
Padday J F 1969 *Surf. Colloid Sci.* (ed.) E Matijevic (New York: Wiley Interscience) Vol. 1  
Ramesh Babu S 1984 *Proc. 29th Congress of The Indian Society of Theoretical and Applied Mechanics, KREC, Surathkal* (to appear)  
Ramesh Babu S 1985a *Proc. Int. Conf. on progress in metallurgy; Fundamental and applied aspects*, Indian Institute of Technology, Kanpur  
Ramesh Babu S 1985b *Studies on drop formation at conical tips*, Ph.D. Thesis, Indian Institute of Science, Bangalore  
Ramesh Babu S 1985c *An alternative algorithm for least square polynomial fitting* (unpublished research)  
Richardson F D 1973 *Trans. ISIJ* **13** 369  
Richardson F D 1974 *Trans. ISIJ* **14** 1  
Stauffer C E 1965 *J. Phys. Chem.* **69** 1933  
Szekely J 1979 *Fluid flow phenomena in metals processing* (New York: Academic Press)  
White D W G 1962 *Trans. Q.* **55** 757  
Winkel D 1965 *J. Phys. Chem.* **69** 348

## Personal computer-based CAMAC system for data acquisition

S K KATARIA, V S RAMAMURTHY, V G GAONKAR and  
SURENDRA KUMAR\*

Nuclear Physics Division and \*Electronics Division, Bhabha Atomic Research Centre  
Bombay 400 085, India

**Abstract.** A single board auxiliary CAMAC crate controller for a Z80-A based personal computer ZX-spectrum to drive the CAMAC crate housing multiple ADC, TDC, DAC and 16 ports has been developed. The CAMAC crate controller used in this system is of A2 type which supports multiple auxiliary crate controllers. A CAMAC exerciser/training software for the use of CAMAC commands in process control as well as data acquisition has been developed.

**Keywords.** Personal computer; Z80-A CPU; CAMAC; auxiliary crate controller; CAMAC training software.

### 1. Introduction

Data gathering and analysis in experimental sciences has been undergoing a major revolution in the last quarter of this century due to the appearance of low cost digital computers. It has significantly altered the instrumentation around an accelerator or nuclear research reactor, which are being increasingly made with built-in microprocessor ( $\mu P$ ). These inexpensive  $\mu P$  can very easily and rapidly transform the raw data into elaborate computed results in a user friendly form. We are all aware of the concept of modularity in nuclear electronics equipment. The first internationally accepted standard in nuclear electronics is the well known NIM standard. As digital information began to supplement the analogue instrumentation in nuclear environment a new standard CAMAC (computer automation in measurement, acquisition and control) was designed about a decade ago by ESOR group (EUR 4100e, 1969). It is now being widely used in industrial process control and nuclear instrumentation around a reactor or in an accelerator laboratory. A very large number of CAMAC modules including intelligent crate controllers (CC), analog-to-digital converters (ADC), multichannel digital-to-analog converters (DAC), time-to-digital converters (TDC), scalers, module controllers, are available off the shelf from a number of competitive vendors. One can easily configure a spectrometer, or a multiparameter data acquisition system or an accelerator control panel using these standard CAMAC modules. The use of CAMAC-based systems is being favoured (Satyamurthy and Kataria 1984) since one can easily enhance or reconfigure the system using alternate functional units in the CAMAC crate. Kataria (1984) had earlier developed a pulse height analyzer and data analysis system based on a Sinclair ZX-spectrum personal computer. In the present work we report the interfacing of the ZX-spectrum (PC) through a locally designed auxiliary crate controller (ACC). In this way, we can easily use the various standard CAMAC modules without any further hardware interfacing.



facility to address or to respond to any normal station is given through the crate controller (CC) in order to accommodate ACCs, two features are required: (i) access to the N and L lines at normal stations and (ii) priority arbitration for control of dataway

Access to the N lines is necessary to allow an ACC to issue a complete addressed command operation. Access to the L-lines is necessary for an ACC to respond to "look at me" (LAM) signals from the modules or controllers or both. Priority arbitration protocol ensures that at any time only one controller is permitted to have control of the crate. It also provides the means for assigning control of the dataway on the basis of preassigned priority. Access to the N and L lines and other signals necessary for priority arbitration protocol is provided through auxiliary controller bus (ACB) as shown in figure 2.

## 2.2 Hardware developments

Figure 2 shows a general block diagram of the ACC developed in-house. Data transfer over Z-80 bus is 8-bit wide and on CAMAC dataway it is 24-bit wide. As shown in the block diagram, ACC first assembles the CAMAC commands from the information received from personal computer properly in accordance with the CAMAC dataway protocol, then it raises request flag (Req) for taking command of dataway. After getting grant-in, ACC starts its dataway cycles operation. During the dataway operation, the status of X, C and B signals are latched. During CAMAC read operation, it latches the information from R-lines, so that one can transfer the 24-bit data to personal computer byte by byte later on. Wired OR (VECTOR) interrupt facility is provided for L lines, so that the personal computer can respond to the request from the modules for servicing. In the present system, the data are being acquired in interrupt mode.

In the present design, two modes of priority arbitration protocol have been provided: (i) request/grant (R/G) and (ii) auxiliary controller lockout (ACL); the preferred mode is the R/G protocol. In this mode, when a request is raised, it checks for grant-in signal. If grant-in is present, busy and request inhibit signals are generated and the sequence of timing signals for dataway operation is started. If grant-in is not present i.e. dataway is already in command of some other controller, the auxiliary controller requesting dataway, waits for that operation to be completed. In R/G protocol, this type of delay is to be accounted for. In ACL mode, where a controller cannot wait for this delay, the dataway operation of lower priority controller will be aborted and dataway will be given to higher priority controller. The lower priority controller will resume its operation subsequently.

## 3. Functional description

ACC receives the CAMAC commands operation to be performed on CAMAC modules from personal computer. During addressed command operation, it generates the 5-bit binary code (EN) for the station number associated with the command and then transmits it via the EN lines of the ACB. The CC receives this station number code (EN) decodes it and then addresses the appropriate normal station. ACC also establishes other necessary signals on the B, AN, FN, S1 and S2 lines appropriate for the command operation to be performed and to define the timing of the operation. During addressed command operations involving data, the ACC transmits or receives data via W or R lines. The

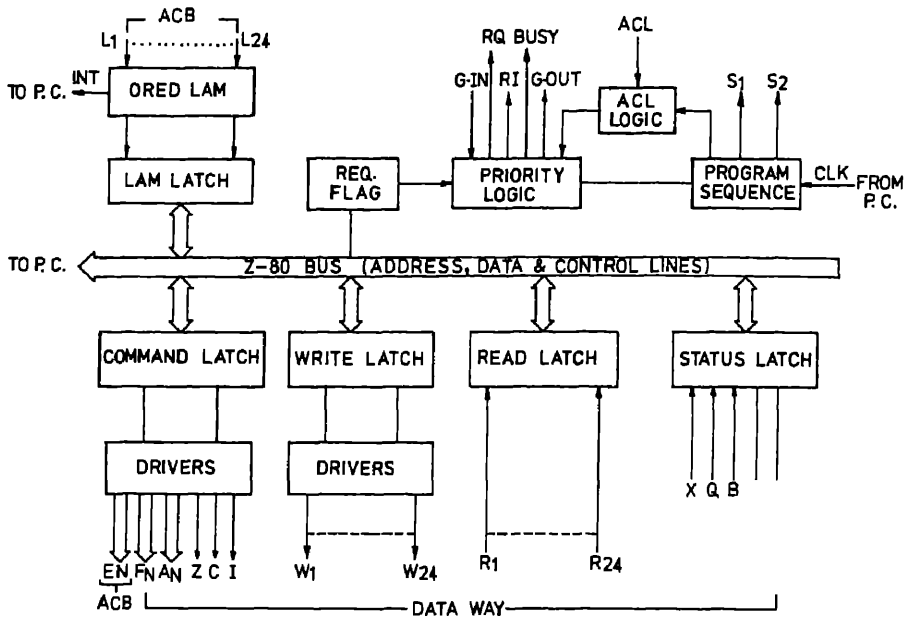


Figure 2. Block diagram of auxiliary crate controller.

unaddressed operations, e.g. dataway initialize Z and dataway clear C, do not require use of EN-signals of the ACB. But ACC still establishes the necessary signals B, S1 and S2 and Z or C lines. Figure 3 shows the sequence of signals for an ACC to gain control of dataway for an addressed command operation.

### 3.1 Software developments

A general purpose software for training in the use of various CAMAC commands has been developed. In the help mode (H), the software displays at a glance all the CAMAC commands e.g. common control commands Z, C, I and dataway commands. In debug-mode (D), one can execute each CAMAC command one by one, using friendly mnemonic symbols (R for read, W for write) and thus debug the CAMAC modules and the associated software. In one session with the training software, one achieves remarkable familiarity with CAMAC system. In the extended mode (X), one can easily write CAMAC subroutines for data acquisition from multiple units in CAMAC crate and debug them extensively from both the software and hardware aspects. This software is written in BASIC language, and can therefore be easily transported to other personal computers.

A dedicated software package for multiparameter data acquisition using a 12-channel nuclear ADC and a 8 channel TDC and display and test module has also been written. In order to achieve faster rate of data acquisition, parts of the software are in machine code e.g. the interrupt service routines, real time one and two parameter data display routines etc. The main program controlling the data acquisition, and setting up the various initial conditions e.g. (choosing the no. of ADC, TDC) is in BASIC language, and has been planned carefully keeping in view the needs of the experimentalists. After defining the parameters of an experiment, the data acquisition is carried out using



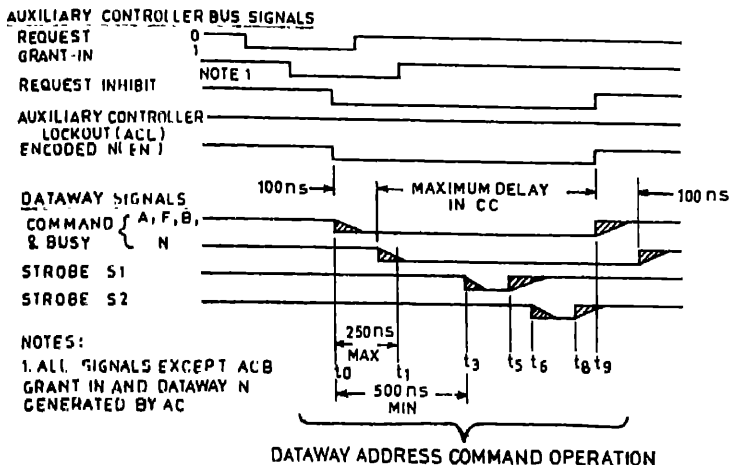


Figure 3. Sequence of signals for an ACC to gain control of dataway for an address command operation.

interrupt facilities; and data display and control is carried out in the background. number of BASIC routines for spectrum analysis are also available and further they are easy to modify to suit the individual requirements of the experimentalists. At present the acquired data can be stored only on audio cassette tape at a speed of 1100 baud rate

## Acknowledgement

We are thankful to Dr S S Kapoor for encouragement.

## References

- CAMAC 1969 A modular instrumentation system for data handling, ESONE report EUR4100
- Satyamurthy N S and Kataria S K 1984 Keynote address in RCA Workshop of IAEA on the "Use of microprocessors in research reactor utilisation", BARC/I-806
- Kataria S K 1984 Personal computers, p. 323, BARC/I-806



## Image analysis system for quantitative metallography

V K CHADDA, D G JOSHI, S N MURTHY, S V KULGOD,  
C BABURAO\*, D K BHATTACHARYA\* and BALDEV RAJ\*

Reactor Control Division, Bhabha Atomic Research Centre, Trombay, Bombay 400 085, In  
\*Radio Metallurgy Programme, Indira Gandhi Centre for Atomic Research, Kalpakkam  
603 102, India

**Abstract.** This paper describes a Z-80 microprocessor-based image analyzer developed for global parameter evaluation of images over a  $256 \times 256$  pixel frame. It consists of a microscopical CCD scanner, 6-bit video ADC, Z-80 computer and an image display monitor. Facilities provided for feature erosion/dilation and halo correction. The paper also presents the details of another more powerful user microprogrammable HP1000 minicomputer-based image analysis system under development. This system consists of an optical microscope/epidiascope coupled to a chalnicon scanner. Here the  $512 \times 512$  pixel image is acquired with 8 bit resolution. It provides for shading correction, auto-delineation, image processing and image analysis functions for evaluation of various basic and derived parameters.

Both the systems are software intensive and are realised according to requirements for quantitative metallography. They can also be used for analysis of images obtained in the fields of biology, medicine, geological survey, photography and space.

**Keywords.** Pixel; erosion; dilation; bit quad; global parameters; feature extraction; image analysis; metallography.

### 1. Introduction

Metallographic image analysis is essential for objective correlation of material properties with its microstructure. It is carried out by examining them under suitable electronic/optical instruments and analysing the image obtained.

A Z-80 microprocessor-based image analysis system with  $256 \times 256$  pixel resolution has been developed indigenously. It provides estimation of different phases and microstructures through grey level detection (64 levels) and computation of their geometrical parameters.

An HP-1000 computer based image analysis system is also being developed with  $512 \times 512$  pixel resolution incorporating facilities for image enhancement, auto-delineation, shading correction, light pen interaction and feature spectral measurements.

### 2. Z-80-based image analysis system

A block diagram of the system is shown in figure 1 and described below:

#### 2.1 Imaging

The image to be analyzed is obtained from samples observed under an optical microscope/epidiascope. It is projected on to the sensor array of a CCD video camera.



For image analysis 256 lines, 256 pixel matrix is selected. The remaining part of frame is used to display a band of 64 grey levels and two cursors indicating the selected grey slice as shown in figure 2.

## 2.2 Data acquisition

The scanner output is presented to a 6-bit video ADC for digitization. A simple scheme based on threshold detection was employed with upper and lower threshold. Detection constitutes obtaining a binary image (logic 0-1 pattern) containing selected features. Logic '1' in the binary image corresponds to pixels lying in the selected slice and logic '0' for the background (Jenkinson 1982).

This binary image is compacted into byte format and stored into an 8 K × memory for flicker-free image display and transferred to the computer memory for analysis.

## 2.3 Data analysis

Image analysis is carried out for evaluation of desired basic metallographic parameters on global basis. The system has facilities for erosion, dilation and halo error correction.

**2.3a Basic parameter evaluation:** Here sets of  $2 \times 2$  pixel patterns called bit quads are computed as shown in figure 3a. Each pixel  $A_0$  of the binary image is selected and its associated bit quad ( $A_0, A_1, A_0^N, A_1^N$ ) is examined. These are represented as  $C_0, C_1, \dots, C_{15}$  where  $C_1 = 2^3 A_1^N + 2^2 A_0^N + 2^1 A_1 + 2^0 A_0$ . At each pixel position the 16 combinations are encountered. A table is created in the memory to determine the count of each  $C_i$  over the entire frame. Based on combination of these  $C_i$  values, counts  $Q_1, Q_2, Q_3, Q_4$  and  $Q_D$  are computed as shown in figure 3b. Basic parameters of an image over the entire frame are expressed in terms of the quad counts as follows (Pratt 1978).

$$\begin{aligned} A_{(\text{area})} &= 1/4 (Q_1 + 2Q_2 + 3Q_3 + 4Q_4 + 2Q_D), \\ P_{(\text{perimeter})} &= Q_2 + 0.707 (Q_1 + Q_3 + 2Q_D), \\ E_{(\text{Euler count})} &= 1/4 (Q_1 - Q_3 - 2Q_D). \end{aligned}$$

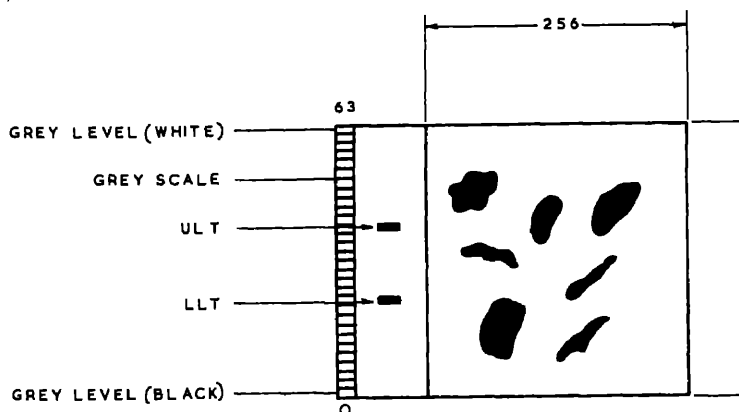


Figure 2. Format of image display on monitor.

Feature count  $C$  is related to Euler count by  $E = (C-H)$  where  $H$  = number of holes. If the number of holes is small in comparison with number of features, Euler number can be taken as a good estimate of feature count.

For horizontal projection  $H_p$ , 0-1 transition in the horizontal direction is observed as shown in figure 3c and  $H_p$  is given by

$$H_p = C_2 + C_6 + C_{10} + C_{14}.$$

Similarly 0-1 transition in the vertical direction is observed as shown in figure 3d and vertical projection  $V_p$  is given by

$$V_p = C_4 + C_8 + C_{12} + C_{14}.$$

Estimation of these parameters requires about 2.5 seconds.

**2.3b Erosion and dilation;** In the process of erosion, the touching objects are uniformly shrunk along their perimeters until a separation is achieved. Dilation is used to join separated parts of detected images.

For erosion and dilation, a reference pixel is considered in relation to its four nearest structuring elements as shown in figure 3e. During erosion the reference pixel is

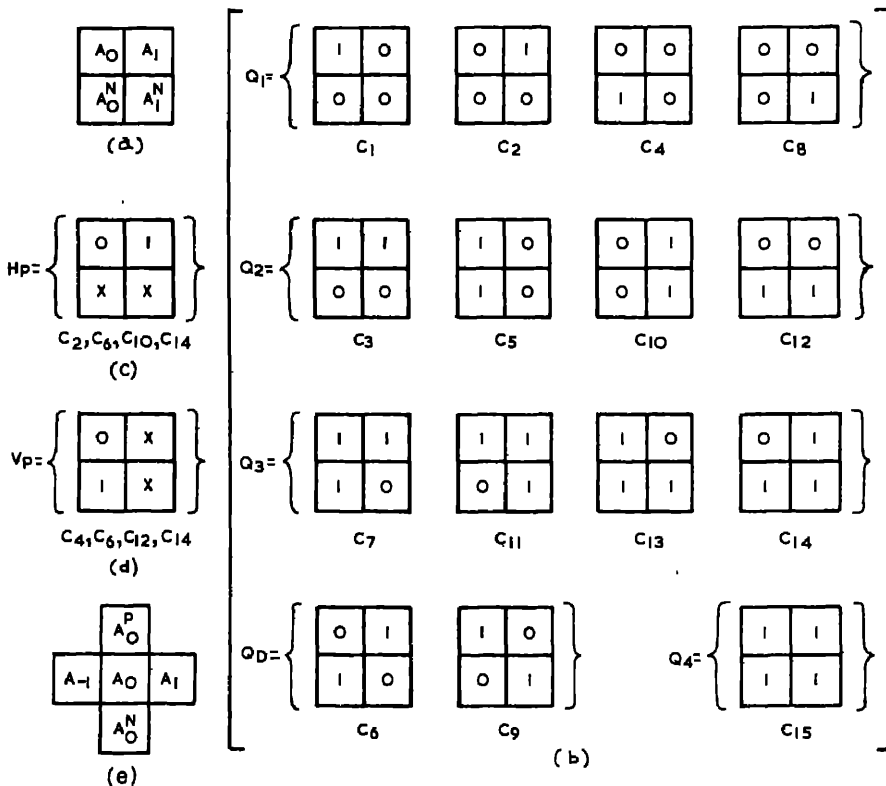


**Figure 3.** Image computation patterns. (a) Typical 2x2 pixel pattern. (b) Area, perimeter and feature count computation patterns. (c) Horizontal intercept pattern. (d) Vertical intercept pattern. (e) Structuring element for erosion and dilation. Note: 0 = logic '0'; 1 = logic '1'; X = don't care.

replaced by 'ANDING' of all the five pixels whereas dilation is accomplished by 'ORing' the same over the entire image frame. Time of execution for one step of erosion/dilation operation is about 0.7 sec.

**2.3c Halo error correction:** In a multiphase sample, when an intermediate phase is detected for computation using threshold level detection errors can occur due to system resolution. This has the effect of producing a 'halo' i.e. an apparent perimeter around a dark feature which is detected. Special algorithm has been developed based on repeated dilation and logical operations for halo error correction.

## 2.4 Operator interaction

Operator interaction with the system is accomplished under the control of a system monitor (Terrell 1978). A query procedure guides the user step by step making the dialogue user friendly. Additionally, the monitor provides for execution of operations like setting of undetected, detected and computed image display. Also there is a provision for print out of results in a standard format as shown in table 1.

## 3. HP1000-based image processing and analysis system

A powerful image processing and analysis system is being developed with 512 pixel resolution incorporating facilities such as shading correction, auto-delineation, image enhancement, light pen interaction and feature-specific measurements.

### 3.1 Schematic details

The system is based on a user microprogrammable HP1000-model 27 computer system. Figure 4 shows the block diagram of this system. Its imaging section consists of an optical microscope/epidiascope coupled to a chalnicon scanner. The video output is stored into a  $512 \times 512 \times 8$  pixel frame grabber. Peripheral operations like light pen interaction, autofocus, stage control, console scanning and image monitor control are carried out by the Apple II computer. The image is transferred to the HP1000 computer system via IEEE-488 bus for processing and analysis.

### 3.2 System software

After shading correction and auto-delineation image processing and analysis functions for various basic and derived parameters are carried out in FORTRAN-77. Results are shown in table 1.

**Table 1.** Micromet. (Radiometallurgy Programme, Kalpakkam)

Sl. No.	UT	LT	Count	Area	Peri	Vert	H
1	16	09	38	8402	2391	818	
2	38	26	86	19410	10017	3313	2
3	51	45	54	11692	3939	1391	

User: ABC; Specimen: Sensitized nuclear grade SS 316 sample.

Date: 19 January 1985; SP No. 1147.

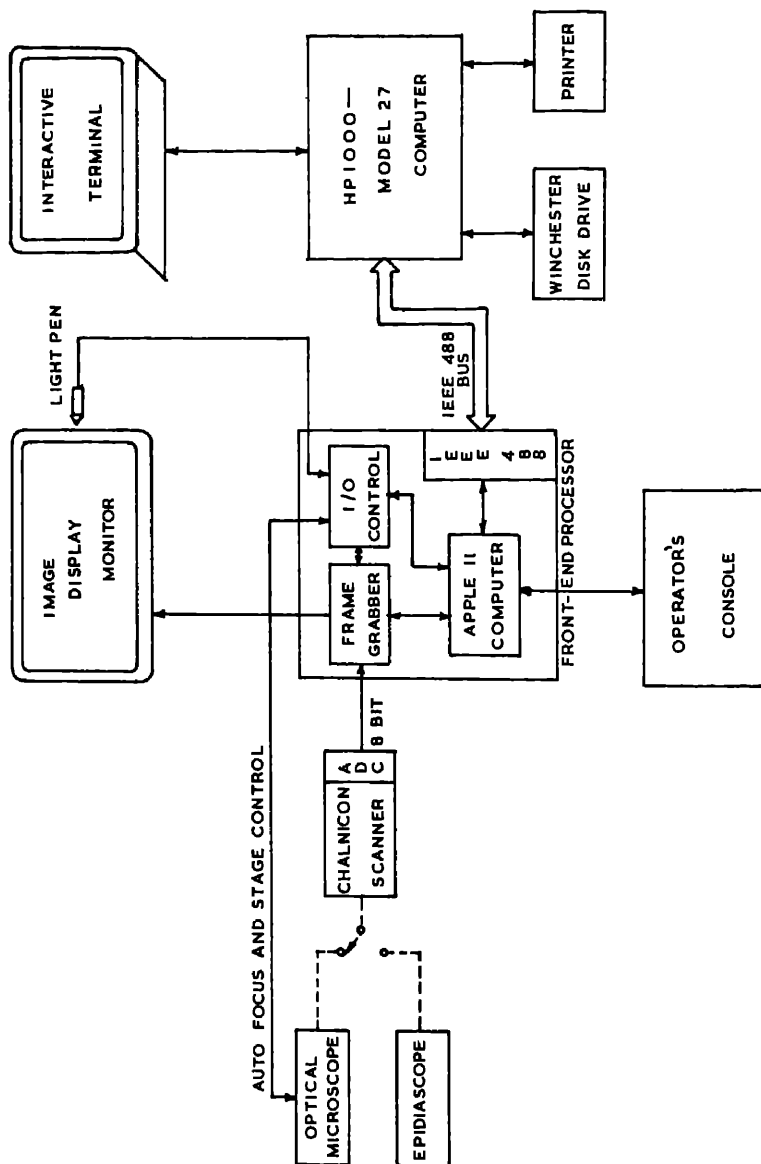


**Figure 4. Block diagram of HP 1000 computer processing and analysis system.**



operations are microprogrammed for fast execution. Two specific schemes adopted for image analysis are continuous scan and features extraction methods.

**3.2a Continuous scan method:** Here parameters of each individual feature are measured separately. The detected binary image is continuously scanned. When a feature is encountered it is indexed and the basic parameters are accounted for the feature. This technique provides accurate size distribution, spatial distribution and various derived parameters.

**3.2b Feature extraction method:** During evaluation of length, breadth and perimeter of a particular feature, the presence of other features interferes with the analysis. This is avoided by using feature extraction method. In this technique, the contour of the feature is traced. The complete feature is copied into another sector of memory and analysed independently.

#### **4. Conclusion**

The Z-80 based image analyser is an inexpensive solution for measuring straight line features in the image frame under view with limited resolution. It is a versatile tool for field-specific basic parameter evaluation. Provision exists for erosion/dilation and error correction. An HP1000 computer based image processing and analysis system is under development. The features being incorporated in this system are image enhancement, 2-D detection, shading correction, light pen interaction and field-specific measurements. Both the systems being software intensive provide flexibility in selecting a particular operation and are open ended for further upgradation.

Though the image analysis is automated, the results obtained are still subject to human factors involved in the preparation of samples/micrographs, selection of desired features and in editing of images. Therefore, expert attention is indispensable for obtaining accurate results.

The systems are being realized taking into consideration the requirements of quantitative metallography. They are equally powerful for analysis of images obtained in the fields of photography, biology, medicine, geology, meteorology and so on.

#### **Acknowledgements**

The authors are grateful to Dr P R Dastidar, Dr P Rodrigues and Sri S N Seshadri for their constant encouragement and providing facilities to develop the image analysis system.

#### **References**

- Jenkinson G W 1982 Technical Exchange and Symposium on Image Analysis, University of Iron and Steel, Beijing
- Pratt W K 1978 *Digital image processing* (New York: John Wiley & Sons)
- Terrell A C 1978 *Microscope* 26 49



## Modern computer assisted methods in metallurgy

G W JENKINSON and T KELLY

Cambridge Instruments Limited, Rustat Road, Cambridge, England

**Abstract.** Image analysis systems have been used in metallurgy for over two decades and play a vital role in quality assessment for the steel industry. One major application is the characterization of steel by counting and measuring the non-metallic inclusion content for steel assessment, relying on the comparison with idealized 'charts' of varying inclusion content, for example as defined by ASTM and SEP, is the most common manual method employed.

However, this has proved to be most difficult to automate due to the degree of subjectivity associated with the manual methods. This has previously restricted the acceptance of image analysis systems for routine quality control. The increased software power of the more recent instruments has enabled the installation of systems which satisfactorily mimic the observer in a reproducible manner. These work with an economically attractive throughput and produce results in the accepted standard format.

A limitation of these systems is that they grade a field on the basis of the majority inclusion type present. This can lead to significant but lesser inclusions being ignored altogether, presenting a false picture of the sample. This paper describes a new method which identifies individual inclusions in a field. The grade number of a field can then be determined for each inclusion type. This is known as the mixed field method. This paper describes the method and its implementation on the Cambridge Instruments' QUANTIMET 92 image analysis system.

**Keywords.** System operation; inclusion type; inclusion grade; mixed fields; worst

### 1. Introduction

The mechanical properties of steel are greatly influenced by the type and dispersion of non-metallic inclusions, and the inclusions themselves are often characteristic of the steel making practice.

The evaluation and description of the inclusion content of steel is carried out on a routine basis in every quality monitoring laboratory in the steel industry, and for economic and historical reasons, visual chart comparison procedures such as the E45 method (American Society for Testing and Materials, 1963) and the SEP method (Stahl-Eisen-Prüfblatt 1971), are frequently used. Despite their shortcomings (Johansson 1974) these chart-based methods do provide a common ground for intercompany and manufacturer-user dialogue but the precision of the results obtained by the visual methods is often far from satisfactory. Repeat evaluations by different operators, and evaluations obtained by different operators examining the same sample, show wide variations, and to such a degree that it can be difficult to draw conclusions concerning assessment carried out at different times and places by different operators (Johansson 1974). This is precisely the effect that the visual method is supposed to avoid. Automatic image analyzers such as the Cambridge Quantimet systems set out to minimize this effect by providing a standardized operation procedure for the evaluation of the inclusion fields, so that results are independent of where the evaluation is performed or who operates the system.

It has been shown (Pohl 1979a, b) that the same measurements can be obtained by automatic image analysis as by visual comparison for the assessment of non-metallic inclusions. The first analyzer to do this for ASTM E45 and SEP 1570-71 was the Quantimet 720 Steelscan (Polzin 1977, 1978). Since then, however, more rigorous application of the standards has called for the ability to determine the content of each type of oxide in a field rather than to classify a field on the basis of the most likely single inclusion type. This is a significantly more difficult function and this paper describes the methods used and illustrates the implementation on the Quantimet 920 image analyser.

## **2. General description of system operation**

A conventionally prepared specimen either mounted in plastic or as a free block, in accordance with local practice, is scanned automatically by a motorized XY stage under a microscope equipped with a high-speed autofocus system. There are few limitations on specimen size; samples up to 10 cm × 10 cm can be accommodated though a total inspection area of 250 or 500 mm<sup>2</sup> is typical. Specimens are examined under the conditions prescribed in the chart method (× 100) so the images are familiar to the operator and this allows direct confirmation of the system interpretation of field ratings.

The optical image is presented to a high resolution (720 line) plumbicon scanner, necessary to allow correct separation of the sulphide and oxide inclusions at the relatively low magnifications involved. The parameters required for the evaluation of inclusion type and rating are measured and the decoding of this quantitative data into the familiar chart terms is carried out by the systems' microprocessor. On completion of an analysis, the traditional evaluation table is printed (table 1 shows an ASTM example) and if required the 'worst fields' of any inclusion type can be recalled, displayed and rejected if necessary.

## **3. Determination of inclusion type**

The primary classification into oxide and sulphide inclusion types is performed by an automatic detector which is sensitive to the grey tone differences of these two major inclusion types. It duplicates therefore the discrimination process of a human operator but includes fine detail enhancement to ensure that all visually recognised inclusions are identified to the system. The detection system also compensates for variations in background illumination generated in all optical microscopes and whose presence could severely limit the useful field of measurement. The separation of the oxide and sulphide inclusion types is therefore a straightforward process and is illustrated in figure 1.

The next requirement, the classification of the oxide inclusion into the three visual types (recognized as B, C, D in the ASTM procedure and OA, OS, OG in the SEP method) is more complex. The essential differences between the three oxide types are of morphology and patternness as can be seen from the schematic representation of the chart fields in figure 2. The silicate type is characterized by having an elongated morphology relative to the alumina and globular types which are morphologically very similar. There is a very different patternness for the alumina and globular types which

Table 1. Typical ASTM E45 chart print-out

Grade	Sulphides		Aluminates		Silicates		Globular	
	Thin	Thick	Thin	Thick	Thin	Thick	Thin	Thick
Based on observed specimen area of 199.091 mm <sup>2</sup>								
0.5	121	59	6	0	115	40	108	118
1.0	91	102	0	1	34	12	0	168
1.5	7	22	1	0	2	38	0	18
2.0	0	142	0	2	0	137	0	0
2.5	0	8	0	3	0	3	0	0
3.0	0	2	0	0	0	1	0	0
3.5	0	0	0	0	0	0	0	0
4.0	0	0	0	0	0	0	0	0
4.5	0	0	0	0	0	2	0	0
5.0	0	0	0	0	0	0	0	0
Based on standard specimen area of 250 mm <sup>2</sup>								
0.5	152	74	8	0	144	50	136	148
1.0	114	128	0	1	43	15	0	211
1.5	9	28	1	0	3	48	0	23
2.0	0	178	0	3	0	172	0	0
2.5	0	10	0	4	0	4	0	0
3.0	0	3	0	0	0	1	0	0
3.5	0	0	0	0	0	0	0	0
4.0	0	0	0	0	0	0	0	0
4.5	0	0	0	0	0	3	0	0
5.0	0	0	0	0	0	0	0	0

Number of fields rejected: 0

can be characterized by the degree of clustering along and about the direction elongation as described by the charts.

Figure 3 describes the decision logic which classifies a given field in terms of measurements made by the Quantimet. This logic requires the individual classification of each inclusion in the field and this is achieved by measurement of the aspect ratio and Y position and vertical length of each inclusion. The photographs of figure 4, which show identified inclusions, can be compared with figure 2. The annotation on photographs is performed by the system while operating in 'review mode' which allows the operator to check the decisions being made by the system. The codes used to annotate the inclusions are as follows:-

SUL - Thick } sul - Thin }	Sulphide	(A or SS)
ALU - Thick } alu - Thin }	Alumina oxide	(B or OA)
SIL - Thick } sil - Thin }	Silicate oxide	(C or OS)
GLO - Thick } glo - Thin }	Globular oxide	(D or OG)

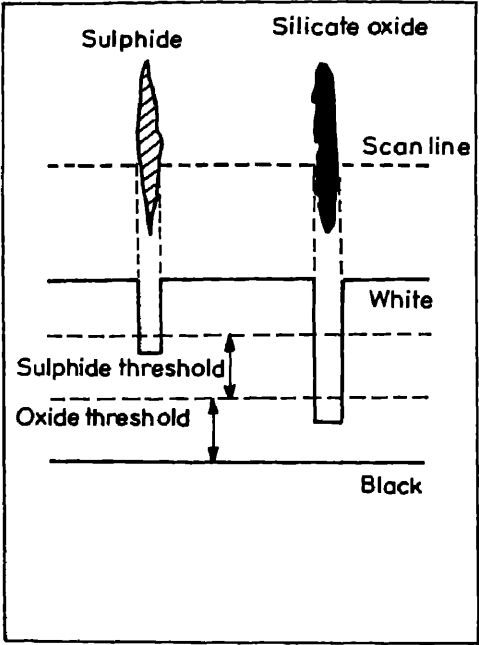


Figure 1. Separation of oxides from sulphides by grey-level

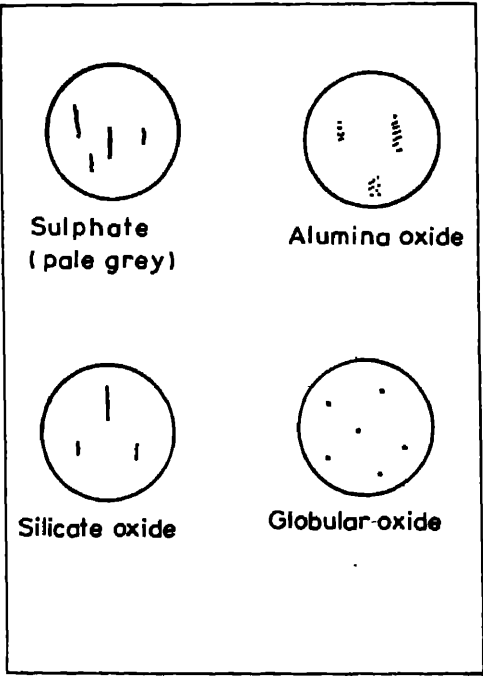
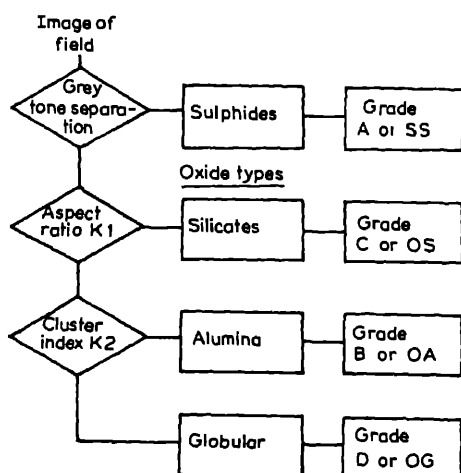


Figure 2. Schematic representation of chart fields



**Figure 3.** Classification algorithm for automatic rating: K1 is a constant which is specified to separate silicates from other oxides on the basis of aspect ratio; K2 is a constant which is specified to determine the cluster spacing which separates alumina and globular oxides.

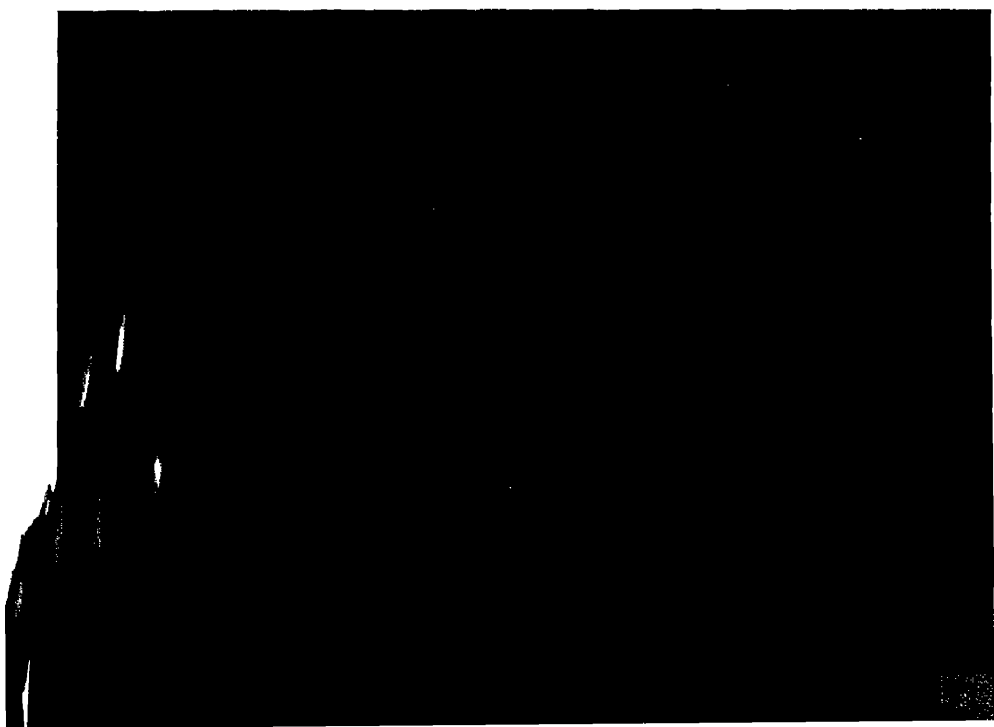
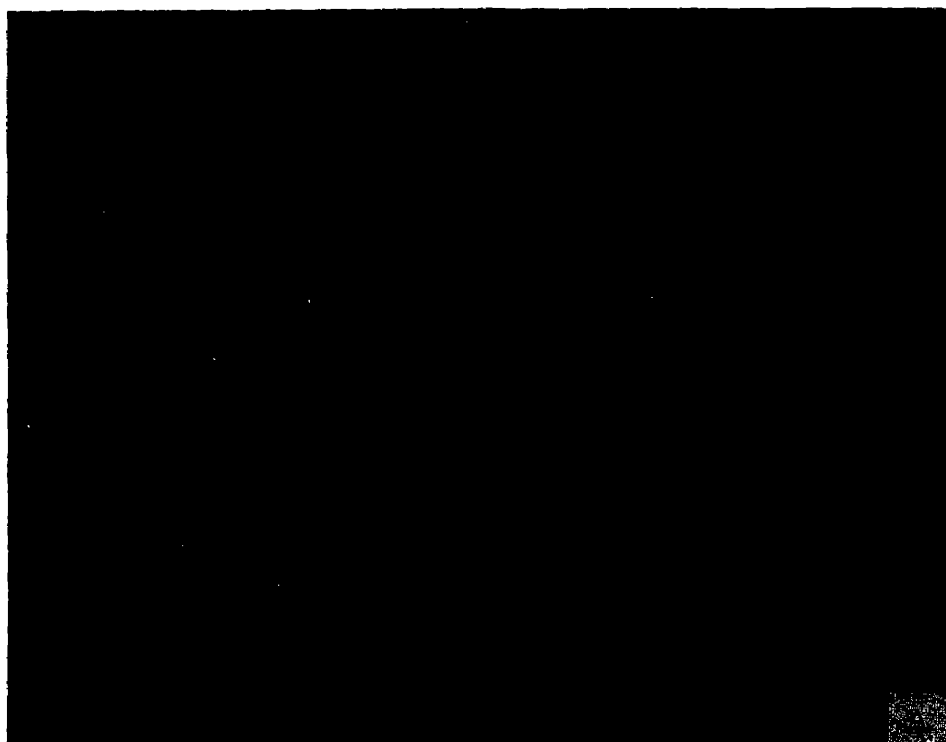
#### 4. Determination of inclusion grade

Having identified the inclusion type as described, it is then a straightforward matter to assign a grade number (0–8) to the type. Each column of the ASTM or SEP chart shows an increase in total inclusion length as we progress through the range 0–8 and since this is a parameter measured by the Quantimet it can be used to assign a grade number to the observed field. If required the grading can be further refined into the 'thick' or 'thin' categories allowed for in the charts. The values characteristic of each ASTM or SEP grade are defined in the respective standard so these are used in the analysis programme. As can be seen from table 1, two tables are printed. The first table shows the actual number of 0.5 mm<sup>2</sup> fields which have been measured. The lower table has been normalized to the standard specimen area of 250 mm<sup>2</sup>. It is often preferable to scan a reduced area but this is of sufficient accuracy while improving throughput.

#### 5. Mixed fields

Assigning a grade number to an observed field by comparing it with the chart representation is subjective and influenced by several factors. The occurrence of a 'severe' sulphide field will influence the operator's decision concerning the oxides in the field. Automatic image analysis gives unbiased results. The presence of 'mixed' oxide fields (alumina with globular or silicate with globular) also causes confusion.

In previous systems mixed oxide fields were not partitioned into different types and a majority field type was assigned. In the logic implemented by the Quantimet 920, each individual inclusion is identified, and its contribution to the grade number determined even for mixed oxide fields. Clearly this is a much more demanding protocol to implement and reproduction of human classification cannot be perfect. However, the provision of a review facility allows the operator to verify that the system is performing satisfactorily before making fully automatic analysis.





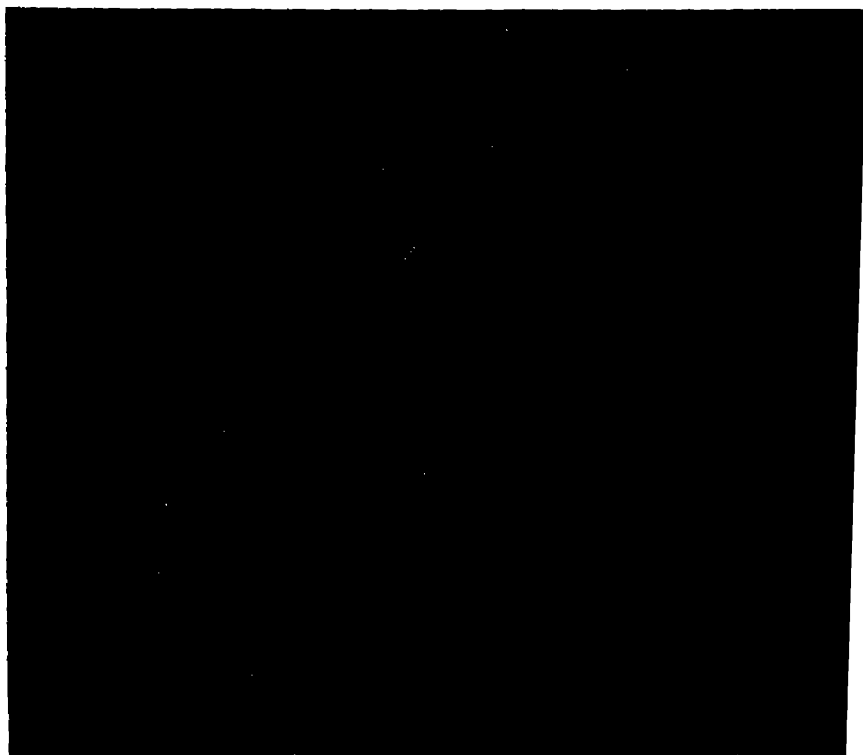


**Figure 4.** (A) Identified sulphide inclusions. (B) Identified alumina inclusions. (C) silicate and globular inclusions.

## **6. Worst fields**

Preparation methods used for automatic analysis need to be of a consistent quality. However, dust or dirt cannot be entirely avoided. The worst field review enables the operator to check on the fields which have unusually high ratings, be excluded from the analysis if found to be due to dirt or debris.

The worst field for each inclusion type can also be recalled. The system recalls the X-Y location of the worst fields. The operator selects from the list (figure 5) which type of field to examine. The system moves this field of the inclusion into the analysis field of view by moving the automatic motorised microscope. The operator can decide to accept or reject this field. The next worst field is then presented and so on until sufficient fields have been reviewed.

## **7. Conclusions**

This paper has described how the image analysis techniques for chart grade classification have been extended to work with mixed fields of oxides.

**\*\*\* WORST FIELD REVIEW \*\*\***

- 0- TERMINATE
- 1- THIN SULFIDE
- 2- THICK SULFIDE
- 3- THIN SILICATE
- 4- THICK SILICATE
- 5- THIN GLOBULAR
- 6- THICK GLOBULAR
- 7- THIN ALUMINA
- 8- THICK ALUMINA

**SELECT FIELD TYPE TO REVIEW**

**Figure 5.** World field review selection.

if necessary of the worst fields found after this analysis run is complete. A verify facility permits system operation to be checked for each field.

## **References**

- ASTM 1963 American Society for Testing and Materials. "Recommended practice for determining the inclusion content of steel," ASTM E45-63
- Johansson S 1974 Tech. Rept. Sandviken. "The rating of nonmetallic inclusions by image analysis."
- Pohl W and Fischer A 1979a Microscopia Acta, Supplement 3, S. 77-82. "Experience in Steel Cleanliness Assessment by the Automatic Image Analyser QUANTIMET 720/10M"
- Pohl W and Fischer A 1979b Sonderbande der Praktischen Metallographie, Band 10, S631-640. "Erfahrungen bei der Reinheitsgradbestimmung mit dem Automatischen Bildanalysator QUANTIMET 720/10M."
- Polzin T 1977 Microscopia Acta, Supplement 1, S 19-31
- Polzin T 1978 Praktische Metallographic, Band 15, S 277-286. "QUANTIMET 360/2 and QUANTIMET 720/10M—two new systems for microscopic evaluation of non-metallic inclusion content in steel."
- Stahl-Eisen-Prüfblatt 1971 Verlag Stahleisen, Dusseldorf. "Microscopic examination for non-metallic inclusions with reference inclusion charts."

## Computer simulation of dislocation-carbon interaction in nickel

B PURNIAH and S SRINIVASAN

Indira Gandhi Centre for Atomic Research, Kalpakkam 603 102, India

**Abstract.** An atomistic computer model based on a rigid boundary method has been developed to estimate the interaction energy between a single edge dislocation and an impurity carbon interstitial in nickel. The simulation was carried out using the static relaxation technique on a total of 600 atoms, using an appropriate host-host pair potential. The impurity host potential has been chosen to be a cubic function in this calculation. In the absence of the dislocation the dipole tensor for the octahedral site is seen to be spherical. Two impurity positions, one above and one below the slip plane were investigated. The carbon-dislocation interaction energies obtained were 1.4 eV and 0.7 eV respectively for the two impurity positions. The dipole tensor for the impurity in the presence of the dislocation was found to be non-diagonal.

**Keywords.** Computer simulation; impurity defects; dislocation; lattice statics; interaction

### 1. Introduction

Many important physical and technological phenomena occur as a direct consequence of the interaction between impurity point defects and dislocations. A well-known example is that of strain aging which involves the migration of interstitial impurities to dislocations. This interaction can be studied very effectively by internal friction experiments (Nowick and Berry 1972). The quantitative interpretation of internal friction experiments needs the estimation of the dipole tensor which is a measure of the elastic distortion caused by the defect in question. In this paper we describe such a calculation for a straight edge dislocation and a carbon impurity interstitial in nickel. The simulation is carried out in two steps. Section 2 describes the choice of the interatomic potential. Section 3 describes the simulation of an edge dislocation and section 4 describes the simulation of the dislocation-point defect interaction.

The simulation of an edge dislocation described here is based on a rigid boundary method (Bullough and Tewary 1979). To obtain the atomic configurations associated with the straight edge dislocation, a rectangular parallelepiped of freely interacting atoms was set up. The defect configuration is introduced at the centre of this crystal which has two regions. In the inner region (region I), the atoms are allowed to freely relax to the equilibrium positions via a given nonlinear potential. In the outer region (region II), the atoms are constrained to remain in positions given by the linear elastic theory. Region I was chosen to be sufficiently large compared to region II such that the influence of the surface or boundary effects are minimized. Some improved methods involving flexible boundaries (Hoagland *et al* 1976) have been developed and used for dislocation simulation. However, these flexible boundary methods cannot be used for a combined point defect-dislocation model.

There are two main techniques followed in literature to relax the atoms in Region I. These are the static and the dynamic relaxation techniques. The static method which

basically a gradient method is used here to minimize the total energy of this region (Sahu *et al* 1980). To determine the interaction energy, we need to evaluate the difference in the energy of formation of the point defect in a perfect and a lattice with a dislocation. This is accomplished by a separate evaluation of the energy of the dislocation and the point defect-dislocation combination.

## 2. Interatomic potentials

The interatomic potential is of crucial importance in atomistic models. They can be classified into two broad categories, namely the empirical potentials and the pseudopotentials. The pseudopotential method, which has been successful in predicting various physical properties of the perfect lattice has been shown to be inadequate for defects such as vacancies, dislocations, surfaces etc., which produce large inhomogeneities in the electron distribution. Empirical potentials are, however, more suited for defect studies (Johnson 1973). The simulation of dislocations in fcc metals require pair potentials which incorporate stacking-fault energies. We have used such a potential developed by Baskes and Melius (1979) for the host lattice where the cut-off distance for the potential is taken to be between the third and fourth neighbour. The functional form of the potential is a cubic spline between a number of fixed nodal points. The impurity-host potential was chosen to be a cubic function (Johnson *et al* 1964). The general shape was similar to the host-host potential i.e. a strong repulsion at close distances, a minimum at some intermediate distance and going to zero with zero slope at a cut-off distance. The potential parameters were determined with the help of experimental quantities like the carbon atom migration energy, activation volume and carbon-vacancy binding energy.

## 3. Simulation of edge dislocation

The edge dislocation studied in this case lies along  $[11\bar{2}]$  direction. Its Burger's vector was of the type  $a/2\langle 110 \rangle$  (see figure 1). The faces of the crystallite were appropriate  $\{110\}$ ,  $\{112\}$ , and  $\{111\}$  crystallographic planes and the dislocation was arranged to lie through the centre of the assembly and orthogonal to the two  $\{112\}$  faces. In the direction of the dislocation line, specifically the  $[11\bar{2}]$  direction ( $y$ -axis), the assembly was only six lattice planes thick and periodic boundary conditions were imposed across the two end  $(11\bar{2})$  faces (Cotterill and Doyama 1967). In the other two orthogonal directions ( $[1\bar{1}0]$ - the  $x$  direction and  $[111]$ - the  $z$  direction) the assembly was made up of 49  $\{110\}$  lattice planes and 19  $\{111\}$  planes. The parallelepiped was deliberately extended in the  $x$ -direction to accommodate the dissociation into Shockley partials of the glissile edge dislocation. The initial defect configuration was achieved by first imposing the appropriate anisotropic elastic displacements on all the atoms in the crystallite. This configuration is designated as the elasto-atomic model.

Next, the atoms in region I, numbering approximately 600, were allowed to relax towards equilibrium under the influence of the host pair potential already described. During the simulation of the undissociated dislocation (also called complete dislocation) the atoms were *not* permitted to relax in a direction parallel to the dislocation line. The strain energy of a dislocation inside a certain radius is given by

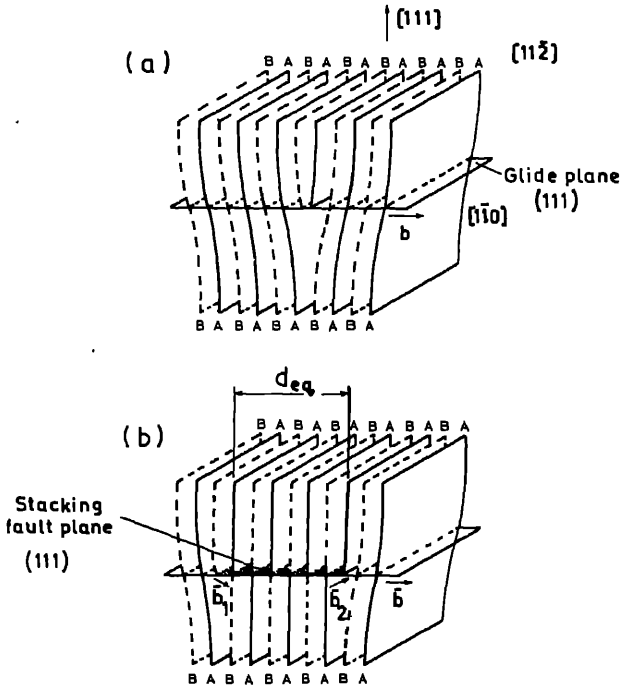


Figure 1. Spatial representation of an edge dislocation with a Burger's vector  $a/2 [1\bar{1}1]$  the fcc structure. (a) Complete edge dislocation. (b) Dissociated edge dislocation. ( $\bar{b}$ ,  $\bar{b}_1$  and  $\bar{b}_2$  indicate the Burger's vector of the complete and the two partial dislocations).

$E_d = 1/2 \sum_i^n (E_i - E_0)$ , where  $n$  is the number of atoms inside that radius,  $E_i$  is energy of the  $i$ th atom *after* relaxation and  $E_0$  in the perfect lattice. The factor  $1/2$  required because each interatomic bond is counted twice in the calculation. Figure 2 shows the energies of the elasto-atomic model and the complete edge dislocation plotted as a function of distance.

It is known in fcc metals that the edge dislocation dissociates into a pair of partial dislocations separated by an intrinsic stacking-fault on the (111) plane (Heidenreich and Shockley 1948). To study this dissociation, the atoms in-region I were also allowed to relax parallel to the dislocation line. The parallelepiped was extended to 49 planes in the  $x$ -direction (as already stated) to accommodate the splitting of the dislocation partials leading to a stacking-fault along this direction. The final positions attained by the atoms in complete dislocation were used as the initial positions for the case of dissociated dislocation. It was found that the complete dislocation splits into partials separated by a distance of  $8b$ . The energy of the dissociated dislocation is also plotted in figure 2. It can be seen that the energy of the dissociated dislocation is indeed less than that of the complete dislocation.

#### 4. Dislocation-carbon interaction

To obtain the interaction energy between the dislocation and carbon impurity, it is necessary to extend the parallelepiped in the  $y$ -direction and drop the peri-

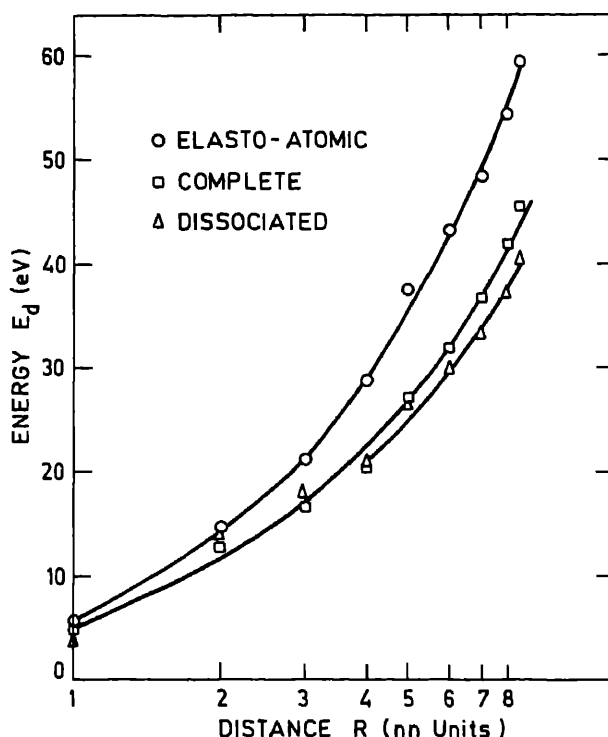


Figure 2. The energy as a function of the radius from the centre of a edge dislocation shown for the three cases, elasto-atomic, complete and dissociated dislocation.

boundary conditions on these faces. The crystallite was made 30 planes thick as against the six originally taken. Of this assembly, the central region containing 627 atoms was allowed to relax. The boundary atoms were held in their previous relaxed dissociated dislocation positions and the position of the point defect (in this case the carbon impurity in octahedral site) relative to the dislocation was varied. Two impurity positions were chosen. One position at (3, -3, 1.5) was above the slip plane and the other at (3, -3, -1.5) was below the slip plane. The co-ordinates are with reference to the dislocation centre located at (0, 0, 0). The carbon interstitial formation energy in the perfect lattice was obtained using a point defect simulation program (Sahu *et al* 1980).

## 5. Results and discussion

The results of the simulation are summarized in table 1. The edge dislocation lying along [112] direction was found to dissociate into partials when the atoms in region I were allowed to relax freely in all three directions. The equilibrium distance of separation between the partials was found to be 8b. For the two impurity configurations, one above and one below the slip plane, the formation energy, interaction energy and dipole tensor were obtained. A few points can be seen from the table. The (undersized) carbon atom prefers to sit above the slip plane as is known from the

## Dislocation-carbon interaction in nickel

**Table 1.** Values of carbon impurity formation energy, interaction energy, dipole tensor stacking-fault distance obtained from computer simulation of an edge dislocation in N

Property	Value
1. (a) Carbon impurity formation energy in perfect lattice	1.624 eV
(b) Dipole tensor of carbon interstitial (eV)	$\begin{pmatrix} 2.56 & 0.0 & 0.0 \\ 0.0 & 2.56 & 0.0 \\ 0.0 & 0.0 & 2.56 \end{pmatrix}$
2. Edge dislocation	
(a) <i>Interstitial above the slip plane</i>	
Formation energy (3, -3, 1.5)	
(with dislocation)	0.25 eV
Carbon-dislocation interaction energy	1.374 eV
(b) <i>Interstitial below the slip plane</i>	
Formation energy (3, -3, -1.5)	0.91 eV
(with dislocation)	
Carbon-dislocation interaction energy	0.714 eV
3. Stacking-fault distance	8.0 b
4. Dipole tensor, $P_{ij}$ (eV)	
(a) Interstitial above the slip plane	$\begin{pmatrix} 6.78 & -0.81 & -0.44 \\ -0.81 & 2.32 & -0.01 \\ -0.44 & -0.01 & 4.25 \end{pmatrix}$
(b) Interstitial below the slip plane	$\begin{pmatrix} 4.09 & -3.05 & -1.59 \\ -3.05 & 9.16 & -2.98 \\ -1.59 & -2.98 & 3.00 \end{pmatrix}$

Cottrell formula using linear elasticity theory. Further, the dipole tensor which spherical in the absence of the dislocation has a monoclinic symmetry in the vicinity the dislocation. This is true both above and below the dislocation.

## References

- Abrahamson A 1969 *Phys. Rev.* **178** 76  
 Baskes M I and Melius C F 1979 *Phys. Rev.* **20** 3197  
 Bullough R and Tewary V K 1979 in *Dislocations in solids* (ed.) F R N Nabarro (New York: North-Holla. Vol. 2, p. 1  
 Cotterill R M J and Doyama M 1967 in *Lattice defects and their interactions* (ed.) R R Hasiguti (New Yo Gordon and Breach), p. 20  
 Heidenreich R O and Shockley W 1948 Report on Conference in Strength of Solids, p. 57  
 Hoagland R G, Hirth J P and Gehlen P C 1976 *Philos. Mag.* **34** 413  
 Johnson R A 1973 *J. Phys.* **F3** 295  
 Johnson R A, Dienes G J and Damask A C 1964 *Acta Metall.* **12** 1215  
 Nowick A S and Berry B S 1972 *Anelastic relaxation in crystalline solids* (New York: Academic Press  
 Sahu H K, Srinivasan S and Krishan K 1980 *Pramana (J. Phys.)* **15** 189





## **Water reactor fuel performance code PROFESS and its application predicting the behaviour of the fuel elements of D-Com blind problem**

**D N SAH, D VENKATESH and E RAMADASAN**

Radiometallurgy Division, Bhabha Atomic Research Centre, Trombay, Bombay 400 001, India

**Abstract.** This paper gives a brief description of the sub-models of important phenomena treated in computer code PROFESS and presents some results of PROFESS calculations for fuel elements of D-Com blind problem.

**Keywords.** Computer modelling; computer code; nuclear fuel element; water reactor; verification; fuel performance; irradiation effects; irradiation behaviour.

### **1. Introduction**

The first version of computer code PROFESS (performance analysis of rod-type oxide elements under steady state) was completed in the beginning of 1983. To check the predictive capability of the code and its sub-models, it was necessary to simulate a documented irradiation experiment and to compare the predictions with experimental results. At that time, a code exercise was being organized as part of an co-ordinated research programme on development of computer models (D-Com) to investigate the predictive capability of the existing codes. A detailed data package for an irradiation experiment was made available to the participants of the exercise and it was known as D-Com blind problem. The predictions of the different codes participating in this exercise were to be compared with the actual experimental findings, which had been held secret till calculations of all codes had been submitted. This provided a good opportunity to check the predictive capability of PROFESS by participating in the exercise. This paper briefly describes the models of some important phenomena treated in the code and gives some of the results obtained on the fuel elements of D-Com blind problem.

### **2. Computer code PROFESS**

Computer code PROFESS is applicable to rod-type fuel elements used in water-cooled nuclear reactors. A typical water reactor fuel rod consists of a number of sintered or  $\text{UO}_2$ - $\text{PuO}_2$  fuel pellets stacked inside a zircaloy cladding tube which is sealed at both ends.

The general features of PROFESS have been described elsewhere (Sah *et al* 1983 and Venkatesh 1984). The flow chart of calculation followed in PROFESS is given in figures 1 and 2. The models incorporated in this code are listed in table 1. The ge-

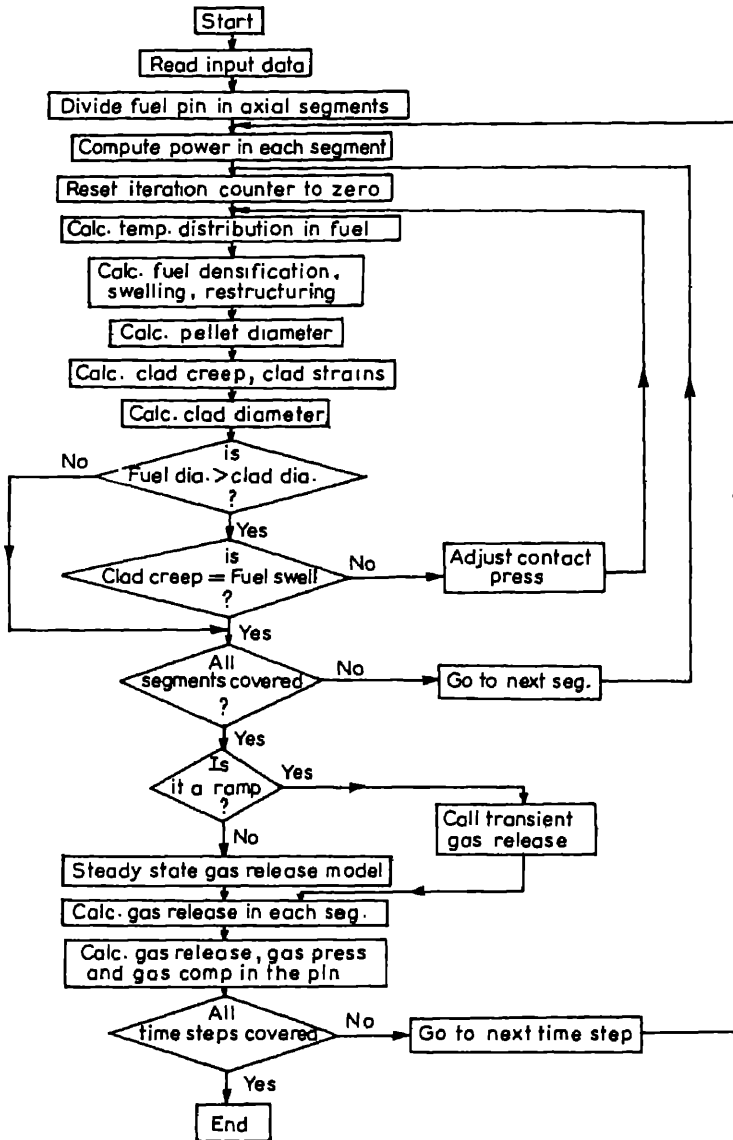


Figure 1. Flow chart of the calculations followed in PROFESS.

method of thermal and mechanical analysis of fuel element is described elsewhere (Roy and Sah 1985). Models of important phenomena treated in PROFESS are briefly described below.

### 2.1 Gap conductance model

The heat flow through the fuel clad gap/interface is considered to take place by thermal conduction and radiation. The gap conductance is evaluated by the Ross-Stout model

## *Water reactor fuel performance code*

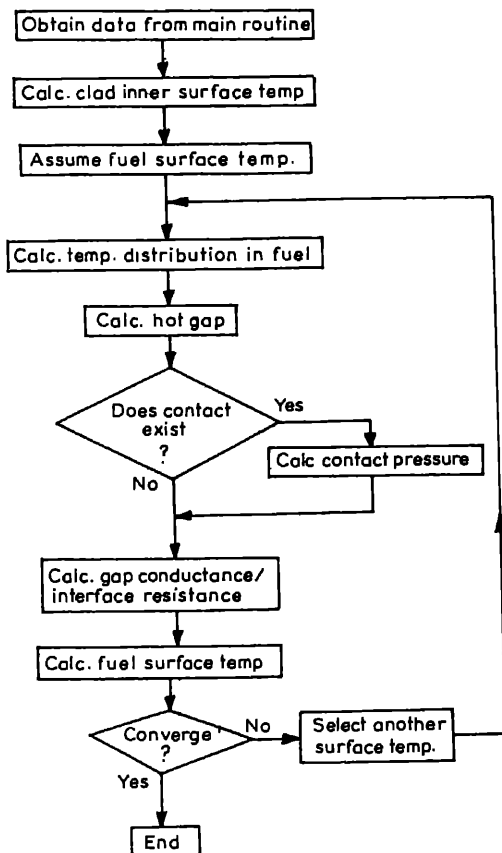


**Figure 2.** Flow chart of the calculation of radial temperature distribution in the cross-section.

**Table 1.** Models in computer code PROFESS

<i>Analytical models</i>	<i>Material properties models</i>	<i>Phenomenological models</i>
Cladding surface temperature	Thermal expansion of $\text{UO}_2$	Fuel clad gap conductance
Temperature drop across cladding	Thermal expansion of zircaloy	Solid and gaseous fission product swelling
Temperature drop across fuel clad-gap	Thermal conductivity of $\text{UO}_2$	In pile fuel densification
Radial temperature distribution in fuel	Thermal conductivity of zircaloy	Fission gas release (steady state)
Elastic deformation of cladding	Thermal conductivity of gases, He, Xe	Fission gas release (transient)
Void volume	Thermal conductivity of gas mixture	Equiaxed grain growth
Internal gas pressure	Jump distance of gases	Columnar grain growth
Fission gas generation	Yield strength of zircaloy	Fuel relocation
Gap gas dilution	Poisson's ratio of zircaloy	Zircaloy in-pile creep
Plenum temperature	Meyer's hardness of zircaloy	
Neutron flux depression	Elastic modulus of zircaloy	

(Ross and Stout 1962) modified to account for the effect of fission gas, gas pressure and pellet eccentricity.

When the fuel-clad gap is open, the heat transfer coefficient in the gap is given by

$$h_{\text{gap}} = h_{\text{cond}} + h_{\text{rad}},$$

where 
$$h_{\text{cond}} = K_{\text{gas}} / (X_{\text{gap}} + \delta + g_f + g_c),$$

$$h_{\text{rad}} = (4\sigma T^3) / \{ [(1/E_f) + (1/E_c)] \} - 1,$$

$K_{\text{gas}}$  = thermal conductivity of the gas,  $\delta$  = sum of the surface roughness of fuel and cladding,  $g_f, g_c$  = jump distances of the gas in the fuel and in the cladding,  $X_{\text{gap}}$  = fuel-clad gap,  $\sigma$  = Stefan-Boltzmann constant,  $E_f, E_c$  = emissivity of the fuel and the cladding and  $T$  = temperature in the fuel clad gap. When the fuel-clad gap is closed i.e. the fuel and cladding are in contact with each other, the heat transfer co-efficient through the interface ( $h_{\text{cont}}$ ) is given by

$$h_{\text{cont}} = \frac{K_{\text{gas}}}{\delta + g_c + g_f} + C \frac{2K_f K_c}{(K_f + K_c)} \cdot \frac{P_c}{\delta^{1/2} H},$$

where  $K_f, K_c$  are thermal conductivities of fuel and cladding,  $P_c$  is the contact pressure between fuel and cladding,  $H$  is the Meyer's hardness of cladding and  $C$  is a constant.

In the gap conductance model used in PROFESS it is assumed that when the pellet is placed eccentrically, its effect can be evaluated by assuming that even in the open gap condition a certain fraction of fuel surface is in pressureless contact with the cladding. This contact area fraction depends upon the existing gap and is defined as follows:

$$CA = 1 - \left( \frac{\text{hot gap}}{\text{cold gap} - A_0} \right)^{1.5\epsilon^2},$$

where  $\epsilon$  denotes the extent of eccentricity and has a value between 0 and 1, for a fully concentric pellet,  $\epsilon$  is zero resulting in a contact area fraction of zero and  $A_0$  is a constant. The method of solution in the gap conductance model used in PROFESS is similar to the method used in COMETHE code (Hoppe *et al* 1982).

## 2.2 In-pile fuel densification

The irradiation-induced densification of uranium dioxide fuel is considered to be a function of the initial fuel density, the amount of unstable porosity in the fuel and the fuel burn-up. The model in PROFESS considers that the initial unstable pores disappear exponentially with the progress of fuel irradiation. The volume change in the fuel due to in-pile densification is given by the following correlation (Pedersen 1978),

$$(\Delta V/V)_{\text{dens}} = (P_0 - P_s) \left[ \exp \left( \frac{-\text{BU}}{500} \right) - 1 \right],$$

where  $(\Delta V/V)_{\text{dens}}$  is the volumetric change in the fuel,  $P_0$  is the initial porosity fraction,  $P_s$  is the fraction of stable porosity in the fuel and BU is fuel burn-up. The densification is considered isotropic.

### 2.3 Solid and gaseous fission product swelling

The fission product swelling model incorporated in PROFESS considers free swelling fuel when the fuel clad gap is open and a restrained swelling occurs when the fuel and cladding are in pressure contact with each other. The swelling correlations have been derived from the experimental data reported in literature (Zimmermann 1979; Hilb *et al* 1971). Below 900°C free swelling is a linear function of fuel burn-up and above this temperature the swelling is considered as a function of fuel burn-up and fuel temperature both. The restrained swelling is linearly related to fuel burn-up and is taken as 1% ( $\Delta V/V$ ) per at. % burn-up.

### 2.4 Fission gas release

There are five optional fission gas release models (Sah *et al* 1984) in PROFESS for calculating the steady state fission gas release from fuel. The transient fission gas release is estimated by a model given below (Pati and Ritterbusch 1980).

$$F = 1 - \exp(-mt^n),$$

where  $F$  = fraction of pre-transient gas released during the transient,  $t$  = time transient (seconds),  $m$  = temperature dependent variable (given by  $2.22 \times 10^{-7} (T - 1000)^2$ ),  $T$  = fuel temperature °C and  $n = 0.25$ . In the above model the gas release occurs only if the fuel temperature exceeds 1000°C. The generation of fission gas during transient is ignored and the release occurs from the retained gas available in the fuel. For fuel burn-up higher than 20,000 MWD/MTU a correction factor is used to account for burn-up enhancement of the steady state release.

### 2.5 Fuel restructuring

Two important microstructural changes in fuel e.g. equiaxed grain growth and columnar grain growth have been modelled in PROFESS. The correlations used are given below.

Equiaxed grain growth is represented by the following correlation

$$D^2 = D_0^2 + 2.92 \times 10^{-8} \left[ \exp - \frac{2.67 \times 10^5}{8.314 T} \right] \cdot t,$$

where  $D_0$  is the initial grain size and  $D$  the final grain size. The grains are allowed to grow to a limiting size which is given by

$$D_{\max} = 2.23 \times 10^{-3} \exp(-7620/T).$$

The columnar grain growth is represented by a time temperature relationship given by  $t = t_0 \exp(A/T + 273)$ , where  $t$  is the time required to form columnar grains at temperature  $T$  (°C),  $A$  and  $t_0$  are constants.

### 2.6 Cladding creep

The creep rate of zircaloy cladding is considered a function of cladding stress, fission neutron flux ( $> 1$  MeV) and the cladding temperature. The correlation used in PROFESS is given below (Wood and Watkins 1971).

$$\dot{\epsilon} = A \exp\left(-\frac{14000}{RT}\right) \phi^{0.85} \sin(\sin h(0.165\sigma))$$

where  $A$  is a constant,  $\phi$  is the fast neutron flux,  $\sigma$  is cladding stress  $\text{kg/mm}^2$ ,  $T$  is cladding temperature ( $^{\circ}\text{C}$ ) and  $R$  is the gas constant.

### 3. Results of PROFESS calculation of D-Com blind problem

#### 3.1 D-Com blind problem

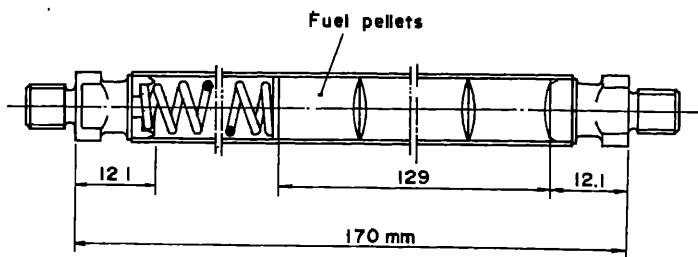
The D-Com blind problem refers to an irradiation experiment in which three (AG11-8, AG11-9 and AG11-10) pre-pressurised mini-fuel elements were irradiated together to a fuel burn-up of about 32000 MWD/MTU at fairly low heat ratings. Two of these fuel elements were subjected to a power ramp (referred as bump test) at the end of life. The third fuel element (AG11-8) had been taken out of reactor prior to the bump test. The design of the fuel elements, the axial power profile in the fuel assembly and the power history of irradiation is shown in figure 3. Misfeldt (1982) compiled the details of this irradiation experiment and the data package used for the code calculations.

#### 3.2 PROFESS calculations

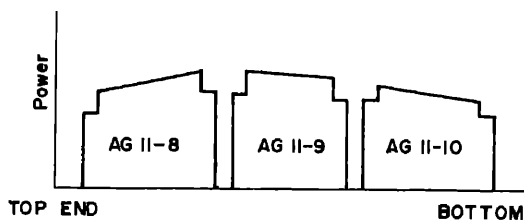
PROFESS was used to calculate the following parameters as a function of irradiation time (i) fuel centre temperature (ii) gap conductance (iii) fission gas release in the fuel element (iv) fuel restructuring and (v) fuel element diameter. The detailed results of the calculation have been reported elsewhere (Sah *et al* 1984). Some important results related to the gap conductance, fission gas release and fuel restructuring are presented below.

**3.2a Fuel-clad gap conductance:** The variation of gap conductance as a function of irradiation time in the three fuel elements at their mid-stack location is shown in figure 4. A gradual increase in the gap conductance is observed in all the three fuel elements in the beginning, followed by an abrupt increase to a comparatively high value at about 10,000 hrs. The sudden increase in the gap conductance indicates the occurrence of fuel-cladding contact in the fuel elements. However it is seen that the value of gap conductance in the three elements is different from each other, even though the fuel clad gap has closed in all the three. This difference is because of the different amount of fission gas released in the three fuel elements (see §3.2b). Since fission gases, Xe and Kr, have very low thermal conductivity a higher gas release in a fuel element results in a lower value of gap conductance. The results presented in this figure, when compared with the experimentally measured fission gas release in the three fuel elements, indicates that PROFESS is able to simulate the gap conductance behaviour very well.

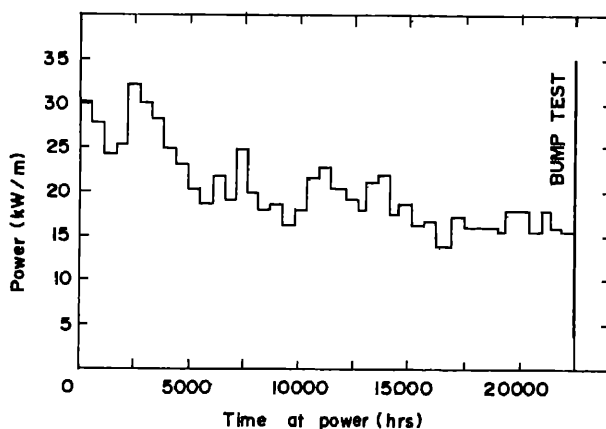
**3.2b Fission gas release:** The amount of gas release calculated by PROFESS in the three fuel elements is given in table 2 along with the experimentally measured values. There is satisfactory agreement between the predicted and measured gas release in the fuel element AG 11-8. However an underprediction of about 30% is noted in the bump tested elements AG11-9 and AG11-10. Comparison of the PROFESS predictions with the



(a)



(b)



(c)

**Figure 3.** The design and the irradiation history of the fuel elements of D-Corn blir problem; (a) fuel pin schematic design (b) power profile in the fuel pin assembly ar (c) irradiation power history.

prediction of some other codes (figure 5) revealed that most of the codes tended to underpredict the gas release in these fuel elements. This indicates that the model of transient gas release adopted by the codes are presently inadequate for accurate prediction.

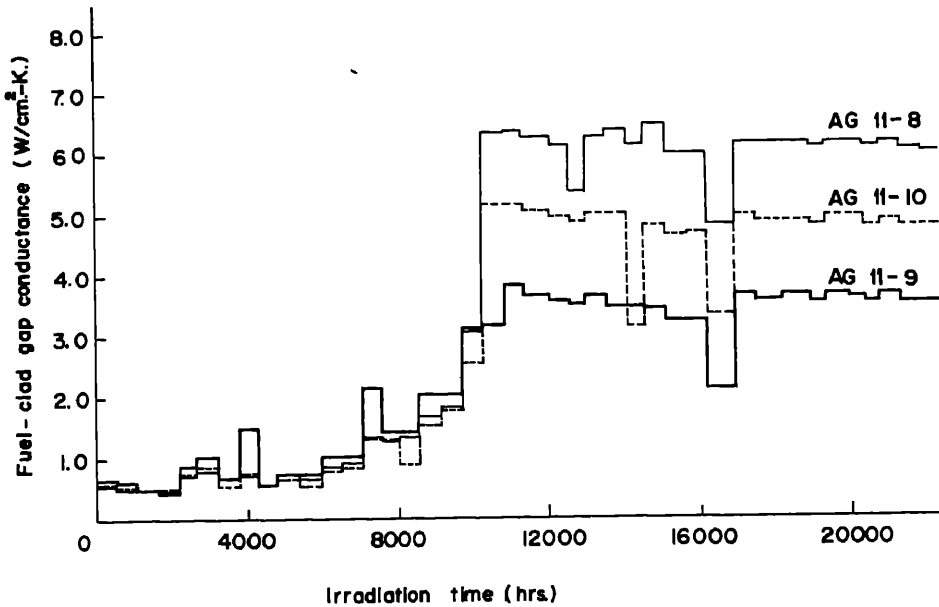


Figure 4. Fuel-clad gap conductance at the mid-stack location in the three fuel elements, as a function of irradiation time.

Table 2. Comparison of the predicted and the measured values of fission gas release in the three fuel elements of D-Com blind problem

Fuel element	Fission gas release (cc STP)	
	PROFESS prediction	Experimentally measured
AG 11-8	1.25	1.5
AG 11-9	9.0	12.5
AG 11-10	2.81	4.5

The gas release behaviour (as a function of irradiation time) calculated by PROFESS in AG 11-9 and AG 11-10 is shown in figure 6. It is interesting to note that in AG 11-9, the major amount (about two third of the total) of gas release occurred during the bump testing. This trend was in agreement with the conclusion arrived from the experiment (Misfeldt 1983).

**3.2c Fuel restructuring:** The calculations indicated that no grain growth occurred in the fuel element AG 11-8. This prediction is in agreement with the experimental finding. PROFESS prediction of the extent of grain growth at fuel centre and the size of the equiaxed grain growth region in the fuel element AG 11-9 was found to be in very good



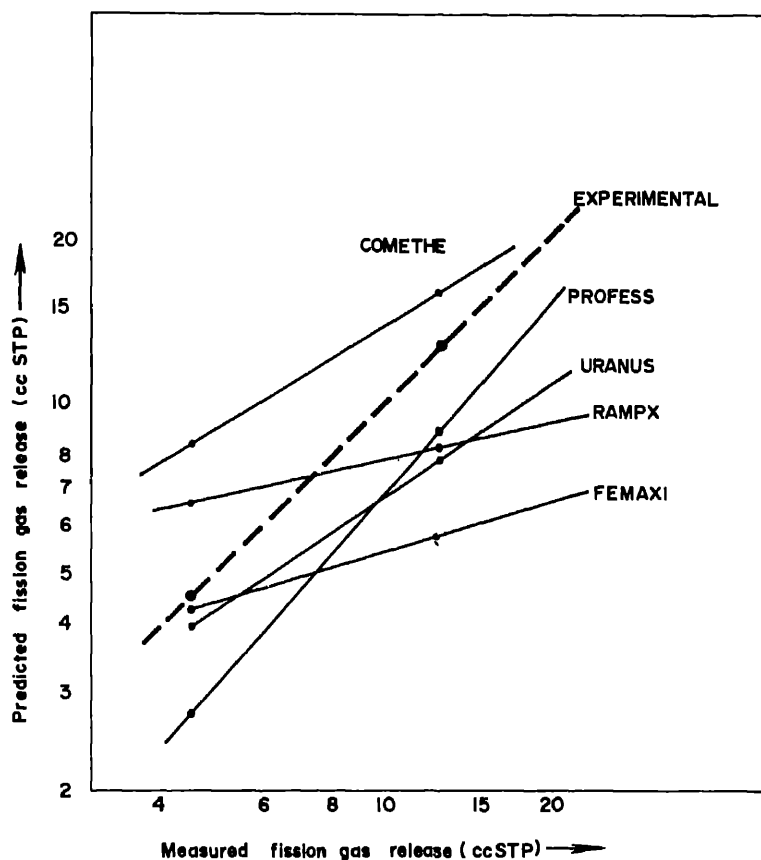


Figure 5. Comparison of the measured fission gas release in AG 11-9 and AG 11-10, with prediction of some codes.

Table 3. Comparison of the grain growth prediction with experimental observation at the mid-stack location in the fuel elements

Fuel element	Fuel grain size at the centre ( $\mu\text{m}$ )		Size of grain growth region (fuel-fractional radius)	
	Predicted	Observed	Predicted	Observed
AG 11-8	No grain growth	No grain growth	0.00	0.00
AG 11-9	32.4	30	0.57	0.50
AG 11-10	24.2	Not measured	0.51	Not measured

agreement with metallographic observations (table 3). The calculations also reveal that the grain growth in AG 11-9 occurred during the initial period of irradiation (figure 7).

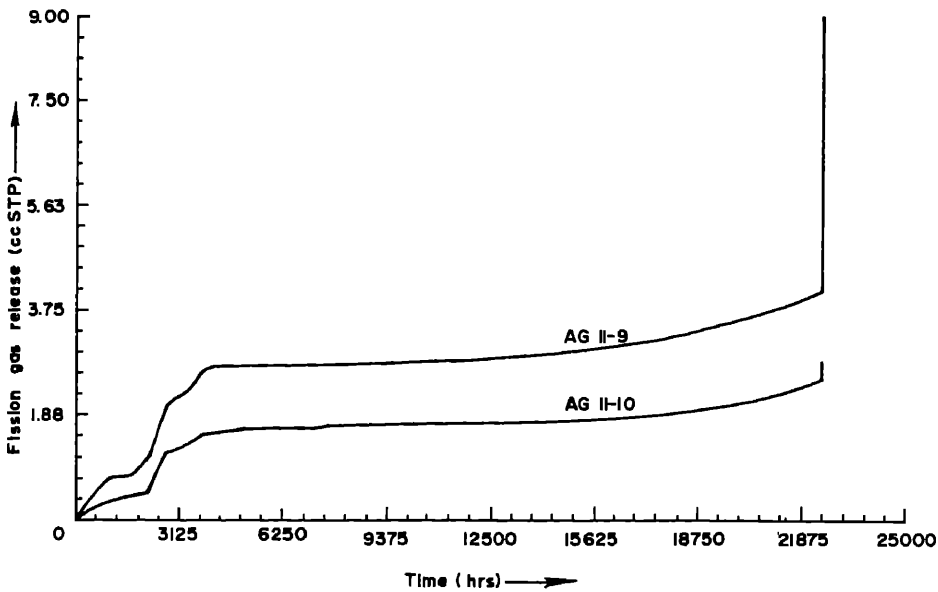


Figure 6. Predicted fission gas release in the fuel elements AG 11-9 and AG 11-10 as a function of irradiation time.

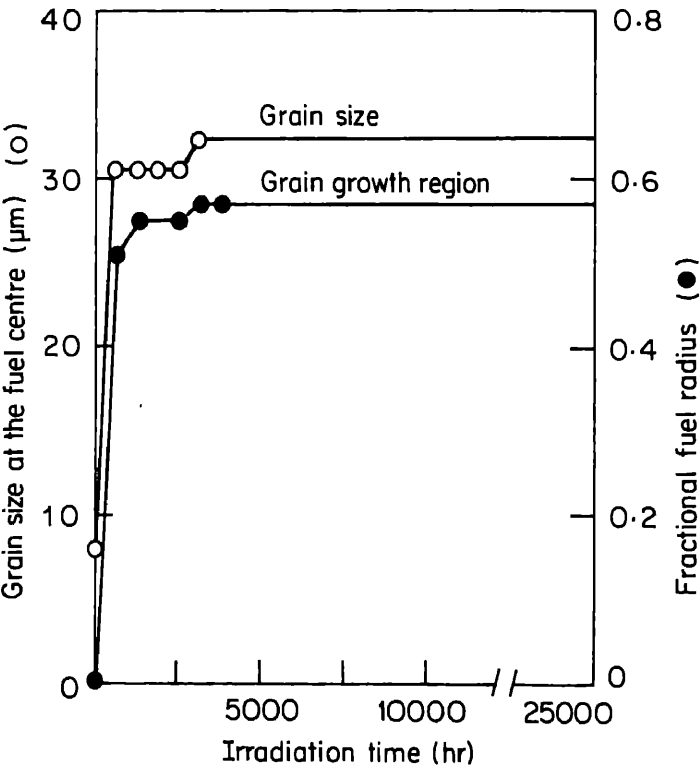


Figure 7. Predicted grain size at the fuel centre and the size of the grain growth region in the pellet cross-section for fuel elements AG 11-9, as a function of irradiation.

#### **4. Conclusion**

Computer code PROFESS was successfully used to calculate the performance parameters of the three fuel elements of an irradiation experiment commonly referred to as D-C blind problem. The prediction of the fission gas release in the fuel elements and the restructuring was found to be in reasonable agreement with experimental observations. The fuel-clad gap conductance model gives good simulation of the effect of fission gas and clearly revealed the occurrence of fuel-clad gap closure in the fuel elements during irradiation. It was noted, however, that there is a tendency for under-prediction of release during transient and better models may be required to represent the gas release in the fuel elements during transient conditions.

#### **Acknowledgement**

The authors wish to express their sincere thanks to Shri K S Sivaramakrishnan of I Section and Shri P R Roy, of Metallurgy Group for their keen interest in this work.

#### **References**

- Hilbert R F, Storhok V W, Chubb W and Keller D C 1971 *J. Nucl. Mater.* **38** 26  
Hoppe N, Billaus M and Vliet J U 1982 Belgonuclear Report COMETHE III-L, Report No. BN 8201  
Misfeldt I 1982 Data for The D-Com blind problem on fission gas release, Report B-528, Metallurgy Division, RISØ National Laboratory, Denmark  
Misfeldt I 1983 *OECD-NEA-CSNI/IAEA Specialists meeting on Water Reactor Fuel Safety and Fission release in off normal and Accident Condition*, RISØ National Laboratory, Denmark  
Pati S R and Ritterbusch S E 1980 *Fission gas release during anticipated transient*; IAEA Specialists Meeting on Water Reactor Fuel Element Performances Modelling, Blackpool, UK  
Pedersen N K 1978 *Proc. IAEA Specialists Meeting on Water Reactor Fuel Performance Computer Model*, Blackpool, UK  
Ross A M and Stout R L 1962 Heat Transfer Coefficient between  $\text{UO}_2$  and Zircaloy-2, Report AECL 1  
Roy P R and Sah D N 1985 *Pramana (J. Phys.)* **24** 397  
Sah D N, Venkatesh D and Sivaramakrishnan K S 1983 *Proc. Symp. on Irradiation Effects in Solids* (Bombay BARC) p. 203  
Sah D N, Venkatesh D and Ramadasan E 1984 *IAEA Specialists Meeting on Water Reactor Fuel Element Performance Modelling*, Bowness on Windermere UK (to be published).  
Wood D S and Watkins B 1971 *J. Nucl. Mater.* **41** 327  
Zimmermann H 1979 *IAEA Specialists Meeting on Behaviour of defected zirconium alloy clad ceramic fuel water cooled reactors*, Chalk River, Canada p. 147



## **FOREWORD**

Thin film techniques find wide applications not only in basic research but applied work in many areas such as Defence, Space, Lasers etc. The possibility of preparing tailor-made coatings for specific requirements by controlling the deposition conditions has given a new thrust to this activity. In fact it is a frontier area of research and technology. Thin film work is now being carried out in many universities and R & D organisations in the country.

The Instrumentation and Services Unit, Indian Institute of Science, organised the National Symposium on Thin Film Science and Technology during 9-11 January 1975 as part of the Platinum Jubilee celebrations of the Institute. The objective of the symposium was to bring together scientists and engineers actively involved in the field of thin film science and technology and provide a forum for presentation of papers on various topics with an emphasis on preparation and analysis of thin film coating devices.

The symposium was cosponsored by the Indian Institute of Science, University Grants Commission, Department of Science and Technology, Defence Metallurgical Research Laboratory, Indian Space Research Organisation, Solid State Ionics Laboratory, Committee on Science and Technology in Developing Countries (COSTED), USAF European Office of Aerospace Research and Development (OEAR) and the US Army Research Development and Standardisation Groups (USARDAG).

The three-day symposium was attended by about 250 delegates from about 40 institutions all over the country. The European Office of Aerospace Research and Development was represented by Dr Larell K. Smith and Dr Hussain.

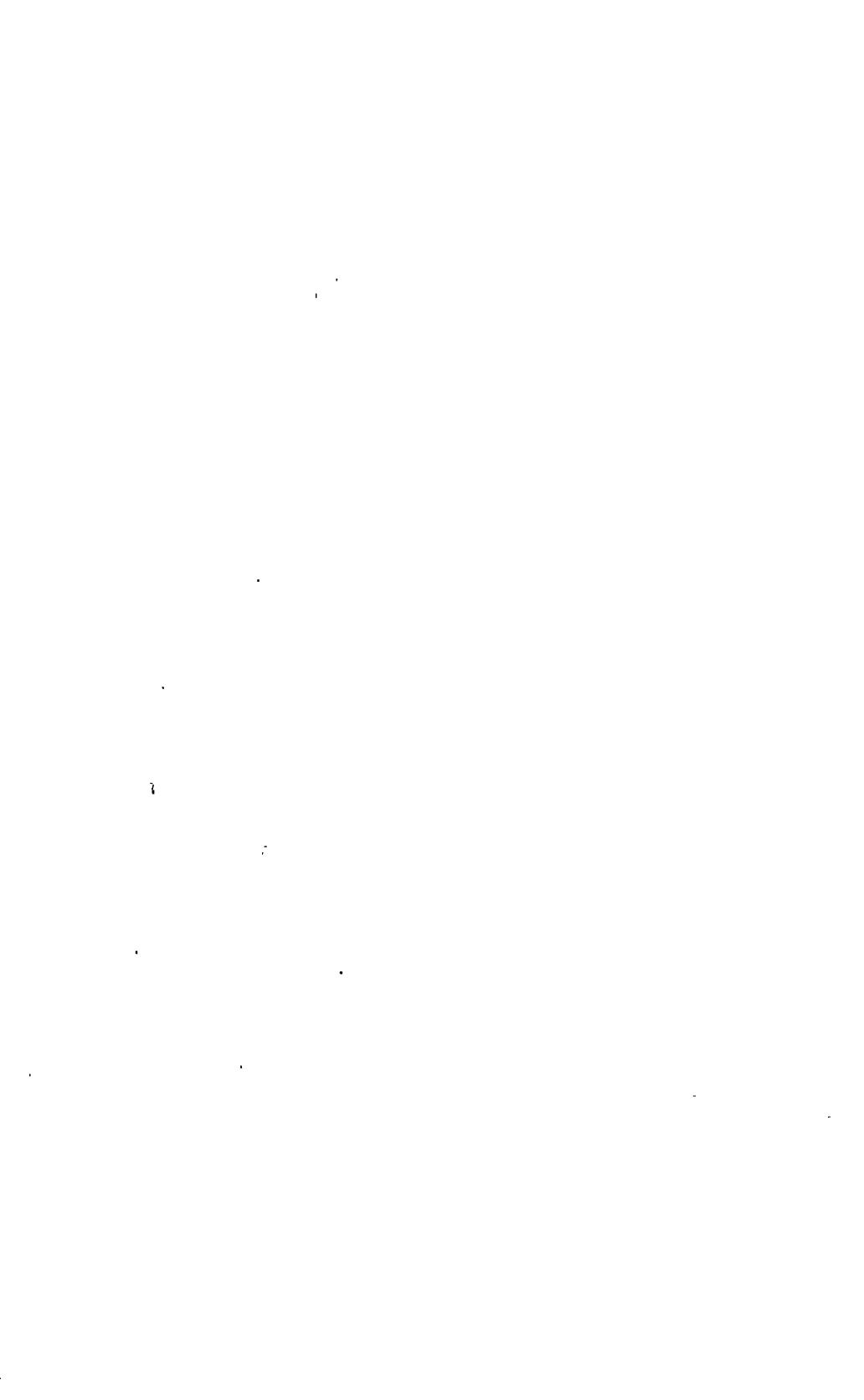
The technical sessions included about 75 technical papers covering areas such as photovoltaics, tribological coatings, selective coatings, amorphous films, their thermoelectrical and mechanical properties, optical, electrooptical and electronic properties, thin film instrumentation, characterization and analytical techniques.

It was felt that the proceedings of the symposium would be useful to a wider scientific community interested in thin films and it is indeed most gratifying that it has been possible to bring out a special issue of the Bulletin of Materials Science.

Thanks are due to the various sponsors of the symposium for the financial support and to the members of the National Advisory Committee, the Organising Committee and the Sub-Committees for their support and cooperation.

**M. Ramakrishna Rao**  
**S. Mohan**  
Conveners, National Symposium  
on Thin Film Science and Technology

**C. N. F.**  
Editor of Publication



## Electrical and optical properties of $\mu$ c-SiH films

G C DUBEY, R A SINGH, S N MUKHERJEE, SURENDRA PAL  
M G RAO

Solid State Physics Laboratory, Lucknow Road, Delhi 110007, India

**Abstract.** Microcrystalline silicon films have been found quite useful in amorphous solar cells as a contact material in n-i-p cells. Microcrystalline silicon films are obtained amorphous silicon films are prepared by R.F. glow discharge of  $\text{SiH}_4 + \text{H}_2$  at higher pressures. These films possess higher conductivity as well as high transmission than amorphous silicon films. The present paper reports the preparation technique of  $\mu$ c-SiH films using capacitive glow discharge of hydrogen-diluted silane. X-ray studies and TEM studies of the films indicate microcrystallinity of the films. The electrical and optical properties are also reported.

**Keywords.** Amorphous silicon; solar cells; plasma deposition; thin films

### 1. Introduction

During recent years several approaches have been adopted for increasing the efficiency of a-SiH solar cells. These include attempts to obtain new configurations of the structure and various materials. Use of microcrystalline silicon films for front window material for n-i-p solar cells is one such attempt in this direction. These films have been used for other thin film devices like thin film transistors. The advantage of microcrystalline film in amorphous silicon solar cell is two-fold; it enhances transmittance and increases the conductivity of the front layer, thus contributing to an increase in the efficiency of the solar cells. In fact cells upto efficiency of 9.1 % have been reported using  $\mu$ c-SiH films as a front window material in n-i-p cells (Hamakawa and Okamoto 1983).

Veprek and Marecek (1968) were the first to report  $\mu$ -crystalline films of silicon by chemical transport of silicon in hydrogen plasma. Their aim was to investigate the growth of  $\mu$ c-silicon at low temperature. Recently, various groups have reported  $\mu$ c-films using glow discharge (Uchida *et al* 1982) or reactive sputtering technique (Hirata *et al* 1981). There are several methods of producing  $\mu$ c-SiH films i.e. transportation of silicon in hydrogen plasma, reactive sputtering technique, increased R.F. power in glow discharge system (Uchida *et al* 1981; Dubey *et al* 1983) and higher substrate temperature. In the present paper  $\mu$ c-SiH films having increased R.F. power as well as higher concentration of hydrogen in silane gas (i.e. 99 %  $\text{H}_2 + 1$  %  $\text{SiH}_4$ ) have been grown. At higher concentration of hydrogen the deposition rate also decreases (Varshney *et al* 1984) helping in increasing the crystallite size in the film (Kamuro *et al* 1984). These films have been analyzed by x-ray diffraction and TEM for their microcrystallinity. The electrical and optical properties of these films have been studied and discussed.

## 2. Experimental

The  $\mu\text{-SiH}$  films were deposited in a capacitively coupled R.F. glow discharge of 1  $\text{SiH}_4 + 99\% \text{H}_2$ . The glow discharge system designed incorporates a stainless steel cross-type chamber as shown in figure 1. This has a parallel plate type of capacitor 14 cm dia. The distance of the plates can be varied from 1 to 3 inch with provision incorporated in the top electrode. The bottom electrode on which substrates are kept can be heated through a resistance heater located outside the chamber, up to temperature of  $350^\circ\text{C}$ . The temperature is monitored with a thermocouple provided beneath the bottom electrode of the capacitor and outside the discharge chamber to avoid any contamination. The stainless steel chamber is cooled from outside by circulating cold water through copper tubing cold welded with thermally conductive epoxy. Matsuda (1983) pointed out that higher concentration of hydrogen ions in the plasma tends to yield microcrystalline-hydrogenated silicon films. In the present system, therefore, a higher concentration of hydrogen ( $99\% \text{H}_2 + 1\% \text{SiH}_4$ ) has been used to prepare  $\mu\text{-SiH}$  films by increasing the R.F. power and the concentration of hydrogen in the mixture.

The system is evacuated to  $10^{-6}$  mm of Hg using a diffusion pump. Fomblin oil (HVAC18/8), which is more resistant to reactive gases like silane etc has been used in the diffusion pump. The plumbing line connecting various gaseous systems to the glow discharge chamber is evacuated by a second rotary pump before silane gas mixture ( $1\% \text{SiH}_4 + 99\% \text{H}_2$ ) is admitted into the glow discharge chamber to avoid any contamination of the silane gas mixture. The whole system is also flushed with hydrogen before starting the gas flow. The pressure in the glow discharge chamber measured by Pirani gauge is kept constant by balancing the constant flow of the gas as monitored by rotameter. The compound gauge has been provided close to the rotameter to monitor the pressure in the plumbing line prior to the gas flow. During the gas flow, the constant pressure as indicated in the compound gauge helps in maintaining precise flow control.

The films have been grown on a variety of substrates such as 7059 corning glass, quartz, rocksalt, silicon, cover slips and stainless steel. To study the pattern of delineation for device fabrication, the films have been deposited on the substrate through metal masks. The thickness of the films grown ranges from 300 Å to  $1.6\ \mu\text{m}$ . Films with lower thicknesses were used for TEM studies.

R.F. power is fed through a coaxial cable having n-connector and fed to the parallel plate capacitor through power meter (model 4410). Both the transmitted and the reflected power is measured from which the actual power fed to the system is computed. No provision was made to scavenge the exhaust silane gas by burning as is normally the practice, since highly diluted silane is used in the experiment.

The substrate temperature has been varied from room temperature to  $200^\circ\text{C}$ . Different gas flow rates have also been tried. Most of the work has been done at slow deposition rates and at substrate temperature of  $200^\circ\text{C}$  where good quality films are obtained.

X-ray diffraction studies have been carried out on Philips x-ray diffractometer and optical absorption measurements on spectrophotometer (Cary 17) TEM has been done on electron microscope (JEOL). For thickness measurements Taly surf and light sectioning microscope have been used.



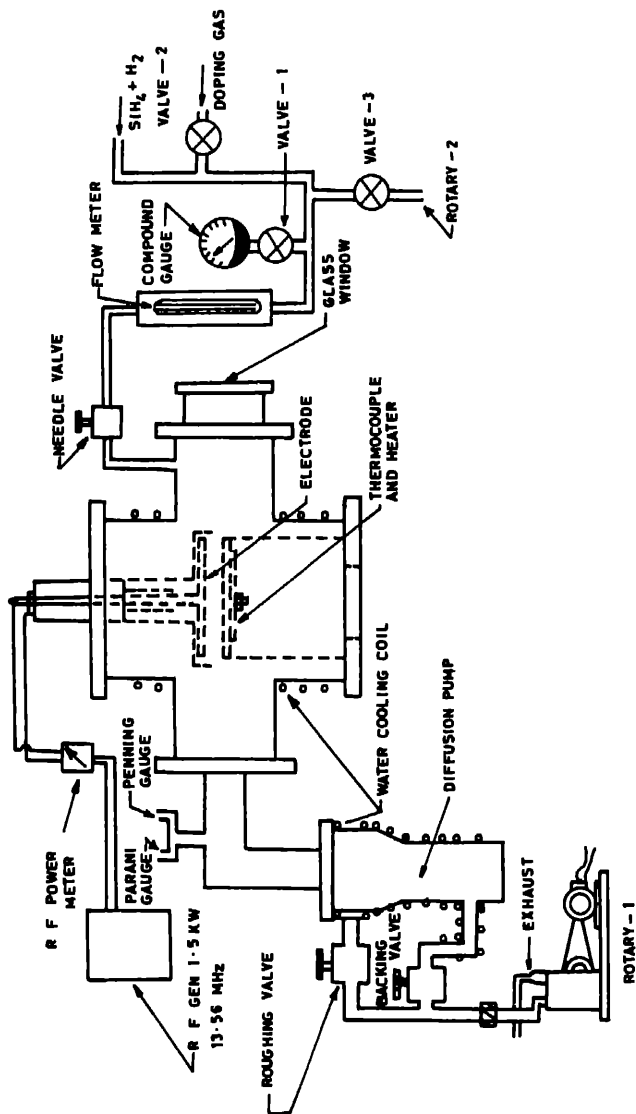


Figure 1. Schematic of glow discharge system.

### 3. Results and discussion

The films obtained were smooth having very good adhesion and difficult to scratch except those which were deposited at room temperature. All the films withstood the tape test as applied to thin films. The pattern delineation showed sharp edges. X-ray diffraction pattern provides information on the crystallite size, its orientation, lattice distortion and the volume fraction of crystalline phase in mixed phase of  $\mu\text{c-SiH}$ . Figure 2 shows the x-diffraction pattern of  $1\ \mu$  thick film deposited on silicon substrate. Similar measurements were carried out by Uchida *et al* (1981) indicating the diffraction line of (111) phase characteristic of silicon. The diffraction pattern of the film taken on glass substrate indicated peaks at  $2\theta = 28.8^\circ$ ,  $48^\circ$  and  $56^\circ$ , showing that the film contains mixed phase of perfect crystalline phases of (111), (220), (311) and others along with amorphous phase.

In order to estimate the degree of crystallinity of the film, the substrate was heated to  $700^\circ\text{C}$  for 1.5 hr in hydrogen atmosphere. This temperature is quite above the transition temperature of  $650^\circ\text{C}$  for crystallization of the entire film. Normally, the complete film is not crystalline. Percent volume fraction of crystalline phase varied from 60 to 80%. Previous studies had reported this value from 20 to 80% depending upon the R.F. power (Nakatani *et al* 1983). Figure 2 enables one to calculate the percentage volume fraction of microcrystals. It is seen that the values of peak heights  $I_p$  and the full width at half maximum (FWHM)  $\Delta 2\theta$  are different before and after annealing. Assuming that the product of  $I_p$  and  $(2\theta)$  is proportional to the volume of microcrystals in  $\mu\text{c-SiH}$  film, the volume fraction in the film has been estimated as 70%. It has been observed that  $\Delta 2\theta$  which is a measure of the micro-crystallite size remains constant upto the annealing temperature of  $\approx 500^\circ\text{C}$ . On annealing at  $700^\circ\text{C}$ , a two-fold increase in the crystallite size is observed. The crystallite size in the as-grown film is calculated to be  $150\ \text{\AA}$  using the Scherrer formula (Cullity 1959).

Figure 3 shows the electron diffraction pattern of the three types of films deposited at

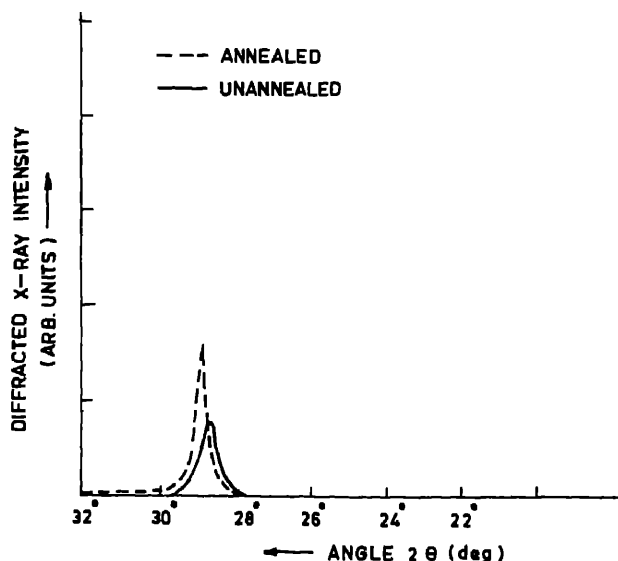
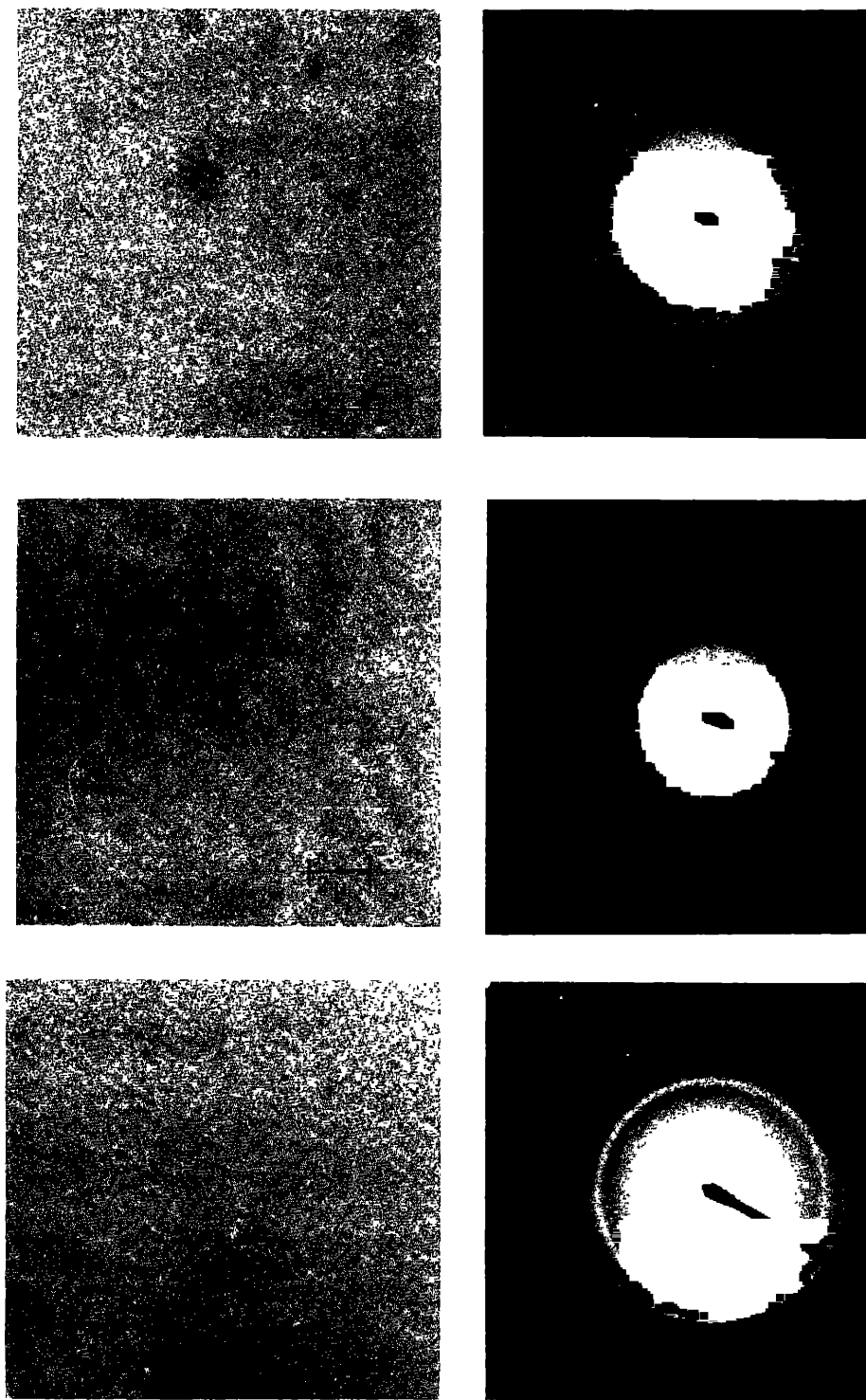


Figure 2. X-ray diffraction pattern.



**Figure 3.** Photomicrograph of amorphous and microcrystalline films along with SAD microcrystallinity increases as the power increases (a) 20 watt (b) 50 watt (c) 150 watt

power level of 20, 50 and 150 watts. The Debye Scherrer rings of the diffracted pattern show a gradual increase in microcrystallinity with increase in power. Also, even at smaller thicknesses in the range of 400–500 Å the films are microcrystalline.

The optical bandgap  $E_0$  of  $\mu\text{c-SiH}$  film has been calculated using figure 4, where  $\alpha^2$  has been plotted against photon energy, since the  $\mu\text{c-SiH}$  films are used for front window material. In the figure,  $\alpha^2$  has been plotted to compare the results with those of other transparent conducting materials like tin oxide films (Dubey *et al* 1985).

The bandgap obtained is  $\approx 1.8\text{ eV}$  which conforms to the data obtained by Uchida *et al* (1981). Figure 5 shows the plots of  $h\nu$  vs  $\sqrt{\alpha h\nu}$  for  $\mu\text{c-SiH}$ , a-SiH and silicon. The data of a-SiH(a) and silicon (c) have been taken from Tanaka and Matsuda (1983). It is seen that the spectra of  $\mu\text{c-SiH}$  and single crystal silicon do not obey the square root law and that a-SiH exhibits a linear variation of  $\sqrt{\alpha h\nu}$  over a wide  $h\nu$  range.

A comparison of the curves shows that the nature of  $\mu\text{c-SiH}$  lies between a-SiH and C-Si. This indicates that with increased power, it is possible to get crystalline films and the optical properties are therefore changed accordingly. This also is indicative of the

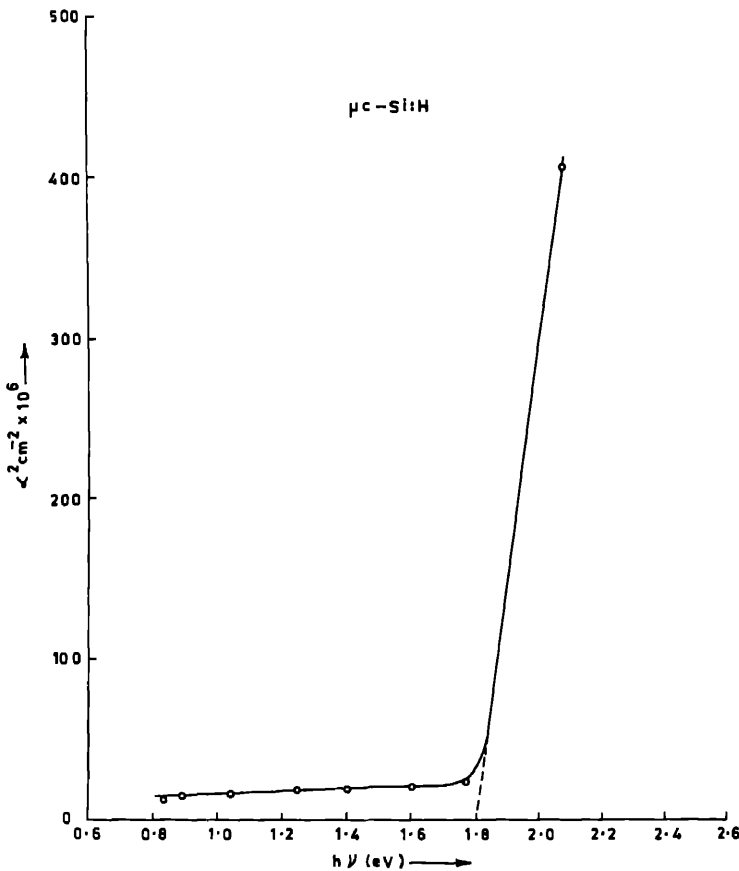


Figure 4. Variation of  $\alpha^2$  with photon energy.

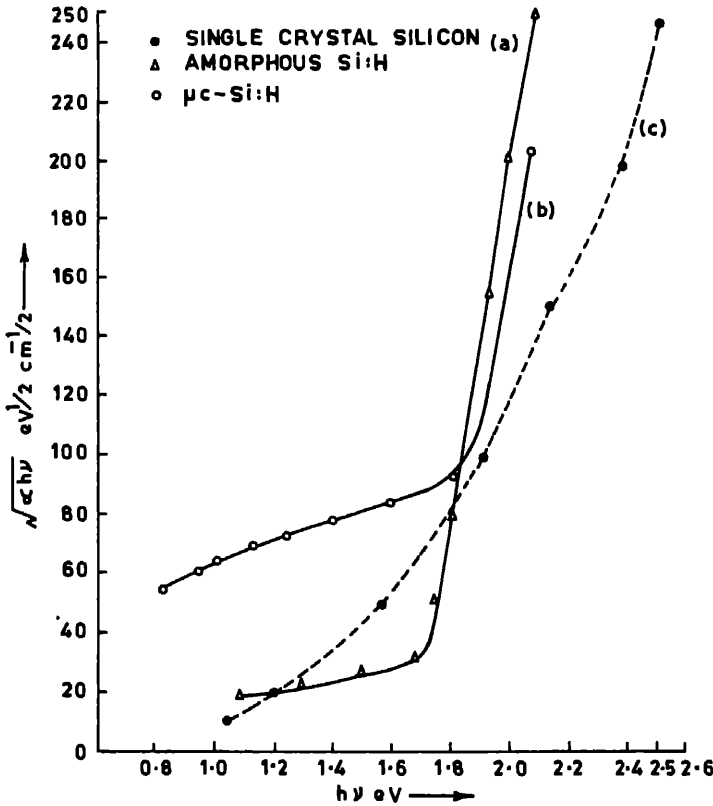


Figure 5. Variation of  $\sqrt{\alpha h\nu}$  with photon energy.

fact that these films have a mixed phase of amorphous and crystalline substances smaller crystallites.

As mentioned earlier these microcrystalline films have been used as window mate in n-i-p solar cells. Therefore, the transmission data of these films is very useful. Figure shows the transmission with varying thickness for  $\lambda = 7,000 \text{ \AA}$ . It has been suggested that a thickness of around  $100 \text{ \AA}$  to  $200 \text{ \AA}$  is required in the fabrication of n-i-p solar cells (Tanaka and Matsuda 1983).

#### 4. Electrical properties

Dark conductivity  $\sigma_d$  of  $\mu\text{c-SiH}$  is in general two or three orders of magnitude higher than a-SiH (Tanaka and Matsuda 1983; Kaya *et al* 1984). Similar results have been observed in the present study. Moreover as shown in figure 7, the resistivity of the film is a function of substrate temperature. It is also seen that as substrate temperature increased the resistivity decreases which can be attributed to increase in crystallite size with increase in substrate temperature. The variation of electrical resistance of the film with temperature is given in figure 8.

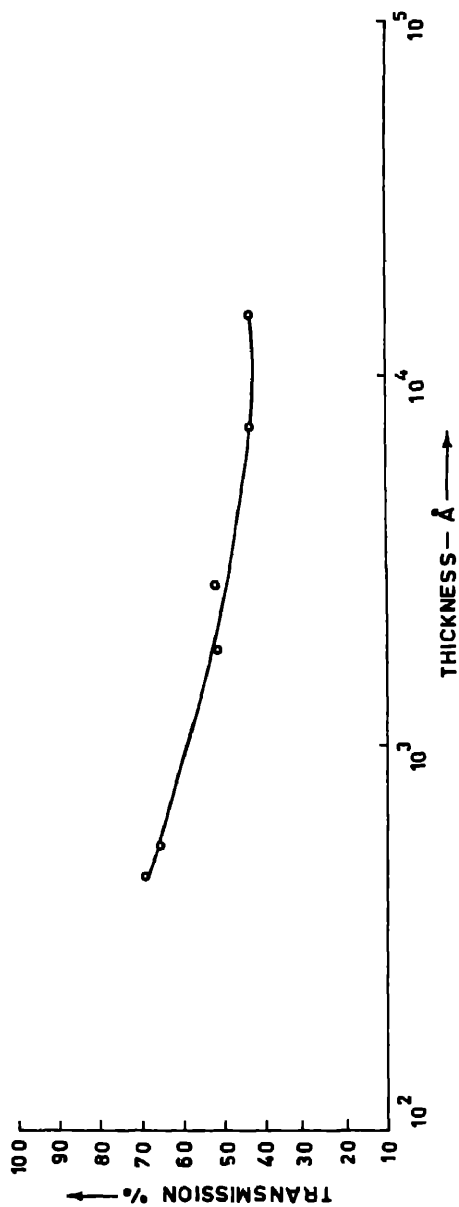
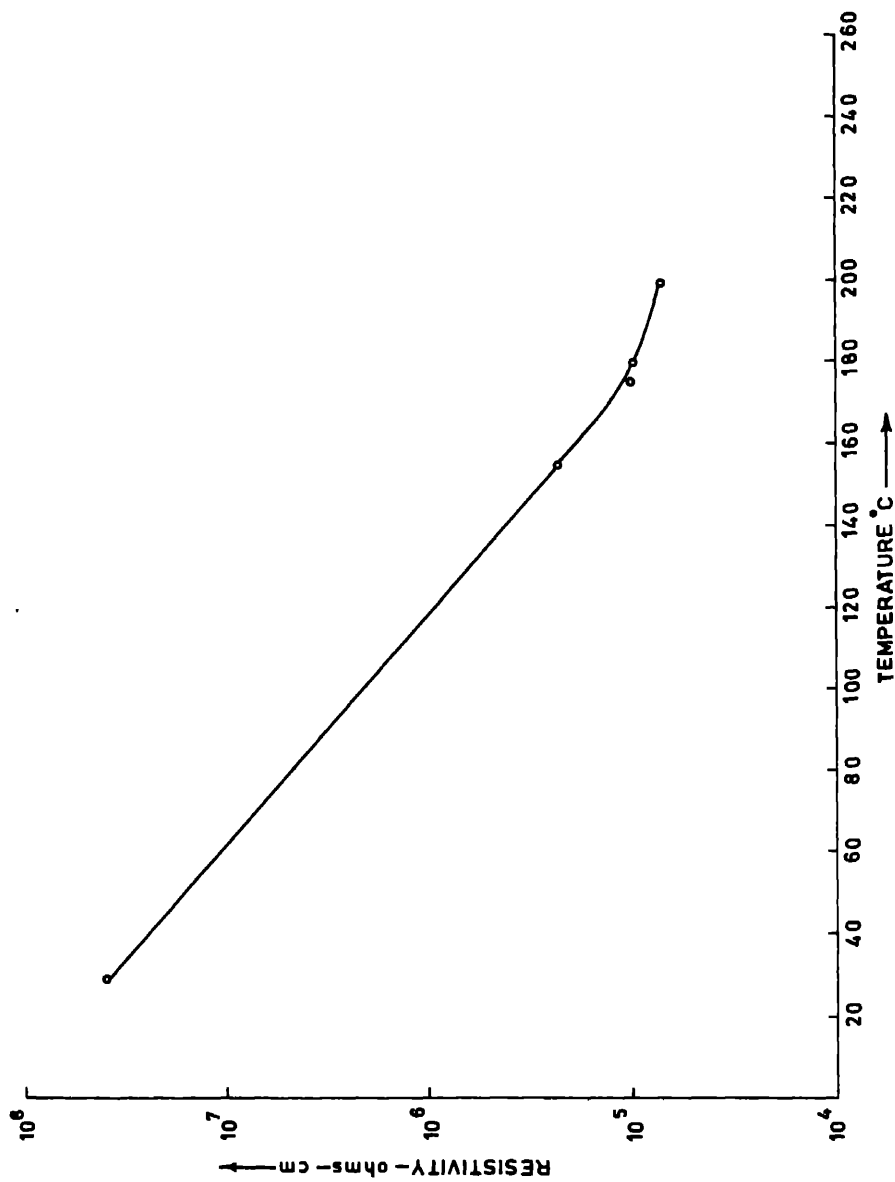


Figure 6. Variation of transmission with thickness of  $\mu$ -crystalline films.

*Properties of  $\mu\text{c-SiH}$  films*



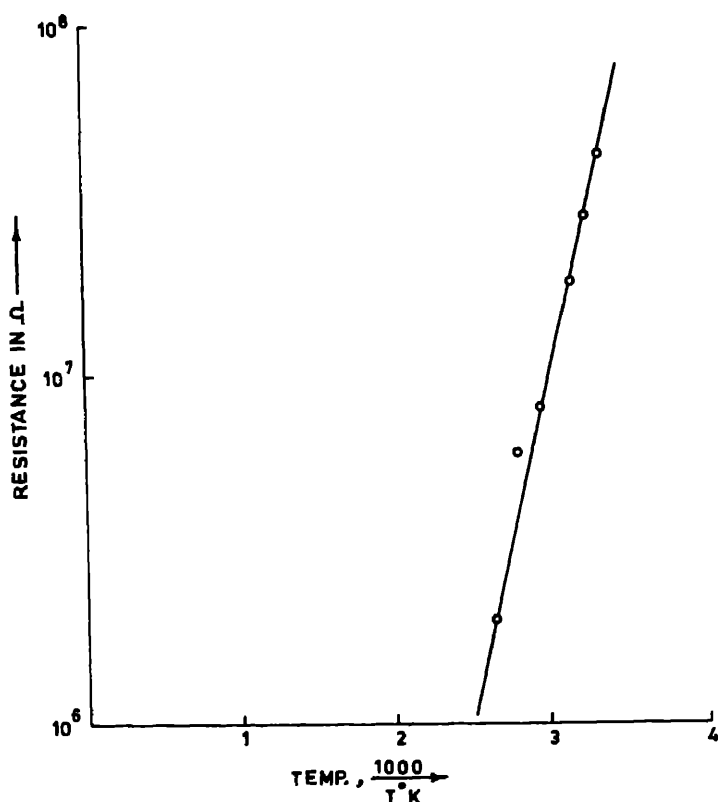


Figure 8. Variation of electrical resistivity with temperature for films grown at 200°C.

## 5. Conclusions

$\mu$ c-SiH films are produced when hydrogen diluted silane is decomposed in a parallel plate capacitive glow discharge system with power level of 50 watt and above. Structurally, these films are of mixed phase of amorphous and crystalline silicon as confirmed by annealing the films upto 700°C in hydrogen atmosphere. The resistivity of the films decreases as the substrate temperature is increased.

## Acknowledgements

The authors are grateful to Dr S K Sharma of the National Physical Laboratory, New Delhi for help in electron diffraction work, and to Dr R P Mall and Dr S S Singh of the Defence Science Centre for x-ray diffraction and optical absorption measurements respectively.

## References

- Cullity B D 1959 *Elements of x-ray diffraction* (Massachusetts: Addison-Wesley) 99
- Dubey G C, Singh R A, Pal S and Gopal Rao M 1983 Second International Workshop on the Physics of Semiconductor Devices, New Delhi



## *Properties of $\mu\text{c-SiH}$ films*

- Dubey G C, Singh R A, Pal S and Gopal Rao M 1985 *Photovoltaic materials and devices, Proc. Symp.* (eds Das and S N Singh (Delhi: Wiley Eastern) p. 254
- Hamakawa Y and Okamoto H 1983 *Amorphous Semiconductor Tech. Devices* 6 182
- Hiraki A, Imura T, Modi K and Tashiro M 1981 *J. Phys. (Paris)*, C-4 277
- Kaya H, Imura T, Kusao T, Hiraki A, Nakamura O, Okayasu Y and Matsumura M 1984 *Jpn. J. Appl. Phys.* 23 L549
- Kamuro S, Aoyagi J, Segawa Y, Namba S, Masuyama A, Matsuda A and Tanaka K 1984 *J. Appl. Phys.* 65 1658
- Matsuda A 1983 *J. Non-Cryst. Solids* 59-60 767
- Nakatani K, Yano M, Suzuki and Okinawa A 1983 *J. Non-Cryst. Solids* 59-60 827
- Tanaka K and Matsuda A 1983 *Amorphous Semiconductor Tech. Devices* 6 161
- Uchida Y, Ichimura T, Veno M and Haruki H 1982 *Jpn J. Appl. Phys.* 21 1586
- Uchida Y, Ichimura T, Veno M and Ohsawa M 1981 *J. Phys. (Paris)* C-4 265
- Vamier P E, Kampas F J, Corderman R R and Rajeswaran G 1984 *J. Appl. Phys.* 56 1812
- Veprek S and Maracek V 1968 *Solid State Electron.* 11 683



## Thin film CdZnS/CuInSe<sub>2</sub> solar cells by spray pyrolysis

P RAJA RAM, R THANGARAJ and O P AGNIHOTRI

Physics Department, Indian Institute of Technology, New Delhi 110016, India

**Abstract.** Cd<sub>1-x</sub>Zn<sub>x</sub>S/CuInSe<sub>2</sub> solar cells having efficiencies in the range of 2% fabricated by spray pyrolysis. The best cell had the following parameters:  $V_{oc} = 0.32$  V,  $J_{sc} = 32$  mA/cm<sup>2</sup>, FF = 0.32 area = 0.4 cm<sup>2</sup> and efficiency = 3.149%.  $V_{oc}$  versus  $J_{sc}$  measurements showed that the electron affinity difference was 0.22 eV. Forward and reverse current versus voltage curves were plotted and a possible current mechanism occurring in the cells has been proposed.

**Keywords.** CuInSe<sub>2</sub> solar cells; thin film solar cells; CdZnS/CuInSe<sub>2</sub>; spray pyrolysis

### 1. Introduction

CuInSe<sub>2</sub> is a I-III-VI<sub>2</sub> ternary chalcopyrite semiconductor which has recently attracted considerable interest as a photovoltaic material. It has a direct band gap of 1.0 eV which falls in the optimum range for terrestrial photovoltaic applications (Kazmer 1976, 1977). Owing to its high absorption coefficient, it requires at the microns of thickness to make devices. Besides, inexpensive thin film deposition techniques can be used in the fabrication. CuInSe<sub>2</sub> when paired with CdS, has a compatible lattice structure with a lattice mismatch of only 1.2% and a small electron affinity difference (0.1 eV) (Tell *et al* 1972; Shay *et al* 1975; Chen and M 1980). The CdS/CuInSe<sub>2</sub> solar cell has been modelled by Ireland *et al* (1979) and has been analysed as one of the highest efficiency photovoltaic heterojunctions available. A 11% thin film CdZnS/CuInSe<sub>2</sub> cell prepared by an elemental three-source evaporation has already been demonstrated by the Boeing Aerospace Co., Washington (H *et al* 1984). The Boeing cells have been found to have excellent stability owing to the tetragonal structure of CuInSe<sub>2</sub> (Mickelsen and Chen 1982).

### 2. Experimental procedure

#### 2.1 CuInSe<sub>2</sub> films

Aqueous solutions of cupric chloride, indium trichloride and seleno-urea were mixed together in the Cu:In:Se ratio of 1:1:4 and sprayed onto glass substrates heated at 300°C to obtain CuInSe<sub>2</sub> films about 1 μ thick. The films were characterized by x-ray diffraction, optical transmission spectra, transmission electron microscopy, scanning electron microscopy (SEM), x-ray photoelectron spectroscopy (XPS) and electrical measurements. The properties of these sprayed films have been reported elsewhere (Agnihotri *et al* 1983; Raja Ram *et al* 1985).

## 2.2 Fabrication of cells

A number of  $\text{Cd}_{0.85}\text{Zn}_{0.15}\text{S}/\text{CuInSe}_2$  solar cells having efficiencies in the 2–3% range were prepared by spray pyrolysis. Indium tin oxide films of high transmission and low sheet resistance ( $1\text{--}5\ \Omega/\square$ ) were used as the substrates for the junctions.

The ITO substrates were placed on a hot plate, partially covered and heated to  $350^\circ\text{C}$ . A  $1.5\ \mu$  thick layer of  $\text{Cd}_{1-x}\text{Zn}_x\text{S}$  ( $x = 0.15$ ) was grown on the uncovered portion of the ITO by spraying a mixture of aqueous solutions of  $\text{CdCl}_2$ ,  $\text{ZnCl}_2$  and thiourea. Indium (5–10%) in the form of  $\text{InCl}_3$  solution was also added to reduce the resistivity of the  $\text{CdZnS}$  layer. The substrates were further covered and about  $2\ \mu$  of  $\text{CuInSe}_2$  were grown at  $300^\circ\text{C}$ . The junctions were then removed from the hot plate and fitted inside a vacuum coating chamber to deposit the gold contact on the  $\text{CuInSe}_2$  back layer. Thus junctions of the type  $\text{ITO}/\text{CdZnS}/\text{CuInSe}_2/\text{Au}$  were formed.

## 2.3 Characterisation of the cells

The cells were illuminated at  $100\ \text{mW}/\text{cm}^2$  through the glass, ITO and  $\text{CdZnS}$ , and the I-V characteristics were plotted on an automatic I-V plotter. The values of  $V_{oc}$  versus

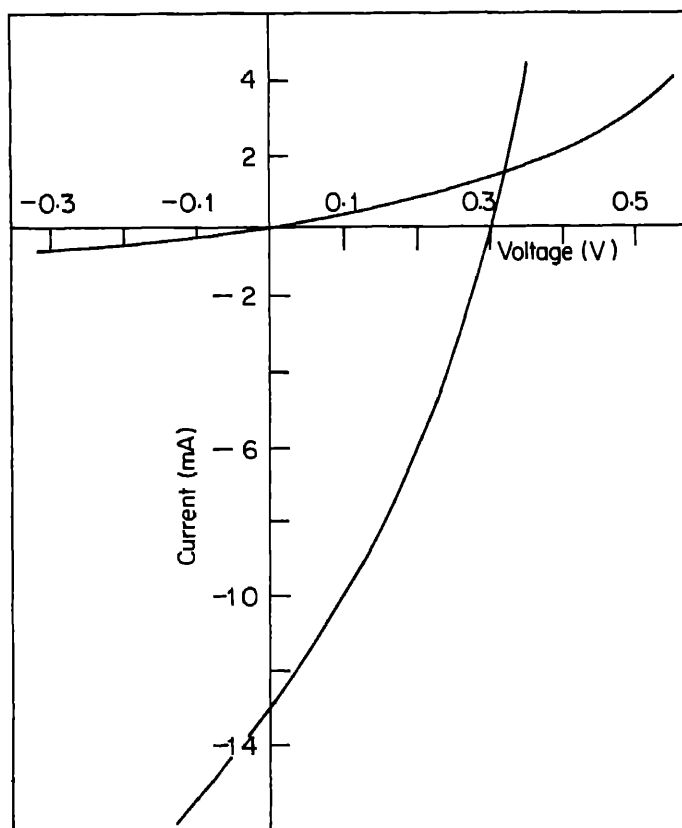


Figure 1. I-V characteristics of a  $\text{CdZnS}/\text{CuInSe}_2$  solar cell illuminated at  $100\ \text{mW}/\text{cm}^2$ .

temperature and dark I-V plots at various temperatures were obtained by fitting device in a copper cryostat cooled by liquid air.

### 3. Experimental results and discussion

Figure 1 shows the light I-V characteristics of the best CdZnS/CuInSe. The parameters of the cell illuminated at 100 mW/cm<sup>2</sup> are:  $V_{oc} = 30$  mV,  $J_{sc} = 32$  mA/cm<sup>2</sup>, FF = 0.324, area = 0.40 cm<sup>2</sup> and efficiency  $\eta = 3.149\%$ .

In general the cells had high short circuit currents, but low open circuit voltage and consequently low efficiencies.

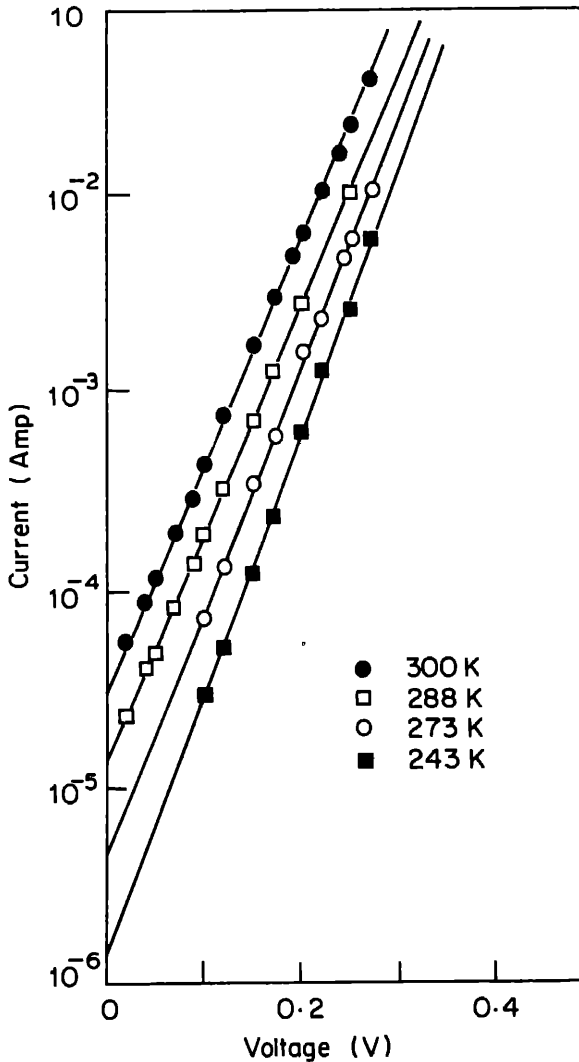


Figure 2. Dark current vs voltage at various temperatures for CdZnS/CuInS

If the cell is dominated by interface recombination, the current through the junction is of the form (Kazmerski *et al* 1978):

$$J = J_o \exp(qV/nkT)$$

where

$$J_o = J_{\infty} \exp \left\{ -\frac{(E_{g1} - \Delta\psi)}{nkT} \right\},$$

where  $q$  is the charge of an electron,  $V$  is the applied voltage,  $n$  is the diode factor,  $E_{g1}$  is the band gap of CuInSe<sub>2</sub>,  $\Delta\psi$  is the electron affinity difference between the CuInSe<sub>2</sub> and CdZnS.

The diode factor  $n$  of the best cell was about 1.5, confirming that interface recombination is the dominant mechanism in these junctions. Figure 2 shows the dark I-V plots for the best cell for various device temperatures. The intercept on the current axis gives the  $(J_o \times \text{area})$  value for each temperature. Figure 3 shows the  $J_o$  versus  $1/nkT$  plot whose slope gives the diffusion voltage in the dark. Here it is 0.63 V. For a planar diode, the open circuit voltage  $V_{oc}$  can be written as:

$$qV_{oc} = E_{g1} - \Delta\psi + nkT \cdot \ln \left( \frac{J_{sc}}{qN_{C2}S_1} \right) - \delta_1 - \delta_2,$$

where  $\delta_1$  and  $\delta_2$  are the energy differences between the fermi level and the valence and conduction band edges as shown in figure 5. The  $V_{oc}$  versus  $T$  plot is shown in figure 4. The intercept on the  $V_{oc}$  axis gives the value of  $E_{g1} - \Delta\psi = 0.82$  eV. Thus the value of  $\Delta\psi$  is 0.22 eV assuming that the band gap of sprayed CuInSe<sub>2</sub> is 1.04 eV.

From the above results the energy band diagram has been drawn for these CdZnS/CuInSe<sub>2</sub> cells. This is shown in figure 5.

The resistivities of the CuInSe<sub>2</sub> and CdZnS layers forming the junction are about 100  $\Omega$  cm and 50  $\Omega$  cm respectively. The values for the carrier concentrations  $p$  and  $n_e$  given in the figure are typical values obtained from Hall and thermoelectric measurements conducted on the films.

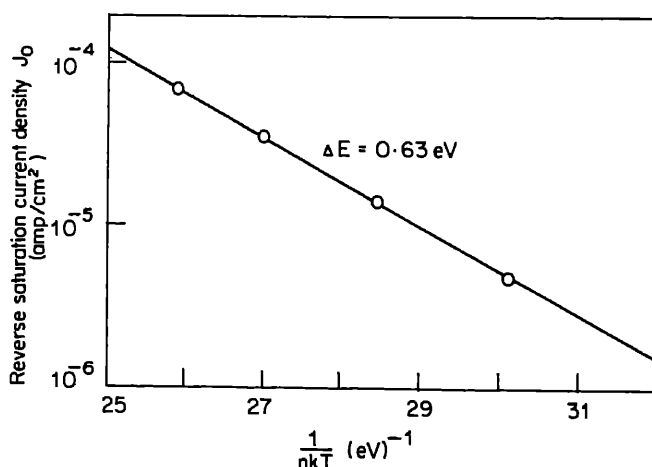


Figure 3.  $J_o$  vs  $(nkT)^{-1}$  for the cell.

## Thin film $\text{CuInSe}_2$ solar cells

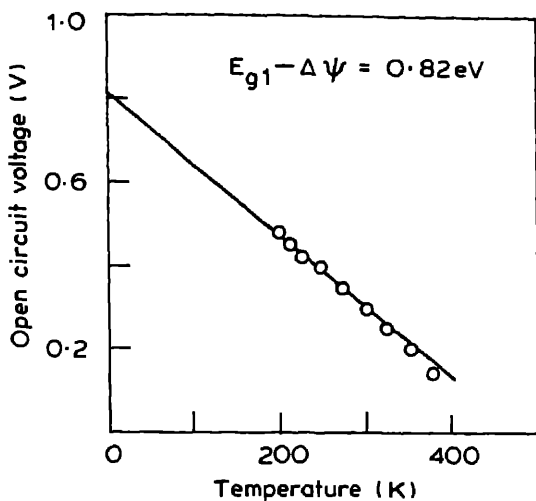


Figure 4.  $V_{oc}$  vs temperature for the cell.

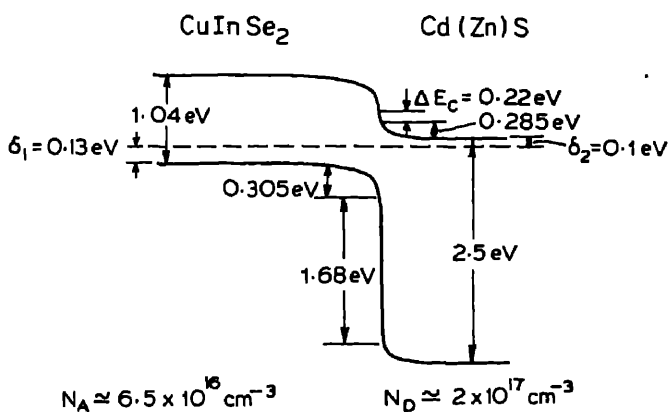


Figure 5. Proposed energy band diagram for the  $\text{CuInSe}_2/\text{CdZnS}$  junction.

The proposed band diagram explains some of the properties like low efficiency of the cells. The  $V_{oc}$  is low due to: (i) the spreading of the junction field into the  $\text{CdZnS}$  because the condition  $n_e \gg p$  does not hold. A part of the voltage appears across the  $\text{CdZnS}$  and only the remaining part contributes to (ii) The high values of  $\delta_1$  and  $\delta_2$  which can be reduced only if the resistivity of  $\text{CdZnS}$  is further decreased without compromising the film quality.

Another important factor which causes a reduction in both  $V_{oc}$  and the fill factor is the low shunt resistance. The shunt resistance is small due perhaps to the high recombination along the grains and the defects which are in large numbers in sprayed films. The low values of  $V_{oc}$  and FF thus result in low efficiencies of the cells.

ons

$\text{SnSe}_2$  solar cells with efficiencies around 3% were prepared by spray  
e efficiency can be increased by reducing the resistivity of the CdZnS layers  
ving the quality of the sprayed CuInSe<sub>2</sub> and CdZnS films. We are grateful  
nistry of Defence, Government of India for financial support.

- Raja Ram P, Thangaraj R and Sharma A K 1983 *Thin Solid Films* **102** 291  
Mickelsen R A 1980 *Proceedings of the Society of Photo-optical Instrumentation Engineers*,  
Washington p. 62  
Reibel K and Mitchell R 1984 *Proceedings of the 17th Photovoltaic Specialists Conference*,  
I  
Gerner S, Kazmerski L L and Hulstrom R L 1979 *Science* **204** 611  
White F R and Morgan G K 1976 *Appl. Phys. Lett.* **29** 268  
White F R, Ayyagari M S, Juang Y L and Patterson R P 1977 *J. Vac. Sci. Technol.* **14** 65  
Ireland P J, White F R and Cooper R B 1978 *Proc. 13th IEEE Photovoltaic Specialists*  
Washington, 184  
and Chen W S 1982 *Proc. 16th IEEE PVSC* 781  
Thangaraj R, Sharma A K and Agnihotri O P 1985 *Solar Cells* **14** 123  
r S, Bachmann K, Buchler E and Kasper H M 1975 *Proc. 11th IEEE PVSC*, Phoenix, 503  
and Kasper H M 1972 *J. Appl. Phys.* **43** 1972



## a-Si:H/CuInS<sub>2</sub> heterojunctions for photovoltaic conversion

SATYENDRA KUMAR, A N TIWARI, O S SASTRY, D K PA  
and K L CHOPRA

Department of Physics, Indian Institute of Technology, New Delhi 110016, India

**Abstract.** Heterojunctions of hydrogenated a-Si films prepared by r.f. sputtering and pyrolyzed CuInS<sub>2</sub> films have been studied. Capacitance-voltage measurements establish formation of abrupt heterojunction. The barrier height varies from 0.26 to 0.52 eV. The resistivity of CuInS<sub>2</sub> film decreases from  $1.5 \times 10^3$  to 65  $\Omega\text{cm}$ . These junctions show photovoltaic behaviour with  $V_{oc} = 220$  mV and  $I_{sc} = 0.20$  mA/cm<sup>2</sup>.

**Keywords.** Heterojunction; a-Si:H; CuInS<sub>2</sub>; photovoltaics

### 1. Introduction

Hydrogenated a-Si is a promising material for low cost and large area solar cells. The main photogenerated carrier transport mechanism in an a-Si:H solar cell is drift of carriers, which depends on the strength and distribution of electric field in the i-p-i-n junction. Further, because of the relatively short carrier diffusion length, the optimum thickness of the i-layer is restricted to 0.5–0.7  $\mu\text{m}$  although the penetration depth of 1.8 eV photons (for the same band gap of a-Si:H) is around 5.0  $\mu\text{m}$ . One of the major limitations in attaining higher efficiency in such cells is the loss of incident radiations because of the large bandgap and small thicknesses used for the fabrication of solar cells. Also, the cells have poor response at higher wavelengths. Attempts to make low band gap a-Si:H with tolerably low density of gap states have been unsuccessful as there appears a correlation between optical bandgap and disorder in the material. To improve the performance of the solar cell, effective utilization of unabsorbed high energy photons ( $> E_g$ ) and that of low energy photons is required. One way to improve upon the efficiency of a-Si solar cell is to utilize carrier confinement by employing highly reflecting back electrode and a textured back surface. Solar cells having efficiency  $\sim 9.3\%$  have been reported (Hamakawa and Okamoto 1984) using such principles. Another promising way is to use the concept of tandem cells of varying bandgap. Theoretically more than 30% efficiency can be achieved for two stacked cells (Fan and Palm 1983). Hamakawa and Okamoto (1984) developed ITO/n-i-p-a-Si:H/n-a-Si:H/poly c-Si/Ag stacked cells having 12.5% efficiency. Since the device is fabricated on Si wafer, it is not cost-effective. However, if thin films of semiconductors having optimum bandgap ( $\sim 1.5$  eV) are used, cost-effective high efficiency devices are expected. Among many others, Cu chalcopyrite compound semiconductors CuInX<sub>2</sub> (where X = S, Se, Te), are promising because of high absorption coefficient and bandgap in the range of  $\sim 1$ –1.6 eV, valence controllability (p- or n-type) with control on varying electrical parameters and producibility of large area of films. A heterojunction of this material with a-Si:H will make best use of their optimum material properties for efficiency improvement.

hieve this an understanding of the material and its junction behaviour is essential. With this in view, we have prepared junctions of  $p\text{-CuInS}_2$  with  $a\text{-Si:H}$  in the ructure  $\text{Al}/p\text{-CuInS}_2/a\text{-Si:H}/\text{SnO}_x\text{:F}/\text{glass}$ . This paper describes the junction haviour of such devices.

### Experimental details

lms of  $a\text{-Si:H}$  (bandgap 1.8 eV and resistivity  $\sim 10^8 \Omega\text{m}$ ) were deposited by r.f. uttering on  $\text{SnO}_x\text{:F}$  coated glass substrates of sheet resistance  $\sim 10 \Omega/\square$  acting as ck electrode.  $p\text{-CuInS}_2$  films were deposited by spray pyrolysis (Tiwari *et al* 1985). sistivity of the sprayed  $\text{CuInS}_2$  films can be varied by changing the Cu/In ratio in the ray solution. The substrate temperature for this deposition was kept at  $\sim 200\text{--}250^\circ\text{C}$ , suring that during the deposition of  $\text{CuInS}_2$  film there is no hydrogen evolution from e hydrogenated  $a\text{-Si}$  film. At this stage annealing in inert ambient is carried out at  $0^\circ\text{C}$  for 45 minutes and finally Al is evaporated on  $\text{CuInS}_2$  to make the top contact. The frequency dependence of capacitance was measured using an LCR bridge for low quencies and a Wayne-Kerr bridge for higher frequencies ( $> 10 \text{ kHz}$ ). An automatic V plotter was used to plot the capacitance-voltage characteristics of the junction at 0 kHz. The C-V at 1 MHz was measured using an MSI junction profiler model 893. ie current-voltage characteristics (I-V) of the junctions were plotted using an automatic I-V plotter. For light I-V an ORIEL solar simulator having intensity  $100 \text{ mW/cm}^2$  was used. Details of the experimental set-up have been described ewhere (Purushotam *et al* 1982, 1985).

### Results and discussion

order to study the nature of traps, the frequency dependence of capacitance was asured from 100 Hz to 1 MHz. Figure 1 shows the results. At 500 Hz, the measured

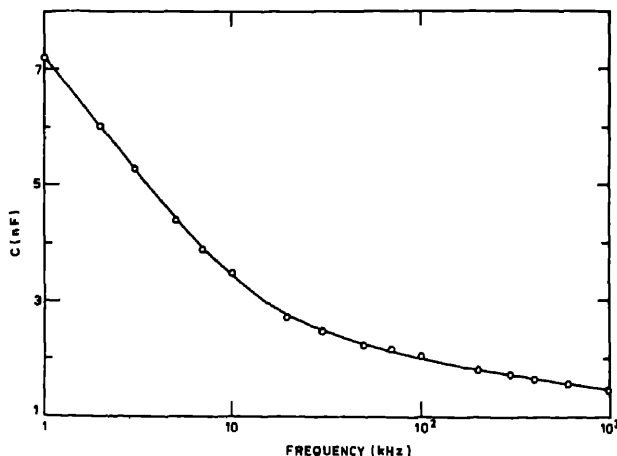


Figure 1. Frequency dependence of capacitance for a typical junction.

capacitance was 90 nF and it varied almost linearly with  $\log f$  in the region 1 to 1 and 30 kHz to 1 MHz implying that the time constant of traps is varying indic band of deep donor levels with the response time having an exponential distributi higher frequencies ( $f > 1/\tau$ ), deep traps respond very slowly but the shallow having fast response time respond to the applied a.c. voltage and the capac decreases. As the frequency of a.c. signal decreases, deep traps start responding, c shielding of the bulk traps (shallow) and dielectric relaxation, thus increas capacitance. Note that frequencies  $\geq 100$  kHz are high enough to neglect die relaxation phenomena and thus C-V characteristics can be studied for the evalua depletion layer width,  $\omega$ , and barrier voltage,  $V_b$ .

Figure 2 shows the variation of  $1/C^2$  and  $\omega^2$  with bias voltage of junctions C 0.32  $\mu\text{m}$  thick *a*-Si:H films with a  $\text{CuInS}_2$  (resistivity  $1.5 \times 10^3 \Omega\text{m}$ ) film. We se  $1/C^2$  varies almost linearly with reverse bias establishing the formation of : junction. For 0.32  $\mu\text{m}$  *a*-Si:H film junction, deviation from linear behaviour is ob above 2.5 V because the whole of *a*-Si:H is depleted at this voltage and breakd expected. Another interesting aspect is the sublinearity in the forward bias regio could be because of the interface states introduced during the junction form Figure 3 shows the  $\omega^2$  vs bias voltage for three junctions with  $\text{CuInS}_2$  of  $1.5 \times 1 \times 10^2$  and 65  $\Omega\text{m}$  resistivities and *a*-Si:H film of  $\sim 0.5 \mu\text{m}$  thickness. We calculated the donor density ( $N_D$ ) and barrier height from the slope and inter these curves. The calculated carrier density ranges from  $3.1$  to  $6.8 \times 10^{22} \text{ m}^{-3}$  a barrier height varies with the resistivity of  $\text{CuInS}_2$  films from 0.26 to 0.55 V. Jur made with  $\lesssim 10 \Omega\text{m}$  resistivity show insignificant bias dependence and som give unusually high  $V_b$  ( $\geq 1.0$  V).

I-V characteristics of the sample indicate that a good rectifying junction b *a*-Si:H and  $\text{CuInS}_2$  is formed. As-deposited samples show some hysteresis vanishes in annealed samples. It is observed that series resistance decrease decreasing  $\text{CuInS}_2$  resistivity but the samples made with lower resistivity  $\text{CuInS}_2$  ( $\lesssim 10 \Omega\text{m}$ ) always show capacitive-type hysteresis behaviour although in such s the series resistance is relatively low ( $\lesssim 100 \Omega$ ) with high rectification. The ju show photovoltaic behaviour when illuminated under light. Figure 4 shows the V of samples 1 and 3, dark I-V of sample 3 is also included. The cross-over of lig

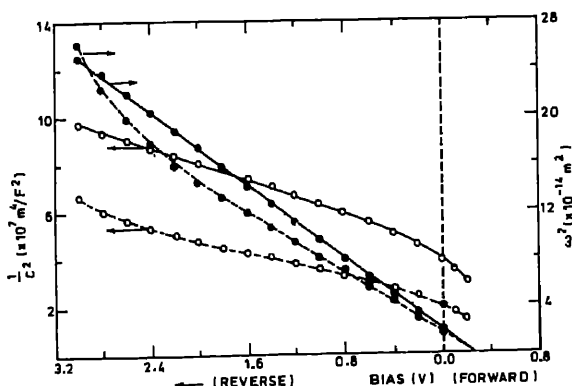
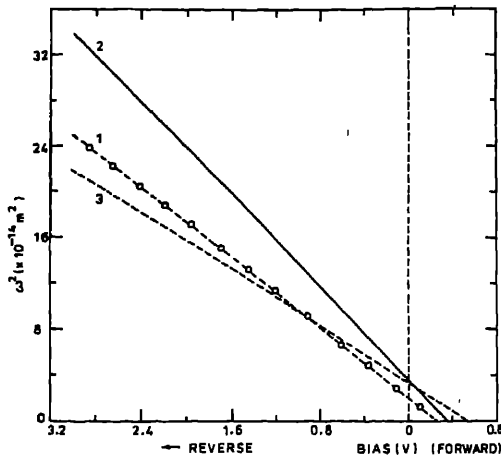
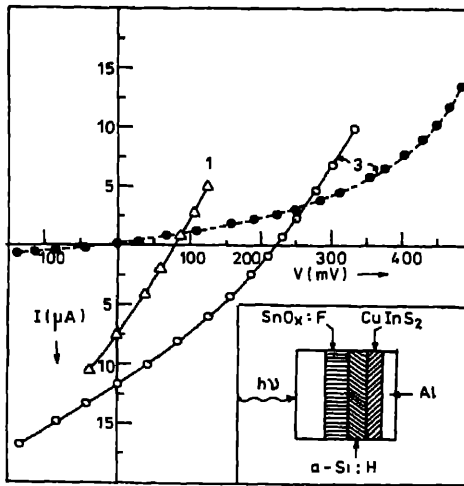


Figure 2. Variation of  $1/C^2$  (O) and  $\omega^2$  (●) with bias voltage for 0.5  $\mu\text{m}$  (—) 0.32  $\mu\text{m}$  (-----) thick *a*-Si:H film.



**Figure 3.** Variation of  $\omega^2$  with bias voltage for junctions with different  $\text{CuInS}_2$  resistivities. 1.  $1.5 \times 10^3 \Omega\text{m}$ ; 2.  $3.6 \times 10^2 \Omega\text{m}$  and 3.  $65 \Omega\text{m}$ .



**Figure 4.** Current-voltage characteristics of junctions 1 and 3 (as described in figure 3). Inset shows the structure of the junction.

dark I-V may be because of photoconductivity of a-Si:H. Spectral response measurements show a broad peak from 0.6 to 0.87  $\mu\text{m}$ . Detailed analysis of the junction behaviour and its photoresponse analysis will be published separately (Tiwari *et al* 1985).

#### 4. Conclusions

- (i) Rectifying junctions have been formed between a-Si:H and  $\text{CuInS}_2$ .
- (ii) Barrier voltage of the junction is found to depend on the resistivity of  $\text{CuInS}_2$

films and increases from 0.26 to 0.55 V on decreasing the resistivity of CuInS<sub>2</sub> film from  $1.5 \times 10^3 \Omega\text{m}$  to 65  $\Omega\text{m}$ .

(iii) Junctions show photoresponse which depend on the resistivity of CuInS<sub>2</sub> film  $V_{oc} = 0.22$  V and  $I_{sc} = 0.2$  mA/cm<sup>2</sup> have been observed in good junctions.

## References

Fan J C C and Palm B J 1983 *Solar Cells* **10** 81

Hamakawa Y and Okamoto H 1984 *Jpn Annu. Rev. Electron. Comput. Telecommun.; Amorphous semiconductor technologies and devices* (ed.) Y Hamakawa **16** 208

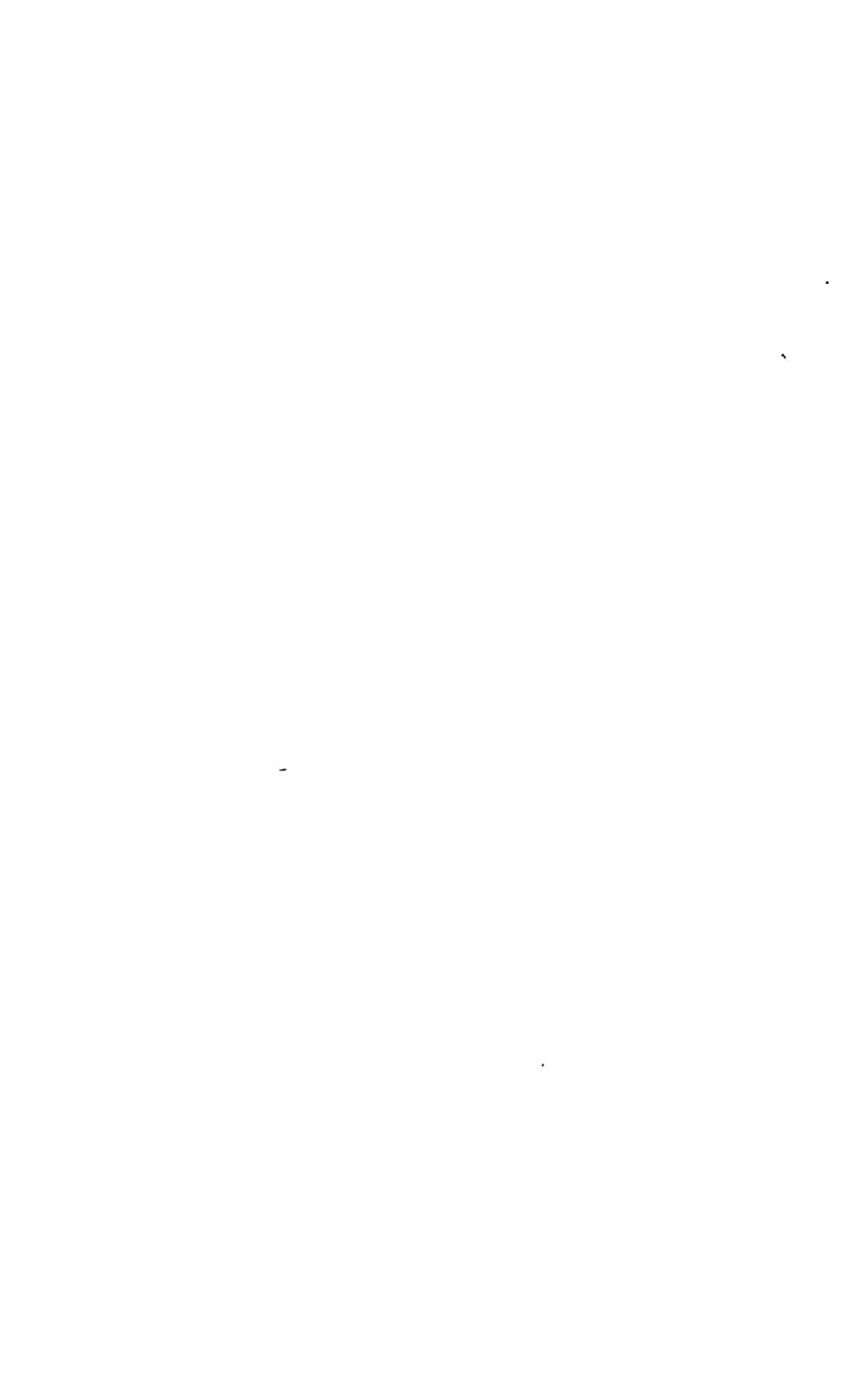
Purushotam M, Mukerjee A K and Chopra K L 1982 *Rev. Sci. Instrum.* **53** 1749

Purushotam M, Mukerjee A K and Chopra K L 1985 *Indian J. Pure Appl. Phys.* (accepted)

Tiwari A N, Pandya D K and Chopra K L 1985 *Thin Solid Films* (accepted)

Tiwari A N, Kumar S, Sastry O S, Pandya D K and Chopra K L 1985 (to be communicated)

Uchida K 1984 *Jpn. Annu. Rev. Electron. Comput. Telecommun.; Amorphous semiconductor technologies and devices* (ed.) Y Hamakawa **16** 186



## Flash-evaporated thin films of $\text{CuInSe}_2$

R D PACHORI, A BANERJEE and K L CHOPRA

Thin Film-Solid State Technology Laboratory, Indian Institute of Technology, New Delhi 110016, India

**Abstract.** Flash-evaporated technique has been developed for deposition of  $\text{CuInSe}_2$  films. A control over the stoichiometry and chemical composition of the films has been obtained by varying the deposition parameters. Single phase chalcopyrite structure films with optical gap  $\sim 1.15$  eV have been obtained. The electronic properties of the films have been tailored for solar cell applications.

**Keywords.** Flash evaporation; copper; indium; selenium.

### 1. Introduction

The attainment of conversion efficiency, greater than 10% using  $\text{CuInSe}_2$  as an active material in all thin film solar cell has led to considerable research interest in this material (Mickelsen *et al* 1984). Thin film heterojunction  $p\text{-CuInSe}_2/n\text{-CdS}$  and  $p\text{-CuInSe}_2/\text{Zn}_{1-x}\text{Cd}_x\text{S}$  cells have yielded efficiencies around 9.5 and 11.5%, respectively. A number of investigations have since been undertaken to understand the properties of  $\text{CuInSe}_2$  relevant to photovoltaic conversion (Kazmerski 1978; Kazmerski *et al* 1981; Sobczak *et al* 1980; Naufi *et al* 1984; Abernathy *et al* 1984). It has been established that Cu to In ratio and metal (Cu + In) to selenium ratio in the films are critical parameters affecting the film properties (Shay and Wernick 1975; Masse and Redjai 1984). As a consequence only three source evaporation techniques for deposition of  $\text{CuInSe}_2$  films have succeeded for solar cell applications. However, with an increased understanding of the dependence of the properties of  $\text{CuInSe}_2$  on stoichiometry and structure, new techniques for film deposition have been used which yield properties comparable to those of films prepared by the three-source technique. These techniques include single source pyrolysis (Pamplin and Feigelson 1979; Gorska *et al* 1980; Abernathy *et al* 1981), sputtering (Piekoszewski *et al* 1980; SERI Report 1981), chemical vapour deposition (SERI Report 1981) and screen printing (Pachori *et al* 1985).

Flash evaporation technique has been used earlier for the deposition of  $\text{CuInSe}_2$  films but discarded due to the difficulty of producing films of reproducible quality (Horig *et al* 1978; Durny *et al* 1980). We have revived this technique due to its simplicity and potential to deposit multi-component films with widely varying vapour pressure constituents. Further, with a vastly improved knowledge of the properties of  $\text{CuInSe}_2$  we have succeeded in producing  $\text{CuInSe}_2$  films with excellent and reproducible photovoltaic properties. Since our objective is to fabricate thin film  $\text{CuInSe}_2/\text{CdS}$  solar cells,  $p$ -type  $\text{CuInSe}_2$  films have been studied in greater detail. This paper describes the preparation and properties of  $\text{CuInSe}_2$  films obtained by the flash evaporation technique. Preliminary results on  $\text{CuInSe}_2/\text{CdS}$  junction are also given.

## 2. Experimental details

Ingots of  $\text{CuInSe}_2$  were prepared from its constituent elements, viz copper, indium and selenium. The elements weighed in the stoichiometric proportion were sealed in a quartz ampoule under vacuum ( $\sim 10^{-5}$  torr) and homogenized at  $\sim 1000^\circ\text{C}$  for 48 hr in a furnace. The ingots were then powdered to a mean particle size  $\sim 150\ \mu\text{m}$ . The  $\text{CuInSe}_2$  powder was gradually dropped onto a closed molybdenum boat heated to  $\sim 1400^\circ\text{C}$  in vacuum ( $\sim 10^{-5}$  torr). The substrate temperature was maintained at  $450 \pm 10^\circ\text{C}$  using a temperature controller. The thickness and rate of deposition were monitored by a quartz crystal thickness monitor. After deposition, the films were annealed at  $\sim 475^\circ\text{C}$  for 30–45 min in vacuum. The selenium concentration in the films was varied by controlling the concentration in the powder itself. For Se-deficient cases, the starting alloy was prepared in a non-stoichiometric manner with pre-determined Se deficiency. Se-excess films were prepared by mixing a weighed amount of free selenium powder with the stoichiometric  $\text{CuInSe}_2$  powder before evaporation. It may be noted that the Se concentration mentioned in the text refers to the concentration in the powder before evaporation and not in the final film. Auger analysis was, however, used to determine the chemical composition of the films. In the text the Se-deficient films have been indicated with negative Se at.wt. % concentration whereas Se excess films are denoted by positive concentration.

The thickness of the films was measured by the Taylor-Hobson Talystep instrument. The electronic properties of the films were determined from d.c. Hall measurements using van der Pauw geometry. The optical transmittance at various wavelengths was measured using Hitachi 330 Spectrophotometer. Solar cells were fabricated by evaporating 2–3  $\mu\text{m}$  thick CdS layer on top of the annealed  $\text{CuInSe}_2$  films at a substrate temperature  $200^\circ\text{C}$ . The resistivity of CdS layer was in the range of 1–20 ohm-cm. Silver paste was used for taking contacts from both materials.

## 3. Results and discussion

The structural properties of the films were studied using x-ray diffraction (XRD) and transmission electron microscopy (TEM). XRD results show that the films are polycrystalline and the as-deposited flash-evaporated films are multiphase containing sphalerite  $\text{CuInSe}_2$  and excess-free selenium distributed throughout the films. By vacuum annealing of the as-deposited films, single phase chalcopyrite  $\text{CuInSe}_2$  films with lattice constants  $a = 8.70\ \text{\AA}$  and  $c = 11.70\ \text{\AA}$  have been obtained. The values of lattice constants for annealed  $\text{CuInSe}_2$  films are quite close to the reported values (Kazmerski *et al* 1976). Annealing of as-deposited films in vacuum produces two important changes in the films, namely, structural transformation from sphalerite to chalcopyrite and reevaporation of excess-free selenium. No traces of indium oxide and copper oxide have been found. The average grain size of the as-deposited and the annealed films, as determined by TEM, are  $\sim 60$ – $80\ \text{nm}$  and  $\sim 90$ – $120\ \text{nm}$ , respectively.

Figure 1 shows the transmittance spectra of the as-deposited (+ 17 at. wt. % excess Se) and the corresponding vacuum-annealed films. For the as-deposited films, two distinct slopes corresponding to the absorption edges of  $\text{CuInSe}_2$  and free selenium are discernible. On vacuum annealing, the slope corresponding to free selenium absorption



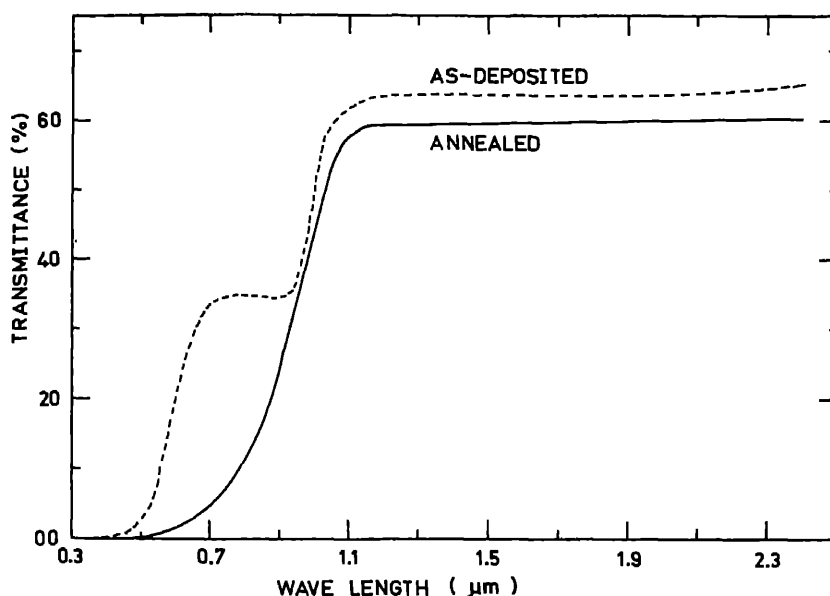


Figure 1. Transmittance of flash-evaporated CuInSe<sub>2</sub> films (+ 17 at. wt. % Se).

edge disappears. This suggests that the as-deposited films are multiphase in nature containing CuInSe<sub>2</sub> and free selenium. The undesirable excess Se is removed in vacuum annealing step.

The optical absorption coefficient of the films has been calculated at various wavelengths from the transmittance values of two films of different thickness using formula

$$\alpha = \frac{\ln [T_1/T_2]}{(t_2 - t_1)},$$

where  $\alpha$  = absorption coefficient,  $T_1$  and  $T_2$  are the transmittance of the film of thickness  $t_1$  and  $t_2$  respectively. Figure 2 shows a plot of the variation of  $\alpha^2$  with  $h$ . A straight line behaviour establishes that the films have a direct bandgap of  $\sim 1.1$  eV. The value of  $\alpha$  at  $0.55 \mu\text{m}$  is  $\sim 10^5 \text{ cm}^{-1}$  for the annealed films and compares well with reported data (Sun *et al* 1978).

The chemical composition and metal-to-Se ratio for various vacuum-annealed films as determined from Auger results are shown in table 1. The analysis shows that the Se evaporated is not entirely incorporated in the film which is attributed to the high vapour pressure and low sticking coefficient of Se. The metal-to-Se ratio is less than unity for films prepared from excess Se concentration powder and greater than unity for deficient Se concentration powder.

The dependence of the electronic properties of the films on the Se concentration of the powder is shown in figure 3. Three different regions can be identified in the figure: (1)  $n$ -type (left side), (2)  $p$ -type (right side), and (3) high resistivity intrinsic-like behaviour (central region). Correlation with Auger results (see table 1) shows that the conductivity type of the films is governed by the metal-to-Se ratio. The films are  $n$ -type if the ratio is greater than one and  $p$ -type if the value is less than one. Figure 3 shows that as

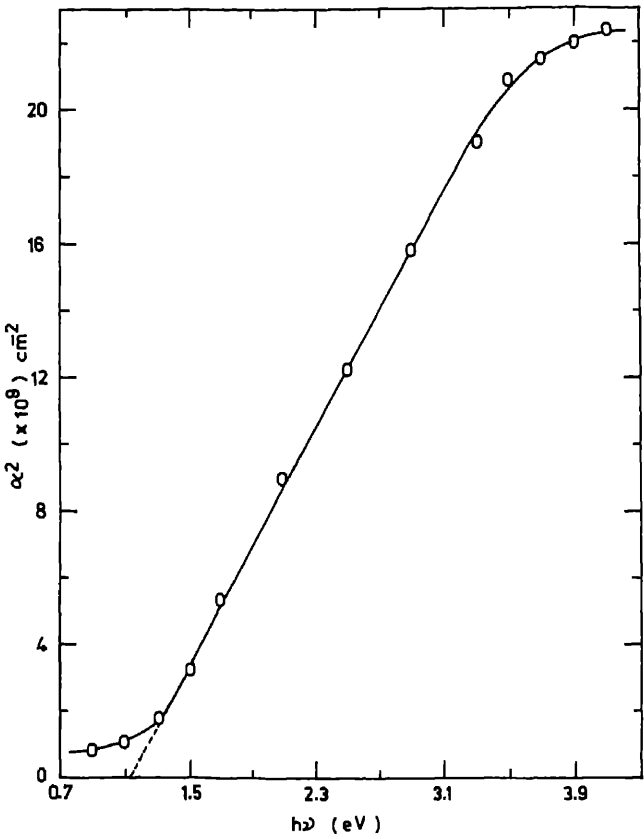


Figure 2. Variation of  $\alpha^2$  with  $h\nu$  of vacuum-annealed  $\text{CuInSe}_2$  films (+ 17 at. wt. % Se).

Table 1. Auger composition analysis of flash-evaporated  $\text{CuInSe}_2$  films

Selenium concentration in powder (at. wt. %)	Copper (at. %)	Indium (at. %)	Selenium (at. %)	Metal/ selenium ratio
-10	25.2	31.6	43.2	1.32
- 5	24.0	30.3	45.7	1.19
0	22.3	30.2	48.5	1.08
+ 5	22.0	26.8	51.2	0.95
+10	20.2	26.5	53.3	0.88
+15	19.0	25.2	55.8	0.79
+16	18.8	24.8	56.4	0.77
+17	18.5	24.5	57.0	0.76
+18	18.0	24.5	57.7	0.74
+19	17.7	24.3	58.0	0.72

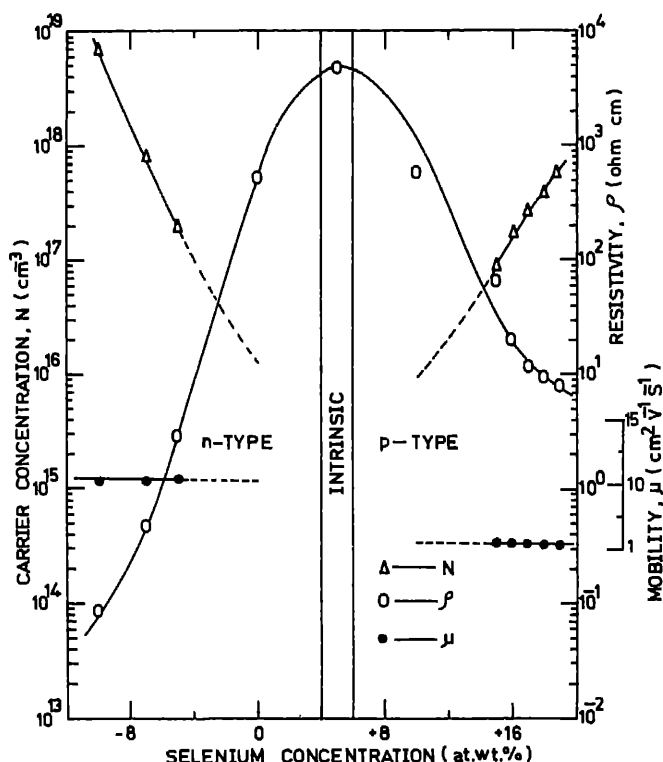


Figure 3. Variation of carrier concentration ( $N$ ), mobility ( $\mu$ ) and resistivity ( $\rho$ ) of vacuum annealed CuInSe<sub>2</sub> films with deficit/excess selenium in powder.

concentration is increased or decreased beyond the stoichiometric composition resistivity decreases as the films become more and more of  $p$ -type or of  $n$  respectively. Further, the decrease in resistivity is almost entirely due to an increase in the free electron or hole concentration as the case may be. Mobility essentially remains constant at  $\sim 10 \text{ cm}^2 \text{V}^{-1} \text{s}^{-1}$  for  $n$ -type films and  $\sim 1 \text{ cm}^2 \text{V}^{-1} \text{s}^{-1}$  for  $p$  films. The films with Se concentration +20 at. wt. % are of  $p$ -type but multiphase nature containing both CuInSe<sub>2</sub> and Se.  $p$ -type films with carrier concentration of  $\times 10^{17} \text{ cm}^{-3}$ , resistivity of  $\sim 1.2 \times 10^1 \text{ ohm cm}$  and mobility of  $\sim 1.0 \text{ cm}^2 \text{V}^{-1} \text{s}^{-1}$  have been used to fabricate junctions of  $p$ -CuInSe<sub>2</sub>/ $n$ -CdS. The CdS films have been deposited on the CuInSe<sub>2</sub> films by vacuum evaporation. The junction has exhibited an open circuit voltage of the order of 350–375 mV. Having established the feasibility of using the CuInSe<sub>2</sub> films for making junctions, present efforts are directed towards attaining high conversion efficiencies.

#### 4. Conclusions

The feasibility of using a flash evaporation technique for the deposition of thin film CuInSe<sub>2</sub> has been established. The properties of the films can be tailored by controlling the selenium concentration.

the stoichiometry of the films, and vacuum-annealing treatments. CuInSe<sub>2</sub>/CdS junctions fabricated using these films have shown high  $V_{oc} = 350\text{--}375$  mV.

## References

- Abernathy C R, Mates C W, Anani A A, Haba B and Smestad G 1984 *Appl. Phys. Lett.* **45** 890
- Durny R, Hill A E and Tomlinson R D 1980 *Thin Solid Films* **69** L11
- Gorska M, Beaulieu R, Loferski J J, Roessler B and Beall J 1980 *Solar Energy Mater.* **2** 343
- Horig W, Neumann H and Sobota H 1978 *Thin Solid Films* **48** 67
- Kazmerski L L, Ayyagiri M S, Sanbora G A, White F R and Merrill A J 1976 *Thin Solid Films* **37** 323
- Kazmerski L L 1978 *Solid State Electron.* **21** 1545
- Kazmerski L L, Jamjoum O, Ireland P J, Mickelson R A and Chen W S 1981 *J. Vac. Sci. Technol.* **21** 486
- Masse G and Redjai E 1984 *J. Appl. Phys.* **56** 1154
- Mickelson R A, Chen W S, Hsio Y R and Lowe V 1984 *IEEE Trans. Electron Devices* **ED31** 542
- Naufi R, Axton R, Herrington C and Deb S K 1984 *Appl. Phys. Lett.* **45** 668
- Pachori R D, Banerjee A and Chopra K L 1985 Paper presented at the National Solar Energy Conference, Bhopal
- Pamplin B and Feigelson R S 1979 *Thin Solid Films* **60** 41
- Piekoszewski J, Loferski J J, Beaulieu R, Beall J, Roeslev R and Shewchun J 1980 14th IEEE Photovoltaic Specialists Conference, San Diego
- SERI Semi Annual Report No. SERI/STR-211-2203 1981 Solar Energy Research Institute, Golden Colorado, USA
- SERI Final Report No. SERI/STR-211-2247 1981 Solar Energy Research Institute, Golden Colorado, USA
- Shay J L and Wernick J H 1975 *Ternary chalcopyrite semiconductor growth; Electronic properties and applications* (New York: Pergamon Press)
- Sobotta H, Neumann H, Riede V, Kuhn G, Seletmann J and Oppermann D 1980 *Phys. Status Solidi* **60** 531
- Sun L Y, Kazmerski L L, Clark A H, Ireland P J and Morton D W 1978 *J. Vac. Sci. Technol.* **15** 265

## Growth of polysilicon and silicide films for MOS-VLSI application

S K AGARWAL, M BAL, G D SHARDA, MAHAVIR SINGH and  
K K LAROA

Solid State Physics Laboratory, Lucknow Road, Delhi 110007, India

**Abstract.** Doped and undoped polycrystalline silicon films were grown by APCVD thermal evaporation techniques. The effect of growth and annealing conditions on crystalline nature of the films and their properties were studied by electrical, optical, x diffraction and SEM techniques. Metal silicides such as  $\text{TiSi}_2$  and  $\text{PtSi}_2$  were prepared by evaporation technique over polysilicon layers to study their suitability in microelectronic applications. Some of the properties of polysilicon and silicides are discussed.

**Keywords.** Metal-oxide semiconductor; atmospheric pressure chemical vapour deposition; very large scale integration; polycrystalline silicon films

### 1. Introduction

Polycrystalline silicon films have many applications in microelectronics technology. These films are being used to simplify the fabrication technology and to obtain improved parameters of semiconductor devices.

Undoped polycrystalline films are used in planar high voltage diodes, transistor dielectrically isolated circuits and in integrated circuits made with silicon on insulated substrate (Clarke and Zoroglu 1970; Davidson and Lee 1969; Kuhn and R 1973). Doped polycrystalline films have been used as interconnect lines, as gate electrodes in silicon gate MOS integrated circuits (Faggin and Klein 1970), and as load value resistors in static memory circuits. Other applications include distributed RC filters, lossy dielectric in SiPOS devices, low cost solar cells, a dopant source in bipolar and in self-aligned contact metal-oxide semiconductor (MOS) technology (Fripp and Sterner 1970).

Use of polycrystalline silicon films is therefore of special importance in preparation and characterization of these films (Kamins 1975; Mai *et al* 1971; Ric and Ley 1981; Feldman *et al* 1978; Anderson 1973).

A major limitation of polycrystalline silicon films as a gate material for very large scale integration (VLSI) applications is their limited conductivity which restricts their usefulness as an interconnection level (Crowder and Zirinsky 1979). Metal silicides such as  $\text{TiSi}_2$ ,  $\text{PtSi}_2$  were prepared to study their suitability in microelectronic applications.

This paper examines some of the properties of polysilicon and silicides, grown by atmospheric chemical vapour deposition and by thermal/electron beam evaporation techniques.

## 2. Experimental

### 2.1 Atmospheric pressure chemical vapour deposition (APCVD) technique

Polycrystalline silicon films were deposited from  $\text{SiH}_4\text{-N}_2$  mixtures at temperatures ranging 600–750°C in a horizontal resistance heated reactor shown in figure 1. These films were grown on polished fused quartz substrates and  $\text{SiO}_2$  deposited silicon wafers. However, the best films were deposited at 650°C with a silane-to-nitrogen ratio of  $1:1.5 \times 10^2$ . The deposition rate was kept at about 500 Å/min.

### 2.2 Evaporation technique

High purity (5 N) silicon powder was evaporated using either a beryllium oxide crucible heated by tantalum helical filament surrounded by tantalum heat shields or an electron beam gun, on polished quartz substrates and  $\text{SiO}_2$  deposited silicon wafers at a working pressure of about  $2 \times 10^{-5}$  torr. The substrates were heated by a radiation heater made of tantalum sheet positioned on top of the substrate holder. Films were deposited at different substrate temperatures ranging from 600°C to 900°C and annealed at the deposition temperature for about 1 hr. This enabled reduction of the internal stresses developed during deposition and ensured better film adhesion on the quartz substrates. The rate of deposition was of the order of 1000 Å/min.

### 2.3 Formation of silicides

Several potential fabrication techniques were investigated including sputtering, chemical vapour deposition and coevaporation of elements with a multihearth electron beam

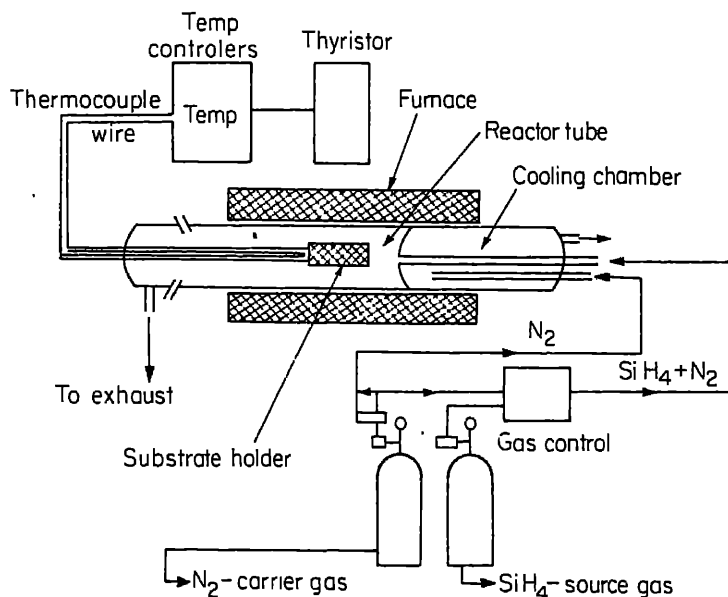


Figure 1. Schematic layout of polysilicon deposition system.

evaporation unit. Direct reaction between silicon and the refractory metal was employed because of the strong dependence of this reaction upon the interface between the metal and silicon (e.g. native oxides) (Kumar 1976; Locker and Capico 1976).

The following techniques were used: coevaporation from the elements on polished quartz substrates, and evaporation of titanium metal on single crystal silicon wafers having sheet resistance of the order of 60 ohms/ $\square$ . Using an electron beam gun, titanium was evaporated at a pressure of about  $10^{-6}$  torr at 3500°C. The vacuum chamber was flushed a number of times with argon to remove traces of oxygen which are detrimental to silicide formation (Murarka *et al* 1980). Samples were annealed at temperatures ranging from 600 to 750°C in a vacuum coating chamber at  $10^{-6}$  torr for about 30 min.

### 3. Results and discussion

#### 3.1 Effect of annealing temperature

When annealed at higher temperatures the grains grow in size. The effect of annealing temperature on the grain size was investigated between 700 and 1100°C for APCVD polysilicon grown at 650°C. Heat treatment was performed in a standard resistance heated furnace in an inert atmosphere of argon gas for 30 minutes. The effect of annealing temperature upon grain size is shown in figure 2. No noticeable increase was observed in grain size with annealing between 700°C and 1000°C. Above 1000°C grain size increase from 0.2  $\mu\text{m}$  to 1.2  $\mu\text{m}$ . SEM micrographs of polysilicon film grown at 650°C followed by annealing at 1050°C are shown in figure 3. These results agree with published data (Wada and Nishimatsu 1978; Mei *et al* 1981).

#### 3.2 Effect of deposition temperature

X-ray diffraction patterns of polysilicon films deposited at different substrate temperatures are shown in figure 4. Using Scherrer formula the grain size of these films was determined.

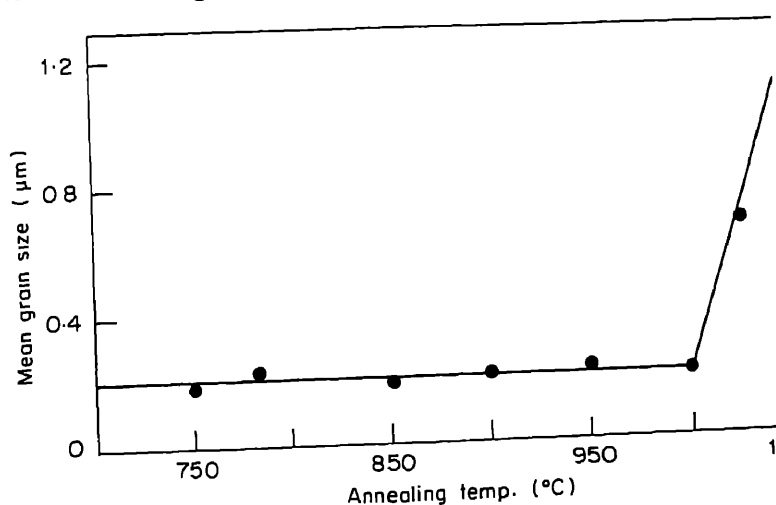
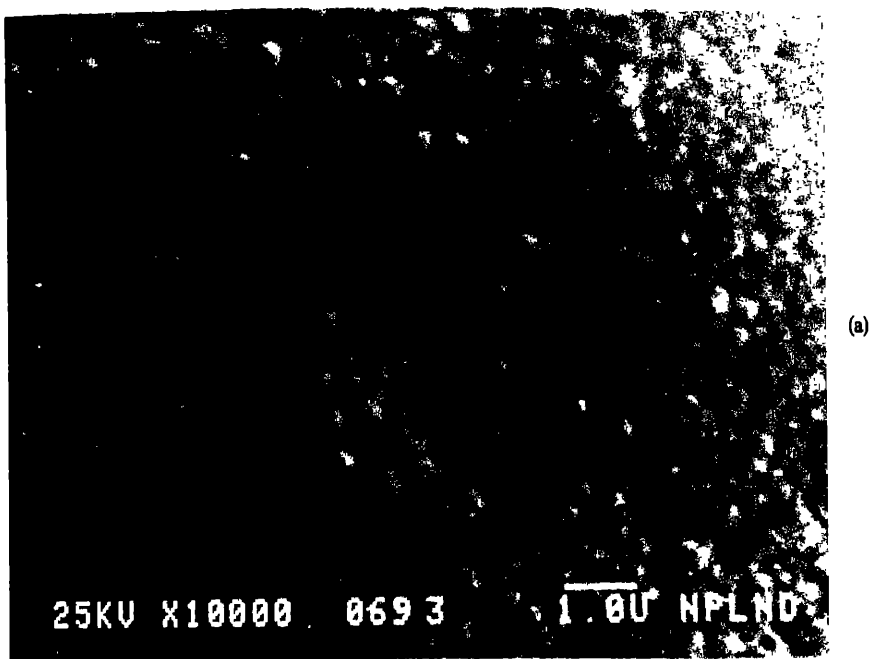


Figure 2. Annealing temperature vs mean grain size of polysilicon films grown at 650°C.



**Figure 3.** SEM micrograph of polysilicon films (a) deposited at 650°C. (b) annealed 1050°C for 30 min.



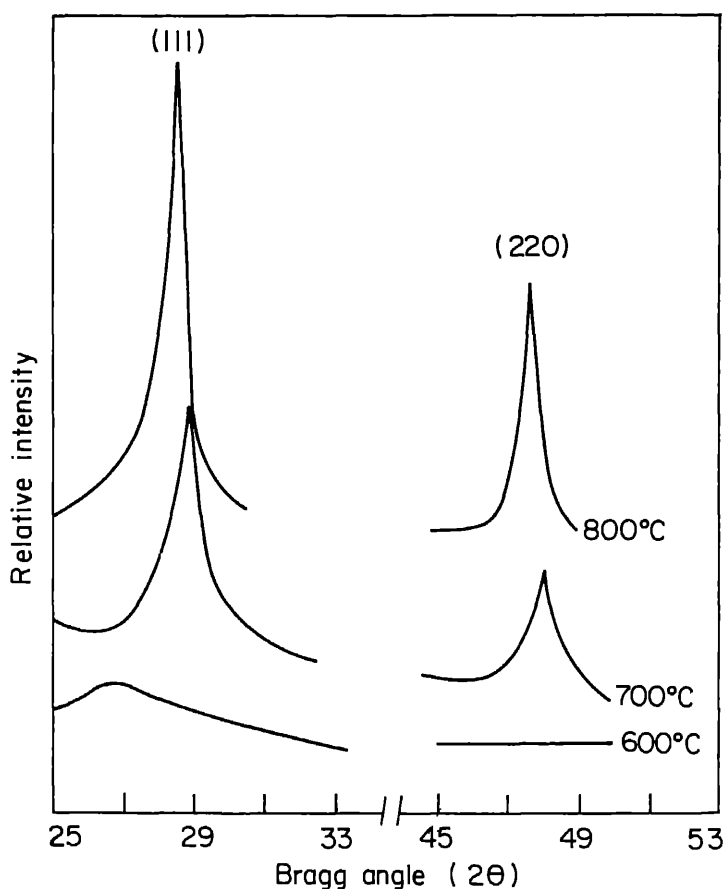


Figure 4. X-ray diffraction pattern of polysilicon films, deposited at different temperatures.

can be calculated from x-ray diffraction pattern. The x-ray diffraction patterns of the films deposited at different substrate temperatures are almost identical; however, an increase in crystallinity with increasing substrate temperature is observed. With increasing substrate temperatures, the width of diffraction peaks decreases and the intensity ratio of (220) to (111) peak increases due to the change in the preferential orientation of the crystallites. This has also been observed by Veprek *et al* (1981). The grain size calculated using Scherrer formula for films deposited from 700°C to 900°C varies from 100 Å to 200 Å. The films grown below 600°C, however, show an amorphous nature.

### 3.3 Effect of doping

A mixture of high purity silicon with 1% aluminium was evaporated at  $10^{-5}$  to pressure on mirror polished quartz substrates kept at 500°C followed by annealing (for 30 min) at the deposition temperature. The following conclusions have been drawn:

- (i) Grains are uniformly distributed and their size increases as a result of aluminium doping.

- (ii) An undoped poly Si film deposited below 600°C shows amorphous nature. On aluminium doping films grown at 500°C show polycrystalline nature.
- (iii) The resistivity of the films decreases as a result of aluminium doping and sheet resistance of the order of 150 ohm/ $\square$  has been obtained.

The Arrhenius plots of doped and undoped polysilicon films are shown in figures 5 and 6. For the undoped films the calculated activation energy is 0.55 eV which is half the band gap of single crystal silicon. For doped films the activation energy decreases and its value is 0.19 eV which has also been observed earlier (Richter and Ley 1981).

### 3.4 Optical absorption

Figure 7 shows a typical dependence of the absorption coefficient on photon energy in the range of 1 to 3 eV for thermally evaporated Si samples deposited at 900°C and 700°C respectively. The APCVD film grown at 650°C is also shown in figure 7 as also the data of Dash and Newman (1955) for single crystal silicon. It can be seen that the absorption coefficient of a polycrystalline Si film is high in the photon energy range of 1 to 3 eV and exceeds that of a single crystal silicon by an order of magnitude and decreases as the substrate temperature increases. With increasing deposition temperature the crystalline size increases as has been seen from SEM and x-ray studies.

In figure 8 the value of  $(\alpha h\nu)^{1/2}$  vs  $h\nu$  is plotted in the limited range of 0.5–2.5 eV. As expected in the case of indirect transitions there is linear dependence with a threshold at 1.1 eV. This value is in agreement with the indirect band gap of single crystal silicon at room temperature. There is a tail of optical absorption extending to about 0.5 eV. This suggests that at low energies the absorption is associated with some rather well-defined

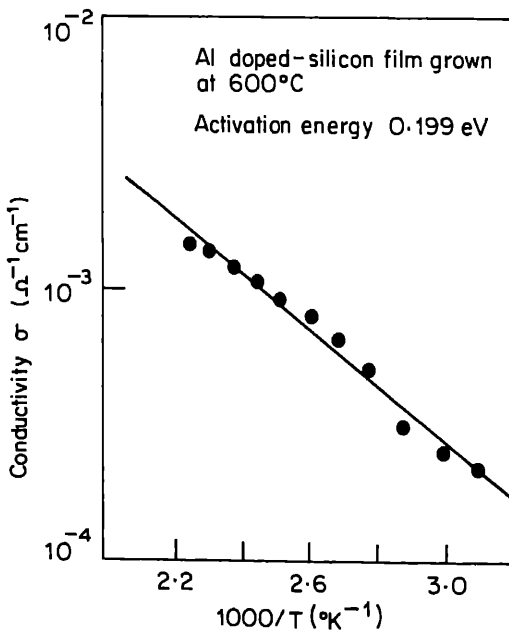


Figure 5. Arrhenius plot for undoped polysilicon films.

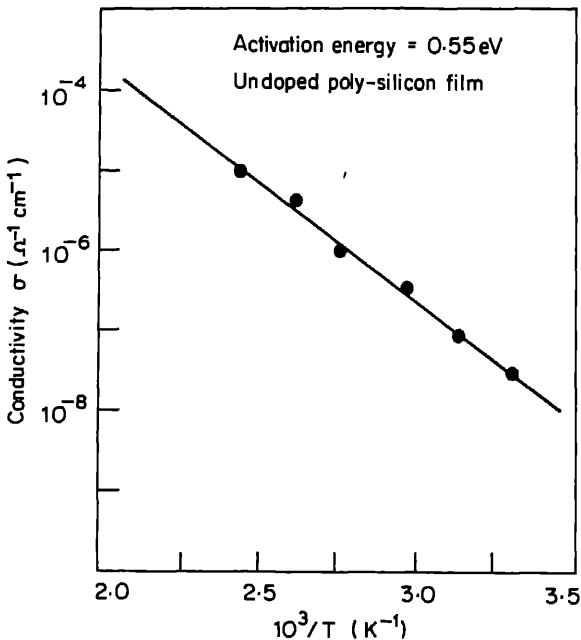


Figure 6. Arrhenius plot for doped polysilicon films.

states in the gap which might be due to (paired) dangling bonds at the surface of the crystallites or due to other defects.

### 3.5 Silicide characteristics

Sheet resistance of titanium silicide as measured by the four-point probe is of the order of 5 to 7  $\Omega/\square$ . Sheet resistance vs annealing temperature is shown in figure 3. Decrease in sheet resistance at higher temperature may be due to either an intermetallic formation or recrystallization of film or both. The lowest resistance obtained is due to complete transformation of metal into its silicide. The thickness of the film is measured by creating a step (by etching the film in buffered hydrofluoric acid solutions) and measuring the step height using the talley step. Silicide thickness of the order of 2000 to 6000 Å is obtained by changing the deposition time. The titanium: silicon ratio in the silicide is 33:67 as observed by EDAX measurements.

## 4. Conclusions

Polycrystalline silicon films grown by CVD and vacuum evaporation techniques were characterized using x-ray diffraction, optical absorption, electrical and SEM techniques. It was found that the doped and the undoped Si films meet all the requirements for gate material and load resistors in MOS devices. Initial experiments on the fabrication and characterization of silicides were carried out.

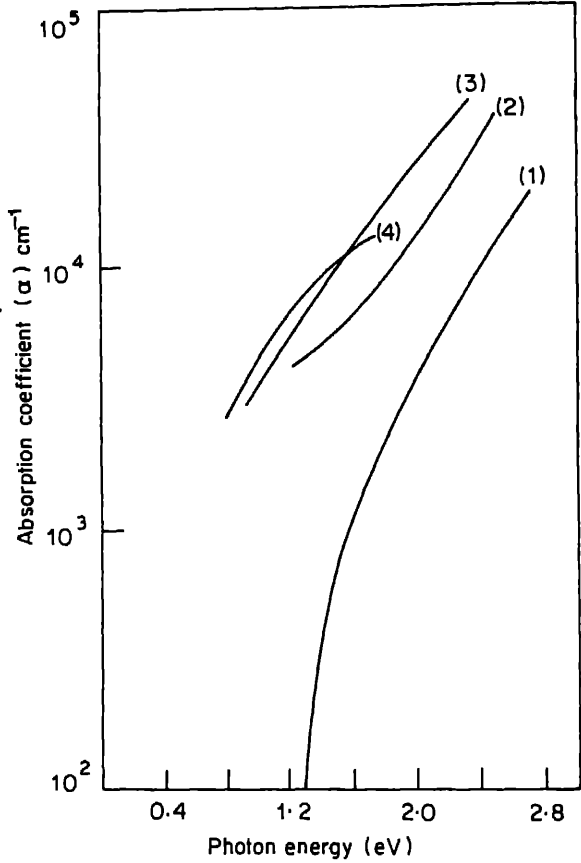


Figure 7. Absorption coefficient vs photon energy for polysilicon films deposited at different temperatures.

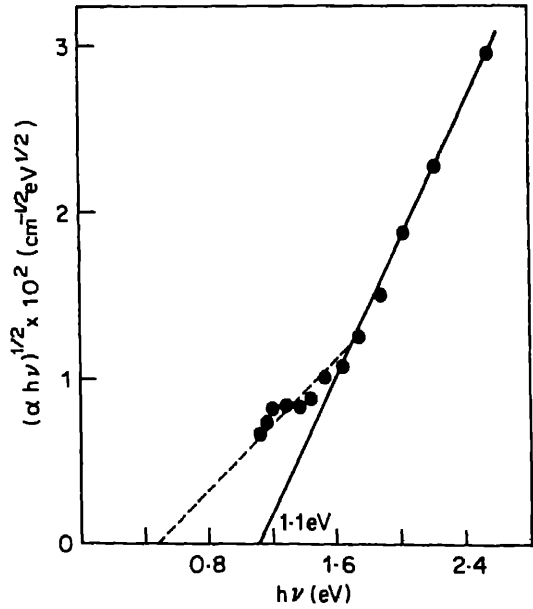


Figure 8.  $h\nu$  vs  $(\alpha h\nu)^{1/2}$  for polysilicon films deposited at 900°C by vacuum evaporation.

## Growth of polysilicon and silicide films

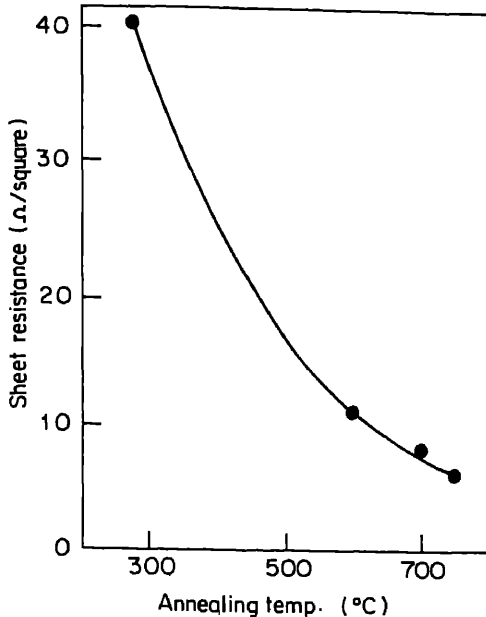


Figure 9. Sheet resistance vs annealing temperature of TiSi<sub>2</sub> films grown by coevaporation of Ti and Si at 300°C.

## References

- Anderson R M 1973 *J. Electrochem. Soc.* **120** 1540
- Clarke L E and Zoroglu D S 1970 *Solid State Electron.* **15** 653
- Crowder B L and Zirinsky S 1979 *IEEE J. Solid State Circuits* Sc-14, **2** 291
- Dash W C and Newman R C 1955 *Phys. Rev.* **99** 1151
- Davidson U and Lee F 1969 *Proc. IEEE* **57** 1532
- Faggin F and Klein T 1970 *Solid State Electron.* **13** 1125
- Feldman C, Norman A B, Charlis H K Jr. and Satkiewicz F G 1978 *J. Electron. Mater.* **7** 309
- Fripp A L and Sterner R L 1970 *J. Electrochem. Soc.* **117** 1569
- Kamins T I 1975 *J. Appl. Phys.* **46** 5247
- Kuhn G L and Rhee C J 1973 *J. Electrochem. Soc.* **120** 1563
- Kumar V 1976 *J. Electrochem. Soc.* **123** 262
- Locker L D and Capio C D 1973 *J. Appl. Phys.* **44** 4366
- Mai C C, Whitehouse T S, Thomas R C and Goldstein D R 1971 *J. Electrochem. Soc.* **118** 331
- Mei L, Rivier M, Kwark Y and Dutton R W 1981 *Silicon Semiconductor* **81-5** 1007
- Murarka S P, Fraser D B, Sinha A K and Levinsten H J 1980 *IEEE Trans. Electron Device* ED-27
- Richter H and Ley L 1981 *J. Appl. Phys.* **52** 7281
- Veprék S, Iqbal Z, Oswald H R and Webb A P 1981 *Solid State Phys.* **14** 295
- Wada Y and Nishimatsu S 1978 *J. Electrochem. Soc.* **125** 1499



## Electrical and structural characteristics of oxides grown from polycrystalline silicon

B B DIXIT, P D VYAS, W S KHOKLE, K MAHADEVAN\*  
and H N ACHARYA\*

Solid State Devices Division, Central Electronics Engineering Research Institute,  
333 031, India

\*Department of Physics and Meteorology, Indian Institute of Technology, Kharagpur,  
721 302, India.

**Abstract.** A comparative study of dielectric properties of polysilicon oxide with silicon dioxide, grown on single crystal silicon, shows that the former is more conducting due to the presence of asperities at polysilicon/SiO<sub>2</sub> interface. This paper also reports attempts to improve the electrical properties of polysilicon oxide by investigating the effects of oxidation temperature, polysilicon deposition temperature and doping on current field characteristics of the polyoxide. Higher doping and higher oxidation temperature yield smoother interfaces, higher breakdown voltages and lower leakage currents. Surface morphology of polysilicon oxide under different process conditions is also studied.

**Keywords.** Polycrystalline silicon; inter level insulator; polyoxide.

### 1. Introduction

Thermal oxide film grown over polysilicon, often referred to as polyoxide, is an important material for integrated circuit technology. These films are used to provide protection layers of polysilicon gate and also as an interlevel insulator in multilevel structures. In very large scale integrated (VLSI) circuits, where thinner dielectric films and high temperature processing are used, the dielectric breakdown of the oxides grown over polysilicon is a major yield and reliability problem. Hence it is necessary to improve the electrical properties of the polyoxide taking into account the usual process conditions. The present investigation is devoted to understanding some of the physical and electrical properties of polyoxide. The effects of oxidation temperature, doping, growth temperature of polysilicon on leakage currents through the polyoxide and morphological change in polyoxide/polysilicon interface are reported.

A comparative study of dielectric properties of polysilicon oxides with oxides grown on single crystal silicon has shown that the former oxides are more conductive than the latter given average field (DiMaria and Kerr 1975) and have a lower breakdown strength. Electrical conduction through polyoxide involves effects of asperities present at polysilicon/polyoxide interface, which causes higher leakage current through the polyoxide (Anderson and Kerr 1977).

### 2. Sample preparation and measurements

Phosphorus doped silicon wafers (0.8–1.2 ohm cm) were thermally oxidized at 1000°C in dry oxygen to grow about 900 Å thick silicon dioxide films. Polycrystalline silicon

Table 1. Breakdown field of samples processed under different conditions.

Sample	Dopant	Doping temp. (°C)	Oxidation temp. (°C)	Oxidation time (min)	Thickness Å	Breakdown field (MV/cm)	
						Poly-Si negative	Field plate negative
1	None	—	850	500	525	5.3	5.6
2	None	—	1050	20	520	7.3	7.2
3	Phosphorous	900	850	20	500	6.1	6.3
4	Phosphorous	900	1050	8	500	8.1	8.2
5	Phosphorous	900	950	6	485	7.8	7.9
6	Phosphorous	1000	950	4	520	8.5	8.4
7	Phosphorous	900	1050	10	800	7.5	7.5
8	Phosphorous	900	1050	12	1000	7.2	7.2

films (5000 Å) were deposited by atmospheric chemical vapour deposition technique. Oxide thickness and polysilicon thicknesses were measured with ellipsometer, bevelling and observation under scanning electron microscope (SEM) respectively. Some of the polysilicon films were phosphorus doped ( $1 \times 10^{20} \text{ cm}^{-3}$ ) in a diffusion furnace. Polyoxide was then grown in dry  $\text{O}_2$  under different process conditions (table 1). With the help of aluminium metallization and photolithography, 20 mils diameter electrodes were fabricated on polyoxide and polysilicon surfaces (figure 1). I-V measurements were carried out using electrometer (Keithley 620) with positive as well as negative field polarities.

### 3. Results

#### 3.1 SEM study of polysilicon/polyoxide interface

Samples were prepared for SEM examination of the polysilicon/polyoxide interface by stripping off the polyoxide in buffered hydrofluoric acid (HF). Direct evidence of the asperites, which is one of the causes of high conductivity observed in polyoxide is best illustrated in the SEM photograph (figure not shown). The flattening of asperites with increase in oxidation temperature of polysilicon is also evident (figure not shown). For phosphorus doped polysilicon samples, no asperites were found at the polysilicon/polyoxide interface (even up to  $15000 \times$  magnification).

#### 3.2 Current field characteristics

The current density field characteristics of polyoxide grown at two different temperatures (850°C and 1050°C) over undoped polysilicon is shown in figure 2. The leakage current density for 1050°C oxidized polysilicon is one decade lower than that of 850°C oxidized polysilicon and it remains almost constant up to 3 MV/cm field strength. The effect of doping ( $1 \times 10^{20} \text{ cm}^{-3}$ ) of polysilicon on current density field characteristics of polyoxide is depicted in figure 3. Here again, leakage current through polyoxide grown at higher temperature is less. It is evident from figures 2 and 3 that leakage current through polyoxide grown over doped polysilicon is about one decade less than that of



## Properties of polycrystalline silicon

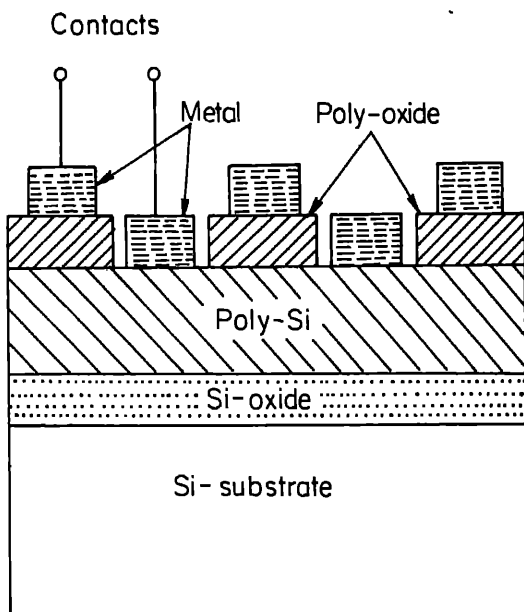


**Figure 1.** Final structure of MOS capacitor with polyoxide as insulator.

undoped polysilicon. Leakage current density field characteristics of Heimann *et al* (1982) have also been plotted in figure 3. The effect of polysilicon deposition temperatures (650°C and 750°C) on leakage currents through polyoxide is shown in figure 4. Higher deposition temperature gives less leakage current.

## 4. Discussion

Surface roughness of polysilicon is a direct result of intergranular oxidation of polysilicon (Suzuki *et al* 1977). As oxidation ensues, a stress builds up in grain boundaries due to increase in volume resulting from intergranular oxide formation. Silicon atoms creep towards midgrain regions to relieve the strain. This motion of silicon atoms depletes the amount of silicon at the grain boundaries and enhances the amount at the midgrain regions thereby elongating the grains normal to the stress.

Simultaneous with the silicon motion, oxidation also occurs and silicon is absorbed both in the grain boundaries and at midgrain regions. The net result is thinner oxide formed at previous grain boundaries due to silicon depletion and thicker oxide at midgrain regions that receive excess silicon atoms. At higher oxidation temperatures where oxidation is predominantly diffusion-controlled, a smooth polysilicon/polyoxide interface is produced.

In the case of oxidation of doped polysilicon, dopants segregate and precipitate in grain boundaries. Because the dopant is electrically active within the grain, oxidation of a grain is a surface reaction and is equivalent to oxidation of single crystal silicon. On the other hand, large amount of segregated dopant atoms in the grain boundaries can lead to increased leakage current.

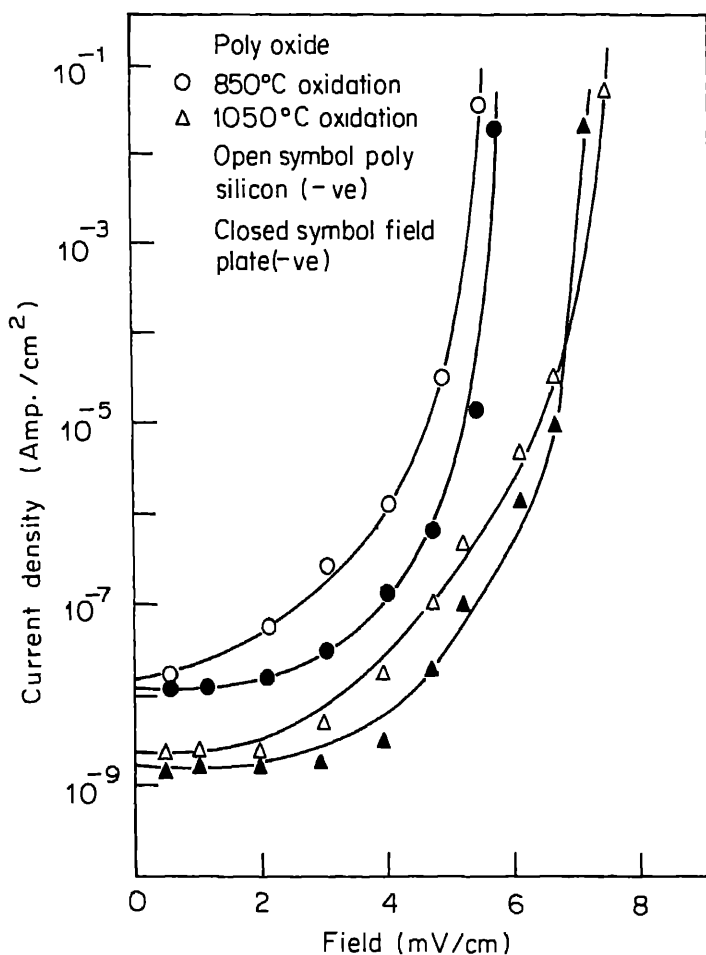


Figure 2. Current density vs field for oxides grown at two different temperatures for undoped polycrystalline silicon.

boundaries leads to an enhanced oxidation rate caused by an increase in the surface reaction rate and oxidant diffusivity through the grown SiO<sub>2</sub> (Barnes *et al* 1979; Ho *et al* 1978).

The higher conductivity observed in oxides grown from polysilicon can be explained as follows: The electrical conduction of the polyoxides is controlled by traps in the polyoxide (Huff *et al* 1980; Lee and Feng 1980). Most of the electrons are trapped close to the polysilicon/polyoxide interface. The difference in the leakage currents is due to the difference in the size and quantity of protuberances and bumps at the polysilicon/polyoxide interface (Irne *et al* 1980; Mandurah *et al* 1980). These protuberances and bumps cause enhanced local electric fields which increase the injection of electrons into the polyoxide, yielding high leakage currents (Pidley 1975). Higher oxidation temperatures and doped polysilicon give smooth polysilicon/polyoxide interface. Hence leakage currents in these cases are lower (figures 2 and 3). A high temperature

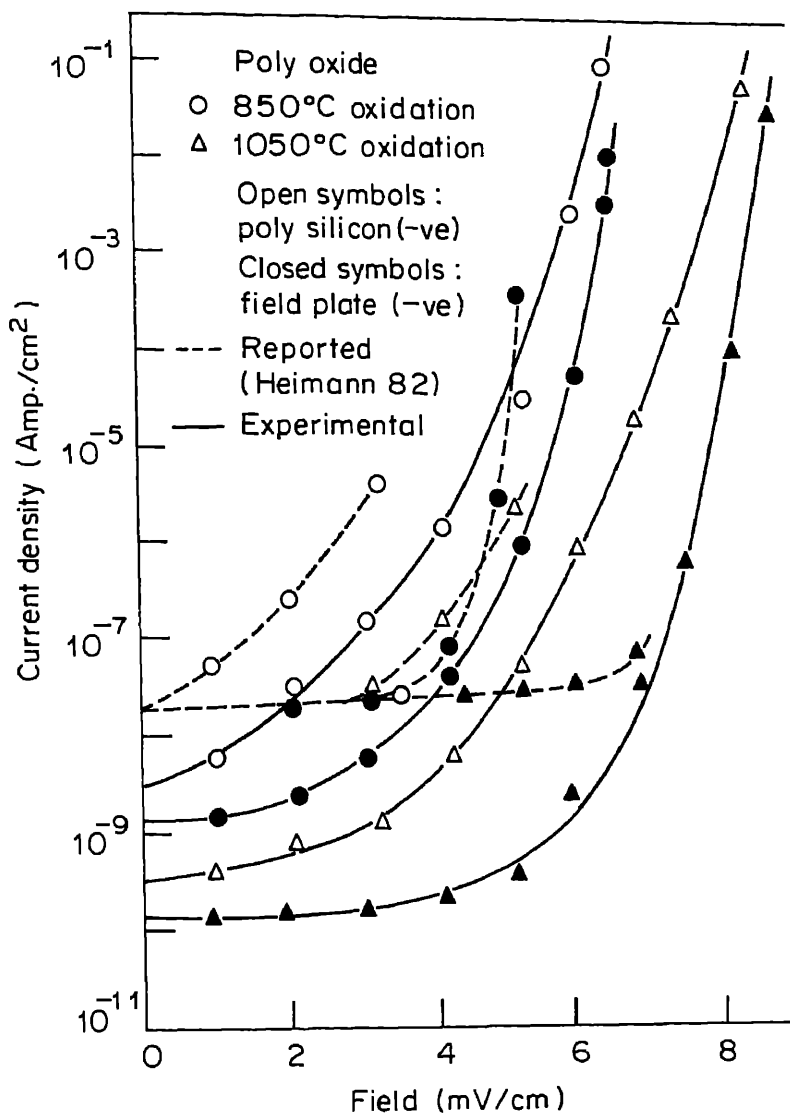


Figure 3. Current density vs field for oxides grown at two different temperature polysilicon doped at 900°C.

polysilicon deposition leads to higher grain size or lesser grain boundaries an thickness undulations and hence an improvement in leakage current and break voltage.

## 5. Conclusion

A strong correlation between asperites present at polysilicon/polyoxide interfac leakage currents through polyoxides has been established. The surface morphol polyoxides as a function of oxidation temperature for doped as well as un

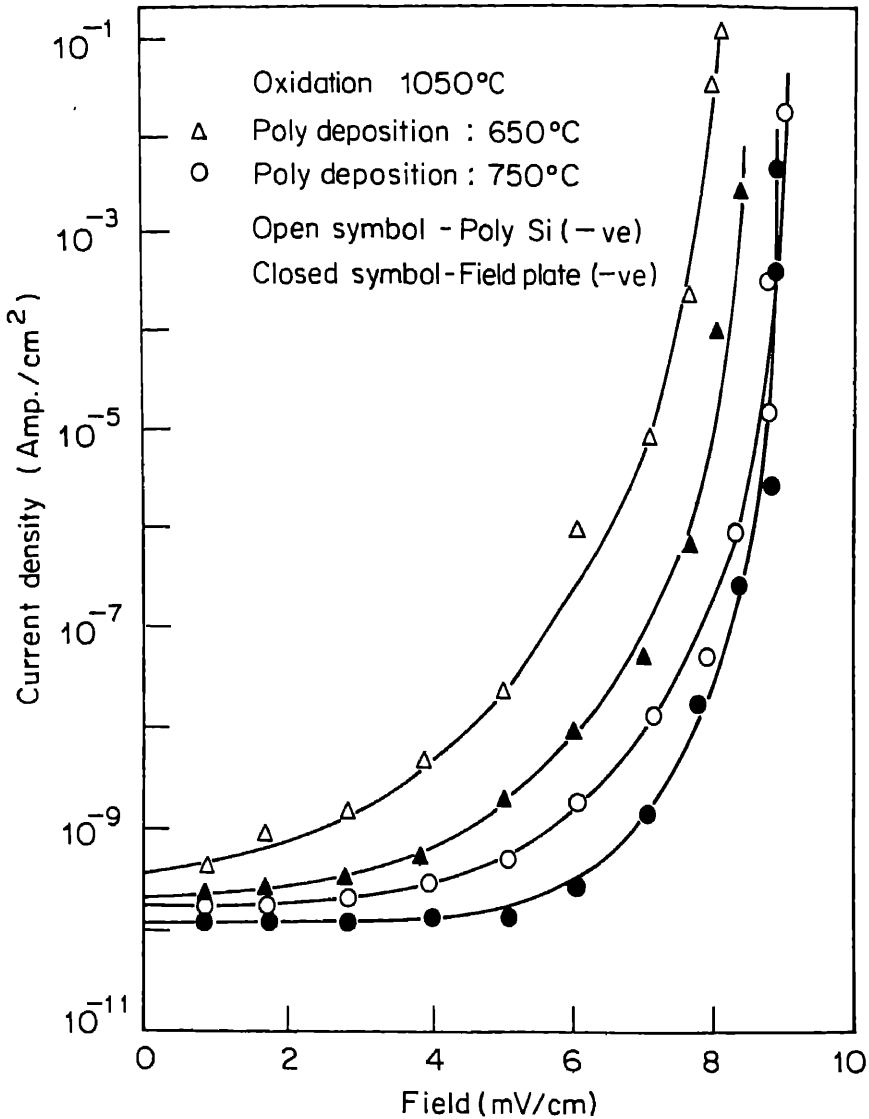


Figure 4. Current density vs field for oxides grown at 1050°C from polysilicon deposited at two different temperatures.

polysilicon films is examined. Higher polysilicon deposition temperature, doping and higher oxidation temperatures yield oxides with higher breakdown fields and lesser leakage currents.

Acknowledgements

Authors thank Mr P N Andhare for help in measurements and Mr D P Runthala, Mr Satish Kumar and Mr H Lal for fabrication help.

## *Properties of polycrystalline silicon*

### **References**

- Anderson R M and Kerr D R 1977 *J. Appl. Phys.* **48** 4834  
Barnes J J, DeBlasi J M and Deal B E 1979 *J. Electrochem. Soc.* **126** 1779  
DiMaria D J and Kerr D R 1975 *Appl. Phys. Lett.* **27** 505  
Heimann P A, Murarka S P and Sheng T T 1982 *J. Appl. Phys.* **53** 6240  
Ho C P, Plummer J D, Meindl J D and Deal B E 1978 *J. Electrochem. Soc.* **125** 665  
Huff H R, Halverson R D, Chu T L and Gutermann D 1980 *J. Electrochem. Soc.* **127** 2482  
Irne E A, Tierney E and Dong D W 1980 *J. Electrochem. Soc.* **127** 705  
Lee H S and Feng C H 1980 *Appl. Phys. Lett.* **37** 1080  
Mandurah M M, Saraswat K C, Helms C R and Kamins T I 1980 *J. Appl. Phys.* **51** 5755  
Pidley B K 1975 *J. Appl. Phys.* **46** 998  
Suzuki T, Minura A and Ogawa T 1977 *J. Electrochem. Soc.* **124** 1776



## **SnO<sub>2</sub>:F films synthesized by chemical vapour deposition technique using hydrofluoric acid as doping material**

A K SAXENA, R THANGARAJ, S P SINGH and O P AGNIHOTRI

Physics Department, Indian Institute of Technology, New Delhi 110016, India

**Abstract.** Highly transparent and highly conducting films of SnO<sub>2</sub>:F were prepared by chemical vapour deposition technique. The films prepared at 350°C substrate temperature and 2.5 lit. min<sup>-1</sup> flow rate of oxygen showed maximum figure of merit. The optimum concentration of fluorine was 1.02 wt %. The Hall experiment showed that the films prepared at optimum conditions had high carrier concentration and high mobility.

**Keywords.** Thin films; SnO<sub>2</sub>:F; transparent conductors; chemical vapour deposition

### **1. Introduction**

SnO<sub>2</sub>, In<sub>2</sub>O<sub>3</sub>, Cd<sub>2</sub>SnO<sub>4</sub> etc are wide band gap semiconductors and have high transparency when prepared under certain conditions (Haacke 1977). They are transparent to visible solar radiations and are reflecting to infrared radiations. These properties make them suitable for application in solar absorbers (Fan *et al* 1977) where they minimize emittance. The optical refractive indices of these coatings are such that they act as antireflection coatings for Si, GaAs and Ge (Chambouleyron and Sarrasin 1979; Cheek *et al* 1979). Low resistive films of these transparent conductors are therefore suitable for use as top conducting layers in solar cells such as SnO<sub>2</sub>/Si etc. Transparent conducting coatings are also used to prevent the windscreens of vehicles from freezing and misting. These coatings are also used to control the indoor environment of houses by their application to windows.

SnO<sub>2</sub> is an n-type material with a direct band gap of about 4.27 eV and an indirect band gap of about 2.73 eV (Bhardwaj *et al* 1981–82). The electron concentration in the conduction band arises due to non-stoichiometry produced by oxygen deficiency. The conductivity of these films can be increased by doping for instance with fluorine or antimony. Several processes such as spray pyrolysis (Bhardwaj *et al* 1981–82; Murthy and Rodriguez 1980; Pommier *et al* 1981), chemical vapour deposition (Murthy and Furukoshi 1978; Kane *et al* 1975; Murty and Jawalekar 1983; Ghoshtagore 1978), sputtering (Lehmann and Widmer 1975; Leja *et al* 1980) have been employed to deposit pure and doped SnO<sub>2</sub> onto semiconductor wafers and glass substrates. In this paper we report the effect of substrate temperature, flow rate of oxygen and concentration of fluorine on SnO<sub>2</sub> films prepared by chemical vapour deposition technique.

### **2. Experimental technique**

Figure 1 shows the schematic diagram of the CVD apparatus, used for the deposition of SnO<sub>2</sub>:F films. This consists of a 0.8 m long quartz furnace. A constant temperature

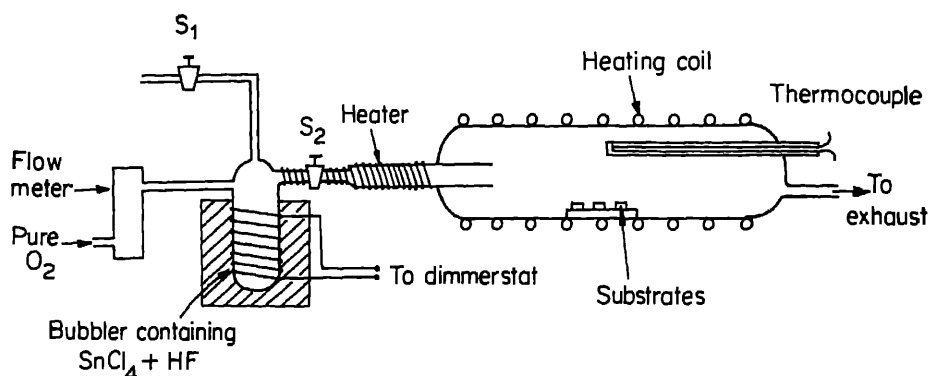


**Figure 1.** Schematic diagram of the experimental set-up used for the deposition of SnO<sub>2</sub>:F films.

zone of about 0.4 m in the middle of the furnace was maintained at a required temperature using electronic temperature controller (accuracy  $\pm 5^\circ\text{C}$ ). Stannic chloride ( $\text{SnCl}_4 \cdot 5\text{H}_2\text{O}$ ) was used as the source material and dilute HF was used as doping material. The glass apparatus was not affected by dilute HF during deposition. High purity oxygen gas was used as the carrier gas and oxidizing agent. Doping was done by mixing required amounts of HF in molten stannic chloride. The temperature of the bubbler containing the mixture of stannic chloride and HF was maintained at  $200^\circ\text{C}$ . The tubes connecting the bubbler and furnace were also maintained at  $200^\circ\text{C}$  to avoid condensation of vapours. The flow of oxygen was regulated by using a flow meter. After attaining the required temperature in the furnace cleaned glass substrates were loaded into the reaction zone. Stop cock S<sub>2</sub> was kept closed and after attaining the required temperature in the bubbler, oxygen gas was bubbled and initial vapours were allowed to escape through S<sub>1</sub>. After adjusting the required flow rate S<sub>1</sub> was closed and S<sub>2</sub> was opened. Before establishing the optimum substrate temperature, films of various doping concentrations were deposited at a fixed substrate temperature ( $400^\circ\text{C}$ ) and a fixed flow rate of oxygen ( $2.0 \text{ lit. min}^{-1}$ ). For that optimum doping concentration, films were deposited at various substrate temperatures and different flow rates of oxygen. Then for optimum substrate temperature and flow rate of oxygen, doping concentration of fluorine was systematically changed.

The transmission spectra of the films were taken by putting a blank glass substrate in the reference beam of a spectrophotometer (Pye Unicam, SP 8–100). The Hall experiment was performed as described by Seeger (1973). Ohmic contacts were made by evaporating aluminium and thickness of the films was measured by Talystep instrument.

### 3. Results and discussion

SnO<sub>2</sub>:F films for fixed doping concentration of fluorine were deposited at various substrate temperatures and different flow rates of oxygen. The figure of merit  $F_r$ , defined by Jain and Kulshreshta (1981) which is independent of film thickness and depends only on the parameters of coating material and preparation technique is



given by:

$$F_t = R_{sh} \ln T$$

where  $R_{sh}$  is the sheet resistance and  $T$  is the transmission. The value of  $F_t$  was maximum for the films deposited at substrate temperature of  $350^\circ\text{C}$  and oxygen rate of  $2.5 \text{ lit. min}^{-1}$ . Figure 2 shows the dependence of sheet resistance, transmission and figure of merit on doping level of fluorine. Figure 3 shows the dependence of carrier concentration and mobility on doping level of fluorine. At a low doping level the carrier concentration is low; therefore the films are highly resistive. As we increase the doping level  $F_t$  becomes maximum ( $-1.11$ ) at  $1.02 \text{ wt } \%$  of fluorine. Further increase in doping level reduces the carrier concentration because at a higher doping level the fluorine atoms start compensating the effect of other fluorine. The reduction in mobility at higher doping level is due to the deteriorated crystallinity (Saxena *et al* 1985). Therefore we conclude that the substrate temperature of  $350^\circ\text{C}$ , flow rate of oxygen of  $2.5 \text{ lit. min}^{-1}$  and doping level of fluorine of  $1.0$  are the optimum conditions to deposit fluorine doped tin oxide films by CVD technique using HF as the doping material.

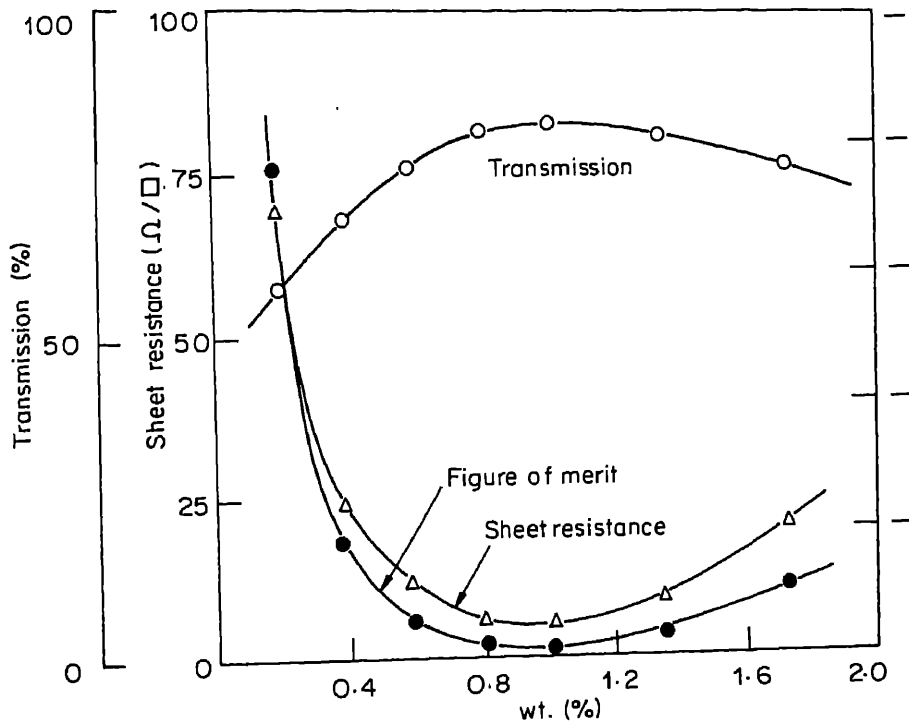


Figure 2. Dependence of sheet resistance, transmission and figure of merit on doping fluorine.

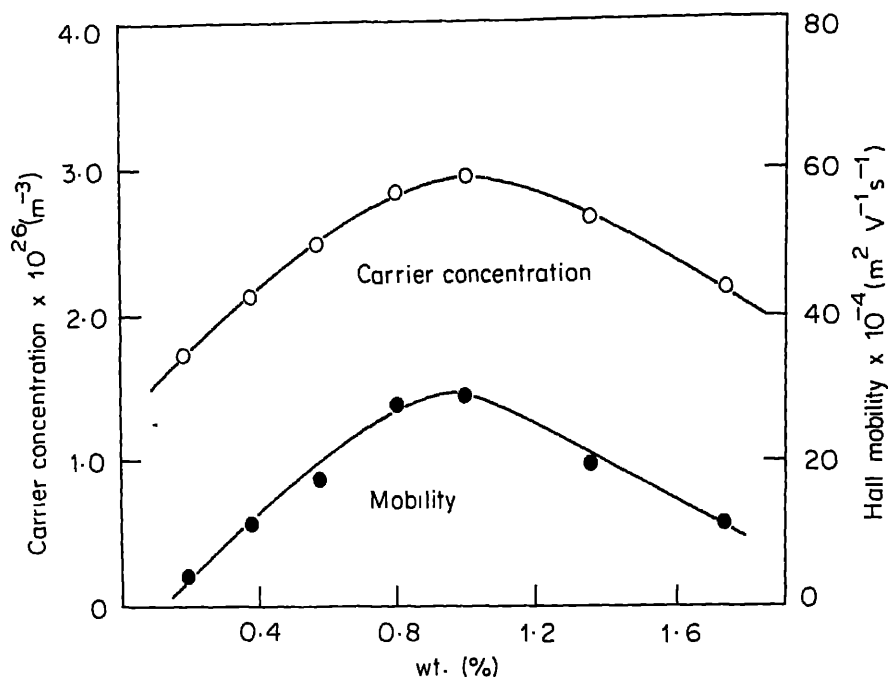


Figure 3. Dependence of carrier concentration and mobility on doping level of fluorine.

### Acknowledgements

The authors are grateful to the Defence Research and Development Organisation, Ministry of Defence and the Department of Non-conventional Energy Sources, Ministry of Energy for financial support.

### References

- Bhardwaj A, Gupta B K, Raza A, Sharma A K and Agnihotri O P 1981-82 *Solar Cells* **5** 39
- Chambouleyron and Saucedo E 1979 *Sol. Energy Mater.* **1** 299
- Check G, Genis A, DuBow J B and Verneker V R P 1979 *Appl. Phys. Lett.* **35** 495
- Fan J C C, Reed T B and Goodenough J B 1974 *Proc. Ninth Intersociety Energy Conversion Engineering Conference*, San Francisco, CA, Society of automotive engineers, New York, pp. 341-346
- Ghoshtagore R N 1978 *J. Electrochem. Soc.* **125** 110
- Haacke G 1977 *Annu. Rev. Mater. Sci.* **7** 73
- Jain V K and Kulshreshta A P 1981 *Sol. Energy Mater.* **4** 151
- Kane J, Schweizer H P and Kern W 1975 *J. Electrochem. Soc.* **122** 1144
- Lehmann H W and Widmer R 1975 *Thin Solid Films* **27** 359
- Leja E, Pisarkiewicz and Kolodziej A 1980 *Thin Solid Films* **67** 45
- Maudes J S and Rodriguez T 1980 *Thin Solid Films* **69** 183
- Muranoi T and Furukoshi M 1978 *Thin Solid Films* **48** 309
- Murty N S and Jawalekar S R 1983 *Thin Solid Films* **108** 277
- Pommier R, Gril C and Marucchi J 1981 *Thin Solid Films* **77** 91
- Saxena A K, Thangaraj R, Singh S P and Agnihotri O P 1985 *Thin Solid Films* (accepted)
- Seeger K 1973 *Semiconductor physics* (New York: Springer) p. 71

## Preparation and characterization of flash-evaporated CuInSe<sub>2</sub> thin films

D SRIDEVI, J J B PRASAD and K V REDDY

Department of Physics, Indian Institute of Technology, Madras 600 036, India

**Abstract.** Thin films of CuInSe<sub>2</sub> have been evaporated onto glass substrates by evaporation. The as-deposited films are amorphous and annealing in selenium atmosphere produces polycrystalline films. The films were characterized by TEM and x-ray diffraction techniques. The optical absorption of the films shows three energy gaps of 1.03, 1.01 and 1.22 eV. The crystal field and spin-orbit splitting are thus found to be 0.04 eV and 0.18 eV respectively. The percentage *d*-character of the valence band states is ~ 35%. The Arrhenius plot of electrical conductivity of films showed impurity ionization of  $E_A = 75$  meV.

**Keywords.** Thin films; chalcopyrites; optical absorption; electrical conductivity.

### 1. Introduction

The semiconductor CuInSe<sub>2</sub> belongs to the I-III-VI<sub>2</sub> group of compounds with chalcopyrite structure. This compound has attracted considerable interest in the decade after the demonstration of 12.5% efficiency of *p*-CuInSe<sub>2</sub>/*n*-CdS heterojunction solar cells (Shay *et al* 1975). Thin film *p*-CuInSe<sub>2</sub>/CdS cells have given > 10% efficiency (Mickelson *et al* 1984). Garcia and Tomar (1983) recently reported sputtered CuInSe<sub>2</sub>/CdS thin film cells of 3% efficiency. Although research on these cells is only of recent origin, it has already warranted a review (Herman and Zwerger 1983). Various methods of preparing thin films of CuInSe<sub>2</sub> have been investigated to make these solar cells economically viable. Pamplin and Feigelson (1979) developed a spray-pyrolysis technique for the preparation of CuInSe<sub>2</sub> thin films. R.F. sputtered films have been characterized by Krishnaswamy *et al* (1983). Loferski (1981) reviewed the performance of CuInSe<sub>2</sub>/CdS thin film solar cells prepared by various techniques and concluded that flash-evaporated and R.F. sputtered films were more nearly stoichiometric and of more reproducible compositions.

In this paper we report the characterization of flash-evaporated CuInSe<sub>2</sub> thin films using optical and electrical characterization techniques. Structural characterization of the films was done by TEM and x-ray diffraction techniques.

### 2. Experimental

The polycrystalline bulk CuInSe<sub>2</sub> was prepared by melting the stoichiometric mixture of 99.999% pure Cu, In and Se at 1050°C in evacuated quartz ampoules. The charge was powdered and remelted two or three times to ensure thorough mixing and reaction of the components. The formation of single-phase, chalcopyrite CuInSe<sub>2</sub> was verified by x-ray diffraction and the exact composition verified by EPMA. The CuInSe<sub>2</sub> prepared is powdered finely and used in the flash evaporation.

A simple flash deposition technique developed in our laboratory was employed for coating  $\text{CuInSe}_2$  thin films. A calling-bell type plunger was used as the vibrator, the frequency of which was varied using a variac. The hopper was filled with finely powdered  $\text{CuInSe}_2$  and a tantalum boat at  $1300^\circ\text{C}$  evaporated the powder instantaneously. The evaporation was carried out using a vacuum coating unit (Hind High Vacuum Co.) under a vacuum of  $10^{-5}$  torr. Thin films of thickness in the range  $0.1\text{ }\mu\text{m}$  to  $0.3\text{ }\mu\text{m}$  were coated on glass substrates.

The glancing angle x-ray diffractogram of the films showed all the prominent reflections of the chalcopyrite structure. Films with minimum thickness were used for TEM. The TEM analysis of as-deposited films showed them to be amorphous in nature. A 45 min anneal in Se atmosphere at  $250^\circ\text{C}$  converted the films to polycrystalline. A typical SAD of selenium-annealed films is shown in figure 1. From this, the values of the lattice parameters were calculated as  $a = 5.85\text{ }\text{\AA}$  and  $C = 11.76\text{ }\text{\AA}$  which are in good agreement with previously reported values (Shay and Wernick 1975). Only selenium annealed films were used throughout the study.

The optical absorption spectrum of  $\text{CuInSe}_2$  thin films was recorded in the spectral range  $800\text{--}1300\text{ nm}$  using spectrophotometer (Cary 2300), and shown in figure 2. It was analyzed by the usual procedures. The electrical conductivity of the films was measured by a four-probe technique in the temperature range  $400\text{--}77\text{ K}$ . The films were evaporated through a special contact mask, which gave films with four specific contact geometries. The steady state electrical conductivity measurements were in argon atmosphere. Indium pressure contacts gave good ohmic contacts. Figure 3 shows the Arrhenius plot of conductivity of  $\text{CuInSe}_2$  films.

### 3. Results and analysis

The optical absorption spectrum shown in figure 2 shows three distinct regions of absorption. The absorption coefficient  $\alpha$  rises sharply initially, then becomes rather flat and again increases sharply. This may be considered as due to a direct transition in the

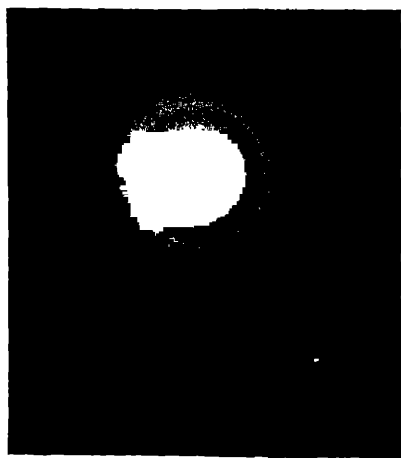


Figure 1. SAD of selenium annealed  $\text{CuInSe}_2$  thin films.

## Characterization of CuInSe<sub>2</sub> films

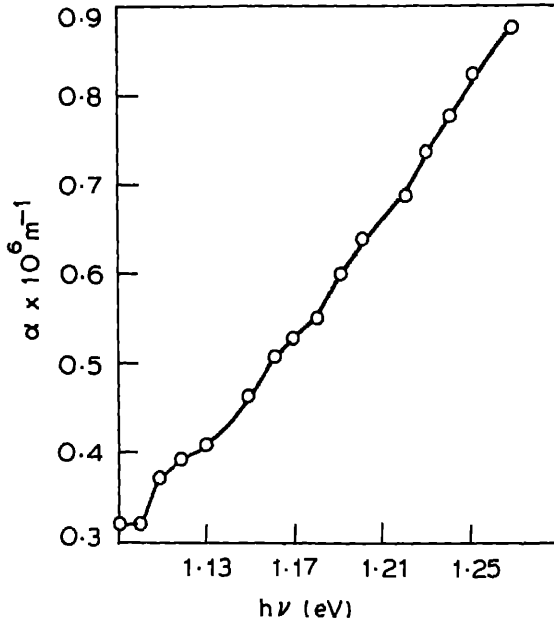


Figure 2. Absorption spectrum of CuInSe<sub>2</sub>.

low energy regions. The flat portion at 1.15 eV is due to the onset of a forbidden transition, the absorption of which is much less than that due to a direct transition. The increase of  $\alpha$  beyond 1.2 eV is due to the onset of another allowed transition. The absorption spectrum was analyzed following Neumann *et al* (1979).

The initial rise of  $\alpha$  below the photon energy  $h\nu \leq 1.15$  eV was a direct allowed transition given by

$$\alpha = \frac{A_1}{h\nu} (h\nu - E_{g1})^{1/2},$$

with  $E_{g1} = 1.03$  eV and  $A_1 = 1.45 \times 10^6$  cm eV<sup>1/2</sup>. This value of the energy  $g$  compares well with the reported direct band gap of 1.04 eV (Shay *et al* 1973) for the material.

For energies greater than 1.15 eV, if we calculate  $\alpha$  using equation (1) and the observed values of  $E_{g1}$  and  $A_1$ , we find that the calculated  $\alpha_1$  is always less than the experimental values. This is due to the onset of additional absorption mechanisms. Hence, the additional absorption coefficient,  $\alpha_2 = \alpha - \alpha_1$  was analyzed for  $h\nu \geq 1.15$  eV. It was found that  $\alpha_2$  satisfies quite well the relation,

$$\alpha_2 = \frac{A_2}{h\nu} (h\nu - E_{g2})^{3/2}, \quad (2)$$

for  $1.15 \leq h\nu \leq 1.20$  eV, with  $E_{g2} = 1.07$  eV, which corresponds to a direct forbidden transition.

Once again, the values of  $\alpha_2$  calculated using (2) beyond  $h\nu = 1.2$  eV were always less than the experimental values. This is due to the onset of a third interband transition. Therefore, now  $\alpha_3 = \alpha - \alpha_1 - \alpha_2$  was analyzed and it was found that  $\alpha_3$  can also be described by equation (1) with  $E_{g3} = 1.22$  eV.

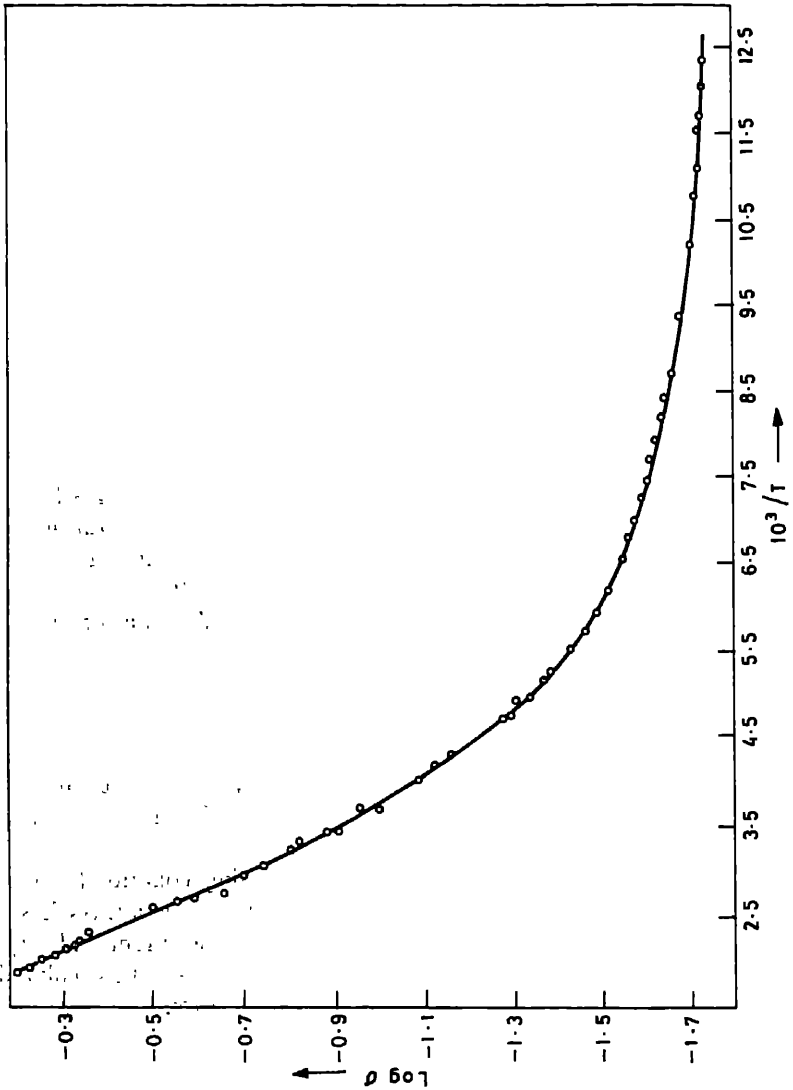


Figure 3. Arrhenius plot of conductivity of  $\text{CuInSe}_2$  thin films.

#### 4. Discussion

From the above analysis, three characteristic band gaps for CuInSe<sub>2</sub> were found  $E_{g1} = 1.03$  eV,  $E_{g2} = 1.07$  eV and  $E_{g3} = 1.22$  eV. These are in good agreement with previously reported values for this material both by optical absorption studies (Neumann *et al* 1982) and by modulation spectroscopic techniques (Shay and Wernick 1975). From the above results, we may draw the zone-centre valence band structure of CuInSe<sub>2</sub> as in figure 4. The three transitions A, B and C correspond to  $E_{g1}$ ,  $E_{g2}$  and  $E_{g3}$  respectively. The values of the crystal field splitting and the spin orbit splitting were calculated using the method of Rowe and Shay (1971) to be  $\Delta_{cf} = -0.05$  eV and  $\Delta_{so} = 0.16$  eV. The percentage *d*-character of the uppermost valence band level was calculated by the procedure of Shay *et al* (1973) to be approximately 35%.

The Arrhenius plot of conductivity in the temperature region 400–77 K is shown in figure 3. Near the room temperature the activation energy is 80 meV and in the temperature range 120–77 K, the activation energy is a few meV. All the films were found to be *p*-type with a hot probe test. Hence the activation energy of 80 meV is attributed to shallow acceptors. Within the hydrogenic approximation of shallow acceptors, the acceptor ionization energy is given by

$$E_A = 13.6(m_p^*/m_0)/\epsilon^2, \quad (1)$$

where  $\epsilon$  is the static dielectric constant of CuInSe<sub>2</sub> and the hole effective mass  $m_p^* = 0.73 m_0$ . This gives a calculated value of  $E_A = 110$  meV which agrees quite well with that observed here. The low temperature activation energy is probably due to surface or grain boundary migration energy.

#### 5. Conclusions

From the analysis of the optical absorption spectrum of thin films of CuInSe<sub>2</sub> near the band edge, the zone centre valence band structure has been determined. The

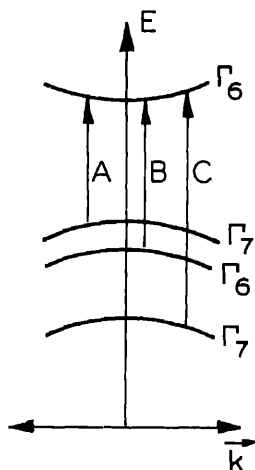


Figure 4. Zone centre band structure of CuInSe<sub>2</sub>.

electrical conduction in thin film is dominated by impurity levels of activation energy  $E_A = 80$  meV above 200 K and by grain boundary scattering below 200 K.

## References

- Garcia F J and Tomar M S 1983 *Jpn. J. Appl. Phys. Suppl.* **53**  
Herman A and Zweibel K 1983 *Proc. SPIE Int. Soc. Opt. Eng.* **407** 96  
Krishnaswamy S V, Manocha A S and Szedon J R 1983 *J. Vac. Sci. Technol.* **A1** 510  
Loferski J J 1981 *Proc. International workshop on physics and semiconductor devices, India*, pp 408  
Mickelsen R A, Chen W S, Hsiao Y R and Lowe V E 1984 *IEEE Trans. Electron Devices* **31** 542  
Neumann H, Horig W, Reccius E, Sobotta H, Schumann B and Kuhn G 1979 *Thin Solid Films* **61** 13  
Neumann H, Perl B, Abdul Hussein N A K, Tomlinson R D and Hill A E 1982 *Crystal Res. Technol.* **17** 469  
Pamplin B and Feigelson R S 1979 *Thin Solid Films* **60** 141  
Rowe J E and Shay J L 1971 *Phys. Rev.* **B3** 451  
Shay J L, Tell B, Kasper H M and Schiavone L M 1973 *Phys. Rev.* **B7** 4485  
Shay J L, Wagner S and Kasper H M 1975 *Appl. Phys. Lett.* **27** 89  
Shay J L and Wernick J H 1975 Ternary chalcopyrite semiconductors: Growth, electronic properties and applications (New York: Pergamon)



## Deposition and assessment of thin dielectric films on photocathode substrate made of Kodial glass

V R KATTI and L M RANGARAJAN

Bhabha Atomic Research Centre, Trombay, Bombay 400 085, India

**Abstract.** The development of  $\text{Cs}_3\text{Sb}$  transmissive interference cathode technology processing of such photocathodes on thin dielectric films coated on glass substrate; use of such films as light resonators is made for reducing the light losses due to reflection at the cathode surface. Consequently the sensitivity of the photocathode is enhanced.  $\text{TiO}_2$  films are chosen for their good optical properties with  $\text{Cs}_3\text{Sb}$  photocathodes in photoemission. Deposition methods and instrumentation in assessing their properties are discussed.

**Keywords.** Interference photoemission; dielectric films; refractive index.

### 1. Introduction

Recent developments in electro-optical instrumentation with advanced technology, light sources, optical components and electronics have set the situation where photocathode quantum efficiency places a limit on the total performance. Increasing the efficiency of the photocathode by optical interference phenomena (Kossel *et al* 1969) is one of the methods. Thin films in conjunction with photocathodes act as light resonators, due to the formation of standing wave within them, facilitating a large amount of light for photoemission. In the development of transmissive interference photocathode (TIC) of S-9( $\text{Cs}_3\text{Sb}$ ) type,  $\text{TiO}_2$  and  $\text{SiO}_2$  films were selected for their matching optical properties such as high refractive index, transmission and chemical compatibility with the photocathode (Katti *et al* 1981). This paper describes the deposition methods of the above films, instrumentation techniques of measuring their optical properties and the application of interference photoemission.

### 2. Experimental techniques

The interference photoemission needs processing of photocathode in conjunction with non-absorbing thin dielectric films of known thickness, required refractive index and transmittance in useful spectral region.

#### 2.1 Method of deposition

Among various methods, reactive evaporation (Pulker *et al* 1976) of  $\text{TiO}_2$  (supplied by Balzers Ltd, W. Germany) in the ambient of oxygen is followed to assess its suitability for the special photodiodes employing Kodial glass to Kovar glass-to metal

Electron beam evaporation method is used. The  $O_2$  pressure, rate of evaporation and substrate temperature are controlled so as to get fully oxidized and non-absorbing films of high  $n_1$  value. Thin SiO films are deposited by vacuum evaporation of SiO powder (supplied by Merk, W. Germany) in a high vacuum of  $< 1 \times 10^{-5}$  torr (Holland 1961). The evaporation source temperature in the range of  $1250^\circ\text{C}$  to  $1350^\circ\text{C}$  is maintained to prevent decomposition of SiO at elevated temperatures.

## 2.2 Thickness measurement

Thickness is the single most film parameter on which the end application of thin films for any device is greatly dependent. The phase condition for TFC is  $n_1 t_1 + n_2 t_2 = (\lambda/2) \rightarrow 1$  where  $n_1$  and  $n_2$  are refractive indices and  $t_1, t_2$  the thicknesses of the film and photocathode respectively.  $\lambda$  is the wavelength of exciting radiation. The values of  $n_2$  and  $t_2$  for the  $Cs_3Sb$  photocathode are 3.2 and 300 Å approximately. The quartz crystal thickness monitor was employed for simultaneously monitoring the film thickness during growth as well as the evaporation rate. A sensitive AT cut quartz crystal with a natural frequency of 5 MHz which was temperature-resistant and water-cooled was used. The change in oscillation frequency  $\Delta f$  is related to the thickness  $t$  of the growing film by the equation  $\Delta f = 0.6 \times t \times d \rightarrow 2$ ,  $d$  being the bulk density of the film material ( $d = 4.3$  g/cc for  $TiO_2$  and 2.1 g/cc for SiO).

The thickness by the quartz crystal was monitored for different films by measuring the exact geometrical thickness using Tolansky's interferometric method. The experimental set-up is shown in figure 1. An interference filter transmitting the

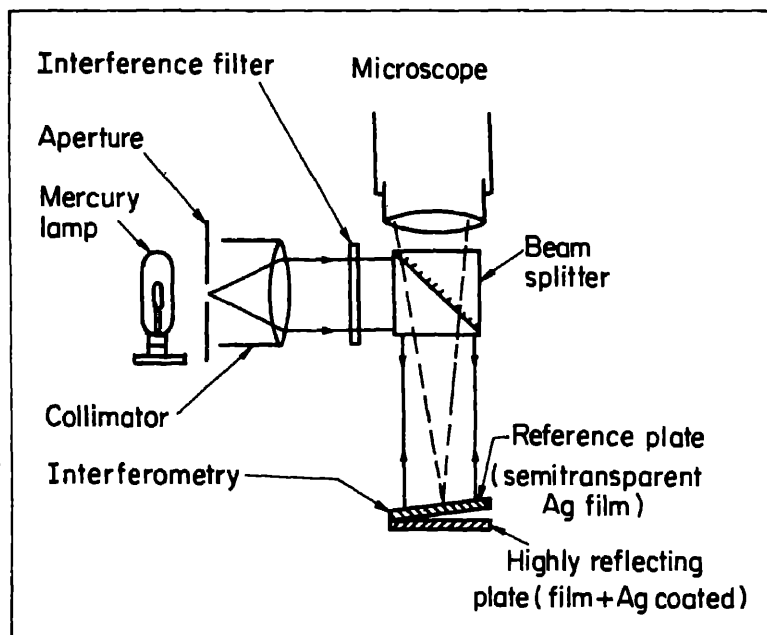


Figure 1. Schematic diagram for multiple beam Fizeau fringe interferometry.

## Dielectric films coated glass substrates

wavelength ( $\lambda = 5460 \text{ \AA}$ ) in front of a Hg-discharge lamp gives monochromatic light. The film thickness is given by the equation

$$t = (\lambda/2)(\Delta/d) \rightarrow 3$$

where  $\Delta$  is the fringe shift and  $d$  the fringe width. Since surface planarity of the plate is important, silver or aluminium step-coatings are given for high contrast array of the fringes. The calibration curves relating both methods of thickness measurement for  $\text{TiO}_2$  and  $\text{SiO}$  films are shown in figure 2.

### 2.3 Refractive index and transmission measurements

In interference photoemission, a knowledge of RI of dielectric films is necessary for selecting suitable films for the photocathode to satisfy the amplitude condition. Measurement of Brewster's angle by Able's method is used here. The reflectance of coated and uncoated substrate is measured using a plane-polarized, monochromatic light at different angles of incidence. The RI of the film is given by the equation  $n = \sqrt{4 \tan^2 \theta + 1}$  for equal reflection from coated and uncoated region,  $\theta$  being the angle of incidence (Brewster's angle). The photomultiplier tube and M4Q III spectrophotometer are used.  $\theta$  is determined graphically (figure 3). The spectral transmittance of the film is measured by using a quartz prism monochromator (M4Q III-Carl Zeiss) and is shown in figure 4. These data are essential for the TIC technology and interpretation of results.

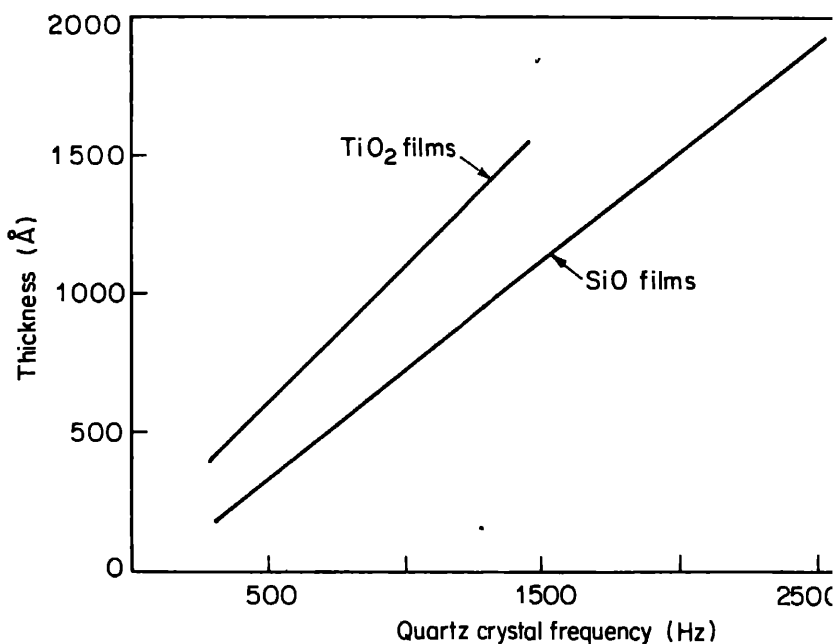


**Figure 2.** Relation between quartz crystal monitor and actual thickness for dielectric films.

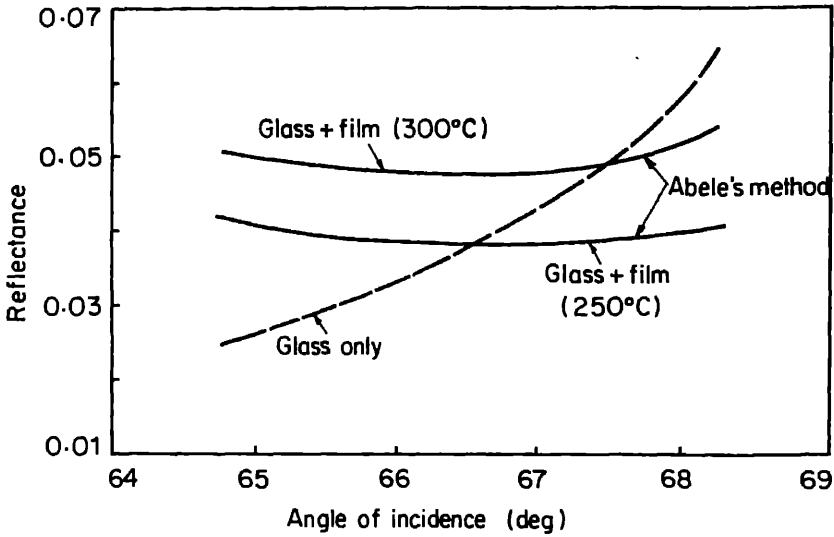


Figure 3. RI measurement for  $\text{TiO}_2$  films made by reactive evaporation method at different substrate temperatures.

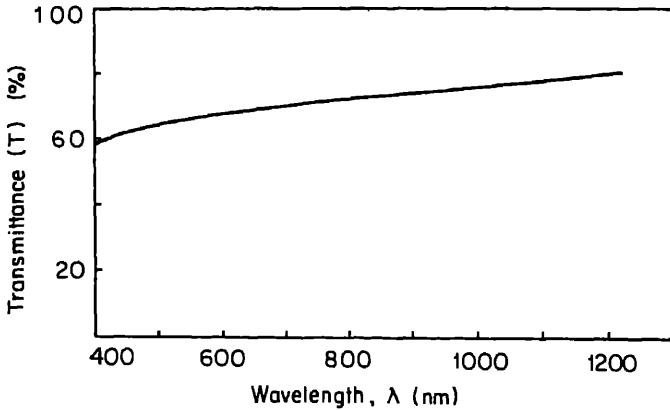


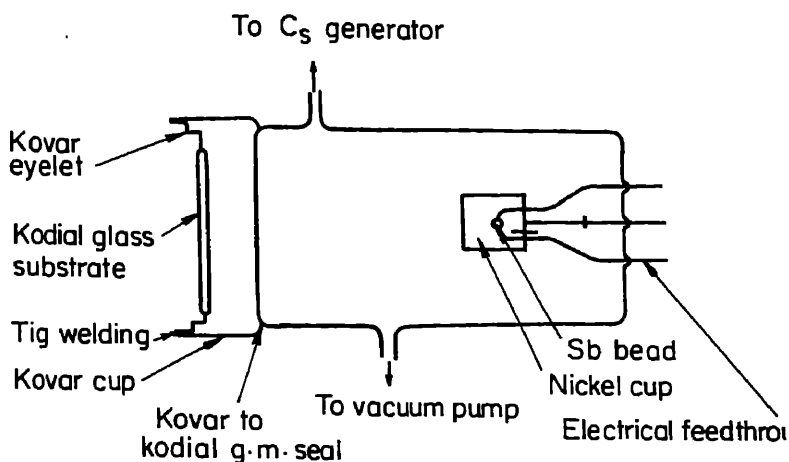
Figure 4. Spectral transmittance of  $\text{TiO}_2$  film (scanned by M4Q III monochromator).

The photodiode tube assembly is shown in figure 5. Films of required thickness are deposited on Kodial glass plate sealed to metallic Kovar eyelets by glass-to-metal seals. These components are used as photocathode substrates in image converter and image intensifier tubes.

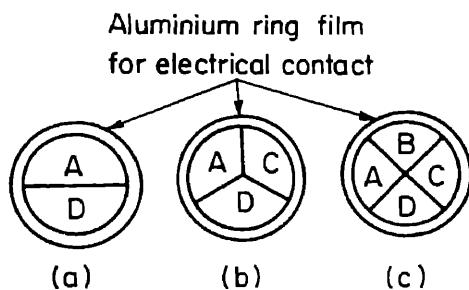
3. Results and Discussion

Film properties such as RI and transmittance depend on the conditions of deposition. In order to process  $\text{TiO}_2$  films by reactive evaporation of  $\text{TiO}$  material, oxygen pressure is

## Dielectric films coated glass substrates



(a)



A = Tuning at 560nm , B = Tuning at 600nm  
C = Tuning at 620nm , D = Uncoated region

(b)

Figure 5. (a) Experimental photodiode tube and (b) substrate configurations.

kept at  $1.5 \times 10^{-4}$  torr so that the films are fully oxidized and non-absorbing (1968). The rate of evaporation is 7 Å/sec for films processed at two different substrate temperatures of 250°C and 300°C; the  $n_i$  values for  $\text{TiO}_2$  are 2.42 and 2.30 respectively at 300°C and 250°C (figure 3). This variation in  $n_i$  is due to crystal imperfections established by Bright Field (BF) and Selected Area Diffraction (SAD) electron micrographs. The films are polycrystalline, tending towards anatase. However, oxidation of Ti films in air at 450°C yields  $\text{TiO}_2$  of  $n_i$  value 2.6, which is required. We could not pursue this method further because of its unsuitability to Kodial substrates with glass to metal seals. Thin films of  $\text{SiO}_2$  are deposited in a vacuum better than  $1 \times 10^{-5}$  torr, the substrate temperature being 250°C. The evaporation

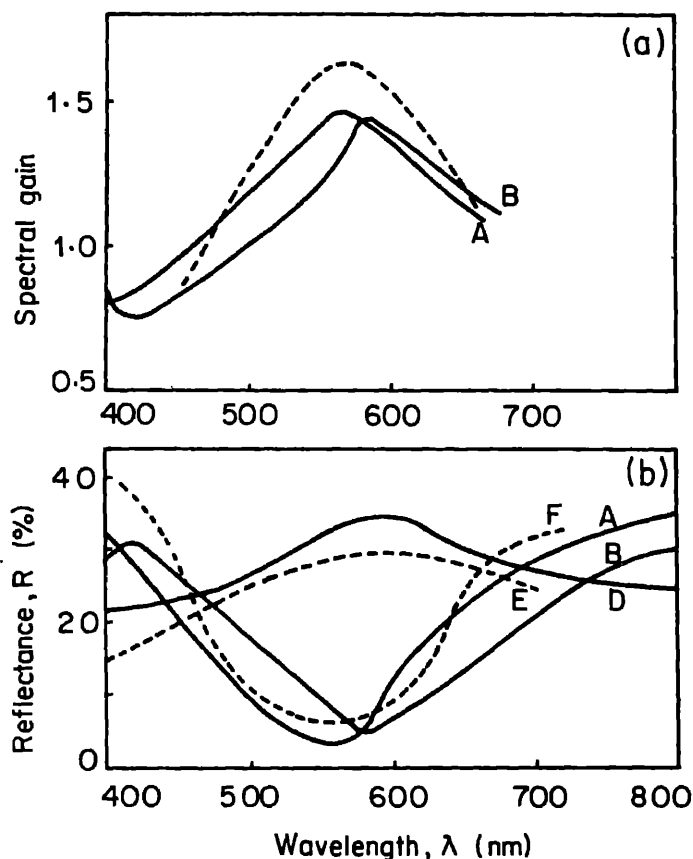


Figure 6. (a) Spectral gain and (b) reflectance characteristics for  $\text{TiO}_2\text{-TiC}$  samples: A.  $\text{TiO}_2\text{-TiC}$  at 560 nm; B.  $\text{TiO}_2\text{-TiC}$  at 600 nm; D. S-9 Photocathode; E. Computed (R) for S-9; F. Computed (R) for  $\text{TiO}_2\text{-TiC}$  at 560 nm.

temperature was kept within  $1350^\circ\text{C}$  because the films above this temperature are likely to contain Si and  $\text{SiO}_2$ .  $\text{SiO}$  films of  $n_1$  value 1.82 can be obtained with the above conditions in addition to the rate of evaporation of 12 Å/sec.

The quartz crystal thickness monitor and Tolansky's interferometric instrument for the assessment of thickness of the films are complementary to each other.  $n_1$  measurement for these optical films by Able's method is quite simple; however the use of photomultiplier tube spectrometer with fine angular graduations and the optical arrangement of lenses, slits and monochromator increase the accuracy of measuring techniques. The accuracy obtained in  $n_1$  value is  $\pm 0.05$ , fairly sufficient for the TiC development work.

The enhancement in photocathode sensitivity by interference mode is achieved to the tune of 1.45 for  $\text{TiO}_2\text{-TiC}$  (Rangarajan and Katti 1978) in the tuned spectral region as shown in figure 6. The agreement obtained between experimental results and theoretical computations shows the right optimization of the deposition parameters of these films as well as the reliability of the instrumentation in assessing their properties.

A gain of 1.25 in photocathode sensitivity in tuned spectral region is recorded for SiO-TiC.

#### 4. Conclusions

TiO<sub>2</sub> films deposited at 300°C substrate temperature by reactive evaporation of TiO<sub>2</sub> at pressure of  $1.5 \times 10^{-4}$  torr are polycrystalline, tending towards anatase, of  $n_1$  value 2.42 and nonabsorbing, in the useful spectral region. SiO films of  $n_1 = 1.8$  are obtained by evaporation of SiO in a vacuum  $< 1.0 \times 10^{-5}$  torr. The enhancement in photocathode sensitivity is 1.45 times over the normal mode for TiO<sub>2</sub>-TiC in the tuned spectral region.

#### Acknowledgements

We thank S S Ramamurthi and S N Seshadri for their encouragement.

#### References

- Holland L 1961 *Vacuum deposition of thin films* (London: Chapman & Hall)
- Katti V R 1979 *A study of Cs<sub>3</sub>Sb transmissive interference photocathode*, M.Sc. thesis, University of Bombay
- Katti V R, Rangarajan L M and Bhide G K 1981 *Vacuum* **30** 497
- Kossel D, Deutscher K and Hirschberg K 1969 *Physics of thin films* (eds) G Hass and R E Thun (London: Academic Press) Vol. 5, 1-45
- Pulker H K, Paesold G and Ritter E 1976 *Appl. Opt.* **15** 2986
- Rangarajan L M and Katti V R 1978 *Proceedings of Symposium on Electron Devices, Pilani, CEE India*, p. 3-31
- Ritter E 1968 *Blazers High Vacuum Information* **16** 385





## Development of high resolution thin film patterns on curved photocathode substrates of image tubes

L M RANGARAJAN and V R KATTI

Bhabha Atomic Research Centre, Trombay, Bombay 400085, India

**Abstract.** Fabrication of thin film patterns involves a sequence of photolithographic and chemical processes to define the high resolution features in thin films on the surface of optical substrates. The substrates used in the present work were curved fused silica with radii of curvature 58 mm and 18 mm which are used as photocathode substrates for image converter and image intensifier tube devices. The resolution pattern and bar chart were successfully printed on these substrates using a secondary conformable photomask of Mylar.

**Keywords.** Photolithography; electron-optics; image tube; resolution; photoemission; integrated-circuits.

### 1. Introduction

The study of experimental electron optics of photoelectronic imaging devices either practical electron valves or in demountable systems is possible only by using good photocathode resolution patterns. An important aspect of the experimental electron optical demountable system (EEDS) is the photocathode and lamp combination, for this depends the simplicity of the day-to-day operation. This requires a photocathode that can be exposed to air without being damaged. Metals, which are, ultraviolet sensitive can satisfy this requirement. The required test pattern is defined in a mask on quartz substrate and a photocathode evaporated on the top (Picat *et al* 1972). The mask is then illuminated from behind with an uv lamp so that electrons are emitted from clear areas of the mask and the pattern is converted into an electron image. These photoelectrons are then accelerated by a high electric field onto the phosphor screen (figure 1). Among the photocathode materials Au, Pd and CsI are typical examples. The photoelectric work function of Au film is 4.492 eV ( $\lambda_{th} = 2760 \text{ \AA}$ ). Hence uv excitation from an Hg-lamp is sufficient to generate the required electron current density. Photolithographic contact printing method (IEEE 1975) was employed in this work for the replication of high resolution patterns from flat master masks to Mylar and curved quartz substrates.

### 2. Experimental techniques

The three important resolution test charts used as master masks for the entire study for analysis of electron optics of image devices were (a) RETMA pattern (b) Westinghouse bar chart (ET-1332A) (c) USAF 1951 resolving power target. The finest line of the pattern was 6  $\mu\text{m}$ , 6  $\mu\text{m}$  and 2  $\mu\text{m}$  width. Since the pattern cannot be directly transferred from the emulsion plate flat master mask to the curved quartz substrates, a second

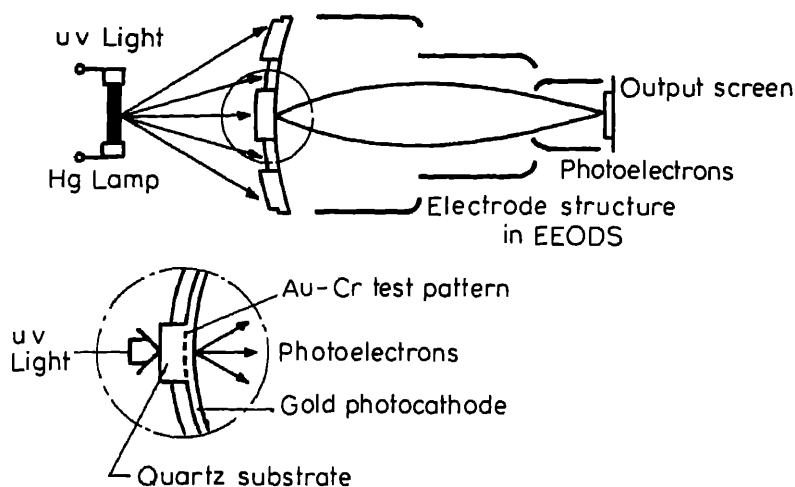


**Figure 1.** A gold photocathode resolution pattern inside a demountable electron-optical system

conformable master mask was developed to be copied on the curved substrates, by contact printing. Of the many organic sheet materials, Mylar sheet has an attractive combination of properties such as mechanical strength, resistance to organic solvents, optical transparency and availability in various thicknesses with optical quality surfaces. The Mylar substrate is completely transparent so that optical realignment of masks is possible. The masks are durable and handling is easier than glass masks now used in photolithography. The dimension of Mylar does not change with temperature and humidity at ambient conditions. It was therefore selected as the substrate material for secondary mask. Photolithographic techniques involved deposition of metallic films on the given substrate followed by selective removal of portions of the film using organic solvents dispersed in photoresists which protect the film in the desired regions, while the unwanted and unprotected regions are etched away chemically. In general pattern delineation by optical lithography gives satisfactory resolution for features as small as  $2\ \mu\text{m}$ . Limit of line resolution is set by wavelength of uv light,  $0.2\ \mu\text{m}$ .

Deposition of Cr-Au films as well as Ti-Pd-Au films on Mylar samples was independently carried out for getting satisfactory patterns. A Mylar sheet ( $30 \times 20 \times 0.4\ \text{mm}$ ) was washed with trichloroethylene and ultrasonically cleaned to remove fine dust particles and organic solvents on the surface, which are a potential source of pinholes. An aluminium strip placed below the Mylar (which buckles at  $150^\circ\text{C}$ ) served as a heat sink. Uniform layers of chromium (100 nm) and gold (100 nm) films were deposited in sequence on the Mylar substrate, using fast evaporation and employing double filament methods in a vacuum of  $< 10^{-5}$  torr. The filaments were of basket type made of tungsten. Chromium, in fact, sublimes above  $1800^\circ\text{C}$  and gold evaporates at  $1000^\circ\text{C}$ . Shutter mechanism and double filaments were incorporated inside the vacuum evaporation plant.

A thin uniform layer ( $0.3\ \mu\text{m}$ ) of Kodak negative photoresist or KTR was coated on the AuCr layer by a photospinner. The centrifugal whirling of photoresists is the standard application technique for producing sub-micron thickness films of these materials. The viscosity of the resist solution and the speed of rotation of the whirler

were optimized to obtain a thin, uniform, bubble and agglomeration-free photoresist coating on the Mylar substrate. For different samples tried with varying thickness resist films, the resolution was found to vary inversely with resist thickness. It was prebaked at a temperature of 80°C for half an hour. Baking the photoresist layer prior to exposure is often helpful for this particular photofabrication process. The purpose of the prebake is to remove any residual photoresist solvent that has not been eliminated by air drying. Failure to prebake the layer of resist usually results in either degradation or complete failure of the image in the developer. The photoresist coated substrate was exposed for 7 sec, in a system which included a light source, provision for holding the substrate and mask in close contact and a microscope to observe the mask. The pattern was exposed with a high pressure Hg vapour lamp which produced near collimated light. Typical value of the exposure of light energy at the substrate was 10 mW/cm<sup>2</sup>. Details of developing, postbaking and chemical etching were reported earlier (Sunita Singh *et al* 1980). A resolution of 6 µm (80 lp/mm) was observed on the secondary mask. To develop a conformable mask pattern of very high resolving power of 2 µm (250 lp/mm) like the one of USAF 1951 target, the experimental techniques were modified (Rangarajan 1982). Uniform layers of Ti (40 nm) and Pd-Au (50 nm) films were deposited sequentially on the Mylar sample in a pressure < 10<sup>-5</sup> torr. Ti wire (8 mil) was wound on tungsten ribbon-stranded filament, for evaporation. Ti evaporates at 1800°C. Pd-Au wire (60% Pd and 40% Au alloy composition) from basket type filament evaporates at 900°C. The photofabrication process was similar excepting the following changes: the negative photoresist used in the present study was from Way-Coat (USA); the thickness of NPR coating was kept below 1 µm; line broadening due to light scattering under the dark portions of the mask was eliminated with well adjusted exposures and negligible mask-to-substrate separation as well as by using dark field and bright field patterns at appropriate times; chemical etching for Ti film was done from a solution of 70 cc H<sub>2</sub>O, 10 cc of 48% Hf and 20 cc of HNO<sub>3</sub> and the rate of etching was 18 µm per min at 32°C. The strong adhesive property of Ti on silica Mylar substrates retained the fine details of the pattern after chemical etching. As many as 25 samples were prepared in the course of experiments. A resolution of 2 µm was observed on the secondary mask which had very good contrast and high edge definition.

### 3. Experimental results and discussion

To evaluate the quality of the mask, the transmittance of different regions was measured with a micro-densitometer (type: Jarrel-ash Company) and a high precision recording microphotometer (model-23-500/501). Density of lines was 0 to 3.5 with a width of 1.4 µm. Consider a series of periodic bars and spaces such as a picket fence. The spatial dimension is the period. The spatial frequency, as with time frequency, is the inverse of this period i.e. 1/T (figure 2). This is expressed in lines per millimetre; resolution as lp/mm. The contrast of the mask pattern is the difference in optical density of the opaque and transparent regions at that spatial frequency. The optical density, is defined as

$$D = \log_{10}(I_0/I_T),$$

where  $I_0$  and  $I_T$  are intensity of incident and transmitted light. In figure 2, 1 is the bl

or grey bar and 2 is the white or full transmission bar,

$$\text{contrast} = C = D_1 - D_2 = \log_{10}(I_{T_2}/I_{T_1}). \tag{2}$$

This contrast value was determined at different resolution values,  $R$ . While expressing the results of  $C = f(R)$ , values were normalized. A thumb rule is that the slit width should be at least one-third of the resolving power. The output of the microdensitometer was plotted on a recorder and looked like a square wave response. The method is analogous to obtaining the pulse response of an amplifier. The contrast of the pattern details described on the Mylar samples and the reference photographic emulsion mask is shown in figure 3.

The curved quartz substrates were coated with Cr and Au films in sequence and a thin layer ( $0.5\ \mu\text{m}$ ) of positive photoresist spun on them. The Mylar pattern was transferred on the silica glass substrates as a contact print by making the Mylar sheet take the shape of curved substrates of 60 mm and 18 mm radii of curvature in the two cases. This is possible by using a specially designed fixture (figure 4). Close contact between the Mylar mask and quartz substrate was achieved by applying mechanical pressure. While the top and bottom metallic flanges are tightened (with bolts and nuts), the teflon

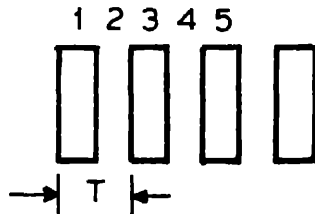


Figure 2. Spatial frequency.

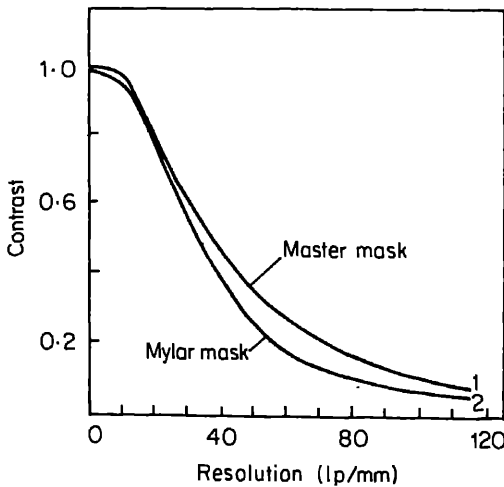
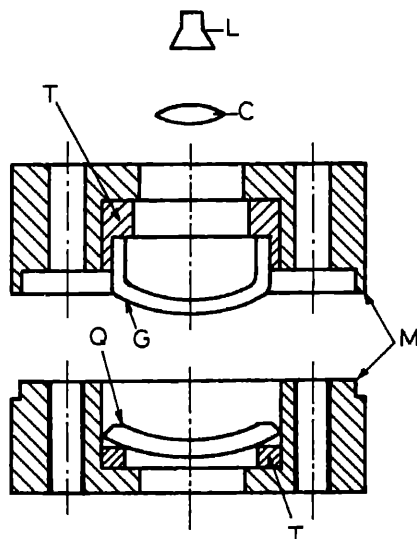


Figure 3. Contrast curves.



**Figure 4.** Mechanical and optical set-up for photomasking (L-Lamp; C-Collimating lens; T-Teflon runners; M-Special fixture; G-Glass plate; Q-Curved quartz plate (RC = 18 mm)).

runners take care of the extra-pressure and guide the glass plate and quartz plate for proper alignment. Here again, the usual photolithographic techniques were employed for printing the resolution pattern on the quartz substrate. While transferring details to cathode substrates, special precaution has to be exercised to completely eliminate the line width variations in photoresist patterns on profiled surfaces. This has been made possible by using (i) mask alignment apparatus with new techniques such as optical contact or coupling liquid (DoW Corning Q2-3067, Refractive index is 1.45, quartz, FoP coupling of image tubes) between the Mylar pattern and the resist surface and (ii) by using dark field and bright field patterns appropriately with PPR or during printing.

After transferring the pattern on the curved substrate, a thin film of gold of thickness 25 nm was evaporated over the pattern in a vacuum of  $10^{-6}$  torr to form a semitransparent gold photocathode. The curved gold photocathode and the electron gun of an image tube were mounted and aligned on an electron-optical bench contained in an evacuated chamber, whose dynamic vacuum was  $10^{-5}$  torr. A Hanovia uv lamp (500 W) was used for exciting the Au photocathode. Photocurrents of the order of  $10^{-8}$  to  $10^{-7}$  A cm<sup>-2</sup> could be obtained from the photocathode. The electron optical image was reconverted into visible image at the screen by cathodoluminescence, which could be viewed externally by a naked eye or by an optical microscope when necessary. The limiting resolution of the tube in the position of best focus was read on the screen. By measuring the widths of the pattern on the image at centre and at known distances from the centre, the magnification and distortion characteristics were obtained. For a typical tube with a radius of curvature of gold photocathode substrate as 18 mm, the paraxial resolution obtained was 50 lp/mm and the magnification is 0.978.

#### 4. Conclusions

While employing conventional photolithographic methods, new techniques have been introduced in the preparation of a conformable Mylar mask with resolution details of  $2\text{ }\mu\text{m}$  and, in the final process of printing such test patterns on curved quartz substrates. Such electronic patterns contribute immensely to the experimental electron optics studies of image tubes, and analysis of tube characteristics such as image details, aberrations etc which give image tube performance of practical importance. An important aspect of EEODs and allied techniques is that it forms the basic requirements of electron image projection systems for making master masks of  $1\text{ }\mu\text{m}$  details or smaller features required in integrated circuit technology. This is a fast growing field utilizing the principles of electron optics of photoelectronic imaging devices and electron-resist technology.

#### Acknowledgements

The authors thank Professor K V Ramanathan, Head, Solid-State Electronics Group, Tata Institute of Fundamental Research for allowing use of facilities and for guidance during the course of this work.

#### References

- IEEE 1975 *Pattern generation and microlithography*, IEEE Trans Special issue ED-22, 369
- Picat J P, Cambes M, Felenbok P and Fort B 1972 The electron Camera used in a reflective mode; *Adv. Electron. Electron Phys.* **A33** 557
- Rangarajan L M 1982 A study of electron-optics in photoelectronic imaging devices, Ph.D. Thesis, Bombay University, Bombay
- Sunita Singh, Rangarajan L M and Pishorady T U 1980 Application of photolithography to development of photocathodes for electron optical imaging devices; *J. IETE* **26** 190

## Dielectric mirrors for high power laser applications

K V S R APPARAO

Spectroscopy Division, Bhabha Atomic Research Centre, Trombay, Bombay 400085, India

**Abstract.** Development of low loss dielectric high reflecting mirrors for high power laser applications presents some problems in selecting suitable thin film materials and understanding their optical constants. Some of these problems have been solved by a systematic study of the dependence of optical constants on different evaporation parameters for a number of thin film materials. Using the data thus obtained high reflecting dielectric mirrors for different laser applications in the UV, visible and near-infrared regions have been successfully developed indigenously by the method of vacuum evaporation.

**Keywords.** Mirrors; lasers; thin films; optics; multilayers; coatings.

### 1. Introduction

With correct choice of thin film constants, film thicknesses and number of films, it is possible to design different dielectric mirrors and other thin film devices (Dobrowol 1965, 1981; Apparao 1977). But practical realization of low loss, stress free and high reflecting thin film devices which can withstand high power lasers presents some problems (Pawlewicz *et al* 1980; Carniglia 1981; Kuster and Ebert 1980). Selection of appropriate thin film materials having the required optical and mechanical properties, knowledge of optical losses and constants and their dependence on the process parameters are some of the involved problems. In order to meet the specific needs of research activities using lasers some of these problems have been solved and different thin film devices including dielectric mirrors for high power laser applications were developed indigenously. Some of the important results derived during the development work are presented in this paper.

### 2. Thin film devices development

It is well known that a multilayer dielectric thin film device is made up of at least two materials and depending on the application the films of each material should have the desired refractive index, transmission, scattering, thickness, stress, hardness, defect free, low optical losses, resistance to laser radiation etc. Unfortunately despite all the advances in materials science and sophisticated instrumentation during the last few years, it is difficult to achieve all the desired film properties in any process because the film growth during the process of evaporation, as is well known, is complex and depends upon different process parameters like evaporation method, rate of evaporation, substrate temperature, ambient pressure, vapour angle, vapour chopping, glow discharge starting material, substrate material etc. For example, for laser applications, optical loss of the coatings is one of the important factors to be controlled during the evaporation

process. These losses, which include losses due to absorption, adsorption, scattering and fluorescence, depend upon the bulk absorption, stoichiometry, voids in the structure, surface roughness, rough internal boundaries, density changes, pin holes, cracks, microdust etc in the films which are all process-dependent except the bulk absorption. So exact and reproducible process and chamber parameters which give the desired film properties with the specified tolerance limits are very essential to develop high quality thin film devices for laser applications. The present situation is such that although basic optical properties of different thin film materials are available (Jenkins 1958; Hass and Ritter 1967; Macleod 1969; Ritter 1975; Pulker 1979), full details of optical constants and mechanical properties of the films and their dependence on process parameters are not available in the voluminous literature published in the field, particularly for the films in the uv region from 240 nm to 400 nm. This is because most of the parameters are considered as trade secrets and patents and are not published. The few results published are not exactly reproducible and are different for different experimental set-ups. In addition human element in the form of experience, skill and judgement plays a role in achieving the required film properties in the given process.

In our programme to develop thin film devices indigenously, studies have been undertaken to evaluate all necessary film data for different thin film materials like  $\text{TiO}_2$ ,  $\text{CeO}_2$ ,  $\text{Al}_2\text{O}_3$ ,  $\text{MgF}_2$ ,  $\text{SiO}_2$ ,  $\text{MgO}$ ,  $\text{Ta}_2\text{O}_5$ ,  $\text{Na}_3\text{AlF}_6$ ,  $\text{ZrO}_2$  etc. using the method of vacuum evaporation. Using the data thus obtained low loss, stress force and hard high reflecting mirrors of conventional design having reflection as high as 99.5 % with losses as low as 0.5 % were developed for different wavelengths ranging from 300 to 1060 nm. The coatings developed are in constant use in our laboratories and are found to withstand the available lasers operating upto 1 MW maximum power with 10 nsec pulse widths. High reflecting mirrors developed so far include the coatings working at  $\text{XeCl}$ ,  $\text{N}_2$ ,  $\text{HeCd}$ , visible dye, II YAG,  $\text{Ar}^+$ , Cu vapour,  $\text{HeNe}$  and YAG glass laser wavelengths.

### 3. Development work

Space does not permit a discussion of the entire development work and so some details of the investigations carried out for developing the dielectric mirrors for the uv region from 240 nm to 400 nm are presented in this paper. The uv coatings were developed, using  $\text{ZrO}_2$  as high index and  $\text{SiO}_2$  as low index materials, by the method of reactive evaporation. The results concerning the optical losses of  $\text{ZrO}_2$  films prepared under different evaporation parameters are given. The dependence of the optical losses and constants on the rate of evaporation, ambient oxygen pressure, substrate temperature, film thickness and chopping the vapour before reaching the substrate have been studied and the results of the most significant evaporation parameters are briefly discussed and the results presented.

#### 3.1 Experimental

$\text{ZrO}_2$  films were deposited on a 25 mm diameter fused silica substrates by evaporating optical grade  $\text{ZrO}_2$  using the electron beam gun in a conventional 500 mm vacuum coating unit. The chamber was evacuated to better than  $2 \times 10^{-6}$  mbar before evaporating the material. For reactive evaporation IOLAR grade pure oxygen from a high pressure cylinder was admitted into the chamber and maintained at the required



value ranging from  $3 \times 10^{-4}$  mbar to  $5 \times 10^{-6}$  mbar by controlling the needle valve pressure regulating valves. The substrate was heated to the assigned temperature ranging from  $50^\circ\text{C}$  to  $400^\circ\text{C}$  and the evaporation rate ranging from  $1 \text{ \AA}/\text{sec}$  to  $100 \text{ \AA}/\text{sec}$  was measured and controlled with the quartz crystal monitor. Chopped films prepared by introducing suitable rotating mask between the substrate and the source. A total of 35 samples were prepared for the present studies, each with different evaporation conditions. For all the samples prepared, uniformity of film thickness over the whole surface was found to be within  $\pm 2\%$  of the average thickness. The transmittance spectrum of each substrate was recorded before and after depositing film using double beam spectrophotometer (Hitachi model 330). The optical losses were taken as the difference of transmission peak maxima and the substrate transmission at the respective peak wavelengths. Refractive index  $n$ , physical thickness and the effective extinction coefficient  $k$  of each sample film were deduced by the method of Swanepoel (1983).

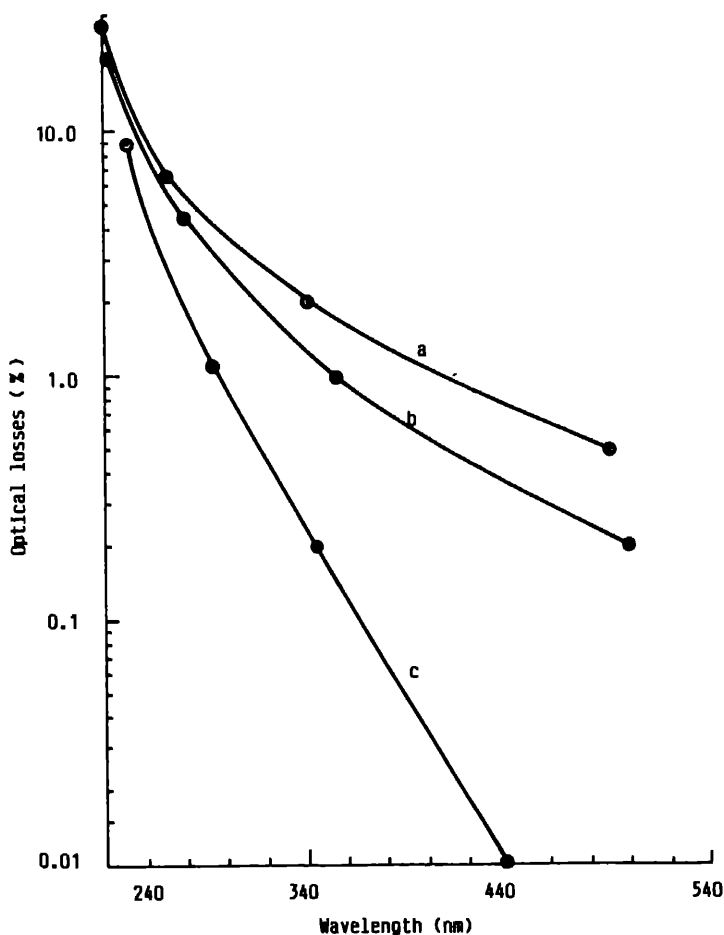


**Figure 1.** Dependence of optical losses of  $\text{ZrO}_2$  films on rate of evaporation. (a)  $20 \text{ \AA}/\text{sec}$ ,  $t = 250 \text{ nm}$ , (b)  $10 \text{ \AA}/\text{sec}$ ,  $t = 275 \text{ nm}$  and (c)  $5 \text{ \AA}/\text{sec}$ ,  $t = 320 \text{ nm}$

### 3.2 Results and discussion

The measured percentage losses  $L$  were plotted against the wavelength  $\lambda$  for each set of films prepared under identical conditions with one parameter variable. Figure 1 shows one such plot where the variation of optical losses is shown for films prepared at different evaporation rates. All the films shown in figure 1 were prepared at the same ambient oxygen pressure ( $2 \times 10^{-4}$  mbar) and substrate temperature ( $260^\circ\text{C}$ ). As can be seen from figure 1 the optical losses are minimum for  $\text{ZrO}_2$  films evaporated at  $5 \text{ \AA}/\text{sec}$ . The present investigation also indicated that the losses are further reduced as expected at higher substrate temperatures and low oxygen ambient pressures. It was also found that the losses in the visible region (where the absorption is negligible) remained almost constant with increasing film thickness indicating that the losses were greater due to surface scattering than bulk scattering. Such changes can be attributed to changes in the film structure, grain size, density fluctuations, stoichiometry and the extent of reoxidation of the film (Pulker 1976; Baumeister and Arnon 1977). For the best 275 nm thick  $\text{ZrO}_2$  films prepared the optical constants  $L$ ,  $n$  and  $k'$  respectively at different uv laser wavelengths are found to be 8%, 2.35,  $7.0 \times 10^{-3}$  at 248 nm, 0.6%, 2.16,  $4.7 \times 10^{-4}$  at 308 nm, 0.24%, 2.12,  $1.2 \times 10^{-4}$  at 337 nm and 0.14%, 2.11,  $8.8 \times 10^{-5}$  at 351 nm. The data from the present investigations were used successfully to develop uv coatings for laser applications. Full details of the present investigations and those connected with other materials for developing dielectric mirrors for visible and near infrared region will be published elsewhere.

### References

- Apparao K V S R 1977 *Indian J. Pure. Appl. Phys.* **15** 270  
Baumeister P and Arnon O 1977 *Appl. Opt.* **16** 439  
Carniglia C K 1981 *Thin Solid Films* **77** 225  
Dobrowolski J A 1965 *Appl. Opt.* **4** 937  
Dobrowolski J A 1981 *Appl. Opt.* **20** 74  
Hass G and Ritter E 1967 *J. Vac. Sci. Technol.* **4** 71  
Jenkins F A 1958 *J. Phys. Rad.* **19** 301  
Kuster H and Ebert J 1980 in *Laser induced damage in optical materials* (eds) H E Bennett, A A Glass, A H Guenther and B E Newnam (Washington: Nat. Bur. Stand.) Spec. Publ. 568, 269  
Macleod H A 1969 in *Thin film optical filters* (London: Adam Hilger) 316  
Pawlewicz W T, Hays D D and Martin P M 1980 *Thin Solid Films* **73** 169  
Pulker H K 1976 *Thin Solid Films* **34** 343  
Pulker H K 1979 *Appl. Opt.* **18** 1969  
Ritter E 1975 in *Physics of thin films* (New York: Academic Press) Vol. 8  
Ritter E 1981 *Appl. Opt.* **20** 21  
Swanepoel R 1983 *J. Phys.* **E16** 1214

## Design and development of a thin film dielectric beam combiner

K V S R APPARAO and N K SAHOO\*

Spectroscopy Division, MDRS\*, Bhabha Atomic Research Centre, Trombay, B-400085, India

**Abstract.** A multilayer thin film device called a beam combiner for a specific photodissociation experiment was designed and developed. The device when operated at  $45^\circ$  at incidence transmits a UV laser beam and reflects a visible laser beam at the same time with minimum energy loss. The efficiency of the device was found to be better than 90%.

**Keywords.** Thin films; beam combiner; edge filter; optics.

### 1. Introduction

Dielectric beam combiner is a multilayer thin film device which can be used to combine optical electromagnetic radiation of two different frequencies collinearly with minimum energy loss. The device has an application in a certain photodissociation process wherein the reaction target zone has to be irradiated collinearly with two laser beams within a few nanoseconds of delay. The wavelength of one laser is in the UV region and the other in the visible region. Since the efficiency of the dissociation process is proportional to the intensity of the laser radiation reaching the target, the device should have minimum energy loss. Since no device of the required specification is commercially available, a multilayer thin film device called a beam combiner was designed and developed for the specific application. Details involving the design and development of the beam combiner are briefly discussed in this paper.

### 2. Design of the beam combiner

The main requirements of the beam combiner were when operated at  $45^\circ$  at incidence it should transmit 337 nm  $N_2$  laser beam and at the same time reflect a tunable dye laser beam from 420 nm to 450 nm completely without any energy loss. These requirements can be achieved ideally with a  $45^\circ$  angle of incidence low pass dielectric edge filter having the edge anywhere between 350 nm and 380 nm and having about 150 nm to 200 nm wide high reflection zone.

A simple design of a conventional quarter wave stack with alternate low and high index films can be used as a beam combiner with low transmission efficiency. The reduction of the transmission in the UV region for such a simple design is because of the presence of the characteristic ripple of the quarterwave stack in the pass region. The computed transmission (average of P- and S-polarized components) of such a simple design is shown in figure 1 (design A). The UV efficiency of the design can be increased by reducing the ripple in the pass band region from 300 nm to 400 nm by using multi-

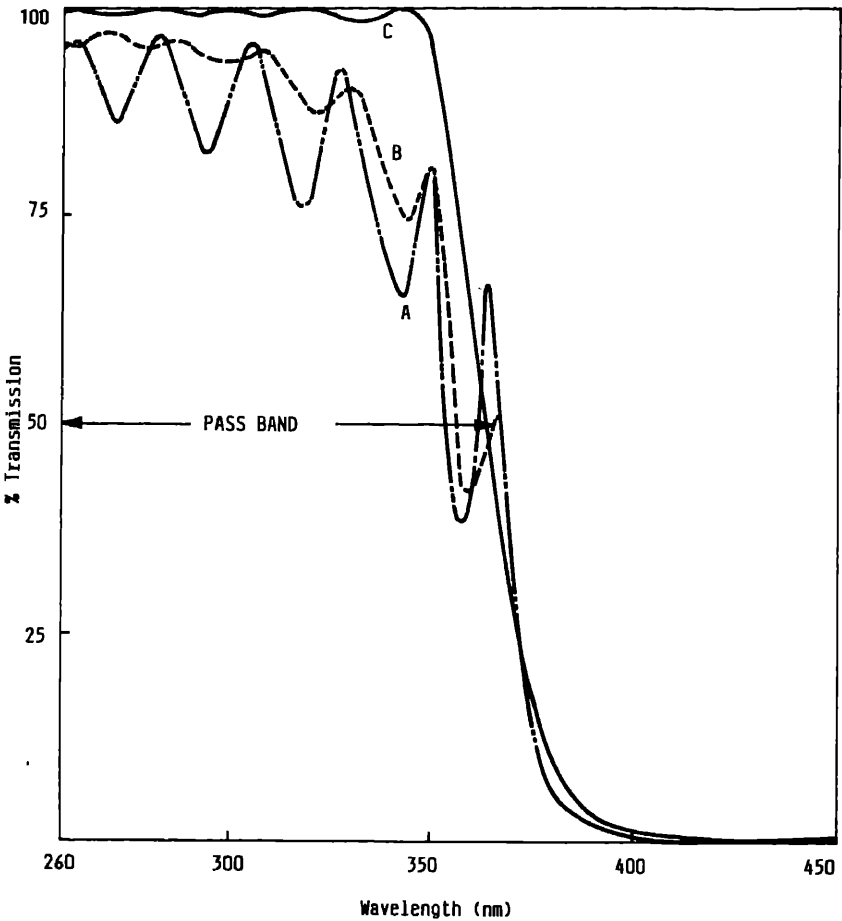


Figure 1. Transmission characteristic of beam combiner designs operating at 45° angle of incidence. A, B, C refer to the respective designs.

techniques. The simplest approach for such design (Macleod 1969) is to add matching layers at either side of the quarterwave stack to match it to the substrate and to the medium. A quarterwave layer of admittance  $\eta_s$  inserted between the stack and the substrate, another quarterwave layer of admittance  $\eta_1$  between the stack and the medium according to the following relations becomes a good match

$$\eta_s = (n_s \cdot E)^{1/2} \quad \text{and} \quad \eta_1 = (n_0 \cdot E)^{1/2},$$

where  $E$  is the equivalent optical admittance of the stack,  $n_s$  the refractive index of the substrate and  $n_0$  is that of the medium. These additional quarterwave layers at the required wavelength (337 nm) act as antireflection coatings in reducing the reflection ripple in the pass band. But in practice it is difficult to get suitable thin film materials having matching indices. The solution to the problem is then to have eighth wave thick low index layers on either sides of the stack which act as antireflection coatings to a first approximation. The transmission characteristic of such a 17-layer stack design is shown in figure 1 (design B). As seen in figure 1, design B has less ripple in the pass band

compared to design A. To correct the ripple further in the pass band more advanced design methods have to be used. Using such an advanced method, a beam combiner was designed having less than 2% ripple in the pass band and its transmission characteristic is included in figure 1 (design C). The design method used was based on a technique called "limited scan damped least squares optimization", the details of which were described elsewhere (Apparao 1975 and 1977). The transmission characteristic of such an ideal beam combiner design is also shown in figure 1 (design C). The design data for all the three designs are given in table 1. Design B which is relatively easy to develop and which serves the application is chosen for the present development.

### 3. Development of the beam combiner

The beam combiner according to design B was developed and successfully fabricated using the method of vacuum evaporation using a conventional 300 nm vacuum coating plant. Optical grade  $\text{Sb}_2\text{O}_3$  and  $\text{Na}_3\text{AlF}_6$  were chosen as high and low index films respectively and were evaporated in boat sources. Fused silica substrate (50 mm dia) was used for the device.  $\text{Sb}_2\text{O}_3$  films evaporated at a rate less than 5 Å/sec and  $\text{Na}_3\text{AlF}_6$  films evaporated at about 20 Å/sec were found to give homogeneous stable films with minimum energy losses, particularly in the UV region. Optical and quartz crystal monitors were used during the evaporation time for monitoring optical thickness and rate of evaporation respectively. Computer-simulated data was used to monitor film thicknesses. The performance of the 17-layer beam combiner thus fabricated was evaluated at the required wavelength points using lasers and power meter. The beam

Table 1. Optical description of 17 laser beam combiner designs

No. of layers	Ref. index	Optical thickness of the film in nm		
		Design A	Design B	Design C
	1.0	Massive	Massive	Massive
1	1.35	120.0	60.0	65.13
2	2.30	120.0	120.0	126.32
3	1.35	120.0	120.0	124.03
4	2.30	120.0	120.0	122.45
5	1.35	120.0	120.0	122.45
6	2.30	120.0	120.0	119.70
7	1.35	120.0	120.0	118.23
8	2.30	120.0	120.0	118.52
9	1.35	120.0	120.0	119.11
10	2.30	120.0	120.0	119.11
11	1.35	120.0	120.0	118.81
12	2.30	120.0	120.0	119.40
13	1.35	120.0	120.0	120.91
14	2.30	120.0	120.0	123.08
15	1.35	120.0	120.0	125.98
16	2.30	120.0	120.0	134.08
17	1.35	120.0	60.0	156.35
	1.48	Massive	Massive	Massive

combiner when operated at  $45^\circ$  angle of incidence showed more than 90 % transmission at 337 nm ( $N_2$  laser) and more than 99 % reflection in the region from 420 nm to 450 nm (tunable dye laser). The device is being used successfully in the photodissociation experiments in our laboratories.

## References

Apparao K V S R 1975 *Indian J. Pure Appl. Phys.* **13** 183

Apparao K V S R 1977 *Indian J. Pure Appl. Phys.* **15** 270

Macleod H A 1969 in *Thin film optical filters* (London: Adam Hilgers) p. 128

## Optical constants in the ultraviolet region of evaporated high index thin films

K V S R APPARAO and T C BAGCHI

Spectroscopy Division, Bhabha Atomic Research Centre, Trombay, Bombay 400 085, India

**Abstract.** A suitable method to determine the optical constants of high index thin film essential for developing high efficiency dielectric thin film devices in the UV region from 240 to 400 nm. A quick and accurate method is established to determine these constants. Using this method the optical losses, refractive index, absorption coefficient and extinction coefficient of  $ZrO_2$  films prepared by the method of reactive evaporation were evaluated in the UV region.

**Keywords.** Thin films; refractive index; optical constants; absorption coefficient; extinction coefficient.

### 1. Introduction

Knowledge of optical losses and constants of thin films is essential for the development of efficient low-loss high reflecting dielectric mirrors for different laser and Fabry-Perot interferometer applications in the UV region from 240 nm to 400 nm. Such applications require suitable high index ( $n \geq 2.0$ ) optical films with minimum extinction coefficient ( $k \leq 5 \times 10^{-4}$ ). Very few high index films are known to be suitable for UV region and even for these materials complete data of optical constants and their dependence on various process parameters used during the preparation of the films are not available. Development work to study and establish such thin film data for each material involves preparing as many as 60 sample films each deposited with different process parameters and determining the optical constants of each sample film accurately. A quick and accurate method is established to determine the optical constants of thin films using transmittance spectrum of the film.

### 2. Experimental

$ZrO_2$  films were prepared on a 25 mm diameter fused silica substrates by evaporating optical grade  $ZrO_2$  using the electron beam gun in a conventional 500 mm vacuum coating unit. A total of 35 samples of  $ZrO_2$  films were prepared for the present study each with different evaporation parameters. For all the samples prepared uniformity of film thickness over the whole surface was found to be within  $\pm 2\%$  of average thickness. The transmittance spectrum of each sample substrate was recorded using double beam spectrophotometer (Hitachi model 330, photometric accuracy  $\pm 0.2\%$ ).

### 3. Method of determination

Optical losses and constants of each sample film were determined using its transmittance spectrum. A typical spectrum of about 300 nm thick  $\text{ZrO}_2$  film of refractive index  $n$  deposited on a substrate of index  $s$  is shown in figure 1. The transmittance spectrum of the substrate before coating the film is also shown in figure 1.

#### 3.1 Optical losses

The percentage optical losses  $L$  of thin films include losses due to bulk absorption  $A$ , scattering  $S$ , fluorescence  $F$  and are given by

$$L = (A + S + F) = 100 - (R + T),$$

where  $R$  and  $T$  are the specular reflection and transmission of the film respectively. It is well known that the transmittance spectrum of a dielectric film consists of a series of transmittance maxima and minima corresponding to the interference fringes as shown in figure 1. For a film of zero losses the peak maxima  $T_{PM}$  (corresponding to even multiples of half wave optical thickness) should be the same as the substrate transmittance  $T_s$  at respective wavelength points. The attenuation of  $T_{PM}$  as seen in figure 1 at the lower wavelengths can be attributed to the losses in the film. The percentage losses  $L$  of the film at wavelength  $\lambda_0$  were determined from the spectrum using the relation

$$L = 100 (T_s - T_{PM}).$$

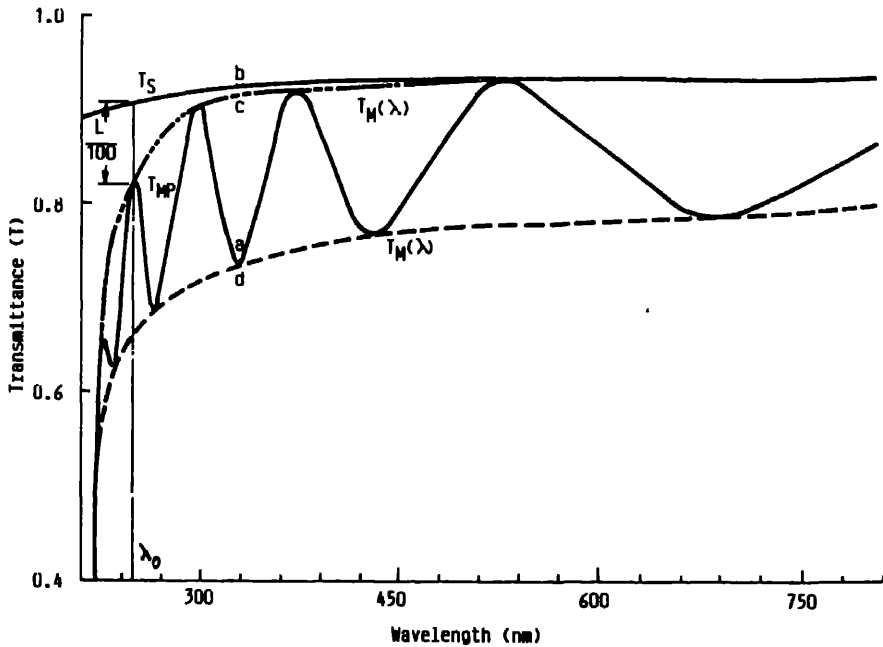


Figure 1. Transmittance spectrum of (a) 300 nm thick  $\text{ZrO}_2$  film of index  $n$  coated on a substrate index of  $s$ , (b) the substrate before coating, (c) continuous function  $T_M(\lambda)$  and (d) the continuous function  $T_m(\lambda)$ .



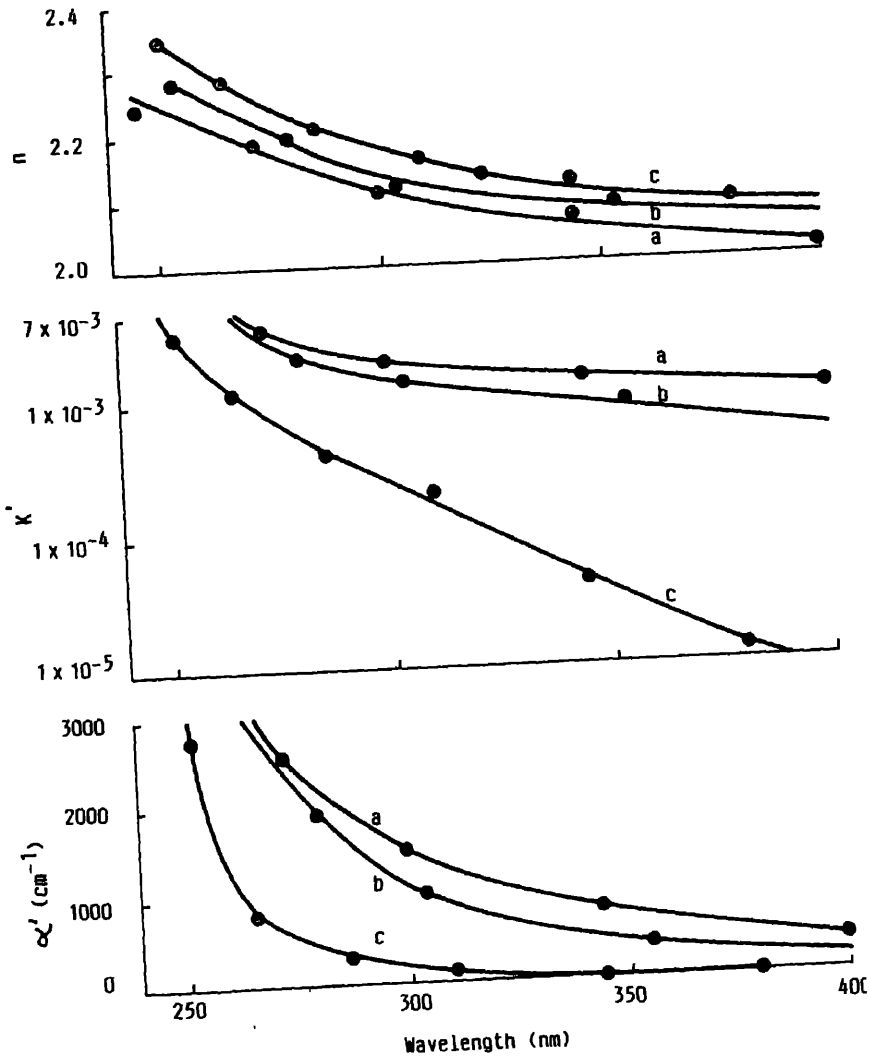


Figure 2. Dependence of optical constants of  $\text{ZrO}_2$  film on rate of evaporation. (a) 20 Å/sec, (b) 10 Å/sec and (c) 5 Å/sec.  $t \approx 275$  nm,  $T = 260^\circ\text{C}$  and  $\text{O}_2 = 2 \times 10^{-4}$  mbar.

### 3.2 Optical constants

The refractive index  $n$ , absorption coefficient  $\alpha$ , extinction coefficient  $k$  of the film at different wavelength points and its physical thickness  $t$  were determined by the method of Swanepoel (1983) using the continuous functions  $T_M(\lambda)$  and  $T_m(\lambda)$  as shown in figure 1. The formulae used in this method to compute  $\alpha$  and  $k$  were derived assuming that the attenuation of the functions  $T_M(\lambda)$  and  $T_m(\lambda)$  at shorter wavelength region was due to pure absorption losses in the film. But in practice thin films prepared by vacuum evaporation suffer losses due to scattering and fluorescence in addition to absorption. So the constants  $k$  and  $\alpha$  deduced by this method are now called effective constants  $k'$  and  $\alpha'$ .

**Table 1.** Optical losses and constants (275 nm thick)  $\text{ZrO}_2$  films in the UV region.

Wavelength $\lambda$ nm	Optical losses $L$ %	Optical constants		
		$n$	$\alpha'$ $10^3 \text{cm}^{-1}$	$k'$
250	8.00	2.35	3.547	$7.0 \times 10^{-3}$
300	0.60	2.16	0.192	$4.7 \times 10^{-4}$
350	0.13	2.10	0.031	$8.5 \times 10^{-5}$
400	0.03	2.06	0.010	$5.0 \times 10^{-5}$

#### 4. Results and discussion

The measured percentage losses and constants were plotted against wavelength for all the film samples of  $\text{ZrO}_2$  films each prepared with different evaporation conditions. The results of the relevant samples were grouped into different sets. Each set of films were prepared under identical conditions but with one parameter variable. Figure 2 shows the results of one such set wherein the dependence of optical constants of  $\text{ZrO}_2$  films on rate of evaporation is shown. The optical losses and refractive index at 250 nm ( $L = 8\%$  and  $n = 2.35$ ) for our films of 275 nm thick were found to be comparable with those films prepared by the method of sputtering ( $L = 9\%$  and  $n = 2.47$ ) as reported by Pawlewicz *et al* (1980). The losses of these films in the visible region above 440 nm are less than 0.01 % and the constants at 515 nm are found to be compatible with those reported by Pulker (1976). The optical constants and losses at different wavelength points for the  $\text{ZrO}_2$  films (275 nm thick) as prepared by us are given in table 1.

#### References

- Pawlewicz W T, Hays D D and Martin P M 1980 *Thin Solid Films* 73 169  
 Pulker H K 1976 *Thin Solid Films* 34 343  
 Swanepoel J 1983 *J. Phys.* E16 1214

## Quality and reliability of optical coatings

C L NAGENDRA and G K M THUTUPALLI

ISRO Satellite Centre, Bangalore 560017, India

**Abstract.** Quality and reliability of optical coatings can be evaluated by studying their and durability properties. A simple experimental technique is developed which facilitates and quick estimation of the quality and reliability of optical coatings as well as optimization of process parameters. This technique has been successfully applied for process optimization of anti-reflection coatings (ARCS) for Ge optics in the IR region.

**Keywords.** Optical coating; anti-reflection coatings; germanium.

### 1. Introduction

In the early 60s optical coatings were confined to simple systems such as reflector and antireflection coatings whose applications were limited in nature. In recent years, the science and technology of optical coatings have undergone remarkable changes, resulting in the development of a variety of optical coatings ranging from simple coatings to semiconductor, dielectric and refractory coatings. Since quality and durability are the basic factors responsible for satisfactory performance of systems, along with the growth and necessity of a variety of optical coatings, their quality and reliability also have become equally important. Therefore, development of high quality and reliable coatings for a particular application needs a better understanding of coating materials and their associated process technology.

Quality and reliability of any system, in general, are assessed in terms of its performance, under given environmental conditions. Hence, to evaluate the quality and reliability of optical coatings, it is necessary to study their behaviour under various environments. This calls for a detailed investigation of the physical properties of optical coatings. We have studied different physical properties which reflect the quality and reliability of optical coatings and the experimental techniques to evaluate these parameters. Based on this, a simple experimental method has been developed to demonstrate their quality and reliability. In this paper, different physical properties of the coatings, salient features of the new experimental technique and its results are presented.

### 2. Physical properties of optical coatings

Different physical properties of optical coatings that are normally considered are spectral characteristics such as reflectance, transmittance and absorptance, mechanical properties such as hardness, adhesion, abrasion resistance and durability properties such as ageing characteristics under high humidity, salinity and extreme temperature conditions. These, as a whole, can be broadly classified into basic and durability properties.

## 2.1 Basic properties

In optical coatings, spectral characteristics form the basis of their development. The materials and the process parameters are chosen so as to meet the required optical properties. Since coatings are normally deposited on optical elements such as lenses, wedges and plane parallel plates known as substrates, the deposited coatings should have satisfactory adhesion to the substrate. The optical properties and mechanical adhesion can, therefore, be considered as the basic properties.

## 2.2 Durability properties

For given conditions, the coatings should have reliable performance over a specified length of time. By studying the durability properties, it is possible to know whether they are capable of withstanding the particular environment over a given duration. In this study, the coatings are exposed to the specified environmental conditions and the basic properties are verified for any significant change. This will give the time after which the coatings will show signs of deterioration. Considering the various external conditions that the coatings are subjected to, the total number of tests could be enormous. However, to rationalize and follow certain standard test procedures, military specifications are universally adopted (Guenther 1981).

The coating properties, in general, depend on the choice of the materials used for preparing the coating and on the process parameters such as cleaning procedures and method of evaporation. The properties affected by different process parameters are presented in table 1 (Ritter 1981). It is seen that to produce good coatings, it is necessary to optimize these parameters and ascertain their durability/reliability of the coatings by conducting accelerated life tests according to military standards. Considering the various test procedures followed in military standards and process parameters, the task of optimization and demonstration of quality and reliability becomes stupendous. Hence, simplification of the test procedures greatly helps in this direction. The

Table 1. Influence of process parameters on coating properties

Coating property	Substrate cleaning	Ionic cleaning	Evaporation method	Evaporation rate	High vacuum pressure	Substrate temperature
Ref. index	—	—	—	A <sup>+</sup>	A <sup>+</sup>	A <sup>+</sup>
Transmission absorption	—	—	A	A <sup>-</sup>	A	A
Stress	A <sup>-</sup>	A <sup>-</sup>	—	A <sup>-</sup>	A <sup>-</sup>	A <sup>+</sup>
Adherence	A <sup>+</sup>	A	—	A	A <sup>+</sup>	A <sup>+</sup>
Temperature stability	A	—	—	A	A	A <sup>+</sup>
Insolubility	A <sup>-</sup>	—	—	A <sup>-</sup>	A	A <sup>+</sup>
Resistance to radiation	A	A	A	A	A	A
Defects	A	A	A <sup>+</sup>	A	A <sup>-</sup>	A

A<sup>+</sup>, strong dependence; A, moderate dependence; A<sup>-</sup>, possible dependence.

proposed experimental technique, because of its composite nature, makes the test an evaluation simpler and at the same time, it also includes the salient features of the majority of the test procedures followed in military specifications. It makes use of simple laboratory facilities.

### **3. Boiled water scotch tape test**

The various specifications and standards commonly used for optical coatings are discussed in detail by Guenther (1981). Considering the effect of these tests on the coating properties they can be classified into three groups:

- (i) Tests in which effect of solvents/vapours are studied; e.g., humidity, salt spray, boiling water and solubility tests etc.
- (ii) Tests in which the effect of temperature is studied; e.g., the temperature cycling and thermal shock tests.
- (iii) Radiation resistance tests where the effect of high energy radiations on the coating properties is studied.

Normally after these tests are conducted individually or collectively, basic properties namely mechanical adhesion and optical properties are studied (sometimes, it is also necessary to conduct abrasion resistance test). The military specification tests basically make use of solvent/vapour environment and extreme temperature conditions. The dual effect of solvent/vapour environment and extreme temperature conditions can be effectively brought about by adopting the boiled water scotch tape test. In this, the samples are immersed in boiled water at regular intervals of 5, 10, 20 minutes and cooled to ambient conditions quickly and tested for adhesion using standard scotch tape. The percentage peel-off at each interval of time is recorded by visual observation. By comparing the time intervals at which 50 % coating is peeled off, it is possible to identify the particular group of samples which have higher probability of survival. This essentially demonstrates the reliability of the coatings. Apart from this, the additional advantages of this procedure are:

- (i) By studying the mode of failure and its relation to the properties of the coating material and the substrate, it is possible to choose proper evaporation materials for a given substrate.
- (ii) Since this test is a combination of humidity, solubility, temperature cycling and thermal shock tests, the observations and its conclusions are helpful in anticipating the behaviour of the coating when subjected to individual tests.
- (iii) By extending this test over a large number of samples, reliability figures of optical coatings can be estimated experimentally. This, however, needs a thorough study on the sampling procedure for a given application.

### **4. Application to infrared antireflection coatings**

The above method has been applied to optimize the various process parameters of Al on Ge, such as temperature, evaporation rate and ionic cleaning time. After depositing the coatings, the boiled water scotch tape test is carried out and the time at which initial failure starts and 50 % coating peels, are noted down for each sample. The

**Table 2.** Experimental results of boiled water scotch tape test

Substrate temperature (°C)	Time at which visual deterioration observed (minutes)	Time at which 50 % peeling observed (minutes)
Room temp.	5	10
100	5	10
150	10	50
200	60	250
250	10	50
300	10	60

The normal adhesion is satisfactory in all cases.

**Table 3.** Quality and reliability characteristics of anti-reflection coatings (ARCS) on Ge

Tests conducted	Specification followed	Test results	Remarks
<i>Basic properties</i>			
Spectral transmission	—	80 % in 14–16 $\mu\text{m}$ (100 % improvement over bare Ge)	Same transmission levels achieved in other wavelength
Spectral reflection	—	8 % in 14–16 $\mu\text{m}$ (90 % improvement in reducing the reflection loss of Ge)	Same reflection levels achieved in other wavelength
Adhesion	MIL-M-13508	Meets specifications	
<i>Durability properties</i>			
Thermal/cleaning durability test	MIL-F-48616	Meets specifications	
Salt solubility test	MIL-C-675A	Meets specifications	
	MIL-F-48616	Meets specifications	
Humidity test	MIL-C-675A	Meets specifications	—
	MIL-F-48616		—
Abrasion test	MIL-C-675A	Meets specifications	—
<i>Long term durability properties</i>			
Thermal cycling test	+70°C to –30°C .150 cycles	No change in the basic properties and passes abrasion test as per MIL-C-675A	—
Thermal soak test	100°C for 24 hr	No change in the basic properties and passes abrasion test as per MIL-C-675A	
Extended salt solubility test	Total duration of soaking 125 hr	Passes the test as per specification MIL-C-675A and MIL-F-48616	—

results with respect to the different substrate temperatures are summarized in table 2 is evident that samples deposited at 200°C survived for a longer duration without a failure. The corresponding 50 % peel-off time is also about five times greater than other samples. This indicates that samples deposited at 200°C have higher probability of survival and are more reliable than others.

To compare the results of the present test with those of military specification tests similar samples were subjected to the military specification tests such as salt solubility and humidity tests (MIL-C-675A and MIL-F-48616) and few longer durability tests. The various tests conducted on the samples and the corresponding observations presented in table 3 show that the coated samples not only withstand the military specification tests but are also stable even after long term durability tests. Therefore it can be concluded that the method can be adopted for process optimization of optical coatings and as a quick look quality control test. It is also very effective in arriving at optimized process parameters.

## **References**

- Ritter E 1981 *Appl. Opt.* **20** 21  
Guenther K H 1981 *Appl. Opt.* **20** 3487





## Optical and electrical properties of $\text{SnO}_2$ films prepared by chemical vapour deposition

S RAGHUNATH REDDY, A K MALLIK and S R JAWALEKAR\*

Regional Sophisticated Instrumentation Centre, \*Department of Electrical Engineering  
Indian Institute of Technology, Bombay 400 076, India

**Abstract.** Transparent and conducting  $\text{SnO}_2$  films are prepared at  $500^\circ\text{C}$  on quartz substrates by chemical vapour deposition technique, involving oxidation of  $\text{SnCl}_2$ . The effect of oxygen gas flow rate on the properties of  $\text{SnO}_2$  films is reported. Oxygen with a flow from  $0.8$ – $1.35 \text{ l min}^{-1}$  was used as both carrier and oxidizing gas. Electrical and optical properties are studied for  $150 \text{ nm}$  thick films. The films obtained have a resistivity between  $\times 10^{-3}$  and  $4.95 \times 10^{-3} \text{ ohm cm}$  and the average transmission in the visible region ranges from  $86$ – $90\%$ . The performance of these films was checked and the maximum figure of merit value of  $2.03 \times 10^{-3} \text{ ohm}^{-1}$  was obtained with the films deposited at the flow rate of  $1.16 \text{ l min}^{-1}$ .

**Keywords.** Chemical vapour deposition; figure of merit;  $\text{SnO}_2$  film; transparent conducting film.

### 1. Introduction

Tin oxide films are being used in a variety of applications, such as transparent heating elements, transparent electrodes and antistatic coatings (Manificier and Fillard 1979). In the last few years interest in tin oxide films has further increased because of its potential application in semiconductor-insulator-semiconductor (sis) solar cells (Nagatomo *et al* 1979; Ghosh *et al* 1980). In the present study a simple and inexpensive chemical vapour deposition (cvd) method involving oxidation of  $\text{SnCl}_2$  has been selected for the deposition of  $\text{SnO}_2$  films for solar cell application. Murthy and coworkers (Murthy *et al* 1983; Murthy and Jawalekar 1983) deposited  $\text{SnO}_2$  films using a similar method and studied the effect of deposition temperature (range:  $300$ – $500^\circ\text{C}$ ) on their properties. It was reported that the films deposited at  $500^\circ\text{C}$  have low resistivity with uniform and large grain size ( $0.3$ – $3 \mu\text{m}$ ). Thus,  $500^\circ\text{C}$  was considered as optimum deposition temperature for deposition of  $\text{SnO}_2$  films. The aim of the present work is to study the effect of oxygen flow rate on the electrical and optical properties and to find out the optimum oxygen flow rate for the deposition of  $\text{SnO}_2$  films. In the present study, the depositions are carried out at  $500^\circ\text{C}$  with an oxygen flow rate between  $0.8$  and  $1.35 \text{ l min}^{-1}$ . The dependence of electrical and optical properties on oxygen flow rate is also reported.

### 2. Experimental details

An open tube cvd system has been used to deposit  $\text{SnO}_2$  films. The schematic of the experimental set-up is shown in figure 1. Chemically and ultrasonically cleaned P-type or quartz substrates (about  $4 \text{ cm}^2$  in area) were loaded into quartz reactor tube

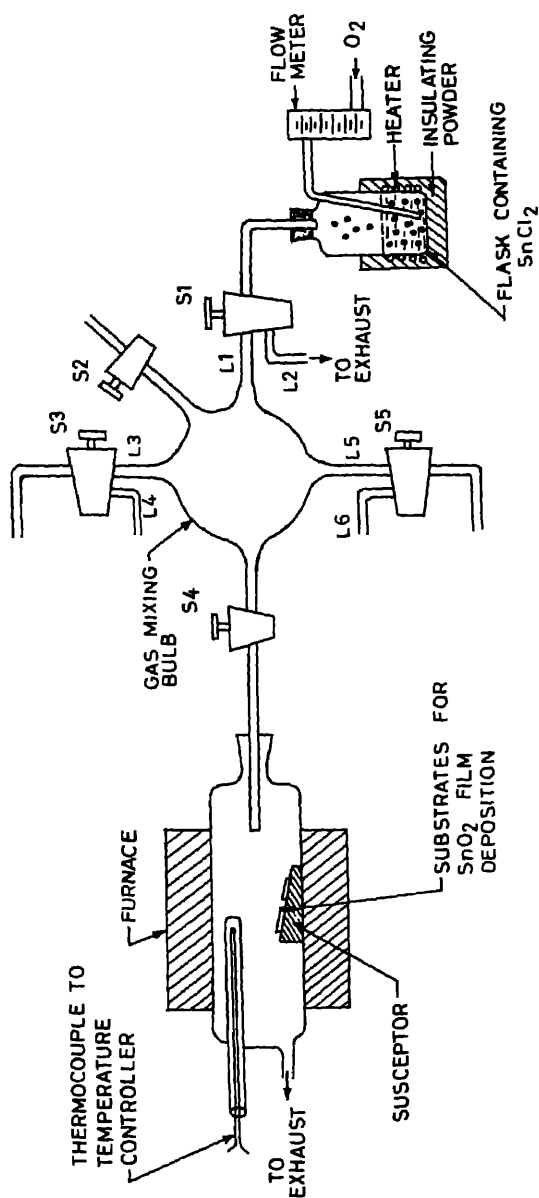


Figure 1. Schematic of the CVD experimental set-up for the deposition of  $\text{SnO}_2$  films.

placed inside the constant temperature zone. The deposition temperature maintained at the required value within  $\pm 2^\circ\text{C}$  by using a temperature control. Anhydrous stannous chloride produced by heating  $\text{SnCl}_2 \cdot 2\text{H}_2\text{O}$  (purity 99.9%) used as a source material.  $\text{SnCl}_2 \cdot 2\text{H}_2\text{O}$  was heated to its melting point ( $248^\circ\text{C}$ ); oxygen (purity 99.9%) gas was bubbled through it, which acts as a carrier and oxidizing gas. While heating to this temperature, the stopcock  $S_1$  was adjusted to position  $L_1$  that water vapour could be vented out. After adjusting the required oxygen flow rate vapours are allowed to pass through the gas mixing bulb to the heated substrates turning  $S_1$  to position  $L_2$ . The bulb was continuously heated to avoid any condensate of vapours inside the bulb. Any required dopant vapours can also be introduced through the stopcocks  $S_3$  and  $S_5$ . However no doping was carried out in this study; therefore  $S_3$  and  $S_5$  are kept closed.

The thickness of the film was measured by an optical interference method. The sheet resistance was measured by the conventional four-probe technique. For this measurement direct current through the films was maintained low (1 mA) and was passed less than 30 sec to avoid heating of the films. The optical transmission in the visible region was measured using a spectrophotometer (Aminco DW2A).

### 3. Results and discussion

The properties of  $\text{SnO}_2$  films are strongly dependent on deposition parameters, such as deposition temperature ( $T$ ), deposition time ( $t$ ) and oxygen flow rate ( $F$ ). All depositions were carried out in the flow range  $0.8\text{--}1.35\text{ lmin}^{-1}$  at  $500^\circ\text{C}$  and the effect of oxygen flow rate on electrical and optical properties is discussed in detail. Films deposited on quartz substrates were used for electrical and optical measurements.

#### 3.1 Electrical properties

The variation of film thickness ( $d$ ), deposited in the flow range  $0.8\text{--}1.35\text{ lmin}^{-1}$  with deposition time ( $t$ ) is shown in figure 2. It can be seen that  $d$  also increases with  $F$ . This is because at higher flow rates more  $\text{SnCl}_2$  vapours will be carried out from the source flask by oxygen and thereby the rate of deposition will be greater, hence the thickness increases. The dependence of sheet resistivity ( $R_{\text{sh}}$ ) on the film thickness, deposited in the flow range  $0.8\text{--}1.35\text{ lmin}^{-1}$  is shown in figure 3. It can be observed that  $R_{\text{sh}}$  decreases with  $d$  and the variation of  $R_{\text{sh}}$  is less beyond 150 nm. To study the effect of oxygen flow rate on  $R_{\text{sh}}$  and resistivity  $\rho$ , a fixed thickness film should be deposited under different flow conditions. In this case 150 nm film thickness has been chosen to study the effect of oxygen flow rate. To deposit 150 nm thick film, in the flow range  $0.8\text{--}1.35\text{ lmin}^{-1}$ , corresponding deposition times are found out from figure 1 and the films are deposited accordingly. The variation of  $R_{\text{sh}}$  and  $\rho$  with  $F$  for these films are shown in figure 4. It can be seen from these curves, that initially when  $F$  is increased,  $R_{\text{sh}}$  and  $\rho$  decrease; they pass through a minimum value at  $1.16\text{ lmin}^{-1}$  and a further increase in  $F$  results in an increase in  $R_{\text{sh}}$  and  $\rho$ .

The above results can be explained in the following way. It is well known that  $\text{SnO}_2$  is an oxygen-deficient semiconductor and  $\text{SnO}$  is an insulator. At low flow rates all the tin atoms may not be oxidized to the  $\text{SnO}_2$  state. A few molecules in the  $\text{SnO}$  phase may also be present, resulting in relatively high resistivity. As the flow rate

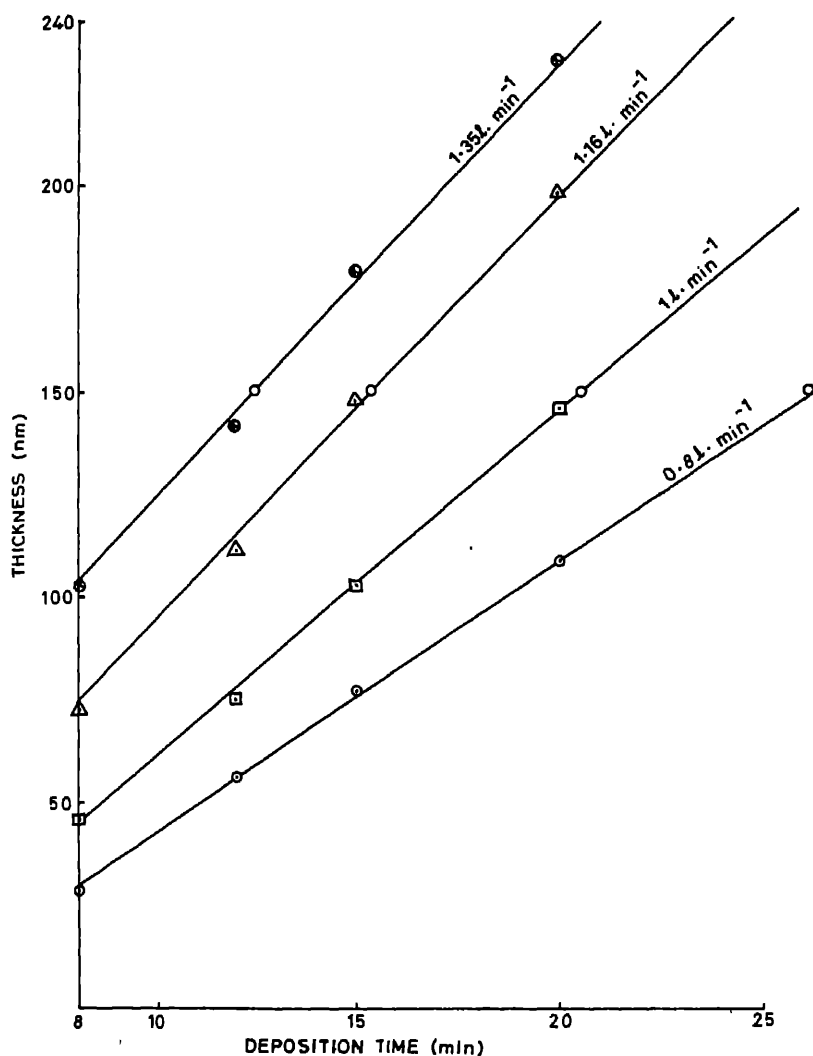


Figure 2. Variation of  $\text{SnO}_2$  film thickness on deposition time at various oxygen flow rates.

increased, the concentration of  $\text{SnO}$  may decrease, thereby decreasing  $\rho$ . Thus  $\rho$  reaches a minimum and  $\text{SnO}_2$  obtained in this region will have the optimum concentration of oxygen vacancies to give rise to the lowest  $\rho$ . As the flow rate is increased further, the oxygen content in the reaction tube increases. This may result in infilling of the oxygen vacancies in the  $\text{SnO}_2$ , and hence the oxygen-deficient  $\text{SnO}_2$  becomes nearly stoichiometric  $\text{SnO}_2$ . Thus  $\rho$  again increases as  $F$  increases.

### 3.2 Optical properties

The transmission spectra in the visible region 400–800 nm was recorded for 150 nm thick  $\text{SnO}_2$  films, deposited in the flow range of 0.8–1.35 l min<sup>-1</sup>. From these spectra the

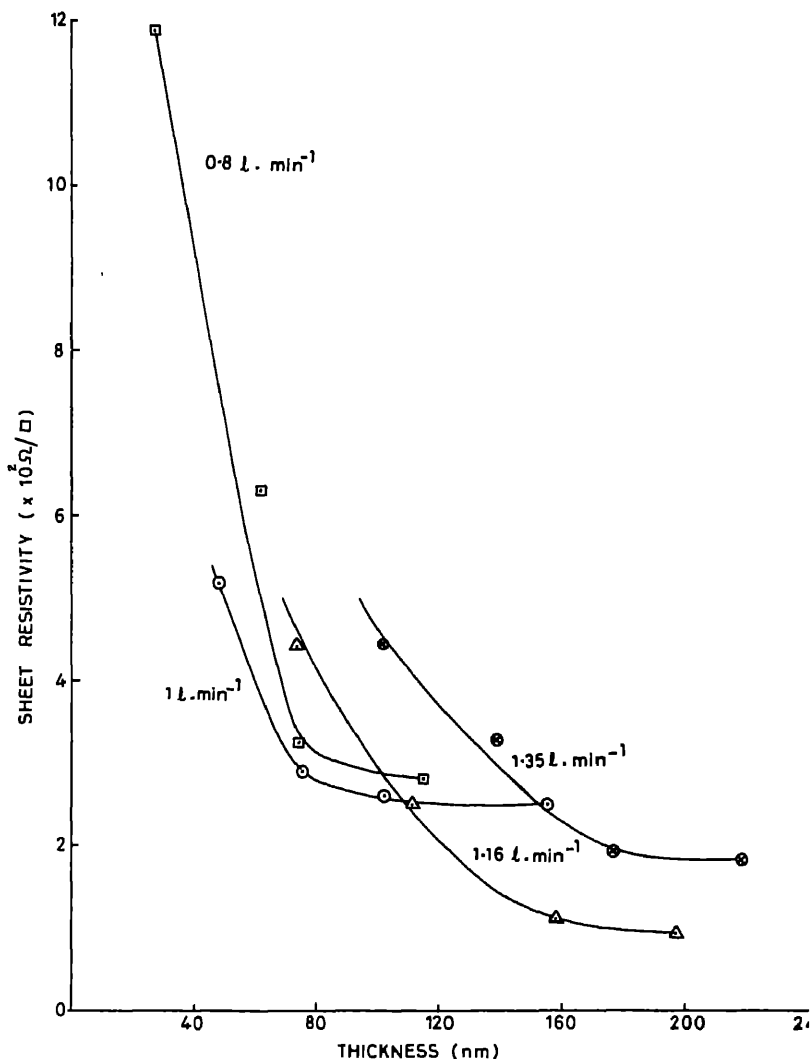


Figure 3. Dependence of  $\text{SnO}_2$  film sheet resistivity on film thickness at various oxygen flow rates.

average transmission ( $T_{r(\text{av})}$ ) is calculated and is plotted as a function of  $F$  (figure 4). It can be seen from this curve that the transmission initially decreases as  $F$  increases, and reaches a minimum for films deposited at  $1.16 \text{ lmin}^{-1}$ . The reason for this is an increase in absorption by free carriers with an increase in  $F$ . It is also evident from resistivity curves that  $\rho$  decreases as  $F$  increases. As  $\rho$  decreases the carrier concentration increases and hence the absorption by the free carriers also increases. A further increase in  $F$  results in an increase in transmission. This is again because  $\rho$  increases and hence the absorption by free carriers decreases. This explains the variations of transmission with  $F$ .

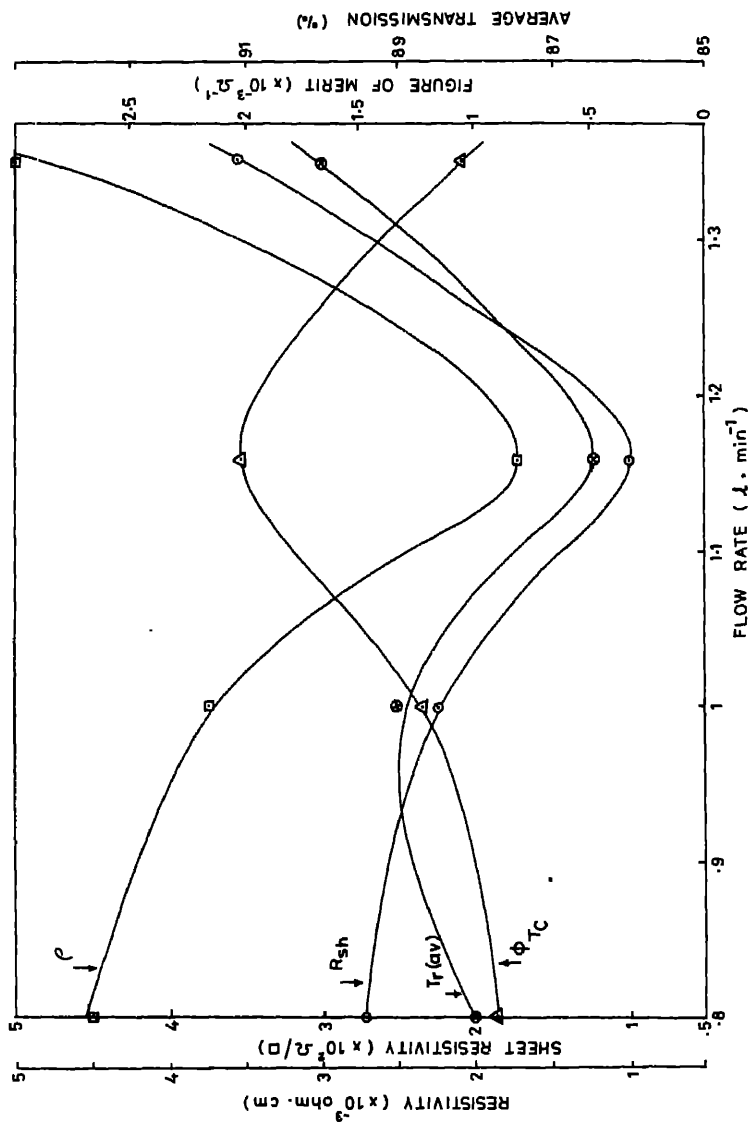


Figure 4. Variation of sheet resistivity ( $R_{sh}$ ), resistivity ( $\rho$ ), average transition ( $T_{r(av)}$ ) and figure of merit ( $\phi_{TC}$ ) with oxygen flow rate ( $F$ ).

### 3.3 Figure of merit

In order to compare the performance of the films deposited at various flow rate most commonly used definition of figure of merit  $\phi_{\text{TC}}$  as proposed by Haacke (1971) been used. It is defined as

$$\phi_{\text{TC}} = T_r^{1/2}/R_{\text{sh}},$$

where  $T_r$  is the transmission and  $R_{\text{sh}}$  is the sheet resistivity. The variation of  $\phi$  as a function of oxygen flow rate is shown in figure 4. It can be seen that the deposited at a flow rate  $1.16 \text{ lmin}^{-1}$  exhibit the maximum  $\phi_{\text{TC}}$ . The highest figure of merit  $2.03 \times 10^{-3} \text{ ohm}^{-1}$  obtained in this study is of the same order of magnitude reported by Kane *et al* (1975) and Shanthi *et al* (1982).

The above results show that the optimum oxygen flow rate for the deposition of  $\text{SnO}_2$  films is  $1.16 \text{ lmin}^{-1}$ . The corresponding film properties are  $R_{\text{sh}} = 115 \text{ square}^{-1}$ ,  $T_{\text{r(av)}}$  = 86.5 % and  $\phi_{\text{TC}} = 2.03 \times 10^{-3} \text{ ohm}^{-1}$ .

### 4. Conclusions

In this study tin oxide films deposited by CVD technique involving oxidation of  $\text{SnO}$  at  $500^\circ\text{C}$  with an oxygen flow rate between  $0.8$  and  $1.35 \text{ lmin}^{-1}$ . Electrical and optical properties are studied as a function of oxygen flow rate. On the basis of figure of merit values it is concluded that  $1.16 \text{ lmin}^{-1}$  is the optimum flow rate for the deposition of  $\text{SnO}_2$  films.

### Acknowledgements

We are thankful to the Head, Department of Electrical Engineering, Indian Institute of Technology, Bombay for providing the facilities. One of the authors (SRR) is thankful to the Head, RSIC, IIT, Bombay for sponsoring this research work.

### References

- Ghosh A K, Feng T and Maruska P 1980 *Proceedings 14th IEEE Photovoltaic Specialist Conf.*, Institute of Electrical and Electronics Engineers, New York, p. 1370
- Haacke G 1976 *J. Appl. Phys.* **47** 4086
- Kane J, Schweitzer H P and Kern W 1975 *J. Electrochem. Soc.* **122** 1144
- Mamlacier J C and Fillard J P 1981 *Thin Solid Films* **77** 67
- Murthy N S, Bhagavat G K and Jawalekar S R 1983 *Thin Solid Films* **92** 347
- Murthy N S and Jawalekar S R 1983 *Thin Solid Films* **102** 283
- Nagatomo M, Endo M and Omoto O 1979 *Jpn J. Appl. Phys.* **18** 1103
- Shanthi E, Banerjee A and Chopra K L 1982 *Thin Solid Films* **88** 93





## Pyroelectric polymer films for infrared detection

P JAYARAMA REDDY and M SIRAJUDDIN

Department of Physics, Sri Venkateswara University, Tirupati 517 502, India

**Abstract.** Some of the polymers have been recognised as potential materials for application in pyroelectric detectors because of their large and durable electric polarization. These materials are preferred over conventional ceramics due to their unique features which make them very sensitive and fast to the infrared radiation detection. The present paper discusses the special characteristics of polymer films, namely PVDF, PVC and PVF, their preparation and characterization and their pyroelectric behaviour.

**Keywords.** Pyroelectricity; polymer films; infrared detection.

### 1. Introduction

Pyroelectric detectors are of recent origin and are of special interest. These detectors which are sensitive to the changes in detection temperature rather than to the absolute temperature itself, respond to radiation which is chopped, pulsed or otherwise modulated, but ignore steady background radiation. These are less sensitive compared to the photon detectors, but are capable of operating at ambient temperature and give a consistent response over a long wavelength.

Since the discovery of piezo- and pyroelectricity in polyvinylidene fluoride (1969; Bergman *et al* 1972), polymers are recognized as potentially important transducer materials. Polymers are preferred for pyroelectric detectors over conventional ceramics because of their unique features, namely, toughness, flexibility, low mechanical impedance, low density and ability to sustain to high fields. However, due to their relatively poor dimensional stability, the melting and softening temperatures are lower than ceramics. As a result when the temperature increases the pyroelectric effect deteriorates due to the increased segmental motion of the molecular chains which leads to depolarization.

The change in polarization  $dP$  of a pyroelectric crystal due to the change in temperature  $dT$  is given by

$$dP = p \cdot dT$$

where  $p$  is the pyroelectric coefficient of the crystal.

If the temperature change is caused by the absorption of infrared radiation, the observed pyroelectric effect is equivalent to the detection of incident radiative current  $i$  in the external circuit is given by (Chynoweth 1956)

$$i = A \frac{dP}{dT} \frac{dT}{dt},$$

where  $A$  is the area of the radiation receiving electrode and  $dT/dt$  is the heating rate.

Combining (1) and (2), we get

$$p = i/[A(dT/dt)]. \quad (3)$$

## 2. Experimental

### 2.1 Film formation

Solvent casting (Sirajuddin and Jayarama Reddy 1984) and laser evaporation (Sirajuddin and Jayarama Reddy 1984a, 1985) were employed in the present investigation to prepare the films of polyvinyl fluoride, polyvinylidene fluoride and polyvinyl chloride.

**2.1a Solvent casting:** The polymer materials were dissolved in a suitable solvent. The temperature of the solution was maintained at 60°C and the films of required thickness were obtained by immersing the glass substrates in the solution of known concentration and deposition time as described elsewhere (Sirajuddin *et al* 1984). Metal electrodes were vacuum evaporated before and after the film formation to characterize the films in sandwich configuration.

The films were dried in an oven at 100°C for about 48 hr to evaporate the solvent present before the top electrode was deposited.

**2.1b Laser evaporation:** The polymer material was evaporated on glass substrates by laser radiation. A high power carbon dioxide laser of 60 watts was employed to evaporate polymer materials. The laser beam was allowed to pass through a zinc selenide window and reflected from gold-coated concave mirror onto the polymer. The pressure in the chamber was run down to  $10^{-4}$  torr during the formation of films. The details of the evaporation technique were described elsewhere (Sirajuddin and Jayarama Reddy 1984a).

### 2.2 Film characterization and measurement of pyroelectric currents

The films were characterized by studying (i) infrared spectra in the range 2.5  $\mu\text{m}$  to 25  $\mu\text{m}$  using Perkin Elmer IR spectrophotometer, (ii) x-ray diffraction profiles using Philips x-ray unit and (iii) molecular weight.

Capacitance and dielectric loss were measured using 4275A Hewlett Packard LCR meter. The resistivity was measured using 4140B digital pA meter by applying a small voltage across the films.

The film thickness was determined using Stanton monopan microbalance by measuring the weight change of the substrate and assuming the density of the film and cross-checked by capacitance measurements.

The films sandwiched between Al electrodes were poled by applying a constant electric field ( $6 \times 10^5$  V/cm) at a constant temperature 400 K. The samples were cooled in the presence of the field and the pyroelectric currents were measured using the direct method similar to that used by Byer and Roundy (1972). The poled samples were heated to 363 K under short-circuit condition for about 2 hr at a chamber pressure of  $10^{-5}$  torr and then cooled to room temperature. The first thermal cycle, known as the depolarization current or irreversible cycle, is a measure of absorbed charges during poling process. The subsequent cycles, namely, heating the short-circuited samples at a

Table 1. Properties of the films formed by solvent casting and laser evaporation

Material	Method of film formation	Thickness of the films ( $\mu\text{m}$ )	Area of the film ( $\text{cm}^2$ )	Dielectric constant	Dielectric loss	Resistivity ( $\text{ohm-cm}$ )	Structure	Pyroelectric coefficient ( $\text{nC/cm}^2\text{K}$ )	Reference
Polyvinylidene fluoride	Solvent casting	0.1-2	0.04	10	0.6	$4 \times 10^{13}$	Amorphous	1.2	
	Laser evaporation	0.1-2	0.04	8	0.05	$1 \times 10^{13}$	Semicrystalline	2.4	
	Commercial film	25	1.2	—	—	—	Semicrystalline	2.0	Das Gupta and Duffy (1979)
Polyvinyl fluoride	Solvent casting	0.1-2	0.04	7	0.4	$2 \times 10^{14}$	Amorphous	0.8	
	Laser evaporation	0.1-2	0.04	5	0.03	$1 \times 10^{14}$	Semicrystalline	1.2	
	Commercial film	18	1.86	—	—	—	Semicrystalline	1.0	Phelan <i>et al</i> (1971)
Polyvinyl chloride	Solvent casting	0.1-2	0.04	5	0.1	$5 \times 10^{13}$	Amorphous	0.08	
	Laser evaporation	0.1-2	0.04	5	0.1	$5 \times 10^{14}$	Amorphous	0.1	
	Commercial film						Amorphous	0.3	Broadhurst <i>et al</i> (1973)

constant rate to a desired temperature and subsequent cooling were observed to give 'reversible' or 'true pyroelectric' currents. Pyroelectric currents were measured using 4140B digital pA meter. The temperature of the sample was monitored by a digital multimeter (Keithley 160B). The samples were gradually heated (1 K/min) by circulating hot water. The temperature and pyroelectric currents were plotted on a X-Y/t recorder as a function of time.

### 3. Results and discussion

Table 1 gives the experimental results. The data of other workers wherever available are also given. The films obtained by laser evaporation are found to be uniform, pin hole-free and crystalline with low dielectric loss and high pyroelectric coefficient compared to solvent cast films.

#### 3.1 IR and x-ray diffraction studies

The infrared spectral studies reveal that the solvent cast films retain their chemical structure as that of the starting material whereas the laser-evaporated films have undergone structural changes. The changes were partial in the case of PVF<sub>2</sub> and PVF whereas they were predominant in PVC. Figure 1 shows the infrared spectra of laser-evaporated PVF films. The decrease in the intensity of the peak corresponding to the C-F bond suggests a partial decomposition of the polymer. A similar observation was made in PVF<sub>2</sub>. In the case of PVC, the peaks corresponding to the C-C1 stretchings and C-H vibrations were found missing suggesting the decomposition of PVC during evaporation.

The x-ray diffraction studies show that the solvent-cast films were amorphous whereas laser-evaporated PVF<sub>2</sub> and PVF films were crystalline. Figure 2 shows the diffraction pattern of typical PVF<sub>2</sub> films prepared by both the techniques. Because of their crystallinity the laser-evaporated films exhibited high pyroelectric activity in spite of partial structural deviation.

#### 3.2 Molecular weight measurement

The molecular weight of the films was determined using gel permeation chromatography and the results are shown in table 2. It was found that laser evaporation

**Table 2.** Molecular weight comparison of laser evaporated films with starting material

Material	Number average angstrom size extended chain length		Number average molecular weight	
	Starting material	Laser-evaporated	Starting material	Laser-evaporated
PVF <sub>2</sub>	2,500	360	20,400	5,420
PVF	1,800	250	15,000	5,300
PVC	1,500	100	12,000	3,500

## Pyroelectric polymers for infrared detection

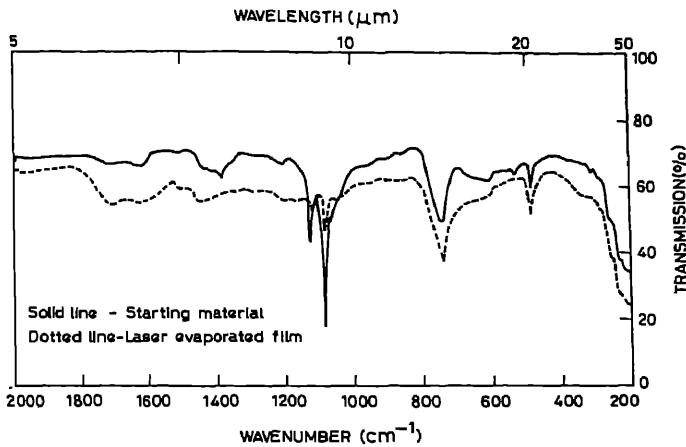


Figure 1. IR spectra of polyvinyl fluoride film.

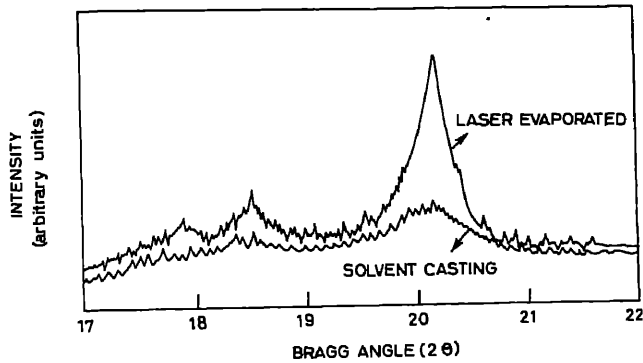


Figure 2. X-ray diffraction pattern of  $\text{PVF}_2$  film ( $2\ \mu\text{m}$  thick).

drastically reduced the molecular weight of the polymer. The shortening of the length of the laser-evaporated films suggest that the materials transferred into phase rather than as solid particles during evaporation.

### 3.3 Pyroelectric coefficient

The pyroelectric coefficient of the films was derived from the pyroelectric current temperature plot using equation (3).

It was observed that the polarity of the short circuit current in these films is opposite to that of the charging current suggesting that the pyroelectric activity may be due to the dipolar orientation (Nakamura and Wada 1971). The polarization obtained by integrating the liberated charges during the pyroelectric current measurement after the first thermal cycling of these films are shown in Figure 3. From the rigid dipolar model (Lines and Glass 1977) the polarization induced

Table 3. A comparison of experimental and theoretical values of residual polarization in vinyl halogen polymers

Polymer	Residual polarization ( $\mu\text{C}/\text{cm}^2$ )	
	Laser-evaporated films	From the rigid dipolar model
PVF <sub>2</sub>	0.5	0.3
PVF	0.3	0.1
PVC	0.1	0.08

materials was evaluated and shown in table 3 for comparison with observed values. It is seen that the observed values are significantly higher than the evaluated values. This suggests that the injection of charge carriers during poling may also be contributing to the pyroelectric activity in these materials. The studies on PVF films with asymmetrical electrode configuration (Jayarama Reddy 1984) also revealed that the polarization in these films was due to the injection of charge carriers during poling process together with dipolar orientation. The fact that injection of charge carriers was taking place further supported by the steady state current voltage characteristics revealed Schottky emission in these films (Sirajuddin and Jayarama Reddy 1984b). Similar conclusions were also drawn by Pfister *et al* (1973) and Takahashi *et al* (1977) in studying PVF<sub>2</sub> films with different electrode configurations. The Schottky type conduction in PVC (Rastogi and Chopra 1975) and the effect of metal electrodes on the depolarization currents of PVC electrets (Talwar and Behari 1981) also support the contribution of injection of charge carriers from the electrodes to the polarization of the sample. These observations suggest that the pyroelectricity in these materials can be accounted by taking both the injection of charge carriers and the dipolar orientation.

#### 4. Conclusions

(i) Laser evaporation appears to give uniform and pin hole-free polymer films compared to solvent casting method, (ii) Laser evaporated films of PVF<sub>2</sub> and PVF are found to be crystalline with low dielectric loss and high pyroelectric coefficient, and are comparable to commercial polymer films in performance. (iii) Laser evaporated films of PVC are amorphous and suffered degradation during film formation and (iv) the origin of pyroelectricity in these films can be accounted by taking both the space charge model and dipolar orientation.

#### Acknowledgement

The authors are grateful to the Department of Science and Technology, New Delhi for providing financial assistance to carry out the present work under SERC project.

## References

- Bergman J G, Crane G R, Ballman A A and O'Bryan H 1972 *Appl. Phys. Lett.* **21** 497
- Broadhurst M G, Harris W P, Mopsik F I and Malmberg C G 1973 *Polymer Reprints* **14** 820
- Byer R L and Roundy C B 1972 *Ferroelectrics* **3** 333
- Chynoweth A G 1956 *J. Appl. Phys.* **27** 78
- Das-Gupta D K and Duffy J S 1979 *J. Appl. Phys.* **50** 561
- Jayarama Reddy P 1984 *Proc. 2nd All India Conf. on Thin film State Phenomena*, IIT, Madras
- Kawai M 1969 *Jpn. J. Appl. Phys.* **8** 975
- Lines A E and Glass A M 1977 *Principles and applications of ferroelectrics and related materials* (Clarendon) p. 608
- Nakamura K and Wada Y 1971 *J. Polym. Sci.* **9** 161
- Phelan Jr R J, Mahler R J and Cook A R 1971 *Appl. Phys. Lett.* **19** 337
- Pfister G, Abkowitz M and Crystal R G 1973 *J. Appl. Phys.* **44** 2064
- Rastogi A C and Chopra K L 1975 *Thin Solid Films* **26** 61
- Sirajuddin M, Kesava Raju V and Jayarama Reddy P 1984 *Phys. Status Solidi* **A81** K-37
- Sirajuddin M and Jayarama Reddy P 1984a *Proc. Natl. Symp. Inst. Kashmir*
- Sirajuddin M and Jayarama Reddy P 1984b *J. Phys. Chem. Solids* (Communicated)
- Sirajuddin M and Jayarama Reddy P 1985 *Thin Solid Films* **124** 149
- Takahashi K, Lee H, Salomon R E and Labes M M 1977 *J. Appl. Phys.* **48** 4697
- Talwar I M and Behari S 1981 *Proc. Nucl. Phys. Solid State Phys. Symp.* (Bombay. Bhabha Res. Centre) **C24** 615





## Photoresponsive measurements on $\text{InAs}_{0.3}\text{Sb}_{0.7}$ infrared detector

M RAJA REDDY, B SRINIVASULU NAIDU and  
P JAYARAMA REDDY

Department of Physics, Sri Venkateswara University, Tirupati 517 502, India

**Abstract.** This paper presents a study of responsivity of  $\text{InAs}_{0.3}\text{Sb}_{0.7}$  infrared detector films of  $\text{InAs}_{0.3}\text{Sb}_{0.7}$  semiconducting compound were prepared by vacuum evaporation on glass and mica substrates held at 473° K under a pressure of  $10^{-6}$  torr with deposition rate of 20 Å/sec. The isothermal annealing process was employed to improve the quality of the films. The responsivity variation with blackbody temperature (333° K to 673° K), detector temperature (80° K to 303° K) and frequency (10 Hz to 10 kHz) was measured. The experimental results and the results are presented and discussed.

**Keywords.** Thin films; photoresponsivity; semiconductor; infrared detector.

### 1. Introduction

For the fabrication of the infrared detectors in the wavelength range 3  $\mu\text{m}$  to 12  $\mu\text{m}$  III–V ternary alloy system  $\text{InAs}_{1-x}\text{Sb}_x$  is of particular interest (Clawson *et al* 1973; Andrews *et al* 1975; Chenug *et al* 1977; Gertner *et al* 1980). Previous studies (Raja Reddy *et al* 1984a, b, c) carried out by the preparation and characterization of  $\text{InAs}_{1-x}\text{Sb}_x$  films revealed that films with  $x$  between 0.6 and 0.8 have favourable properties as infrared detector, since these showed maximum mobility and minimum optical energy gap among the composition range investigated. Hence in the present study the photoconductive properties of solid solutions of  $\text{InAs}_{0.3}\text{Sb}_{0.7}$  prepared by thermal evaporation are reported.

### 2. Experimental

#### 2.1 Film preparation and characterization

$\text{InAs}_{0.3}\text{Sb}_{0.7}$  films were prepared from homogeneously mixed 5 N pure InAs and Sb compounds. The films (1  $\mu\text{m}$  thick) were deposited onto glass by discrete evaporation technique using a vacuum coating technique (Balzers Automatic 510E) and cleaved mica (surface smoothness: average atomic value 1.73  $\mu\text{m}$ ) substrate under a pressure of  $10^{-6}$  torr. The thickness and deposition rate of the films were monitored using a calibrated quartz crystal thickness monitor (QM101). The source temperature (1700° K), substrate temperature (473° K), thickness (1  $\mu\text{m}$ ) and the deposition rate (20 Å/sec) were controlled by a built-in microprocessor.

The composition of the films analysed by EDAX technique showed that the films were stoichiometric. The films were found to be polycrystalline from the selected area electron diffraction pattern taken with Philips TEM. The carrier concentration and carrier mobility were measured using van der Pauw technique. The as-deposited

( $T_s = 473^\circ\text{K}$ ) were  $p$ -type with a carrier concentration of  $4.8 \times 10^{18}\text{ cm}^{-3}$  and Hall mobility,  $110\text{ cm}^2\text{V}^{-1}\text{sec}^{-1}$ . These films did not exhibit any photoresponse, probably due to the low mobility of charge carriers, high carrier concentration and  $p$ -type conduction.

The films were annealed at  $700^\circ\text{K}$  in arsenic vapour at 1 atm pressure, to compensate the native acceptors. After annealing, the films were found to be  $n$ -type with carrier concentration  $6.2 \times 10^{17}\text{ cm}^{-3}$  and mobility  $1.4 \times 10^3\text{ cm}^2\text{V}^{-1}\text{sec}^{-1}$  and exhibited good photoresponse.

## 2.2 Photoconductive measurements

The annealed  $\text{InAs}_{0.3}\text{Sb}_{0.7}$  films with dimensions  $0.2\text{ cm} \times 0.2\text{ cm} \times 1\text{ }\mu\text{m}$  were used for photoconductive measurements. The electrical contacts were provided by evaporating indium and attaching silver leads using indium solder.

The blackbody photoconductive response of the films was measured using the experimental set-up shown in figure 1. A blackbody (Model 11-210) obtained from M/s Barnes Engineering Company, USA was used as a radiation source. A variable mechanical chopper (Barnes Model 11-200/201-10A and 10C) placed between the source and the sample film, modulated the radiation frequency in the range 10 Hz to 10 kHz. The film sample was mounted in a specially designed cryostat and the temperature was controlled by a temperature controller (Specac 20-100) with an accuracy of  $\pm 1^\circ\text{K}$  in the temperature range,  $80^\circ\text{K}$  to  $303^\circ\text{K}$ . A  $\text{CaF}_2$  infrared transmitting window was fixed to the cryostat with  $90^\circ$  field of view. The film sample i.e. the detector was connected in series with load resistor and a bias power supply. The signal voltage ( $V_s$ ) developed across the detector due to the incident radiant power from the blackbody was measured using a lock-in amplifier (Princeton Applied Research, model 124A) with a plug-in (PAR 184) pre-amplifier.

The measurements were repeated by varying the blackbody temperature from  $333^\circ\text{K}$  to  $673^\circ\text{K}$ , maintaining the detector always at  $80^\circ\text{K}$ .

The spectral response of the detector was measured using a monochromator (M/s Central Electronics Limited, New Delhi, model HM104) with interchangeable

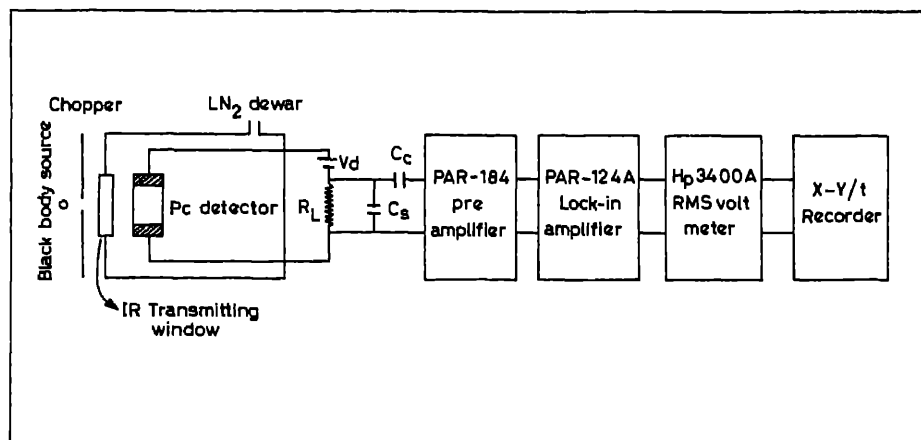


Figure 1. Experimental set-up for photoconductive measurements.

gratings in the wavelength range  $2\text{ }\mu\text{m}$  to  $10\text{ }\mu\text{m}$ . The detector temperature was from  $80^\circ\text{K}$  to  $303^\circ\text{K}$ .

The noise voltage of the detector in the frequency range  $10\text{ Hz}$  to  $10\text{ kHz}$  measured using a voltmeter (Hewlett Packard 3400A RMS) with a full scale acc of  $\pm 1\%$ .

The photoresponsivity ( $R$ ) of the detector, was determined using the relation

$$R = V_s / H A$$

where  $H$  is the irradiance on the plane of the detector and  $A$  is the effective area detector.

In order to specify the effect of noise on the performance of the detector, a independent figure of merit,  $D^*$ , was evaluated using the relation (Kruse *et al*

$$D^* = (1/H)(V_s/V_n)(\Delta f/A)^{1/2},$$

where  $V_n$  is the noise voltage and  $\Delta f$  the electrical bandwidth.

### 3. Results and discussion

The variation of blackbody photoresponse with its temperature is shown in figure 2. The responsivity slowly increases with increasing blackbody temperature and saturates beyond  $500^\circ\text{K}$ . The initial increase is due to the increase of photo density. The blackbody temperature was therefore fixed at  $500^\circ\text{K}$  for spectral responsivity and detectivity.

From the measured spectral response of the detector,  $D^*$  was calculated and plotted against wavelength.  $D^*$  showed a maximum around  $8\text{ }\mu\text{m}$  (figure 3). Further, detectivity was high at  $80^\circ\text{K}$  and decreased as the temperature increased. This is due to the substantial increase of the thermally generated charge carriers overshadow the photogenerated charge carriers resulting in the decrease of signal to noise ratio.

The variation of detectivity with frequency and temperature is shown in figure 4. It is observed that the detectivity is frequency-dependent up to about  $200\text{ Hz}$  and

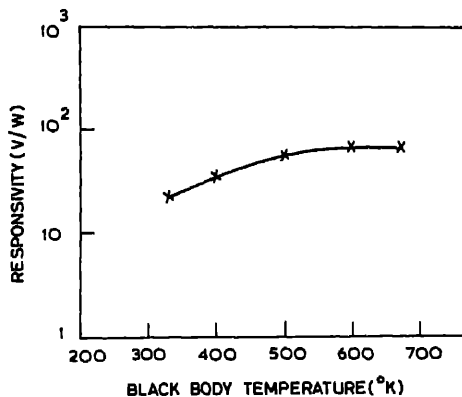


Figure 2. Variation of photoresponse with blackbody temperature.

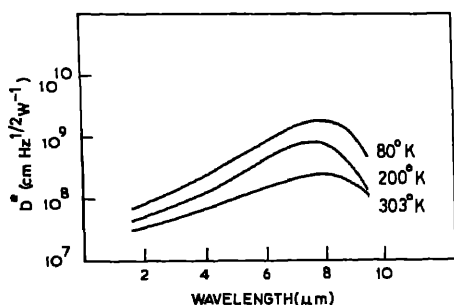


Figure 3. Variation of detectivity ( $D^*$ ) with wavelength.

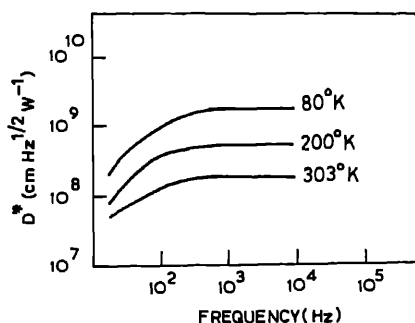


Figure 4. Variation of detectivity ( $D^*$ ) with frequency.

becomes independent. At low frequencies the detectivity is generally limited by  $1/f$  noise arising due to the presence of potential barriers at the electrical contacts, surface or interior (Hanafi and van der Ziel 1978) of the sample. In the present case, the potential barriers appearing at the electrical contacts were taken as negligible, because the contacts used were perfectly ohmic. Also, the surface states contribution to  $1/f$  noise was reduced by depositing antireflecting layer (polystyrene) on the surface of the detector, i.e. the low value of  $1/f$  noise (figure 4) was mostly due to the interior potential barriers of the semiconducting film which was polycrystalline in nature. At frequencies  $> 200$  Hz, the detectivity is limited by amplifier or generation-recombination (g-r) noise. Because of the use of a low noise amplifier and a proper design of the electronic circuit, the amplifier noise may be taken as negligible in the present study. The g-r noise is generally proportional to the minority carrier density and is dependent on the nature of conduction and the quality of the films. In the present film samples (i.e. detectors), even after annealing, there are likely to be some uncompensated native defects which act as recombination centres, contributing significantly to the g-r noise and limiting the detectivity. The performance of the detector however, can be improved by preparing films free from impurities and defects and having a low minority carrier concentration. The g-r noise decreases with increasing temperature (figure 4), because the majority carrier concentration increases at higher temperatures.

#### 4. Conclusions

$\text{InAs}_{0.3}\text{Sb}_{0.7}$  films were deposited on glass and mica substrates held at 473° K using discrete evaporation at a pressure of  $10^{-6}$  torr. As-deposited films were  $p$ -type and did not exhibit photoresponse. The films were annealed in arsenic ambient to convert them to  $n$ -type. The annealed films exhibited high mobility and good photoresponse. The photoresponse of annealed  $n$ -type films were studied as a function of frequency, wavelength and detector temperature. The performance of the detector was limited by  $1/f$  noise at low frequencies ( $< 200$  Hz) and then g-r noise at higher frequencies. The detector showed maximum detectivity ( $2.78 \times 10^9 \text{ cm Hz}^{1/2} \text{ watt}^{-1}$ ) at 80° K around 8  $\mu\text{m}$ . The performance of the detector may be improved by preparing epitaxial films free from defects and impurities.

## *InAsSb infrared detector*

### **Acknowledgement**

The authors are grateful to the Department of Science and Technology, New D financial assistance.

### **References**

- Andrews A M, Chenug D T, Gertner E R and Longo J T 1975 *J. Vac. Sci. Technol.* **13** 961
- Bubalac L O, Andrews A M, Gertner E R and Chenug D T 1980 *Appl. Phys. Lett.* **36** 734
- Chenug D T, Andrews A M, Gertner E R, Williams G M, Clarke J E, Pasko J G and Longo J T 1980 *Phys. Lett.* **30** 587
- Clawson A R, Lile D L and Wieder H H 1972 *J. Vac. Sci. Technol.* **9** 976
- Gertner E R, Andrews A M, Bubalac L O, Chenug D T, Ludowise M J and Riedel R A 1979 *J. Mater.* **8** 545
- Hanafi H I and van der Ziel A 1978 *Solid State Electron.* **21** 1019
- Kruse P W, McGlauchlin L D and McQuistan R B 1962 *Elements of infrared technology: Generation, transmission and detection* (New York: John Wiley) p. 271
- Raja Reddy M, Srinivasulu Naidu B and Jayarama Reddy P 1984a *Proc. Int. Conf. Metallurgical Engineering* San Diego, USA
- Raja Reddy M, Srinivasulu Naidu B and Jayarama Reddy P 1984b *Natl. Symp. Instrumentation, Electronics and Optics* India
- Raja Reddy M, Srinivasulu Naidu B and Jayarama Reddy P 1984c *Proc. Sixth Int. Conf. Thermochemical Analysis* (Lausanne: Elsevier) Stockholm, Sweden
- Wieder H H and Clawson A R 1973 *Thin Solid Films* **15** 217



## R.F. magnetron sputtered tungsten carbide thin films

P K SRIVASTAVA, V D VANKAR and K L CHOPRA

Department of Physics and Centre for Materials Science and Technology, Indian Ins Technology, New Delhi 110016, India

**Abstract.** Thin films of tungsten carbide have been deposited on stainless steel substrate at 500°C by r.f. reactive magnetron sputtering in two different modes of introducing argon and acetylene gases called normal and high rate mode. A single phase fcc-WC is formed in normal mode whereas a mixture of A-15-W<sub>3</sub>C, hexagonal-WC and graphitic- and diamond-carbon is found in the high rate mode. A microhardness value as high as 3200 kgf/mm<sup>2</sup> compared to the bulk value of 1800 kgf/mm<sup>2</sup> is obtained in the film deposited by high rate mode.

**Keywords.** Tungsten carbide; magnetron sputtering

### 1. Introduction

High rate reactive magnetron sputtering process for thin film deposition is important for industrial applications. Several workers (Aronson *et al* 1980; Schiller *et al* 1981; Kaiza *et al* 1981) have developed such techniques to deposit thin films of various transition metal carbides, nitrides, oxides etc for wear-resistant and protective coatings on various substrates like cemented carbide tools, high speed steel, copper and copper alloys. Efforts to enhance the deposition rate by effective control of the flow of reactive gases into sputtering chamber have been made. The processes that occur on the magnetron target surface are dependent on the interaction between sputtered particles and reactive gaseous products as well as on the degree of coverage of the target by the products obtained on the target. Generally in reactive sputtering, the target metal is carburized, nitrided or oxidized by the reactive gases and subsequently sputtered at very high rates since the sputtering yield for carbides, nitrides or oxides is much lower than that of the corresponding metals. Schiller *et al* (1980) deposited various compounds at very high rates by using a dc magnetron-plasmatron system in such a way as to achieve practically complete separation of solid component sputtering at the target and reaction of the produced particles with the gaseous component during condensation on the substrate. They were able to sputter various compounds with very high rates (~1 µm/min for Ta<sub>2</sub>O<sub>5</sub>). Recently Scherer and Wirz (1984) used a similar configuration for sputtering of Al<sub>2</sub>O<sub>3</sub>.

We have prepared tungsten carbide films by reactive r.f. magnetron sputtering on stainless steel substrates. The substrate temperature, flow of gases and bias potential at the cathode were controlled to obtain hard adherent coatings. Two different methods of introducing argon and acetylene gases were studied. In one, called the normal mode (NM), the two gases were homogeneously mixed in the plasma region whereas in the other, called the high rate mode (HRM), separate zones of argon and acetylene were created by controlling the flow of the two gases such that the carbide formation

tungsten target could be reduced (Srivastava *et al* 1985). The  $WC_x$  films formed in both the modes were analyzed by x-ray diffraction (XRD) and Auger electron spectroscopy (AES) for their structure and compositional analysis. The microhardness was measured by Vicker's microhardness tester fitted onto Carl Zeiss optical microscope. The indents produced during the microhardness measurements were also analyzed in a scanning electron microscope (SEM).

## 2. Experimental details

Figure 1 shows the magnetron sputtering system used for deposition of tungsten carbide films on stainless steel substrates held at 500°C in the normal mode (a) and in the high rate mode (b). Preparation of substrates for deposition and various conditions for sputtering is reported elsewhere (Srivastava *et al* 1984). Flow rates of argon and acetylene gases were maintained at 30 scc/min and 6 scc/min, respectively for both systems. An r.f. power density of 4.5 watt/cm<sup>2</sup> was maintained during sputtering. This developed a target bias voltage of 500 volts. For each run, the substrate temperature, flow of gases and the bias potential developed on the cathode were kept constant. Under similar conditions the deposition rate of tungsten films and tungsten carbide films in normal and high rate mode are 825, 600 and 825 Å/min respectively.

An x-ray diffractometer (Philips PW 1730/10) was used for x-ray analysis in  $\theta - 2\theta$  scan mode using  $CuK_{\alpha}$ , (1.54 Å) radiation and 1°/min scan speed. For compositional analysis, a scanning Auger microprobe (PH1 590) with electron beam of 0.2 µm diameter was used. The sputter depth profile was performed with an ion gun of ~200 µm diameter operated at 5 kV and current density 600 µA/cm<sup>2</sup>.

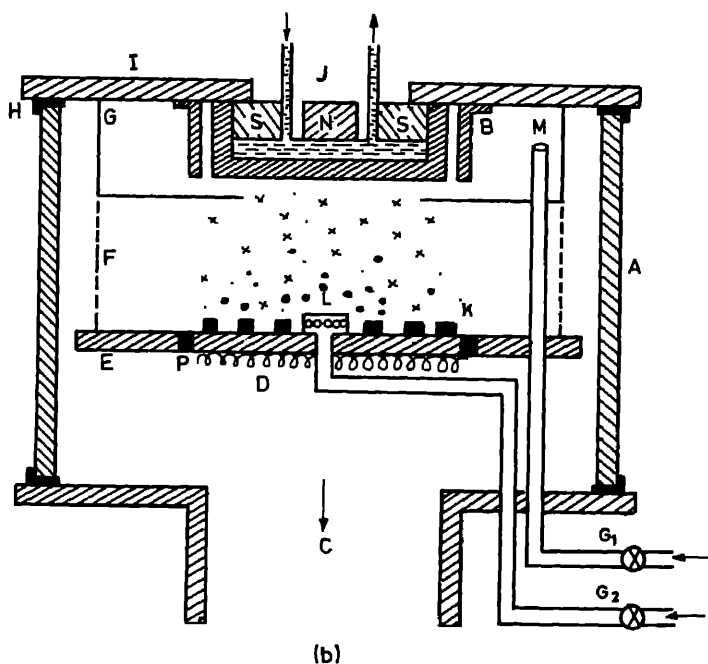
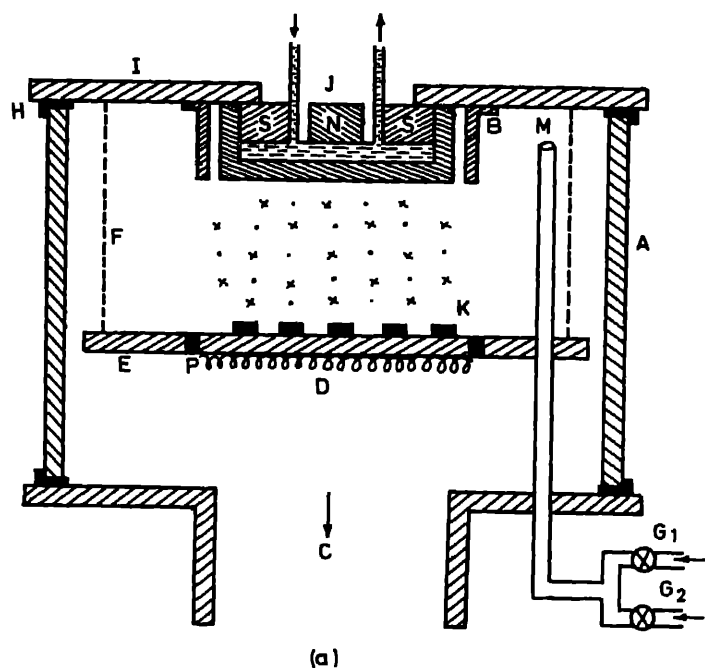
## 3. Results and discussion

Figure 2 shows the XRD profiles for 4.2 µm thick films deposited at 500°C in the normal mode (a) and in the high rate mode (b). The maximum grain size as calculated from the broadening of x-ray peaks is ~300 Å for both types of films. Since at different temperatures the structure and composition of the film are different, correlation of the grain size variation with temperature is not possible. The interplanar spacings  $d$  were calculated from the XRD and compared with standard data (ASTM data cards). The NM films deposited at 500°C on stainless steel are cubic tungsten monocarbide (f.c.c. B1 structure) while the HRM films deposited at 500°C are a mixture of various phases, namely A-15  $W_3C$ , hexagonal WC, graphitic carbon and diamond carbon.

Figure (3a) shows the AES traces of the surface of  $WC_x$  films which is a typical feature of all the films sputtered in both modes. Oxygen ( $KL_{2,3}L_{2,3}$ -512 eV) is a major impurity on the surface. The presence of carbon is indicated by a peak ( $KL_{2,3}L_{2,3}$ -271 eV) which has a characteristic shape suggesting the formation of graphitic phase on the surface. Inside the bulk of the NM film the shape of this peak changes and additional features at 252 eV and 260 eV appear (figure 3b). Such features are characteristic of carbide phase formation (Moyoshi and Buckley 1982). Similar peaks at 252 eV and 260 eV appear in the HRM films but these peaks are not very sharp suggesting that the carbide phase formation is not complete and a mixture of graphitic and carbidic phases are present (figure 3c). Thus XRD and AES profiles are found consistent with each other. AES



# Magnetron sputtered tungsten carbide films



**Figure 1.** Schematic diagram of reactive r.f. magnetron system in (a) normal mode, (b) rate mode showing metallic belljar (A), target shield (B), vacuum pump (C), substrate heat grounded base plate (E), perforated aluminium mesh (F), aluminium metallic partition (H), top plate (I), target (J), substrate (K), opening of inert gas (M), insulator ring (P), and precision needle valves (G<sub>1</sub> and G<sub>2</sub>).

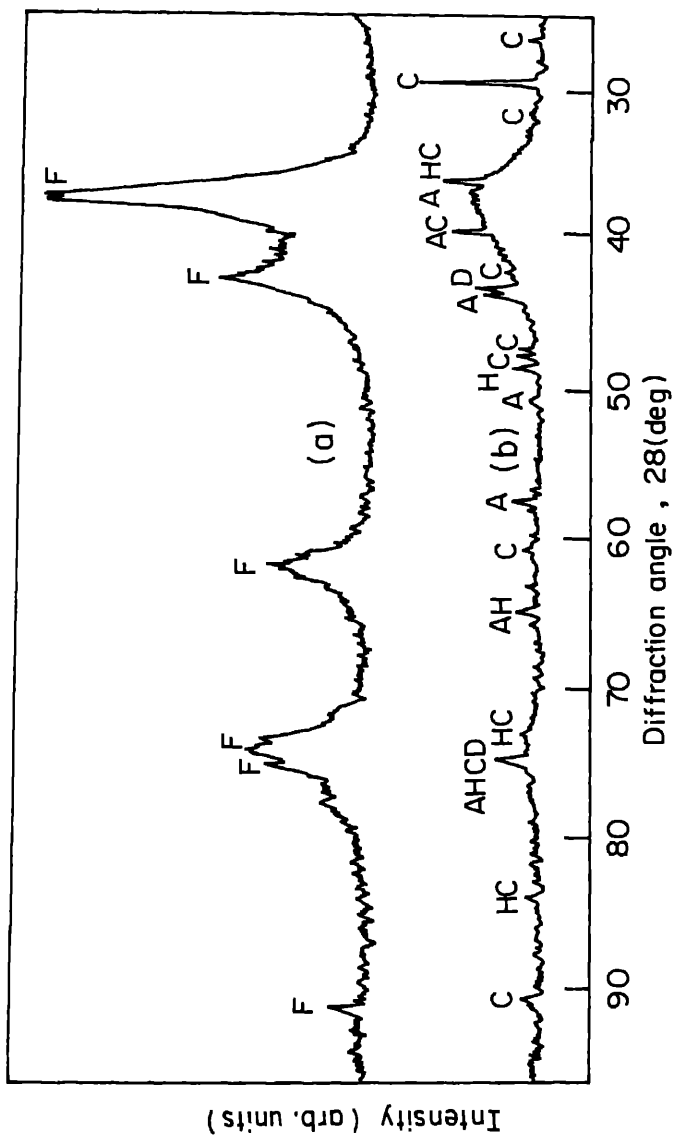
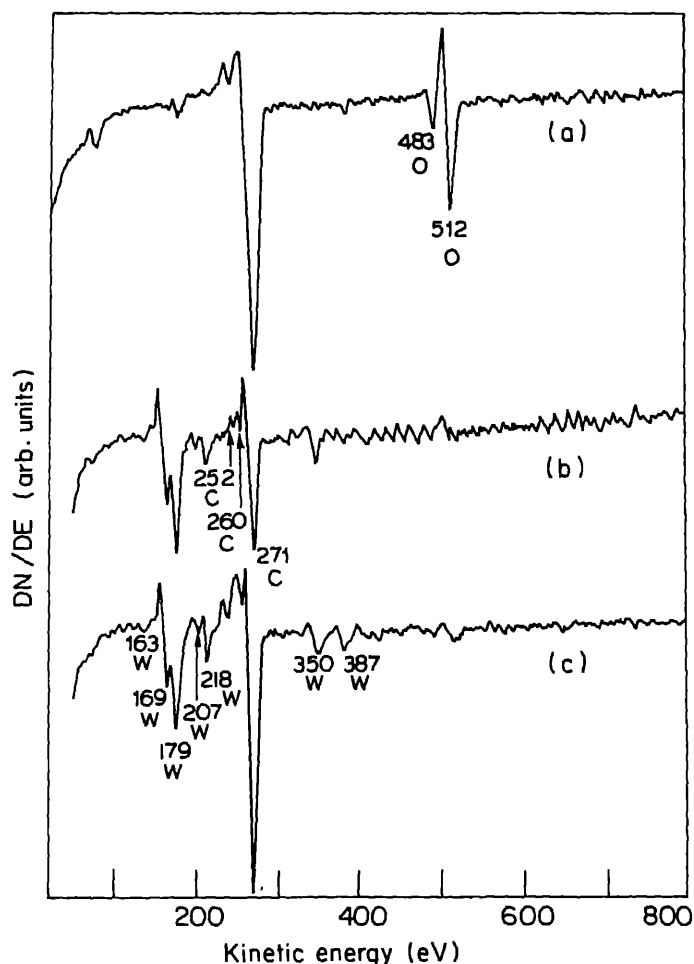


Figure 2. X-ray diffraction profiles of  $WC_x$  films prepared on stainless steel substrates at  $500^\circ C$  in (a) normal mode, (b) high rate mode showing A-15  $W_3C$  phase (A), hexagonal  $WC$  phase (H), graphitic carbon (C) and diamond carbon phase (D), and for  $WC_x$  phase (F).



**Figure 3.** AES profile of  $WC_x$  films deposited at  $500^\circ\text{C}$  on stainless steel substrate at surface of HRM films, (b) 100 Å depth from the surface of NM films, and (c) 100 Å depth from the surface of HRM films.

analysis yields the composition of these films as 50% W, 50% C for NM films, and W, 60% C for HRM films.

The microhardness of the films has been measured by Vicker's microhard indenter and value of 3200 and 2365 kgf/mm<sup>2</sup> is observed at 10 g load for NM and HRM films respectively. It should be noted that the bulk hardness of tungsten carbide (hexagonal phase) is 1800 kgf/mm<sup>2</sup>. The higher values observed in NM films may be due to fine grain size and B1 fcc crystal structure. HRM films crack during the microhardness measurement and a circular crack pattern is developed around the indentation. The number of the circles increases with increasing load and three concentric circles formed at a load of 160 g. In the case of NM films such cracks around the indentation were not observed.

The XRD and AES studies suggest that the HRM films have excess free carbon in graphitic and diamond form which is dispersed in  $W_3C$  (A-15 phase) and WC (hex-

phase) resulting in brittle films (as observed in microhardness measurements) which develop cracks at higher loads. On the other hand, NM films have single phase and are less brittle and, therefore, do not crack at loads as high as 160 g.

#### 4. Conclusions

- (i) Rates of deposition of  $WC_x$  films as high as that of pure tungsten have been achieved by dividing the inert and reactive gases in separate zones and controlling their flow patterns in such a way that the carbide formation on target surface is avoided.
- (ii)  $W_3C$  (A-15 phase), WC (hexagonal) and carbon (graphitic and diamond form) are obtained in the films prepared in the modified geometry whereas in the normal geometry a single phase fcc tungsten monocarbide is formed.
- (iii) A microhardness value as high as  $3200 \text{ kgf/mm}^2$  at 10 g load has been obtained in single phase fcc  $WC_x$  films whereas the films containing a mixture of phases and dispersed carbon have lower microhardness ( $2365 \text{ kgf/mm}^2$ ) at 10 g load.

#### Acknowledgements

The authors are grateful to the Department of Science and Technology, New Delhi, for financial support, to Dr K C Nagpal for help and advice with x-ray diffraction work, to M Bhatnagar for AES work, to Vandana Agrawal and R S Rastogi for technical discussion.

#### References

- Aronson A J, Chen D and Class W H 1980 *Thin Solid Films* **72** 535
- ASTM Data Card Nos. 20-1316, 5-728, 22-1069, 6-675
- Kaiza K, Tsunetaka S and Mitsunori K 1981 *Thin Solid Films* **78** 41
- Moyashi and Buckley D H 1982 *Appl. Surf. Sci.* **10** 357
- Scherer M and Wirz P 1984 *Thin Solid Films* **119** 203
- Schiller S, Heisig U, Strumptel K and Sieber W 1980 *Vakuumtechnik* **30** 1
- Schiller S, Beister G and Sieber W 1984 *Thin Solid Films* **111** 259
- Srivastava P K, Rao T V, Vankar V D and Chopra K L 1984 *J. Vac. Sci. Technol.* **A2** 1261
- Srivastava P K, Vankar V D and Chopra K L 1985 *J. Vac. Sci. Technol.* **A3** 2129

## Cobalt oxide-iron oxide selective coatings for high temperature applications

C S UMA, L K MALHOTRA and K L CHOPRA

Department of Physics, Indian Institute of Technology, New Delhi 110016, India

MS received 1 January 1985; revised 9 January 1986

**Abstract.** Cobalt oxide-iron oxide coatings on stainless steel have been prepared by pyrolysis technique. These coatings have absorptance ( $\alpha$ ) = 0.94 and emittance ( $\epsilon_{100}$ ), which are much better values than for cobalt oxide or iron oxide alone on stainless substrates. The coatings have been found to be stable for temperatures upto 400°C.

**Keywords.** Selective coatings; absorptance; emittance; cobalt-iron oxide

### 1. Introduction

The spectral profile of an ideal absorber surface in a photothermal converter for spectrum comprises of a low reflectance region from 0.3–2.0  $\mu\text{m}$  and a high reflect at higher wavelength. Such a spectral profile can be generated in many ways by us combination of thin film materials (selective coatings). An absorber-reflector tandem structure is one of the important selective coatings. The tandem structure is made a thin layer of a material (which absorbs the solar radiation but is transparent infrared) on a metal having a high infrared reflectance and hence low emittance.

Cobalt oxide as an absorber layer has been studied by many workers (Kokorop *et al* 1959; Gillette 1960; Kruidhoff and Van der Leij 1979; McDonald 1980; Smitl 1980; Chidambaram *et al* 1982) on a variety of substrates like polished nickel, platinum and stainless steel. Different techniques such as thermal oxidation, electrodeposition and spray pyrolysis have been utilized to deposit thin cobalt oxide. The resulting absorber/reflector tandem structure gives integrated absorptance range 0.87–0.92 and thermal emittance  $\sim$  0.14–0.24. The reflectance spectrum of an oxide coating on metal substrate shows a rise around 1.05  $\mu\text{m}$  which limits ultimate integrated absorptance. Addition of other materials like cobalt sulphide (Chidambaram *et al* 1982) modifies the reflectance spectrum but the presence of sulphide reduces the stability of the coating to  $\sim$  250°C. If this modification is achieved by the addition of another stable oxide, a higher stability is expected. Such a combination of cobalt oxide-iron oxide was studied by Kruidhoff and Van der Leij (1980) by thermally oxidizing an electroplated layer of Fe and Co. Iron oxide has a lower refractive index compared to cobalt oxide and hence one expects such a combination to give rise to a high absorptance. However, an integrated absorptance of only 0.5 and thermal emittance of 0.3 was obtained by these workers. The coatings were found to be stable up to 300°C. In the present work a simple spray process has been used to prepare cobalt oxide-iron coatings on stainless steel. The results are presented in the following section.

## 2. Experimental details

The coatings were prepared by spray pyrolysing aqueous solution of cobalt nitrate and ferric nitrate on stainless steel substrates. The substrates were initially cleaned by a mild scrubbing with detergent, thoroughly washed with water and then chemically etched for 2–3 min at 60°C in a solution having 200–250 g/l of sodium dichromate and 20–30 ml/l of sulphuric acid. This was followed by cleaning with distilled water. Good, uniform and adherent coatings were obtained at a deposition temperature of  $\sim 170^\circ\text{C}$ . Various parameters like volume of the solution sprayed, concentration of cobalt nitrate and ferric nitrate solution, spray rate were optimized to give the best values of absorbance and emittance.

Total reflectance was measured using a Hitachi 330 spectrophotometer with an integrating sphere attachment. Freshly prepared MgO was used as a standard. The absorbance ( $\alpha$ ) was calculated by integrating the reflectance data over AM 1.5 spectrum. The emittance ( $\epsilon$ ) was measured by using the standard radiometric method. The temperature of measurement was kept at 100°C. The stability of the coating was tested by annealing in air at 400°C and 500°C for 24 hr and in a separate test, by boiling in a 5% NaCl solution. The absorption and emittance were measured before and after each test.

Electron diffraction analysis was carried out using AEI/EM 802 transmission electron microscope. A scanning auger microprobe (PHI 590A) was used to determine the composition of the coating.

## 3. Results and discussion

Figure 1 shows the reflectance spectra of cobalt oxide, iron oxide and cobalt oxide-iron oxide coatings on stainless steel. The deposition parameters for all the coatings have

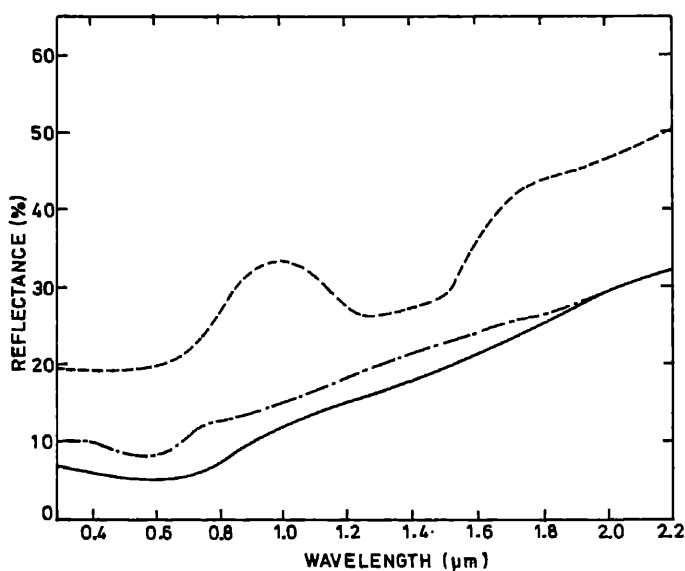


Figure 1. Reflectance spectrum of cobalt oxide (-----), cobalt oxide-iron oxide (——) and iron oxide (— · — · —) for the same deposition parameters.

been kept similar for comparison. The characteristic rise in reflectance spectrum cobalt oxide is quite evident. The coating with this reflectance spectrum has  $\alpha = 0.89$  only and  $\epsilon_{100} \sim 0.15$ . The optimized values of  $\alpha$  and  $\epsilon$  for cobalt oxide/stainless steel were 0.89 and 0.2 respectively. Since iron-oxide has a lower refractive index than cobalt oxide, one expects cobalt oxide-iron oxide coatings to have lower reflectance and hence higher absorptance. Incorporation of iron oxide thus decreases the reflectance in entire spectral range of interest and particularly around  $1.05 \mu\text{m}$  and consequently goes up to 0.94. The emittance has a value of 0.20. The reflectance spectrum of cobalt oxide alone is also shown. This coating has  $\alpha = 0.89$ . This indicates that the high absorption in cobalt-oxide iron oxide is partly due to the inherent low reflectance of material compared to either cobalt oxide or iron oxide and partly due to textural effects. Dependence of absorptance and emittance on the volume of solution sprayed (and hence the thickness of the absorber layer) for a particular concentration is shown in figure 2. The absorptance initially rises and then saturates to a value of 0.94. This value is limited by the front surface reflection of the absorber layer. As expected, emittance increases with thickness of the absorber layer.

The coatings were stable up to  $400^\circ\text{C}$ . When heated up to  $500^\circ\text{C}$  in air for 24 hr absorptance decreased to 0.91 and emittance increased to 0.22. The reflectance spectrum of such a heated sample is shown in figure 3.

Auger analysis showed the presence of Fe, Co and O. The composition profile as a function of etch time is shown in figure 4. The ion etching was done using a differentially pumped ion gun with  $\text{Ar}^+$  ions (ion beam voltage  $\sim 3 \text{KV}$ , current density  $\sim 600 \mu\text{A}/\text{cm}^2$ , raster area  $2 \text{mm} \times 2 \text{mm}$ , corresponding to a precalibrated rate of  $120 \text{ \AA}/\text{min}$  of  $\text{Ta}_2\text{O}_5$ ). The depth profile was started after sputter cleaning. The percentage of iron was greater than that of cobalt throughout the film. Electron diffraction studies showed these coatings to consist of  $\text{Fe}_2\text{O}_3$  and  $\text{CoO}$  with small traces of  $\text{Fe}_3\text{O}_4$ .  $\text{Fe}_2\text{O}_3$  and  $\text{CoO}$  are known to be the stable oxides of Fe-O and Co-O systems. The general decomposition mechanism of aqueous solution of salts is similar

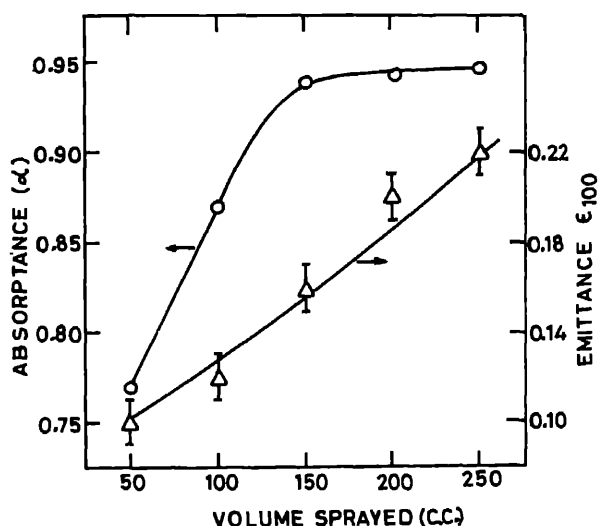


Figure 2. Dependence of absorptance and emittance on the amount of absorptant emittance on the amount of volume of solution sprayed.

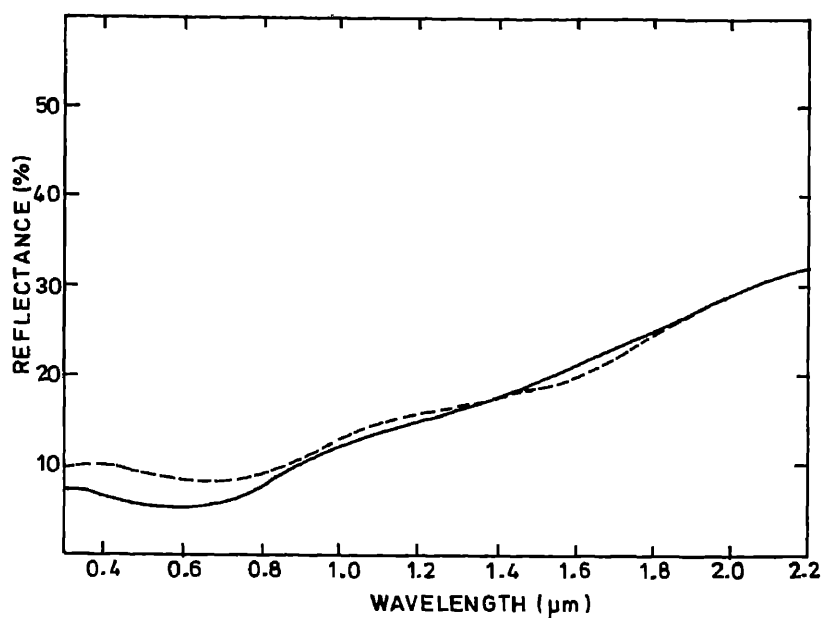


Figure 3. Change in reflectance spectrum of cobalt oxide-iron oxide coating on stainless steel after heating (-----) at 500°C for 24 hr in air. (—) is reflectance spectrum before heating.

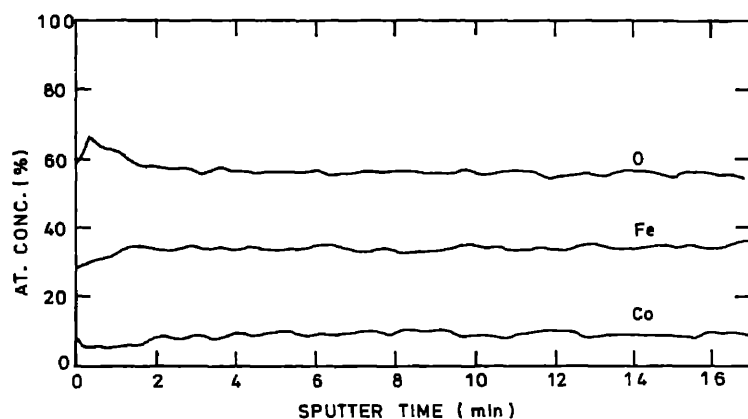
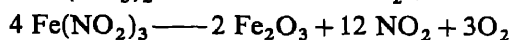
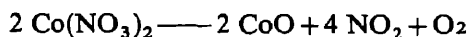


Figure 4. Auger depth profile showing the variation of Fe, Co and O concentrations with depth.

to that of decomposition of salts in air. The following chemical reactions lead to the formation of CoO and Fe<sub>2</sub>O<sub>3</sub>.



This explains the presence of the above mentioned oxides in the bulk of the coating.



## *Selective coatings for high temperature applications*

### **4. Conclusions**

Mixed oxides of cobalt and iron have been prepared on stainless steel by s pyrolysis. The integrated absorptance of the mixed oxide is 0.94 which is higher than that of either cobalt oxide ( $\alpha = 0.80$ ) or iron oxide ( $\alpha = 0.89$ ) on stainless steel obtained under similar conditions. The emittance increases slightly from 0.15 for pure cobalt oxide to 0.20 for mixed oxide. As far as stability is concerned, cobalt oxide coating is stable up to 600°C whereas the mixed oxide coatings of cobalt and iron are stable up to 400°C.

### **References**

- Chidambaram K, Malhotra L K and Chopra K L 1982 *Thin Solid Films* **87** 365  
Chaudhary C and Sehgal H K 1982 *Solar Energy* **28** 25  
Gillette R B 1960 *Solar Energy* **4** 24  
Kokoropoulos P, Salam E and Daniels F 1959 *Solar Energy* **3** 19  
Kruidhof W and Van der Leij M 1979 *Solar Energy Mater.* **2** 69  
McDonald G E 1980 *Thin Solid Films* **72** 83  
Smith G B, Ignatiev A and Zajac G 1980 *J. Appl. Phys.* **51** 4186



## Transistors made in laser recrystallized polysilicon on insulator films

S CHANDRASEKHAR, P R APTE and S K ROY

Solid State Electronics Group, Tata Institute of Fundamental Research, Bombay 400 India

**Abstract.** LPCVD polycrystalline silicon films were deposited on thermally oxidized silicon as well as on LPCVD silicon nitride deposited on silicon. A cw argon ion laser was used to recrystallize the polysilicon film into large grains (grain size from 5  $\mu\text{m}$  to 40  $\mu\text{m}$ ). Boron was then implanted and standard N-channel silicon gate process and N-channel metal gate process were carried out to realise MOSFETs on this material. Channel mobilities upto 450  $\text{cm}^2/\text{V}\cdot\text{s}$  for electrons have been measured. This thin film MOSFET has a four-terminal structure with top and a bottom gate and the influence of one gate on the drain current due to the other has been investigated. Comparison of the  $I_D-V_D$  curves of the devices with physical model found in good agreement.

**Keywords.** Recrystallisation; semiconductor; silicon; laser; MOSFET; silicon-gate process

### 1. Introduction

Polycrystalline silicon formed by low pressure chemical vapour deposition (LPCVD) is commonly used in integrated circuits for interconnections, gate electrodes and resistors. However, the relatively small grain size (of the order of 500 Å) tends to limit application since the grain boundaries usually affect the transport properties. The earliest MOSFETs fabricated on thin films of polysilicon have shown poor mobilities and transconductances (Kamins 1972). It has now been well demonstrated that the grain size of polysilicon deposited on thermally-oxidized silicon can be increased dramatically by annealing the material with either a scanning cw laser beam (Gat *et al* 1980; Kamins *et al* 1980) or a heated graphite strip (Tsaur *et al* 1981). The grain size can be made as large as 100  $\mu\text{m}$  by 100  $\mu\text{m}$  extending through the thickness of the film. This has generated a considerable amount of work (Lam *et al* 1982; Colinge *et al* 1983) devoted to the fabrication of device-worthy silicon-on-insulator (SOI) films as an alternative to the classical silicon-on-sapphire (SOS). A variety of applications such as large flat panel displays and 3-D integrated circuits offer a significant promise for the future.

We report here our results of MOSFETs made by laser recrystallization.

### 2. Experimental

The samples were made on 2 inch diameter P type  $\langle 100 \rangle$  silicon wafers. A 1  $\mu\text{m}$  oxide was grown in steam ambient and a 500 nm thick film of polysilicon was deposited by low pressure chemical vapour deposition (LPCVD) of silane. A capping layer of silicon nitride was then deposited by LPCVD of dichlorosilane and ammonia. The thickness of the nitride was 60 nm which gives the optimum antireflection effect for the two

wavelengths (488 nm and 514.5 nm) used in the recrystallization. The wafers were then recrystallized using a cw argon ion laser operating in the multiline mode. The substrate was heated to 350°C on a vacuum held chuck and the laser beam was scanned in a serpentine fashion using an X-Y mirror galvanometer deflection system. A plano convex lens of focal length 250 mm was used to focus the beam on to the substrate to give a spot size of about 60 to 70  $\mu\text{m}$ . The scan speed was 10 cm/sec with spacing between successive scan lines of about 20  $\mu\text{m}$ . The laser power used was between 11 W and 13 W.

As a result of the recrystallisation, long crystallites (upto 40  $\mu\text{m}$  in length, 5 to 10  $\mu\text{m}$  in width) were formed in a chevron shape. The capping nitride was then stripped in hot phosphoric acid. Boron was implanted into the large grain silicon at 80 keV to a dose of  $1 \times 10^{12}$  ions/cm<sup>2</sup>. (This dose was calculated to make the recrystallised polysilicon *p*-type with an average concentration of  $1.2 \times 10^{16}$  atoms/cm<sup>2</sup>). Standard *N*-MOS silicon gate process was carried out from this stage. A 100 nm silicon nitride was deposited, active areas of transistors defined by photolithography and nitride etched in a CF<sub>4</sub> plasma. Local oxidation was then carried out to convert the unwanted polysilicon into oxide. The nitride was then stripped, a gate oxide of 100 nm was grown at 1050°C in oxygen, 0.5  $\mu\text{m}$  polysilicon was deposited and patterned into gates. The source, drain and gates were then doped by POCl<sub>3</sub> at 975°C. After opening contact holes, aluminium was evaporated and patterned. The devices were then sintered at 500°C in N<sub>2</sub> for 45 min. Figure 1 shows the cross-section of the completed structure. Some wafers were processed for *N*-MOS meal gate devices.

### 3. Results and discussion

The MOSFET device characteristics were measured with an automated measurement system controlled by a desktop computer. Figure 2 shows a typical drain current  $I_D$  versus drain voltage  $V_D$  family of curves as a function of the top gate voltage  $V_{G1}$  for a particular bottom gate voltage  $V_{G2}$ . Referring back to figure 1, we notice that the 1  $\mu\text{m}$  silicon dioxide on which the recrystallized film is sitting acts as a second gate dielectric with the underlying support of silicon as the gate electrode. This four-terminal structure of the laser recrystallized film is thus unique and consequently, the device has two channels for current to flow from source to drain—a top channel below gate 1 and a bottom channel above gate 2.

The MOSFET, now called MISIMFET (metal-insulator-semiconductor-insulator-metal), has therefore four cases of operation:

- (i) When the voltages on both gates are large and negative the silicon below the gates are accumulated and the transistor is in the OFF state.
- (ii) The voltage on one gate forms an inversion layer (i.e. a channel) while the other gate is in accumulation.
- (iii) The voltage on one gate forms a channel while the other gate forms a depleted region.
- (iv) Both the gate voltages are such that a channel is formed below each gate.

The drain current  $I_D$  therefore is a function of drain voltage  $V_D$ , gate 1 voltage  $V_{G1}$  and gate 2 voltage  $V_{G2}$ . This dependence can be seen in figure 3 which is the  $I_D$ - $V_{G1}$  curve for a small drain voltage ( $V_D = 100$  mV) as a function of the back gate voltage  $V_{G2}$ . For

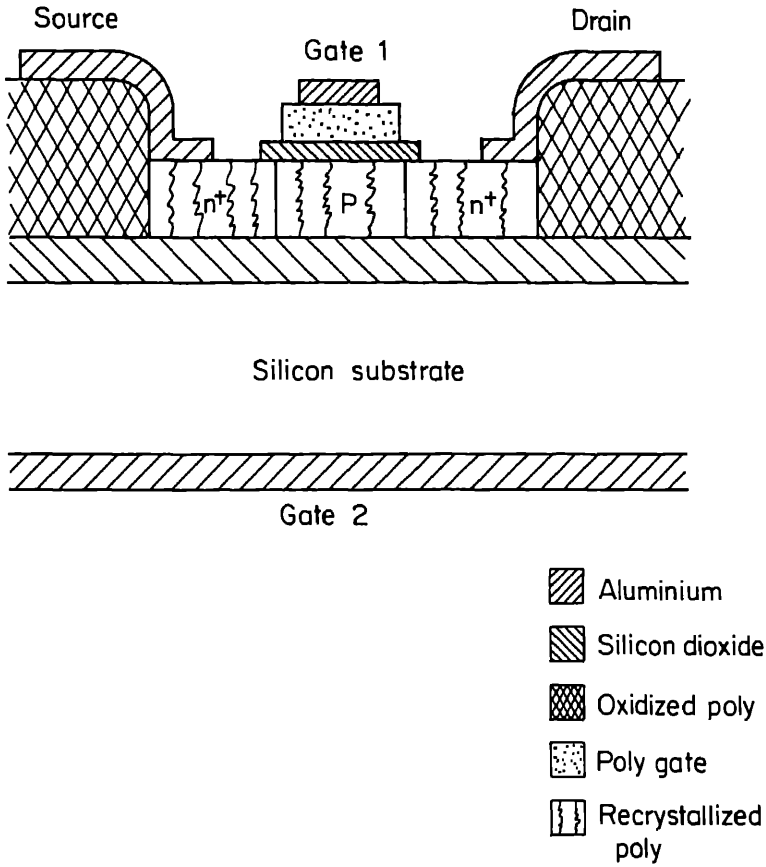


Figure 1. Cross-sectional view of completed MOSFET on laser recrystallized polysilicon

For  $V_{G2} < -45$  V and  $V_{G1} < -4$  V, we see the drain current is practically zero. This is case 1. For  $V_{G1} > -4$  V and  $V_{G2} < -45$  V, the drain current starts increasing showing that channel 1 has inverted while channel 2 is still in accumulation. For  $V_{G2} > -45$  V and  $V_{G1} < -4$  V, we see that the drain current again starts increasing showing that channel 2 has inverted while channel 1 is off. This is case 2. For  $V_{G1} > -4$  V and  $V_{G2} > -45$  V both channels are conducting and we have case 4. Case 3 is between these two voltage limits.

The expression for the drain current when channel 2 is accumulated is

$$I_D = \mu \frac{W}{L} C_{01} (V_G - V_{T1}) V_D,$$

where  $\mu$  is the mobility,  $W$  and  $L$  are the device width and length,  $C_{01}$  is the gate capacitance,  $V_D$  is the drain voltage ( $= 100$  mV),  $V_{T1}$  is the turn on voltage of channel 1. The slope is

$$\partial I_D / \partial V_G = \mu \frac{W}{L} C_{01} V_D$$

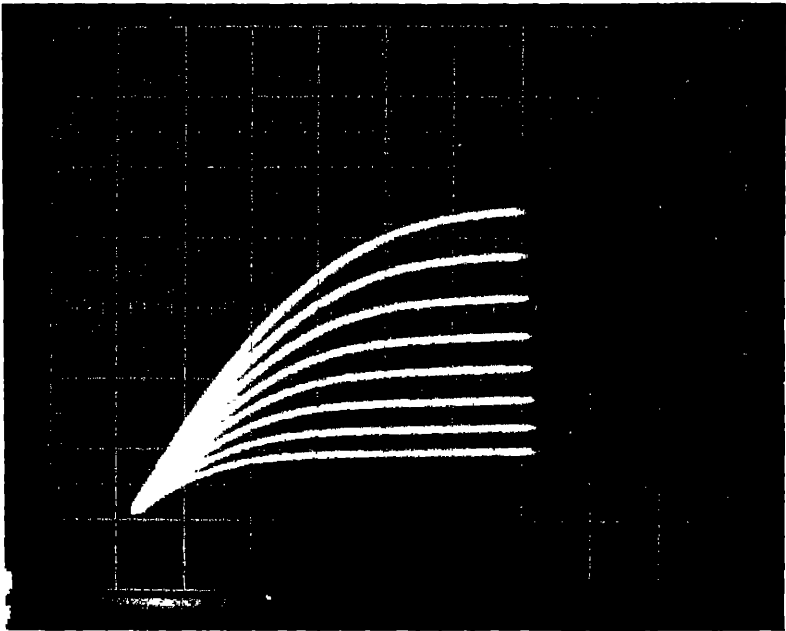


Figure 2. Photograph of the  $I_D$ - $V_D$  characteristics of the  $n$ -channel Si gate MOSFET as a function of front gate voltage  $V_{G1}$  for a fixed back gate voltage  $V_{G2}$

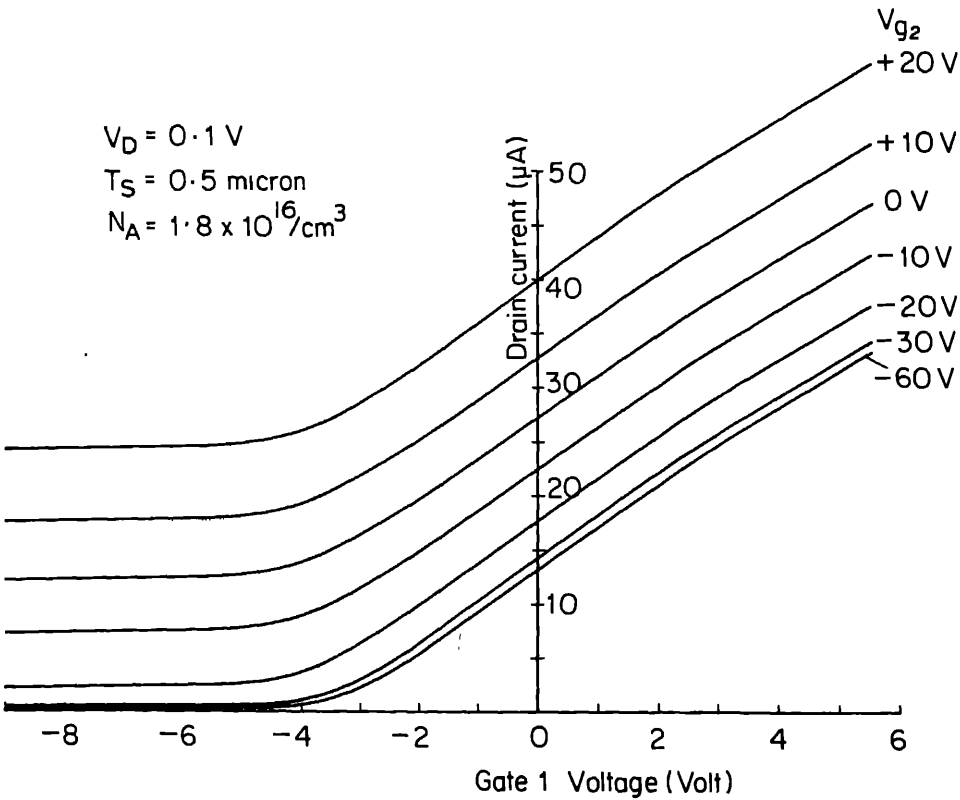


Figure 3. Drain current vs front gate voltage  $V_{G1}$  as a function of back gate voltage  $V_{G2}$ .

and the intercept is  $V_{T1}$ . We have measured mobilities from 250 cm<sup>2</sup>/V-sec to 450 cm<sup>2</sup>/V-sec with the front channel threshold voltage of -3.2 to -3.5 V and channel threshold voltage of -30 V to -35 V.

There have been two models proposed in literature for explaining the  $I_D$ - $V_D$  behavior of the MISIM structure, one by Lim and Fossum (1984) and the other by Barth (1983). The second model is exact while the first one makes some approximations. Both models take into consideration the fact that silicon is finite in extent (0.5  $\mu$ m in our case) and so far a given impurity concentration, the depletion regions from the top and bottom will meet at some point making the entire film depleted. As a result, the "communication" between the top and bottom gates, thereby controlling the current. We have matched our data with the Barth-Apte-Angell model and this is shown in figure 4 with a good fit.

Since our device has a  $W$  of 100  $\mu$ m and  $L$  of 20  $\mu$ m, there are a couple of grain boundaries in the active region of the transistor perpendicular to the current flow. Mobility and threshold voltages are thus modulated by these grain boundary charges and this gives a small error to our modelling effort. We have taken care of these effects by a voltage-dependant mobility (as can be seen in figure 3, where the slope is constant).

The parameters which were used to fit the data are the mobilities  $\mu_{n1} = 295$  V-sec of front channel and  $\mu_{n2} = 310$  cm<sup>2</sup>/V-sec of back channel,  $V_{FB1}$ , the front channel flat band voltage of -6.1 V and  $V_{FB2}$ , the back channel flat band voltage of -52 V. The front gate oxide is 1000 Å while the back gate oxide is 1  $\mu$ m.

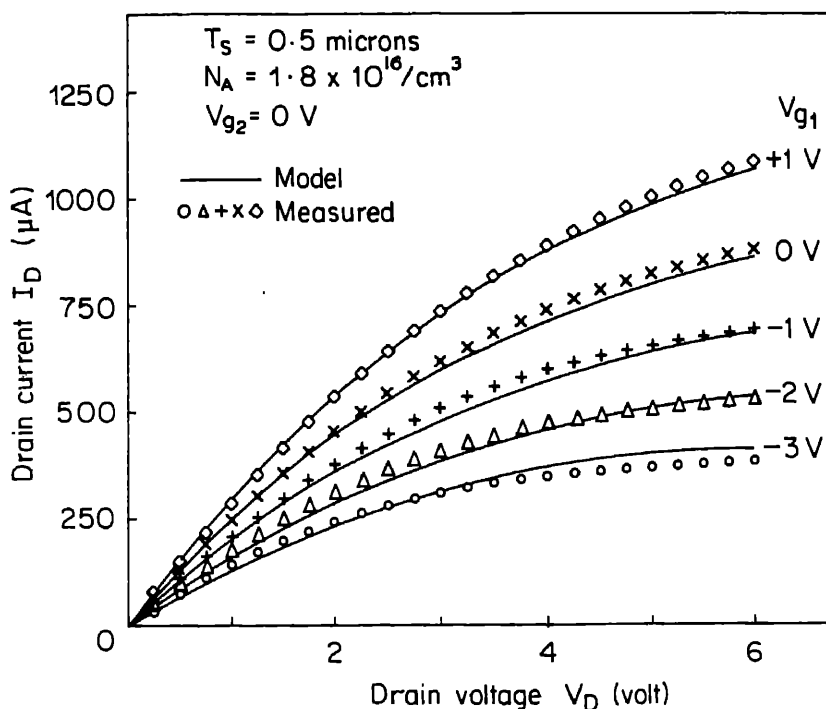


Figure 4. Experimental and calculated  $I_D$ - $V_D$  curves for the MISIMFET.

#### 4. Conclusions

We have fabricated N-channel silicon gate and metal gate MOSFETs by recrystallization, using a cw laser beam, LPCVD polysilicon deposited on thermally oxidized silicon. Surface electron mobilities upto  $450 \text{ cm}^2/\text{V-sec}$  have been measured. We have demonstrated the 4-terminal behaviour of our structure and applied a model to explain the  $I_D-V_D$  curves as functions of the two gate voltages. Laser beam recrystallized polysilicon films on insulators have a bright future for realising device-worthy silicon-on-insulator films and making 3-D integrated circuits.

#### Acknowledgements

The authors are grateful to the Department of Science and Technology for financing the laser. The authors would like to thank Prof. K V Ramanathan for his keen interest and continuous encouragement during the course of this investigation.

#### References

- Barth P W, Apte P R and Angell J B 1983 *IEEE Trans. Electron Devices* **ED-30** 1717  
Colinge J P, Demoulin E, Bensahel D, Auvert G and Morel H 1983 *IEEE Electron Device Lett.* **EDL-4** 75  
Gat A, Gerzberg L, Gibbons J F, Magee T J, Peng J and Hong J D 1978 *Appl. Phys. Lett.* **33** 775  
Kamins T I 1972 *Solid State Electron.* **15** 789  
Kamins T I, Lee K F and Gibbons J F 1980 *Appl. Phys. Lett.* **36** 550  
Lam H W, Sobczak Z P, Pinizotto R F and Tasch A F Jr 1982 *IEEE Trans. Electron Devices* **ED-29** 389  
Lim H-K and Fossum J G 1984 *IEEE Trans. Electron Devices* **ED-31** 401  
Tsaur B-Y, Fan J C C, Geiss M W, Silversmith D J and Mountain R 1981 *Appl. Phys. Lett.* **39** 561



## Effect of bulk and thin film dielectric overlay on the characteristic microstrip rejection filter and simple microstriplines

K VIJAYA, M L JADHAV, S A GANGAL and R N KAREKAR

Department of Physics, University of Poona, Pune 411 007, India

**Abstract.** The changes in the characteristics of microstrip rejection filter and simple microstriplines due to bulk and thin film dielectric overlay are reported in this paper. A dielectric overlay both bulk and thin film increases the  $Q$  of the filter. All other overlays decrease the  $Q$ . A thin film of  $\text{TiO}_2$  shows improvement in  $Q$  whereas with bulk  $\text{TiO}_2$  the filtering property is not observed. The effect of overlays on simple lines is to reduce the transmission without effect in the reflection.

**Keywords.** Microstrip rejection filter; simple microstriplines; dielectric overlay; thin film

### 1. Introduction

The structure of the microstripline may lend itself to the study of microwave properties of materials in the thin film form by using overlay/underlay techniques which result in a change in the effective dielectric constant (Farrar and Adams 1974; Pande and Kar 1976; Pande 1976).

For a given dielectric substrate the characteristic impedance ( $Z_0$ ) of the microstripline is governed by the  $w/h$  ratio where  $w$  is the width of the line on top of the substrate and  $h$  is the dielectric thickness (Wheeler 1965). The impedance of the measuring system is normally  $50 \Omega$ . Thus for maximum power transfer the value of  $Z_0$  should also be  $50 \Omega$ . For alumina substrate with  $\epsilon = 9.6$ ,  $Z_0$  is  $50 \Omega$  for  $w/h$  ratio of about 1 (Gupta and Singh 1974).

Open microstrip resonators are often employed in MIC techniques as absorbers and filters. One form is the standard half-wave resonator, open at both sides and coupled over a quarter wavelength with the main transmission line (figure 2). In the design of coupled microstrip structures the odd-mode impedance value is often used (Mumford Tech. Comm. 1972) for arriving at the coupling and the corresponding geometry. Unfortunately a considerable portion of the odd mode field exists in the air (Weirauch 1974) which leads to fringing fields and radiative losses, particularly in open circuit resonators. The overlay technique, using  $\text{Bi}_2\text{O}_3$  overlay on Au microstrip circuit (Pande 1976), is reported to be one of the solutions to this problem.

The aim of the present work is to fabricate copper microstriplines and rejection filters and study their transmission and reflection properties with and without overlay of various dielectric materials. From these observations the properties viz the characteristic impedance,  $Q$ , rejection, etc are calculated.

## 2. Experimental

The microstrip lines were obtained using chromium/copper on standard  $1'' \times 1'' \times 0.025''$  99.66% pure alumina substrates. Initially a thin film of chromium (thickness  $\sim 300 \text{ \AA}$ ) was vacuum-evaporated at about  $2 \times 10^{-5}$  torr onto heated alumina substrates, the substrate temperature being optimized to  $100^\circ\text{C}$  for best adhesion.

After cooling the substrates to room temperature copper was deposited onto the Cr to a thickness of approximately  $3000 \text{ \AA}$  in the same cycle. After repeating the process on the other side of the alumina substrate, the thickness of Cu was increased to about  $5 \mu$  by electroplating in a  $\text{CuSO}_4\text{-H}_2\text{SO}_4$  bath using the arrangement shown in figure 1. The bath required about 2 litres of plating solution ( $\text{CuSO}_4\text{—}200 \text{ g/l}$ ,  $\text{H}_2\text{SO}_4\text{—}56 \text{ g/l}$ , potash alum  $12 \text{ g/l}$ ).

The size of the anode was twice that of the cathode so as to obtain a uniform field around the cathode. The pH of the solution was approximately 2. This electroplating system was optimized to obtain a uniform pinhole free deposit which did not oxidize easily. For a fixed separation between the electrodes ( $7.5 \text{ cm}$ ) and for a fixed voltage ( $10 \text{ V}$ ) a current of  $80 \text{ mA}$  gave the best films. When run for  $30 \text{ min}$ , a thickness of  $5 \mu$  was obtained.

The rejection filters and microstriplines were photolithographically delineated on one side of these metallized substrate. The geometry was arrived at by using the standard tables and curves reported by Wheeler (1965) and Bryant and Weiss (1978). We designed a  $\lambda/2$  open circuit resonant, single section maximally flat rejection filter (see figure 2) without overlay, at  $f = 9.57 \text{ GHz}$ ,  $\lambda_g = 1.271$  with bandwidth of  $2\%$ . In addition stripline masks of different widths were used to study the effect of width on  $Z_0$  and to optimize the mask width.

For circuit evaluation, the microstrip circuits were mounted in resilient contact MIC test fixture. The performance of the filter and microstripline was evaluated using a network analyser (Hewlett-Packard 8410B). On this system the amplitude as well as the phase of the reflection and transmission coefficients can be measured. Using Smith chart overlay fixed on the polar display, direct evaluation of the input impedance ( $Z_{in}$ ) is

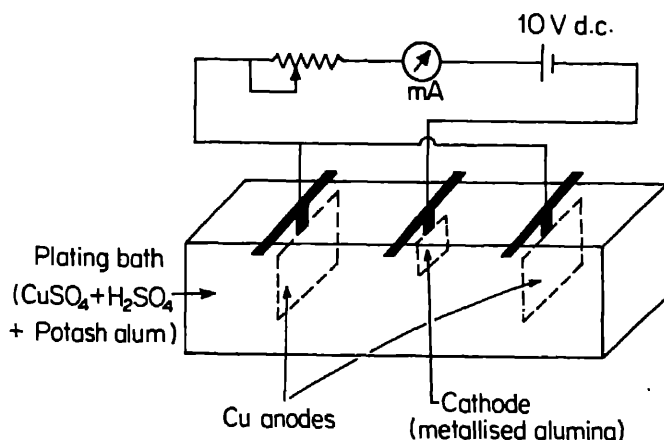


Figure 1. Arrangement for copper electroplating.

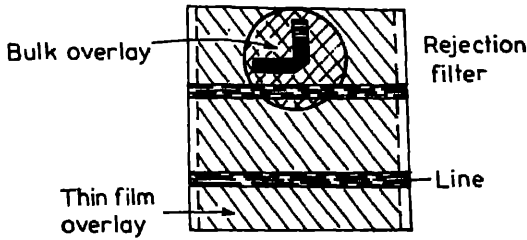


Figure 2. Sketch of the rejection filter and single microstripline with thin film overlay ( $\lambda_g = 1.271$  cm).

possible. The  $Z_{in}$  data, obtained in the frequency range of 2 to 12 GHz, were used to calculate the characteristic impedance  $Z_0$  of the microstripline, using the equation

$$Z_{in} = Z_0 \left( \frac{Z_L + Z_0 \tan \beta l}{Z_0 + j Z_L \tan \beta l} \right)$$

where  $Z_L$  is the load impedance =  $50 \Omega$ ,  $\beta$  is the propagation constant and  $l$  is the length of the stripline. Both the bulk and thin film overlays were tried on the filter microstriplines. The bulk overlays of  $\text{Bi}_2\text{O}_3$ ,  $\text{TiO}_2$  and  $\text{ZnS}$  were in pellet form (1 cm in diameter and 2 mm thick). Those of  $\text{Al}_2\text{O}_3$  and 0211 corning glass were in the form of plates of size 2 cm  $\times$  1 cm. The thickness was 0.5 mm for corning glass and 0.26 mm for  $\text{Al}_2\text{O}_3$ . In any case the dimensions of these bulk overlays were such that they covered the entire coupler area of the filter.

For the film overlays,  $\text{Al}_2\text{O}_3$ ,  $\text{Bi}_2\text{O}_3$ ,  $\text{TiO}_2$  and  $\text{ZnS}$  and PAN were tried.  $\text{Al}_2\text{O}_3$  was deposited by chemical vapour deposition. The substrates were heated in a nitrogen atmosphere to  $375^\circ\text{C}$  and a mixture of aluminium isopropoxide ( $\text{Al}(\text{OC}_3\text{H}_7)_3$ ) and  $\text{N}_2$  gas was passed over them. Due to the pyrolysis of  $\text{Al}(\text{OC}_3\text{H}_7)_3$  at  $375^\circ\text{C}$ ,  $\text{Al}_2\text{O}_3$  is deposited on the substrate.  $\text{Bi}_2\text{O}_3$  films were obtained by vacuum evaporation of bismuth and subsequent oxidation in atmospheric air at a temperature of  $165^\circ\text{C}$  for about 90 min, and also by reactive ion plating. These overlays of  $\text{Al}_2\text{O}_3$  and  $\text{Bi}_2\text{O}_3$  had some problem of oxidation and peeling because of the heat treatment required and  $\text{ZnS}$  was obtained by vacuum evaporation without much difficulty. PAN (polyacrylonitrile) films were obtained by plasma polymerization. In all the cases the area covered by overlay was such that it covered the whole substrate except for the coupler areas as shown in figure 2.

### 3. Results and discussion

#### 3.1 Rejection filter

Figure 3 shows the typical curves of rejection (db) (i.e. transmission) vs frequency for the filter with and without bulk overlay for various overlay materials. Figure 4 shows the rejection vs frequency curves for filters with thin film overlay. It is seen from the curves that the bulk overlays shift the centre frequency ( $f_0$ ) to the lower frequency side. For  $\text{Al}_2\text{O}_3$  all other overlays have the effect of reducing the  $Q$ .  $\text{TiO}_2$  overlay does not reduce the transmission at all frequencies from 8–12 GHz and the sample does not show

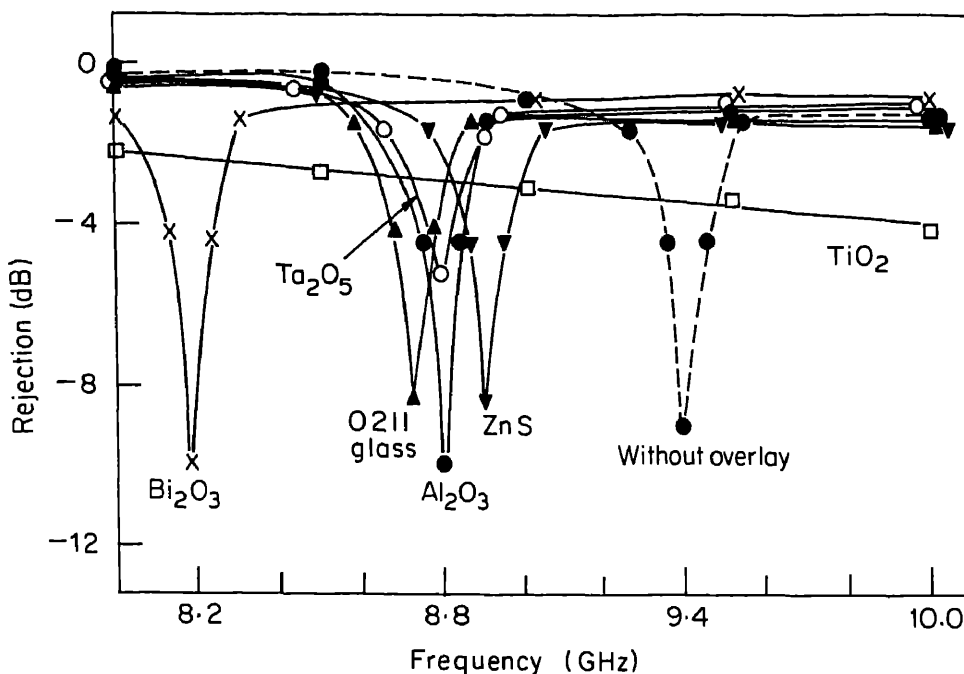


Figure 3. Graph of rejection (db) vs frequency (GHz) for rejection filter with and without bulk overlay.

properties. This shows that the higher thickness of the overlay in some way makes the filter more lossy. This may be due to the presence of some other higher modes, like surface waves. The thickness effect was studied only for  $\text{Bi}_2\text{O}_3$  bulk overlay which shows improvement in  $Q$  (even compared to the one without overlay) at a lower thickness of 0.9 mm.

Table 1a gives the data of  $Q$  for filter with and without  $\text{Al}_2\text{O}_3$  and 0211 corning glass bulk overlay. It shows that there is an increase in  $Q$  and rejection after  $\text{Al}_2\text{O}_3$  bulk overlay (except in one sample). This shows that the overlay has tightened the coupling and reduced the losses. For 0211 glass there is decrease in  $Q$  for all the samples. Table 1b gives the data for other bulk overlays.

From figure 4 (for the thin film overlay) it is seen that for  $\text{Al}_2\text{O}_3$  (thickness  $\sim 4000$  Å deposited by cvd) there is a shift in frequency and also improvement in  $Q$  from 84.08 to 112.  $\text{Bi}_2\text{O}_3$ ,  $\text{TiO}_2$  and  $\text{Ta}_2\text{O}_5$  do not show any shift in frequency.  $\text{TiO}_2$  film of thickness 900 Å also shows improvement in  $Q$  from 158.5 to 172.9. Thin film overlay of  $\text{TiO}_2$  is better than bulk  $\text{TiO}_2$  overlay. For  $\text{Bi}_2\text{O}_3$  and  $\text{Ta}_2\text{O}_5$ , there is decrease in  $Q$ , for  $\text{Bi}_2\text{O}_3$  from 189 to 118 and for  $\text{Ta}_2\text{O}_5$  from 188 to 156.6. ZnS films reacted with copper, spoiling the microstrip structure itself, so the effect of ZnS thin film overlay could not be studied. Plasma-polymerized PAN overlay gave rise to shift in  $f_0$  from 9.52 to 9.49 and decrease in  $Q$  from 190 to 158.

An attempt was also made to use the frequency shift and  $Q$  of filters with overlay to get an idea about the material properties of the overlay. The procedure was as follows.

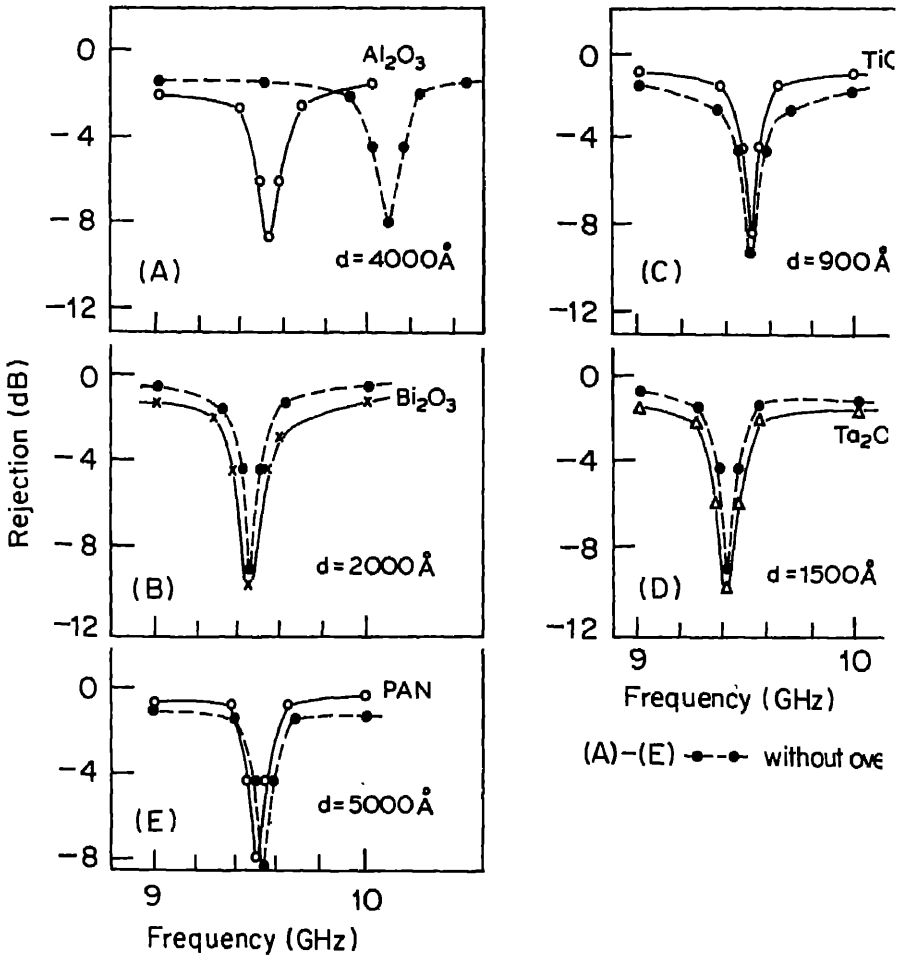


Figure 4. Graph of rejection (db) vs frequency (GHz) for rejection filter with and without thin film overlay.

The  $\epsilon_{\text{eff}}$  of the stripline without overlay was calculated using the formula of (1976).

$$\epsilon_{\text{eff}} = \frac{\epsilon_r + 1}{2} \left\{ 1 + \frac{29.98}{Z_0} \left( \frac{2}{\epsilon_r + 1} \right)^{1/2} \left( \frac{\epsilon_r - 1}{\epsilon_r + 1} \right) \left( \ln \frac{\pi}{2} + \frac{1}{\epsilon_r} \ln \frac{4}{\pi} \right) \right\}^2$$

where  $\epsilon_r = 9.6$ , the dielectric constant of the alumina substrate.  $Z_0$  was assumed  $50 \Omega$  as an approximation. From this formula  $\epsilon_{\text{eff}}$  without overlay comes out to be Using this value of  $\epsilon_{\text{eff}}$  and the experimental resonant frequency  $f_0$  without overlay guide wavelength  $\lambda_g$  was calculated for each sample using the relation,

$$\lambda_g = \frac{\lambda_0}{\sqrt{\epsilon_{\text{eff}}}},$$

$\lambda_0$  is the free space  $\lambda_0 (c/f_0)$ . This is done to account for changes in  $\lambda_g$  due to delin

**Table 1a.** Data of  $Q$  and rejection of filter with and without bulk  $\text{Al}_2\text{O}_3$  and 0211 glass overlays

Sample No.	Bulk overlay of $\text{Al}_2\text{O}_3$ and 0211 glass								
	Without overlay			$\text{Al}_2\text{O}_3$			0211 glass		
	$f_0$ GHz	$Q$	Rej db	$f_0$ GHz	$Q$	Rej db	$f_0$ GHz	$Q$	Rej db
3	9.64	160	4.9	9.05	181	5.4			
41	9.47	145.6	4.9	8.82	147	5.6	8.72	96.8	4.3
44	9.51	158.5	6.1	8.78	175.6	6.1	8.76	109.5	4.5
48	9.52	190.4	5.4	8.94	149	5.4	8.67	123.8	4.8
53	9.40	188.0	6.1	8.80	251.4	6.9	8.72	158.5	5.4
B	9.57	106.3	3.9	8.92	111.5	4.5	8.81	80.10	3.9
D	9.65	175.4	4.9	8.88	253.8	6.1	8.87	108.75	4.9
H	9.71	107.8	3.9	9.19	13.13	4.5	9.0	90.0	4.1
I	9.56	73.5	3.0	8.85	126.4	3.9	8.82	76.7	3.0
Average values	$\epsilon_{\text{eff}} = 6.077$ $\tan \delta_{\text{eff}} = 5.7 \times 10^{-3}$ $\sigma_{\text{eff}} = 2.99 \times 10^{-9} \text{ } \Omega\text{-cm}$			$\epsilon_{\text{eff}} = 7.169$ $\tan \delta_{\text{eff}} = 3.94 \times 10^{-3}$ $\sigma_{\text{eff}} = 3.98 \times 10^{-9} \text{ } \Omega\text{-cm}$			$\epsilon_{\text{eff}} = 7.19$ $\tan \delta_{\text{eff}} = 9.19 \times 10^{-3}$ $\sigma_{\text{eff}} = 1.70 \times 10^{-9} \text{ } \Omega\text{-cm}$		

**Table 1b.** Data of  $Q$  and rejection of filter with other bulk overlays

Without overlay			Bulk overlays of								
			$\text{Bi}_2\text{O}_3$			$\text{ZnS}$					
$f_0$ GHz	$Q$	Rej db	$f_0$ GHz	$Q$	Rej db	$f_0$ GHz	$Q$	Rej db	$f_0$ GHz	$Q$	Rej db
9.64	160	4.9	8.52	31.5	1.4	9.12	102	3.9	8.79	46.3	2.2
9.52	190.4	5.4	9.28	42.2	3.2						No filter characteristics
9.40	188	6.1	8.18	204.5	6.9						No filter characteristics
(thin pellet)											
			$\epsilon_{\text{eff}} = 7.5$			$\epsilon_{\text{eff}} = 6.7$			$\epsilon_{\text{eff}} = 7.3$		

As a result of overlay,  $\epsilon_{\text{eff}}$  will change to  $(\epsilon_{\text{eff}})_0$ , thus changing the resonant frequency to  $(f_0)_0$ . Hence by knowing experimental  $(f_0)_0$  and calculated  $(\lambda_g)_0$  and using equation (3) again one can get  $(\epsilon_{\text{eff}})_0$ . The values of  $(\epsilon_{\text{eff}})_0$  thus calculated are given in tables 1a and 1b.

From the experimental value of  $Q$ , the effective loss tangent of the overall configuration can be calculated using the relation

$$\tan \delta = 1/Q. \tag{4}$$

Some typical values are given in tables 1a and 1b. Assuming the rejection filter to be a parallel resonant circuit the effective conductivity can be estimated to a first

approximation using the formula for parallel resonant circuits.

$$\sigma_{\text{eff}} \approx Q/\omega \epsilon_{\text{eff}}$$

It is seen that with overlay there is a reduction in the effective  $\tan \delta$  as compared to one without overlay. Only  $\tan \delta$  of  $\text{Al}_2\text{O}_3$  is available in literature and is  $\sim 6 \times 10^{-4}$ . Our values are effective and further analysis is being done to separate the dielectric properties from the effective values.

### 3.2 Single microstriplines

Figure 5 shows the variation of  $Z_0$  with frequency in the range of 2 to 12 GHz microstriplines with widths varying from 18 to 28 mils. It is seen that  $Z_0$  varies in range of 20  $\Omega$  to 95  $\Omega$  randomly about the expected value of 50 ohms. Although some sort of oscillatory behaviour is observed, it is difficult to relate this to width variation in all cases, except for the 18 mils line the scatter is more pronounced at the high

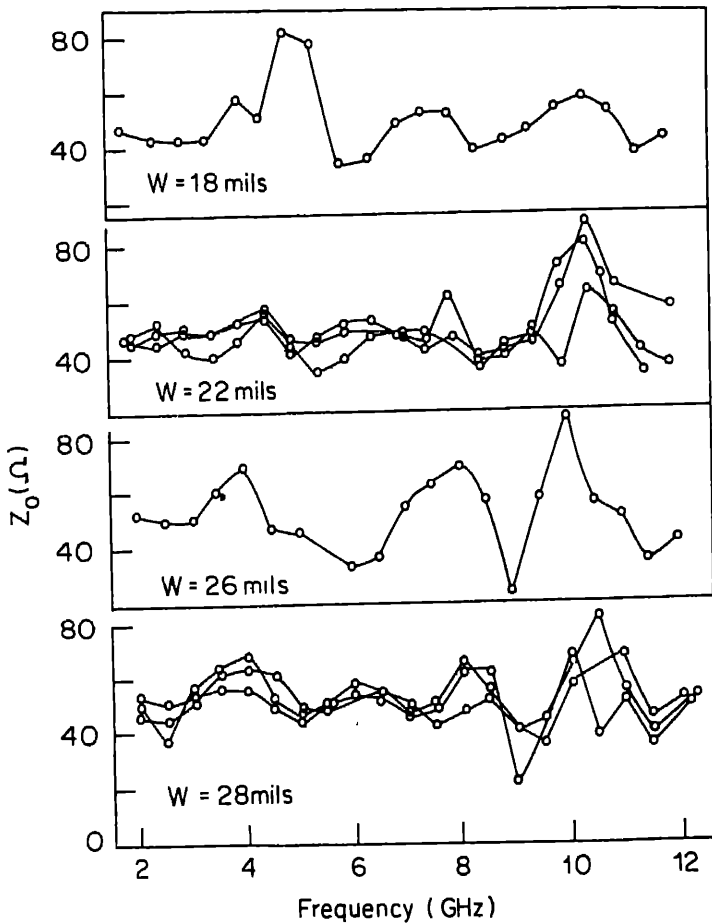


**Figure 5.** Variation of characteristic impedance ( $Z_0$ ) with frequency for striplines of different widths.

frequencies (8–12 GHz). In the microwave range,  $Z_0$  is expected to show a steady increase with frequency (Krage and Haddad 1972). This is because of the change in the effective dielectric constant with frequency and also changes in the resistivity of conductor material.

The observed random variation of  $Z_0$  with frequency could be due to the contacts between the microstrip and the omni spectra (osm) launchers which are actually co-axial to microstrip connectors used to connect the microstrip to the rest of the measuring system. Bianco *et al* (1976) characterized the effect of launcher on a system of microstrips and active devices. They too report random oscillatory behaviour of the scattering parameter  $S_{11}$  and  $S_{22}$ . Since the results are heavily affected by launcher discontinuities, there seems to be no justification to discuss the frequency dependence of  $Z_0$  in any further depth.

**3.2a Overlay effects on losses:** In order to study the effect of overlay on the losses present in the microstripline the power reflection and transmission coefficients were studied for both bulk and thin film overlays. The typical graphs of  $\rho^2$  and  $T^2$  versus frequency for bulk overlay effect are shown in figure 6. In all cases except for  $\text{TiO}_2$  the reflection reduced as a result of bulk overlay. The transmission is also slightly reduced except in  $\text{TiO}_2$ , where it reduced almost by 50 %. However, the values of  $\rho^2$  and  $T^2$  are very critically dependant on size and position of the overlays. Since thin film overlays had to be tried on different samples only  $\Delta T$  and  $\Delta \rho$  were studied as a result of overlay. Only PAN (reactive ion-plated),  $\text{Bi}_2\text{O}_3$  and  $\text{TiO}_2$  showed increased average transmission as shown in table 2. The reflection coefficient measured at 8 GHz did not show much change (within variability limits). More careful experimentation is needed after considering the effect of discontinuities and variabilities.

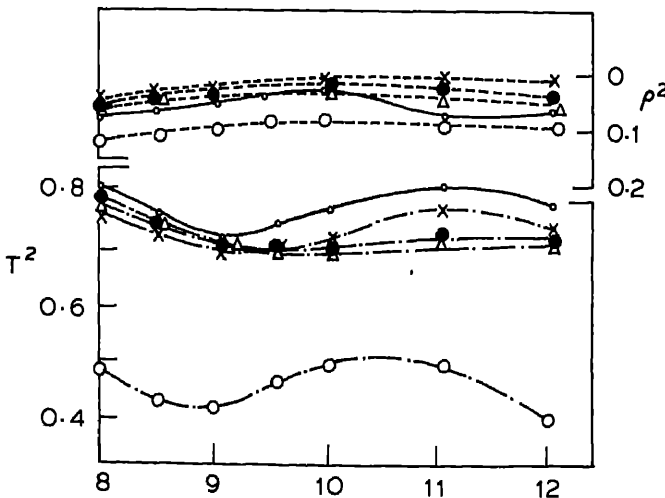


**Figure 6.** Variation of transmission and reflection coefficients as a function of frequency for single stripline with and without bulk overlay. (●)  $\text{Al}_2\text{O}_3$ ; (×)  $\text{Bi}_2\text{O}_3$ ; (Δ) 0211 glass; (○)  $\text{TiO}_2$ .



## *Studies on microstrip filter and microstriplines*

**Table 2.** Effect of thin film overlay on microstripline,  $\rho^2$  and  $T^2$

Material	$\Delta T^2$ (average)	$\Delta \rho^2$ (8 GHz)
PAN	+0.09	-0.04
TiO <sub>2</sub>	+0.13	0
ZnS	-0.67	—
Bi <sub>2</sub> O <sub>3</sub> (oxidized)	-0.05	0
Bi <sub>2</sub> O <sub>3</sub> (reactive ion-plated)	+0.13	-0.004
Al <sub>2</sub> O <sub>3</sub> (CVD)	-0.05	—

### **Acknowledgements**

The authors gratefully acknowledge the permission given by Mr R P Arora Pune for the extensive use of network analyser. Thanks are also due to Mr D for helping in CVD of Al<sub>2</sub>O<sub>3</sub>. The authors also acknowledge the financial assistance from the Department of Science and Technology, New Delhi.

### **References**

- Bianco B *et al* 1976 *IEEE Trans. Instrum. Meas.* **1M-25** 320  
Bryant T G and Weiss J A 1978 *IEEE Trans. Microwave Theory Tech.* **MTT-16** 1021  
Farrar A and Adams A T 1974 *IEEE Trans. Microwave Theory Tech.* **MTT-22** 889  
Gupta K C and Singh A 1974 *Microwave Integrated Circuits* (New York: Wiley, Eastern) p. 13  
Krage M K and Haddad G I 1972 *IEEE Trans. Microwave Theory Tech.* **MTT-20** 678  
Mullard Tech. Commun. No. 116 1972 p. 117-187  
Owens R P 1976 *Radio Electron. Eng.* **46** 360  
Pande M K and Karekar R N 1976 *IEEE Trans. Microwave Theory Tech.* **MTT-24** 262  
Pande M K 1976 Ph.D. Thesis, Poona University, Pune  
Weirather R R 1974 *IEEE Trans. Microwave Theory (Lett.)* **MTT-22** 70  
Wheeler A 1965 *IEEE Trans. Microwave Theory Tech.* **MTT-13** 172



## Thermoelectroluminescence in thin films of zinc and copper phthalocyanines

L. N. TRIPATHI and Y. MISRA

Department of Physics, University of Gorakhpur, Gorakhpur 273 001, India

**Abstract.** Thermoelectroluminescence studies were performed on zinc phthalocyanine and copper phthalocyanine films deposited on transparent and conducting glass substrate. Thermoluminescence glow curves were recorded. The trap depths and frequency factors have also been determined using three different methods.

**Keywords.** Thermoelectroluminescence; zinc phthalocyanines; copper phthalocyanine

### 1. Introduction

Thermoelectroluminescence (TEL) is one of the thermally stimulated processes to study the thermal activation of inorganic and organic phosphors under a superimposed or a.c. electric fields. This method gives information about the traps and their distribution like the simple glow curve experiment, viz thermoluminescence (TL), thermally stimulated current (TSC) or thermally stimulated electron emission (TSEE) experiments. Trapping action in EL processes can be understood by studying the variation of brightness as a function of temperature.

In organic hydrocarbons, the temperature dependence of space charge limited current in d.c. electroluminescence has been studied in anthracene (Nakada and Ishihara 1964; Bierman 1963) and metal-free phthalocyanines (Heilmann and Weiser 1963). Thermally stimulated current measurements on the trapping levels of copper phthalocyanine have been reported by Hoshino (1981). No attempt, has, however, been made to determine parameters such as trap depths and recombination rate constants or frequency factors in ZnPc and CuPc. The present study attempts to record the thermoluminescence glow peaks for these materials to determine the above parameters.

### 2. Theoretical

EL brightness is strongly dependent on the variation in temperature, which in turn brings about a number of changes; for example, electrons/holes are detrapped from the traps and the mean trapping time of the carriers is also affected. The degree of ionization of the trap levels also affects the potential in the space charge region. An increase of brightness at a particular field frequency may be due to the release of electrons/holes at a particular temperature, which interact with excitons to lead to enhanced EL. These electrons may associate themselves with holes supplied from the positive contact forming excitons which decay radiatively giving EL emission. Carriers released from the traps are over and above those which are injected from the electrodes.

electrode contacts during the positive half cycles and which eventually form space-charge region leading to the formation of excitons. The release from traps, therefore, depends both on temperature and time. It therefore becomes necessary to consider the effect of temperature and the frequency of the alternating voltage together.

Chukova (1972), Johnson *et al* (1956) and Haake (1955) showed that the effect of temperature and frequency on EL brightness can be expressed by the relation

$$f = S \exp(-E/kT), \quad (1)$$

where  $E$  is the trap activation energy,  $S$  the frequency factor or carrier attempt to escape frequency,  $f$  the frequency of the electric field and  $T$ , the temperature at which the brightness is maximum.

If the experiment is performed at a number of frequencies  $f_1, f_2, f_3 \dots$  at a constant fixed voltage and  $T_1, T_2, T_3 \dots$  be the corresponding temperatures of maximum brightness for a particular peak, then the slope of the line drawn between  $\log f$  and  $1/T$  would give  $-E/K$  and the intercept on the  $\log f$  axis would give  $\log S$ . From these data,  $E$  and  $S$  could be found out.

There is a second approach to determine the trap depth. If the experiment is performed at different heating rates, a particular peak is shifted towards the higher temperature side at a higher rate of heating. The shift in EL brightness is also expected with change in frequency of the field. At higher frequencies the peak would shift towards higher temperature side. Therefore, the different maxima at a particular frequency  $f$ , can be represented by an equation similar to (1)

$$f_1 = S_n \exp(-E_n/kT_n), \quad (2)$$

where  $E_n$  is the energy of the  $n$ th trap corresponding to temperature  $T_n$  and  $S_n$  is the frequency factor for that trap.

If the experiment is repeated at another frequency  $f_2$  but at the same voltage, then

$$f_2 = S_n \exp(-E_n/kT'_n), \quad (3)$$

where  $T'_n$  is the new temperature at which the new peak maxima occur. From (2) and (3), we have

$$E_n = K \frac{(\log f_1 - \log f_2)}{\left(\frac{1}{T'_n} - \frac{1}{T_n}\right)}. \quad (4)$$

$S$  can now be calculated from (2) and (3).

We use a third method known as the initial rise method to determine trap depth. Here, the probability that the electrons/holes will be excited by thermal energy is proportional to  $\exp(-E/kT)$ . At lower temperatures, a smaller number of electrons/holes will be released and their number will increase with increase in temperature. After reaching a maximum, it falls as the traps are depleted. The resulting TL curve has a single peak, the peak maxima denoting the depth of the level. If  $\log I$  (at a constant frequency and voltage) versus  $1/T$  is plotted, we could get a straight line, which would give the trap depth. The peak shape and the temperature of peak maxima depend not only on the intrinsic parameters such as  $E$  and  $S$ , but also on the heating rate, the intensity of EL emission and also on the concentration of traps and excitons. Several types of traps with different activation energies usually result in several TL peaks which

may superimpose. There may be as many glow peaks as the number of trap levels in the TEL curve. The brightness maxima correspond to the exhaustion of certain group of trap levels.

### 3. Measuring arrangement and procedure

All the TEL curves were recorded above 200°K. The phosphor samples were in the form of thin films. The EL cell was fixed on a metallic plate of the cryostat, over which heating element was wound, thin mica sheet providing an insulation.

The temperature of the EL cell was measured by a chromel-alumel thermocouple. One junction of the thermocouple was securely fixed in the metallic electrode of the cell using thin mica insulation and the other junction was dipped in ice. The EMF generated in the thermocouple was recorded by a digital multimeter and the value corresponding temperature was computed from the standard table with an accuracy of 1°C. The heating rate was adjusted at 0.68°K/sec by controlling the current in the heating coil.

To obtain EL, the cell terminal was connected to a wide band amplifier capable of giving a.c. voltages up to 1000 V and frequencies from 1 Hz to 10 kHz. The integrated light output was measured using photomultiplier tube (1P21) operated by a stabilized power supply unit giving voltages up to 1200 V. The output terminals of the photomultiplier tube were connected to a multiflex galvanometer of current sensitivity  $10^{-9}$  amp/mm to record the relative intensity in arbitrary scale.

For recording TEL emission, 500 V (r.m.s.) was applied between the plate of the cell and the heating was then started. The light output was recorded at 3.14 frequencies, 1.5, 2.0 and 2.5 kHz respectively for every sample.

### 4. Results and discussion

The TEL glow curves for ZnPc and CuPc are shown in figures 1 and 2 respectively. The maxima of the brightness temperature curves are seen to shift to lower temperatures with increasing field frequencies. In inorganic systems so far known, the peak maxima are reported to shift towards the higher temperature side (Tripathi *et al* 1974). Normally such systems have a majority of electron traps. This probably implies that in ZnPc and CuPc, the presence of hole traps might cause this behaviour.

The  $\log f$  versus  $1/T$  plots for each sample show a straight line. This gives the activation energy directly and intercept the value of  $S$ . The calculated values of  $E$  and  $S$  are shown in table 1 for each system.

Trap depths have also been calculated using equation (4) at three different frequencies 1.5, 2.0 and 2.5 kHz and the results are presented in table 1. The initial method ( $\log B$  versus  $1/T$ ) curves are shown in figures 5 and 6 and the values of  $E$  are shown in table 1. The value of  $S$  for each sample is of the order of  $10^6 \text{ sec}^{-1}$ .

Hwang and Kao (1974) studied the d.c. electroluminescence and its temperature dependence in anthracene single crystals and reported one glow peak maxima at 300°K. This has been interpreted as arising due to competing behaviour of two types of processes: (i) due to exciton-trapped-exciton interaction and (ii) due to exciton-exciton interaction. The exciton-trapped-exciton interaction dominates at temperatures

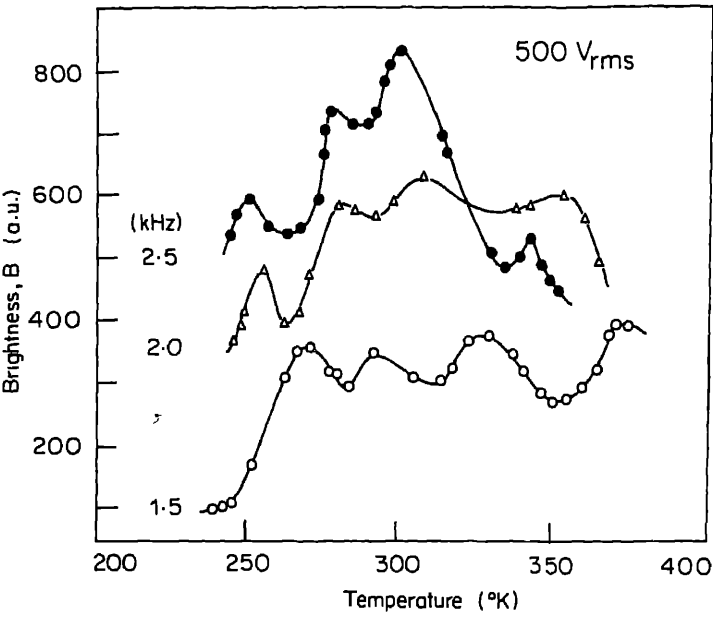


**Figure 1.** TEL curves for ZnPc (150 nm thick).

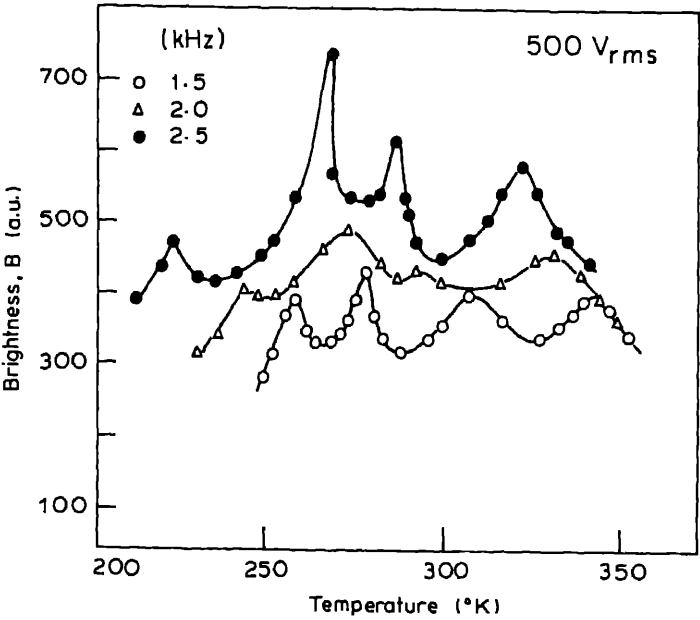


**Figure 2.** TEL curves for CuPc film (200 nm thick).

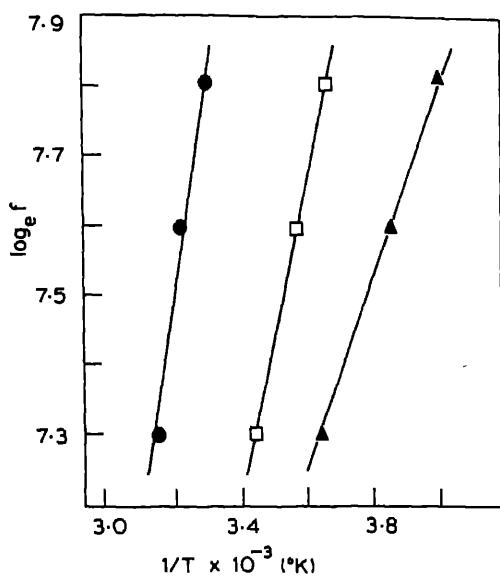


Figure 3.  $\log f$  vs  $1/T$  for ZnPc film (200 nm thick).

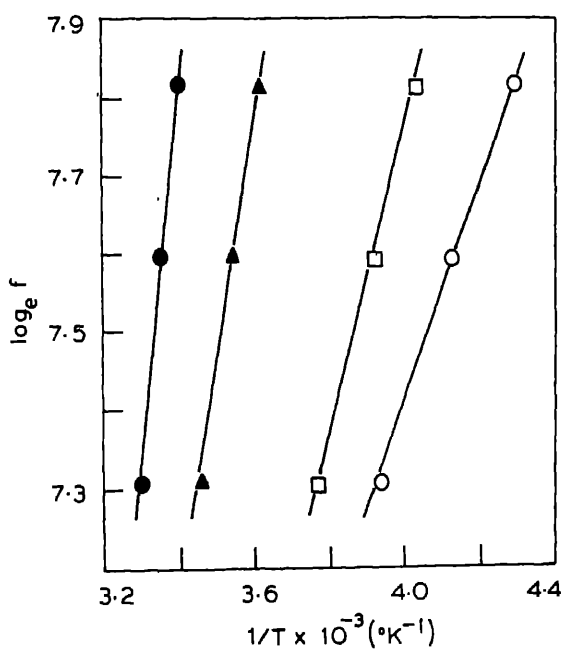


Figure 4.  $\log f$  vs  $1/T$  for CuPc film (200 nm thick)

Table 1. Values of trap depths *E* and the frequency factor *S* ZnPc and CuPc

Phosphor film	From glow curve at low temperature trap depth (eV)			Trap depth (TEL)	Trap depth	Escape frequency (sec <sup>-1</sup> )
	<i>f</i> <sub>1</sub> - <i>f</i> <sub>2</sub>	<i>f</i> <sub>2</sub> - <i>f</i> <sub>3</sub>	<i>f</i> <sub>3</sub> - <i>f</i> <sub>4</sub>	log <i>f</i> vs 1/ <i>T</i>	log <i>B</i> vs 1/ <i>T</i>	
ZnPc	0.10	0.12	0.11	0.14	0.16	10 <sup>6</sup>
	0.21	0.21	0.21	0.22	0.23	
	0.50	0.47	0.49	0.26	0.27	
CuPc	0.14	0.07	0.08	0.13	0.16	10 <sup>6</sup>
	0.16	0.19	0.17	0.16	0.18	
	0.36	0.27	0.29	0.24	0.25	
	0.83	1.16	—	0.74	—	

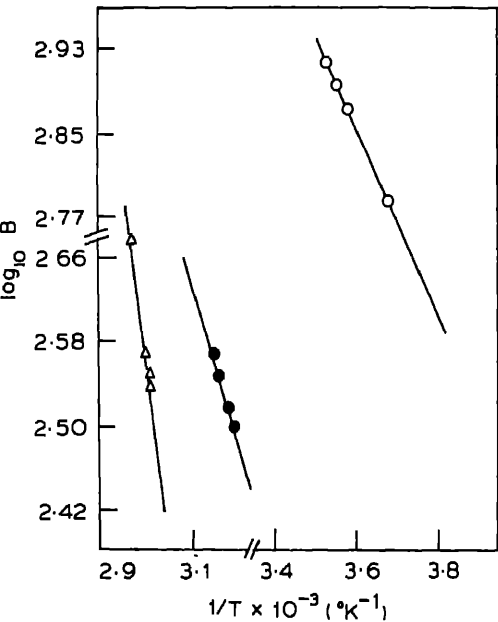


Figure 5. Log *B* vs 1/*T* for ZnPc.

maximum while the exciton carrier interaction dominates at higher frequencies. In the temperature range shown, we find four peaks corresponding to 4 groups of phosphors. As pointed out that in EL experiment, the phosphors are excited by photons at room temperatures for some time to fill the trap levels with electrons/holes and later the temperature is raised to get the stored energy released. But no such excitation was done in the present study. The EL radiation itself acts as excitation source for filling the traps



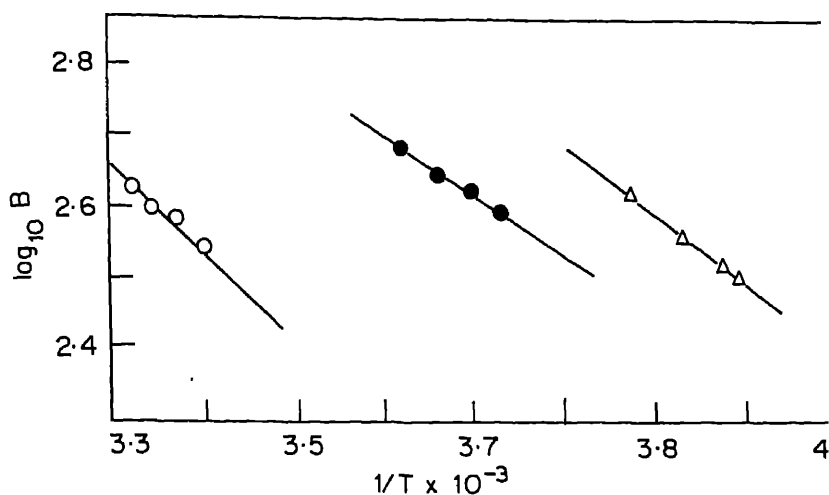
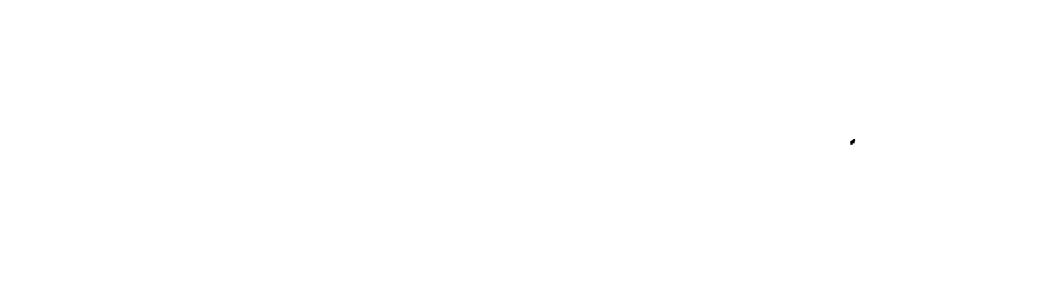


Figure 6. Log B vs  $1/T$  for CuPc.

and these trapped electrons/holes are released by the combined action of frequency and temperature.

## References

- Bierman A 1963 *Phys. Rev.* **130** 2226  
 Chukova Y P 1972 *Electrolum. Proc., P. N. Lebedev Phys. Institute*, **50** 97  
 Haake C H 1957 *J. Electrochem. Soc.* **104** 291  
 Heilmair G H and Warfield G 1963 *J. Chem. Phys.* **38** 163  
 Hoshino Y 1981 *J. Appl. Phys.* **52** 5655  
 Hwang W and Kao K C 1974 *J. Chem. Phys.* **60** 3845  
 Johnson P D, Piper W W and Williams F E 1956 *J. Electrochem. Soc.* **103** 221  
 Nakada I and Ishahara Y 1964 *J. Phys. Soc. Jpn* **19** 695  
 Tripathi L N, Chaube B R and Misra C P 1982 *Pramana (J. Phys.)* **19** 385



## Characterization of $\text{Pb}_3\text{O}_4$ films by electrochemical techniques

M SHARON, SUDHIR KUMAR and S R JAWALEKAR\*

Department of Chemistry, \*Department of Electrical Engineering, Indian Institute of Technology, Bombay 400 076, India

**Abstract.** The band gap of semiconductor is determined by photovoltage spectrum. Photovoltage sign shows the semiconductor to be of  $n$ -type conductivity. Mott-Schottky gives the position of Fermi level, the approximate position of band edges, donor density of semiconductor and space charge layer thickness. The results agree with other reported

**Keywords.** Electrochemistry; photovoltage; photoelectrochemical

### 1. Introduction

The practical application of the concepts of semiconductor electrochemistry is still a sufficiently developed field, although sufficient information regarding its characteristics is available since the last two decades. In many semiconductors, electrochemical characterization has been used successfully (Faktor *et al* 1980) to determine band gap, donor density, space charge layer width, absorption coefficient, type of conductivity, carrier concentration, composition, diffusion length etc. In the present investigation the semiconductor  $\text{Pb}_3\text{O}_4$  is characterized by photovoltage spectrum and capacitance-voltage characteristics.

### 2. Experimental details

The  $\text{Pb}_3\text{O}_4$  films (thickness  $6.3 \mu\text{m}$ ) were obtained by annealing the electrodeposited  $\text{PbO}_2$  films on nickel substrates for 24 hr at  $450^\circ\text{C}$  (Sharon *et al* 1984c). These films exhibited low conductivity ( $\sim 10^{-4} \text{ ohm}^{-1} \text{ cm}^{-1}$ ). The photovoltage spectrum was obtained by measuring the open circuit photovoltage between  $\text{Pb}_3\text{O}_4$  electrode and platinum counterelectrode dipped in redox electrolyte  $\text{IO}_3^-/\text{I}^-$  (0.2 M) at different wavelengths of light (200–800 nm). The semiconductor electrode was illuminated by a xenon arc lamp (Oriel, 500 W) through a monochromator (Oriel) keeping the cell 7 cm away from the latter. Capacitance-voltage characteristics were studied with the electrode system i.e. semiconductor, platinum and saturated calomel electrode (s.c.e.) reference dipped in buffer solution ( $\text{pH} = 7$ ). The capacitance was measured by a bridge (Systronics) at various electrode potentials (vs s.c.e.) of semiconductor electrode. AnalaR grade of chemicals were used in all the experiments without any further purification. All the solutions were prepared in triple distilled water.

### 3. Results and discussion

The criteria for electrolyte selection, validity of photovoltage spectrum for band-gap determination and interpretation of Mott-Schottky plot are discussed below.

#### 3.1 Electrolyte selection

The criteria for the most suitable electrolyte in contact with semiconductor are that it should not react chemically with the semiconductor and should produce sufficient band bending. Based on earlier studies (Sharon *et al* 1984c), the redox couple  $\text{IO}_3^-/\text{I}^-$  (0.2 M, pH = 7) satisfies both the conditions. Therefore,  $\text{IO}_3^-/\text{I}^-$  was selected for further studies.

#### 3.2 Photovoltage spectrum

Open-circuit photovoltages of the photoelectrochemical (PEC) system  $\text{Pb}_3\text{O}_4/\text{IO}_3^-$ ,  $\text{I}^-/\text{Pt}$  were measured at various wavelengths of light. The photovoltage sign gives conductivity type of semiconductor (Peter 1983; Faktor *et al* 1980). In this system anodic behaviour of photovoltage of the semiconductor was observed which indicates its *n*-type of conductivity.

A plot of photovoltage against the wavelength of light is shown in figure 1. The absorption edge of the spectrum gives the band-gap value 2.12 eV which is in good agreement with the value of 2.18 eV reported earlier (Pamfilov *et al* 1967). This value is also comparable with that measured earlier by photocurrent method ( $E_g = 2.0$  eV) (Sharon *et al* 1984a) and reflectance spectrum (Sharon *et al* 1984b) ( $E_g = 2.1$  eV). The exact explanation of photovoltage spectrum is not available till date. However, Williams

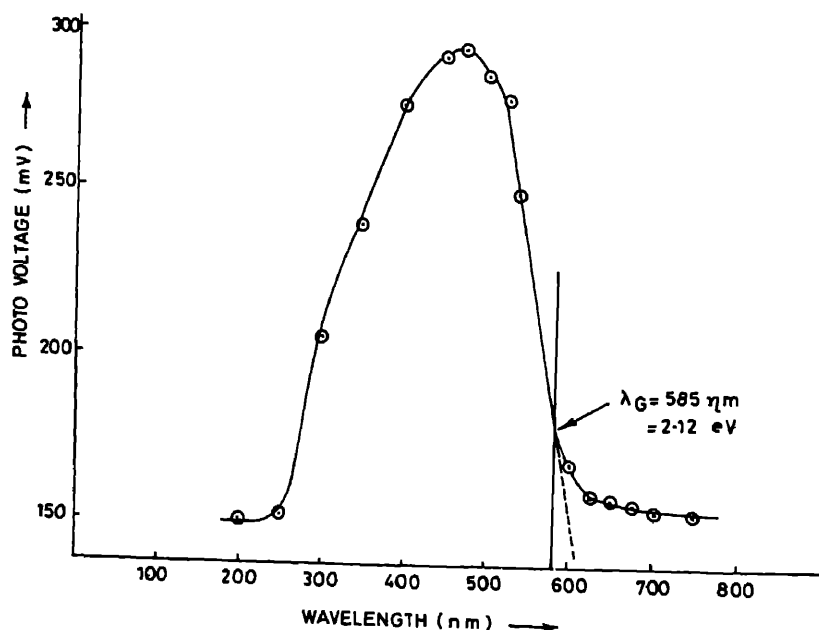


Figure 1. Photovoltage vs wavelength of light for the system  $n\text{-Pb}_3\text{O}_4/\text{IO}_3^-$ ,  $\text{I}^-/\text{Pt}$  to determine the band gap of  $\text{Pb}_3\text{O}_4$ .

(1959) observed that the photovoltage spectra of ZnO and CdSe exactly behave optical density vs wavelength plot and give similar absorption edge. This can explained as follows:

Based on the equation for the generation rate  $g_p(x)$  as a function of depth ( $x$ ) for semiconductor electrolyte junction (Myamlin and Plaskov 1967)

$$g_p(x) = P(1 - R)\alpha \exp(-\alpha x),$$

an expression for small signal photovoltage is given as (Faktor *et al* 1980),

$$KP \left[ \frac{(1 - R)\alpha L_p}{1 + L_p} \right]$$

where  $K$  is the constant for the given material;  $P$ , the photon flux;  $R$ , the surf reflectivity;  $\alpha$ , the absorption coefficient and  $L_p$  = hole diffusion length. In the ab expression, if  $\alpha \cdot L_p \ll 1$  which is always true when band gap is not too low,  $V_{ph} = K[(1 - R)L_p \times \alpha]$ . At constant photon flux  $KP(1 - R)L_p = A = \text{constant}$   $V_{ph} = A\alpha$ . Her  $V_{ph}$  is directly related to  $\alpha$  and consequently shows the same spectral distribution

### 3.3. Capacitance-voltage characteristics

The capacitance-voltage characteristics were studied by using the well-established Mott-Schottky plot for semi-conductor-electrolyte junction (Gerischer 1979).  $1/C^2$  (capacitance) $^{-2}$  vs electrode potential plot for the electrochemical syst  $Pb_3O_4$ /buffer solution (pH = 7)/Pt is given in figure 2. The condition when electrode potential is equal to zero gives the flat-band potential. The value of flat-band poten ( $V_{fb}$ ) as obtained from this plot is  $-0.405$  V vs SCE which is comparable to that repor

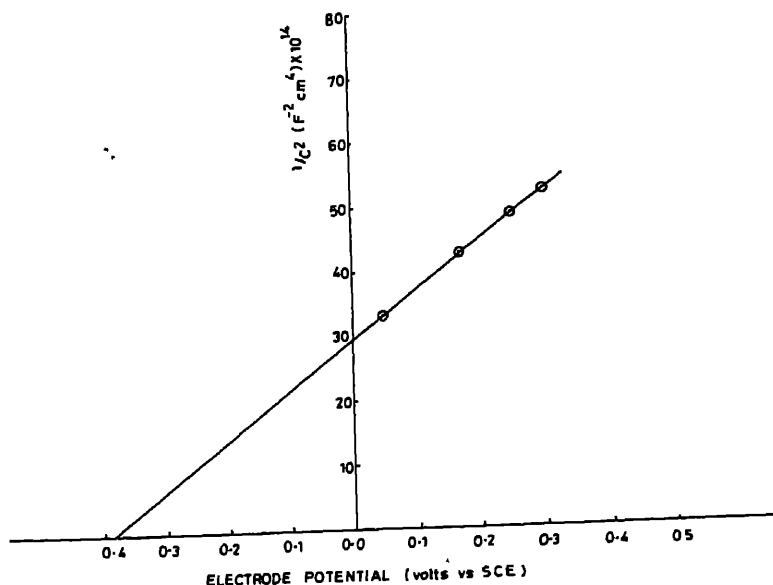


Figure 2. Mott-Schottky plot for the system  $n-Pb_3O_4$ /Buffer solution (pH = 7)/Pt to si capacitance voltage characteristics. Electrode potential is measured with respect to satur calomel electrode (SCE)

earlier (i.e.  $-0.31$  V vs SCE) using photocurrent method (Sharon *et al* 1984a) for polycrystalline  $\text{Pb}_3\text{O}_4$  pellets.

The flat band potential gives the position of Fermi-level in semiconductors. The position of Fermi-level with respect to vacuum level is given by

$$E_F = e V_{fb} \text{ (vs SCE)} - 4.781 \text{ eV (Gerischer 1975)} \\ = 4.376 \text{ eV}$$

In highly doped semiconductors the Fermi level position lies  $0.1$  eV below that of conduction band edge (Scaife 1980). However, these  $\text{Pb}_3\text{O}_4$  films have low conductivity. Therefore, if we assume this difference as  $0.2$  eV, the approximate positions of conduction and valence band edges can be given as  $-4.176$  eV and  $-6.356$  eV, respectively. The donor density in the semiconductor is calculated from the slope of Mott-Schottky plot (figure 2). Using the reported value of dielectric constant ( $\epsilon = 15$ ) for  $\text{Pb}_3\text{O}_4$  (Oehme 1964) the donor density is calculated to be  $1.19 \times 10^{-16} \text{ cm}^{-3}$ . Putting the appropriate values of donor density, dielectric constant and flat band potential, the space charge layer width in semiconductor was calculated to be  $7.80 \times 10^{-5} \text{ cm}$ .

#### 4. Conclusions

The electrochemical characterization methods are fast and much less complicated. Specially the band gap measurement is very simple and reliable. The value of  $E_{fb}$  ( $-0.405$  V vs SCE) is also in good agreement with that determined by photocurrent method ( $-0.31$  V vs SCE). However, detailed studies are needed to explain the experimental behaviour of photovoltage spectrum and this is now in progress.

#### Acknowledgement

We are grateful to CSIR for providing a research grant to complete this project. One of us (SK) is specially thankful to the Director, IIT, Bombay for a research fellowship.

#### References

- Faktor M M, Ambridge T, Elliott C R and Regnault J C 1980 *Current topics in material science* (ed.) E Ka (Amsterdam: North-Holland) Vol. 6, p. 1
- Gerischer H 1979 *Topics in applied physics* (Solar Energy Conversion) (ed.) B O Seraphin (Berlin: Springer-Verlag) Vol. 31, p. 214
- Gerischer H 1975 *J. Electroanal. Chem. Interf. Electrochem.* **58** 263
- Myamlin V A and Plaskov Y V 1967 *Electrochemistry of semiconductors* (New York: Plenum Press) p. 1
- Oehme F 1964 *Chemiker Ztg.* **88** 657 (*Chem. Abstr.* **61** 15459f)
- Pamfilov A V, Evanchevka E G and Drogomeretskie P V 1967 *Russ. J. Phys. Chem.* **41** 565
- Peter M 1983 *J. Electroanal. Chem. Interf. Electrochem.* **144** 315
- Scaife D E 1980 *Solar Energy* **25** 41
- Sharon M, Kumar S, Sathe N P and Jawalekar S R 1984a *Renewable energy sources*, (ed) T N Vezirc (Amsterdam: Elsevier) p. 321
- Sharon M, Kumar S, Sathe N P and Jawalekar S R 1984b *Solar Cells* **12** 353
- Sharon M, Kumar S and Jawalekar S R 1984c *Proc. Symp. photovoltaic materials and devices*
- Williams R 1959 *J. Chem. Phys.* **32** 1505

## Electrochemical bath deposition technique: Deposition of CdS thin films

S H PAWAR, C H BHOSALE and L P DESHMUKH

Department of Physics, Shivaji University, Kolhapur 416004, India

**Abstract.** Cadmium sulphide thin films have been deposited onto chromium plated stainless steel substrates under the influence of electric field. The various deposition parameters such as speed of rotation of the substrates, temperature of the chemical bath, molar concentrations of the solution and the strength of the electric field were kept at optimized conditions. Thin electrochemical photovoltaic (ECPV) cells are formed with CdS film electrodes. The properties of CdS films and ECPV cells are monitored with selective values of the electric field employed in the controlled precipitation technique. This relatively new technique is described and a possible film formation mechanism suggested.

**Keywords.** Anodic chemical film; cathodic chemical film; electrochemical photovoltaic cell

### 1. Introduction

Recent investigations have developed considerable interest in CdS thin film due to its intermediate band gap, high absorption coefficient and considerable energy conversion efficiency. This resulted from the discovery of Ellis *et al* (1976) that photo-decomposition of CdS can be quenched by adding polysulphides to the aqueous solution. Much work has been done on the CdS thin films and their use in electrochemical photovoltaic (ECPV) cells. Various preparative and post-preparative treatments have been given to CdS photoanode (Lokhande *et al* 1983; Mukherjee and Das 1980) to improve the performance and efficiency of these cells.

In this investigation an attempt has been made to improve the output current and voltage of the ECPV cell formed with CdS photoanode, prepared under the influence of an electric field. This paper also presents the formation mechanism of CdS film prepared anodically and cathodically.

### 2. Experimental

The reaction mixture was prepared as under: 20 c.c. of desired molar  $\text{CdSO}_4$  solution was taken in 250 c.c. beaker and an appropriate amount of 14 M liquor ammonia was slowly added into it at room temperature, with continuous stirring, to redissolve the white precipitate of  $\text{Cd}(\text{OH})_2$ . The pH of the deposition mixture was adjusted to 1. The mixture was then diluted to a total volume of 120 c.c. by adding double-distilled water. This reaction vessel containing the turbid solution of  $\text{Cd}(\text{OH})_2$  was kept in an ice bath maintained at  $90^\circ\text{C}$ . The ultrasonically-cleaned chromium-plated stainless-steel substrates fixed in a specially designed substrate holder were rotated by 75 r.p.m. by a motor, in a reaction vessel for 30 min at  $85^\circ\text{C}$ . The desired molar thiourea solution was added into the reaction vessel at the rate of 0.7 ml/min. Before adding thiourea

electric field of proper magnitude was applied between chromium plated stainless steel substrates and a ring-shaped stainless steel electrode, the distance between the electrode and the substrate being 1 cm. The CdS film was deposited onto the chromium-plated stainless steel substrates first with positive bias (by applying positive potential to the substrates), and then cathodically (by applying negative potential to the substrates) by applying d.c. 900 mV voltage. The current maintained during the deposition was 0.15 mA. The films so deposited were taken out of the reaction vessel, washed several times with double-distilled water, dried and then heated in a furnace for an hour at 200°C. The photoanode area was defined by the coal tar.

The ECPV cell was formed simply by immersing the photoanode and the counter electrode in an electrolyte. Platinum was used as a counter electrode in the cell and the properties of the films were investigated.

### 3. Results and discussion

The method of formation of thin films by controlled precipitation technique, also called chemical bath deposition technique, was modified by employing additional electric fields between conducting substrates and the counter electrode made up of chemically inert metallic cylinder. The chemical mixture was stirred into the electric cylindrical cell. The CdS films were formed by sustaining the conducting substrates both at positive and negative potentials, known as anodic and cathodic chemical films respectively.

A systematic investigation was made to reveal the role of the preparative parameters such as speed of rotation of substrates, temperature of the electrochemical bath, pH of the solution, strength of electric field etc on the properties of the films. It was found that, at low speeds of substrates (50-60 rpm), films were thick, nonspecular, and nonuniform. At higher speed (150 rpm), films were thin, specular and adhesive, while at intermediate speeds (70-80 rpm), films were smooth, specularly reflecting, adhesive and uniform. The films formed on the stationary substrates were porous, powdery, thick and nonuniform. Rotation of substrates into the electric cylindrical cell may help to increase the deposition of CdS molecules on the substrates, affecting the quality of the film.

The dissociation of complex and anion compounds depends on the temperature of the electrochemical bath. The optimum temperature of the electrochemical bath, for the growth of CdS films, was determined as  $85 \pm 5^\circ\text{C}$ . Similarly the concentrations of the chemical ingredients used, the strength of the electric field and the pH of the mixture were optimized.

In chemical bath deposition technique, Kaur *et al* (1980) suggested the growth mechanism for CdS film formation, according to which, film formation takes place either by ion-by-ion condensation of  $\text{Cd}^{2+}$  and  $\text{S}^{2-}$  ions or by adsorption of colloidal CdS particles formed in the reaction mixture. Formation of CdS nuclei by combination of ions on the substrate surface requires some catalytic solid phase on the substrate surface, which can preferentially adsorb  $\text{Cd}^{2+}$  or  $\text{S}^{2-}$  ions to form CdS.

In our electrochemical bath deposition technique, the above mechanism was modified by applying electric field. The CdS molecules thus formed are in dispersed state due to the stirring of the chemical mixture. Generally the dispersed CdS and CdSe molecules exhibit negative charges. These negatively-charged particles under the influence of electric field are bound to attract or repel from the electrically-energized substrate electrode, depending on its polarity. The influence of the electric field on the



growth mechanism of CdS and CdSe films was earlier studied by Ueno *et al* (1983) electrophoretic technique. In the present investigation, chromium-plated stainless steel substrate dipped in a suspension of  $\text{Cd}(\text{OH})_2$  has a layer of  $\text{Cd}(\text{OH})_2$  on it, which acts as a catalytic solid phase, to stimulate the decomposition of thiourea. Decomposition of thiourea in the deposition mixture supplies  $\text{S}^{2-}$  ions which then combine with  $\text{Cd}(\text{OH})_2$  to form CdS molecule. It is therefore quite obvious that, if positive potential is given to the conducting substrates, these negatively-charged CdS molecules attract towards the substrates and get deposited on the substrates. Thus the growth of CdS thin film takes place molecule-by-molecule. The rate of deposition of CdS molecules on the substrate surface is increased due to the application of electric field with substrate at the positive potential. Stirring of the solution under the influence of electric field increases the rate of deposition of CdS molecules on the substrates.

For cathodic chemical CdS films, the rate of deposition of CdS molecules onto the substrate surface is decreased. This automatically decreases the deposition rate of CdS molecules on the substrate surface, but at the same time the deposition rate of CdS molecules on the ring shaped metallic counter electrode is increased as it is at the positive potential. It is thus clear that the anodic films are more adherent, physically coherent and smoother than the latter.

The properties of CdS films were studied by the method of semiconductor electrolyte junction. In the present investigation, ECPV cells, termed as Cr/CdS-NaOH/Na<sub>2</sub>S-S/Pt, were fabricated with both anodic and cathodic chemical CdS films. Their current-voltage (*I* – *V*) characteristics, both in dark and light for anodic and cathodic

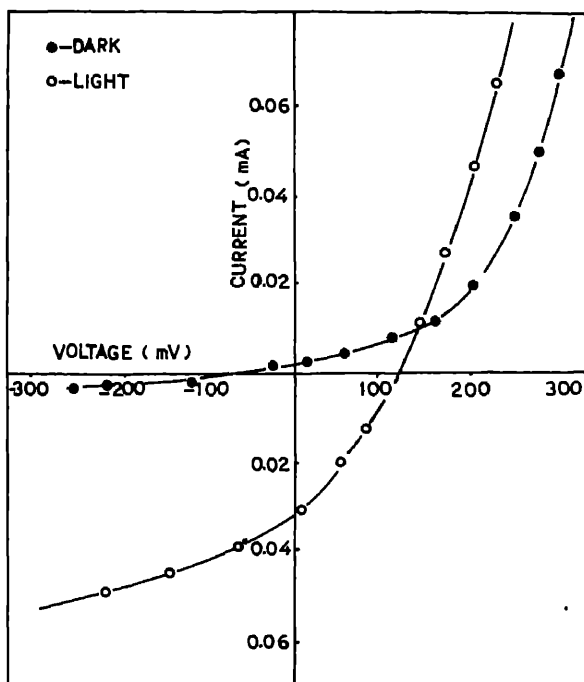


Figure 1. Current-voltage characteristics in the dark and light for the ECPV cell formed with anodic chemical CdS film.

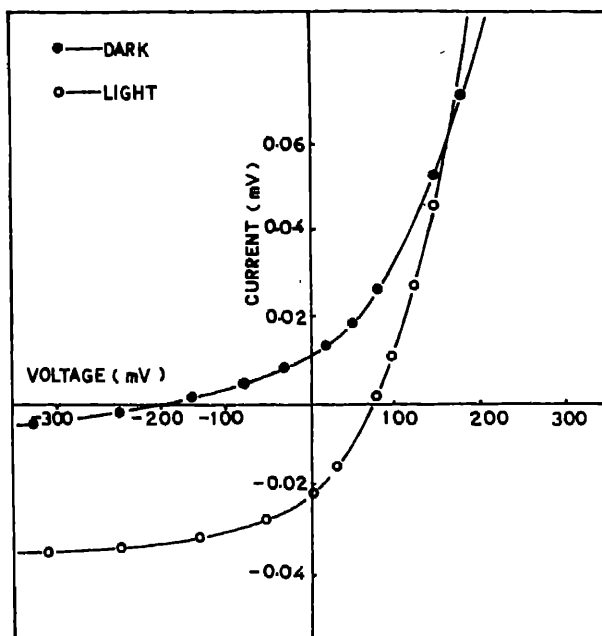


Figure 2. Current-voltage characteristics in the dark and light for the ECPV cell formed with cathodic chemical CdS film.

chemical CdS films are, shown in figures 1 and 2 respectively. It is seen that the photovoltaic output performance for the ECPV cell formed with anodic chemical CdS films is better than that formed with the cathodic chemical CdS film. This is attributed to the superiority of the anodic chemical CdS film.

### Acknowledgements

The authors are grateful to the University Grants Commission, New Delhi for financial support. One of the authors (CHB) is indebted to Rayat Shikshan Sanstha, Satara for granting study leave.

### References

- Ellis A B, Kaiser S W and Wrighton M S 1976 *J. Am. Chem. Soc.* **98** 1635
- Kaur I, Pandya D K and Chopra K L 1980 *J. Electrochem. Soc.* **127** 943
- Lokhande C D, Uplane M D and Pawar S H 1983 *Indian J. Pure Appl. Phys.* **21** 78
- Mukherjee M K and Das S K 1980 *Proc. National Solar Energy Conversion* (Madras: Allied Publishers) 326
- Ueno Y, Minoura H, Nishikawa T and Masayasu T 1983 *J. Electrochem. Soc.* **130** 43

## Spray pyrolytic deposition of $\text{CuBiS}_2$ thin films

S H PAWAR, A J PAWAR and P N BHOSALE

Department of Physics, Shivaji University, Kolhapur 416 004, India

**Abstract.** Thin films of  $\text{CuBiS}_2$  have been deposited on glass substrates using spray pyrolysis technique. The effect of substrate temperature on the growth of  $\text{CuBiS}_2$  thin films is studied in the range of 150 to 400°C. The best quality films are grown at substrate temperature 200°C with 0.1 M composition. Other preparative parameters like spray rate, pressure, height of spray solution, etc are optimized with respect to substrate temperature. Some optical and electrical properties of  $\text{CuBiS}_2$  films are also studied and reported.

**Keywords.** Spray pyrolysis technique; ternary chalcogenide films; spray rate.

### 1. Introduction

Ternary systems of the compound semiconductors are particularly interesting because of their technological applications in thin film devices and photovoltaic energy converters. Among the ternary semiconducting materials sulphur-containing compounds occupy an important place. These compounds can be prepared by employing various deposition methods, namely vacuum evaporation, chemical bath deposition, spray pyrolysis etc (Austin *et al* 1956; Rajebhosale and Pawar 1978; Pawar and Upadhyay 1983).

Spray pyrolysis technique has been successfully used in the deposition of a number of chalcogenide semiconductors (Feigelson *et al* 1977). However, no information is available on the preparation of  $\text{CuBiS}_2$  thin films of the type I-III-VI<sub>2</sub> by spray pyrolysis technique. In the present study  $\text{CuBiS}_2$  thin films were deposited on glass substrates to study the conditions for obtaining pure, uniform and adherent  $\text{CuBiS}_2$  films. The effect of preparative parameters on optical and electrical properties of grown  $\text{CuBiS}_2$  films has also been studied.

### 2. Experimental

Thin films of  $\text{CuBiS}_2$  were deposited on ultrasonically cleaned glass substrates employing spray pyrolysis technique (Chamberlin and Skarman 1966; Pawar and Upadhyay 1985). The basic ingredients used were cuprous chloride ( $\text{CuCl}$ ), bismuth trichloride ( $\text{BiCl}_3$ ) and thiourea [ $(\text{NH}_2)_2\text{CS}$ ].

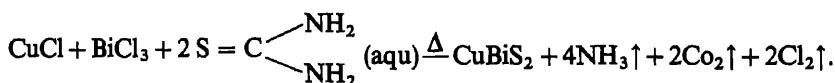
The starting solution was prepared by adding 100 c.c. of 0.1 M  $\text{CuCl}$  solution to 100 c.c. of 0.1 M  $\text{BiCl}_3$  solution to maintain a Cu:Bi ratio of 1:1. Then 200 c.c. of 0.1 M thiourea solution was added to the solution to obtain a CuBi:S ratio of 1:2. The starting solution was sprayed through a specially designed glass nozzle. Air was used to atomize the spray. The substrate temperature was varied from 150°C to 400°C with an interval of 50°C. Fast cooling was used at the termination of spray, as slow cooling

produces film with higher resistivity, possibly because of the reaction with oxygen in air over a longer time used in cooling (Feigelson *et al* 1977). The films were taken out and preserved for further study.

Films prepared at different substrate temperatures are described as  $S_{150}$ ,  $S_{200}$ ,  $S_{250}$ ,  $S_{300}$ ,  $S_{350}$  and  $S_{400}$ , the subscripts denoting the substrate temperature. The bandgap of the deposited material was determined by taking optical absorption using a monochromator (Carl Zeiss Jena). The resistivity was measured employing routine techniques. Thermovoltage of the films was recorded by using d.c. microvoltmeter (P.P.9004) in the temperature range between 300 K and 450 K.

### 3. Results and discussion

The  $\text{CuBiS}_2$  thin films were prepared by spray-pyrolysis technique. The aqueous complex solution was fed via an atomizer to hot substrates, where they decompose forming a heat-resistant compound of the copper, bismuth and sulphur. The reaction is as follows:



The decomposition of the complex compound depends on substrate temperature, spray rate, height of solution etc. It is observed that at lower temperature the films are powdery and porous in nature indicating that the decomposition of the complex compound is not complete. As substrate temperature increases, the decomposition rate increases. At higher substrate temperatures thin reflecting films are obtained which is ascribed to the evaporation rate of initial ingredients reducing the volumetric proportion of Cu, Bi and S in the film. The same effect is observed when the spray rate is high (10 cc/min) and the substrate temperature suddenly drops reducing the decomposition rate of the solution. When the spray rate is low the evaporation is high reducing the thickness of the thin film.

The  $\text{CuBiS}_2$  thin films prepared by spray pyrolysis technique at different substrate temperatures are found to be uniform and adhere tightly to the substrate. However, the thickness of the films decreases with increase in the substrate temperature (Ugai *et al* 1978) which is attributed to the increase in evaporation rate of the initial products. The crystallinity of the films increases with substrate temperature. In order to optimize the substrate temperature of the films their optical and electrical properties were studied.

#### 3.1 Optical and electrical properties

The optical absorption of the films was recorded in the wavelength range between 400 nm and 800 nm. The absorption coefficient  $\alpha$  attained a minimum value at higher wavelength region and increases with decrease in wavelength ( $\lambda$ ). This is attributed to the absorption edge of the semiconductor and homogeneity of the film.  $\alpha$  lies in the order of  $10^{-4} \text{ cm}^{-1}$  indicating that the material is of direct energy gap in accordance with the pure  $\text{Bi}_2\text{S}_3$  and  $\text{Cu}_2\text{S}$  compounds. Figure 1 shows the variation of  $(\alpha h\nu)^2$  versus energy for the typical sample  $S_{250}$ . The linear extrapolation of this curve to the energy axis gives the value of optical gap of the film. In the present study the value of bandgap ( $E_g$ ) obtained is 1.65 eV, which is somewhat larger than the bandgap of  $\text{Bi}_2\text{S}_3$  (1.4 eV).

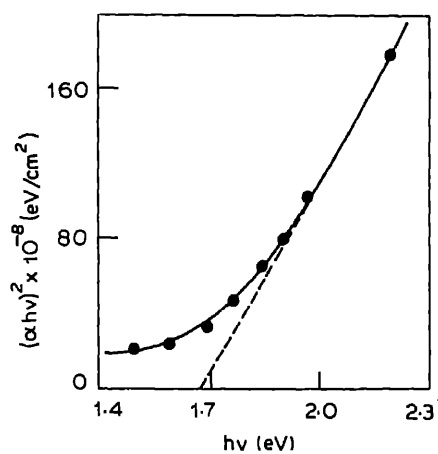


Figure 1. Plot of  $(\alpha hv)^2$  versus energy ( $h\nu$ ) for a typical sample  $S_{250}$ .

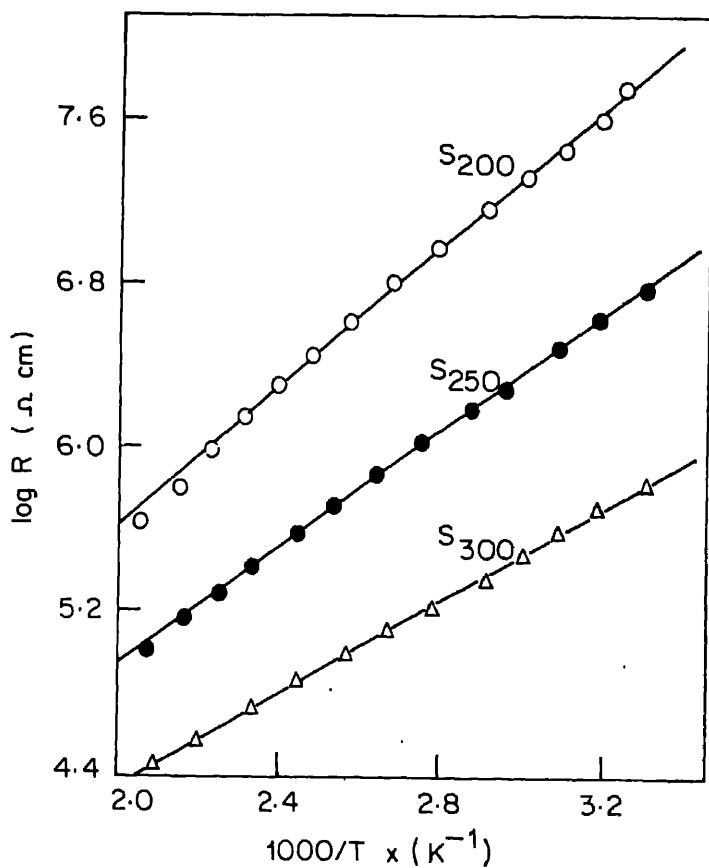


Figure 2. Variation of  $\log R$  versus  $1/T$  for the samples  $S_{200}$ ,  $S_{250}$ ,  $S_{300}$ .

(Pawar *et al* 1983) and  $\text{Cu}_2\text{S}$  (1.2 eV) (Mytton 1974). At higher substrate temperature excessive evaporation from the film takes place giving a nearly ionic ratio of 1:1:2. Beyond 450°C of substrate temperature, the evaporation rate of sulphur increases thereby forming the oxides of copper and bismuth. Better quality films were obtained between the substrate temperatures of 250°C and 300°C.

The dark resistivity measurements were carried out in the range between 300°k and 600°k. Figure 2 shows the variation of  $\log R$  with the reciprocal of temperature for typical samples  $\text{S}_{200}$ ,  $\text{S}_{250}$  and  $\text{S}_{300}$ . Films prepared at lower substrate temperature show greater resistance than films prepared at higher substrate temperature. Resistance decreases with increase in temperature confirming that  $\text{CuBiS}_2$  is a semiconducting material. The activation energies for the samples  $\text{S}_{200}$ ,  $\text{S}_{250}$  and  $\text{S}_{300}$  are 0.64 eV, 0.52 eV and 0.40 eV respectively. In the present investigation the resistivity of the films lies in the range of  $10^4$  to  $10^7$  ohm-cm.

Thermovoltage of the films was recorded to understand the conductivity and the as-grown  $\text{CuBiS}_2$  thin films showed *n*-type conduction.

## Acknowledgements

The authors are grateful to the University Grants Commission, New Delhi for financial support. One of the authors (AJP) is indebted to Rayat Shikshan Sanstha, Satara for granting study leave.

## References

- Austin I G, Goodman C H L and Pengelly A E 1956 *Electrochem. Soc.* **103** 609
- Chamberlin R R and Skarman J S 1966 *J. Electrochem. Soc.* **113** 86
- Feigelson R S, N' Dioye A, Yin Shaiw-Yih and Bube R-H 1977 *J. Appl. Phys.* **48** 3162
- Mytton R J 1974 *Solar Energy* **16** 33
- Pawar S H and Uplane M D 1983 *Solar Cell* **10** 177
- Pawar S H, Bhosale P N, Uplane M D and Tamhankar S P 1983 *Thin Solid Films* **110** 165
- Pawar S H, Uplane M D, Pawar S K and Desai J S 1985 *J. Shivaji Univ.*
- Rajebhosale M R and S H Pawar 1978 *J. Shivaji Univ.* **18** 45
- Ugai Ya A, Semenov V N and Averbakh E M 1978 *Izv. Nauk SSIR, Neorganicheskie Materialy* **14** 1529

## Preparation and properties of $\text{Bi}_{2-x}\text{As}_x\text{S}_3$ thin films by solution-gas interface technique

S H PAWAR and P N BHOSALE

Department of Physics, Shivaji University, Kolhapur 416 004, India

**Abstract.** The solution gas interface technique by which thin films of  $\text{Bi}_{2-x}\text{As}_x\text{S}_3$  were deposited is described in this paper. The semiconducting properties of the interface grown  $\text{Bi}_{2-x}\text{As}_x\text{S}_3$  thin films are studied. The optical absorption, dark resistivity and thermoelectric power of the films were studied and results are reported.

**Keywords.** Solution-gas interface technique;  $\text{Bi}_{2-x}\text{As}_x\text{S}_3$  films; resistivity.

### 1. Introduction

During the last few years, mixed semiconductors, especially chalcogenides, have been extensively studied because of their proven and potential applications in thin film technology. Among the compound semiconductors, sulphides of arsenic, antimony and bismuth are important due to their photoconductive and photovoltaic properties (George and Radhakrishnan 1979; Curran *et al* 1982; Bhattacharya and Pramanik 1982; Andreichin 1970; Ghosh and Verma 1979). We have recently reported the growth of thin films of  $\text{As}_2\text{S}_3$ ,  $\text{Sb}_2\text{S}_3$  and  $\text{Bi}_2\text{S}_3$  by our newly developed solution-gas interface (sgi) technique (Pawar and Bhosale 1984; Pawar *et al* 1983). Thin films of the compounds can be obtained by vacuum evaporation, spray pyrolysis, dip and dry as well as solution growth techniques (Ghosh and Verma 1979; Pawar *et al* 1984; Nayak *et al* 1982; Pramanik and Bhattacharya 1980). Amongst these techniques sgi technique is relatively new, inexpensive, simple and convenient for the deposition of uniform large area thin films. In order to devise a simple method of controlling the composition of the individual metal ions in the chemically grown films, we have studied their optical and transport properties and the results are reported in this paper. These results are used to deduce the variation in optical gap ( $E_g$ ) as a function of composition ( $x$ ).

The mixed  $\text{Bi}_2\text{S}_3$ - $\text{As}_2\text{S}_3$  system can be one of the promising materials for thin film photovoltaic energy conversion, because of the availability of the bandgap between 1.4 eV and 2.4 eV to cover the maximum portion of the solar spectrum. Therefore attempts have been made to establish the feasibility of producing this system in thin film form using sgi technique and to investigate the energy gap and dark resistivity of the material as a function of  $x$ .

### 2. Experimental

Thin films of  $\text{Bi}_{2-x}\text{As}_x\text{S}_3$  were deposited onto the glass substrates in the following manner. The solutions were prepared using analytical grade bismuth and arsenic salts

adding together clear solutions of  $\text{BiCl}_3$ ,  $3\text{H}_2\text{O}$  (0.1 M) and  $\text{AsCl}_3$  (0.1 M) in the volumetric ratio by varying the relative proportion of  $\text{BiCl}_3$  and  $\text{AsCl}_3$  so as to get Bi:As ratio from  $x = 0-2$ . The solutions were mixed thoroughly and the final solution was exposed to hydrogen sulphide ( $\text{H}_2\text{S}$ ) gas. The experimental set-up was described earlier (Pawar *et al* 1983; Pawar and Bhosale 1984). In brief, it consists of a gas chamber filled with pure and dry  $\text{H}_2\text{S}$  gas at a desired pressure, solution container which is specially designed to remove the solution from its bottom without disturbing the solution surface and uniform gas exposure unit. Cleaned and dry glass substrates (size  $2.5 \text{ cm} \times 1 \text{ cm}$ ) which were kept on a rectangular glass stand in the container were immersed in the solution. The solution was exposed to  $\text{H}_2\text{S}$  gas. A thin solid film is formed at the interface of the solution and gas. The solution is drained slowly from the bottom of the solution container and a uniform large area film remained on the glass substrates. The films were washed, dried and preserved in dark desiccator for further study. The films prepared with different Bi:As ratios are denoted as,  $S_{20:0.0}$ ,  $S_{1.5:0.5}$ ,  $S_{1.0:1.0}$ ,  $S_{0.5:1.5}$  and  $S_{0.0:2.0}$ , where subscripts denote the Bi:As ion ratios. The band gap of the deposited material was determined by recording the absorption spectrum in the wavelength range between 4000 and 8000  $\text{\AA}$  using a spectrophotometer (Carl Zeiss Jena). The dark resistivity measurements were carried out in the temperature range between 300 and 600 K, while thermovoltage was recorded in the temperature range between 300 and 450 K using d.c. microvoltmeter (PP 9004).

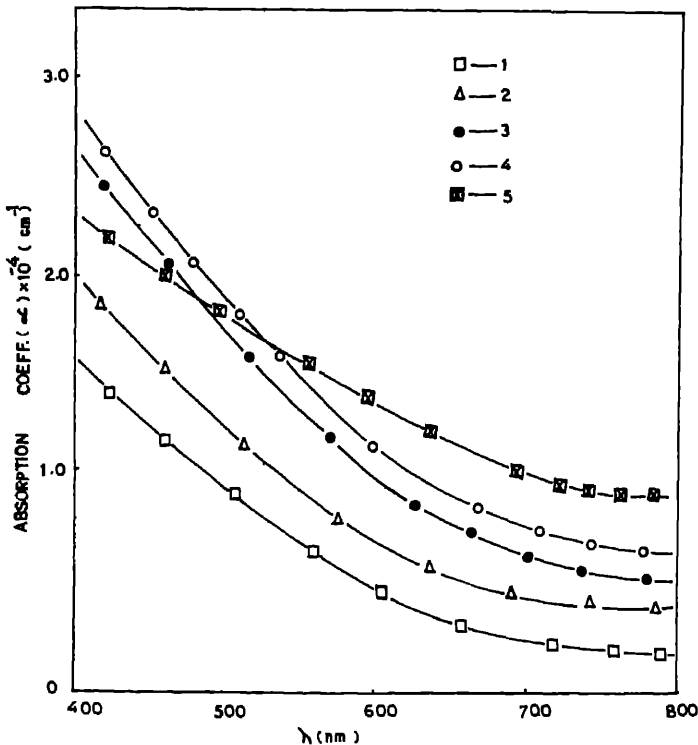


Figure 1. Variation of absorption coefficient  $\alpha$  as a function of wavelength ( $\lambda$ ) for the samples, (1)  $S_{20:0.0}$  (2)  $S_{1.5:0.5}$  (3)  $S_{1.0:1.0}$  (4)  $S_{0.5:1.5}$  (5)  $S_{0.0:2.0}$ .



### 3. Results and discussion

It is well known that the fifth group elements Bi, Sb and As have a strong affinity towards chalcogen ions and form stable chalcogenide compounds. Based on experimental evidence a new deposition method is being proposed for the mixed film semiconductors. Similar to solution growth techniques, the growth of  $\text{Bi}_{2-x}\text{As}_x\text{S}_3$  thin films takes place at the interface of the solution and gas. Due to cation-anion interaction of the arsenic, bismuth and sulphide ions a thin solid film of  $\text{Bi}_{2-x}\text{As}_x\text{S}_3$  is formed at the interface of solution and gas.

The quality and uniformity of the  $\text{Bi}_{2-x}\text{As}_x\text{S}_3$  thin films prepared by the technique depend on various preparative conditions, including the composition of mixed solution, pH, surface tension, temperature, gas exposure time and gas pressure. Keeping all these parameters constant the composition of  $\text{AsCl}_3$  and  $\text{BiCl}_3$  solution was taken to vary from 0–2. The  $\text{Bi}_{2-x}\text{As}_x\text{S}_3$  thin films in the present investigation were formed using 0.1 M bismuth and arsenic chloride solutions with pH range between 2 and 4 at room temperature.

Variation of absorption coefficient ( $\alpha$ ) with wavelength ( $\lambda$ ) is shown in figure 1. A steep fall in  $\alpha$  is ascribed to the absorption edge of the semiconductor. The value of  $\alpha$  for all the films lies in the order of  $10^{-4} \text{ cm}^{-1}$  which is characteristic of the direct transition. Figure 1 shows that the absorption edge shifts towards the shorter wavelength side with increase in the arsenic composition in the film. This reveals that the bandgap of  $\text{Bi}_{2-x}\text{As}_x\text{S}_3$  film increases with increasing composition of arsenic in the film. Figure 2 shows that the variation of  $(\alpha h\nu)^2$  vs photon energy ( $h\nu$ ) for a typical

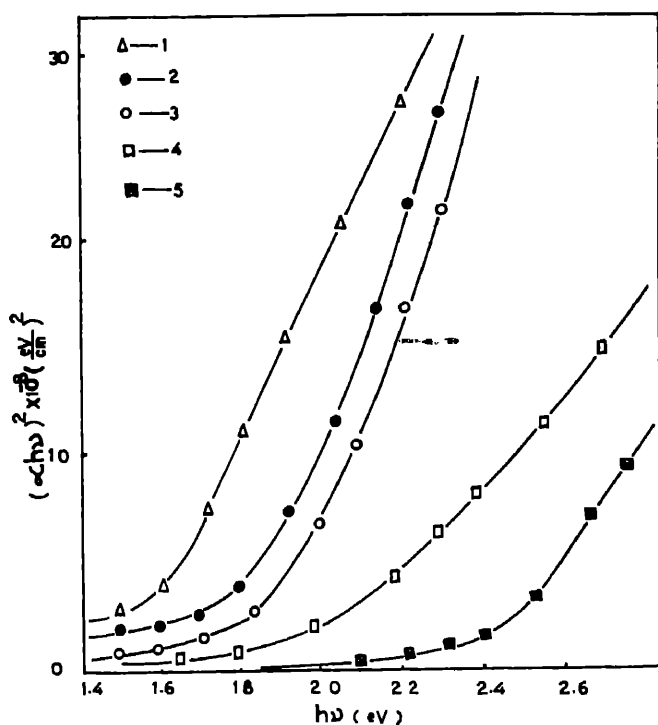


Figure 2. Plots of  $(\alpha h\nu)^2$  vs  $(h\nu)$  for the samples. Details same as in figure 1.

is linear and shows strong absorption near the bandgap region. Extrapolation of this plot to energy axis gave the bandgap varying from 1.5 eV for pure  $\text{Bi}_2\text{S}_3$  to 2.42 eV for pure  $\text{As}_2\text{S}_3$  thin films. Figure 3 shows the experimental curve of  $E_g$  vs  $x$ . The dependence of energy gap  $E_g$  on  $x$  is obtained from the position of the symmetry point  $x$  which has been selected in accordance with the values for pure compounds of  $\text{Bi}_2\text{S}_3$  and  $\text{As}_2\text{S}_3$ .

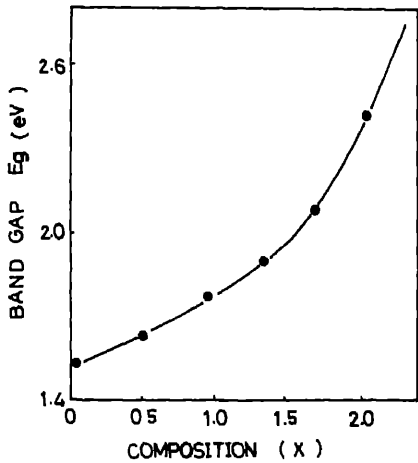


Figure 3. Variation of bandgap ( $E_g$ ) as a function of composition ( $x$ ) for  $\text{Bi}_{2-x}\text{As}_x\text{S}_3$  films.

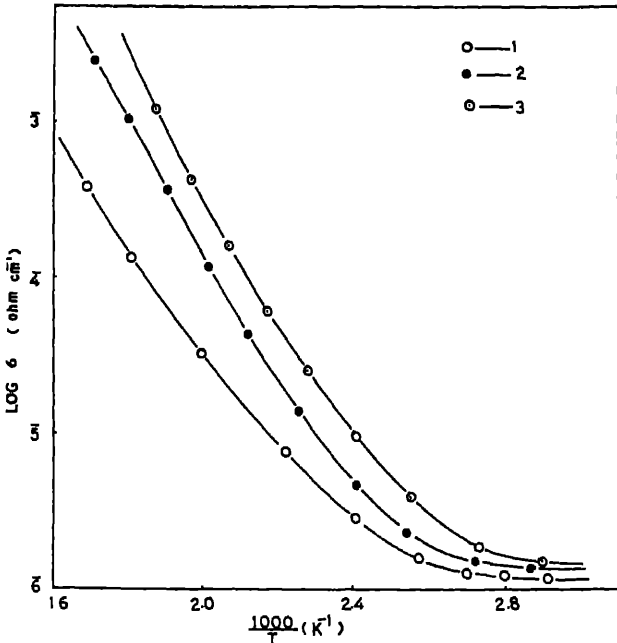


Figure 4. Plot of  $\log \sigma$  vs  $1/T$  for the typical samples (1)  $S_{2.0.00}$  (2)  $S_{1.0.10}$  (3)  $S_{0.0.20}$ .

The nonlinear variation of  $E_g$  with  $x$  is similar to the results reported by other workers in case of  $Cd_{1-x}Zn_xS$  thin films (Agnihotri and Gupta 1979; Mbow *et al* 1982).

In the present investigation variation of resistivity with reciprocal of temperature studied for all films. The films have high electrical resistance in comparison to single crystals of  $Bi_2S_3$  and  $As_2S_3$  (Andreichin 1970; Bhattacharya and Pramanik 1982). The resistivity lies in the range of  $10^8$  to  $10^9$  ohm cm at room temperature. The resistance generally high for films prepared by solution growth techniques, presumably due to the discontinuity and thickness of the films. The activation energy of the films deposited by the SGT technique is high as compared to single crystals, perhaps due to high specific resistivity. The plot of  $\log \sigma$  vs  $1/T$  for three typical samples are shown in figure 4. The slope of the plots gives two activation energies at lower and higher temperature regions which can be attributed as follows. At higher temperatures, excessive evaporation of sulphur from the films takes place with a pronounced reduction in resistance (Krishnamoorthy and Shivakumar 1984), while at lower temperature conduction of electrons takes place in the extrinsic region of the semiconductor. The  $Bi_{2-x}As_xS_3$  films show  $n$ -type conduction in accordance with pure  $Bi_2S_3$  thin films.

## Acknowledgements

Authors are grateful to the Department of Non-Conventional Energy Sources (DNES), Ministry of Energy, Govt. of India for financial assistance. They would like to thank Mr S K Jamadar and the Energy Conversion group for experimental help.

## References

- Agnihotri O P and Gupta B K 1979 *Jpn J. Appl. Phys.* **18** 141
- Andreichin R 1970 *J. Non-Crystall. Solids* **4** 73
- Bhattacharya R N and Pramanik P 1982 *J. Electrochem. Soc.* **129** 332
- Curran J S, Philippe R, Joseph J and Gagnaire 1982 *Chem. Phys. Lett.* **89** 511
- George J and Radhakrishnan M K 1979 *Solid State Commun.* **33** 987
- Ghosh C and Verma B P 1979 *Thin Solid Films* **60** 61
- Gildert L, Kline J M and Mattox D M 1961 *J. Phys-Chem. Solids* **18** 286
- Krishnamoorthy P A and Shivakumar G K 1984 *Mater. Lett.* **2** 223
- Mbow C M, Cohen C W and Laplace D 1982 *Thin Solid Films* **87** 141
- Nayak B B, Acharya H N, Chaudhury T K and Mitra G B 1982 *Thin Solid Films* **92** 309
- Pawar S H and Bhosale P N 1984 *Mater. Chem. Phys.* **11** 461
- Pawar S H, Bhosale P N, Uplane M D and Tamhankar S P 1983a *Thin Solid Films* **110** 165
- Pawar S H, Bhosale P N, Deshmukh L P and Uplane M D 1984a *Thin Solid Films* (In press)
- Pawar S H, Bhosale P N, Tamhankar S P and Uplane M D 1983b *Ind. J. Pure & Appl. Phys.* **21** 66.
- Pawar S H, Tamhankar S P and Lokhande C D 1984b *Mater. Chem. Phys.* **11** 401
- Pramanik P and Bhattacharya R N 1980 *J. Electrochem. Soc.* **127** 2087

■

” ” ”

## Electron microscopy study of chemically deposited Ni-P films

S V S TYAGI, V K TANDON and S RAY\*

Department of Physics, \*Department of Metallurgy, University of Roorkee, Roorkee 247 66, India

**Abstract.** The structure of electroless thin films of Ni-P has been studied. The microstructure and the selected area diffraction pattern of the samples reveal that certain samples transform to crystalline Ni with P in solid solution by nucleation and growth, whereas others transform to crystalline state by growth alone. The former set of thin films having a P-content of 19–21 at. % is characterized as amorphous. Films with a P-content of 13–15 at. % fall in the latter category and are characterized as microcrystalline. Those with a P-content of 16–18 at. % contain both amorphous and microcrystalline regions.

**Keywords.** Amorphous; microcrystalline; electroless; nickel-phosphorous; electron microscopy.

### 1. Introduction

Electroless deposition of Ni with different metalloids like P, B etc has produced both crystalline and amorphous thin films depending upon the composition of the bath (P and Marton 1972; Gorbunova *et al* 1973; Hedgecock *et al* 1975; Yamasaki *et al* 1981; Cortijo and Schlesinger 1983). These metalloids have very restricted solid solubilities in Ni (Maeda 1970). When the amount of metalloid exceeds the limit of solid solubility, the film at equilibrium has a suitable precipitate containing the excess metalloid in the matrix of Ni with the metalloid up to the limit of solid solution. However, electroless deposition, being a low temperature process, the system is constrained to remain in a single non-equilibrium phase due to its kinetic limitations.

As the metalloid content increases beyond the solubility limit, they produce excess strain in the crystalline structure resulting in a higher density of defects (Graham *et al* 1965). Normally one expects that the defects increase with increase in metalloid content and the system becomes microcrystalline. Moreover, when the metalloid content is increased beyond a limit, it becomes difficult to retain the long range order and the system passes into a non-equilibrium amorphous state.

To distinguish between the as-deposited state of an amorphous sample and that of a microcrystalline sample is a difficult task, because responses which are similar to those in diffraction studies in the two states. Bagley and Turnbull (1970) provided the following conceptual framework by arguing that on heating, a microcrystalline sample will undergo grain growth to pass on to a crystalline state but the amorphous sample will transform only by nucleation and growth. While there will be a critical temperature only above which it is possible to surmount the activation barrier for nucleation, for microcrystalline samples the grain growth will take place at all temperatures depending upon the magnitude of the diffusion coefficient.

In the present investigation we have examined the thin films of electroless deposited Ni-P alloys with different P-contents. The thin films were subjected to electron microscopy while heating on the stage of the microscope. The electron micrographs a

selected area diffraction pattern (SAD) of the films with different P contents were analyzed to determine the nature of the as-deposited electroless films. Makhsoos *et al* (1978) undertook similar investigations on electrodeposited films by heating the samples with electron beam itself. However, the extent of heating could not be determined in their investigation. In the present study the sample temperature was monitored throughout.

## 2. Experimental

The Ni-P films were deposited using electroless deposition technique. The details of the bath and conditions are given in table 1. The concentration of components in the solution was optimized to get a deposition rate of about 800 Å/min. The glass slides, used as substrates, were first washed with liquid detergent (Teepol), then by acid and degreased with hot NaOH solution. Finally substrates were washed with hot double distilled water. For deposition, these properly cleaned substrates were given a sensitizing treatment (by dipping in a 1% SnCl<sub>2</sub> solution for 60 sec) and activation treatment (by dipping in a 0.1% PdCl<sub>2</sub> solution for 30 sec). The film was deposited for about 40 sec for examination under transmission electron microscope.

The samples were chemically analyzed by using wet chemical method, the accuracy of which is less than  $\pm 1\%$ . Transmission electron microscopy (Philips model EM 400 T/ST with a heating holder PW 6592) was carried out and the general form of the holder was similar to that of other holders for the goniometer stage.

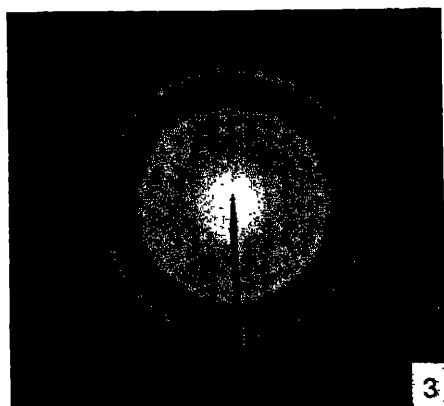
## 3. Results and discussion

Ni-P samples have been deposited by varying the amount of the reducing agent, NaH<sub>2</sub>PO<sub>2</sub>, in the bath so that the composition falls in three ranges—sample I containing 13–15 at. % of P, sample II 16–18 at. % P and sample III 19–21 at. % P. The composition of the deposits could not be controlled more closely due to limited facilities.

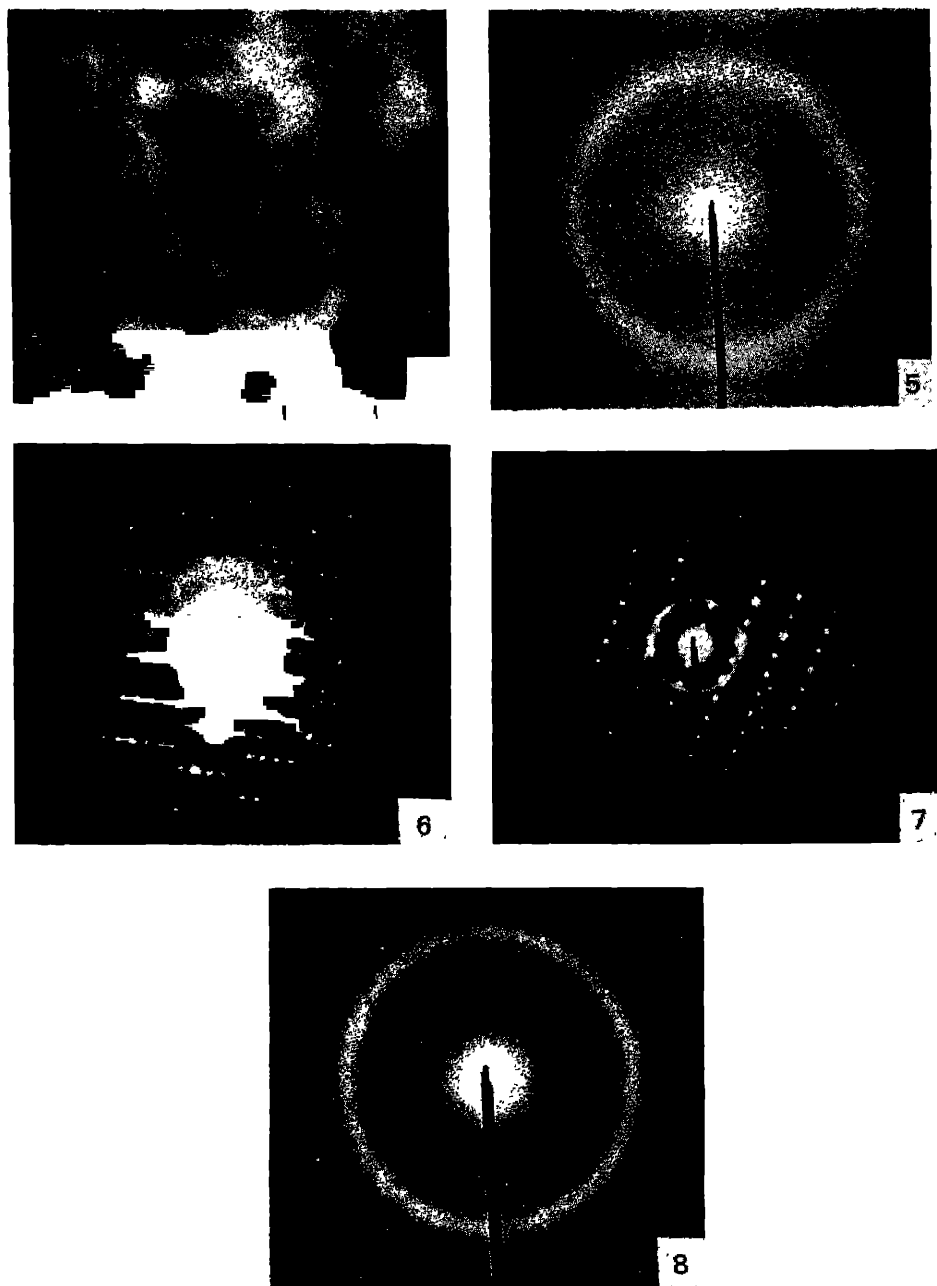
The electron micrograph of sample I is shown in figure 1. The deposit shows unevenness, but the SAD as in figure 2 shows a diffuse ring at  $2\theta = 1.063^\circ$  and  $\Delta 2\theta = 0.08^\circ$ . If it is assumed to be microcrystalline the lattice parameter is approximately 3.46 Å on the average. However, the diffuse ring may have been a characteristic of an amorphous state; while heating this sample the width of the diffuse ring decreases continuously leading to rather sharp rings as given in figure 3 showing

Table 1. Bath and conditions of Ni-P films

Plating variables	g/l of H <sub>2</sub> O	
NiSO <sub>4</sub> ·7H <sub>2</sub> O	24	pH-(8.5–9.5)
(NH <sub>4</sub> ) <sub>2</sub> SO <sub>4</sub>	50	adjusted with NH <sub>4</sub> OH
Na <sub>3</sub> C <sub>6</sub> H <sub>5</sub> O <sub>7</sub> ·2H <sub>2</sub> O	88	temperature-85 $\pm$ 2°C
NaH <sub>2</sub> PO <sub>2</sub>	(10–45)	No stirring



**Figures 1-3.** Electron micrograph and SAD of Ni-P sample I (13-15 at. %). 1, 2. As-deposit state. 3. Heated at 350°C for 2 min.



Figures 4-8. Electron micrograph and SAD of Ni-P sample II. 4-7. 16-18 at. %. 4, 5. As-deposited state. 6. Heated at 340°C for 2 min. 7. Heated at 340°C for 2 min in a region different from that of 6. 8. 19-21 at. % in as-deposited state.



the SAD of sample I heated to 350°C for 2 min in TEM. The reduction in broadening may be attributed to the lowering of defect density and growth of the grains in microcrystalline state. Following the arguments of Bagley and Turnbull (1970), we believe that the sample class I is not in amorphous state but in a microcrystalline state.

The electron micrographs of as-deposited sample II and its SAD pattern are shown in figures 4 and 5. The SAD pattern has a diffuse ring at  $2\theta = 1.057^\circ$  and its width  $\Delta 2\theta = 0.13^\circ$ . Clearly it is identical to that observed for as-deposited sample I excepting for a slight shift in the position of the ring and an increase in width. If the sample is microcrystalline, the higher P content of the sample will change the lattice parameter causing a shift in position of the ring. The resulting strain may also have been accommodated by larger concentration of defects and reduced grain size. Thus, the diffraction ring has a higher width. But again SAD may be attributed to that of an amorphous state.

On heating sample II to 340°C and holding it for 2 min certain areas of the sample showed an SAD pattern as given in figure 6. The SAD pattern shows broad diffuse rings superimposed over a spot pattern. The retention of width at a high temperature (340°C) is in sharp contrast with the behaviour observed in sample I. Thus in sample II there is a barrier to the change in state from the one characterized by the broad diffuse ring. In addition, the spot pattern is characteristic of a crystalline state with a crystallite size exceeding the width of focus. It can be inferred that in this region of the sample, an amorphous state transforms to a crystalline state by nucleation and growth. However, in certain other regions of this sample one observes continuous sharpening of broad rings, resulting in sharp rings superimposed on the spot pattern (figure 7). This region appears to consist of microcrystallites and a crystallite of size greater than the size of focus indicating a grain growth and an abnormal grain growth. Sample II contains both amorphous and microcrystalline regions, which may have resulted due to the variation of P distribution from one region to the other.

Sample III shows an SAD pattern (figure 8) and again consists of a broad diffuse ring with  $2\theta = 1.055^\circ$  and  $\Delta 2\theta = 0.16^\circ$ . The position of the ring has slightly been shifted and the width increased obviously due to an increase in P content. However, it is not possible to infer about the structural state of the sample from this SAD pattern. On heating this sample to 345°C and holding for 2 min, one observes superposition of broad diffuse rings on the spot pattern similar to that observed in some regions of sample II.

#### 4. Conclusions

The electron microscopy study of the Ni-P samples containing 13–21 at.% P show that the as-deposited film passes from a microcrystalline state to amorphous state with increasing P content. At intermediate compositions the microcrystalline and amorphous state co-exist. But it is not clear whether it is a result of composition variation or whether it is possible to achieve these two states together at the same composition. In the composition range of 19–21 at.% P it is amorphous. Several investigations have noted that the samples with low-P are crystalline (Yamasaki *et al* 1981). Thus, it appears that with increase of P, the as-deposited Ni passes from crystalline to microcrystalline state continuously and then beyond a certain composition to an amorphous state.

### **Acknowledgements**

The authors are highly grateful to Dr Kailash Chandra for all facilities at the University Service and Instrumentation Centre and to Dr R C Bembi for chemical analysis of the samples. Thanks are also due to Mr NK Saini for transmission electron microscopy.

### **References**

- Bagley B G and Turnbull D 1970 *Acta Metall.* **18** 857  
Cortiju R O and Schlesinger M 1983 *J. Electrochem. Soc.* **130** 2341  
Gorbunova K M, Ivanov M V and Moiseev V P 1973 *J. Electrochem. Soc.* **120** 613  
Graham A B, Lindsay R W and Read J 1965 *J. Electrochem. Soc.* **112** 401  
Hedgecock N, Tung P and Schlesinger M 1975 *J. Electrochem. Soc.* **122** 866  
Maeda H 1970 *J. Phys. Soc. Jpn* **29** 311  
Makhsoos E V, Thomas E L and Toth L E 1978 *Metall. Trans.* **A9** 1449  
Pai S T and Marton J P 1972 *J. Appl. Phys.* **43** 282  
Yamasaki T, Izumi H and Sunada H 1981 *Scripta Met.* **15** 177

## Liquid phase epitaxy growth of GaAs:Si by temperature difference method

C C WEI, Y K SU, C C CHANG and S C LU

Research Institute of Electronic and Electrical Engineering, National Cheng Kung University, Tainan, Taiwan, Republic of China

MS received 26 October 1985

**Abstract.** The LPE growth of a horizontal sliding system by temperature difference method is used to grow single and multiple layers of GaAs compounds from dilute solution. The weight ratio of Si to Ga solvent is  $10^{-4}$  wt%. The growth rate, surface morphology, carrier concentration and Hall mobility are studied. Relationship between the above properties and the growth temperature and temperature difference ( $\Delta T$ ) is also discussed. In general, the present results appear quite consistent with the diffusion limited model. The growth rate can be precisely controlled. The stability of the solid-liquid interface can be obtained in the epilayer growth at a constant temperature of the system which can avoid the effect of constitutional supercooling. Under proper control, a perfect epilayer and multiple smooth layers can be obtained.

**Keywords.** Liquid phase epitaxy; GaAs:Si doping; temperature difference method; growth rate; surface morphology; carrier concentration; Hall mobility.

### 1. Introduction

Liquid phase epitaxy (LPE) is a technique normally used to grow single or multiple layers of III–V compound semiconductor materials from dilute solution. It can also be used to grow other materials, such as II–VI compounds and magnetic materials, and offers good quality epilayers for devices such as injection lasers, solar cells, varactor, LED and FET etc.

The steady state temperature difference method with horizontal sliding boat system was adopted in this experiment (Nishizawa and Okuno 1978). This technique is easier for temperature control compared with the transient method. The desired thickness of epilayers can be obtained by precisely controlling the growth time. The other advantage associated with this method is that constitutional supercooling can be avoided (Long *et al* 1974; Tiller 1968). In this experiment, silicon was used as the *n*-type dopant. The weight ratio of Si to Ga solvent was  $10^{-4}$  wt%. The Cr-doped semi-insulated GaAs wafer was used for substrate which was oriented on the (100) crystal plane. Gallium was used as a solvent and GaAs polycrystal wafer was adopted as the source.

The growth rate, surface morphology, Hall mobility and carrier concentration were measured. Relationship between the above properties and growth temperature and  $\Delta T$  (temperature difference between substrate and source) is also discussed.

The growth temperature and temperature difference ranged from 650°C to 800°C and from 4.5°C to 25.7°C respectively. The thickness of epilayer ranged from 1  $\mu\text{m}$  to 20  $\mu\text{m}$ .

## 2. Growth apparatus and measurements

The schematic diagram of the apparatus is shown in figure 1. The principal components are graphite boat, quartz tube, gold-coating transparent furnace, purifier, vacuum system and exhaust system. Small quartz tubes were used as pull rod, graphite boat holder and thermal couple protector. Since temperature difference method was adopted (Nishizawa and Okuno 1978) the tungsten filament should be designed and wound around crucibles as heater. Certainly, a small cylindrical quartz tube was needed to cover the environment of graphite crucible to obtain a more uniform temperature distribution.

Gold-coating transparent furnace can be tuned to a constant temperature within  $\pm 1^\circ\text{C}$  over 70% of its length. The boat was set in the middle of the furnace for a stable temperature. Only one zone was needed.

Vacuum system had a cold trap with liquid nitrogen for preventing the oil vapour from contaminating the system.

After loading the boat and substrate, the reactor was flushed with flowing gas, evacuated and then backfilled with purified  $\text{H}_2$ . A slow flowing  $\text{H}_2$  (about 0.5 l/min) was used as purge (30 min) and the furnace was then moved into the position of the boat. The furnace temperature was increased gradually to the growth temperature. After the stable operating temperature was reached,  $\Delta T$  was established between substrate and source with AC power supply. A few minutes later, the substrate was pushed to contact source solution and the desired LPE layers were grown. During the growth run, the variation of the system temperature was kept within  $\pm 0.5^\circ\text{C}$  or less. After the growth run ended, the substrate was pushed out of the solution, the furnace moved away and the boat cooled to room temperature. Hydrogen stopped and then the growth was finished.

When the epilayer was grown, the surface morphology and cleavage surface of the epilayer were examined by optical microscopy. The carrier concentration and

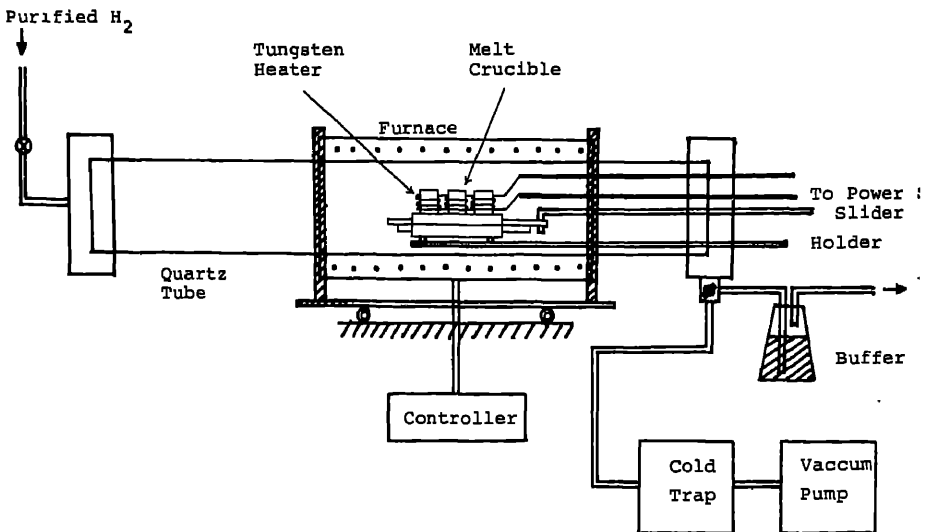


Figure 1. The apparatus of horizontal system for temperature difference method.

mobility was measured with van der Pauw measurement and Hall effect. Ti multilayer Ge/Au/Ni (about 400 Å/2500 Å/400 Å), evaporated onto the wafer surface, was used for ohmic contacts.

### 3. Results and discussion

#### 3.1 Growth rate

With a solution temperature of 704.5–725.7°C, a substrate temperature of 700°C and a growth time of 4 hr, the thickness vs temperature difference  $\Delta T$  between the source and the substrate is shown in figure 2. The experimental data are compared with theoretical values (Long *et al* 1974; Hsieh 1980). It can be shown that the thickness of the epilayer increases as  $\Delta T$  is increased. The furnace temperature was varied from 650°C to 800°C ( $\Delta T=18.8^\circ\text{C}$ , growth time=1 hr) and the thickness vs growth temperature is shown in figure 3. It is assumed that the diffusion constant is determined by growth temperature ( $T_G$ ) (dashed curve) and that it is determined by growth temperature and temperature difference between the source and the substrate (i.e.  $T_G + \Delta T$ ) (dashed line b). The experimental data in figure 2 are more consistent with the latter case.

The growth rate of epilayer was apparently proportional to the growth time in our measurement (see figure 4). Further, the carrier concentration showed a strong dependence on the value of  $\Delta T$ . Two interesting experimental results are shown in figure 5. Figure 5(a) shows that two layers were grown on substrate in the same solution and at the same growth temperature but  $\Delta T$  was different during the epilayer growth. The first and the second layers were grown with a temperature difference of 25.7°C and 11.2°C respectively for 2 hr. The growth temperature was set at 700°C and the height of the solution was 0.34 cm. The thickness of the second layer was greater than the normal growth, because the temperature difference was

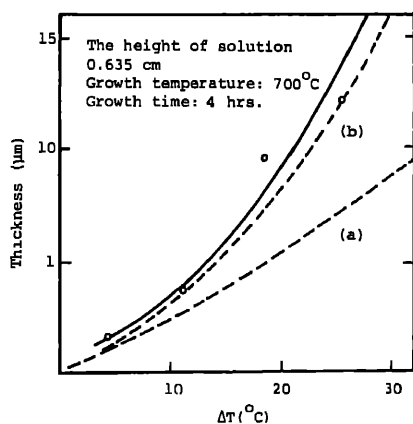


Figure 2. Epilayer thickness vs temperature difference ( $\Delta T$ ) curve. The dashed lines are the theoretical data and the solid line is the experimental data.

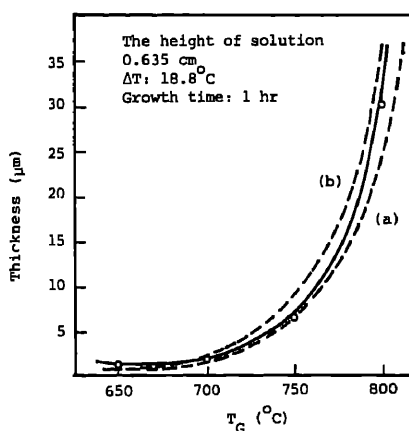


Figure 3. Epilayer thickness vs growth temperature curve. The dashed lines are the theoretical data and the solid line is the experimental data.

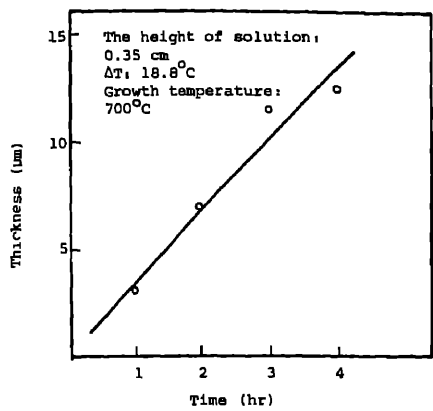


Figure 4. Epilayer thickness vs time

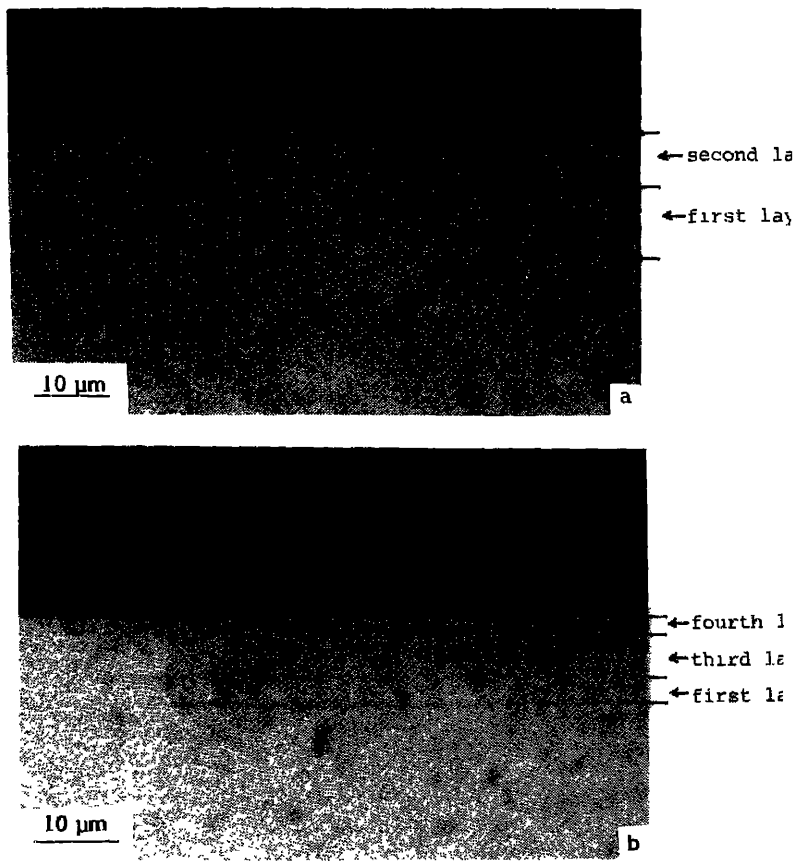


Figure 5. Cleavage surface of grown layer. (a) Double epilayers ( $T_g = 700^\circ\text{C}$ ,  $W = \Delta T:t = 25.7^\circ\text{C}:2\text{ hr}$  then  $11.2^\circ\text{C}:2\text{ hr}$ ). (b) Multilayer ( $T_g = 700^\circ\text{C}$ ,  $W = \Delta T:t = 25.7^\circ\text{C}:1\text{ hr}$ ,  $11.2^\circ\text{C}:1\text{ hr}$ ,  $18.8^\circ\text{C}:1\text{ hr}$  then  $4.5^\circ\text{C}:1\text{ hr}$ ).

## LPE growth of GaAs:Si

reduced from 25.7°C to 11.2°C producing the condition of equilibrium co step cooling in the solution.

A similar condition is shown in figure 5b. The temperature difference was 11.2, 18.8 and 4.5°C respectively for 1 hr during each growth. Here, it appears the fourth layer is much thicker than the normal growth, while the first layer is thinner than the normal growth, although the secondary layer has disappeared. Back etching seems to have occurred when the temperature difference changed from 11.2°C to 18.8°C.

### 3.2 Electric characteristics of epilayers

Figure 6 shows the dependence of resistivity and Hall mobility on concentration. The dashed line from Sze (1981) shows the dependence of resistivity and Hall mobility on impurity concentration which can be compared with experimental data. The Hall mobility and the resistivity of experimental data are lower than the comparative values of dashed lines. Perhaps it is influenced by the dopant because Si is an amphoteric impurity in GaAs layers (Casey and 1978). Since carrier concentration is  $n = N_D - N_A$  for n-type material and the in

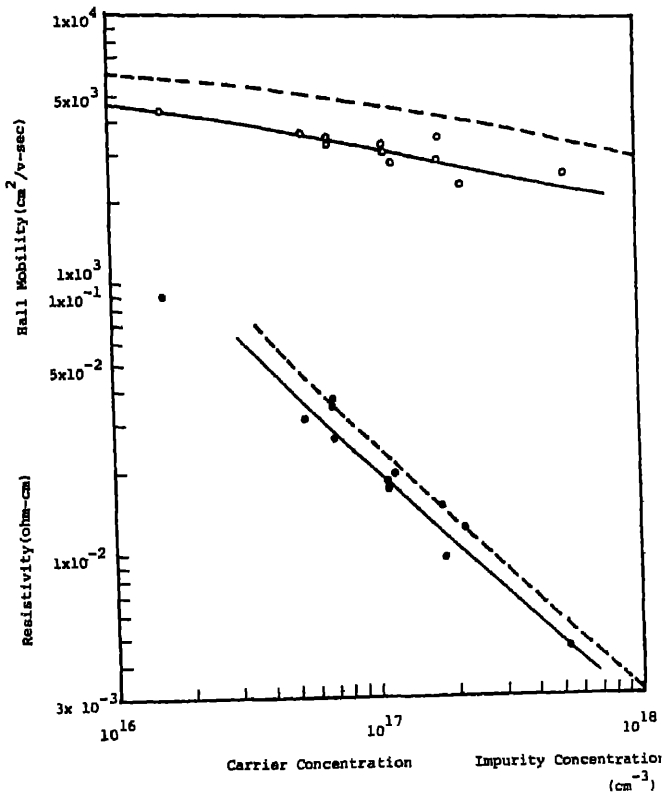


Figure 6. Dependence of resistivity and Hall mobility on carrier concentration (circles) and impurity concentration (dashed lines).

concentration is  $C_B = N_D + N_A$ , the carrier concentration is lower than impurity concentration. In our measurements the carrier concentration decreased with increasing growth temperature and  $\Delta T$ . It may be that the solution ahead of the advancing interface gets depleted of Si, as a result of the limited diffusion of Si for faster growth rate. Certainly, the As vacancy may increase with temperature, but its influence is much less than the depletion effect of Si about 700°C.

For the depletion effect of Si, the carrier concentration decreased with increasing  $\Delta T$  (figure 7). Hall mobility increased as  $\Delta T$  increased (figure 8). The inhibition of constitutional supercooling also helps in increasing the Hall mobility. The saturation of this curve may be due to the increasing domination of As vacancy. The same is the

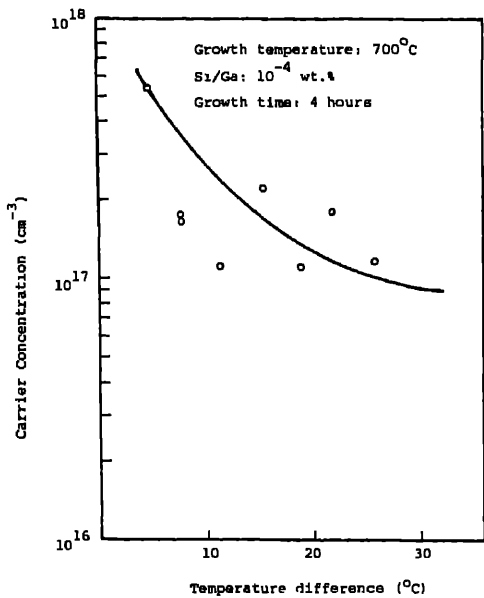


Figure 7. Dependence of carrier concentration on the temperature difference between source and substrate.

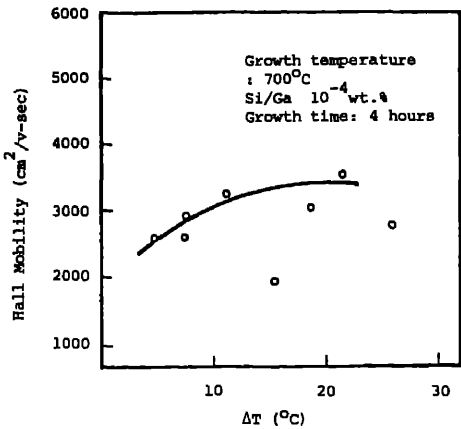


Figure 8. Dependence of Hall mobility on the temperature difference between source and substrate.



### *LPE growth of GaAs:Si*

reason for the changes of carrier concentration and Hall mobility followed by variation of growth temperature. From figures 9 and 10 similar results can be found. When the variation of growth time was used as a parameter, a minimum carrier concentration and a maximum Hall mobility were measured in the vicinity of growth (figures 11 and 12).

#### 3.3 Surface morphology

Figures 13(a) to 13(d) show some pictures of the surface grown at 700°C for different growth times. The temperature difference was 4.5, 11.2, 18.8 and 25.7°C respectively. On the scale

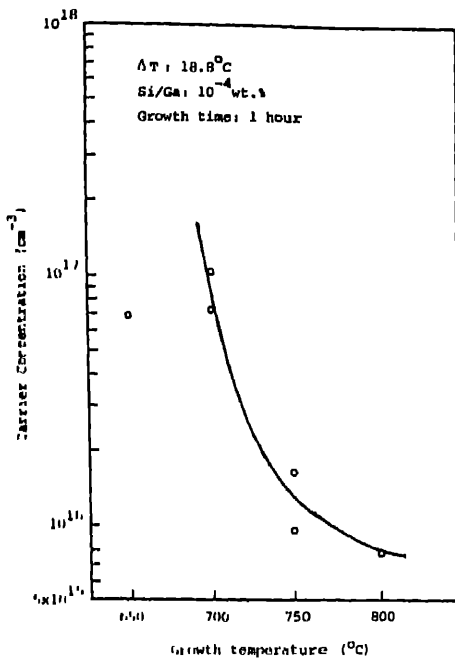


Figure 9. Dependence of carrier concentration on the growth temperature.

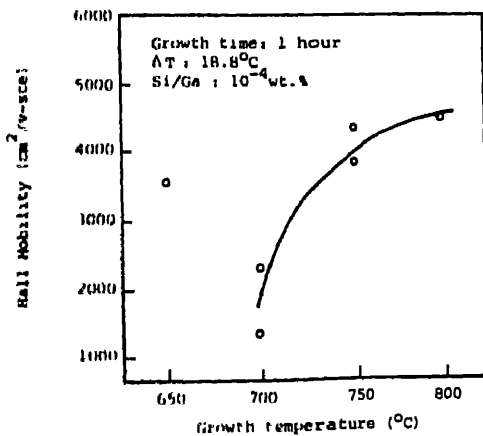


Figure 10. Dependence of Hall mobility on the growth temperature.

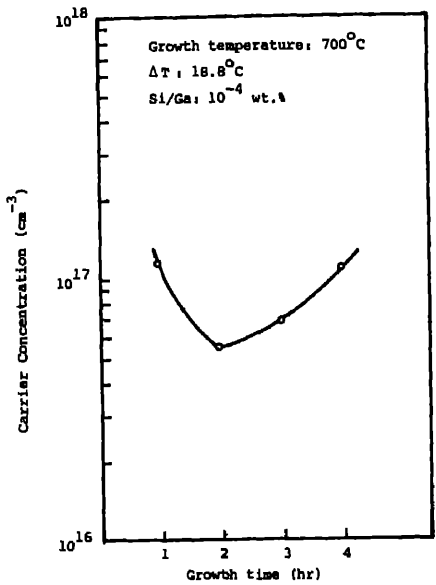


Figure 11. Dependence of carrier concentration on the growth time.

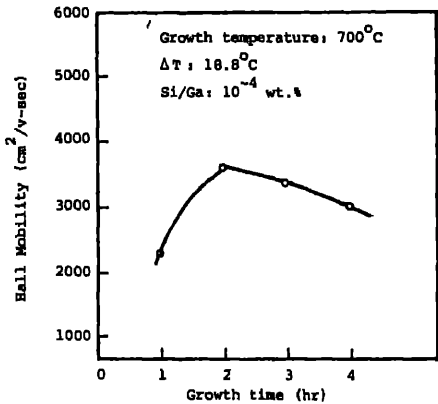


Figure 12. Dependence of Hall mobility on the growth time.

those photographs, the surface has a rough appearance although both to the eye and at higher magnifications the surface appeared smooth. Those photographs of high magnification are shown in figures 13(e) and 13(f) with temperature difference 4.5°C and 18.8°C. It is found that with higher  $\Delta T$ , the surface morphology is better because the constitutional supercooling is inhibited more for the higher  $\Delta T$ .

4. Conclusion

The LPE growth was studied using the temperature difference method. The epilayers with uniform doping were grown. The results show that the electric characteristics and the thickness of the epilayers strongly depend on the growth temperature and

*LPE growth of GaAs:Si*

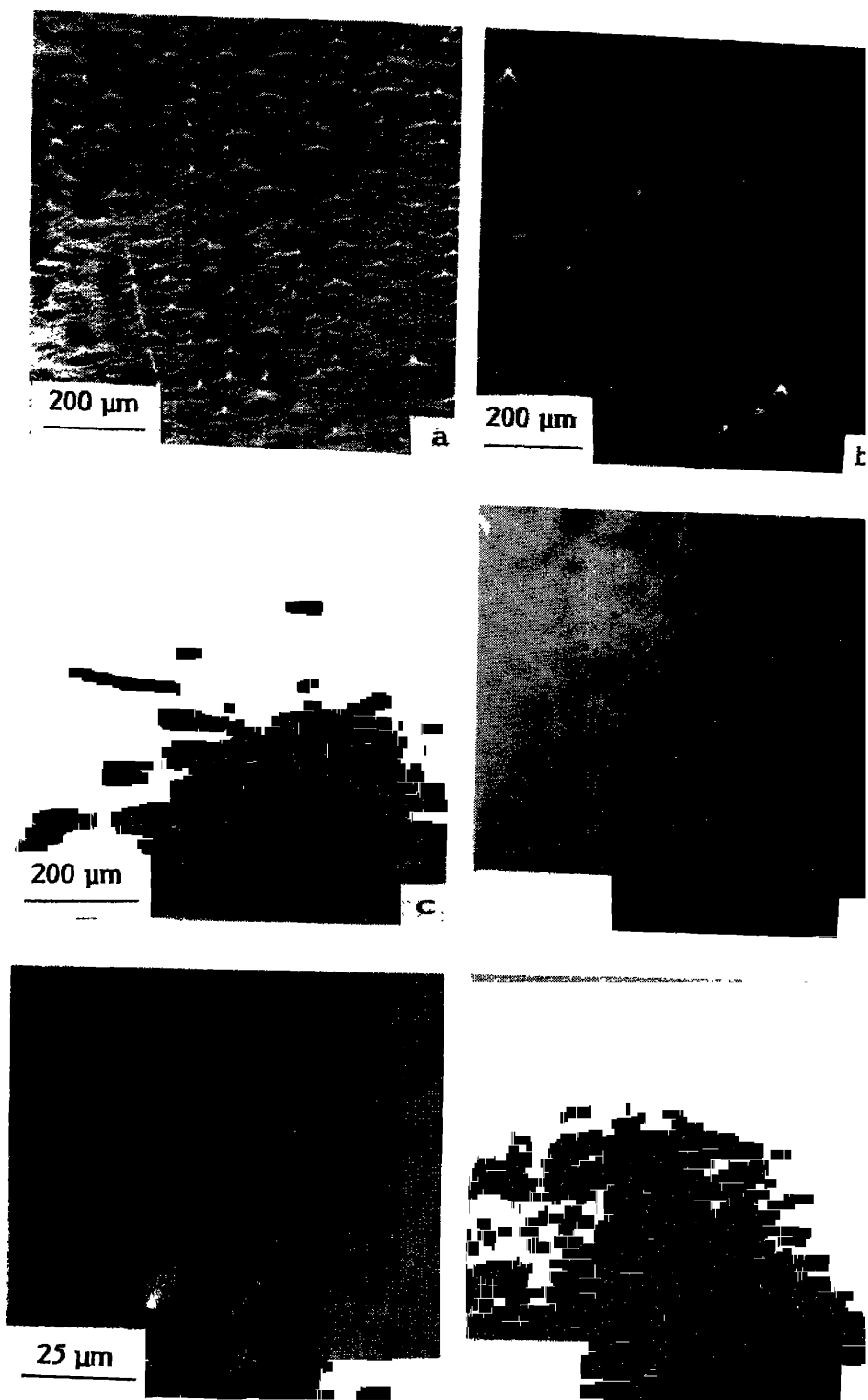


Figure 13. Photomicrographs of the substrate morphology  $T_0 = 700^\circ\text{C}$ ,  $W = 0.635$ ,  $t = 4$  hr, (a)  $\Delta T = 4.5^\circ\text{C}$ , (b)  $\Delta T = 11.2^\circ\text{C}$ , (c)  $\Delta T = 18.8^\circ\text{C}$ , (d)  $\Delta T = 25.7^\circ\text{C}$ , (e) high magnification.

temperature difference. With proper control, a perfect epilayer and multiple smooth layers can be obtained.

Even the thickness is limited by edge effects. However, the uniformity of thickness is well away from the edge. Therefore by utilizing a larger size of substrate epilayer better uniformity suitable for fabrication of devices can be obtained.

In general, diffusion limited model is consistent with this experiment. The growth rate can be controlled well. The stability of solid-liquid interface can be acquired at constant temperature of system, which can avoid the effect of constitutional supercooling.

As the solution ahead of the advancing interface becomes depleted of Si, the reducing carrier concentration can be obtained at higher growth rate. Due to this effect, it increases the complication of epilayer growth. Although the variation of vacancy influences the carrier concentration, depletion effect dominates the growth temperature about 700°C. With proper control, a perfect epilayer can be obtained.

## Acknowledgements

The authors gratefully acknowledge Dr T S Wu for his fruitful discussions and suggestions. The authors also thank National Science Council, Republic of China for financial support of this research project.

## References

- Casey Jr H C and Panish M B 1978 *Heterostructure lasers*, Part B (New York: Academic Press) p 1
- Hsieh J J 1980 *Handbook on semiconductors* (eds) T S Moss and S P Keller (Amsterdam, New York: Oxford: North-Holland) Vol. 2, p 418
- Long S I, Ballantyne J M and Eastman L F 1974 *J. Cryst. Growth* 26 13
- Nishizawa J and Okuno Y 1978 RIEC Technical Report TR-41, April
- Sze S M 1981 *Physics of semiconductor devices* (New York: John Wiley) pp 29-33
- Tiller W A 1968 *J. Cryst. Growth* 2 69

## X-ray diffraction study of epitaxial zinc and cadmium films prepared by hot-wall technique

A V KULKARNI and R PRATAP\*

D B J College, Chiplun 415 605, India

\*Department of Physics, University of Bombay, Vidyanagari, Bombay 400 098, India

MS received 12 May 1986

**Abstract.** Hot-wall technique greatly improves the quality of zinc and cadmium deposited on glass substrate. At substrate temperature the growth of such films is ordered, showing highly preferred orientation along *c*-axis. However, if the substrate temperature is increased beyond certain limit, we get polycrystalline growth of the films. This shows that the growth of zinc and cadmium films on glass substrate strongly depends on the substrate temperature.

**Keywords.** X-ray diffraction; epitaxial growth; hot-wall technique; zinc films; cadmium films.

### 1. Introduction

The conventional method of vacuum deposition of cadmium films does not give good quality homogeneous films deposited on glass substrate (Bandopadhyay and Pal 1979). We have already shown that, by using the hot-wall technique, good quality cadmium films consisting of large crystal domains with only [002] orientation, can be obtained (Kulkarni *et al* 1984). The present paper reports the effect of elevated substrate temperature on the epitaxial growth of zinc as well as cadmium films. The growth process is strongly influenced by the temperature as well as the nature of the substrate. Cadmium films deposited on NaCl (100) single crystal substrate show preferred orientations in [101], [102], [103] and [002] directions in decreasing order (Kulkarni *et al* 1984). The polycrystalline nature of the films deposited on glass substrate is due to the lattice mismatch and relative positioning of cadmium atoms (Chopra 1969). However, if an amorphous substrate like glass is used, the lattice mismatch plays a smaller role in the growth process. After initial deposition of atomic layers of the film, the auto-epitaxy plays an important role in further development of the film structure. Thus, we get ordered structure with highly preferred orientation. It is also observed that a vacuum of the order of  $10^{-5}$  torr is suitable for such growth.

### 2. Experimental

The apparatus used to deposit cadmium and zinc films was essentially the same as described earlier (Kulkarni *et al* 1984). The only modification was to replace the conical glass tube with quartz tube having larger dimensions (height 6.0 cm; outer diameter 2.9 cm; inner diameter 2.6 cm). Cadmium metal (purity 6N) (obtained from Koch-Light Laboratories, UK) and zinc metal (purity, 5N) (from Fluka A G, Buchs, Switzerland) were used as source material for depositing the films. The vacuum during deposition

was maintained at  $2 \times 10^{-5}$  torr. Cleaned glass substrates were used to deposit all the films. The thickness of the films was determined by gravimetric method and for the purpose a Mettler, M5, balance with sensitivity  $1 \mu\text{g}$  was used.

### 3. Results and Discussion

Visual observation showed that all the films deposited on the glass were continuous and shining like mirror at the back of the films, while the front surfaces had silvery-white shine. To understand the film structure, x-ray diffractometry was carried out using fully computerised, SIEMENS-RE 2400 diffractometer. During x-ray scanning, the sample was kept rotating at a constant speed of 30 rev/min about an axis perpendicular to its plane and passing through its centre. This gave an overall picture of the complete film structure.

Figure 1 shows the XRD patterns of cadmium and zinc films deposited by HWT at different substrate temperatures. Tables 1 and 2 give the relative intensities of the

**Table 1.** X-ray diffraction measurement on cadmium films prepared by HWT on glass substrate.

hkl	Relative intensity (%)		
	$70^\circ < T_s < 80^\circ\text{C}$	$100^\circ < T_s < 110^\circ\text{C}$	ASTM-data
002	100	100	65
100	—	2.5	32
101	—	32.2	100
102	—	12.4 ( $K\alpha_1$ )	32
102	—	6.7 ( $K\alpha_2$ )	—
103	—	15.4 ( $K\alpha_1$ )	26
103	—	8.3 ( $K\alpha_2$ )	—
004	9.4 ( $K\alpha_1$ )	23.5 ( $K\alpha_1$ )	3
004	5.0 ( $K\alpha_2$ )	12.3 ( $K\alpha_2$ )	—

\* $T_s$ , Substrate temperature.

**Table 2.** X-ray diffraction measurement on zinc films prepared by HWT on glass substrate.

hkl	Relative intensity (%)		
	$40^\circ < T_s < 50^\circ\text{C}$	$60^\circ < T_s < 70^\circ$	ASTM-data
002	100	100	53
100	0.4	0.7	40
101	0.2	1.9 ( $K\alpha_1$ )	100
101	—	1.1 ( $K\alpha_2$ )	—
102	—	2.6 ( $K\alpha_1$ )	28
102	—	1.6 ( $K\alpha_2$ )	—
103	0.1	4.1 ( $K\alpha_1$ )	25
103	—	2.2 ( $K\alpha_2$ )	—
110	—	0.2	21
004	9.4 ( $K\alpha_1$ )	17.6 ( $K\alpha_1$ )	2
004	4.7 ( $K\alpha_2$ )	10.2 ( $K\alpha_2$ )	—
112	—	0.7	23
200	—	0.2	5

# Study of zinc and cadmium films by hot-wall technique

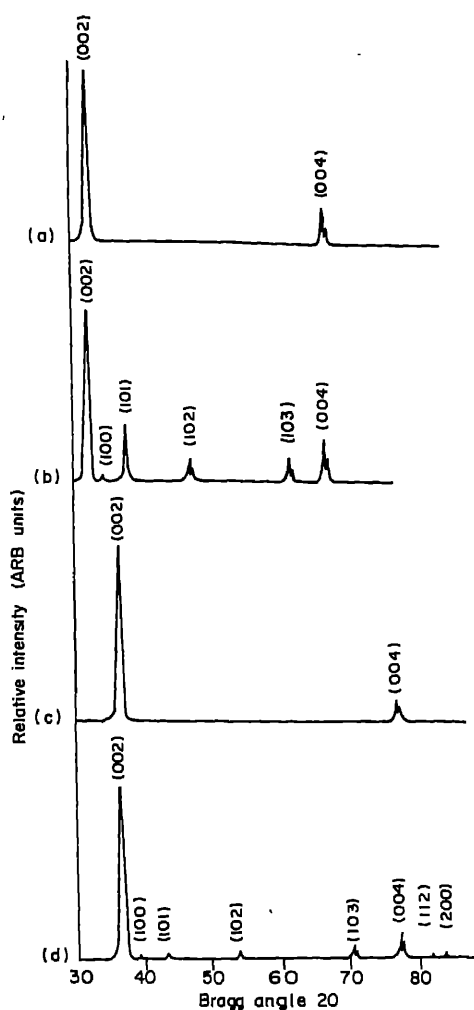


**Figure 1.** X-ray diffraction pattern (obtained with  $\text{CuK}\alpha$  radiation) for the films deposited onto glass substrate by HWT. (a) Cd film ( $70^\circ < T_s < 80^\circ\text{C}$ ); (b) Cd film ( $100^\circ < T_s < 110^\circ\text{C}$ ); (c) Zn film ( $40^\circ < T_s < 50^\circ\text{C}$ ); (d) Zn film ( $60^\circ < T_s < 70^\circ\text{C}$ ).  $T_s$  = substrate temperature.

peaks observed for cadmium and zinc films respectively. Figures 1a, c indicate the film structure is well ordered with perfect epitaxial growth along [002] direction. The diffraction pattern at elevated substrate temperature ( $100\text{--}110^\circ\text{C}$ ) clearly shows the appearance of Cd peaks corresponding to the planes (100), (101) and so on (figure 1b). This shows that cadmium films deposited at elevated temperature (approximately greater than one third of the melting point of the metal) are polycrystalline.

Similar trend is observed in zinc films deposited at higher substrate temperatures ( $60\text{--}70^\circ\text{C}$ ) (figure 1d), the newly appeared reflection peaks (showing polycrystalline nature of the film) have very low intensity. Such preferentially oriented growth of zinc films along [002] direction has also been reported in the thickness range  $500\text{--}5000\text{ \AA}$  (Nandi *et al* 1978). But the perfect epitaxial growth (figure 1c) in zinc films

**Table 3.** Deposition parameters of the films prepared by HWT

Film	Temperature (°C)			Thickness ( $\mu\text{m}$ )	Growth rate ( $\mu\text{m/hr}$ )
	Source	Wall	Substrate		
Cd	400–450	375–425	70–80	5.2	25
Cd	450–500	400–450	100–110	4.5	35
Zn	500–550	300–400	40–50	6.5	39
Zn	550–600	350–450	60–70	2.3	45

has been observed for the first time in thick films at the substrate temperature 40–50° C.

Table 3 gives the deposition parameters for cadmium and zinc films. The films are thick, the thickness being in the range 2 to 6  $\mu\text{m}$ . The rate of deposition is in the range of 25 to 45  $\mu\text{m/hr}$ . Single heating coil was used to heat the quartz tube and therefore, the source and wall temperatures could not be precisely defined. The glass substrate was radiation-heated from the same heating coil.

#### 4. Conclusion

By using hot-wall technique, thick zinc and cadmium films having perfect orientation can be deposited on glass substrate, keeping the substrate temperature sufficiently low (below one third of the melting point of the metal). We have also shown that such films usually consist of large crystallites ( $\sim 5 \mu\text{m}$ ) (Kulkarni *et al* 1984). Thus, this simple version of HWT is useful wherever highly epitaxial on (even thick) films of cadmium and zinc are required.

#### Acknowledgements

The diffractometer facility was provided by the Tata Institute of Fundamental Research, Bombay. One of us (AVK) gratefully acknowledge the fellowship awarded by the University Grants Commission, New Delhi. The authorities of DBJ College, Chiplun, were kind enough to grant AVK the necessary study leave to take up the fellowship.

#### References

- Bandopadhyay S K and Pal A K 1979 *J. Mater. Sci.* **14** 2989
- Chopra K L 1969 *Thin film phenomena* (New York: McGraw-Hill) 226
- Kulkarni A V, Bose S and Pratap R 1984 *Thin Solid Films* **120** L73–L77
- Nandi R K, Suchitra Sen and Sen-Gupta P 1978 *Thin Solid Films* **51** 141



## Concept of thermodynamic capacity

R AKILA\*†, K T JACOB\* and A K SHUKLA\*\*

\*Department of Metallurgy, \*†Materials Research Laboratory,

\*\*Solid State and Structural Chemistry Unit, Indian Institute of Science, Bangalore 560 012, India.

MS received 15 April 1986

**Abstract.** The thermodynamic capacity of a species ( $C_i$ ) in a homogeneous phase is defined as  $(\partial n_i / \partial \mu_i)_{P, T, n_j}$  where  $n_i$  is the total number of moles of  $i$  per unit quantity of the system, irrespective of the actual system chemistry and  $\mu_i$  is its chemical potential. Based on this definition, the thermodynamic capacity of oxygen in non-reactive and reactive gas mixtures and in binary and ternary liquid solutions has been computed. For reactive gas mixtures containing stable chemical species which do not undergo significant dissociation such as  $\text{CO} + \text{CO}_2$ ,  $\text{H}_2 + \text{H}_2\text{O}$  and  $\text{H}_2 + \text{CO}_2$ , the capacity curves show a maximum at equilibrium ratio and a minimum at higher oxygen potentials. If one of the chemical species dissociates as in the case of  $\text{H}_2\text{S}$  in  $\text{H}_2 + \text{H}_2\text{S}$  mixtures or  $\text{SO}_3$  in  $\text{SO}_2 + \text{SO}_3$  mixtures, capacity curves do not exhibit such maxima and minima, especially at high temperatures would be difficult to produce stable oxygen fugacities when the capacity has a low value, for example at compositions near the minimum. Oxygen capacities of non-ideal solutions,  $\text{Cu}-\text{O}$  and  $\text{Cu}-\text{O}-\text{Sn}$ , and heterogeneous systems formed at saturation with their respective oxides are discussed.

**Keywords.** Thermodynamic capacity; ideal gas mixture; reactive gas mixture; condensed phase.

### 1. Introduction

While the concept of thermodynamic potential is well established and widely used in chemical literature, the corresponding capacity function has not been discussed in the textbooks on thermodynamics (Prigogine and Defay 1954; Swalin 1972; Kottler 1979; Lupis 1983). As such, chemical potentials are appropriate to determine the direction of transport of a species or of a reaction in a chemical system. However, being an intensity factor, chemical potentials do not provide any information on the amount of species transported or on the extent of reaction, even in the absence of kinetic restrictions. A suitably defined capacity factor can be useful in quantifying the amount of a species that can be drawn from a chemical reservoir at a specified chemical potential. Consider, for example, the synthesis of a non-stoichiometric oxide or a Magneli phase at high temperatures by equilibrating the solid with a flowing gas of defined oxygen potential. As oxygen is being added or removed from the oxide, the oxygen potential of the gas phase will usually change. If an  $\text{Ar} + \text{O}_2$  mixture with  $p_{\text{O}_2} < 10^{-4}$  atm is used for controlling the stoichiometry, the change in oxygen potential of the gas accompanying a finite oxygen exchange with the solid will be very large. In other words, the gas phase is unable to supply or remove a significant amount of oxygen from the solid at a defined potential. The oxygen capacity of the  $\text{Ar} + \text{O}_2$  mixture may therefore be considered to be low at these low oxygen partial pressures. A gas mixture consisting of  $\text{CO} + \text{CO}_2$  or  $\text{H}_2 + \text{H}_2\text{O}$  will have higher capacity to supply or remove oxygen at low potentials. The purpose

this communication is to define thermodynamic capacity and to illustrate its variation for some typical systems. A potential application of the concept in high temperature material synthesis and solid state device research is projected.

## 2. Definition of thermodynamic capacity

Just as the electrical potential increases as electrons are put into a condenser, the chemical potential of a species increases in a homogeneous medium with the addition of that species. While the electrical potential rises linearly with charge, the chemical potential increases logarithmically with concentration for ideal or dilute solutions. The thermodynamic capacity of a species (*i*) in a homogeneous phase may be defined by the expression,

$$C_i = (\partial n_i / \partial \mu_i)_{P, T, n_{j|j \neq i}}, \quad (1)$$

where  $n_i$  is the total moles of *i* in any state of chemical combination per unit amount of the phase and  $\mu_i$  is the chemical potential of *i*. Thermodynamic capacity of species *i* may be visualized as the moles of *i* that is added or removed from a specified quantity of a homogeneous system when the chemical potential of *i* is given a unit increment or decrement.

It is interesting to explore the variation of thermodynamic capacity with composition for an ideal gas mixture ( $\text{Ar} + \text{O}_2$ ), reactive gas mixtures usually used in chemical synthesis ( $\text{CO} + \text{CO}_2$ ,  $\text{H}_2 + \text{H}_2\text{O}$ ,  $\text{SO}_2 + \text{SO}_3$ ,  $\text{H}_2 + \text{CO}_2$  and  $\text{H}_2 + \text{H}_2\text{S}$ ) and condensed phase solutions ( $\text{Cu}-\text{O}$  and  $\text{Cu}-\text{O}-\text{Sn}$ ). For simple mixtures, analytical expressions may be derived relating capacity and composition. However, in systems containing several complex species, numerical procedures are more convenient. In the numerical technique, one starts with a preset composition and computes the chemical potential of species *i*. The chemical potential is then incremented by a small amount and the new composition is computed. From the change in composition, the amount of the species added is calculated. The capacity

$$C_i = \Delta n_i / \Delta \mu_i.$$

## 3. Capacity of an ideal gas mixture

An example of a simple gas mixture is  $\text{Ar} + \text{O}_2$ . In the ideal gas approximation, chemical potential of oxygen in the mixture is given by

$$\mu_{\text{O}_2} = \mu_{\text{O}_2}^\circ + RT \ln p_{\text{O}_2}. \quad (2)$$

Implicit differentiation gives

$$d\mu_{\text{O}_2} = (RT/p_{\text{O}_2}) dp_{\text{O}_2}. \quad (3)$$

The partial pressure of oxygen is defined by

$$p_{\text{O}_2} = n_{\text{O}_2} / (n_{\text{O}_2} + n_{\text{Ar}}). \quad (4)$$

This on differentiation gives

$$dp_{\text{O}_2} = (p_{\text{Ar}}/n) dn_{\text{O}_2} = (p_{\text{Ar}} RT/PV) dn_{\text{O}_2}, \quad (5)$$

## Concept of thermodynamic capacity

where  $n = n_{O_2} + n_{Ar}$  is the total moles of oxygen plus argon in the gas and  $P$  total pressure. Combining (3) and (5), one gets

$$C_{O_2} = \frac{dn_{O_2}}{d\mu_{O_2}} = \frac{p_{O_2}PV}{(RT)^2 p_{Ar}} = \frac{p_{O_2}PV}{(RT)^2 (P - p_{O_2})} = \frac{p_{O_2}V}{(RT)^2 [1 - (p_{O_2}/P)]}$$

When  $p_{O_2} \ll P$ , the thermodynamic capacity of oxygen is proportional to the oxygen partial pressure. As  $p_{O_2}$  tends to  $P$ , the infinite capacity of pure oxygen is approached.

In the numerical procedure for the calculation of  $C_{O_2}$ , the relative chemical potential is computed for an initial mixture of  $n_{O_2}$  moles of  $O_2$  and  $n_{Ar}$  moles of argon using (4). The chemical potential is then changed by 100 or 1000 cal by addition or removal of oxygen. This changes the number of moles of oxygen in the system to  $\Delta n_{O_2}$ , which is given by

$$\Delta n_{O_2} = \frac{[p'_{O_2}(n_{Ar} + n_{O_2}) - n_{O_2}]}{(1 - p'_{O_2})},$$

where  $p'_{O_2}$  is the new oxygen partial pressure, corresponding to  $\mu'_{O_2}$ . The thermodynamic capacity is given by

$$C_{O_2} = \Delta n_{O_2} / (\mu'_{O_2} - \mu_{O_2}).$$

The calculations have been carried out per mole of the mixture. The variation of  $\log C_{O_2}$  with  $\log p_{O_2}$  is shown in figure 1 at 1 atm total pressure for different temperatures. Both analytical and numerical techniques give essentially the same result.

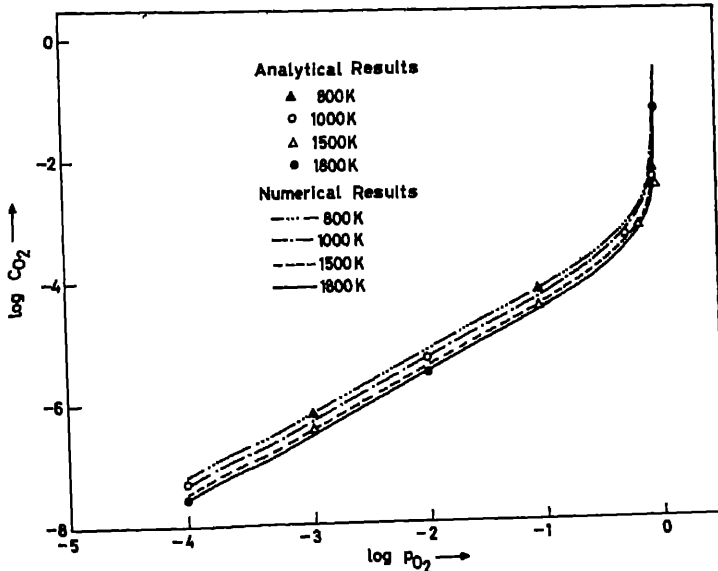


Figure 1. Variation of the thermodynamic capacity,  $C_{O_2}$ , with  $p_{O_2}$  in  $Ar + O_2$  gas mixture at different temperatures.

#### 4. Reactive gas mixtures containing stable species

##### 4.1 $\text{CO} + \text{CO}_2$ mixtures

In a  $\text{CO} + \text{CO}_2$  gas mixture, the system is buffered against changes in oxygen potential by the formation or dissociation of  $\text{CO}_2$  according to the reaction



The equilibrium constant  $K$  is given by

$$K = (p_{\text{CO}}/p_{\text{CO}_2})p_{\text{O}_2}^{1/2}. \quad (10)$$

Based on the approach similar to the one used for an  $\text{Ar} + \text{O}_2$  mixture, the thermodynamic capacity of oxygen,  $\text{C}_{\text{O}_2}$ , at a given oxygen partial pressure  $p_{\text{O}_2}$  can be approximated by

$$\text{C}_{\text{O}_2} = \frac{V}{(RT)^2} \left[ p_{\text{O}_2} + \frac{P(p_{\text{O}_2}/K^2)^{1/2}}{4[1 + (p_{\text{O}_2}/K^2)^{1/2}]^2} \right] \frac{1}{(1 - p_{\text{O}_2}/P)}. \quad (11)$$

At  $p_{\text{O}_2} \simeq K^2$  or a  $p_{\text{CO}}/p_{\text{CO}_2}$  ratio equal to unity,  $\text{C}_{\text{O}_2}$  is a maximum. A minimum in capacity is observed at a value of  $p_{\text{O}_2}$  given by

$$p_{\text{O}_2} \simeq \frac{1}{4}(P^{2/3} K^{2/3}), \quad (12)$$

or

$$\frac{p_{\text{CO}_2}}{p_{\text{CO}}} \simeq \frac{1}{4}(P^{1/3} K^{-2/3}). \quad (13)$$

In the numerical technique, we consider a starting gaseous mixture of carbon dioxide, carbon monoxide and oxygen with initial number of moles of the species being  $n_{\text{CO}_2}$ ,  $n_{\text{CO}}$  and  $n_{\text{O}_2}$  respectively. The equilibrium composition at a given temperature may be reached by the decomposition of a certain amount of  $\text{CO}_2$ , say  $\alpha$ , according to the reaction (9). Each of the partial pressures in (10) may be expressed in terms of mole fractions of the particular species. For example

$$p_{\text{CO}_2} = \frac{n_{\text{CO}_2} - \alpha}{n_{\text{CO}_2} + n_{\text{CO}} + n_{\text{O}_2} + \alpha/2}. \quad (14)$$

Substituting for the partial pressures in (10), the value of  $\alpha$  is given by the solution of the equation

$$\alpha^3(1 - K^2)/2 + \alpha^2(1 - K^2)(n_{\text{O}_2} + n_{\text{CO}}) + \alpha[K^2 n_{\text{CO}_2}(3/2 n_{\text{CO}_2} + 2n_{\text{CO}} + 2n_{\text{O}_2}) + n_{\text{CO}}(n_{\text{CO}}/2 + 2n_{\text{O}_2})] - [K^2 n_{\text{CO}_2}^2(n_{\text{CO}_2} + n_{\text{CO}} + n_{\text{O}_2}) - n_{\text{CO}}^2 n_{\text{O}_2}] = 0. \quad (15)$$

Let  $\Delta n_{\text{O}_2}$  be the change in total number of moles of oxygen corresponding to a change in chemical potential by 1000 calories. Equilibrium is reached by the formation of  $x$  additional moles of  $\text{CO}_2$ . The new values of the partial pressures are represented as  $p'_{\text{CO}_2}$ ,  $p'_{\text{CO}}$  and  $p'_{\text{O}_2}$ . The values of  $x$  and  $\Delta n_{\text{O}_2}$  are then given by the expressions

$$x = (n_{\text{CO}} + \alpha) - \frac{p'_{\text{CO}}(n_{\text{CO}_2} + n_{\text{CO}})}{(1 - p'_{\text{O}_2})} \quad (16)$$

and

$$\Delta n'_{O_2} = \left( \frac{n_{CO}}{2} - n_{O_2} \right) - \frac{(n_{CO_2} + n_{CO})(p'_{CO} - 2p'_{O_2})}{2(1 - p'_{O_2})}$$

Hence

$$C_{O_2} = \Delta n'_{O_2} / \Delta \mu_{O_2}$$

Two separate cases of  $CO + CO_2 + O_2$  mixtures can be considered. In the first the equilibrium  $O_2$  concentration is generated solely by the dissociation of  $CO_2$   $CO + CO_2$  mixture. For this case, initial oxygen  $n_{O_2} = 0$ . In the second case equilibrium  $CO$  is generated by dissociation of  $CO_2$  in a  $CO_2 + O_2$  mixture therefore  $n_{CO} = 0$ .

Case 1: When  $n_{O_2} = 0$ , the expressions (15) and (17) reduce to

$$\alpha^3(1 - K^2)/2 + \alpha^2 n_{CO}(1 - K^2) + \alpha[(3/2)K^2 n_{CO_2}^2 + 2K^2 n_{CO_2} n_{CO} + n_{CO}^2/2] - K^2 n_{CO_2}^2 (n_{CO_2} + n_{CO}) = 0,$$

$$\Delta n_{O_2} = \frac{n_{CO}}{2} - \frac{(n_{CO_2} + n_{CO})(p'_{CO} - 2p'_{O_2})}{2(1 - p'_{O_2})}$$

When  $n_{CO}$  is large,  $p'_{CO}$  is also large, therefore  $\Delta n'_{O_2}$  is small. As  $n_{CO}$  decreases  $p'_{CO}$  also decreases. However,  $\Delta n'_{O_2}$  increases with decreasing  $n_{CO}$ . As the  $n_{CO_2}/n_{CO}$  approaches unity, the value of  $\Delta n'_{O_2}$  and hence the thermodynamic capacity increases. A maximum value is obtained at a ratio of one. With increasing value of the  $n_{CO_2}/n_{CO}$  ratio, capacity decreases and passes through a minimum. It is difficult to control oxygen potential near the minimum in capacity. Other systems should be considered if it is necessary to control oxygen potential in this range.

Case 2: When  $n_{CO} = 0$ , i.e. at very high oxygen potentials, decomposition of  $C$  alone cannot account for the free oxygen in the system. The starting mixture will therefore have  $CO_2$  and  $O_2$  as the initial species, the  $CO$  content at equilibrium being set up by dissociation of  $CO_2$ . Then  $\alpha$  and  $\Delta n'_{O_2}$  are given by the solution:

$$\alpha^3(1 - K^2)/2 + \alpha^2(1 - K^2)n_{O_2} + \alpha[(3/2)K^2 n_{CO_2}^2 + 2K^2 n_{CO_2} n_{O_2}] - K^2 n_{CO_2}^2 (n_{CO_2} + n_{O_2}) = 0$$

and

$$\Delta n'_{O_2} = \frac{(2p'_{O_2} - p'_{CO})n_{CO_2}}{2(1 - p'_{O_2})} - n_{O_2}$$

respectively. As  $n_{O_2}$  and  $p'_{O_2}$  increase, the thermodynamic capacity of oxygen increases. For pure oxygen, the capacity will be infinite.

Figure 2 gives the thermodynamic capacity of oxygen as a function of equilibrium  $n_{CO_2}/n_{CO}$  ratio per mole of gas mixture. The equilibrium constants were taken from the JANAF tables (Stull and Prophet 1971). The values given by analytic expression (11) and the numerical technique match well. The plot shows a peak at a 1:1 ratio, where the system is buffered well against changes in oxygen potential. At higher oxygen potentials, the capacity coincides with that of  $Ar + O_2$  mixture as shown in figure 3. The capacity values at 1500 K are tabulated for various input compositions in table 1.

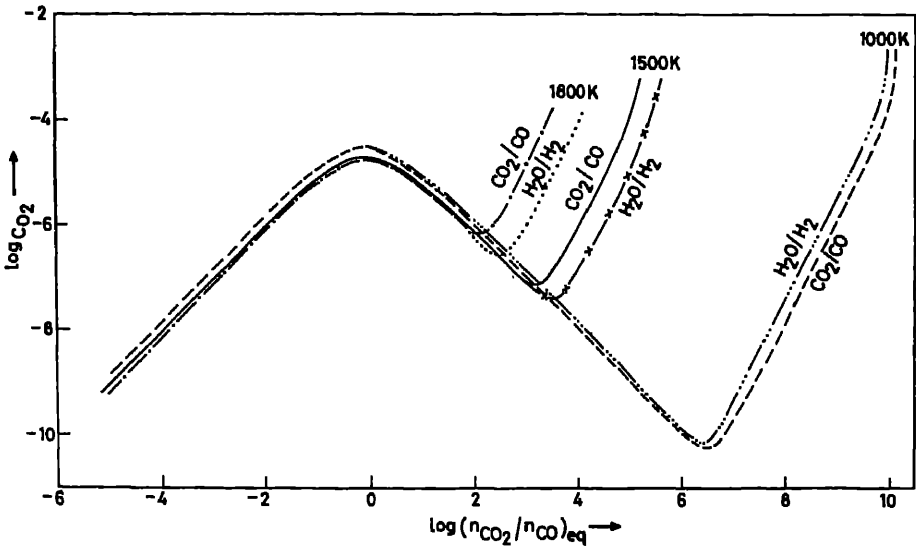


Figure 2. Variation of  $C_{O_2}$  with the equilibrium  $n_{CO_2}/n_{CO}$  or  $n_{H_2O}/n_{H_2}$  ratios at various temperatures.

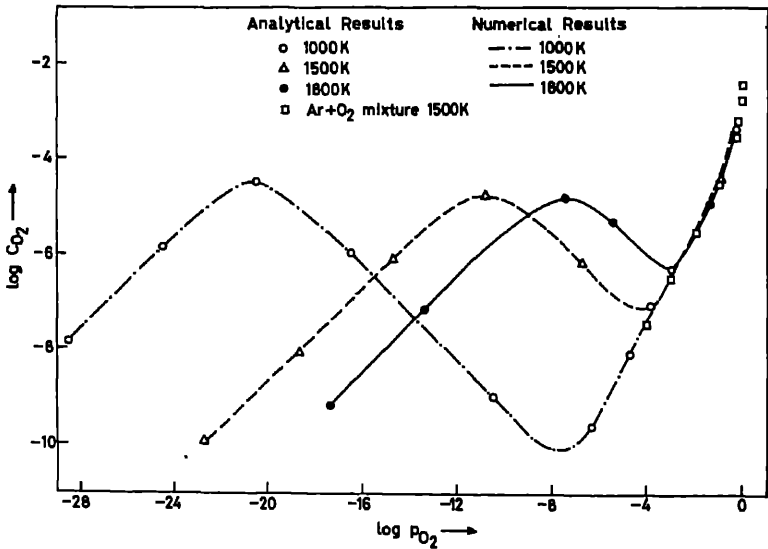


Figure 3. Variation of  $C_{O_2}$  as a function of  $\log p_{O_2}$  in a  $CO + CO_2$  gas mixture at various temperatures.

4.2  $H_2 + H_2O$  mixtures

The procedure for calculating  $C_{O_2}$  is similar to that for a  $CO + CO_2$  gas mixture. As seen in figure 2, the small differences in the values of the equilibrium constants for the dissociation reactions in the two gas mixtures give rise to significant differences in the values of  $C_{O_2}$  only at higher oxygen potentials.

## Concept of thermodynamic capacity

**Table 1.** Values of thermodynamic capacity of oxygen in a  $\text{CO} + \text{CO}_2$  mixture for defined values of the equilibrium ratio  $n_{\text{CO}_2}/n_{\text{CO}}$  in the input mixture at 1500 K, obtained by the numerical technique.

$n_{\text{CO}_2}/n_{\text{CO}}$	$p_{\text{O}_2}$ atm	$\text{C}_{\text{O}_2}$ moles/cal
$10^{-7}$	$2.13 \times 10^{-25}$	$1.19 \times 10^{-10}$
$10^{-5}$	$2.13 \times 10^{-21}$	$8.94 \times 10^{-10}$
$10^{-3}$	$2.13 \times 10^{-17}$	$9.15 \times 10^{-8}$
$10^{-1}$	$2.13 \times 10^{-13}$	$7.45 \times 10^{-6}$
1	$2.13 \times 10^{-11}$	$2.10 \times 10^{-5}$
10	$2.13 \times 10^{-9}$	$6.49 \times 10^{-6}$
$2.59 \times 10^3$	$1.43 \times 10^{-4}$	$8.72 \times 10^{-8}$
$2.16 \times 10^4$	$9.92 \times 10^{-3}$	$4.03 \times 10^{-6}$
$6.53 \times 10^4$	$9.09 \times 10^{-2}$	$4.17 \times 10^{-5}$
$1.53 \times 10^5$	0.5	$6.68 \times 10^{-4}$

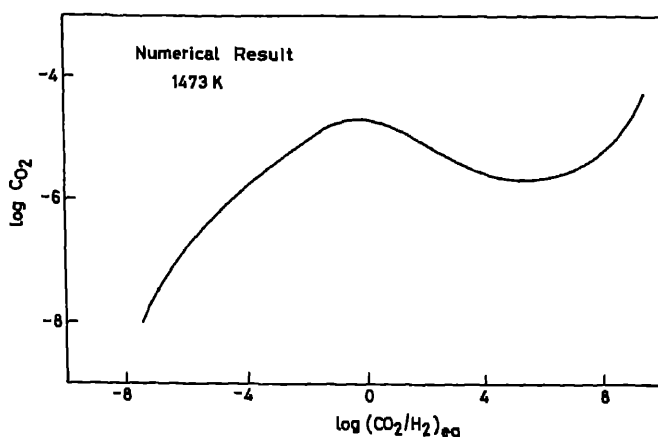


**Figure 4.** Dependence of  $\text{C}_{\text{O}_2}$  on  $n_{\text{CO}_2}/n_{\text{H}_2}$  at 1473 K.

### 4.3 $\text{H}_2 + \text{CO}_2$ mixtures

The equilibrium gas composition at 1473 K was calculated considering the species  $\text{CO}_2$ ,  $\text{CO}$ ,  $\text{H}_2\text{O}$ ,  $\text{H}_2$  and  $\text{CH}_4$ , using the SOLGAS program (Eriksson 1971). The oxygen capacity was then computed using the numerical procedure. As seen in figure 4, a peak is seen at a ratio of  $n_{\text{CO}_2}/n_{\text{H}_2}$  equal to unity, at which the equilibrium  $n_{\text{CO}_2}/n_{\text{CO}}$  and  $n_{\text{H}_2\text{O}}/n_{\text{H}_2}$  values are also close to one. The trend is similar to that of other reactive gas mixtures.

## 5. Reactive gas mixtures containing unstable species

### 5.1 $\text{SO}_2 + \text{SO}_3$ mixtures

The equilibrium constant for the decomposition of  $\text{SO}_3$  is large even at a temperature of 1000 K. Figure 5 gives the  $\text{C}_{\text{O}_2}$  values in an  $\text{SO}_2 + \text{SO}_3$  mixture

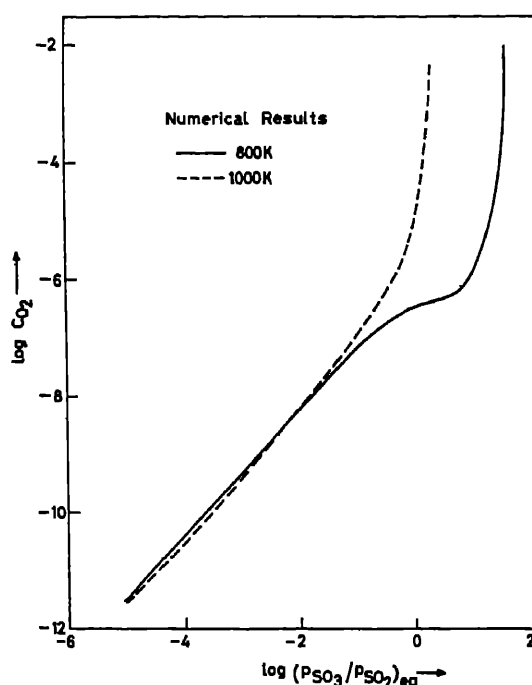


Figure 5. Variation of  $C_{O_2}$  with equilibrium  $n_{SO_3}/n_{SO_2}$  in an  $SO_2 + SO_3$  gas mixture at 800 K and 1000 K.

function of the equilibrium  $n_{SO_3}/n_{SO_2}$  ratio. No peak is observed even at 1000 K and it is not clearly defined at 800 K. For identical ratios of  $n_{SO_3}/n_{SO_2}$  and  $n_{CO_2}/n_{CO}$  at a given temperature, the thermodynamic capacity of oxygen in an  $SO_2 + SO_3$  mixture is lower.

## 5.2 $H_2 + H_2S$ mixtures

The thermodynamic capacity of sulphur  $C_{S_2}$  in a  $H_2 + H_2S$  gas mixture at temperatures of 800, 1000, 1500 and 1800 K has been calculated on similar lines. The peak again occurs at a ratio of unity as seen in figure 6. At higher temperatures where  $H_2S$  is unstable, no peak is seen and the capacity continuously increases.

## 6. Condensed phase calculations

In the copper-oxygen system, when oxygen is added to molten copper, its chemical potential rises. However, more oxygen is required at higher potentials to produce a given rise and the capacity increases with increasing oxygen content. While the mathematical equation referring to this curve has no upper limit, there are very real chemical limits. When the oxygen potential exceeds  $-32,860$  cal at 1373 K,  $Cu_2O$  will precipitate as a separate phase. Attempts to increase the oxygen content of molten copper will result in the formation of  $Cu_2O$ , which is equivalent to a "leak" at



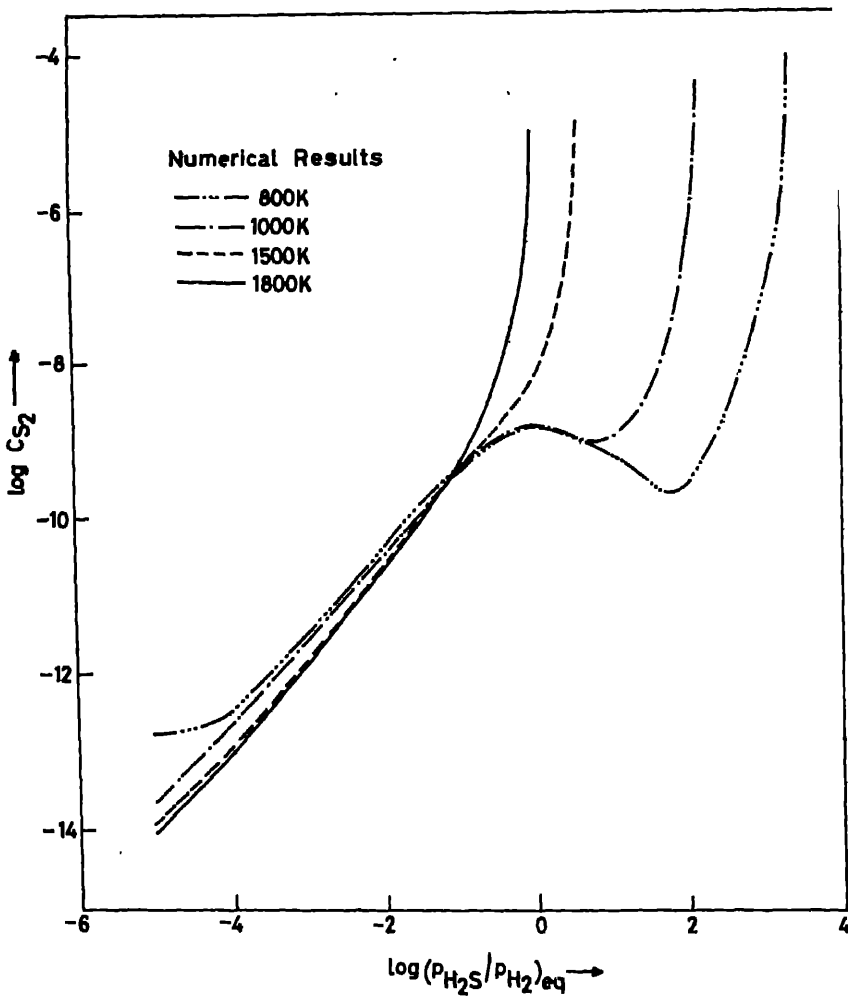


Figure 6. Thermodynamic capacity of sulphur in an  $H_2 + H_2S$  gas mixture at different temperatures.

this level into another phase with unlimited capacity. The whole copper can oxidized at this potential.

Similarly, if copper contained dissolved tin, it would not be possible to raise the oxygen potential above the value corresponding to the formation of  $SnO_2$ . The oxygen potential for the formation of  $SnO_2$  will be a function of the tin concentration. Here, the leak is to another oxide  $SnO_2$ . As the tin concentration decreases due to the formation of  $SnO_2$  the permissible oxygen potential in the metal goes up. Since the oxygen potential does not remain constant during the formation of  $SnO_2$ , the capacity does not go to infinity as in the Cu-O system, but increases a very large value at the saturation solubility limit for oxygen at the given tin concentration.

6.1 *Molten Cu-O system*

Dissolution of oxygen in molten copper may be represented by the reaction



where  $\Delta G^\circ$ , the free energy change associated with the above reaction is given by (Jacob and Jeffes 1971)

$$\Delta G^\circ = RT \left( \frac{\ln(\% \text{O} f_{\text{O}}^\circ)}{p_{\text{O}_2}^{1/2}} \right) = -20,542 + 1.723 T \text{ cal/g.at.} \quad (24)$$

The standard state for dissolved oxygen is chosen such that  $a_{\text{O}} = \text{atom \% O as atom \% O} \rightarrow 0$ . The variation of the Henrian activity coefficient of oxygen with concentration at 1373 K is given by

$$\log f_{\text{O}}^\circ = -0.042 \text{ (at \% O)} \quad (25)$$

Differentiating (24) with respect to the change in number of moles of oxygen,  $dn_{\text{O}_2}$ , the thermodynamic capacity,  $C_{\text{O}_2}$ , is given by the expression

$$C_{\text{O}_2} = \frac{dn_{\text{O}_2}}{d\mu_{\text{O}_2}} = \frac{X_{\text{O}_2}}{2RT(1 + 2\varepsilon_{\text{O}}^\circ X_{\text{O}_2})}, \quad (26)$$

where  $X_{\text{O}_2}$  is the oxygen content in molten copper expressed as a mole fraction of  $\text{O}_2$  and  $\varepsilon_{\text{O}}^\circ$  is the self interaction parameter,  $(\partial \ln f_{\text{O}} / \partial X_{\text{O}})_{X_{\text{O}} \rightarrow 0}$ .

In the numerical technique, the equilibrium constant  $K$  for (23) given by

$$K = a_{\text{O}} / p_{\text{O}_2}^{1/2} \quad (27)$$

was used to calculate the oxygen partial pressure in equilibrium with a given amount of dissolved oxygen in molten copper. The chemical potential of oxygen was then incremented by 100 cal and the new oxygen content computed. The analytic and numerical results agree well. The saturation solubility limit for oxygen corresponding to the formation of  $\text{Cu}_2\text{O}$  at 1373 K is 2.4 atom % O. As seen from figure 7, the

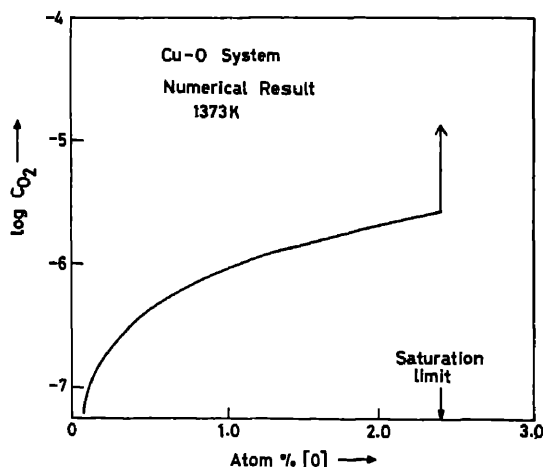


Figure 7.  $C_{\text{O}_2}$  as a function of dissolved oxygen in molten copper at 1373 K.

## Concept of thermodynamic capacity

thermodynamic capacity,  $C_{O_2}$ , plotted as a function of dissolved oxygen in , expressed in atom % becomes infinite at the saturation value. The phase  $n$   $Cu-O+Cu_2O$  provides a composition invariant buffer for oxygen.

### 6.2 Molten Cu-O-Sn system

The calculations were done at 1373 K for various alloy compositions in the 1-14 atom % Sn. The interaction parameter  $\epsilon_O^{Sn}$  is (Jacob *et al* 1970)

$$\epsilon_O^{Sn} = \left( \frac{\partial \ln f_O}{\partial X_{Sn}} \right)_{X_{Sn}, X_O \rightarrow 0} = -4.6.$$

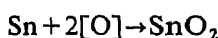
The corresponding expression for  $\log f_O$  is

$$\log f_O = -0.042 (\text{atom \% O}) - \frac{4.6}{2.303} X_{Sn}.$$

The activity coefficient of tin in molten copper is given by (Jacob *et al* 1970)

$$\log \gamma_{Sn} = (-1.38 + 3.333 X_{Sn}) X_{Cu}^2$$

Combining (24) with the free energy of formation of  $SnO_2$ , the free energy change of the reaction



is

$$\Delta G^\circ = -98,566 + 47.174 T \text{ cal/mol}$$

The upper limit to the oxygen activity corresponding to saturation can be calculated. The capacity values for various oxygen contents upto the saturation were computed by the numerical technique. At saturation, the formation of  $SnO_2$  provides an additional sink for oxygen. The analytic expression for oxygen capacity in saturated solutions of Cu-Sn is obtained as shown below:

$$\begin{aligned} \frac{d\mu_{O_2}}{dX_{Sn}} &= \frac{d}{dX_{Sn}} (\ln X_{Sn} \gamma_{Sn}) \\ &= -\frac{RT}{X_{Sn}} - RT \left( \frac{d \ln \gamma_{Sn}}{dX_{Sn}} \right). \end{aligned}$$

$$\text{Now } dX_{Sn} = -dX_{SnO_2} = -dn_{O_2}.$$

Hence

$$C_{O_2} = \frac{dn_{O_2}}{d\mu_{O_2}} = \frac{X_{Sn}}{RT\{1 + 2.303 X_{Sn}(1 - X_{Sn})(2.76 + 3.333[1 - 3X_{Sn}])\}}$$

At saturation the rise in capacity is by 2-3 orders of magnitude as shown in fig . The capacity of the two-phase mixture of  $SnO_2$  and the homogeneous solution is larger than that of the single phase alloy. The saturation oxygen concentration in the ternary alloy increases as the tin concentration decreases. The oxygen capacity therefore does not go to infinity at saturation. As the tin concentration in the alloy

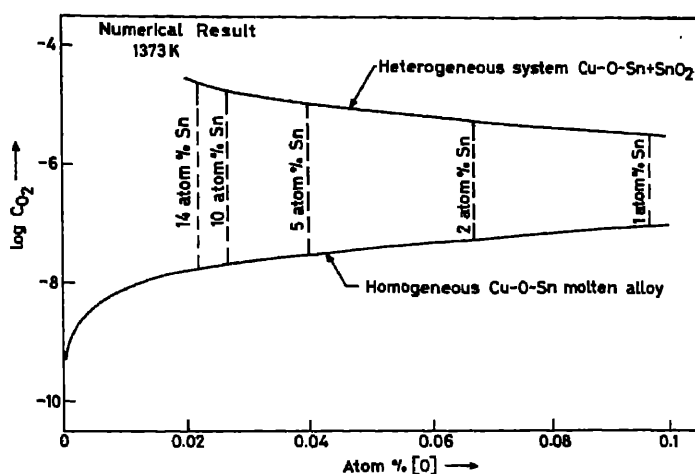


Figure 8. Variation of  $C_{O_2}$  with the concentration of dissolved oxygen in Cu-Sn alloy different compositions at 1373 K.

depleted by the formation of  $SnO_2$ , the thermodynamic capacity of oxygen va along the upper curve corresponding to the two-phase mixture. This exan illustrates a composition variant two phase buffer.

## 7. Applications

In the preparation of inorganic solids of controlled compositions, the samples often equilibrated with a gas phase of controlled chemical potential. If thermodynamic capacity of the gas is low, then a large volume of the gas is requi unless the amount of oxygen to be exchanged is small. Similarly, when using mixtures containing molecules that differ considerably in molecular weights, a  $H_2 + H_2S$  mixtures, the flow rate must be kept high to minimize thermal segregat The experiments using large volumes of high purity gases are inherently expens Sometimes disposal of large volumes of toxic gases can also be problematic solution to the problem is to use a recirculating system which provides regeneration of the gas to the required composition. Solid state sensors can be pla in the recirculating stream to ensure that the composition is maintained at pr values. In gas mixtures, for the control of oxygen potential, injection or withdra of oxygen from the stream can be accomplished by an electrochemical oxygen pu Coulometric oxygen pumps depend on Faraday's law relating current to oxygen and are based on solid electrolytes with mobile oxygen ions. In principle the pum similar to a sensor. The sensor operates in open circuit mode while the pu operates in the non-zero current mode. The current through the oxygen pump can regulated by the emf feedback from the solid state sensor. The feedback amplific may be automated. It can be shown that the correct value of the pump curren related to the thermodynamic capacity of oxygen in the gas

$$I = \frac{4Fn_V}{1 - t_e} \int_{\mu_{O_2}}^{\mu_{O_2}^0} \frac{C_{O_2}}{V} d\mu_{O_2}$$

## *Concept of thermodynamic capacity*

where  $n_V$  is the volume flow rate of the gas,  $\mu'_{O_2}$  and  $\mu''_{O_2}$  are the actual and chemical potentials of oxygen in the gas,  $\bar{t}_e$  is the average electronic transfer number of the solid electrolyte and  $C_{O_2}/V$  is the oxygen capacity of the gas per volume. The pumping current is a highly nonlinear function of oxygen pressure.

## **8. Conclusion**

A new thermodynamic variable, thermodynamic capacity, which is a measure of the ability of a chemical system to exchange a species without a change in its chemical potential, has been proposed. The variation of thermodynamic capacity for ideal and non-ideal solutions and systems with strong and weak compounds have been computed using analytical and numerical techniques. The capacities in two-phase and heterogeneous systems are illustrated using  $Cu-O + Cu_2O$  and  $Cu-O-Sn + SnO$  as examples. Multiphase systems can be devised that have higher thermodynamic capacity than homogeneous phases. The concept of thermodynamic capacity is useful in high temperature chemical vapour transport and solid state devices incorporating electrochemical pumps.

## **References**

- Eriksson G 1971 *Acta Chem. Scand.* **25** 2651  
Jacob K T and Jeffes J H E 1971 *Trans. Inst. Min. Metall.* **C80** 32  
Jacob K T, Seshadri S K and Richardson F D 1970 *Trans. Inst. Min. Metall.* **C79** 274  
Kestin J 1979 *A course in thermodynamics* (Washington: McGraw Hill) Vols 1 and 2  
Lupis C H P 1983 *Chemical thermodynamics of materials* (New York: North Holland)  
Prigogine I and Defay R 1954 *Chemical thermodynamics* (London: Longmans, Green and Co.)  
Stull D R and Prophet H 1971 *JANAF thermochemical tables*, 2nd ed. NSRDS-NBS37, U.S. Department of Commerce, Washington D C  
Swalin R A 1972 *Thermodynamics of solids* (New York: John Wiley)



## Growth of low dislocation density single crystals of nickel

S K KHANNA and K GOVINDA RAJAN

Materials Science Laboratory, Indira Gandhi Centre for Atomic Research, Kalpa  
603 102, India

MS received 16 January 1986; revised 24 April 1986

**Abstract.** Low dislocation density single crystals of nickel have been grown at ambient pressure by the Czochralski method. X-ray Laue picture shows that the crystals are strain-free. The dislocation density was determined to be  $<10^3/\text{cm}^2$  by the etch procedure. It was found that the necking and cone regions are very critical in the dislocation introduction in the crystals. An increase in the ambient pressure used during the growth seems to aid the crystal quality.

**Keywords.** Nickel crystals; high pressure growth; Czochralski technique.

### 1. Introduction

The physical properties of the crystalline materials are sensitive to the presence of lattice imperfections such as dislocations which may be present in the as-grown crystals. A significant contribution was made by Dash (1958) who discovered the method of eliminating dislocations in the melt-grown crystals. A thin neck was grown on top of the growing crystal by employing large pulling rates. The defects in the neck grow out to the nearby surface. Moreover, only a very small number of dislocation lines are allowed from the seed crystal. Dash's technique is particularly suitable for growing nearly perfect single crystals of metals where the necking procedure will ensure a sufficiently small temperature gradient in the middle body of the crystal. We have employed this procedure to grow low dislocation density single crystals of nickel. The other objective of the present work has been to study the influence of higher ambient pressure on the quality of the crystal.

### 2. Experimental details

We have employed the Czochralski technique for the growth of single crystals where the crystal cools in an unconstrained manner thus making it possible to produce low dislocation density crystals. Moreover, the necking procedure can be employed, and the shape of the growing crystal can be controlled to a considerable extent. Details of the main equipment used for the Czochralski growth have been described elsewhere (Khanna *et al* 1986). The initial charge in the form of pellets (99.99% pure nickel) was placed in an alumina crucible which was completely supported by a graphite container. A 99.99% pure nickel wire was used for the seed. The system was filled with high purity argon to a pressure of 6 bars. The seed crystal was carefully wetted in the melt before initiating the crystal pulling. The seed crystal and the crucible were rotated in the opposite direction at 10 rpm. This was done to interface the molten mass and to ensure a constant circumferential temperature. A thin neck of 0.4 mm was grown on the top of the crystal. The diameter was controlled only

continuously monitoring the melt temperature, and the pulling speed during the growth was maintained at a constant level of 0.2 mm/min. This way it was ensured that there were no sudden mechanical shocks given to the solid-liquid interface. The pulling speed  $v_p$  does not coincide with the growth rate  $V$ . As the crystal grows, the melt level lowers. The two rates are related to each other by the following relation (Paorici 1982)

$$V = \frac{V_p}{1 - [(\rho_s/\rho_L) (d_s/d_L)^2]}$$

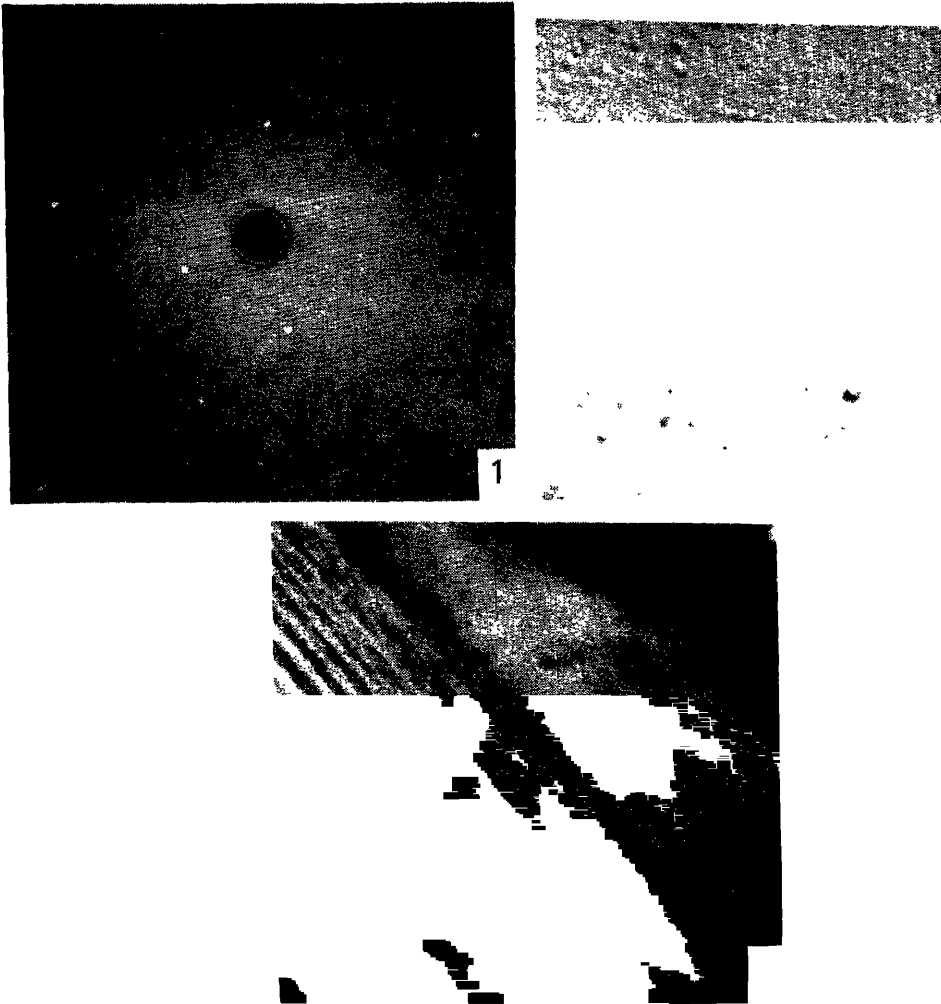
where  $d_s$ ,  $d_L$  are diameters of the growing crystal and the melt in the crucible,  $\rho_s$  and  $\rho_L$  are the densities of nickel in solid and liquid phases. The crucible lift rate was fixed at 0.02 mm/min. On completion of the growth the crystal was cooled down very slowly at 10°C/min to avoid dislocation generation due to thermal gradients.

### 3. Results and discussion

By using high pressure Czochralski technique we have grown single crystals of nickel (6 mm diameter and 25 mm long). Single crystallinity was examined by exposing the crystal to the x-ray beam and recording the Laue back reflection picture. Figure 1 shows that the crystal is both a single crystal and strain-free. The nickel crystals reported so far (Hayashi *et al* 1974; Kuriyama *et al* 1977) have been grown from melt either in vacuum or in an inert gas environment maintained at 1 atm. pressure. The dislocation density reported in these crystals was fairly high (Hayashi *et al* 1974). In order to find out the dislocation density of the present high pressure Czochralski grown crystals, these were cut normal to the growth axis and then characterized by metallographic techniques. The crystals were mechanically polished by using diamond paste down to a 3  $\mu\text{m}$  surface finish and etched in a solution of  $\text{HNO}_3$  and acetic acid (Brandes 1983). The dislocation density was measured by first identifying those etch pits which were due to dislocations. For this the crystal surface was successively etched and the continuity of etch pits was followed. Etching resulted in well-defined etch pits which were triangular in shape (figure 2) and which persisted even after the removal of successive layers from the crystal surface. Slight roughness of the etched surface, seen in the photograph, could be due to the effects of mechanical polishing. We have used only upto 3  $\mu\text{m}$  grain size diamond paste. This procedure yielded an estimate of  $< 10^3$  dislocations/cm<sup>2</sup>, indicating that the crystal grown in an argon gas atmosphere at a pressure slightly higher than the ambient is of good quality. Low dislocation density was obtained by eliminating the dislocations from the seed crystal in the neck, and the dislocations can be reintroduced if the diameter of the cone region is not controlled. The growth of the cone region was very important for obtaining low dislocation density single crystals of nickel. The cone region was grown such that the top angle was small. The cone could thus grow out with minimum dislocations. On the other hand, with large top angles, the internal stresses in the growing crystal would have been high and that would cause dislocation generation in the cone region. With dislocations being kept at minimum level in the cone region, further growth of the crystal was accomplished such that the crystal diameter stayed more or less constant. With this the dislocation multiplication in the lower part of the crystal was prevented to a great extent.



## Growth of nickel single crystals



Figures 1-3. 1. X-ray back reflection picture of single crystal of nickel. 2. Dislocation et pits in nickel crystal. 3. Radial growth striations in nickel single crystal.

Striations observed normal to the growth axis  $\langle 111 \rangle$  (figure 3) showed the shape of the solid-liquid interface. No axial growth striations were observed. Since the crystals were not doped with any other material, these striations are not due to the solute variations. These were found to be not periodic over the length of the crystal and were observed at an extremely small number of places. The unintentional dopants that might exist in 99.99% pure nickel will, on the other hand, give rise to striations which will be periodic over the entire length of the crystal. Also no discoloration of the alumina crucible material was observed after the growth experiments, implying that there was no reaction of nickel with  $\text{Al}_2\text{O}_3$  crucible. The spacing between the two adjoining striations was measured to be  $2-3 \mu\text{m}$ . These striations can be attributed to the possible thermal fluctuations present across the interface due to the thermal expansion of the solid and liquid phases.

and temperature gradients commonly used in the growth of single crystals of nickel are not very low to eliminate thermal convection. A spacing of the above mentioned magnitude is typical of such fluctuations. Although low temperature gradients in the crystal were favourable for the low dislocation density growth, with such low temperature gradients in the melt, the melt convection reduces making the heat transfer from the crucible wall to the crystal interface small. Subsequently it became very difficult to control the crystal diameter.

Low dislocation density ( $< 10^3$  dislocations/cm<sup>2</sup>) observed in nickel single crystals grown in argon gas at 6 bar pressure indicates that the high ambient pressure does not reduce the quality of the crystal. On the other hand, the crystal is mechanically extremely soft at its melting temperature and a slight ambient pressure perhaps prevents dislocation generation by reducing the thermal stresses at the interface. Compared to the vacuum-grown crystals these crystals have lower dislocation density and their microstructure does not show any grain boundaries.

#### 4. Conclusions

Strain-free single crystals of nickel have been grown at 6 bar inert gas pressure. In a slight hydrostatic pressure environment and the necking are found to improve the crystal quality. The dislocation density of these crystals was determined to be less than  $10^3$  dislocations/cm<sup>2</sup>.

#### Acknowledgement

The authors are thankful to Shri M Sekar for assistance in the experiments and S G V N Rao for help in x-ray work.

#### References

- Brandes E A 1983 *Smithells metals reference book* (London: Butterworths) p. 10
- Dash W C 1958 *J. Appl. Phys.* **29** 736
- Hayashi S, Echigoya J, Hariu H, Sato T, Nakamichi T and Yamamoto M 1974 *J. Cryst. Growth* **24** 422-425
- Khanna S K, Sekar M, Michael David A, Govinda Rajan K and Bhaskar Rao P 1986 *Pramana (J. Phys.)* **26** 151
- Kuriyama M, Boettinger M J and Burdette H E 1977 *Advances in x-ray analysis* (New York: Plenum Press) (eds) H F McMuradie, C S Barrett, J B Newkirk and C O Rund Vol. 20, p. 245
- Pamplin B R 1975 *Crystal growth* (New York: Pergamon Press)
- Paorici C 1982 *Proc. international school on synthesis, crystal growth and characterization* (ed) K. (Amsterdam: North-Holland) p. 170

## Emission spectrographic technique for the quantitative determination of trace elements in granitic rocks

A EL BIALY, M RASMY\*, L A GUIRGUIS\*\* and W MOUSSA

Women's College, Ain Shams University, Cairo, Egypt

\*Earth Sciences Laboratories, National Research Centre, Cairo, Egypt

\*\*Nuclear Materials Corporation, Cairo, Egypt

MS received 14 March 1985; revised 29 July 1985

**Abstract.** An emission spectrographic technique was developed to estimate 16 trace elements in some samples of Egyptian granite. The detection limits were: 0.1 ppm for Pb, Ba, Mn, Cr, Yb and Ni, 0.3 ppm for Sn, Ga and Be, 1 ppm for Co, Sc and V, 3 ppm for Bi and 10 ppm for La. The relative deviation of the two-thirds limits ranges between  $\pm 1.5$  and

**Keywords.** Emission spectrography; granitic rocks; trace elements.

### 1. Introduction

Crystalline rocks, including igneous and metamorphic types, constitute more than 60% of the earth's crust. Granites are the most common igneous rocks. Many valuable deposits are genetically related to granitic rocks. Therefore, the determination of trace elements in granite is essential for both genetic and economic reasons. The technique of emission spectrographic analysis of granites has drawn the attention of a great number of authors (Ahrens and Taylor 1961; Sighinolfi 1966; Peter 1969; Fleischer 1972; Gallet 1975; Watson and Russell 1978). Granites are coarse-grained acid igneous rocks which are mainly composed of alkali feldspars, acid plagioclases, mica and some other accessory minerals. Granites contain high  $\text{SiO}_2$  content (usually above 65%) and are therefore considered acidic and responsible for the dense silica bands in spectrographic analysis. Besides, the increased ratio of alkalies perceptibly lowers the arc temperature. These factors give rise to a dense background and low sensitivity of the analytical elements.

The aim of the present work is to develop a specific technique by which analytical conditions of granite are improved and sensitivities of the elements increased.

### 2. Experimental

The emission spectrographic technique was developed to determine 16 trace elements in some samples of Egyptian granite using a Zeiss Jena grating spectrograph. Graphite was used as a buffering material while  $\text{CdF}_2$  was added as a carrier. The current intensity was 1.4 A, time was 50 sec and Pd was used as the internal standard for the elements.

The optimum conditions of spectrographic analysis of granite can be achieved by studying some factors. These are discussed in this paper.

### 1.1 Electrode type

For practical reasons, only rod-type graphite electrodes were experimented. Four forms of each of the sample and counter electrodes were alternatively tested. These forms are similar to the Ringsdroff types (RW0006, RW0021, RW0068, RW0070, RW0083, RW0028 and RW0067) with tip angles  $20^\circ$  and  $30^\circ$ . The best forms that gave good burning conditions and high line intensities are those similar to the sample form RW0021 and counter form RW0028. The electrodes (electrode gap: 3.5 mm) were shaped from JMC specpure graphite rods. These are shown in figure 1 and are given the

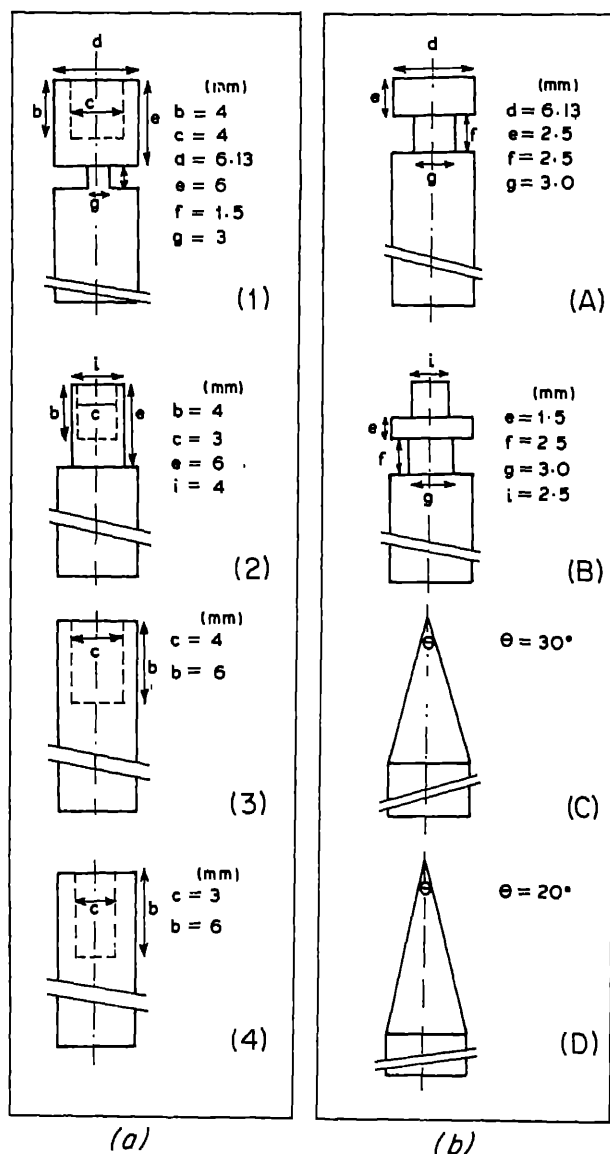


Figure 1. Electrode shape.

## *Trace elements in granitic rocks*

symbols 1, 2, 3 and 4 for sample electrodes (anode) and A, B, C and D for electrodes (cathode) respectively.

### *2.2 Current intensity*

According to Bowmans (1966) the intensities of the spectral lines are influenced by arc current. It is important to obtain the best current intensity to have a smooth arc and a stable arc spot.

The dependence of the current densities of the test lines: Ba: 455.4 nm, Ti: 337.280 nm, Cr: 425.434 nm, Zr: 339.198 nm, Zn: 328.233 nm, V: 431.4 nm, Pb: 283.307 nm, Mo: 317.035 nm, Be: 213.042 nm, Yb: 328.937 nm and Y: 330.2 nm on the arc current from 6 to 15 A is represented graphically in figure 2. It is clear that line densities increase gradually with current intensity. Moreover some of the elements such as Y and Yb did not appear except at a high current intensity (14 A). The best practical current intensity was 14 A.

### *2.3 Buffers and carriers*

A wide range of additives was used. They include graphite powder, alkali and earth carbonates and halides, oxides of Mg, Zn, Zr and Ga as well as heavy metal halides (Rasmy 1983) in varying ratios. It was observed that the best buffer and carriers are graphite powder and cadmium fluoride respectively. The ideal mixing ratio of sample, graphite and  $\text{CdF}_2$  is 2:2:1. Figure 3 shows a moving plate study of spectral line intensities for three cases, from which the following can be concluded:

- (a) When the sample is arced alone, the distillation period exceeds 160 sec till volatile elements, e.g. Y, attain their peaks.
- (b) When a mixture of equal amounts of the sample and graphite powder is used, the distillation period is rather shortened and arcing is improved. However, some elements like Y and Mo exhibit double peaks.
- (c) When the ideal mixture of the sample, graphite and  $\text{CdF}_2$  is arced, the distillation period is greatly shortened. Each element exhibits one peak and all peaks appear within the first 50 seconds of arcing. Besides, densities of spectral lines of the elements are perceptibly increased. It seems that the most suitable exposure time is 50 sec, at which time a reasonable background intensity is developed.

### *2.4 Sample preparation*

Samples of granite, each about 2 kg, were crushed by hammering. Small representative samples were prepared by quartering method and ground to about 200 mesh in an agate mortar. Contamination was always avoided.

### *2.5 Synthetic standards*

A matrix was prepared, the composition of which is close to the average composition of granite given by Wedepohl (1969). The small content of Mn, Ti and P was excluded as  $\text{P}_2\text{O}_5$  was not provided as a separate chemical while Mn and Ti were added as a part of the trace elements to be analysed. After thorough mixing of matrix components, they were sintered in a platinum dish at 1200°C for 6 hours and ground to 200 mesh. The final composition of the matrix was expected to be as follows:

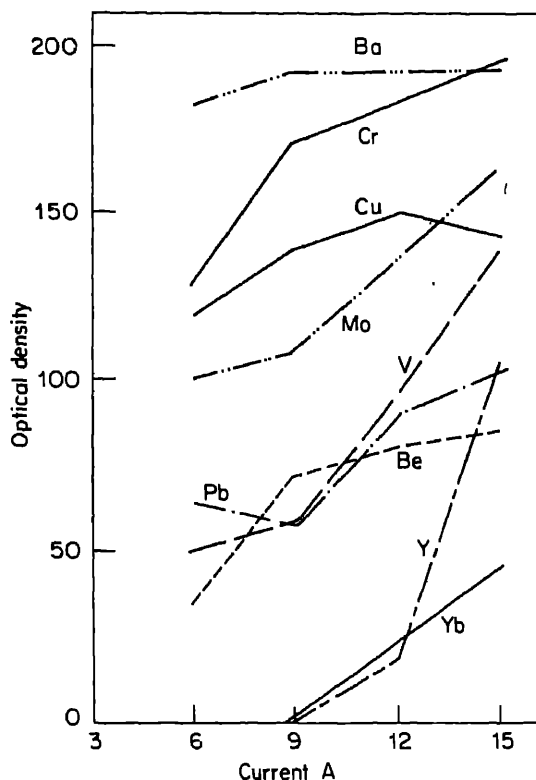


Figure 2. Current effect.

72.91 %  $\text{SiO}_2$ , 14.02 %  $\text{Al}_2\text{O}_3$ , 2.56 %  $\text{Fe}_2\text{O}_3$ , 0.53 %  $\text{MgO}$ , 1.35 %  $\text{CaO}$ , 3.12 %  $\text{Na}_2\text{O}$  and 5.52 %  $\text{K}_2\text{O}$ .

The first standard, containing 3000 ppm of each of the trace ingredients, was prepared from the calculated amount of JMC Spectromel No. 1 mixture containing 1.18 % of 53 different trace elements, to which the corresponding amounts of the oxides of Y, La and Yb are added and finally diluted with the weighed amount of the matrix. From this first standard, other standards containing 1000, 300, 100 . . . down to 0.1 ppm of the trace elements were prepared by successive dilution with the matrix.

## 2.6 Internal standard

An amount equivalent to 100 ppm palladium, as chloride, was added to each of the samples and standards for internal standardization. The intensities of the less volatile elements (Ahrens and Taylor 1961) are related to that of Pd. No other internal standard could be used for volatile elements including Ga, Pb, Cu and Sn. They were related to their adjacent background.

## Trace elements in granitic rocks

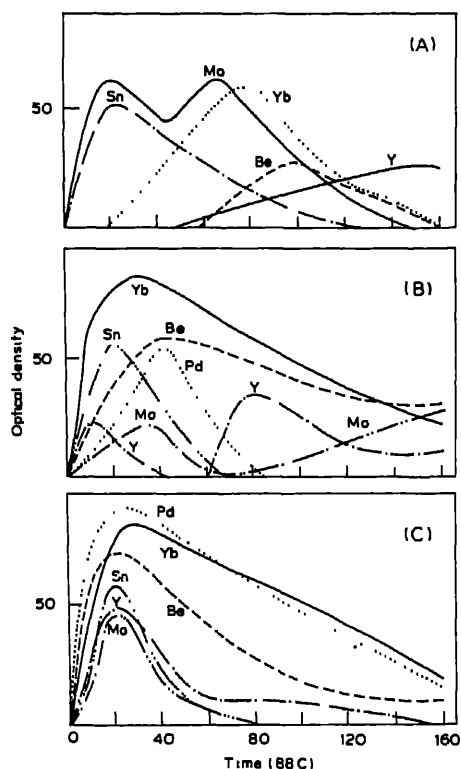


**Figure 3.** Time-intensity diagrams of granite standard with about 100 ppm trace the effect of buffer and carrier: (A) Standard alone, (B) Standard: Buffer 1/1, (C) Buffer:  $\text{CdF}_2$  2/2/1.

### 2.7 Slit width adjustments

The slit width of the spectrograph is of great importance when the background is considered. The background intensity, due to continuous radiation, increases with slit width. Therefore the slit must be adjusted to give maximum line intensity with a reasonable background. The granitic sample was arced using variable slit widths such as 10, 12, 14 and 16  $\mu$ . It is clear from the results obtained (figure 4) that a slit width of 12  $\mu$  was most preferable, considering the exposure time of 50 sec and the above conditions.

### 2.8 Calibration and evaluation

Calibration curves were drawn by plotting blackness  $D$  of some Fe spectral line against their log intensities using a six-step diminisher with 100, 40, 16, 10, 6 transmissions. Four curves were drawn covering the whole wavelength range 282–456 nm (figure 5). The background correction was made using the relation of Mika and Torok (1974).

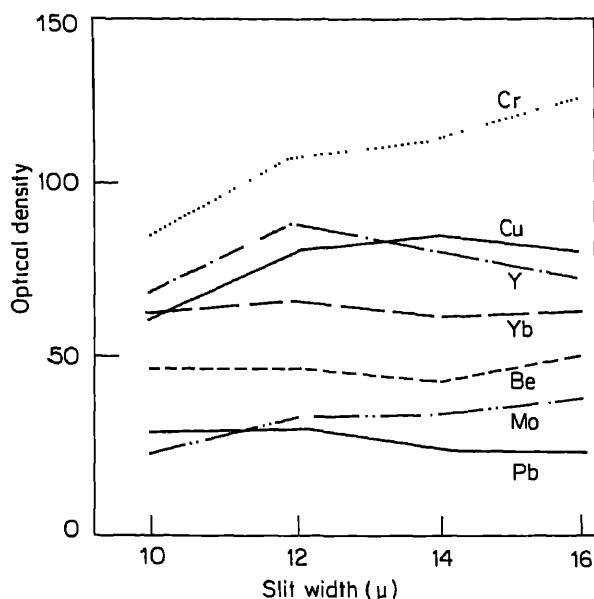


Figure 4. Effect of slit width.

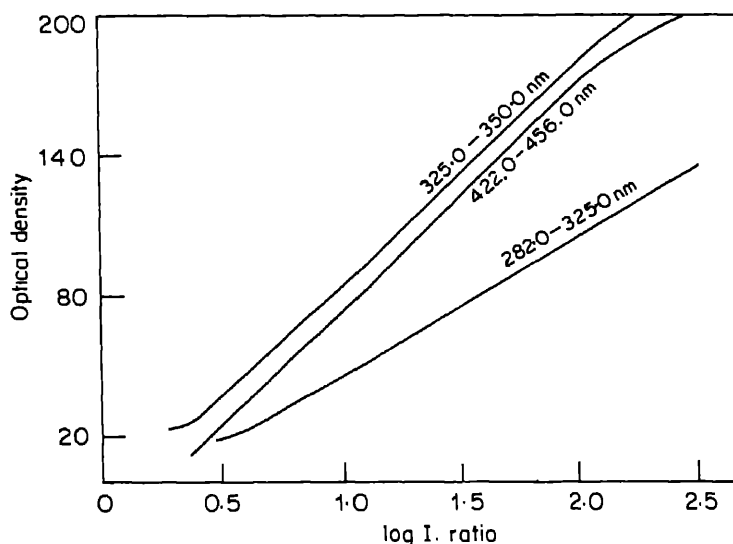


Figure 5. Sample of the calibration curves.

Working curves were drawn between log intensity ratio and log concentration (figure 6). The trace elements content of the analyzed granite samples and its implications were discussed in detail by El Bialy *et al* (1984). The analytical lines and detection limits of the analysed elements of our work and that of Gokun (1975) (the best available compatible work) are shown in table 1.



## Trace elements in granitic rocks

Table 1 shows that the improvements in the minimum detection limit : 1000 for Pb, Mo, Cu, Yb, Ni, Cr and Ba, 333.33 for Ga and Be, 100 for 33.33 for Y and 16.66 for Sn.

### 2.9 Precision and accuracy

Precision expressed as the standard deviation  $S$  and the relative deviation thirds limits is shown in table 2 using data obtained by arcing granite rock distributed by the U.S. Geological survey, as an unknown sample. deviation  $S$  ranges between  $\pm 0.02$  and  $\pm 1.9$  ppm while the relative deviation

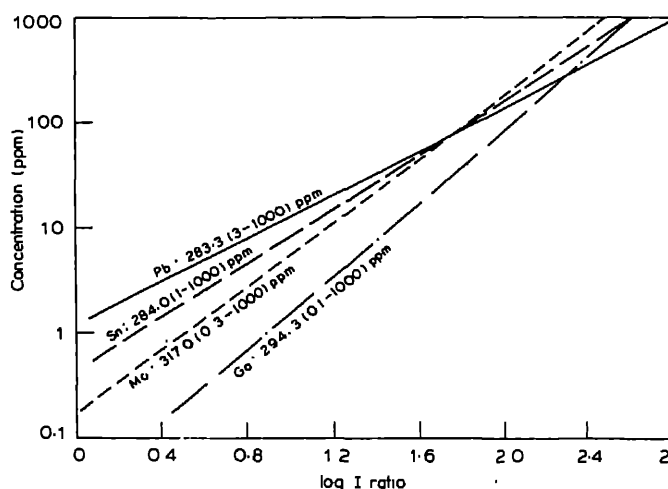


Figure 6. Samples of working curves for the determination of Pb, Sn, Mo

Table 1. Detection limits and wavelength of spectral lines of the analysed present work compared to that of Gokun (1975)

Element	Wave-length (nm)	Detection limit (ppm)		Element	Wave-length (nm)	Detection limit (ppm)
		Present work	Gokun (1975)			Present work
Pb	283.307	0.1	100	Ga	294.364	0.1
Mo	317.035	0.1	100	Be	313.042	0.1
Cu	327.396	0.1	100	Co	345.351	1
Yb	328.937	0.1	N.D.	Sc	424.683	1
Ni	341.477	0.1	100	V	437.924	1
Cr	425.434	0.1	100	Bi	306.772	3
Ba	455.404	0.1	100	Y	332.788	3
Sn	283.999	0.3	5	La	433.347	10

N.D. not detected.

**Table 2.** Results of analysis of granite rock standard USGS-G<sub>2</sub> together with standard deviations (S) and relative deviation (C)

Element	Flanagan (1973)	Present work	S	C
Be	2.6	3.1	0.70	24.7
Ga	22	18	1.9	11.5
Cu	11.7	10.27	1.58	13.8
Mo	0.36	0.5	0.06	11.5
Y	12	11.1	1.69	15.25
Yb	0.88	0.8	0.15	18.8
Sn	1.5	1.33	0.02	1.5
Cr	7	5.3	0.77	14.5
Sc	3.7	3.22	0.16	5.08

between  $\pm 1.5$  and  $\pm 24.7$ . As shown in table 2, the present values of trace elements G<sub>2</sub>, are in good agreement with earlier values (Flanagan 1973). This shows that accuracy of the method is satisfactory. Moreover the reported relative deviation val in table 2 for all the elements are much better than the value of 25% given by Gok (1975).

## References

- Ahrens L H and Taylor S R 1961 *Spectrochemical analysis* (London: Addison-Wesley) 2nd edn  
 Bowmans P W J M 1966 *Theory of spectrochemical excitation* (London: Hilger Watts) pp 192  
 El Bialy A, Rasmy M N, Guirguis L A and Moussa W 1984 *Bull. Nat. Res. Council (Cairo)* (accept)  
 Flanagan F J 1973 *Geochim. Cosmoch. Acta* **37** 1189  
 Fleischer M 1972 *Science* **199** 6  
 Gokun V N 1975 *Tr. Akad. Nauk USSR* **35** 105  
 Mika J and Torok T 1974 *Analytical emission spectroscopy Fundamentals (Hung)*, Eng. Transl. P A F (London: Butterworth)  
 Peter S 1969 *Math. Natur. Wiss. Reihe* **1**, 8, 8 971  
 Rasmy M 1983 *Bull. Nat. Res. Council (Cairo)*  
 Sighinolfi G P 1966 *Period Minerel Rome* **35**, 3 769  
 Watson A F and Russell G U 1978 *Spectrochim. Acta part 2*, **33**, 5 173  
 Wedepohl K H (ed.) 1969 *Data of geochemistry* (Berlin: Springer) Vol. 1

## Determination of oxygen to metal ratio of U-Pu mixed oxides by diffraction

RAVI VERMA and P R ROY

Radiometallurgy Division, Bhabha Atomic Research Centre, Bombay 400 085, India

MS received 13 March 1986

**Abstract.** The possibility of measuring the oxygen-metal ratio (O/M) of U-oxides by x-ray diffraction technique has been explored. In single-phase U-Pu mixed oxides the lattice parameter vs O/M plots for different plutonium concentrations are interpolation of lattice parameter values between those of  $\text{UO}_2$ ,  $\text{PuO}_2$  and  $\text{Pu}_2\text{O}_3$  plots are then used for determining the O/Ms of unknown samples against experimentally measured lattice parameter values. In two-phase mixed oxides, fractions of the two phases are determined from the intensities of their selected lines. The O/M of the mixed oxide is then given by the mole average of the individual O/Ms of the two phases.

**Keywords.** Oxygen-metal ratio; uranium plutonium oxides; x-ray diffraction.

### 1. Introduction

The oxygen-to-metal ratio (O/M) is an important parameter governing properties of the U-Pu mixed oxide fuels. It is well known that deviating from stoichiometry assists in the sintering of mixed oxide compacts (Belle 1961; Lyon 1965; Gibby 1969) and melting point (Lyon and Baily 1965). Diffusion coefficients and vapour pressures have also been reported to change by 3 or more orders of magnitude for a minor change of 0.02 in the O/M near the value of 2.00 (Lyon 1976). A knowledge of O/M of the mixed oxide fuel, therefore, is very essential.

A variety of O/M measurement techniques have been developed and used in the past several years with varying degree of success. Lyon (1963) reviewed several of these techniques and recommended a thermogravimetry method for O/M measurement. McNeilly and Chikalla (1971) improved upon the two-step method and suggested a single heat treatment of the sample at 1073 K for 6 h in an atmosphere of Ar-8%  $\text{H}_2$  passed over a water trap maintained at 273 K. This method has an accuracy of  $\pm 0.002$ . The thermogravimetry method requires an accurate balance, a furnace and a gas handling system which make it difficult to adopt it as an on-line method of O/M measurement in a commercial fuel processing plant. Lattice parameter measurement can be conveniently used to measure O/M in single-phase mixed oxides. In this paper, different methods of O/M measurement based on x-ray diffraction analysis are presented for single-phase and for two-phase mixed oxides. The results of O/M measurements obtained using these methods are discussed.

### 2. U-Pu-O system

Before discussing the x-ray methods, it is worthwhile to examine some of the relationships in the ternary U-Pu-O system. Since the recommended fuel

metal fast breeder reactors is a hypostoichiometric mixed oxide, the discussion would be restricted only to this region of the ternary phase diagram.

The phase diagram in figure 1 (Markin and Street 1967) shows that for plutonium concentrations less than 30–35%, the hypostoichiometric mixed oxide exists as a single fcc phase. The remarkable ability of the mixed oxide to lose oxygen without undergoing a phase transformation is attributed to the conversion of  $\text{Pu}^{4+}$  ions to  $\text{Pu}^{3+}$  ions. The O/M limit of the single phase region corresponds to a state in which all the plutonium in the mixed oxide is reduced to  $\text{Pu}^{3+}$ . Uranium, on the other hand, remains tetravalent throughout the reduction of the mixed oxide. For plutonium concentrations more than 30–35%, the hypostoichiometric mixed oxide exists as a mixture of two phases—the stoichiometric  $\text{MO}_{2.00}$  phase and a substoichiometric  $\text{MO}_{2-x}$  phase. The O/M of the latter phase corresponds to all the plutonium in  $\text{Pu}^{3+}$  state. The phases,  $\text{MO}_{2.00}$  and  $\text{MO}_{2-x}$ , have the fcc structure upto a plutonium concentration of 50% (Brett and Russell 1963), beyond which the  $\text{MO}_{2-x}$  phase shows a bcc structure (Brett and Russell 1963; Dean 1965). Further, it has been shown (Dean *et al* 1970) that the hypostoichiometric mixed oxide containing 76% plutonium shows a rhombohedral phase in equilibrium with the fcc  $\text{MO}_{2.00}$  phase. The O/M of the rhombohedral phase is reported to be 1.70, which means that only a part of plutonium in this phase exists in  $\text{Pu}^{3+}$  state.

### 3. Methods

#### 3.1 Single-phase mixed oxide

The x-ray diffraction method for determining O/M in a single-phase mixed oxide is based on finding a correlation between the lattice parameter and the O/M of the

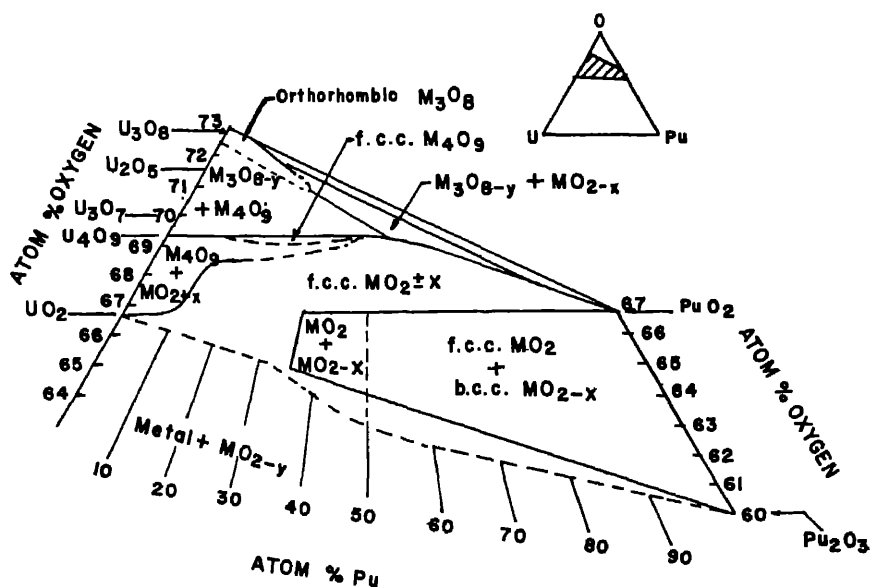


Figure 1. A section of U-Pu-O ternary equilibrium diagram.

mixed oxide. Lattice parameter values determined by the x-ray diffraction technique are plotted against O/M values measured by the thermogravimetric method for different plutonium concentrations of the mixed oxide (Dean and Pascard 1967; Markin and Street 1967). These plots are then used to obtain O/M values for unknown samples.

The lattice parameter vs O/M plots for different plutonium concentrations also be drawn on the basis of the following consideration.

The lattice parameter of a stoichiometric mixed oxide varies linearly with plutonium content from  $\text{UO}_2$  to  $\text{PuO}_2$  (Mufford and Ellinger 1958). Dean *et al* showed that the lattice parameter of a fully reduced mixed oxide (i.e. all plutonium in  $\text{Pu}^{3+}$  state) varies linearly with plutonium content, from  $\text{UO}_2$  to  $\text{Pu}_2\text{O}_3$ . From there is ample evidence (Dean and Pascard 1967; Blank *et al* 1967; Markin and Street 1967) indicating that the lattice parameter of a mixed oxide of given plutonium concentration varies linearly with its oxygen content. These observations suggest that, in general, the lattice parameter of a hypostoichiometric mixed oxide can be obtained by linear interpolation between the lattice parameter values of  $\text{UO}_2$  and  $\text{Pu}_2\text{O}_3$ . Details of the interpolation are shown in figure 2. Dean's lattice parameter vs plutonium content plot for fully reduced mixed oxide (line a

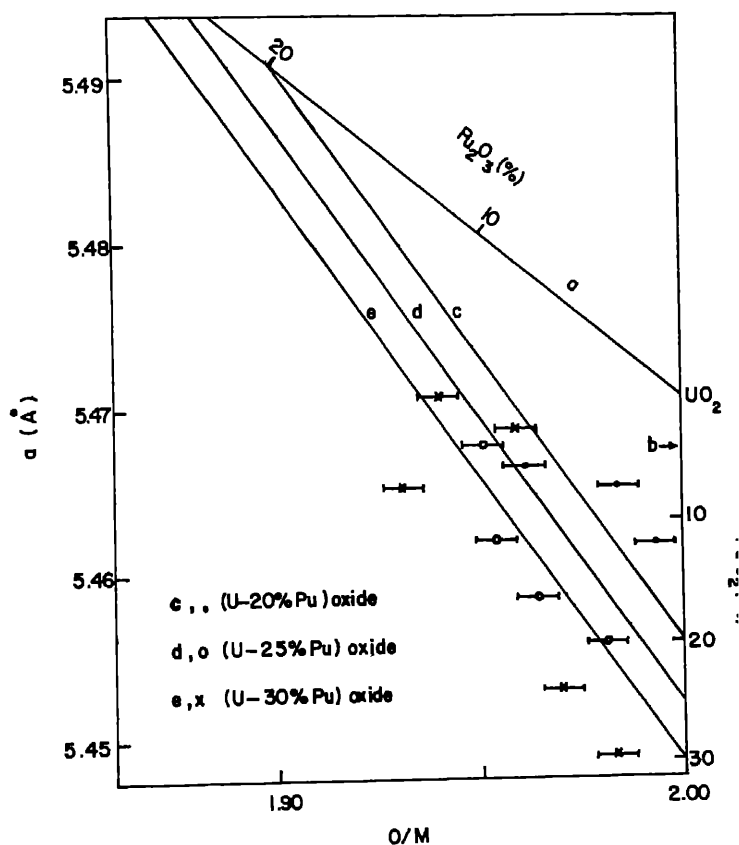


Figure 2. Dependence of lattice parameter on O/M for different compositions of phase mixed oxide; theoretical plots (—) and the experimental data points.

figure) is drawn by assigning limit stoichiometry according to the trivalent state plutonium, to each composition of the limiting phase. The linear variation of the lattice parameter with the  $\text{PuO}_2$  content of the stoichiometric mixed oxide is plotted as line b. Since the lattice parameter vs O/M plot for a mixed oxide of given plutonium concentration, say  $\text{U}_{1-c}\text{Pu}_c\text{O}_{2-0.5c}$  oxide, is also a straight line (Dean and Pascard 1967; Blank *et al* 1967; Markin and Street 1967), the plot is simply obtained by joining with a straight line the limit compositions,  $\text{U}_{1-c}\text{Pu}_c\text{O}_{2-0.5c}$  on plot a and  $\text{U}_{1-c}\text{Pu}_c\text{O}_{2.00}$  on plot b. This way the lattice parameter vs O/M plots for different plutonium concentrations of the mixed oxide are drawn. By knowing the lattice parameter of a mixed oxide of known plutonium concentration its O/M can be obtained from a suitable plot in figure 2.

### 3.2 Two-phase mixed oxide

The overall O/M of a mixed oxide consisting of two phases can be obtained by taking the weighted mean of the individual O/Ms of the two phases. If  $m$  denotes the mole fraction of  $\text{MO}_{2-x}$  phase in a mixture of  $\text{MO}_{2.00}$  and  $\text{MO}_{2-x}$  phases, the overall O/M of the mixed oxide will be given by

$$\begin{aligned} \text{O/M} &= (1-m) \times 2.00 + m(2-x) \\ &= 2.00 - mx \end{aligned} \quad (1)$$

To find the O/M of a two-phase mixed oxide, therefore, the values of  $x$  and  $m$  should be known. The deviation from stoichiometry of the  $\text{MO}_{2-x}$  phase is given, based on the trivalent state of plutonium, as

$$x = 0.5 C_{\text{Pu}} / (C_{\text{U}} + C_{\text{Pu}}) \quad (2)$$

where  $C_{\text{U}}$  and  $C_{\text{Pu}}$  are atomic concentrations of uranium and plutonium in the mixed oxide.

In the  $\text{MO}_{2-x}$  phase containing 76% plutonium, all the plutonium do not exist in the trivalent state as shown by Dean *et al* (1970). The departure from stoichiometry in this phase, therefore, is not given by (2). This phase has been shown to have an O/M of 1.70 (Dean *et al* 1970), and so, an  $x$  equal to 0.3. The value of  $m$  can be obtained experimentally by measuring the x-ray line intensities of some selected reflections of the two phases as described below.

The ratio of the volumes of two phases,  $\alpha$  and  $\beta$  in a mixture is given in terms of the integrated intensities of their selected x-ray reflections, as

$$V_{\alpha}/V_{\beta} = \frac{I_{\alpha}(hkl)}{I_{\beta}(h'k'l')} \frac{K_{\alpha}(hkl)}{K_{\beta}(h'k'l')} \quad (3)$$

where  $K(hkl)$  is a factor characteristic of the selected reflection ( $hkl$ ) and the crystal structure of the particular phase.

In mixed oxides having 35 to 50% plutonium, both  $\text{MO}_{2.00}$  and  $\text{MO}_{2-x}$  phases have a fluorite-type cubic structure. Their lattice parameter values are nearly the same. They differ in their oxygen contents, but this is not of much consequence in so far as the  $K$  factors of the two phases are concerned since the atomic scattering factors of oxygen is much smaller than those of uranium and plutonium. Thus, for a given reflection ( $hkl$ ), the  $K$  factor values for the two phases can be regarded as equal

$$K_{\alpha}(hkl) = K_{\beta}(hkl).$$

red oxides containing more than 50% Pu, the bcc structure of the  $\text{MO}_{2-x}$  is in fact identical in atomic arrangement to the fluorite structure of the  $\text{MO}_2$  phase, except that the vacancies in its oxygen sublattice are ordered, giving a bcc super lattice (Gardner *et al* 1965). Thus, for the same reasons as cited in the preceding paragraph, for a given reflection ( $hkl$ ), the  $K$  factors for  $\text{MO}_2$  and  $\text{MO}_{2-x}$  phases can be regarded as equal.

x-ray diffraction pattern of hypostoichiometric mixed oxide containing 76% plutonium is shown in figure 3. It is seen that the lines of the rhombohedral  $\text{MO}_{2-x}$  closely precede the corresponding lines of the cubic  $\text{MO}_{2.00}$  phase. Because of the symmetry of the rhombohedral structure *vis-a-vis* the cubic structure, some lines are split into two. It has been shown (Dean *et al* 1970) that the rhombohedral structure of the  $\text{MO}_{2-x}$  phase is a slightly distorted form of the fluorite structure of the  $\text{MO}_{2.00}$  phase (rhombohedral:  $a=5.5087 \text{ \AA}$  and  $\alpha=89.525^\circ$ ;  $a=5.4147 \text{ \AA}$ ,  $\alpha=90^\circ$ ). Therefore, the  $K$  factors for equivalent reflections of  $\text{MO}_{2-x}$  and  $\text{MO}_{2.00}$  phases should be nearly equal. In the case of the split lines of the rhombohedral phase, the combined  $K$  factor for the pair of split lines is equal to the  $K$  factor for the corresponding single line of the cubic phase. The  $\{200\}$  line of the rhombohedral phase is not split into two (figure 3). Therefore,

$$K_r\{200\} = K_c\{200\}.$$

where the subscripts  $r$  and  $c$  denote rhombohedral and cubic phases respectively. Thus, for all compositions of the mixed oxide,

$$K_{\text{MO}_{2.00}}(hkl) = K_{\text{MO}_{2-x}}(hkl),$$

where ( $hkl$ ) can be any reflection for mixed oxides containing 35 to 50% plutonium

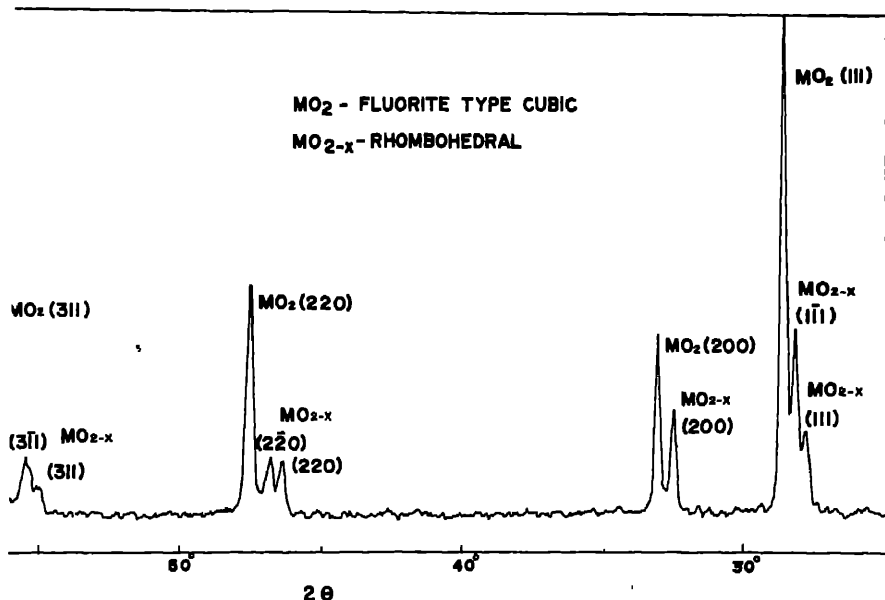


Figure 3. Recorded trace of (U0.24 Pu0.76)  $\text{O}_{2-x}$  diffraction pattern by  $\text{CuK}_\alpha$  radiation.

and only the {200} reflection in case of mixed oxide containing 76% plutonium. Using the above equality in (3), one gets

$$V_\alpha/V_\beta = I_\alpha(hkl)/I_\beta(hkl). \quad (4)$$

The subscripts  $\alpha$  and  $\beta$  represent the  $\text{MO}_{2-x}$  and the  $\text{MO}_{2.00}$  phases respectively. Since all the different crystal structures associated with  $\text{MO}_{2-x}$  phases are closely related to the fluorite-type cubic structure of the  $\text{MO}_{2.00}$  phase, both these phases will have the same number of molecules per unit cell or per unit volume. Now, if  $m_\alpha$  and  $m_\beta$  represent the number of moles of  $\text{MO}_{2-x}$  and  $\text{MO}_{2.00}$  phases, respectively, in a given mixed oxide sample, then

$$m_\alpha/m_\beta = V_\alpha/V_\beta.$$

Substitution from (4) gives

$$m_\alpha/m_\beta = I_\alpha(hkl)/I_\beta(hkl),$$

$$\text{or } m = m_\alpha/(m_\alpha + m_\beta) = I_\alpha(hkl)/[I_\alpha(hkl) + I_\beta(hkl)], \quad (5)$$

where  $m$  is mole fraction of the  $\text{MO}_{2-x}$  phase in the mixed oxide. Knowing the values of  $x$  and  $m$  from (2) and (5) respectively, the O/M of unknown mixed oxide can be obtained from (1).

With the help of (1)  $m$  vs O/M plots for three different mixed oxide compositions U-35, 50 and 76% Pu, have been drawn in figure 4. The values of O/M for unknown

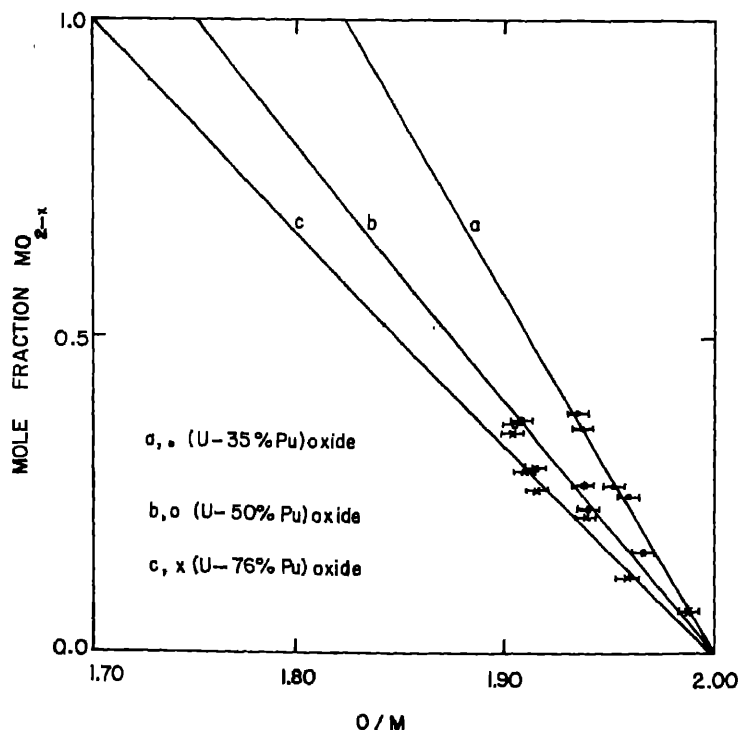


Figure 4. Amount of substoichiometric phase versus overall O/M of the two-phase mixed oxide; theoretical plots (—) and experimental data points (—o—)



mixed oxides belonging to these compositions can be read from these plots against their  $m$  values obtained from (5).

#### 4. Experimental

Mixed pellets of compositions  $\text{UO}_2$ -20, 25, 30, 35, 50 and 76%  $\text{PuO}_2$  homogenized at 2073 K for 30 hr in a dry (100 ppm moisture) Ar+8% atmosphere. The measurement of O/Ms of representative pellets by thermogravimetric method showed that all the mixed oxides were highly reduced. The process of O/M measurement by the thermogravimetric method adjusted O/M of the mixed oxide pellet to 2.00. These O/M adjusted pellets are free of oxygen inhomogeneity and other phases and are thus suitable for assessing metal atom homogeneity in the mixed oxides by the x-ray diffraction technique. The diffraction patterns of all the O/M adjusted pellets showed sharp lines belonging to a single fcc phase. They also showed well-resolved ( $K\alpha_1$ - $K\alpha_2$ ) doublets for the reflection, confirming that all the mixed oxides were well homogenized.

As-homogenized (non adjusted) pellets were heated at 373 K in air. For each of various mixed oxide compositions, one pellet was removed from the furnace every 15 min of heating and stored in an inert atmosphere. This was continued until the last set of pellets was removed. Thus, pellets of different O/Ms were obtained for all the mixed oxide compositions. Each of these pellets was broken into two halves; one half was used to determine O/M by the thermogravimetric method and the other half was used to record the x-ray diffraction pattern. For mixed oxides containing 25 and 30% plutonium (single-phase mixed oxides) precise lattice parameters were determined by 'extrapolation' method using high angle lines. For mixed oxides containing 35 and 50% plutonium, the {311} reflection and in the case of the oxide containing 76% plutonium, the {200} reflection was recorded at a scanning speed of  $1/8^\circ$  in  $2\theta/\text{min}$ . These reflections consisted of two peaks corresponding to the  $\text{MO}_{2.00}$  and the  $\text{MO}_{2-x}$  phases. The integrated peak intensities  $I_{\text{MO}_{2.00}}$  and  $I_{\text{MO}_{2-x}}$  were obtained by measuring areas under individual peak profiles. In mixed oxide containing 35% plutonium, however, the two peaks overlapped as shown in figure 5 and measuring the area under the individual peak was very difficult. This difficulty was overcome by correcting the peak profiles for instrumental broadening by line profile analysis technique described elsewhere (Verma 1983). The measured integrated intensities were substituted in (5) to obtain mole fractions of the  $\text{MO}_{2-x}$  phase in mixed oxide samples of different compositions.

#### 5. Results and discussion

The experimental data points based on measured lattice parameter and O/M of the single phase mixed oxides are plotted in figure 2. It is seen that the data are scattered not too closely on both sides of the theoretical lattice parameter O/M plots. The O/M values of various mixed oxide samples were also plotted against the respective measured lattice parameter values from these theoretical plots. The differences between the O/M values thus obtained and the O/M values measured by the thermogravimetric method are plotted against the latter in figure 3. In the case of two-phase mixed oxides, the experimental data points based

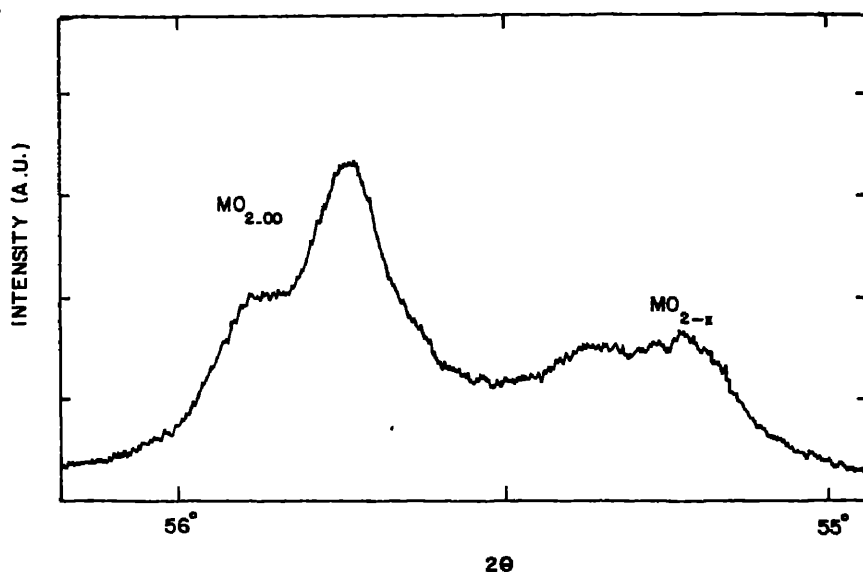


Figure 5. (311) Reflection profile recorded from ( $\text{UO}_2$ -35%  $\text{PuO}_2$ ) mixed compact sinter in a reducing atmosphere.

measured  $\text{MO}_{2-x}$  phase fractions and O/M values obtained by thermogravimetry method are plotted in figure 4. The data points in this case fit the theoretical  $\text{MO}_{2-x}$  phase fraction versus O/M plots fairly well. The differences in the O/M value obtained from the theoretical plots and those measured by the thermogravimetry method are plotted against the latter in figure 6.

It could be seen that the differences between the calculated and the measured O/M values are larger in the case of single phase mixed oxides than those of two-phase mixed oxides. The points in figures 6a and 6b show standard deviations of  $\pm 0.0$  and  $\pm 0.005$  respectively, from the O/M values measured by the thermogravimetry method. The thermogravimetry method of O/M measurement being the reference method in this study, the O/M values obtained by this method may be treated as absolute. The standard deviations of  $\pm 0.01$  and  $\pm 0.005$ , therefore, represent the accuracies of O/M measurement by the x-ray method in the context of single-phase and two-phase mixed oxides respectively. The accuracy of the x-ray method in single-phase mixed oxides is thus rather poor whereas in two-phase mixed oxides the accuracy of this method is comparable to that reported for the thermogravimetry method.

An O/M measurement by the x-ray method takes less than an hour which is much shorter a period as compared to 6–8 hr required by the thermogravimetry method.

## 6. Conclusions

The x-ray diffraction technique provides a convenient method for measuring the O/M of U-Pu mixed oxides. In single-phase mixed oxides ( $\text{Pu} < 30\%$ ), the x-ray method is based on measurement of the lattice parameter of the mixed oxide. The

## X-ray diffraction of O/M in U-Pu mixed oxides

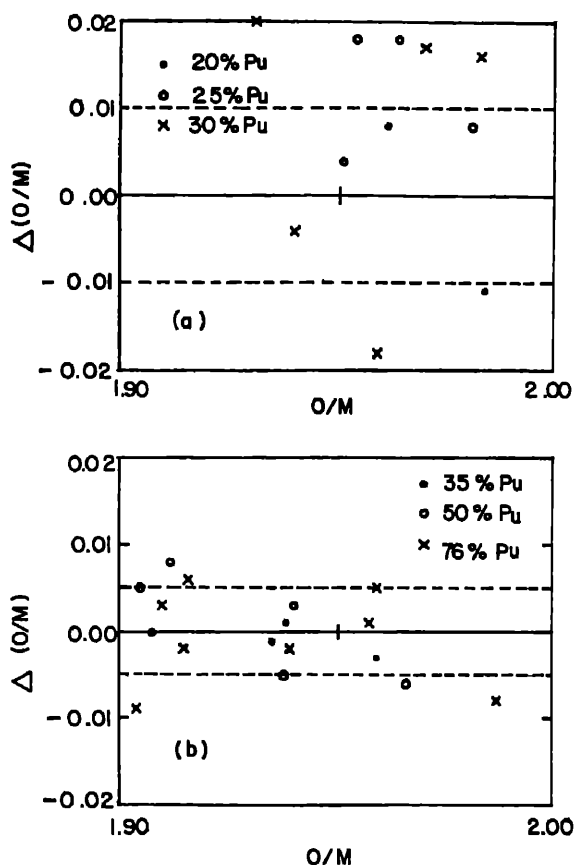


Figure 6. Difference in O/M determined by x-ray method and that determined by thermogravimetric method versus the latter; (a) single-phase mixed oxides, (b) two-phase mixed oxides.

accuracy of the method is approximately  $\pm 0.01$  which is poor compared to that of the thermogravimetric method.

For two-phase mixed oxides, the x-ray method of O/M measurement is based on measuring the volume fractions of the stoichiometric and the sub-stoichiometric phases in the mixed oxide. In this case the x-ray method has an accuracy of  $\pm 0.01$  which is comparable to that reported for the thermogravimetric method.

As compared to the thermogravimetric method, the x-ray method is faster, non-destructive and does not require a furnace or gas handling system. The method can be easily automated for on-line applications.

## References

- Belle J 1961 Uranium dioxide: Properties and nuclear applications Naval Reactors, Division of Research and Development, USAEC
- Blank H, Benedict U and Sari C 1967 in Technical Report Series (Vienna:IAEA) No. 79 p. 56
- Brett N H and Russell L E 1963 *Trans. J. Br. Ceram. Soc.* 62 97

- Dean G 1965 *Proc. 3rd Int. Conf. on Plutonium* (ed) A E Kay and M B Waldron (London: Chapman and Hall)
- Dean G and Pascard R 1967 in Technical Report Series (Vienna:IAEA) No. 79 p. 56
- Dean G *et al* 1970 *Proc. 4th Int. Conf. on Plutonium and other actinides Santa Fe, New Mexico* (ed) William N Miner (New York: Metallurgical Society)
- Gardner E R, Markin T L and Street R S 1965 *J. Inorg. Nucl. Chem.* **27** 541
- Gibby R L 1969 Battelle Northwest (USA) Report BNWL 927
- Lay K W 1971 *J. Am. Ceram. Soc.* **54** 18
- Lyon W L 1963 General Electric (USA) Report GEAP 4271
- Lyon W L and Bailey W E 1965 *Trans. Am. Nucl. Soc.* **8** 376
- Markin T L and Street R S 1967 *J. Inorg. Nucl. Chem.* **29** 2265
- Matzke H J 1976 in *Plutonium and other actinides* (Amsterdam: North Holland) p. 801
- McNeilly C E and Chikella T D 1971 *J. Nucl. Mater.* **39** 77
- Mufford R N R and Ellinger F H 1958 *J. Am. Ceram. Soc.* **80** 2023
- Schmidt H E 1968 Progress Report 4, European Institute for Transuranium Elements
- Van Craeynest J C and Weilbacher J C 1968 *J. Nucl. Mater.* **26** 132
- Varma R 1983 *J. Nucl. Mater.* **118** 325
- Zebroski E L, Lyon W L and Baily W E 1965 Int. Conf. on Safety, Fuels and Core Design in Large Fast Breeder Reactors, Argonne

## Kinetics of calcium molybdate crystallization

N M BATRA and S K ARORA

Department of Physics, Sardar Patel University, Vallabh Vidyanagar 388 120, India

MS received 17 June 1985; revised 24 October 1985

**Abstract.** Kinetics of crystallization of calcium molybdate from unstirred molten solution of lithium chloride of low to medium supersaturation in platinum crucibles by the process of continuous cooling at  $5^{\circ}\text{C hr}^{-1}$  from temperatures  $T_0 = 700$  and  $750^{\circ}\text{C}$  are investigated. The crystal size measured by optical microscopy for different crystallization periods shows that both crystal length and width generally increase with cooling period. The degree of crystallization  $\alpha_c$  also increases with cooling period, attaining a maximum of 0.9. Diffusion rate constants,  $K_{Di}$ , at 700 and  $750^{\circ}\text{C}$  are 0.0776 and 0.1138 respectively. The effect of variation of the crystallization temperature on the crystal size and their number has been studied.

**Keywords.** Calcium molybdate; crystallization kinetics.

### 1. Introduction

Crystallization of inorganic materials from high temperature solution has been studied by many workers (Laudise 1963; Kroger 1964; White 1964; Schroedger 1966; Linares 1966; Elwell and Scheel 1975). Alkaline earth metal molybdates and tungstates have been prepared by crystallization from lithium chloride and sodium tungstate or molybdate metals (Groot 1947; Moon 1948; Klick 1949; Anikin 1956; Uiter 1960; Ouwetjes 1965; Packter and Roy 1971). Packter and Roy (1973, 1975) studied some of the crystallization kinetics of alkaline earth metal compounds. Kinetics of precipitation of alkaline earth metal molybdates have also been studied (Packter 1977). However, only preliminary reports on the kinetics of crystal growth of calcium molybdate are available in literature and therefore we have undertaken further studies of the crystallization kinetics of calcium molybdate from an unstirred supersaturated solution in molten lithium chloride. These results are reported here.

### 2. Experimental

#### 2.1 Materials

The chemicals used were  $\text{CaMoO}_4$  powder (ICN Pharmaceuticals, New York) and hydrated  $\text{LiCl}$  (Burgoyne, Bombay). A 100 ml platinum crucible was employed to hold the growth charge.

#### 2.2 Solubility

Calcium molybdate solubilities in  $\text{LiCl}$  melt at 650 to  $900^{\circ}\text{C}$  were determined by the supersaturation method. For this purpose, lithium chloride powder (5 g) was n

in a platinum crucible and the temperature was measured with a chromel/alumel thermocouple and controlled using a variable voltage transformer. Increasing amounts of ground metal molybdate were then added to the molten solvent until a saturated solution was attained; the solution was considered saturated when traces of excess solute were visible at the bottom of the crucible. The solubility was thus determined from the weight of solute dissolved.

### 2.3 Crystallization

From the solubility data, appropriate quantities of flux and solute were weighed, mixed thoroughly using a pestle and mortar and then packed into the platinum crucible with a loosely fitting lid to prevent excessive evaporation. The saturated solutions were prepared at temperature, given by

$$T_i = T_0 + \Delta T,$$

where  $T_0$  is the temperature at which the crystallization is intended to be studied and  $\Delta T = 50^\circ\text{C}$ . The charge was heated at  $T_i$  for an hour. The furnace was then rapidly cooled to the crystallization temperature  $T_0$  and then soaked for an hour. After soaking, it was cooled at a uniform rate of  $5^\circ\text{C hr}^{-1}$  for different periods ranging from 1 to 17 hr, after which the crucible was withdrawn from the furnace and the undissolved crystals were separated from the solidified matrix by leaching with hot distilled water. The crystallization was studied at  $T_0 = 700$  and  $750^\circ\text{C}$  and the crystals were characterized essentially by EDAX and XRD. Crystal sizes were measured by optical microscopy.

Crystallization was next studied at  $T_0 = 650, 700$  and  $750^\circ\text{C}$ , but the charge was cooled from  $T_0$  to the eutectic ( $550^\circ\text{C}$ ) at  $5^\circ\text{C hr}^{-1}$ . The furnace power was then turned off and the crucible allowed to cool to room temperature. The effect of variation of crystallization temperature on the final crystal sizes and number was also studied.

### 3. Observations and discussion

The solubility of calcium molybdate at different temperatures is shown in figure 1. The observed increase in solubility with temperature is quite favourable for the crystal growth. The charge was deliberately heated at  $50^\circ\text{C}$  above  $T_0$ , to ensure removal of any undissolved excess nuclei which might have remained at  $T_0$ ; failure to carry this out usually resulted in considerable spurious nucleation. Calcium molybdate crystallized as tetragonal bipyramids with well-developed (011) faces. The average crystal lengths  $l_t$  and widths  $w_t$  were both measured using a travelling microscope (least count  $0.001\text{ cm}$ ). The  $l_t$  (cm) vs  $t$  (hr) and the  $w_t$  (cm) vs  $t$  (hr) plots are shown in figure 2. One observes that the crystal size increases with increasing crystallization period and the growth rate is higher at larger temperatures. However, after about 10 hr of cooling the change in crystal size was very small, giving a final, almost consistent size,  $l_{\text{fin}}$  and  $w_{\text{fin}}$ . Probably, the limiting growth rate is imposed by surface kinetic processes, such as dissolution, ledge integration of kinks and steady removal of solvent molecules from the surface. At times, spontaneous nucleation of further crystals might also limit the experimental, maximum feasible, growth rate (Laudise 1963).

## Kinetics of calcium molybdate crystallization

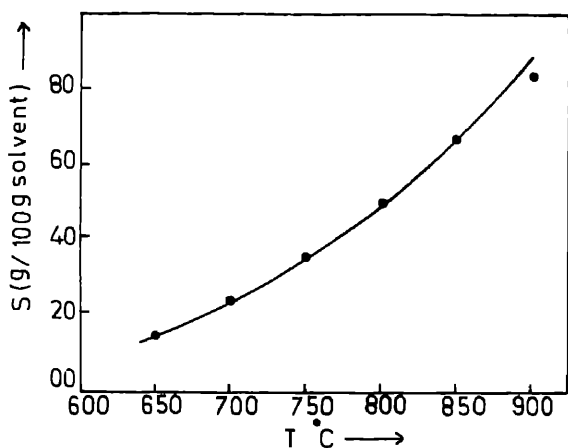


Figure 1. Solubility of  $\text{CaMoO}_4$  in LiCl at different temperatures.

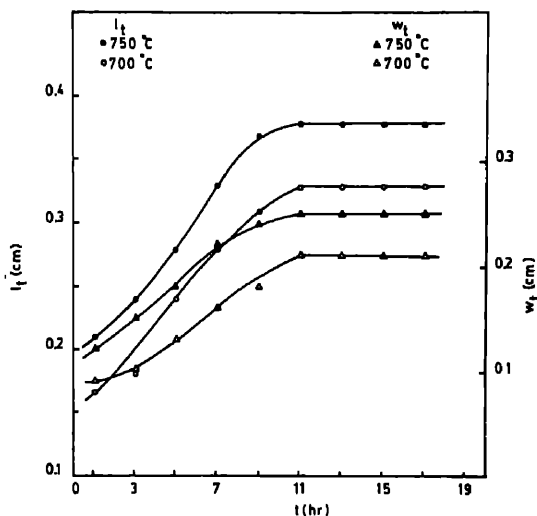


Figure 2. Variation of average crystal length and width at different cooling periods 700° and 750°C.

The degree of crystallization,  $\alpha_t$ , measured by the ratio between the amount of substance crystallized to the total amount able to crystallize, is defined as (N 1964)

$$\alpha_t = (C_0 - C_t) / (C_0 - S),$$

where  $C_0$  is the concentration at  $t=0$ ,  $C_t$  the instantaneous concentration  $S(=C_{\text{sat}})$  the solubility. One can also write,

$$\alpha_t = l_t^3 / l_{\text{fm}}^3$$

where  $l_t$  and  $l_{fin}$  are instantaneous and final lengths, respectively. It is evident that since  $l_t$  is sensitive to the cooling time (figure 2),  $\alpha_t$  becomes a function of the crystallization period and this relationship for 700° and 750°C is plotted in figure 3a,  $\alpha_t$  increases monotonically with time, reaching >0.9 after about 9 hr of crystallization.

Crystal growth rates in unstirred solutions of low permeability are generally controlled by the rate of diffusion of material on different growth faces. The deposition rate of the metal salt ions on growing surfaces from low viscosity LiCl melt, at any time, would then be expressed by the relation (Mullin 1961; Nielsen 1964; Treybal 1968)

$$\frac{dl}{dt} = \frac{2 \text{ Sh } \Phi_1(\varepsilon) D \Delta C_t}{l_t} \frac{\rho_f}{\rho_x} \text{ cm/sec} \quad (3)$$

where Sh is the Sherwood dimensionless function,  $\Phi_1(\varepsilon)$  an overall shape permeability factor,  $D$  the diffusion coefficient of metal salt ion,  $\text{Ca}^{+2}$ ,  $\Delta C_t$  the instantaneous excess  $\text{CaMoO}_4$  concentration expressed in g/g solution ( $dl/dt$  however depends on  $\alpha_t$  through  $\Delta C_t$ ),  $\rho_x$  the crystal density and  $\rho_f$  the fluxed-melt density.

In the present case of unstirred molten solution where the natural convection is very poor,  $\text{Sh} \approx 2$  (Treybal 1968), one obtains

$$dl/dt = (2 K_{Dl} \Delta C_t) / l_t \text{ cm/sec}, \quad (4)$$

where  $K_{Dl}$  is the rate constant (dependent on the permeability factor) for diffusion-controlled growth of the longer crystal-pyramid side. A general solution of equation

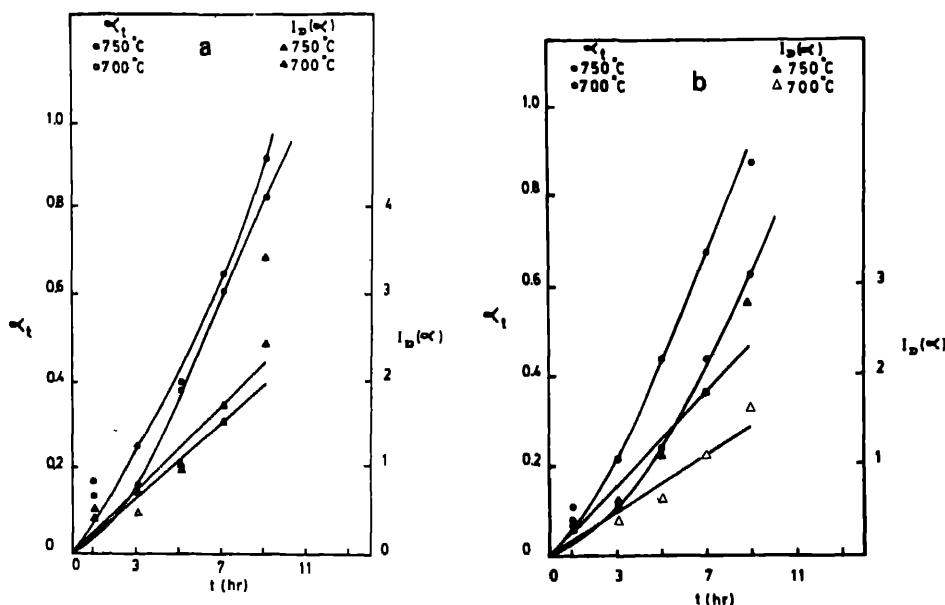


Figure 3. Degree of crystallization  $\alpha_t$  and  $I_D(\alpha)$  at different cooling periods for 700° and 750°C. a. for length b. for width.



(4) for all  $\alpha_t$  values can be given as,

$$I_D(\alpha) = \int_0^\infty \frac{d\alpha}{\alpha^{1/3}(1-\alpha)} = \left( \frac{12K_{DI}\Delta C_0}{l_{fin}^2} \right) t = t/K_D.$$

The rate constant of metal salt deposition  $K_D$ , having the dimension of time, contains all physical constants of the process, including  $K_{DI}$ ,  $\Delta C_0$  and  $l_{fin}^2$ . Furthermore,  $I_D$  is identified as the dimensionless time, or chronomal, which is a characteristic parameter for diffusion-controlled and polynuclear-layer controlled growth mechanisms. It signifies that if the size of a particle is known at a certain time, one can calculate at constant concentration the time at which it started with zero size. The integral in (5) can be solved using standard methods (Lamer and Dinegar 1950) to give

$$I_D(\alpha) = \frac{1}{2} \ln \left[ \frac{(1-\alpha)}{(1-\alpha^{1/3})^3} \right] - \sqrt{3} \tan^{-1} \left[ \frac{\sqrt{3}}{1+2\alpha^{-1/3}} \right].$$

This equation predicts the overall kinetics of crystallization. The values of the chronomal  $I_D(\alpha)$  obtained with the help of Nielsen's table (Nielsen 1964) are plotted with time as shown in figure 3a for 700°C and 750°C respectively. The two plots are seen to be linear up to  $\alpha_t \approx 0.61$  for 700°C and  $\alpha_t \approx 0.65$  for 750°C. Similarly, the rate of diffusion-controlled growth of the shorter side of the crystal bipyramid

$$dw/dt = (2K_{Dw}\Delta C_t)/w_t, \text{ cm/sec}$$

the Nielsen's relation for this case would be

$$I_D(\alpha) = \left( \frac{12K_{Dw}\Delta C_0}{w_{fin}^2} \right) t = t/K_D,$$

$\alpha_t$  and  $I_D(\alpha)$  vs  $t$  (hr) plots are shown in figure 3b. Both the plots are linear up to  $\alpha_t \approx 0.44$  and  $\alpha_t \approx 0.68$  for 700°C and 750°C respectively.

It is interesting to find the rate constant  $K_{DI}$  and  $K_{Dw}$  at different crystallization temperatures from  $I_D(\alpha)$  vs  $t$  (hr) plots using the relation,

$$K_{DI} = \frac{\text{Grad}[I_D(\alpha) \text{ vs } t \text{ plot}] \times l_{fin}^2}{12\Delta C_0} \frac{\text{cm}^2}{\text{sec}}$$

and

$$K_{Dw} = \frac{\text{Grad}[I_D(\alpha) \text{ vs } t \text{ plot}] \times w_{fin}^2}{12\Delta C_0} \frac{\text{cm}^2}{\text{sec}}.$$

The required  $\Delta C_0$  values were estimated from solubility vs temperature data (figure 1), and the results are shown in table 1.

In order that a crystal may grow from solution, the solute must essentially be transported through the solution to the growing surface, desolvated and arranged in conformity with the crystal structure. Therefore, both diffusion and convection are important in controlling the growth velocity. But, when the crystal was relatively smaller than say about 10  $\mu$ , convection may be neglected in view of the very low velocity of growth fronts in normal gravity fields. At this stage, when convection is insignificant, crystal growth takes place principally due to Fick's steady diffusion

concentration gradients. The fact that this state is established around the crystal at a much faster rate than the rate at which the solution in its close vicinity would be replenished, has been proved by Nielsen (1964). This also explains the initially faster growth rate. Such a situation, on an average, exists in the present case upto about 63% (corresponding to  $\alpha_i \approx 0.61$  at  $700^\circ$  and  $0.65$  at  $750^\circ\text{C}$ ) and the remaining growth may, however, be surface-reaction-controlled, approximated by

$$l_t^3 = l_0^3 + K_R(t - t_0),$$

where  $K_R$  is the surface-reaction rate constant.

The fact that the remaining 37% of growth occurs by surface-reaction needs confirmation. This could not be done experimentally because it is not possible to measure the surface tension of solid substances, though some attempts have been made in this direction (Kuznetsov 1957) with non-convincing results. Nonetheless, the fact that the lateral growth rate is diffusion-controlled to only about 44% is corroborative of the pyramidal morphology of the crystal with its  $C$ -axis much larger than either lateral axis.

Further, to understand the effect of crystallization temperature on the final crystal size and the crystal numbers, the final crystal lengths ( $l_{\text{fin}}$ ) and widths ( $w_{\text{fin}}$ ) were measured, and the number  $N$  of crystals that grew from 100 g solution was

**Table 1.** Initial excess solute concentration  $\Delta C_0$  and rate constant at different temperatures

Temp. ( $^\circ\text{C}$ )	$\Delta C_0$ (g/g solution)	Rate constant ( $\text{cm}^2 \text{sec}^{-1}$ )	
		$10^{-4}K_{Dl}$	$10^{-4}K_{Dw}$
700	0.069	0.0776	0.0234
750	0.071	0.1138	0.0526

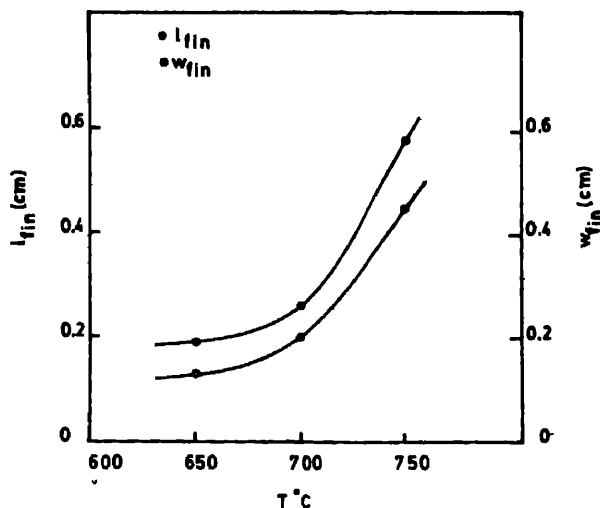


**Figure 4.** Variation of final crystal length and width at different crystallization temperatures.

## Kinetics of calcium molybdate crystallization

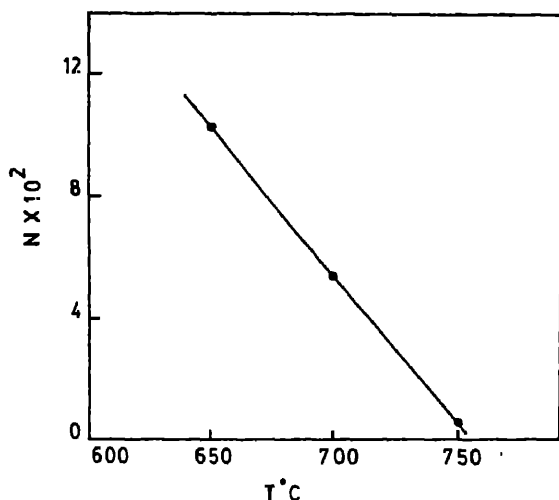


Figure 5. Variation in crystal numbers at different crystallization temperatures.

determined from the average crystal lengths using the relation (Roy and P: 1980)

$$N = (\Delta w_{\text{tot}} / \rho_x f_s l_{\text{fin}}^3) 100 \text{ g solution}^{-1},$$

where  $\Delta w_{\text{tot}}$  is the total weight of crystals forming from 100 g solution cooled the temperature range  $T_0$  to  $T_{\text{eut}}$  (eutectic temperature = 550°C),  $\rho_x$  is the density and  $f_s$  is the shape factor determined by the volume  $V$ ,

$$V = f_s l^3.$$

The effect is shown graphically in figures 4 and 5, revealing that the crystal increases while the crystal number decreases with increasing crystallization temperature. This supports the general expectation that the smaller the crystal concentration the larger will be the crystal size in a growth process.

## Acknowledgement

One of the authors (NMB) thanks UGC, New Delhi for a fellowship.

## References

- Anikin I N 1956 *Dokl. Akad. Nauk.* 110 259
- Elwell D and Scheel H J 1975 *Crystal growth from high temperature solutions* (London: Academic Press)
- Groot W DE 1947 *Phillips Tech. Rev.* 9 321
- Klick C C 1949 *Phys. Rev.* 75 1606
- Kroger F A 1964 *Chemistry of imperfect crystals* (Amsterdam: North Holland) p. 31
- Kuznetsov V D 1957 *Surface energy of solids* (London: HMSO) translated from Russian.
- Lamer V K and Dinegar R H 1950 *J. Am. Chem. Soc.* 72 4847
- Laudise R A 1963 *The art and science of growing crystals*, (ed) J J Gilman (New York: John Wiley)

- Moon R J 1948 *Phillips Tech. Rev.* **73** 1210  
Mullin J W 1961 *Crystallization* (London: Butterworths) ch. 3  
Nielsen A E 1964 *Kinetics of precipitation* (Oxford: Pergamon) ch.3  
Ouwetjes J C 1965 *Mod. Mater.* **5** 188  
Packter A and Roy B N 1971 *Kristall. Tech.* **6** 39  
Packter A and Roy B N 1974 *Kristall. Tech.* **9** 1361  
Packter A and Roy B N 1975 *Kristall. Tech.* **10** 385  
Packter A and Roy B N 1973 *J. Cryst. Growth* **18** 86  
Packter A 1977 *Kristall Tech.* **12** 729  
Roy B N and Packter A 1980 *J. Cryst. Growth* **49** 368  
Schroedger J B and Linares R C 1966 *Prog. Ceram. Sci.* **4** 195  
Treybal R E 1968 *Mass transfer operation* (New York: McGraw Hill) ch. 3  
Van Uitert L G 1960 *J. Appl. Phys.* **31** 328  
White E A D 1964 *Tech. Inorg. Chem.* **4** 31

## Thermal transformation in a chrysotile asbestos

A K DATTA, B K SAMANTARAY and S BHATTACHERJEE  
Department of Physics, Indian Institute of Technology, Kharagpur 721 302, India  
MS received 19 December 1985

**Abstract.** Structural changes accompanying thermal transformation in a chrysotile sample of Indian origin upto a temperature of 900°C have been investigated by x-ray diffraction method. The changes in lattice parameters have been systematically measured by the least square refinement technique and the crystallite size and strain defects at different temperatures have been estimated by line profile analysis of the diffraction peaks. The present study confirms the earlier results on stepwise transformation of chrysotile fibres. This sequential transformation has been explained assuming two different types of crystallites as reprotochalcocite and kaolinite.

**Keywords.** Dehydration; transformation; chrysotile; asbestos; x-ray diffraction.

### 1. Introduction

Chrysotile asbestos is of great scientific interest and commercial value because of its complex structure and multiple uses. It belongs to the serpentine group of minerals with 1:1 layers which curl into cylindrical rolls. Its ideal formula per unit cell is  $\text{Mg}_3\text{Si}_2\text{O}_5(\text{OH})_4$  and is built up of alternate half layers of silicate and brucite (magnesium hydroxide). Misfit between the two half layers results in curvature with the longer brucite layer lying on the convex side. The curved layers form cylindrical fibrils with the  $a$ -axis along the fibre axis,  $b$  along the circumference and  $c$  along the radius of the fibres (Brindley and Brown 1980).

Several studies have been reported (Brindley and Zussman 1957; Glasser 1962; Martin 1977; Hey and Bannister 1948; Santos and Yada 1979) using different methods. These results show that chrysotile with the loss of structural water transforms into an anhydrous phase around 600°C followed by formation of enstatite. Finally above 810°C the anhydrous phase recrystallizes into enstatite. However, the exact nature of the entire sequence of this transformation mechanism is yet to be fully understood.

No attempt has so far been made to study this transformation by applying the technique of line profile analysis for estimating the extent of lattice defects which are likely to increase with temperature in this type of mineral with cylindrical structure. Systematic estimation of the crystallite size and strain defects which are present in this type of sample with curved structure as described earlier, in conjunction with accurate measurements of the changes of lattice parameters from the x-ray diffraction patterns at different temperatures may reveal several new information which might suggest a satisfactory model of the entire sequence of transformation. The present work reports the results of studies carried out on a chrysotile sample of Indian origin following this approach.

## 2. Experimental methods

### 2.1 Chemical and differential thermal analysis

A specimen of chrysotile from Cuddapah (India) was selected for the present investigation. The sample was silky fibrous in form and about 1 to 2 cm long. The average chemical composition of the sample is shown in table 1. The result of the thermal analysis is shown in figure 1. It consists of a strong and broad endothermic band with peak at about 660°C followed by a sharp exothermic peak at 814°C characteristic of chrysotile. The broad endothermic peak is, however, marked by a number of small humps resembling necks on either side of the peak corresponding to 595, 715 and 753°C respectively. The finely powdered samples were heated below and above the DTA peak temperatures at 580, 640, 700, 750, 800 and 900°C respectively each for 5 hr.

**Table 1.** Chemical analysis of chrysotile sample at room temperature.

Component	Percentage
SiO <sub>2</sub>	36.72
Al <sub>2</sub> O <sub>3</sub>	Trace
Fe <sub>2</sub> O <sub>3</sub>	2.48
FeO	Trace
TiO <sub>2</sub>	Trace
MnO	0.04
CaO	1.50
MgO	40.10
Na <sub>2</sub> O	0.07
K <sub>2</sub> O	0.04
H <sub>2</sub> O	18.53

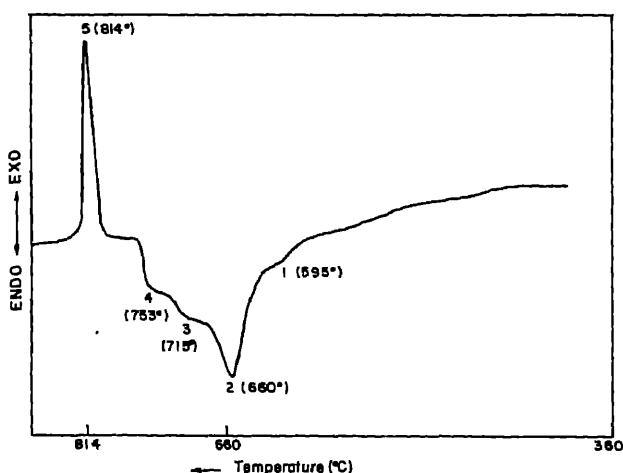


**Figure 1.** Differential thermal analysis curve of chrysotile.

## 2.2 X-ray diffraction analysis

The sample preparation and the x-ray diffraction techniques followed were similar to those described earlier (Mitra and Bhattacharjee 1969, 1970). X-ray Debye Scherrer powder photographs were taken and from the observed  $d$ -values, the changes in lattice parameters were studied by adopting Ito's (1949) method followed by a least square refinement using LAPOD programme (Langford and Marriner 1973).

Diffraction profiles of the samples were recorded in a Norelco x-ray diffractometer at a scanning speed of  $1/4^\circ/\text{min}$  ( $2\theta$ ) using  $\text{CuK}_\alpha$  radiation. Crystallite size and microstrain were obtained from the variance of the corrected line profiles and the relation (Mitra 1965)

$$\frac{W \cos \theta}{\lambda \sigma} = \frac{1}{2\pi^2 P} + \frac{\lambda n^2}{\sigma \cos \theta} \frac{\langle e^2 \rangle}{d^2},$$

where  $W$  is the variance in ( $2\theta$ ) unit of the line profile,  $P$  is the apparent crystallite size in the direction normal to the reflecting planes with interplanar spacing  $d$ ,  $\lambda$  the wavelength,  $n$  the order of reflection,  $\sigma$  the angular range of the profile;  $\langle e^2 \rangle$  the mean square strain and  $\theta$  the Bragg angle of reflection. Thus a plot of  $W \cos \theta / \lambda \sigma$  against  $\lambda n^2 / \sigma \cos \theta d^2$  will be a straight line whose slope gives  $\langle e^2 \rangle$  and the intercept  $P (= t/k)$  where  $t$  is the true particle size and  $k$  is the Scherrer constant.

The partially overlapped lines were resolved accurately by following the method of Mitra and Bhattacharjee (1970) and corrected for instrumental broadening by comparing the profiles of standard silicon sample. The values of crystallite size along the  $a$ ,  $b$  and  $c$  directions and the microstrain values were determined from the variance range plots of the (002), (004), (008) and (0010) reflections. The mean values of these parameters are shown in table 2.

## 3. Results and discussion

The broad endothermic peak which extends between  $568$ – $768^\circ\text{C}$  and marked by several small maxima clearly indicates that dehydration takes place in several steps. It is quite likely that there are different groups of particles affected at different stages. The sharp exothermic peak at  $814^\circ\text{C}$  indicates that rapid recrystallization occurs at this temperature. These results are in conformity with those of the previous workers as mentioned earlier. The x-ray diffraction patterns of samples heated up to  $500^\circ\text{C}$

**Table 2.** Values of crystallite size and r.m.s. strain as obtained from variance analysis of (001) line profiles of chrysotile asbestos.

Temperature ( $^\circ\text{C}$ )	Crystallite size ( $\text{\AA}$ )	r.m.s. strain $\langle e^2 \rangle^{1/2} \times 10^3$
30	425	1.894
580	615	0.245
640	705	0.653
700	1010	0.334
750	2850	0.733
800	730	0.699
900	625	0.698

exhibited the usual lines, characteristic of chrysotile only. However, the patterns of samples at 640, 700 and 750°C were marked by prominent peaks of forsterite also at 3.88, 3.72, 2.77, 2.81 and 2.46 Å in addition to the existing lines of chrysotile. On the other hand, diffraction patterns of the samples at 800 and 900°C contained, besides these peaks of forsterite and chrysotile, characteristic peaks of enstatite at 2.91, 2.55, 2.31 Å respectively. These observations clearly indicate that chrysotile is converted to forsterite and enstatite in steps during this thermal transformation. During dehydration a part of chrysotile is converted to forsterite only, corresponding to the endothermal peak while partial conversion of chrysotile to both forsterite and enstatite takes place at higher temperatures which correspond to the exothermal region.

Table 3 shows the refined values of the lattice parameters of samples heated to different temperatures. Since prolonged heating even for 100 hr at high temperatures does not fully convert chrysotile (Brindley and Hayami 1965), heating for 5 hr in the present case converts only 40% at 800°C. Hence quite justifiably, the lattice parameters measured from the patterns of samples at higher temperatures and shown in table 2, are considered to be that of the unaffected chrysotile. The room temperature data clearly demonstrate the monoclinic symmetry of the present sample. Table 2 shows that the *a*-values initially decrease systematically up to 640°C and thereafter increase gradually till 900°C. The *b*-values also follow the same pattern of variation. On the other hand *c*-values increase steadily till 750°C beyond which they decrease slowly up to 900°C. However, the *b*-values do not follow any systematic variation. Thus the temperature variation of lattice parameters in general shows a contraction along the axial *a*-direction up to 640°C accompanied by an expansion in the radial *c*-direction up to 750°C. Contraction of the lattice in general and along the fibre axis, in particular, has been observed in fibrous chain silicate clay minerals (Bhattacharjee and Lokanatha 1984). Hence the present results are on expected lines.

On heating cavities possibly open up (Martin 1977) resulting in decrease of curvature of the rolled layers. This may lead to an extension of *c* along the radial direction with release of strain and subsequent increase in crystallite size upto 750°C as shown in table 3. The curvature along the surface is likely to change nonuniformly resulting in irregular variation of *b* with dehydration and perhaps is responsible for the slight increase of *a*-values above 640°C. It may be noted here that this process relates only to chrysotile sample and its dehydration products as the measurements are on the pattern of chrysotile only. After completion of dehydration above 750°C,

**Table 3.** Variation of lattice parameters of chrysotile with temperature.

Temperature (°C)	<i>a</i> (Å)	<i>b</i> (Å)	<i>c</i> (Å)	β(deg)
30	5.4158	9.1959	14.5424	95.46
580	5.3529	9.1610	14.8328	90.62
640	5.3433	9.4868	14.8435	89.88
700	5.3667	9.5028	15.0812	90.47
750	5.3736	9.5146	15.1236	92.10
800	5.3927	9.4628	15.0560	95.39
900	5.4022	9.5318	14.9318	96.12



the process proceeds at a faster rate due to mutual migration of Mg and Si leading to the conversion of greater proportion of chrysotile to forsterite and enstatite. The straightening of the lattice probably causes slight decrease of  $c$ -value and increase of  $a$ -values. However, these points need further convincing explanation which is not possible at the present state of our knowledge.

A possible alternative explanation of the gradual transformation of the chrysotile sample into forsterite and enstatite in various steps can be given by assuming existence of two types of crystallites, namely type I and type II, type I being more prone to dehydration than II as reported in kaolinite (Mitra and Bhattacharjee 1969). At lower temperatures only crystallites of type I get dehydrated and as temperature increases, more and more of type II get affected, while the already affected type I crystallites get converted into forsterite. The reaction rate increases above 800°C and conversion to enstatite also starts. This process will continue unabated even beyond 900°C till the conversion is complete.

The electron micrographs of the samples clearly reveal the usual cylindrical form of the fibres. Measurements of the length and width of the fibrils from 10 micrographs show that the average length is of the order of 20,000 Å whereas the breadth is about 2000 Å. Dimensions of the fibrils are not changed appreciably at the initial stage of heating. However at very high temperatures (900°C) the fibres collapse and take the form of lumps possibly due to the formation of forsterite and enstatite. Two representative micrographs of the samples, one at room temperature and the other at 900°C (at magnification 50,000) have been shown in figures 2a, b to illustrate these characteristics.

The values of the crystallite size giving the thickness of the layers along the radial  $c$ -direction and the corresponding microstrain as calculated from the variance analysis of the 001 reflections are shown in table 3. It is seen that the crystallite size increases rapidly from about 400 Å at room temperature to 2800 Å at 750°C beyond which the size falls sharply. The corresponding strain values show a gradual decrease till 700°C and thereafter statistically remain more or less the same upto 900°C. Since the diffraction peaks of forsterite were too small to be accurately measured by variance-range analysis, a rough estimate of the crystallite size has been made from the integral width of the peaks. It has been observed that the crystallite size of forsterite remains almost the same at about 400 Å in the temperature range 600–750°C which corresponds to the endothermal peak in the DTA. Thereafter the size rises sharply in two successive jumps to 700 and 1000 Å at 800 and 900°C respectively. It can be inferred from these data that there is a sharp increase in crystallite size accompanied by decrease of microstrain of the forsterite product above 750°C which marks the end of dehydration and the beginning of recrystallization as shown by DTA. The rapid growth may be attributed to an annealing effect at such high temperature. The rapid fall in crystallite size of chrysotile accompanied by increase of size of forsterite above 750°C is indicative of conversion to forsterite at a faster rate and larger proportion above 750°C. Also the rapid growth of size of the forsterite suggests that defects are removed from the converted forsterite in this temperature range.

As has been observed (Ball and Taylor 1961) and recently confirmed by several workers (Santos and Yada 1979; Martin 1977) the dehydration of chrysotile goes through several steps. In the first stage there is a removal of the hydroxyl ions, in the second stage there is a slow growth of forsterite because of SiO<sub>2</sub> rich regions

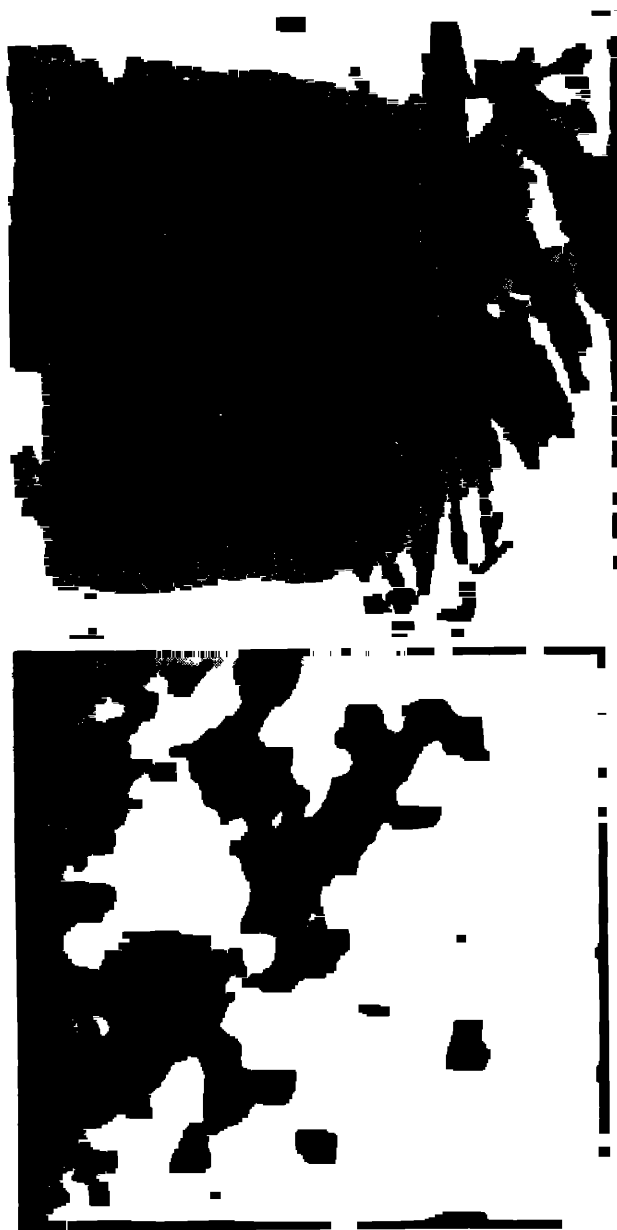


**Figure 2.** Transmission electronmicrographs of chrysotile sample at different temperatures (a) 30°C. (b) 900°C.  $\times 50,000$

inhibiting further recrystallization and a rapid formation of forsterite and enstatite through mutual migration of Mg and Si ions at high temperatures beyond 800°C.

The present observations also confirm the stepwise transformations of the chrysotile fibres leading to the formation of forsterite and enstatite as discussed. However, the present study shows that in the first stage which extends upto about 640°C when dehydration starts with the expulsion of hydroxyl water, the lattice

## *Thermal transformation in asbestos*

transforms rather slowly mainly due to the contributions of the first type crystallites. At the next stage which extends upto 750 marking the complete dehydration, slow conversion of the already affected crystallites of type I forsterite starts while more of type II gets dehydrated with further transformation accompanied by increase of crystallite size in the radial direction owing to release of strain consequent upon possible opening up of cavities in the curved layer as mentioned earlier. This process continues till 750°C. In the final stage beyond 750°C, rapid recrystallization of the already affected crystallites of forsterite and enstatite takes place with changes of a and c in reverse directions. Consequently the size of chrysotile reduces at the expense of development of forsterite and enstatite as revealed by the gradual increase of forsterite and enstatite peaks. As the process continues more and more of type II crystallites are converted till the process is complete.

## **References**

- Ball M C and Taylor H F W 1961 *Mineral. Mag.* **32** 754  
Bhattacharjee S and Lokanatha S 1984 *Trans. Indian Ceram. Soc.* **43** 149  
Brindley G W and Brown G 1980 *Crystal structure of clay minerals and their x-ray identification* (London: Mineralogical Society) p 13  
Brindley G W and Hayami R 1965 *Mineral. Mag.* **35** 189  
Brindley G W and Zussman J 1957 *Am. Mineral.* **42** 461  
Glasser L S D, Glasser F P and Taylor H F W 1962 *Q. Rev. Chem. Soc.* **16** 343  
Hey M H and Bannister F A 1948 *Mineral. Mag.* **28** 333  
Ito T 1949 *Nature (London)* **164** 755  
Langford J I and Marriner G F 1973 Powder pattern programmes, Univ. of Birmingham, Dept. of Physics  
Martin C J 1977 *Mineral Mag.* **41** 453  
Mittra G B 1965 *Acta Crystallogr.* **18** 464  
Mittra G B and Bhattacharjee S 1969 *Am. Mineral.* **54** 1409  
Mittra G B and Bhattacharjee S 1970 *Acta Crystallogr.* **B26** 2124  
Santos H D S and Yada K 1979 *Clays Clay Miner.* **27** 161



## Effect of $H^+$ ion irradiation on surface morphology of $Fe_{40}Ni_{40}$ metallic glass

A J K PRASAD and VAKIL SINGH\*

School of Materials Science and Technology, \*Department of Metallurgical Engineering, Banaras Hindu University, Varanasi 221 005, India

MS received 26 June 1986

**Abstract.** The effect of irradiation by  $H^+$  ions on surface modifications of metallic  $Fe_{40}Ni_{40}B_{20}$ , in the as-quenched, structurally relaxed and crystallized state, has been studied. Swollen regions develop on the surface of the as-quenched and structurally relaxed specimens, whereas blisters form on the surface of the crystallized specimen, under the conditions of irradiation. The results are explained in terms of the distribution of hydrogen in the amorphous and crystallized conditions.

**Keywords.** Metallic glass;  $H^+$  ion irradiation; surface morphology.

### 1. Introduction

The effect of irradiation by gaseous ions like  $He^+$ ,  $Ar^+$  and  $H^+$  on amorphous materials has been reviewed by Nandedkar and Tyagi (1984) and the irradiation effect has been found to be strongly influenced by a number of factors such as the state of the material, specific composition, the implanting ion and the defects resulting from irradiation.

The present study aims at bringing out the effect of  $H^+$  ion implantation on the surface morphology of  $Fe_{40}Ni_{40}B_{20}$  metallic glass in three different states, namely as-quenched, structurally relaxed and crystallized.

### 2. Experimental

Amorphous  $Fe_{40}Ni_{40}B_{20}$  (Vitrovac 0040), 12 mm wide and 40  $\mu m$  thick ribbon was used. Segments (20 mm long) were vacuum sealed ( $\approx 10^{-3}$  torr) and annealed at  $423 \pm 2$  K and  $723 \pm 2$  K separately for 40 min to cause structural relaxation and crystallization respectively in the material (Toloui *et al* 1985). The completely amorphous nature of the structurally relaxed specimen was confirmed by x-ray diffraction.

The as-quenched, structurally relaxed and crystallized specimens were subjected to pre-irradiation electropolishing in an electrolyte containing acetic acid and perchloric acid in 10:1 proportion at 15 V. Irradiation was carried out with  $H^+$  ions of 250 keV to a fluence in the range of  $2 \times 10^{18}$  to  $4 \times 10^{18}$  ions/cm<sup>2</sup> using an analyzed and collimated beam of 3 mm diameter from an AN-400 Van de Graaff accelerator as described earlier (Yadava *et al* 1980).

The changes in surface morphology of the specimens resulting from  $H^+$  ion irradiation were examined by using a scanning electron microscope (Philips PSM 500).

### 3. Results

The scanning electron micrographs in figures 1–3 respectively show the surface features of the as-quenched, structurally-relaxed and crystallized specimens of  $\text{Fe}_{40}\text{Ni}_{40}\text{B}_{20}$  metallic glass following implantation of  $\text{H}^+$  ions to a fluence of  $4 \times 10^{18}$  ions/cm<sup>2</sup>. A large number of swollen regions developed on the irradiated surfaces of the as-quenched and structurally relaxed specimens and consequently the irradiated surface became rough (figures 1 and 2). The average size of the swollen regions developed on the surface of the structurally relaxed specimen (figure 2a) is smaller than that developed on the surface of the as-quenched specimen (figure 1a).

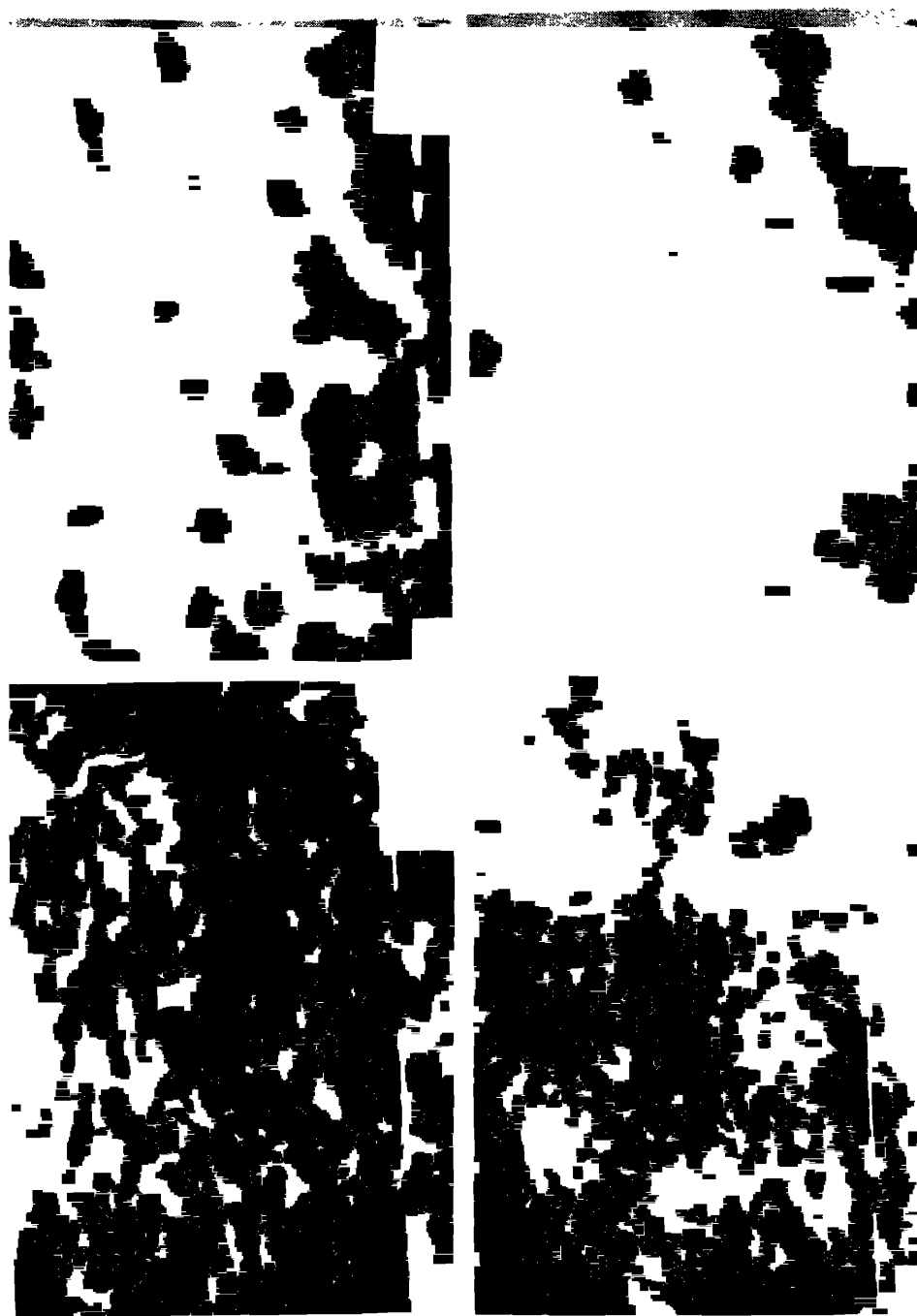
The dark regions in figures 2a, b arise from excessive localized swelling of the matrix around them. The enlarged views of the irradiated surfaces of the as-quenched and structurally relaxed specimens in figures 1b and 2b respectively show that tiny globular features are associated with the swollen surface of the as-quenched specimen (figure 1b), however, no such features are seen on the swollen surface of the structurally relaxed specimen (figure 2b).

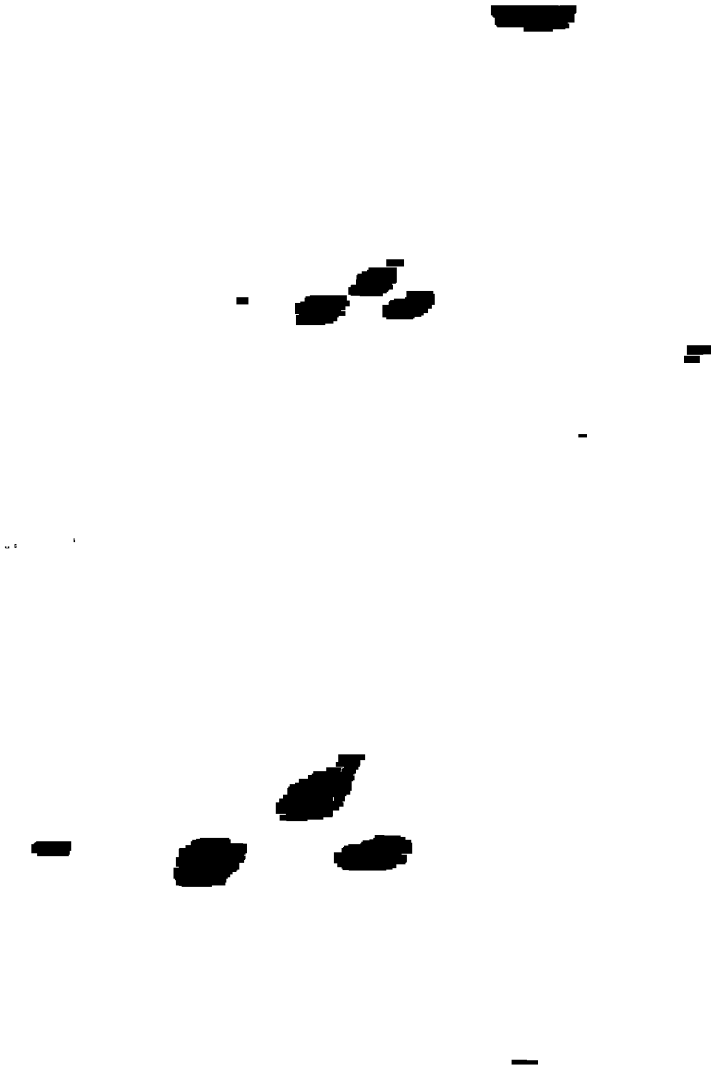
Contrary to these observations, in the case of crystallised specimen, distinct blisters are seen on the surface following  $\text{H}^+$  ion implantation (figure 3a). The domes of the blisters (figure 3b) appear quite smooth.

### 4. Discussion

The implanted  $\text{H}^+$  ions produce defects through displacement damage process before they get thermalized at short depths in the near-surface region. Vacancy like defects produced in the amorphous specimens are usually unstable and collapse into the distributed free volume. The major fraction of the implanted hydrogen remains entrapped, particularly in the thin irradiation-affected zone of the amorphous specimens due to increase in the free volume and absence of any potential trapping site and preferential path, to cause inward migration of hydrogen below the irradiation affected zone. Due to neutron irradiation the amorphous  $\text{Fe}_{40}\text{Ni}_{40}\text{B}_{20}$  has been found to dissociate into small amorphous regions enriched with boron to approach  $(\text{Fe}, \text{Ni})_3\text{B}$  composition and others depleted of boron (Gerling *et al* 1983; Toloui *et al* 1985). Localized stress fields with tensile and compressive stress systems have also been reported to develop simultaneously (Toloui *et al* 1985). Similar compositional fluctuations and stress fields could develop in this material on irradiation by  $\text{H}^+$  ions. High concentration of hydrogen and its clustering at preferred sites in localized regions, with favourable chemical composition and stress system, results in formation of gas bubbles in those regions. The growth and consequent coalescence of the underlying gas bubbles, below those seen as tiny globules at the surface, result in formation of swollen regions (figure 1b).

The smaller size of the swollen regions on the surface of the structurally-relaxed specimen (figure 2a), as compared to the as-quenched one (figure 1a) may be attributed to relatively lower concentration of hydrogen in the irradiation affected zone of the structurally-relaxed specimen. It may occur due to a wider distribution of hydrogen even below the irradiation zone because of the presence of pre-irradiation chemical inhomogeneities which have higher solubility for hydrogen in the structurally-relaxed condition. Also the solubility and diffusivity of hydrogen in the





Figures 3a,b. Crystallized.

structurally-relaxed condition would be less than that in the as-quenched state a  $\text{Fe}_{40}\text{Ni}_{40}\text{P}_{14}\text{B}_6$  (Lin and Johnson 1982). The absence of globules on the two surface of the structurally-relaxed specimen (figure 2b) may thus be attributed to low concentration of hydrogen in the irradiation-affected zone and hence the small number of gas bubbles. Swollen features have also been observed earlier in  $\text{H}^+$  irradiated amorphous  $\text{Ni}_{40}\text{Fe}_6\text{Co}_{20}\text{Cr}_{12}\text{Mo}_6\text{B}_{16}$  (Yadava *et al* 1981) but at a much higher fluence of  $1 \times 10^{19} \text{ H}^+$  ions/ $\text{cm}^2$ . It may be attributed to the higher resistance of amorphous  $\text{Ni}_{40}\text{Fe}_6\text{Co}_{20}\text{Cr}_{12}\text{Mo}_6\text{B}_{16}$  against irradiation-induced decomposition because of its complex chemical composition. The formation of blisters on the surface of the crystallized specimen, following  $\text{H}^+$  ion implantation (figure 3) may be due to the crystalline nature of the material. Crystallization of amorphous  $\text{Fe}_{40}\text{Ni}_{40}\text{B}_{20}$  results in the formation of different phases such as  $\gamma$  (Fe-Ni), (Fe, Ni



and (Fe, Ni)<sub>23</sub>B<sub>6</sub> of varying sizes. Since hydrogen resides in interstitial position metals and alloys and diffuses by jumps between the interstitial sites, solubility and diffusivity of hydrogen would be different in the various crystal phases, depending upon the size, number and interconnectivity of the interstitial sites per unit cell. The distribution of implanted hydrogen would not be limited only to the irradiation-affected zone, but also below the irradiation zone because of high solubility of hydrogen in some of the crystalline phases referred to above. The wide distribution of implanted hydrogen in the crystallized state of the material is further favoured by the interphase boundaries. Though the defect sites produced in the irradiated region would act as trap sites for hydrogen, the interaction of hydrogen with defect sites in metals is weak and hence the interphase boundaries, particularly those associated with tensile stress fields and triple junctions with high stresses would be potential sites for trapping of hydrogen in the crystalline specimen.

The high concentration of hydrogen above a critical level at potential trap sites, at a depth of several hundred Å from the surface, results in nucleation of bubbles. The coalescence of bubbles leads to the formation of penny-shaped cavities. The increase in cavity pressure leads to plastic bulging of the thin layer of material above the cavity to form blisters on the surface of the crystallized specimen (figure 1). Formation of blisters on the surface of the crystallized Fe<sub>40</sub>Ni<sub>40</sub>B<sub>20</sub> following hydrogen ion implantation in the present investigation is in agreement with the earlier observation made in the crystallized Ni<sub>40</sub>Fe<sub>6</sub>Co<sub>20</sub>Cr<sub>12</sub>Mo<sub>6</sub>B<sub>16</sub> (Yadava *et al* 1987).

## Acknowledgements

The authors are grateful to Prof. T R Anantharaman, for his encouragement and interest in the work. Useful discussions with Prof. P Ramachandra Rao, P C Suryanarayana and Prof. S Lele are gratefully acknowledged.

## References

- Gerling R, Schimansky F P and Wagner R 1983 *Scr. Metall.* **17** 203
- Lin R W and Johnson H H 1982 *J. Non-Cryst. Sol.* **51** 45
- Nandedkar R V and Tyagi A K 1984 in *Metallic glasses* (ed) T R Anantharaman (Switzerland: Tl Tech. Pub.) p. 165
- Yadava R D S, Singh N I, Nigam A K and Singh Vakil 1980 *J. Nucl. Mater.* **92** 366
- Yadava R D S, Singh N I, Nigam A K and Singh Vakil 1981 *J. Nucl. Mater.* **101** 124
- Toloui B, Kursumovic A and Cahn R W 1985 *Scr. Metall.* **19** 947



## Periodic crystallization of barium oxalate in silica hydrogel

S M DHARMA PRAKASH and P MOHAN RAO

Department of Physics, Mangalore University, Mangala Gangotri, Mangalore 574 15  
India

MS received 1 March 1986; revised 5 May 1986

**Abstract.** The experimental conditions for obtaining periodic crystallization of barium oxalate in silica hydrogel are investigated. The Liesegang rings formed by the reaction of oxalic acid and barium chloride are studied. The dependence of velocity constant and the spacing coefficient on pH, concentrations of inner and outer electrolytes and temperature have also been studied and a possible mechanism for the behaviour is suggested. The deviations from Isemura's general observations are interpreted by considering the microcrystals constituting the rings and the irreversibility of inner and outer electrolytes.

**Keywords.** Barium oxalate; silica hydrogel; periodic crystallization.

### 1. Introduction

Periodic precipitation in the form of concentric rings was first observed by Liesegang (1896) during his experiments of chemical reactions in gels. Several theories of the Liesegang ring phenomenon have been proposed viz the supersaturation theory (Ostwald 1897; Wagner 1950), the absorption theory (Bradford 1922; Dhar and Chatterji 1922; Shinohara 1970), the coagulation theory (Dhar and Chatterji 1922), the diffusion wave theory (Ostwald 1925), the comprehensive theory (Hedges 1935) and the flocculation theory (Shinohara 1970). All these theories only partially explain the experimental observations. Two laws govern the Liesegang phenomenon. The first one is the spacing law given by Jablczynski (1923)

$$X_n = aS^n,$$

where  $X_n$  is the distance of the  $n$ th ring from the origin of diffusion, and  $a$  and  $S$  are constants,  $S$  being known as the spacing coefficient. The second law is the time law of Morce and Pierce (1903),

$$(X_n/t_n^{1/2}) = K$$

where  $X_n$  is the distance to which the precipitate penetrates in time  $t_n$  and  $K$  is the velocity constant.

The present paper reports our investigation of the conditions for obtaining periodic crystallization of barium oxalate in silica hydrogel. The effects of various factors like the temperature, the concentration of the inner and outer reactants and the pH of the gel medium are considered.

### 2. Experimental

Experiments were carried out in Corning glass test tubes (inner diameter 2.5 cm, length 25 cm). The chemicals used were: sodium metasilicate, oxalic acid (AR) and

$\text{BaCl}_2 \cdot 2\text{H}_2\text{O}$  (AR). The gel was set by mixing sodium metasilicate solution of specific gravity, 1.03 with aqueous solution of 0.5 M oxalic acid in proportions such that the pH of the resulting solutions lay at 4.15, 4.35, 4.55, 4.75 and 4.95 measured immediately after mixing. Barium chloride solutions of 0.7, 0.5, 0.3 and 0.1 M concentration were carefully poured into the tubes over the set gel. The experiments were performed at 31, 37, 43 and 49°C. Cathetometer was used for measuring the position of the rings. Well-spaced rings were nucleated after 20–30 minutes. The time of formation and distance of each ring was recorded. The constants  $K$  and  $S$  for individual rings and hence for each experimental tube were computed. The Liesegang rings formed in the range are displayed in figure 1.

### 3. Observations and discussion

In accordance with the time law of Jablczynski (1923), the velocity constant  $K$  is independent of  $X_n$  and  $t_n$ . Similarly the spacing co-efficient  $S$  is independent of the order of the ring according to the spacing law of Morcé and Pierce (1903). But it is observed that both  $K$  and  $S$  depend on the concentration of the inner and outer electrolytes and their diffusion coefficients.

#### 3.1 Variation of $K$ and $S$ with pH

In figure 2, time and space constants are plotted against pH of the reaction medium, taking temperature and concentration of the outer electrolyte as fixed parameters. The graphs reveal that as the pH of the gel medium increases, the velocity constants ( $K$ ) and the space constants ( $S$ ) decrease. The points on the graph for  $S$  at different temperatures overlap and show small changes in the value of  $S$  with temperature.

Though the pH is the measure of acidity of the gel, it also indicates the concentration of inner electrolyte (or oxalate ions in the present case). Hence, for a particular concentration of the outer electrolyte both  $K$  and  $S$  decrease almost linearly with increase in the concentration of the inner electrolyte. Similar results have been reported from the studies of Liesegang phenomena of various systems (Gnanam *et al* 1979; Kanniah *et al* 1979; Arora *et al* 1982). Thus the inner electrolyte also plays an important role in the Liesegang phenomenon (Matalon and Packter 1955).

The observed decrease of  $K$  can be attributed to the increased hardness of the gel which in turn decreases the diffusion rate and increases the time of ring formation. The decrease of  $S$  in the present study may be explained as follows: At higher pH, though a lesser amount of  $\text{Ba}^{2+}$  ions diffuse through the pores of the hardened gel, the concentration of the uniformly spread oxalate ions is quite high. So, when a ring is formed, oxalate ions in the immediate vicinity would be sufficient to complete the reaction with the incoming barium ions. The region from which the oxalate ions diffuse upwards is small and consequently the rings tend to form more closely separated in harder gels, thereby showing relatively lower values of  $S$ .

#### 3.2 Variation in space and time constants with the concentration of the outer electrolyte

Figure 3 depicts the variation of  $K$  and  $S$  with the change in the concentration of feed solution at different pH of the reaction medium and different temperatures.

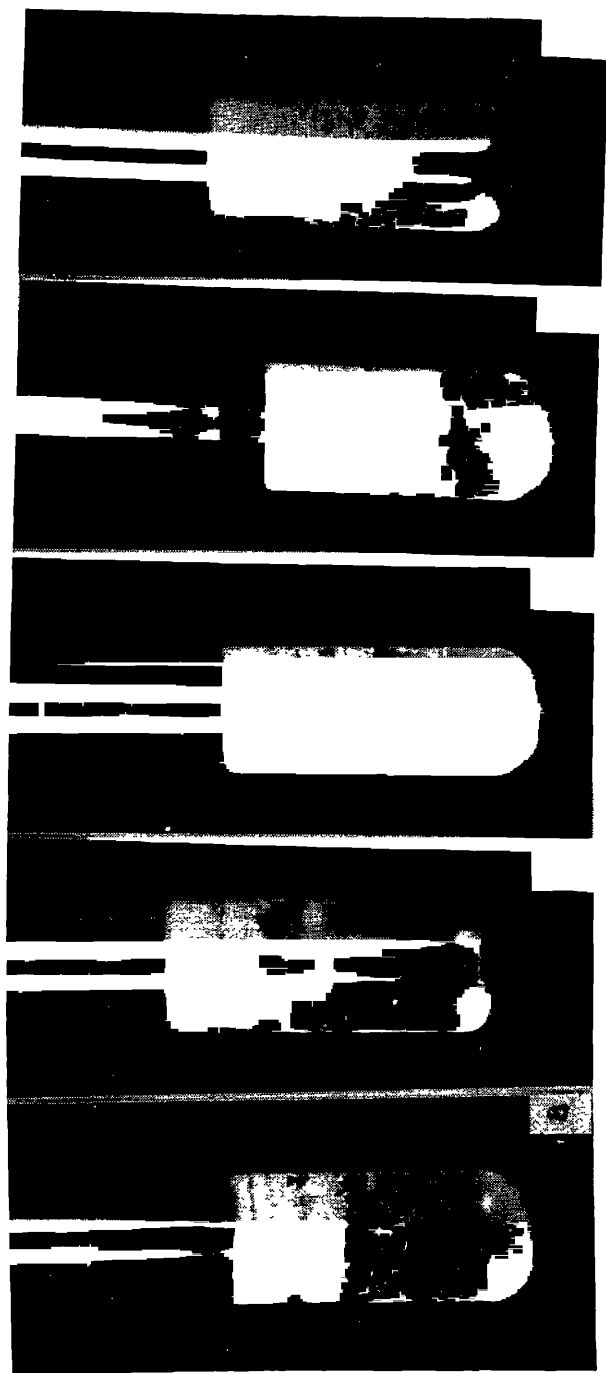


Figure 1. Liesegang rings formed in gel at room temperature (31°C) 0.5 M oxalic acid as inner and (a) 0.1, (b) 0.3, (c) 0.5, (d) 0.7 M barium chloride as outer electrolytes (e) band of precipitation in the gel of basic pH.

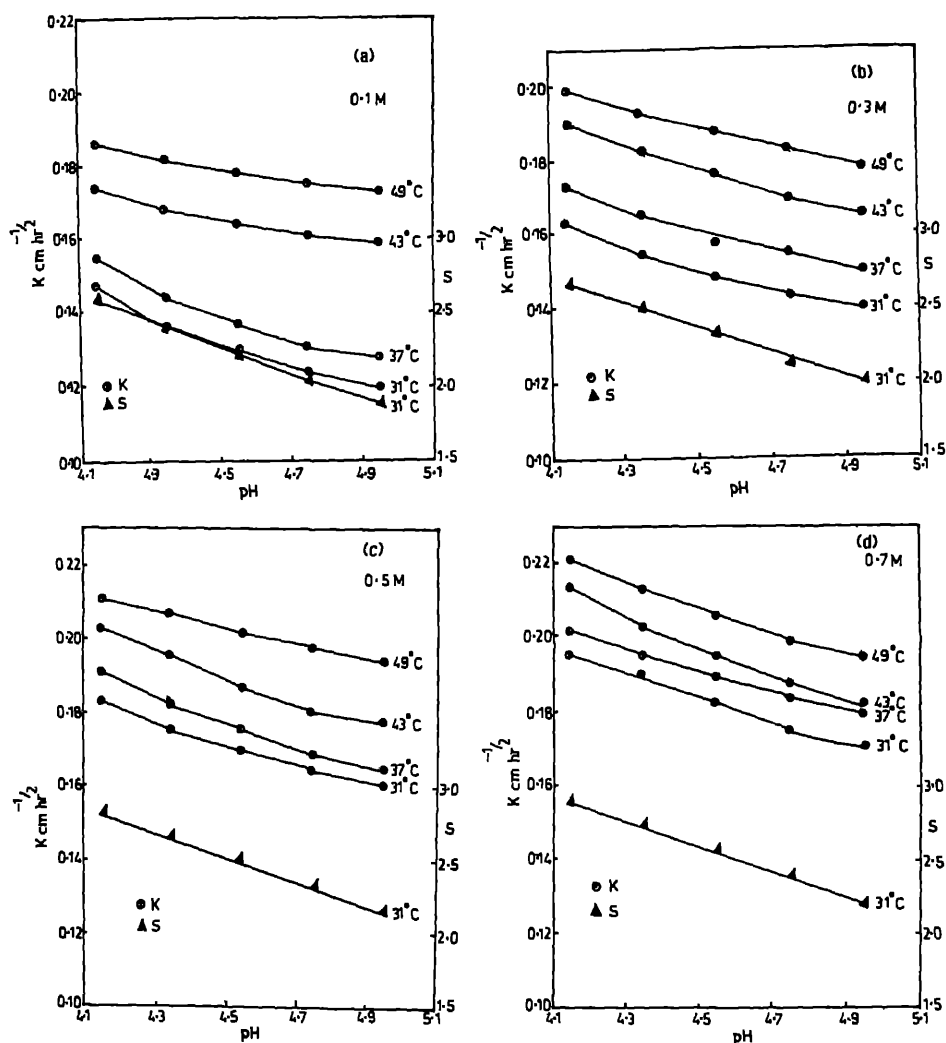


Figure 2. Plot of time constant  $K$  and space constant  $S$  against gel pH at various temperatures using (a) 0.1 M (b) 0.3 M (c) 0.5 M (d) 0.7 M  $\text{BaCl}_2$  solutions.

With increased concentration, the diffusion rate of  $\text{Ba}^{2+}$  ions is enhanced which explains the greater value of velocity constant  $K$ . When a larger amount of outer electrolyte diffuses fast into the system containing uniformly distributed inner electrolyte, precipitation begins at the interface and the ring formation occurs below the interface, the growth of which is facilitated from the stoichiometric interior ions diffusing up to the position of the nucleated ring to provide nutrients to the growing crystals. This leaves a larger space below the ring which is depleted of inner electrolyte. Therefore, for the next ring to nucleate, the outer ions have to cross over this barren depletion region to meet with the other reactant. Since the passage is clear without any inner electrolyte, and  $\text{Ba}^{2+}$  ions diffuse more rapidly, it leads to increase in  $K$ .

# Periodic crystallization of barium oxalate

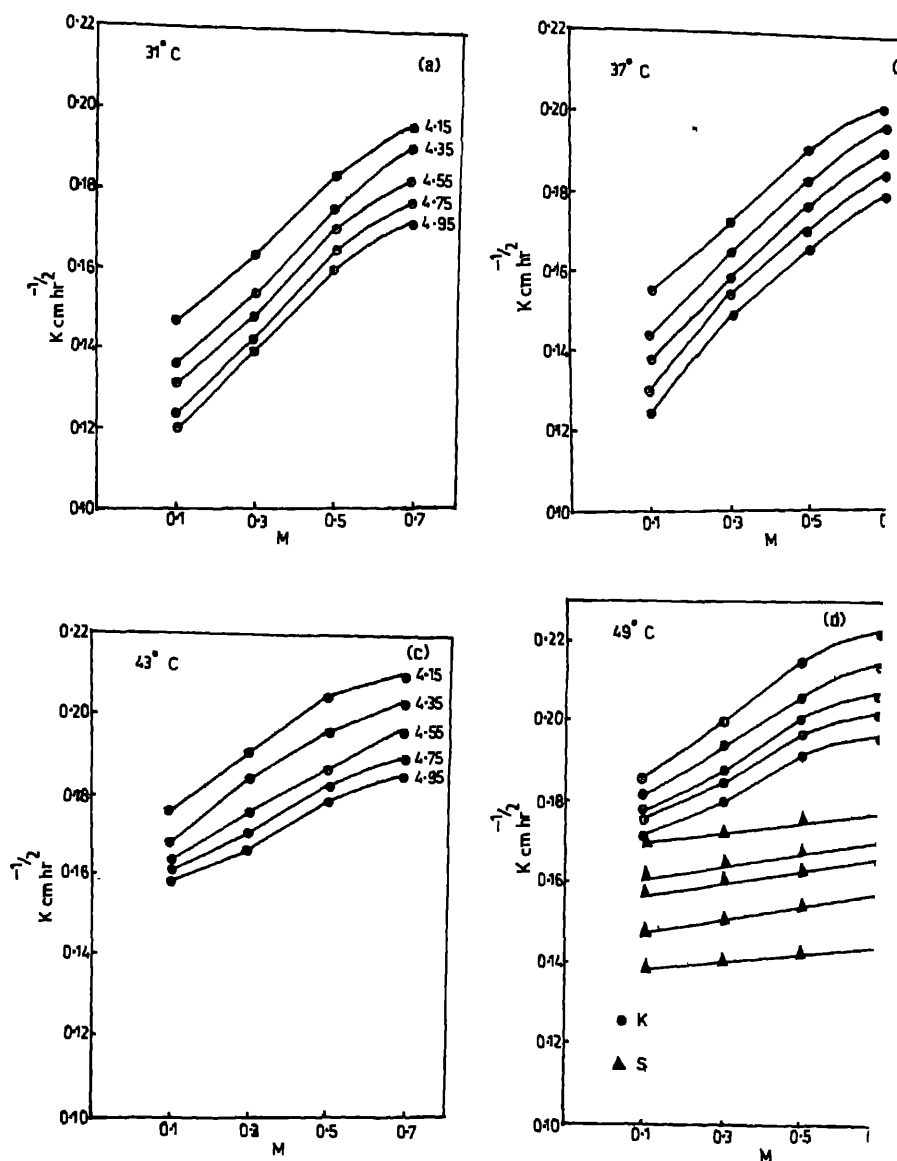


Figure 3. Plot of time constant  $K$  against concentration of  $\text{BaCl}_2$  as outer electrolyte at different pH values at (a) 31°C (b) 37°C (c) 43°C (d) 49°C as well as space constant

According to Isemura (1939), as the concentration of the outer electrolyte increases, the number of bands also increases and the successive interval between them decreases. Barium oxalate rings exhibit a different behaviour so that the number of bands formed does not vary but the spacings between them increase noticeably with higher concentrations of barium chloride. The contradiction results when compared to Isemura's observation can be understood if we consider the nature of rings in both the cases. In amorphous or microcrystalline rings

particles do not tend to grow up after the ring formation, whereas in rings the nucleated crystals do receive nutrients from larger distance growth of the already nucleated crystal is energetically favourable. This is the separation between crystalline rings.

Plot of  $K$  and  $S$  with temperature

As the plot of  $K$  versus temperature and figure 5 the plot of  $S$  versus temperature. The increased diffusion rate at higher temperature may be responsible for the increase in velocity constant. There is no appreciable change of space constant with change of temperature for a given pH and outer electrolyte

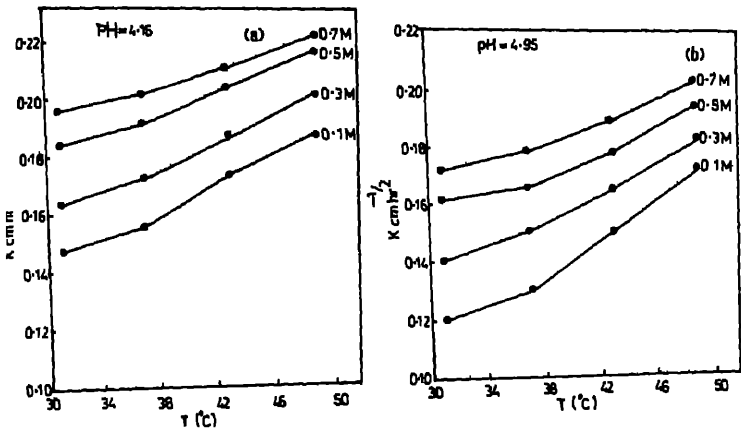


Figure 4. Plot of time constant  $K$  against temperature using different concentration of the outer electrolyte at pH values of (a) 4.15 and (b) 4.95.

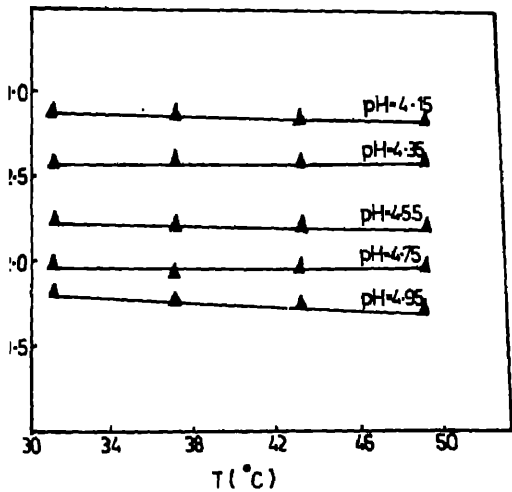


Figure 5. Plot of space constant  $S$  against temperature at different pH values.



## *Periodic crystallization of barium oxalate*

concentration. This may be because of the competitive increase in the rate of diffusion of both the electrolytes.

Another interesting observation is that the barium chloride incorporated gel with oxalic acid as the supernatant solution produces no rings but only a precipitate. This again contradicts Isemura's (1939) results according to which interchanging of the reactants (as inner and outer electrolytes) will not affect the appearance of periodic precipitation. The nonappearance of rings when BaCl<sub>2</sub> is impregnated with the gel is perhaps due to non-diffusion of the heavier barium ions in the upward direction with sufficient velocity required for the ring formation. Continuous diffusion of oxalate ions from the top results in continuous precipitation.

## **References**

- Arora S K, Tomy Abraham and Godebole 1982 *Crystal Res. Technol.* **17** 979  
Bradford S C 1922 *Kolloid Zh.* **30** 364  
Dhar N R and Chatterji A C 1922 *Kolloid Zh.* **31** 151  
Gnanam F D, Krishnan S, Ramasamy P and Laddha G S 1979 *J. Colloid Interface Sci.* **73** 193  
Hedges E 1932 *Liesegang and other periodic structures* (London: Chapman)  
Isemura T 1939 *Bull. Chem. Soc. Jpn* **14** 179  
Jablczynski K 1923 *Bull. Chem. Soc. France* **33** 1592  
Kannaiah N, Gnanam F D and Ramasamy P 1979 *J. Colloid Interface Sci.* **80** 377  
Liesegang R E 1896 *Naturwiss Wochenschr* **11** 353  
Matalon R and Packter A 1955 *J. Colloid Sci.* **10** 46  
Morce H W and Pierce G W 1903 *J. Phys. Chem.* **45** 589  
Ostwald W 1897 *Lehrbuch der allgemeinen Chemie*, Leipzig 788  
Ostwald W 1925 *Kolloid Zh* **36** 380  
Shinohara S 1970 *J. Phys. Soc. Jpn* **29** 1073  
Wagner C 1950 *J. Colloid Sci.* **5** 85



## Studies on etching of gel-grown barium oxalate dihydrate crystals

S M DHARMAPRAKASH and P MOHAN RAO

Department of Physics, Mangalore University, Mangala Gangotri 574 199, India.

**Abstract.** Etch pits produced by selective etchants such as 1 M HCl, 1 M  $\text{HNO}_3$ ,  $\text{BaCl}_2$ , 4 M  $\text{NH}_4\text{Cl}$  and 4 M  $\text{NH}_4\text{Cl}$ –1 M HCl solutions on the as-grown {110} face of barium oxalate dihydrate crystals are illustrated and explained. The kinetics of etching is studied. From Arrhenius plots, the activation energy of etching and the pre-exponential factor are computed. An empirical equation governing the kinetics has been suggested.

**Keywords.** Etching; gel growth; barium oxalate dihydrate.

### 1. Introduction

Etching technique is a powerful tool to study the nature of crystal dislocations. Gilman and Johnston (1956) and Keith and Gilman (1960) showed that etch pits nucleate at the points of emergence of dislocations and other defects on the crystal surfaces. Though a voluminous literature can be cited on the study of dislocation chemical etching, a generally complex etching mechanism (Batterman 1957; Gilman and Lavine 1960; Warikose *et al* 1962) which is at variance with the material and etchant, is not understood properly to-date. Hence, a trial and error method was adopted for the determination of suitable etchant for a material. Since there exist reports in the literature about etching studies on barium oxalate dihydrate crystals, it was considered better to subject the crystals to various dislocation etchants.

The present study reports the effect of etching parameters like temperature, composition and time on selective etch rate with the different etchants used. All etching experiments were conducted on as-grown {110} faces.

### 2. Experimental procedure

The barium oxalate dihydrate crystals employed for etching studies were grown by the gel method (Dharmaprakash and Mohan Rao 1985). A number of analytical grade chemical reagents were examined for possible use as dislocation etchant; viz  $\text{HNO}_3$ ,  $\text{BaCl}_2$ ,  $\text{NH}_4\text{Cl}$ . It was felt necessary to establish the reliability of an etchant to determine the dislocation on crystal faces, for which microscopic examination was made of the successively etched faces. Etch pit size was determined by taking the average of measurements on a number of etch pits at a constant magnification using a filar micrometer eye piece fitted to the optical microscope. Crystals were etched at different constant temperatures between room temperature (31°C) and 40°C. Temperature was controlled using a bath regulated within  $\pm 0.5^\circ\text{C}$ . Etch rate at different compositions of the etchants was calculated from a number of measurements of the pit size.

### 3. Observations, results and discussion

Figures 1–3 depict the etch patterns produced by 1 M hydrochloric acid, 1 M  $\text{BaCl}_2$  and 4 M barium chloride after etching for 30 seconds. The etch pits

produced by 4 M ammonium chloride after etching for one minute is shown in figure 4. Figure 5 represents etch pits formed by a mixture of 1 M HCl and 4 M  $\text{NH}_4\text{Cl}$  after 30 seconds. It can be seen from these figures that the etch pit morphology depends on the nature of etchant used. Some shallow pits on the etched planes are seen together with deep ones. Micropits are also found (figures 1, 2 and 5) which indicate the general dissolution of the surface, because point defects are too sensitive to etching. Individual pits, not endowed with regular symmetry, are formed some of which are flat-bottomed and the others point-bottomed. Such shallow, flat and micropits formed during etching need not necessarily be related to the sites of dislocation intersection with the surface. Point defect clusters, impurity inclusions, surface damage, foreign particles on the surface, and other often in tractable factors, may also lead to the formation of pits on the habit faces. In order to test whether the etch pits are produced at the emergent sites of dislocation, successive etching is tried with each of the etchants. Successive etching results in pit widening and deepening in all the etchants, thus providing reliability of etchants. Some of the etch pits on the same face are not of the same size and depth. This discrepancy can be explained by the studies of Patel and Desai (1965) who postulated that, while the surface is dissolved by the micropit mechanism, new layers are exposed during continued etching, which means that new end points of defects terminating in the layer just below the cleavage face are attacked by the etchants. At the sites of these newly exposed defects the etch points are therefore bound to form. The time lag in the formation of pits is responsible for the non-uniform sizes of etch. In figures 2–4 the point bottoms of some of the rectangular shaped pyramidal pits are shifted from their geometric centre. The eccentricities of the pits can be explained by postulating the existence of inclined dislocation lines in the body of the crystal (Patel 1961). When the etchant attacks the dislocation sites, the pits thus produced will follow the dislocation lines into the body of the crystal. If the dislocation lines are perpendicular to the face, symmetric pits will be produced. On the other hand, for inclined dislocation lines asymmetric pits will result. When a series of dislocations lying in the same slip plane meet a barrier such as a grain boundary, the dislocation pile-up takes place. The row of etch pits shown in figure 6 represents such an example of the pile-up.

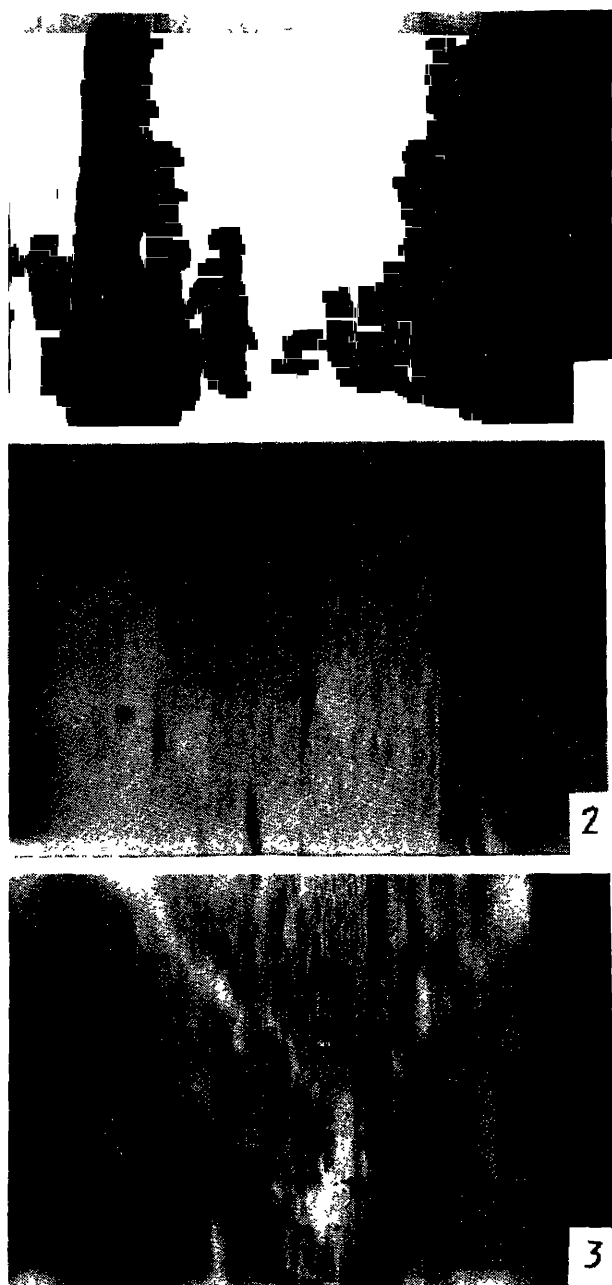
In order to study the kinetics of etching in barium oxalate dihydrate crystals, the etch rates are determined at various temperatures for different concentrations of the etchants. The plots of logarithm of etch rate  $\ln R$  vs reciprocal temperature  $T^{-1}$  of the etchant in the temperature range 31–49°C for 1 M  $\text{HNO}_3$ , 1 M HCl, 4 M  $\text{BaCl}_2$ , 4 M  $\text{NH}_4\text{Cl}$  and a mixture of 4 M  $\text{NH}_4\text{Cl}$  and 1 M HCl are illustrated in figures 7, 8 and 9. Evidently the curves follow the Arrhenius equation:

$$R = A \exp(-E/KT),$$

where  $A$  is the pre-exponential factor,  $E$  the activation energy of the etching process,  $K$  the Boltzmann's constant and  $T$  the temperature of etchant. From these Arrhenius plots, the values of activation energy and pre-exponential factor are calculated and the results are presented in table 1.

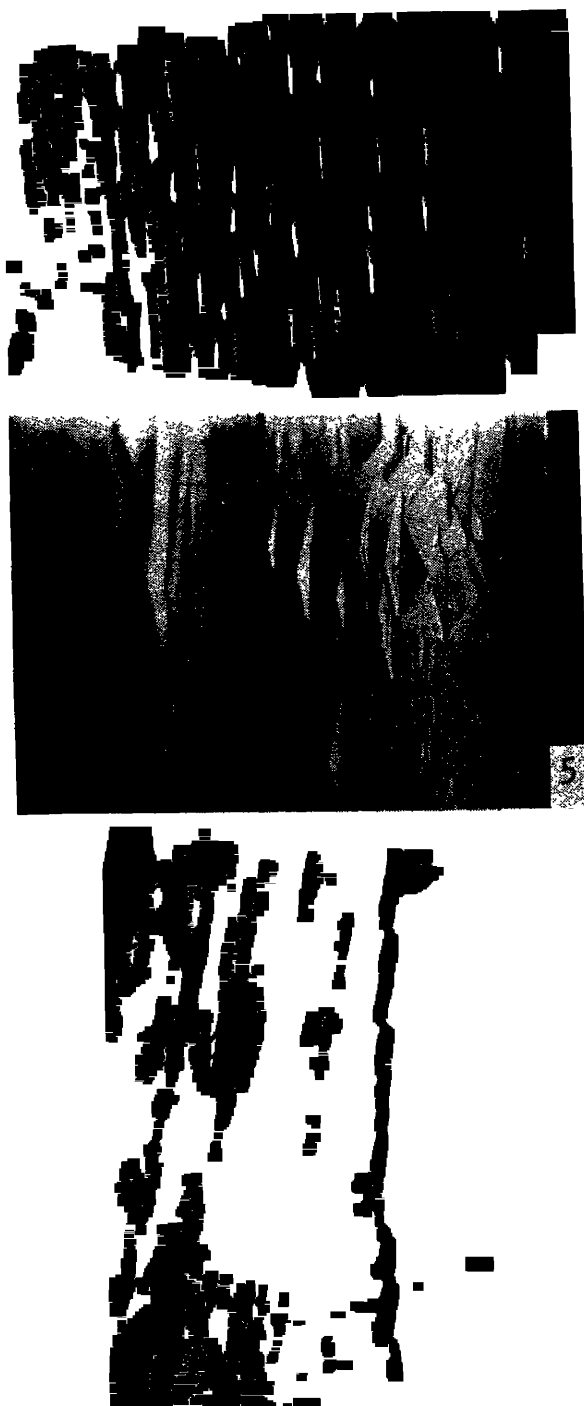
The faster etch rate in  $\text{NH}_4\text{Cl}$ -HCl may be because the fast etching is not sensitive to the energies of the atoms at the surface or to their geometrical configuration (Gatos 1975). It may be the fact that the chemical reaction and diffusion both operate simultaneously making the etching or dissolution process less sensitive to

*Etching of barium oxalate crystals*



Figures 1-3. Etch patterns produced (at 30 sec) by: 1. 1 M HCl. 2. 1 M HNO<sub>3</sub>. 3. 1 M BaCl<sub>2</sub>.

temperature change, thus giving a very low value of activation energy. As the etching proceeds, etchants such as HCl, HNO<sub>3</sub> react with crystals to form oxalic acid which in turn dissolves in water. Therefore these dissolutions are reaction rate-controlled. Among the etchants presently investigated, the etch rate in BaCl<sub>2</sub> is low giving



Figures 4-6. 4, 5. Etch patterns produced (at 30 sec) by. 4. 4 M  $\text{NH}_4\text{Cl}$ . 5. 4 M  $\text{NH}_4\text{Cl}$ +1 M HCl. 6. A row of etch pits on a surface etched with 4 M  $\text{NH}_4\text{Cl}$  (1 min)

## Etching of barium oxalate crystals

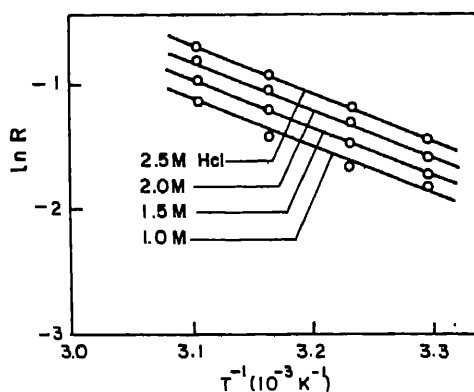


Figure 7. Plot of  $\ln R$  against reciprocal temperature for HCl

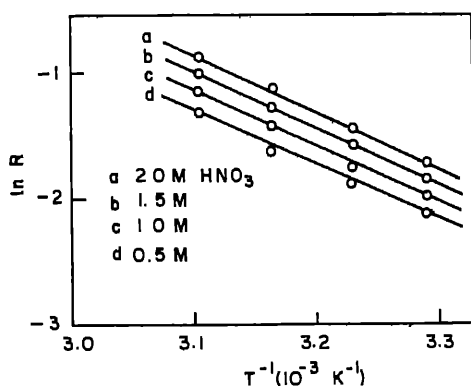


Figure 8. Plot of  $\ln R$  against reciprocal temperature for  $\text{HNO}_3$

highest activation energy. Also the dissolution in  $\text{BaCl}_2$  is diffusion-controlled because of the common ion of the solution and the solvent. The observation of high activation energy characterizes diffusion-controlled dissolution (as of oxalate in barium chloride) is contrary to the observation by Abramson and Tuck (1939) and Tuck (1975) on certain semiconductor materials in which the activation energy for a diffusion process was found to be less than that for a chemically controlled dissolution. It follows, therefore, that the other conclusion of Tuck that the diffusion-controlled mechanism of dissolution is not sensitive to change in temperature is contradicted in the present situation. The values of activation energy are independent of acid concentration (table 1) indicating the dependence of rate on temperature alone. Further, since the value of pre-exponential factor increases with increasing acid concentration, it implies that  $A$  has to be the function of etch concentration. Figure 10 illustrates the graph of  $\ln A$  vs  $\ln C$  from which it can be expressed by the empirical relations

$$A = 11.896 C^{0.3143}, \quad A = 10.8519 C^{0.4444}$$

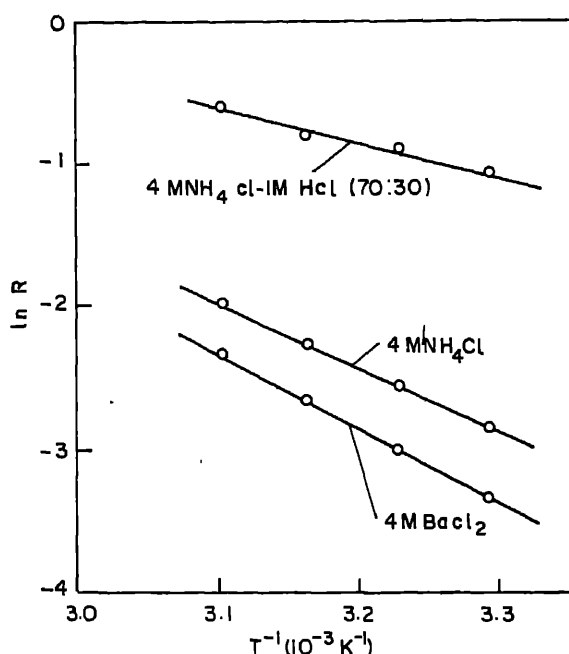


Figure 9. Plot of  $\ln R$  against reciprocal temperature for  $\text{BaCl}_2$ ,  $\text{NH}_4\text{Cl}$  and  $\text{NH}_4\text{Cl-HCl}$

Table 1. Activation energies and pre-exponential factors calculated from Arrhenius plots.

Dislocation etchants	Etchant concentration (M)	Activation energy $E$ (in eV)	Arrhenius pre-exponential factor ( $\times 10^4$ )
$\text{HNO}_3$	0.5	0.36	12.53
	1.0	0.36	14.64
	1.5	0.36	16.33
	2.0	0.36	18.84
$\text{HCl}$	1.0	0.34	5.87
	1.5	0.34	6.82
	2.0	0.34	7.77
	2.5	0.34	8.93
$\text{NH}_4\text{Cl}$	4	0.38	10.28
$\text{BaCl}_2$	4	0.44	92.72
$\text{NH}_4\text{Cl}$ and $\text{HCl}$	4	0.22	00.13

in the case of  $\text{HNO}_3$  and  $\text{HCl}$  respectively. This would enable us to represent the dissolution of barium oxalate dihydrate crystals by writing the Arrhenius equation in the form

$$R = 11.896 C^{0.3143} \exp(-E/KT);$$

$$R = 10.8510 C^{0.4444} \exp(-E/KT),$$

where  $C$  is the etch concentration of  $\text{HNO}_3$  and  $\text{HCl}$  respectively.



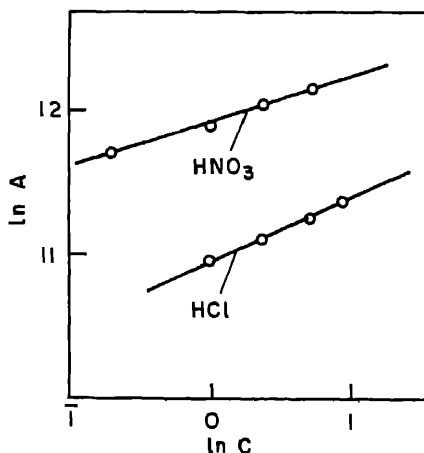


Figure 10. Plot of  $\ln A$  vs  $\ln C$

## References

- Abramson M B and King C V 1939 *J. Am. Ceramic Soc.* **61** 2290  
 Batterman E P 1957 *J. Appl. Phys.* **28** 1236  
 Dharmaparakash S M and Mohan Rao P 1985 *J. Mater. Sci. Lett.* **4** 787  
 Gatos H C 1975 *Crystal growth and characterization* (eds) R. Ueda and J. B. Mullin (Amsterdam: North Holland)  
 Gatos H C and Lavine M C 1960 *J. Appl. Phys.* **31** 743  
 Gilman J J and Johnston W G 1956 *J. Appl. Phys.* **27** 1018  
 Keith R E and Gilman J J 1960 *Acta Metall.* **8** 1  
 Patel A R 1961 *Physica* **27** 1097  
 Patel A R and Desai C C 1965 *Acta Crystallogr.* **18** 373  
 Tuck B 1975 *J. Mater. Sci.* **10** 321  
 Warikose E P, Lavine M C, Mariano A N and Gatos H C 1962 *J. Appl. Phys.* **33** 690



## Determination of molecular weight distribution of polyethylene terephthalate by gel permeation chromatography

K SREENIVASAN and PRABHA D NAIR

Biomedical Technology Wing, Sree Chitra Tirunal Institute for Medical Sciences Technology, Poojapura, Trivandrum 695 012, India.

MS received 18 March 1985; revised 25 April 1986

**Abstract.** Gel permeation chromatography was used to determine the molecular weight distribution of polyethylene terephthalate. Chloroform was used as the mobile phase. Average molecular weights calculated from the chromatogram closely agree with the known values of the samples used in this experiment.

**Keywords.** Polyethylene terephthalate; gel permeation chromatography; Styragel.

### 1. Introduction

A knowledge of molecular weight distribution (MWD) of a polymer is important for understanding the relationship between its structure and properties. Gel permeation chromatography (GPC) is commonly used for determining the MWD. However, the number of solvents which could be used for polyethylene terephthalate (PET) in conjunction with GPC is limited due to the insoluble nature of the polymer in most solvents. Phenols and mixed solvents containing phenols as one of the constituents have been widely used as solvents for PET (Panaris and Pallas 1970; Ede and Dideley 1972). The analysis requires, in certain cases, higher temperatures and this affects the detector response of the instrument. Moreover, the use of phenols as a mobile phase drastically affects the performance of the crosslinked polystyrene gels which are widely used as GPC column material (Snyder and Kirkland 1976). Recently hexafluoroisopropanol (HFIP) has been used as a GPC solvent for PET (Drott 1977). However, HFIP is incompatible with low pore size as well as crosslinked polystyrene packings (Drott 1977; Snyder and Kirkland 1979). Further, the toxic hazards of HFIP are still not clearly known despite its wide use as a solvent for a variety of polymers. Also, the high cost of HFIP restricts its use as a solvent for PET.

In this paper, we describe a GPC method using chloroform as the mobile phase for determining the MWD and average molecular weights of PET.

### 2. Experimental

#### 2.1 Materials

PET samples were from SITRA, India, Analytical grade phenol and chloroform from BDH, India.

## 2.2 Method

About 25 mg of the PET samples were dissolved in 10 ml of chloroform-phenol mixture (1:1 V/V) at about 50°C. One ml of this solution was diluted with 4 ml of chloroform and filtered through a millipore membrane. 100  $\mu$ l of the solutions were used for the analysis.

## 2.3 Chromatography

The instrument employed consisted of a solvent delivery pump (Waters Associates Model 6000A), 440 absorbance detector, U6K injector and a set of five  $\mu$  Styrag columns of pore size  $10^5$ ,  $10^4$ ,  $10^3$ , 500 and 100 Å (particle size 10  $\mu$ m). Freshly distilled chloroform at a flow rate of 1 ml/min was used as the mobile phase and columns effluents were monitored at 254 nm. The columns were calibrated using polystyrene standards (Waters Associates Inc, USA) in chloroform.

## 2.4 Calibration curve

0.1% solutions of polystyrene standards in chloroform were prepared. Peak average molecular weights of the standards chosen were 2,40,000, 1,10,000, 50,000, 9,000 and 4,000. These solutions were filtered and 100  $\mu$ l of the filtered solution were injected into the chromatograph. Chromatography was performed under the same condition as used for the samples above. The retention time of each standard i.e. from the start of the injection to the maximum of the chromatographic peak was plotted on the linear x-axis on semilog paper vs the corresponding value on the logarithmic y-axis of the peak molecular weight of the respective standard. A smooth curve was drawn through the points plotted to obtain the calibration curve.

## 2.5 Computation

The direct calibration method was employed for determining the weight average molecular weight of the PET samples. The data obtained were computed as in DS (1974). The retention times for the start ( $t_1$ ) and finish ( $t_2$ ) of the polym chromatogram were marked and a baseline drawn from  $t_1$  to  $t_2$ . Peak heights of 10 equally spaced points along the GPC curve were measured and tabulated under the following headings: col.1: retention time; col.2: height (mm); col.3: molecular weight; col.4: col.2/col.3; col.5: col.2  $\times$  col.3. The molecular weight averages were determined by the following equations

$$M_n = \Sigma \text{col.2} / \Sigma \text{col.4},$$

$$M_w = \Sigma \text{col.5} / \Sigma \text{col.2}.$$

The equations are based on the theoretical equation

$$\bar{M}^* = \sum_0^i NiMi^b / \sum_0^i NiMi^{b-1},$$

Where  $b$  is a constant, any whole integer, and  $\bar{M}^* = M_n$ , when  $b = 1$ ,  $M_w$  when  $b = 2$ ,  $M_z$  when  $b = 3$ , respectively.

### 3. Results and discussion

Figure 1 shows a typical chromatogram of PET in the mobile phase. The number average and the weight average molecular weights were determined from the chromatogram according to the method discussed above and summarized in table 1

Table 1 also gives the known values of viscosity average molecular weights  $M_v$  for the three PET samples A, B and C. The molecular weights obtained by the chromatographic method can be said to be in good agreement with the known values of  $M_p$  as known that  $M_v$  lies between  $M_n$  and  $M_w$  but closer to  $M_w$  (Allcock and Lampe 1961)

PET is widely used commercially and as a biomedical polymer. In this context, it should be noted that subtle batch-to-batch variation in MWD and molecular weights of PET can cause significant differences in end use performances.

Table 1. Molecular weights of PET samples

Sample	Number average molecular weight ( $M_n$ )	Viscosity average molecular weight ( $M_v$ )	Weight average molecular weight ( $M_w$ )	Dispersity ( $M_w/M_n$ )
A	24,000	54,767	58,175	2.42
B	25,000	40,553	54,669	2.19
C	24,009	56,099	62,147	2.59

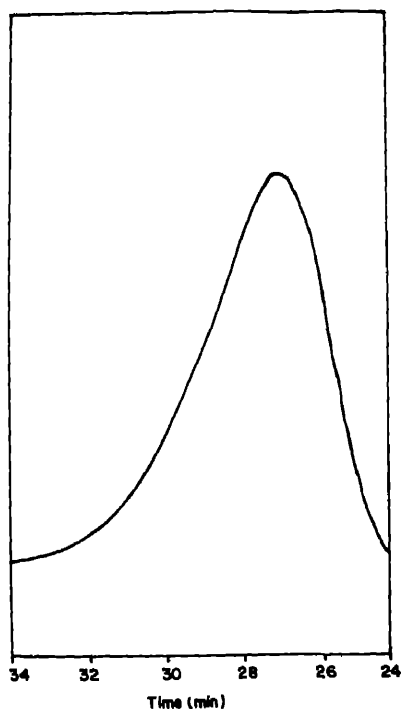


Figure 1. A representative chromatogram of PET.

dependability of a number of properties such as mechanical strength, glass transition temperature etc on MWD and molecular weight further emphasize the need for a simple and rapid method for the determination of molecular weights and dispersity.

Light scattering and viscometric methods, which are also used for molecular weight determinations, however require extensive sample preparation and are too cumbersome for routine determinations. Further, these techniques are incapable of providing any information on MWD.

The hydrodynamic volume of PET molecules in chloroform relative to the conformational status in other good solvents and solvent mixtures has not been assessed. However, the close agreement of the data obtained from the present method with the known values of the viscosity average molecular weight of the samples indicates the absence of any substantial deviation of molecular size in chloroform.

A small quantity of phenol introduced along with the samples elutes after a considerable time and does not interfere with the analysis.

#### 4. Conclusion

The reported method allows the MWD determination of PET at ambient temperature without affecting the efficiency of the crosslinked polystyrene gel columns.

#### Acknowledgement

The authors thank Mr G S Bhuvaneshwar for the PET samples.

#### References

- Allcock H R and Lampe F W 1981 *Contemporary polymer chemistry* (New Jersey: Prentice-Hall) p. 388
- Didely M A 1972 *J. Appl. Polym. Sci.* **16** 493
- Drott E E 1977 *Chromatographic science series* (ed.) Jack Cazes (New York: Marcel-Dekker) Vol. 8, p. 41
- DSO 1974 Waters Associates Application brief, DSO 47, April
- Ede P S 1971 *J. Chromatogr. Sci.* **9** 275
- Panaris R and Pallas G 1970 *J. Polym. Sci.* **16** 493
- Snyder L R and Kirkland J J 1979 *Introduction to modern liquid chromatography* (New York: Wiley-Interscience) Ch. 12

## Space charge limited currents in chlorazole black E dye

J P S CHAUHAN, D C DUBE and S C MATHUR

Department of Physics, Indian Institute of Technology, Hauz Khas, New Delhi 1  
India

MS received 19 September 1985; revised 18 January 1986

**Abstract.** Space-charge-limited-currents have been studied in Chlorazole Black E dye to understand the current-voltage relationship and the nature and distribution of traps present in the dye. Three distinct regions of voltage-current characteristics have been observed probably for the first time. The results have been discussed on the basis of injection theory. There are non-uniformly distributed deep as well as shallow traps.

**Keywords.** Space-charge-limited-current; traps; carrier injection; chlorazole black E

### 1. Introduction

Photovoltaic studies on merocyanine dyes (Morel *et al* 1983; Morel *et al* 1978) generated a lot of interest in the studies of electrical properties of organic solar cells. Sharma (1985) collected the various organic solar cells studied so far along with their efficiencies, open-circuit voltages, fill factors and stabilities. These cells were prepared as polycrystalline thin film. Though a lot of work has been done on organic dye solar cells (Kudo and Moriizumi 1981; Chamberlain *et al* 1981; Kudo *et al* 1981; Yoshimura *et al* 1981; Chamberlain *et al* 1982; Skotheim *et al* 1982; Chauhan 1983; Sharma *et al* 1983; Loutfy *et al* 1983; Sharma 1985), very little attention has been paid towards studying other electrical properties of the dyes. An important parameter controlling the photovoltages in thin film solar cells and the electrical conductivity of solids is the nature of the traps. In most organic molecular crystals the trap distribution is Gaussian (Silinsh 1970; Silinsh *et al* 1974; Nespor 1976; Silinsh 1976; Silinsh *et al* 1978). However other types of distribution cannot be ruled out. The nature of the traps is reflected in the current-voltage relationship. A space-charge-limited-current (SCLC) is considered a good probe into the nature and distribution of traps. We have therefore studied the current-voltage characteristics of Chlorazole Black E dye. Since thin films of dyes in solar cells are polycrystalline our interest was in the study of polycrystalline samples. Therefore powder compacts of unpurified as well as purified material were used for the present studies. The results have been discussed to understand the nature of the traps and their distribution in the dye.

### 2. Experimental

The CBE dye obtained from Sigma Chemical Company, USA was only 50% pure. Since the presence of impurities in organic dyes is a major impediment to the investigation of their electrical properties, the dye was subjected to purification by chemical precipitation, column chromatography and sublimation techniques. For chemical precipitation, a saturated solution of CBE was prepared in triple distilled dimethyl formamide and filtered to remove the

impurities. The pure dye was precipitated out by adding chloroform to the filtrate. This process, repeated three times, gave a high purity material but the yield was low. For chromatographic purification, the dye purified by chemical technique, was dissolved in a mixture of propanol, acetone, triple distilled water and acetic acid in 5:5:3:1 ratio. Finally the dye was sublimed under a vacuum of  $10^{-6}$  torr. Unfortunately the dye could not be put to zone refining. But the purity of the dye was estimated to be better than 99.99%. For space-charge-limited-current studies thin pellets were prepared in a evacuable die (Pyel Unicam). The pressure applied to the die, having  $\frac{1}{2}$  inch diameter was 10 tons. In some preliminary studies it was found that the conductivity of the CBE dye pellet became constant at a pelletising pressure of 10 tons and more. It was also noted that the pelletising pressure does not effect the I-V characteristics at these pressures. The thickness of the samples prepared ranged between 0.09 mm and 0.16 mm. The measuring set-up consisted of a conductivity cell (Chauhan *et al* 1983), a regulated power supply and an electrometer (Keithley 610C). The measurement of current as a function of applied field was taken in dark at room temperature ( $\sim 300^\circ\text{K}$ ). The samples were cycled six times with electric field and all the measurements were taken under steady state conditions. No hysteresis was observed on increasing and decreasing the field. Also no aging effect was observed on I-V curves.

### 3. Results and discussion

Figure 1 shows the current-voltage characteristics of unpurified and purified samples. The applied electric field was cycled between 300 volts/cm and 12000 volts/cm. As

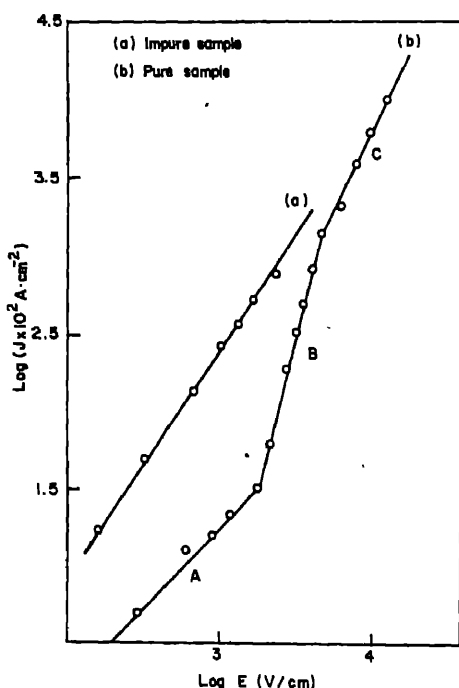


Figure 1. Log  $J$ -log  $E$  plot for chlorazole black E dye.



can be seen the current-voltage curve, for unpurified sample, follows a straight line on a log-log plot, having a slope of 1.5 yielding  $J \propto E^{3/2}$ . For purified sample current-voltage curve on log-log plot can be divided into three distinct straight lines marked A, B and C. Straight line A extends upto  $E = 1800$  volts/cm and has a slope of 0.96 ( $\approx 1$ ) indicating an ohmic behaviour. Line B has a slope of 3.4. It starts at  $E = 1800$  volts/cm and extends upto  $E = 4500$  volts/cm. The third region starts at  $E = 4500$  volts/cm and extends upto 12000 volts/cm.

It is reported (Lyons and Gutmann 1967; Kao and Hwang 1981) that in traps in solids and in solids having only the shallow traps the injected currents follow the Langmuir law after the ohmic region. But when there are shallow as well as deep traps and the distribution of the traps is nonuniform, the current varies as  $E^n$  where  $n > 2$ . This is the situation presently observed for the region marked B. In case there are shallow as well as deep traps and the trap distribution is uniform the injected current varies exponentially with the applied field. Further it has also been reported (Silinsh that the constancy of slope in the  $\log J$  vs  $\log E$  curve in the superlinear region of current-voltage characteristic (region B) with  $n > 2$  within a wide range of intensity values is an absolutely indispensable condition for the validity of the exponential distribution of traps. In the region C the injected current follows the Langmuir law. This suggests that at this stage all the traps are filled and the injection is in the conduction band only. In this situation the injected currents follow the Langmuir law, a situation consistent with our observation in region C. So far no other study on the traps in chlorazole black E dye which we can use to check our conclusions.

Further studies on the CBE dye are in progress and will be reported elsewhere.

## Acknowledgement

Authors wish to thank Professor M L Gulrajani for many useful discussions regarding the purification of the dye. Our thanks are also due to Mr Bala for estimating the purity of vacuum sublimed dye.

## References

- Chamberlain G A 1982 *J. Appl. Phys.* **53** 9
- Chamberlain G A, Cooney P J and Dennison S 1981 *Nature (London)* **289** 45
- Chauhan J P S, Rai R C, Tripathi A K and Mathur S C 1983 *J. Mater. Sc. Lett.* **2** 149
- Kao K C and Hwang W E 1981 *Electrical transport in solids* (New York: Pergamon Press) pp 1-10
- Kudo K and Morizumi T 1981 *Jpn. J. Appl. Phys.* **20** L553
- Kudo K, Shinohara T, Morizumi T, Iriyama K and Sugi M 1981 *Jpn. J. Appl. Phys.* **20** 135
- Loutfy R O, Shing Y H and Murti D K 1983 *Solar Cells* **5** 331
- Lyons L E and Gutmann F 1967 *Organic semiconductors* (New York: John Wiley) pp. 558
- Morel D L, Ghosh A K, Feng T, Stogryn E L, Purwin P E, Shaw R F and Fishman C 1978 *J. Mater. Sc. Lett.* **328** 495
- Morel D L, Stogryn E L, Ghosh A K, Feng T, Purwin P E, Shaw R F and Fishman C 1983 *J. Mater. Sc. Lett.* **88** 923
- Nespurek S and Silinsh E A 1976 *Phys. Status Solidi* **A34** 747
- Sharma G D 1985 *Photovoltaic studies on some organic dyes*, Ph.D thesis, Department of Physics, Institute of Technology, New Delhi
- Sharma G D, Tripathi A K, Mathur S C and Dube D C 1983 *J. Mater. Sc. Lett.* **2** 433
- Silinsh E A 1970 *Phys. Status Solidi* **A3** 817

- Silinsh E A, Jurgis A, Gailis A K and Taure L F 1974 Electrical properties of organic solids, Summer School, Karpacz, Wroclaw, p. 40
- Silinsh E A, Muzikante I J and Taure L F 1978 Electrical and related properties of organic solids, Paper of Int. Conf., Karpacz, Poland, p. 71
- Skotheim T, Yang J M, Otvos J and Klein M P 1982 *J. Chem. Phys.* **77** 6144
- Yoshimura T, Kiyota K, Ueda H and Tanaka M 1981 *Jpn. J. Appl. Phys.* **20** 1671

## Microstrip losses with $\text{Al}_2\text{O}_3$ overlay

K K JOSHI, C DHANAVANTRI, S A GANGAL and R N KAREI  
Department of Physics, University of Poona, Pune 411 007, India

MS received 19 December 1985; revised 20 June 1986

**Abstract.** Microstriplines were coated with  $\text{Al}_2\text{O}_3$  by chemical vapour deposition homogeneous thin film overlay. The paper reports the decrease in the total power loss in such microstrips. The frequency response from 2-6 GHz is studied for the overlay effect.

**Keywords.** Microstrip; attenuation; microwave power; overlay; aluminium oxide; chemical vapour deposition.

### 1. Introduction

Open microstrip is the most convenient type of transmission line for fabricating hybrid and monolithic microwave integrated circuits (MICs). This inhomogeneous open structure has quasi-TEM mode of propagation with electric lines of force dispersing into air which contribute to radiation losses. Pucel *et al* (1968) has an expression for conductor and dielectric losses of microstrips. Denlinger (1974) expressed radiation loss from microstrip resonator as a function of effective dielectric constant ( $\epsilon_{\text{eff}}$ ), substrate thickness ( $h$ ) and a free space wavelength ( $\lambda_0$ ). This depends on the substrate dielectric constant and the distribution of field between substrate and air. This distribution is a function of frequency due to contribution of higher order modes propagating which are unavoidable because of its structure (Young and Sobol 1974).

The fringing fields from microstrip are often used for coupling the power between two close-by strips. The dielectric overlay technique can be used to improve coupling and directivity as analyzed by Haupt and Delysh (1974), Speilman and Lee (1974). Speilman (1974) reported theoretical analysis for machined dielectric overlay on the alumina substrate; this study of course cannot be directly applied to thin film overlay. Experimental observations on thin film overlay on alumina (Weirather 1974) and  $\text{Bi}_2\text{O}_3$  (Karekar and Pande 1976) have been reported, the latter showing an improvement in the quality factor ( $Q$ ) of rejection filter. However, the overlays are inhomogeneous with  $\text{Al}_2\text{O}_3$  substrate.

Only thin film  $\text{Al}_2\text{O}_3$  overlay can give a near homogeneous structure as reported in this study. The improvement in the parameters of microstrip resonators and couplers can be analyzed if the effect of overlay on parameters of a microstrip (like characteristic impedance ( $Z_0$ ), attenuation and radiation) is studied. The total loss of power which includes attenuation and radiation is studied using transmission and return loss observations, with swept frequency technique (2-6 GHz) using WILTRON, computer-aided scalar network analyzer. The effect of overlay on total loss is studied and is further analyzed to distinguish between the effect of overlay on reducing radiation and the effect giving better matching  $Z_0$  changes.

## 2. Experimental

Alumina substrates (1 inch  $\times$  1 inch Alsimag 772) were locally metallized (at IIT, Bombay) by Cr-Au successive vacuum evaporation. The thickness of gold film was then increased by electroplating upto  $8\ \mu$ . The three masks for three-line patterns and one mask for five-line pattern were prepared and photolithographically delineated on the substrate. For each mask three sample sets were taken, out of which sixteen lines could be finally used for this experiment. The  $\text{Al}_2\text{O}_3$  homogeneous overlay was deposited on these patterns by metal organic chemical vapour deposition (MOCVD). The MOCVD system consisted of a resistively heated horizontal flow system (Dhanvantri *et al* 1985). Aluminium isopropoxide was used as a reactant material. The thickness of the overlay was kept constant at nearly  $3000\ \text{\AA}$ . The microwave measurements of transmission and return loss (RL) were performed on a WILTRON network analyzer with an HP-85 microcomputer for correcting the system errors. This gives high accuracy of  $56\ \text{dB} \pm 1.5\ \text{dB}$  (i.e. the limiting power level is about  $\pm 10^{-6}\ \text{mW}$ ).

## 3. Results and discussion

Figure 1 shows a typical transmission and return loss curves before and after overlay, measured using the same connectors, transitions and other components. The average improvement in transmission measured for 16 lines is  $0.3\ \text{dB}$  over the frequency range of  $2\text{--}6\ \text{GHz}$ . For the same samples and frequency range the average decrease in RL is  $5.6\ \text{dB}$  which is further used to calculate the power reflection coefficient ( $\rho^2$ ).

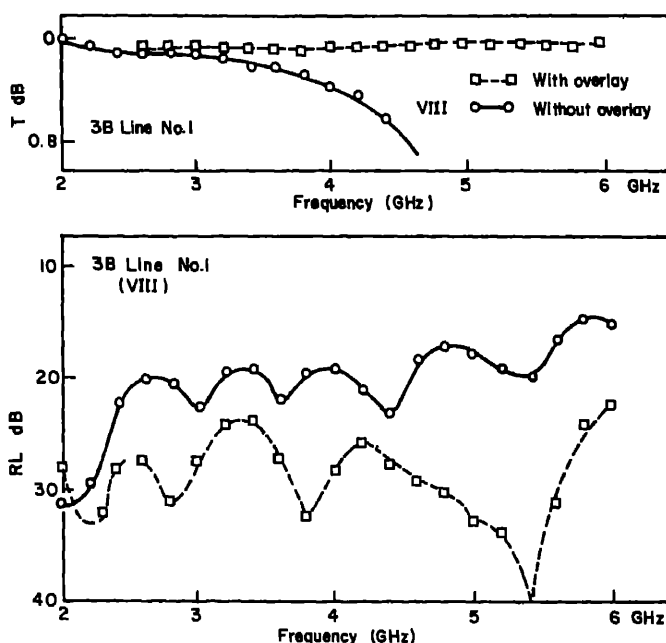
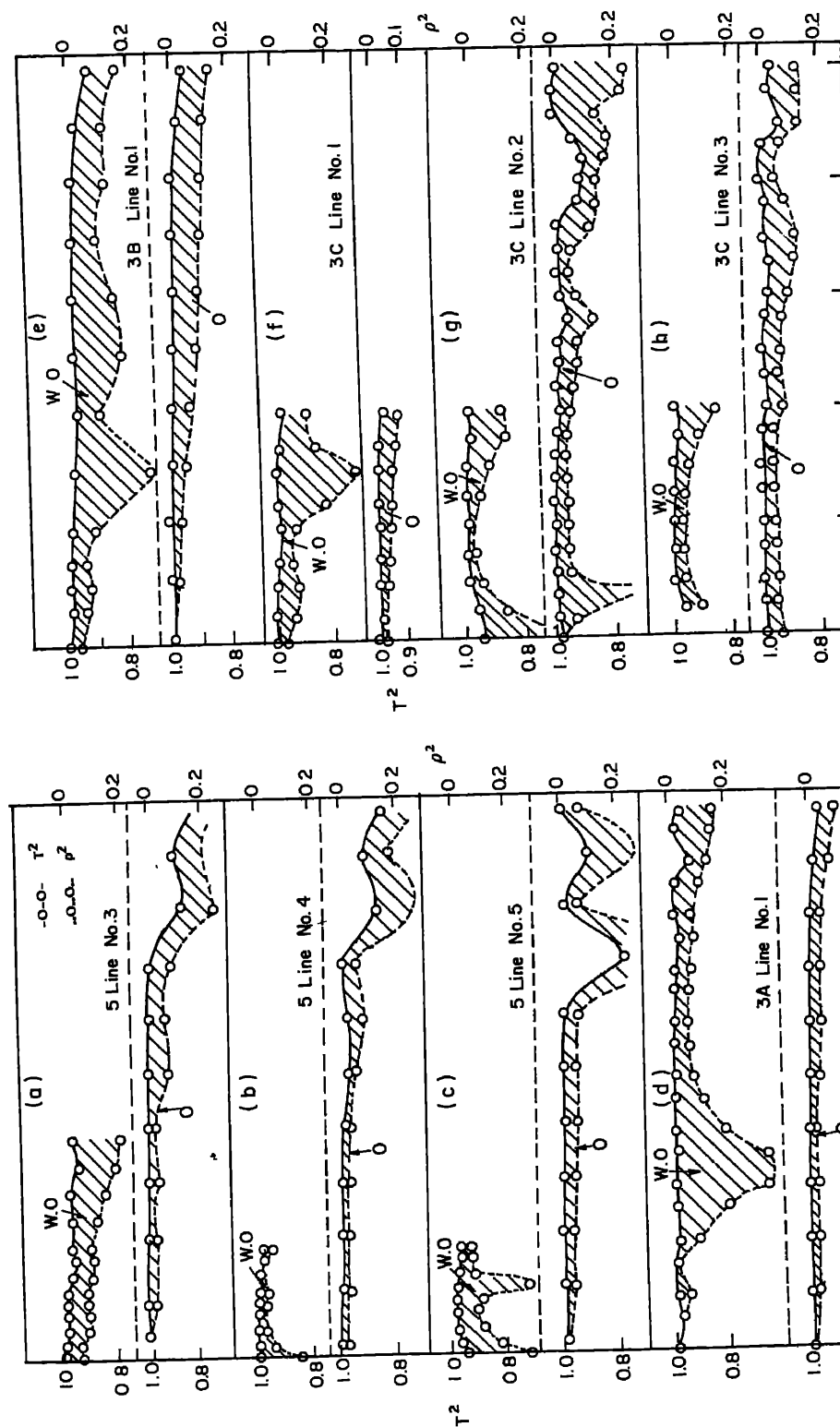


Figure 1. Typical transmission and return loss curves with and without  $\text{Al}_2\text{O}_3$  overlay.

# Microstrip losses with $Al_2O_3$ overlay



The variation of transmission and RL with frequency show resonant dips at harmonic frequencies. Though the coupling effects are not analyzed in detail, the amplitudes of dips decrease with overlay. The complete data of eight different microstrip widths for  $\rho^2$  and  $T^2$  with and without overlay are given in figure 2, where the shaded portion shows the relative power loss ( $1-\rho^2-T^2$ ). Table 1 gives the corresponding average decrease in the loss due to  $\text{Al}_2\text{O}_3$  overlay but no specific relationship between percentage loss and strip width is observable. Further the decrease, which is present at all frequencies between 2 and 10 GHz, is more prominent at higher frequencies (in some cases where the readings are available). On an average the decrease is 1.7% at 4 GHz and 8.8% at 6 GHz indicating better wide band operations. The results are sometimes over shadowed due to the coupling between neighbouring parallel lines.

The decrease in total loss of power from microstrip leads to increased transmission of power, whereas increase in the return loss (i.e. reflection coefficient) indicates change in  $Z_0$ . Characteristic impedance given by  $1/V_p C$  is therefore affected by change in effective permittivity. Our observations show increase in transmitted power ( $T^2$ ) by about 5% and decrease in the reflected power by about 0.8% at 3 GHz. These figures indicate that the increase in transmission is mainly due to the decrease in microstrip losses. If the change in  $\rho^2$  is comparable to the change in transmission ( $T^2$ ) then it can be attributed to the improvement in matching, which is not the case. Thus the decrease in total loss is attributed to the following phenomenon.

When a homogeneous overlay is placed on a microstrip substrate a layer of air is replaced by the  $\text{Al}_2\text{O}_3$  thin film. Thus the propagation mode will tend to move from quasi-TEM towards TEM propagation, reducing the surface mode or other higher order modes, due to increased homogeneity of the medium. Secondly, the fringing field otherwise dispersing in air will be compressed, to some extent, into the overlay region because of its high permittivity. Hence the radiating fields will be confined more to the overlay dielectric region which may have manifested in the observed reduction of radiation loss (particularly because the dielectric and conductor losses cannot be expected to decrease with overlay (Pucel *et al* 1968)). Denlinger (1961) predicted a similar decrease in the radiation loss with increase in the effective permittivity. The reported change in  $\epsilon_{\text{eff}}$  for  $\text{Bi}_2\text{O}_3$  overlay is 0.9 for the thickness

**Table 1.** Actual line widths and average percentage loss for the samples at 4 and 6 GHz.

Width $W$ (cm)	Decrease in percentage loss ( $1-\rho^2-T^2$ ) $\times$ 100%	
	4 GHz	6 GHz
0.057	4.5	15.0
0.050	2.0	9.0
0.052	1.0	4.0
0.054	5.0	2.0
0.062	0.0	8.0
0.064	3.5	15.0
0.066	1.0	—
0.069	0.5	—

## *Microstrip losses with $Al_2O_3$ overlay*

1.3  $\mu$  (Pande 1976). The change in percentage radiation loss is about 1–2% for change in  $\epsilon_{eff}$ , which can be considered as the maximum limit of change in percentage radiation in our study. Hence the rest of the average decrease in radiation loss, especially at a higher frequency, may be attributed to the change in the propagation mode.

## **Acknowledgements**

One of the authors (KKJ) is thankful to Prof. S Mahapatra and Prof. S M Shrivastava of IIT Bombay for making available fabrication and measurement facilities for this work.

## **References**

- Dhanavantri C, Karekar R N and Rao V J 1985 *Thin Solid Films* **127** 85  
Denlinger E J 1969 *IEEE Trans. Microwave Theory Tech.* **17** 235  
Haupt G and Delysh H 1974 *Electron. Lett.* **10** 142  
Karekar R N and Pande M K 1976 *IEEE Trans. Microwave Theory Tech.* **24** 262  
Lee Y S 1974 *IEEE Trans. Microwave Theory Tech.* **22** 66  
Pande M K 1976 *Studies on microstrip circuits with special reference to thin film  $Bi_2O_3$  overlay* Thesis, University of Poona, 142  
Pucel R A, Masse D J and Hertwig C P 1968 *IEEE Trans. Microwave Theory Tech.* **16** 6  
Spielman B 1974 *Analysis of Electrical characteristics of edge-coupled microstriplines with a  $Bi_2O_3$  overlay* NRL Report 7810  
Weirather R R 1974 *IEEE Trans. Microwave Theory Tech.* **22** 71  
Young L and Sobol H (eds) 1974 *Advances in microwaves* (New York: Academic Press) Vol. 8, 1





## Thermoluminescence of alkali halides doped with alkaline earth impurities

A R LAKSHMANAN and S V MOHARIL\*

Division of Radiological Protection, Bhabha Atomic Research Centre, Bombay 400  
India

\*Department of Physics, Nagpur University, Nagpur 400 010, India

MS received 31 March 1986; revised 12 May 1986

In this note we elaborate some points on LiF mentioned in the review article "Thermoluminescence of alkali halides doped with alkaline earth impurities" Deshmukh and Moharil (1985), hereafter referred to as paper I.

(1) The last sentence in § 3.1 of paper I states "In recent years, the 285°C peak been correlated with the 310 nm band (Lakshmanan *et al* 1982)". This should be as "In recent years, the 285°C peak (peak No. 7 according to the notation of St *et al* 1971) has been correlated by Lakshmanan *et al* (1982) with two-electron centres". Lakshmanan *et al*'s (1982) studies have shown that there is a conversion between peak 7 and 450°C (peak 10) centres just as one would expect from  $Z_2 \rightleftharpoons Z_3$  trap conversion. This has prompted them to suggest that peak 7 correlates with  $Z_2$  centres; not to be confused with 310 nm band as assigned by Jain and Kos (1976). Peak 7 optical absorption (OA) is not yet identified unambiguously because of the presence of intense F(250 nm) band.

Mayhugh (1970) established that the 200°C TL peak (peak No. 5) corresponds to the 310 nm OA band. It is now generally agreed that Nink and Kos's (1976) identification of 310 nm OA with  $Z_2$  centres in LiF:Mg, Ti is not correct (Jain and Kathuria 1978; Nepomnyashchikh and Radzhabov 1980; Horowitz 1982; Caldwell *et al* 1983; McKeever 1984; Lakshmanan 1984).

(2) Mort (1966) and Mort and Zimmerman (1966) empirically predicted the TL centre absorption maximum at 225 nm in LiF:Mg. Nepomnyashchikh and Radzhabov (1980) again predicted the absorption of  $Mg^0$  type centres from an empirical relation at 225 nm. Lopez and Lopez (1981) predict that Mg should act as an electron trap. On the contrary, Bosi and Nimis (1985) in a recent analysis predict that Mg should form  $Z$  centres in LiF. All these diverse predictions show that an analysis is premature.

(3) The arguments concerning 310 nm  $\rightarrow$  225 nm conversion during low temperature optical bleaching and the correlation of 310 nm and 225 nm OA bands with  $Mg^0$  centres by Nepomnyashchikh and Radzhabov (1980) (refer § 4.1) have been questioned recently by Lakshmanan *et al* (1985). If the argument that all centres change to  $Mg^0$  centres when peak 5 readout is correct, then one should have observed peak 5 at all. Even if one assumes that only some  $Mg^+$  centres convert to  $Mg^0$  centres, then the peak 10 (correlated with 225 nm OA) TL in virgin TLD-100 should have been considerably greater than that for the 140°C irradiation annealed sample, because peak 5 (correlated with 310 nm OA) TL

and hence the electrons released from them are a factor of 20 to 30 times higher in the former sample than in the latter one. But experiments show no appreciable difference in peak 10 TL between the two samples (Lakshmanan *et al* 1985).

(4) In §4-1 of paper I, it is also mentioned that ESR measurements by Watterich *et al* (1980) show that in LiF:Mg, the  $g$  value is 2.006 for the  $F$  band and 2.029 for the 225 nm band suggesting that the latter is not a  $Z_3$  band. Nevertheless, this band seems to be definitely related to the presence of Mg. Subsequently Watterich *et al* (1984) stated that the presence of OH in LiF:Mg made the ESR investigation of any  $Mg^+$  ions impossible upto now.

Landreth and McKeever (1985) have recently reported that from their optical absorption data on LiF:Mg,Ti, they find no compelling evidence to relate either the 4.4 eV or the 5.3 eV bands to Z-type centres. The 5.7 eV may be a Z-type defect but of unknown structure. Hence more detailed experimental studies including optical absorption, ESR, ENDOR, Faraday rotation etc are needed to identify the TL trap centres bearing in mind that the behaviour of LiF could be different from other alkali halides.

As mentioned in paper I, the ultimate photon emission step is not satisfactorily elaborated in any of the models in literature. The mobile electron and mobile interstitial models have led to two groups of researchers, each proceeding almost independently and ignoring the work of the other. The recent article by Lakshmanan *et al* (1985) attempts to answer these questions in LiF TLD-100 and suggests that both the processes may be operating at the same time.

## References

- Bosi L and Nimis M 1985 *Phys. Status Solidi* **B131** K111  
 Caldas L V E, Mayhugh M R and Stoebe T G 1983 *J. Appl. Phys.* **54** 3431  
 Deshmukh B T and Moharil S V 1985 *Bull. Mater. Sci.* **7** 427  
 Horowitz Y S 1982 *Phys. Status Solidi* **A69** K29  
 Jain V K and Kathuria S P 1978 *Phys. Status Solidi* **A50** 329  
 Lakshmanan A R, Chandra B and Bhatt R C 1982 *J. Phys.* **D14** 1683  
 Lakshmanan A R 1984 *Radiat. Prot. Dosim.* **6** 52  
 Lakshmanan A R, Bhuwan Chandra, Bhatt R C, Hoffmann W and Spallek R 1985 *J. Phys.* **D18** 1673  
 Landreth J L and McKeever S W S 1985 *J. Phys.* **D18** 1919  
 Lopez F and Lopez F A 1981 *Cryst. Lattice Defects* **9** 131  
 McKeever S W S 1984 *Radiat. Prot. Dosim.* **8** 3  
 Mayhugh M R 1970 *J. Appl. Phys.* **41** 4776  
 Mort J and Zimmerman D W 1966 *Phys. Lett.* **21** 273  
 Mort J 1966 *Phys. Lett.* **21** 124  
 Nepomnyashchikh and Radzhabov E A 1980 *Opt. Spectrosc. (USSR)* **48** 154  
 Nink R and Kos H J 1976 *Phys. Status Solidi* **A35** 121  
 Sunda C M, Bapat V N and Kathuria S P 1971 *Proc. Third Int. Conf. on Lum. Dosimetry*, Riso Report No. 249, Danish AEC and IAEA p 146  
 Watterich A, Foldvari I, Corradi G and Opyrchal H 1984 *Phys. Status Solidi* **B121** 117  
 Watterich A, Foldvari I and Voszka R 1980 *J. Phys. (Paris)* **41** C6-159

## A simple hydrothermal cell for synthesis at moderate temperatures pressures

J A K TAREEN, B BASAVALINGU, M A SHANKARA and  
REZA FAZELI

Mineralogical Institute, Manasagangotri, Mysore 570 006, India

MS received 27 February 1986; revised 7 April 1986

**Abstract.** A simple hydrothermal cell without threaded parts has been developed for routine synthesis of materials at moderate temperatures (upto 500°C) and pressure (5 kb). The sealing of the fluid pressure in the cell has been achieved with a cap arrangement, but the sealing pressure has been through a hydraulic ram instead of a threaded cap. Experience showed that this cell is more convenient for rapid and experimentation.

**Keywords.** Hydrothermal cell; material synthesis.

### 1. Introduction

The hydrothermal method has increasingly been recognised as a potential technique for synthesis of inorganic materials, crystal growth (Laudise 1973) and even for large scale preparation of pure ultrafine oxides (Stambaugh 1982). To mineralogical investigation of the mineral reactions is of immense value to understand their paragenesis and the conditions of their formation. Hydrothermal reactors employing different kind of sealing systems (Morey and Ingerson 1950; Walker and Buchler 1950; Bridgman 1914; Roy and Tuttle 1956) have been in use in the past few decades. The authors have also designed and fabricated such reactors in this laboratory for hydrothermal studies. All these reactors invariably consist of threaded parts and call for an extremely precise machining. Except for the 'cold seal' type reactors, other systems such as Bridgman type etc also need the deformable gaskets and such gaskets are to be replaced after every experiment. Further, all these hydrothermal reactors which employ threaded caps for sealing need frequent machining for cleaning and dressing the threads.

The high cost for precision machining and the considerable loss of time due to frequently required machining of these reactors was a disadvantage for the experimentation. This prompted the authors to develop a more simpler and compact cell which was found to be extremely convenient for routine exploratory runs at moderate temperatures and pressures. This paper is a report of this cell.

### 2. The new hydrothermal cell

As shown in figure 1\*, the cell consists of two parts:

(a) the lower part is the furnace assembly with supporting shell made from m

---

\*Engineering drawing can be obtained from the author on request.

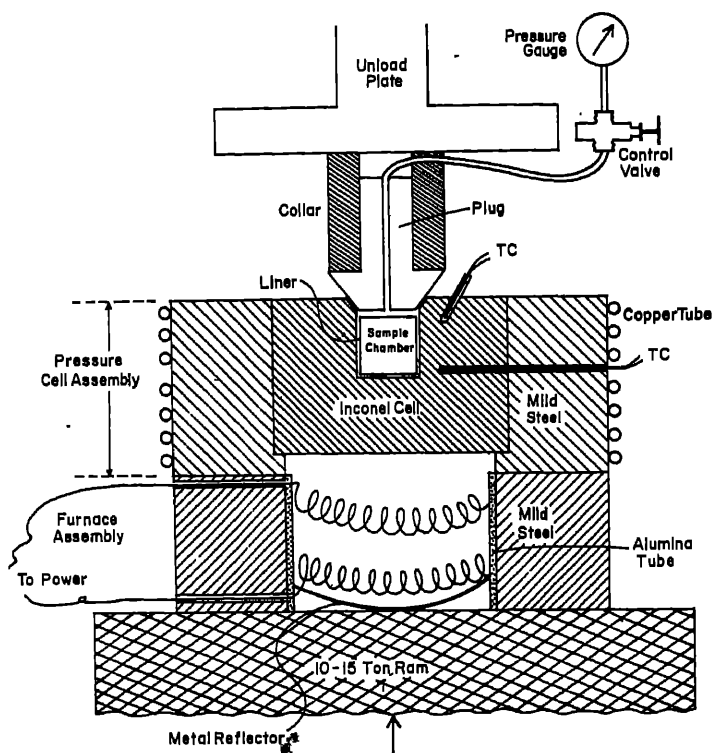


Figure 1. The new hydrothermal cell (scale 1:1).

18 series. The resistance heating coil is wound from kanthal AI placed spirally the ceramic sleeve tightly fitted into the supporting shell. The coil power be limited to 30 amp and 50 V to raise the temperature of the sample er to a maximum of 500°C. The power supply is through a voltage stabilizer 50 A variac.

upper part of the system consists of the pressure cell made from inconel. This pressure cell has been tightly heat-fitted into another concentric shell of mild r EN-18 series. The pressure cell (10 cc capacity) has been provided with a seating closure. The seating cone is made from stainless steel 316, preferably ed by heating upto 400°C and quenching in water.

ater or any non-corrosive fluid is used as mineralizer, the cell can be used at a protective liner in the sample chamber. But, with corrosive fluid, the has to be encapsulated in a noble metal ampoule. A small silver liner can also d in which case the pressure generated inside the liner has to be balanced by ting equal pressure outside the liner by using appropriate percent fill of water. Pressure generated in the cell depends on the initial fluid filled into the cell. For le, if 80% of free volume of the cell is filled with H<sub>2</sub>O at 500°C, it generates 3200 bars fluid pressure. The P-V-T diagrams for some fluids such as H<sub>2</sub>O (edy 1950), CO<sub>2</sub> (Kennedy 1954), HCl (Rau and Kutty 1972), etc are reported make the pressure reading straightforward. Alternatively the fluid pressure

### *A simple hydrothermal cell*

could also be read on Bourden gauge connected to the sample chamber through stainless steel high pressure tubing. This is possible only when the chamber is encapsulated and the pressurising fluid is water or gas.

The quenching of the vessel to arrest the reaction in equilibrium can be achieved by flushing compressed chilled air or water through the copper tubing on the shell. The quenching time to cool from 500°C to ambient by this process is 10 minutes.

The cell, after being charged with the sample is placed between the two ram-operated hydraulic press of 15 ton capacity (figure 2) and pressed with 5–6 tons of load. The sealing thus achieved will be effective to retain up to 1000 atm pressure inside the chamber. The use of hydraulic press eliminates the threaded joints in the system which makes the sealing as well as opening of the cell considerably simple and rapid, thus reducing the changing time to about 15–20 minutes from one experiment to another. Further, the concentric shell arrangement ensures safety against any rupture. The expected life of the cell is about 10,000 hr. However, due to the reasonably low cost of the cell (Rs. 500 to 600) it enables any laboratory to afford a few spare cells and change them after about 2000 hr of running use. The authors, in fact, have been using a cell for over 2000 hr which still does not require replacement or re-machining.

Finally, the authors would like to emphasize that the new sealing device suggested in this report is not a total substitute to the other type of reactors but it is an extremely convenient and low cost device for rapid experimentation at moderate hydrothermal conditions.

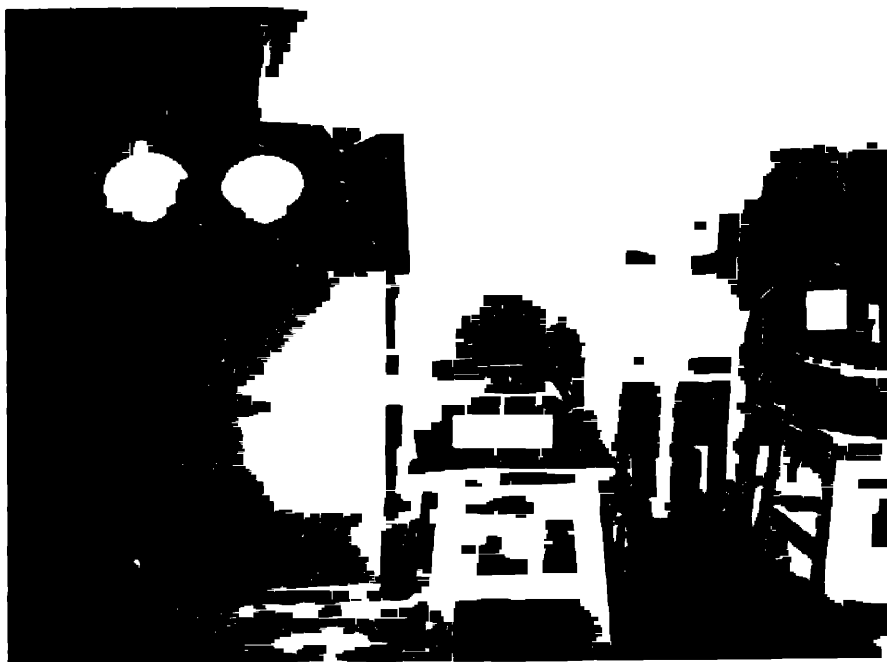


**Figure 2.** Positioning of the cell between the rams of the hydraulic press.

## Acknowledgements

The authors thank Prof. V Venkatachalapathy for encouragement. The skilful machining work of Mr Nadeem-ur-Rehman-Khan is acknowledged.

## References

- Bridgman P W 1914 *Proc. Am. Acad. Arts Sci.* **49** 625  
Kennedy G C 1950 *Am. J. Sci.* **248** 540  
Kennedy G C 1954 *Am. J. Sci.* **252** 225  
Laudise R A 1973 *Crystal growth: An introduction* (The Netherlands: North Holland Publishing Co.) p 162  
Morey G W and Ingerson E 1937 *Am. Mineral.* **22** 1121  
Rau H and Kutty T R N 1972 *Ber. Bun. Ges. Phys. Chem.* **76** 645  
Roy R and Tuttle O F 1956 *Phys. Chem. Earth* **1** 138  
Stambaugh E P 1982 *Proc. First Int. Symp. Hydrothermal Reaction* (Japan: Gakujutsu Bunken Fukyu-Kai) p 859  
Walker A C and Buchler E 1950 *Ind. Eng. Chem.* **42** 1369

## Characterization and thermal behaviour of lanthanum tartrate crystals grown from silica gels

P N KOTRU, N K GUPTA, K K RAINA and M L KOUL†

Department of Physics, †Department of Chemistry, University of Jammu, Jammu 180 001, India

MS received 15 February 1986; revised 7 May 1986

**Abstract.** Results obtained on characterization of lanthanum tartrate crystals, grown by the gel method, using chemical analysis, x-ray and electron diffraction, infra-red and mass spectroscopy are reported. The thermal behaviour is studied using DTA, TGA and DTG. The decomposition pattern is reported to be typical of a hydrated metal tartrate. Kinetic parameters like order of reaction, frequency factor and activation energy are evaluated. Contracting cylinder kinetic model is found to be the best fit for the decomposition processes involved. Magnetic susceptibility measurements indicate the material to be diamagnetic.

**Keywords.** Lanthanum tartrate crystal; thermal behaviour; silica gels.

### 1. Introduction

Rare-earth materials have attracted considerable attention on account of their luminescent and magnetic properties (Eyring 1964). The present efforts have been initiated to obtain rare-earth tartrates for various investigations. However, it is necessary to establish the exact chemical composition and other characteristics of the material. In the present work the crystals of  $\text{La}_2(\text{C}_4\text{H}_4\text{O}_6)_3 \cdot 7\text{H}_2\text{O}$  were grown by using the controlled diffusion system of silica gels (Kotru *et al* 1985). Crystals of varied morphologies grown in the gel media are shown in figure 1. A literature survey showed that no studies have been carried out on the growth or the x-ray diffraction data on lanthanum tartrate crystals. The present characterization of lanthanum tartrate crystals is therefore studied and the results obtained from chemical analysis, infra-red and mass spectroscopy, x-ray and electron diffraction and thermal analysis are discussed.

### 2. Experimental details

To determine the contents of lanthanum (metal), carbon and hydrogen, the material was subjected to conventional physical and chemical methods. Carbon-hydrogen analysis was performed and x-ray diffraction pattern recorded on the powdered samples using x-ray powder diffractometer (Phillips model PW1350) with nickel-filtered  $\text{CuK}\alpha$  radiations (30 kV, 15 mA). Electron diffraction was obtained by using transmission electron microscope (AEI TEM-802, UK). Mass spectrum was recorded using JMS-300 at 70 eV. The IR spectrum (range: 300 to  $4000\text{ cm}^{-1}$ ) was recorded by employing Spektromom 2000, using KBr pellet technique. Thermal analysis, involving DTA, TGA and DTG techniques was carried out using a MOM derivatograph (Paulik-Paulik-Eredey Hungary) at the heating rate of  $10^\circ\text{C/min}$ . The

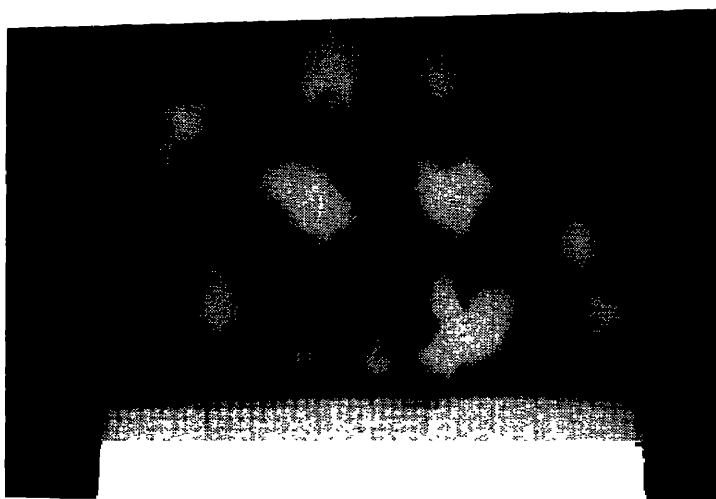


Figure 1. Gel grown crystals of  $\text{La}_2(\text{C}_4\text{H}_4\text{O}_6)_3 \cdot 7\text{H}_2\text{O}$  of different morphologies.

weight of the sample used was 200 mg. To identify the final product in TG analysis, x-ray powder pattern was recorded after heating the original compound to  $850^\circ\text{C}$  in an electronically controlled muffle furnace working within an accuracy of  $\pm 10^\circ\text{C}$ . Kinetic parameters of solid state reactions from the thermal analysis such as activation energy, order of reaction and frequency factor were determined by using different thermo-analytical kinetic equations and Gouy's balance was used for magnetic susceptibility measurements.

### 3. Results and discussion

#### 3.1 Chemical analysis

To establish the chemical composition of crystals grown, the metal and carbon-hydrogen analysis was made use of. The chemical composition of the material was  $\text{La}_2(\text{C}_4\text{H}_4\text{O}_6)_3 \cdot 7\text{H}_2\text{O}$ . These results are further supported by TGA in which after the mass loss of 63%  $\text{La}_2\text{O}_3$  is formed. The TGA results also agree with those obtained from chemical analysis.

#### 3.2 X-ray analysis

The x-ray diffractogram recorded (figure 2) indicates the crystallinity of the sample. Table 1 shows the x-ray diffraction data for  $\text{La}_2(\text{C}_4\text{H}_4\text{O}_6)_3 \cdot 7\text{H}_2\text{O}$ .

#### 3.3 TEM results

TEM was used to establish the crystallinity of the sample. It is seen that there is a decomposition resulting in the change of the diffraction pattern. Figures 3(a) and 3(b)



*Thermal behaviour of lanthanum tartrate crystals*

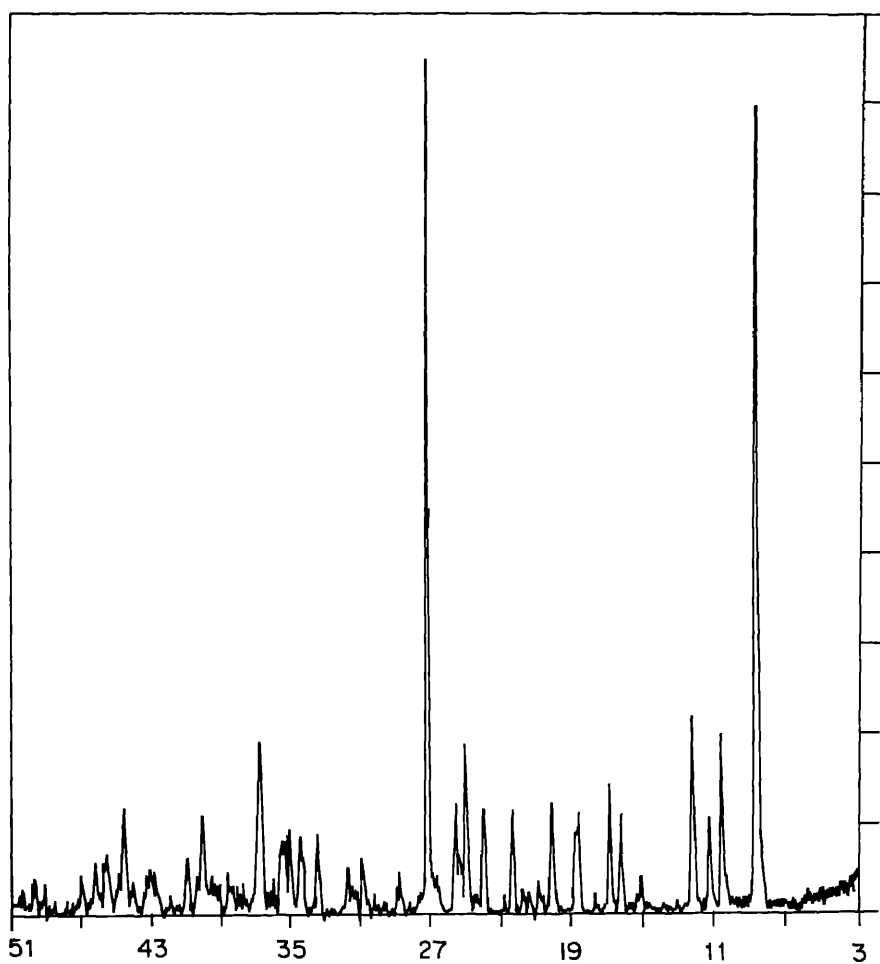


**Figure 2.** X-ray diffraction trace.

**Table 1.** X-ray powder data.

d values	Intensity values
10.0480	89.5
8.2678	20.0
7.0810	22.0
5.3402	9.0
5.1257	12.0
4.6707	9.0
4.3532	10.0
3.9342	11.5
3.5339	19.0
3.2433	95.0
2.4332	19.0
2.2378	11.0
2.0273	12.0

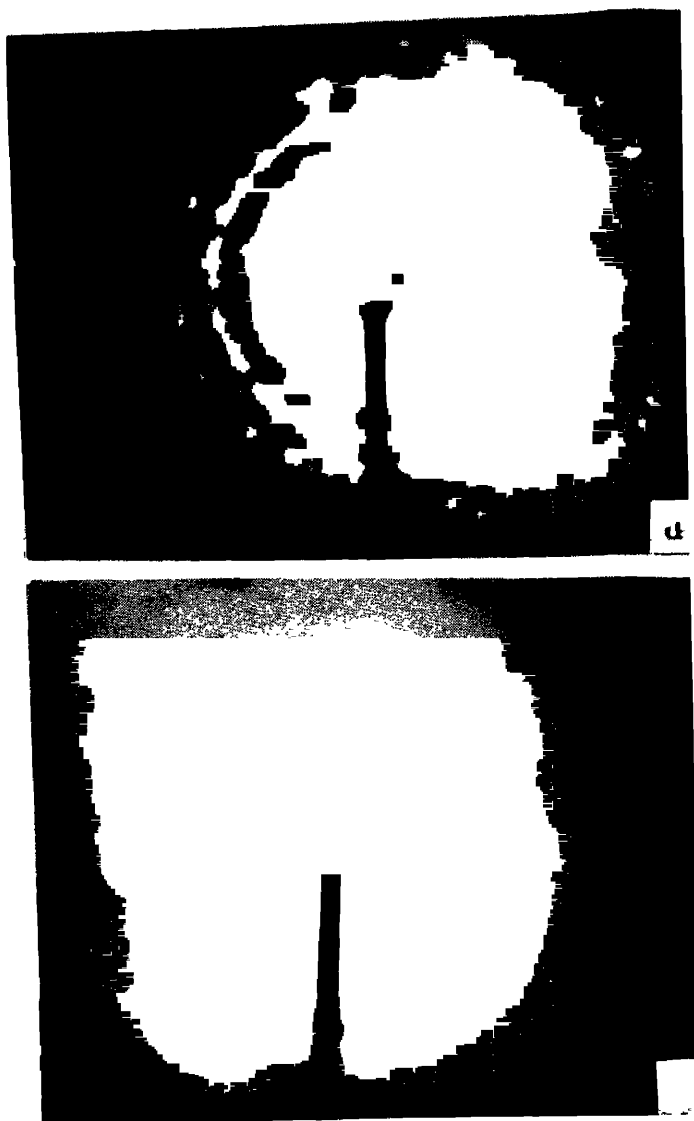


**Figure 3.** (a) Electron diffraction pattern recorded immediately on loading and (b) electron diffraction pattern recorded after some time of loading.

are electron diffraction patterns of the material recorded immediately or after some time of loading. The pattern shown in figure 3(a) indicates the crystallinity of the material. A comparison between figures 3(a) and 3(b) shows that the diffraction pattern changed from polycrystalline to nearly amorphous pattern (Kotru and Gupta 1983). This could be due to the presence of water in the original material.

### 3.4 Mass spectroscopy

Mass spectrum of the crystal sample was recorded using 70 eV electron bombardment for ionization. Figure 4 shows the mass spectrum of  $\text{La}_2(\text{C}_4\text{H}_4\text{O}_6)_3 \cdot 7\text{H}_2\text{O}$ .

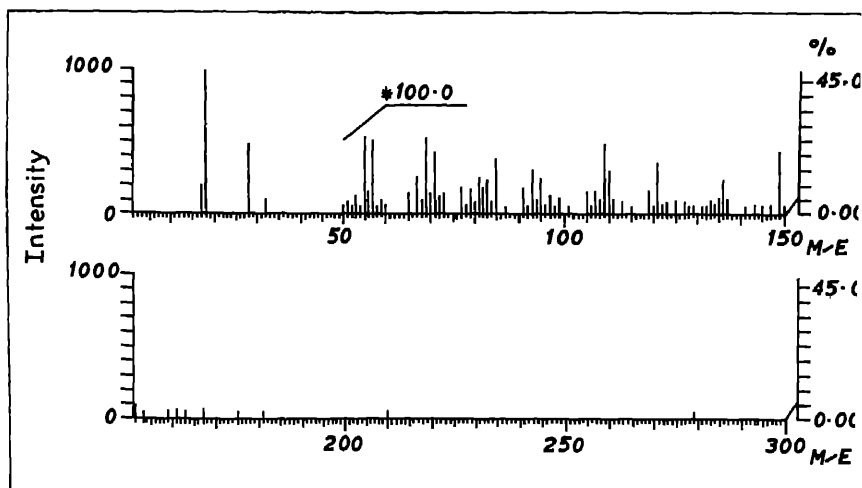


Figure 4. Mass spectrum of  $\text{La}_2(\text{C}_4\text{H}_4\text{O}_6)_3 \cdot 7\text{H}_2\text{O}$  crystals.

Table 2. Mass spectrum data corresponding to significant peaks of  $\text{La}_2(\text{C}_4\text{H}_4\text{O}_6)_3 \cdot 7\text{H}_2\text{O}$ .

M/E	Raw int.	Relative intensity	Sigma (%)
16.0	11.1	13.9	0.68
17.0	169.9	212.0	10.40
18.0	801.2	1000.0	49.04
28.0	388.8	485.2	23.79
32.0	87.0	108.5	5.32
43.0	10.3	12.9	0.63
44.0	16.9	21.0	1.03
149.0	3.4	4.3	0.21

The mass fragmentography corresponding to prominent peaks is indicated in Figure 3. The base peak of M/E 18 suggests the possible presence of water of crystallization. The M/E peak at 149 may be due to the tartrate constituent of the parent material.

The mass spectrum suggests the decomposition of the material and supports the presence of water, carbon and oxygen as constituents of the sample which is expected on fragmentation of the tartrate and water of crystallization in the parent material. To find out if there was any volatility, mass spectrometry experiments were performed to capture the molecular ion along with the mass fragments. They failed to yield the desired results indicating that the molecule got decomposed before it was captured.

### 3.5 IR spectrum results

Figure 5 shows the infra-red spectra of  $\text{La}_2(\text{C}_4\text{H}_4\text{O}_6)_3 \cdot 7\text{H}_2\text{O}$ . The peak 3400  $\text{cm}^{-1}$  is due to water and strongly stretching modes of OH group. The bands near 1600  $\text{cm}^{-1}$  are due to the C=O stretching of the tartrate.

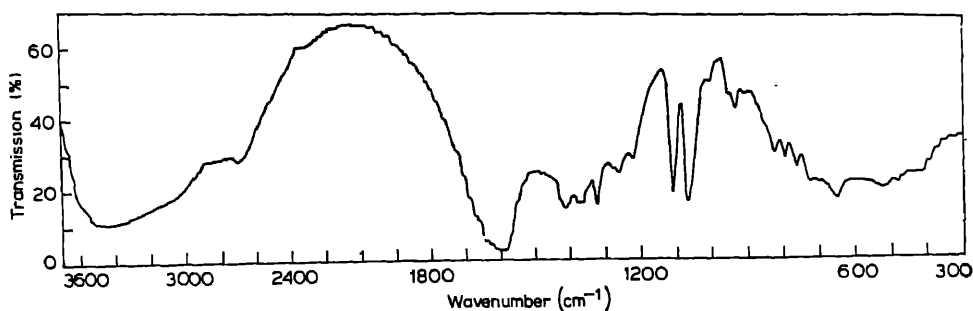


Figure 5. Infra-red spectrum of  $\text{La}_2(\text{C}_4\text{H}_4\text{O}_6)_3 \cdot 7\text{H}_2\text{O}$  crystals.

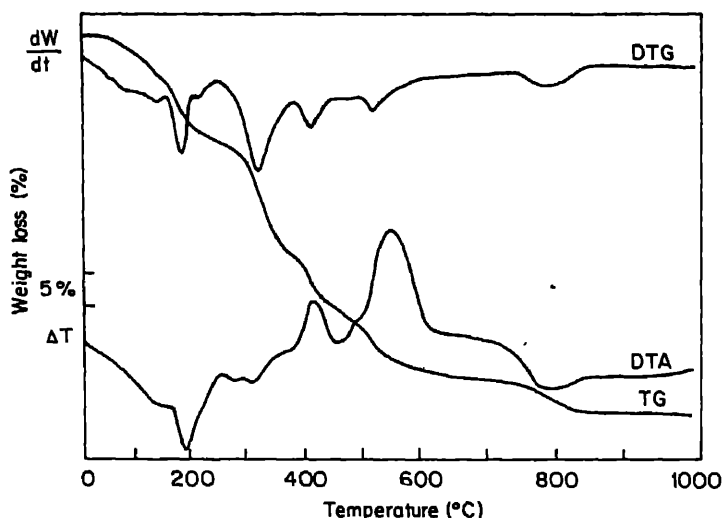


Figure 6. Thermogram showing TGA, DTA and DTG curves for  $\text{La}_2(\text{C}_4\text{H}_4\text{O}_6)_3 \cdot 7\text{H}_2\text{O}$  crystals.

and  $1370\text{ cm}^{-1}$  may be attributed to OH in plane bending. While the band at  $1590\text{ cm}^{-1}$  is due to C=O stretch, those at  $1415$  and  $1325\text{ cm}^{-1}$  are due to CO sym +  $\delta$  O-C=O modes. The modes of  $\delta$  C-H and  $\pi$  C-H are indicated by bands at  $1115$  and  $1070\text{ cm}^{-1}$ . A significant band is observed at  $650\text{ cm}^{-1}$  which is attributed to the presence of crystal water (Niekerk and Schoening 1951). Besides, there are some peaks below  $500\text{ cm}^{-1}$  indicating metal oxygen bond.

### 3.6 Thermal analysis

Figure 6 shows the thermogram for TGA, DTA and DTG for  $\text{La}_2(\text{C}_4\text{H}_4\text{O}_6)_3 \cdot 7\text{H}_2\text{O}$ . It is seen from TGA that the material starts decomposing around  $60^\circ\text{C}$  and the process is completed after the mass loss attains saturation. Some of the decomposition steps in the TG show considerable overlapping but are very much distinct in

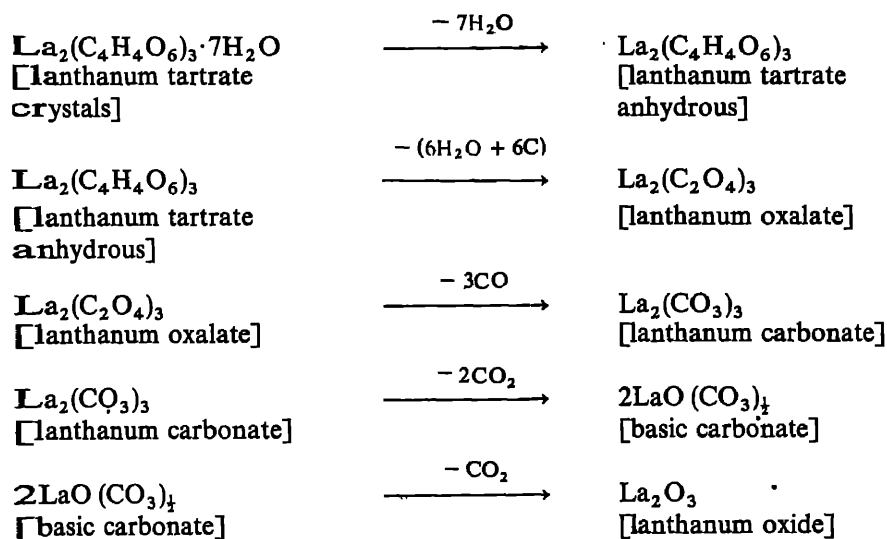
Table 3. Results of decomposition process of  $\text{La}_2(\text{C}_4\text{H}_4\text{O}_6)_3 \cdot 7\text{H}_2\text{O}$ .

Temperature range (°C)	Observed mass loss (%)	Calculated mass loss (%)	Loss of molecules in the step
60-200	14.51	14.85	$7\text{H}_2\text{O}$
200-370	35.00	36.08	$6\text{H}_2\text{O} + 6\text{C}$
370-470	45.00	45.99	$3\text{CO}$
470-610	55.50	56.36	$2\text{CO}_2$
610-835	62.00	61.55	$\text{CO}_2$

TG curve. A combined study of TG and DTG indicates a decomposition pattern as shown in table 3.

DTA curve also indicates peaks corresponding to the DTG peaks. The first stages in DTA are endothermic and hence the involvement of oxidation accompanying the decomposition process is ruled out. However, the subsequent exothermic stages in DTA suggest that decomposition is accompanied by oxidation which may be atmospheric oxygen.

Following is the stoichiometry of the different intermediates involved in the decomposition process of lanthanum tartrate.



The decomposition pattern is typical of a hydrated metal tartrate (Alfred *et al* 1970). Each thermal decomposition study leaves no doubt about the stoichiometry of the reaction.

To study the reaction kinetics of solid state reactions involved, three equations were used for calculating the activation energy, the order of reaction and the pre-exponential factor for the first stage of decomposition only, as in subsequent stages the reaction characteristics cannot be controlled. The equations of Horowitz-Metzger (1963), Piloyan-Novikova (1966) and Coats-Redfern (1964) were used for this purpose.

Application of H-M equation leads to a good linear fit in the case of  $f(\alpha) = (1 - \alpha)^{\frac{1}{2}}$

**Table 4.** Energy of activation, order of reaction and frequency factor calculated from first stage of decomposition.

Relation used	Order of reaction ( $n$ )	Frequency factor ( $Z$ )	Energy of activation ( $E_a$ ) (Kcal/mol)
Horowitz-Metzger	$\frac{1}{2}$	—	9.426
Piloyan-Novikova	—	$5.49 \times 10^6$	6.669
Coats-Redfern	—	$3.653 \times 10^4$	7.254

which indicates a contracting cylindrical mechanism of decomposition. The Coats-Redfern method also gives a linear fit for  $g(\alpha) = 2[1 - (1 - \alpha)^{\frac{1}{2}}]$ , thereby suggesting the same mechanism of decomposition. Table 6 gives the activation energy, order of reaction and frequency factor as calculated from the first stage of decomposition. As is evident from table 4, the values of kinetic parameters like activation energy and frequency factor obtained by the application of three kinetic equations (viz. H-M, P-N and C-R for  $E_a$  and P-N and C-R for frequency factor as well) are in reasonably good agreement. An agreement on the reaction mechanism leading to decomposition as suggested by the application of Coats-Redfern and Horowitz-Metzger relation is noteworthy: both indicating contracting cylinder-kinetic model as the appropriate one to explain the results obtained in the present case.

### 3.7 Magnetic characteristics

Magnetic characteristic of the material grown was studied using Gouy's balance at room temperature (34°C). The magnetic susceptibility measurements indicated the material to be diamagnetic.

## 4. Conclusion

- (i) The gel-grown system involving the use of lanthanum nitrate or lanthanum chloride as the upper reactant and sodium metasilicate gel impregnated with tartaric acid leads to crystallization of lanthanum tartrate.
- (ii) Chemical analysis supplemented by the results of infra-red spectroscopy and TGA establish the crystals to be hydrated; the chemical composition being  $\text{La}_2(\text{C}_4\text{H}_4\text{O}_6)_3 \cdot 7\text{H}_2\text{O}$ .
- (iii) The x-ray and electron diffraction results reveal crystallinity of the gel-grown lanthanum tartrate crystals.
- (iv) The results of thermal analysis (DTA, TGA and DTG) suggest the material to be thermally unstable beyond 60°C. The decomposition of the material at 70 eV of energy is suggested by the fragmentography in the mass spectrum. Changes in the electron diffraction pattern recorded immediately or after some time of loading also reveal changes in the crystalline character of the material due to electron beam heating and the presence of waters of hydration (Lorento 1975); the diffraction patterns revealing transition from poly-crystalline to nearly amorphous pattern.
- (v) Application of Horowitz-Metzger and Coats-Redfern relations in understanding the reaction kinetics of solid state reactions leading to decomposition of the

## *Thermal behaviour of lanthanum tartrate crystals*

crystalline material suggests the contracting cylinder-kinetic model to explain decomposition.

(vi) Magnetic susceptibility measurements indicate the material to be diamagnetic.

### **Acknowledgements**

The authors (NKG and KKR) are thankful to UGC and to the university authorities for research fellowships. The research work has been partially supported by UGC. We are thankful to Prof. Y Prakash for his interest.

### **References**

- Alferd C, Latz G, Litant I and Rubin B 1970 *Analytical calorimetry* (New York & London: Plenum)
- Coats A W and Redfern J P 1964 *Nature (London)* **201** 68
- Eyring L 1964 *Progress in science and technology of rare earths* (New York: Pergamon Press) **1&2**
- Horowitz H H and Metzger G 1963 *Anal. Chem.* **35** 1464
- Kotru P N and Gupta N K 1983 *Bull. Elect. Microsc. Soc. India* **7** 119
- Kotru P N, Gupta N K and Raina K K 1985 *J. Mater. Sci.* **21** 90
- Lorento M H 1975 *Physicochemical methods of mineral analysis* (ed) A W Nicol (New York: Plenum)
- Niekerk J V and Schoening F R L 1951 *Acta. Crystallogr.* **4** 35 381
- Piloyan G O and Novikova O S 1966 *Russ. J. Inorg. Chem.* **12** 313





## Glass ceramics containing ferroelectric phases

OM PARKASH, DEVENDRA KUMAR\* and LAKSHMAN PANDEY

School of Materials Science and Technology, \*Department of Ceramic Engineering  
Institute of Technology, Banaras Hindu University, Varanasi 221 005, India

MS received 31 March 1986

**Abstract.** Glass ceramics prepared by controlled crystallization of glasses produce fine dispersion of crystallites in a glassy matrix. Glasses containing a major portion of constituents of a ferroelectric phase produce crystallites of ferroelectric phase in glass through suitable heat treatment. The amount of network former in the initial glass has a profound influence on its crystallization behaviour and microstructure of the resulting ferroelectric glass ceramics. The value of dielectric constant and the nature of ferroelectric to paraelectric transition depend on the crystallite size and volume fraction of the ferroelectric phase. These glass ceramics are transparent for crystallite size less than  $0.1\ \mu\text{m}$  and exhibit large quadratic-electro-optic effect.

**Keywords.** Glass ceramics; ferroelectric; crystallization; heat treatment.

### 1. Introduction

Stookey (1959) discovered the method of controlled nucleation and crystallization of glass to produce ceramic bodies. Such materials are referred to as glass ceramic (McMillan 1979) in which crystallites of a particular phase are dispersed in continuous glassy matrix. Their preparation consists of making a homogeneous glass, its shaping in the desired form and finally heat-treating it to produce microcrystalline glass ceramic body. These glass ceramic bodies are free from pores in contrast to conventionally sintered ceramics. Absence of pores imparts them high mechanical and dielectric breakdown strengths. Glass ceramic bodies having intricate shapes and close tolerance in dimensions can be produced using commercial methods of glass production. This is because the conversion of glass into glass ceramic is rarely accompanied by more than 3-5% change in volume.

Soon after the discovery of the glass ceramic process, attempts were made to produce glass ceramics having high permittivity, low dielectric loss, high electric resistance and dielectric breakdown strength by precipitating ferroelectric phases in the glassy matrix (Bergeron 1961; Herczog 1964; Borrelli *et al* 1965). These materials find applications as capacitor dielectrics (Herczog 1967), as electronic components (Herczog 1973) and as infrared detectors (Takahashi *et al* 1975) etc. The ferroelectric phases are generally  $\text{ABO}_3$  perovskite type where  $A$  ion is from first, second and third group and  $B$  ion is from second to fifth group of the periodic table.

The ferroelectric perovskites can be produced in the glassy form in the pure state without addition of a network former (Ulrich and Smoke 1966; Glass *et al* 1979; Nassau *et al* 1979a, b, 1981). The viscosity of the melt without network former is low. This requires rapid quenching of the melt of the order of  $10^6$  degrees/sec or more, producing only very small thin platelets. On the other hand crystallization of bodies made of glass powder may produce undesirable porous structure. The addition of network formers, such as  $\text{SiO}_2$ ,  $\text{B}_2\text{O}_3$ ,  $\text{Al}_2\text{O}_3$  etc increases the viscosity of the melt.

This helps in producing a few millimeter thick discs or plates by cooling of the melt at a moderate rate of a few hundred degrees/sec. The devitrification of a glass to crystalline phase of the same composition produces crystals of varying sizes which are difficult to control. The glasses containing network formers yield two or more phases during crystallization. The minor phase acts as grain growth inhibitor of the major phase. With this, an exact control of grain size in glass ceramics is possible. Due to these various factors, the glasses prepared from the melts of pure perovskites and the crystalline product obtained therefrom are not yet usable and have academic interest only. In this review, we attempt to present the processing, crystallization and electrical properties of various glass ceramic systems containing ferroelectric phases studied so far. These glass ceramics are prepared from glasses containing network formers.

## 2. Processing

The glasses are prepared by melting batches containing a major amount of constituents of desired ferroelectric phase and an optimum amount of network formers in inert crucibles. The use of inert crucibles is recommended because any contamination during melting may adversely affect the crystallization behaviour of the glass and dielectric properties of the resulting glass ceramic product (Grossman and Isard, 1969a). The melt is quenched by pouring it into a suitably designed mould provided with an arrangement of pressing. The pressing time and temperature are adjusted to avoid the devitrification and development of thermal cracks in the quenched glass body. Fully or semi-automatic arrangements are used for this purpose (Herczog, 1964, 1984). The glass melt is transferred to a mechanized glass delivery system designed to ensure reproducible glass forming conditions. It consists of a platinum crucible which discharges molten glass droplets through a platinum tube. The falling droplets sensed by a photocell are caught in a horizontal mould and transferred to a miniaturized water cooled press. The pressed pieces are annealed to relieve the stress. The annealed glasses are subjected to differential thermal analysis (DTA) to determine the nucleation  $T_N$  and growth  $T_G$  temperatures of various crystal phases which would precipitate during ceramization of the glass (Herczog, 1981; Bergeron and Russel 1965; Layton and Herczog 1967). A typical DTA plot for glass (21 PbO–21 BaO–42 TiO<sub>2</sub>–6 SiO<sub>2</sub>–10 B<sub>2</sub>O<sub>3</sub> mole%) is shown in figure 1.

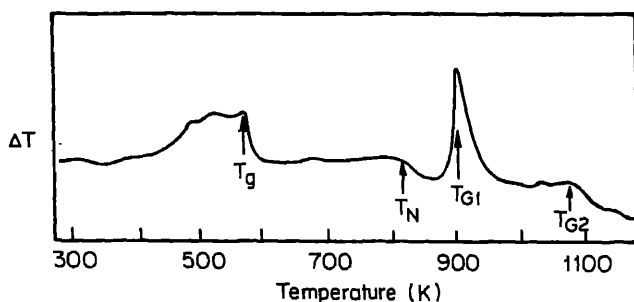


Figure 1. DTA curve for the glass in the system BaO–PbO–TiO<sub>2</sub>–B<sub>2</sub>O<sub>3</sub>–SiO<sub>2</sub> (Om Parkash *et al* 1986).

first endotherm at 575 K represents the glass transition. The second endotherm at 810 K corresponds to nucleation of crystalline phases. The exothermic peak at 900 K and 1075 K represent the growth temperatures  $T_g$  of two phases respectively which are developed during heat treatment of this glass (Om Parkash *et al* 1984).

The glasses are then subjected to various heat treatment schedules based on results. The crystalline phases precipitated during ceramization are identified by diffraction (XRD) and their respective nucleation and growth temperatures are identified. In figure 1, 900 K corresponds to the growth of  $\text{BaTiO}_3$ , while 1075 K represents the growth of second crystalline phase. An optimum heat treatment schedule is determined based on the measurements of optical and electron microscopy and dielectric properties of the glass ceramics obtained by different treatment schedules.

When crystallization of glasses in the system  $\text{BaO-TiO}_2\text{-Al}_2\text{O}_3\text{-SiO}_2$  is carried out in reducing atmosphere, interconnected dispersion of semiconducting  $\text{BaTiO}_3$  in glassy matrix is obtained. Oxidation of this semiconductor leads to surface with very high dielectric strength and resistivity about 100 times higher than the resistivity obtained by direct crystallization of the glass in air (Herczog 1984).

### 3. Systems

As mentioned in §1, the ferroelectric phases which are precipitated during crystallization of glasses in these glass ceramics are of  $\text{ABO}_3$  perovskite type. Ferroelectric glass ceramics studied can be put into two categories depending on crystallite size and resulting properties: (1) those glass ceramics with crystallites having size  $>0.1 \mu\text{m}$ . They are opaque and have potential applications as dielectric and permittivity materials, and (2) those with crystallites having size  $<0.1 \mu\text{m}$ . These glass ceramics are transparent and exhibit interesting electro-optic properties.

The different systems investigated are given in table 1.  $\text{BaTiO}_3$  and  $\text{PbTiO}_3$  crystals have been precipitated in different glass ceramic systems (Herczog, Bergeron and Russell 1965). Solid solution ferroelectric ceramics possess desirable properties than pure ferroelectric materials. Various attempts have been made to precipitate similar solid solution crystallites in the glass ceramic systems. Formation of pure lead titanate has been reported during ceramization of glasses in the system  $\text{PbO-BaO-TiO}_2\text{-B}_2\text{O}_3\text{-SiO}_2$  (Grossman and Isard 1981, Lynch and Shelby 1984). However,  $\text{BaTiO}_3$  was obtained in the same system (Rajgopalan 1985). From these studies it is concluded that the ratio of  $\text{PbO}$  and  $(\text{PbO} + \text{BaO})$  to  $\text{TiO}_2$  determines whether  $\text{PbTiO}_3$  or  $\text{BaTiO}_3$  would precipitate out during heat treatment. Other substitutions such as Sr for Ba and Zr for Ti have been made in precipitation of different phase rather than solid solutions. Formation of crystallites of various ferroelectric niobates and tantalates in the pure and solid solution form over wide ranges of composition has been reported in glass ceramic systems (Borrelli 1967; Borrelli and Layton 1971) as shown in table 1. Most of the glass ceramics can be obtained with crystallite size  $<0.1 \mu\text{m}$  and are transparent. Thin crystals having large surface area have been obtained by ceramic processing in the system  $\text{Pb}_5\text{Ge}_{3-x}\text{Si}_x\text{O}_{11}$  (Takahashi 1975).

Table 1. Glass ceramic systems containing ferroelectric phases.

Glass system	Ferroelectric phase	Reference
BaO-TiO <sub>2</sub> -SiO <sub>2</sub> -B <sub>2</sub> O <sub>3</sub>	BaTiO <sub>3</sub>	Herczog (1964)
BaO-TiO <sub>2</sub> -SiO <sub>2</sub> -Al <sub>2</sub> O <sub>3</sub>	BaTiO <sub>3</sub>	Herczog (1984)
PbO-TiO <sub>2</sub> -B <sub>2</sub> O <sub>3</sub>	PbTiO <sub>3</sub>	Bergeron and Russell (1965)
PbO-TiO <sub>2</sub> -Al <sub>2</sub> O <sub>3</sub> -SiO <sub>2</sub>	PbTiO <sub>3</sub>	Kokubo and Tashiro (1973/74)
PbO-BaO-TiO <sub>2</sub> -B <sub>2</sub> O <sub>3</sub>	PbTiO <sub>3</sub>	Lynch and Shelby (1984)
PbO-BaO-TiO <sub>2</sub> -B <sub>2</sub> O <sub>3</sub> -SiO <sub>2</sub> -Al <sub>2</sub> O <sub>3</sub>	PbTiO <sub>3</sub>	Grossman and Isard (1969a, b)
PbO-BaO-TiO <sub>2</sub> -B <sub>2</sub> O <sub>3</sub> -SiO <sub>2</sub>	BaTiO <sub>3</sub>	Om Parkash <i>et al</i> (1986)
Na <sub>2</sub> O-Nb <sub>2</sub> O <sub>5</sub> -SiO <sub>2</sub>	NaNbO <sub>3</sub>	Layton and Herczog (1967)
CdO-Na <sub>2</sub> O-Nb <sub>2</sub> O <sub>5</sub> -SiO <sub>2</sub>	Na <sub>1-x</sub> Cd <sub>x/2</sub> NbO <sub>3</sub>	Layton and Smith (1975); Borrelli and Layton (1971)
PbO-Na <sub>2</sub> O-Nb <sub>2</sub> O <sub>5</sub> -SiO <sub>2</sub>	Na <sub>1-x</sub> Pb <sub>x/2</sub> NbO <sub>3</sub>	Borrelli and Layton (1971)
Na <sub>2</sub> O-K <sub>2</sub> O-Nb <sub>2</sub> O <sub>5</sub> -SiO <sub>2</sub>	Na <sub>1-x</sub> K <sub>x</sub> NbO <sub>3</sub>	-do-
SrO-Na <sub>2</sub> O-Nb <sub>2</sub> O <sub>5</sub> -SiO <sub>2</sub>	Na <sub>1-x</sub> Sr <sub>x/2</sub> NbO <sub>3</sub>	-do-
PbO-MgO-Nb <sub>2</sub> O <sub>5</sub> -SiO <sub>2</sub>	Pb <sub>3</sub> MgNb <sub>5</sub> O <sub>9</sub>	-do-
SrO-K <sub>2</sub> O-Nb <sub>2</sub> O <sub>5</sub> -SiO <sub>2</sub>	Sr <sub>2</sub> KNbO <sub>5</sub>	-do-
Li <sub>2</sub> O-Na <sub>2</sub> O-K <sub>2</sub> O-Nb <sub>2</sub> O <sub>5</sub> -SiO <sub>2</sub>	Li <sub>x</sub> Na <sub>4-x</sub> K <sub>x</sub> NbO <sub>3</sub>	-do-
BaO-CaO-PbO-Nb <sub>2</sub> O <sub>5</sub> -SiO <sub>2</sub>	Ba <sub>x</sub> Ca <sub>y</sub> Pb <sub>z</sub> Nb <sub>2</sub> O <sub>6</sub>	-do-
BaO-SrO-PbO-Nb <sub>2</sub> O <sub>5</sub> -SiO <sub>2</sub>	Ba <sub>x</sub> Sr <sub>y</sub> Pb <sub>z</sub> Nb <sub>2</sub> O <sub>6</sub>	-do-
Li <sub>2</sub> O-Na <sub>2</sub> O-K <sub>2</sub> O-Ta <sub>2</sub> O <sub>5</sub> -SiO <sub>2</sub>	Li <sub>x</sub> Na <sub>4-x</sub> K <sub>x</sub> Ta <sub>2</sub> O <sub>6</sub>	-do-
PbO-GeO <sub>2</sub> -SiO <sub>2</sub>	Pb <sub>5</sub> Si <sub>x</sub> Ge <sub>3-x</sub> O	Takahashi <i>et al</i> 1975

#### 4. Nucleation and crystallization

An understanding of the mechanism of nucleation and crystallization in these glasses helps in better control of properties of resulting glass ceramics. Bergeron and Russell (1965) investigated the rate of growth of PbTiO<sub>3</sub> crystals from a PbO-TiO<sub>2</sub>-B<sub>2</sub>O<sub>3</sub> glass at different temperatures. The Brown-Ginell equation satisfactorily explained the growth rate data. It was also observed that temperature of maximum growth rate was 100–150°C above the exotherm associated with the growth of lead titanate crystals in DTA plots of solid and powdered glass samples. It was ascribed to the large surface area of the powdered sample. The large number of nuclei present in such samples may result in a large heat effect even at low growth rate at the temperature of the exotherm. Most of the total quantity of the crystals which can be in equilibrium at the higher temperatures were precipitated below the temperature of maximum growth rate.

The crystallization behaviour of glasses in the system Na<sub>2</sub>O-Nb<sub>2</sub>O<sub>5</sub>-SiO<sub>2</sub> has been investigated by measuring the viscosity, grain size and crystalline content as a function of temperature at different constant heating rates (Layton and Herczog 1967). The crystallization was very rapid and exothermic, making the measurements at constant temperatures very difficult. From electron microscopic observations at various stages of heat treatments it was observed that in the beginning of crystalli-

zation, particles of 500–1000 Å in diameter appear in the glass. These particles v agglomerates of very fine crystallites of diameter 100 Å or less. These fine crystal constituting a particle, formed a star-like configuration indicating a growth f central nucleus. Slightly crystallized specimens also showed the presence of a li number of phase separated regions of 20–50 Å in diameter. On further heating, tl regions subsequently coalesced until a critical size was reached forming a st nucleus. At low SiO<sub>2</sub> content, uniform and very large concentration of these nu are formed indicating a high rate of nucleation. The transformation of the glas the crystalline phase is complete with minimum of grain growth and sintering. T the final glass ceramic product is transparent due to crystallite size being less 1 0.1 μm. At high SiO<sub>2</sub> content, the nucleation rate is slower resulting in growt crystals upto 1 μm or more in diameter making the glass ceramic opaque.

Phase separation occurring during heat treatment may be due to the mi heterogeneities in the structure of glass having the same size and composition as phase separated regions. This can be understood in terms of the ratio of number multivalent cations (such as Ti<sup>4+</sup> and Nb<sup>5+</sup>) and network forming cations N ( as Si<sup>4+</sup>, B<sup>3+</sup>, Al<sup>3+</sup> etc) present in the initial glass composition (Layton and Her 1969). The randomness of the glass network is attributed to flexibility of Si-bond angle or to that of angle formed by other network formers. Ti<sup>4+</sup> and Nb<sup>5+</sup> normally octahedrally coordinated to oxygen in oxide lattices and they can rej the network forming ions upto a certain limit in oxide glasses. These ions lack bility of bond angles. When these cations are not associated with a true net former as their nearest neighbours, they become structurally ordered with respe each other. These structurally ordered regions represent microheterogeneities i glass structure. It is reasonable to assume that the ratio B/N=1 represents the of substitution of network forming cations by these ions without causing r structural inhomogeneities in the glass. As the ratio exceeds 1, microheterogen are formed and on heating, phase-separated regions are produced in sufficien centration, approaching the size of a stable nucleus allowing rapid interaction ween them. This explains high rate of nucleation and rapid completion of cry zation without substantial grain growth in glasses with low network forming co

The DTA curve in figure 1 shows the presence of second exothermic peak 1 senting the growth of another crystalline phase beside barium titanate. Ther when the glass or the glass ceramic samples are heated at higher temperature (g temperature of second phase) the second phase separates out along with Ba This is shown in the scanning electron micrograph (figure 2) of the glass ce sample obtained by heat treatment at this temperature (Om Parkash *et al* 198 order to obtain the maximum recovery of a ferroelectric phase during ceramiz it is recommended to start with a glass composition corresponding to stoichio composition of two crystal phases; the ferroelectric phase and a secondary containing all network forming additions. Presence of any residual glass reduc yield of ferroelectric phase either by keeping it in solution or by secondar temperature reaction with it (Herczog 1984).

## **5. Electrical properties**

Uniform fine-grained microstructure is very desirable in ferroelectric cerami imparts mechanical and dielectric stability suitable for various device applic



**Figure 2.** Microstructure of the glass ceramics in the system  $\text{PbO-BaO-TiO}_2\text{-B}_2\text{O}_3\text{-SiO}_2\text{-P}_2\text{O}_5$ , heat treated at 975 K for 12 hours,  $\sim 10\mu\text{m}$  (Om Parkash *et al* 1986).

This type of microstructure can be easily produced in ferroelectric glass ceramics by controlled heat treatment. The dielectric constant depends on the particle size and content of crystalline phase in these materials. A high percentage (75–80 volume%) of a ferroelectric phase can be obtained starting with a suitable composition.

Variation of dielectric constant and loss tangent with temperature at 1 kHz with  $\text{BaTiO}_3$  content and particle size is shown in figure 3 (Herczog 1964). The curves on the left side show the characteristics of the materials containing different percentages of  $\text{BaTiO}_3$  but having the same particle size. The right side curves are for materials of different particle size and of same barium titanate content. Dielectric anomaly was distinctly seen in samples having particle size  $\geq 0.8\mu\text{m}$  (curves (a), (b) and (c)) becoming diffuse with decreasing particle size (curves (d) and (e)) and disappear completely below  $0.1\mu\text{m}$ . A maxima in dielectric constant as a function of grain size at  $0.8\mu\text{m}$  was observed. A similar maxima in dielectric constant of microcrystalline  $\text{PbTiO}_3$  crystallized from  $\text{PbO-TiO}_2\text{-Al}_2\text{O}_3\text{-SiO}_2$  glass was observed at a grain size of  $0.15\mu\text{m}$  (Kokubo and Tashiro 1973/74). Similar dielectric behaviour has been reported in glass ceramics containing  $\text{NaNbO}_3$  (Borrelli and Layton 1971).

This dielectric behaviour as a function of crystallite size has been explained in terms of internal stresses generated in these submicrometer range crystallites and suppression of ferroelectric-to-paraelectric transition due to crystal clamping in the rigid surrounding glass matrix. This model was proposed by Buessem *et al* (1966) to explain the high permittivity in fine-grained  $\text{BaTiO}_3$ . Kokubo and Tashiro (1973/74) through careful experimentation using XRD showed that the maximum dielectric constant was obtained at the same grain size at which the two-dimensional stress was maximum. The decrease in dielectric constant at higher grain size was ascribed to  $90^\circ$  twinning within the grain as proposed by Buessem *et al* (1966), which leads to reduction in two-dimensional stresses. Similarly, temperature-independent behaviour for submicron range can be understood due to the absence of domain walls in these

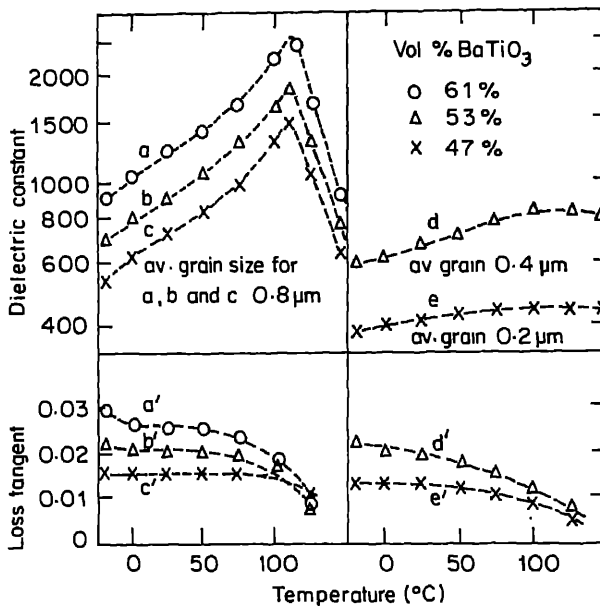


Figure 3. Variation of dielectric constant and loss tangent with temperature at 1 kHz glass ceramics containing different contents and size of  $\text{BaTiO}_3$  crystallites (Herczog 19

crystallites. For particles  $\geq 1 \mu\text{m}$  or so,  $90^\circ$  twinning of domain wall becomes possible and hence glass ceramics containing particles in this range show a non dielectric anomaly at the Curie point.

These glass ceramics show a higher dielectric breakdown strength and resistivity as compared to normally-sintered ferroelectric ceramics due to absence of pores.

When the crystallite size in these glass ceramics is  $\leq 0.1 \mu\text{m}$ , they become transparent and exhibit interesting electro-optic properties. A quadro-electro optic effect is observed when an electric field  $E$  is applied on the as crystallized glass ceramic. The induced birefringence  $\Delta n_2$  is expressed by the equation

$$\Delta n_2 = \frac{1}{2} n^3 g \epsilon^2 E^2,$$

where  $n$ ,  $g$  and  $\epsilon$  are the refractive index, electro-optic coefficient and dielectric constant of the glass ceramic. When an electric field is applied on the prepoled glass ceramic, however, a linear electro-optic effect is observed and the induced birefringence  $\Delta n_1$  is expressed by

$$\Delta n_1 = \frac{1}{2} n^3 g P_1 \epsilon E,$$

where  $P_1$  is the remanent polarization of the glass ceramic. The ferroelectric-electric transition is suppressed below the crystallite size of  $0.1 \mu\text{m}$ . This represents the upper limit upto which these materials are transparent. Therefore linear electro-optic effect cannot be observed in these transparent materials. However, they have a large value of dielectric constant even when the particle size  $< 0.1 \mu\text{m}$ . Therefore, a large quadro-electro-optic effect is observed (Borrelli and Layton 1971).

Observation of a hysteresis loop between polarization and applied electric field

the true test of the presence of ferroelectricity in a given material. Fully developed hysteresis loops have been observed for glass ceramics containing crystallites having size  $> 1 \mu\text{m}$  while some hysteresis effects have been observed down to  $0.2 \mu\text{m}$  (Herczog 1964). For transparent glass ceramics containing particles having size  $< 0.1 \mu\text{m}$ , no hysteresis loops were observed and it can be understood by the absence of domain walls in these small crystallites (Borrelli and Layton 1971). However, the pyroelectric measurements on these glass ceramics show that the sign of the pyroelectric signal reversed on the reversal of the maximum bias field, a positive proof of reversible spontaneous polarization, establishing ferroelectricity in transparent glass ceramics (Layton and Smith 1975).

## 6. Conclusions

Glass ceramics containing a variety of ferroelectric phases can be produced with a precise control of microstructure. The value of dielectric constant can be varied by controlling the crystal content and its size. A high and an almost temperature-independent value of dielectric constant is obtained for crystallite size in the submicron range. If the crystallite size is  $< 0.1 \mu\text{m}$ , these are optically transparent and exhibit a large quadratic electro-optic effect. These characteristics make them potentially useful in various electronic components and devices in different forms (Kokubo *et al* 1968; Herczog 1973; Devendra Kumar and Om Parkash 1985).

Various attempts to precipitate ferroelectric crystallites in the solid solution form to obtain improved properties have not yielded any encouraging results in the case of titanates. Though the formation of extensive solid solution in niobates and tantalates in glass ceramics have been reported, yet no conclusive evidence is given in its support. Therefore problems associated with precipitation of solid solution ferroelectric crystallites in the glass ceramics require detailed investigations. This problem, if solved, will enhance the utilization of ferroelectric glass ceramics.

## References

- Bergeron C G 1961 *Crystallization of perovskite lead titanate from glass*, Ph.D. Thesis, University of Illinois
- Bergeron C G and Russell C K 1965 *J. Am. Ceram. Soc.* **48** 115
- Borrelli N F 1967 *J. Appl. Phys.* **38** 4243
- Borrelli N F, Herczog A and Maurer R D 1965 *Appl. Phys. Lett.* **7** 117
- Borrelli N F and Layton M M 1971 *J. Non-Cryst. Solids* **6** 197
- Buessem W A, Cross L E and Goswami A K 1966 *J. Am. Ceram. Soc.* **49** 33
- Devendra Kumar and Om Parkash 1985 Ferroelectric glass ceramics, Symposium on Emerging Frontiers in Ceramic Engineering, Banaras Hindu University, Varanasi
- Glass A M, Nassau K and Negram T J 1978 *J. Appl. Phys.* **49** 4808
- Grossman D G and Isard J O 1969a *J. Am. Ceram. Soc.* **52** 230
- Grossman D G and Isard J O 1969b *J. Mater. Sci.* **4** 1059
- Herczog A 1964 *J. Am. Ceram. Soc.* **47** 107
- Herczog A 1967 *Glass Ind.* **48** 455
- Herczog A 1973 *IEEE Trans PHP* **9** 247
- Herczog A 1984 *J. Am. Ceram. Soc.* **67** 484
- Kokubo T, Kung C T and Tashiro M 1968 *J. Ceram. Assn. Jpn.* **76** 89
- Kokubo T and Tashiro M 1973/74 *J. Non-Cryst. Solids* **13** 328
- Layton M M and Herczog A 1967 *J. Am. Ceram. Soc.* **50** 369
- Layton M M and Herczog A 1969 *Glass Technol.* **10** 50



## *Glass ceramics containing ferroelectric phases*

- Layton M M and Smith J W 1975 *J. Am. Ceram. Soc.* **58** 435
- Lynch S M and Shelby J E 1984 *J. Am. Ceram. Soc.* **67** 424
- McMillan P W 1979 *Glass ceramics* (2nd ed) (London: Academic Press)
- Nassau K, Wang C A and Grasso M 1979a *J. Am. Ceram. Soc.* **62** 74
- Nassau K, Wang C A and Grasso M 1979b *J. Am. Ceram. Soc.* **62** 503
- Nassau K, Cava R J and Glass A M 1981 *Solid State Ionics* **2** 163
- Om Parkash, Devendra Kumar and Rajgopalan R 1986 *Bull. Mater. Sci.* **8** 13
- Rajgopalan R 1985 *Preparation and characterization of glass ceramic containing ferroelectric*  
M.Tech. Thesis, Institute of Technology, Banaras Hindu University
- Stookey S D 1959 *Glasstech. Ber.* 32K (Fifth International congress on glass, Verlag der De  
Glastechnischen Gesellschaft, Frankfurt am Main) p 574
- Takahashi K, Cross L E and Newnham R E 1975 *Mater. Res. Bull.* **10** 599
- Ulrich D R and Smoke E J 1966 *J. Am. Ceram. Soc.* **49** 210



## Magnetic hysteresis and crystallization studies on metallic glass $\text{Fe}_{67}\text{Co}_{18}\text{B}_{14}\text{Si}_1$

A M VARAPRASAD and C RADHAKRISHNAMURTHY\*

Naval Chemical and Metallurgical Laboratory, Naval Dockyard, Bombay 400 023

\*Tata Institute of Fundamental Research, Bombay 400 005, India

MS received 10 February 1986; revised 21 May 1986

**Abstract.** Magnetic hysteresis studies were carried out on Metglas 2605 Co ( $\text{Fe}_{67}\text{Co}_{18}\text{B}_{14}\text{Si}_1$ ) samples, cut parallel and perpendicular to the ribbon axis and annealed at different temperatures. The samples annealed at  $450^\circ\text{C}$  for 2 hr show a coercive force of 8.75–0.60 Oe in the parallel and perpendicular directions respectively. Electron probe analysis studies revealed the onset of primary crystallization at  $400^\circ\text{C}$  and a displacement of B and Si from the lattice as the annealing temperature was increased to  $450^\circ\text{C}$ . The observed large coercive force is due to an increase in anisotropy resulting from an intergrowth pattern of the type  $\text{Fe}_x\text{Co}_{1-x}\text{B}$ ,  $0.3 < x < 1.0$ , including boron-rich phases such as  $(\text{FeCo})\text{B}$ ,  $(\text{FeCo})_2\text{B}$ ,  $(\text{FeCo})_3\text{B}$ , developed by the displacement of atoms from the original amorphous lattice.

**Keywords.** Amorphous alloys; anisotropy; crystallization; magnetic hysteresis.

### 1. Introduction

Recently, amorphous alloys have emerged as a new class of materials for construction of high performance transducers and sensors. Both isotropic and anisotropic forms of amorphous alloys find applications in device construction (Mohri 1984; Sarin *et al* 1984). The material under study, commercially known as Metglas 2605 (composition  $\text{Fe}_{67}\text{Co}_{18}\text{B}_{14}\text{Si}_1$ ), has a high magnetostriction constant ( $\lambda = 35$  (Allied 1981)) coupled with a higher saturation induction and is suitable for water transducer applications (Mohri 1984). The magnetic properties of this material could be conveniently modified by adopting suitable annealing procedures. The magnetic hysteresis properties, crystallization aspects and its relation to the anisotropy of this material annealed to different temperatures have been reported in this paper.

### 2. Experimental

Metglas 2605 Co ribbon, 50 mm wide,  $27\ \mu$  thick (supplied by Allied Corp USA) was cut into strips of dimensions  $50\text{ mm} \times 4\text{ mm}$  and of equal weight parallel and perpendicular to the ribbon axis. These were annealed at 100, 200, 400 and  $450^\circ\text{C}$  for a constant period of 2 hr.

Hysteresis studies were carried out on the strip samples using a hysteresis tracer (Radhakrishnamurthy *et al* 1978) suitably modified to minimize magnetization effects. The coercive force  $H_c$  measured on the original sample was 0.08 Oe, which corresponds well with the value given in the specification of the material. The crystallization and composition analysis were carried out

electron probe micro analyser (model: Camebax, Chemica, France) (Beaman and Isasi 1972). Phase analysis, if any, was carried out using a Siemens Kristalloflux x-ray diffractometer. The statistical data on the crystallite dimensions were obtained using a TAS plus image analyser.

### 3. Results and discussion

Figures 1(a) to (f) depict the hysteresis of the Metglas samples taken parallel to the ribbon axis and annealed for 2 hr at temperatures (a) as obtained, (b) 100°C, (c) 200°C, (d) 300°C, (e) 400°C and (f) 450°C. The hysteresis loops for samples taken perpendicular to ribbon axis are shown in figures 2(a) to (f). The  $H_c$  data are presented in table 1.

From figures 1(a) and 2(a) a slight difference is seen in the  $H_c$  of the original sample in either direction. It can be inferred, therefore, that the starting samples possess little anisotropy due to magnetostriction and/or magnetoelastic effects (Haregawa 1976; Suja *et al* 1975; Takahashi *et al* 1976). Samples annealed at 400°C have shown clusters of tiny crystallites (figure 3a), without a significant change in the magnetic hysteresis (figures 1e and 2e). The crystallite dimensions range from a few hundred to about a thousand Ångströms. Due to their small size such small crystallites formed with the onset of crystallization may be considered as single domain regions (Chaugule *et al* 1983). At 450°C these crystallites coalesce to form into narrow regions of nearly 50–100  $\mu$  length and about 10  $\mu$  width (figure 3b). The hillock type crystallization products show a regular pattern elongated perpendicular to the ribbon axis. Texture Analysis System (TAS) image analysis revealed that the form factor of the regions is about 0.528 with an equivalent diameter of about 107  $\mu$ .

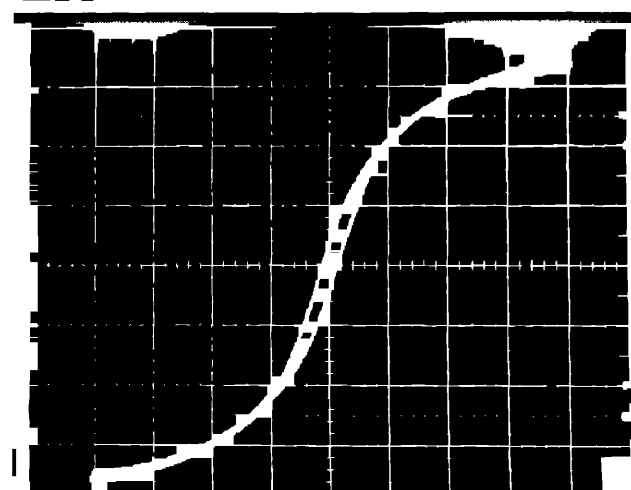
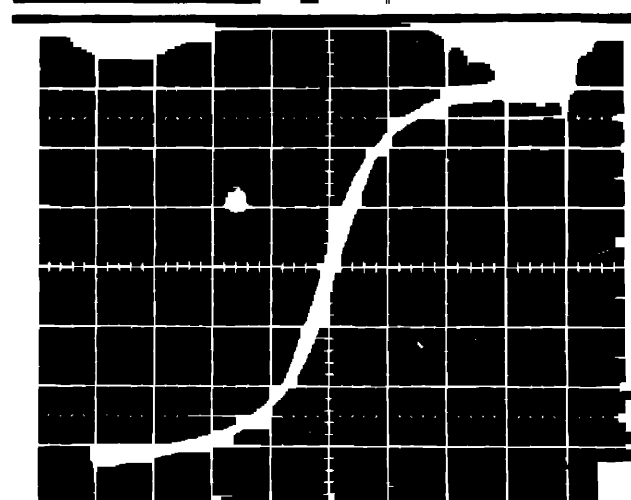
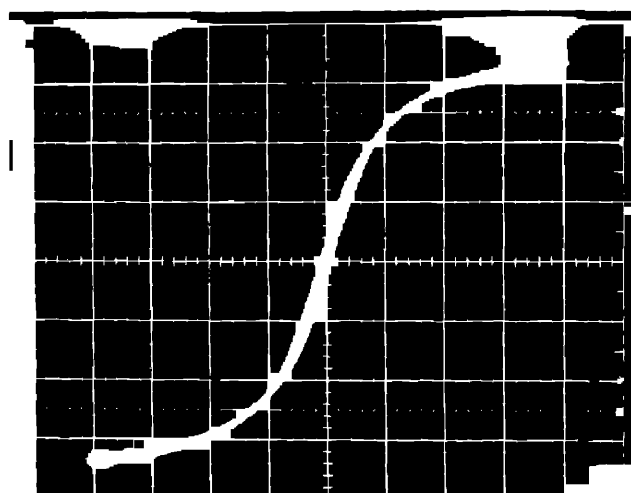
#### 3.1 X-ray diffraction studies

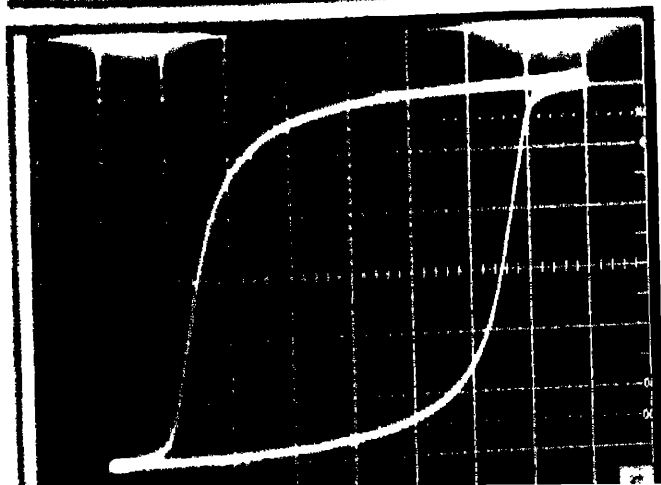
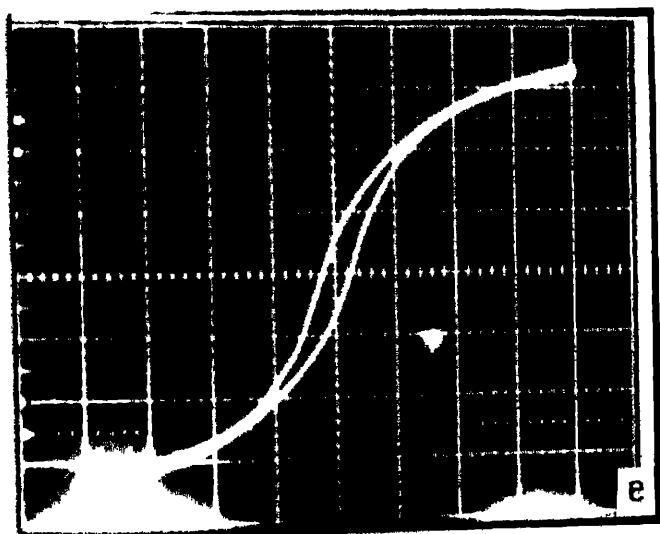
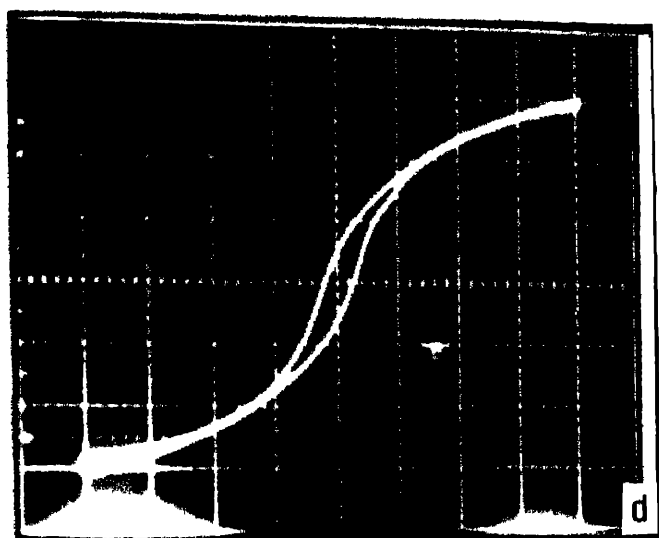
X-ray diffraction analysis revealed a consistent amorphous structure with the samples annealed at 100, 200, 300 and 400°C. The sample annealed at 450°C shows a distinct crystalline diffraction pattern with  $d$ -values at 2.03, 1.43 and 1.17 Å. A variety of phases such as  $\alpha$ -Fe,  $\text{Fe}_x\text{Co}_{1-x}$  (FeCo)B,  $(\text{FeCo})_2\text{B}$ ,  $(\text{FeCo})_3\text{B}$  are expected (Baburaj *et al* 1985; Harold and Kosten 1978; Takacs *et al* 1975). Thus the observed XRD lines possibly belong to some of these phases. Further, distinct regions of  $\alpha$ -Fe or (FeCo) type phases were not identified in the electron probe analysis (see table 2), suggesting that these could be intergrowth regions of submicron dimensions.

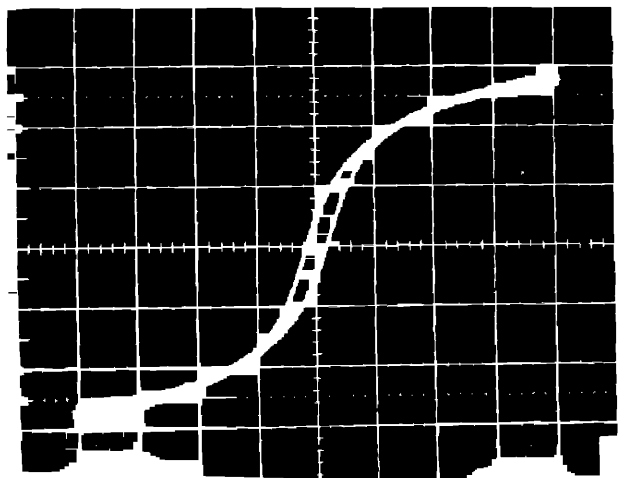
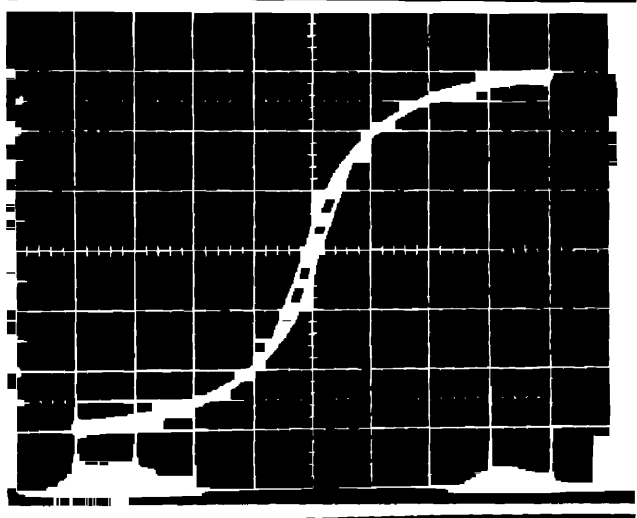
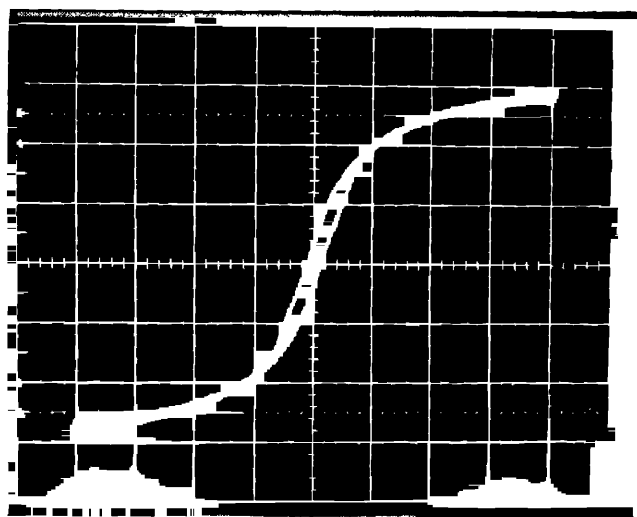
#### 3.2 Electron probe micro analysis

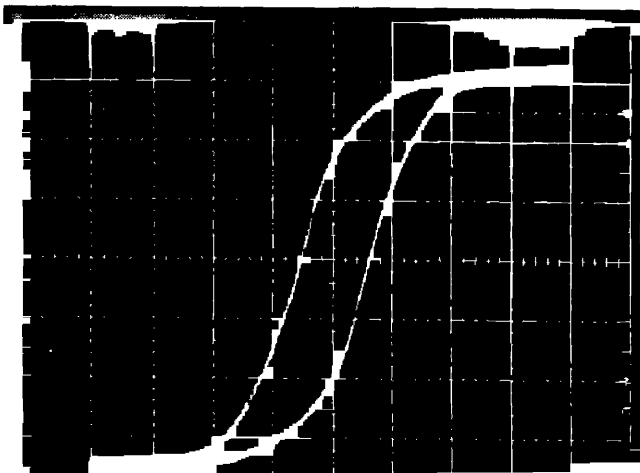
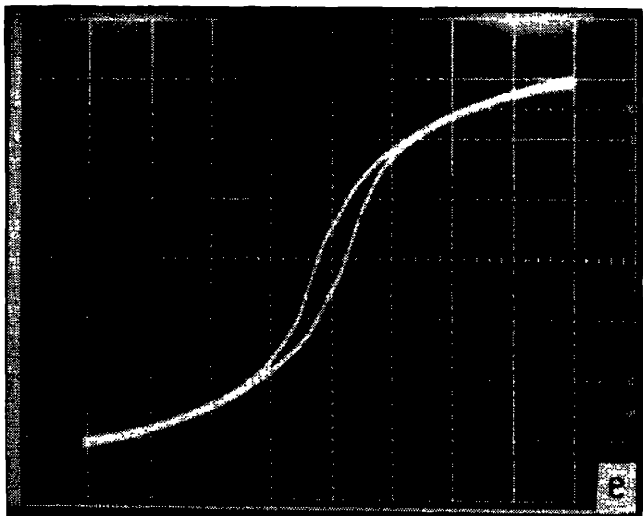
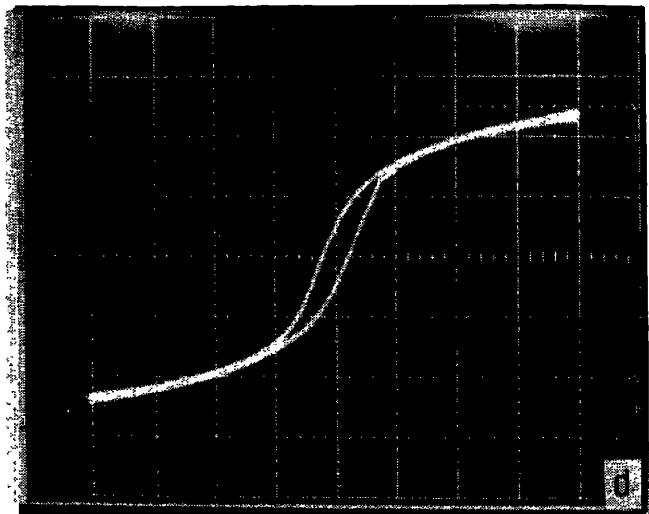
Electron probe micro analysis was carried out at nearly 20, 40, 60 and 80  $\mu$  distance from one end to the other for several crystallites. The percentage composition of

Figure 1. Hysteresis loops of Metglas 2605 Co parallel to the ribbon axis. Annealing temperatures (a) As obtained, (b) 100°C, (c) 200°C, (d) 300°C, (e) 400°C, (f) 450°C. Scale: X-axis (a) to (e) one big division = 2.5 Oe and for (f) it is 3.5 Oe.











**Table 1.** Coercive force  $H_c$  of Metglas 2605 in the directions parallel and perpendicular to ribbon axis.

Annealing temperature (°C)	Coercive force (Oe)	
	Parallel	Perpendicular
30	0.08	0.15
100	0.08	0.15
200	0.15	0.20
300	0.30	0.30
400	0.35	0.35
450	8.75	0.60

Fe, Co, Si was obtained against calibrated standards with a statistical accuracy of 0.5% of the measured value and B concentration was obtained by calculation difference. The error estimated is about +1% of the measured concentration (Beaman and Isasi 1972; Heinrich 1981). The results show a significant variation in composition as given in table 2. These results indicate that the sample is boron-deficient at its centre. When there is a gradual increase in boron away from the centre the composition around the periphery of the sample is enriched in boron and silicon. Also, there seems to be a preferential rejection of boron at the first instance when compared to that of silicon as inferred from enrichment at 20 and 80  $\mu$  (see table 2). The crystallization process could be categorized as the primary crystallization (Baburaj *et al* 1985; Harold *et al* 1978; Takacs *et al* 1975) which involved preferential displacement of boron by silicon into the amorphous matrix. Distinct regions of iron have been observed suggesting that the  $\alpha$ -Fe phase identified in x-ray diffraction study is possibly present as intergrowth regions of submicron dimensions during the crystallization process.

### 3.3 Magnetic anisotropy

The hysteresis loops for the samples annealed at 450°C (figures 1f and 2e) enhanced anisotropic effects.  $H_c$  increased to a value of 0.60 Oe perpendicular to ribbon axis, while it is 8.75 Oe in the parallel direction. However, the sample annealed at 400°C showed an  $H_c$  value of 0.35 Oe in either direction (figure 2e), despite the fact that microcrystalline regions appeared due to the crystallization (figure 3a). The composition of such crystallites is, therefore, expected to be nearly the same as that of the bulk. The crystallization may proceed through the formation of intergrowth structures with complex repeat sequences (Rao *et al* 1981) are possible with the evolution of textures based on Bernal polyhedra (Fisher and Wallace 1981). Further, as seen in figure 3b the hillock regions are elongated perpendicular to the long axis of the ribbon. The hysteresis loops in figures 2d and 2e reveal that the hard axis of the 450°C annealed ribbon lies in a direction perpendicular to the ribbon axis. These results suggest that the intergrowth pattern is likely to be in a direction perpendicular to the long axis of the hillock structure which indicates that the intergrowth patterns are parallel to the ribbon axis.

**Figure 2.** Hysteresis loops of Metglas 2605 Co perpendicular to the ribbon axis: (a) as obtained, (b) 100°C, (c) 200°C, (d) 300°C, (e) 400°C.

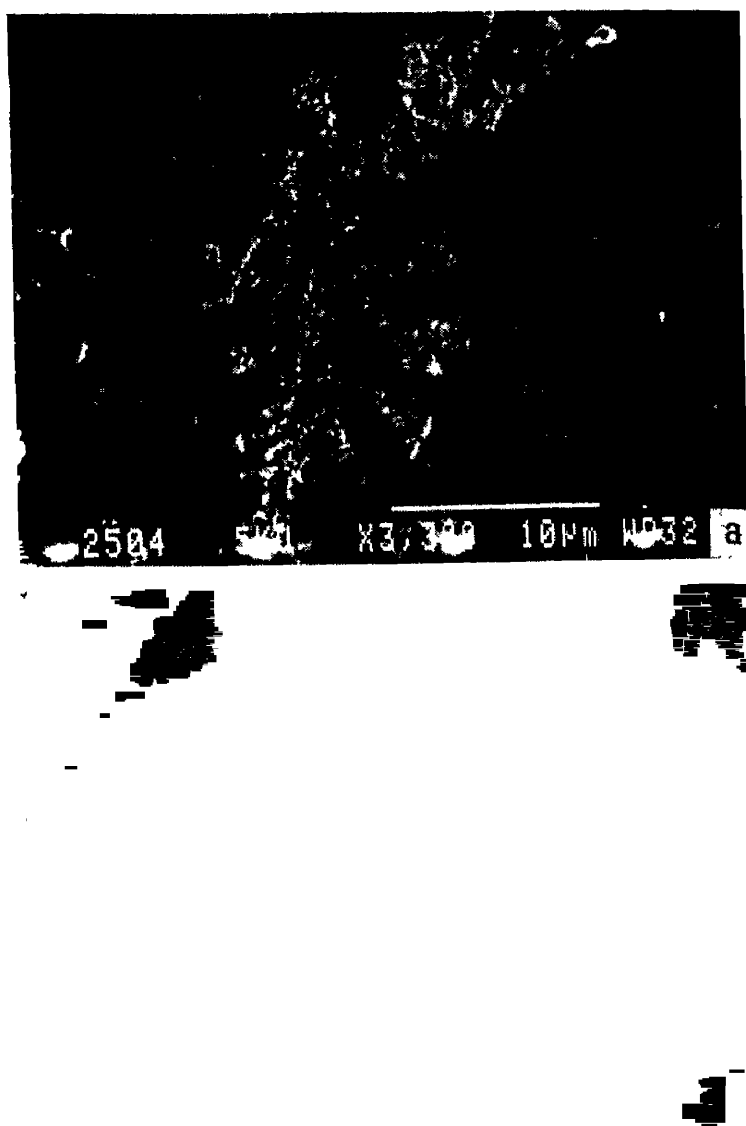


Figure 3. (a) Microcrystallites formed at 400°C. Scale: the bar represents 10  $\mu$ . (b) Hillock type crystallization formed at 450°C. Scale: the larger rectangle represents 100  $\mu$ . Arrow indicates the direction of the ribbon axis.

In accordance with the recent Mössbauer investigations (Bhatnagar *et al* 1985) and in the wake of preferential rejection of boron and silicon, we propose that the intergrowth regions may comprise of compositions of the form  $\text{Fe}_x\text{Co}_{1-x}$ ,  $0.3 < x < 1.0$ ,  $\alpha$ -Fe including the boron-containing phases  $(\text{FeCo})\text{B}$ ,  $(\text{FeCo})_2\text{B}$ ,  $(\text{FeCo})_3\text{B}$  preferentially grown parallel to the ribbon axis. The compositions  $\text{Fe}_x\text{Co}_{1-x}$  with  $0.3 < x < 1.0$  were known to be strongly anisotropic with anisotropic constant  $K$  for  $\alpha$ -Fe,  $\text{Fe}_{0.7}\text{Co}_{0.3}$  and  $\text{Fe}_{0.3}\text{Co}_{0.7}$  being 460, -430 and 102 respectively (Gray 1963). Thus the observed anisotropy

**Table 2.** Typical composition of a crystallite from end to end—EPMA data.

Element	Composition from one end at ( $\mu$ )			
	20	40	60	80
Fe	73.37	75.99	75.49	70.10
Co	20.16	20.56	20.36	19.22
Si	1.01	0.92	0.67	1.14
B By difference	5.46	2.53	3.47	9.54

Note: Fe, Co and Si were estimated against calibrated standards and B concentration was obtained by difference. Estimated error is of the order of  $\pm 1\%$  of the measured value.

$\text{Fe}_{0.3}\text{Co}_{0.7}$  and FeCo among the various compositions that appear as intergrowth regions preferentially formed parallel to the ribbon axis.

#### 4. Conclusions

(i) Thermal annealing of Metglas 2605 Co at  $450^\circ\text{C}$  leads to pronounced magnetic anisotropy with respect to ribbon axis. (ii) The thermally-induced anisotropy in Metglas 2605 Co samples could be explained on the basis of the intergrowth pattern formed preferentially parallel to the ribbon axis leading to local compositions of type  $\alpha\text{-Fe}$ ,  $\text{Fe}_x\text{Co}_{1-x}$  ( $0.3 \leq x \leq 1.0$ ), FeCo,  $(\text{FeCo})\text{B}$ ,  $(\text{FeCo})_2\text{B}$ ,  $(\text{FeCo})_3\text{B}$  etc.

#### Acknowledgements

Sincere thanks are due to Mr V V Modak and Mr K K Karmakar for EPMA/SEM studies. We gratefully acknowledge the useful discussions with Dr S Bar BARC, Bombay. AMV acknowledges his sincere regards to Dr R Krishnan, Director NCML, for initiation, guidance and encouragement.

#### References

- Allied Corporation 1981 Bulletin No. 15M-10/81 on Metglas electromagnetic alloys p 16
- Baburaj E C, Dey G K, Patni M J and Krishnan R 1985 *Scr. Metall.* **19** 305
- Beaman D R and Isasi J A 1972 Electron probe micro analysis: The fundamentals and applications STP 506, Am. Soc. Test Mater. pp 23-28
- Bhatnagar A K, Bhanuprasad B and Jagannathan R 1985 *J. Appl. Phys.* **57** 3514
- Chaugule R S, Radhakrishnamurthy C, Sampathkumaran E V, Mallik S K and Vijayaraghavan M 1985 *Mater. Res. Bull.* **18** 817
- Finney J L and Wallace J 1981 *Proc. Fourth Int. Conf. Rapidly Quenched Metals*, (ed) T Masumoto, K Suzuki Sendai Japan p 253
- Gray D E (ed.) 1963 *AIP Handbook* (2nd edition) (New York: McGraw-Hill) Chapter 5 p 190
- Haregawa R 1976 *AIP Conf. Proc.* **29** 216
- Harold V and Koster U 1978 *Proc. Third Int. Conf. Rapidly Quenched Metals Brighton* (ed) B Cantor p 355
- Heinrich K F J 1981 *Electron beam micro analysis* (New York: Van Nostrand) p 355
- Mohri K 1984 *IEEE Trans. Mag.* **20** 942
- Radhakrishnamurthy C, Lkhite S D and Sahasrabudhe P W 1978 *Proc. Indian Acad. Sci. (Earth Planet. Sci.)* **87A** 245
- Rao C N R 1985 *Bull. Mater. Sci.* **7** 155
- Sasada I, Hiroike A and Harada K 1984 *IEEE Trans. Mag.* **20** 951
- Suza N T, Arai K I, Shiirja Y and Masumoto T 1975 *Phys. Lett.* **A51** 121
- Suza N T, Arai K I, Shiirja Y and Masumoto T 1975 *J. Phys.* **F5** 800



## Influence of eutectic addition on the electrical conductivity of $\text{Li}_2\text{O}:\text{B}_2\text{O}_3$ system

V K DESHPANDE and K SINGH

Department of Physics, Nagpur University, Nagpur 440 010, India

MS received 4 July 1986; revised 13 November 1986

**Abstract.** Addition of three eutectics,  $\text{Li}_2\text{SO}_4:\text{Li}_2\text{CO}_3$ ,  $3\text{Li}_2\text{O}:\text{Nb}_2\text{O}_5:\text{LiNbO}_3$  and  $\text{AgI}:\text{Ag}_2\text{SO}_4$  has been tried in the  $\text{Li}_2\text{O}:\text{B}_2\text{O}_3$  glass system. The electrical conductivity increases with the addition of eutectic. The amount of lithium fraction and the melting point of the eutectic govern the conductivity.

**Keywords.** Eutectic; lithium fraction; electrical conductivity.

### Introduction

In recent years, considerable research has been devoted to electrolytes based on Li ion conducting glasses suitable for solid state batteries. Non-crystalline solid electrolytes have definite advantages over their crystalline counterparts, like isotropic properties, ease of thin film formation, flexibility of size and shape (at satisfactory cost) etc. One of the important features of glass as a solid electrolyte is the possibility of continuous change of the composition over a wide range. A major characteristic of oxide glasses concerns the large variation in the conductivity with alkali oxide content. Recently, more complex glasses have been synthesized by dissolving salts in an oxide based glass (Smedley and Angell 1978; Levasseur *et al* 1979a).

A number of workers have reported fast ion conduction in lithium borate glasses (Otto 1966; Charls 1966; Levasseur *et al* 1979b; Biefeld *et al* 1978; Audier *et al* 1976; Malugani and Robert 1979; Glass *et al* 1978). As reported by Singh and Rokade (1984), conventionally quenched  $\text{Li}_2\text{O}:\text{B}_2\text{O}_3$  (40:60 m%) is the best homogeneous glass-forming composition with maximum conductivity. Tuller and Button (1985) have suggested that an enhancement in the conductivity of  $\text{Li}_2\text{O}:\text{B}_2\text{O}_3$  system can be obtained by increasing the alkali ion concentration. According to Øye (1963) the mobility of Li ion increases in the presence of silver ions. Low melting point is one of the important criteria responsible for high ionic conductivity (Reau *et al* 1978). In a binary system, an eutectic is the lowest melting point composition.

By considering the above factors, an attempt has been made to study the influence on the electrical conductivity of  $\text{Li}_2\text{O}:\text{B}_2\text{O}_3$  (40:60) system by the addition of  $\text{Li}_2\text{SO}_4:\text{Li}_2\text{CO}_3$ ,  $3\text{Li}_2\text{O}:\text{Nb}_2\text{O}_5:\text{LiNbO}_3$  and  $\text{AgI}:\text{Ag}_2\text{SO}_4$  eutectics. It is expected that the presence of these eutectics in the glass system under study will provide an enhancement in the conductivity.

### 2. Experimental details

In the present work, the starting materials,  $\text{Li}_2\text{SO}_4$ ,  $\text{Li}_2\text{CO}_3$ ,  $\text{B}_2\text{O}_3$ ,  $\text{AgI}$ ,  $\text{Ag}_2\text{SO}_4$  and  $\text{Nb}_2\text{O}_5$  of 99.9% purity were used for the synthesis of the glasses. For preparing

$\text{Li}_2\text{SO}_4:\text{Li}_2\text{CO}_3$  eutectic, about 10 g of raw material in eutectic ratio (60:40) m% was weighed to an accuracy of 0.0001 g and mixed under acetone. The mixture was then heated in an electric furnace. It was maintained at a temperature of 20 K above the melting point for 2 hr to homogenize the melt. Then the melt was quenched in an aluminium mould at room temperature. This eutectic was then crushed to a fine powder and added in the host  $\text{Li}_2\text{O}:\text{B}_2\text{O}_3$  system.

Similarly, other eutectics of  $3\text{Li}_2\text{O}:\text{Nb}_2\text{O}_5:\text{LiNbO}_3$  and  $\text{AgI}:\text{Ag}_2\text{SO}_4$  were prepared. Later, these eutectics were added in different concentrations to the lithium borate glass. In all these compositions, the ratio of  $\text{Li}_2\text{O}:\text{B}_2\text{O}_3$  was maintained to be 40:60 m%. After quenching the glasses in aluminium mould, they were immediately transferred to an annealing furnace maintained at 473 K. After 4 hr of annealing, the samples were subjected to furnace cooling.

The glasses thus obtained were polished flat. Silver paint was used to ensure the ohmic contact before loading the sample in the sample holder which has been described elsewhere (Deshpande and Singh 1982). The conductivity of these samples was measured at 1 kHz as a function of temperature.

### 3. Results and discussion

Figure 1 shows the variation of  $\log \sigma T$  vs  $10^3/T$  for  $\text{Li}_2\text{O}:\text{B}_2\text{O}_3$  glass system with addition of three eutectics;  $\text{Li}_2\text{SO}_4:\text{Li}_2\text{CO}_3$ ,  $3\text{Li}_2\text{O}:\text{Nb}_2\text{O}_5:\text{LiNbO}_3$  and  $\text{AgI}:\text{Ag}_2\text{SO}_4$ . In general, the conductivity increases with increase in temperature. Typical conductivity values at two different temperatures, lithium fraction and the melting point of the dopant eutectic, are given in table 1 and it is evident that the addition of all the

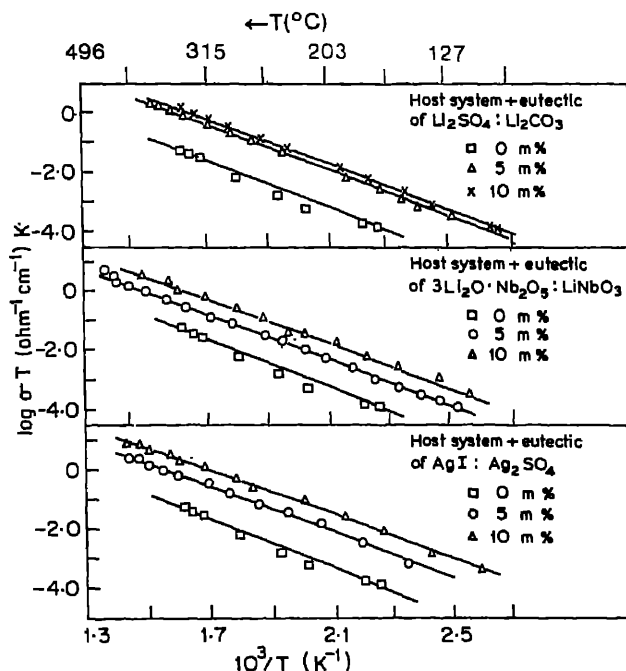


Figure 1. Variation of  $\log \sigma T$  vs  $10^3/T$  for  $\text{Li}_2\text{O}:\text{B}_2\text{O}_3$  host system with the addition of three different eutectic.

## Eutectic addition in $\text{Li}_2\text{O}:\text{B}_2\text{O}_3$

**Table 1.** Conductivity values at 623 and 523 K, lithium fraction and melting point dopant eutectic.

$\text{Li}_2\text{O}:\text{B}_2\text{O}_3$ (40:60) + 10 m% of eutectic	$\sigma$ in $\text{ohm}^{-1} \text{cm}^{-1}$ at		$*f_{\text{Li}}+$	Melting point of the eutectic
	623 K	523 K		
$\text{Li}_2\text{SO}_4:\text{Li}_2\text{CO}_3$	$1.15 \times 10^{-4}$ $2.02 \times 10^{-3}$	$5.70 \times 10^{-5}$ $1.51 \times 10^{-4}$	0.80 0.92	530°C (Amadori 1912)
$3\text{Li}_2\text{O}:\text{Nb}_2\text{O}_5:\text{LiNbO}_3$	$1.60 \times 10^{-3}$	$1.35 \times 10^{-4}$	0.84	1160°C (Reisman 1958)
$\text{AgI}:\text{Ag}_2\text{SO}_4$	$4.03 \times 10^{-3}$	$5.3 \times 10^{-4}$	0.72	158°C (Takahashi <i>et al</i> )

$$*f_{\text{Li}} = \frac{2^n \text{Li}_2\text{O} + 2^n \text{Li}_2\text{SO}_4 + 2^n \text{Li}_2\text{CO}_3}{n \text{Li}_2\text{O} + n \text{B}_2\text{O}_3 + n \text{Li}_2\text{SO}_4 + n \text{Li}_2\text{CO}_3}$$

where  $n_i$  is the number of moles of constituent  $i$  in the mixture.

three eutectics enhances the conductivity of the host system by more than an order of magnitude. The enhanced conductivity for higher concentration of the first eutectics is due to increased  $\text{Li}^+$  fraction. Similar enhancement in the conductivity with increasing  $\text{Li}^+$  fraction has been reported earlier (Deshpande *et al* 1985).

Among the three eutectic samples, the conductivity for  $3\text{Li}_2\text{O}:\text{Nb}_2\text{O}_5:\text{LiNbO}_3$  is minimum. This is because of its higher melting point and lower lithium fraction than that for  $\text{Li}_2\text{SO}_4:\text{Li}_2\text{CO}_3$ . The lithium fraction for 10 m%  $\text{Li}_2\text{SO}_4:\text{Li}_2\text{CO}_3$  composition sample (0.92) is higher than that observed for 7 m%  $\text{Li}_2\text{SO}_4$  containing  $\text{Li}_2\text{O}$  glass (0.88) (Deshpande *et al* 1985). Also the conductivity in this case is higher than what was reported earlier for 7 m%  $\text{Li}_2\text{SO}_4$  added sample. Thus, the melting point of the eutectic and the lithium fraction governs the conductivity for eutectic compositions.

For 10 m%  $\text{AgI}:\text{Ag}_2\text{SO}_4$  eutectic, maximum conductivity is observed. This is because of the lowest melting point of this sample over all the others studied in the present investigation. This sample was a homogeneous glass without any crystallization in it suggesting that, upto 10 m%,  $\text{AgI}:\text{Ag}_2\text{SO}_4$  gets adjusted in the amorphous matrix of the host system. The  $\text{SO}_4$ , being tetrahedra might expand in the  $\text{BO}_3/\text{BO}_4$  glass network. Due to the larger size of the iodine, it expands the network which enhances the mobility of the mobile ion. In this case, silver ions might contribute to the conduction. However, due to non-availability of the experimental facilities, it was not possible to separate out the contribution of silver and boron ions. The study of  $\text{AgX}$  ( $\text{X}=\text{I}, \text{Br}$ ) containing borate glasses suggests that containing glasses give more conductivity (Minami *et al* 1982). According to (1983), those  $\text{Ag}^+$  ions surrounded by halide ions in the glass contribute to the conduction. In  $\text{B}_2\text{O}_3$  containing glasses,  $\text{Ag}^+$  ions interacting with  $\text{BO}_4$  groups contribute to the conduction as well as the  $\text{Ag}^+$  ions surrounded by halide ions.

## 4. Conclusion

From the present investigation it can be concluded that, lower the melting point of the eutectic, higher is the conductivity of the system. The maximum conductivity,  $\sigma \approx 4.03 \times 10^{-3} \text{ ohm}^{-1} \text{cm}^{-1}$  at 623 K obtained for 10 m%  $\text{AgI}:\text{Ag}_2\text{SO}_4$  eutectic can be used for technical applications.

## References

- Amadori M 1912 *Atti Reale Acad. Lincei* **21** 68
- Audier M, Ravaine D and Souquet J C 1976 *C R Acad. Sci.* **C282** 499
- Biefeld R M, Johnson R T and Baughman R J 1978 *J. Electrochem. Soc.* **125** 179
- Charls R J 1966 *J. Am. Ceram. Soc.* **49** 55
- Deshpande V K and Singh K 1982 *Solid State Ionics* **6** 18
- Deshpande V K, Rokade S and Singh K 1985 *Proc. Sixth Riso Int. Symp. on Transport-structure Relations in fast ion and Mixed Conductor*, (eds) F W Poulsen, N Hessel Andersen, K Clausen, S Skaarup and O Toft Sørensen (Denmark: RISØ National Laboratory) 227
- Glass A M, Nassau K and Negran T J 1978 *J. Appl. Phys.* **49** 4808
- Levasseur A, Kbala M, Brethous J C, Reau J M and Hagenmuller P 1979a *Solid State Commun.* **32** 839
- Levasseur A, Brethous J C, Reau J M and Hagenmuller P 1979b *Mater. Res. Bull.* **14** 921
- Malugani J P and Robert G 1979 *Mater. Res. Bull.* **14** 1075
- Minami T, Ikeda Y and Tanaka M 1982 *J. Non-Cryst. Solids* **52** 159
- Minami T 1983 *J. Non-Cryst. Solids* **56** 15
- Otto K 1966 *Phys. Chem. Glasses* **7** 29
- Øye H A 1963 Thesis, Trondheim, Norway
- Reau J M, Portier J, Levasseur A, Villeneuve and Pouchard M 1978 *Mater. Res. Bull.* **13** 1415
- Reisman A and Holtzberg F 1958 *J. Am. Chem. Soc.* **18** 6503
- Singh K and Deshpande V K 1982 *Proc. DAE Symp. on Interactions at electrode Electrolyte Interfaces* Indian Inst. Technol., Madras, p 167
- Singh K and Rokade S 1984 *J. Power Sources* **13** 151
- Smedley S I and Angell C A 1978 *Solid State Commun.* **27** 21
- Takahashi T, Nomura E and Yamamoto O 1972 *J. Appl. Electrochem.* **2** 51
- Tuller H L and Button D P 1985 *Proc. Sixth Riso Int. Symp. on Transport-structure Relation in fast ion and Mixed conductors, Denmark*, 119



## Optical black coatings for space applications

K RAMASESHAN, M VISWANATHAN and G K M THUTUPALLI

ISRO Satellite Centre, Bangalore 560 017, India

MS received 19 October 1985; revised 2 January 1986

**Abstract.** The durability properties of PTX-205 optical black coatings deposited on metallic and non-metallic substrates are studied. The coatings are stable against adverse environmental requirements for space applications. Typically, coatings with 8-11  $\mu$  thickness are opaque and have an average reflectance loss (<5%) in the spectral range of 200-1500 nm. The absorption to emission ratio is 1.01.

**Keywords.** Black coatings; opaque coatings.

### 1. Introduction

Electrically conducting optical black coatings are extensively used in various terrestrial and space-oriented optical, thermal and electrical appliances (Birnbau *et al* 1982). A few important applications among these are: (i) in high absorbing and low scattering of optical devices in far infrared cryogenic systems; (ii) as spectral masks in satellite-based electro-optical sensors; (iii) in thermal detectors and so on as absorbers to increase their efficiency; and (iv) in space-borne systems to keep differential charging of spacecraft external surfaces and equipment to a minimum and prevent problems due to electrostatic fields, arc etc.

For these, a variety of optical black coatings ranging from simple carbon soot to layers of burning camphor, wax, kerosene etc., to vacuum-evaporated metallic and non-metallic blacks are available (Harris *et al* 1948; Okamoto and Hatanaka 1979). However, when these coatings are used for defence and space applications, they should not only meet the basic optical and electrical properties needed for terrestrial systems, but also should functionally be stable against the adverse environmental conditions (table 1) to which they are exposed to, over an extended period of time. But, our experience shows that the majority of these black coatings cannot meet these requirements.

Even among the limited black paints available, there are hardly any studies available on their durability properties although their optical and electrical properties are known. In many cases, the details of the process technology are treated as guarded trade secrets.

Keeping these in view, a systematic study of the functional and durability properties of various organic and inorganic blacks has been carried out and in this paper, the coating process technology, the functional and durable properties of PTX-205 of Polytronix brand are reported (Bach 1982).

### 2. Process technology

The various performance requirements and specifications to be met for a space/terrestrial borne black paint are summarized in tables 1 and 2. While sc

Table 1. Performance specifications.

Adhesion	Cellotape peel test (MIL-F-48616)
Abrasion	Eraser abrasion for 50 strokes with 0.5 kg continuously applied.
Humidity	Steady state ( $48^{\circ} \pm 2^{\circ}\text{C}$ ) and 95–100% relative humidity for 24 hr (MIL-C-675A)
Temperature	
(a) Soaking	at high temp. $+85^{\circ}\text{C}$ for 24 hr at low temp. $-85^{\circ}\text{C}$ for 24 hr
(b) Thermal shock	100 cycles, each cycle consisting of a dwell time of 10 min each, at $+85^{\circ}\text{C}$ , ambient, $-85^{\circ}\text{C}$ , ambient and then back at $+85^{\circ}\text{C}$ with a transfer time from one temperature to another in less than 15 sec
Vacuum baking	At $85^{\circ}\text{C}$ and $10^{-3}$ torr for 24 hr
Salt solubility	Immersed in a salt solution of 4%, (common salt in water) at room temperature for 24 hr (MIL-C-675A)

Table 2. Performance specifications.

Parameter	Desired value
Substrate for coating	Metallic/non-metallic
Outgassing (total mass loss)	Less than 1%
Pinholes on the coated area	Class-A (number of pinholes of size 0.05 mm per square cm will be less than 1).
Transmittance	1% in the visible and near IR
Total reflectance	< 5%
Emissivity	> 0.8

the applications such as thermal control of devices require only deposition of black coatings on suitable metallic/non-metallic substrates, some other applications such as (space borne sensor masks etc) also require a suitable pattern generation on the black paints. Therefore, its optimized process technology is presented in this paper. The functional and durability properties of the black paint so deposited on metallic/non-metallic substrates with and without pattern are also reported.

## 2.1 Substrate preparation

For non-metallic substrates, optically plane glass and quartz (25 mm  $\times$  25 mm size and 1.5 mm thick) are taken and their surface quality is better than 60:40 in the optical standards. Aluminium and copper foils (25 mm  $\times$  25 mm square and 100  $\mu\text{m}$  thick) and free from streaks, scratches and wrinkles etc., are used for metallic substrates.

Substrate cleaning prior to deposition of coating plays a vital role and the following cleaning procedure is adopted. The glass and quartz substrates are vapour degreased to remove grease, oil etc in reagent grade trichloroethylene, followed by sequential ultrasonic cleaning in alkaline solution, distilled water and chromic acid. They are then rinsed in distilled water and finally, ultrasonically, cleaned in reagent

grade isopropyl alcohol. The aluminium and copper foils are vapour-degreased and cleaned in dilute hydrochloric acid, distilled water and dried. The substrates are baked at 200°C for 30 min.

## 2.2 Coating process and generation of pattern

The cleaned dry surface on which the black coating has to be deposited is treated with silane type adhesion promoter (Polytronix) and spin-dried at 4000 rpm. The black paint is then spread uniformly, spin-coated and baked at 90°C for 45 min. The photoresist (Waycoat HPR-204 positive photoresist) is similarly spin-coated on the dried black surface and pre-baked at 90° for 45 min. The photoresist is exposed under the desired photomask, developed and post-baked at 90°C for 45 min. The unprotected black is etched in a warm dilute alkaline solution at 50°C to realize the final pattern. The treated surface is rinsed in distilled water and dried. The undeveloped photoresist is stripped and the sample is baked at 200°C for 60 min.

## 2.3 Thickness measurement

Thickness of black coatings is maintained in the range of 8–12  $\mu$ . Films with thickness lower than 8  $\mu$  on the non-metallic substrates cannot meet the required opacity level. On the other hand, for films, thicker than 12  $\mu$  on both metallic and non-metallic substrates, although the functional properties remain unaltered the adhesion is poor. The thickness is measured at various points randomly on the coatings using vertical metroscope (Carl Zeiss, Jena ABBE P 01) having a resolution of 0.1  $\mu$ .

It has been observed that due to variations in the speed of the spinning system used in this Laboratory, a non-uniformity upto  $\pm 0.5 \mu$  is noticed in the coating. But as it can be seen later, these variations do not have adverse effect on the required properties of the coatings when subjected to environmental test conditions.

## 3. Test results

### 3.1 Functional properties

**3.1a Thermo-optical properties:** The transmission spectra of the coated samples are measured in the range of 400–1000 nm and 2–15  $\mu$  on spectrometers (Schimat Model VV-120-02 and Perkin Elmer Model 783). The reflection spectra are measured in the same ranges on the photospectrometer (Beckmann Model AC MIV and Perkin Elmer Model 783). For non-metallic substrates, the average reflectance is <5% in the entire spectral range and transmittance is <0.1% in range 400–1500 nm and zero in the range 2–15  $\mu$ . For metallic substrates, while transmittance is zero, the reflectance values are less than 5% in the entire spectral range. Typical reflectance spectra on metallic/non-metallic substrates are shown in figures 1a and 1b. The noise spectrum in the range 6 to 7  $\mu$  seen in figure 1b is due to the ambient water vapour and is not the intrinsic property of the coatings. Reflectance values are measured using an emissometer (Devices and Serv

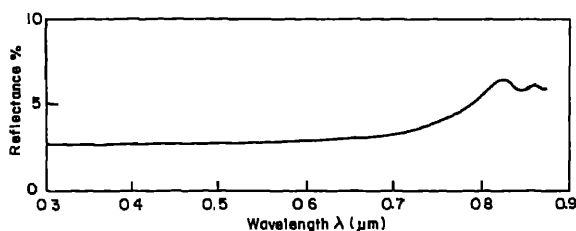


Figure 1a. Reflection spectra of PTX-205.

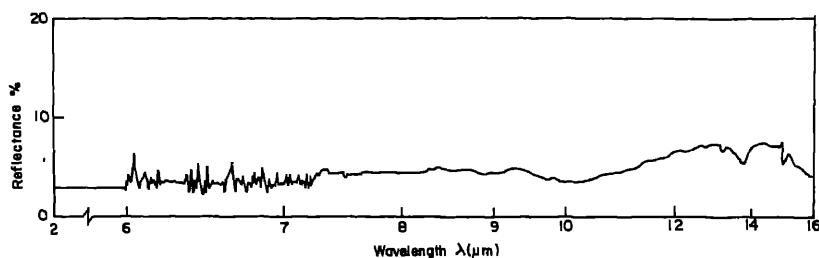


Figure 1b. Reflection spectra of PTX-205.

Company Model 4, E.S.No. 175) and the values range from 0.83 to 0.86 depending upon the surface finish. However, the results are reproducible to an accuracy of  $\pm 1\%$ . The corresponding absorption to emission (a/e) ratio is calculated to be 1.01.

**3.1b Electrical properties:** To estimate the volume and surface resistivities, the following simple method is adopted.

A conducting foil is cut and placed exactly over the painted area of a metallic substrate and compressed firmly against the paint surface. Resistance is measured from the top surface of the conducting foil to the bottom of the substrate. From this the volume resistivity is calculated. The measurements on different samples show that the volume resistivity is in the range of 18.14 ohm metre to 6.1 ohm metre for the coating thickness corresponding to the range of 10 to 8  $\mu$ . The surface resistivity is deduced from this and the corresponding values range from 1.814 ohms per square to 0.76 ohms per square.

**3.1c Mechanical properties:** Five samples are selected at random in a batch of 30 samples and the adhesion test is conducted according to military standards (MIL-F-48616). A scotch tape (peel strength 0.5 kg/cm) is uniformly adhered to the coating surface by pressing it against the surface. The tape is peeled rapidly at an angle between  $45^\circ$  and  $90^\circ$  to the surface. The coating is evaluated for peel-off and other surface defects such as pin holes, scratches etc. Also, the optical properties are measured as post-adhesion test. The bonding is extremely good in all the samples and no deterioration in the optical properties and no defects in the coating surface quality are found.

## Optical black coatings

A moderate abrasion test is conducted on the same set of samples. The surface is abraded with a standard eraser mounted in an eraser abrasion cou tester. The rubbing is done across the surface from one point to another over same path for 50 strokes with a load of 0.5 kg continuously applied. The length of stroke is approximately 3 times the diameter of the eraser piece. The surface is evaluated for cosmetic defects and the optical properties measured as post-abrasion tests. No deterioration is observed suggesting the good abrasion resistance of the black paint system.

### 3.2 Durability properties

Stability of the functional properties of the samples, when subjected to accelerated environmental conditions (table 1), is evaluated to ascertain the usefulness of the black coatings for various other applications in space. A batch of samples is divided at random into sets, each consisting of 5 numbers, and tests are conducted on the set of samples in the sequence given in figure 2. Commonly available environmental test chambers are used and the standard procedure adopted (MIL-C-675A). The results are summarised in table 3.

## 4. Conclusion

The PTX-black coatings are stable functionally against adverse environmental conditions such as humidity, thermal shock cyclings, etc. These coatings are

Table 3. Summary of test results under accelerated environmental conditions.

Type of test	Inference
Adhesion	Surface quality —Good Optical properties —Good
Abrasion	—do—
Humidity	—do—
Thermal shock	—do—
Thermal soaking	
(i) Hot soaking	*Pinholes (5–10 number) appear randomly on samples. But their sizes are <0.05 mm The integrated optical transmission is less than the visible and near IR
(ii) Cold soaking	No change in the surface quality or pinhole number
Vacuum baking	*Pinholes appear randomly. But their size is <0.05 mm The integrated optical transmission is not affected <0.1%. Total mass loss <1%
Salt solubility	Surface quality —Good Optical properties —Good

\*(In hot soaking and vacuum baking, except for the vacuum environment, the temperature and duration of heating are the same. Therefore, with extended heating, the pinholes appear due to the release of entrapped air lockets during coating)

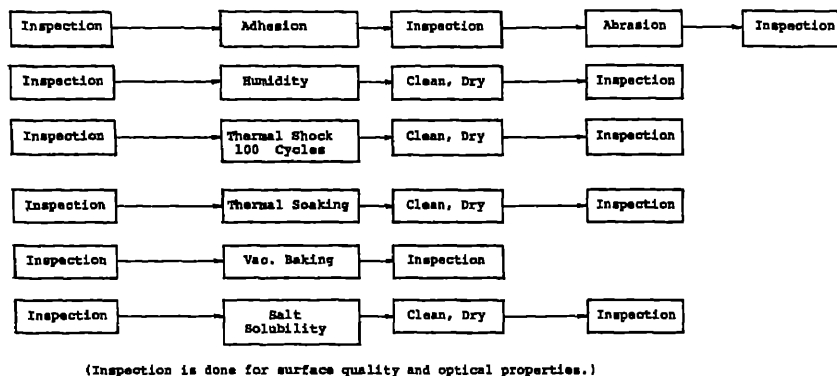


Figure 2. Test sequence.

applied on metallic/non-metallic substrates, either as a uniform layer or as layer with required pattern generation and these can find immense applications in various terrestrial and space-borne systems.

## References

- Birnbaum M, Mettler E C and Cieland E L 1982 *Proceedings of SPIE* **362** 60  
 Harris L, McGinnies R T and Siegel B M 1948 *J. Opt. Soc. Am.* **38** 582  
 Lineback R J 1982 *Electronics* April 21 42  
 Okanto S and Hatanaka Y 1981 *Bull. Bismuth Inst.* **33** 8  
 Polytronix data sheet P O Box 3024 Richardson Texas 75081  
 US Military Specification MIL-C-675A 1976 Coating of glass optical elements  
 US Military Specification MIL-F-48616 1977 Federal Specification L-T-90 Tape pressure sensitive adhesive cellophane and cellulose acetate

## Dislocation density in electrolytically-coloured KCl crystals

N L BHOLE\* and B T DESHMUKH

Department of Physics, Nagpur University, Nagpur 440 010, India

\*Department of Physics, Vidarbha Mahavidyalaya, Amravati 444 604, India

MS received 5 May 1986; revised 6 August 1986

**Abstract.** Dislocation densities have been investigated in potassium chloride crystals electrolytically coloured in the temperature range of 550–710°C. The results show an increase in the dislocation density with coloration temperature upto 650°C and decrease thereafter. This is attributed to the movement of dislocations and interactions between them during electrolytic coloration of the crystals.

**Keywords.** Dislocation density; electrolytic coloration; coloration temperature; dislocation annihilation.

### 1. Introduction

It is well known that dislocations play an important role in the coloration of alkali halide crystals (Seitz 1954; Belyaev *et al* 1968; Koikov *et al* 1967). Dislocation densities in electrolytically-coloured alkali halides have been studied earlier (Deshmukh and Soman 1976; Kolomiitsev *et al* 1978). However, there is no work on the temperature variation of dislocation density in electrolytically-coloured crystals. An attempt is therefore made in this paper to study the effect of variation of coloration temperature on dislocation density in electrolytically-coloured KCl crystals.

### 2. Experimental procedure

Single crystals of KCl used in the present work were grown from melt by the Czochralski technique. Two crystals (each of size  $10 \times 5 \times 5 \text{ mm}^3$ ) obtained from the as-grown block were used in the experiments. One of them (to be electrolytically coloured) was mounted between two platinum electrodes (one pointed electrode and the other flat) and the other was placed beside it in the coloration furnace. The temperature of the crystals was measured with an accuracy of  $\pm 5^\circ\text{C}$  by chromel-alumel thermocouple. The crystals were kept at the required temperature for near an hour. The crystal clamped between the electrodes was coloured with a pointed cathode by applying a DC electric field of 120 V. After coloration, both the coloured and uncoloured crystals were quenched by rapidly removing them from the furnace and placing them on the metal plate. In this manner the crystals were coloured at desired temperatures ranging from 550°C to 710°C.

The coloured and uncoloured crystals were cleaved from the central part of the crystals and etched with an etchant consisting of an ethanol (99%) saturated at 50°C with  $\text{PbCl}_2$ . This etchant is found to attack at dislocation sites on (100) faces of KCl crystals. The dislocation density was measured with a  $\text{NU}_2$  research microscope on a number of crystal specimens and the average dislocation density was obtained at each temperature.

## Results and discussion

It is observed that electrolytic coloration proceeds at a faster rate with increase of coloration temperature i.e. the efficiency of formation of colour centres increases with increase of coloration temperature. For example, the coloration over the entire crystal takes 4 min at 550°C and about 30 sec at 710°C.

Figures 1a and 1b respectively show the variation of dislocation density with temperature in KCl crystals for uncoloured and coloured crystals. The dislocation density varies linearly with temperature in uncoloured crystals and nonlinearly in coloured crystals. Dislocation density in coloured crystals reaches a maximum at 650°C and decreases on either side of 650°C. Figures 2a, b and c show the photomicrographs of dislocation patterns in KCl crystals electrolytically-coloured at 550°C, 650°C and 710°C respectively. Figure 2b shows the maximum dislocation density at 650°C.

The observed increase of dislocation density linearly with quenching temperature in uncoloured crystals can be attributed to severe surface stresses developed in the crystals with increasing quenching temperature (Rao and Hari Babu 1976; Chawre *et al* 1978).

For coloured crystals the coloration temperature range can be divided into two parts (i) coloration temperature from 550°C to 650°C in which the dislocation density increases with temperature and (ii) coloration temperature above 650°C in which dislocation density decreases with temperature. In the range 550–650°C, as the dislocation density increases linearly with coloration temperature the behaviour of a coloured crystal is similar to that of the uncoloured one and the increase in dislocation density can again be attributed to surface stresses. In other words, the electrolytic coloration has only a little effect on the increase of dislocation density up to coloration temperature 650°C. Its effects in decreasing the dislocation density in KCl crystals are, however, seen above the coloration temperature of 650°C.

Electrolytic coloration occurs at high temperature with large electric field gradient. Under these conditions, dislocations move inside the crystals. In the range of coloration temperature 550–650°C, the dislocations during their motion may take vacancies (possibly anion vacancies) with them thereby forming positive jogs in them.

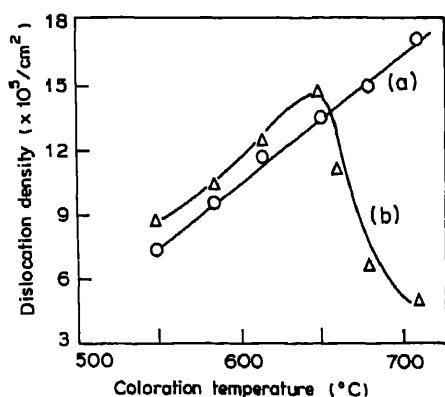


Figure 1. Variation of dislocation density with temperature in KCl crystals (a) uncoloured, (b) electrolytically coloured.



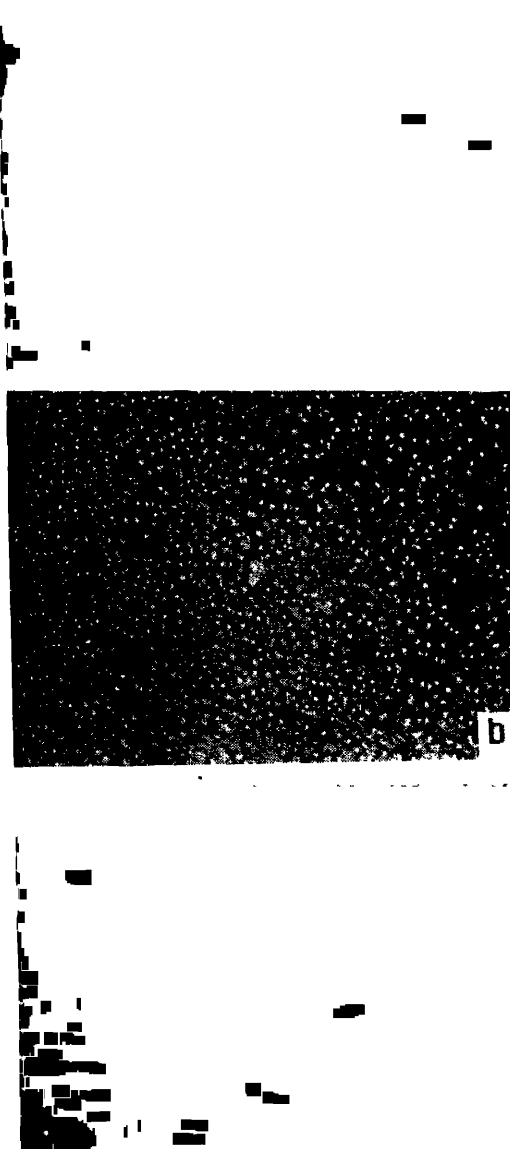


Figure 2. Photomicrographs of electrolytically coloured KCl crystals. a. Coloured at 550°C; b. Coloured at 650°C; c. Coloured at 710°C.

These anion vacancies may be formed due to the dissociation of *F*-centres by dislocations (Sierra and Cabrera 1975). This presence of jogs in the dislocation impedes its motion. The dislocations will thus move comparatively slowly which will lead to an increase in the dislocation density. The jogs in the dislocation may increase with increase of coloration temperature which will provide greater resistance to the motion of dislocation. As a result, dislocations will move slowly with increasing coloration temperatures thereby giving rise to an increase in dislocation density with increasing coloration temperatures.

In the range of coloration temperature 650–710°C the decrease of dislocation density can be attributed to the mutual annihilation of opposite edge dislocations. This might occur because, in this temperature range the dislocations become sufficiently mobile to cause their annihilation. The annihilation of opposite dislocations may result from the following two processes: (i) when two opposite dislocations glide on the same plane, their mutual interaction results in a perfect lattice; (ii) when two opposite edge dislocations glide on neighbouring planes, their interaction will leave a row of vacancies or interstitials. This row of vacancies or interstitials diffuse away under the conditions of high temperature and high electric field gradient of electrolytic coloration leaving a perfect lattice. This process of diffusion of vacancies or interstitials is energetically costly and thus occurs at high temperatures only. The above two processes contribute to the decrease in dislocation density above 650°C. Deshmukh and Soman (1976) observed such a decrease in dislocation density in alkali halides on electrolytic coloration. The process of annihilation of dislocations increases at increasingly high temperatures which results in decrease in dislocation density at temperatures beyond 650°C. At temperatures upto 650°C the energy supplied is insufficient for the diffusion of vacancies produced during the interaction of opposite dislocations. Hence the process of annihilation of opposite dislocations does not occur before 650°C.

#### 4. Conclusions

Our results show that the dislocation density in the electrolytically coloured KCl crystals increases with coloration temperature upto 650°C and decreases thereafter. The following conclusions can be drawn: (i) The efficiency of electrolytic coloration increases with coloration temperature in KCl crystals, (ii) dislocation density in electrolytically coloured KCl crystals varies nonlinearly with coloration temperature, (iii) dislocations in electrolytically coloured KCl crystals are generated in the temperature range 550–650°C whereas they are annihilated in the temperature range 650–710°C.

#### Acknowledgement

NLB is thankful to the UGC, New Delhi for financial assistance.

#### References

- Belyaev V D, Semuskin G B and Tsikin A N 1968 *Sov. Phys. Solid State* **9** 2564
- Chawre R S, Jain S K and Shrivastava R N 1976 *Indian J. Pure Appl. Phys.* **16** 434
- Deshmukh B T and Soman S T 1978 *Pramana (J. Phys.)* **7** 423
- Koikov S N, Semuskin G B and Tsikin A N 1967 *The Physics of dielectrics and semiconductors* (Leningrad)
- Kolomiitsev A I, Svetashov A A and Tyapunina N A 1978 *Sov. Phys. Crystallogr.* **23** 138
- Rao M L and Hari Babu V 1976 *Indian J. Pure Appl. Phys.* **14** 769
- Seitz F 1954 *Rev. Mod. Phys.* **26** 64
- Sierra J and Cabrera J M 1975 *Phys. Status. Sol.* **A27** K43

## Low-temperature attachment for a four-circle neutron diffractometer

A SEQUEIRA, SANDHYA BHAKAY-TAMHANE and S R SAWANT\*

Neutron Physics Division, \*Physics Group Workshop, Bhabha Atomic Research Centre, Trombay, Bombay 400 085, India

MS received 29 September 1986

**Abstract.** A single-stage closed-cycle helium gas cryogenerator, capable of cooling between 77 K and 300 K, has been installed on the 4-circle neutron diffractometer at CIRUS. The cryo-tip assembly has been incorporated directly on the  $\phi$ -circle of the full-circle crystal orienter in place of the goniometer head used in room temperature experiments. The salient features of this low-temperature attachment and its performance are discussed.

**Keywords.** Low temperature diffraction; diffractometer cryo-assembly; helium gas cryo-tip; closed-cycle cryogenerator.

### Introduction

A cryostat mounted on a conventional four-circle diffractometer (with an Eulerian cradle) must be capable of tilting at least  $90^\circ$  off the vertical and work for long periods without interruption. This places severe limitations on the type of cryotips used on these diffractometers. A number of different cryo-systems for use on x-ray and neutron single-crystal diffractometers have been reported; the various methods (table 1) can be broadly classified (Rudman 1976) into: (a) gas stream i.e. a stream of cold gas ( $\text{He}$ ,  $\text{N}_2$  or air) is directed over the sample, (b) conduction i.e. the sample is cooled by means of a good thermal conductor (cold finger) in contact with a cooling unit; the cooling unit may be a cold bath, mechanical refrigerator, thermoelectric cooler, Joule-Thomson expansion device or a closed-cycle cryorefrigerator and (c) immersion, where the entire camera is immersed in cold liquid in which cold liquid is dripped over sample.

The immersion method does not allow a fine temperature control. The gas stream method (Lippman and Rudman 1976; Burbank 1973), though easily adaptable to an instrument, is not so convenient due to the cumbersome nature of cryogen handling (liquid  $\text{N}_2$  or compressed gas), temperature instability during cryogen refilling and other problems, which persist even with proper insulations during the actual working of a cryo-system over prolonged periods of time as in neutron diffraction. The conduction cooling apparatus with liquefied gasses (Coppens *et al* 1974) was not favoured as the levels of performance of these systems seem to be directly proportional to their cost and complexity. Thermoelectric coolers (working on the Seebeck-Peltier thermoeffect), though very clean and simple to operate, are capable of cooling to only  $-45^\circ\text{C}$  with a single-stage (Agron *et al* 1972) and to  $-80^\circ\text{C}$  with multi-stages (Khan and Erickson 1970) and hence are of limited use. Alternately, regulating Joule-Thomson coolers are also not convenient to use, due to stringent requirements on the purity and dryness of gas, the cleanliness of gas lines and the open cycle nature of the operation.

The introduction of closed-cycle cryo-refrigerators has made available a new range of cryogenic devices inexpensive in use and simple to operate, as against the ear-

Table 1. Different cryo-systems in use.

Type of apparatus	Manufacturers
Gas stream cooling apparatus	Enraf-Nonius, Netherlands; Philips X-ray Instruments, Netherlands; Rich Seifert, West Germany; Syntex Analytical Instruments, USA; Techna-bexport, USSR.
Conduction cooling with liquid N <sub>2</sub> or liquid He continuous-flow cryostats.	Air-Products and Chemicals USA; Cryogenic Associates, USA; Oxford Instruments, UK.
Thermoelectric coolers	Borg-Warner Corp., USA; Jepson Thermoelectrics, USA; Cambion Thermoelectrics, USA.
Self-regulating J-T coolers	Hymatic Engineering, UK; Air-Products and Chemicals, USA.
Closed-cycle cryo-refrigerators.	Air-Products and Chemicals, USA; Custom-built according to specified requirements.

cryo-systems which have liquids as refrigerants or are somewhat uneconomical in prolonged operations. Further, the cold-tip is so compact that its adaptation on a full-circle diffractometer is not a problem; with minor modifications the same design can be used on a x-ray diffractometer. The cryo-tip opted for was a compact single-stage Air-Products DISPLEX (model CS-1003) closed-cycle cryo-system capable of cooling in the range 45–300 K. The DISPLEX system is a closed-cycle cryogenerator, consisting of a single-stage displacer/expander cooler, a compact air-cooled, oil-lubricated compressor module with integral oil clean-up package and electrical controls. The compressor is connected to the valve assembly with flexible metal lines, the valve assembly in turn is connected to the displacer/expander cold end with more flexible nylon tubings. M/s Air-Products have modified the cold head, embedding a standard 30 Watt heater and chromel/gold (0.07 atomic% iron) thermocouple according to our requirements and supplied a compatible temperature controller. The refrigeration capacity of the cooler is 1 W at 77 K. A two-stage DISPLEX cooler was not favoured as the system is not as compact as a single stage one and could not be incorporated on our diffractometer.

## 2. General description

The neutron diffractometer (Sequeira *et al* 1978) has a 45 cm-dia full-circle crystal orienter which is sturdy enough to carry a cryostat. The single-stage displacer-expander is mounted directly on the  $\phi$ -circle of the Eulerian cradle. A schematic drawing of the displacer-cryo-tip assembly (similar to the ILL, Grenoble assembly (Allibon *et al* 1981)) as incorporated on the  $\phi$ -circle of the full-circle Eulerian cradle is shown in figure 1. The total height of the cryo-tip is  $\sim 10.1$  cm while the space available on the  $\chi$ -circle is  $\sim 10.6$  cm. Thus no vertical adjustment has been provided for the cold tip. The crystal is mounted directly on the cryo-tip using OFHC copper mounting studs of  $\sim 2$ –3 mm height; the exact height of the stud is matched so that the centre of the sample crystal comes to the centre of the full circle. The crystal orientation is determined directly (without goniometer head) using optimized  $\chi$  and  $\phi$  angles for a few reflections. The  $\phi$ -motion entails the rotation of the cryo-tip on

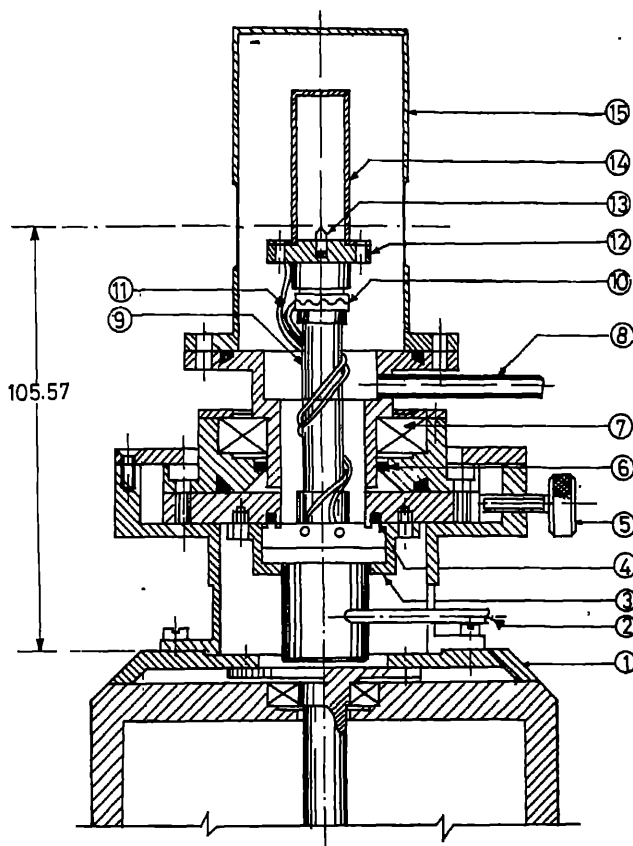


**Figure 1.** A schematic drawing of the dispex cryo-tip assembly as incorporated on the circle of the neutron full circle crystal orientor. The parts indicated are the  $\phi$ -drive bolt (1), helium lines to/from cold head (2), split-cup which provides rigid support to cryo-tip (3), teflon O-ring isolates the vacuum chamber from the lower half of the assembly (4), lateral translation screws (5), rotary vacuum seal (6) and ball-bearings (7) for decoupling  $\phi$ -rotation from vacuum pumping port (8) and vacuum shroud (15). The DISPLEX CS-cryo-tip (9) has a heater (10) and a thermocouple (11) embedded in the cold head flange. The centre of the diffractometer (13), the inner (14) and outer (15) aluminium vacuum shrouds are also indicated. The cold finger is of OFHC copper, all adapter parts fabricated using anti-magnetic SS-304.

which the crystal has been mounted. The  $\phi$ -rotation is decoupled from the vacuum port and vacuum shroud by use of a rotating vacuum seal and ball-bearing to avoid mechanical instabilities arising from a rotating vacuum port. This places limitations on the ultimate vacuum reached ( $> 10^{-4}$  torr). A simple rotary pump does the job within half an hour.

Figure 2 shows the various components (valve-motor, cables, gas lines and vacuum inlet) placed to avoid excessive twisting of the lines, fouling up of the moving parts of the diffractometer by cables or lines or obstructing the incident and diffracted beams of neutrons. The rotation of  $\phi$  has to be limited to  $300^\circ$  both by hardware as well as software to avoid twisting of the nylon tubing connecting the cold head to the vacuum motor assembly. The vacuum port and the external vacuum shroud is held in place by using two clamps which hold on to the  $\chi$ -ring.

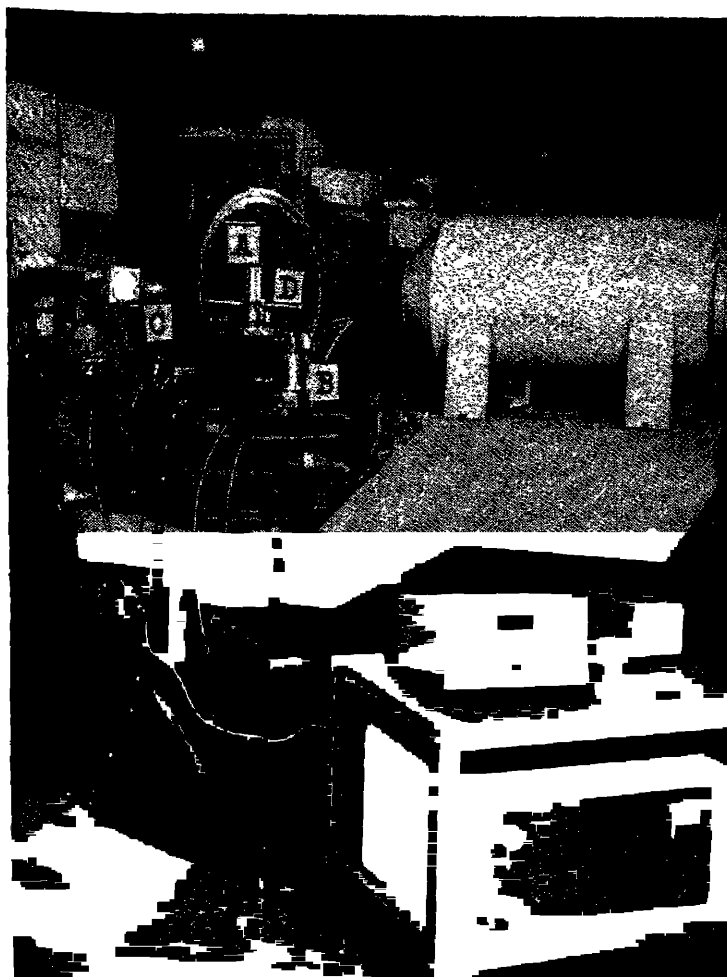


**Figure 2.** Photograph of the low-temperature assembly after installation on the four-circle diffractometer. (A) is the vacuum shroud over the cryo-tip, (B) is the valve assembly held onto the  $\omega$ -plate of the diffractometer, (C) is the vacuum port and (D) are the clamps which hold onto the  $\chi$ -circle. The compressor and temperature controller are placed on a trolley visible in the foreground. The positions of all the components are optimized to minimize the twists/strains on the tubes and possible entangling with the diffractometer moving parts.

The heat and vacuum shields are made of Al; both shields are designed in the form of cylinders  $\sim 0.5$  mm thick. The external heat shroud has been ground to  $\sim 0.3$  mm to provide a window in the region where the beam is incident. In x-ray diffractometer the vacuum shields will have to be preferably of Be so as to be 'invisible' to x ray radiation.

### **3. Use and performance**

As the positions of all the components have been determined, the mounting of the low-temperature device onto the diffractometer can be accomplished within 10 min. The sample is mounted directly on the cryo-tip using a mounting stud of suitable

the vacuum shields. The Cu cold tip which falls within the beam area has to be covered with Cd to minimize the contamination and background scattering.

The space between the inner and outer vacuum shields is pumped till a vacuum of better than  $10^{-3}$  torr is obtained and cooling is then started. The system cools to 130 K in about 1 hr and to  $\sim 80$  K in approximately 2 hr. The cooling curve is nearly exponential. Temperature control is achieved by using the resistance heater embedded in the cold head along with the chromel/gold (iron) thermocouple and the temperature controller unit. The temperature indicator displays temperature on a 4-digit readout, the resolution is 0.1 K and the stability  $\pm 0.5$  K. The calibration was done using the room temperature, liquid nitrogen and dry ice temperatures. Though the low temperatures match perfectly well (within  $\pm 1^\circ$ ), the room temperature display is off by  $10^\circ$  and remains so even with all the zero and span adjustments. The low temperature calibration points, however, reproduce themselves.

The assembly is extremely simple to use and can be used without interruption for long periods. The charging of the system with commercial-grade helium gas has to be done once in approximately six months (nominal He-gas pressure 115 psi). Long-term measurements (as required in neutron diffraction experiments) are not possible at temperatures below 90 K as accurate temperature control becomes a problem. Also, if the compressor is used continuously for very long periods (exceeding a month or so), the temperature starts wandering. Further, continuous long usage of the compressor increases the risk of oil cross-over from the compressor; hence regular servicing of the cold head assembly is necessary. The filters installed in the compressor module must also be changed periodically.

The installation of the device introduces limits on the  $\chi$  and  $\phi$  angles in addition to the intrinsic blind areas of the diffractometer. The  $\chi$  accessibility has been nominally restricted to the range  $-10^\circ < \chi < 100^\circ$  and  $\phi$  accessibility to the range  $45-300^\circ$ . Even with these restrictions on the diffractometer angles, half the reciprocal space is accessible for crystals of all space groups other than the triclinic. The facility has so far been used to record over 1500 reflections in five low-temperature data sets to investigate the low-temperature structural phase transitions in  $\text{LiKSO}_4$  (Bhakar Tamhane and Sequeira 1986).

## Acknowledgement

We are grateful to Dr R Chidambaram for useful suggestions and encouragement.

## References

- Agron P A, Levy H A and Bogardus B J 1972 *J. Appl. Crystallogr.* **5** 432
- Allibon J R, Filhol A, Lehmann M S, Mason S A and Simms P 1981 *J. Appl. Crystallogr.* **14** 326
- Bhakar-Tamhane S and Sequeira A 1986 *Ferroelectrics* **69** 241
- Burbank R D 1973 *J. Appl. Crystallogr.* **6** 437
- Coppens P, Ross F K, Blessing R H, Cooper W F, Larsen F K, Leipoldt J G, Rees B and Leonard R I 1976 *J. Appl. Crystallogr.* **7** 315
- Khan D C and Erickson R A 1970 *Rev. Sci. Instrum.* **41** 107
- Lippman R and Rudman R 1976 *J. Appl. Crystallogr.* **9** 220
- Rudman R 1976 'Low temperature x-ray diffraction': *Monographs in low-temperature physics* (New York: Plenum)
- Tamhane S N, Bhakar-Tamhane S N, Bhaskar H, Soni J N, Chidambaram R, Dilip Kumar, Ramana Rao A





## SUBJECT INDEX

- Absorptance**  
Cobalt oxide-iron oxide selective coatings for high temperature applications 385
- Absorption coefficient**  
Optical constants in the ultraviolet region of evaporated high index thin films 347
- Aluminium oxide**  
Microstrip losses with  $\text{Al}_2\text{O}_3$  overlay 535
- Amorphous alloys**  
Magnetic hysteresis and crystallization studies on metallic glass alloy  $\text{Fe}_{67}\text{Co}_{18}\text{B}_{14}\text{Si}_1$  567
- Amorphous**  
Electron microscopy study of chemically deposited Ni-P films 433
- Amorphous silicon**  
Electrical and optical properties of  $\mu\text{c-SiH}$  films 267
- Anisotropy**  
Magnetic hysteresis and crystallization studies on metallic glass alloy  $\text{Fe}_{67}\text{Co}_{18}\text{B}_{14}\text{Si}_1$  567
- Anodic chemical film**  
Electrochemical bath deposition technique: Deposition of CdS thin films 419
- Anti-reflection coatings**  
Quality and reliability of optical coatings 351
- Apex angle**  
Computer-aided roll pass design for continuous billet mill 183
- Asbestos**  
Thermal transformation in a chrysotile asbestos 497
- a-Si:H**  
a-Si:H/CuInS<sub>2</sub> heterojunctions for photovoltaic conversion 285
- As-Sb-Se glasses**  
Thermal expansion studies on As-Sb-Se glasses 53
- Atmospheric pressure chemical vapour deposition**  
Growth of polysilicon and silicide films for MOS-VLSI application 297
- Attenuation**  
Microstrip losses with  $\text{Al}_2\text{O}_3$  overlay 535
- Auxiliary crate controller**  
Personal computer-based CAMAC system for data acquisition 225
- Barium oxalate**  
Periodic crystallization of barium oxalate in silica hydrogel 511
- Barium oxalate dihydrate**  
Studies on etching of gel-grown barium oxalate dihydrate crystals
- Beam combiner**  
Design and development of a thin film dielectric beam combiner
- Beta alumina**  
Kinetics of electrophoretic deposition of alumina
- $\text{Bi}_{2-x}\text{As}_x\text{S}_3$  films**  
Preparation and properties of  $\text{Bi}_{2-x}\text{As}_x\text{S}_3$  films by solution-gas interface technique
- Binary diagrams**  
Computer calculations of phase diagrams
- Bit quad**  
Image analysis system for quantitative metrography
- Black coatings**  
Optical black coatings for space application
- Cadmium films**  
X-ray diffraction study of epitaxial zinc cadmium films prepared by hot-wall technique
- Calcium molybdate**  
Kinetics of calcium molybdate crystallization
- CAMAC**  
Personal computer-based CAMAC system for data acquisition
- CAMAC trainer software**  
Personal computer-based CAMAC system for data acquisition
- Carrier concentration**  
Liquid phase epitaxy growth of GaAs:Li by temperature difference method
- Carrier injection**  
Space charge limited currents in chlorazole E dye
- Cathodic chemical film**  
Electrochemical bath deposition technique: Deposition of CdS thin films
- $\text{CdZnS/CuInSe}_2$**   
Thin film  $\text{CdZnS/CuInSe}_2$  solar cells by pyrolysis
- Ceramics**  
Dielectric properties of the system  $\text{Pb}_{2-x}\text{Nb}_{1.5}\text{O}_{6+\delta}$

# Index

- characterization of flash-  
 $\text{Al}_2\text{O}_3$  thin films 319
- composition  
 with  $\text{Al}_2\text{O}_3$  overlay 535
- synthesized by chemical vapour  
 deposition using hydrofluoric acid as  
 catalyst 315
- optical properties of  $\text{SnO}_2$  films  
 by chemical vapour deposition 357
- photoconductive dye  
 induced currents in chlorazole black  
 531
- production in a chrysotile asbestos  
 497
- generator  
 for attachment for a four-circle  
 diffractometer 591
- materials for high power laser appli-  
 cations 339
- on oxide selective coatings for  
 catalytic applications 385
- properties  
 and activities in the Co-Ni-O  
 system 71
- solid oxide solid solution  
 and activities in the Co-Ni-O  
 system 71
- thermochemical performance code PROFESS  
 application for predicting the behaviour  
 of elements of D-Com blind problem  
 253
- thermochemical  
 analysis of silver base Ag-Cd-  
 alloys 61
- temperature  
 sensitivity in electrolytically coloured  
 films 587
- design  
 of design of rolling mills 123
- model  
 of roll pass design for continuous  
 casting 183
- thermochemical performance code PROFESS  
 application for predicting the behaviour  
 of elements of D-Com blind problem  
 253
- rolling  
 of design of rolling mills 123
- rolling  
 of design of composition-treatment-struc-  
 ture correlation studies in steels 193
- Computer model  
 Computer modelling application in life predic-  
 tion of high temperature components 133
- Computer modelling  
 Computer models for fuel element behaviour 93
- Water reactor fuel performance code PROFESS  
 and its application for predicting the behaviour  
 of the fuel elements of D-Com blind problem  
 253
- Computer simulation  
 Computer-aided design of rolling mills 123
- Computer simulation of defects and radiation  
 damage 155
- Computer simulation of pressure sintering 199
- Computer simulation of dislocation-carbon inter-  
 action in nickel 247
- Concentration  
 Kinetics of electrophoretic deposition of  $\beta$ -  
 alumina 1
- Condensed phase  
 Concept of thermodynamic capacity 453
- Copper  
 Flash-evaporated thin films of  $\text{CuInSe}_2$  291
- Copper phthalocyanines  
 Thermoelectroluminescence in thin films of zinc  
 and copper phthalocyanines 407
- Correlation  
 Computer-aided composition-treatment-struc-  
 ture-property correlation studies in steels 193
- Crack growth model  
 Computer modelling application in life predic-  
 tion of high temperature components 133
- Creep modulus  
 Computer simulation of pressure sintering 199
- Crystallization  
 Glass ceramics containing ferroelectric phases  
 557
- Magnetic hysteresis and crystallization studies  
 on metallic glass alloy  $\text{Fe}_{67}\text{Co}_{18}\text{B}_{14}\text{Si}_1$  567
- Crystallization kinetics  
 Kinetics of calcium molybdate crystallization  
 489
- $\text{CuInS}_2$   
 a-Si:H/ $\text{CuInS}_2$  heterojunctions for photovoltaic  
 conversion 285
- $\text{CuInSe}_2$  solar cells  
 Thin film CdZnS/ $\text{CuInSe}_2$  solar cells by spray  
 pyrolysis 279
- Czochralski technique  
 Growth of low dislocation density single crystals  
 of nickel 467
- Deformation  
 Computer models for fuel element behaviour 93
- Dehydration  
 Thermal transformation in a chrysotile asbestos  
 497

- Development of ductile permanent magnet  
 Magnetic and Mössbauer studies on ductile Fe-Cr-Co permanent alloys 39
- Dielectric behaviour  
 Microstructural and dielectric behaviour of glass ceramics in the system  $\text{PbO-BaO-TiO}_2\text{-B}_2\text{O}_3\text{-SiO}_2$  13
- Dielectric films  
 Deposition and assessment of thin dielectric films on photocathode substrate made of Kodial glass 325
- Dielectric overlay  
 Effect of bulk and thin film dielectric overlay on the characteristics of microstrip rejection filter and simple microstriplines 397
- Dielectric properties  
 Dielectric properties of the system  $\text{Pb}_{2-x}\text{Nd}_x\text{Li}_{0.5}\text{Nb}_{1.5}\text{O}_{6+x}$  23
- Differential thermal analysis  
 Microstructural and dielectric behaviour of glass ceramics in the system  $\text{PbO-BaO-TiO}_2\text{-B}_2\text{O}_3\text{-SiO}_2$  13
- Diffractionmeter cryo-assembly  
 A low-temperature attachment for a four-circle neutron diffractometer 591
- Dilation  
 Image analysis system for quantitative metallography 231
- Dislocation  
 Computer simulation of dislocation-carbon interaction in nickel 247
- Dislocation annihilation  
 Dislocation density in electrolytically coloured KCl crystals 587
- Dislocation density  
 Dislocation density in electrolytically coloured KCl crystals 587
- Dislocations  
 Computer simulation of defects and radiation damage 155
- Displacement damage  
 Computer simulation of defects and radiation damage 155
- Drop profiles  
 An absolute method for the determination of surface tension of liquids using pendent drop profiles 217
- Dynamic method  
 Computer simulation of defects and radiation damage 155
- Edge filter  
 Design and development of a thin film dielectric beam combiner 343
- Electrical conductivity  
 Preparation and characterization of flash-evaporated  $\text{CuInSe}_2$  thin films 319
- Influence of eutectic addition on the electric conductivity of  $\text{Li}_2\text{O}:\text{B}_2\text{O}_3$  system 57
- Electrochemical photovoltaic cells  
 Electrochemical bath deposition technique: Deposition of CdS thin films 4
- Electrochemistry  
 Characterization of  $\text{Pb}_3\text{O}_4$  films by electrochemical techniques 4
- Electrode separation  
 Kinetics of electrophoretic deposition of alumina
- Electroless  
 Electron microscopy study of chemically deposited Ni-P films 4
- Electrolytic coloration  
 Dislocation density in electrolytically coloured KCl crystals 58
- Electromotive force  
 Phase relations and activities in the Co-Ni system at 1373 K
- Electronic analog  
 Computer simulation of serrated yielding 2
- Electron microscopy  
 Electron microscopy study of chemically deposited Ni-P films 4
- Electron-optics  
 Development of high resolution thin film patterns on curved photocathode substrates image tubes 3
- Electron tunnelling  
 Tunnelling of electrons from deep traps of  $\text{Mg}$
- Electrophoretic deposition  
 Kinetics of electrophoretic deposition of alumina
- Electrophoretic kinetics  
 Kinetics of electrophoretic deposition of alumina
- Emission spectrography  
 Emission spectrographic technique for quantitative determination of trace elements granitic rocks 4
- Emittance  
 Cobalt oxide-iron oxide selective coatings high temperature applications
- Epitaxial growth  
 X-ray diffraction study of epitaxial zinc and cadmium films prepared by hot-wall technique
- Erosion  
 Some fundamental considerations to precise image analysis  
 Image analysis system for quantitative metallography
- Etching  
 Studies on etching of gel-grown barium oxalate dihydrate crystals

- Eutectic  
Influence of eutectic addition on the electrical conductivity of  $\text{Li}_2\text{O}:\text{B}_2\text{O}_3$  system 577
- Extinction coefficient  
Optical constants in the ultraviolet region of evaporated high index thin films 347
- Failure  
Computer models for fuel element behaviour 93
- Fatigue life  
Computer modelling application in life prediction of high temperature components 133
- Feature extraction  
Image analysis system for quantitative metallography 231
- Ferroelectric  
Glass ceramics containing ferroelectric phases 557
- Figure of merit  
Optical and electrical properties of  $\text{SnO}_2$  films prepared by chemical vapour deposition 357
- Finite element analysis  
Computer simulation of pressure sintering 199
- Fission gases  
Computer models for fuel element behaviour 93
- Fission products  
Computer models for fuel element behaviour 93
- Flash evaporation  
Flash-evaporated thin films of  $\text{CuInSe}_2$  291
- Fracture  
Effect of texture and grain size on the mechanical properties of warm-worked cadmium, zinc and zinc-0.35% aluminium alloys 81
- Free energy of mixing  
Phase relations and activities in the Co-Ni-O system at 1373 K 71
- Fuel performance  
Water reactor fuel performance code PROFESS and its application for predicting the behaviour of the fuel elements of D-Com blind problem 253
- Furnace design  
Computer applications in the field of furnace design 147
- GaAs:Si doping  
Liquid phase epitaxy growth of GaAs:Si by temperature difference method 439
- GaAs thin films  
Surface morphology and properties of GaAs epilayers controlled by temperature difference method of liquid phase epitaxy 29
- Gel growth  
Studies on etching of gel-grown barium oxalate dihydrate crystals 519
- Gel permeation chromatography  
Determination of molecular weight distribution of polyethylene terephthalate by gel permeation
- Geometrical dimensions  
Computer-aided roll pass design for continuous billet mill 183
- Germanium  
Quality and reliability of optical coatings 351
- Glass ceramic  
Microstructural and dielectric behaviour of glass ceramics in the system  $\text{PbO}-\text{BaO}-\text{TiO}_2-\text{B}_2\text{O}_3-\text{SiO}_2$  13
- Glass ceramics  
Glass ceramics containing ferroelectric phases 557
- Glass transition region  
Thermal expansion studies on As-Sb-Se glasses 53
- Global parameters  
Image analysis system for quantitative metallography 231
- Grain size  
Effect of texture and grain size on the mechanical properties of warm-worked cadmium, zinc and zinc-0.35% aluminium alloy 81
- Granitic rocks  
Emission spectrographic technique for the quantitative determination of trace elements in granitic rocks 471
- Growth rate  
Liquid phase epitaxy growth of GaAs:Si by temperature difference method 439
- Hall mobility  
Liquid phase epitaxy growth of GaAs:Si by temperature difference method 439
- Heating furnaces  
Computer applications in the field of furnace design 147
- Heat transfer  
Computer models for fuel element behaviour 93
- Heat treatment  
Glass ceramics containing ferroelectric phases 557
- Heat treatments  
Magnetic and Mössbauer studies on ductile Fe-Cr-Co permanent magnet alloys 39
- Helium gas cryo-tip  
A low-temperature attachment for a four-circle neutron diffractometer 591
- Heterojunction  
a-Si:H/CuInS<sub>2</sub> heterojunction for photovoltaic conversion 285
- High pressure growth  
Growth of low dislocation density single crystals of nickel 467
- High temperature components  
Computer modelling application in life prediction of high temperature components 133
- Hill climbing technique

- H<sup>+</sup> ion irradiation**  
 Effect of H<sup>+</sup> ion irradiation on surface morphology of Fe<sub>40</sub>Ni<sub>40</sub>B<sub>20</sub> metallic glass 505
- Hot-wall technique**  
 X-ray diffraction study of epitaxial zinc and cadmium films prepared by hot-wall technique 449
- Hydrothermal cell**  
 A simple hydrothermal cell for synthesis at moderate temperature and pressure 543
- Ideal gas mixture**  
 Concept of thermodynamic capacity 453
- Image analysis**  
 Some fundamental considerations to precede image analysis 169  
 Image analysis system for quantitative metallography 231
- Image tube**  
 Development of high resolution thin film patterns on curved photocathode substrates of image tubes 333
- Impurity defects**  
 Computer simulation of dislocation-carbon interaction in nickel 247
- Inclusion grade**  
 Modern computer assisted methods in metallurgy 239
- Inclusion type**  
 Modern computer assisted methods in metallurgy 239
- Indium**  
 Flash-evaporated thin films of CuInSe<sub>2</sub> 291
- Infrared detection**  
 Pyroelectric polymer films for infrared detection 365
- Infrared detector**  
 Photoresponsive measurements on InAs<sub>0.3</sub>Sb<sub>0.7</sub> infrared detector 373
- Integrated circuits**  
 Development of high resolution thin film patterns on curved photocathode substrates of image tubes 333
- Interaction**  
 Computer simulation of dislocation-carbon interaction in nickel 247
- Interatomic potential**  
 Computer simulation of defects and radiation damage 155
- Interference photoemission**  
 Deposition and assessment of thin dielectric films on photocathode substrate made of Kodial glass 325
- Inter level insulator**  
 Electrical and structural characteristics of oxides grown from polycrystalline silicon 307
- Iron-chromium-cobalt alloys**  
 Magnetic and Mössbauer studies on ductile Fe-Cr-Co permanent magnet alloys 30
- Irradiation behaviour**  
 Water reactor fuel performance code PROFES and its application for predicting the behaviour of the fuel elements of D-Com blind problem 25
- Irradiation effects**  
 Water reactor fuel performance code PROFES and its application for predicting the behaviour of the fuel elements of D-Com blind problem 25
- Isothermal decay**  
 Tunnelling of electrons from deep traps of MgO 4
- Lanthanum tartrate crystals**  
 Characterization and thermal behaviour of lanthanum tartrate crystals grown from silic gels 54
- Laser**  
 Transistors made in laser recrystallized polysilicon on insulator films 39
- Lasers**  
 Dielectric mirrors for high power laser applications 33
- Lattice stability**  
 Computer calculations of phase diagrams 10
- Lattice statics**  
 Computer simulation of dislocation-carbon interaction in nickel 24
- Life prediction**  
 Computer modelling application in life prediction of high temperature components 13
- Line profile analysis**  
 X-ray line profile analysis of silver base Ag-Cu alloys 6
- Liquid phase epitaxy**  
 Surface morphology and properties of GaAs epilayers controlled by temperature difference method of liquid phase epitaxy 2  
 Liquid phase epitaxy growth of GaAs:Si by temperature difference method 43
- Lithium fraction**  
 Influence of eutectic addition on the electrical conductivity of Li<sub>2</sub>O:B<sub>2</sub>O<sub>3</sub> system 57
- Low temperature diffraction**  
 A low-temperature attachment for a four-circle neutron diffractometer 59
- Machine equations**  
 Computer simulation of serrated yielding 20
- Magnetic hysteresis**  
 Magnetic hysteresis and crystallization studies on metallic glass alloy Fe<sub>67</sub>Co<sub>18</sub>B<sub>14</sub>Si<sub>1</sub> 56
- Magnetic properties**  
 Magnetic and Mössbauer studies on ductile Fe-Cr-Co permanent magnet alloys 3
- Magnetron sputtering**  
 R.F. magnetron sputtered tungsten carbide thin films 37

# Index

l synthesis	
iple hydrothermal cell for synthesis at	
rate temperature and pressure	543
atical models	
uter applications in the field of furnace	
1	147
: glass	
of H <sup>+</sup> ion irradiation on surface	
hology of Fe <sub>40</sub> Ni <sub>40</sub> B <sub>20</sub> metallic glass	505
graphy	
e analysis system for quantitative metallo-	
ly	231
xide semiconductor	
with of polysilicon and silicide films for	
3-VLSI application	297
crystalline	
ron microscopy study of chemically depo-	
Ni-P films	433
trip	
rostrip losses with Al <sub>2</sub> O <sub>3</sub> overlay	535
trip rejection filter	
ct of bulk and thin film dielectric overlay on	
characteristics of microstrip rejection filter	
simple microstriplines	397
structure	
rostructural and dielectric behaviour of glass	
mics in the system PbO-BaO-TiO <sub>2</sub> -B <sub>2</sub> O <sub>3</sub> -	
2	13
y line profile analysis of silver base Ag-Cd-	
lloys	61
wave power	
rostrip losses with Al <sub>2</sub> O <sub>3</sub> overlay	535
rs	
lectric mirrors for high power laser appli-	
ons	339
ility gap	
puter calculations of phase diagrams	107
i fields	
ern computer assisted methods in metal-	
gy	239
FET	
nsistors made in laser recrystallized poly-	
con on insulator films	391
bauer studies	
agnetic and Mössbauer studies on ductile Fe-	
-Co permanent magnet alloys	39
ilayers	
electric mirrors for high power laser appli-	
ions	339
lymium doping	
electric properties of the system Pb <sub>2-x</sub> Nd <sub>x</sub>	
0.5Nb <sub>1.5</sub> O <sub>6+x</sub>	23
el crystals	
rowth of low dislocation density single crystals	
nickel	467
el-phosphorous	
atron microscopy study of chemically depo-	
sited Ni-P films	433
Noise	
Computer simulation of serrated yielding	209
Nuclear fuel element	
Water reactor fuel performance code PROFESS	
and its application for predicting the behaviour	
of the fuel elements of D-Com blind problem	253
Nuclear fuels	
Computer models for fuel element behaviour	93
Opaque coatings	
Optical black coatings for space applications	581
Optical absorption	
Preparation and characterization of flash-	
evaporated CuInSe <sub>2</sub> thin films	319
Optical coating	
Quality and reliability of optical coatings	351
Optical constants	
Optical constants in the ultraviolet region of	
evaporated high index thin films	347
Optics	
Dielectric mirrors for high power laser appli-	
cations	339
Design and development of a thin film dielectric	
beam combiner	343
Overlay	
Microstrip losses with Al <sub>2</sub> O <sub>3</sub> overlay	535
Overture	
Some fundamental considerations to precede	
image analysis	169
Oxide fuels	
Computer models for fuel element behaviour	93
Oxygen-metal ratio	
Determination of oxygen to metal ratio of U-Pu	
mixed oxides by x-ray diffraction	479
Oxygen potential	
Phase relations and activities in the Co-Ni-O	
system at 1373 K	71
Pass sequence	
Computer-aided roll pass design for continuous	
billet mill	183
Periodic crystallization	
Periodic crystallization of barium oxalate in	
silica hydrogel	511
Personal computer	
Personal computer-based CAMAC system for	
data acquisition	225
Phase diagram	
Phase relations and activities in the Co-Ni-O	
system at 1373 K	71
Phase diagrams	
Computer calculations of phase diagrams	107

- Phase identification  
 Magnetic and Mössbauer studies on ductile Fe-Cr-Co permanent magnet alloys 39
- Photoelectrochemical  
 Characterization of  $\text{Pb}_3\text{O}_4$  films by electrochemical techniques 415
- Photoemission  
 Development of high resolution thin film patterns on curved photocathode substrates of image tubes 333
- Photolithography  
 Development of high resolution thin film patterns on curved photocathode substrates of image tubes 333
- Photoresponsivity  
 Photoresponsive measurements on  $\text{InAs}_{0.3}\text{Sb}_{0.7}$  infrared detector 373
- Photovoltage  
 Characterization of  $\text{Pb}_3\text{O}_4$  films by electrochemical techniques 415
- Photovoltaics  
 a-Si:H/CuInS<sub>2</sub> heterojunctions for photovoltaic conversion 285
- Pixel  
 Image analysis system for quantitative metallography 231
- Plasma deposition  
 Electrical and optical properties of  $\mu\text{c-SiH}$  films 267
- Point defects  
 Computer simulation of defects and radiation damage 155
- Polycrystalline silicon films  
 Growth of polysilicon and silicide films for MOS-VLSI application 297
- Polycrystalline silicon  
 Electrical and structural characteristics of oxides grown from polycrystalline silicon 307
- Polyethylene terephthalate  
 Determination of molecular weight distribution of polyethylene terephthalate by gel permeation chromatography 527
- Polymer films  
 Pyroelectric polymer films for infrared detection 365
- Polyoxide  
 Electrical and structural characteristics of oxides grown from polycrystalline silicon 307
- Pressure sintering  
 Computer simulation of pressure sintering 199
- Pressure vessel  
 Computer modelling application in life prediction of high temperature components 133
- Process parameters  
 Computer applications in the field of furnace design 147
- Property  
 Computer-aided composition-treatment-structure-property correlation studies in steels 193
- Pyrochlore-structured system  
 Dielectric properties of the system  $\text{Pb}_{2-x}\text{Nd}_x\text{Li}_{0.5}\text{Nb}_{1.5}\text{O}_{6+\delta}$  23
- Pyroelectricity  
 Pyroelectric polymer films for infrared detection 365
- Reactive gas mixture  
 Concept of thermodynamic capacity 453
- Recrystallisation  
 Transistors made in laser recrystallized polysilicon on insulator films 391
- Refractive index  
 Deposition and assessment of thin dielectric films on photocathode substrate made of Kodial glass 325  
 Optical constants in the ultraviolet region of evaporated high index thin films 347
- Regression analysis  
 An absolute method for the determination of surface tension of liquids using pendant drop profiles 217
- Resistivity  
 Preparation and properties of  $\text{Bi}_{2-x}\text{As}_x\text{S}_3$  thin films by solution-gas interface technique 427
- Resolution  
 Development of high resolution thin film patterns on curved photocathode substrates of image tubes 333
- Rolling force  
 Computer-aided roll pass design for continuous billet mill 183
- Rolling mills  
 Computer-aided design of rolling mills 123
- Runge-Kutta method  
 An absolute method for the determination of surface tension of liquids using pendant drop profiles 217
- Selective coatings  
 Cobalt oxide-iron oxide selective coatings for high temperature applications 385
- Selenium  
 Flash-evaporated thin films of  $\text{CuInSe}_2$  291
- Semiconductor  
 Photoresponsive measurements on  $\text{InAs}_{0.3}\text{Sb}_{0.7}$  infrared detector 373  
 Transistors made in laser recrystallized polysilicon on insulator films 391
- Serrated yielding  
 Computer simulation of serrated yielding 209
- Silica gels  
 Characterization and thermal behaviour of lanthanum tartrate crystals grown from silica gels 549
- Silica hydrogel  
 Periodic crystallization of barium oxalate in silica hydrogel 511

# Index

- n-gate process
- insistors made in laser recrystallized polycon on insulator films 391
- n
- insistors made in laser recrystallized polycon on insulator films 391
- r base ternary alloys
- ray line profile analysis of silver base Ag-Cd-alloys 61
- le microstriplines
- fect of bulk and thin film dielectric overlay on characteristics of microstrip rejection filter
- d simple microstriplines 397
- $z:F$
- $IO_2:F$  films synthesized by chemical vapour deposition technique using hydrofluoric acid as etching material 315
- $z$  film
- optical and electrical properties of  $SnO_2$  films prepared by chemical vapour deposition 357
- ware
- computer-aided composition-treatment-structure-property correlation studies in steels 193
- r cells
- lectrical and optical properties of  $\mu c$ -SiH films 267
- d state cell
- hase relations and activities in the Co-Ni-O system at 1373 K 71
- ution-gas interface technique
- 'reparation and properties of  $Bi_{2-x}As_xS_3$  thin films by solution-gas interface technique 427
- ution models
- Computer calculations of phase diagrams 107
- ice-charge-limited-current
- space charge limited currents in chlorazole black E dye 531
- ray pyrolysis
- Thin film CdZnS/CuInSe<sub>2</sub> solar cells by spray pyrolysis 279
- ray pyrolysis technique
- Spray pyrolytic deposition of CuBiS<sub>2</sub> thin films 423
- ray rate
- Spray pyrolytic deposition of CuBiS<sub>2</sub> thin films 423
- quare-diamond pass
- Computer-aided roll pass design for continuous billet mill 183
- acking fault probabilities
- X-ray line profile analysis of silver base Ag-Cd-In alloys 61
- atic method
- Computer simulation of defects and radiation damage 155
- eel
- Computer-aided composition-treatment-structure-property correlation studies in steels 103
- Structure
- Computer-aided composition-treatment-structure-property correlation studies in steels 193
- Styragel
- Determination of molecular weight distribution of polyethylene terephthalate by gel permeation chromatography 527
- Surface morphology
- Surface morphology and properties of GaAs epilayers controlled by temperature difference method of liquid phase epitaxy 29
- Liquid phase epitaxy growth of GaAs:Si by temperature difference method 439
- Effect of  $H^+$  ion irradiation on surface morphology of  $Fe_{40}Ni_{40}B_{20}$  metallic glass 505
- Surface tension
- An absolute method for the determination of surface tension of liquids using pendant drop profiles 217
- System operation
- Modern computer assisted methods in metallurgy 239
- Temperature
- Kinetics of electrophoretic deposition of  $\beta$ -alumina 1
- Temperature difference method
- Liquid phase epitaxy growth of GaAs:Si by temperature difference method 439
- Template matching
- Some fundamental considerations to precede image analysis 169
- Ternary chalcogenide films
- Spray pyrolytic deposition of CuBiS<sub>2</sub> thin films 423
- Ternary diagrams
- Computer calculations of phase diagrams 107
- Texture
- Effect of texture and grain size on the mechanical properties of warm-worked cadmium, zinc and zinc-0.35% aluminium alloy 81
- Thermal expansion coefficient
- Thermal expansion studies on As-Sb-Se glasses 53
- Thermodynamic capacity
- Concept of thermodynamic capacity 453
- Thermodynamic properties
- Phase relations and activities in the Co-Ni-O system at 1373 K 71
- Thermoelectroluminescence
- Thermoelectroluminescence in thin films of zinc and copper phthalocyanines 407
- Thermoluminescence
- Tunnelling of electrons from deep traps of MgO 49
- Thin films
- Electrical and optical properties of  $\mu c$ -SiH films 267



- $\text{SnO}_2$ :F films synthesized by chemical vapour deposition technique using hydrofluoric acid as doping material 315  
 Preparation and characterization of flash-evaporated  $\text{CuInSe}_2$  thin films 319  
 Dielectric mirrors for high power laser applications 339  
 Design and development of a thin film dielectric beam combiner 343  
 Optical constants in the ultraviolet region of evaporated high index thin films 347  
 Photoresponsive measurements on  $\text{InAs}_{0.3}\text{Sb}_{0.7}$  infrared detector 373  
 Effect of bulk and thin film dielectric overlay on the characteristics of microstrip rejection filter and simple microstriplines 397  
 Thin film solar cells  
   Thin film  $\text{CdZnS/CuInSe}_2$  solar cells by spray pyrolysis 279  
 Torque  
   Computer-aided roll pass design for continuous billet mill 183  
 Trace elements  
   Emission spectrographic technique for the quantitative determination of trace elements in granitic rocks 471  
 Transformation  
   Thermal transformation in a chrysotile asbestos 497  
 Transparent conducting film  
   Optical and electrical properties of  $\text{SnO}_2$  films prepared by chemical vapour deposition 357  
 Transparent conductors  
    $\text{SnO}_2$ :F films synthesized by chemical vapour deposition technique using hydrofluoric acid as doping material 315  
 Trapping groups  
   Tunnelling of electrons from deep traps of  $\text{MgO}$  49  
 Traps  
   Space charge limited currents in chlorazole black E dye 531  
 Tungsten carbide  
   R.F. magnetron sputtered tungsten carbide thin films 379  
 Uranium plutonium oxides  
   Determination of oxygen to metal ratio of U-Pu mixed oxides by x-ray diffraction 479  
 Very large scale integration  
   Growth of polysilicon and silicide films for MOS-VLSI application 297  
 Warm working  
   Effect of texture and grain size on the mechanical properties of warm-worked cadmium, zinc and zinc-0-35% aluminium alloy 81  
 Water reactor  
   Water reactor fuel performance code PROFESS and its application for predicting the behaviour of the fuel elements of D-Com blind problem 253  
 Worst fields  
   Modern computer assisted methods in metallurgy 239  
 X-ray diffraction  
   X-ray diffraction study of epitaxial zinc and cadmium films prepared by hot-wall technique 449  
   Determination of oxygen to metal ratio of U-Pu mixed oxides by x-ray diffraction 479  
   Thermal transformation in a chrysotile asbestos 497  
 Yield stress  
   Effect of texture and grain size on the mechanical properties of warm-worked cadmium, zinc and zinc-0-35% aluminium alloy 81  
 Z 80-A CPU  
   Personal computer-based CAMAC system for data acquisition 225  
 Zinc films  
   X-ray diffraction study of epitaxial zinc and cadmium films prepared by hot-wall technique 449  
 Zinc phthalocyanines  
   Thermoelectroluminescence in thin films of zinc and copper phthalocyanines 407

# AUTHOR INDEX

arya H N		Bhosale C H	
see Dixit B B	307	see Pawar S H	419
Arora S K		Bhosale P N	
Growth of polysilicon and silicide films for MOS-VLSI application	297	see Pawar S H	423
		see Pawar S H	427
Chhoti O P		Bialy A El	
see Ram P Raja	279	Emission spectrographic technique for the quantitative determination of trace elements in granitic rocks	471
see Saxena A K	315		
Chakraborty R		Chadda V K	
Concept of thermodynamic capacity	453	Image analysis system for quantitative metallography	231
Chakraborty K V S R		Chandrasekaran V	
Dielectric mirrors for high power laser applications	339	Magnetic and Mössbauer studies on ductile Fe-Cr-Co permanent magnet alloys	39
Design and development of a thin film dielectric beam combiner	343	Chandrasekhar S	
Optical constants in the ultraviolet region of evaporated high index thin films	347	Transistors made in laser recrystallized polysilicon on insulator films	391
Chakraborty P R		Chang C C	
see Chandrasekhar S	391	see Su Y K	29
Chakraborty S K		see Wei C C	439
see Batra N M	489	Chauhan J P S	
Chakraborty V S		Space charge limited currents in chlorazole black E dye	531
see Ramakrishnan N	199	Chopra K L	
		see Kumar Satyendra	285
Chakraborty C		see Pachori R D	291
see Chadda V K	231	see Srivastava P K	379
Chakraborty S Ramesh		see Uma C S	385
An absolute method for the determination of surface tension of liquids using pendant drop profiles	217	Datta A K	
Chakraborty T C		Thermal transformation in a chrysotile asbestos	497
see Apparao K V S R	347	Deshmukh B T	
Chakraborty M		see Bhole N L	587
see Agarwal S K	297	Deshmukh L P	
Chakraborty A		see Pawar S H	419
see Pachori R D	291	Deshpande V K	
Chakraborty M N		Influence of eutectic addition on the electrical conductivity of $\text{Li}_2\text{O}:\text{B}_2\text{O}_3$ system	577
Tunnelling of electrons from deep traps of MgO	49	Dhanavanti C	
		see Joshi K K	535
Chakraborty D		Dharmaprakash S M	
see Rao D U Krishna	1	Studies on etching of gel-grown barium oxalate dihydrate crystals	519
Chakraborty B		Dixit B B	
see Tareen J A K	543	Electrical and structural characteristics of oxides grown from polycrystalline silicon	307
Chakraborty N M		Dube D C	
Kinetics of calcium molybdate crystallization	489	see Chauhan J P S	531
		Dubey G C	
Chattacharya D K		Electrical and optical properties of $\mu\text{c-SiH}$ films	267
see Chadda V K	231	Dwarakadasa E S	
Chattacherjee S		see Vijayaraju K	193
see Datta A K	497		
Chatt T Balakrishna			
see Ramakrishnan N	199		
Chhole N L			
Dislocation density in electrolytically coloured KCl crystals	587		

- Fazeli Ali Reza  
*see* Tareen J A K
- Gangal S A  
*see* Vijaya K  
*see* Joshi K K
- Gaonkar V G  
*see* Kataria S K
- Giridhar A  
 Thermal expansion studies on As-Sb-Se glasses 53
- Guirguis L A  
*see* Bialy A El
- Gupta N K  
*see* Kotru P N
- Iyengar G N K  
*see* Jacob K T
- Jacob K T  
 Phase relations and activities in the Co-Ni-O system at 1373 K 71  
*see* Akila R 453
- Jadhav M L  
*see* Vijaya K 397
- Jawalekar S R  
*see* Reddy S Raghunath 357  
*see* Sharon M 415
- Jenkinson G W  
 Modern computer assisted methods in metallurgy 239
- Jha Sudhakar  
*see* Kumar Ashok 183
- Joshi D G  
*see* Chadda V K 231
- Joshi K K  
 Microstrip losses with  $Al_2O_3$  overlay 535
- Karekar R N  
*see* Vijaya K 397  
*see* Joshi K K 535
- Kataria S K  
 Personal computer-based CAMAC system for data acquisition 225
- Katti V R  
 Deposition and assessment of thin dielectric films on photocathode substrate made of Kodial glass 325  
*see* Rangarajan L M 333
- Kelly T  
*see* Jenkinson G W 239
- Khanna S K  
 Growth of low dislocation density single crystals of nickel 467
- Khokle W S  
*see* Dixit B B 307
- Kotru P N  
 Characterization and thermal behaviour of lanthanum tartrate crystals grown from silica gels 547
- Koul M L  
*see* Kotru P N 547
- Krishan K  
 Computer simulation of defects and radiation damage 155
- Kulgod S V  
*see* Chadda V K 231
- Kulkarni A V  
 X-ray diffraction study of epitaxial zinc and cadmium films prepared by hot-wall technique 449
- Kumar Ashok  
 Computer-aided roll pass design for continuous billet mill 183
- Kumar Devendra  
*see* Parkash Om 13  
*see* Parkash Om 557
- Kumar Satyendra  
 a-Si:H/CuInS<sub>2</sub> heterojunctions for photovoltaic conversion 285
- Kumar Sudhir  
*see* Sharon M 415
- Kumar Surendra  
*see* Kataria S K 225
- Lakshmanan A R  
 Thermoluminescence of alkali halides doped with alkaline earth impurities 541
- Laroia K K  
*see* Agarwal S K 297
- Lu S C  
*see* Su Y K 29  
*see* Wei C C 439
- Mahadevan K  
*see* Dixit B B 307
- Malage A B  
*see* Rao D U Krishna 1
- Malhotra L K  
*see* Uma C S 385
- Mallik A K  
 Computer calculations of phase diagrams 107  
*see* Reddy S Raghunath 357
- Mathur S C  
*see* Chauhan J P S 531
- Matthews J R  
 Computer models for fuel element behaviour 93
- Misra Y  
*see* Tripathi L N 407
- Moharil S V  
*see* Lakshmanan A R 541
- Moussa W  
*see* Bialy A El 471
- Mukherjee S N  
*see* Dubey G C 267
- Murthy C H Sreerama  
*see* Chandrasekaran V 39

- Murthy S N  
see Chadda V K 231
- Nagendra C L  
Quality and reliability of optical coatings 351
- Naidu B Srinivasulu  
see Reddy M Raja 373
- Nair D Prabha  
see Sreenivasan K 527
- Neelakantan K  
Computer simulation of serrated yielding 209
- Pachori R D  
Flash-evaporated thin films of  $\text{CuInSe}_2$  291
- Pakala V S  
Computer applications in the field of furnace design 147
- Pal Surendra  
see Dubey G C 267
- Pandey K G  
Computer-aided design of rolling mills 123
- Pandey Lakshman  
see Parkash Om 557
- Pandya D K  
see Kumar Satyendra 285
- Parkash Om  
Microstructural and dielectric behaviour of glass ceramics in the system  $\text{PbO-BaO-TiO}_2\text{-B}_2\text{O}_3\text{-SiO}_2$  13  
Glass ceramics containing ferroelectric phases 557
- Pawar A J  
see Pawar S H 423
- Pawar S H  
Electrochemical bath deposition technique:  
Deposition of CdS thin films 419  
Spray pyrolytic deposition of  $\text{CuBiS}_2$  thin films 423  
Preparation and properties of  $\text{Bi}_{2-x}\text{As}_x\text{S}_3$  thin films by solution-gas interface technique 427
- Phadnis S G  
Dielectric properties of the system  $\text{Pb}_{2-x}\text{Nd}_x\text{Li}_{0.5}\text{Nb}_{1.5}\text{O}_{6+x}$  23
- Prakash S M Dharma  
Periodic crystallization of barium oxalate in silica hydrogel 511
- Prasad A J K  
Effect of  $\text{H}^+$  ion irradiation on surface morphology of  $\text{Fe}_{40}\text{Ni}_{40}\text{B}_{20}$  metallic glass 505
- Prasad J J B  
see Sridevi D 319
- Pratap R  
see Kulkarni A V 449
- Purniah B  
see Krishan K 155  
Computer simulation of dislocation-carbon interaction in nickel 247
- Radhakrishnamurthy C  
see Varaprasad A M 567
- Radhakrishnan V M  
Computer modelling application in life prediction of high temperature components 133
- Raina K K  
see Kotru P N 547
- Rajagopalan R  
see Prakash Om 13
- Rajan K Govinda  
see Khanna S K 467
- Rajan R  
see Phadnis S G 23
- Raj Baldev  
see Chadda V K 231
- Ramadasan E  
see Sah D N 253
- Ramakrishnan N  
Computer simulation of pressure sintering 199
- Ramamurthy V S  
see Kataria S K 225
- Ramaseshan K  
Optical black coatings for space applications 581
- Ramaswamy V  
see Kumar Ashok 183
- Ram P Raja  
Thin film  $\text{CdZnS/CuInSe}_2$  solar cells by spray pyrolysis 279
- Ranganathan S  
see Rao K Ratnaji 81
- Rangarajan L M  
see Katti V R 325  
Development of high resolution thin film patterns on curved photocathode substrates of image tubes 333
- Rao D U Krishna  
Kinetics of electrophoretic deposition of  $\beta$ -alumina 1
- Rao K Ratnaji  
Effect of texture and grain size on the mechanical properties of warm-worked cadmium, zinc and zinc-0.35% aluminium alloy 81
- Rao M G  
see Dubey G C 267
- Rao P Mohan  
see Prakash S M Dharma 511  
see Dharmaparakash S M 519
- Rasmy M  
see Bialy A El 471
- Ray S  
see Tyagi S V S 433
- Reddy K V  
see Sridevi D 319
- Reddy M Raja  
Photoresponsive measurements on  $\text{InAs}_{0.3}\text{Sb}_{0.7}$  infrared detector 373

- Reddy P Jayarama  
Pyroelectric polymer films for infrared detection 365  
see Reddy M Raja 373
- Reddy S Raghunath  
Optical and electrical properties of  $\text{SnO}_2$  films prepared by chemical vapour deposition 357
- Reddy S Venkat  
X-ray line profile analysis of silver base Ag-Cd-In alloys 61
- Roy P R  
see Verma Ravi 479
- Roy S K  
see Chandrasekhar S 391
- Sah D N  
Water reactor fuel performance code PROFISS and its application for predicting the behaviour of the fuel elements of D-Com blind problem 253
- Sahoo N K  
see Apparao K V S R 343
- Samantaray B K  
see Datta A K 497
- Sandhya Bhakay-Tamhane  
see Sequena A 591
- Sastry D H  
see Rao K Ratnaji 81
- Sastry O S  
see Kumar Satyendra 285
- Sawant S R  
see Sequena A 591
- Saxena A K  
 $\text{SnO}_2$  films synthesized by chemical vapour deposition technique using hydrofluoric acid as doping material 315
- Sequeira A  
A low-temperature attachment for a four-circle neutron diffractometer 591
- Shankara M A  
see Tareen J A K 543
- Sharda G D  
see Agarwal S K 297
- Sharon M  
Characterization of  $\text{Pb}_3\text{O}_4$  films by electro-chemical techniques 415
- Shukla A K  
see Akila R 453
- Singh A K  
see Giridhar A 53
- Singh K  
see Deshpande V K 577
- Singh Mahavir  
see Agarwal S K 297
- Singh R A  
see Dubey G C 267
- Singh S P  
see Saxena A K
- Singh Vakil  
see Prasad A J K
- Sirajuddin M  
see Reddy P Jayarama
- Sivaraman S  
see Bapat M N
- Sreenivasan K  
Determination of molecular weight distribution of polyethylene terephthalate by gel permeation chromatography
- Sridevi D  
Preparation and characterization of flame evaporated  $\text{CuInSe}_2$  thin films
- Srikanth S  
see Jacob K T
- Srinivasan S  
see Krishan K 1  
see Purniah B 2
- Srivastava P K  
R.F. magnetron sputtered tungsten carbide thin films 2
- Subbarao E C  
see Rao D U Krishna
- Subramaniam P  
see Chandrasekaran V
- Subramanian M  
see Phudnis S G
- Sudha Mahadevan  
see Giridhar A
- Suryanarayana S V  
see Reddy S Venkat
- Su Y K  
Surface morphology and properties of Ga epilayers controlled by temperature difference method of liquid phase epitaxy 4  
see Wei C C
- Tandon V K  
see Tyagi S V S 4
- Tareen J A K  
A simple hydrothermal cell for synthesis moderate temperatures and pressures 5
- Thangaraj R  
see Ram P Raja 2  
see Saxena A K 3
- Thutupalli G K M  
see Nagendra C L 3  
see Ramaseshan K 5
- Tiwari A N  
see Kumar Satyendra 2
- Tripathi L N  
Thermoelectroluminescence in thin films of zinc and copper phthalocyanines 4
- Tyagi S V S  
Electron microscopy study of chemically deposited Ni-P films 2

- Uma C S  
Cobalt oxide-iron oxide selective coatings for  
high temperature applications 385
- Vankar V D  
see Srivastava P K 379
- Varaprasad A M  
Magnetic hysteresis and crystallization studies  
on metallic glass alloy  $\text{Fe}_{67}\text{Co}_{18}\text{B}_{14}\text{Si}_1$  567
- Venkatesh D  
see Sah D N 253
- Venkateswarlu G  
see Chandrasekaran V 39
- Verma Ravi  
Determination of oxygen to metal ratio of U-Pu  
mixed oxides by x-ray diffraction 479
- Vijaya K  
Effect of bulk and thin film dielectric over  
the characteristics of microstrip rejection  
and simple microstriplines
- Vijayaraju K  
Computer-aided composition-treatment-  
ture-property correlation studies in steels
- Viswanathan M  
see Ramaseshan K
- Vollath Dieter  
Some fundamental considerations to pr  
image analysis
- Vyas P D  
see Dixit B B
- Wei C C  
see Su Y K  
Liquid phase epitaxy growth of GaAs:  
temperature difference method

### 3. Results

For the sake of better comparison, the same accelerating voltage has been maintained (60 kV) throughout the experiment, which gives the wavelength of the incident radiation as 0.0487 Å. Since the same camera constant is used, it is possible to compare the spots/rings of one figure with that of the other.

Figures 1a,b show the electron micrograph and the electron diffraction pattern respectively of the film deposited at room temperature. The electron micrograph shows formation of small granular structures indicating formation of crystalline state. The electron diffraction pattern had a number of rings. The diameter of these rings given in table 1 shows that the ratios of  $d^2$  for the outer ring to the next ring in order is a constant

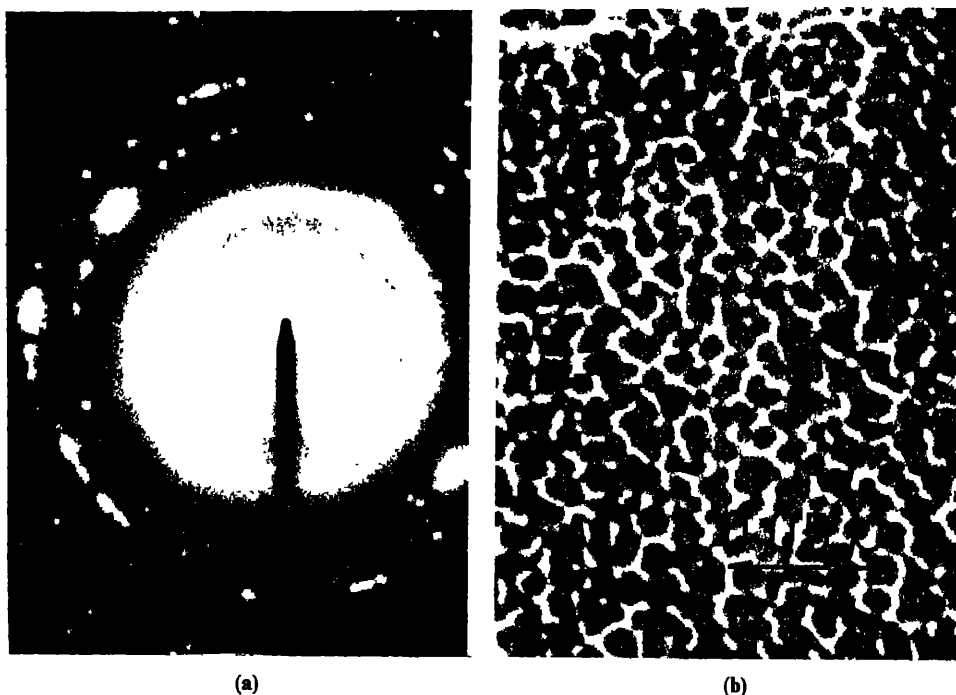


Figure 1. a. Electron diffraction pattern b. Electron micrograph of the antimony film deposited at room temperature

Table 1. Diameter of electron diffraction rings and the ratio of their squares, substrate being at room temperature.

Ring No.	$d_n$ = diameter of the ring $n$	$d_n^2$	$\Sigma = (d_n/d_{n-1})^2$
1	3.07	9.43	—
2	3.92	15.37	1.63
3	4.94	24.40	1.59
4	6.22	38.69	1.59
5	7.83	61.31	1.59

1·59. Reference to the camera geometry and Bunn charts reveals that the structure is hcp and the distance corresponds to (10 $\bar{1}$ 0) plane. The constants of the hcp crystal were according to the previous literature, i.e.  $a = 3\cdot33 \text{ \AA}$  and  $c/a = 1\cdot58$  (Dilshad Akhter *et al* 1979).

Figures 2a,b show the diffraction patterns and the electron micrograph respectively of the films deposited at 323 K. It has been observed that the grain size has become larger and the crystal structure has started changing. The electron diffraction pattern corresponds to a spot pattern showing (110) planes of a cubic structure and some traces of the previous ring pattern are also seen.

At further elevated temperatures i.e. at 373 K, the cubic pattern becomes predominant and large crystals are formed. The previous ring pattern is faintly visible (figures 3a,b).

At 423 K the pattern becomes more complicated and absolutely polycrystalline (figures 4a,b). We get a number of rings in the diffraction pattern. Nine rings which were predominantly seen were taken for comparison. Starting from the outermost ring, squares of the ratios of the diameters of the inner ones were taken and are shown in table 2.

A close look at the table shows that the ratios 9/7, 8/6, and 6/4 are around 1·59. Since the magnification, incident radiation and camera constant have remained the same, it can be concluded that these rings resemble the previous hcp structure with  $a = 3\cdot33 \text{ \AA}$  and  $c/a = 1\cdot58$ . The second commonly occurring ratio is between 6/5, 5/4, 4/3 and 9/8 and is 1·12.

Excepting these two ratios there are no more ratios which are repeating. We can

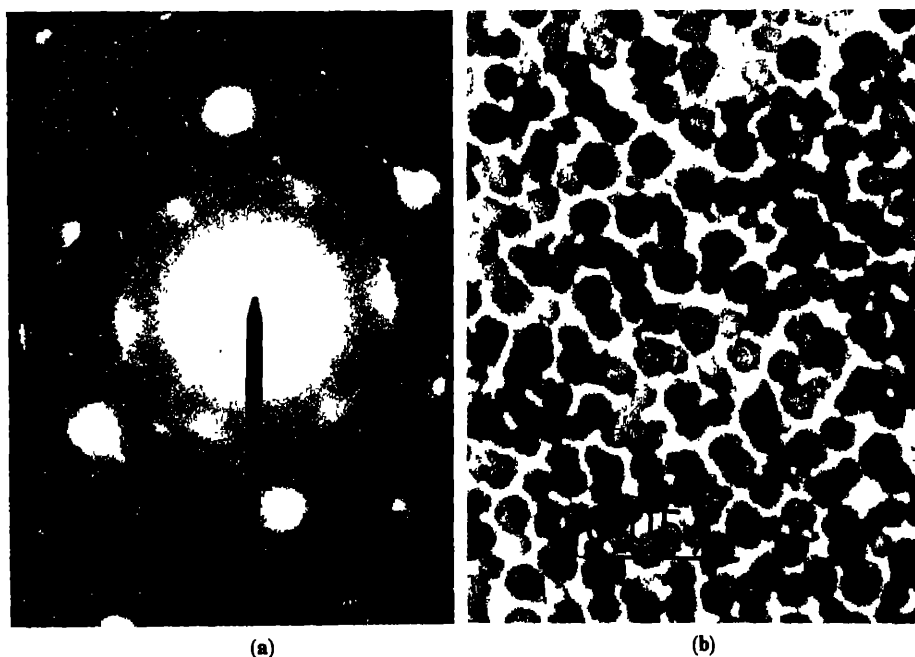
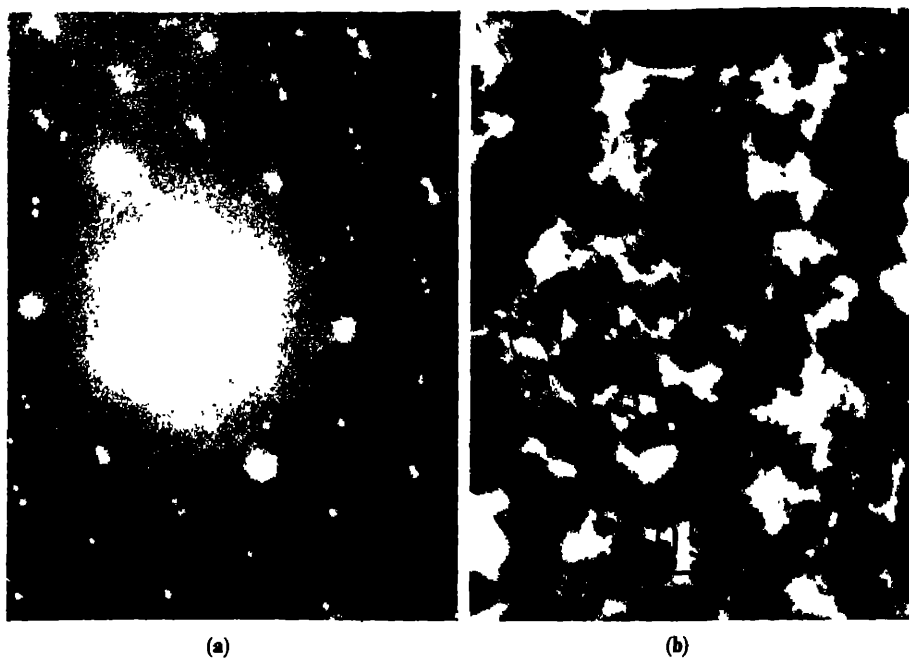
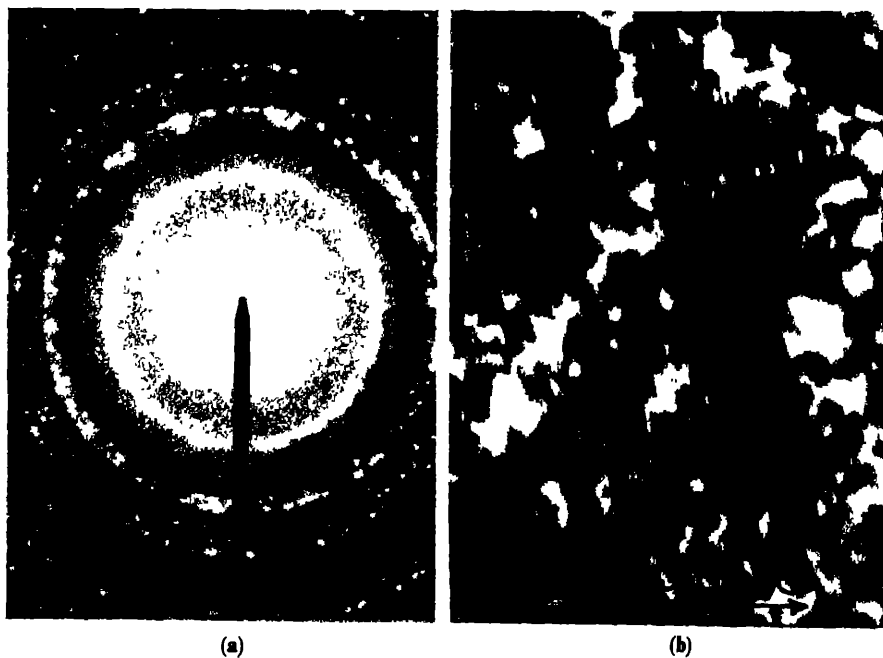


Figure 2. a. Electron diffraction pattern b. ( $\times 44000$ ) Electron micrograph deposited at 323K.





**Figure 3.** a. Electron diffraction pattern b. ( $\times 44\,000$ ) Electron micrograph of the film deposited at 373K.



**Figure 4.** a. Electron diffraction pattern b. ( $\times 44\,000$ ) Electron micrograph of the film deposited at 423K.

Table 2. Squares of the ratios of the outer diameter to the inner one.

Ring No.	Value for various ratios $\sum = (d_m/d_N)^2$							
	$N = 98$	7	6	5	4	3	2	1
9	— 1.14	1.57	2.25	2.48	3.11	3.93	6.90	13.08
8	—	1.43	1.67	1.84	2.33	2.92	5.14	9.73
7	— —	—	1.57	1.98	2.50	3.10	4.39	8.31
6	— —	—	—	1.12	1.59	1.75	2.78	5.27
5	— —	—	—	—	1.12	1.45	2.80	5.30
4	— —	—	—	—	—	1.12	1.76	3.32
3	— —	—	—	—	—	—	1.76	3.32
2	— —	—	—	—	—	—	—	1.89

attribute this second ratio to the cubic phase seen in the previous figures. Other ratios may be due to the metastable phases of other crystals in the process of formation or might be some other reflections of the existing crystals. They were not considered as they were not significant in number.

Since the photographs were taken under the same magnification and since we know that the cubic plane is (110), and the hexagonal one is (10 $\bar{1}$ 0), the interatomic distance of the cubic phase is estimated to be 3.4 Å.

#### 4. Discussion

The present study shows that because of the variation of the substrate temperature a number of additional phases are developed in the vapour-deposited antimony film. If the series of the diffraction patterns are observed carefully, it is found that the sample gradually changes from a polycrystalline hcp to crystalline cubic and then back to polycrystalline hcp and cubic mixture. In figure 3 the hcp structure has almost vanished. Similarly it is also expected that at some temperature between 373 and 423 K this hcp structure may reappear again. The study of this point is worth undertaking; however it would need a better control of substrate temperature. The cubic phase observed has a larger interatomic distance *i.e.* 3.4 Å. In previous studies by splat cooling (Dilshad Akhter *et al* 1979), such a structure with  $a = 3.16$  was observed.

#### 5. Conclusions

(i) hcp phase of antimony is observed by vapour deposition also. (ii) By increasing the substrate temperature, the cubic phase is also observed. (iii) The cubic phase has larger interatomic distances than usual. (iv) At intermediate substrate temperature hcp phase vanished and reappeared at higher temperatures. (v) At the substrate temperature of 423 K both hexagonal and cubic phases become polycrystalline.

## **Acknowledgments**

Thanks are due to Dr C S Harendranath for making the TEM facility available. The authors also thank Mr Nageshwar Rao and Miss Mruga H Joshi for help in the use of TEM.

## **References**

- Boyer A, Des B, Chacht and Groubert 1981 *Thin Solid Films* **76** 119  
Dilshad Akhtar Venkar V D and Chopra K L 1979 *Thin Solid films* **58** 327  
Kabalkina S S and Mylov V P 1964 *Sov. Phys-Dokl* **8** 917

## Formation of lamellar $M_{23}C_6$ on and near twin boundaries in austenitic stainless steels

B SASMAL

Department of Metallurgical Engineering, Indian Institute of Technology, Kharagpur 721 302, India

**Abstract.** Thin foil electron microscopy studies were made on the precipitation of lamellar  $M_{23}C_6$  during aging at 973 K and 1073 K in water-quenched specimens of two austenitic stainless steels. After the precipitation on incoherent twin boundaries  $M_{23}C_6$  formed on coherent twin boundaries and in the regions adjacent to incoherent twin boundaries. These precipitates showed lamellar morphology and were aligned in a specific manner with respect to the twin boundaries. Such lamellar precipitates were absent in the specimens which were isothermally treated at 1073 K after being transferred from the solution treatment temperature. The lamellar morphology of  $M_{23}C_6$  is suggested to be developed by the influence of residual specific stress field around twin boundaries resulted from quenching.

**Keywords.** Electron diffraction; lamellar  $M_{23}C_6$ ; precipitation morphology; twin boundaries.

### 1. Introduction

Precipitation of  $M_{23}C_6$  in austenitic stainless steels was studied by many investigators. In quenched and aged conditions  $M_{23}C_6$  precipitates (Lewis and Hattersley 1965; Wolff 1966; Beckitt and Clark 1967; Singhal and Martin 1967; Wilson 1971; Weiss and Stickler 1972) on incoherent twin boundaries after the precipitation on grain boundaries. During the later stages of aging, precipitation occurs on coherent twin boundaries and within the grains. The precipitates adjacent to an incoherent twin boundary grow as plates on both sides of the boundary, which are parallel to the coherent twin boundaries (Lewis and Hattersley 1965; Beckitt and Clark 1967; Singhal and Martin 1967; Hattersley 1964 and Lewis 1964).

Two models have been put forward to explain the formation of these lamellar precipitates. Beckitt and Clark (1967) suggested that the stress generated due to growth of precipitates nucleated on an incoherent twin boundary drives the twinning dislocations out of the boundary. These dislocations have been attributed to act as sites for nucleation continuously as they move out into the matrix and thus to form the plates of  $M_{23}C_6$  on the  $\{111\}$  (twinning) planes. Singhal and Martin (1967) however observed the stacking faults formed possibly by bowing of the twinning dislocation out of the incoherent twin boundary after the precipitation on the boundary. They have suggested that  $M_{23}C_6$  precipitation occurs by nucleation along the bounding Shockley dislocation and by growth across the stacking fault to form a sheet of carbide. Shockley partial might again be repelled by the precipitate and the repetition of the precipitation process might cause further growth of the plate.

In order to examine these models a detailed electron microscopy study was made on

the formation of lamellar  $M_{23}C_6$  adjacent to incoherent twin boundaries and on the precipitation at coherent twin boundaries.

## 2. Experimental

The chemical composition of two austenitic stainless steels (AISI 316L and DIN 4981, hereafter referred to A and B respectively) studied are given in table 1. The cold-rolled sheet specimens (about 150  $\mu\text{m}$  thick) were solution-treated (5.4 Ksec (1 hr 30 min) at 1433 K for steel A and 1.8 Ksec (30 min) at 1550 K for steel B) inside sealed silica tubes in argon atmosphere and quenched in water. The quenched specimens were then aged at 973 K and 1073 K inside evacuated silica tubes for various durations from 3.6 Ksec (1 hr) to 14.4 Msec (4000 hr). A few bulk specimens (10  $\times$  5  $\times$  3 mm) of A after being solution-treated were transferred to 1073 K, held for 360 Ksec and 1.8 Msec and then cooled in air. Thin foils for electron microscopy examination were prepared by twin-jet electrolytic polishing with a mixture of 10% perchloric acid and 90% acetic acid.

## 3. Results and discussion

Steel A was fully austenitic in the as-quenched condition, while B contained a considerable amount of undissolved NbC particles.  $M_{23}C_6$  was the only carbide to be precipitated in A during aging at 973 K and 1073 K. In B both NbC and  $M_{23}C_6$  formed. Because of the precipitation of NbC in very fine form on grain boundaries, on dislocations, in association with stacking faults and as dot-like particles, the precipitation of  $M_{23}C_6$ , in general, was appreciably low and was delayed in B (Sasmal 1980).  $M_{23}C_6$  first precipitated on grain boundaries and later on incoherent twin boundaries followed by intragranular precipitation on continued aging. After the precipitation on incoherent twin boundaries a preferential precipitation of  $M_{23}C_6$  was noted in the regions adjacent to these boundaries (figure 1). Precipitation on coherent twin boundaries also occurred simultaneously. In B, though the intragranular precipitation was rarely observed, a new mode of precipitation of  $M_{23}C_6$  around undissolved NbC particles was noted. This is reported earlier (Terao and Sasmal 1978, 1981).

Electron diffraction analysis showed that the  $M_{23}C_6$  precipitates were face-centred cubic and had almost the same lattice parameter in both the steels:  $a = 10.7 \text{ \AA}$ . They were found to grow at all the sites with the cube orientation relationship with austenite matrix, i.e.

$$\begin{aligned}\{100\}_{M_{23}C_6} &\parallel \{100\}_\gamma, \\ \langle 100 \rangle_{M_{23}C_6} &\parallel \langle 100 \rangle_\gamma.\end{aligned}$$

Table 1. Chemical analysis of steels.

Steel	Composition, wt. %							
	C	Ni	Cr	Mn	Mo	Si	Nb	B
A	0.014	11.5	17.3	1.15	2.2	0.56	—	—
B	0.057	15.8	16.2	1.12	1.84	0.41	0.77	0.0003

Balance

"



Figures 1-3. Steel A, aged for 28.8 Ksec (8 hr) at 1073 K. Lamellar  $M_{23}C_6$  formed close to incoherent twin boundaries and on coherent twin boundaries. 2. Steel A, aged for 1.80 Ksec (50 hr) at 1073 K.  $M_{23}C_6$  plates increased in number on both sides of the incoherent twin boundary. The specimen foil is nearly parallel to the (110) of the matrix and the twin axis is  $[T11]$ . 3. Steel B, aged for 14.4 Msec (4000 hr) at 1073 K.  $M_{23}C_6$  plates formed on coherent twin boundaries and adjacent to incoherent twin boundaries, but considerably less in number.

The results agree with those reported earlier (Lewis and Hattersley 1965; Weiss and Stickler 1972; Singhal and Martin 1968). The morphology of these precipitates after a long aging period, however, depends on the precipitating sites (Sasmal 1980). Whatever may be the morphology of these particles, their interfaces always consist of  $\{111\}$  and  $\{110\}$  types of planes. This result confirms the suggestion made by Beckitt and Clark (1967).

In the adjacent regions of an incoherent twin boundary  $M_{23}C_6$  grew as plates into the austenite matrix on both sides of the boundary (figure 1). The plates grew in a direction parallel to the coherent twin boundaries. On longer aging, more and more lamellar  $M_{23}C_6$  formed in a similar fashion and gradually grew away from the incoherent twin boundaries (figure 2). The number of lamellae however decreased progressively with increase in distance. On the coherent twin boundaries also,  $M_{23}C_6$  grew as similar plates which on longer aging joined one another making almost a continuous layer of precipitates. In B,  $M_{23}C_6$  plates also formed on coherent twin boundaries and in the vicinity of incoherent twin boundaries, but to a lesser extent, (figure 3). A few examples of morphology of the lamellar precipitates in the vicinity of an incoherent twin boundary are shown schematically in figure 4. The large planes of these plates are parallel to the twinning planes. A detailed study of the characteristics of these lamellar precipitation has been reported elsewhere (Terao and Sasmal 1980). The

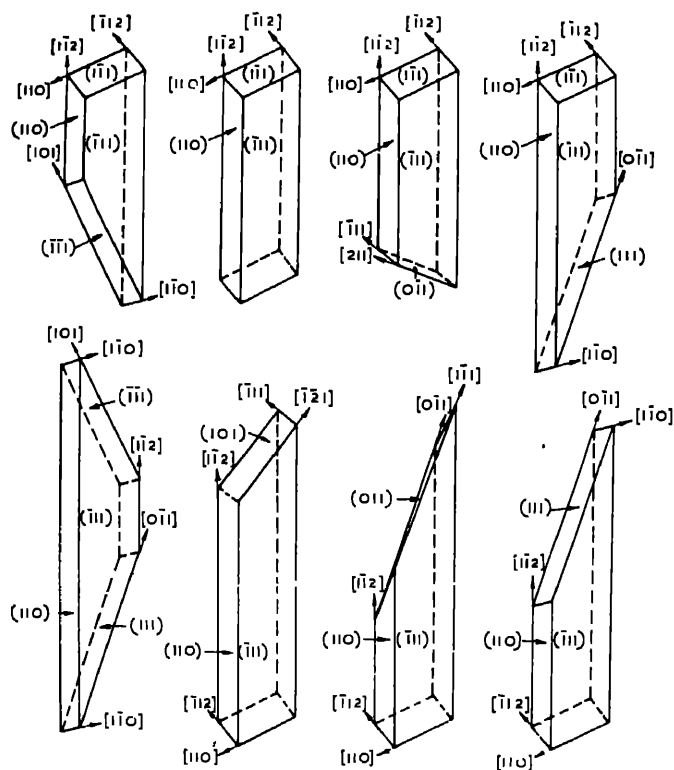


Figure 4. Several examples of morphology of  $M_{23}C_6$  lamellae formed adjacent to an incoherent twin boundary, the twinning plane being  $(\bar{1}11)$ .

specific features of the formation of these  $M_{23}C_6$  lamellae were observed to vary from one twin to another.

The lamellar  $M_{23}C_6$  precipitates, as reported by the previous investigators (Beckitt and Clark 1967; Singhal and Martin 1967) were assumed to result from emanation into the grains of the precipitates nucleated earlier, on incoherent twin boundaries. On the basis of this assumption in the mechanisms suggested for their formation the glide of the twinning dislocations possibly repelled from the incoherent twin boundaries by the stress field of growing particles at the boundaries has been proposed to play the most important role. The plate morphology has been attributed to result by a repeated nucleation (Beckitt and Clark 1967) on these gliding Shockley particles, or by the formation of stacking faults, nucleation on the outer particals and subsequent growth across the stacking faults (Singhal and Martin 1967). A close examination (by tilting the thin foils about different axes) of these lamellae, however revealed that most of them stood separate from the precipitates formed on incoherent twin interfaces, having no contact whatsoever. On the other hand, if any one of these mechanisms were operative, the lamellar  $M_{23}C_6$  might not form in B since dislocations are more preferable sites for precipitation of NbC. Further, none of these mechanisms is able to explain the lamellar precipitation on coherent twin boundaries.

To examine further the validity of these models another experiment was made. A few bulk specimens of A were held at 173 K for sufficiently long periods, after being transferred directly from the solution-treatment temperature. As shown in figure 5,  $M_{23}C_6$  precipitated in these specimens only on incoherent twin boundaries. No lamellar precipitation occurred either on coherent twin boundaries or in the regions adjacent to the incoherent twin boundaries. These observations indicated that quenching from the solution-treatment temperature is essential to induce lamellar precipitation during aging, and the existing models have no provisions to accommodate this fact.

Due to differential contraction between cooler and hotter parts of a metallic body, quenching from a high temperature induces pronounced stress. The state of stress inside a specimen becomes complicated in the vicinity of a barrier such as grain boundaries, twin boundaries and undissolved particles. The effect of the quenching stress near twin boundaries would, however, be different from that near a grain boundary owing to the inherent difference in characteristics of these two types of boundaries. In this respect coherent twin boundaries would once again behave differently from incoherent twin boundaries. Quenching stress produces residual stresses in the specimens, the maximum value of which has been calculated (Lang 1965) to be

$$\sigma_{\max} = \frac{E\alpha\Delta T}{1-\nu} \cdot \frac{S^2}{3at_0},$$

where  $E$  = Young's modulus;  $\alpha$  = coefficient of thermal expansion;  $\Delta T$  = temperature range ( $T_q - T_{\text{room}}$ );  $\nu$  = Poisson's ratio ( $= 0.3$ );  $2S$  = thickness of the plate;  $a$  = thermal diffusivity in  $\text{cm}^2/\text{sec}$ ;  $t_0$  = total transient time.

The change of orientation of a crystal in a specific manner across twin boundaries is expected to induce a specific stress field around the boundaries since the elastic constants of a material are different along different directions. In these regions,  $M_{23}C_6$  which always nucleates on  $\{111\}$  austenite planes, because of least misfit (Beckitt and Clark 1967) across these interfaces has to choose one of the possible habits in order to



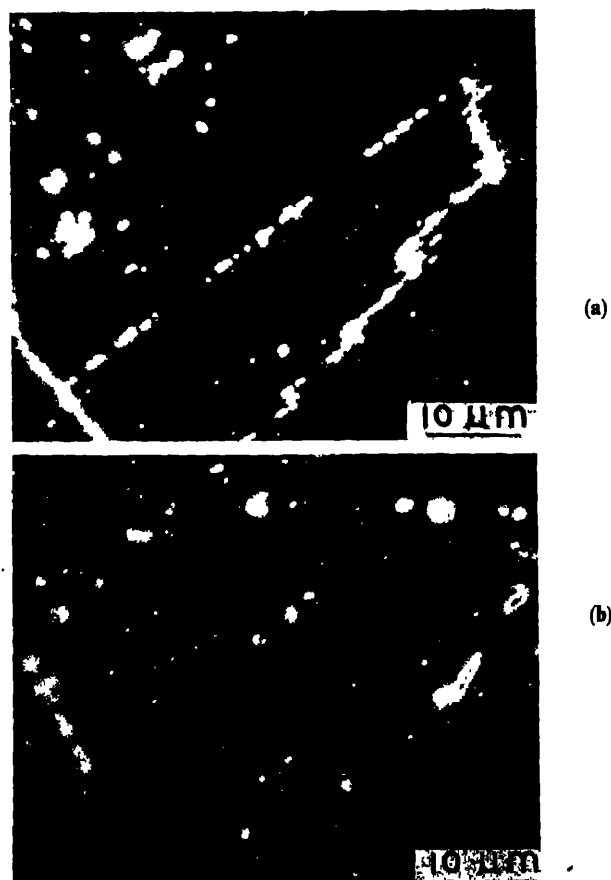


**Figure 5.** Dark-field optical micrographs of steel A. **a.** Water quenched and aged at 1073 K for 1.8 Msec (500 hr).  $M_{23}C_6$  precipitated on incoherent and coherent twin boundaries and also in the regions adjacent to incoherent twin boundary. **b.** Quenched to 1073 K and held for 1.8 Msec (500 hr). Coherent twin boundaries and regions close to the incoherent twin boundaries are free from lamellar  $M_{23}C_6$ .

minimise the coherency strain. This is in conformity with the observations made. It is therefore, proposed that the presence of a residual specific stress field around twin boundaries in the quenched specimens is responsible for the formation of lamellar  $M_{23}C_6$  precipitates on coherent twin boundaries and in the regions close to incoherent twin boundaries. Possibly vacancies play an important role in the process of their nucleation.

#### 4. Conclusions

The lamellar  $M_{23}C_6$  precipitates on coherent twin boundaries and near incoherent twin boundaries form during aging in the quenched samples only. The morphology and the specific orientation of these precipitates are influenced by the residual stress developed around twin boundaries due to quenching. The nucleation of these precipitates is aided by vacancies.

## References

- Beckitt F R and Clark B R 1967 *Acta Metall.* **15** 113  
Hattersley B and Lewis M H 1964 *Philos. Mag.* **10** 1075  
Lang W 1965 *Keruforschungszentrum Karlsruhe Report No 274*  
Lewis M H and Hattersley B 1965 *Acta Metall.* **13** 1159  
Sasmal B 1980 Ph.D. Thesis, Indian Institute of Technology, Kharagpur  
Singhal L K and Martin J W 1967 *Acta Metall.* **15** 1603  
Singhal L K and Martin J W 1968 *Acta Metall.* **16** 1159  
Terao N and Sasmal B 1978 *C. R. Acad. Sci. (Paris)* **C287** 487  
Terao N and Sasmal B 1980 *Metallography* **13** 117  
Terao N and Sasmal B 1981 *Trans. Jpn. Inst. Metals* **22** 379  
Weiss B and Stickler R 1972 *Met. Trans.* **3** 851  
Wilson F G 1971 *J. Iron Steel Inst.* **209** 126  
Wolff V E 1966 *Trans. MS-AIME* **236** 19



## FOREWORD

The mechanical behaviour of materials is of vital interest to many branches of engineering and technology. Although at one time physicists were interested in this subject, at present its study is pursued mainly by metallurgists and mechanical engineers. However, the recent focus on topological defects etc., made some of us wonder whether the time was ripe for physicists to renew their interest in mechanical properties. In order to explore this, a Discussion Meeting was held at the Reactor Research Centre, Kalpakkam on February 7, 8 and 9, 1983. The Meeting was sponsored by the Indian Academy of Sciences, the Department of Science and Technology, the Defence Metallurgical Research Laboratory and the Department of Atomic Energy. About 70 scientists belonging to various disciplines took part.

We present in this volume the written version of the talks given at the Meeting, the record of the discussions that followed the oral presentations, and of the Panel Discussion that took place in the concluding session. Owing to restrictions of space, and in the interests of reasonable uniformity of style and notation, we have been forced to make (generally minor) editorial changes in the manuscripts submitted by the speakers, and on occasion, prune the material in places. While great care and pains have been taken to preserve the essential spirit of every point the authors have intended to make, we do accept the responsibility for the changes necessitated by the reasons stated.

The Meeting itself was quite lively and absorbing, with a variety of views expressed by people with varying specializations. In offering the Proceedings we hope that the excitement of the Meeting would be shared by a wider audience, and enthrust at least some physicists to enter this area.

The task of preparing the Proceedings for publication has been quite strenuous and could not have been accomplished but for the unstinted help and cooperation we have received from many. Particular mention should be made of G Ananthakrishna, B Purniah, Radha Ranganathan, V Sridhar, P Subba Rao and T D Sundarakshan. We also would like to express our personal indebtedness to Prof. S Ramaseshan for support and encouragement in organising the Discussion Meeting.

February, 1984  
C N R Rao  
Editor of Publications,  
Indian Academy of Sciences

Guest Editors  
V BALAKRISHNAN  
G VENKATARAMAN

11

1

1

1

1

1

1

1

1

1

1

1

## Observations on the physical basis of mechanical behaviour

S RAMASESHAN

Indian Institute of Science, Bangalore 560 012, India

### 1. General remarks

It gives me great pleasure to participate in this Discussion Meeting. This is perhaps the first time that physicists, materials scientists and metallurgists in India have planned a meeting to understand each other and to see whether phenomena not completely comprehended by one group can be looked into by another or jointly. The motivations are so praiseworthy that I am sure something will come out of such meetings. If these meetings are to be successful many obstacles have to be surmounted. The first, of course, is that of language. Each person here must understand the jargon of the other. The second is to make a conscious attempt to change one's attitudes.

The metallurgists and physicists today appear to be two different animals. The purpose of this meeting is to see that the barriers that have been artificially raised are removed. One has only to read the fascinating books by Cyril Stanley Smith, *From Art to Science* and *A Search for Structure* to realise that metallurgy which has been an empirical science for a long time has been eminently successful; and yet what is common to the village blacksmith is very mysterious to the physicist. Science was injected into metallurgy only recently. Most metallurgists, like chemists, are pragmatists. They reduce many sophisticated theories to thumb rules which work and which have advanced the fields most spectacularly. However, there is a tendency among many of them not to go too deeply into the fundamentals of the phenomena they observe. The physicist, on the other hand, choose rather simple ideal systems and model them. As this approach has been rather successful in physics he feels that by using a similar one he can "clean" up many of the problems which the metallurgist does not understand. In this connection, I must recall what Prof. Andrew Huxley—a physicist himself who entered biology and distinguished himself—said when he lectured at the Indian Institute of Science, Bangalore on Physical Sciences and Biology. Biology, according to him, is inherently complex. Simplistic models sometimes hinder rather than advance the subject. It is the complexity and the basis of this complexity that one must try to understand and describe. The physicist, if he is to be useful at all, must enter biology with great humility, with a genuine intent to understand the subject and its spirit. What Huxley said of biology is, in my view, applicable to metallurgy and materials science.

In each field of science when sufficient knowledge accumulates, a great step is usually taken which throws new light and opens up new vistas. This happened to biology about 25 years ago when biologists and crystallographers combined to unravel the structure of DNA and caused a revolution which biology is still experiencing.

For metallurgy there was one such great flash in 1934 when the theory of dislocation was put forward by physicists which opened the gates for the understanding of the mechanism of strengthening, crystal growth etc. Fifty years have now passed and one

feels that a coming together of scientists in related fields may possibly help is taking another important step even if it is not as revolutionary as the dislocation theory. Being an experimenter myself I must stress the importance of experiments. Unfortunately the experimental approach is sometimes neglected by physicists in India. Experiment forms the backbone of progress in any field. I am told that Prof. Mott often stressed that every theoretical paper or idea must suggest a clean interesting experiment which can be performed. I do hope that at the end of this meeting crucial experiments will be suggested which will help to bring about the proper understanding of some of the puzzling phenomena in this field.

If such meetings are held often they would create a community of scientists interested in mechanical behaviour of materials. They may also provoke individuals or groups with complementary competences to collaborate. One hopes that the theorists and experimenters would join hands to look into some of the exciting problems in this field. Following the spirit advocated by the organisers of this Meeting, in this inaugural talk I shall mention a few experiments which I and my group have performed (many of which are unpublished) and others which are not so well-known, that have come my way. I shall also raise some questions which have troubled me particularly those connected with crack generation, hardness and its variation, friction, wear, surface states and the nature of grain boundaries.\*

## 2. Welding of surfaces and generation of cracks

In some experiments done in 1944 I noticed that diamond surfaces freshly cleaved in vacuum ( $10^{-5}$  torr) do not rejoin when brought together almost immediately after cleaving. It was also possible to show by studying the Jamin effect (*i.e.* by ellipsometric methods) that a thin film is formed on the cleaved surface. In 1948 Gwathmey showed that cleaved copper single crystal welded together in vacuum ( $10^{-8}$  torr) a phenomenon now common in space.\*\*

At the surface of a metal due to discontinuity there would be a spill-over of electrons and the consequent charge imbalance is prevented by the electrons collectively conspiring to set themselves into oscillations. When two clean metal surfaces are brought close to each other these oscillations in each piece (which are independent) can become coupled and they go backwards and forwards from one piece to the other, bonding the two surfaces. Another crucial question is: Can stress concentration in a metal cause an instability in the electron oscillations so that decoupling can take place causing the formation of two surfaces (*i.e.* a crack?) These are topics of great interest worthy of some thought and discussion.\*\*\*

\* No attempt is made to pad it up to make it more intelligible!

\*\* I am not aware of any experiments done in space attempting to join or weld diamonds. It is not clear to me why diamond surfaces should not also weld as copper surfaces do. The dangling bonds in diamond may help to chemisorb atoms to form a thin film. In metals also thin films are formed by physical adsorption. One wonders whether the difference in the magnitude of the energies of chemisorption and physisorption is the real cause of the two types of behaviour.

\*\*\* Some may disagree with the conjecture that two metal surfaces weld together in vacuum because the surface plasmons go backwards and forwards from one piece to another. It is strange that the magnitude of the surface energy is very close to the contribution of the correlation part of the electron energy. Does this imply that for some reason there is a cancellation of some of the very large terms like the lattice contribution, the kinetic energy of the electron etc? Similarly, when one considers the cohesive energy (next section) is there also a cancellation of the Madelung term, corresponding to the kinetic energy of the electron so that the electrons are mostly responsible for the cohesive energy.

Crude measurements (by us) of the stress optic coefficients of metals indicate that stress has considerable effect on the electrons. Stress distorts the lattice and due to this there are two optical effects. Firstly, the anisotropic distribution of the polarisable atoms in the strained lattice alters the index ( $n$ ) and absorption ( $k$ ) tensors. Secondly, electrons moving in the strained lattice can also alter the  $n$  and  $k$  tensors. The latter effect appears to be quite large and is opposite to that of the former.

### 3. Do electrons contribute to the hardness of metals?

Since electrons do contribute so much to the cohesive energy of a solid, it seems very probable (at least to me) they contribute to the hardness of a metal.†

Some compounds like rare earth chalcogenides (example SmS which has the NaCl structure) are semiconductors and become metals under pressure, undergoing isostructural semiconductor-to-metal transformation. There is a volume change and the resistance drops by five to six orders of magnitudes. These are peculiar metals which have positive and negative ions inside with 'free electrons' in them. By measuring the hardness of the two phases one can get an idea as to whether electrons do contribute to hardness or not. To make measurements at high pressures is not easy although the method mentioned in the next section could be adopted for this purpose. The effect of the density change on hardness must also be taken into account.

A similar isostructural semiconductor-metal-transition can be effected by adding adequate amounts of rare earth metal which simulates the effects of pressure (*e.g.* SmS is a semiconductor while Sm<sub>0.85</sub>, Gd<sub>0.15</sub>S is a metal). The hardness of the metal is much higher than that of the semiconductor. But one cannot be certain whether this increase is due to the electrons, the change of density or the additional Gd atoms in the substance.

### 4. The hardness pendulum—The measurement of the variations of hardness

The hardness pendulum, devised by experimentors in USSR, in which a loaded cylinder oscillates on the surface under study can be used to measure hardness of the metal under a variety of conditions. The hardness is estimated from the rate of damping of the oscillations. Liquids can be placed between the surface and the cylinder to study the effects of adsorption and hardness. With an electrolyte, variation of hardness can be studied with varying potentials applied on the system. The hardness of the material increases with increasing potential and becomes maximum when the charge on the surface is zero and it decreases as the surface becomes progressively negatively charged. In fact, this curve is very similar to the variation of the interfacial tension of Hg solution interface with applied voltage indicating clearly that the surface energy (which changes with the application of potential) is involved in the phenomenon of hardness. By

† I am not at all happy using the word 'electron' in this loose manner as I am aware that there are several contributions to the energy from electrons themselves and they even have opposite signs.

‡ To my mind the question "do electrons" contribute to the hardness of metals is an important one and deserves further theoretical and experimental investigation.



analogy with the Hg solution interface the effect of atoms absorbed on the surface was studied. Many patents on additives to increase the machining rates have resulted from this work.

It is also found that the effect of absorption of neutral atoms decreases the hardness. It is also a known fact that the work function  $W(\phi)$  of a refractory transition metal is lowered by as much as 4 eV by a monolayer of Cs. This is possibly the reason why adsorption can decrease hardness. Theoretical calculations of the electron distribution on the surface have also been done. When a tin crystal is coated with liquid gallium the crystal becomes brittle. Laue photographs show that a single crystal becomes polycrystalline. It is thought that the grains are held together by surface tension forces of the liquid. The strength of the solid decreases considerably although its ductility is not affected.

## 5. Friction, surface roughness and surface states

The second law of friction discovered by the great Leonardo da Vinci (which states that the coefficient of friction ( $\mu$ ) is independent of the surface area) appears mysterious to many when they first come to know of it. To explain this experimental law one must seek a phenomenon by which a true area of contact is proportional to load (the first law states that the  $\mu \propto$  load). The real surface of any material consists of microscopic hills and valleys (asperities). When two surfaces touch, the area of contact being small the stress is very large. An elastic deformation takes place first and this is followed by a plastic one till the total area of contact increases to a value which can support the load. This phenomenon can be elegantly demonstrated by observing intensively the total internal reflection in a right angle prism. When the surface (with its asperities) is laid on the hypotenuse of the prism wherever there is a real contact there is no total internal reflection, and where there is no contact, evanescent wave returns into the medium of the prism. The intensity of the totally reflected beam decreases with load.

The existence of the asperities has also been demonstrated by measurements of the AC surface resistance (at very high frequencies 24000 MHz when the skin depth is as low as  $0.4 \mu$ ) and this surface resistance is much greater than the DC resistance. If the surface is bathed in carbon monoxide, the AC resistance increases considerably indicating that the electrons are trapped in the surface states created by CO.

## 6. Electrons and metals

There are many other questions which require consideration. What is the sub-microscopic beilby layer which forms when one metal is rubbed against another? And which spalls off during wear producing hard particles? Why is it harder and more brittle than the parent metal—although it is said to have the same composition? Has the metal turned amorphous due to the high temperatures and pressures produced during wear? Does the contribution of the electron to cohesive energy increase in amorphous metals, making them harder and corrosive resistant? Electron micrographs definitely indicate that the boundaries in large angle polycrystalline metals and alloys are extremely thin (about 3 to 5 atomic layers). Are these really "amorphous" regions with coordination polyhedra postulated by Bernal for "liquids"? Are polycrystals stronger than the monocrystals because dislocation cannot wander across the grain boundaries or is it

because electron “lattice” interactions at the grain boundaries contribute to the cohesive energy?

We know that the dislocation theory has been very successful but are we leaning a bit too heavily on it, relegating the effect of free electrons on the mechanical properties, to the background?

Soon after the discovery of the quantum theory, it was appreciated that the physical basis for the optical and magnetic properties of solids must be found at the microscopic level. Unfortunately, the physical basis of mechanical behaviour was relegated as engineering. Only some outstanding scientists like Mott and Pierls appreciated that one must look at microscopic phenomena to understand mechanical behaviour also. Soon after the advent of the dislocation theory, their interest shifted to other problems and physicists have been very reluctant to contribute to this complex but important field. It is a bit ironical because the most dramatic and obvious property of a solid is, of course, its mechanical strength. This meeting clearly shows that we in India have a unique opportunity to make some important contributions before the rest of the world wakes up, so to say.

[REDACTED]

## Shocks and high velocity deformation

R CHIDAMBARAM

Physics Group, Bhabha Atomic Research Centre, Bombay 400085, India

**Abstract.** The shock Hugoniot curves of a large number of materials up to a few Mbar have been obtained experimentally. Metallurgical examination and physical measurements on metallic and other samples recovered after shock loading up to several 100 kbar indicate the existence of large concentrations of point, line and planar defects. Dislocation mechanisms have been invoked to explain shock wave propagation and the phenomena related to the quick homogenisation of stress and strain behind the shock front. Computer simulation models using molecular dynamics calculations have also been used to understand some aspects of shock wave propagation at an atomistic level. For very strong shocks, the material is expected to melt under shock heating, but the experimental evidence regarding this is inconclusive. A combination of shock temperature measurement and theory may be able to answer this question.

**Keywords.** Shock propagation; shock deformation; shock melting.

### 1. Introduction

During the last decade or two, our understanding of the mechanical effects of shock waves on materials has advanced considerably. There is now a wealth of metallurgical information on samples recovered after being subjected to shock loading. Active measurements of physical parameters such as the electrical resistivity have also been attempted in a few cases. Physical phenomena like shock deformation, phase transformations under shock loading and shock melting have been understood to a somewhat smaller extent at the microscopic level. We shall discuss some of these aspects in this paper.

If the shock wave propagating in a material is considered to be a sharp discontinuity in stress, then, using the laws of conservation of mass, momentum and energy, it can be shown that the undisturbed state is related to the shocked state at the shock front as follows:

$$U_s \rho_0 = \rho_1 (U_s - U_p), \quad (1)$$

$$P_1 - P_0 = \rho_0 U_s U_p, \quad (2)$$

$$E_1 - E_0 = \frac{1}{2} (P_1 + P_0) (V_0 - V_1), \quad (3)$$

where  $U_s$  is the shock front velocity,  $U_p$  is the particle velocity in the compressed region;  $P$ ,  $E$ ,  $\rho$  and  $V (= 1/\rho)$  are respectively the pressure, specific internal energy, density and specific volume: the suffixes 1 and 0 represent quantities in the shocked and the unshocked regions respectively.

If the equation of state  $E = E(P, V)$  of the material is also known, we can use (3) to write  $P$  as a function of  $V$  (for all practical purposes,  $P_0 \simeq 0$ ). The locus of all states  $(P, V)$  which can be obtained by a single shock from an initial state  $(P_0, V_0)$  is known as the Rankine-Hugoniot curve or simply the Hugoniot curve (figure 1).

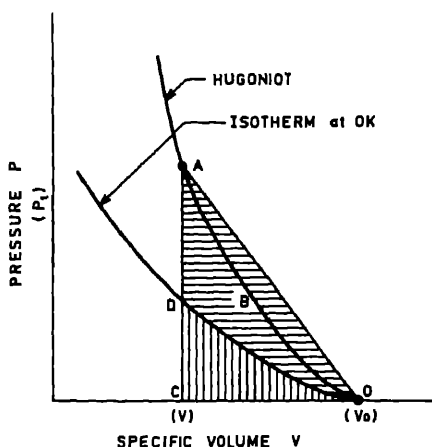


Figure 1. The Hugoniot curve. The vertically-hatched area is a measure of the cold compressive energy. The horizontally-hatched area is a measure of the heat energy in the shocked sample.

It is evident from (3) that the internal energy deposited in the compressed body is the area of the triangle  $OAC$ . If the compression is carried out isothermally at  $0^\circ\text{K}$  to the same final volume  $V$ , the material will be at the point  $D$ . The area of the curved triangle  $ODC$  therefore represents the "cold" elastic energy. The difference between the areas of  $OAC$  and  $ODC$  is a measure of the heat energy deposited by the shock in the compressed sample; the contribution from defects created by the shock, such as vacancies and dislocations, is relatively negligible. To give some numbers, a shock pressure of 1 Mbar\* will compress a sample of aluminium from a density of  $2.78$  to  $4.30 \text{ g/cm}^3$  and heat it to  $3540 \text{ K}$ . The corresponding shock velocity is  $10.1 \text{ mm}/\mu\text{sec}$  and the particle velocity is  $3.6 \text{ mm}/\mu\text{sec}$ .

After the shock wave has passed, the sample will unload along the curved path  $ABO$  doing work on the surroundings represented by the area of the curved triangle  $OBAC$ . (For simplicity we assume that the terminal specific volume  $\approx$  the initial value  $V_0$ , which would be true in the absence of porosity in the initial sample, etc.) The difference in the areas  $OAC$  and  $OBAC$  represents the (waste) heat deposited in the terminal sample. In aluminium, the residual temperature is  $1440 \text{ K}$ . If the amount of waste heat exceeds the enthalpy of vaporization (or melting), the terminal sample will be in the vaporised (or molten) state. In peaceful nuclear explosions (*e.g.*, see Chidambaram and Ramanna 1975), when a nuclear explosive is detonated underground in a rock medium, about 20% of the explosive energy is utilised in vaporising approximately 70 tons of rock, and another 20% in melting approximately 300 tons of rock for every kton of yield.

## 2. Range of shock pressures achieved experimentally

By keeping chemical explosives (usually in the form of lenses and pads) in contact, shock pressures of a few 100 kbar can be transmitted into materials. Alternately, a metal plate (flyer plate) can be accelerated by a contact explosive or a gas gun, and can subsequently be made to deliver its momentum to a target plate by impact. Pressures up

\* 1 Mpa = 10 bar, 1 Gpa = 10 kbar, 1 Tpa = 10 Mbar.

to several Mbars can be achieved in this manner, though the pressure pulse widths are smaller (typically a few mm in space); still higher pressures can be obtained using curved rather than plane geometries. Exploding foils and rail guns can also be used to accelerate flyer plates. The highest shock pressures achieved to date have been through laser—or nuclear explosive-driven shocks and are in the range of tens of Mbars (for a more detailed discussion see Godwal *et al* 1983a). The metallurgical and physical observations to be discussed below have generally been on samples shocked to pressures less than about 1 Mbar.

### 3. Finite elastic-plastic deformation by shock waves

When a plane shock wave propagates through a material, the change in density occurs—from a macroscopic point of view—through uniaxial compression. Consider a volume element of cross-sectional area  $A$  (perpendicular to the direction of shock propagation) and length  $L$ . During shock compression,  $A$  remains unchanged while  $L$  decreases in direct proportion to the decrease in the specific volume (see figure 2). If the element were allowed to expand from the final compressed state without lateral constraints it would reach normal density at the boundaries shown by the broken lines, provided it had been in a state of hydrostatic strain and stress in the compressed state. This gives us the elastic and plastic strain components in the direction of shock propagation and in the lateral directions, as indicated in the figure.

The time scales involved in shock propagation are typically in the  $\mu\text{sec}$  region, while the rise times are well below a nsec. Are conditions of hydrostatic stress and strain achieved behind the shock front, and, if so, how quickly? The answer to this question comes from the beautiful flash x-ray diffraction experiments of Johnson and Mitchell (1980) with single crystals of LiF, Al and graphite. Specific Bragg reflections were recorded using a Mo x-ray pulse synchronised with the duration of the shock compression of the crystal. These authors concluded that: (a) single crystals transform to the hydrostatically-compressed state within less than 20 nsec—there is no immediate conversion to a polycrystalline state; (b) the unit cell volume compression is in agreement with the conventional macroscopic volume compression data to within 1 %, independent of crystal orientation (shocks of strengths between 400 kbar and 1.1 Mbar were propagated along [100] and [111] in LiF). In related experiments at Trombay (Gupta 1980) we shocked polycrystalline samples of zirconium (hexagonal crystal

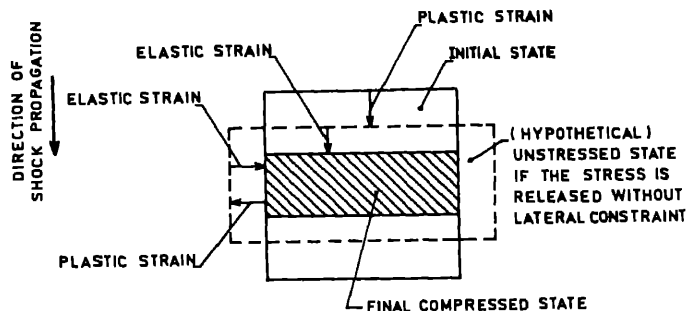


Figure 2. Finite elastic-plastic deformation created by a shock wave.

system) which showed a prominent texture ( $\{100\}$  planes preferentially normal to the axis of the cylindrical sample). The texture was retained to a substantial extent in the terminal sample, after shock loading to about 150 kbar.

At very low pressures, the unit cell of the crystal may be expected to respond by one-dimensional compression. Correspondingly, in the Hugoniot curve, there is a pressure value known as the Hugoniot elastic limit (HEL) below which the response of the material to the shock pressure is nearly linear; the Hugoniot really begins to curve (concave upwards) from this point. The HEL is related to the shear strength of the material; one may expect that, for shock pressures lower than this limit, no rearrangement of the crystal lattice occurs (unlike in strong shocks discussed below). However, Jamet (1980) found, in some recent flash x-ray experiments with NaCl single crystals (HEL = 280 bar), that the one-dimensional deformation must be taken into account even for shock pressures above 10 kbar. Some experiments on the measurement of triaxial stress components using piezo-resistive gauges for shock pressures below, around and above the HEL are now being carried out for several materials (see, *e.g.* Chartagnac 1982).

Computer simulation of shock propagation in crystal lattices has also been attempted (Tsai and Macdonald 1976). Shock compression is initiated in a semi-infinite lattice by moving the lattice along the x-axis towards the origin with (mass) average velocity corresponding to the particle velocity  $U_p$  defined in (1)–(3), and making it collide with its image at  $x = 0$ . Many effects are correctly predicted by these molecular dynamics calculations including the achievement of thermal equilibrium and a state of hydrostatic stress, and also the right temperature. However, the strain in the compressed state turns out to be far from hydrostatic! This is related, we believe, to the computer limitation that necessitates a small-sized crystal lattice without scope for the generation of dislocations. As we shall see, the introduction of mobile-dislocation mechanisms is unavoidable in the description of shock propagation in solids.

#### 4. Defect-generation during shock propagation

A variety of point, line and planar defects can be induced by shocks. Solid samples are usually examined after recovery following shock loading, and there is always the question of the relation of the residual defects to those present during the different stages of shock loading. On the one hand, shock heating may anneal out defects; on the other, the shock unloading process may lead to further plastic deformation. The former may be prevented to some extent by doing the experiment at liquid nitrogen temperatures, and then ejecting and storing the sample also at the same low  $T$ ; electrical resistivity annealing measurements in copper shock-loaded (70–380 kbars) in this manner yield typical vacancy concentrations  $\sim 10^{-4}$  (Mogilevskii 1970). The vacancy concentrations estimated from active resistance measurements in shock-loaded silver foils are perhaps ten times higher (Dick and Styrís 1975; Graham 1981). Similarly, the density of dislocations in metals increases with shock pressure-approximately as  $P^{1/2}$ , according to Murr and Kuhlmann-Wilsdorf (1978). This density is about  $10^{10}$ – $10^{11}$   $\text{cm}^{-2}$  in recovered samples shock-loaded up to 100–200 kbar, although once again the dislocation density could be much higher *during* shock propagation (Graham 1981; Svensson 1981).

---

In the original model of Smith (1958) for shock wave propagation, an interface of dislocations was postulated between the shocked and unshocked regions so that the deviatoric stresses arising from the shock could be relieved. The dislocation interface separates two lattices with different parameters. This interface of dislocations would, according to Smith, move with the shock front. If the dislocations move on a slip plane making an angle  $\phi$  with the shock-front plane, the velocity of the dislocations becomes  $U_s \csc \phi$  which produces the necessary plastic strain. Such supersonic dislocations are, however, unacceptable for several reasons (Meyers and Murr 1981). This had led Meyers to postulate a new model whose essential features are as follows: (a) Dislocations are homogeneously at (or close to) the shock front by the deviatoric stresses set up by the state of uniaxial strain; the generation of these dislocations relaxes the deviatoric stresses. Adjacent dislocation layers are made up of dislocations with Burgers vectors of opposite signs; (b) The dislocations move short distances at subsonic speeds; (c) New dislocation interfaces are generated as the shock wave propagates through the material.

This model qualitatively explains many experimental results. Meyers and Murr also believe that the rarefaction part of the wave (corresponding to shock unloading) plays only a minor role in dislocation generation.

The shock front has a width  $W$  extended over a few lattice spacings, i.e.,  $W \sim 10^{-6}$  cm. The strain rate  $\dot{\epsilon}$  can be written as (Gilman 1979)

$$\dot{\epsilon} \approx \frac{U_s}{2W} \frac{(\rho_1 - \rho_0)}{\rho_0}. \quad (4)$$

If the shock velocity is taken to be 1 cm/ $\mu$ sec and a density compression of 2 is achieved by the shock,  $\dot{\epsilon} \approx 10^{12}$  sec $^{-1}$ , which is enormous. What is the mechanism of the transport of momentum down the steep velocity gradient? It is through atoms and dislocations, and the dislocation velocity may be expected to be proportional to  $U_s$ . The drag pressure  $D$ , which acts in opposition to the driving pressure  $P$  and equals it under steady motion conditions, can be written as a product of an effective viscosity  $\eta$  and the strain rate  $\dot{\epsilon}$ . Gilman finds that the value of the viscosity that arises from the dislocations is of the order of 1 poise. As both  $\eta$  and  $\dot{\epsilon}$  are proportional to  $U_s$ ,  $D \sim U_s^2$ , and hence can be very large for strong shocks. I have discussed this aspect in detail to emphasize the complexity that a first-principle calculation of shock wave structure, shock width, etc., would entail. The heating of the material by the shock wave can, however, be calculated using (1)–(3) and condensed matter theory, because the contribution of the various defects produced by the shock wave propagation to the free energy of the material is small.

What about shock propagation in liquids? One has to re-interpret the mobile-dislocation mechanisms in this case, taking into account the short-range order in liquids on the one hand, and the narrow width of the shock front on the other. To the best of my knowledge, no work has been done along these lines.

## 5. Phase transformations and melting under shock

Most phase transitions observed under static pressures are also observed under shock pressures. In fact, many sluggish phase transitions are readily observed under shock conditions because the deviatoric shear stress provides a driving force to overcome any



activation barrier. The phase transformation is best examined in terms of  $U_s$  and  $U_p$ , rather than the conventional variables  $P$ ,  $V$ . The plot of  $U_s$  vs  $U_p$  is (surprisingly) linear for a given phase (up to pressures of several megabars), and shows a discontinuity and change of slope upon the occurrence of a phase transformation. There is one important point which must be kept in mind when discussing shock-induced phase transformations: unlike static pressures, shock pressures also induce heating, and the rise in temperature may influence or inhibit the transformation. For example, in the alpha (hcp) to omega (simple hexagonal) phase transformation in Ti, the amount of  $\omega$ -phase formed increases continually with pressure in the 'static' case; in contrast, under shock this amount first increases and then decreases as the shock pressure is increased. The reason for this behaviour is the change in temperature (Sikka *et al* 1982).

As one keeps on increasing the shock pressure, does the shock heating lead to melting in the compressed state, and, if so, what is the melting temperature? There is still considerable controversy with regard to this point. This is because the slope changes in the  $U_s - U_p$  curves are either small or else have an alternative interpretation in terms of certain electronic changes. The shock-Hugoniot measurements show, for example, the existence of a relatively less-compressible high-pressure phase (beyond 300 kbar) in all members of the rare-earth series. This 'stiffening' of the Hugoniot curves has been identified with melting by Carter *et al* (1975), but Gust and Royce (1973) attribute it to the onset of a repulsive interaction between the noble-gas atomic cores. McMahan *et al* (1981), on the other hand, have analysed this phenomenon in terms of the completion of  $s - d$  transfer in La. Again, in Pb, the various estimates of shock melting pressures range from 220 kbar to 1.24 Mbar (Duvall and Graham 1977).

The melting temperature under shock compression increases as indicated schematically in figure 3. We feel that the onset of shock melting may be established by a combination of shock temperature measurement and theoretical considerations (Godwal *et al* 1983b). The Hugoniot curves obtained by equation-of-state calculations in the solid and liquid states are quite distinct in the  $T - P$  plane, as shown schematically in figure 3. There is a mixed solid-liquid region in the middle. (We have done these calculations for Al and Pb by the pseudopotential method. At  $\rho_1/\rho_0 = 1.8$  in Al, for example, the temperatures predicted are 12500 K and 8100 K respectively using the corresponding solid and liquid state theories.) Thus, a measurement of shock temperatures over a range of shock pressures will presumably yield information of the type shown in figure 3, so that the onset of melting may be discerned clearly.

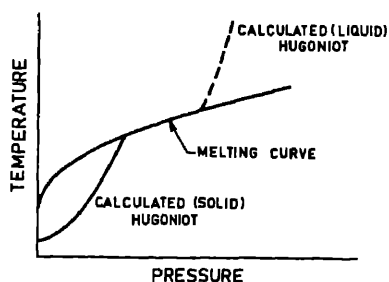


Figure 3. Schematic phase diagram for melting by shock heating.

## 6. Conclusions

There are many problems in the shock deformation of metals which are not yet fully understood. Most of the metallurgical studies have been on terminal samples shock-loaded to a few 100 kbar or less. Large concentrations of a variety of defects are found in these samples. These concentrations are presumably even greater during the various stages of shock propagation, since shock heating is supposed to anneal out many of the defects. The generation and motion of dislocations are essential in explaining shock front propagation which leaves behind a shocked region in a state of essentially hydrostatic strain (at least for strong shocks). Some computer simulation studies on atomistic models have also been attempted, but they do not account for all the experimental facts. Evidence for the melting of materials under very strong shocks is still in some doubt and may need a combination of theory and shock temperature measurement in order to be established conclusively. Much theoretical and experimental work still remains to be done in the field of shock deformation and related effects in materials.

## Acknowledgements

The author thanks Dr S K Sikka and Dr B K Godwal for many helpful discussions.

## References

- Carter W J, Fritz J, Marsh S P and McQueen R G 1975 *J. Phys. Chem. Solids* **36** 741  
 Chartagnac P F 1982 *J. Appl. Phys.* **53** 948  
 Chidambaram R and Ramanna R 1975 *Proc. Tech. Commun. PNE IV* (Vienna: International Atomic Energy Agency) p 421  
 Dick J J and Styris D L 1975 *J. Appl. Phys.* **46** 1602  
 Duvall G E and Graham R A 1977 *Rev. Mod. Phys.* **49** 523  
 Gilman J J 1979 *J. Appl. Phys.* **50** 4059  
 Godwal B K, Sikka S K and Chidambaram R 1983a *J. Phys. Rep.* (under publication)  
 Godwal B K, Sikka S K and Chidambaram R 1983b (unpublished)  
 Graham R A 1981 in *Shock waves and high-strain-rate phenomena in metals* (eds) M A Meyers and L E Murr (New York: Plenum Press) p 375  
 Gupta S C 1980 Ph.D Thesis, University of Bombay (unpublished)  
 Gust W H and Royce E B 1973 *Phys. Rev.* **B8** 3595  
 Jamet F 1980 in *High pressure science and technology* (eds) B Vodar and Ph Marteau (Oxford: Pergamon Press) Vol 2 p 974  
 Johnson Q and Mitchell A C 1980 in *High pressure science and technology* (eds) B Vodar and Ph Marteau (Oxford: Pergamon Press) Vol 1 p 977  
 McMahan A K, Skriver H L and Johansen B 1981 *Phys. Rev.* **B23** 5016  
 Meyers M A and Murr L E 1981 *Shock waves and high strain-rate phenomena in metals* (eds) M A Meyers and L E Murr (New York: Plenum Press) p 487  
 Mogilevskii M A 1970 *Combustion, explosion and shock waves* Vol 6 p 197  
 Murr L E and Kuhlmann-Wilsdorf D 1978 *Acta Met.* **26** 847  
 Sikka S K, Vohra Y K and Chidambaram R 1982 *Prog. Mater. Sci.* **27** 245  
 Smith C S 1958 *Trans. AIME* **212** 574  
 Svensson T 1981 *Shock waves and high strain rate phenomena in metals* (eds) M A Meyers and L E Murr (New York: Plenum Press) p 547  
 Tsai D H and Macdonald R A 1976 *High Temp. High Pressures* **8** 403

## Discussion

C K Majumdar: Entropy production is not taken into account satisfactorily in any essentially hydrodynamics-based formalism. Eckart's work (1945) may perhaps indicate how this aspect should be incorporated into the description of shocks.

K Srinivasa Raghavan: There is nothing unusual about nonhydrostatic strain due to hydrostatic stress, because one is dealing with nonhomogeneous structures.

R Chidambaram: The question here is whether, in Tsai's molecular dynamics calculation on a bcc crystal, unit cells can be strained nonhydrostatically under hydrostatic stress. This has been achieved here by 'buckling' of neighbouring cells—akin to twinning. This picture appears to be somewhat artificial to me, the problem arising from the neglect of mechanisms of plastic deformation.

K A Padmanabhan: Can the amount of explosive charge be estimated, when, say, a hollow cylinder of Al is cald on to a hollow inner cylinder of steel?

Chidambaram: The attenuation behind the shock front is related to the ratio of the mass of the metal to the mass of the explosive. In the problem of explosive welding one has to strike a balance between having too little explosive (the attenuation is then too high) and having too much explosive (the metal cylinder is then damaged).

A P Pathak: Can channeling by charged particles be used to extract information about the defects while experiments on mechanical properties (including shock wave propagation) are in progress?

Chidambaram: I think the penetration of charged particles into the specimen could pose problems, as the diameter of the metal plates under study  $\gtrsim 1$  cm

R Krishnan: In uniaxial tensile testing, an increased strain rate is equivalent to a reduction in test temperature. Is this so also for hydrostatic stress?

Chidambaram: For shock induced deformation, a higher strain rate implies a higher shock pressure which would lead to increased shock heating.

S Ramaseshan: How long does the rise in  $T$  due to the shock wave take to cool down?

Chidambaram: The fall from the high temperature in the compressed state to the residual temperature after shock unloading usually occurs in  $\mu\text{sec}$ . The cooling beyond that is by normal mechanisms.

Ramaseshan: How are boundary conditions specified in the molecular dynamics study of the shock front? How does this method differ from the finite element approach?

Chidambaram: As in usual solid state theory, cyclic boundary conditions were used by Tsai and Macdonald. The finite element method is a more general mathematical technique that is useful even in problems where there are no periodic lattices.

P Rodriguez: What is an ideal powder?

Chidambaram: In the context of diffraction, it is one in which there is no preferred orientation of the grains.

Rodriguez: For melting to occur, the dislocation density must be of the order

$10^{13}/\text{cm}^2$ , but experimentally it is  $10^{11}/\text{cm}^2$ . How is this discrepancy explained?

Chidambaram: The high temperatures prevailing probably cause annealing of some of the dislocations, reducing their density.

Rodriguez: The high strain rates used in shock experiments are also used in metallurgical techniques like explosive forming and welding. The physical basis of these methods needs to be understood.

Rodriguez: In the flyer plate method used for welding and forming the interface is wavy. Could you comment on this?

Chidambaram: The uniformity with which one can produce a plane wave or shock wave by any of these methods is about 100 nsec. Within this time a non-uniformity of the order of 0.1–1 mm sets in. This has to be carried through.

D Kumar: In the energy diagram, a part of the triangle is the recoverable elastic energy and a part is the dissipated heat energy. Does the rest go into the formation of dislocations?

Chidambaram: The energy required to create dislocations is small and is generally ignored in the book-keeping.

S N Bandopadhyay: What is the evidence that the *strain* is hydrostatic?

Chidambaram: Flash x-ray diffraction experiments on cubic crystals indicate that the crystal behind the shock front reaches a state of hydrostatic strain within 20 nsec.

—

.

—

## Computer simulation of tensile testing\*

V SRIDHAR

Materials Science Laboratory, Reactor Research Centre, Kalpakkam 603 102, India

**Abstract.** A brief overview of the molecular dynamics method, with emphasis on the work of Parrinello and Rahman, is presented. Molecular dynamics is a method for studying classical statistical mechanics of well-defined systems through a numerical solution of Newton's equations. A set of  $N$  particles with coordinates  $r_i$  ( $i = 1, \dots, N$ ) and confined in a cell are allowed to interact through a potential. The bulk is usually simulated by periodically repeating the cell in space. Newton's equations are then solved numerically and the statistical averages of dynamical properties are calculated as temporal averages over the trajectory of the phase space. This method has already been used to simulate a liquid. Now, based on a Lagrangian formulation, it is possible to study systems under the most general conditions of externally applied stress. Unlike the earlier calculations, in this procedure, shape and size are governed by equations of motion obtained from the Lagrangian. Thus it allows us to study structural transformations which may be brought about by an interplay of external and internal stresses. By applying this technique to a single crystal of Ni, Parrinello and Rahman observe that the stress-strain relations obtained confirm with reported results. Under compressive loading it is found that Ni shows a bifurcation in its stress-strain relation and the system changes from cubic to hexagonal close packing. Such a transformation could perhaps be observed under extreme conditions of shock. Finally the scope of computer simulation is highlighted and the limitations of employing such a method are pointed out.

---

\*only summary of the talk



## Instabilities in yielding

G VENKATARAMAN

Reactor Research Centre, Kalpakkam 603 102, India

**Abstract.** This paper addresses itself to instabilities observed during tensile testing, and complements the papers of Rodriguez and Ananthakrishna presented at this Meeting. The work of Caglioti *et al* on the elastic to plastic transformation is first reviewed. The work of Kubin *et al* on the serrated (repeated) yielding observed at liquid helium temperatures is then discussed in brief. Finally, our own work relying on electronic simulation is described. We conclude with some brief remarks on a few important questions that merit attention in the future.

**Keywords.** Tensile testing; yielding; instabilities; electronic simulation.

### 1. Introduction

Yielding observed during a tensile test is being discussed by several speakers at this Meeting. While metallurgists are by and large interested in the deformation mechanisms, for physicists the nonlinearities and the instabilities arising thereof are perhaps attractive avenues for investigation. Dr Rodriguez will present the metallurgist's point of view while Dr Ananthakrishna will discuss how he views the phenomena as a physicist. My talk will deal with some work on the subject that is pertinent to the present Meeting but not touched upon by them.

### 2. Elastic to plastic transition

The work done by Prof. Caglioti and coworkers (Boffi *et al* 1980) who address themselves to the instability associated with the elastic to plastic transition is first reviewed. They adopt a hydrodynamic approach, and their basic idea is as follows. One starts with the Helmholtz free energy  $F$  expressed as a function of the temperature  $T$  and strain  $\varepsilon$ , since these are quantities which can be measured in real time during an experiment.  $F(T, \varepsilon)$  is expanded in a series in  $\varepsilon$  and  $\theta = (T - T_0)/T_0$ ,  $F(T_0, 0)$  being the free energy of the undeformed solid at temperature  $T_0$ , assuming that a uniaxial tension is applied. By differentiating  $F(T, \varepsilon)$  appropriately with respect to the state variables, expressions are deduced for the entropy  $S$  and the equilibrium stress  $\sigma_e$ . These are substituted in the space- and time-dependent partial differential equations representing entropy and momentum balance. This is the starting-point for the subsequent stability analysis, the procedure up to this point being identical to what is normally done in hydrodynamics.

We are interested in the question of stability as the material deforms through the elastic region. Let us suppose that the applied (constant) strain rate is  $\dot{\varepsilon}_a$ . To investigate the stability of a particular state  $\varepsilon_a (= \dot{\varepsilon}_a t$ ,  $t$  being the elapsed time) and temperature  $\theta$ ,



# MODE STABILITY

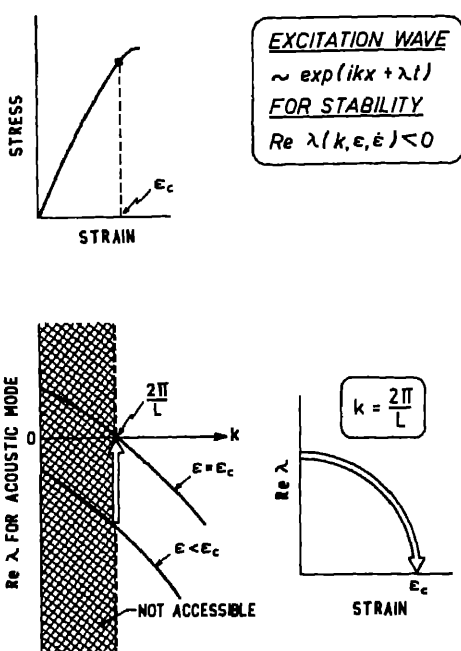


Figure 1. Instability of acoustic mode as  $\varepsilon \rightarrow \varepsilon_c$ . Owing to finite size of the specimen, the shaded region is not accessible.

one imposes small fluctuations  $\delta\varepsilon$  and  $\delta\theta$  around the reference state. Linearization yields a set of three coupled first-order equations for the quantities  $\delta\theta$ ,  $(\delta\dot{\varepsilon}/\varepsilon_a)$  and  $\delta\varepsilon$ , on which the standard normal-mode analysis may be performed. (In fluid dynamics, one would obtain the Rayleigh and Brillouin modes in this manner.) For a given mode to be stable, it is necessary that  $\text{Re } \lambda(k) < 0$ , where  $\lambda$  is the corresponding eigenfrequency and  $k$  is the wavevector. It turns out that all the modes are stable as long as  $\varepsilon_a$  is smaller than a critical strain  $\varepsilon_c$ . At the critical strain, the acoustic mode with the longest wavelength (i.e.,  $k \approx 2\pi/L$  where  $L$  is the length of the sample) becomes unstable (figure 1). There is an obvious analogy with phase transitions; Boffi *et al* (1980) have indeed drawn a parallel with the nonequilibrium transition in the laser. As yet there is only partial experimental confirmation of these ideas, but I understand (Bottani, private communication) that efforts are in progress to monitor the transition more completely by measuring the associated temperature fluctuations.

## 3. Repeated yielding

Let us consider next the instability aspects of serrated yielding. Dr Rodriguez in his presentation offers a comprehensive survey of the various mechanisms responsible for repeated yield drop. Dr Ananthakrishna considers one of these models, namely, that due to Cottrell, and analyzes how instabilities can arise. I shall complete the picture by discussing the work of Kubin *et al* and some of our own work.

### 3.1 Low-temperature yielding

Kubin and coworkers (Estrin and Kubin 1981; Kubin *et al* 1982, 1983) are concerned with repeated yield drops observed at liquid helium temperatures. These arise due to thermomechanical instabilities for which a model is proposed. The stability analysis is rather similar to that carried out by Boffi *et al* (1980) (the applied stress and the temperature are now chosen as the state variables characterizing the material undergoing deformation). These two variables are coupled through two nonlinear differential equations, the mechanical equation and the equation describing heat removal, in which the experimental conditions are suitably introduced. Linearization, stability analysis, etc., are then performed as usual, and contact is made with elementary bifurcation theory (Haken 1977).

The parameters that enter into the thermomechanical model of Kubin and coworkers (Estrin and Kubin 1981; Kubin *et al* 1982, 1983) are: the specimen dimensions, the applied strain rate, the combined elastic modulus of the specimen and the machine, the specific heat of the specimen and the coefficient of heat transfer. These parameters are combined into three dimensionless quantities  $\dot{\Sigma}_a$  (the reduced elastic slope of the straining curve),  $\alpha$  (the reduced activation volume) and  $\nu$  (representing, apart from a factor, the ratio of the elastic and thermal energies). These are the control parameters. Figure 2 shows the  $(\nu/\alpha, \dot{\Sigma}_a\alpha)$  plane in control parameter space. The different regions represent qualitatively different kinds of mechanical behaviour, the nature of which is amplified in figure 3. The types of trajectories in the phase space  $(\sigma, \theta)$  associated with the various regions in figure 2 are sketched in figure 3a, and the corresponding yield curves are shown in figure 3b. While one has an asymptotic steady state in region II, one obtains serrations in region III. The crossing of the II-III boundary corresponds to a hard-mode instability. (A similar instability is discussed by Ananthakrishna with reference to his model.) To sum up, the work of Kubin *et al* demonstrates that it is possible to predict whether plastic deformation at low (cryogenic) temperatures will be smooth or jerky, depending on the values of a specified set of mechanical, geometric and thermal parameters, by using bifurcation theory and stability analysis.

### 3.2 Electronic simulation

I now turn to the work on serrated yielding which Neelakantan and myself (1983) have been engaged in recently. Our work was triggered by a fascinating paper by Franck

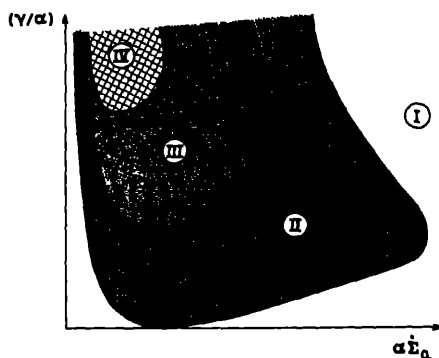


Figure 2. Regions of different types of mechanical behaviour in the parameter plane  $(\dot{\Sigma}_a\alpha, \nu/\alpha)$  (Kubin *et al* 1983).

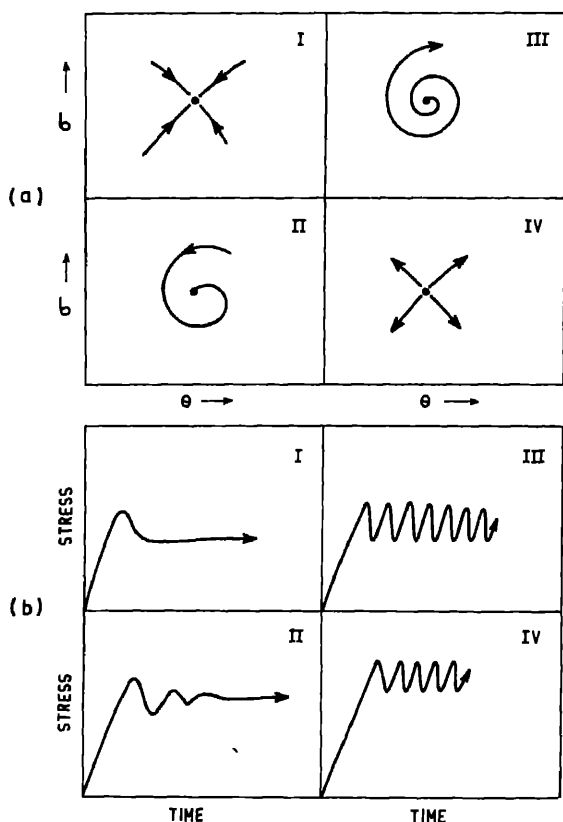


Figure 3. a. Phase space plots corresponding to the different regions shown in figure 2. b. Stress vs time curves corresponding to the different regions of figure 2 (Kubin *et al* 1983).

(1974) which gives an overview of feedback oscillations occurring in widely different chemical and biological systems. According to Franck, these diverse systems exhibit very similar behaviour because they share an underlying "negative resistance" feature. In serrated yielding, it is well known that at least for one class of models, *viz.*, the Cottrell-Bilby model (1949) (see also the paper by Rodriguez at this Meeting), there is such a negative resistance feature. We (Neelakantan and Venkataraman 1983) therefore explored how some of the observed features of repeated yielding could be understood along the lines indicated by Franck. It was most convenient to map the problem onto an equivalent electronic problem, and essentially carry out an analog simulation.

Skiping the details, the essential idea underlying our work may be understood by referring to figure 4. Shown here is a typical negative resistance characteristic, the detailed nature of which is dependent (in the physical problem under consideration) on parameters such as the dislocation density, temperature, etc. The applied strain rate prescribes the *load line*; the behaviour of the specimen during the test depends on where the load line cuts the characteristic curve. If the intersection is in the negative resistance region, then there is instability and oscillations (in stress) ensue.

Now, in contrast to the situation obtained usually in an electronic device, the characteristic curve itself evolves during the test for a specimen undergoing plastic

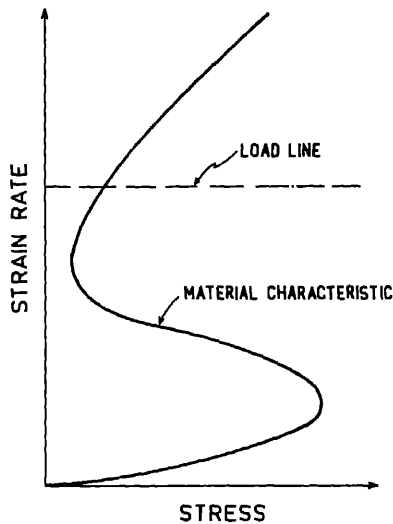


Figure 4. Schematic plot of the strain rate vs stress curve for a material exhibiting serrated yielding. (For examples of such curves in the Fe-C system, see Neelakantan and Venkataraman 1983). The negative resistance feature arises due to dislocations breaking away from their atmospheres.

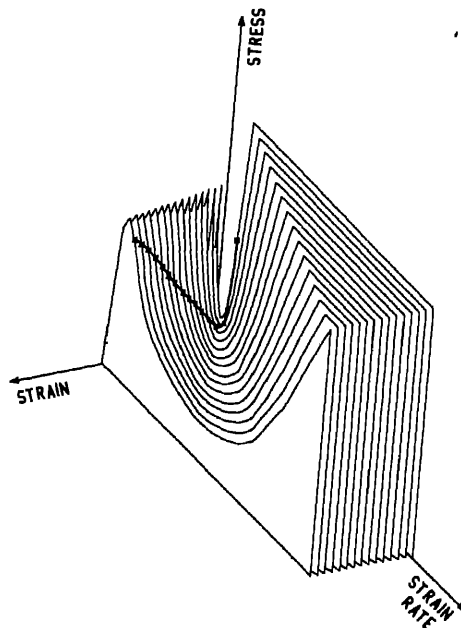


Figure 5. Perspective plot of a family of characteristic curves, simulating the evolution during an actual test. The valley associated with the negative resistance feature is seen to widen as the test progresses. The trajectory obtained by the load line method is also partially indicated. Serrations occur during the test only when the load line intercepts the characteristic in a region of negative slope.

yields. Thus, at a fixed temperature, and for the *same* material, the intersection of the load line and the characteristic may occur in a region of positive slope at one instant and in a region of negative slope at the next. The general form of the characteristic also suggests why serrations occur only in a certain region of the test curve. Figure 5 shows a schematic plot of a family of evolving characteristic curves for a material at a particular temperature. The trajectory resulting from the load line is also indicated, and one can see that instability can occur in certain ranges of the strain and not in others.

Our approach demonstrates that numerous aspects of tensile test curves observed in practice are readily reproduced and studied under convenient, controlled conditions in a suitably constructed analog device. One can begin to understand some of the observed trends in depth. For example, it is known that at a given temperature, serrations are absent both at very high and low strain rates; likewise, at a given strain rate, serrations appear only in a certain temperature band. There is therefore a well-defined region in the  $\dot{\epsilon} - T$  plane within which serrations occur. Our study shows that such a bounded region is indeed to be expected.

#### 4. Conclusions

One common feature of all the models cited is that they tacitly assume the medium to respond homogeneously during repeated yielding. There are, however, reasons to believe that the deformation is in fact spatially inhomogeneous. This aspect has not received the attention it deserves in theoretical studies of the phenomenon, and one hopes that in the years to come this will be set right.

Another relatively neglected aspect is the important role played by noise: a considerable amount of irregularity exists in the observed serrations. Ananthakrishna discusses the effects of fluctuations to some extent in his paper. In our work, too, some thought has been given to the matter. Our preliminary finding is that when noise is included, the simulated tensile test curves begin to resemble real-life curves such as, *e.g.*, those found in Hall (1970). This work is still in progress. One's experience with the study of fluctuations in other areas of physics suggests that here, too, such an analysis would be a fruitful avenue of investigation.

#### References

- Boffi S, Bottani C E, Caglioti G and Ossi P M 1980 *Z. Phys.* **B39** 135
- Cottrell A H and Bilby B A 1949 *Proc. Phys. Soc.* **A62** 49
- Estrin Y and Kubin L P 1981 in *Deformation of polycrystals Proc. 2nd Risø Int. Symp. Metal. Mat. Sci.*, (eds) N Hansen, A Horserrell, T Leffers and H Lilholt p. 179
- Franck U C 1974 in *Physical chemistry of oscillatory phenomena Symp. Faraday Soc.* No. 9, p. 137
- Haken H 1977 *Synergetics* (Berlin: Springer)
- Hall E O 1970 *Yield point phenomena in metals and alloys* (New York: Plenum)
- Kubin L P, Spiesser Ph and Estrin Y 1982 *Acta Metall.* **30** 385
- Kubin L P, Estrin Y and Spiesser Ph 1983 preprint, Low temperature plastic deformation of metals and bifurcation theory (to appear in *Res. Mechanica*)
- Neelakantan K and Venkataraman G 1983 *Acta Metall.* **31** 77

#### Discussion

G Srinivasan: The introduction of noise seems to produce bands. Is it that you are seeing some kind of a beat phenomenon?

G Venkataraman: We have not explored all the possibilities to say something at this stage.

R Ramaswamy: The kind of bunching phenomenon that occurs does have a practical

analogue. This is the phenomenon of intermittency—shortly before the onset of a truly turbulent phase, long range periodicity appears in bursts.

K R Rao: Referring to Caglioti *et al*'s work, in the yield instability region, the soft mode may go to zero giving rise to an incommensurate phase reciprocal lattice point. Has this been experimentally observed?

Venkataraman: It has not been observed. This is only a model.

\_\_\_\_\_

## Serrated plastic flow

P RODRIGUEZ

Metallurgy Programme, Reactor Research Centre, Kalpakkam 603 102, India

**Abstract.** This paper attempts an assessment of the current understanding of the phenomenon of "serrated plastic flow", which manifests itself as serrations, load drops, jerkiness or other discontinuities in the stress-strain curves obtained in constant extension rate tensile tests, and as sudden bursts of strain in constant loading rate tests and in constant load (stress) creep tests (the so called staircase creep). Though one can identify at least seven physical processes that can cause serrations, the discussion here is restricted mainly to serrated yielding in tension tests originating from dynamic strain ageing (DSA). The characteristics of the five types of serrations that have been identified so far and the experimental conditions under which they occur are discussed. The various models of serrated flow that have been put forward are reviewed critically. Some recent results on 316 stainless steel are presented to illustrate the effects of grain size, temperature and strain rate on serrated flow. Manifestations of DSA other than serrations such as a negative strain rate sensitivity, positive temperature dependence for flow stress and work hardening, and the ductility minimum are also discussed. Finally the various issues to be resolved are enumerated.

**Keywords.** Serrated flow; dynamic strain ageing; continual mechanical twinning; flow stress; work hardening peaks; ductility minimum.

### 1. Introduction

The organisers of this discussion meeting in their invitation requested that I should present here the metallurgist's viewpoint of 'serrated plastic flow'. At the outset let me state that whatever I say in the following should be considered as my own understanding of the phenomenon. There will be many materials scientists and engineers (including those with both physics and metallurgy backgrounds) who may not agree with all the views propounded here; there must also be an equally large number of physicists and metallurgists who may find common ground with the interpretations offered. It is interesting to note that in a recent international conference on deformation, two different treatments of the phenomenon, both by metallurgists have been given. One is based on a strain ageing mechanism involving the diffusion of solute atoms to temporarily arrested dislocations (McCormick 1983) and the other interprets it as an example of catastrophe theory in physical metallurgy (Strudel 1983).

The objective of the present paper is an assessment of the current understanding of the phenomenon of serrated plastic flow. We start with a brief description of the methodology of the tensile test. The physical processes that can cause serrated flow are then identified. Subsequent discussions are restricted to serrations due to dynamic strain ageing (DSA) or the Portevin-Le Chatelier (PL) effect (Portevin and Le Chatelier 1923) arising from interactions between diffusing solute atoms and mobile dislocations. The characteristics of five types of serrations observed under conditions of DSA are then discussed. The various quantitative models for serrated flow that have been put forward are then critically reviewed. Some recent results on 316 stainless steel are presented to



illustrate the effects of grain size, temperature and strain rate on the DSA behaviour. This is followed by a discussion of the various manifestations of DSA in tensile test results. Finally, the various issues to be resolved are considered and catalogued.

## 2. Phenomenology

In a tension test, (the specimen suitably gripped between two crossheads, one moving and the other fixed) is deformed at a constant nominal strain rate determined by the velocity of the moving crosshead. At any instant of time, the total strain  $\varepsilon$ , the plastic strain  $\varepsilon_p$  in the specimen, and the elastic strain  $\varepsilon_e$  of the specimen-machine system are related by

$$\varepsilon = \varepsilon_p + \varepsilon_e, \quad (1)$$

$$\dot{\varepsilon} = \dot{\varepsilon}_p + \dot{\varepsilon}_e. \quad (2)$$

Equation (2) can be rewritten as

$$\dot{\varepsilon} = \dot{\varepsilon}_p + \frac{1}{E_s} \dot{\sigma}, \quad (3)$$

where  $\sigma$  is the stress and  $E_s$  the elastic modulus of the specimen-machine system. The condition for serrations or load drops is that the plastic strain rate  $\dot{\varepsilon}_p$  exceeds the imposed strain rate  $\dot{\varepsilon}$ , i.e. whenever there is a sudden increase in  $\dot{\varepsilon}_p$ , a load drop occurs.

The phenomenon can also occur in creep tests in which strain in a specimen under a constant stress is measured as a function of time. Sudden bursts of plastic strain occur periodically, with the result that the creep curve has the shape of a staircase (hence the name 'staircase creep'). This manifestation of DSA in creep tests is discussed in another paper (Ananthakrishna 1983) presented at this Meeting.

## 3. Physical processes that can cause serrated flow

A survey of the literature shows that we can identify at least seven physical processes that can lead to serrations in the flow curve:

- (i) The plastic strain rate under dislocation glide is given by

$$\dot{\varepsilon}_p = \rho_m b \bar{v}, \quad (4)$$

where  $\rho_m$  is the mobile dislocation density,  $\bar{v}$  the average velocity of dislocations and  $b$  the Burgers vector. Serrations will therefore occur whenever there is an instantaneous increase in  $\rho_m$  or in  $\bar{v}$  or in both.

- (ii) Interaction of moving dislocations with DSA can lead to sudden increases in  $\rho_m$  and/or  $\bar{v}$  and we shall be mainly examining this particular phenomenon.

- (iii) In alloys undergoing order-disorder transformations, gradients or modulations in order encountered by moving dislocations can cause serrated flow (Mannan and Rodriguez 1972; Samuel and Rodriguez 1975, 1980).

- (iv) Another phenomenon that can cause serrations is continual mechanical twinning as has been reported for an Fe-25 at% Be alloy (Bolling and Richman 1965). Twinning is characterised by a positive temperature dependence and a negative strain rate sensitivity for the flow stress which are also obtained under conditions of DSA.

(v) A sudden increase in the specimen temperature due to adiabatic heating is another possibility (Ramachandran 1983; Ramachandran *et al* 1970; Kubin *et al* 1982). This has been found to occur in tests at cryogenic temperatures. Dissipation of the heat of deformation becomes difficult since the specimen surface is covered by a layer of gas molecules of the cryogenic liquid. The resultant increase in specimen temperature satisfies the condition for a load drop since a higher plastic strain rate can now occur at the applied stress level.

(vi) Phase transformations induced by stress and strain can also cause serrated flow. This aspect is covered in another paper presented at this Meeting (Seetharaman 1983).

(vii) Weertman (1967) has pointed out that yielding across fracture surfaces in brittle materials when tested under both hydrostatic pressure and triaxial non-hydrostatic stresses can cause serrations.

#### 4. Types of serrations

Five types of serrations due to DSA termed A, B, C, D and E have so far been identified (figure 1). Types A, B and C are well-known and their characteristics are also well documented (Russel 1963; Macherauch and Munz 1966; Solar-Gomez and McG-Tegart 1969; Brindley and Worthington 1970; Cuddy and Leslie 1972) whereas serrations of types D and E have been referred to only relatively recently (Pink and Grinberg 1981; Wijler *et al* 1972). The characteristics of the different types of serrations and the experimental conditions that produce them are as follows.

(i) Type A serrations are periodic serrations from repeated deformation bands initiating at the same end of the specimen and propagating in the same direction along the gauge length. These are considered as locking serrations, characterised by an abrupt rise followed by a drop to below the general level of the stress-strain curve. They occur in the low temperature (high strain rate) part of the DSA regime.

(ii) Type B serrations are oscillations about the general level of the stress-strain curve that occur in quick succession due to discontinuous band propagation arising from the DSA of the moving dislocations within the band. (This contrasts with the smooth propagation of the band that occurs after initiation with a type A load drop). Type B

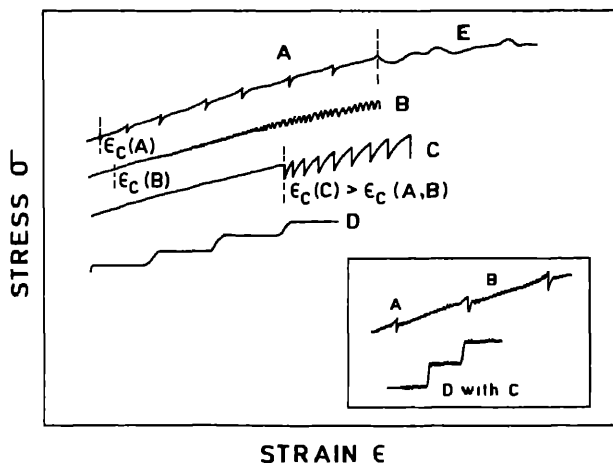


Figure 1. Types of serrations.

serrations often develop from those of type A with increasing strain (figure 1 inset) or occur at the onset of serrated yielding at high temperatures and low strain rates.

(iii) Type C serrations are yield drops that occur below the general level of the flow curve and are therefore considered to be due to dislocation unlocking. They occur at higher temperatures and lower strain rates than in the case of types A and B serrations.

(iv) Type D serrations are plateaus in the  $\sigma$ - $\epsilon$  curve due to band propagation similar to Luders band with no work hardening or strain gradient ahead of the moving band front. Like type A serrations, they can occur alone or with type B serrations during the band propagation (figure 1 inset). In Au-Cu 14 wt % alloy, Wijler *et al* (1972) produced type D serrations by homogeneous prestraining at high temperatures.

(v) Type A serrations change over to type E serrations at high strains. The latter are similar to type A serrations, but with little or no work hardening during band propagation.

## 5. Models for serrated flow from DSA

Any theory or model for serrated flow should account for the different types of serrations that appear in different alloys and for the influence of temperature, strain and strain rate on these various types. For the onset of serrations in substitutional alloys, a critical strain  $\epsilon_c$  is required. The  $\epsilon_c$  value is dependent on both  $\dot{\epsilon}$  and the temperature  $T$  (figure 2). At high strain rates and low temperatures where the first serrations are of type A or B,  $\epsilon_c$  increases with increasing strain rate and decreasing temperature. At high temperatures and low strain rates, where serrations of type C are observed,  $\epsilon_c$  increases with increasing temperature and decreasing strain rate. While current theoretical models are unable to account for this latter behaviour, the variation of  $\epsilon_c$  with  $T$  and  $\dot{\epsilon}$  in the low temperature (high strain rate) regime has been rationalized by a number of theoretical models based on the interaction of diffusing solute atoms and mobile dislocations.

### 5.1 Interpretations of $\epsilon_c$

The oldest quantitative model for serrated yielding is due to Cottrell (1953) in which the mobile solutes are assumed to interact with quasi-viscously moving dislocations; serrations are attributed to repeated locking and unlocking of dislocations in solute atmospheres, which occurs when  $\bar{v}$  equals the drift velocity of the solutes in the stress field of the dislocations. In subsequent modifications of this model that integrate it with the theory of thermally activated deformation processes, it was recognised (Sleeswyk

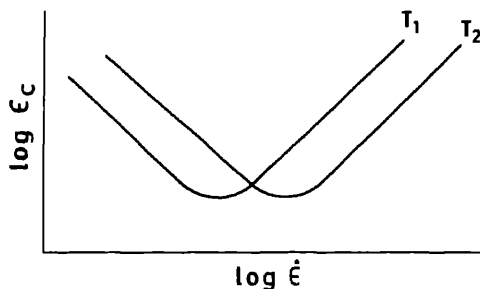


Figure 2. Effect of strain rate and temperature on critical strain;  $T_2 > T_1$ .

1958; McCormick 1972) that the "ageing" of the dislocations would take place during the waiting time of the dislocations at discrete obstacles rather than during their actual motion. When the diffusion coefficient is high enough to saturate the dislocation with a solute atmosphere during the waiting time, serrated yielding will start. In the model of van den Beukel (1975) though the same picture of solute-dislocation interaction was adopted,  $\varepsilon_c$  was chosen (following the ideas of Sleeswyk 1958; Penning 1972) to be the strain at which the strain rate sensitivity  $\gamma = \partial \sigma / \partial \ln \dot{\varepsilon}$  became negative. In all the three approaches, the final result is that at  $\varepsilon_c$

$$\rho_m^{(c)} C_v^{(c)} = K_1 \dot{\varepsilon} \exp(E_m/kT), \quad (5)$$

where  $C_v$  is the vacancy concentration  $E_m$  is the vacancy migration energy and  $T$  the absolute temperature. The three models yield widely different values for the constant  $K_1$  (the value in the original Cottrell model does not account for the experimental values of  $\varepsilon_c$ ). The vacancy concentration is enhanced due to the strain (Van Bueren 1955) according to

$$C_v = A \varepsilon^m. \quad (6)$$

Similarly, the strain dependence of  $\rho_m$  can be expressed as

$$\rho_m = B \varepsilon^\beta. \quad (7)$$

From (5), (6) and (7) we get

$$\varepsilon_c^{m+\beta} = K_2 \dot{\varepsilon} \exp(E_m/kT). \quad (8)$$

DSA due to interstitial solutes (8) reduces to

$$\varepsilon_c^\beta = K'_2 \dot{\varepsilon} \exp(E_m/kT). \quad (9)$$

Experimental results in the low temperature-high strain rate region have given reasonable values for  $m$ ,  $\beta$  and  $E_m$ . Typical  $(m + \beta)$  values are between 2 and 3 for substitutional alloys; for interstitial alloys (Van den Beukel 1980),  $\beta$  lies between 0.5 and 1.

It has generally been observed that the critical strain  $\varepsilon_c$  increases with increasing grain size (Brindley and Worthington 1970; Charnock 1968, 1969; Mannan 1981; Mannan *et al* 1983). Relating this increase to the grain size dependence of  $\rho_m$ , Charnock (1968, 1969) has shown that (8) can be modified to include the grain size dependence of  $\varepsilon_c$  according to

$$\varepsilon_c = K_3 d^p \dot{\varepsilon}^q \exp[E_m/kT(m + \beta)] \quad (10)$$

where  $p = n''/(m + \beta)$ ,  $q = 1/(m + \beta)$  and the parameter  $n''$  arises from the  $\rho_m - d$  relationship of Conrad and Christ (1963):  $\rho_m = N \varepsilon^\beta / d^{n''}$ .

## 5.2 Some results on 316 stainless steel

The flow curves obtained in the temperature range 523–923 K at a strain rate of  $3 \times 10^{-4} \text{ sec}^{-1}$  for 316 stainless steel of two different grain sizes (0.04 and 0.125 mm) are shown in figures 3 and 4 (Mannan 1981; Mannan *et al* 1982, 1983). (The serration types are labelled as in §4). The observed effects of the grain size on DSA are the following: (a) The DSA temperature region gets shifted to higher temperatures with increasing grain size; (b) For all grain sizes (8) is valid with  $(m + \beta) = 2.3$ ,  $\beta$  was estimated to be  $\approx 0.9$ , in

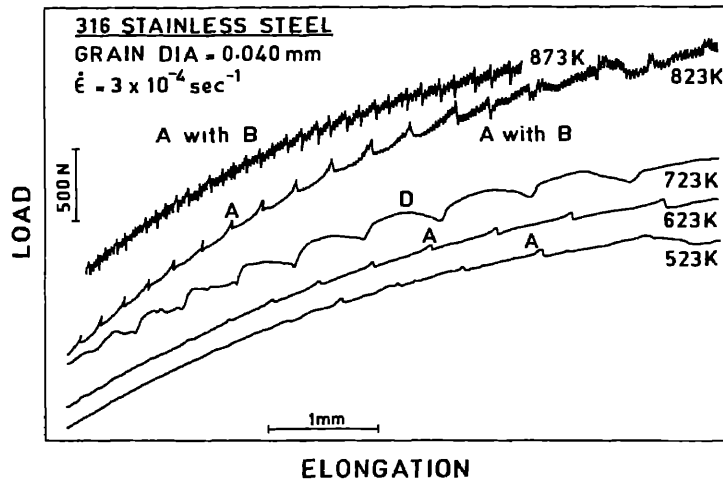


Figure 3. Serrated plastic flow in 316 stainless steel with grain size  $d = 0.040$  mm.

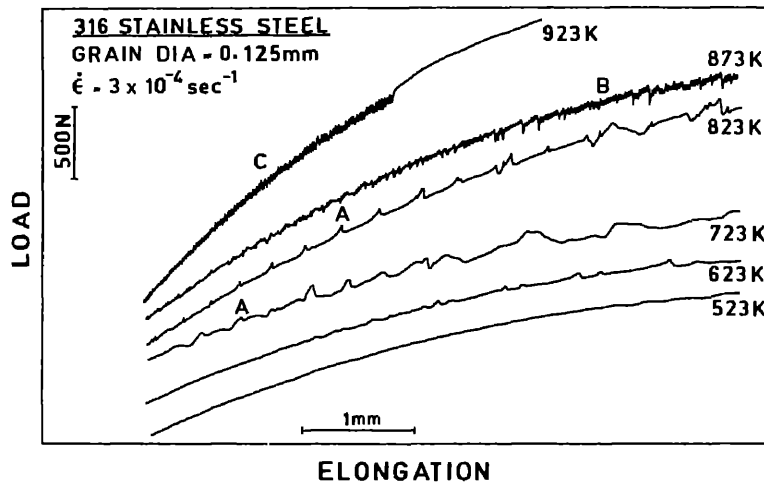


Figure 4. Serrated plastic flow in 316 stainless steel with grain size  $d = 0.125$  mm.

good agreement with the prediction of  $\beta = 1$  for a linear increase in dislocation density with strain; (c) The relationship between  $\epsilon_s$  and  $d$  follows (10) with  $p = 0.6$ ; (d) An apparent activation energy for DSA of 255 kJ/mol is obtained for all grain sizes from the variation of  $\epsilon_s$  with  $T$ , (8); (e) A fit to the Hall-Petch equation for the variation of the flow stress  $\sigma_s$  with grain size  $d$ , namely,  $\sigma_s = \sigma_{0s} + K_s d^{-1/2}$  where  $K_s$  and  $\sigma_{0s}$  are constants (called the Hall-Petch slope and intercept respectively), yields a monotonic decrease of  $\sigma_{0s}$  with temperature; whereas  $K_s$  though it generally decreases with temperature, shows a peak in the temperature region 523–723 K. This indicates that grain boundary regions are preferred sites for dynamic strain ageing (Armstrong 1968); (f) A peak in the variation of work hardening with temperature is also obtained but towards the upper

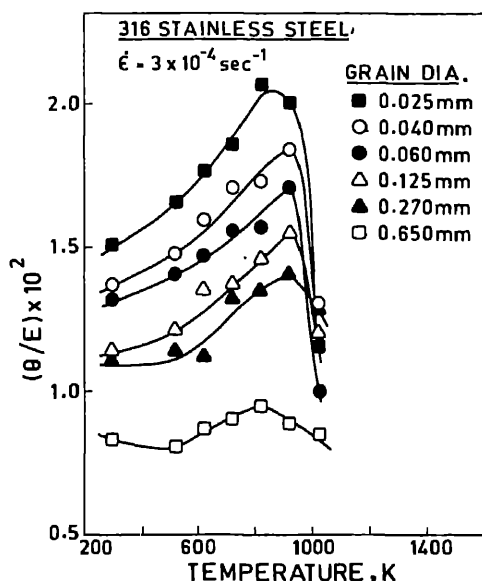


Figure 5. Variation in work hardening with temperature for 316 stainless steel with different grain sizes.  $E$  is the Young's modulus.  $\theta = \Delta\sigma/\Delta\epsilon$ ,  $\Delta\sigma$  is the flow stress increment over the strain interval  $\Delta\epsilon$  from  $\epsilon = 0.005$  to  $\epsilon = 0.05$ .

end of the DSA temperature range (figure 5). Consistent with the fact that this temperature range represents conditions for strong pinning and accordingly the most rapid and strongest dislocation immobilisation, leading to an increased rate of dislocation accumulation (Reed-Hill 1974), the DSA peak for work hardening also becomes more pronounced with decreasing grain size.

### 5.3 Other interpretations of serrated flow

Equation (4) allows serrations to occur for sudden increases in  $\rho_m$  or in  $\bar{v}$  or in both of them. The models discussed in §5.1 assume that the average velocity is unchanged, and that serrations occur due to changes in  $\rho_m$  owing to the locking and unlocking of dislocations during deformation. It has also been pointed out that the solute atmospheres formed could be dragged along with the moving dislocations, and that such atmospheres would exert a drag stress on the dislocation which varies with dislocation velocity as schematically illustrated in figure 6(a) (Hirth and Lothe 1968; Schmidt and Miller 1982). With this drag stress contribution included, the normal stress-velocity variation for dislocations shown in figure 6(b) assumes the shape shown in figure 6(c). Nabarro (1967) has suggested that serrations will occur in the strain rate (dislocation velocity) region between the points B and D in this figure since the dislocation velocity is a multivalued function of stress in this region; for a given value of the applied stress it is possible for the velocity to increase suddenly to a higher value. The region between C and D where the moving dislocation requires a lower stress for a higher velocity (negative strain rate sensitivity) is more commonly identified with the dynamic instability of plasticity leading to the PL effect (Sleeswyk 1958; Sleeswyk and Verel 1972; Wilcox and Rosenfield 1966; Yoshinaga and Morozumi 1971; Penning 1972; Malygin 1973). Suggestions have also been made that serrated yielding could be considered as a manifestation of 'chaotic' behaviour (Neelakantan and Venkataraman 1982) or as an example of a 'catastrophe' in plastic deformation (Strudel 1983) arising from the negative-resistance feature between C and D.

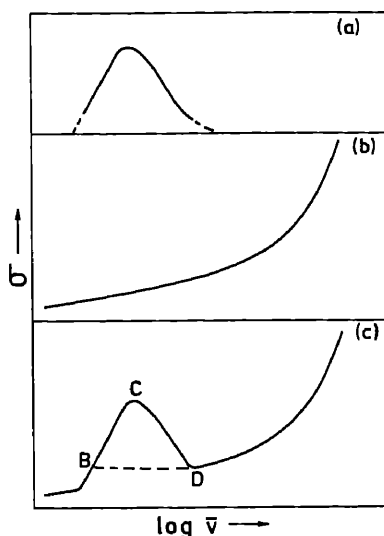


Figure 6. (a) The solute drag stress on a dislocation as a function of dislocation velocity. (b) Normal stress-velocity relation for dislocation in the absence of the drag stress. (c) Actual stress-velocity variation due to the presence of a drag stress at intermediate velocities.

That negative strain rate sensitivity is a crucial factor for the PL effect is now recognised in all the models. The treatment of McCormick (1983), for example, points out that the critical strain for the onset of serrated flow can be rationalised by matching the critical velocity (for negative resistance) with the solute diffusion coefficient. In the models of Van den Beukel (1975, 1980) and of Mulford and Kocks (1979) it is held that any solute mobility makes a negative contribution to the total strain rate sensitivity and that this contribution increases with strain; when the total strain rate sensitivity becomes negative plastic flow becomes unstable. In arriving at the strain dependence of the strain rate sensitivity, Van den Beukel retains the notions of a strain-dependent solute diffusion coefficient and strain-dependent mobile dislocation density from the older models. Mulford and Kocks (1979), on the other hand, describe the strain rate sensitivity in terms of the flow stress  $\sigma$  which is the sum of two components—the friction stress  $\sigma_f$  and the dislocation flow stress  $\sigma_d$ ; solute mobility affects  $\sigma_d$ , the strain-hardening component of the flow stress. More recently, Van den Beukel and Kocks (1982) have arrived at a unified approach which enables the negative strain rate sensitivity to arise as a consequence of the influence of solute mobility on both the friction stress (by decreasing the obstacle spacing along the dislocation) and forest hardening (by increasing the strength of dislocation junctions).

In a paper that has not received the attention that it deserves, Weertman (1967) has suggested that the PL effect occurs as a result of an instability of the dislocations in going back and forth between a slow moving state and a fast moving state due to dynamic frictional stress drops. The effect occurs because of the inherent instability of the position that separates the fast slip region from the slow slip region in the slipped zone. The similarity between earthquakes and the behaviour of groups of dislocations in a slip band when the frictional force is reduced for any reason has also been pointed out: "Earthquakes are merely, the PL effect exhibited in a sample whose dimensions happen to have a grand scale".

Mention should also be made of attempts to understand serrated yielding through mechanical and electronic models. Dry friction models that simulate the strain bursts in

staircase creep (Bodner and Rosen 1967) and the load drops in tensile tests (Rosen and Bodner 1969) have been devised which consider some of the features of DSA such as the negative strain rate sensitivity, work hardening and deformation by band propagation. Similar electronic analogs for the tensile test situation have also been demonstrated (Neelakantan and Venkataraman 1983).

## 6. Other manifestations of DSA

As we have mentioned earlier, serrations represent only one of the manifestations of dynamic strain ageing. In figure 7 the various other anomalies associated with DSA are illustrated schematically. These are (i) a peak in the variation of  $\sigma$  with  $T$  (ii) a peak in the variation of the work hardening  $\theta = \Delta\sigma/\Delta\epsilon$  with  $T$ , (iii) a peak in the variation of the Hall-Petch slope  $K_\epsilon$  with  $T$ , (iv) a minimum in the variation of the ductility with  $T$  and (v) a minimum in the strain rate sensitivity  $\gamma = \Delta\sigma/\Delta \ln \dot{\epsilon}$  with  $\gamma$  going negative in the temperature region of serrated flow. The variations in  $\gamma$  with stress and strain at different temperatures are also shown in figure 7. The types of serrations normally observed in the different temperature regions are also indicated.

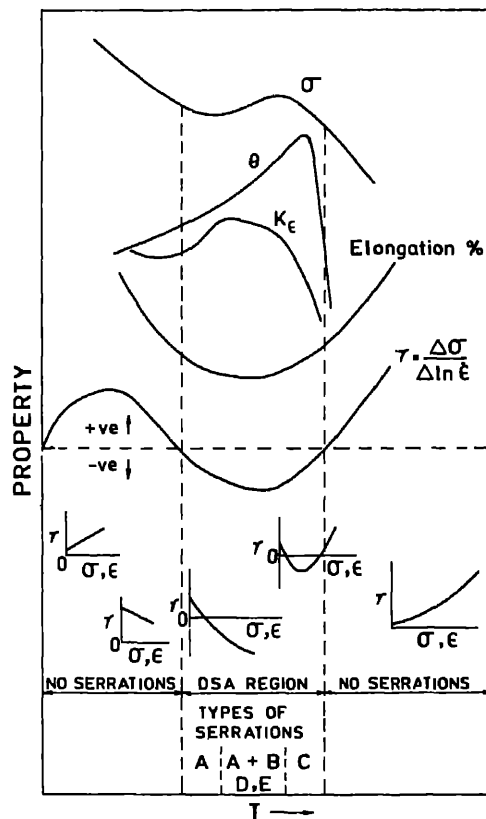


Figure 7. Schematic illustration of the various manifestations of dynamic strain ageing.



## 7. Issues to be resolved

(i) The main issue to be resolved unambiguously is whether the load drops are caused by a sudden increase in  $\rho_m$  or in  $\bar{v}$  or in both. We are handicapped by the fact that we do not so far have an experimental technique to measure  $\rho_m$  or  $\bar{v}$  during deformation. Acoustic emission measurements hold out promise as a potential method of attack on this problem.

(ii) Deformation during serrated flow is inhomogeneous and localised in bands. The actual strain rate in the deformation band is much higher than the imposed or assumed strain rate. Measurements and analysis of deformation band parameters such as the band velocity, band strain, band width and the average strain rate in the band should therefore receive greater attention than they have hitherto (McCormick 1983).

(iii) Current theoretical models are unable to account for the inverse effects ( $\epsilon_c$  increasing with increasing temperature and decreasing strain rate) observed in the high temperature-low strain rate region in which type C serrations are observed.

(iv) Most of the models are incomplete in that they make *ad hoc* assumptions or use empirical relationships; there is no detailed understanding either experimentally or theoretically of the effect of strain on diffusion, of the dependence of mobile dislocation density on strain or of the effect of a solute atmosphere on dislocation-dislocation interactions.

(v) Though it is often recognised that only short range diffusion in dislocation core (pipe diffusion) is involved in many manifestations of DSA, we are handicapped by the lack of an adequate knowledge of the appropriate diffusion coefficients.

(vi) In analysing the dependence of  $\sigma$  on  $\dot{\epsilon}$  and  $T$ , is the splitting of the flow stress into additive contributions from forest interactions, solutes, lattice friction, justified? How is such an approach reconciled with the idea that the obstacle with the highest energy barrier will be rate-controlling?

This list is evidently not an exhaustive one, but it does highlight some of the aspects of DSA that deserve greater attention from both experiment and theory in future.

## References

- Ananthakrishna G 1984 *Bull. Mater. Sci.*  
 Armstrong R W 1968 in *Dislocation dynamics* (eds) A R Rosenfield, G T Hahn, A L Bement and R I Jaffee (New York: McGraw Hill) p. 293  
 Bodner S R and Rosen A 1967 *J. Mech. Phys. Solids* **15** 63  
 Brindley B J and Worthington P J 1970 *Met. Rev.* **15** 101  
 Bolling G F and Richman R H 1965 *Acta Metall.* **13** 709, 723, 745  
 Charnock W 1968 *Philos. Mag.* **18** 89  
 Charnock W 1969 *Philos. Mag.* **20** 209  
 Conrad H and Christ B 1963 in *Recovery and recrystallization of metals* (ed) L Himmel (New York: Interscience) p. 124  
 Cottrell A H 1953 *Philos. Mag.* **44** 829  
 Cuddy L J and Leslie W C 1972 *Acta Metall.* **20** 1157  
 Hirth J P and Lothe J 1968 *Theory of crystal dislocations* (New York: McGraw-Hill)  
 Kubin L P, Spiesser Ph and Estrin Y 1982 *Acta Metall.* **30** 385  
 Macherauch E and Munz D 1966 *Z. Metall.* **57** 552  
 Malygin G A 1973 *Phys Status Solidi* **A15** 51  
 Mannan S L 1981 *Influence of grain size on the flow and fracture in AISI type 316 stainless steel at elevated temperatures* Ph.D. Thesis, Indian Institute of Science, Bangalore

- Mannan S L and Rodriguez P 1972 *Philos. Mag.* **25** 673
- Mannan S L, Samuel K G and Rodriguez P 1982 in *Proc. 6th Int. Conf. Strength of Metals and Alloys*, Melbourne, Aug. 1982 (ed) R C Giffkins (New York: Pergamon Press) Vol 2 pp. 637-642
- Mannan S L, Samuel K G and Rodriguez P 1983 *Trans. Indian Inst. Metals* **36** 313
- McCormick P G 1972 *Acta Metall.* **20** 351
- McCormick P G 1983 in *Deformation—All aspects, Int. Conf. on Metal Sci., ICMS, Ranchi* (Calcutta: Indian Institute of Metals)
- Mulford R A and Kocks U F 1979 *Acta Metall.* **27** 1125
- Nabarro F R N 1967 *Theory of crystal dislocation* (Oxford: University Press) p. 431
- Neelakantan K and Venkataraman G 1983 *Acta Metall.* **31** 77
- Penning P 1972 *Acta Metall.* **20** 1169
- Pink E and Grinberg A 1981 *Mater. Sci. Eng.* **51** 1
- Portevin A and LeChatelier F 1923 *CR Acad. Sci.* **176** 507
- Ramachandran V 1983 in *Deformation—All aspects, Int. Conf. on Metal Sci., ICMS, Ranchi* (Calcutta: Indian Institute of Metals)
- Ramachandran V, Baldwin D H and Reed-Hill R E 1970 *Metall. Trans.* **1** 3011
- Reed-Hill R E 1974 *Rev. High Temp. Mater.* **2** 214
- Rosen A and Bodner S R 1969 *Mater. Sci. Eng.* **4** 115
- Russel B 1963 *Philos. Mag.* **8** 615
- Samuel K G and Rodriguez P 1975 *Trans. Indian Inst. Metals* **28** 323
- Samuel K G and Rodriguez P 1980 *Trans Indian Inst. Metals* **33** 285
- Schmidt C G and Miller A K 1982 *Acta Metall.* **30** 615
- Seetharaman V 1984 *Bull Mater. Sci.* **6**
- Sleeswyk A W 1958 *Acta Metall.* **6** 598
- Sleeswyk A W and Verel D J 1972 *Scr. Metall.* **6** 1972
- Solar-Gomez A J R and McG Tegart W J 1969 *Philos. Mag.* **20** 507
- Strudel J L 1983 in *Deformation—All Aspects, Int. Conf. on Metal Sci., ICMS, Ranchi*, (Calcutta: Indian Institute of Metals)
- Van Bueren H G 1955 *Acta Metall.* **3** 519
- Van den Beukel A 1975 *Phys Status Solidi A* **30** 197
- Van den Beukel A 1980 *Acta Metall.* **28** 965
- Van den Beukel A and Kocks U F 1982 *Acta Metall.* **30** 1027
- Weertman J 1967 *Can. J. Phys.* **45** 797
- Wijler A, Schade Van Westrum J and Van den Beukel A 1972 *Acta Metall.* **20** 355
- Wilcox B A and Rosenfield A R 1966 *Mater. Sci. Eng.* **1** 201
- Yoshinaga H and Morozumi S 1971 *Philos. Mag.* **23** 1351, 1367

\_\_\_\_\_

## Repeated yield drop phenomena as a cooperative effect

G ANANTHAKRISHNA

Materials Science Laboratory, Reactor Research Centre, Kalpakkam 603 102, India

**Abstract.** We present a theoretical model of repeated yielding (RY) which reproduces many experimentally observed features, apart from showing how the temporal behaviour of the phenomenon emerges as a consequence of the cooperative behaviour of defects. We first consider the case of step-like creep curves. Our model leads to a coupled set of nonlinear differential equations which admit limit cycle solutions, and thence jumps on the creep curve. Approximate closed form solutions for the limit cycles and the steps on the creep curve are obtained. The model is then extended to the constant strain rate experiment by including the machine equation. The temporal ordering of RY is shown to follow, as well as several other features characteristic of RY. Chaotic flow is also exhibited: the model has a sequence of period-doubling bifurcations with an exponent equal to that of the quadratic map. Finally, we have analysed the fluctuations during the onset of RY using nonlinear Langevin equations. Fluctuations in the periodic (RY) phase are also investigated. We conclude that RY is another example of a dissipative structure.

**Keywords.** Repeated yield drop; defects; cooperative behaviour; limit cycle solutions; nonlinear Langevin equations.

### 1. Introduction

There have been numerous phenomenological treatments of repeated yielding (RY) in the metallurgical literature (Bell 1973; Bodner and Rosen 1967; Cottrell 1953; McCormic 1972; Penning 1972; van den Beukel 1975, 1980). The best known model is Cottrell's dynamic strain-ageing model and its extensions (Mc Cormic 1972; van den Beukel 1975, 1980). In these models, expressions are derived for such quantities as the critical strain, the critical strain rate, the dependence of the flow-stress on the strain rate, etc. Little attention has been paid to relating these quantities to the basic dislocation mechanisms such as cross glide, the Frank-Read mechanism, the formation of dislocation locks, etc. Also, there has been no attempt to investigate how the temporal behaviour of repeated yielding could arise naturally as a consequence of the basic dislocation mechanisms. From this point of view Cottrell's model is essentially static in character.

The transition from a single yield drop to a situation where RY occurs when certain 'drive' parameters (*e.g.*, the strain rate, temperature, etc.), are varied has the physical features of a nonequilibrium phase transition. (For examples of such transitions which arise only when the system is driven away from equilibrium, see Nicolis and Prigogine 1977; Haken 1978). We have constructed dislocation-dynamical model (Ananthakrishna and Sahoo 1981; Ananthakrishna and Valsakumar 1982; Valsakumar and Ananthakrishna 1983) which exhibits most of the experimentally observed features of RY and demonstrates that RY is a nonequilibrium phase transition. Needless to say, we consider somewhat idealized conditions, and further do not attempt to fit any actual data. In §2, we start with the simplest case, namely, steps on the creep curve. Based on

well-known dislocation mechanisms, we introduce a model which transforms one type of dislocation into another, giving rise to a set of coupled nonlinear differential equations for the corresponding densities. For a range of values of the rate constants, these equations are shown to admit *limit cycle* solutions. These lead immediately to jumps on creep curves. The model predicts a temperature range in which these jumps appear. In §3, we outline how approximate closed form solutions for the limit cycles and the steps on the creep curve are obtained. The results are shown to agree with experiments on zinc (Zagorukuyko *et al* 1977). Section 4 contains the extension of the model to the constant strain rate case by coupling the equations of §2 to the machine equations. The temporal ordering of  $\dot{\epsilon}$  is shown to follow (Ananthakrishna and Valsakumar 1982). Also demonstrated are several important features typical of  $\dot{\epsilon}$  such as bounds on the strain rate, bounds on the concentration of solute atoms, the negative strain rate dependence of the flow stress, the dependence of the amplitude on the strain rate and strain, etc.

Our model also exhibits chaotic flow, which finds some support from experiments. We find a sequence of period doubling bifurcations (Ananthakrishna and Valsakumar 1983) with an exponent identical to that for a quadratic map. This is presented in §5. Section 6 is devoted to the study of fluctuations during the onset of  $\dot{\epsilon}$  using nonlinear Langevin equations. We have used the Monte-Carlo and Gaussian decoupling methods (Valsakumar *et al* 1983). As the strain rate approaches its critical value, the variance not only diverges, but also shows the periodic nature of the fluctuations. Fluctuations within the periodic phase ( $\dot{\epsilon}$ ) are also investigated. Our entire analysis shows that  $\dot{\epsilon}$  is another example of a dissipative structure (Nicolis and Prigogine 1977). In the final section, some unresolved problems are discussed.

## 2. Steps on the creep curve

### 2.1 The model

Perhaps the simplest manifestation of instability in plastic flow, from a conceptual point of view, is a creep curve with steps. However, there are not many instances of measurements where stepped response has been observed (Ardley and Cottrell 1953; Navratil *et al* 1974; Stejskalova *et al* 1981; Zagorukuyko *et al* 1977; Da Silveira and Monteiro 1979; Lubahn and Felgar 1961). There appears to be no detailed theory for the phenomenon. The model we propose (Ananthakrishna and Sahoo 1981; Valsakumar and Ananthakrishna 1983) is a natural extension of our earlier work (Sahoo and Ananthakrishna 1982) where a theory of creep was developed under the assumption that mobile dislocations (denoted by  $g$ ) and immobile dislocations (denoted by  $s$ ) transform into each other and are in dynamical balance. In the present case, we introduce a third species of dislocations (denoted by  $i$ ) which are surrounded by clouds of solute atoms. These are dislocations moving much slower than the mobile species, ultimately becoming immobile. The introduction of this species is reminiscent of the basic feature of Cottrell's (1953) theory, so that the model is in keeping with the essential spirit of Cottrell's theory.

Let  $N_g$ ,  $N_s$  and  $N_i$  denote the densities of the  $g$ ,  $s$  and  $i$  species respectively. The rate equations for these quantities are (a dot denotes the time derivative):

$$\dot{N}_g = \theta V_g N_g - \mu N_g^2 - \mu' N_g N_s + \lambda N_s - \alpha N_g, \quad (1)$$

$$\dot{N}_s = k\mu N_g^2 - \mu' N_g N_s - \lambda N_s + \alpha' N_i, \quad (2)$$

$$\dot{N}_i = \alpha N_g - \alpha' N_i. \quad (3)$$

Here  $V$  denotes the dislocation velocity. We assume that  $\theta$ ,  $\bar{\mu}$ ,  $\mu'$ ,  $\alpha$ ,  $\alpha'$ , and  $\lambda$  are constants for a given stress at a given temperature. The first term in (1) corresponds to the production of dislocation by the cross glide mechanism; the second corresponds to the immobilization of two mobile dislocations and the annihilation of pairs of dislocations at a rate  $(l-k)\mu$ ; the third corresponds to the annihilation of a mobile dislocation with an immobile one; and the last arises from solute atoms gathering around dislocations. Once a certain number of solute atoms gather around a moving dislocation, its mobility is reduced, and it becomes a type  $i$  dislocation (hence the source term  $\alpha N_g$  in (3)). As the size of the solute atom cloud increases, the dislocation eventually becomes immobile (hence the source term  $\alpha' N_i$  in (2)). The term  $\lambda N_s$  comes from the (thermal or athermal) activation of immobile dislocations. The parameter  $\alpha$  is expected to depend on the diffusion constant of the solute atoms, their concentration and the velocity of dislocations of type  $i$ . The parameter  $\alpha'$  is the rate of immobilization, and hence should be expected to depend on the critical velocity ( $k$  is a parameter close to unity).

It is convenient to make equations (1)–(3) dimensionless by setting

$$x = (\mu/\lambda)N_g, \quad y = (\mu/\theta V_g)N_s, \quad z = (\mu\alpha'/\lambda\alpha)N_i. \quad (4)$$

Then

$$dx/d\tau = (l-a)x - bx^2 - xy + y, \quad (5)$$

$$dy/d\tau = b(kbx^2 - xy - y + az), \quad (6)$$

$$dz/d\tau = c(x-z), \quad (7)$$

where

$$\lambda = \theta V_g t, \quad a = \alpha/\theta V_g, \quad b = \lambda/\theta V_g, \quad c = \alpha'/\theta V_g. \quad (8)$$

(We have set  $\mu = \mu'$  in order to reduce the number of parameters.)

## 2.2 Stability analysis and existence of limit cycles

Equations (5)–(7) form a nonlinear system. Under well-known conditions (Minorsky 1962), these admit periodic solutions called limit cycles for a certain range of values of the parameters  $a, b, c$  and  $k$ . Although the method of investigation is well known, for the sake of completeness we briefly outline the procedure used. Limit cycles are special classes of solutions which are isolated closed trajectories in the phase space  $(x, y, z)$  such that any trajectory which is sufficiently close to it either approaches it or recedes from it. Such closed trajectories can arise only in nonlinear systems. The search for limit cycles is generally preceded and aided by an investigation of the properties of the system around the steady state values  $x_a, y_a$ , and  $z_a$ . The stability of the system is decided by the nature of its singular points—node, focus, saddle point or centre. Linearising the set of equations around  $(x_a, y_a, z_a)$ , one obtains an equation of the form

$$d\psi/d\tau = W\psi, \quad (9)$$

where  $\psi$  is the column vector with components  $(x - x_a), (y - y_a), (z - z_a)$ , and  $W$  is a  $3 \times 3$  matrix. A node arises when all three eigenvalues of  $W$  are of the same sign, and a saddle point when only two of these are of the same sign; a focus occurs when there are two complex conjugate eigenvalues, and a centre when one eigenvalue is identically zero

and the other two are pure imaginary. (In the last case the nature of the singular point may have to be analysed more carefully; see Minorsky 1962).

An attractive limit cycle exists if there is a surface surrounding an unstable focus into which all trajectories enter: in the present case, we first look for a domain in the parameter space  $(a, b, c, k)$  when two of the eigenvalues are complex with at least one of them having a positive real part, and then show that such a surface exists (Ananthakrishna and Sahoo 1981). The only constraints that we have on the values of the parameters are  $a < 1$  (which arises because the total rate of production of dislocations is positive);  $k < 1$ ; and  $a, b, c > 0$ . ( $N_g$ ,  $N_s$  and  $N_t$  are obviously positive).

### 2.3 Staircase creep

An analytical solution of (5)–(7) for arbitrary values of the parameters, and valid for all times, is difficult. To obtain numerical solutions,  $V_g$  must be known as a function of  $N = N_t + N_s + N_g$  and  $\sigma^*(N)$ , where  $\sigma^*$  is the effective stress. For simplicity we assume  $V_g$  to be constant. Although this assumption is not physical, it can be argued that it will not alter the qualitative features of staircase creep (Ananthakrishna and Sahoo 1981). The creep curve obtained by integrating the Orowan equation is shown in figure 1. The steps on the creep curve appear only in the secondary region, which is consistent with the existing experimental results (Zagorukuyko *et al* 1977; Da Silveira and Monteiro 1979).

Our model also predicts a feature which is in agreement with experiment, namely, that there are upper and lower bounds for the asymptotic creep rates for which staircase creep occurs. These arise because the frequency of oscillation  $\sim V_g \text{Im } \omega_1$ , where  $\omega_1$  is one of the two complex conjugate eigenvalues of  $W$ . Bounds can be put on  $\text{Im } \omega_1$ ,

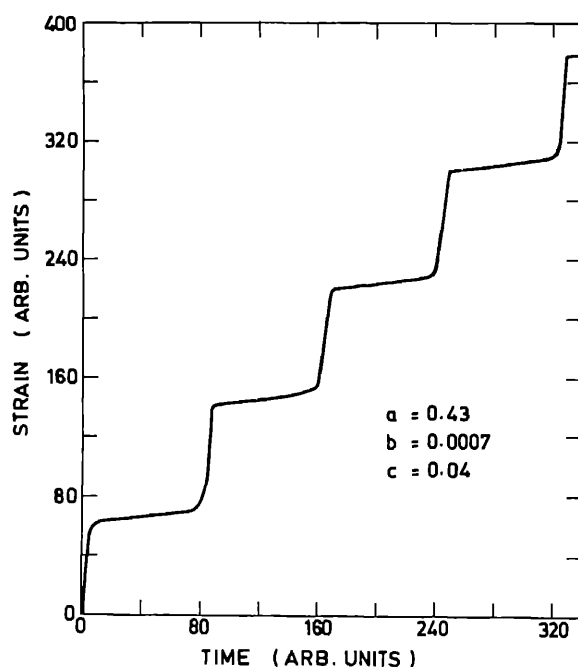


Figure 1. Staircase creep for typical values of the parameters  $a$ ,  $b$  and  $c$ .

depending on the basic mechanism prevailing in the system. This implies corresponding bounds on  $V_g$  in order to have *observable* steps on the creep curve. This in turn implies that the phenomenon can only be observed over a finite range of  $\dot{\epsilon}$  (in practice, somewhat less than three orders of magnitude). Moreover, since  $V_g$  is temperature dependent (for a fixed stress), this phenomenon can only occur over a fixed range of temperature, as corroborated by the experimental results of Zagorukuyko *et al* (1977).

### 3. Approximate solutions

We outline an analytic procedure for obtaining asymptotic solutions to our equations. This is essential if one wants to relate the theoretical rate constants to accessible parameters such as the applied stress  $\sigma_a$ , temperature  $T$ , concentration of solute atoms  $C$ , etc. Our method follows that of Tyson (1977) for the Belousov-Zhabotinski oscillating chemical reaction. The main point is to identify a fast mode and adiabatically eliminate it to obtain a reduced set of two coupled equations from the original set of three equations (5)–(7). Approximate solutions are then obtained by using the method of relaxation oscillations (Minorsky 1962; Tyson 1977). Defining  $X = x - x_a$ ,  $Y = y - y_a$ ,  $Z = z - z_a$ , and  $\tau' = b\tau$ , (5)–(7) may be re-written in the form

$$b\dot{X} = -[\alpha X + \beta Y + bX^2 + XY], \quad (10)$$

$$\dot{Y} = -[\gamma X + \delta Y - bX^2 + XY - aZ], \quad (11)$$

$$\dot{Z} = \frac{c}{b}[X - Y], \quad (12)$$

where the dot now refers to differentiation with respect to  $\tau'$ . Further, the constants  $\alpha, \dots, \delta$  are

$$\alpha = a + 2bx_a + y_a - 1, \quad \beta = x_a - 1, \quad \gamma = y_a - 2bx_a, \quad \delta = x_a + 1 \quad (13)$$

(The constant  $\alpha$  used here is distinct from that appearing in (1) of §2.) Since  $b \ll a, c$ , we see that  $|\dot{X}| \rightarrow \infty$  as  $b \rightarrow 0$  unless the right side in (10) vanishes identically. This amounts to saying that  $X$  must change with a characteristic time  $\sim b$  to maintain the condition

$$\alpha X + \beta Y + bX^2 + XY = 0 \quad (14)$$

Thus  $X$  is a fast variable that can be adiabatically eliminated from (10)–(12), and the resulting pair of independent equations used for further analysis.

We use the results of stability analysis and further express  $\alpha, \beta, \gamma, \delta, x_a, y_a$  and  $z_a$  as power series in  $b$ . We then determine the 'null clines'

$$\dot{Y} = 0 \leftrightarrow Z_1 = Z(Y) = X(Y) + \frac{2}{a}[x_a + X(Y)]Y, \quad (15)$$

and

$$\dot{Z} = 0 \leftrightarrow Z_2 = X(Y), \quad (16)$$

and again express  $Z(Y)$  in powers of  $b$ . To find the limit cycles, we look for the intersection of the null clines in the region of negative slope. From the expressions for the null clines  $Z_1$  and  $Z_2$  we obtain a reasonable idea of the phase portrait. For  $a < 1/3$  and for  $1/\sqrt{2} < a < 1$ , the steady state is stable. For  $1/3 < a < 1/\sqrt{2}$ , the null clines intersect in the negative slope region, which means that a limit cycle exists. Figure 2



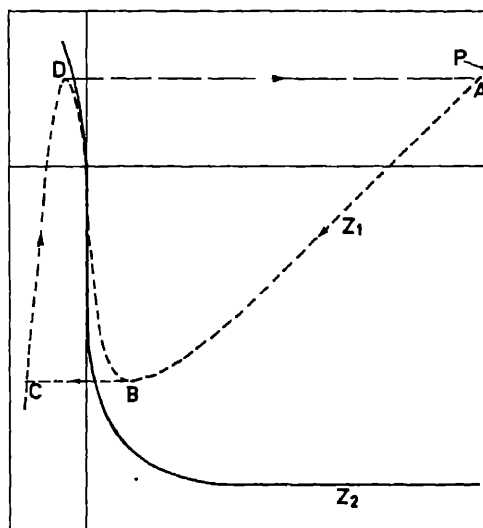


Figure 2. Phase plane portrait (the null clines  $Z_1$  and  $Z_2$  plotted as a function of  $Y$ ) in the case  $1/3 < a < 1/2$ . The limit cycle is ABCDA.

shows a typical phase portrait for  $1/3 < a < 1/2$ . Starting from an arbitrary point, the trajectory moves along the null cline  $\dot{Y} = 0$  until it reaches the turning point  $D$ , from where it almost instantaneously jumps to  $A$ . Thereafter it moves along the branch  $\dot{Y} = 0$  (slowly) until it reaches the second turning point  $B$  from where it jumps to  $C$ , and the process continues. Thus the trajectory is a closed one and the limit cycle is  $A \rightarrow B \rightarrow C \rightarrow D \rightarrow A$ . From the expressions for  $Z_1$  and  $Z_2$ , it is possible to calculate also the period, the amplitude and the wave form of the limit cycle solution. Finally, as already stated, we can integrate the Orowan equation to obtain the steady state creep curve which exhibits steps (Valsakumar and Ananthakrishna 1983).

Although the results of the model (in its present form) are not directly applicable to the detailed results on zinc (Zagorukuyko *et al* 1977), they still permit qualitative comparison. That the steps are seen only in the secondary creep region is obviously consistent with our theory, since the latter predicts a bifurcation from the steady state solution to a periodic one. Zagorukuyko *et al* (1977) report a rapid monotonic increase of the magnitude of the step in the strain as a function of  $\sigma_a$ ; a weak, decreasing dependence of the period of the jump on  $\sigma_a$ ; and a decrease of the magnitude of the jump in strain with increasing  $T$ . All these features are consistent with our work.

#### 4. Repeated yield drop

Our model can be extended to a constant strain rate experiment by augmenting equations (1)–(3) with the machine equation representing the load sensed by the load cell, namely

$$\dot{\sigma}_a = K[\dot{\epsilon} - b_0(N_0 + \gamma N_1)V_0(\sigma^*)], \quad (17)$$

where a dot denotes the time derivative. Here  $\dot{\epsilon}$  is the imposed strain rate,  $K$  is the effective compliance,  $b_0$  is the Burgers vector and  $\sigma^*$  is the effective stress. The second term on the right in (17) is the plastic strain rate  $\dot{\epsilon}_p$ . We assume the power law  $V_0 = V_0(\sigma^*/\sigma_0)^n$ , with  $\sigma^* = \sigma_a - HN^{1/2}$ , where  $H$  is a constant characteristic of

hardening and  $m$  is a velocity exponent. Following a procedure similar to that of § 2, it can be shown that there is a domain in the space of the relevant parameters for which limit cycle solutions exist. Choosing values of the parameters in the domain of instability so as to be consistent with the expected values of the dislocation densities and the yield drops, numerical solutions of the system of equations may be obtained, and various characteristic features of the  $\sigma\epsilon$  exhibited may be studied. These appear to be generally consistent with the experimental results. (Note that the latter are in the nature of averages over the sample dimensions.) We list these salient features: (a) There is a range of  $\dot{\epsilon}$  over which serrations are seen. (b) The model exhibits the negative strain rate behaviour of the flow stress at a fixed value of the plastic strain. The inset in figure 3 shows a typical plot of  $\sigma_a$  vs  $\dot{\epsilon}_p$ , with a minimum in  $\sigma_a$  at a point  $\dot{\epsilon}_p = \dot{\epsilon}_{\min}$ . Curves corresponding to larger  $\epsilon_p$  are displaced successively upwards. This feature has been both theoretically (Penning 1972; van den Beukel 1975) and experimentally verified (Bodner and Rosen 1967). (c) Figure 3 shows a typical plot of serrated yielding. The serrations are asymptotically periodic. Since it is not possible to identify them (from the plot itself) as serrations of type A or type B, a strain rate change test (Wijler and van Westrum 1971) must be carried out, from which it is found that beyond  $\dot{\epsilon}_{\min}$  the serrations are of type B. (d) The amplitude of the serration increases up to  $\dot{\epsilon}_{\min}$  and decreases thereafter. (e) The amplitude increases and saturates as a function of  $\epsilon$ , consistent with experiments (McCormic 1971). (f) There are upper and lower bounds on the parameter  $\alpha$  of (1) within which serrated yielding occurs. Since  $\alpha$  depends on the concentration of solute atoms, this implies that there is a range of the solute atom concentration in which the phenomenon occurs. (g)  $\epsilon_c$  (the critical strain), as a function of  $\dot{\epsilon}$ , first decreases and then increases (McCormic 1971). (h) Beyond the range of  $\dot{\epsilon}$  where serrated yielding occurs, the 'normal' behaviour of  $\sigma_a(\epsilon)$  is resumed.

It should be pointed out that there has so far been no attempt to derive the negative strain rate behaviour of flow stress (which is crucial for any meaningful description of the phenomenon) starting from dislocation *interactions*. In the existing theories this is either assumed (Penning 1972) or derived (van den Beukel 1975) through a phenomenological treatment of waiting times involving in any case only individual dislocations. In contrast, this property emerges naturally in the present model from a consideration of dislocation interactions.

We have shown that the new temporal order represented by serrated yielding is the consequence of a bifurcation from a temporally homogeneous steady state plastic flow

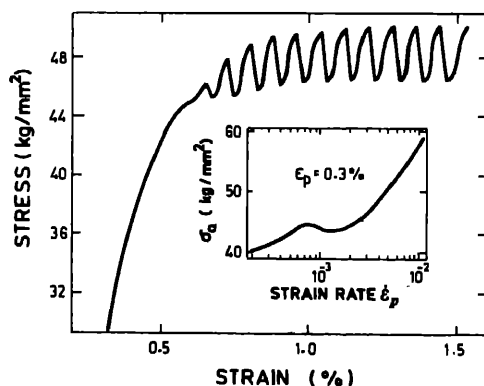


Figure 3. Calculated stress-strain curve showing repeated yielding. The inset is a graph  $\sigma_a$  vs  $\dot{\epsilon}_p$  for the same values of the parameters.

beyond some critical values of the parameters. This order is a result of a balance between the energy input (in the form of dislocation multiplication) and dissipation (annihilation, immobilisation and other processes). The phenomenon is obviously a far-from-equilibrium situation and is an example of a dissipative structure (Nicolis and Prigogine 1977).

## 5. Chaotic flow

We now turn to the chaotic flow exhibited by our model over a certain range of a drive parameter, the applied strain rate. (There is also some experimental evidence for such a flow, which will be discussed subsequently in brief). This adds to the growing list of models and physical situations exhibiting chaos (Ott 1981; Eckmann 1981; Lauterborn and Kramer 1981; Jefferies 1982). The model has an infinite sequence of period-doubling bifurcation eventually leading to chaos. The region over which chaos is exhibited is very small compared to the range of  $\dot{\epsilon}$  over which  $\text{RY}$  is seen ( $\text{RY}$  is considered to be periodic). We have calculated the value of the associated exponent and found it to be the same as the exponent for the quadratic map. We have also obtained the associated one-dimensional map. As the parameter of interest is the applied strain rate  $\dot{\epsilon}$ , we fix the values of all the other parameters within the instability region and study the bifurcation sequence with respect to the parameter  $e = \dot{\epsilon}(\mu/\lambda V_0 b_0)$ . The region where the period doubling bifurcation occurs is small, and is located near the upper end of the range of  $e$  (the dimensionless strain rate) over which  $\text{RY}$  is observed. For the chosen values of the parameters, the first bifurcation from the periodic state with period  $T$  to a state with a period  $2T$  occurs at  $e_1 = 159.98444$ , while the successive bifurcation to states with period  $2^2T$ ,  $2^3T$ , . . . , occur at  $e_2 = 173.7178$ ,  $e_3 = 175.8974$ , . . . . The exponents  $\delta = \lim(e_n - e_{n-1})/(e_{n+1} - e_n)$  appears to be very close to that obtained by for the quadratic map (Grossman and Tnomae (1977), Feigenbaum (1978)). The estimated value of  $e_\infty$  is 176.4669, beyond which we find chaotic motion. Figures 4 and 5 show the variation of the stress  $\sigma_a$  with time (equivalently, the strain) for  $e = 174.679$  (motion with period  $4T$ ) and  $e = 178.205$  (chaotic motion) respectively. A log-log plot of the projection of the strange attractor in the  $N_g - \sigma_a$  plane is shown in figure 6. The associated one-dimensional map is shown in figure 7. Unlike the corresponding map for the Lorenz model (Ott 1981), our map has a smooth rounded maximum similar to the quadratic map except that it is very much skewed.

The fact that our model can exhibit chaotic flow has prompted us to look for experimental evidence for the plots of repeated yield drops. (Of course, the value of the parameter which controls the magnitude of the variation in  $\sigma_a$ , i.e., the magnitude of the yield drop, has to be appropriately chosen). Even though we are constrained by the fact that the *average* stress level remains constant in our model, we have found evidence (Hall 1970) in support of such flows. Experimentally, too, this occurs towards the end of the  $\dot{\epsilon}$  range for which  $\text{RY}$  is seen. If we subtract the normally observed slow increase in the base level of the stress, there appear to be many more situations which perhaps correspond to chaos (Rosen and Bodner 1969).

## 6. Fluctuations during the onset of repeated yielding

We have discussed so far the possibility of a new temporal phase arising as a drive parameter (here,  $\dot{\epsilon}$ ) is varied. The situation corresponds to a *hard mode instability* in

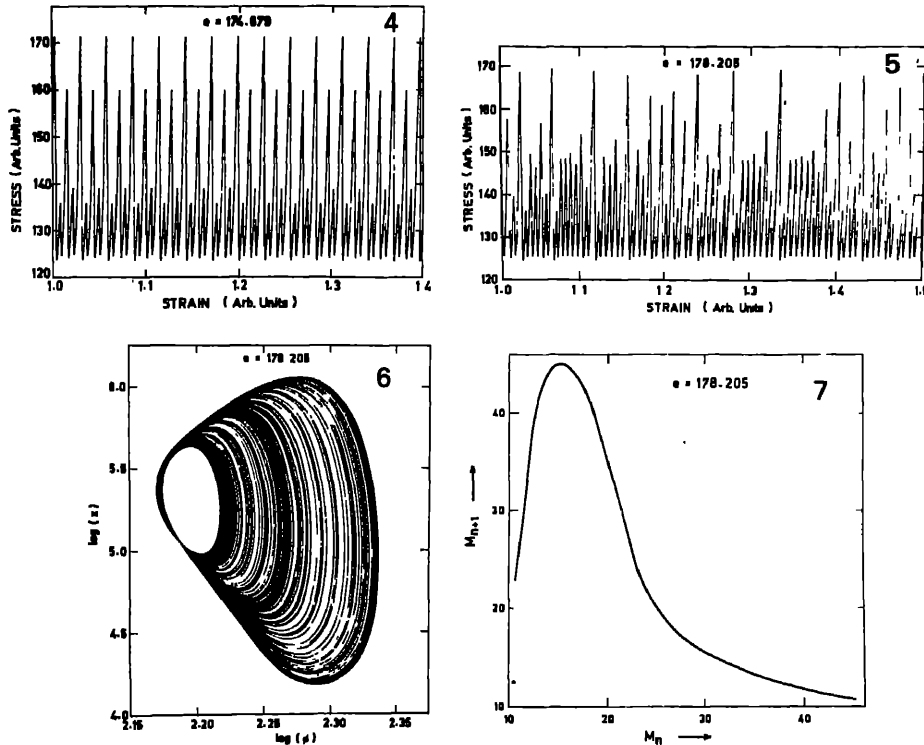


Figure 4. Stress-strain curve for  $e = 174.679$  with period  $4T$ .

Figure 5. Stress-strain curve for  $e = 178.205$ , i.e., in the chaotic region.

Figure 6. A log-log plot of the projection of the strange attractor for  $e = 178.205$  in the  $x - \phi$  plane. Here  $x = (\mu/\lambda) N_g$  and  $\phi = \sigma_a/\sigma_0$ .

Figure 7. The one-dimensional map associated with chaotic flow in the model.

which the real part of complex conjugate modes changes sign (from negative to positive) in the frequency plane, as the drive parameter crosses its critical value. The foregoing analysis is completely deterministic. We now analyse the nature of the fluctuations when the parameter is in the neighbourhood of its critical value.

Our analysis begins with the nonlinear Langevin equations obtained by adding Gaussian white noise terms to the deterministic equations. We have used both the Monte Carlo technique and a Gaussian decoupling method (Valsakumar *et al* 1983) to study the fluctuations. (However, in the present context the second method can be applied only in the special case  $H = 0$ ; otherwise powers of  $N^{1/2}$  are present, which cannot be handled without further approximations). It is convenient to discuss the general features of the fluctuations with the help of the equivalent Fokker-Planck equation. The standard form of the Fokker-Planck equation is

$$\frac{\partial \pi}{\partial t}(\xi, t) = \frac{\partial}{\partial \xi} [K(t) \cdot \xi \pi(\xi, t)] + \frac{1}{2} \frac{\partial^2}{\partial \xi^2} [D(t) \pi(\xi, t)], \quad (18)$$

where

$$K(t) = \frac{\partial C_1(y)}{\partial y}, D(t) = C_2(y), \quad (19)$$

and

$$\frac{dy}{dt} = C_1(y) \text{ and } \xi = \varepsilon^{-1/2}[x - y]. \quad (20)$$

Here,  $x$  is the random variable,  $y$  its mean,  $C_1(y)$  the first jump moment and  $C_2(y)$  the second moment. ( $K$  is the regression matrix.)  $\varepsilon$  is the (system-size) expansion parameter. To identify the onset of the periodic state beyond the critical value of the drive parameter, it is convenient to use the concept of the 'irreversible circulation of fluctuation' defined by (Tomita and Tomita 1974; Tomita *et al* 1974)

$$\alpha = \frac{1}{2}[(K\sigma)^T - K\sigma] \quad (21)$$

where  $\sigma$  is the variance ( $T$  represents the transpose).  $K$  and  $\sigma$  are related by

$$\frac{1}{2}\sigma = \alpha + K\sigma + \frac{1}{2}D. \quad (22)$$

If a periodic state occurs as a result of the hard mode instability both  $\alpha$  and  $\sigma$  diverge; the instability is incurred through  $\alpha$ , which becomes increasingly large as the transition point is approached from below.

Our preliminary investigations reveal that as  $\varepsilon \rightarrow \varepsilon_c$  from below, the fluctuations show an overall growth which is indicative of the divergence of the variance, in addition to exhibiting a near periodic modulation which is indicative of the approach to a periodic state. For  $\varepsilon > \varepsilon_c$ , the fluctuations have the normal characteristics expected when limit cycle solutions are supported. The details of this study will be reported elsewhere.

## 7. Concluding remarks

We have shown that the state of temporal order represented by steps on the creep curve or by repeated yield drops is a consequence of a bifurcation from a temporally homogeneous, steady-state plastic flow. (A similar approach has been used by Kubin *et al* (1984) for low temperature  $\text{Pb}$ .) A major criticism that can be raised is that the theory does not take into account the inhomogeneous deformation that normally accompanies the phenomenon. (Although, to the best of the author's knowledge, experiments do not show which is the cause and which is the effect, *i.e.*, whether an inhomogeneous deformation is the cause and a yield drop is the effect, or *vice versa*. We believe that it is not possible to disentangle the two. Nor is there any theory that takes the inhomogeneous deformation into proper account. The closest is that of Penning (1972) in which the feature is simply assumed). However, we argue (Ananthakrishna and Valsakumar 1982) that if the space dependence is properly taken into account, the inhomogeneity of the deformation should follow automatically. The point is that such an extended model would still exhibit the negative strain rate behaviour of the flow stress (which has been assumed by Penning (1972) to show that hopping and propagating band type solutions are supported). Attempts are underway to demonstrate explicitly that such solutions indeed occur when appropriate space dependence is included.

Another possible criticism could be that the model merely 'mimics' the effects of the waiting of dislocations at obstacles which van den Beukel (1975) has used to derive  $\sigma(\dot{\epsilon}_p)$ . However, this work deals with individual dislocations whereas what is observed in an actual experiment is an ensemble average over participating dislocations. Therefore, for such a theory to hold good, there must be a 'phase coherence' between the dislocations, if the effects are to manifest themselves at a gross level. Further, it is known that the negative strain rate behaviour is essential for  $\text{RY}$ . (For a detailed analysis of various tensile test conditions using the negative strain rate behaviour, see Neelakantan and Venkataraman 1983). Our analysis shows that this behaviour is a consequence of the competition between different dislocation interaction mechanisms. We have also checked (Ananthakrishna and Sahoo 1981) that the incorporation of certain other basic dislocation mechanisms (pile up, pinning and depinning of dislocations from obstacles) leads to similar results.

Finally, it should be pointed out that several materials like nylon (Schultz 1974), metallic glasses (Takayama 1979), wood, etc. are known to show  $\text{RY}$ . The present work suggests that the *mathematical mechanism in all these cases must be the emergence of limit cycle solutions which are characteristic of non-linear systems. As plastic flow is basically nonlinear, such solutions are an intrinsic possibility.* The basic microscopic physical mechanisms of course are bound to be different in different materials.

### Acknowledgement

The author thanks Dr G Venkataraman for arousing his interest in this problem.

### References

- Ananthakrishna G and Sahoo D 1981 *J. Phys.* **D14** 2081  
Ananthakrishna G and Valsakumar M C 1982 *J. Phys.* **D15** L171  
Ananthakrishna G and Valsakumar M C 1983 *Phys. Lett.* **A95** 69  
Ardley G W and Cottrell A H 1953 *Proc. R. Soc.* **A219** 328  
Bell J F 1973 *Handbuch der Physik Band VIa/1* (Berlin: Springer-Verlag)  
Bodner S R and Rosen A 1967 *J. Mech. Phys. Solids* **15** 63  
Cottrell A H 1953 *Philos. Mag.* **44** 829  
Da Silveira T L and Monteiro S N 1979 *Met. Trans.* **A10** 1795  
Eckmann J P 1981 *Rev. Mod. Phys.* **53** 643  
Feigenbaum M J 1978 *J. Stat. Phys.* **19** 25  
Grossman S and Tnomae S 1977 *Z. Naturforsch.* **32a** 1353  
Haken H 1978 *Synergetics* (Berlin: Springer-Verlag)  
Hall E O 1970 *Yield point phenomena in metals and alloys* (Macmillan: London)  
Jefferies D J 1982 *Phys. Lett.* **A90** 317  
Kubin L P, Estrin Y and Spiesser Ph 1984 *Res. Mechanica* **10** 25  
Lauterborn W and Kramer E 1981 *Phys. Rev. Lett.* **47** 1445  
Lubahn J D and Felgar R P 1961 *Plasticity and creep of metals* (New York: John Wiley)  
McCormic P G 1971 *Acta Metall.* **19** 463  
McCormic P G 1972 *Acta Metall.* **20** 351  
Minorsky N 1962 *Nonlinear oscillations* (New Jersey: Van Nostrand)  
Navratil V, Hammersky M and Blazkova 1974 *Czech. J. Phys.* **B24** 907  
Neelakantan K and Venkataraman G 1983 *Acta Met.* **31** 77  
Nicolis G and Prigogine I 1977 *Self organization in non-equilibrium systems* (New York: Wiley)  
Ott E 1981 *Rev. Mod. Phys.* **53** 643  
Penning P 1972 *Acta Metall.* **20** 1169

- Rosen A and Bodner S R 1969 *Mater. Sci. Eng.* **4** 115  
 Sahoo D and Ananthakrishna G 1982 *J. Phys.* **D15** 1439  
 Schultz J 1974 *Polymer materials science* (New Jersey: Princeton-Hall)  
 Stejskalova V, Hammersky M, Luckac P, Vostry P and Sprusil B 1981 *Czech J. Phys.* **B31** 195  
 Takayama 1979 *Scr. Met.* **13** 463  
 Tomita K, Ohta T and Ohta H 1974 *Prog. Theor. Phys.* **52** 1744  
 Tomita K and Tomita H 1974 *Prog. Theor. Phys.* **51** 1731  
 Tyson J J 1977 *J. Chem. Phys.* **66** 905  
 Valsakumar M C and Ananthakrishna G 1983 *J. Phys.* **D16** 1055  
 Valsakumar M C, Murthy K P N and Ananthakrishna G 1983 *J. Stat. Phys.* **30** 637  
 van den Beukel A 1975 *Phys. Status Solidi* **A30** 197  
 van den Beukel A 1980 *Acta Metall.* **20** 965  
 Wijler A and van Westrum S 1971 *Scr. Metall.* **5** 531  
 Zagarkukyo L N, Ostasky A L and Soldatov V P 1977 *Phys. Met. Metallogr.* **43** 156

### Discussion

P Rodriguez: You cited some results on zinc. In your model, the Cottrell type of solute locking is envisaged. What was the solute species?

G Ananthakrishna: Zinc is a poor example (the dislocations are actually produced due to inhomogeneities at the surface).

Rodriguez: Many of the conclusions with respect to the critical strain, the magnitude of the strain burst, the delay time for the strain burst to occur, etc., follow automatically once Cottrell locking is introduced. It is therefore not surprising that the model gets these right.

Ananthakrishna: Cottrell locking is not manifest in the equations of the model.

N Kumar: You get period doubling bifurcations even though your maps are not discrete. Is this because of the higher dimensionality of the system of equations?

Ananthakrishna: One-D are the simplest of systems which exhibit chaos. Coupled system of differential equations also exhibit such a behaviour. The associated 1-D map can be obtained.

C K Majumdar: It would be interesting to examine the structure of your set of equations from the point of view of catastrophe theory.

## **Mechanisms and empirical equations for deformation and some principles of alloy design**

**T BALAKRISHNA BHAT**

Defence Metallurgical Research Laboratory, Kanchanbagh, Hyderabad 500 258, India

**Abstract.** Some aspects of the deformation behaviour of solids at very high, moderately high and low strain rates are discussed. In the very high strain rate region, deformation equations and the physics of the shock front are analysed to propose a route to lower energy dissipation at the shock front. In the moderately high strain rate region, alloy design principles for maximizing the deformation resistance are outlined. In the low strain rate region, an analysis of the physical basis for the power law creep equation is presented. Some physical arguments are presented as a rationale for the high stress exponents and activation energies often observed in particle-strengthened alloys. The additivity of strain rates by various mechanisms is also briefly discussed.

**Keywords.** Deformation mechanisms; empirical equations; dislocation dynamics; shock front; impact resistance; alloy design.

### **1. Introduction**

The behaviour of solids under deformation depends on the operating stress level, the temperature, and many material properties such as the elastic modulus, the microstructure and the properties of the individual constituents. The behaviour is indeed complex and can be described only by semiquantitative and quasi-empirical relations. In the very high strain rate region where shock waves predominate in the flow process, the microstructure and initial temperature are relatively unimportant. The crystalline state and basic material properties such as the modulus and density are important in this region. In the lower strain rate region such as that observed in the ballistic testing of materials, the stress-strain diagrams, the glide resistances, the phonon drag and the temperature play important roles. In the low strain rate region as in creep, the operating temperature and stress are most important. A smaller but significant role is also played by the microstructure. The regimes of deformation rates and stresses of interest in the present discussion are shown in figure 1.

### **2. Deformation at very high pressures and strain rate**

Pressure impulses injected into materials generate shock waves. At low pressures the shock front consists of purely elastic strains and the wave propagates over large distances with relatively little attenuation. A typical example of such a wave is that of sound waves generated by gentle knocks on any solid. More intense waves such as those generated during hollow charge collisions or in implosions intended for thermonuclear fusion generate high nonelastic strains at the wave-fronts. Such waves suffer large drags and tend to get dissipated. This drag is in some cases undesirable, for example in



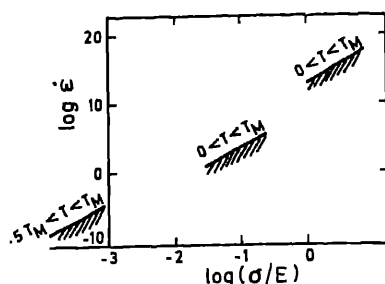


Figure 1. Stress-strain rate regimes considered in this paper.

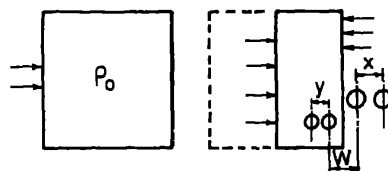


Figure 2. Schematic diagram illustrating the strain at a shock front:  $\varepsilon = (x - y)/x$ .

thermonuclear experiments. We may therefore analyse the drag mechanisms in terms of a specific question, namely, how to reduce the drag.

At the shock front a low density phase is transformed to a high density phase. This transition induces both bulk and shear strains at the front (Gilman 1979). Figure 2 illustrates the situation at the shock front. The strain there may be written as

$$\varepsilon = (\rho - \rho_0)/\rho_0, \quad (1)$$

where  $\rho_0$  is the initial density and  $\rho$  is the shocked density. The power dissipated at the moving front is

$$G = B\dot{\varepsilon} = Bv_{sh}/W, \quad (2)$$

where  $B$  is the drag coefficient,  $v_{sh}$  is the speed of the shock front, and  $W$  is the width of the transition region between the shocked and the unshocked state. The power dissipated at the shock front is thus controlled by the parameters  $B$  and  $W$ .

In crystalline solids the shock front moves *via* the coordinated motion of atoms. The interface between the shocked and the unshocked regions is thought to consist of a set of interface dislocations and a compressed zone (figure 3). The areal density of dislocations,  $\rho_{dis}$ , depends on the compression ratio according to

$$\rho_{dis} = \frac{1}{\sqrt{2}b} [1 - (\rho_0/\rho)^{1/3}], \quad (3)$$

where  $b$  is the Burgers vector. Figure 4 is a plot of this dependence. The dislocation spacing approaches  $b$  at high compression ratios. The shear strain rate at those dislocations (which travel with the shock front) becomes  $\dot{\varepsilon} = v_{sh}/b$ . Typical values are  $v_{sh} \approx 10^7$  cm/sec and  $b = 2.5 \times 10^{-8}$  cm, so that  $\dot{\varepsilon} \approx 4 \times 10^{14}$  sec $^{-1}$ . At such a high strain rate, even in a material as fluid as water (viscosity  $\sim 10^{-2}$  poise) the drag becomes  $4 \times 10^4$  kg/mm $^2$ ! Shock pulses therefore attenuate extremely rapidly. One way to reduce this drag pressure would be the use of metallic glasses which have a liquid-like structure on either side of the shock front. The intense localisation of strains arising from the smallness of the Burgers vector of the dislocations is then avoided.

### 3. Deformation at moderately high strain rates

At lower stress levels (the middle shaded region in figure 1), the deformation front advances at subsonic speeds. A typical example in this range of strain rates is the

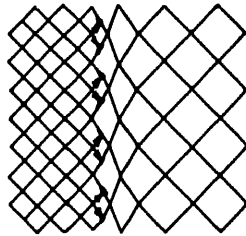


Figure 3. Schematic illustration of the interface structure at shock fronts in crystalline materials.

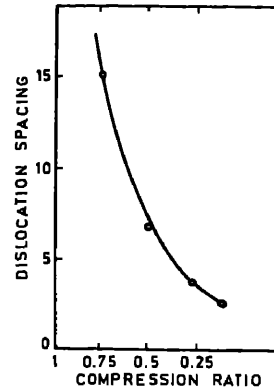


Figure 4. Variation of dislocation spacing (in units of  $b$ ) at the shock front as a function of the compression ratio.

deformation armour under ballistic attack. Strain in this regime normally occurs by dislocation movement. The flow is governed by high-velocity dislocation dynamics. The equation of motion for a dislocation line is of the form (Kocks *et al* 1973)

$$M\ddot{y} + B\dot{y} = b(\sigma - \tau), \quad (4)$$

where  $M$  is the 'mass' of the dislocation,  $B$  is the viscous drag coefficient,  $\sigma$  is the applied stress, and  $\tau$  is the lineglide resistance of the dislocation element against slow glide. Clearly,  $M$ ,  $B$  and  $\tau$  must be maximised for increasing the strength of the material. The 'mass'  $M$  of the dislocation can be shown to be

$$M = U/v_s^2 = 1/2 b^2 \rho, \quad (5)$$

where  $U$  is the line energy per unit length of the dislocation,  $v_s$  is the velocity of sound, and  $\rho$  is the material density of the material. Hence high density materials (*e.g.*, steel) and materials with large Burgers vectors (*e.g.*, intermetallics) offer greater resistance to dynamic flow. The drag coefficient  $B$  is controlled by the Peierls potential and the phonon-dislocation interaction. Dissipation of energy occurs when dislocations interact with phonons. In addition, shear-stress fluctuations due to phonons cause dislocations to flutter. Nonlinear elastic strains near dislocations also scatter phonons because of local changes of modulus and density (and hence of the speed of elastic waves). These mechanisms retard moving dislocations. Further, a moving dislocation has to build up and relax elastic strains, and this process is also retarded by the interaction with phonons. All these factors lead to a drag coefficient of the form (Kocks *et al* 1973)

$$B = k_B T / \Omega \omega, \quad (6)$$

where  $\Omega$  is the atomic volume and  $\omega$  is the atomic frequency. In contrast to the other mechanisms resisting flow, the drag  $B$  increases with temperature. Moreover, there is also a rapid increase of  $B$  when the speed of the dislocation  $\gtrsim 0.5 v_s$ . This is because the strain field of the dislocation begins to be compressed into smaller volumes (for lack of time!) at any given location. However, the discrete nature of the atoms and the low compressibility of atomic cores puts an upper limit to this contraction and allows

'supersonic' speeds to be reached at high stress levels, as in the shock waves discussed earlier.

Turning to the parameter  $\tau$  (the line glide resistance) in (4), we observe first that this resistance normally varies with the location on the glide plane. The Peierls resistance, for instance, varies periodically with a wavelength  $b$ . Solute atoms provide small discrete obstacles. Precipitates, interphase interfaces and cell or grain boundaries provide a coarser but stronger set of obstacles. Some of these obstacles are repulsive to dislocations, some are attractive and some are energy-storing. A schematic glide-resistance diagram is shown in figure 5. The spatial variation of the effective driving force on the dislocation results in an oscillatory motion superposed on its steady state motion. This induces radiation of elastic energy from the moving dislocation into the crystal. As this energy must also be supplied by the applied stress, the hills and valleys in the glide-resistance diagram contribute to the drag. The varying effective driving force also causes rapid acceleration or deceleration of the dislocation as it moves in the glide plane. The dislocation may then be able to overcome an obstacle on its path at least in part through its inertia. Attractive obstacles are specially prone to this phenomenon, for the energy picked up in the 'downhill' motion of the dislocation can facilitate its subsequent travel 'uphill'. Similarly, many small obstacles met with after passage through a large repulsive obstacle can be overcome dynamically. It is also possible for a moving dislocation to interact with near-by dislocations and transfer energy to them. Thus, under dynamic conditions obstacles incorporated in the matrix begin to lose their individuality and efficacy and the macroscopic concepts of flow stress may no longer be valid.

The onset of this dynamic behaviour is influenced by many factors. Higher values of the viscosity and larger obstacles sizes or spacing postpone the onset to higher dislocation velocities. Larger values of  $M$  and  $b$  favour an early transition. For obstacles of width smaller than a few Burgers vectors, dynamic effects emerge when (Kocks *et al* 1973)

$$(\sigma/G) > (k_B T / \Omega G)^2, \quad (7)$$

where  $\sigma$  is the stress level and  $G$  is the shear modulus. A rationale for specifying low- $T$  impact properties for armour materials is hidden in this above equation, because low temperatures bring out the dynamic effects at lower stresses and strain rates. This also suggests that the results of low- $T$  tensile tests may correlate better with ballistic performance when the highest suitable test temperature is chosen by the onset of simultaneous decrease in strength and ductility.

Certain alloy design criteria (for good ballistic performance) also emerge from this discussion. A material that must resist flow at the strain rates, presently under

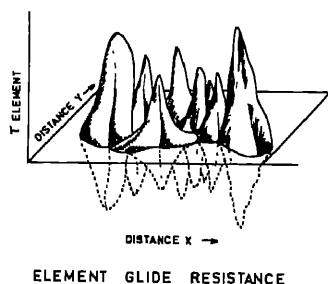


Figure 5. Schematic glide-resistance diagram in multiphase materials.

consideration, should not exhibit significant dynamic weakening. Thus, a high Peierls stress is particularly detrimental. Also undesirable are microstructures with precipitates that almost touch each other, as are attractive precipitates, even when they are strong. Long range barriers such as subgrains, martensite lath boundaries, strong and large ( $> 2000 \text{ \AA}$ ) repulsive precipitates, or repulsive-type solute elements would be the ideal candidates for the purpose at hand.

#### 4. Deformation at low stresses and strain rate

Even at low stresses materials can deform provided the temperature is sufficiently high to permit thermal activation of certain microscopic processes. This deformation mode, called creep, has been extensively studied over the years and a variety of equations, mechanisms and explanations have been proposed by various workers.

One particular widely-used semi-empirical equation is the 'power law', according to which the creep rate  $\dot{\epsilon}$  can be expressed as the product of a (small) power of the stress and an exponential function of  $T$ :

$$\dot{\epsilon} = A (Gb/KT) (\sigma/G)^n D_0 \exp(-Q/RT). \quad (8)$$

Here  $A$  is a constant,  $D_0$  is the preexponential in the diffusion coefficient,  $R$  is the gas constant and  $Q$  is the activation energy for diffusion. This equation has been shown to work for simple metals and ionic solids (Bird *et al* 1969). Nevertheless, many difficulties and unexplained modes of behaviour persist. The magnitude of the creep rate predicted by (8) is often incorrect (Evans and Knowles 1981). The index  $n$  lies anywhere between 1 and 6 and sometimes can be as high as 40 (Benjamin and Cairns 1971). The observed activation energy for creep often deviates significantly from that for diffusion, and in addition varies with  $T$  and  $\sigma$  (Poirier 1978). Moreover, even if there is a correlation between the activation volumes for self-diffusion and creep, one cannot unequivocally conclude that the creep is diffusion-controlled, because it can be shown that any process that depends on the pressure through the modulus will also have the same activation volume (Beyeler 1969). In spite of the large literature extant on the subject, a generally-agreed upon theory is lacking as yet.

##### 4.1 The stress exponents and the creep deformation mechanisms

The index  $n$  is unity for viscous flow in solids, as in fluids. This is a characteristic of microscopically homogeneous or structureless flow. Diffusional flow as in polycrystalline materials at elevated temperatures also exhibits a linear stress dependence. Basically, the applied stress serves only to generate higher point defect concentrations on grain boundaries under tensile stress relative to boundaries under no stress. The concentrations are exponential functions of  $(\sigma\Omega/k_bT)$  which approximate to linear functions of  $\sigma$  at low stress levels (Nabarro 1948; Coble 1963).

Several anomalies exist in the dislocation creep region. Stocker and Ashby (1973) have used a heuristic statistical analysis to prove that  $n = 3$  is the most probable value for dislocation creep. A simple way to see this is as follows: The dislocation density  $\propto \sigma^2$ , while the dislocation velocity  $\propto \sigma$ , in a viscous flow picture. Orowan's equation then directly leads to  $\dot{\epsilon} \propto \sigma^3$ . The same conclusion can also be reached if we treat the creep as being controlled by the coarsening of dislocation networks (Evans and Knowles 1981).

Dislocation creep that is controlled by recovery processes generally has a larger stress exponent. One such process is the mutual annihilation of dislocations with opposite Burgers vectors (or their segments) when they meet each other. If  $\rho_+$  and  $\rho_-$  denote the densities of dislocations with Burgers vectors of opposite signs, the annihilation can be considered as a second order reaction with a rate given by  $\dot{\rho} = K_1 v \rho_+ \rho_-$  where  $\rho$  is the total dislocation density and  $K_1$  is a reaction constant. The rate of reaction, and hence of recovery, is evidently greater the higher the dislocation velocity. The strain rate associated with the recovery can be written as  $\dot{\epsilon} = \dot{\rho} b s$  where  $s$  is the average distance travelled by a dislocation before annihilation. Substituting a quadratic dependence of the dislocation density on  $\sigma$  and a linear dependence of  $v$  on  $\sigma$ , we get

$$\dot{\epsilon} \sim \sigma^4. \quad (9)$$

This recovery strain rate leads to a proportional but larger glide strain rate, which is the observed strain rate. Thus, recovery-controlled creep is expected to have a stress exponent equal to four.

One may be tempted to combine such power laws into a general functional form

$$\dot{\epsilon} = \sum_n a_n (\sigma/G)^n, \quad (10)$$

where the  $a_n$  are independent of  $\sigma$ , a particular mechanism being associated with each distinct  $n$  value. Equation (10) implies that the control of the creep rate shifts to the mechanisms corresponding to higher  $n$  values with increasing stress. Often, however, this is not the case. One plausible conclusion from this is that the index  $n$  has no specific connection with any mechanism. Alternatively, one may invoke a back stress concept, such that the effective stress for creep is given by

$$\sigma_{\text{eff}} = \sigma - \sigma_b = \sigma - f_n(\sigma),$$

where  $\sigma$  is the applied stress and the function  $f_n$  depends on the specific mechanism concerned. The back stress can be considered as a measure of the energy spent on athermal steps that are essential for creep but do not directly lead to any significant creep strain. A specific illustration of the use of back stress concept is in the creep behaviour of particle-strengthened systems. Unusually large  $n$  values are often observed in both diffusional creep and dislocation creep regions (Benjamin and Cairns 1971). Recently, we have shown how the anomalous stress exponents in TD Nichrome and Mar M-200 superalloys fall in line with that for nickel once the back stress arising from strong dislocation-particle interactions is taken into account (Balakrishna Bhat and Arunachalam 1980; Balakrishna Bhat 1981). When the particles are attractive, the back stress appears as a threshold stress; when they are repulsive, the back stress increases with applied stress, reaching a limiting value as shown in figure 6. The back stress for diffusion creep is believed to be associated with the interaction of grain boundary dislocations with particles at the grain boundaries. It must be mentioned that the term 'back stress' has also been used in several different contexts. For example, it has been identified with the internal stress which includes the average stress field of the dislocation structure together with the cell boundaries (Pahutova and Cadek 1973; Argon *et al* 1981). In reality, the power law discussed earlier is the result of the interaction of defects among themselves and with the background stress field; the average stress field of the other defects is therefore already taken into account, and it is incorrect to include it once again in the back stress.

#### 4.2 Activation energy for deformation

**4.2a Activation energy and the bulk modulus:** The activation energy can be considered as the work a solid under load has to perform on itself in temporarily expanding against its own bulk modulus to accommodate the moving unit of flow. Figure 7 is a plot of  $Q/[\Omega(1 - P_f)]$  vs the bulk modulus for various metals. ( $P_f$  is the packing factor for the crystal). The approximately linear fit is noteworthy. It is interesting to note also that the activation energy is the energy that gets stored in the empty space  $\Omega(1 - P_f)$  as the solid momentarily dilates or contracts!

**4.2b Activation energy for dislocation creep and the creep mechanism:** A power law for creep presupposes that the activation energy for creep is equal to that for diffusion. However, the observed value of the activation energy is not constant. It increases with  $T$

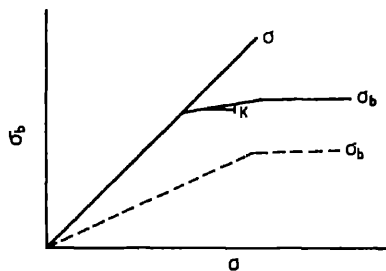


Figure 6. Schematic variation of back stress  $\sigma_b$  with applied stress  $\sigma$  in particle-strengthened alloy systems.

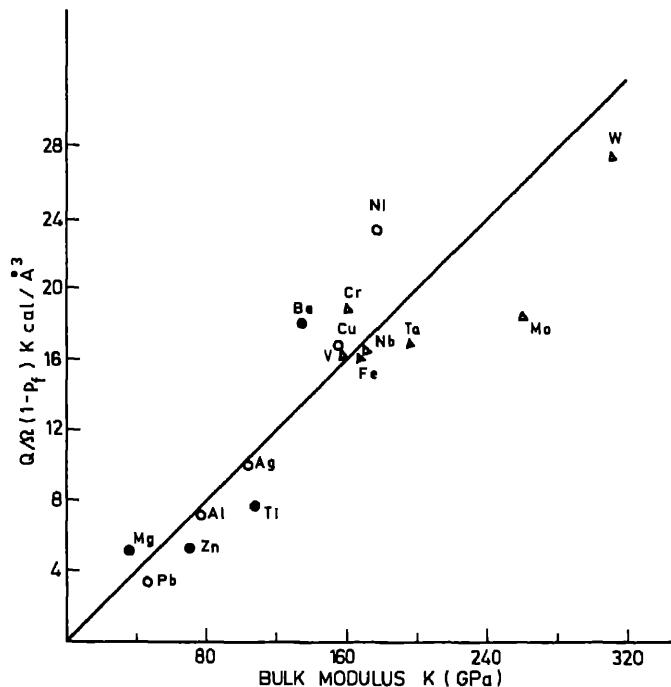


Figure 7. Dependence of  $Q/[\Omega(1 - P_f)]$  on bulk modulus for metals.

to match the activation energy for diffusion only in some small range of homologous temperature which, moreover, is different for each material (Poirier 1978). In particle-strengthened systems anomalously high and variable activation energies have often been reported.

It has often been suggested that the variation of the elastic modulus with temperature should account for the anomaly (Shewfelt and Brown 1974). However, this is not very convincing. Consider a force-displacement diagram between the atoms in a crystal as shown in figure 8. The elastic modulus reflects the rate of energy storage for infinitesimal displacements from the equilibrium value whereas the activation energy reflects the energy needed for a displacement equal to a lattice parameter which is more like the *area* under the curve. The inadequacy of the effect of  $T$  on  $E$  as a measure of its effect on  $Q$  is obvious.

The apparent activation energy for creep in particle-strengthened systems also depends on the back stress and its variation with temperature. This contribution to the apparent activation energy is given by (Balakrishna Bhat 1981)

$$\Delta Q = [nRT^2/(\sigma - \sigma_b)] [\partial \sigma_b / \partial T]. \quad (11)$$

For diffusion creep with low  $n$  and  $\sigma_b$ , the contribution is relatively small. For dislocation creep with large  $n$  and  $\sigma_b$  (as in TD nichrome), the contribution can be large. Further,  $\sigma_b$  varies an order of magnitude more rapidly with  $T$  than is predicted by the variation of the elastic modulus alone. The reason for this difference is not clear at the moment. Perhaps, with increasing  $T$  dislocation climb increases exponentially, facilitating the selection of easier flow paths by a sampling of the field of glide resistance along all three axes. The effective glide resistance (which one may call the 'volume glide resistance') or the back stress for creep will be different from the 'plane glide resistance' derived for a planar distribution of obstacles and a largely in-plane overcoming of obstacles by the dislocations. During creep, dislocations accumulate in difficult-to-glide locations and direct the other dislocations to climb over to easier regions of flow. When once climb has become possible, the back stress changes only slowly with temperature (figure 9).

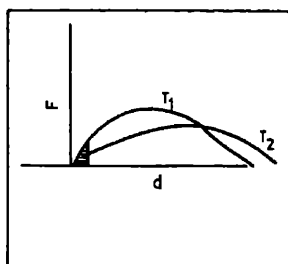


Figure 8. Atomic force-displacement diagram for two different temperatures.

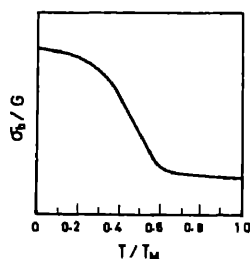


Figure 9. Temperature dependence of the back stress in particle-strengthened alloys.

A consequence of the volume-sampling hypothesis is that high  $n$  and high  $Q$  are not necessarily coupled. Even at high temperatures,  $\sigma_b$  in ODS alloys can be relatively large, giving a large effective  $n$ . The volume-sampling process reaches saturation above a particular temperature and the back stress then drops slowly with further increase of  $T$ . The apparent activation energy would then be small in spite of a large  $n$  value. Indeed, the results of Benjamin and Cairns (1971) on ODS alloys show a modulus-compensated activation energy close to that for self-diffusion in spite of a high apparent stress exponent of 32.8 at  $T = 1350^\circ\text{C}$ . At a lower temperature, a lower  $n$  value is obtained, but  $Q$  is still twice the activation energy for self-diffusion. Another consequence of volume-sampling is that there will be no influence of particle shape on the  $T$ -dependence of  $\sigma_b$  for a random distribution of obstacles, since the  $T$ -dependence arises primarily from the climb-controlled volume-sampling of weaker regions from the same random distribution of obstacles, and not from climb around individual particles. This observation is substantiated by the experiments of Shewfelt and Brown (1974). It would be of interest to perform a computer simulation of this volume-sampling glide process during the creep of particle-strengthened systems, in order to optimize the particle size and distribution for effective resistance to creep flow.

### 5. Additivity of creep rates

An unsolved problem in creep relates to the additivity of creep rates through various mechanisms. The expansion of (10) presupposes such additivity. All theoretical treatments to date have also made this assumption. However, the basic physical processes involved cast a doubt on the validity of this assumption.

Consider for instance diffusion creep and grain boundary sliding. Diffusion creep elongates the grains; when added over all the grains, this leads to directional elongation. However, grain sliding events as in superplastic flow introduce new directions for diffusional creep, with the net result of eliminating diffusion creep on the average.

Then again, dislocation creep pre-empts diffusion creep by consuming vacancies en route as they move from one grain boundary to the other. Dislocation creep also generates ledges on grain boundaries and hinders both diffusion creep and grain boundary sliding. On the other hand, diffusion creep tends to retard the onset of grain boundary sliding by generating nonequiaxed grains. It also retards dislocation creep by not allowing large stress concentrations to build up at the grain boundaries. Thus, each mechanism appears to possess an intrinsic inhibiting effect on the others, which may explain why one obtains well-delineated deformation mechanisms in creep experiments. The opposite can also happen in some cases. For example, dislocation glide and climb favour each other. Dislocation activity at the grain boundary zone can enhance grain boundary diffusivity and hence superplastic strain rates. Computer simulation of the deformation process should be of help in understanding these coupled processes.

### 6. Summary

Our discussion above may be summarized in the form of the following specific questions:

(a) Will metallic glasses exhibit low damping of shock waves? (b) Can low temperature tensile and compressive tests be used to design alloys for good ballistic performance?



(c) Will attractive precipitates prove inferior to repulsive precipitates in the context of ballistic resistance? (d) Can the Arrhenius term in the creep rate be rewritten as a combination of the bulk modulus, the atomic volume and the packing factor? (e) Is the back stress concept relevant, and is it correct to subtract internal stresses due to defects which move to cause strain? (f) Can a microstructure suitable for optimal creep resistance be designed using the concept of volume glide resistance? (g) Can the strain rates arising from different mechanisms be considered to be additive, even though some of them appear to be mutually inhibiting?

### Acknowledgements

The author acknowledges many useful and inspiring discussions with Dr V S Arunachalam and Prof. K Srinivasa Raghavan during the course of this work. He is also grateful to Dr P Rama Rao for inspiring him to write this article. The curves in figure 9 are a result of discussions with Shri A K Gogia.

### References

- Argon A S, Print F and Moffatt W C 1981 in *Creep and fracture of engineering materials and structures* Proc. Int. Conf., Swansea, U.K.
- Balakrishna Bhat T and Arunachalam V S 1980 *J. Mat. Sci.* **15** 1614
- Balakrishna Bhat T 1981 *Effect of second phase on microstructural development and engineering properties* Ph.D. Thesis, Indian Institute of Technology, Madras
- Balakrishna Bhat T 1983 *Principles for protection* Trans. I.I.M. (to be published)
- Benjamin J S and Cairns R L 1971 in *Modern developments in powder metallurgy* (ed) H Hausner (New York: Plenum) **5** 47
- Beyeler M 1969 Report CEAR 3715
- Bird J E, Mukherjee A K and Dorn J E 1969 in *Quantitative relations between properties and microstructure* (eds) D G Brandon and A Rosen, (Jerusalem: Israel University Press) p 255
- Coble R L 1963 *J. Appl. Phys.* **34** 1679
- Evans H E and Knowles G 1981 in *Creep and fracture of engineering materials and structure* Proc. Int. Conf. at Swansea, U.K. (eds) B Wilshire and D R Owen J. p 169
- Gilman J J 1979 *J. Appl. Phys.* **50** 4059
- Kocks U F, Argon A S and Ashby M F 1973 *Thermodynamics and kinetics of slip* (Illinois: Argonne National Laboratory)
- Malu M and Tien J K 1975 *Scr. Met.* **9** 1117
- Nabarro F R N 1948 Report of a Conference on the strength of solids 1963 The Physical Society, London 1.
- Pahutova M and Cadek 1973 *J. Mater. Sci. Eng.* **11** 151
- Poirier J P 1978 *Acta Metall.* **26** 629
- Shewfelt A S W and Brown L M 1974 *Philos. Mag.* **30** 1125
- Stocker R L and Ashby M F 1973 *Scr. Met.* **7** 115

### Discussion

K A Padmanabhan: Your statement that dislocations could move as fast as the shock front does not appear to tally with the detailed analysis of J D Eshelby on dynamical effects on dislocations. Moreover, as in special relativity, the mass of a dislocation increases with its velocity. Incidentally, Dr Chidambaram's observation that the density of dislocations at the shock wave front is  $\sim 10^{11} \text{ cm}^{-2}$  also indicates that the total strain arises from a larger number of dislocations rather than a few moving at extremely high speeds.

N Kumar: In his book, Frank describes what led him to the theory of the Frank-Read mechanism: the realization that the velocity of a dislocation could never exceed the velocity of sound.

Bhat: When the width and amplitude of the incident impulse are large, shock waves travelling at speeds higher than the speed of sound develop. The strain gradients at the front have to be established in the short duration of the passage of the front, so that the strain rate becomes high. This strain rate can be achieved by either or both the terms in the classical equation  $\dot{\epsilon} = \rho b v + \dot{\rho} b s$  where the symbols are as explained in the text. Clearly, movement of the dislocations is required,  $v$  being associated with  $\rho$  and  $s$  with  $\dot{\rho}$ . If quasistatic dislocations alone account for the shock front, the shocked stress state would acquire permanence in the material. When shock waves can travel faster than the speed of sound, dislocations too can do the same. Physically both share the same important characteristics—strains and strain gradients in their vicinity.

S N Bandhopadhyay: The basic equations of plasticity like those for the velocity field, strain field, localized modes of deformation etc., do not appear to be taken care of properly in the finite element modelling of deformation.

Bhat: I think that the finite element method specialises in taking care of localized modes of deformation *without* sacrificing the basic equations of plasticity.

K A Padmanabhan: Did you measure the back stress in your experiment by either the stress reduction or stress relaxation method? Otherwise you are just introducing an adjustable variable.

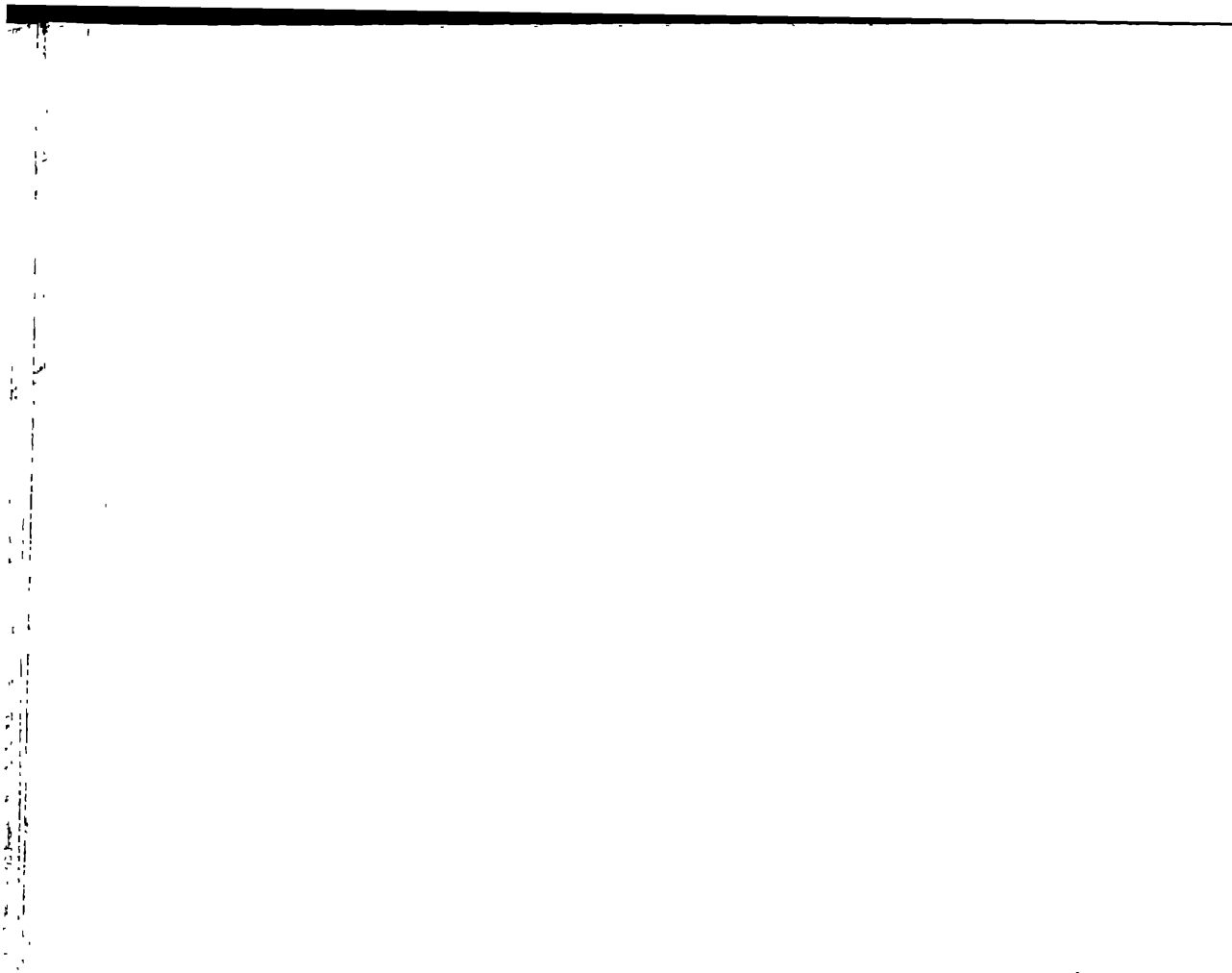
Bhat: The existence of the back stress has not been experimentally established, and it cannot be measured directly. It is felt only by the dislocation that is moving in a structure. Even though the back stress is an adjustable empirical variable it has a certain consistency associated with it. When we introduce this parameter in order to bring the stress exponents to normal values, the anomalous activation energies in such materials automatically come down to normal values for diffusion. This certainly suggests that back stress is a parameter that has some fundamental significance associated with it.

V Balakrishnan: Regarding the computer simulation results on deformation, if you begin with empty spaces between grains, should you not expect further cavitation to occur? Or do you have hydrostatic stress, and the cavities just get filled in?

Bhat: We apply hydrostatic or uniaxial compressive loading in order to simulate hot pressing conditions.

V Balakrishnan: Within a single grain or element, what sort of compatibility conditions do you put in to ensure that no holes are formed?

Bhat: Strain compatibility conditions are put in to ensure that any particular mode has a unique displacement. Regarding your observations on the additivity *vs* interdependency of various creep mechanisms, another interesting example is provided by grain boundary sliding and diffusion creep. Grain boundary sliding occurs via the climb as well as glide of dislocations at the boundary. Climb generates vacancies which can in turn lead to vacancy creep.



## Superplasticity

K SRINIVASA RAGHAVAN

Department of Metallurgical Engineering and Department of Physics, Indian Institute of Technology, Madras 600 036, India

**Abstract.** Superplasticity is the phenomenon of extraordinary ductility exhibited by some alloys with extremely fine grain size, when deformed at elevated temperatures and in certain ranges of strain rate. To put the phenomenology on a proper basis, careful mechanical tests are necessary. These are divided into (i) primary creep tests, (ii) steady state deformation tests, and (iii) instability and fracture tests, all of which lead to identification of macroscopic parameters. At the same time, microstructural observations establish those characteristics that are pre-requisites for superplastic behaviour. Among the macroscopic characteristics to be explained by any theory is a proper form of the equation for the strain rate as a function of stress, grain size and temperature. It is commonly observed that the relationship between stress and strain rate at any temperature is a continuous one that has three distinct regions. The second region covers superplastic behaviour, and therefore receives maximum attention. Any satisfactory theory must also arrive at the dependence of the superplastic behaviour on the various microstructural characteristics. Theories presented so far for microstructural characteristics may be divided into two classes: (i) those that attempt to describe the macroscopic behaviour, and (ii) those that give atomic mechanisms for the processes leading to observable parameters. The former sometimes incorporate micromechanisms. The latter are broadly divided into those making use of dislocation creep, diffusional flow, grain boundary deformation and multimechanisms. The theories agree on the correct values of several parameters, but in matters that are of vital importance such as interphase grain boundary sliding or dislocation activity, there is violent disagreement. The various models are outlined bringing out their merits and faults. Work that must be done in the future is indicated.

**Keywords.** Superplasticity; ductility; stress and strain rate; grain boundary; dislocation creep; diffusional flow.

### 1. Introduction

Structural superplasticity is a high-homologous-temperature phenomenon exhibited by some metals and alloys which suffer extended or anomalous ductility under restricted circumstances. Elongations amounting to a few thousands per cent have been reported. When the conditions of deformation are changed, the same material does not possess the same ductility, and this has led to serious inquiries into the fundamental reasons for this behaviour. The technological off-shoot of this research, *viz.*, the development of many commercial alloys as well as forming processes, has not lagged behind. The aim of this paper is to summarize the observations made on superplastic materials and to identify their characteristics, to list the most important mechanisms identified as responsible for this behaviour, and to outline the more important models/theories presented so far. For recent reviews, see Edington *et al* (1976), Gifkins (1982), Hazzledine and Newbury (1976) and Padmanabhan and Davies (1980). Some points of controversy, which needs to be eliminated, are indicated.

## 2. Observations

The first systematic study on low-melting eutectics displaying superplasticity (Pearson 1934) is by now familiar. Observations on superplastic materials may be divided broadly into two classes: (i) those involving macroscopic aspects, from mechanical deformation studies; and (ii) those involving microscopic aspects, from microstructural observations.

### 2.1 Macroscopic observations

The variables are stress, strain, strain rate and temperature. However, a curve as shown in figure 1 is most common, showing the relationship between the flow stress  $\sigma$  and the strain rate  $\dot{\epsilon}$ . This relationship can be mathematically written as

$$\sigma = A \dot{\epsilon}^m, \quad (1)$$

where  $A$  is a constant and  $m$  is the strain rate sensitivity index (on a log-log plot, the slope of the curve). Three regions can be recognized which may conveniently be labelled I, II and III. Region II is the one of interest, where superplasticity is displayed. The peak values of  $m$  in this region coincide with maximum elongation, indicating a direct, if not linear, relation between them. In the superplastic region,  $m$  has values from 0.3 to 0.9. It may be mentioned here that all the three regions of figure 1 may not be found with a single experimental set-up.

The steady state strain rate in region II may be expressed in the familiar form of a diffusion-controlled process according to

$$\dot{\epsilon} \propto \frac{Gb}{k_B T} (b/d)^p (\sigma/G)^n D_0 \exp(-Q/RT), \quad (2)$$

where  $G$  is the shear modulus,  $b$  is the magnitude of the Burgers vector, and  $d$  the grain size.  $D_0$  and  $Q$  denote a pre-factor and activation energy, respectively, while  $p$  and  $n$  are indices to be determined. Alternative equations to describe the behaviour of  $\dot{\epsilon}$  are also available in the literature. Their relative merits will be discussed in a later section.

The (thermal) activation energy in (2) may be determined by three different methods (Langdon 1982): (i) changing the temperature very rapidly during a test on a single

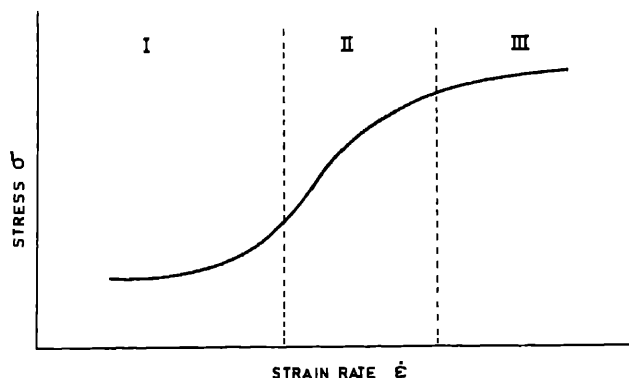


Figure 1. Flow stress plotted against strain rate.

specimen at constant stress; one finds

$$Q = \frac{R \ln (\dot{\epsilon}_2 G_2^{n-1} T_2) (\dot{\epsilon}_1 G_1^{n-1} T_1)}{[(T_2 - T_1)/(T_1 T_2)]}, \quad (3)$$

where  $\dot{\epsilon}_1$  and  $\dot{\epsilon}_2$  are the strain rates before and after the increase in temperature, and  $G_1$  and  $G_2$  the values of the shear modulus at the respective temperatures. (ii, iii) data from different specimens tested to steady state flow yield either

$$Q_\sigma = -R \left( \frac{\partial \ln \dot{\epsilon} G^{n-1} T}{\partial (1/T)} \right)_{d, \sigma}, \quad (4)$$

or, in another version,

$$Q_\epsilon = R \left( \frac{\partial \ln (\sigma^n / G^{n-1} T)}{\partial (1/T)} \right)_{d, \epsilon}. \quad (5)$$

We shall assume the equality of these two versions. Typical values of  $Q$  for the three regions suggest an activation energy for self-diffusion,  $Q_{SD}$ , in region I, an activation energy for grain boundary diffusion in region II, and an activation energy equal to or lower than  $Q_{SD}$  in region III.

The different activation energy values led to the belief that several mechanisms were operative. It must be noted here that  $m (= 1/n)$  varies with strain rate at different temperatures. The index  $m$  itself can be measured in several ways (Edington *et al* 1976). With the experimental values of  $n$  and  $Q$ , the grain size index  $p$  can be obtained by plotting  $\dot{\epsilon}$  vs the grain size at constant stress and temperature. A  $p$  value between 2 and 3 is typical of a number of superplastic materials in region II.

## 2.2 Metallographic observations

The microstructural study of superplastic materials includes surface observation through optical microscopy, replica electron microscopy and scanning electron microscopy, and internal structure determination through transmission electron microscopy. On a few specimens, fracture and cavitation have also been studied. Of great importance is the relative contribution of grain boundary sliding to the total strain. Microstructural observations made on specimens undergoing superplastic deformation show that: (i) there is no massive recrystallisation, (ii) there is grain rotation (both ways), (iii) a new surface is created, (iv) texture is generally reduced: (a) texture weakens continuously with strain; (b) texture weakens to a steady distinct lower level; (c) texture generally weakens, while retaining some components. (In some cases, new texture is introduced). (v) there is little dislocation activity, (vi) there is deformation near grain boundaries, (vii) grain boundary sliding takes place, (viii) there is diffusional flow in region I.

It is clear that any model proposed to explain superplastic behaviour must satisfactorily account for these observations. It must also lead to the proper constitutive equations to give the activation energy, strain rate sensitivity index and the grain size index. The general conclusions that may be drawn from the results of metallographic observations are listed in the next section.

### 3. Characteristics of superplastic materials

From the various observations made, the following general conclusions may be drawn (Sherby and Ruano 1982): (i) The superplastic material must have a fine grain size ( $\leq 10 \mu\text{m}$ ), which must remain so, (ii) the presence of a second phase is necessary to inhibit grain growth, (iii) the mechanical strength of the second phase must generally be of the same order as that of the matrix, (iv) the second phase, if harder, should be finely distributed within the matrix, (v) the grain boundaries between the matrix grains should be of the high angle kind, (vi) the grain boundaries should be mobile so as to reduce stress concentration at triple points, (vii) the grains should be equiaxed in order to enable a grain boundary to experience a shear stress, allowing grain boundary sliding to occur, (viii) the grain boundaries must resist tensile separation.

### 4. The role of grains

Noting that superplasticity is confined to materials with fine grains which remain fine-grained and equiaxed, one can conclude that the grain centres must move as if the material were deforming homogeneously (Hazzledine and Newbury 1976). Thus it is necessary that the grains slide past one another during deformation. Sherby and Ruano (1982) have considered two phenomenological equations

$$\dot{\epsilon} = 10^9 \frac{D_{\text{GB}} b}{d^3} (\sigma/E)^2 \quad (6)$$

when grain boundary diffusion is thought to be the rate-controlling step, and

$$\dot{\epsilon} = 10^8 \frac{D_{\text{latt}}}{d^2} (\sigma/E)^2, \quad (7)$$

when lattice diffusion is considered to be the rate-controlling step. Experimentally a plot of  $(\dot{\epsilon} d^3 / b D_{\text{GB}})$  vs  $(\sigma/E)$  gives the correct exponent, namely, 2. Grain boundary sliding is therefore conceded to be the dominant mechanism.

Grain boundary sliding has been sought to be explained as brought about either by the motion of dislocations or by diffusion. In the dislocation model, crystal dislocations gliding to a grain boundary confine their subsequent motion to its vicinity. Special grain boundary dislocations whose Burgers vector is different and is related to a particular boundary may also move conservatively with the grain boundary. In this model, the strain-rate sensitivity  $m$  could be manipulated to be less than one, but then the grains would have to be elongated, which is not observed. On the other hand, the diffusion model considers the easy sliding of grains on smooth portions. If further sliding is opposed by irregularities, the rate of sliding is controlled by the movement or elimination of irregularities by diffusion. Such sliding could take place also at interphase boundaries. (These are classical notions and have been questioned by Padmanabhan and Davies 1980). However, since the strain rate is directly proportional to the applied stress,  $m$  will have a value of 1, which is at variance with experimental values. It would therefore appear that changes in the grain shape must also be taken into account.

#### 4.1 Grain strain

Since structural continuity must be preserved, the grains must undergo some strain. This can be thought of in two different ways. Vacancy diffusion in the bulk can result in a change of shape, when the path of diffusion is fully across the grain. This Herring-Nabarro creep is given by the expression

$$\dot{\epsilon} = (20 D_{\text{lat}} \Omega) / (k_B T d^2), \quad (8)$$

where  $\Omega$  is the atomic volume. When the diffusion path is confined to the grain boundary region, one has Coble creep, given by

$$\dot{\epsilon} = 50 D_{\text{GB}} \Omega \delta / (k_B T d^3). \quad (9)$$

Here  $\delta$  is the width of the diffusion path. It may be noted that in both the above expressions,  $m = 1$ .

On the other hand, matter can be moved by conservative and non-conservative motion of dislocations. Nabarro (1967) has given two expressions, the first being a power dependence  $\dot{\epsilon} \propto \sigma^3$ ; the second for pipe-diffusion along the cores of dislocations, leads to  $\dot{\epsilon} \propto \sigma^5$ . It may be mentioned that the grain size does not figure in these expressions. Friedel creep envisages a pile-up of dislocations against a grain boundary, from which the leading dislocation climbs into the grain boundary. The process is controlled by the climb rate of dislocations. This has been utilized to yield a relation  $\dot{\epsilon} \propto \sigma^2$ . However, it is clear that grain elongation is unavoidable, and that as the grains elongate, the process must be exhausted. There is nothing in this picture to indicate the rotation of the grains. Moreover, no dislocation pile-ups have been observed in superplastic alloys.

#### 4.2 Interaction between grain strain and grain boundary sliding

It is commonly believed that neither of the above can take place without the other, as they must together produce strain rates compatible with one another. The amount of strain produced by grain sliding is usually measured by surface markers, even though there is considerable controversy about the measurement. However experimentally the value ( $\epsilon_{\text{GBS}}/\epsilon_{\text{tot}}$ ) varies between wide limits. It may be pointed out here that such measurements have been made at a strain of about 0.2, which is not typical of superplastic deformation. Stevens (1971) puts an upper limit of 0.62 to this ratio. Hazzledine and Newbury (1976) point out that at any instant the strain rate due to sliding is of the same order as the rate of strain of the grain.

Nevertheless, the idea has persisted that the strain due to grain boundary sliding must necessarily be less than the total strain. Consequently, an overwhelming majority of the mechanisms suggested invoke some process or the other to accommodate grain boundary sliding. It is against this background that different mechanisms are outlined in the next section. It is instructive to reproduce the figure from Edward and Ashby (1979) illustrating the different accommodation processes (figure 2).

### 5. Atomic mechanisms for superplasticity

It has been pointed out earlier that mechanisms employing diffusion creep or slip are unable to account for many of the observations satisfactorily, in particular for the large



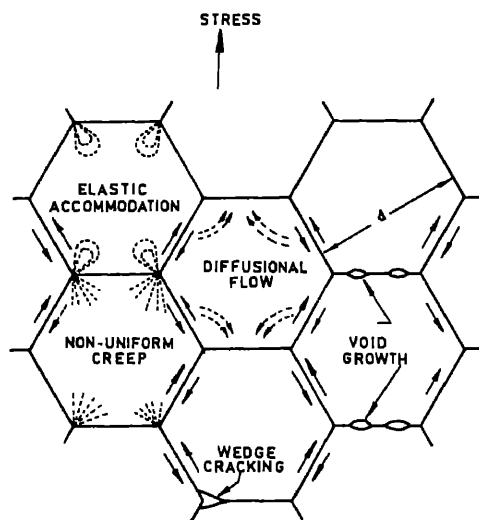


Figure 2. Consequences of grain boundary sliding (After Edward and Ashby 1974).

amount of grain boundary sliding. In this section, some more mechanisms will be listed where grain boundary sliding (GBS) is considered along with some accommodating processes.

### 5.1 GBS accommodated by dislocation motion

Ball and Hutchison (1968) put forward the idea that several groups of grains slide at once. When there is an unfavourably oriented grain, a stress concentration results which can be relieved by dislocation motion. The dislocations, which are necessarily in a pile-up, prevent further sliding until the lead dislocation climbs. Mukherjee (1971) contended that the grains move individually. Again a pile-up is invoked because dislocations are produced by irregularities in the grain boundaries. This itself is a major difficulty since, as mentioned earlier, no pile-ups have been seen. Moreover, the same dislocation motion will be rate controlling in region III too, and it would be impossible to distinguish between the two.

### 5.2 GBS and diffusion creep

Ashby and Verrall (1973) proposed a grain switching event as central to their model. A group of four grains reacts to a tensile stress, sliding past each other and changing their shape to maintain continuity. These switching events occur randomly throughout the specimen with various clusters in different stages of the process. The accommodation strain is accounted for by bulk and boundary diffusion. While the model, which considers the topological aspects of the sliding process, satisfactorily explains most of the observations, there are large variations in the predicted values of parameters.

Hazzledine and Newbury (1976) have used the concept of grain emergence: as a group of adjacent grains slide, a grain from the layer below emerges at a location where a fissure would otherwise open up. Grain boundary migration occurs at the same time to restore the dihedral angles, resulting in the rounding off of the emergent grain and

the curvature of all other grain boundaries. Having conceded that the phenomenon is too complicated for analysis, Hazzledine and Newbury proceed to give a viscoelastic model of superplasticity with several dashpot elements representing Nabarro, Coble and Friedel creep, as well as grain boundary and interphase sliding. The general conclusion is that a single comprehensive mechanism is not possible.

### 5.3 *GBs and core-mantle theory*

Gifkins (1976) proposed for each grain a non-deforming core surrounded by a mantle in which flow occurs. While the core contains statistically stored dislocations, the mantle, which is a few per cent of the grain diameter, contains geometrically necessary dislocations. The grain boundary dislocations piled-up against a triple edge are responsible by their movement for grain boundary sliding. The stress concentration of the pile-up is regarded as that of a freely slipping crack. By climb and glide the lead dislocations accommodate grain boundary sliding. Gifkins arrived at an appropriate equation to account for the observed parameters. Since the widths of the core and mantle are adjustable parameters, the experimental verification has been criticised as "an exercise in curve fitting". Further, no single mechanism has been identified as responsible for superplasticity.

Arieli and Mukherjee (1980) have also criticised this model on the ground that the deformation will slow down in time and eventually come to a stop, since many dislocations will be lost by annihilation. Also the stress concentration has been calculated by the Eshelby, Frank and Nabarro method, which does not apply to climb or any other deformation process.

Arieli and Mukherjee themselves employed a modified mantle behaviour. The small number of pre-existing dislocations are attracted to the boundary under the action of the applied stress and their own line-tension. The individual dislocations climb the short distance to the boundary and, in the process, create new dislocations by the Bardeen-Herring mechanism. At the boundary, the dislocations are annihilated. The eventual stress concentration created by the dislocations climbing into the boundary are relaxed by grain boundary diffusion. It may be noted here that there has been no experimental evidence for the Bardeen-Herring mechanism.

### 5.4 *Micromultiplicity*

As the grain boundary network has alternate sets of shear paths, the deformation continues even if grain boundary sliding is obstructed locally. In other words, the local stress conditions would alternatively enhance or decrease the importance of the obstacles. A number of processes, mentioned above, could be appropriately combined to give the total strain rate. It is obvious that this is also merely a curve-fitting exercise since the arbitrary constants of the constitutive equations can be adjusted appropriately.

### 5.5 *Unaccommodated GBs*

There has been considerable controversy as to whether grain boundary sliding is independent of diffusional strain. The work of Raj and Ashby (1972), Speight (1975) and Beere (1976) has shown that specimen strain can only develop when both sliding

and diffusion can operate simultaneously. Therefore the deformation can be attributed to either sliding or diffusion, and can be described as diffusion-accommodated sliding or sliding-accommodated diffusion; in no sense can they contribute independently (Burton 1977).

Accordingly, Padmanabhan (1977) regards the upper limit of 60–65 % placed on the contribution from sliding to be a consequence of the assumption that both diffusion and sliding are present as separate steps. It is also held that the ideas concerning sliding in coarse-grained materials were not necessarily relevant to sliding in ultrafine-grained alloys, and that superplastic deformation is a result of pure grain boundary sliding of non-deformation grains that require no accommodation. Starting from the fundamental rate equation one arrives at a constitutive equation

$$\dot{\epsilon} = C \frac{\delta}{d^2} \sigma^n \exp(-Q_0/RT), \quad (10)$$

where  $C$  is a constant and  $\delta$  is the jump distance in the grain boundary region. The stress exponent  $n$  may be recognized as the inverse of the strain-rate sensitivity index,  $m$ , and is shown to be a function of stress, grain size and temperature. Excellent agreement with experimental results is achieved, as is a demonstration of the transition to the region III in which climb-controlled motion of dislocations occurs.

## 6. The activation energy for superplasticity

The activation energy  $Q$  has been introduced in (2). It was mentioned there that different values are obtained for  $Q$  in the three regions of figure 1. This is done by treating the sigmoidal curve as a combination of three linear curves. The assumption of the equality of  $Q_s$  and  $Q_b$  ((4) and (5)) has also been mentioned. Padmanabhan (1981) has objected to the procedure on the grounds that (2) is empirical, that for each range a constant but different  $n$  value is assumed, and that within each range the activation energy is assumed to be independent of the temperature and the stress level of its evaluation. He has pointed out that the evaluation of the activation energy from an equation that has no physical basis is bound to lead to erroneous results, and that since  $n$  is continuously variable, there is no justification for treating this as a constant. At the junctions of region II with regions I and III the  $n$  value becomes ambiguous. Topologically and microstructurally regions I and II are not different. Only region III indicates a change of mechanism. Another serious objection is the treatment of an expression containing a  $T$ -dependent pre-factor as a true Arrhenius form. Padmanabhan (1981) has derived expressions for  $Q_s$  and  $Q_b$  (the values corresponding to the shear mode) and has pointed out that the best estimates of the real activation energy are only attained when data pertaining to the range in which  $m$  is large ( $\sim 1$ ) are used. It is regrettable that many of the leading workers in the field have not recognized the force of these arguments.

## 7. The role of dislocations in superplasticity

Even though many of the models invoke dislocations to explain superplasticity, there has been no direct experimental evidence to support dislocation activity. However,

Edington *et al* (1976) have argued, taking Nicholson's (1972) experiments as an example, that dislocations might have been active or that they might have been obstructed by precipitates. Padmanabhan (1980) has argued that this was unlikely. He has further held that any dislocation seen was the residue of the initial configuration or the existence of local stress concentrations or a favourable strain rate at which dislocation motion commences. *In situ* experiments have also failed to reveal substantial quantities of dislocation.

Melton and Edington (1973) have maintained that since (i) statistically significant differences in the angular distance of the dislocations from their nearest possible glide planes were found as a function of the deformation rate; (ii) the Burgers vector distribution changed as a function of strain rate; (iii) increasing the initial density by cold working prior to superplastic deformation did not produce any detectable differences in the Burgers vectors and densities after superplastic deformation; (iv) there is an equilibrium dislocation density typical of superplastic flow and (v) dislocations are also observed at strain rates an order of magnitude less than that corresponding to  $m_{\max}$ , one must conclude that crystallographic slip plays a small but significant role in superplasticity. Padmanabhan (1980) has countered these arguments by citing experimental results accepted by Melton and Edington themselves. It therefore appears that the available experimental evidence could support either point of view. Lücke (1974) has pointed out that any sequence of deformation processes leading to a given strain tensor will give the same texture. Hence the operating mechanisms cannot be deduced solely from texture results. TEM has provided no evidence for dislocation activity.

## 8. Future work

To set at rest the controversy regarding the mechanism of superplasticity, work is required along the lines indicated below: (i) a better understanding of the structure of grain boundaries and interphase boundaries, (ii) a correct analytical form for the flow stress as a function of strain rate, temperature and grain size, (iii) unequivocal experimental evidence to support or discount dislocation activity, (iv) an understanding of the role of the stacking fault energy, (v) an unambiguous interpretation of experimental curves such as the double sigmoidal plot of figure 1.

It is to be hoped that there will be a happier conclusion to superplasticity than in the case of work hardening, in which field the workers have apparently agreed not to agree.

## Acknowledgements

The author is indebted to Prof. K A Padmanabhan of IIT, Madras for many valuable clarifications.

## References

- Arieli A and Mukherjee A K 1980 *Mater. Sci. Eng.* **45** 61
- Ashby M F and Verrall R A 1973 *Acta Metal.* **21** 149
- Ball A and Hutchison M M 1968 *Met. Sci. J.* **3** 1
- Beere W B 1976 *Met. Sci. J.* **10** 133
- Burton B 1977 *Diffusional creep in polycrystalline materials* (Ohio: Trans Tech Publications)

- Edington J W, Melton K N and Cutler C P 1976 *Prog. Mater. Sci.* (eds) B Chalmers, J W Christian and T B Massalski (Oxford: Pergamon Press) Vol. 21 p. 61
- Edward G and Ashby M F 1979 *Acta Metal.* **27** 1505
- Gifkins R C 1976 *Met. Trans.* **A7** 1225
- Gifkins R C 1982 in *Superplastic forming of structural alloys* (eds) N E Paton and C H Hamilton, The Metallurgical Society of AIME 3-26
- Hazzledine P M and Newbury D E 1976 in *Grain boundary structure and properties* (eds) G A Chadwick and D A Smith (New York: Academic Press) Chap. 7
- Langdon T E 1982 in *Superplastic forming of structural alloys* (eds) N E Patson and C H Hamilton, The Metallurgical Society of AIME 27-40
- Lücke K 1974 *Can. Metall. Q.* **13** 261
- Melton K N and Edington J W 1973 *Met. Sci. J.* **7** 172
- Mukherjee A K 1980 *Mater. Sci. Eng.* **8** 83
- Nabarro F R N 1967 *Philos. Mag.* **16** 231
- Nicholson R B 1972 in *Electron microscopy and structure of materials* (ed) G Thomas (University of California) 682
- Padmanabhan K A 1977 *Mater. Sci. Eng.* **29** 1
- Padmanabhan K A 1980 *Met. Sci.* **14** 506
- Padmanabhan K A and Davies G J 1980 *Superplasticity* (Berlin: Springer Verlag)
- Padmanabhan K A 1981 *J. Mater. Sci. Lett.* **16** 531
- Pearson C E 1934 *J. Inst. Met.* **54** 111
- Raj R and Ashby M F 1972 *Met. Trans.* **3** 1937
- Sherby O D and Ruano O A 1982 in *Superplasticity forming of structural alloys* (eds) C E Paton and C H Hamilton, The Metallurgical Society of AIME 241-256
- Speight M V 1975 *Acta Metall.* **23** 779
- Stevens R N 1971 *Philos. Mag.* **23** 265

## Grain boundary-dislocation interactions\*

S RANGANATHAN

Department of Metallurgy, Indian Institute of Science, Bangalore 560012, India

**Abstract.** Our current understanding of the structure of grain boundaries will be described first. The structure of low angle boundaries can be rigorously described in terms of arrays of dislocations. The structure of high angle boundaries continues to defy a complete and rigorous description. A model has been developed based on coincidence site lattices. This model postulates the presence of grain boundary dislocations even at high angles of misorientation to accommodate the deviation from exact coincidence conditions. The Burgers vectors of such grain boundary dislocations can be found by the translation vectors of the DSC lattice. An interesting point is that the Burgers vectors are not lattice translations. Hence the dislocations are confined to the surface of the boundary and cannot move into the grain. Alternative descriptions of the structure of grain boundaries make appeal to the Bernal type of polyhedral voids that occur in metallic glasses. A brief discussion of the strength of this approach will be outlined. Dislocations at grain boundaries can affect both grain boundary migration and sliding. The possible mechanisms for these phenomena will be described. The importance of understanding these mechanisms to explain deformation of metals at high temperatures will be stressed.

### Discussion

M Youssuff: Is it possible to include vacancies in the approach you have described?

S Ranganathan: This is an important question; the answer is not known.

P Rodriguez: How do you explain migration with the help of imprisoned grain boundary dislocations?

Ranganathan: It is easy to explain this migration in a framework similar to Aronson's theory of the growth of precipitates. For example, in cases where the ledge mechanism operates, the ledges move along the plane in which the precipitate is growing.

Rodriguez: If we provide energy in the form of stress, is it possible that the smaller grain boundary dislocations combine to form larger mobile lattice dislocations?

Ranganathan: It should be possible, but no clear evidence is available.

S Ray: Can only certain lattice vectors be split into DSC vectors?

Ranganathan: Any lattice vector can be broken into DSC vectors, since the DSC lattice consists of both the lattice positions.

Ray: Are ledges inherited from the energetics of growth? Are these a common feature?

Ranganathan: They need not be inherited from the growth. Yes, they are a reasonably common feature.

\* Only a summary is presented.

S Ramaseshan: Why is a polycrystalline material stronger than a real single crystal?

Ranganathan: In a polycrystalline material, the dislocations are stopped at the grain boundaries, thereby impeding their movement.

Ramaseshan: In the Bernal picture, could a polycrystalline material be considered as a composite of grains and grain boundaries?

Ranganathan: One could think of the polycrystalline material as a two phase material—the grain boundaries and the grains. The idea, though found in the literature, has no validity. We have to consider the boundary as a whole.

T V Ramakrishnan: Is there any evidence for the existence of dislocations and their movement?

Ranganathan: We can actually see dislocations by etch, pit techniques, field-ion microscopy, electron microscopy, etc.! There is no doubt about the movement of the boundary of a bicrystal when it is loaded in the form of a cantilever.

G Srinivasan: Should not the energetics contain all sorts of things, including contributions from the electrons?

Ranganathan: I am tempted to agree with this since all existing theories seem to be succeeding only up to a point. There seems to be something basic that is missing.

Srinivasan: Could the unique microscopic properties shown by a metallic glass (*e.g.*, the electronic properties and ductility) be translated to a microscopic description of grain boundary sliding?

Ranganathan: One would indeed like to do that. However we are rather ignorant about both these areas and hence not much progress has been made.

Srinivasan: Is this analogy being used only with reference to structure?

Ranganathan: Right now, for the structure and the geometry.

K R Rao: As the dislocation structure can change owing to a variety of factors, it appears that the structure of the specimen is really transient—how does one ensure reproducible conditions in this sense?

Ranganathan: The underlying structures are not as transient as appears at first sight, but careful investigation of this point is certainly in order.

A P Pathak: Is there a study of the variation of the strength with respect to the orientation of the boundaries?

Ranganathan: I think this has been done for bicrystals, but not for polycrystals.

## Instabilities in first order phase transitions\*

S BANERJEE

Metallurgy Programme, Bhabha Atomic Research Centre, Bombay 400 085, India

**Abstract.** Majority of the metallurgical phase transformations are first-order transitions which occur by the nucleation and growth process near equilibrium conditions. In recent years, homogeneous transformation has been reported in some of these cases at conditions significantly away from those of equilibrium. In this paper some of these transformations will be discussed. In the first part of the presentation the thermodynamic and the mechanistic distinctions between first and higher order phase transformations will be discussed and a comparison made between homogeneous and heterogeneous modes of phase transformations and those of deformation. Based on Landau's free energy *vs* generalised order parameter plots, an instability temperature is defined for first order phase transformations below which the transformation can occur by a continuous amplification of a concentration or a strain fluctuation. In the second part experimental evidence in support of the continuous mode of transformations in two ordering reactions are presented. These are: (i) a transition from the short range to the long range chemical order in  $\text{Ni}_4\text{Mo}$  (D1a structure) and (ii) a hybrid displacive-replacive ordering in  $\text{Zr}_2\text{Al}$  (B8<sub>2</sub> structure). In order to make the continuous mode operative in these first order transformations (which is possible at a high "supercooling"), radiation in the former and rapid quenching in the latter were employed. In the last part, the martensitic transformation and the shape memory effect is described in terms of Landau's plots and the mechanical and thermodynamical consequences of the model are discussed.

### Discussion

M Youssuff: What is the criterion by which we can distinguish whether the development of long-range order is by nucleation and growth or by a continuous mechanism?

S Banerjee: The only criterion is whether we are below  $T_0$  or not. Also, not all ordering can be described in terms of compositional modulations.

V K Wadhawan: What is order parameter in  $\text{Ni}_4\text{Mo}$ ?

Banerjee: The population density of Mo atoms on a given lattice site.

V C Sahni: Is there any example where there is a formation volume and the transformation is homogeneous?

Banerjee: It is possible that the volume change is very small like in  $\text{Ni}_4\text{Mo}$ .

Sahni: How is the expansion of free energy in terms of the order parameter justified in a first order phase transition (since the opm is discontinuous)?

Banerjee: It cannot be justified.

---

\* Only a summary is presented.





## Deformation and martensitic transformation

V SEETHARAMAN

Metallurgy Programme, Reactor Research Centre, Kalpakkam 603 102, India

**Abstract.** The influence of applied stresses and imposed plastic deformation on the martensitic transformation of a parent phase is described. Changes in mechanical properties such as flow stress, work hardening rate, fracture toughness, etc brought about by strain-induced martensitic transformation are briefly examined. In the absence of appreciable dislocation glide, atomic displacements associated with glissile boundaries are highly ordered and reversible modes of (plastic or nonlinear pseudoelastic) deformation. Such processes lead to large strains and are encountered in deformation twinning, martensitic transformations and in the reorientation of martensite units. The reversibility leads to phenomena such as elastic twinning, thermoelastic martensites, superelasticity, shape memory and two-way shape memory effects, and rubber-like behaviour. These are discussed using a unified approach based on thermoelastic equilibrium. The shape memory effect suggests several potential applications of the martensitic transformations in non-ferrous alloys in which the effect is most commonly observed. Recent developments in this area are reviewed with special reference to the prerequisites for the effect and the influence of metallurgical processing on the extent of shape recovery.

**Keywords.** Plastic deformation; pseudoelasticity; shape memory effect; martensitic transformation.

### 1. Introduction

A martensitic transformation is a first-order solid-state structural transformation that is diffusionless, involves relative atomic motion by amounts smaller than the interatomic spacing, and exhibits a lattice correspondence between the parent and product structures. The transformation is generally adiabatic, athermal and exhibits hysteresis. It proceeds by a shear mechanism, and the net macroscopic distortion of the crystal can be regarded as an invariant plane strain. This implies that the interface between the parent phase and the growing martensite crystal is a plane of zero average macroscopic distortion. This feature has been verified in several experiments on the surface relief effect produced by the transformation. According to the phenomenological theories proposed by Wechsler *et al* (1953) and by Bowles and Mackenzie (1954) it is possible to consider the invariant plane strain as a superposition of the following components: a lattice strain (Bain strain), a lattice-invariant shear, a rotation and a dilation. The lattice-invariant shear required can manifest itself as slip, twinning or faulting of the martensite units. Besides, the different variants of martensite units formed from a parent phase crystal are generally arranged as three dimensional self-accommodating groups such that the total macroscopic strains are minimised.

Martensitic transformations can be induced by the application of external stress or by lowering the temperature. The former possibility arises because the free enthalpies of the parent phase and the martensite, and their equilibria, depend not only on the temperature and the composition but also on the stress; moreover, the nucleation and

growth processes are associated with shear strains and these couple to the internally or externally applied stresses. This paper deals with the relationship between martensitic transformations and deformation (both recoverable and nonrecoverable). We first consider the thermodynamic and kinetic aspects of stress-assisted and strain-induced martensitic transformations. This is followed by an account of an experimental study of the influence of plastic deformation at cryogenic temperatures on the martensitic transformation in an austenitic stainless steel. Next, we deal with the phenomenon of transformation-induced plasticity and its applications. Finally, a series of related phenomena including thermoelasticity, pseudoelasticity and the shape memory effect are discussed from a unified point of view based on the reversibility of the deformation caused by the migration of glissile interfaces.

2. Stress-assisted and strain-induced martensitic transformations

The driving force for the spontaneous martensitic transformation is the difference  $\Delta G^c$  in the chemical free energy between the parent and the martensite phases. It is known that the transformation does not set in at the equilibrium temperature  $T_0$  ( $\Delta G^c(T = T_0) = 0$ ). Instead, it requires substantial undercooling, and commences at a temperature  $M_s < T_0$ . If the parent phase is stressed at a temperature  $T(T_0 > T > M_s)$ , a mechanical driving force,  $U$ , is added to the chemical driving force; stress-assisted martensitic transformation occurs at  $T$  if

$$|\Delta G^c(T)| + U \geq |\Delta G^c(M_s)|. \tag{1}$$

$U$  is a function of the stress and the orientation of the martensite crystal with respect to the parent phase. Patel and Cohen (1953) have shown that

$$U = \tau \gamma_0 + \sigma \epsilon_0, \tag{2}$$

where  $\tau$  is the shear stress resolved along the transformation shear direction on the habit plane,  $\gamma_0$  is the transformation shear strain,  $\sigma$  is the dilatational stress resolved normal to the habit plane, and  $\epsilon_0$  is the normal component of the transformation strain. If a single crystal of the parent phase is stressed according to the geometry shown in

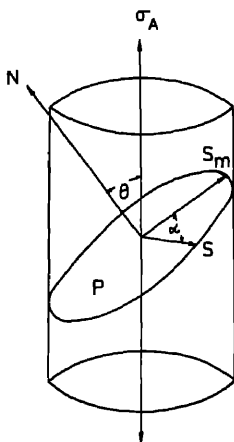


Figure 1. Geometry of stressing in a single crystal. P is the habit plane having N as its normal. S is the shear direction and  $S_m$  is the maximum shear direction of the applied stress on the habit plane. (The other symbols are explained in the text).

figure 1,  $\tau$  and  $\sigma$  can be expressed for any given orientation of the martensite plate as

$$\left. \begin{aligned} \tau &= 0.5 \sigma_A \sin 2\theta \cos \alpha \\ \sigma &= \pm 0.5 \sigma_A (1 + \cos 2\theta) \end{aligned} \right\} \quad (3)$$

where  $\sigma_A$  is the absolute value of the applied stress,  $\theta$  is the angle between the axis of the applied stress and the normal to the habit plane, and  $\alpha$  is the angle between the shear direction of the transformation and the maximum shear direction of the applied stress on the habit plane (the sign of  $\sigma$  specifies whether the stress is tensile or compressive). If the chemical driving force ( $\Delta G^\circ$ ) decreases linearly with an increase in temperature above  $M_s$ , it is logical to expect that the critical applied stress for martensite formation should increase linearly with temperature. In practice, it is observed that the critical stress shows a linear dependence only between  $M_s$  and  $M_s^\sigma$  (figure 2). Beyond  $M_s^\sigma$  the stress required would exceed the flow stress of the parent phase and thus cause plastic deformation of this phase. Olson and Cohen (1972) have postulated that in the temperature range  $M_s^\sigma < T < M_d$  the nucleation of martensite is aided by the large number of defects caused by the plastic deformation, and hence the transformation is considered to be strain-induced ( $M_d$  is the highest temperature at which the

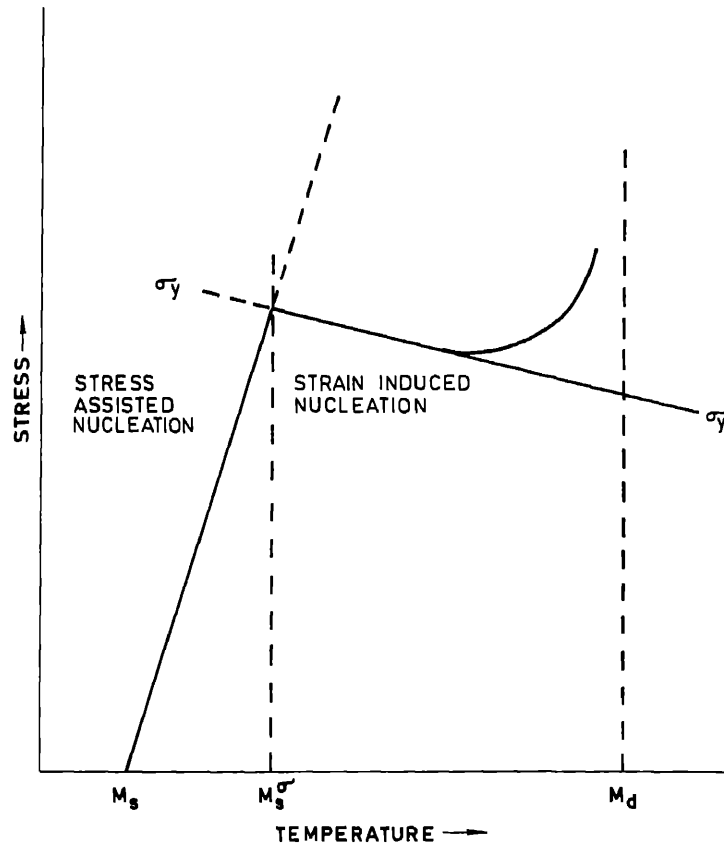


Figure 2. Variation of the critical stress required for the onset of the transformation at different temperatures. (The regimes of stress-assisted and strain induced transformation are indicated.)

transformation can be induced;  $M_d < T_0$ ). There is thus a fundamental difference between stress-assisted and strain induced transformations.

The volume fraction  $f$  of the martensite formed at any given level of plastic strain  $\epsilon_p$  is given by (Olson and Cohen 1975; Murr *et al* 1982)

$$f = 1 - \exp \{ -\beta [1 - \exp(-\alpha \epsilon_p)]^n \} \quad (4)$$

where  $\alpha$ ,  $\beta$  and  $n$  are temperature dependent parameters. Recently, Tamura (1982) has suggested that the transformation kinetics should be based on the stress rather than the strain, and has proposed a different expression for  $f$  that depends on  $\sigma_A$ ,  $\gamma_0$  and  $\epsilon_0$ . The role of plastic deformation in the strain-induced nucleation of martensite has been a subject of controversy. Olson and Cohen (1972, 1976) firmly believe that the intersection of slip bands produced as a result of plastic deformation acts as a nucleation site for martensite. In contrast, Suzuki *et al* (1977) and Onodera and Tamura (1979) have expressed the view that the local stress concentration near the grain boundaries due to the pile-up of dislocations would raise the applied stress to values obtained by the extrapolation of the straight line in figure 2 well beyond  $M_s^*$ .

### 3. Strain-induced martensitic transformation in a type 316 austenitic stainless steel

Type 316 austenitic stainless steel does not transform to martensite spontaneously even when it is cooled down to 77 K. In contrast, plastic deformation at low temperatures leads to the formation of two different types of martensites:  $\epsilon$  martensite with an hcp structure and  $\alpha$  martensite with a bcc structure. Figure 3 illustrates the variations in the volume fractions of these phases with plastic strain at 77 K. The main conclusions that can be drawn from this plot are: (i) With increasing plastic strain, the amount of  $\epsilon$  phase present increases to a maximum and then decreases gradually, (ii) Detectable amounts of the  $\alpha$  phase are formed only beyond a certain minimum value of the plastic strain, beyond which its volume fraction increases continuously with the plastic strain. These results imply that the  $\alpha$  martensite forms at the expense of the  $\epsilon$  martensite.

Plastic deformation of the austenite ( $\gamma$ ) at temperatures below 220 K leads to the progressive formation of wide stacking faults, clusters of overlapping stacking faults, and finally, thin sheets the  $\epsilon$  martensite. Transmission electron microscopy of the deformed samples reveals a large number of shear bands on  $\{111\}_\gamma$  planes. These bands

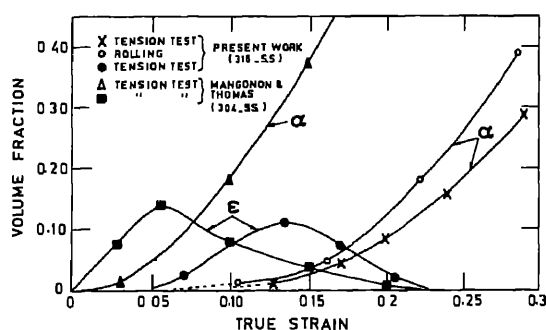
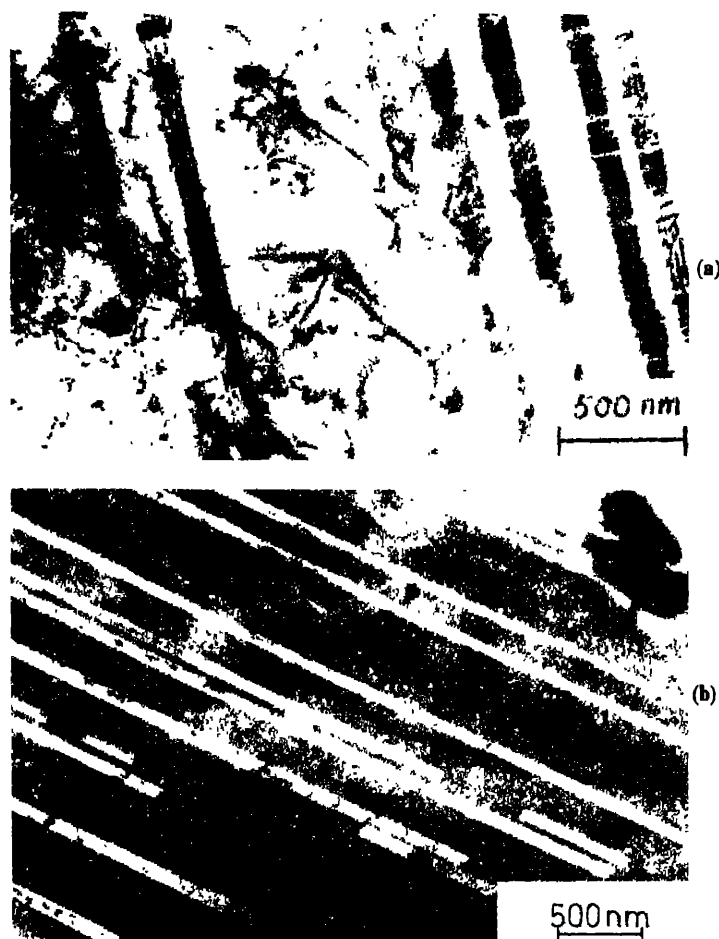


Figure 3. Variation of the volume fraction of the  $\epsilon$  and  $\alpha$  martensites in a type 316 stainless steel as a function of the true strain at 77 K. The results of Mangonon and Thomas (1970) in a type 304 stainless steel are shown for comparison.



**Figure 4.** Transmission electron micrographs of type 316 stainless steel deformed at 77 K up to 5% strain. (a) wide stacking faults forming on the  $\{111\}_\gamma$  planes, (b) dark field micrograph showing one of the variants of the deformation bands.

consist of overlapping faults, deformation twins and the  $\epsilon$  martensite, the relative proportions of which vary with the temperature, strain rate and the extent of deformation. Typical examples of the microstructure obtained after tensile deformation at 77 K up to 5% strain are shown in figure 4. When the austenite is subjected to strains larger than 15% at 77 K, tiny crystals of  $\alpha$  are observed at the intersections of two different variants of the shear bands. On continuing the deformation, the  $\alpha$  nuclei grow along the cylindrical axes of the rod-shaped volumes comprising the intersections of these bands. The above experimental evidence obtained by x-ray diffraction and electron microscopy techniques proves conclusively that the  $\epsilon$  martensite forms as an intermediate phase in the  $\gamma \rightarrow \alpha$  transformation, the sequence being representable as  $\gamma \rightarrow \epsilon \rightarrow \alpha$  (Seetharaman 1976; Seetharaman and Krishnan 1981).

#### 4. Transformation-induced plasticity (TRIP)

As already mentioned, martensitic transformation can be considered as a mode of plastic deformation of the parent phase that competes with other modes such as slip and twinning. Therefore, if martensite forms dynamically during the mechanical testing of any alloy, the mechanical properties of the alloy would inevitably be altered considerably. Figure 5 shows the stress-strain curves of the Fe-29 Ni-0.26 C austenitic alloy deformed in tension at different temperatures (Tamura *et al* 1970a). The values of  $M_s$  and  $M_d$  for this alloy are 213 K and 298 K, respectively. The large serrations observed in the curves at 223 K and 203 K are due to the formation of stress-assisted martensite. On the other hand, the curves corresponding to 243 K or 263 K exhibit very fine serrations and also substantial tensile elongation: the samples corresponding to these curves show evidence of the presence of strain-induced martensite. Such an enhancement in the ductility of an alloy owing to the onset of strain-induced martensitic transformation is known as 'transformation-induced plasticity (TRIP)'.

The tensile properties of three different austenitic steels in the temperature range  $M_s^c < T < M_d$  are shown in figure 6 (Tamura *et al* 1970b). The inverse temperature dependence of the 0.2 % proof stress observed between  $M_s^c$  and  $M_d$  (figure 6a) is due to the transformation strain caused by the stress-assisted martensite formed before the yielding of the parent austenite phase. The total elongation exhibits a maximum at temperatures just above  $M_s^c$ . Such an enhancement in elongation has been attributed to the suppression of the necking phenomenon. This, in turn, is due to the increase in the work-hardening rate caused by the strain-induced martensitic transformation. Similar increases in the work-hardening rates have also been encountered in austenitic stainless steels (Angel 1954; Ludwigson and Berger 1969; Seetharaman 1976). The hardness of the martensite increases with increase in the carbon content of the steel. It follows that, for a given volume fraction of martensite, the increase in the work-hardening rates will be high for high carbon steels. Thus the TRIP phenomenon will be dominant in austenitic steels containing high levels of carbon.

Although ductility can be enhanced markedly by TRIP, strengthening must be achieved by other methods. Zackay *et al* (1967) developed an ultra-high-strength steel called TRIP steel in which the ductility is enhanced by the TRIP of the retained austenite

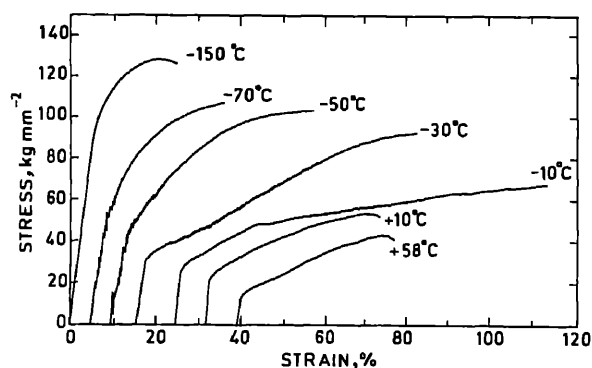


Figure 5. Stress strain curves of Fe-29Ni-0.26C austenitic alloy deformed in tension at different temperatures.

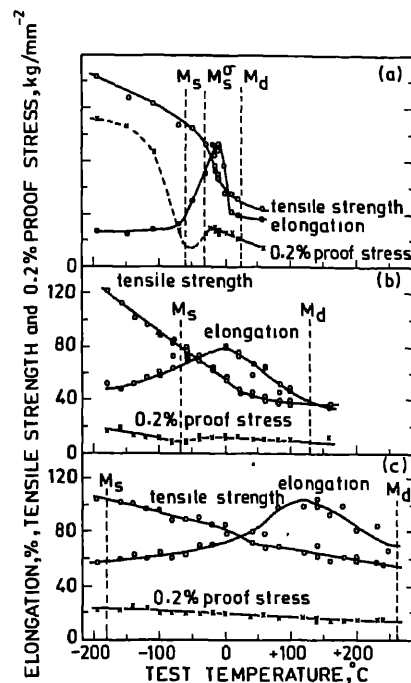


Figure 6. Effect of test temperature on tensile properties in three different types of metastable austenitic steels (a) Fe-29Ni-0.26C, (b) Fe-19-Cr-11Ni, (c) Fe-24Mn-0.26C.

while the strength is increased by the ausformed martensite. TRIP steels exhibit good properties at low temperatures because of the retained austenite, and are therefore suitable structural materials for chemical plants, containers for liquified gases, armour plates and earthquake dampers. Furthermore, the TRIP phenomenon is very effective in improving the formability, particularly the deep drawability, of austenitic stainless steels (Divers 1964).

##### 5. Thermoelasticity, pseudoelasticity and shape memory effect

The thermodynamics of the growth of the martensite plate can be represented by the following energy balance:

$$G_r^c + U \geq \tau_0 \gamma_0 + \sigma_0 \varepsilon_0 + S_M A + \xi \gamma_0, \quad (5)$$

where  $\tau_0$  is the intrinsic shear resistance of the parent phase against the shear strain  $\gamma_0$ ,  $\sigma_0$  is the intrinsic tensile resistance of the parent phase against  $\varepsilon_0$ ,  $S_M$  is the specific surface energy of the parent-martensite interface,  $A$  is the shape factor of the martensite, and is a dissipation factor. Let us exclude the trivial case of the stoppage of a growing plate by a grain boundary or some equivalent obstacle. Then an equality in (5) implies that any small change in the thermal or mechanical components of the driving force will cause growth or shrinkage of the martensite plate. This equilibrium condition forms the basis of the thermoelastic martensitic transformation. A thermoelastic martensite forms and grows continuously as the temperature is lowered, and shrinks and vanishes as the temperature is raised. Figure 7(a) gives a schematic representation of this transformation indicating the increase in the internal stress  $\sigma_i$  and the volume fraction  $f$  of the martensite, these being measures of the progress of the transformation.



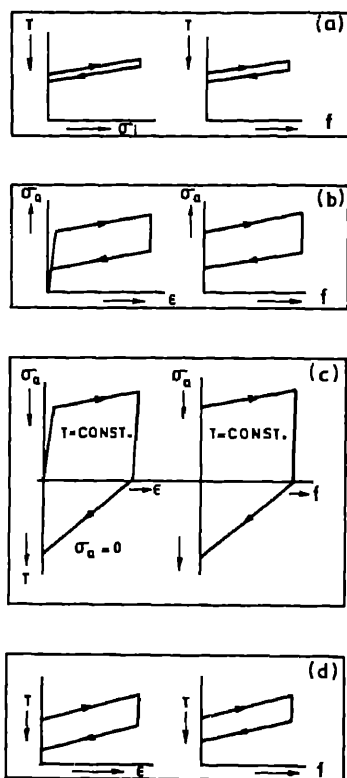


Figure 7. Schematic representation of (a) thermoelasticity (b) pseudoelasticity (c) shape memory effect and (d) two-way shape memory effect.

There is no sudden appearance or disappearance of large groups of martensite plates (the burst phenomenon).

Pseudoelastic behaviour (figure 7b) is a complete mechanical analogue of the thermoelastic transformation. In this case, the transformation proceeds continuously with increased applied stress. The 'plastic' strain is caused by the shape strain accompanying the formation of martensite. Recovery of the shape strain therefore occurs when the transformation is reversed. This type of pseudoelastic behaviour is obtained when the material is stressed at temperatures higher than the finish temperature  $A_f$  for the reverse transformation. Pseudoelasticity can also occur by the reorientation of the existing martensite variants (Krishnan *et al* 1974). Other terms such as superelasticity, ferroelasticity, rubber-like behaviour etc. have sometimes been used to describe pseudoelastic behaviour.

The shape memory effect arises if a macroscopic deformation is accompanied, as before, by a martensitic transformation which is not reversed on removal of the applied stress; in a second step the reverse transformation and a concomitant reversal of the macroscopic deformation are induced by heating. Figure 7(c) shows this behaviour schematically. The upper half represents the response of the specimen to the isothermal heating. The idealised curves shown in figure 7(a-c) suggest close interrelations between these processes. If the stress hysteresis in a pseudoelastic transformation is so large that the reverse transformation is incomplete at  $\sigma_a = 0$ , then the residual martensite can be

reverted by heating, *i.e.*, by employing the shape memory effect. This clearly demonstrates the interchangeability of stress and temperature as state variables.

A two-way shape memory effect occurs when the specimen deforms spontaneously during the cooling half-cycle and recovers during the heating half-cycle (figure 7d). An alloy which exhibits the one-way or normal shape memory effect can often be converted into a reversible memory alloy by "training" with a few cycles of the one-way type, or (more effectively), a few pseudoelastic cycles above  $M_s$  (Christian 1982). The maximum strains of the reversible effect are normally much smaller than those of the simple shape memory effect for a given alloy.

## 6. Common characteristics of materials exhibiting the memory effect

On the basis of extensive investigations conducted on Au-Cd, In-Tl, Ni-Ti, Cu-Zn, Fe-Pt and Cu-Al-Ni alloys, Wayman and Shimizu (1972) have concluded that the following conditions are necessary for an alloy to exhibit the shape memory effect: (i) The martensitic transformation should be a thermoelastic one; (ii) the parent phase and the martensite should be ordered; (iii) the lattice-invariant shear must occur by twinning rather than by slip.

While the first two conditions hold good for all the alloys investigated so far, the last condition, namely, the internal twinning of martensite does not appear to be very general. In fact, there is ample evidence in the literature to show that martensites in silver- and copper-based ordered alloys contain extensive and periodic faulting in the stacking sequence of the close packed planes, and these alloys do exhibit the shape memory effect to a significant extent.

### 6.1 Thermoelastic martensites

A thermoelastic martensite is generally characterised by (i) a small driving force, (ii) a small shear component of the shape strain, (iii) a small volume change, and (iv) a matrix with a high elastic limit (Dunne and Wayman 1973; Tong and Wayman 1975). It is clear that a thermoelastic martensite-crystal must have a perfectly coherent interface with the surrounding matrix and that the coherence must be maintained during the whole process of growth or shrinkage. This is possible only if the volume change associated with the transformation is small. Furthermore, the small value of the thermal hysteresis is a direct consequence of the smallness of the driving force.

### 6.2 Effect of ordering

It is found that some degree of ordering (usually, long range ordering) is present in all parent phases which are known to transform thermoelastically. As a case in point, the ordered  $\text{Fe}_3\text{Pt}$  alloy undergoes a thermoelastic martensitic transformation and also exhibits the shape memory effect, while disordered specimens of the same composition display neither.

According to the phenomenological theory of martensitic transformation (Wayman 1964), the habit plane is a plane of zero average distortion. However, localised distortions still persist at the interface though they are macroscopically arranged out by the lattice-invariant shear. This fine-scale distortion is not expected to exceed the elastic limit of the matrix in ordered alloys (because of the order-hardening effects), but in

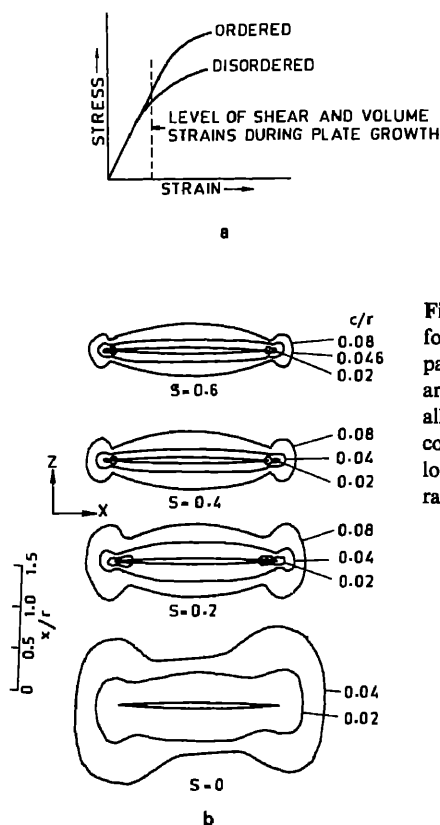


**Figure 8.** (a) Schematic stress-strain curves for the disordered and ordered states of the parent phase. (b) Matrix yield stress contours around an oblate spheroidal plate of an Fe-Pt alloy. The plate is in the x-y plane and the contours are drawn for varying values of the long range order parameter,  $S$  and the aspect ratio,  $c/r$ .

disordered alloys the elastic limit is evidently exceeded and the interface eventually becomes incoherent. This is explained with the help of the hypothetical stress-strain curves shown in figure 8(a). Ling and Owen (1979) have re-examined the plastic deformation around a growing thermoelastic plate, and have predicted the size of the plastic zone around plates of various shapes and in materials with varying long-range order (figure 8b). In the disordered alloy (longrange order parameter  $S = 0$ ), general yielding has occurred all around the isolated plate with an aspect ratio  $c/r = 0.02$ . However, when  $S > 0.4$ , such yielding is confined to a small volume near the radial edge. It is therefore clear that the primary role of ordering is to strengthen the parent and the martensite phases without affecting significantly the value of the shear modulus,  $\mu$ , thereby increasing the ratio  $\sigma_y/\mu$  of the yield strength to  $\mu$ .

The ordered arrangement of atoms is also important when one considers the reverse transformation upon heating. If a material is to exhibit the shape memory effect, it is essential that all the martensite plates formed in a single crystal of the parent phase should revert as a unit to the original orientation of the parent phase. When an ordered parent phase transforms to an ordered martensite, the arrangement of atoms, though ordered, exhibits a lower symmetry in the latter phase (following the deformation of the lattice). Considering that another lattice distortion must be operative during the inverse transformation, it follows that the number of reverse lattice correspondences is more limited than in cooling transformation, one imposes the restriction that the original ordered arrangement in the parent phase be recovered. In fact, in Cu-Al-Ni alloys it has been shown that there is only one lattice correspondence between the parent and the

martensite phases which maintains the original order (Wayman and Shimizu 1972). Accordingly, the ordered martensite is obliged to revert to the original orientation of the parent phase in this case.

### 6.3 Lattice softening

Shape memory alloys exhibit interesting and anomalous behaviour with respect to the temperature dependence (near  $M_s$ ) of the electrical resistivity, elastic constants, etc. Moreover, 'extra' reflections appear in the x-ray and electron diffraction patterns taken at temperatures just above  $M_s$ . The damping capacity of these alloys increases anomalously to reach a maximum near  $M_s$ . Among all these pre-martensitic phenomena, the most important and striking feature is that the temperature derivative of the elastic shear constant  $dC'/dT$  (where  $C' = (C_{11} - C_{12})/2$ ) is large and positive. Zener (1947) has explained the low values of  $C_{11} - C_{12}$  observed in  $\beta$ -brass for  $T \approx M_s$  on the basis of the instability of the bcc lattice with respect to a  $(110)[\bar{1}\bar{1}0]$  shear. Thus it is suggested that the very low value of the thermodynamic driving force required at  $M_s$  is due to the assistance by long wavelength phonon instabilities of the nucleation of martensite in a soft lattice. As with ordering, it is probable that the major, and certainly the most direct consequence, of lattice softening in the nature of martensite growth would be with regard to the ratio  $\sigma_y/\mu$ . A decrease in  $\mu$  increases the magnitude of the shear strain which can be accommodated elastically.

### 6.4 Mechanisms for the shape memory and related effects

The most remarkable consequence of deformation by interface migration is that the substantial strains produced this way are often completely recoverable when the chemical or mechanical driving force is removed. This 'shape recovery' is a consequence of the highly ordered nature of the atomic displacements during thermoelastic interface deformation. It contrasts with the irreversibility of the plastic deformation produced by dislocation glide or by the formation of martensite plates or deformation twins with an accompanying dislocation deformation. The most important mechanisms based on interface migration which have been put-forward for the effects under consideration include (i) the stress-assisted reversible growth of martensite; (ii) the reorientation of the martensite plates under an applied stress; (iii) inter-twin growth; and (iv) martensite-to-martensite transformation under stress. We now discuss these mechanisms in brief.

**6.4a Stress-induced reversible growth of martensite:** The essential feature of this mechanism is that those plates of martensite grow which have orientation and shear directions favoured by the dominant shear due to the imposed macroscopic change in shape; while other less favourably oriented variants shrink. The growth must be mechanically reversible (and hence thermoelastic) if the shape is to be completely recoverable. The martensite plates which participate in this mechanism may be nucleated under the action of the applied stress, in which case only the favourably-oriented variants will be produced; or they may be plates which may have been formed athermally before the external stress is applied.

**6.4b Reorientation of martensite plates:** Macroscopic shape deformation can be achieved by an externally applied stress through the growth of martensite plates

favourably oriented in the stress field at the expense of less suitably oriented plates. It is to be noted that when the martensite interface moves, the habit plane itself remains unchanged, suggesting that ratio of the thickness of alternate segments of transformation twins within the plates remains unchanged. A special and specific mechanism whereby martensite plates can be reoriented under stress has been proposed by Wasilewski (1975). It is described as a 'stress-assisted double transformation'. When a stress is applied at a temperature between  $A_d$  and  $M_f$ , the martensite transforms to the  $\beta'$ -phase by the stress-assisted reverse transformation; ( $M_f$  is the martensite finish temperature during cooling and  $A_d$  is the lowest temperature at which martensite reverts to austenite under deformation) and then, because it is both thermally unstable and subject to an external stress, it transforms instantaneously to a martensite variant more favourably oriented with respect to the applied stress field than the original plate. However, there is no experimental evidence as yet for the transitory existence of an intermediate  $\beta'$ -phase.

If the specimen is fully martensitic and consists of self-accommodating groups of martensite, then on the application of external stress, movements of the existing plate boundaries or creation of new ones together with changes in internal structure will occur. Because no untransformed parent phase is present, no invariant plane strain conditions need to be satisfied; only a three-dimensional strain minimisation is necessary.

6.4c *Inter-twin growth*: Macroscopic deformation by change in the thickness of two twin variants under an applied stress was first reported by Olander (1932) and studied in detail in Au-Cd and In-Tl alloys by Chang and Read (1951). This mechanism does not involve any movement of the martensite-martensite interfaces. On applying a stress the twin boundaries move so as to thicken those twins which are favourably oriented with respect to the applied stress. On removal of the stress, the twin boundaries return (relatively slowly) to their original positions, and the specimen recovers its original shape. The strains thus recoverable may be as large as 0.08 in Au-Cd.

6.4d *Martensite-to-martensite transformation under stress*: In Cu-Ni-Al alloys two different martensites  $\beta'_1$  and  $\gamma'_1$  form from the parent  $\beta_1$ . It is reported that the  $\beta'$  martensite can be transformed partially to  $\gamma'_1$  by applying a stress below  $M_s$ . Similarly, athermally formed  $\beta'_1$  martensite in Cu-Al alloys can transform either to an fcc or hcp structure by deformation. Delaey and Warlimont (1975) have demonstrated a similar martensite-to-martensite-transformation in a Cu-Zn-Al alloy.

The different possible routes in a pseudoelastic cycle and a shape memory cycle are illustrated in figure 9 (Cook 1981). This diagram compares the changes involved in a shape memory cycle (VABCDEZ) with those in a pseudoelastic cycle (VWXYZ). If the same martensite phase is produced in the two cycles, the structure at X is identical with that at C and D, and the state X may be converted into D by cooling at a constant strain.

## 7. Applications of the shape memory effect

One of the earliest applications of the shape effect was the introduction of tubing or pipe couplings that shrink during heating. Ni-Ti alloy couplings are used for connecting aircraft hydraulic lines. These are expanded by 4% in the martensitic

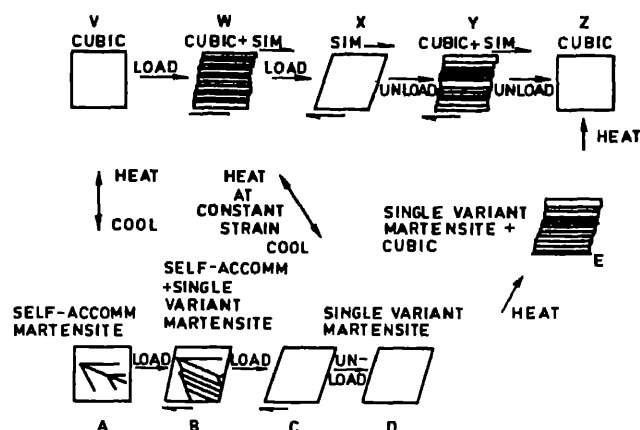


Figure 9. Schematic structural changes during a pseudoelastic cycle VWXYZ and a shape memory cycle VABCDEZ.

condition at liquid nitrogen temperatures, and placed around the tubes to be joined. Warming at room temperature produces a tight seal. Substantial developments have taken place in the field of copper-based shape memory alloys, particularly the Cu-Zn-Al alloys, with emphasis on their applications as thermostats, automotive control devices and actuators. Applications in the field of medicine include the use of such materials for orthodontic dental arch wires, blood clot filters and orthopaedic devices.

## References

- Angel T 1954 *J. Iron Steel Inst.* **177** 165
- Bowles J S and Mackenzie J D 1954 *Acta Metall.* **2** 129
- Chang L C and Read T A 1951 *Trans. Met. Soc. AIME* **191** 47
- Cook J M 1981 Ph.D. Thesis, Cambridge University (unpublished)
- Christian J W 1982 *Met. Trans.* **A13** 509
- Delaey L, Krishnan R V, Tas H and Warlimont H 1974 *J. Mater. Sci.* **9** 1521
- Delaey L and Warlimont H 1975 *Proc. conf. shape memory effects in alloys*, (eds) J Perkins (New York: Plenum Press) p. 59
- Divers C K 1964 *Met. Prog.* **86** 115
- Dunne D P and Wayman C M 1973 *Met. Trans.* **4** 137
- Olsen G B and Wayman C M 1972 *J. Less Common Metals* **28** 107
- Ling H S and Owen W S 1979 *Proc. int. conf. martensitic transformation (ICOMAT 1979)*, (Cambridge: MA) p. 368
- Ludwigson D C and Berger J A 1969 *J. Iron Steel Inst.* **207** 63
- Manganon Jr P L and Thomas G 1970 *Met. Trans.* **1** 1587
- Murr L E, Staudhammer K P and Hecker S S 1982 *Met. Trans.* **A13** 627
- Olsen G B and Cohen M 1975 *Met. Trans.* **A6** 791
- Olsen G B and Cohen M 1976 *Met. Trans.* **A7** 1905
- Olander A 1932 *J. Am. Chem. Soc.* **54** 3819
- Onodera H and Tamura I 1979 US-Japan seminar on *Mechanical behaviour of metals and alloys associated with displacive transformation*, (Troy, NY) p. 24
- Patel J R and Cohen M 1953 *Acta Metall.* **1** 531
- Seetharaman V 1976 *Effect of thermomechanical treatments in stainless steels* M.Sc. (Tech) Thesis, University of Bombay

- Seetharaman V and Krishnan R 1981 *J. Mater. Sci.* **16** 523  
Suzuki T, Kojima H, Suzuki K, Hashimoto T and Ichihara H 1977 *Acta Metall.* **25** 1162  
Tamura I 1982 *Met. Sci.* **16** 245  
Tamura I, Maki T and Hato H 1970a *Trans. Iron Steel Inst. Jpn* **10** 163  
Tamura I, Maki K, Hato H, Tomoto Y and Okada M 1970b *Proc. ICSMA 3*, (ASM, Metals Park Ohio) p. 900  
Tong H C and Wayman C M 1975 *Acta Metall.* **23** 209  
Wasilewski R J 1975 *Met. Trans.* **A6** 1405  
Wayman C M 1964 *Introduction to the crystallography of martensitic transformation* (London: Macmillan)  
Wayman C M and Shimizu K 1972 *Met. Sci. J.* **6** 175  
Wechsler M S, Lieberman D S and Read T A 1953 *Trans. AIME* **197** 1503  
Zackay V F, Parker E R, Fahr D and Busch R 1967 *Trans. ASM* **60** 252  
Zener C 1947 *Phys. Rev.* **71** 846

## Discussion

V K Wadhawan: What is the role of the superlattice structure in the shape memory effect?

V Seetharaman: Ordering of the parent and martensite phases has two consequences. (i) It increases the yield strength of the parent and product phases by the 'Fisher's order hardening mechanism' (ii) It reduces the number of variants available for the reverse transformation so that strain recovery can occur efficiently.

S Ray: Does the shape memory effect occur only in isothermal martensite systems (through mode softening) or is it possible in athermal martensites also?

Seetharaman: It is seen in athermal martensites though the mode may not soften completely.

R Krishnan: Are there examples of transformation induced plasticity in ceramic materials?

Seetharaman: I know only a few examples of these. The material must have a residual plasticity before we can introduce TRIP.

## Strength and electronic structure

K GOVINDA RAJAN

Materials Science Laboratory, Reactor Research Centre, Kalpakkam 603 102, India

**Abstract.** The main attribute of a solid is its resistance to deformation, or its 'strength'. We discuss first the interpretation of the strength parameter. The current situation with regard to the central problem of providing a microscopic description of the strength parameter is briefly reviewed. Electrons in metals provide the cohesion, so that an understanding of the role played by electronic structure in the strength attribute should lead to practical hints for building stronger materials. The useful 'aircraft alloy' (Ti + Al + V) illustrates one such important relationship, viz., that the addition of a non *d*-character metal to a *d*-electron host strengthens the latter. Again, metals are distinguished from non-metals by the Fermi surface they possess, and it is interesting to examine any possible relationship between the anisotropy of the Fermi surface with the observed anisotropy in hardness (or yield strength). Next, we turn to cleavage, and point out that the assumption that it is the exact opposite of cohesion faces objections. Cohesion is an average property, whereas cleavage is a crack-tip phenomenon. Finally, among the processes familiar to the metallurgist wherein a metal is hardened, electron-moderated mechanisms have been identified in at least two cases, and we conclude with a brief account of these.

**Keywords.** Strength; cohesive energy; electronic energy; electron-mediated interactions; strengthening mechanisms.

"... merely corroborative details to lend an aspect of verisimilitude to what would otherwise be a bald and unconvincing narrative ..."

Gilbert and Sullivan—The Mikado

### 1. Introduction

A solid is characterized by its resistance to deformation, or its strength. In particular, the ability of a solid to resist shearing forces is used to distinguish it from a fluid. Three broad characteristics can be recognized when the meaning of 'strength' is considered. Resilience or elasticity, when subjected to transient forces—that is, how strongly does the solid attempt to regain its original shape if a force is applied to it for a time and then removed? The Young's modulus, which is a measure of such resistance, varies over three orders of magnitude ( $10^{10}$ – $10^{13}$  dyn/cm<sup>2</sup>). Resistance to flow is the next characteristic and it concerns the question: how much applied force is required to obtain a particular rate of flow? Flow resistance varies even more—from  $10^5$  to  $10^{12}$  dyn/cm<sup>2</sup>—and the measured rates of flow vary over 12 orders of magnitude. Third, by applying sufficient tension, solids can be pulled apart into two pieces. How much applied force is required to fracture a solid? Fracture resistance is the resistance of a material to crack propagation. It is measured in terms of the fracture surface energy, which may be as little as 10 dyn/cm or as high as  $10^8$  dyn/cm, i.e., varies over 7 orders of magnitude.

Owing to these diverse and variable aspects, the problem of strength is one of great complexity. Strength depends on the collective response of a crystal to applied stress, so



that its description is quite involved. That is, strength depends on the behaviour of aggregates of particles, and the central problem in the science of strength has been to learn how to describe mechanical behaviour in terms of the fundamental properties of matter, so that the shapes of stress-strain or strain-time curves and their dependence on loading conditions can be predicted from a small number of experimental relationships (Gilman 1969).

Turning to metals, we know that the properties of metals arise from the behaviour of the free electrons, and their interaction with the metallic ions. Much attention has therefore been directed to the properties of electrons (in particular, the free electrons) in metals, and features such as electrical conduction, magnetic properties and structure in metals have been understood. This success provides the motivation to look into the question of whether progress with regard to the strength attribute too can be made using this approach.

## 2. Perfect cleavage

We begin by discussing how the strength of a solid is calculated in order to understand the role of electronic structure.

The separation of a crystal into two or more parts by the propagation of a geometrically plane crack through the solid is called cleavage. Perfect cleavage is portrayed in figure 1. A crystal is stressed in tension vertically to the point of theoretical cohesive strength (figure 1a), and then this stress is exceeded simultaneously at every one of the atomic bonds across the cleavage plane extending interminably and mathematically all the way across the stressed crystal (figure 1b), with no intermediate stages. The crystal goes directly from cohesion to cleavage with no crack propagation direction. The more recent, and present, concept of perfect cleavage is that the elastic bonds connecting the atoms are individually overcome one by one in chronological order, as shown in figure 1c. In this visualization, perfect cleavage is the propagation of an atomically sharp crack with the applied stress overcoming the elastic stresses in a purely elastic manner, and with the atoms separating in geometrically opposite directions, along the direction of the tensile stress.

### 2.1 Ideal strength of a crystalline solid

The maximum stress required to produce, in an ideal crystal, a perfect cleavage of the form imagined above is called the ideal strength or the theoretical strength of a solid

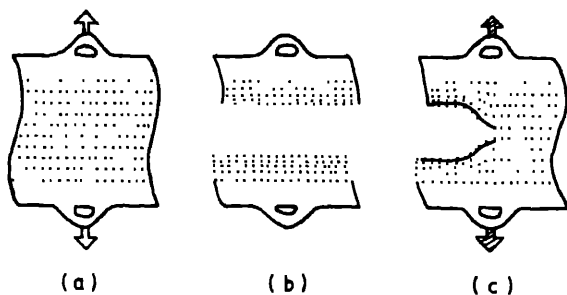


Figure 1. Perfect cleavage: (a) and (b) Original picture; (c) present concept of perfect cleavage.

( $\tau_s$ ). Before the development of the dislocation theory of solids, this problem was of considerable interest because calculated values of the strength were typically greater than experimental values by a factor of 100 or more. Even at the present time, this problem is of theoretical and practical importance, as a knowledge of the  $\tau_s$  is useful in determining the stress distribution and other properties in the region at the tip of a crack; in determining the dislocation core radii; in defining the point at which coherency breakdown occurs at a particle-matrix interface; and in providing insight into the phenomenon of melting. The reviews by Milstein (1982) and Macmillan (1972) exemplify these points. Macmillan also reviews the practical approach to the measurement of  $\tau_s$ . The measurements are carried out either on specially grown whiskers or on single crystals of materials in which the dislocation density is very small ( $\sim 10^1$ – $10^2$  cm<sup>2</sup>). Table 1 provides a comparison between the calculated and measured strength for a few solids.

A simple way of estimating the cleavage stress of a perfect crystal is as follows (Kelly 1973). It is assumed that the crystal is pulled at  $T = 0$ , and the restoring force per unit area between two adjacent atomic planes is assumed to vary with distance according to  $\sigma = K \sin \pi/a (x - a_0)$ , where  $a_0$  is the equilibrium separation between the atomic planes, and  $a$  is the range of the interatomic force. The latter is evaluated by setting

$$2\gamma = \int_{a_0}^{a_0+a} \sigma dx$$

at cleavage,  $\gamma$  being the surface energy of the solid; the factor 2 appears because a pair of surfaces is created when cleavage occurs. Thus  $a = \pi\gamma/K$ . The maximum value of  $\sigma$  is identified as the  $\tau_s$  of the solid, so that we have simply  $\sigma_{\max} = K$ .  $K$  is evaluated from the definition of the Young's modulus  $Y$  for the appropriate direction in the solid, namely,  $Y = a_0 d\sigma/dx$ . For  $x \simeq a$ , this gives

$$Y = K\pi \frac{a_0}{a} \cos \frac{\pi}{a} (a - a_0) \simeq \frac{K\pi a_0}{a},$$

Table 1. Comparison of calculated and measured values of the strength of a few solids.

Calculated values of $\tau_s$				Experimental data		
Material	Tensile direction	Theoretical strength (calculated) $\times 10^{-11}$ dyn/cm <sup>2</sup>		Material	Max. tensile stress $\sigma_{\max} \times 10^{-10}$ dyn/cm <sup>2</sup>	$\frac{\sigma_{\max}}{Y} \approx$ strain
		equation (1)*	equation (2)			
Ag	$\langle 111 \rangle$	2.4 (0.20)	—	Whiskers		
Ag	$\langle 111 \rangle$	2.7 (0.25)	—	Ag	1.73 $\langle 100 \rangle$ tension	0.040
Cu	$\langle 111 \rangle$	3.9 (0.20)	3.796	Cu	2.94 $\langle 111 \rangle$ tension	0.028
Cu	$\langle 100 \rangle$	2.5 (0.51)	3.60	Fe	13.10 $\langle 111 \rangle$ tension	0.049
W	$\langle 100 \rangle$	6.1 (0.22)		Cd	2.80 $\langle 1120 \rangle$ tension	0.040
$\alpha$ -Fe	$\langle 100 \rangle$	3.0 (0.34)				
$\alpha$ -Fe	$\langle 111 \rangle$	4.6		Crystal		
C(dia)	$\langle 111 \rangle$	20.5		Ge	7.12	0.05– 0.08
Si	$\langle 111 \rangle$	3.2				
Ni	$\langle 100 \rangle$		2.3			

\* Values indicated in parentheses are the calculated strains.

so that we have, finally,

$$\sigma_{\max} = (\Upsilon\gamma/a_0)^{1/2}. \quad (1)$$

This simple treatment indicates that the strength goes as  $\sqrt{\Upsilon}$  and  $\sqrt{\gamma}$ . The values of strengths obtained from this approach are indicated in table 1.

## 2.2 More exact calculations of $\tau$ s

After Born's work on the necessary conditions for the thermodynamic stability of a crystal lattice with respect to arbitrary (but small) homogeneous deformations, many attempts have been made to refine the calculations of the theoretical strength (Esposito *et al* 1980; Milstein 1982). The current approach is to proceed along the following lines: (a) The solid under consideration is defined by specifying its crystal structure, parameters of the unit cell, etc. (b) The interaction between the ions and electrons is specified next. For simplicity, pair potentials (Lennard-Jones, Morse, etc.) are used. However, for metals where there is a clear deviation from the Cauchy relation  $C_{12} = C_{44}$ , the pair potential approximation is not applicable. Recently, the so-called "ab-initio potential" method for the calculation of the  $\tau$ s has been developed to overcome the limitations of the pair-potential approximation (Carlsson *et al* 1980). (c) The Born stability criteria are applied, and the suitability of the potential is checked. (d) The cohesive energy per atom (or unit cell) is calculated as a function of the parameters of the potential and other geometric parameters. (e) The unit cell is stretched, and the energy is calculated as a function of the strain. (f) Considering for the moment a cubic crystal with lattice parameter  $a_0$  (thus  $a_1 = a_2 = a_3 = a_0$ ), it is clear that a stretch, for example along  $[100]$ , will impart a tetragonal distortion. For computational ease the deformation is imagined to increase  $a_1$  and decrease  $a_2$  and  $a_3$  in such a manner as to keep  $a_2 = a_3$  and the transverse stress  $\sigma_2 = \sigma_3 = 0$ . In practice, this is achieved by an iterative technique. The relevant stress  $\sigma_1$  is calculated from the expression

$$\sigma_1 = \frac{4}{a_0^3} \frac{\partial U}{\partial (a_1/a_0)}. \quad (2)$$

where  $U$  is the cohesive energy. The theoretical strength is identified as

$$\tau = (\sigma_1)_{\max}. \quad (3)$$

Figure 2 gives an idea of the way  $\sigma_1$  varies with extension along  $[100]$  in nickel. The maximum  $\sigma_1$  value is the  $\tau$ s, and the corresponding  $a_1$  value gives the strain at fracture. Obviously, the cleavage process is imagined to be the exact opposite of cohesion, with all bonds snapping simultaneously when  $\sigma_1$  reaches  $(\sigma_1)_{\max}$ .

Further details may be found in the references listed at the end (*e.g.*, Milstein 1982). Table 1 also contains the  $\tau$ s values calculated by these more exact methods. It is interesting to note that even the naive calculations outlined in §2.1 are already in reasonably good agreement with the observed values. The more exact calculations, in addition to improving this agreement, also help us in understanding the correlation between the electronic structure and strength of metals.

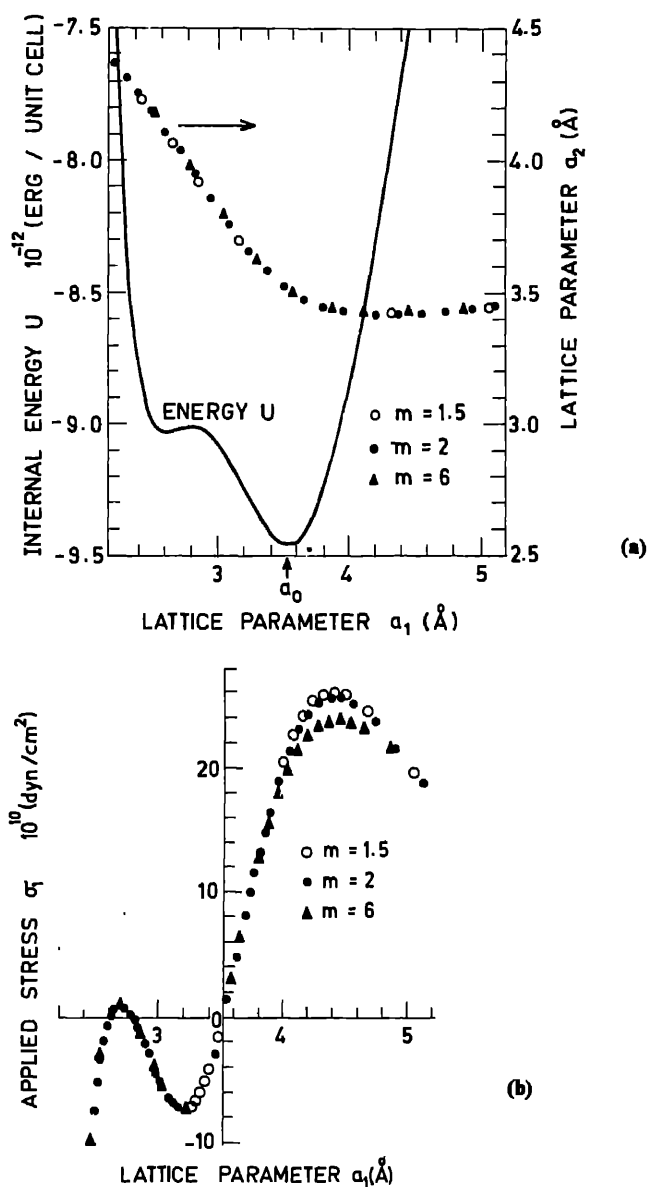


Figure 2. (a) The internal energy (cohesive energy) as a function of the axial lattice parameter  $a_1$  for [100] uniaxial loading in fcc Ni. (b) Computation of the true axial stress  $\sigma_1$  as a function of  $a_1$  for [100] loading. The maximum value of  $\sigma_1$  is the theoretical strength. The calculations were performed using a Morse potential  $\phi(r) = D[\exp\{-2m\alpha(r-r_0)\} - 2\exp\{-m\alpha(r-r_0)\}]$ . Results for a few values of  $m$  are shown (after Milstein 1982).

### 3. Cohesion and electronic structure

We have seen that in strength calculations, the cohesive energy of the solid has to be first determined. It therefore becomes necessary to see how the electronic structure enters the calculation of cohesive energy, for a better understanding of the relationship between strength and electronic structure (especially in metals).

The calculations of the total energy of a metallic structure is formulated as the determination of the energy of an assembly of  $N$  ions (each with volume  $\Omega$ ) at sites  $\mathbf{r}_n$ , arranged on a crystal lattice, and  $NZ$  valence electrons. The total energy  $U$  is first separated into the energy of the ions, which is purely potential and comes from their mutual repulsion, and that of the electrons, which contains both kinetic and potential terms. The energy of an electron with momentum  $k$  is given (to a second order of approximation) by

$$E(k) = \frac{\hbar^2 k^2}{2m} + V_0 + \sum_q' \frac{V_q^2}{E_k - E_{k+q}}, \quad (4)$$

in standard notation. To obtain the total energy of the electrons, we must sum  $E(k)$  over all occupied states, *i.e.*, over all  $k \leq k_F$ , the Fermi momentum of the electrons. The first two terms on the right in (3) are free-electron terms, this being the zeroth approximation for the perturbation theory. All such terms are *structure-independent*. The first term is the kinetic energy of the free electron gas, and the second is the average value of the lattice potential. Both terms depend upon the total volume. All the structure dependence of  $E(k)$  resides in the third term, which contains the strengths of atomic potentials expressed in some suitable form. If the potentials are weak, a second-order correction is adequate and this leaves  $E(k)$  only slightly structure-dependent. The corresponding mechanical characteristic is softness; *e.g.*: Na, K, etc. As the strength of the atomic potentials in a sequence of metals increases more terms have to be added to  $E(k)$ , making it more and more structure-dependent. As a result, these metals fall into a sequence of increasing hardness (or strength). It has been suggested that the parameter  $E_g/\Delta$  can also be used as a measure of atomic potential strength, where  $E_g$  is the width of a low-lying band gap at the zone boundary and  $\Delta$  is the width of the energy band itself.

The cohesive energy of a metal can be written as a sum

$$U = U_0 + U_s, \quad (5)$$

of a structure-independent part  $U_0$ , and a structure-dependent term  $U_s$ . The former is given by

$$\begin{aligned} U_0 &= U_e + ZV_0 + W_e \\ &= \frac{3}{5} ZE_F + ZV_0 - 0.9 \frac{Z^2 e^2}{R}. \end{aligned} \quad (6)$$

The first two terms represent the free electron energy averaged over all the occupied states. ( $E_F$  is the free electron Fermi energy.)  $ZV_0$  is the mean value of the pseudopotential in a sphere of  $\Omega$ , *i.e.* the mean potential energy per electron multiplied by the number of electron per ion.  $W_e$  is the electrostatic energy of the ions in the uniform free electron gas. In determining its value, the ions are imagined to be spheres immersed in the electron gas. When crystal structures are taken into account, the geometric factor 0.9 is modified to other values very close to 0.9. Correction terms like

**Table 2.** Comparison between the observed values of the cohesive energy  $U$  with the calculated values of the structure independent part of  $U$ .

Element	$-U_0$ (in ry) calculated	Measured cohesive energy (ry)
Li	0.513	0.512
Na	0.457	0.460
K	0.369	0.388
Be	0.995	1.13
Mg	0.852	0.892
Zn	0.991	1.05
Cd	0.937	0.993
Al	1.32	1.38
Sn	1.69	1.77
Pb	1.73	1.81

the electrostatic self-energy, that is, the interaction of the electron gas with itself, also have to be considered. The structure-independent energy  $U_0$  is thus

$$U_0 = \frac{3}{5} Z E_F + Z V_0 - 0.9 \frac{Z^2 e^2}{R} - \frac{e^2}{2Z} \int \frac{\rho(\mathbf{r})(\mathbf{r})}{|\mathbf{r} - \mathbf{r}'|} d\mathbf{r} d\mathbf{r}'. \quad (7)$$

Further correction terms to allow for correlation and exchange effects among the conduction electrons and for the exclusion of conduction electrons from the core, enable  $U_0$  to be determined more accurately.

A comparison (table 2) between the observed and calculated cohesive energies for a number of metals shows that the structure-independent energy dominates the volume dependence of the total energy; so that, by choosing a particular pseudopotential form,  $U_0$  can be evaluated as a function of  $\Omega$ . From this, the structure, compressibility and strength follow readily.

The structure-dependent energy  $U_s$  has the following terms:

$$U_s = U_{BS} + \Delta W_E. \quad (8)$$

The band structure energy  $U_{BS}$  is the change in energy in going from the free electron model to one containing a periodic potential.  $\Delta W_E$  is a structure-dependent correction to  $W_E$ . In one dimension, if the Fermi level lies just below a band gap, the effect of the band structure is a lowering of the energy below the free electron level. If the Fermi level were far above a band gap, the net effect would leave the free electron energy unaltered. However, the actual Fermi surfaces in metals and other crystals always lie close to the first few reciprocal lattice vectors so that the effect of the band gaps always decreases the total energy, i.e.  $U_{BS}$  is always negative. Figure 3 shows this schematically. This structure-dependent part of the electron energy can be expressed as

$$U_{BS} = \sum_{k < k_F} \sum_g' \frac{V_g V_g^*}{E_k - E_{k+g}}. \quad (9)$$

This is a perturbation-theoretic result, and is not accurate close to the Brillouin zone boundary—it diverges when the Bragg condition is exactly satisfied. The way the

structure controls  $U_{BS}$  can be seen by writing the final form of  $U_{BS}$  as

$$U_{BS} = \sum'_{\substack{g \\ g \neq 0}} [S(g)]^2 [V(q)]^2 \chi(q) \varepsilon(q), \quad (10)$$

where  $S(g)$  is zero except at reciprocal lattice vector points and is thus the sole repository for the influence of the structure. The remaining factors are characteristic only of the nature of the atoms in question, and they are usually collectively termed the energy-wavenumber characteristic  $F(q)$ :

$$F(q) = V(q)^2 \chi(q) \varepsilon(q), \quad (11)$$

$F(q)$  has the form as shown in figure 4 for various metals.

The theory described so far has been used by metal physicists to understand the crystal structure of metals, to provide the basis for the Hume-Rothery rules, and to explain the stability of alloy phases at the absolute zero of temperature (Harrison 1966; Wilkes 1973). Calculation of the theoretical strength has been attempted only for copper and fcc iron. Once  $U$  is calculated the calculation of the strength proceeds on the lines explained in § 2.2. Table 3 indicates the values of theoretical strengths obtained for copper using three different potentials. Obviously, this approach of treating the

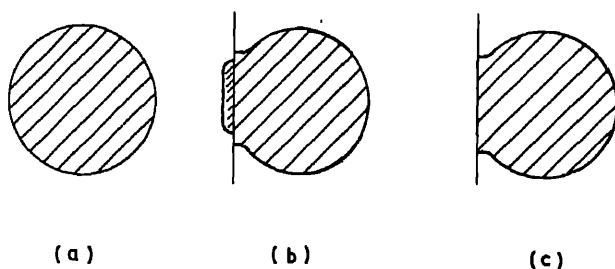


Figure 3. (a) Free electron Fermi surface—a sphere. (b) The Fermi sphere intersected by a Brillouin zone. This gives rise to little energy change. (c) Sphere touching plane—energy gain.

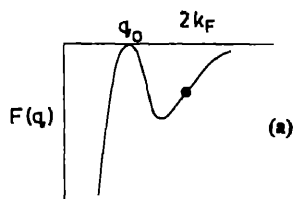
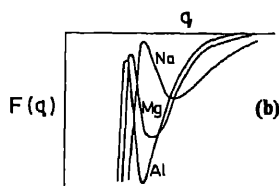


Figure 4. (a) Schematic diagram of energy-wavenumber characteristic. (b) Energy-wavenumber characteristic for some metals.



**Table 3.** The theoretical strength of copper calculated using three different model potentials.

Potential	Theoretical strength, $\sigma_t$ (dyn/cm <sup>2</sup> )	Strain $\epsilon_t = \sigma_t/\Upsilon$
Nonself-consistent KKR	$5.5 \times 10^{11}$ ( $\Upsilon/2.3$ )	0.5
Self-consistent ASW with Ewald correction	3.6 ( $\Upsilon/4.0$ )	0.3
Pair potential	3.6 ( $\Upsilon/4.0$ )	0.5

electrons as nearly free cannot be used when dealing with transition and rare-earth metals, as these possess narrow *d* and *f* bands respectively.

It may be observed from tables 1 and 3 that while there is satisfactory agreement between the computed and observed  $\sigma_t$  values, the calculated values of the strains  $\epsilon_t$  at failure are nearly an order of magnitude greater than those found experimentally. Brenner's (1956) early experiments on single crystal copper whiskers indicated for [111] tension, a maximum stress  $\sim \Upsilon/40$ , where  $\Upsilon$  is the measured Young's modulus for polycrystalline copper, and a strain of only 0.03 (3%). Brenner noticed that in his experiments, all the specimens did not cleave, but sheared apart. It might also be of interest to note that in another study (McQueen and Marsh 1962), flat single crystal samples of Cu were subjected to shock waves of sufficient intensity to cause fracture. Because of the geometry of the experiment, the transverse dimensions of the sample remain essentially fixed. For the [100] orientation, the yield strength obtained was  $\Upsilon/7.5$ . However, the derivation of this value from the known shock-wave intensity involved the use of hydrodynamic equations and equations of state whose validity is difficult to assess.

The substantial difference between the calculated and the observed strains prompts us to examine closely how good the foregoing picture of cleavage is. It is true that in some experiments a shear yield rather than a clean cleavage was observed. Yet, this alone cannot account for the entire difference. It must be that, after all, fracture is not as simple as pure cleavage, which is just the antithesis of cohesion. Finally, it should be mentioned that the strength calculations have so far been performed for a simple cubic unit cell; it is not known at present just how complicated these calculations are for other lower symmetries.

#### 4. Cohesion vs cleavage

Cohesion may be described as a process holding the atoms together and cleavage as a process parting the atoms, and it is tempting to imagine these processes being exactly opposite in character. In tensile tests crystals are held together by cohesion until a load is reached where cleavage (or other fracture) occurs. From the measured load and the cross-sectional area one can compute the average force per unit area which existed at the time of fracture. This is the fracture, or cleavage, stress. It is not the cohesive strength; up to the point of fracture, the crystal had cohesion, and every atomic bond across the future cleavage plane was certainly strained in something close to perfectly-elastic tension. The moment a crack formed, however, be it 10 Å or 2000 Å, a new condition came into being—the crack tip. In short, cleavage is a crack-tip phenomenon,



whereas cohesion is an average property of a crystal. It is appropriate to quote Beachem (1978) here: "Cohesive energies, or cohesive forces, do account for the loads to which tensile or bend specimens can be subjected before they break. Once fracture starts, however, events become localized and average properties become less important than local stresses, general microstructures become less important than local crack-tip microstructures, and bulk environments become less important than local crack-tip environments. Those average macroscopic bulk properties which were used in predicting the forces to which the whisker (or other specimen) could be loaded, before fracture, no longer apply. Local properties and events become decisive. Once fracture starts, it is a whole new ball game."

5. Yield strength, hardness and related parameters

The hardness of materials is a very useful quantity from the practical viewpoint. It is an empirical parameter; depending on the material, and is measured on a suitable scale. Figure 5 shows how the Vicker's hardness varies across the periodic table for the various elements. The hardness of a crystalline material and its yield strength are proportional to each other (Gilman 1973; Havner 1979). Thus the same trend in variation is expected for the strength attribute. The first prominent peak at around  $e/a \sim 7$  lies among the transition metals possessing narrow  $d$ -bands. The second, higher peak is found among the group IV metalloid elements. This latter peak in the

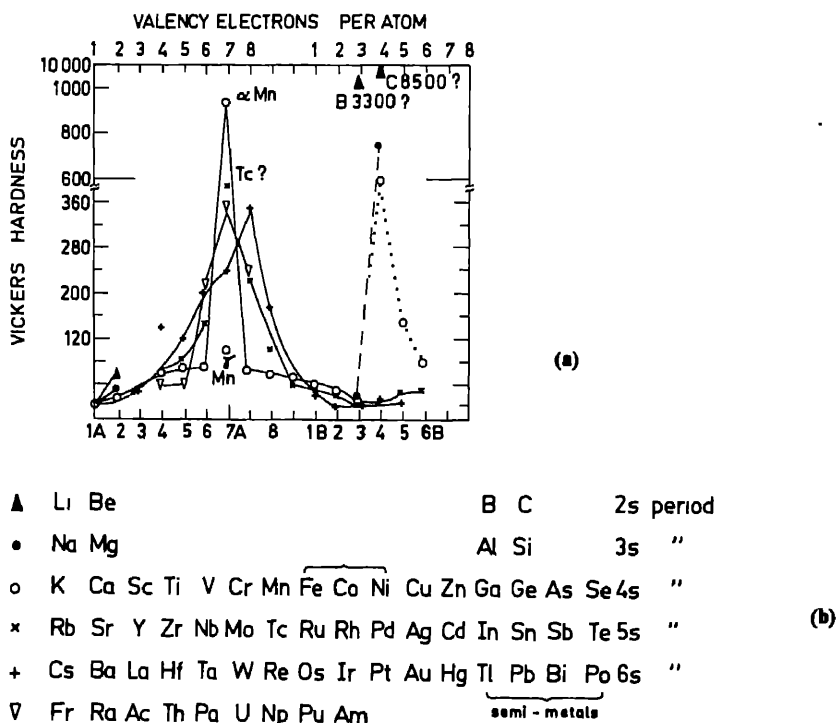


Figure 5. Vickers hardness at room temperature for various metals (after O'Neill 1967).

strength is interpreted in terms of the progressive changeover from metallic to covalent bonding. The second peak will *still* be there, even if one questions the validity of inclusion of diamond (metastable phase) in the figure.

Extensive data on the hardness of metals and alloys are available in the literature. In recent years, the microhardness parameter of metals and alloys has come to be regarded as the 'strength' microprobe (Westbrook and Conrad 1973). Two recent results concerning the behaviour of microhardness are relevant here and serve to illustrate the subtle interplay between the electronic structure and the strength. The first is the rather surprising correlation found between the microhardness and the semiconductor-to-metal transition pressure in group IV elements (Gerk and Tabor 1978). The hardness values of Ge, Si and C (diamond) were found to be 800, 1200 and  $10^4$  kg/mm<sup>2</sup> respectively. These values are remarkably close to the hydrostatic pressure values necessary to initiate semiconductor-to-metal transition in these elements (1000, 1550 and  $\sim 10^4$  kg/mm<sup>2</sup>). This indicates that plastic flow has been sustained (ductility indicates the presence of the metallic phase) in these brittle materials, and is probably because the indentation process involves a large component of hydrostatic stress inhibiting brittle failure. The second point concerns the now-established anisotropy with respect to crystallographic direction of the hardness of crystals. The elegant experiments of Tabor and his school, especially those of Brookes, have established the scratch hardness technique on an analytical basis, and data on the hardness along different crystallographic directions is available (Brookes 1981; O'Neill 1967; Westbrook and Conrad 1973). Results for copper appear in figure 6. One interprets the anisotropy in terms of the variation in the resolved shear stress for a specified indenter orientation, and therefore with the relevant active slip system. Since hardness and yield strength can be imagined to be directly related in metals, the question arises whether the

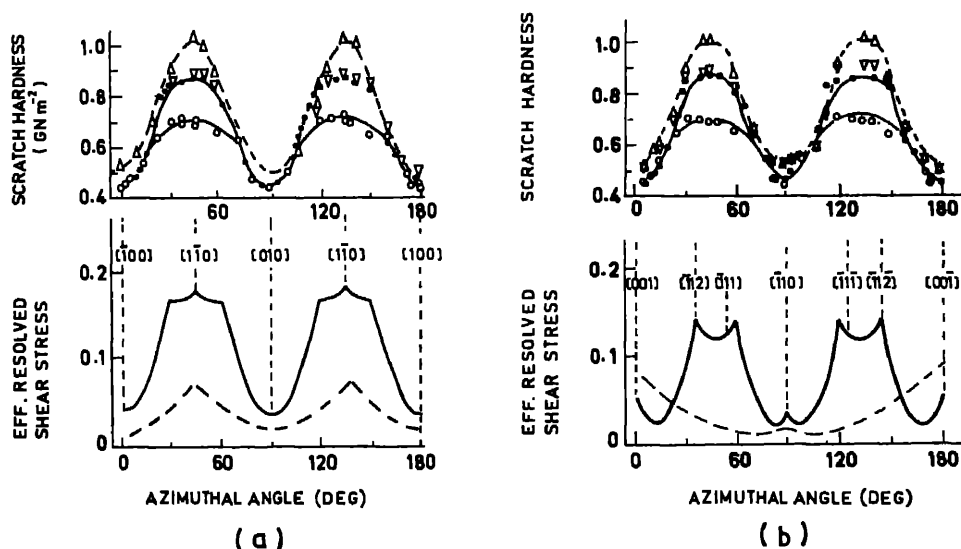


Figure 6. The measured scratch hardness results for copper. The indenter used was diamond with a  $120^\circ$  cone and an edge-leading  $136^\circ$  pyramid, and with a normal load of 500 g. (a) (001) surface and (b) (110) surface. The bottom curves represent the calculated stress values along various directions, all lying in the plane on which measurements are made (Brookes 1981).

above anisotropy can emerge from the calculation of the cohesive energy. The structure-dependent term  $U_{\text{BS}}$  in the total energy (equation (9)) must therefore be subjected to a closer examination. This involves analysing the band structure and Fermi surface in the presence of an applied stress. A beginning has been made in Watts (1979). It appears that by calculating the electron density from these Fermi surface results, one can discuss the influence of external stress on the elastic constants and, consequently the hardness. It is suggested that this line of approach might help in the endeavour to correlate the anisotropy in hardness with the anisotropy in the Fermi surface.

## 6. Strengthening mechanisms: role of electron mediated processes

There are a number of processes, well-known to metallurgists, available for enhancing the strength of elemental metals. The chief methods are (Peckner 1967): (a) dislocation strengthening, (b) strain hardening, (c) solid-solution hardening, (d) precipitation hardening, (e) dispersed-phase strengthening, (f) diffusionless (martensitic) transformation strengthening, (g) superlattice strengthening, and (h) radiation hardening. If we ask whether a definite electron-mediated effect has been identified with the strengthening mechanism in any of the above processes, the answer is a tentative 'yes' for mechanisms (c) and (g). We therefore start with the discussion of solid-solution strengthening.

### 6.1 Solid-solution strengthening

The simplest method of strengthening or hardening is by alloying the host element with other suitable elements/impurities. According to Conrad (1981), the solubility of the impurities will have a different value in the vicinity of dislocations than in other regions, and that the solute distribution will be such as to minimize the energy of the alloy. As the dislocations move under external stress this minimum energy configuration of the impurities is disturbed, raising the energy; the impurities thus tend to act as pinning centres for dislocations. The actual detailed mechanism could either be elastic or electronic in origin. (Ultimately, of course, elastic energy can be traced to an electronic origin). The problem of solution hardening in alloy physics can be related to that of calculating the change in energy of an impurity as its nearest neighbours vary their relative positions. The impurities are assumed to be arranged such that the distortion around the impurity is part of a macroscopic and uniform distortion of the surrounding host. The distortion is produced by first considering a single impurity in the host, undistorted except for the elastic distortion produced by a possible size mismatch. Thus a macroscopic and uniform distortion  $\Delta S$  is applied to the host so as to produce the desired distortion around the impurity. Changes in the energy of the system as a function of the distortion are calculated and  $\Delta E_i$ , the part due to the presence of the impurity, is isolated. The interaction between the impurities is neglected (assuming the impurity to be sufficiently dilute). The magnitude of  $\Delta E_i/\Delta S$  is a measure of the solution strengthening; the larger it is, the greater is the solution strengthening. Figure 7 shows the strengthening coefficient for a few Ti-based alloys (Collings and Gegel 1975). It can be deduced from these figures that the solid solution strengthening increases roughly in proportion to the distance between the columns in the periodic table of the solvent and solute. In Ti, when such an impurity is added, its lack of *d*-character causes a larger perturbation in the wave function of the system in its vicinity.

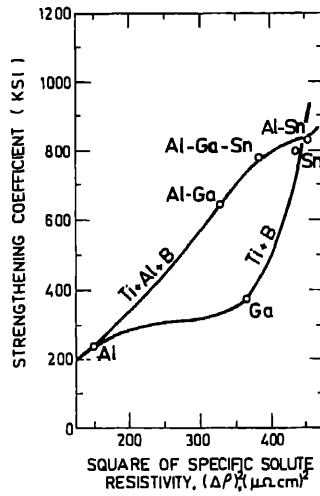


Figure 7. Correlation between the strengthening coefficient ( $d\sigma/dC$ ) (equivalently,  $dE_i/da$ ) and the electrical resistivity for a set of Ti + B alloys and a set of Ti + Al + B alloys ( $B = \text{Ga, Sn, etc.}$ ) (Collings and Gegel 1975).

Assuming that the wavefunction in the vicinity of an atom is the same as it is in the atomic configuration, the problem is simplified by imagining the perturbation introduced by the impurity to be spherically symmetric and highly localized. This then permits the definition of phase shifts introduced by the presence of the impurity. The phase shift (for a general  $l$ -character:  $l = s, p, \dots$ ) has the form

$$\delta_l = \pi Z_l / (4l + 2), \quad (12)$$

where  $Z_l$  is the difference in the number of valence electrons between the impurity and the host. The introduction of the impurity and the corresponding phase shifts disturbs the wave function in the vicinity of the impurity. The distortion is appreciable and causes a given Bloch state to scatter into other states and decay with time. This leads to electrical resistivity; and indeed, a significant correlation has been found in experimental studies between the increase in electrical resistivity  $\Delta\rho$  and the solution hardening. It is of interest to look at the form of the final expression for the strengthening coefficient  $dE_i/da$  (Stern 1975)

$$\frac{dE_i}{da} = \frac{1}{6\pi} \frac{dW}{da} \left[ E_i + \frac{2}{\pi} \int_{-\infty}^0 \frac{\epsilon_0 I(\epsilon) d\epsilon}{\{1 - \epsilon_0 R(\epsilon)\}^2 + \{\epsilon_0 I(\epsilon)\}^2} \right]. \quad (13)$$

This is entirely equivalent to  $d\sigma/dC$ , the variation of the conductivity with the impurity concentration. In (13),  $W$  is the band width and  $a$  is the lattice parameter. ( $\epsilon$  is the reduced energy parameter,  $E/W$ )  $\epsilon_0$  is six times the ground state energy of the impurity in units of  $W$ .  $R$  and  $I$  are certain functions that involve the phase shifts. As  $dW/da$  in (13) is independent of the impurity, the variation of interest is the expression in square brackets. If the impurity forms a bound state level below the bottom of the band ( $U_0 \ll -1$ ), then  $(dE_i/da)$  is proportional to  $U_0$ ; thus larger the magnitude of  $U_0$ , greater is the  $dE_i/da$ , and greater the solid solution strengthening.

Thus, it seems that an impurity with an electronic structure very different from that of the host causes a large perturbation of the wavefunction of the latter, leading to large phase shifts and consequently to high solution hardening. It would be worthwhile to measure the changes in the various elastic constants of the alloy with impurity concentration, in particular to confirm the expected increase in elastic constants with the addition of impurities of the above type (Conrad 1981).

## 6.2 Superlattice strengthening

In a solid solution, the atoms of the different components of the alloy form a common crystal lattice, generally that of the solvent. The metallic type of bond is found in all metal-based solid solutions regardless of the type of bond peculiar to the solute in the solid state. Nonmetallic atoms (C, N, Si, etc.) do not change the metallic bond of metallic solid solutions. In a number of metallic systems (Cu + Au, Fe + Al, Fe + Si, Ni + Mn, etc.) the atoms of both components occupy entirely definite positions in the solid solution lattice if the alloy has been slowly cooled or has been heated for a long time at a definite temperature. Such ordered solid solutions are distinct from those in which the components assume statistically random positions in the lattice. This new order superimposed on the solvent lattice results in a structure called a 'superlattice'. Ordered solid solutions occur when the ratios of the alloyed components (in atomic %) are equal to whole numbers, and are designated  $\text{Cu}_3\text{Au}$ ,  $\text{Fe}_3\text{Al}$  etc. The formation of an ordered solid solution is accompanied by a sharp fall in electrical resistivity and a sharp increase in hardness and strength.

The 'order-disorder' compounds are regarded as intermediate phase between solid solutions and chemical compounds. Much work has been done on these alloys (Warlimont 1974), including the correlation between their mechanical properties (in particular, the strength) and their electronic structure. Experimentally, correlations are found between a typical strength attribute, namely, hardness, and the so-called short-range-order (SRO) parameter, which is related to the ordering energy  $V(k)$ . The SRO parameter can be determined from diffuse x-ray scattering measurements, as in these measurements one really probes the chemical nature of the nearest neighbours of an atom, and thus the SRO. Interesting Fermi surface effects giving rise to satellites in the diffuse x-ray scattering have been seen (Scattergood *et al* 1970), and thus the SRO and the Fermi surface effects in these compounds can be imagined to be related. If only the connection between any elastic constant (or any other suitable strength attribute) and the SRO parameter, can be established, the correlation between the strength and electronic structure in this mode of strengthening can be understood. This last step constitutes the lacuna in this area of investigation.

## 7. Summary

Elucidating the physical basis of one of the important mechanical attributes of a solid, namely, its strength, continues to be a challenging problem. Much success has, no doubt been achieved using the dislocation idea. We have examined the problem of understanding the strength of a crystalline solid on the basis of its electronic properties. The attempts that have been made so far adopted the view that cleavage can be regarded as the exact opposite of cohesion. This enables one to use in full the electronic theory of the cohesion of solids. The strength values calculated on this assumption agree by and

large with the limited experimental values available. However, as pointed out in §3, there is an order of magnitude difference between the calculated and measured strains at failure. Also, it is true that the way the unit cell is assumed to deform in calculating the strength is not realistic. There is scope for refinements here, both in terms of allowing for more realistic deformations as well as extending the calculation to non-cubic symmetries of the unit cell. Nevertheless, it appears that as far as the problem of cleavage is concerned, well-known dislocation mechanisms and dislocation-crack-tip interactions are adequate to account for the strength of materials. The electronic theory (in the form of a phase shift analysis) meets with reasonable success when applied to the solution-strengthening problem. Systematic measurements of the elastic constants of sequences of alloys with, say, titanium as the host metal will be valuable. In the case of order-disorder compounds, an analysis of the relationship between the short-range-order parameter and the elastic constants (and thus the strength) would be very desirable. We have not commented in this article on the possible correlations that may exist between the electronic structure and the other strengthening mechanisms listed in §6.

### Acknowledgement

The author thanks Dr G Venkataraman for suggesting this problem.

### References

- Beachem C D 1978 in *Proceedings of the Second International Conference on Mechanical Behaviour of Materials* (Ohio, Metals Park, ASM) 322ff  
 Brenner S S 1956 *J. Appl. Phys.* **27** 1484  
 Brookes C A 1981 *Philos. Mag.* **A43** 529  
 Carlson A E, Gelatt C D and Ehrenreich H 1980 *Philos. Mag.* **A41** 241  
 Collings E W and Gegel H L 1975 *Physics of solid solution strengthening* (New York: Plenum Press)  
 Conrad H 1981 *Prog. Mater. Sci.* **26** 2  
 Esposito E, Carlsson D D, Ehrenreich H and Gelatt C D (Jr) 1980 *Philos. Mag.* **A41** 251  
 Gerk A P and Tabor D 1978 *Nature (London)* **271** 732  
 Gilman J J 1969 *Micromechanics of flow in solids* (New York: McGraw Hill)  
 Gilman J J 1973 *J. Appl. Phys.* **44** 982  
 Hall E O 1970 *Yield phenomena in metals and alloys* (London: Macmillan and Co.)  
 Harrison W 1966 *Pseudopotentials in the theory of metals* (Massachusetts: Benjamin Inc.)  
 Havner K S 1979 *J. Mech. Phys. Solids* **27** 393  
 Kelly A 1973 *Strong solids* (Oxford: Clarendon Press)  
 Macmillan N H 1972 *J. Mater. Sci.* **7** 239  
 McQueen R G and Marsh S P 1962 *J. Appl. Phys.* **33** 654  
 Milstein F 1982 in *Mechanics of solids* (eds) H G Hopkins and M J Sewell (Oxford: Pergamon Press) 417ff  
 O'Neill H 1967 *Hardness measurement of metals and alloys* (London: Chapman and Hall)  
 Peckner D 1967 *The strengthening of metals* (New York: Reinhold Publishing Co.)  
 Scattergood R O, Moss S C and Bever M B 1970 *Acta Metall.* **18** 1087  
 Stern E A 1975 in Collings and Gegel (1975)  
 Warlimont H 1974 *Order-disorder transformations in alloys* (Berlin: Springer-Verlag)  
 Watts B K 1979 *J. Phys.* **F9** 1565  
 Westbrook J H and Conrad H 1973 *The science of hardness testing and its research applications* (Ohio, Metals Park, ASM)  
 Wilkes P 1973 *Solid state theory in metallurgy* (London: Cambridge University Press)

### Discussion

K R Rao: Could you comment on the nature of the electronic systems you are considering and their relation to the strength of materials?

K Govinda Rajan: The kind of electrons being considered will be specified once the potential is specified. It may also be useful to think in terms of electron charge densities around ion cores and their distortion during loading to understand strength phenomena.

A P Pathak: Instead of talking about the "effects of electronic structure on strength", it appears to be preferable to consider the *correlation* of electronic and mechanical properties. After all, all cohesion in solids is due to electronic structure (either orbital core electrons or conduction/valence electrons), and strength must necessarily be due entirely to electronic structure. Evidently the strength does not depend simply or directly upon, say, the band gap or the conduction electron density (as do the electrical properties), but on combinations of these properties, the core electrons, and of course the structure of the solid. Would you like to comment on this?

Govinda Rajan: In the exhaustive review by K A Gschneider (Solid State Physics, Vol. 16), one finds graphs of electronic properties (resistivity, valence electrons per atom, etc.) *vs* mechanical properties (yield strength hardness) for elemental metals. No significant microscopic picture, however, has emerged. What I have attempted instead is to identify—from the plethora of mechanical properties—the "strength" attribute, and to discuss the role of electronic structure in this context. This is because the strength parameter is, in a sense, the final stage of the mechanical response of a solid, and thus should be amenable to simple calculations. Even this view in which, for instance, cleavage is imagined to be the exact opposite of cohesion has met with serious objection from the metallurgists, as I have taken care to point out

G Venkataraman: It might be interesting to measure the hardness of a semiconductor after pumping electrons into the conduction band by, say, using a laser. This would also have practical relevance to devices like GaAs diode lasers.

## Ferroelasticity

V K WADHAWAN

Neutron Physics Division, Bhabha Atomic Research Centre, Trombay, Bombay 400 085, India

**Abstract.** This paper surveys the present-day description of ferroelasticity in terms of the notion of symmetry descent. Based on the work of earlier authors, a symmetry classification of phase transitions is presented. A general classification of twinning in crystals is also attempted on the basis of this scheme. Most kinds of twinning fall into two broad categories: nonferroelastic and ferroelastic. The shape-memory effect associated with martensitic transitions is discussed briefly. The interesting possibilities of this effect in the case of ferroelectric ferroelastics, for which the electric field provides an additional control parameter, are also mentioned.

**Keywords.** Ferroelasticity; symmetry; phase transitions; twinning; ferroelectric ferroelastics.

### 1. Introduction

The elastic (or recoverable) response of a material to a small external stress can be nonlinear in general, although it is predominantly linear in a large number of crystalline substances, glass, and many cross-linked polymers. The elastic response is markedly nonlinear in cellular structures like wood and in "elastomers" like rubber, which consist of long, spaghetti-like, entwined molecules. The recoverable strain in materials of either the linear or the nonlinear type is usually a *single-valued* function of the small applied stress. There is, however, a technologically important class of materials for which the elastic response is neither linear nor single-valued. Ferroelastic materials belong to this class.

A good deal of our present understanding of ferroelastics has been obtained by considering them as the mechanical analogues of ferroelectric and ferromagnetic materials. In fact, the concept of ferroelasticity itself was introduced by direct analogy with ferroelectricity and ferromagnetism. In particular, one associates stress-strain hysteresis with a ferroelastic, which implies that the spontaneous strain is a double-valued function of stress, even for vanishingly small values of the stress (figure 1). The key to such mechanical behaviour lies in the domain structure of the ferroelastic. As we shall see, the most elegant and rational description of the domain structure of a crystal comes from considerations of broken symmetry at a real or hypothetical phase transition. A proper understanding of ferroelastic behaviour is hardly possible unless one pays attention to the ferroelastic phase transition.

The most significant factor contributing to this understanding has been the approach, initiated by Aizu (1970) and developed by a number of other workers, (Janovec *et al* 1975; Tolédano and Tolédano 1976, 1977, 1980, 1982), according to which ferroelastic phase transitions form part of the larger class of *ferroic phase transitions*: these are transitions which result in a change of the point-group symmetry of the crystal. A *ferroelastic* phase transition, by definition, entails not only a change of the



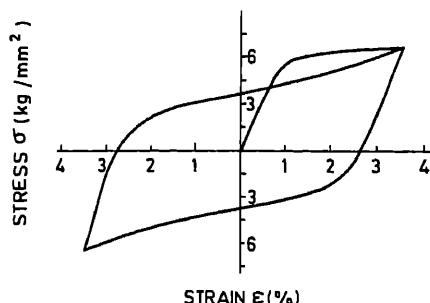


Figure 1. Stress-strain hysteresis curve for the ferroelastic  $\beta'$ -Au<sub>26</sub>Cu<sub>30</sub>Zn<sub>44</sub> martensite at 298 K (Nakanishi *et al* 1971).

point symmetry, but also a change of the crystal system (if we regard the hexagonal and trigonal crystal systems as a single system) (Tolédano and Tolédano 1980).

Ferroc behaviour of crystals encompasses not only ferroelasticity but also other, more subtle, types of mechanical properties like ferrobielasticity. Here I shall describe the salient features of the formalism of ferroicity, developed over the last decade and a half. It will be further argued that the notion of ferroicity also provides a very rational and fairly comprehensive description of the occurrence of twinning in crystals. Twinning, in its general sense, is a far more common feature of crystals than has been realized so far. Ferroelasticity itself is a type of mechanical twinning "with change in form" (Klassen-Neklyudova 1964).

## 2. Ferroelasticity

The term "ferroelasticity" has had a number of connotations, all similar, and yet not quite the same. It was first used in physical metallurgy by Frank in the early 1950's to describe the "rubber-like" memory effect in the gold-cadmium alloy (see Lieberman *et al* 1975). A piece of Au<sub>1.05</sub>Cd<sub>0.95</sub> or InTl, when deformed severely (with up to 10% strain) at room temperature, exhibits almost complete crystallographic and morphological recovery when the external stress is removed. As has been pointed out by Lieberman *et al* (1975), there is a tendency in the literature to use the term "ferroelasticity" somewhat indiscriminately in this context. It is important to distinguish clearly between two situations for describing this pseudoelastic behaviour, depending on whether the deforming stress is applied just above the phase transition temperature  $T_c$ , or at temperatures below  $T_c$ . Figure 2 depicts the two cases schematically. The first case represents "pseudoelasticity by transformation", and the second "pseudoelasticity by reorientation" (Warlimont 1976). In the first case the crystal is initially in the parent phase and the application of a deforming stress causes a reversible stress-induced phase transition. When the stress is removed, all parts of the specimen revert to the parent phase. This behaviour is also described as *superelasticity* (Wasilewski 1975; Barrett and Massalski 1980), or *martensitic thermoelasticity* (Lieberman *et al* 1975). But it must not be called ferroelasticity. Ferroelastic response does not involve any phase transition. Pseudoelastic recovery by reorientation, depicted on the right in figure 2, does correspond to ferroelasticity (Lieberman *et al* 1975). The material is already in the lower-temperature, or ferroelastic phase. It is also capable of existing in more than one twin state or domain. The rubber-like pseudoelastic behaviour results from the reversible migration of the twin boundaries or

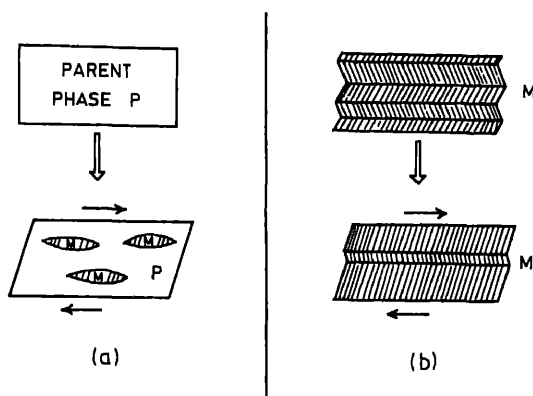


Figure 2. (a) Pseudoelasticity by transformation (or superelasticity), and (b) pseudoelasticity by reorientation (or ferroelasticity).

domain walls. This property is also referred to as *piezomorphic memory* by Lieberman *et al* (1975). As we shall see presently, shape recovery or memory is not regarded by physicists as an essential feature of ferroelasticity; the shape recovery at temperatures below  $T_c$  results from a volume-dependent restoring force, which may not always be present in a ferroelastic crystal.

The stress-assisted double phase transition in TiNi also leads to a mechanical response which resembles ferroelasticity (Wasilewski 1975). However, in keeping with the usage in the rest of physics, the term “ferroelastic” should not be used for those switching phenomena which involve a stress-assisted or any other kind of *phase transition*.

The term “ferroelasticity” was introduced in 1969 (Alefeld *et al* 1969; Aizu 1969) and was used in quite different contexts. Alefeld and coworkers (see Alefeld 1971) were dealing with the problem of hydrogen and other point defects in metals like Nb and Pd, whereas Aizu viewed ferroelastic behaviour as resulting from the occurrence of domain structure (or “orientation states”), taking no note of the presence of any defects in the crystal. We first consider the question of hydrogen or other interstitial impurities in crystals in brief, followed by an exposition of Aizu’s approach and its subsequent development by other workers.

Hydrogen occupies interstitial sites in metals and causes a displacement of the surrounding metal atoms, thus creating local strain fields, as well as a net macroscopic strain. Point defects like hydrogen which distort the host lattice are called *elastic dipoles* (see, *e.g.* Peisl 1978). In general the distortion may be anisotropic and one needs a second-rank polar tensor, ( $\epsilon_{ij}^d$ ), to describe the strain field around a defect. If a uniaxial stress is applied to such a system, a stress-induced diffusion of the interstitial defects to neighbouring sites occurs, resulting in a reorientation of the anisotropic elastic dipoles (figure 3). This time-dependent or anelastic relaxation is known as the *Snoek effect*. Obviously, a stress-strain hysteresis loop looking like the ferroelastic curve of figure 1, will result from such a process. If the defects are highly mobile, one observes the so-called *Gorsky relaxation*, in which the directed diffusion of the defects over many lattice distances occurs under a stress *gradient*. The strain field created by an elastic dipole is long-ranged and is felt by the other elastic dipoles in the metal. This “elastic interaction”

is believed to be largely responsible for the  $\alpha \rightarrow \alpha'$  phase transition in the H-Nb and H-Pd systems (see Wagner 1978). The reason is that Landau's mean field theory works well for this phase transition and it is known that this theory is good for transitions driven by long-range interactions.

Clearly, ferroelastic behaviour resulting from the presence of point defects will disappear in the absence of these defects. This is where Aizu's concept of ferroelasticity differs from that of Alefeld *et al.* In the former, ferroelastic properties arise from the pseudosymmetry resulting from a (real or hypothetical) structural phase transition, and not from the presence of defects. The concept of a *prototype symmetry* plays a central role here. The prototype is the highest supergroup symmetry attainable by, or conceivable for, a given crystal without requiring a rupture or reconstructive rearrangement of chemical bonds. A ferroelastic phase (more generally, a ferroic phase) emerges from the prototype symmetry owing to a small, spontaneous, symmetry-breaking "distortion" when some control parameter such as the temperature is varied. Figure 4 provides an illustration of this, where an orthorhombic symmetry  $mmm$  ( $D_{2h}$ ) is assumed for the prototype. A phase transition to monoclinic symmetry can lead to two possible *orientation states*,  $S_1$  and  $S_2$ , both of which are equally stable in the absence of an external force. Although the actual symmetry of the ferroelastic phase is monoclinic, it is also pseudo-orthorhombic because it differs only slightly from the prototype configuration. Since the two states  $S_1$  and  $S_2$  also differ only slightly from each other, it should be possible to switch  $S_1$  to  $S_2$  and *vice versa* by applying a small, suitably oriented, uniaxial stress, as shown in the lower part of figure 4. This possibility of the occurrence of more than one orientation state, (*i.e.*, the presence of domain structure), is what is responsible for ferroelastic behaviour, in particular the stress-strain hysteresis. Aizu (1969) defined a ferroelastic as a crystal which has two or more equally stable

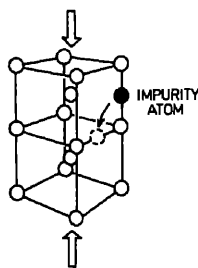


Figure 3. Stress-induced diffusion of an interstitial impurity (Snoek effect).

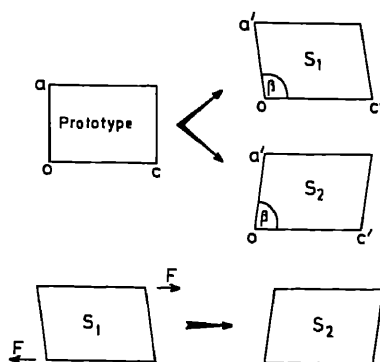


Figure 4. Schematic of an orthorhombic-to-monoclinic ferroelastic phase transition, giving two equivalent orientation states  $S_1$  and  $S_2$  in the lower-symmetry phase.

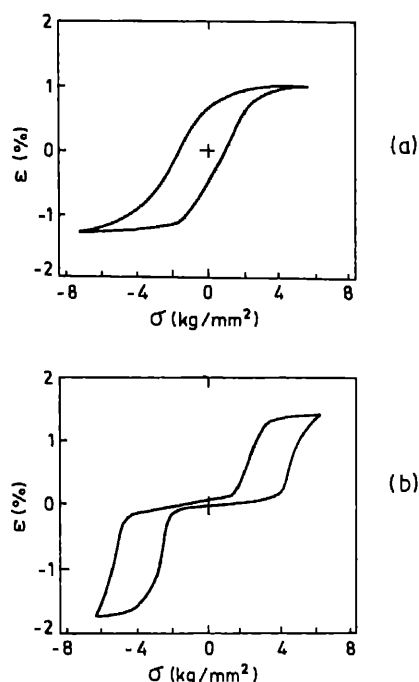


Figure 5. Illustrating the distinction made in physical metallurgy between (a) ferroplastic behaviour and (b) ferroelastic behaviour. The curves shown are for the alloy  $\text{Au}_{1.05}\text{Cd}_{0.95}$  (Lieberman *et al* 1975).

orientation states, and which can be switched from one such state to another by the application of a suitable uniaxial stress. Since all the orientation states are equally stable, the system may not bounce back to the initial state when the stress is removed. It is clear from the above definition that what is called ferroelasticity by Aizu would be described as *ferroplasticity* by physical metallurgists (see Lieberman *et al* 1975). The distinction between ferroelastic and ferroplastic behaviour is illustrated in figure 5 for a gold-cadmium alloy. Very often this distinction is not made in physics, because the term "ferroelastic" is used to imply "ferromechanical", in the sense that the driving force conjugate to the 'order parameter' (strain) is mechanical or elastic in nature (and not electric or magnetic).

Aizu's definition of ferroelasticity also supersedes the earlier usage of this word in physics for describing magnetostrictive and electrostrictive distortions in ferromagnetic and ferroelectric crystals. It is possible for a crystal to be ferroelastic without also being ferroelectric or ferromagnetic. The present concept of ferroelasticity has led to the development of an elegant, symmetry-based, classification of a very large class of phase transitions, and we turn now to an outline of this scheme.

### 3. A symmetry classification of phase transitions in crystals

Figure 6 presents a symmetry classification of phase transitions in crystals based on the work of various authors (Tolédano and Tolédano 1982 and references therein). We exclude from this scheme reconstructive phase transitions like the graphite-to-diamond transition. We also exclude those martensitic and other phase transitions where the lattice distortion is so drastic that it results in a change of coordination number. An example of this is the transition occurring in  $\text{CsCl}$ , where the structure changes from

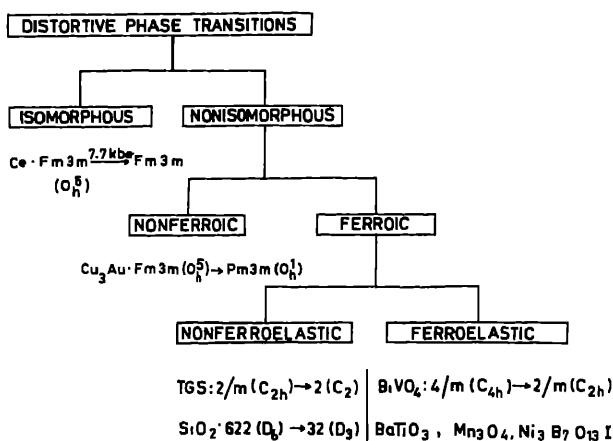


**Figure 6.** A classification of phase transitions based on considerations of symmetry descent from a prototype symmetry.

simple cubic to fcc on heating through the phase transition at 733 K, resulting in a change of the coordination number from 8 to 6.

We use the term *distortive* for the phase transitions considered in figure 6, although even this term is not entirely adequate. It is intended to cover both displacive and order-disorder phase transitions (Muller 1981). The term "group-subgroup type phase transitions" would be perhaps more appropriate if we remember that a group permits the trivial possibility of being its own subgroup or supergroup. In this scheme, all phases of a crystal are regarded as derived from a certain supergroup symmetry called the *prototype* (Aizu 1981). The prototype is the highest conceivable crystallographic symmetry from which a given phase can result by a small distortion. Phase transitions in this classification are therefore not always between two consecutive phases, but between the prototype and the phase under consideration. All phase transitions in crystals can be divided into two categories: *isomorphous phase transitions* and *nonisomorphous phase transitions*. In the former, there is no change in the space-group symmetry of the crystal. A well-known example is the transition occurring in Ce at a pressure of 7.7 kbar (0.77 GPa), involving a volume collapse of about 14 %, but leaving the space-group symmetry unchanged as  $Fm\bar{3}m$  ( $O_h^5$ ). The change of space-group symmetry at a nonisomorphous phase transition can be of two types: *nonferroic* and *ferroic*. In a nonferroic phase transition there is a change in only the translational symmetry, but no change in the point-group symmetry (Tolédano and Tolédano 1982). Perhaps the best known example of this type is the order-disorder transition occurring in the alloy  $\text{Cu}_3\text{Au}$  at 667 K, where the symmetry changes from  $Fm\bar{3}m$  ( $O_h^5$ ) to  $Pm\bar{3}m$  ( $O_h^1$ ). The high pressure transition occurring in EuS at 215 kbar (21.5 GPa) is another example, involving the same symmetry change as  $\text{Cu}_3\text{Au}$ . Ferroic phase transitions involve a change of the point-group symmetry with or without a change of the translational symmetry. If there is a change of the point-group symmetry but no change of the crystal system (provided we do not regard the hexagonal and trigonal crystal systems as distinct for the purposes of this definition), the phase transition is defined as *nonferroelastic* (Tolédano and Tolédano 1976). Examples of nonferroelastic transitions include the ferroelectric transition in triglycine sulphate (symmetry changing from

$2/m(C_{2h})$  to  $2(C_2)$ ), and the  $\beta \rightarrow \alpha$  transition in quartz (symmetry changing from  $622(D_6)$  to  $32(D_3)$ ). With the above proviso about hexagonal and trigonal crystal systems, a change of crystal system becomes a necessary as well as a sufficient condition for a phase transition to be called *ferroelastic* (Tolédano and Tolédano 1980). A ferroelastic phase transition may be either purely ferroelastic, as in  $\text{BiVO}_4$ , or it may be simultaneously ferroelectric as in  $\text{BaTiO}_3$ , or simultaneously ferromagnetic as in  $\text{Mn}_3\text{O}_4$ . The Ni-I boracite undergoes a phase transition which is simultaneously ferroelastic, ferroelectric and ferromagnetic.

I have recently come across a statement by Fleury and Lyons (1981) according to which a centre of symmetry is always preserved across a ferroelastic phase transition. The rationale behind this statement is not entirely clear; in the cubic-to-tetragonal phase transition in  $\text{BaTiO}_3$ , for example, the centre of symmetry is not preserved even though the phase transition is ferroelastic; the fact that the order parameter of this transition does not have the symmetry of a strain component does not preclude the occurrence of ferroelasticity in the tetragonal and the other lower-symmetry phases of  $\text{BaTiO}_3$  (see also Aizu 1972a).

#### 4. Ferroic crystals

A ferroic crystal is one which can undergo a ferroic phase transition. The definition of a ferroic transition in terms of a change in the point-group symmetry has a deep significance. Among other things, it enables us to classify ferroic crystals in terms of their macroscopic physical properties like polarization, strain, etc. The reason for this is that these properties are described by the point group symmetry of the crystal, and a ferroic phase is derived, by definition, by deleting certain point-group operations of the prototype. The lowering of the point symmetry at a ferroic phase transition must necessarily be accompanied by the emergence of at least one new macroscopic tensor property component. If this component also has the symmetry of the order parameter, the corresponding response function becomes anomalously large in the vicinity of the transition. This is important in many of the device applications of ferroic crystals.

Let us imagine a crystal in a particular orientation state  $S_1$ , under the influence of an external electric field ( $E_i$ ), a magnetic field ( $H_i$ ) and a stress ( $\sigma_{ij}$ ). The free energy density for this orientation state can be written as

$$d\Phi = SdT - P_idE_i - M_idH_i - \varepsilon_{ij} d\sigma_{ij}, \quad (1)$$

where  $S$  denotes the entropy,  $P_i$  the polarization,  $M_i$  the magnetization, and  $\varepsilon_{ij}$  the strain.  $P_i$ ,  $M_i$  and  $\varepsilon_{ij}$  consist of a spontaneous part (if any) and an induced part owing to the presence of the external fields. One can integrate (1) to obtain the free-energy density  $\Phi_1$  for state  $S_1$ . Similarly, the free-energy density  $\Phi_2$  can be obtained for another orientation state  $S_2$ . The difference  $\Delta\Phi = \Phi_2 - \Phi_1$  determines whether the crystal makes a state shift from  $S_1$  to  $S_2$ , or vice versa under the action of the external forces. The final expression for  $\Delta\Phi$  can be written as follows (see Wadhawan 1982 for details):

$$\begin{aligned} -\Delta\Phi = & \Delta P_i^0 E_i + \Delta M_i^0 H_i + \Delta \varepsilon_{ij}^0 \sigma_{ij} + \frac{1}{2} \Delta \kappa_{ij} E_i E_j + \frac{1}{2} \Delta \chi_{ij} H_i H_j \\ & + \frac{1}{2} \Delta s_{ijkl} \sigma_{ij} \sigma_{kl} + \Delta \alpha_{ij} E_i H_j + \Delta d_{ijk} E_i \sigma_{jk} + \Delta Q_{ijk} H_i \sigma_{jk} \\ & + \frac{1}{6} \Delta e_{ijk} E_i E_j E_k + \dots \end{aligned} \quad (2)$$

Here  $\Delta P_i^0 = P_{2i}^0 - P_{1i}^0$  is the difference between the values of the  $i$ th component of the spontaneous polarization in the states  $S_2$  and  $S_1$ . The other difference terms are defined similarly.  $\kappa_{ij}$ ,  $\chi_{ij}$  and  $s_{ijkl}$  are, respectively, the elements of the electric susceptibility tensor, the magnetic susceptibility tensor, and the compliance tensor.  $\alpha_{ij}$ ,  $d_{ijk}$  and  $Q_{ijk}$  are elements of the magnetoelectric, piezoelectric and piezomagnetic tensors respectively, and  $e_{ijk}$  stands for the components of the third-order electric susceptibility tensor. Equation (2) serves to define the various types of ferroic crystals. A ferroelectric crystal is defined as one for which at least one pair of orientation states exists such that  $\Delta P_i^0 \neq 0$  for one or more values of  $i$ . Similarly, a ferroelastic crystal is one for which  $\Delta e_{ij}^0 \neq 0$  for at least one pair of orientation states. A ferromagnetic crystal is defined similarly. Ferroelectric, ferroelastic and ferromagnetic crystals are collectively called *primary ferroics*.

It is clear from (2) that other types of ferroicity are also possible. For example, if  $\Delta s_{ijkl} \neq 0$  for one or more pairs of orientation states, the crystal is said to be a *ferrobielastic*. Quartz is a well-known example of a ferrobielastic crystal. The Dauphiné twins of  $\alpha$ -quartz differ in the sign of the elastic compliance coefficient  $s_{1123}$  (as well as in the signs of other symmetry-related coefficients). Consequently, although the two twin states do not differ in spontaneous strain (and therefore quartz is not a ferroelastic), a difference in *induced* strain can be established between them under the action of a common uniaxial stress. A suitable stress can then act on this difference to cause switching from one twin state to the other. Lead germanate,  $\text{Pb}_5\text{Ge}_3\text{O}_{11}$ , is another crystal which can be expected to exhibit ferrobielastic and ferroelectric switching concomitantly. Hence, for applied stresses smaller than the elastic limit, crystals may exhibit elastic, ferroelastic and ferrobielastic (figure 7) mechanical response, or any combination of these.

Still other types of ferroic behaviour can be anticipated from (2). Differences in the piezoelectric tensor between two orientation states can result in *ferroelastoelectric* switching under the *combined* action of an electric field and a uniaxial stress. In an analogous manner, *ferromagnetoelastic* switching becomes possible through differences in the piezomagnetic tensor, and so on. Ferrobielasticity ( $\Delta\Phi \sim \sigma^2$ ), ferrobielectricity ( $\Delta\Phi \sim E^2$ ), ferrobimagnetism ( $\Delta\Phi \sim H^2$ ), ferroelastoelectricity ( $\Delta\Phi \sim \sigma E$ ), ferromagnetoelasticity ( $\Delta\Phi \sim \sigma H$ ) and ferromagnetolectricity ( $\Delta\Phi \sim HE$ ) are the six types of *secondary ferroicity* possible in crystals (Aizu 1972a, 1973). Aizu (1970) has derived 773 possible "species" of ferroic crystals (a species is characterized by the point symmetry of the prototype and the point symmetry of the ferroic phase in question) by assuming that: (a) every time-symmetric point group can become the prototypic point group in some species of ferroic crystal; (b) when a prototypic point group is specified, every one of its proper subgroups can become the ferroic point group in some species with this prototypic point group; and (c) when a

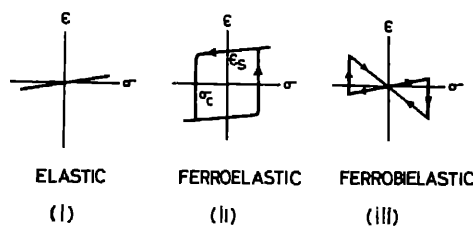


Figure 7. Typical curves illustrating the distinction between elastic, ferroelastic, and ferrobielastic response of crystals to external stress.

prototypic and a ferroic point group are specified, as many species are possible as the number of different ways in which the elements of the ferroic point group can be put in correspondence with the elements of the prototypic point group.

## 5. Domain structure

The mechanical behaviour of a ferroelastic is influenced in a crucial way by its domain structure. In fact, many of the applications of ferroelastics and other ferroic crystals depend on our ability to control the nucleation and mobility of their domain walls. The fracture-toughness achieved in zirconia by exploiting the ferroelastic phase transition is a case in point. A surprisingly large amount of information about the expected domain structure of a crystal can be obtained from symmetry considerations alone. Two or more domains or twin configurations become possible in a crystal because of the lowering of the prototype symmetry at a real or hypothetical phase transition. Regions of the crystal which were completely equivalent under the operations of the prototype symmetry group become nonequivalent either with respect to orientation, or with respect to mutual disposition, or both; this is what gives a crystal its domain structure.

In the spirit of the Landau theory, one holds the emergence of an order parameter responsible for the lowering of the prototype symmetry. The symmetry  $G$  of the daughter phase is determined by the symmetry  $G_0$  of the prototype and the symmetry  $\Gamma$  of the order parameter.  $G$  can be obtained by the principle of superposition of symmetries, commonly known as the *Curie principle* (see Kopstik 1968). Shubnikov and Kopstik (1974) have stated a more updated version of it and called it the Neumann-Minnigerode-Curie principle, (NMC) principle. According to the Curie principle: "When several different natural phenomena are superimposed on one another, forming a single system, their *dissymmetries* add up. As a result, only those elements of symmetry common to all the phenomena remain". If, for example,  $G_1$  and  $G_2$  denote the symmetry groups corresponding to two physical properties of a crystal, the symmetry  $G$  of the crystal cannot be higher than the intersection of  $G_1$  and  $G_2$ . If we consider the symmetry groups  $G_i$ ,  $i = 1, 2, 3, \dots$ , of all possible physical properties of the crystal, the symmetry  $G$  of the crystal is given by the intersection of all these groups:

$$G = G_1 \cap G_2 \cap G_3 \dots = \bigcap G_i \quad (3)$$

The more familiar Neumann's principle follows from the above as an inclusion relation:

$$G_i \supseteq G. \quad (4)$$

In other words, the symmetry element ( $G_i$ ) of any physical property of a crystal include all the symmetry elements ( $G$ ) of the crystal.  $G$  is contained in every  $G_i$ ; in fact, it is a subgroup of every  $G_i$ . Equations (3) and (4) can be combined (Shubnikov and Kopstik 1974) to read

$$G_i \supseteq G = \bigcap G_i \quad (5)$$

In the context of a phase transition accompanied by the emergence of an order parameter having the symmetry group  $\Gamma$ , it follows that the symmetry group  $G$  of the resultant phase is given by

$$G = G_0 \cap \Gamma, \quad (6)$$



where  $G_0$  is the symmetry group of the disordered phase.  $G$  is that maximal subgroup of  $G_0$  which leaves the order parameter invariant (Janovec 1972).

The Curie principle can be applied not only to determine the compatibility or incompatibility of  $G$ ,  $G_0$  and  $\Gamma$ , but also to understand inter-domain relationships. Suppose a crystal undergoes a phase transition from symmetry  $G_0$  to  $G$  on cooling, (that is, under the influence of a scalar control parameter,  $T$ ); it follows that, in the lower-temperature phase, the macroscopic symmetry of the sample crystal *as a whole* would be the intersection of  $G_0$  and the symmetry group of a scalar. The intersection of these two is  $G_0$  itself. Thus, macroscopically speaking, the crystal *as a whole* has an average symmetry  $G_0$  even in the daughter phase. But the microscopic symmetry has actually been reduced from  $G_0$  to  $G$ . The two statements, taken together, imply that the crystal must split into domains in the lower phase. It also follows that, since the symmetry group of each domain is  $G$ , transformation operations which can map one domain to another are those which are *lost* at the phase transitions (Janovec 1976). These are called  $\Phi$ -operations (Aizu 1974). In particular, mirror planes of symmetry lost at a phase transition can become domain walls separating two contiguous domains of the lower phase (Mallard's law). To quote Shubnikov and Kopstik (1974): "The whole process of a phase transition obeys the astonishing law discovered by philosophers—the *symmetry compensation law*: If symmetry is reduced at one structural level, it arises and is preserved at another!"

Let  $G'_0$  and  $G'$  denote the point groups of the space groups  $G_0$  and  $G$  respectively. If  $n_p$  and  $n_f$  are the orders of the groups  $G'_0$  and  $G'$ , the maximum possible number of orientation states or rotational domains possible in the ferroic phase is given by (Aizu 1970; Janovec 1972)  $q' = n_p/n_f$ . Any operation which is a symmetry operation of  $G'_0$ , but not that of  $G'$ , is called an  $F$ -operation. An  $F$ -operation maps one orientation state to another. Choosing a common reference frame for all the orientation states, if  $G'$  is the point group for a particular orientation state  $S_1$  and  $f$  is any  $F$ -operation from  $S_1$  to another orientation state  $S'_1$ , the set of all  $F$ -operations from  $S_1$  to  $S'_1$  is equal to  $fG'$  (Aizu 1970; Janovec 1972). The point group  $G'_0$  can be split into a sum of  $q'$  left cosets of the subgroup  $G'$ :

$$G'_0 = f_1 G' + f_2 G' + \dots + f_{q'} G'. \quad (7)$$

Here a coset  $f_r G'$  comprises all operations mapping the domain  $S_1$  to the domain  $S_r$ . There is a one-to-one correspondence between domains and left cosets. Extending the above considerations from point groups to space groups, if  $G$  is a subgroup of  $G_0$  of index  $q$ ,  $G_0$  can be written as a sum of left cosets as follows

$$G_0 = \phi_1 G + \phi_2 G + \dots + \phi_q G. \quad (8)$$

Once again, there is a one-to-one correspondence between a left coset and a possible structural configuration called a *situation* or a *terrain* (Aizu 1974). The  $\phi$ 's are a representative set of  $\Phi$ -operations from a particular situation to each of the  $q$  situations.

A single domain may consist of one or more terrains, but a uniterrain sample is necessarily unidomain also. The possible occurrence of more than one terrain in a domain is referred to as *domain degeneracy* (Janovec 1976). It can be determined with the help of *Hermann's theorem* (Hermann 1929), according to which, if  $G$  is a subgroup of a space group  $G_0$ , then one can always find a space group  $Z$  which contains  $G$  as a klassengleiche or equipoint-group subgroup, and which is also a maximal equitranslational subgroup of  $G_0$  ( $G \subseteq Z \subseteq G_0$ ). The index of  $Z$  in  $G_0$  is also equal to  $q' (= n_p/n_f)$ . The number of terrains (also called translational domains or antiphase

domains) possible in each (rotational) domain is given by the index  $m$  of  $G$  in  $Z$ . The domain degeneracy is  $m$ . It is also equal to the number of times by which the volume of the primitive unit cell of the daughter phase is nominally larger than that of the primitive cell of the prototype. The total number of situations,  $q$ , is related to the number of orientation states,  $q'$ , through  $m$ :

$$q = q'm. \quad (9)$$

The fact that  $q$  is a finite number is a consequence of the discrete nature of crystallographic space groups. If the prototype symmetry  $G_0$  is described only by a continuous symmetry group, the symmetry group  $G$  of the ordered phase may have an infinite index  $q$ . In such a case the domain structure is replaced by its dynamical counterpart, namely the occurrence of *Goldstone modes*, which are gapless excitations that tend to restore the prototype symmetry (Janovec 1976).

## 6. An unsolved problem of ferroelasticity

The elegant and powerful group-theoretical formalism developed by physicists for describing ferroelastic and other forms of ferroic switching in crystals in a unified way is not without a flaw. This was first pointed out by Laves (1975) by citing the example of mechanical twinning in hcp metals like Mg. Such metals have a point-group symmetry  $6/mmm$  ( $D_{6h}$ ), and apparently undergo ferroelastic switching by shearing along the planes  $\{1\ 0\ \bar{1}\ 2\}$  in the directions  $\langle \bar{1}\ 0\ 1\ 1 \rangle$ . This type of mechanical twinning results in a large reorientation (by  $84^\circ$ ) of the slip plane (0001), and has a drastic influence on the plastic behaviour of these metals (Klassen-Neklyudova 1964). But this apparently ferroelastic twinning does not come within Aizu's formalism because it is not possible to conceive a *crystallographic* prototype symmetry, of which the symmetry  $6/mmm$  of the ferroelastic phase is a subgroup.

Aizu (1970) gave a precise definition of prototype symmetry by demanding that the following two conditions be satisfied: (a) The point-group symmetry of the prototype should contain all the  $F$ -operations from each of the orientation states of the ferroic to all orientation states. (b) If any symmetry operation of the prototype point group is performed on any orientation state, the result must only be one of the possible orientation states, and none other.

The prototype group is also a proper supergroup of the ferroic point group. The example of Mg seems to indicate that ferroelasticity can also occur in materials with a symmetry such that only a subgroup of this symmetry is a subgroup of the prototype symmetry (Laves 1975). If a relaxing of the definition of a prototype is allowed so as to accommodate such a possibility, the prototype would not always contain *all* the symmetry elements of the point group of the ferroelastic phase. Such a modification of the theory does not look very appealing, particularly because it negates a good deal of the elegant description of domain structure of ferroelastic and other ferroic crystals (§5). It also goes against the spirit of the Landau theory of phase transitions. No really good solution of this problem is available at present.

## 7. Twinning

Before the development of x-ray crystallography, the classification of twinning in crystals was based mainly on morphological studies made by contact goniometry and

optical goniometry (Friedel 1926). X-ray diffraction patterns, particularly those obtained with Buerger's precession camera, give us directly a picture of the reciprocal lattice of a twinned crystal. This has led to what may be called the second stage in the classification of twinning (Donnay and Donnay 1974). All twinned crystals are divided into two categories, depending on whether the diffraction pattern reveals a single orientation of the reciprocal lattice for the twins ("obliquity"  $\omega = 0$ ), or two or more orientations with a common origin ( $\omega \neq 0$ ). In the first case one talks of *twinning by twin-lattice symmetry* (TLS), and in the second case *twinning by twin-lattice quasi-symmetry* (TLQS). A further subdivision of each of these main categories is made in terms of the *twin index*  $n$ , defined as the ratio of the volume per node in twin lattice to the volume per node in crystal lattice. The twin lattice is the lattice with the smallest cell that is common to both members of the pair. The twin lattice is perfectly continuous across the twin wall for  $\omega = 0$ , but has a small deviation at the wall when  $\omega \neq 0$ . Twinning by TLS and by TLQS is also called, respectively, "twinning without change of form" and "twinning with change of form" (Klassen-Neklyudova 1964).

This description of twinning concerns itself mainly with geometrical features like orientational relationships of the lattices. Although many crystallographers have indeed dealt with twinning at the structural level, the descriptive terminology available at present does not make evident certain features such as electrical twinning in a ferroelectric crystal, or more subtle effects like differences in the piezoelectric tensor in the twin structure of a crystal like  $\text{NH}_4\text{Cl}$ . I think a stage has now been reached where a more comprehensive and informative classification of twinning can be made in terms of the ideas of symmetry descent discussed in §§3 and 5. We shall use the word "twinning" in a very general sense here, covering all electric, magnetic, elastic or other forms of domain structure possible in a crystal.

Twinning in a crystal implies that the structure can exist in two or more configurations that are energetically equivalent, but differ in mutual orientation, or mutual disposition, or both. The enthalpy barrier for changing one configuration to the other across a twin wall may be either reasonably low (as in Dauphine twins in  $\alpha$ -quartz), or it may be extremely high, even exceeding the breakdown field or the fracture strength (as in Brazil twins in quartz, and also many growth twins). In the former case, barring exceptions like magnesium (§6), an  $F$ - or  $\Phi$ -operation derived from an appropriately assigned prototype symmetry should always be definable. In the latter case, there are two possibilities:

(a) The twins across the interface are lawfully related by an  $F$ - or  $\Phi$ -operation, and the enthalpy barrier just happens to be high; (b) a proper  $F$ - or  $\Phi$ -operation is not definable for mapping one twin into the other; this may happen when, for example, the crystal is in a prototypic phase, and not a ferroic phase (see Aizu 1981).

Thus all twinning can be divided into two types (I and II, say). Type I twins are related by an  $F$ - or  $\Phi$ -operation, whereas type II twins are not. For type I twins a prototype symmetry is always conceivable. In many cases of this type, even if switching from one twin to the other is not possible at room temperature, it may become possible at temperatures sufficiently close to the transition temperature. In any case, demonstration of switching is neither a necessary nor a sufficient condition for assigning a twin to type I; It is necessary and sufficient that an  $F$ - or  $\Phi$ -operation, derived from an appropriate prototype symmetry, is definable. In this scheme, twinning in magnesium will be classified as type II (§6). A better example of type II twinning is provided by Brazil twins in quartz. They are related by a mirror operation, which is not a part of the

symmetry 622 ( $D_6$ ) of  $\beta$ -quartz. The symmetry 622 is prototypic for the symmetry 32 ( $C_6$ ) of  $\alpha$ -quartz, which can consequently exist in two orientation states related by an operation that is a two-fold rotation about the optic axis (Wadhawan 1982). These two orientation states are just the Dauphiné twins. Unless a prototypic symmetry higher than 622 can be conceived for this crystal (which is not possible because that would involve a drastic breaking and reassembling of the structure), Brazil twins do not constitute domains or terrains in the sense discussed in §5. (The concept of the prototype has been discussed with great clarity by Aizu 1978, 1981.)

For type I twins, a nonisomorphous phase transition to the prototypic phase either actually exists, or can be imagined. In  $\text{BaTiO}_3$ , for example, the cubic phase is prototypic to the tetragonal, trigonal and orthorhombic phases, whereas in  $(\text{H}_4)_2\text{SO}_4$  the hexagonal prototypic phase is hypothetical (Sawada *et al* 1976; also Dvorak 1978). A nonisomorphous phase transition can be either nonferroic or ferroic (figure 6). If it is nonferroic, twinning comprises antiphase domains only. About crystals undergoing nonferroic transitions have been listed by Tolédano and Tolédano (1982). This twinning is obviously of the TLS type, and the superlattice reflections resulting from it lead to a smaller primitive unit cell in the reciprocal lattice. In ferroic crystals, twinning can occur either by TLS or by TLQS, depending on whether the phase transition is nonferroelastic or ferroelastic (figure 6).

#### Nonferroelastic twinning

Although all nonferroelastic twinning will be dubbed as just twinning by TLS in the earlier scheme of classification, the advantage of the new scheme suggested here can be seen from the fact that many further subdivisions are possible: We can have ferroelectric twinning (as in TGS, SbSI and  $\text{LiNbO}_3$ ), ferrobielastic twinning (as in quartz), ferroelectric-ferrobielastic twinning (as in  $\text{Pb}_5\text{Ge}_3\text{O}_{11}$ ), ferroelastoelectric twinning (as in  $\text{NH}_4\text{Cl}$ ,  $\text{CuCsCl}_3$  and  $\alpha$ -quartz), ferromagnetoelastic twinning (as in  $\text{F}_2$ ,  $\text{MnF}_2$  and  $\text{FeCO}_3$ ), ferromagnetoelastic twinning (as in  $\text{Cr}_2\text{O}_3$ ), and ferrotrilastic twinning (as in  $\text{Cr}_5(\text{PO}_4)_3\text{Cl}$  and the mineral elapsolite ( $\text{K}_2\text{NaAlF}_6$ )). Twin domains observed in  $\text{Fe}_{36}\text{Cr}_{22-x}(\text{Ti}, \text{Mo})_x$ ,  $\gamma$ -brass,  $\delta$ -NiMo, lithium ferrite  $\text{LiAl}_4\text{Mo}$  (Amelinckx 1976) also constitute a subclass of nonferroelastic twinning. Nonferroelastic twinning may indeed occur in ferroelastic crystals, in the so-called *partial* ferroelastics, in which some twins are ferroelastically related and some are nonferroelastically related. Examples of the latter are the antiparallel ( $180^\circ$ ) domains in  $\text{BaTiO}_3$ . A partial ferroelastic is that for which  $\Delta\epsilon_{ij}^0 = 0$  in (2) for at least one  $i$  (but not all pairs) of orientation states.

An extremely useful tabulation of the "orders" of state shifts in ferroic crystals has been given by Aizu (1972a). The same tabulation can provide a very informative basis for defining the "order" of twinning in a ferroic crystal. For example, ferroelectric twinning can be described as "first-order electrical twinning", and ferrobielastic twinning as "second-order mechanical twinning".

TLS twinning or zero-obliquity twinning has two subclasses: (i) *twinning by merohedry*, for which the twin index  $n = 1$ , and (ii) *twinning by reticular merohedry*, for which  $n > 1$ .

In the second case  $n$  is usually equal to 3, and very rarely equal to 5 (Donnay and Donnay 1974). For purposes of crystal structure determination, twinning by merohedry presents some special problems. Various procedures have been suggested to deal with these (Catti and Ferraris 1976; Rees 1982; Jameson 1982). Both Dauphiné and

Brazil twinning in  $\alpha$ -quartz is described as twinning by merohedry in the old scheme of classification (Donnay and Donnay 1974), whereas, in the present scheme, Brazil twins are type II twins, while Dauphiné twins are type I ferroelastic-ferroelastoelectric twins.

## 7.2 Ferroelastic twinning

This corresponds to twinning by TLQs in the old scheme. Only one further subdivision is made in the old classification: The twinning is said to be by *pseudomerohedry* if  $n = 1$ , and by *reticular pseudomerohedry* if  $n > 1$  (Cahn 1954; Donnay and Donnay 1974). In the new scheme, the twinning is characterized as purely ferroelastic in  $\text{Pb}_3(\text{PO}_4)_2$  and  $\text{BiVO}_4$ , ferroelectric-ferroelastic in  $\text{BaTiO}_3$ , ferromagnetic-ferroelastic in  $\text{Mn}_3\text{O}_4$ , and ferromagnetic-ferroelectric-ferroelastic in  $\text{Ni}_3\text{B}_7\text{O}_{13}\text{I}$ . The presence of any antiphase domains can also be adequately rationalized in terms of reduction of the translational symmetry of the prototype.

## 8. Ferroelastic phase transitions

Ferroelastic phase transitions are characterized by a change of the crystal system, subject to the proviso that hexagonal and trigonal crystal systems are not regarded as distinct for the purpose of defining ferroelastic transitions (§3). The lattice distortion responsible for the change of crystal system is embodied in the spontaneous strain accompanying such transitions.

### 8.1 Proper ferroelastic transitions

A further subdivision of these is sometimes made between *true-proper* and *pseudo-proper* ferroelastic transitions. For the former, the strain itself is the primary order parameter. For the latter, though the strain  $\epsilon$  has the same symmetry as the order parameter  $Q$ , the order parameter is some other primary instability. In  $\text{LaP}_5\text{O}_{14}$ , for example, the driving force of the transition is an instability with respect to a Raman-active optical mode (Errandonea 1980). The strain arises because of a bilinear coupling term of the form  $K_1 Q \epsilon$ . A typical Landau expansion of the free energy density in this case can be written as follows (Wadhawan 1982):

$$\Phi = \Phi_0 + \frac{a}{2} (T - T') Q^2 + \frac{b}{4} Q^4 + \frac{C_0}{2} \epsilon^2 + \frac{B}{4} \epsilon^4 + K_1 Q \epsilon. \quad (10)$$

The elastic stiffness coefficient goes to zero (that is, the response function corresponding to  $\epsilon$  diverges) at the phase transition temperature  $T_c$  given by the equation

$$T_c - T' = K_1^2 / a C_0. \quad (11)$$

Here  $T'$  is the temperature at which the optical soft mode frequency *would* have gone to zero on cooling if the phase transition had not actually occurred at the higher temperature  $T_c$ . The distinction between true-proper and pseudoproper transitions disappears as  $K_1 \rightarrow 0$ . In any case most, if not all, proper ferroelastic transitions are of the pseudoproper type. Luthi and Rehwald (1981), who have listed a large number of them, make no distinction between the two types. Many other authors follow the same

practice. The temperature shift ( $T_c - T'$ ) can be as large as 160 K in  $\text{LaP}_3\text{O}_{14}$ , and 230 K in  $\text{BiVO}_4$ .

The Landau theory of phase transitions works well for systems for which the range of the interaction driving the phase transition is longer than the correlation length characterizing the critical fluctuations of the order parameter. The theory therefore provides a good description of proper ferroelastic transitions for which the critical fluctuations are the acoustic modes (Cowley 1976). (As already stated in §2, the theory holds exactly also for the "ferroelastic" phase transitions in hydrogen-metal systems (Alefeld and Volkl 1978; Wagner 1978), the elastic interaction mediated via the distortion fields around interstitial hydrogen atoms being a long-ranged attractive interaction.)

### 8.2 Improper ferroelastic transitions

In these transitions, the spontaneous strain arises only as a secondary effect, through a nonlinear coupling with the order parameter. The Landau expansion therefore contains a coupling term proportional to  $\epsilon\eta^n$ , where  $\eta$  is the order parameter modulus, and  $n$  is a finite integer called the *faintness index* (Aizu 1972b, c; Dvorak 1974). The spontaneous strain varies as the  $n$ th power of the order-parameter modulus,  $\epsilon_0 \sim \eta^n$ . The higher the value of  $n$ , the smaller is the spontaneous strain. Since strain is no longer the order parameter, the elastic response function does not show very large anomalies at the phase transition. Barring a few exceptions, the Landau theory does not, in general, provide a good description of this class of ferroelastic phase transitions (Wadhawan 1982).

### 8.3 Incommensurate phase transitions

This fundamentally new class of phase transitions (new, that is, for nonmagnetic systems) is currently attracting a good deal of attention (Pynn 1979; Bak 1982). In the usual "commensurate" phase transitions, the pattern of static displacements of atoms in the lower-symmetry phase can be described by a frozen-in wave of wavevector  $\mathbf{k}$ , which is a *rational* fraction of a prototype reciprocal-lattice vector  $\mathbf{r}^*$  along the same direction:

$$\mathbf{k} = (n_1/n_2)\mathbf{r}^*, \quad (12)$$

where  $n_1 = 0, \pm 1, \pm 2, \dots$  and  $n_2 = \pm 1, \pm 2, \dots$ . For example, for a "zone-centre" phase transition  $n_1/n_2 = 0$ , and for a "zone-boundary" phase transition it is equal to  $1/2$ . In an incommensurate transition,  $\mathbf{k}$  is an *irrational* fraction of  $\mathbf{r}^*$ , so that no two atoms have the same static displacement. In other words, in the incommensurate phase no translational symmetry exists in the direction of  $\mathbf{k}$ . Therefore, the notion of antiphase domains or translational domains discussed in §5 does not apply any more for this direction. However, the incommensurate phase still has a well-defined point-group symmetry and the concepts of rotational domains or orientation states and of  $F$ -operations between them are still relevant.

In incommensurate transitions no finite-order coupling between the order parameter and any macroscopic property such as the strain or polarization is possible in the Landau expansion (Riste 1978). Consequently, no spontaneous strain or polarization can appear in the incommensurate phase. Such a polarization or strain gets averaged out to zero because of the zero-energy phase modulation of the displacement pattern.

However, as the temperature of the incommensurate phase is lowered, a point is reached where a "lock-in" transition occurs, at which the fraction connecting  $\mathbf{k}$  to  $\mathbf{r}^*$  becomes rational, and a finite-order nonlinear coupling between the order parameter and one or more macroscopic properties (each with a definite faintness index) can occur. The lock-in transition has been observed to be first-order in all the cases studied so far. The mechanical behaviour of a crystal near an incommensurate transition is influenced by the effect of the transition on its elastic constants. A number of studies of this have already been made, notably by ultrasonic techniques and include the following crystals listed by Luthi and Rehwald (1981):  $\text{K}_2\text{SeO}_4$ ,  $\text{Rb}_2\text{ZnCl}_4$ ,  $\text{N}(\text{CH}_3)_4)_2\text{ZnCl}_4$ ,  $(\text{NH}_4)_2\text{BeF}_4$  and  $\text{K}_2\text{PbCu}(\text{NO}_2)_6$ .

It is pertinent to mention here a relatively new experimental technique, namely,  $\gamma$ -ray diffractometry (Schneider 1981) which is particularly well suited for studying ferroelastic phase transitions, and especially the critical behaviour of the order parameter. Because of the small wavelength involved ( $\lambda = 0.03 \text{ \AA}$  usually),  $\gamma$ -ray diffractometry is a forward-scattering experiment (with scattering angles seldom exceeding  $2^\circ$ ). The change  $\Delta\theta$  in the Bragg angle is related to the change  $\Delta d$  in the interplanar  $d$ -spacing by equation

$$\Delta\theta = -(\Delta d/d) \tan \theta. \quad (13)$$

As  $\theta$  is very small, it follows that changes in the  $d$ -spacings have a vanishingly small effect on the Bragg peak position,  $\theta$ . Therefore, any significant shifts of the peak position in the " $\omega$ -scan" normally employed for recording the diffraction pattern can be attributed almost entirely to a tilting (reorientation) of the concerned lattice planes, with a negligible contribution from changes in their  $d$ -spacing. This is in marked contrast to the situation in conventional x-ray or neutron crystallography where in the back-scattering region ( $\theta \simeq 90^\circ$ ) normally preferred for lattice-parameter determination,  $\Delta\theta$  is extremely sensitive to changes in the  $d$ -spacing.  $\gamma$ -ray diffractometry is therefore ideally suited for studying those phase transitions which entail spontaneous deformation of the crystal lattice, and the consequent tilting of the lattice planes. This is just what happens in ferroelastic phase transitions. The spectral width of the nuclear  $\gamma$ -rays used is extremely small ( $\Delta\lambda/\lambda = 10^{-6}$  for the  $^{198}\text{Au}$  source); this results in excellent angular resolution. A resolution of  $1''$  of arc can be achieved. Further, since the  $\gamma$ -rays are extremely penetrative, the presence of massive high-pressure cells, or elaborate arrangements for achieving a high degree of sample temperature control, do not present any serious problems. The technique looks very promising. Its applications in this direction have begun only recently (see Bastie and Bornarel 1979; Alkire and Yelon 1981).

## 9. The shape-memory effect

The shape-memory effect (SME) in alloys is associated with martensitic phase transitions, which are first order, diffusionless, structural phase transitions involving a distortion of the crystal lattice. Their closeness to ferroelastic phase transitions is obvious. The SME pertains to the shape recovery of a material on heating to a certain temperature, after it has been subjected to a deforming strain of as much as 10% at a lower temperature. As in pseudoelastic recovery (§ 2), two situations are possible for the "one-way" SME: by transformation or by reorientation (Warlimont 1976). In the former

case, the deforming stress induces a phase transition to the martensitic phase, whereas in the latter case the material is already in the martensitic phase and the applied stress makes some domains grow at the cost of others. The shape recovery on heating in both cases involves a phase transition to the parent phase.

In a martensitic transition the parent and the martensitic phase coexist over a certain range of temperatures. For good shape recovery in the SME, it is necessary that the interface between the parent and the martensitic phases be created, annihilated or moved in a reversible manner. A number of conditions should be met for this (Nakanishi 1975; Wasilewski 1975). For example, plastic flow should not occur during deformation. Thus a high yield strength of the initial matrix is required. Also, the driving force required for the nucleation and/or growth of martensite plates should be low. The dominant term in the free energy barrier opposing the nucleation of martensite in the matrix can be written as  $C\epsilon_m^2$ , where  $C$  is the relevant shear elastic constant of the matrix and  $\epsilon_m$  is the effective martensitic strain. A low value of  $C$  would be favourable for the stress-induced nucleation of martensite, but it would also imply a lower yield strength. The optimization of these two requirements indicates that one should apply the deforming stress at a temperature close to  $M_f$ , the martensite finish temperature (Wasilewski 1975).

In a proper ferroelastic phase transition, some stiffness constant, or a combination of stiffness constants, necessarily tends to zero (§8). The presence of such a transition should therefore indicate the possibility of SME in the material (Nakanishi 1975).

Over the last few years, the Landau theory has been increasingly applied to martensitic transitions. The Landau theory was initially formulated for dealing with second-order phase transitions. Further, a Landau expansion like that of (10) presupposes that the order parameter is a slowly varying quantity. Martensitic transitions are first-order phase transitions. One has therefore to employ Devonshire's (1954) generalization of the Landau theory to deal with them. Further, a first-order transition normally exhibits thermal hysteresis. In the temperature range of the thermal hysteresis, the two phases coexist. In addition to this, there also are domain walls associated with the domain structure of the daughter phase. At the domain walls and in the coexistence range of  $T$ , the order parameter changes rapidly. This makes the usual Landau expansion of the free energy inadequate, and one must include terms involving the derivatives of the order parameter, in the spirit of Ginzburg's (1955, 1960) extension of the Landau theory.

For understanding the SME, one has to deal not only with the effect of temperature on the martensitic transition, but also that of stress. In fact, many workers believe that the SME is merely one of the manifestations of the effect of stress on a martensitic phase transition, the martensitic transition for systems exhibiting the SME being taken as just a first-order proper ferroelastic transition (Wasilewski 1975; Falk 1980). In other words, some suitably defined spontaneous strain can be taken as the order parameter of the transition. A very simple but fairly universal model Landau expansion of the free energy has been proposed by Falk (1980), which explains a large number of features in a whole group of alloys exhibiting the SME. Falk's calculation is the mechanical counterpart of Devonshire's (1954) treatment of first-order proper ferroelectric phase transitions driven by the temperature and the electric field. The martensitic alloys CuZn, CuAlNi, AgCd, CuAuZn<sub>2</sub>, NiTi and NiAl are treated together in this phenomenological theory, ignoring their superlattice structure and the differences in the stacking sequence of their close-packed layers. After a suitable rescaling, the



following ansatz is made for the free-energy:

$$f(e, t) = f_0(t) + (t + 1/4)e^2 - e^4 + e^6, \quad (14)$$

where  $f$ ,  $e$  and  $t$  respectively denote the scaled values of the free-energy density, the shear strain (the order parameter), and the temperature. Equation (14) is a universal one for a large number of shape-memory alloys. The properties of specific materials enter through the scaling constants. All mechanical and thermodynamic properties are derived from (14). It is remarkable that this simplest of possible models leads to qualitative agreement with numerous experiments on shape-memory alloys; the stress-strain curves exhibiting elasticity, ferroelasticity and superelasticity in the appropriate temperature regions, the mode softening, the shape-memory effect, the occurrence of the stress-induced and temperature-induced phase transition, and the latent heat of the transition.

At the next level of complication, the electric field must also be brought in. From the point of view of theory, this is naturally a more difficult problem, but it also promises to present a richer variety of physical behaviour. One does not normally think of studying the effect of the electric field in alloys because of their high electrical conductivity. Especially interesting in this regard are materials such as PLZT and BaTiO<sub>3</sub> which are simultaneously ferroelastic and ferroelectric. The presence of ferroelectricity ensures that the spontaneous strain can be manipulated both by a mechanical stress and by an electric field. This is also important in applications of the SME because, by and large, electric fields are easier to apply in practice than mechanical stresses of appropriate magnitude and frequency. Experimental results on the effect of electric fields on the SME are just beginning to come in. Perhaps the first experiment of this type was that on PLZT ceramics (Wadhawan *et al* 1981). The composition of PLZT, that is (Pb, La) (Zr, Ti)O<sub>3</sub>, is conveniently specified by the  $x/y/z$  notation, where  $y/z$  indicates the Zr/Ti ratio, and  $x$  denotes the atomic percentage of La ions substituted for Pb. The composition  $x/65/35$  has received a great deal of attention because of its closeness to the morphotropic phase boundary (Haertling and Land 1971; Haertling 1971). Its ferroelastic nature was first demonstrated by Meitzler and O'Bryan (1971). For  $x > 4.5$ , this material possesses a property known as *perferroelectricity* (Meitzler and O'Bryan 1973), or *quasiferroelectricity* (Carl and Geisen 1973). There is a very interesting phase transition, called the  $\alpha \rightarrow \beta$  transition by Keve and Annis (1973), which is similar in many ways to a martensitic phase transition. Whereas above a temperature  $T_c$  the material behaves like a normal paraelectric, the dielectric behaviour immediately below  $T_c$ , i.e., in the  $\alpha$ -phase, is not that of a normal ferroelectric. The  $\alpha$ -phase is "quasiferroelectric" in which there are polar distorted microregions shorter than the wavelength of light. Application of an electric field between  $T_c$  and a lower temperature  $T_p$  changes the microdomains to macrodomains, which, however, revert back to randomly distributed microdomains (giving a macroscopically nonferroelectric state) when the electric field is switched off. The experimentally observed "slim" hysteresis loops constitute evidence in favour of this model (Carl and Geisen 1973). When the electric field is applied at a temperature below  $T_p$ , stable macrodomains indicative of long-range order are induced and the material behaves like a normal ferroelectric (as well as a ferroelastic), exhibiting "fat" hysteresis loops. Materials showing this type of diffuse phase transition are called "relaxor" ferroelectrics (Smolensky 1970). In the temperature range between  $T_c$  and  $T_p$ , microdomains of polar short-range order coexist with the paraelectric matrix, just as martensite coexists with the parent matrix over a certain temperature range.

The SME in PLZT ceramic of composition  $x/65/35$ , with  $4 \leq x \leq 8$ , was investigated in some detail by Kimura *et al* (1981), and the effect of an electric field on the SME in 6.5/65/35 PLZT was studied by Wadhawan *et al* (1981) by performing very simple bending experiments on thin bars of the ceramic. The modification introduced by the electric field on the SME could be interpreted in terms of the above microdomain model. In the temperature region in which the microdomains exist, the system is "electrically soft", but not "mechanically soft", and the load does not produce a large bending. However, when the electric field is switched on, it changes the microdomains to macrodomains, the material also becomes mechanically soft, and the load produces an additional bending. This was only a preliminary experiment. Much more work is needed to understand the phenomena involved in detail. Since ferroelectricity and ferroelasticity are coupled properties in the case of PLZT, it should be possible to produce changes in strain, including shape-memory bending, purely by electrical means, without the need for any mechanically-produced deformation. Electrically-produced SME would present challenging possibilities for both theory and experiment, as well as for device applications.

## 10. Concluding remarks

The subject of ferroelasticity has gained maturity being viewed as a part of the much larger subject of ferroicity. Much has been learnt or predicted about ferroelasticity by analogy with ferroelectricity. It appears that we can improve, considerably, our understanding of the physical basis of mechanical behaviour by drawing analogies with electrical phenomena (Alefeld 1971).

Based on the symmetry classification of phase transitions, a more rational-looking classification of twinning in crystals has been attempted. Two broad categories of twinning emerge: nonferroelastic and ferroelastic. Although this appears to run parallel to the existing division into twinning by merohedry and twinning by pseudomerohedry, the advantage of the new scheme is that many finer features like piezoelectric twinning can also be distinguished.

As was brought out repeatedly, our present description of ferroelasticity is based on the concept of symmetry descent and the principle of superposition of symmetries (the Curie principle). In fact the Landau theory of phase transitions, which is so effective in explaining a large body of experimental facts, is itself based on the Curie principle. The Landau theory is being increasingly applied to martensitic phase transitions which have a substantial overlap with ferroelastic phase transitions. Although this is a promising development, a certain amount of caution is warranted because we are dealing with *first-order* phase transitions, many of them of so drastic a nature that a change of coordination number and "internal topology" is involved. In some of these transitions there is no group-subgroup relationship between the symmetries of the parent and the daughter phases. While the theoretical apparatus for dealing with second-order phase transitions is very well-developed, in first-order phase transitions only a beginning has been made in some respects (Aizu 1981).

## References

- Aizu K 1969 *J. Phys. Soc. Jpn* **27** 387
- Aizu K 1970 *Phys. Rev.* **B2** 754

- Aizu K 1972a *J. Phys. Soc. Jpn* **32** 1287  
 Aizu K 1972b *J. Phys. Soc. Jpn* **33** 629  
 Aizu K 1972c *J. Phys. Soc. Jpn* **33** 1390  
 Aizu K 1973 *J. Phys. Soc. Jpn* **34** 121  
 Aizu K 1974 *J. Phys. Soc. Jpn* **36** 1273  
 Aizu K 1978 *J. Phys. Soc. Jpn* **44** 683  
 Aizu K 1981 *Phys. Rev.* **B23** 1292  
 Alefeld G, Schaumann J, Tretkowski J and Volkl J 1969 *Phys. Rev. Lett.* **22** 697  
 Alefeld G 1971 in *Critical phenomena in alloys, magnets and superconductors* (ed) R E Mills (New York: McGraw-Hill) p 339  
 Alefeld G and Volkl J 1978 in *Hydrogen in metals, I: Basic properties* (eds) G Alefeld and J Volkl (Berlin: Springer-Verlag) p 1  
 Alkire R W and Yelon W B 1981 *J. Appl. Cryst.* **14** 362  
 Amelinckx S 1976 in *Developments in electron microscopy and analysis* (ed) J A Venables (London: Academic Press) p 417  
 Bak P 1982 *Rep. Prog. Phys.* **45** 587  
 Bastie P and Bornarel J 1979 *J. Phys.* **C12** 1785  
 Cahn R W 1954 *Adv. Phys.* **3** 363  
 Carl K and Geisen K 1973 *Proc. IEEE* **61** 967  
 Catti M and Ferraris G 1976 *Acta Cryst.* **A32** 163  
 Cowley R A 1976 *Phys. Rev.* **B13** 4877  
 Devonshire A F 1954 *Adv. Phys.* **3** 85  
 Donnay G and Donnay J D F 1974 *Can. Miner.* **12** 422  
 Dvorak V 1974 *Ferroelectrics* **7** 1  
 Dvorak V 1978 *Czech. J. Phys.* **B28** 989  
 Errandonea G 1980 *Phys. Rev.* **B21** 5221  
 Falk F 1980 *Acta Metall.* **28** 1773  
 Fleury P A and Lyons K 1981 in *Structural phase transitions I* (eds) K A Muller and H Thomas (Berlin: Springer-Verlag) p 9  
 Friedel G 1926 *Lecons de Cristallographie* (Paris: Berger-Levrault)  
 Ginzburg V L 1955 *Nuovo Cimento* **2** 1234  
 Ginzburg V L 1960 *Sov. Phys. Solid State* **2** 1824  
 Haertling G H and Land C E 1971 *J. Am. Ceram. Soc.* **54** 1  
 Haertling G H 1971 *J. Am. Ceram. Soc.* **54** 303  
 Hermann C 1929 *Z. Kristall.* **69** 533  
 Jameson G B 1982 *Acta Crystallogr.* **A38** 817  
 Janovec V 1972 *Czech. J. Phys.* **B22** 974  
 Janovec V, Dvorak V and Petzelt J 1975 *Czech. J. Phys.* **B25** 1362  
 Janovec V 1976 *Ferroelectrics* **12** 43  
 Keve E T and Annis A D 1973 *Ferroelectrics* **5** 77  
 Kimura T, Newnham R E and Cross L E 1981 *Phase Transitions* **2** 113  
 Klassen-Neklyudova M V 1964 *Mechanical twinning of crystals* (New York: Consultants Bureau)  
 Kopstik V A 1968 *Sov. Phys. Cryst.* **12** 667  
 Laves F 1975 *Acta Crystallogr.* **A31** S9  
 Lieberman D S, Schmerling M A and Karz R S 1975 in *Shape memory effects in alloys* (ed) J Perkins (New York: Plenum Press)  
 Luthi B and Rehwald W 1981 in *Structural phase transitions I* (eds) K A Muller and H Thomas (Berlin: Springer-Verlag) p 131  
 Meitzler A H and O'Bryan Jr H M 1971 *Appl. Phys. Lett.* **19** 106  
 Meitzler A H and O'Bryan Jr. H M 1973 *Proc. IEEE* **61** 959  
 Muller K A 1981 in *Structural phase transitions I* (eds) K A Muller and H Thomas (Berlin: Springer-Verlag) p 1  
 Nakanishi N, Murakami Y, Kanchi S, Mori T and Miura S 1971 *Phys. Lett.* **A37** 61  
 Nakanishi N 1975 in *Shape memory effects in alloys* (ed) J Perkins (New York: Plenum Press) p 147  
 Olson G B and Cohen M 1982 *Proc. Conf. Solid-Solid Transf.* 1981 ICOMAT 1982  
 Peisl H 1978 in *Hydrogen in metals I. Basic properties* (eds) G Alefeld and J Volkl (Berlin: Springer-Verlag) p 53

- Pynn R 1979 *Nature (London)* **281** 433  
Rees D C 1982 *Acta Crystallogr.* **A38** 201  
Riste T (ed) 1978 *Electron-phonon interactions and phase transitions* (New York: Plenum Press)  
Sawada A, Makita Y and Takagi Y 1976 *J. Phys. Soc. Jpn* **41** 174  
Schneider J R 1981 *Nucl. Sci. Appl.* **1** 227  
Shubnikov A V and Kopstik V A 1974 *Symmetry in science and art* (New York: Plenum Press)  
Smolensky G A 1970 *J. Phys. Soc. Jpn* **28** Suppl 26  
Suzuki T 1978 *J. Phys. Soc. Jpn* **45** 860  
Tolédano P and Tolédano J C 1976 *Phys. Rev.* **B14** 3097  
Tolédano P and Tolédano J C 1977 *Phys. Rev.* **B16** 386  
Tolédano J C and Tolédano P 1980 *Phys. Rev.* **B21** 1139  
Tolédano P and Tolédano J C 1982 *Phys. Rev.* **B25** 1946  
Wadhawan V K, Kernion M C, Kimura T and Newnham R E 1981 *Ferroelectrics* **37** 575  
Wadhawan V K 1982 *Phase Transitions* **3** 3  
Wagner H 1978 in *Hydrogen in metals I: Basic properties* (eds) G Alefeld and J Volkl (Berlin: Springer-Verlag) p 5  
Warlimont H 1976 *Mater. Sci. Eng.* **25** 139  
Wasilewski R J 1975 in *Shape memory effects in alloys* (ed) J Perkins (New York: Plenum Press) p 245

## Discussion

G Venkataraman: It is observed that to understand the domain structure, one has to use not only the symmetry of the ferroelastic phase, but also that of the parent phase. This is similar to what Mermin does when he classifies defects using  $G$ , the symmetry of the disordered phase, and  $H$ , the symmetry of the ordered phase.

N Kumar: Is ferroelasticity a noncentrosymmetric phenomenon?

V K Wadhawan: The spontaneous-strain is a second-rank polar tensor. Thus the presence or absence of a centre of symmetry does not effect the occurrence of ferroelasticity in a crystal.

N Kumar: Since there was no prototype group for magnesium, can it be ferroic?

Wadhawan: The  $D_{6h}$  symmetry of magnesium does not admit of a crystallographic prototype group. Therefore we are not able to assign this crystal a place in the existing classification of ferroic crystals.

N Kumar: In order to have one-to-one correspondence is it necessary to have distortion connected with displacement vectors which are not some multiples of lattice spacing?

Wadhawan: We are talking here about the one-way SME and I think the question of one-to-one correspondence is more relevant for the two-way SME.

---

1

## Effects of mechanical deformation: Exoemission

G MUKHOPADHYAY

Department of Physics, Indian Institute of Technology, Bombay 400 076, India

**Abstract.** An introduction to some of the physical effects (*e.g.* exoemission, acoustic emission and mechanoluminescence) associated with the mechanical deformation of solids is presented. Greater emphasis has been given to exoelectron emissions. Experimental information and plausible mechanisms for exoemission have been described briefly. In particular, exoelectron emission from metals and oxide-coated metals has been discussed at some length, with the hope of generating a common interest among physicists and metallurgists.

**Keywords.** Mechanical deformation; stress; defects; dislocations; electron emission.

### 1. Introduction

There exist a number of effects associated with the mechanical deformation of solids. One class of effects is the emission of particles (charged and/or neutral), light and sound, when a material is undergoing deformation or is subjected to a constant strain rate. The emission of particles (in particular, electrons) is called exoelectron emission. The emission of light usually occurs in the form of luminescence from those materials which contain luminescent sources, and such an effect when induced by mechanical deformation is called mechanoluminescence. The emission of sound or stress waves is known to occur from a variety of materials, and is usually called acoustic emission. We shall describe here these effects and their understanding at the present time, with particular emphasis on exoemission, especially from metals and metal oxides during mechanical deformation. We shall see that these effects have some common features, require a great deal of future study and promise to be excellent tools for applied research (especially for metallurgists) in the field of nondestructive testing.

### 2. Exoemission

The phenomenon of exoemission (EE) was reported quite a long time ago (McLennan 1902). However, it was mainly after the introduction of the Geiger tube in the 1920's that the effect was truly recognised. Freshly-prepared Geiger tubes gave high and irregular counting rates for the first few hours or days, before functioning normally, and this led to the discovery that freshly machined metal surfaces emit electrons. This phenomenon was first carefully investigated by Kramer (1950) and sometimes referred to as the Kramer effect. Kramer himself found that all freshly prepared metal surfaces gave off electrons and suggested that the electrons gained the required energy for coming out of a metal by acquiring some of the energy released in the exothermal processes occurring on the surface. The prefix 'exo-' originates from this explanation. Although our present understanding indicates that the actual explanation of the

phenomenon is not as simple as this, the name has survived. It now appears that EE occurs for almost all materials in varying degree.

### 2.1 Main features of EE

The main features of EE occurring in various materials can be summarized as follows:

(i) The material exhibiting EE must be 'excited' externally to produce a perturbation in the form of a structural change. The external excitation may be in the form of cold working, irradiation by electromagnetic radiation (uv or higher frequencies), particle bombardment ( $\alpha$ ,  $\beta$ -rays, neutrons, protons, slow electrons, ions), exposure to gases, abrasion, mechanical deformation, etc.

(ii) The effect is strongly correlated with relaxation processes in the material, both causally and temporally, and it appears only after the generation of the perturbation. The observed time dependence can often be fitted by one or more decaying exponentials. The corresponding time constants reflect the presence of one or more relaxation processes, which normally depend strongly on the amount and nature of the defects in the system. It is this aspect of the EE process that makes it an attractive nondestructive technique of characterizing a material for its defect contents.

(iii) Unlike stationary effects, such as photoemission (PE) and thermionic emission (TE), EE is a nonstationary process, i.e. the EE flux is of transient character. Further, the effect is rather weak compared to PE or TE, with a EE flux typically in the range of  $10^{-13}$  A/m<sup>2</sup>.

(iv) The emission may be spontaneous or may require external stimulation, in addition to the external excitation. The stimulation may be in the form of increased temperature (thermally-stimulated exoemission (TSEE)) or electro-magnetic radiation (photo-stimulated exoemission (PSEE)), usually in the optical range. The EE observed without any photostimulation is usually referred to as 'dark emission'. Normally TSEE is observed non-isothermally, although it can also be observed isothermally. For PSEE, it is necessary that the photon energy is less than the work function of the material under study. Otherwise normal PE will accompany EE making data analysis rather difficult. PSEE can enhance a normal 'dark EE' intensity by a factor as large as  $10^4$  or more. Both TSEE and PSEE have been correlated with several other effects, such as thermally stimulated luminescence (TSL), electron-stimulated desorption (ESD), thermally stimulated conductivity (TSC), thermally stimulated depolarization currents (TSDC), and thermally stimulated desorption (TSD), depending on the material studied. Observations of these effects enhance the understanding of the EE process and are therefore generally desirable. There does not appear to have been any attempt as yet to correlate EE with acoustic emission or mechanoluminescence.

(v) The EE rate is strongly correlated with the work function  $\phi$  of the system. This correlation is of major relevance for PSEE as well as TSEE, and it is necessary to measure the work function simultaneously by an independent method during an EE observation, to facilitate understanding of the EE process.

(vi) The EE effect has two components, one of which is volume dependent and the other, surface dependent. For a particular system one or both may occur depending on the material and its surface condition as well as its surrounding gas medium. The surface effect is strongly related to the surface condition, and in a controlled EE experiment it is often desirable to have an ultra-high vacuum ( $\sim 10^{-10}$  Torr) to separate the surface effect from the volume effect. It is also desirable to have an experimental arrangement for characterizing the surface condition of the sample.

(vii) EE emission can occur continuously, or in large bursts, or with the latter superimposed over the former. It is usually believed that the continuous emission is related to the motion of defects in the sample, whereas the emission in bursts is related to the propagation of cracks (or micro-cracks). Thus the nature of the EE may reveal the nature of its source.

## 2.2 Experimental arrangement

The apparatus for measuring EE consists of an excitation unit, a stimulation unit and a detection unit, attached to an ultrahigh vacuum (UHV) chamber containing the sample. It should be equipped with an Auger spectrometer and a quadrupole mass analyzer for structural and chemical analysis of the surface of the sample and for the identification of the chemical composition of the residual gases in the chamber. A facility for measuring the work function (*eg.*, by the Kelvin or Fowler method) is desirable. In addition, a LEED facility may be used for characterization of the surface structure. A quartz window on the chamber will facilitate optical measurements (*eg.* luminescence, optical absorption, etc.), which often prove valuable for understanding EE.

An apparatus and the technique for observing TSEE has been described by Glaefcke (1979). We describe here an apparatus for observing EE or PSEE (figure 1). This is perhaps one of the most sophisticated versions of this type, developed and used by Rosenblum *et al* (1977) for studying EE during the mechanical deformation of a dogbone shaped sample (marked S in figure 1) of Al, Ni or Ti, with and without oxidised layers. The details of their experimental arrangement are described briefly here. The excitation unit consists of an arrangement for producing uniaxial tensile strain at a constant rate. The sample placed inside an UHV chamber (part of a LEED apparatus) is clamped at both ends, with the fixed end attached to a load cell (LC) and the other end attached to a pulling rod coupled to a linear variable differential transformer (LVDT) for measuring the displacement and thereby the strain rate. Strain at a constant rate is applied at intervals, causing EE in bursts. The vacuum chamber (UHVC) is equipped with a ion-gun (IG) for *in-situ* cleaning of the sample surface. No stimulation unit was used by Rosenblum *et al* (1977), although a LiF window (W) is provided for the purpose of photostimulation. In such experiments the EE flux is usually weak ( $10^4 - 10^6$  particles/sec/m<sup>2</sup>) and it is desirable to have a single-event charged particle and photon

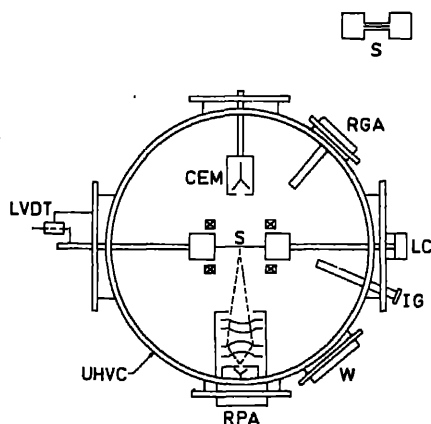


Figure 1. Schematic diagram for EE apparatus. (Rosenblum *et al* 1977).



detector as part of the detection unit. Rosenblum *et al* used a channel electron multiplier (CEM in figure 1) with an input cone (for focussing and accelerating the emitted particles into CEM) with an appropriate shielding and magnetic-discrimination scheme (for identifying the charged particles as electrons, or negative or positive ions). The shield ensured that the electrostatic field developed between the emitting surface and the cone was due to the CEM's biasing potential relative to the specimen rather than to the potential across the CEM. A retarding potential analyser (RPA) was used for Auger and photoelectron spectrometry for studying and characterizing the surface condition of the sample. For the detection of photons (presumably arising from the mechanoluminescence effect), a miniature single-photon counter tube (Bendix BX 754) was used in place of the (removable) RPA unit. For measuring the energy distribution, an electron spectrometer of high resolution (retarding grid potential analyser-RGA in figure 1) was specially designed to suit the way the strain was applied and the EE observed. However, the energy in the energy distribution could be measured only with respect to the Fermi level of the retarding grid, since the work functions of the oxides were uncertain, especially under mechanical strain. Figures 2-5 show the results of EE from Al with an oxide ( $\text{Al}_2\text{O}_3$ ) layer, observed by Rosenblum *et al* (1977, 1977a). In figure 2, curves 1-3 correspond to electron emission intensity plotted against strain for samples with oxide thickness of 2000 Å, 250 Å and 50 Å respectively; the oxides for 2000 Å and 250 Å were grown anodically while the 50 Å thick oxide was grown naturally (*i.e.*, natural air-formed oxide). Curve-4 corresponds to negative ion emission from the 2000 Å thick oxide sample. Curve 5 is the stress-strain curve for the sample. In all cases a constant strain rate of  $\dot{\epsilon} = 2.2 \times 10^{-4} \text{ sec}^{-1}$  was used at an ambient pressure of  $10^{-10}$  Torr. In figure 3, curve 1 corresponds to photon emission from the 2000 Å thick oxide sample

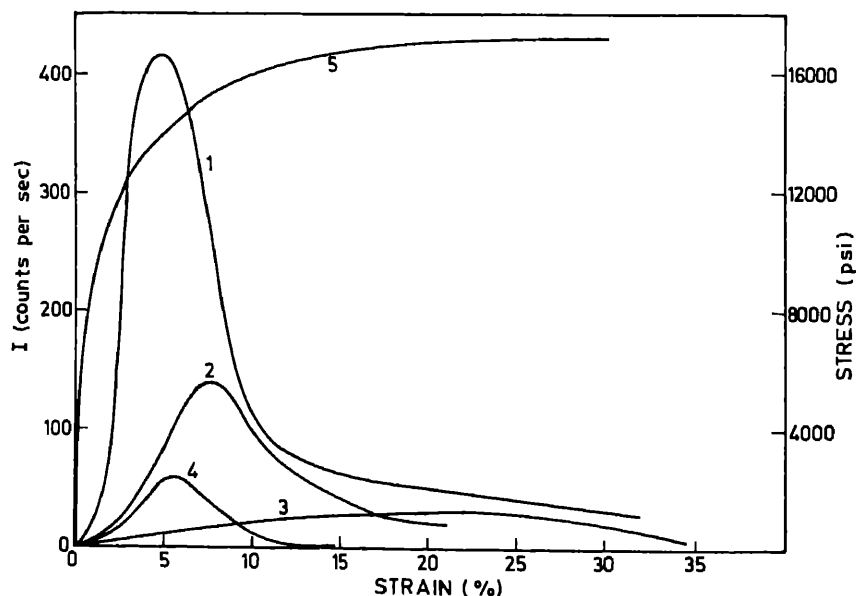


Figure 2. Electron emission intensity vs strain: 1.  $d$  (oxide thickness) = 2000 Å; 2.  $d$  = 250 Å; 3.  $d$  = 50 Å; Negative ion emission: 4.  $d$  = 2000 Å; stress-strain relation: 5. Strain rate  $\dot{\epsilon} = 2.2 \times 10^{-4} \text{ sec}^{-1}$  (Rosenblum *et al* 1977, 1977a).

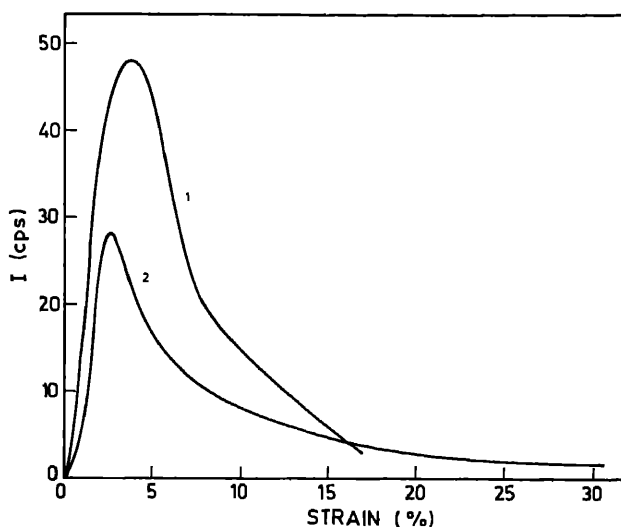


Figure 3. Photon emission intensity vs strain: 1.  $\dot{\epsilon} = 2.2 \times 10^{-4} \text{ sec}^{-1}$ . Positive ion emission: 2.  $\dot{\epsilon} = 5.3 \times 10^{-4} \text{ sec}^{-1}$   $d = 2000 \text{ \AA}$  (Rosenblum *et al* 1977, 1977a).

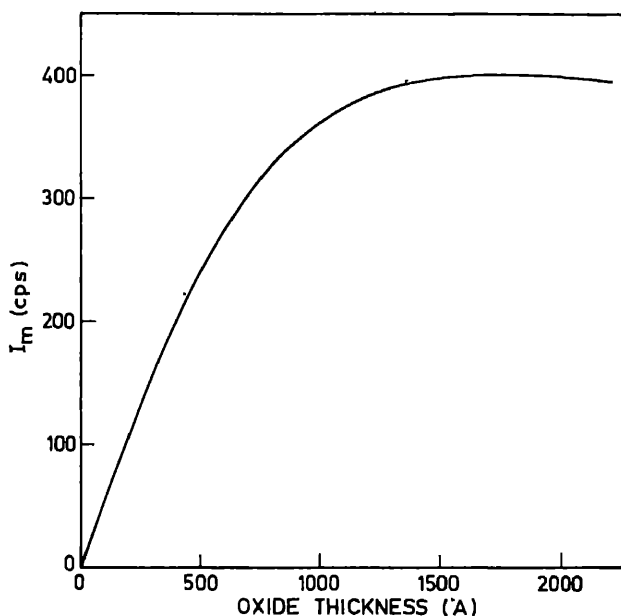


Figure 4. Maximum electron emission intensity vs oxide thickness:  $\dot{\epsilon} = 2.2 \times 10^{-4} \text{ sec}^{-1}$  (Rosenblum 1977a).

for the same strain rate as above, while curve 2 corresponds to positively charged ion emission for the same sample at a strain rate of  $5.3 \times 10^{-4} \text{ sec}^{-1}$ . The general features of the intensity as a function of strain are the same for the emission of electrons, positively or negatively charged ions, or photons. Figure 4 shows the peak electron

### 2.3 Mechanism and general understanding

The mechanisms for EE have always been a subject of controversy, partly because each worker or group of workers has tried to explain the experimental results through phenomenology suitable for that particular experimental situation (which is not easily reproduced), and mainly because of the very complex nature of the EE phenomenon. We now describe briefly some of the mechanisms based on observations under specific situations (see Glaefke 1979 for further details).

**2.3a Excitations induced chemically:** Spontaneous EE can occur when chemically reactive gases interact with initially clean metal surfaces (Bohun 1961; Bohun *et al* 1965; Delchar 1967; McCarrol 1969; Gesell *et al* 1970; Brus and Comas 1971; Born and Linke 1976). The process involved here is adsorption, the subsequent emission occurring from the surface. An adsorption process can be either physical (physisorption) or chemical (chemisorption) in nature. In physisorption, the adsorption-desorption equilibrium (at constant  $T$ ) is reached without activation. The heat of physisorption is typically of the order of 0.1 eV per species, which is too small to trigger EE. In contrast, chemisorption requires an activation energy and is preceded by physisorption. The heat of chemisorption is of the order of several eV per species, sufficient for EE. Compared to physisorption which is reversible and forms multilayers, chemisorption is partially irreversible and ceases at monolayer coverage unless the adsorbed species diffuses into the bulk of the substrate. Such diffusion does occur in the case of oxidation and growth of the oxide layer. The rate of chemisorption may be determined from the chemical kinetic rate equation when the chemical reaction velocity is rate-determining, or from Fick's law of diffusion when the diffusion process is rate-limiting. The EE rate is then assumed to be proportional to the rate of chemisorption. Analysis along these lines then indicates a maximum in the EE current as a function of time. When more than one species is chemisorbed, one would expect a maximum corresponding to each species. Thus, the two observed maxima in the EE from clean Mg surfaces exposed (by abrasion) to  $O_2$  and  $H_2O$  in the dark have been attributed to the two different adsorbing species (Gesell *et al* 1970). It has also been found from a simultaneous measurement of the work function that the maximum in the EE corresponds to a minimum in the work function  $\phi$ . Thus, the EE has been attributed to (a) the lowering of the work function due to adsorption with a dipole moment of the adsorbed complex favouring emission, and (b) transfer of the released heat of chemisorption to generate surface plasmons which in turn transfer their energy to electrons causing EE. For Al, a substantial decrease in the work function  $\phi$  (with the minimum in  $\phi$  coinciding with the maximum in dark EE) during adsorption of water has been reported (Born and Linke 1976, from 4.5 eV to 1.3 eV; Wortmann 1978).

Spontaneous EE can also occur during thermally stimulated desorption (TSD) without any preliminary excitation, and such TSEE is sometimes referred to as self-excited EE (Bohun 1961; Krylova 1976; Krylova *et al* 1976). For *e.g.*, highly hydrated oxides ( $Al_2O_3$ , MgO etc.) and alkali halides (NaCl etc.) show a strong gas desorption accompanied by EE (Krylova 1976). It is believed that the active species at the surface recombine with the sites which have become vacant through desorption due to thermal stimulation. The released recombination energy is then responsible for this TSEE (Krylova *et al* 1976).

TSEE has been observed during heterogeneous catalytic reaction, for example during catalytic oxidation of hydrogen and carbon monoxide on NiO, ZnO and platinum

black (Krylova 1976). Since both TSEE and catalysis depend on chemical thermodynamics, a relationship between the two is to be expected. Indeed, a reproducible linear relation between the two has been demonstrated for catalytic oxidation (Krylova 1976).

**2.3b Excitation by UV and x-rays:** Some alkali halides (especially those with small electron affinity at the surface, *e.g.*, chlorides and fluorides), during exposure to UV light, exhibit PSEE when photostimulated with an additional UV light source. TSEE may be observed during thermal annealing. The mechanism for EE is believed to be a two-step photothermal process involving colour centres generated by the exciting UV light. The first step is the optical transition from the colour centre to the conduction band, and the second step is the thermionic emission from the conduction band to vacuum. The stimulation spectra (*i.e.*, PSEE as a function of the stimulating wavelength) have been studied extensively and found to give information about the colour centres similar to that yielded by their optical absorption spectra (Ford *et al* 1970; Bichevin *et al* 1971; Nink and Holzapfel 1973; Maiste *et al* 1973; Kortov *et al* 1982; Tale *et al* 1982).

TSEE has been reported after excitation with x-rays, and a correlation between TSL and TSEE established (Holzapfel and Krystek 1976). TSEE from oxides irradiated with x-rays has also been investigated (Rudolf and Glaefke 1982). In most cases, a direct liberation of electrons from traps (produced by irradiation) is assumed to explain the EE.

**2.3c Excitation by electrons:** EE has been observed from materials during exposure to electron beams. However, this occurs only for insulators. So far, atomically clean metal surfaces have not exhibited EE on irradiation, and the presence of oxide or adsorbed species seems to be absolutely essential for EE observation here. This seems to be true also for semiconductors. The EE behaviour is strongly dependent on the energy of the exciting electron beam. For low energy electrons (0.2 to 30 eV) the adsorbed species on the surface and the surface states are affected and here EE is essentially a surface phenomenon. These EE spectra are similar to the UV-excited spectra, and electron-stimulated desorption (ESD) can occur. ESD can influence TSEE spectra appreciably. Concepts involving chemical reactions at the surface are utilized to correlate the two (Jakowski and Glaefke 1976; Euler and Scharmann 1976; Brunsmann and Scharmann 1977; Kirihaata and Akutsu 1979). For moderate energy electrons (several hundred to several thousand eV), volume states are excited, generating a complicated space charge inside the insulator. This in turn produces a positive-negative double layer whose electric field (as large as  $10^6$  V cm<sup>-1</sup>) causes EE (Fitting *et al* 1979; Fitting 1981). Systems studied, among others, are Al<sub>2</sub>O<sub>3</sub> (Krylova 1971; Schlenk 1976; Chrysos and Holzapfel 1980), ZnO (Krylova 1971; Hiernaut *et al* 1972; Kriegseis and Scharmann 1975), NiO (Krylova 1971; Hiernaut *et al* 1972), SiO<sub>2</sub> (Krylova 1971; Jakowski and Glaefke 1976), BeO (Euler and Scharmann 1976; Scharmann and Wiessler 1980) and NaF (Brunsmann and Scharmann 1977).

**2.3d Excitation by nuclear radiation:** Reproducible EE has been observed from a number of substances using nuclear radiation as the source of excitation. Among the substances studied are alkali halides, alkaline-earth halides, sulphates, sulphides and a number of metal oxides. TSEE from BeO and LiF have been studied extensively because of their dosimetric applications (see Glaefke 1979 for details). Simultaneous measurement of TSL and TSEE from the same emitter can discriminate between those types of radiation which cause bulk effects (TSL) and those causing surface effects (TSEE).

For example, both  $\alpha$ - and soft  $\beta$ -irradiation yield high TSEE intensity (since the total energy is absorbed near the surface) but rather weak TSL, in BeO. On the other hand,  $\gamma$  irradiation causes very weak TSEE but a very strong TSL. Thus, TSEE and TSL from BeO can distinguish between  $\alpha$  (or soft  $\beta$ ) and  $\gamma$  doses. Fast neutrons can cause EE via recoil protons or  $\alpha$  radiation, and the corresponding TSEE may be separated from the  $\gamma$ -ray TSEE by a subtraction procedure to determine the fast neutron dosage. BeO dosimeters based on these properties may have a dose response range from as low as  $10^{-6}$  rad to  $10^2$  rad. Compared to conventional dosimeters, however, a TSEE-based dosimeter has some technical shortcomings, such as a strong dependence of the TSEE on the mechanical treatment and the ambient atmosphere of the detecting material. This may be responsible for its lack of commercial usage.

**2.3e Excitations through direct structural change:** EE has been observed from a number of materials in which excitation is brought about by direct structural changes. Such changes can be induced by external application of stress, or by generating stress internally through heat treatment of the material.

EE has been observed from metals with atomically clean surfaces in ultrahigh vacuum. Kortov *et al* (1971) observed EE during plastic deformation of Al. Mints *et al* (1973) tried to correlate EE with the process of recovery and recrystallization of metals. Mechanical deformation generates a high concentration of defects (vacancies and dislocations). The relaxation of the stress is accompanied by the diffusion of vacancies towards the surface and the recovery of dislocations. These defects can rearrange themselves exothermally, and the localized release of thermal energy may be taken up by electrons. However, emission of these electrons would require a substantial lowering of the work function  $\phi$ , which is believed to be due to high roughness on a clean metal surface (Lewis 1954; Rhead 1977). Pardee and Buck (1977) and Buck *et al* (1977) considered the roughness-enhanced coupling of incident light with surface plasmons (which can transfer their energy to electrons) to explain PSEE.

EE from oxide covered metals has been observed both in the dark as well as with photostimulation during mechanical deformation. Since most metals in practical situations are oxidised at the surface, these EE observations are of considerable applied interest. The dark emission under UHV has been observed only during mechanical deformation or abrasion of oxide covered metals (Gieroszynski and Sujak 1965; Sujak *et al* 1965; Brotzen 1967; Sujak and Gieroszynski 1970; Linke 1970; Kortov *et al* 1970; Arnott and Ramsey 1971; Kortov and Myasnikov 1972; Kelly and Himmel 1976; Rosenblum *et al* 1977, 1977a). Photostimulated emission during abrasion or plastic deformation of oxide-coated metals can be very large as compared to the dark emission (by a factor of  $10^4$  or more) and a number of oxidised metals have been investigated exploiting this fact (Grunberg 1958; Von Voss and Brotzen 1959; Pimbley and Francis 1961; Mueller and Pontinen 1964; Claytor and Brotzen 1965; Gieroszynski and Sujak 1965; Sujak *et al* 1965; Sujak and Gieroszynski 1970; Baxter 1973; Shorshorov *et al* 1976; Baxter and Rouze 1978; Wortmann 1978; Dickinson *et al* 1978; Komai 1978). Among various oxide coated materials (*eg.*, Al, Ni, Steel, Ti, Mo, etc.), the most widely studied one is  $\text{Al}_2\text{O}_3$ -coated Al. Qualitatively the same emission behaviour has been observed when the oxide covered metal is mechanically abraded or plastically deformed under tension. In the case of tensile strain, dark emission occurs only during a change in the strain and ceases abruptly when the deformation stops. Similarly, when photostimulated, considerable enhancement in electron emission occurs only during constant

strain rate, the emission being regarded as burst emission, even though a continuous component (much smaller in magnitude) may be present. In case of burst emission, typically, for a constant strain rate, the emission increases to a maximum followed by a monotonic decrease with increasing deformation or strain (see figure 2). The emission depends on the strain rate as well as the oxide thickness (see figure 4). The burst emission has been associated with the propagation of cracks or micro-cracks. PSEE from thick oxide layers has been attributed to the propagation of cracks perpendicular to the stress direction, independently of the underlying micro-structure of the metal. In thin oxide layers, it has been attributed to fracture at slip steps (Baxter and Rouze 1978).

The continuous EE is believed to arise from two components, one controlled by the diffusion of point defects (generated by strain) towards the surface, and the other controlled by the relaxation of dislocations. One may dominate over the other, or both may be present. For example, Pimbley and Francis (1961) could explain EE from abraded oxidised Al through a model based on the diffusion of vacancies, while Claytor and Brotzen (1965) explained EE from mechanically deformed oxidised Al in terms of the diffusion of other point defects. On the other hand, Mueller and Pontinen (1964) studied EE from freshly abraded as well as from abraded and aged samples of oxidised Al and concluded against the defect diffusion mechanism. However, Shorshorov *et al* (1976) could correlate PSEE during plastic deformation with the generation of dislocations as well as vacancies by simultaneously studying the behaviour of these defects (using metallographic methods). They found no diffusion of vacancies but found relaxation of dislocations in molybdenum, while both phenomena occurred in  $\alpha$ -iron.

The burst emission, especially in dark, is supposed to originate from cracks or microcracks which develop in the oxide as soon as the local surface strain in the underlying metal substrate exceeds the ultimate tensile strain of the oxide layer (Sujak 1964). Originally it was believed that the opposing surfaces of a propagating fissure (microcrack) become charged, providing a strong electric field that causes field emission (Gieroszynski and Sujak 1965). This so-called electrified-fissure model for EE was reinvestigated by Arnott and Ramsey (1971) who restricted its applicability to polar substances. For non-polar substances, they proposed to interpret EE in terms of rearrangement of dangling bonds created during the propagation of cracks. Rabinowicz (1977) has elucidated this model, but also questioned its feasibility. Rosenblum *et al* (1977a) believe that the release of strain energy in the vicinity (*e.g.* the tip) of a propagating crack results in local heating to a temperature (estimated to be  $\sim 3000$  K for Al) sufficient to cause thermionic emission from the walls. However, they also observed emission of positive and negative ions, which indicates that field-assisted emission of electrons cannot be ruled out.

EE during heat treatment of materials (without external excitation) arises from the internal mechanical stress generated thermally due to the process of phase transformation. Thus EE has been observed during changes of the state of aggregation or modification (first order phase changes, *e.g.*, transition from the hexagonal to the cubic form in thallium, change or modification of hexagonal chromium and selenium, melting of ice, lead, tin, etc.) and during changes of orientation (second order phase changes, *e.g.*, the antiferromagnetic-paramagnetic transition in Ni + NiO and Cr + Cr<sub>2</sub>O<sub>3</sub>). The EE intensity is regarded as proportional to the defect content and a measure of the degree of completion of the phase change. The mechanism is believed to be the same as that for stress-induced EE. The emission has also been observed during

second-order phase changes in crystalline pyroelectrics (*e.g.*, lithium niobate, BeO), where the mechanism is regarded as a thermally stimulated field effect (see Glaefcke 1979 for further details).

#### 2.4 Theoretical models for EE

It is clear from the preceding description that EE is a rather complex phenomenon involving several intermediate steps, depending on the type of material and the actual experimental condition. However, there appear to be three broad steps in the electron emission mechanism: (i) External excitation generates defects and the relaxation of the response to the excitation is associated with the motion or relaxation of these defects. (ii) The defects transfer their energy either directly or via some other agent (*e.g.*, surface plasmons in metals, and possibly phonons) to the electrons by the process of annihilation, or rearrangement, or by chemical reactions (at the surface). (iii) Electrons gaining this energy escape the material in the form of EE when their energy exceeds the work function or the electron affinity, or when an electric field (in electrified fissures) assists the emission. The controlling factors here (*e.g.* work function, etc.) may themselves depend on the nature of the excitation and on the experimental conditions.

Glaefcke (1979) has discussed various theoretical models for the last two steps, especially for dielectrics. Following Kelly (1972), he has described the thermionic emission model, in which the electron concentration is determined by reaction kinetics controlled by the concentration of defects (electron traps) and the retrapping-recombination processes for electrons. The theory has been applied to TSEE with some success. A field-assisted emission model has been developed for space-charge-controlled EE from highly insulating materials (excitation induced by electron bombardment) with the transport and escape of electrons determined by a Monte-Carlo process. The model can explain the intensity, energy and angular distribution of EE, for example in BeO (Kortov and Zolnikov 1975; Fitting *et al* 1979).

In EE from metals with or without an oxide layer, most of the theoretical work has been devoted to step one. Early studies on EE were on the diffusion of vacancies or point defects towards the surface. The rate of arrival of the defects at the surface was determined by Fick's law. This was then assumed to be proportional to the rate at which the electron emitting centres were activated and thereby to the electron emission rate (Grunberg and Wright 1955; von Voss and Brotzen 1959; Pimbley and Francis 1961; Claytor and Brotzen 1965). More recently Nagornykh and Demin (1978) have incorporated into the diffusion equation the generation of vacancies during the straining of oxide coated metals. The diffusion of point defects from the metal into the oxide was matched by the diffusion of oxygen in the opposite direction. The formation of a filled electron trap (F-centre type) at the oxygen vacancy in the oxide was assumed. The electron emission rate was determined from the reaction kinetics involving thermal ionization of traps and recapture of electrons by the traps. The model was applied to EE from oxidised Al with some success.

The model for EE in bursts is based on crack propagation, and is more phenomenological than the model described above (Arnott and Ramsey 1971; Rosenblum *et al* 1977a). These however apply specifically to oxide coated metals. For surface-controlled EE, models based on chemisorption and Auger transitions have been evolved (Kasemo *et al* 1979). Models based on the stress dependence of thermionic emission have also been considered (Tinder 1968).

### 3. Acoustic emission

By acoustic emission (AE) one means the generation of stress waves during structural changes in a material. These may be generated internally (*eg.*, during phase transitions) or by an externally applied stress. The phenomenon is known to occur for almost all kinds of materials, and has been called by different names in different fields of research; for example, it is referred to as 'seismoacoustic activity' when observed in rocks under stress. AE usually refers to all kinds of stress waves even though the emitted frequencies may be far above the audible range. Extensive work has been done in this field, although to a somewhat applied nature (especially in relation to seismic studies of rocks), and some excellent review articles are available (Green 1969; Liptai *et al* 1971; Dunegan and Tatro 1971; Lord 1975). A brief description of the relevant parts of the subject follows:

The first systematic study of AE was by Kaiser in the 1950's, on polycrystalline zinc, steel, aluminium, copper and lead. He observed that AE was irreversible, *i.e.*, emission did not occur during reloading of a material until the stress exceeded its previous value—a phenomenon usually known as the 'Kaiser effect'. This memory effect applies to most metals but generally not to other materials. In 1961 Schofield reported AE from aluminium and zinc single crystals, commercial copper, aluminium, lead and 70–30 brass, and established correlation with dislocations, slips and grain boundary motion. Tatro and Liptai (1962) studied AE from polycrystalline aluminium and steel for various strain values, and from the observed dependence on the surface condition of the specimen, concluded that AE was a surface phenomenon. Later Schofield studied AE from aluminium single crystals, with and without the oxide layer, and found the surface condition to be of secondary importance except for influencing the strain locally at the point where AE commenced in a burst. It was found that the oxide coating was not a source of AE. Further work by Schofield has established AE as primarily a volume effect. The general features of AE derived from the work of several persons can be summarized as follows (Lord 1975).

AE occurs in two forms: continuously, and in bursts. Continuous emissions of rather high frequency ( $\geq 10^2$  kHz) and very low intensity usually occur in metals and metallic systems, and supposedly arise from mobile dislocations and possibly slip movements. Burst emissions occur with much higher intensity and are supposedly associated with failures such as twinning, microcracks, unpinning of dislocations from obstacles, and growth of already existing cracks; they occur at relatively large values of the plastic strain.

Figure 7 shows a typical experimental AE rate as a function of the tensile strain (Dunegan and Harris 1969). This particular result is remarkable in that it fits beautifully with Gilman's mobile dislocation model (Gilman 1966) which gives the mobile dislocation density  $N_m$  as a function of the plastic strain  $\epsilon_p$  through the relation  $N_m = m\epsilon_p \exp(-\phi\epsilon_p)$ , where  $m$  is the dislocation breeding factor, and  $\phi = H/\sigma$ , where  $H$  is the hardening coefficient, and  $\sigma$  is the rms stress. The fit is shown in the dashed curve in figure 7 with  $m = 1.44 \times 10^7$  and  $\phi = 70$  (Lord 1975). This shows that the AE rate is directly related to the mobile dislocation density, so that one may contemplate determining  $H$ , an important mechanical parameter, using the AE technique. Unfortunately such a fit of Gilman's formula does not work for many materials. This has been attributed to the inhomogeneity in the strain caused by the occurrence of Lüder's bands.

At present there does not seem to be any rigorous microscopic theory for the actual



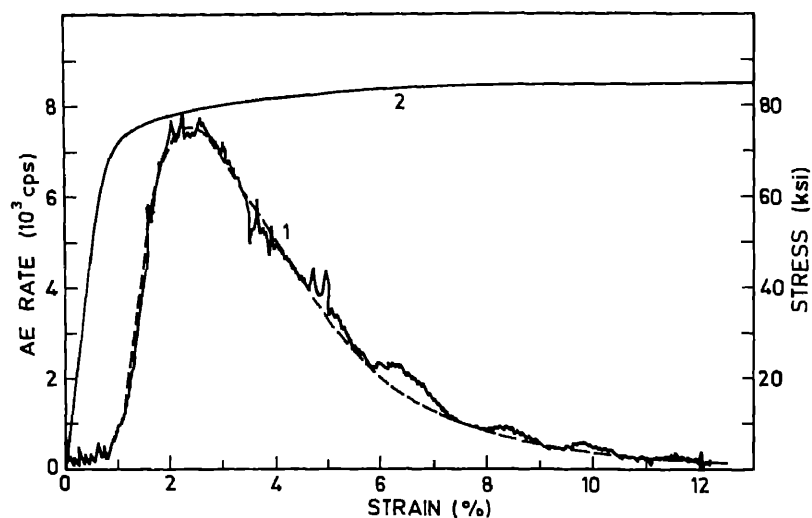


Figure 7. Acoustic emission intensity vs strain: 1. experimental; dashed curve. Gilman's relation. Stress vs strain: 2. (see Lord Jr 1975).

internal mechanism of AE. The major thrust in this area is in the direction of applied research, of establishing empirical relationships between AE and mechanical parameters (Lord 1975). Further, there has been no attempt to correlate AE with EE, although the typical emission intensity vs strain curves for Al are remarkably similar (compare figures 2 and 7).

#### 4. Mechanoluminescence

Some materials emit light when subject to stress beyond a particular level. This phenomenon is broadly called mechanoluminescence (ML) or triboluminescence. (ML is preferred, to avoid confusion with thermoluminescence which is customarily denoted by  $\tau\text{L}$ ). Extensive research has been done in this field on a very large number of materials, and the subject has been reviewed by a number of authors (Meyer *et al* 1970; Walton 1977; Zink 1978). Only a brief account of the relevant aspects is given here.

The most widely-studied materials are the alkali halides where the electron traps are the source of luminescence. ML spectra are similar to the  $\tau\text{L}$  spectra of a given material. Belyaev *et al* (1963) observed ML spectra during the growth of cracks in alkali halides under uniaxial strain, with photon emission in bursts, indicating that ML is associated with crack propagation. ML during fracture can be a hundred times more intense than  $\tau\text{L}$ , the concept of electrified fissures has been used to explain this (Belyaev *et al* 1966; Belyaev and Martyshev 1969). Observations on ML during abrasion or scratching of alkali halides have been correlated with the propagation of cracks and  $\tau\text{L}$  (estimated temperatures as high as  $10^4$  K) at the crack-tip (Meyer *et al* 1970). ML emission has been found to have a memory (analogous to the Kaiser effect) in activated alkali halides and ZnS. In experiments where the strain is repeated, no emission is observed in the elastic or plastic regions; and for a second application of strain, not until its magnitude exceeds that of the previously applied strain. This indicates that the ML intensity depends on the

depinning of dislocations under stress (Alzetta *et al* 1970; Scarmozzino 1971). Simultaneous ML and AE have been observed during mechanical deformation of organic glasses, steel and copper plates, indicating a common origin (Sodomka *et al* 1980). ML during the deformation and fracture of metallic alloys has also been reported (Borisova *et al* 1975). Molotskii (1978) observed ML during the plastic deformation and fracture of copper. Zink and his coworkers have observed ML in many organic and inorganic crystals (Zink 1978; Chandra and Zink 1980). In many cases, explanations on the basis of piezo-electrification, cleavage electrification and triboelectrification, have been given (Meyer *et al* 1970; Walton 1977; Chandra 1981).

Intense ML has been observed from coloured alkali halides (coloured by x- or  $\gamma$ -ray irradiation) by a number of workers. The emission is thought to be a result of the interaction of dislocations with colour centres (Butler 1966; Shmurak 1969; Alzetta *et al* 1970; Guerrero and Alvarez-Rivas 1978; Chandra and Zink 1980). Recently ML emission during the application as well as the release of uniaxial compression in x-ray irradiated alkali halides have been reported by Chandra and Elyas (1978). They have also studied  $\gamma$ -irradiated alkali halides and ML emission from coloured alkali halides under repeated stress, and established a linear relationship between the ML intensity and the measured density of newly-created dislocations at the end of repeated-stress cycles (Elyas 1981). At present a proper theoretical understanding of ML emission, particularly from materials containing active luminescence centres, is still lacking, although some theoretical attempts have been made to understand ML in terms of electric field and pressure effects (Lin *et al* 1980). Studies correlating ML with EE or AE also seem to be inadequate.

## 5. Conclusions

We have tried to present an introduction to the subject of some special physical effects, especially exoelectron emission, in the context of the mechanical deformation of solids. For a better understanding of the exoelectron process, we have also discussed possible mechanisms for EE and two other related phenomena, AE and ML. While a number of possibly important references may have been inadvertently omitted, it is hoped that this article is sufficiently self-contained to generate interest in studying EE in a systematic manner. It can be safely said that, at present, a concrete theory of EE is lacking. Further, extensive, experimental study is required for understanding and correlating EE with AE and ML. For example, one should study more carefully the role of the work function, dislocations (the applicability of Gilman's theory or modification thereof), the mechanism of energy transfer to electrons, and the escape of electrons from metals and oxide-coated metals. On the applications side, one ought to study more extensively the growth of microcracks using spot scanners (PSEE, as in Baxter 1973) and establish empirical relationships with mechanical parameters in the same manner as has been done for acoustic emission studies.

Further references on EE are: Scharmann (1967), Becker (1972), Ramsey (1976), Krylova (1976) and Glaefke (1979).

## Acknowledgements

The author thanks Dr G Srinivasan and Prof. S Ramaseshan for bringing this subject to

his attention. Thanks are also extended to Mr C V Krishna Murthy for providing some of the material presented here.

## References

- Alzetta G, Chudacek I and Scarmozzino R 1970 *Phys. Status Solidi* **a1** 775
- Arnott D R and Ramsey J A 1971 *Surf. Sci.* **28** 1
- Baxter W J 1973 *J. Appl. Phys.* **44** 608
- Baxter W J and Rouze S R 1978 *J. Appl. Phys.* **49** 4233
- Becker K 1972 *CRC Crit. Rev. Solid State Sci.* **3** 74
- Belyaev L M, Nabatov V V and Martyshev Yu N 1963 *Sov. Phys. Crystallogr.* **7** 464
- Belyaev L M and Martyshev Yu N 1969 *Phys. Status Solidi* **34** 57
- Belyaev L M, Nabatov V V, Pisarevskii Yu V and Shaldin Yu V 1966 *Sov. Phys. Crystallogr.* **10** 647
- Bichevin V, Käämbre H and Lushchik Ch. 1971 *Phys. Status Solidi* **a5** 525
- Bohun A 1961 *Czech. J. Phys.* **11** 819
- Bohun A, Sak J and Psenickova M 1965 *Czech-Z-Phys.* **15** 667
- Borisova E A, Glebova R D, Platonov A A and Skyarov N M 1975 *Sov. Phys. Dokl.* **20** 435
- Born D and Linke E 1976 *Proc. 5th Int. Symp. on EE and Dosimetry* (eds) A Bohun and A Scharmann (Prague: Inst. Solid St. Phys. Acad. Sci.) p 265
- Brotzen F R 1967 *Phys. Status Solidi* **22** 9
- Brunsmann U and Scharmann A 1977 *Phys. Status Solidi* **a43** 519
- Brus L E and Comas J 1971 *J. Chem. Phys.* **54** 2771
- Buck O, Pardee W J, Szalkowski F J and Thompson D O 1977 *Appl. Phys.* **12** 301
- Butler C G 1966 *Phys. Rev.* **141** 750
- Chandra B P 1981 *Phys. Status Solidi* **a64** 395
- Chandra B P and Elyas M 1978 *Kristall. U. Tech.* **13** 1341
- Chandra B P and Zink J I 1980 *Phys. Rev.* **B21** 816
- Chrysson E and Holzapfel G 1980 *Phys. Status Solidi* **a59** K49
- Claytor R N and Brotzen F R 1965 *J. Appl. Phys.* **36** 3549
- Delchar T A 1967 *J. Appl. Phys.* **38** 2403
- Dickinson J T, Braunlich P, Larson L A and Marceau A 1978 *Appl. Surf. Sci.* **1** 515
- Dunegan H L and Harris D O 1969 *Ultrasonics* **7** 160
- Dunegan H L and Tatro C A 1971 *Techniques of metals research* (ed) R F Bunshah (New York: Wiley Interscience) Vol V p 273
- Elyas M 1981 *Studies of mechanoluminescence produced during application and release of a uniaxial pressure in x-irradiated KBr, KCl, KI, LiF and NaCl crystals*, Ph.D. Thesis, The Ravishanker University, Raipur, India
- Euler M and Scharmann A 1976 *Phys. Status Solidi* **a34** 297
- Fitting H J 1981 *Phys. Status Solidi* **a63** K47
- Fitting H J, Glaefcke H, Wild W and Lange J 1977 *Phys. Status Solidi* **a42** K75
- Fitting H J, Glaefcke H, Wild W, Franke M and Müller W 1979 *Exp. Tech. Phys.* **27** 13
- Ford L H, Holzapfel G and Kaul W 1970 *Z. Angew. Phys.* **30** 259
- Gesell T F, Arakawa E T and Calcott T A 1970 *Surf. Sci.* **20** 174
- Gieroszynski A and Sujak B 1965 *Acta Phys. Pol.* **28** 311
- Gilmann J J 1966 *Proc. 5th U.S. Nat. Congr. Appl. Mech.* 385
- Glaefcke H 1979 *Topics in applied physics* (ed) P Bräunlich (Berlin: Springer-Verlag) Vol 37 p 224
- Green A T 1969 *Nucl. Safety* **10** 4
- Grunberg L 1958 *Br. J. Appl. Phys.* **9** 85
- Grunberg L and Wright K H R 1955 *Proc. Roy. Soc. London* **A232** 403
- Guerrero E and Alvarez-Rivas J L 1978 *Solid State Commun.* **28** 199
- Hiernaut J P, Forier R P and Van Cakenberghe J 1972 *Vacuum* **22** 471
- Holzapfel G and Krystek M 1976 *J. Phys. (Paris)* **37** C-7-238
- Jakowski N and Glaefcke H 1976 *Thin-Solid Films* **36** 195
- Kasemo B, Tornqvist E, Nørskov J K and Lundqvist B T 1979 *Surf. Sci.* **89** 554
- Kelly P 1972 *Phys. Rev.* **B5** 749
- Kelley P and Himmel L 1976 *Comm. Solid State Phys.* **7** 81

- Kirihata H and Akutsu J 1979 *Phys. Status Solidi* **a51** K 109  
Komai K 1978 *Trans. Jap. Inst. Met.* **19** 119  
Kortov V S and Myasnikov I E 1972 *Phys. Status Solidi* **a9** 119  
Kortov V S and Zolnikov P P 1975 *Phys. Status Solidi* **a31** 331  
Kortov V S, Mints R I, Myasnikov I E and Gaprindoshvily A Y 1970 *Phys. Status Solidi* **a3** 13  
Kortov V S, Mints R I and Teplov V G 1971 *Phys. Status Solidi* **a7** K89  
Kortov V, Isakov V, Glaefke H and Fitting H J 1982 *Phys. Status Solidi* **a73** K275  
Kramer J 1950 *Der metallische zustand* (Gottingen: Vanderhoeck Ruprecht)  
Kriegeis W and Scharmann A 1975 *Phys. Status Solidi* **a29** 407  
Krishna Murthy C V 1982 *Exoelectron emission*, M.Sc. Thesis, Indian Institute of Technology, Bombay, India  
Krylova I V 1971 *Phys. Status Solidi* **a7** 359  
Krylova I V 1976 *Usp. Biol. Khimii* **45** 2138 (English Transl.: 1976, *Russ. Chem. Rev.* **45** 1101)  
Krylova I V, Svitov V I and Konyushkina N I 1976 *Zh. Fiz. Khimii* **50** 933 (English Transl.: 1976 *J. Phys. Chem.* **50** 555)  
Lewis T J 1954 *Proc. Phys. Soc.* **B67** 187  
Lin S H, Wutz D, Ho Z Z and Eyring H 1980 *Proc. Natl Acad. Sci. (USA)* **77** 1245  
Linke E 1970 *Z. Angew Phys.* **29** 241  
Liptai R G, Harris D O, Engle R B and Tatro C A 1971 *Int. J. Nondestruct. Test.* **3** 215  
Lord A E Jr. 1975 *Physical acoustics* (eds) W P Mason and R N Thurston (Academic Press: New York) Vol. XI 289  
McCarrol B 1969 *J. Chem. Phys.* **50** 4758  
McLennan J C. 1902 *Philos. Mag.* **3** 195.  
Maiste A, Sorkin B, Elango M and Käämbre H 1973 *Phys. Status Solidi* **a20** K83  
Meyer K, Obrikat D and Rossberg M 1970 *Kristall. Tech.* **5** 5, 181  
Mints R I, Melekin V P, Segal V M and Icolev I Yu 1973 *Sov. Phys. Solid State* **14** 2153  
Molotskii M I 1978 *Sov. Phys. Solid State* **20** 956  
Mueller R K and Pontinen K 1964 *J. Appl. Phys.* **35** 1500  
Nagornyykh S N and Demin Yu A 1978 *Phys. Met. Metall.* **46** 170  
Nink R and Holzapfel G 1973 *J. Phys. (Paris)* **34** C-9-491  
Pardee W J and Buck O 1977 *Appl. Phys.* **14** 367  
Pimbley W T and Francis E E 1961 *J. Appl. Phys.* **32** 1729  
Rabinowicz E 1977 *Sci. Am.* **236** 74  
Ramsey J A 1976 *Progr. surface and membrane Sci.* (New York: Academic Press) Vol 11 p 117  
Rhead G E 1977 *Surf. Sci.* **68** 20  
Rosenblum B, Carrico J P, Bräunlich P and Himmel L 1977 *J. Phys.* **E10** 1056  
Rosenblum B, Braunlich P and Himmel L 1977a *J. Appl. Phys.* **48** 5262  
Rudolf G and Glaefke H 1982 *Phys. Status Solidi* **a73** K253  
Scarmozzino R 1971 *Solid State Commun.* **9** 1159  
Scharmann A 1967 *Festkörperprobleme* (Berlin: Akad.-Verl.) Vol 6 p. 106  
Scharmann A and Wiessler U 1980 *Phys. Status Solidi* **a60** 117  
Schlenk W 1976 *Phys. Status Solidi* **a33** 217  
Shmurak S Z 1969 *Sov. Phys. Solid State* **10** 1526  
Shorshorov M Kh., Zhebynev D A and Alekhin V P 1976 *Proc. 5th Inter. Symp. on EE and Dosimetry* (ed) A Bohun and A Scharmann (Prague: Inst. Solid St. Phys. Acad. Sci.) p. 229  
Sodomka L, Leistner M, Tessmar H and Karel F 1980 *Kristall. U. Tech.* **15** 1101  
Sujak B 1964 *Acta Phys. Pol.* **26** 1033  
Sujak B and Gieroszynski A 1970 *Acta Phys. Pol.* **A37** 733  
Sujak B, Gieroszynski A and Pega E 1965 *Acta Phys. Pol.* **28** 61  
Sujak B, Gieroszynska K and Gieroszynski A 1982 *Phys. Status Solidi* **a72** K177  
Tale I, Kortov V and Popov V 1982 *Phys. Status Solidi* **a74** 395  
Tatro C A and Liptai R G 1962 *Proc. Symp. on Physics and Non Destructive Testing* (Southwest Research Inst., San Antonio, Texas) p. 145  
Tinder R F 1968 *J. Appl. Phys.* **39** 355  
Von Voss W D and Brotzen F R 1959 *J. Appl. Phys.* **30** 1639  
Walton A J 1977 *Adv. Phys.* **26** 887  
Wortmann J 1978 *Phys. Status Solidi* **a50** 509  
Zink J I 1978 *Acc. Chem. Res.* **11** 289

**Discussion**

M Yussouff: Has the velocity distribution of the emitted electrons been measured?

G Mukhopadhyay: Yes, it has, in some cases.

R Chidambaram: How does thermoluminescence dosimetry compare with exoemission?

Mukhopadhyay: I am sorry, I can't give you a precise answer.

R Krishnan: If there are two or more processes of exoemission occurring simultaneously, can one separate one from the other?

Mukhopadhyay: Only by doing additional experiments.

G Venkataraman: Would the exoemission rate depend on the type of defect migrating to the surface?

Mukhopadhyay: Yes, it would—particularly the temperature dependence, because activation is involved.

C K Majumdar: How long before the actual crack occurs can one detect anything by the techniques you have described?

Mukhopadhyay: This depends on the material. In fatigue cycling with a large stress amplitude, very early detection is possible (at 0.7% of failure).

P Rodriguez: Is the exoemission phenomenon more amenable to measurement in fatigue cycling than in a uniaxial tensile test?

Mukhopadhyay: Not necessarily, but I think this depends on the experimentalist.

M Yussouff: Is exoemission a field emission process?

Mukhopadhyay: No, because the actual explanation depends on the type of sample and environment involved.

## Relevance of liquid state to solid state properties\*

H R KRISHNA MURTHY and T V RAMAKRISHNAN

Department of Physics, Indian Institute of Science, Bangalore 560 012, India

**Abstract.** We outline in this talk the beginning of a new programme to study physical properties of crystalline solids. It is based on considering the latter, a broken symmetry phase, in terms of the higher symmetry liquid phase. The solid is a calculable perturbation on the fluid. This is exactly opposite to the standard approach which relates mechanical properties to the behaviour of defects (mainly dislocations) etc., in an otherwise perfect crystalline solid. However, most other broken symmetry phases (*e.g.* ferromagnets) are discussed starting from a symmetric Hamiltonian or a free energy functional, and earlier work by one of the authors shows that the liquid-solid transition is well described, qualitatively and quantitatively, by this approach. On the other hand, defect theories of melting have a long record of nonsuccess. In the first part of the talk, the density wave theory of freezing will be outlined, and it will be shown how properties such as Debye Waller factor, entropy change of freezing etc. can be calculated with no or one free parameter. The problem of calculating shear elastic constants and dislocation core structures as well as energies in terms only of observable liquid state properties will be set up, and results presented. The method will be contrasted with zero temperature 'atomistic' models which obscure the essential dependence on structure and flounder in a mass of detail. The concluding part will describe further proposed applications, some suggestive experimental results extant in the literature, and some speculations.

### Discussion

G Venkataraman: Is something like the Josephson effect possible in this case of change of phase associated with ballistic motion or diffusion?

T V Ramakrishnan: This is a hard question to answer.

V Balakrishnan: What stabilizes the system against other possible  $\mu_G$ 's? How does the system choose, say, between the fcc and bcc structures?

Ramakrishnan: We examine the stability of the fluid with respect to a *given* structure.

V Balakrishnan: What is it in the system that kills fluctuations with other wavevectors?

Ramakrishnan: The correlation function  $S(q)$  is strongly peaked at a particular  $q$ . Thus the energy to excite this mode is far less than that for any other mode.

G Ananthakrishna: How does one measure the three-point correlation?

Ramakrishnan: This can be estimated either by computer simulation or by doing light scattering experiments on colloidal crystals.

G Srinivasan: Could one find the pressure dependence of the two-point correlation?

Ramakrishnan: This does not give the quantity required here.

---

\* Only a summary is presented.

**K R Rao:** Is it necessary that the three-point correlation measurement be done in solid state?

**Ramakrishnan:** No. A "combination" scattering experiment has to be done in the liquid state for information in the short-range region.

**K R Rao:** What is the difficulty in predicting the melting temperature?

**Ramakrishnan:** The difficulty is that  $\mu_G$  and  $C_G$  are dimensionless quantities.

**S Ranganathan:** Can your theory take into account the liquid-glass transition?

**Ramakrishnan:** No. We are very far from it.

**D Dhar:** How is the effective potential you use related to the effective potential used in cell theories of melting?

**Ramakrishnan:** The two are not related to each other.

**S R Shenoy:** Can one use your theory to handle a crystal with frozen-in defects?

**Ramakrishnan:** Perhaps one could, depending on how perfect these crystallites are and also on how rapidly the phase changes.

**R Chidambaram:** Where is the entropy of melting in this model?

**Ramakrishnan:** We calculate the entropy of melting from the known thermodynamic functions.

**G Ananthakrishna:** How do you describe dislocations and vacancies in your model?

**Ramakrishnan:** I don't know how to describe vacancies, but dislocations can be described in a manner similar to vortices in a superconductor.

## Elastic continuum theories of lattice defects: a review

DEBENDRANATH SAHOO

Materials Science Laboratory, Reactor Research Centre, Kalpakkam 603 102, India

**Abstract.** The presently available elastic continuum theories of lattice defects are reviewed. After introducing a few elementary concepts and the basic equations of elasticity the Eshelby's theory of misfitting inclusions and inhomogeneities is outlined. Kovács' result that any lattice defect can be described by a surface distribution of elastic dipoles is described. The generalization of the isotropic continuum approach to anisotropic models and to Eringen's isotropic but non-local model is discussed. Kröner's theory (where a defect is viewed as a lack of strain compatibility in the medium) and the elastic field equations (formulated in a way analogous to Maxwell's field equations of magnetostatics) are described. The concept of the dislocation density tensor is introduced and the utility of higher-order dislocation density correlation tensors is discussed. The beautiful theory of the affine differential geometry of stationary lattice defects developed by Kondo and Kröner is outlined. Kosevich's attempt to include dynamics in the elastic field equations is described. Wadati's quantum field theory of extended objects is mentioned qualitatively. Some potential areas of research are identified.

**Keywords.** Elastic continuum theory; lattice defects; inhomogeneities; dislocations; disclinations; dislocation density tensor; torsion tensor; curvature tensor; dislocation density correlations; elastic field equations; nonlocal elasticity.

### 1. Introduction

This paper is intended to survey the elastic continuum theories of lattice defects. The understanding of the behaviour of crystal defects is essential for studying such processes as anelasticity, plastic flow, rupture, fatigue and radiation damage, which play a crucial role in materials science. The lattice distortion produced by a defect can be calculated by using elastic models at sufficiently large distances from the defect. In many applications, a continuum theory offers precise analytic expressions for the stress fields of defects, their interaction energies, etc., and hence is of immense practical value. In contrast to this, a discrete atomistic approach (which is unavoidable at short distances from the defects) does not offer analytically convenient working relations, although it yields reliable numerical data.

At present there is no unified theory of defects in continuous media. Most theories are developed with a particular type of defect in view. Thus the methods applicable to point defects are different from those applicable to line defects—for dislocations, see *e.g.*, de Wit (1960), Nabarro (1967), Mura (1968); for volume defects (inclusions), see Eshelby (1957). Moreover, almost all theories are restricted to static defect problems. The dynamical theory of defects in continua is still in its infancy. This review presents a bird's eyeview of the various approaches to defects in a continuous medium.



## 2. Continuum modelling of defects

In the elastic continuum theory, defects are modelled following the procedure given by (See e.g. Eshelby 1956). In order to construct a defect, one marks out in the medium an appropriate surface  $S_C$  bounded by a curve  $C$  and makes a cut coinciding with  $C$ . Then a relative displacement  $\delta u$  is given to each pair of points on either side of  $S_C$ , scraping away material where there would be interpenetration and filling in the remaining gaps with additional material. In general,  $\delta u$  can be written as

$$\delta u_i = b_i + \Omega_{ij} x_j \quad (i, j = 1, 2, 3),$$

where  $x_j$  denotes the coordinates of the point,  $b_i$  the relative translation of this point, and  $\Omega_{ij} (= -\Omega_{ji})$  describes the relative rotation of  $S_C$ . A general dislocation is thus described by six constants—in other words, it consists of six elementary (Volterra) dislocations. Each of the latter can be characterized by a single constant, the other five being set equal to zero. A rotational dislocation with  $b_i = 0$  is actually a disclination. When  $\Omega_{ij} = 0$ , one has the usual (translational) dislocation with a Burgers vector  $\mathbf{b}$ . Some examples of defects created in this manner are shown in figure 1. Figure 1(a) shows an edge dislocation produced by cutting a ring-shaped cylinder across the surface  $S_C$ , choosing the axis of the cylinder as the curve  $C$ , and displacing the upper side of the surface  $S_C$  over the lower by an amount  $\mathbf{b}$  perpendicular to the axis. In figure 1(b), a sector of the cylinder is cut defining the surface  $S_C$  and the axis as  $C$ , and both sides of the surface are pulled apart widening the angle of the sector so as to accommodate a larger sized sector. This produces a wedge disclination,  $\Omega$  being a rotation around the axis. Figure 1(c) shows the Somigliana prescription for creating a substitutional or an interstitial atom. A sphere is cut out of the matrix, its radius altered by adding or removing material, and the sphere is then reinserted in the matrix. This is the familiar misfitting sphere model. Note that there is no boundary curve  $C$  in this case. It can be shown that a knowledge of  $\delta u$  as a function of position  $x_i$  on the surface  $S_C$ , together with the boundary conditions at the surface of the body, completely determines the resulting state of internal stress.

## 3. Basic equations of elasticity theory

In the linear theory of elasticity, the condition of equilibrium is given by

$$\sigma_{il,i} + f_i = 0, \quad (1)$$

where  $\sigma_{il}$  is the stress tensor,  $f_i$  is the body force and the usual comma notation for derivatives and the convention of summation over repeated indices are used.  $\sigma_{ij}$  is related to the strain tensor  $e_{ij}$  by Hooke's law:

$$\sigma_{il} = C_{ilmn} e_{mn}, \quad (2)$$

where

$$e_{mn} = \frac{1}{2} (u_{m,n} + u_{n,m}), \quad (3)$$

is the symmetric part (sym) of the gradient (grad) of the displacement field  $\mathbf{u}$ : thus  $e = \text{sym grad } \mathbf{u} \equiv \text{def } \mathbf{u}$ . For an isotropic homogeneous medium

$$C_{ilmn} = \lambda \delta_{il} \delta_{mn} + \mu (\delta_{im} \delta_{ln} + \delta_{in} \delta_{lm}), \quad (4)$$

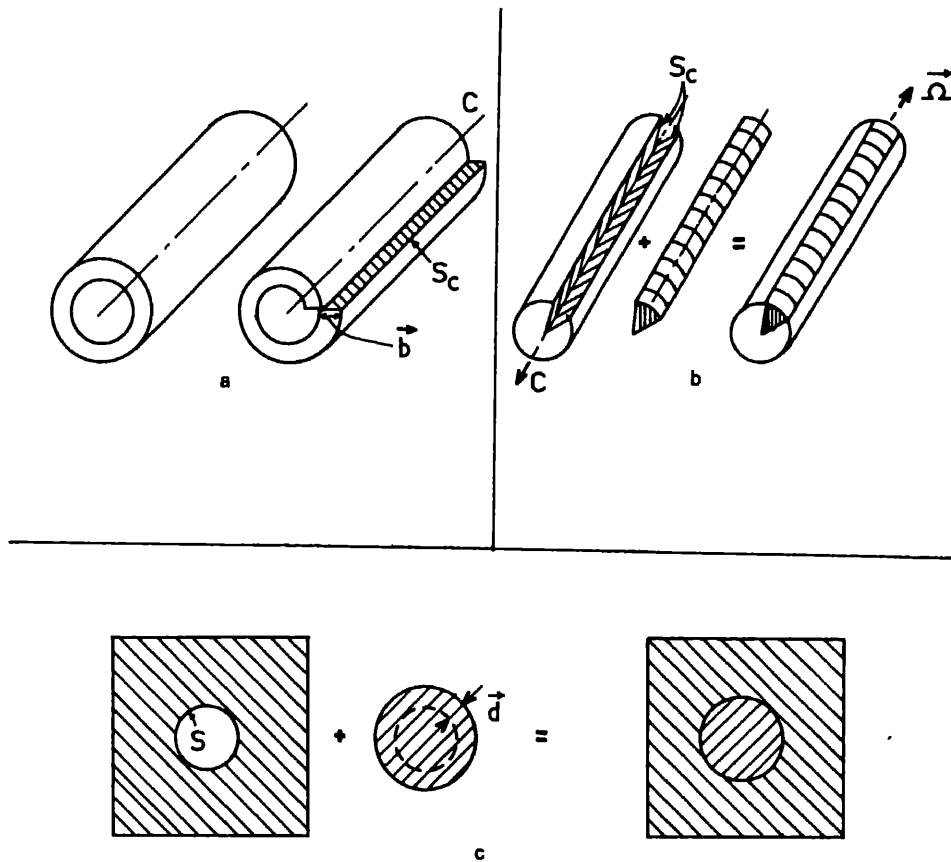


Figure 1. (a) Continuum model of an edge dislocation. (b) Continuum model of a wedge disclination. (c) Misfitting sphere model for a substitutional atom.

where  $\lambda$  is Lamé's constant and  $\mu$  is the shear modulus. Equations (1)–(3) imply the differential equations

$$C_{ilmn} u_{m,nl} + f_i = 0 \quad (5)$$

for  $u$ . Let  $G_{il}$  be the Green function tensor defined by the equation

$$C_{ijkl} G_{km,ij}(|\mathbf{r}|) + \delta_{im} \delta(|\mathbf{r}|) = 0 \quad (6)$$

and the boundary condition  $G_{km}(r \rightarrow \infty) = 0$ . Then

$$G_{km}(\mathbf{r}) = \frac{1}{8\pi\mu} \left[ \delta_{km} r_{,pp} - \frac{\lambda + \mu}{\lambda + 2\mu} r_{,km} \right]. \quad (7)$$

The elastic field due to the body force  $\mathbf{f}$  is given by

$$u_i(\mathbf{r}) = \int f_j(\mathbf{r}') G_{ij}(|\mathbf{r} - \mathbf{r}'|) d^3 r'. \quad (8)$$

The existence of a continuous single-valued displacement field  $u_i$  requires the

incompatibility (inc) of the strain tensor to vanish, i.e.,

$$\text{inc } e = 0, \quad (9)$$

where, in component form,

$$(\text{inc } e)_{ij} = -\varepsilon_{ikl} \varepsilon_{jmn} e_{ln, km} = [\text{curl}(\text{curl } e)]_{ij}, \quad (10)$$

$\varepsilon_{ikl}$  denoting the completely antisymmetric Levi-Civita tensor or the alternator.

There are two broad ways of introducing defects into this picture. One is to start with (1) and assign an effective  $f_i$ , as is usually done in a point defect (Eshelby 1957). In line defects, one puts  $f_i = 0$ , but generalises (8) to include the contribution from the cut surface  $S_C$  (Mura 1968). In the second approach, one must recognise that when defects are present in the medium, the displacement field  $u$  is no longer a continuous single-valued function on  $S_C$ , and therefore the compatibility condition ought to be modified. This is achieved by generalizing (9) to include a source term  $\eta$  characterising the incompatibility distribution of the defect, i.e., (9) is replaced by

$$\text{inc } e = \eta. \quad (11)$$

In the next section we describe briefly the first approach which is due largely to Eshelby (1957).

#### 4. The Eshelby approach

Volume defects such as precipitates, solute atoms, self-interstitials, etc contribute to the change in the elastic state of the medium. A self-interstitial is modelled as a misfitting homogeneous inclusion (MHI). It corresponds to matter of volume  $V + \Delta V$  being forced into a cavity of volume  $V$  in the medium (see figure 2a). Both the inclusion ( $I$ ) and the matrix ( $M$ ) have the same elastic moduli. An MHI is created in a body because of internal stress, i.e., some region  $I$  of volume  $V$  develops internal stress and is transformed to a different shape and size with a volume  $V + \Delta V^C$  while remaining inside the matrix  $M$  (see figure 2b). Thus a constrained stress ( $\sigma_{ij}^C$ ) or a constrained strain ( $e_{ij}^C$ ) is developed both in  $I$  and  $M$ .

Now suppose  $M$  was absent and  $I$  alone were to undergo a transformation (see figure 2c). It would acquire a different shape and size, with volume  $V + \Delta V^T$ . Let  $\sigma_{ij}^T$  and  $e_{ij}^T$  be the stress and strain associated with the transformation. These need not be of elastic origin (they may arise from metallurgical transformations, for example). Thus, symbolically,  $I \xrightarrow{T} I^T$ , and  $M \xrightarrow{T} M$ . Eshelby has posed and answered the following questions:

- (i) How can one relate  $\sigma_{ij}^C$  and  $e_{ij}^C$  to  $\sigma_{ij}^T$  and  $e_{ij}^T$ ?
- (ii) What can one deduce about the behaviour of  $u^C$ ,  $\sigma^C$  and  $e^C$ , the dilation and the self-energy of an MHI of arbitrary shape?
- (iii) What is the interaction energy of an MHI with an applied stress field  $\sigma_{ij}^A$ ?

After answering these questions Eshelby asks the same questions for an "inhomogeneity" (see figure 2d). The inhomogeneity is an inclusion having elastic constants ( $\lambda^*$ ,  $\mu^*$ ) different from those of the matrix ( $\lambda$ ,  $\mu$ ). Note that a perfectly-fitting inhomogeneity (PFI) does not perturb the stress field in the matrix. However, a misfitting inhomogeneity (MFI) would alter the stress field in  $M$ .

An MFI is an appropriate model for a foreign interstitial in a crystal. Eshelby shows:

how to reduce the problem of an MFI to an equivalent MHI problem. The problem of an MFI in the presence of an external stress  $\sigma_{ij}^A$  is of interest in many practical situations such as SIPA creep (Heald and Speight 1974), voids in strained metals, etc. In the presence of  $\sigma_{ij}^A$ , a PFI can undergo an induced transformation strain  $e_{ij}^T$  'proportional' to the applied strain  $e_{ij}^A$ . To illustrate the Eshelby approach, consider an MHI for which the displacement field  $u_i^C$  is given by

$$u_i^C(r) = \int dS_j C_{jlmn} e_{mn}^T(r') G_{ij}(|r-r'|). \quad (12)$$

Eshelby considers a spherical and an ellipsoidal MHI for which  $e_{mn}^T$  is constant, and, using (7) for the Green function, arrives at the familiar relations (for the spherical MHI):

$$\left. \begin{aligned} e_{ij}^C &= 'e_{ij}^C + \frac{1}{3} e^C \delta_{ij} \\ &= \beta 'e_{ij}^T + \frac{1}{3} \alpha e^T \delta_{ij}, \\ e^C &\equiv e_{ii}^C, 'e_{ij}^C \equiv e_{ij}^C - \frac{1}{3} e^C \delta_{ij}, \\ \alpha &= \frac{1}{3} \left( \frac{1+\nu}{1-\nu} \right), \beta = \frac{2}{15} \left( \frac{4-5\nu}{1-\nu} \right). \end{aligned} \right\} \quad (13)$$

Here  $'e_{ij}$  is the deviatoric part of  $e_{ij}$  and  $e$  is the scalar part. The general results for a PFI and an MFI under an applied load are given in Eshelby (1957).

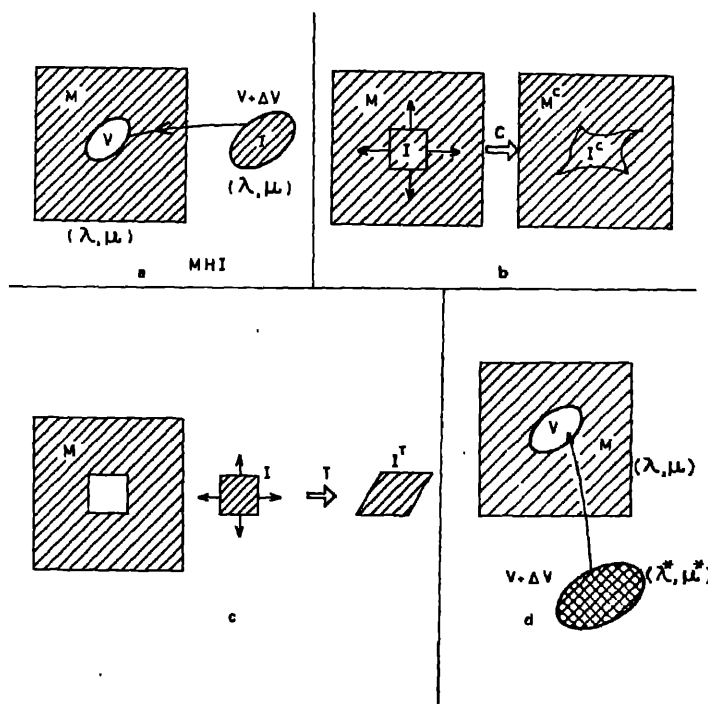


Figure 2. (a) A misfitting homogeneous inclusion (MHI). (b) The rectangular region  $I$  undergoing a constrained transformation in the matrix resulting in a curved shape. (c) The region  $I$ , detached from the matrix, undergoing a  $T$  transformation. (d) A misfitting inhomogeneity (MFI).

A significant feature of Eshelby's theory is the recognition of the important role of surfaces in defect problems. Eshelby was the first to show that the surface contribution to the change in volume of the medium, when defects are present, is quite significant. When defects (internal stresses) are present in a bounded medium, one must invoke image forces such that the boundary of the medium is kept free of stresses (the equilibrium condition), analogous to the method of images in electrostatics. As in the latter case, the image stress in the defect problem should have no internal sources in the medium. A well-known result derived by this method is that the volume change of a finite medium when a single spherical point defect is present is  $\gamma$  times the corresponding volume change in the infinite medium, where  $\gamma = 3(1-\nu)/(1+\nu)$  is the famous Eshelby factor and  $\nu$  is Poisson's ratio. If  $\nu$  is taken as  $1/3$ , then  $\gamma$  is as large as  $3/2$ .

### 5. The elastic dipole tensor

Of central importance in the study of defects is the concept of the elastic dipole. Let a point force  $f_j$  be acting at a point  $\mathbf{r}'$  in an elastic medium. The displacement  $u_i$  at a point  $\mathbf{r}$  caused by the force is

$$u_i(\mathbf{r}) = f_j(\mathbf{r}') G_{ij}(|\mathbf{r} - \mathbf{r}'|). \quad (14)$$

Now suppose that in a small volume centred at  $\mathbf{r}'$ ,  $N$  point forces  $f_k^\alpha(\mathbf{r}' + \mathbf{s}^\alpha)$  are acting at the points  $\mathbf{r}' + \mathbf{s}^\alpha$  ( $\alpha = 1, \dots, N$ ). Then (14) must be generalised to

$$\begin{aligned} u_i(\mathbf{r}) &= \sum_{\alpha=1}^N f_k^\alpha(\mathbf{r}' + \mathbf{s}^\alpha) G_{ik}(|\mathbf{r} - \mathbf{r}' - \mathbf{s}^\alpha|) \\ &= \left[ \sum_{\alpha=1}^N f_k^\alpha \right] G_{ik}(|\mathbf{r} - \mathbf{r}'|) + \left[ \sum_{\alpha=1}^N s_j^\alpha f_k^\alpha \right] G_{ik,j'}(|\mathbf{r} - \mathbf{r}'|) \\ &\quad + \frac{1}{2} \left[ \sum_{\alpha=1}^N s_j^\alpha s_m^\alpha f_k^\alpha \right] G_{ik,j'm'}(|\mathbf{r} - \mathbf{r}'|). \end{aligned} \quad (15)$$

Here the second equality is obtained by expanding the Green function in a Taylor series about  $(|\mathbf{r} - \mathbf{r}'|)$ . (Note that  $G_{ik,j'}$  stands for  $\partial G_{ik}/\partial x_{j'}$ ). The first term in the expansion vanishes, because for physically realizable defects the invariance of the entire system under a rigid infinitesimal translation implies that

$$\sum_{\alpha} f_k^\alpha(\mathbf{r}' + \mathbf{s}^\alpha) = 0. \quad (16)$$

The elastic dipole ( $P_{jk}$ ), tripole ( $P_{jmk}$ ), etc are then defined as the quantities in parentheses in the successive terms that remain:

$$\begin{aligned} P_{jk} &= \sum_{\alpha=1}^N s_j^\alpha f_k^\alpha, \\ P_{jmk} &= \sum_{\alpha=1}^N s_j^\alpha s_m^\alpha f_k^\alpha, \text{ etc.} \end{aligned} \quad (17)$$

The displacement field due to a dipole is thus

$$u_i(\mathbf{r}) = P_{jk} G_{ik,j'}(|\mathbf{r} - \mathbf{r}'|) \text{ and } P_{jk} = P_{kj}. \quad (18)$$

It can be shown easily that a dipole is simulated by a body force according to

$$f_i(r) = P_{ik} \delta_{,k}(r - r'). \quad (19)$$

The importance of the elastic dipole can be judged from the following result due to Kovács (1978): *Any lattice defect can be described by a surface distribution of elastic dipoles.* To establish this fact, consider a surface  $S$  in a medium, and let it undergo a transformation such that the surface element  $dS'_m$  at a position  $r'$  on the surface has a displacement  $a_i(r')$ . Due to this transformation, the surface element  $dS'_m$  becomes a source of an elastic singularity with a dipole strength which can be defined by the expression

$$dP_{ik} = C_{iklm} a_l dS'_m. \quad (20)$$

The total strength of the defect is given by

$$P_{ik} = \int_S C_{iklm} a_l dS'_m. \quad (21)$$

The displacement field of the defect is obtained by applying (18) and integrating over the dipole distribution

$$\begin{aligned} u_n(r) &= \int G_{nl,k'}(r - r') dP_l(r') \\ &= C_{iklm} \int_S G_{nl,k'}(r - r') a_l(r') dS'_m. \end{aligned} \quad (22)$$

To apply this result to a dislocation, consider a cut in the medium over the surface  $S_C$  bounded by a closed curve  $C$ . The positive direction of the normal to  $S_C$  is related to  $C$  by the right hand rule. Now let each point on  $S_C$  be given a displacement  $a_i(r') = b_i$ ,  $b$  being a constant vector. Then we obtain the familiar Burgers (1939) result

$$u_n(r) = C_{iklm} b_l \int_{S_C} G_{ln,m}(r - r') dS'_k, \quad (23)$$

which is the displacement field of a dislocation loop  $C$  of Burgers vector  $b$ .

The displacement field of an MHI can be obtained by choosing for  $S$  a closed surface enclosing a volume  $V \neq 0$  and considering the displacement  $a_i(r')$  inside and outside  $S$ :

$$a_i(r') = \begin{cases} u_i^T(r'), & \text{if } r' \in V \\ 0, & \text{otherwise.} \end{cases} \quad (24)$$

Using (18) and applying Gauss's theorem, one obtains

$$u_n(r) = \int_V C_{iklm} u_i^T G_{nl,k} dV' + \int_V C_{iklm} u_i^T G_{nl,k'm'} dV'. \quad (25)$$

As the Green tensor is symmetric and satisfied the equation

$$C_{iklm} G_{nl,k'm'} = -\delta_{nl} \delta(r - r'), \quad (26)$$

we obtain

$$u_n(\mathbf{r}) = \begin{cases} \int_V \sigma_{ik}^T G_{ni,k} dV' - u_n^T, & \text{if } r \in V, \\ \int_V \sigma_{ik}^T G_{ni,k} dV', & \text{if } r \notin V, \end{cases} \quad (27)$$

where  $\sigma_{ik}^T = C_{iklm} u_{l,m}^T$ . This result is essentially the same as that obtained by Eshelby (1961) if we identify  $\frac{1}{2}(u_{l,m}^T + u_{m,l}^T)$  with the transformation strain  $e_{ml}^T$ . The total strength of this defect is

$$\begin{aligned} P_{ik} &= \oint_S C_{iklm} u_l^T dS'_m \\ &= \int_V C_{iklm} u_{l,m}^T dV' = \int_V \sigma_{ik}^T dV'. \end{aligned} \quad (28)$$

Thus an MHI can be interpreted as a space distribution of dipoles with a volume density  $\sigma_{ik}^T$ . A PFI can be treated similarly (Kovács 1978), and the results of Eshelby (1957) rederived.

The interaction energy  $U$  between the defect, a strain field  $e_{ik}^A$  and the associated force  $F_n^t$  acting on the defect are expressed by the following general relations:

$$\begin{aligned} U &= - \int e_{ik}^A(\mathbf{r}') dP_{ik}(\mathbf{r}') \\ &= - \int_S C_{iklm} e'_{ik}(\mathbf{r}') a_l(\mathbf{r}') dS'_m. \end{aligned} \quad (29)$$

$$\begin{aligned} F_n^t &= \int e_{ik,n}^A dP_{ik} \\ &= C_{iklm} \int_S e_{ik,n}^A(\mathbf{r}') a_l(\mathbf{r}') dS'_m. \end{aligned} \quad (30)$$

These equations are applicable to any type of defect. Thus, substituting in (30) the displacement appropriate for a dislocation and using Stokes' theorem, one recovers the Peach-Koehler (1950) expression for the force

$$F_n^{\text{disl}} = \oint_C \epsilon_{mnk} \sigma_{lm}^A b_l dl'_k, \quad (31)$$

where  $\sigma_{lm}^A$  is the stress field associated with the strain  $e_{lm}^A$  and  $dl'_k$  is a line element along  $C$ .

## 6. Generalizations of elastic continuum models

An important step towards bridging the gap between the elastic continuum approach outlined in the previous sections and the more detailed atomistic calculations has been achieved on two different fronts: the anisotropic continuum approach and the nonlocal continuum approach.

### 6.1 The anisotropic continuum models

These models are well described in the recent book by Teodosiu (1982) which also contains an exhaustive set of relevant references. A point defect in a crystal lattice is better represented by an elastic dipole tensor which is *anisotropic*, conforming to the symmetry of the actual defect site in the lattice, whereas the host lattice may be modelled as an elastically isotropic medium. We mention as an example the calculation of the interaction energy between two point defects with cubic symmetry  $O_h$  by Siems (1968). He showed that two elastic dipoles do not interact, and that the principal singularity of the elastic interaction energy between two such defects is the dipole-octupole interaction. Models along these lines have been proposed for faceted voids in irradiated crystals (Evans *et al* 1972; Malen and Bullough 1971).

Another approach is to consider spherically symmetric point defects in a host medium that is elastically anisotropic. The major drawback of this approach is the nonavailability of a closed form analytic expression for the Green tensor. For symmetries other than hexagonal symmetry (Kröner 1953), the solutions are in the form of series, thus necessitating perturbation-type calculations. For these reasons of mathematical inconvenience, not much work has been done along these lines. (For point defects, see Eshelby 1956; for line defects in an anisotropic host medium, Teodosiu 1982; Steeds and Willis 1979).

### 6.2 The nonlocal elastic continuum models

Eringen and Edelen (1972) and Eringen (1972, 1976) have developed a new theory of elasticity called nonlocal elasticity. This theory makes use of nonlocal elastic constants (a closer approximation to the force constants of the atomistic theories). The basic equations of linear isotropic elastic solids, for the static case and vanishing body forces are:

$$\left. \begin{aligned} \bar{\sigma}_{ik,k} &= 0, \\ \bar{\sigma}_{ik} &= \int_V \sigma_{ik}^{NL}(\mathbf{r}, \mathbf{r}') d^3r', \\ \sigma_{ik}^{NL} &= \alpha(|\mathbf{r} - \mathbf{r}'|) C_{iklm} e'_{lm}, \\ e'_{lm} &= \frac{1}{2}(u_{l,m'} + u_{m,l'}). \end{aligned} \right\} \quad (32)$$

Here  $\alpha(|\mathbf{R}|)$  attenuates rapidly as  $R \rightarrow 0$ , it is a continuous function which depends on a parameter  $a$  such that when  $a \rightarrow 0$ ,  $\alpha(R) \rightarrow \delta(R)$  and the classical equations of elasticity are recovered. Here  $e'_{lm} \equiv e_{lm}(\mathbf{r}')$  and  $u_{l,m'} = \partial u_l / \partial x_{m'}$ . The stress  $\sigma^{NL}(\mathbf{r})$  is the nonlocal stress in the sense that its value at  $\mathbf{r}$  depends on the strain at all  $\mathbf{r}' \in V$ . Eringen has shown that the first equation in (32) is satisfied if and only if  $(C_{iklm} e_{lm})_{,k} \equiv \sigma_{ik,k} = 0$  in  $V$ . This means that the *displacement* field remains the same in the nonlocal theory as in the classical theory. The *stresses* differ in the two theories.

Kovács and Vörös (1979) showed that the appropriate body force  $F_i$  to be included in the generalization of (32) is

$$F_i(\mathbf{r}) = \int \alpha(\mathbf{r} - \mathbf{r}') f_i(\mathbf{r}') dV', \quad (33)$$

where  $f_i(\mathbf{r})$  is the body force in the classical theory (see (1)). The force acting on an elastic



dipole is then

$$F_j(\mathbf{r}) = P_{jk}(\mathbf{r}')\alpha_{,k}(\mathbf{r}-\mathbf{r}') \quad (34)$$

and the interaction energy  $U$  between the elastic dipole and a displacement field  $u_i^A$  is

$$U(r) = - \int P_{jk}(\mathbf{r})\alpha(\mathbf{r}'-\mathbf{r})e_{jk}^A(\mathbf{r}')dV'. \quad (35)$$

Note that the interaction depends on the strain field at *all* points in the medium. The force acting on the dipole is

$$f_n = \int P_{jk}(\mathbf{r})\alpha(\mathbf{r}'-\mathbf{r})e_{jk,n}^A(\mathbf{r}')dV'. \quad (36)$$

Note that (34)–(36) reduce to the corresponding equations of the classical theory, i.e. to (19), (29) and (30) when  $\alpha(\mathbf{r}'-\mathbf{r}) \rightarrow \delta(\mathbf{r}'-\mathbf{r})$ .

Since any defect can be described as a surface distribution of dipoles (discussed in § 5), it is interesting to generalise the results of the local theory for a surface distribution of dipoles. Kovács and Vörös (1979) have shown that (29) then generalises to the form

$$U = - \int_S \bar{\sigma}_{im}^A(\mathbf{r}')a_i(\mathbf{r}')dS'_m, \quad (37)$$

where

$$\bar{\sigma}_{ik}^A(\mathbf{r}) = \int_V \sigma_{ik}^{NL,A}(\mathbf{r}, \mathbf{r}')dV' = \int_V \alpha(|\mathbf{r}-\mathbf{r}'|)C_{iklm}e_{lm}^A dV' \quad (38)$$

and  $a_i(\mathbf{r})$  and  $S$  are as defined in § 5. Similarly, (30) generalises to

$$f_n = \int_S \bar{\sigma}_{im}^A(\mathbf{r}')a_i(\mathbf{r}')dS'_m. \quad (39)$$

It is easy to show that the self-energy of the defect is

$$U_s = -\frac{1}{2} \int_S \bar{\sigma}_{im}^s(\mathbf{r}')a_i(\mathbf{r}')dS'_m, \quad (40)$$

where  $\bar{\sigma}_{im}^s$  is the stress field due to the defect alone.

As expected, the stress singularities and the embarrassing infinite self-energies in the usual defect calculations are replaced by well-defined, finite quantities in the nonlocal theory. This is closer to physical reality, and the advantage of obtaining realistic defect properties without performing tedious atomistic calculations makes this approach very attractive. For lack of space, we quote a single result to substantiate this remark. The interaction energy  $U$  between two dilation centres of volume increments  $\Delta V_1$  and  $\Delta V_2$  is given by

$$U = 2\mu \frac{(1-\nu)}{(1-2\nu)} \Delta V_1 \Delta V_2 \alpha(R), \quad (41)$$

where  $R$  is the distance between the two defects. (Note that when  $\alpha(R)$  is replaced by  $\delta(R)$ ,  $U \rightarrow 0$ , since  $R \neq 0$ .) The self-energy  $U_s$  of a dilation centre of volume increment  $\Delta V$  is

$$U_s = \frac{1}{2} P \Delta V \alpha(0) \quad (42)$$

A convenient representation of the kernel  $\alpha(r)$  is the Gaussian

$$\alpha(R) = \frac{\pi^{3/2} k^3}{a^3} \exp(-k^2 R^2/a^2). \quad (43)$$

It is natural to interpret the parameter  $a$  as the lattice parameter. The other parameter  $k$  is estimated by Eringen (1977a, b) from a consideration of the critical shear stress needed to create a dislocation. This leads to  $k = 0.94$  for fcc metals. In fcc metals  $\Delta V = a^3 \varepsilon/4$  where  $\varepsilon = (V - V_0)/V_0$ , the relative volume difference between the host and the alloying atoms. Then, using  $\nu = 1/3$  and  $k = 0.94$ , one obtains  $U_s = 0.56 \mu a^3 \varepsilon^2$ . This is to be compared with the atomistic model calculation of Flinn and Maradudin (1962) which yields  $U_s \approx 0.54 \mu a^3 \varepsilon^2$ .

Other examples of the application of the nonlocal theory include expressions for the stress field, strain energy, etc. of screw and edge dislocations (Eringen 1977a, b; Eringen and Balta 1979), as well as a nonsingular expression (Eringen *et al* 1977) for the stress-concentration function in the problem of an elastic plate with a sharp crack and subjected to a uniform tension (at infinity) perpendicular to the crack (the Griffith problem). These results show the potential utility of the nonlocal elastic models of defects which certainly needs to be explored much more elaborately. Moreover, calculations in nonlocal elastic theory are much simpler than the corresponding ones in the anisotropic elasticity approach briefly described in § 6.1.

## 7. The linear continuum theory of dislocations

Electron microscopic observations show that deformed crystals have numerous dislocation lines which are very often randomly tangled. A convenient way to describe these dislocations is via the *dislocation density tensor*  $\alpha_{ij}(\mathbf{r})$  (Nye 1953). Consider an arbitrary point  $P$  in the material. In the neighbourhood of  $P$ , within a small area element  $dS$ , there are several dislocation lines with Burgers vector  $\mathbf{b}^{(a)}$  ( $a = 1, 2, \dots, n$ ) in the directions  $\hat{\mathbf{v}}^{(a)}$ , as shown in figure 3. The effective Burgers vector  $d\mathbf{b}$  of  $n$  dislocations threading the surface  $dS$  is then given by

$$dS_i \alpha_{ij} = \sum_{a=1}^n (\hat{\mathbf{v}}^{(a)} \cdot \hat{\mathbf{v}}) b_j^{(a)} \equiv db_j, \quad (44)$$

where  $\hat{\mathbf{v}}$  is the unit vector at  $P$  defining the element  $dS$ . The scalar product  $(\hat{\mathbf{v}}^a, \hat{\mathbf{v}})$  measures the threading of the surface  $dS$  by the  $a$ th dislocation. In integral form, (44) is written as

$$\int_S dS_i \alpha_{ij} = b_j = \oint_C du_j, \quad (45)$$

where  $C$  is the closed curve bounding the surface  $S$ . (Kröner 1964 and Noll 1967 have

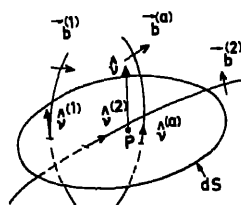


Figure 3. The area element  $dS$  showing the threading of dislocation lines.

defined  $\alpha_{ij}$  somewhat differently; see Teodosiu (1982)). Now

$$\alpha_{ij} = \varepsilon_{ikl} \partial_k \beta_{lj} \quad (\text{or } \alpha = \text{curl } \beta), \quad (46)$$

where  $\beta_{ij}(\mathbf{r}) = u_{j,i}(\mathbf{r})$  is the gradient of the elastic displacement. Using (46) in (45) and invoking Stokes theorem, we find

$$\partial_i \alpha_{ij} = \alpha_{ij,i} = 0, \quad (\text{or } \text{div } \alpha = 0), \quad (47)$$

because the divergence of a curl vanishes. Physically this relation means that dislocations cannot end inside the medium. Another feature of the  $\alpha$ -tensor is worth noting. The first index  $i$  of  $\alpha_{ij}$  denotes the average direction of the dislocation lines whereas the second index  $j$  denotes the direction of the Burgers vector. Thus the diagonal components of  $\alpha$  correspond to screw dislocations and the off-diagonal elements to edge dislocations. Since the diagonal and nondiagonal components of a tensor are not invariant notions, *the classification of dislocations into edge and screw types is not to be taken too seriously.*

The introduction of the  $\alpha$ -tensor has given impetus to the development of the beautiful differential-geometric theory (see § 9). The connection with geometry arises from the physical fact that dislocations involve a certain curvature or bending of the lattice network, thus imparting a curvature to the continuum (Nye 1953). To be more precise, the rotation tensor  $\omega_{ij}$  defined as the antisymmetric part of  $\beta$  leads to an axial rotation vector  $\omega_k = \frac{1}{2} \varepsilon_{ijk} \omega_{ij}$ . The difference in  $\omega$  between two points separated by an infinitesimal distance  $d\mathbf{r}$  is given by

$$d\omega_j = (\varepsilon_{jkl} \partial_k e_{li} + \kappa_{ij}) dx_i,$$

where

$$\kappa_{ij} = \alpha_{ij} - \frac{1}{2} \alpha_{kk} \delta_{ij} \quad (48)$$

is the Nye's curvature tensor (see also Kröner 1981). Thus, in the absence of elastic strains, the presence of a continuous distribution of dislocations alone leads to a rotation  $d\theta$  between two points separated by a distance  $d\mathbf{r}$  given by  $d\theta_j = \kappa_{ij} dx_i$ . It is also straightforward to calculate the incompatibility tensor  $\eta$  associated with the presence of the dislocation distribution. We quote the final result (Kröner 1981):

$$\eta_{ij} = -\varepsilon_{ikm} \varepsilon_{jln} \partial_{kl} e_{mn} = \varepsilon_{ikm} \partial_k \kappa_{mj} = -\frac{1}{2} (\varepsilon_{ilm} \partial_n \alpha_{jn})_{(ij)}, \quad (49)$$

$$\bar{\eta} = \text{inc } e = \text{curl } \kappa = (\alpha \times \nabla)_{\text{sym}} = -\text{curl } \alpha^T.$$

It is evident that the divergence of  $\eta$  vanishes.

## 8. The internal stress problem and Kröner's theory

Defects are characterized by the incompatibility tensor  $\eta$  associated with them. For a continuous distribution of dislocations it is given by (49). A single dislocation is described as a limiting case of the continuous distribution with the help of delta functions:

$$\alpha_{ij} = t_i b_j \delta(p) \delta(q), \quad (50)$$

where  $t_i$  is the tangent to the dislocation line and  $p, q$  are suitable coordinates perpendicular to the dislocation line. For a spherical interstitial atom occupying a

volume  $\Delta V$  and located at  $\mathbf{r}_0$ , the incompatibility tensor is

$$\boldsymbol{\eta} = \Delta V (\vec{\nabla} \times \mathbf{I} \times \vec{\nabla}) \delta(\mathbf{r} - \mathbf{r}_0), \quad (51)$$

where  $\mathbf{I}$  is the unit tensor ( $\delta_{ij}$ ).

The main problem in defect theory is: given the tensor  $\boldsymbol{\eta}$  as a function of  $\mathbf{r}$ , to calculate the internal stress and strain in the body. This is a boundary value problem for the equations  $\partial_i \sigma_{ij} = 0$  (force equilibrium condition in the bulk) and  $\sigma_{ij} n_j = 0$  on the surface  $S$  of the body (the traction boundary condition) together with the incompatibility equation  $\text{inc } \mathbf{e} = \boldsymbol{\eta}$ . There are three ways of calculation of  $\mathbf{e}$ .

(i) *The Eshelby-Eddington method*: Eshelby (1956) uses the fact that, because of the tensor identities

$$\text{inc}(\text{def } \mathbf{u}) = 0 \text{ and } \text{div}(\text{inc } \mathbf{A}) = 0, \quad (52)$$

any solution of the incompatibility equation can be written as

$$\mathbf{e} = \text{def } \mathbf{u} + \tilde{\mathbf{e}}, \quad (53)$$

where  $\tilde{\mathbf{e}}$  is a particular solution of the equation and  $\mathbf{u}$  is an arbitrary vector field. If we put  $\boldsymbol{\eta} = 0$  on the boundary  $S$ , then following the method of Eddington in the general theory of relativity, one can write

$$\tilde{\mathbf{e}}(\mathbf{r}) = \frac{1}{4\pi} \int_V d^3\mathbf{r}' \frac{\boldsymbol{\eta}(\mathbf{r}') - (\text{Tr } \boldsymbol{\eta})\mathbf{I}}{|\mathbf{r} - \mathbf{r}'|}. \quad (54)$$

Next, by substituting (53) into the other field equation and the boundary conditions, one obtains a traction boundary-value problem of classical elasticity theory where  $\mathbf{u}$  plays the role of a displacement field, while the body forces and the surface forces are given by

$$f_k = C_{klmn} \tilde{e}_{mn,l}, \quad (55)$$

$$t_k = -C_{klmn} \tilde{e}_{mn} n_l. \quad (56)$$

(ii) *Mura's method*: This method make use of the elegant Green function technique. The working relation (derived in Mura 1968; Teodosiu 1982) for the calculation of the elastic deformation tensor is

$$\beta_{mr}(\mathbf{r}) = \int d^3\mathbf{r}' C_{plqn} \epsilon_{nrt} \alpha_{qt,l'}(\mathbf{r}') G_{mp}(|\mathbf{r} - \mathbf{r}'|). \quad (57)$$

(iii) *Kröner's method*: Kröner (1981) exploited the analogy of the elastic field with the magnetostatic field. The following is the correspondence between quantities and relations in both theories. (See Seeger 1961 for an excellent review where reference to Kröner's earlier work are given.)

Elasticity	Magnetism
vector quantity	scalar quantity
rank two tensor	vector
rank four tensor	rank two tensor
div	div
inc	curl

Elasticity	Magnetism
$\text{div inc} \equiv 0$	$\text{div curl} \equiv 0$
$\text{def}$	$\text{grad}$
$\text{inc def} \equiv 0$	$\text{curl grad} \equiv 0$
Burgers vector $\mathbf{b}$	current $\mathbf{I}$
incompatibility tensor $\eta$	current density $\mathbf{J}$
strain tensor $\mathbf{e}$	magnetic intensity $\mathbf{H}$
stress tensor $\boldsymbol{\sigma}$	magnetic induction $\mathbf{B}$
elastic constant $\mathbf{C}$	permeability $\mu$
$\boldsymbol{\sigma} = \mathbf{C} : \mathbf{e}$	$\mathbf{B} = \mu \mathbf{H}$
$\text{div } \boldsymbol{\sigma} = 0$	$\text{div } \mathbf{B} = 0$
$\text{inc } \mathbf{e} = \eta$	$\text{curl } \mathbf{H} = \frac{4\pi}{c} \mathbf{J}$
tensor potential $\chi$	vector potential $\mathbf{A}$
$\boldsymbol{\sigma} = \text{inc } \chi$	$\mathbf{B} = \text{curl } \mathbf{A}$

Another auxiliary tensor potential  $\chi'$  is introduced ingeniously by Kröner. This is given by

$$\chi'_{ij} = \frac{1}{2\mu} \left( \chi_{ij} - \frac{\nu}{1+2\nu} \chi_{kk} \delta_{ij} \right), \quad (58)$$

the inverse relation being

$$\chi_{ij} = 2\mu \left( \chi'_{ij} + \frac{\nu}{1-\nu} \chi'_{kk} \delta_{ij} \right). \quad (59)$$

$\chi'$  satisfies the equations

$$\nabla^4 \chi' = \eta \text{ and } \text{div } \chi' = 0. \quad (60)$$

Assuming that  $\eta \rightarrow 0$  at the boundary of the infinite medium one calculates  $\chi'$  from the relation

$$\chi'_{ij}(\mathbf{r}) = -\frac{1}{8\pi} \int d^3 \mathbf{r}' |\mathbf{r} - \mathbf{r}'| \eta_{ij}(\mathbf{r}'). \quad (61)$$

In principle this solves the internal stress problem, since  $\boldsymbol{\sigma}$  can now be calculated using  $\boldsymbol{\sigma} = \text{inc } \chi$ .

Kröner has also put the elastic theory of point defects in a broader perspective. According to him, the elastostatics of a continuum with extrinsic point defects (foreign interstitials) is analogous to electrostatics, whereas in intrinsic defects (vacancies, self-interstitials) the elasticity theory is analogous to magnetostatics:

Electrostatics	Elastostatics with extrinsic defects
$\text{div } \mathbf{D} = \rho$	$\text{div } \boldsymbol{\sigma} = -\mathbf{f}$
$\text{curl } \mathbf{E} = 0$	$\text{inc } \mathbf{e} = 0$
$\mathbf{D} = \epsilon \cdot \mathbf{E}$	$\boldsymbol{\sigma} = \mathbf{C} : \mathbf{e}$
$U = \frac{1}{2} \mathbf{D} \cdot \mathbf{E}$	$U = \frac{1}{2} \boldsymbol{\sigma} \cdot \mathbf{e}$

Magnetostatics	Elastostatics with intrinsic defects (internal sources)
----------------	---

$\text{div } \mathbf{B} = 0$ $\text{curl } \mathbf{H} = \mathbf{J}$ $\mathbf{B} = \mu \cdot \mathbf{H}$ $U = \frac{1}{2} \mathbf{B} \cdot \mathbf{H}$	$\text{div } \boldsymbol{\sigma} = 0$ $\text{inc } \mathbf{e} = \boldsymbol{\eta}$ $\boldsymbol{\sigma} = \mathbf{C} : \mathbf{e}$ $U = \frac{1}{2} \boldsymbol{\sigma} : \mathbf{e}$
--	--

The distinction between extrinsic and intrinsic defects is considered to be a most fundamental one, since this has deeper implications in terms of differential geometry. The terms 'diaelasticity' and 'paraelasticity' now acquire meanings by analogy with electro- and magnetostatics. Carbon atoms in iron are permanent elastic dipoles giving rise to paraelasticity; whereas, in diaelasticity, the induced elastic dipoles  $p_{ij}^{\text{ind}}$  arise only in the presence of an applied elastic strain  $e_{kl}$ , according to  $p^{\text{ind}} = \alpha : e$ . The PFI leads to diaelasticity, while MFI leads to both para- and diaelastic effects. A quantitative measure of the para- or diaelasticity associated with a point defect is the corresponding polarizability. The calculation of this quantity is an important problem in the study of point defect relaxation as in the Snoek effect (see, *e.g.*, Leibfried and Breur 1978). There are also ferroelastic solids possessing permanent macroscopic elastic dipole moment along favoured directions (see, *e.g.*, Wadhwani 1982).

## 9. Differential geometry of defects

The description of defects in the foregoing was confined to linearized theories. When finite deformations are included, the language of differential geometry and tensor calculus becomes indispensable. A summary of these theories is given by Kröner (1981) and we follow his presentation. The nature of the differential geometry is decided by the degrees of freedom associated with the atoms or molecules of the crystal. For constituent particles of the same kind, each having only three translational degrees of freedom (a Bravais lattice), affine geometry seems to be appropriate; whereas for a non-Bravais lattice of molecules possessing rotational degrees of freedom in addition to translational ones, Finsler's geometry (Amari 1962) is required.

Consider for simplicity a cubic primitive Bravais lattice and choose the lattice lines as the Cartesian coordinate lines. The Cartesian coordinates of this defect-free, reference crystal are denoted by  $x^k$ . Let the crystal be deformed and let this configuration have coordinates  $z^k$ . The connection between infinitesimal increments in the coordinates in the two configurations is given by

$$dz^k = B_m^k dx^m, \quad B_m^k = \partial z^k / \partial x^m. \quad (62)$$

Now  $dx^m$  being the corresponding change in the undeformed configuration, the relative displacement is given by

$$du^k = (B_m^k - \delta_m^k) dx^m = \beta_m^k dx^m. \quad (63)$$

With the coordinates  $x^k$  we associate an 'external observer' (also called the Eulerian frame of reference). Consider another observer, the 'internal observer' (the Lagrangian frame of reference) whose reference coordinates are 'dragged along' in the process of deformation. As long as the crystal is defect-free and the deformation is compatible, the internal observer feels no deformation. Let the coordinates of this frame of reference be

$y^{k'}$ . Then the square of the distance between two infinitesimally separated points

$$ds^2 = \delta_{k'l'} dy^{k'} dy^{l'} \quad (64)$$

is an invariant for this observer. In contrast, for the external observer, there is a change in  $ds^2$  after a deformation takes place, given by

$$ds^2 - ds_0^2 = (g_{kl} - \delta_{kl}) dx^k dx^l \equiv 2e_{kl} dx^k dx^l. \quad (65)$$

Here  $ds_0^2$  is the value of  $ds^2$  before deformation, and

$$g_{kl} = \delta_{mn} B_k^m B_l^n. \quad (66)$$

The strain tensor can be easily shown to be

$$e_{kl} = \frac{1}{2}(\beta_{kl} + \beta_{lk}) + \frac{1}{2}\beta_k^m \beta_l^n \delta_{mn}. \quad (67)$$

Next, let us establish a connection between dislocations and torsion. Cartan (1928) introduced the concept of 'torsion' in a purely mathematical context. Later, Frank (1951) constructed the Burgers circuit to define a dislocation. That there is a remarkable similarity between Cartan's procedure for introducing torsion in differential geometry and Frank's construction for a dislocation was noted by Kondo (1952, 1955), Bilby *et al* (1955) and Bilby (1960). Frank considers the nonclosed path  $A'B'C'D'E'$  (see figure 4) around a dislocation in a crystal counting the steps (each step consists of one atomic spacing). The closure failure  $A'E'$  is the Burgers vector. Cartan transports a vector  $\mathbf{CD}$  along the path  $\mathbf{CB}$  from  $C$  to  $B$  and then a vector  $\mathbf{CB}$  along the path from  $C$  to  $D$ . The vectors  $\mathbf{CD} = d_1\mathbf{x}(C)$ ,  $\mathbf{BA} = d_1\mathbf{x}(B)$ ,  $\mathbf{CB} = d_2\mathbf{x}(C)$  and  $\mathbf{DE} = d_2\mathbf{x}(D)$  are all of infinitesimal length. The law of parallel transport of  $d_1\mathbf{x}(C)$  along  $d_2\mathbf{x}(C)$  can be written as

$$d_1x^h(B) = d_1x^h(C) - \Gamma_{ml}^h d_1x^l(C) d_2x^m(C), \quad (68)$$

where  $\Gamma_{ml}^h$  is the affine connection. Similar transport of  $d_2\mathbf{x}(C)$  along  $d_1\mathbf{x}(C)$  gives

$$d_2x^h(D) = d_2x^h(C) - \Gamma_{ml}^h d_2x^l(C) d_1x^m(C). \quad (69)$$

The closure failure is thus

$$\begin{aligned} (AE)^h &= d_1x^h(C) + d_2x^h(D) - d_2x^h(C) - d_1x^h(B) \\ &= \Gamma_{ml}^h (d_1x^l d_2x^m - d_2x^l d_1x^m) \\ &= -\Gamma_{ml}^h dS^{ml}, \end{aligned} \quad (70)$$

where  $dS^{ml} = (d_1x^m d_2x^l - d_1x^l d_2x^m)$  is the area element enclosed by the four infinitesimal vectors. The tensor  $dS^{ml}$  is related to the area vector  $dS_n$  by the relation

$$dS^{ml} = \bar{\epsilon}^{nml} dS_n, \quad dS_n = \frac{1}{2} \bar{\epsilon}_{nml} dS^{ml}, \quad (71)$$

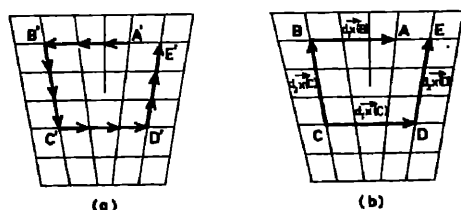


Figure 4. (a) Frank's circuit, (b) Cartan's circuit.

where  $\bar{\epsilon}^{nml} = g\bar{\epsilon}^{nml}$ , with  $g = (\det(g_{lm}))^{1/2}$  (i.e.,  $\bar{\epsilon}^{nml}$  is the contravariant Levi-Civita tensor, etc.). Note that only the antisymmetric part of the connection contributes to the vector  $(AE)^h$  in (70). This is Cartan's torsion tensor,

$$T_{ml}^h = \frac{1}{2}(\Gamma_{ml}^h - \Gamma_{lm}^h). \quad (72)$$

Now, to establish contact with the dislocation density tensor  $\alpha_{ij}$  defined in § 7, note that by definition the Burgers elemental vector is

$$db^k = \alpha^{nk} dS_n \equiv \alpha_{ml}^k dS^{ml}, \quad (73)$$

where

$$\alpha_{ml}^k = \frac{1}{2}\bar{\epsilon}_{nml}\alpha^{nk}, \quad \alpha^{nk} = \bar{\epsilon}^{nml}\alpha_{ml}^k. \quad (74)$$

On comparing  $db^k$  with  $(AE)^k$  we get

$$T_{ml}^k = -\alpha_{ml}^k. \quad (75)$$

This basic identification of the dislocation density tensor with the torsion tensor is the starting point of the differential geometric approach.

The presence of torsion leads to a non-Riemannian geometry. It is known (Schouten 1954) that if the metric is to satisfy the relation  $\nabla_m g_{lk} = 0$  where  $\nabla_m$  is the symbol for covariant derivative, then the most general form of the affine connection possible is related to the torsion as follows: writing  $\Gamma_{ml}^h = g^{hk}\Gamma_{mlk}$ , it turns out that

$$\Gamma_{mlk} = g_{mlk} + h_{mlk}, \quad (76)$$

where

$$g_{mlk} \equiv \frac{1}{2}(\partial_m g_{kl} + \partial_l g_{mk} - \partial_k g_{lm}) \quad (77)$$

and

$$h_{mlk} \equiv T_{mlk} + T_{kml} - T_{lkm}. \quad (78)$$

Here  $g_{mlk}$  is the Christoffel symbol of the second kind, and  $h_{mlk}$  is the *contortion tensor*. The earlier definitions of the distortion tensor  $\beta_{ik}$ , the strain tensor  $e_{ik}$  and the rotation tensor  $\omega_{ik}$  are generalised to read

$$\left. \begin{aligned} d\beta_{ik} &= \Gamma_{mlk} dx^m, \\ de_{ik} &= \Gamma_{m(lk)} dx^m, \\ d\omega_{ik} &= \Gamma_{m[lk]} dx^m, \end{aligned} \right\} \quad (79)$$

where  $(lk)$  and  $[lk]$  respectively stand for symmetric and antisymmetric combinations of these indices. Equation (9) of the linearized theory, which can also be written as

$$\vec{\nabla} \times e \times \vec{\nabla} - \text{sym}\{\alpha \times \vec{\nabla}\} = 0 \quad (80)$$

is generalised in the nonlinear theory to the vanishing of the curvature tensor, i.e.,

$$R_{nmik} = 0, \quad (81)$$

where  $R_{nmik} = g_{kh} R_{nml}^h$  and

$$R_{nml}^h = 2(\partial_n \Gamma_{ml}^h - \Gamma_{mp}^h \Gamma_{nl}^p)[nm]. \quad (82)$$

Equation (81) is the *second basic law* of the differential geometric theory of lattice defects. Physically, this means that if a crystal has dislocations as the only defects in it during deformation, and if it does not develop cracks, then the dislocation distribution must be accompanied by elastic strains such that the curvature tensor vanishes.



The second basic identification states that elementary *extrinsic* defects (extra matter on interstitial sites, fission fragments,  $\alpha$ -particles stuck in the medium, etc) cause a *rotation-like* curvature ( $R_{nm[lk]} \neq 0$ ,  $R_{nm(lk)} = 0$ ). According to the third basic identification, *intrinsic* point defects like self-interstitials and vacancies lead to a *non-metric* curvature ( $R_{nm[lk]} = 0$ ,  $R_{nm(lk)} \neq 0$ ). The non-metric situation is not as well understood in differential geometry as the metric connection. When extrinsic defects are present in addition to dislocations, a beautiful analogy emerges between the field equations of defects and Einstein's equations in the general theory of relativity. To see this, we note that the curvature tensor  $R_{nmik}$  is antisymmetric in  $l$  and  $k$  for the metric geometry, and, by definition, it is also antisymmetric in  $n$  and  $m$ . Thus, without any loss of information, it can be replaced by a second rank tensor  $E^{ij}$  (called the Einstein tensor) given by

$$E^{ij} = \frac{1}{2} \bar{g}^{inm} \bar{g}^{jlk} R_{nmik}. \quad (83)$$

It can be shown that, in the linear approximation, (83) reduces to

$$E = -\text{inc } e + \text{curl } \kappa. \quad (84)$$

Note that when  $R_{nmik} = 0$ ,  $E^{ij} = 0$ . When extra matter is present, the Einstein tensor does not vanish and becomes equal to the matter tensor  $M^{ij}$  or  $E = M$ . This is analogous to the Einstein's field equation. Thus the defects in a crystal are analogous to matter in the universe. "Without matter, the universe is not interesting; without defects, a crystal is dead—" (Kröner 1981).

The approach to defect theories *via* differential geometry is undoubtedly an elegant one. There is a related approach by Wang (1967) and Noll (1967) which starts with the philosophy that the constitutive law of the continuum being fundamental, it must determine the geometry. There are attempts at constructing a Yang-Mills type of minimal coupling theory for materials with dislocations and disclinations (Kadić and Edelen 1982; Edelen 1980). The work of Julia and Toulouse (1979) and that of Dzyaloshinskii and Volovik (1978) are efforts in the same direction. There are further treatments of the differential geometry of defects by Gairola (1979), Zorawski (1967) and Marcinkowski (1979). Marcinkowski in several publications has applied differential geometric techniques extensively to dislocations on surfaces, grain boundaries, cracks, etc.

In spite of its mathematical elegance, the differential-geometric approach to defect problems has not helped much in the development of the phenomenological theory of plasticity. The reason is that, in contrast to the case of electric or magnetic lines of force in electromagnetic theory, dislocation lines almost always form very irregular interconnected networks. This is the main reason why the continuum theory of dislocations and the differential-geometric approach as such can never constitute a good macroscopic theory of plasticity. Dislocations piercing through an area element in the crystal usually appear with positive as well as negative signs so that their resultant Burgers vector is often zero or has a very small value. This results in a very small magnitude for the dislocation density  $\alpha$ . To understand this, consider for example the configuration of dislocations shown in figure 5. All the dislocation lines are in the  $z$  direction; positive (L) and negative (T) dislocations have Burgers vectors  $+b$  and  $-b$ , respectively. Let the domain be divided by a mesh as shown in the figure and let  $a^2$  be the area of each small square. If we consider as the area  $\Delta S_3$  the rectangle AA'B'B,  $\alpha_{31} = -b/a^2$ ; if  $\Delta S_3$  is the rectangle BB'C'C,  $\alpha_{31} = +b/a^2$ ; whereas if area  $\Delta S_3 = AA'C'C$ ,  $\alpha_{31} = 0$ . Note that if we let  $\Delta S_3 \rightarrow 0$  around the point  $P_1$ , then  $\alpha_{31}(P) = \pm b_1 \delta(P - P_1)$ , where the  $+$  sign is applicable if there is a positive dislocation at  $P_1$ , and

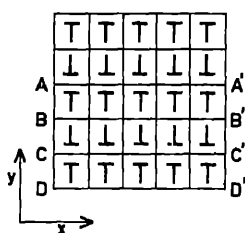


Figure 5. Positive and negative edge dislocations arrays piercing through a rectangular region.

the  $-$  sign if there is a negative dislocation. This means that the microscopic theory of dislocations is built into the formalism, but that in the process of coarse-graining over the distribution of dislocations, too much information seems to be lost.

Kröner (1970) has suggested the following way to rectify this deficiency. According to him, the random distribution of dislocations calls for the use of statistical mechanics. Information about the actual dislocation distribution may be given by  $n$ -point correlation tensor functions  $\langle \alpha(\mathbf{r}_1) \alpha(\mathbf{r}_2) \dots \alpha(\mathbf{r}_n) \rangle$  which give the probability of finding dislocation elements at  $\mathbf{r}_1, \mathbf{r}_2 \dots \mathbf{r}_n$ . Thus one considers, instead of a single real specimen, a whole ensemble of crystals all filled with dislocation line elements in such a way that the ensemble represents all possible realizations of a given macroscopic dislocation state. One may impose extra conditions by prescribing the total energy, the total dislocation length, etc. These would correspond to various types of ensembles (analogous to the well-known microcanonical, canonical and grand canonical ensembles). Kröner (1970) shows that the information contained in the two-point correlation  $\langle \alpha_{ij}(\mathbf{r}) \alpha_{kl}(\mathbf{r}') \rangle$  is quite extensive. For example, it gives information about the total dislocation length in a given volume element, the density of dislocation dipoles, etc. It is (obviously) suitable for describing planar dislocation networks, and, to some extent, dislocation pileups as well. Kröner and Teodosiu (1974) have made the important observation that the internal mechanical state, instead of being represented by the dislocation density tensor and its higher-order correlations, can also be specified by means of the fluctuations of the stress and elastic strain produced by the dislocations. This is of interest because it is the fluctuating stresses and strains that determine the deformation behaviour of materials. This line of approach is very attractive, but much work needs to be done. For example, if the dislocation elements are the basic entities of the system which we want to describe by statistical mechanics, what is the counterpart of Liouville's theorem that would guarantee that the known equations of motion of the dislocation line elements are satisfied? It is worth mentioning here that in another attempt to rectify the shortcomings of the dislocation density tensor, Kroupa (1962) has introduced the dislocation loop density as an additional variable. This approach too has not yet had any practical application.

## 10. Continuum mechanics of moving dislocations

Kosevich (1979) has generalised the basic equations of continuum mechanics taking into account the motion of dislocations during deformation. He has given a very simplified treatment under the (rather drastic) assumption that the energy conservation equation remains unchanged. (This is equivalent to assuming that no heat is generated in the process of dislocation motion). Thus, only the equations of continuity expressing the (local) conservation of mass and (linear) momentum are considered. One begins

with the fundamental equation which introduces dislocations into elasticity theory, namely, (46). If dislocations remain static during the deformation, then the velocity field  $V_k(\mathbf{r})$  is related to the elastic distortion field  $\beta_{ik}(\mathbf{r})$  by  $\partial_i V_k = \partial_i \beta_{ik}$ . However, when dislocations move, this equation must be generalized to

$$\partial_i V_k = \partial_i \beta_{ik} - j_{ik}. \quad (85)$$

Here  $j_{ik}(\mathbf{r})$  is the dislocation flux tensor which must be so chosen that (85) is consistent with (46). Taking the curl of (85) and using (46), one obtains the (local) law of conservation for the Burgers vector

$$\partial_i \alpha_{ik} + \varepsilon_{ilm} \partial_l j_{mk} = 0. \quad (86)$$

If  $C$  is a closed curve bounding a surface  $S$ , then (86) can be expressed in the alternate form

$$db_k/dt = - \oint_C j_{ik} dx_i. \quad (87)$$

The total distortion  $\beta_{ik}^T$  is the sum of the elastic distortion  $\beta_{ik}$  and the plastic distortion  $\beta_{ik}^p$ . Since  $\partial_i V_k = \partial_i \beta_{ik}^T$  by definition, we have evidently  $\partial_i \beta_{ik} = -j_{ik}$ . Hence

$$\partial_i e_{ik}^p = -j_{(ik)}, \quad (88)$$

which is the Orowan equation. For a continuous distribution of dislocations,

$$j_{ik} = \varepsilon_{ilm} \sum_a b_k V_m(\mathbf{r}, \hat{v}^{(a)}) v_l^{(a)}. \quad (89)$$

(compare with (46) which defines  $\alpha_{ik}$ ). The trace  $j_{kk}$  of the flux tensor  $j_{ik}$  is of special interest in connection with the continuity equation for mass. Noting that the relative change in density  $\delta\rho$  is given by  $e_{kk} = -\delta\rho/\rho$  (where  $\rho$  is the density of the medium) and using (85), one obtains

$$\partial_i \rho + \text{div}(\rho \mathbf{V}) = -\rho j_{kk}. \quad (90)$$

The 'complete system' of dynamical equations can then be presented in the form

$$\left. \begin{aligned} \partial_i \sigma_{ik} &= \rho \partial_i V_k \quad (\text{Newton's Law}), \\ \sigma_{ik} &= C_{iklm} \beta_{lm} \quad (\text{elastic constitutive Law}), \\ \varepsilon_{ilm} \partial_l \beta_{mk} &= -\alpha_{ik}, \\ \partial_i V_k &= \partial_i \beta_{ik} - j_{ik}, \end{aligned} \right\} \quad (91)$$

where the tensors  $\alpha_{ik}$  and  $j_{ik}$  must be specified. Note that  $\alpha_{ik}$  and  $j_{ik}$  must satisfy (47) and (86).

We mention here that a lattice defect approach to plasticity and viscoplasticity has been proposed by Kröner and Teodosiu (1974), in which particular emphasis is laid on dislocations. These authors propose a complete set of equations which consist of the continuity equations including the law of conservation of energy, and the thermoelastic constitutive equations for the stress and the heat flux. However, the theory is rather formal and has not yet been tested on any practical problem.

## 11. The quantum field theory approach

Field theorists have recently been interested in defects in crystals. Defects (termed 'extended objects' to stress the generality of the formalism) are viewed as classical

macroscopic objects in a quantum ordered state (a perfect crystal). They are a macroscopic manifestation of the local condensation of bosons associated with a quantum mechanical collective mode (the phonons). There is an efficient tool called the boson transformation technique which describes the condensation process mathematically. In high energy physics, the topological structure of extended objects has been of great interest, being connected with the problems of quark confinement and particle structure. The boson transformation approach to defects was motivated by the success of the theory of solitons. A soliton is a localized wave solution of a classical nonlinear equation which behaves like a particle. The search for soliton solutions in three space dimensions is a challenging problem in itself. Their localized nature suggests that dislocations, point defects, grain boundaries, etc. are somehow related to soliton-like objects in three-dimensions. As it would require a rather lengthy presentation of the field-theoretic background and the boson transformation formalism, we do not describe this approach here. It is best described in the review article of this theory by Wadati (1979). (See also: Umezawa *et al* 1982.) We mention also that Holz (1979, 1980) has given a microscopic Hamiltonian theory of dislocations in crystals.

## 12. Conclusion

The present review was intended to bring out the fact that there is as yet no single unified theory of all defects in crystals. The merits and drawbacks of the various theories available have been pointed out. To the reviewer the following areas seem to need urgent attention. The idea of Kröner (1970) that the loss of information in the coarse-graining process needed to define the dislocation-density tensor can be remedied with the help of higher-order correlation functions, needs to be pursued further. The alternate idea of Kröner and Teodosiu (1974) that it must be possible to describe the deformation behaviour of materials in terms of the fluctuations of the stress and strain (produced by dislocations) clearly suggests a stochastic approach to plastic flow. The difficulty here is the fact that even the deterministic equations needed to completely describe plastic flow are yet to be developed. In fact this was the spirit of the work of Kröner and Teodosiu (1974). Perhaps some extremely simple situations (like steady state creep) must be modelled first in terms of a stochastic description, and the relevant correlation tensors explicitly computed. Both Kosevich (1979) and Kröner and Teodosiu (1974) have proposed hydrodynamic equations for matter undergoing deformation. One testing ground for such hydrodynamic equations could be the work-hardening behaviour of materials. Cottrell (1953) has given a beautiful analogy between stage I of work-hardening and the laminar flow of a fluid, and between stage II and turbulent flow. However, one does not yet know what the 'Reynold number' is which would characterize the transition to 'turbulence' in the case of plastic flow. In the spirit of this analogy, it may be possible to introduce different types of dislocation density tensors to describe the transition from stage I to stage II of the work-hardening curve. It seems that much work remains to be done in developing a hydrodynamic theory of a continuous medium containing dislocations.

## References

- Amari S 1962 in *RAAG memoirs of the unifying study of the basic problems in engineering and physical sciences by means of geometry* (ed) K Kondo (Tokyo: Gakujutsu Bunken Fukyu-kai), Vol 3, p 193

- Bilby B A 1960 in *Progress in solid mechanics* (eds) I N Sneddon and R Hill (Amsterdam: North-Holland), Vol 1, p 329
- Bilby B A, Bullough R and Smith E 1955 *Proc. R. Soc. (London)* **A231** 263
- Burgers J M 1939 *Proc. Acad. Sci. Amsterdam* **42** 378
- Cartan E 1928 *Leçons sur la Géométrie des espaces de Riemann* (Paris: Gauthier-Villars)
- Cottrell A H 1953 *Dislocations and plastic flow in crystals* (Oxford: Clarendon Press)
- de Wit R 1960 in *Solid state physics* (eds) F Seitz and D Turnbull (New York: Academic) Vol 10, p 249
- Dzyaloshinskii I and Volovik G 1978 *J. Phys.* **39** 693
- Edelen D G B 1980 *Int. J. Eng. Sci.* **18** 1095
- Eringen A C 1972 *Int. J. Eng. Sci.* **10** 425
- Eringen A C 1973 *Lett. Appl. Eng. Sci.* **1** 11
- Eringen A C 1976 *Continuum Physics*, Vol IV, (New York: Academic)
- Eringen A C 1977a *J. Phys.* **D10** 671
- Eringen A C 1977b *Int. J. Eng. Sci.* **15** 177
- Eringen A C and Balta F 1979 *Crystal Lattice Defects* **8** 73
- Eringen A C and Edelen D G 1972 *Int. J. Eng. Sci.* **10** 233
- Eringen A C, Speziale C G and Kim B S 1977 *J. Mech. Phys. Solids* **25** 339
- Eshelby J D 1956 in *Solid state physics* (eds) F Seitz and D Turnbull (New York: Academic) Vol 3, p. 79
- Eshelby J D 1957 *Proc. R. Soc. (London)* **A241** 376
- Eshelby J D 1961 in *Progress in solid mechanics* (eds) I N Sneddon and R Hill (Amsterdam: North-Holland) Vol 2, p 89
- Evans J H, Bullough R and Stoneham A M 1972 in *Radiation induced voids in metals* (eds) J W Corbett and L C Ianiello USAEC-CONF-71061
- Flinn P A and Maraduddin A A 1962 *Ann. Phys.* **18** 81
- Frank F C 1951 *Philos. Mag.* **42** 809
- Gairola B K D 1979 in *Dislocations in solids* (ed) F R N Nabarro (Amsterdam: North-Holland) Vol 1, p 223
- Heald P T and Speight M V 1974 *Philos. Mag.* **29** 1075
- Holz A 1979 *Phys. Rev.* **A20** 2521
- Holz A 1980 *Phys. Rev.* **B22** 3678
- Julia B and Toulouse G 1979 *J. Phys.* **40** L-395
- Kadić A and Edelen D G B 1982 *Int. J. Eng. Sci.* **20** 49, 433, 747, (see also Kadić A and Edelen D G B 1983 *A gauge theory of dislocations and disclinations* (Berlin: Springer-Verlag))
- Kondo K 1952 On the geometrical and physical foundations of theory of yielding in *Proc. 2nd Japan Nat. Congr. Applied Mechanics*, Tokyo
- Kondo K 1955 Non-Riemannian geometry of imperfect crystals from a macroscopic viewpoint, in *RAGG memoirs of the unified study of basic problems in engineering and physical sciences by means of geometry* (ed) K Kondo (Tokyo: Gakujutsu Bunken Fukyu-kai)
- Kosevich A M 1979 in *Dislocations in solids* (ed) F R N Nabarro (Amsterdam: North-Holland) Vol 1, p 33
- Kovács I 1978 *Physica* **B94** 177
- Kovács I and Vörös G 1979 *Physica* **B96** 111
- Kröner E 1953 *Z. Phys.* **136** 402
- Kröner E 1964 *Phys. Kondens. Materie* **2** 262
- Kröner E 1970 in *Inelastic behaviour of solids* (eds) M F Kanninen, W F Adler, A R Rosenfeld and R I Jaffee (New York: McGraw-Hill) p 135
- Kröner E 1981 in *Les Houches Session XXXV, 1980 - Physics of defects* (eds) R Balian *et al* (Amsterdam: North-Holland)
- Kröner and Teodosiu C 1974 in *Problems of plasticity*, Int. Symp. on Foundations of Plasticity, Warsaw 1972, (ed) A Sawczuk (Leyden: Noordhoff Intl Publishing) p 45
- Kroupa F 1962 *Czech. J. Phys.* **B12** 191
- Leibfried G and Breur N 1978 *Point defects in metals* (Berlin: Springer-Verlag) Vol I
- Malen K and Bullough R 1971 in *BNES European Conf*, Reading, England, March 1971
- Marcinkowski M J 1979 *Unified theory of the mechanical behaviour of matter* (New York: Wiley)
- Mura T 1968 *Adv. Mater. Res.* **3** 1
- Nabarro F R N 1967 *Theory of crystal dislocations* (Oxford: Clarendon)
- Noll W 1967 *Arch. Rational Mech. Anal.* **27** 1
- Nye J F 1953 *Acta Metall.* **1** 153
- Peach M and Koehler J S 1950 *Phys. Rev.* **80** 436

- Schouten J A 1954 *Ricci-Calculus* (Berlin: Springer-Verlag)
- Seeger A 1961 *Phys. Status Solidi* **1** 669
- Siems R 1968 *Phys. Status Solidi* **30** 645
- Steeds J W and Willis J R 1979 in *Dislocations in solids* (ed) F R N Nabarro (Amsterdam: North-Holland) Vol 1 p 33
- Teodosiu C 1982 *Elastic models of crystal defects* (Berlin: Springer-Verlag)
- Umezawa H Matsumoto H and Tachiki M 1982 *Thermo field dynamics and condensed systems* (Amsterdam: North-Holland)
- Wadati M 1979 *Phys. Rep.* **50** 87
- Wadhawan V K 1982 *Phase Transitions* **3** 3
- Wang C C 1967 *Arch. Rational Mech. Anal.* **27** 33
- Zorawski M 1967 *Théorie mathématique des dislocations* (Paris: Dunod)

### Discussion

T V Ramakrishnan: What is the continuum local theory value for the self-energy of a point defect?

D Sahoo: For a mathematical point defect, it is infinity, but for a rigid 'point' defect occupying a volume  $\Delta V$ , it is  $\frac{2}{3}\mu\Delta V$ , where  $\mu$  is the shear modulus of the medium.

N Kumar: What is  $P$  in the nonlocal theory? Can you go to the local limit through some approximation?

Sahoo:  $P$  is the elastic dipole tensor, as in the local theory. It is the interaction between a dipole and a strain field which is nonlocal. Yes, one can go to the local limit by the replacement  $\alpha(R) \rightarrow \delta(R)$ .

H R Krishna Murthy: Is the nonlocal theory supposed to simulate the lattice?

Sahoo: Yes, it is intermediate between the local continuum theory and the discrete atomistic theory. The lattice appears through the parameter  $a$  occurring in the kernel  $\alpha(R)$ . This  $a$  is essentially the lattice constant.

Ramakrishnan: In that case, where is the dispersion?

Sahoo: Eringen (1972, 1973) has explicitly calculated the dispersion for a one-dimensional lattice. He has also calculated the dispersion curve for Rayleigh surface waves.

A S Parasnis: What exactly is it in the nonlocal theory that removes the infinities in the stress and strain at the core of a (screw) dislocation—a divergence which seems to be almost a necessity in a continuum theory?

Sahoo: It is essentially the replacement of all the  $\delta$  functions by the finite kernel  $\alpha(R)$ . Being a smooth function like a Gaussian, this removes the infinities in the calculation of the integrals involved.

Parasnis: I have two comments: (i) I wonder if mere analogies, such as are implied in the attempt to have a 'unified' theory of defects, are likely to give physically significant theories and results. For example, two decades ago some mathematically-minded people drew an analogy between the closure failure *à la* the Burgers/Frank circuit and Ampere's law and built up a fair edifice. But this could *not* explain the simple fact that like-currents attract whereas like-dislocations repel. What is needed is a *physical* theory

going beyond such analogies. (ii) The difference between a Burgers circuit and a Frank circuit is that since the latter closes in the dislocated crystal/medium, it refers to the Burgers vector in the undislocated reference crystal/medium. You called the circuit a 'Frank circuit' but opened it in the dislocated crystal!

G Srinivasan: I wonder whether in the multiple glide region, the analogy may be with a cross-linked polymer rather than with turbulence. The problem in the polymer case has been made tractable by de Gennes, Edwards and others. The analogy may be worth pursuing.

C K Majumdar: Dr Srinivasan is apparently referring to the calculation of the elastic property of rubber by Prof. S F Edwards. There is a linear part, a plateau and a nonlinear rising part—somewhat similar to the regions I and II you refer to. It is quite possible that this analogy is better than that with laminar and turbulent flow. Now, the rubber and the polymer problems are dominated by entropy. Entropy is always difficult to handle in a mechanistic or hydrodynamic model. This difficulty appears also in the treatment of shocks or grain boundaries discussed earlier. The entropy equation, if written down from the second law, is somewhat different in nature from the hydrodynamic equations or the electrodynamic or the elastic equations (compare for example, the entropy generation equation of Sommerfeld). Edward's calculation of rubber elasticity is statistical mechanical in character, because entropy is involved. (Hydrodynamic equations or electrodynamic equations in continuous media are also statistical in character, but entropy is not so easily expressed in mechanical terms—entropy has an integral character in phase space and is not easily expressed in a differential equation.) If the entropy equation could be written down, or rather, if the entropy could be woven into the framework, the analogy could be exploited—the insight of de Gennes and Edwards in random network problems may perhaps be useful here.

## Fracture of particulate composites

S RAY

Department of Metallurgical Engineering, University of Roorkee, Roorkee 247 672, India

**Abstract.** A thermodynamic analysis of the process of fracture in elastically deformable composites is formulated. The critical dimensions leading either to particle fracture or to matrix-particle decohesion are identified. Fracture in plastically deformable composites is discussed in the light of the experimental evidence regarding void or cavity nucleation. Models of void growth under the application of stress and the role of void growth in causing failure are described in brief.

**Keywords.** Fracture; composite; void nucleation; void growth; cavity.

### 1. Introduction

Particulate composites are materials containing one or more discontinuous phases dispersed in a matrix of a distinctly different phase, such that the length to diameter ratio of each dispersoid is of the order of unity. If the extent of the discontinuous phase (or phases) is small and the load shared by it is insignificant, the material is not effectively regarded as a composite because the mechanical property of the material does not reflect the characteristics of the discontinuous phase. However, many materials that are not originally designed as particulate composites may pick up discontinuous phases during processing in the form of particles of insoluble impurities or inclusions which subsequently exert an important influence on the fracture behaviour of these materials. Particulate composites can be divided into four basic classes depending on the mechanical properties of the continuous phase (the matrix) and the discontinuous phase (the particle). (a) brittle matrix-brittle particle, (b) brittle matrix-ductile particle, (c) ductile matrix-brittle particle, and (d) ductile matrix-ductile particle. The fracture behaviour of the first two classes will be analysed under the broad heading of elastically deformable composites in § 2, and fracture in the other two classes will be examined in § 3.

The first systematic approach to the process of fracture was developed by Griffith (1920) to explain the discrepancy between the ideal strength and the observed strength in a brittle material. The thermodynamics of the process of extension of an atomically sharp pre-existing crack of length  $2c$  under an applied stress of  $\sigma$  was examined. When a crack extends, elastic energy is released due to relaxation of stress around the extended part of the crack; some energy is also expended by the system in creating a fresh crack surface. The extension of the crack becomes feasible only when the former energy exceeds the latter, thereby reducing the total free energy. The fracture stress,  $\sigma_0$ , calculated on the above basis is as given below.

$$\sigma_0 = (2\alpha E/\pi c)^{1/2}, \quad (1)$$

where  $\alpha$  is the specific energy of the crack surface and  $E$  is the Young's modulus.



Orowan (1949) provided a similar analysis for the extension of a crack under the plane stress condition. Sack (1946) and Sneddon (1946) modified the estimate of  $\sigma_0$  in (1) by including the stress concentration effect around the crack. However, the original approach is based on the very general principles of thermodynamics and so provides a *necessary* criterion for the propagation of a crack leading to fracture. Here, we use this simple approach to examine the different possible fracture processes in the problem at hand, to gain an insight into the underlying essentials. Detailed stress calculations will not be of help in this regard because crack propagation is controlled by the local stress and strain which are inhomogeneous and dependent on the exact particle shape and distribution. These material parameters vary considerably from sample to sample, even for the same engineering material.

2. Elastically deformable composites

Any composite with a brittle matrix can be deformed only elastically irrespective of the nature of the reinforcing particle. To determine the fracture behaviour it is necessary to analyse the local stress distribution around the particles. When a particulate composite is deformed, the force is not directly applied to the particles but is transferred through the matrix. We consider the simple model of a particle embedded in a brittle matrix as given in figure 1. To simplify the mathematical treatment the following assumptions are made: (i) Poisson's effect is negligible; (ii) both the particle and the matrix have the same shear modulus. The elastic matrix is subjected to a tensile stress of  $\sigma_m$ . The forces acting on an element extending an angle  $d\theta$  at the centre are shown in figure 1(b). If  $\tau_\theta$  is the shear stress acting at the particle-matrix interface, the elemental force balance in the direction of the applied stress gives

$$d\sigma/d\theta = 2\tau_\theta.$$
 (2)

A special case (*i.e.*, equal elastic moduli for particle and matrix) of the general result derived by Sezawa and Miyazaki (1928) then yields, for the magnitude of the stress distribution  $\tau_\theta$  at the particle-matrix interface, the expression

$$\tau_\theta = (1/2)\sigma_m \sin 2\theta.$$
 (3)

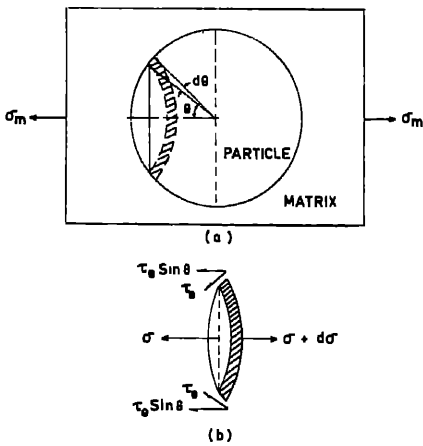


Figure 1. (a) Schematic representation of a single particle composite model. (b) Elemental force balance at a section of the particle.

Inserting this in (2) and integrating, the magnitude of the stress in the particle at a plane labelled by the angle  $\theta$  is

$$\sigma_p = \sigma_m \sin^2 \theta. \quad (4)$$

Let  $\bar{\sigma}_m$ ,  $\bar{\sigma}_p$  and  $\bar{\tau}$  be the fracture strengths of the matrix, particle and interface. Then the matrix, or the particle, or the interface fractures first, if  $\bar{\sigma}_m$ , or  $\bar{\sigma}_p$ , or  $2\bar{\tau}$  is the smallest of the three quantities  $\bar{\sigma}_m$ ,  $\bar{\sigma}_p$ ,  $2\bar{\tau}$ . In the first case, the original analysis of Griffith and its subsequent modifications are applicable, after the inhomogeneous stress distribution is determined. In the second and third cases, a similar analysis brings out certain additional parameters of interest.

### 2.1 Particle fracture

When the particle has fractured at a plane whose angle of extension is  $2\theta$  at the centre, this crack will be able to propagate in the matrix provided it is thermodynamically feasible. If the particle has a radius  $r$ , the change in energy  $\Delta E$  for an infinitesimal extension  $dr$  of the crack is given by

$$\Delta E = -4\pi r^2 dr \sigma_m^2 (1 - \nu_m)^2 \sin^2 \theta / E_m + 2\pi r dr \gamma_m \sin \theta, \quad (5)$$

where  $\nu_m$  and  $E_m$  are Poisson's ratio and the elastic constant respectively of the matrix and  $\gamma_m$  is the surface energy of the matrix. For the crack to propagate spontaneously,  $\Delta E$  should be negative, which implies that

$$r > r_c = E_m \gamma_m / [2(1 - \nu_m)^2 \sigma_m^2 \sin^2 \theta]. \quad (6)$$

Since the particle has fractured when  $\sigma_p = \bar{\sigma}_p = \sigma_m \sin^2 \theta$  the composite will at once satisfy the necessary condition for failure if

$$r > E_m \gamma_m \sin^3 \theta / [2(1 - \nu_m)^2 \bar{\sigma}_p^2]. \quad (7)$$

Otherwise, the load can be increased till it attains the value

$$\sigma_m = [E_m \gamma_m / 2r(1 - \nu_m)^2 \sin^2 \theta]^{1/2}. \quad (8)$$

The matrix will fail at a load different from that causing the fracture of the particles. As a range of particle size is involved in real-life composites, the estimate of  $\sigma_m$  given by (8) must be calculated using the largest value of the particle radius  $r$  that is involved.

### 2.2 Interface fracture

When the interface is weak, let a crack be initiated there at an angle  $\theta$ . The crack will extend along the interface from an angle  $\theta$  to  $\theta + d\theta$  if the corresponding change in energy is negative. This change is given by

$$\Delta E = -\pi r^3 \sigma_m (1 - \nu_p)^2 \sin^4 \theta d\theta / E_p + 2\pi r^2 (\gamma_p + \gamma_m - \gamma_{pm}) \sin \theta d\theta, \quad (9)$$

where  $\nu_p$  and  $E_p$  are Poisson's ratio and the elastic constant, respectively, of the particle;  $\gamma_p$  is the surface energy of the particle and  $\gamma_{pm}$  is the particle-matrix interfacial energy. The debonding between the matrix and the particle will take place as long as  $\Delta E < 0$ , and will extend up to

$$\theta_c = \sin^{-1} \left[ \frac{2(\gamma_p + \gamma_m - \gamma_{pm})E_p}{r(1 - \nu_p)^2 \sigma_m} \right]^{1/2}. \quad (10)$$

Clearly, this crack can propagate into the matrix if the size of the particle is such that

$$r \geq E_m \gamma_m / [2(1 - \nu_m)^2 \sigma_m^2 \sin \theta_c]. \quad (11)$$

If  $r$  is smaller than the quantity on the right, the load must be increased to the level given by (8) in order to fracture the matrix.

The surface energy of the particle, that of the matrix, and the particle-matrix interfacial energy play a vital role in determining the mode of fracture. The experimental determination of these energies is difficult and sometimes unreliable because of the segregation of impurities. The predictions of the above analysis may also become unreliable due to kinetic factors.

### 3. Plastically deformable composites

The phenomenon of fracture in a composite with a ductile matrix is commonly encountered in metals and alloys with inclusions. As composites contain a combination of phases, it is instructive to explore first the mechanism of fracture in a ductile single-phase material.

It is observed that cavities form in front of propagating cracks. It has therefore been assumed that vacancies in the highly strained region condense into voids. Under appropriate conditions of stress, these voids give rise to propagating cracks leading to the failure of the material. However, Balluffi and Siegel (1955) contend that the excess concentration of vacancies produced due to strain is not sufficient to lead to the homogeneous nucleation of voids, and that nuclei for void formation must pre-exist in the specimen. It is well known that cavities may also nucleate through a host of other mechanisms. For example, grain boundary sliding at low strain rates and intermediate temperatures gives rise to voids; and under such circumstances any factors preventing grain boundary sliding would also suppress the nucleation of cavities. Smith and Barnby (1967) have observed the nucleation of cavities at dislocation pile-ups, while Davies and Williams (1969) have observed this process taking place at twin-grain boundary intersections. All these mechanisms are operative at sites with large stress concentrations.

Such stress concentrations exist in the neighbourhood of the particles in a composite, and cavities form there either by cavity nucleation as in pure materials, or by mechanical decohesion of the matrix-particle interface as explained in § 2. Thermodynamic analysis (Greenwood and Harris 1965) shows that if  $\gamma_{pm} < 10^{-3} \gamma_m$ , mechanical decohesion is the most likely mode for cavity formation. Brown and Stobbs (1971) have estimated the critical strain for mechanical decohesion. A comparison of this estimate with the experimental value observed in a composite of silica particles dispersed in copper (Palmer and Smith 1968) indicates that the theoretical value is highly overestimated. This poses a problem, because a thermodynamic analysis provides *necessary* conditions and therefore *minimal* estimates in general. The discrepancy here may be attributed to the relaxation of stress observed around the smaller particles by the formation of prismatic loops. However, no such stress relaxation occurs around large particles and voids are readily formed there. Given a detailed understanding of the mechanisms of void creation, no quantitative theory of the fracture process under consideration is available, because the process is ultimately controlled by local stresses and strains, which in turn are governed by the shape and distribution of the particles in

the matrix. Moreover, once voids are formed, the stress induces further growth and both the volume and the shape of the voids change, with the actual strain history exerting a significant influence.

McClintock (1968) proposed the first model for the growth of a cylindrical hole in a hardening plastic matrix. Subsequently, Rice and Tracey (1969) investigated another model for the growth of a spherical hole in a non-hardening plastic matrix and proposed a nonlinear relation between the radial velocity of the void surface and the applied strain field. Jalinier (1981) applied the linear version of the model to the damage observed in sheet metal. For a void caused by the decohesion of the particle-matrix interface as well as for a void generated by the cracking of the particle,  $\varepsilon_i = B_i \varepsilon_i^\infty$ , where  $\varepsilon_i$  is the relative extension of the void in the  $i$ -direction and  $\varepsilon_i^\infty$  is the applied strain field far from the void. For decohesion,  $B_i$  is a function of the ratio  $\varepsilon_2/\varepsilon_1$  of the principal strains, which for fragmentation is a constant  $\approx 4$ . These theoretical results agree well with experimental observations.

The growth of the voids leads to failure by two possible mechanisms. The material between growing voids starts getting thinner till a necking instability sets in, resulting in the coalescence of the voids and eventual fracture. It is also possible that at some stage in the growth of the voids, conditions become ripe for cracks to originate from the voids, as explained in § 2.

#### 4. Conclusions

Fracture in particulate composites is an important area in need of viable theories. The difficulties arise from the complexity of the stress distribution in an inhomogeneous material and the dependence of the fracture process on highly local stress and strain conditions. Estimates based on energy considerations have led to some understanding of the phenomena involved, but much remains to be done.

#### References

- Balluffi R W and Siegel L L 1955 *Acta Metall.* **3** 170
- Brown L M and Stobbs W M 1971 *Philos. Mag.* **23** 1201
- Davies P W and Williams K R 1969 *J. Metal Sci.* **3** 48
- Greenwood G W and Harris J E 1965 *Acta Metall.* **13** 936
- Griffith A A 1920 *Philos. Trans. R. Soc.* **A221** 163
- Jalinier J M 1981 Thesis, Univ. of Metz, France (unpublished)
- McClintock F A 1968 *J. Appl. Mech.* **35** 363
- Orowan E 1949 *Rep. Prog. Phys.* **12** 185
- Palmer I G and Smith G C 1968 *Oxide dispersion strengthening* (New York: Gordon and Breach) p 253
- Rice J R and Tracey D M 1969 *J. Med. Phys. Solids* **17** 201
- Sack R A 1946 *Proc. Phys. Soc.* **58** 729
- Sezawa K and Miyazaki B 1928 *Proc. Jpn Soc. Mech. Eng.* **31** 625
- Smith E and Barnby J T 1967 *J. Metal Sci.* **1** 1
- Sneddon I N 1946 *Proc. R. Soc.* **A187** 229

#### Discussion

P Rodriguez: Why has the dislocation pile-up at the interface not been taken into account?

S Ray: Dislocation pile-up treatments are suspect. All these effects have been put into an experimental parameter  $\varepsilon_m$ .

V C Sahni: What is the implication if you have an interface of finite thickness?

Ray: I do not know the answer at present.

G Srinivasan: Is there an essential difference between the way a crack propagates in metals and insulators on the one hand, and in crystalline and amorphous materials on the other?

Ray: There is no appreciable difference.

K Srinivasa Raghavan: What about the possibility that the crack nucleates at the interface and goes into the matrix or the particle as decided by the relative moduli?

Ray: It is possible to treat this case along the same lines, but my interest has been in the problem of incipient cracking of the particle.

## Experimental study of fluctuations in materials\*

K R RAO

Nuclear Physics Division, Bhabha Atomic Research Centre, Bombay 400 085, India.

**Abstract.** Mechanical behaviour is decided by the structure and kinetics of defects in materials. External forces play an important role in determining the growth, decay and motion of defects. In addition there is an inherent fluctuation in the various microscopic characteristics of the system as the latter acts as a 'heat bath'. A disturbance that is set up in the system is affected by these fluctuations. The response of the system to external forces can be related to the behaviour of the system due to intrinsic fluctuations in the absence of impressed forces. This is the basis of relation between study of fluctuations in the system and various relaxation phenomena observed. It is proposed to discuss certain features of this subject in relation to various material properties.

### Discussion

A P Pathak: What kind of information does one get about defects and defect structures from small angle neutron (or x-ray) scattering? For thin specimens charged particle scattering (channeling as well as backscattering) gives detailed information about all kinds of defects and defect structures. How do the two techniques compare as regards defect studies?

K R Rao: As I have explained in my talk, small angle scattering (x-ray or neutron) can give information on the *average* size, number and distribution of defects present in a solid (x-rays and neutrons give essentially similar information). Electron microscopy and charged particle scattering give useful information on point defects. Charged ionic particles in channeling experiments, for example, have helped one to decide whether certain impurities are substitutional or interstitial. However, such experiments generally require single crystals, and such studies have mostly been confined to 'ideal' defect studies. Small angle neutron scattering has the advantage that it can be used with bulk systems with large beam diameters, but the intensities are limited at present.

G Venkataraman: It seems to be of interest to consider, say, a creep experiment set up in a neutron beam. By studying the small angle scattering, one could perhaps learn something about the kinematics of defects during the course of deformation.

G Ananthakrishna: How do you measure the two-time correlation function in nonlinear systems?

Rao: I believe that *non-stationary* situations are the ones being investigated currently.

G Ananthakrishna: Binder remarks that coarse graining leads to fuzziness of the spinoidal boundary. How would one measure such an effect?

---

\*Only a summary is presented.

Rao: My *guess* would be that perhaps one ought to start with compositions corresponding to the fuzzy boundary, and then carry out experiments quite similar to the ones I have already described.

## Elementary concepts in chaos and turbulence

RAMAKRISHNA RAMASWAMY

Tata Institute of Fundamental Research, Homi Bhabha Road, Colaba, Bombay 400 005, India

**Abstract.** The phenomenology of aperiodic or chaotic behaviour is described with reference to simple theoretical models and experiments. A brief description is given of the current understanding of how irregular dynamical motions can arise.

**Keywords.** Chaos; nonlinear dynamics; turbulence.

### 1. Introduction

In the past few years, an intense effort has been devoted towards the detailed study of intrinsically random phenomena. Random phenomena are plentiful; in this talk, I will attempt to give a brief introduction to the rather simple concepts that at present underlie a basic understanding of chaos or irregularity, and the onset of turbulence. Many of the ideas are novel and interesting; whether or not these concepts are directly applicable in the context of mechanical behaviour as discussed in this Meeting is not entirely clear, but that is more a problem of application. This talk will be primarily phenomenological and qualitative without much emphasis on the mathematics (although much of the insight in this field really comes from the mathematics). Rather than give explicit references through the text, I prefer to list in the bibliography several articles that discuss these concepts in greater detail.

It is of interest to examine families of (nonlinear) systems rather than particular cases, as this type of study is apt to reveal more of the general behaviour. Typically, such systems can be parametrized by some physical variable such as temperature, pressure, applied voltage, etc. In many situations, the following general pattern has been seen to occur as a function of the relevant control parameter:

Smooth behaviour  $\longrightarrow$  transitional range  $\longrightarrow$  erratic behaviour

periodic  $\longrightarrow$  ?  $\longrightarrow$  aperiodic

A few examples are given below.

(1) *Heart beats* are possibly the most familiar instance of regular, periodic behaviour. As a function of applied stress (for example during physical exertion), we can easily observe the period changing as the heart beats faster. When this exertion is now coupled with oxygen availability, when one is climbing a mountain, say, the period can change drastically, and in fact may become quite erratic. This has unfortunate physiological effects (death is likely), and emphasises the importance of a transition from regular to irregular behaviour under the variation of a control parameter.

(2) A less familiar example occurs in the study of *animal populations*. This assumes



importance in livestock farming or fishery management, where it is necessary to know the behaviour of the population as a function of time, typically from generation to generation. One can in fact write fairly simple equations (of the difference, differential, or differential-delay type) to describe the population, where the control parameters are the food supply and the reproductive ability. These simple equations can give rise to totally chaotic behaviour for some values of these parameters.

(3) An example that I will discuss later on has to do with the *onset of turbulence*. In the classic Rayleigh-Benard experiment, when a liquid is heated, convective motion is established within the liquid. As the rate of heating is increased, the motion can become quite irregular, leading eventually to the full scale turbulence which is seen in the boiling liquid.

(4) It is possible that in a material under stress, this kind of behaviour is present as well, as may be deduced from the equations that model *serrated yielding*, for some values of the applied strain.

There are several more examples that one could cite. What is important, however, is that chaos is a *dynamical* phenomenon, and is abundant, in that it occurs frequently in nonlinear situations. (Nonlinearity of the dynamical system is a necessary condition for chaos, but is not a sufficient one.)

## 2. Dynamics

We define a dynamical system in terms of one independent variable, such as time,  $t$ , one or more dependent variables,  $x_i(t)$ , and an external (control) parameter,  $\mu$ . One requires a prescription to determine the evolution of the dependent variables. This is done via a system of differential equations,

$$\frac{d}{dt} x_i(t) = F_{\mu}(x(t)), \quad (1)$$

or difference equations,

$$x_i(j+1) = F_{\mu}(x(j)). \quad (2)$$

The index  $j$  plays the role of a discrete time in the latter case. The parametric dependence is contained in  $F_{\mu}$ . Given these and a set of initial conditions, it is straightforward to obtain the time evolution of the dependent variables. This defines an *orbit*, and it is the behaviour of these orbits as a function of time that describes the dynamics. It is customary to examine the dynamics in the phase space of the variables  $x_i(t)$ ,  $i = 1, 2, \dots$

We can simply define *regular* behaviour as motion,  $x_i(t)$ , which is predictable. That is, the dynamical variables are periodic functions of time, or combinations of periodic functions, i.e., quasiperiodic functions. Irregular or chaotic motion is, in contrast, unpredictable, and therefore is given by an aperiodic function (equivalently, of infinite period). It is important to emphasize that these motions are discussed entirely in terms of deterministic evolution via (1) or (2). Chaotic motions arise independent of random noise or fluctuations. In fact, it is customary to label such intrinsic erratic behaviour as *self-generated chaos*.

The notions of regular and chaotic motion can be quantified in several ways. A direct and rather obvious means is through the spectral or Fourier analysis of the orbits.

Regular motion leads naturally to a discrete Fourier spectrum, since the motion is either periodic or quasiperiodic. The spectrum for chaotic motion must necessarily be continuous owing to the aperiodicity (*i.e.*, any and all frequencies—in particular, zero-frequency). Another means of distinction is based on the Liapunov instability of orbits. The euclidean distance between regular orbits can grow linearly; whereas, between chaotic orbits, it grows exponentially. It is also possible to examine the orbits themselves, to get an idea of how they develop in phase space. When there are  $n$  dependent variables, corresponding to  $m$  degrees of freedom, the phase space is of dimension  $n$  ( $x_i(t)$ ;  $i = 1, 2, \dots, n$ ). Examining the motion in this  $n$ -dimensional space is a difficult task. One can, however, essentially accomplish this by examining the Poincare surface-of-section. This works best when the number of degrees of freedom is small,  $m = 2$  or  $3$ . To construct a surface of section, one chooses a particular plane in the phase space, and locates the point of intersection each time the orbit passes through this plane. If a given orbit is examined for a sufficiently long time, there are several points of intersection, and these give an idea of the geometry of the orbit. For regular motions, the points of the Poincare section lie on smooth curves, whereas for chaotic motions, these points are scattered apparently randomly in the plane (independent of which particular plane is chosen).

In discussing dynamical systems, it is useful to distinguish between conservative systems (where the volume of phase space is constant in time) and non conservative systems (where this volume changes with time). The behaviour is somewhat different in the two cases. In most physical situations one encounters dissipative, nonconservative systems, owing to the presence of frictional forces, and in that sense these systems are more important. It is however necessary for completeness to describe in brief the behaviour of conservative systems.

## 2.1 Conservative (Hamiltonian) systems

The most common examples of conservative systems are Hamiltonian systems, wherein one can define a Hamiltonian function,  $H(\mathbf{x})$ . As general dynamical systems, these have  $n = 2m$  dependent variables for  $m$  degrees of freedom. Thus, the phase space is of dimension  $2m$ ;  $m$  of these variables are 'coordinates', and  $m$  are their conjugate 'momenta'. Evolution is governed by Hamilton's equations. (In the discrete case, the requirement of constant phase space volume is replaced by the condition that the Jacobian of the transformation in (2) have the value  $\pm 1$ ). One can further separate such systems into two classes: integral systems and nonintegral systems. In the former class, it is possible to make a canonical transformation such that  $H(\mathbf{x})$  is given in terms of  $m$  (in general, new) 'momentum' variables alone. These are constants of the motion, which is then constrained to lie on well-defined geometrical objects, namely,  $m$ -dimensional tori in the phase space of dimension  $2m$ . Thus the motion is *always* regular. We can regard nonintegrable Hamiltonians as arising from integrable ones by the addition of perturbation terms (depending on  $\mu$ ), such that  $H$  can no longer be expressed as a function of  $m$  momentum-like variables alone. There is then no guarantee that the motion will lie on  $m$ -dimensional tori. The powerful KAM theorem applies in such cases. Loosely speaking, this theorem states that, depending on the magnitude of the perturbation, some of the tori that exist in the integrable case get distorted, and some of them are destroyed. When the tori are merely distorted, the motion still remains regular; but when they are destroyed, the orbits are free to wander over all of phase

space, and can therefore become highly irregular and chaotic. The phenomenology of Hamiltonian chaos is in fact extremely bizarre and involved; this erratic behaviour basically arises from the complicated interactions between internal resonances. The foregoing is a cursory description of the bare essentials of the matter. As a simple example, consider the discrete map

$$x_{i+1} = \mu x_i - (y_i - x_i^2)(1 - \mu)^{1/2}, \quad (3)$$

$$y_{i+1} = x_i(1 - \mu)^{1/2} + (y_i - x_i^2)\mu. \quad (4)$$

This roughly models the Poincaré surface of section of an  $m = 2$  degree of freedom Hamiltonian system. Orbits are constructed by iterating points in the  $xy$  plane under the above transformations. Depending on where one starts, successive points in figure 1 can lie on a smooth curve (A) or on a set of smooth curves (B)—these correspond to regular motion on tori; or else the points can be scattered all over the plane (C)—this is a chaotic orbit and is not confined to any simple geometrical object. In general, the motion can be extremely complicated. This is both typical, in the sense that most nonlinear Hamiltonian systems are likely to be nonintegrable, and pathological, in the sense that for any nonzero value of  $\mu$ , a nonintegrable Hamiltonian will exhibit *some* chaotic motions.

## 2.2 Dissipative systems

As already mentioned, dissipative systems are more common, and thus more pertinent. A typical example is provided by the forced-beam problem. A beam of length  $b$  is

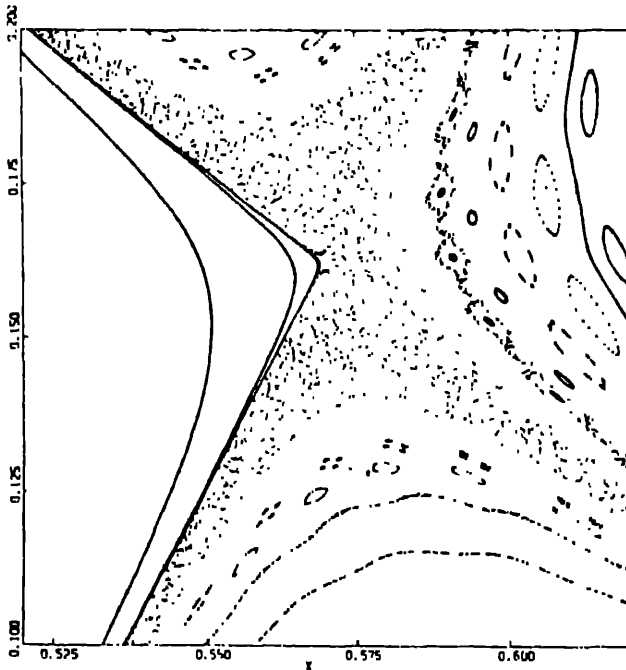


Figure 1. Orbits in the  $xy$  plane induced by the discrete transformation of equations (3)–(4). A and B are examples of regular motion, while the set of points C is typical of the Poincaré section of a chaotic orbit.

pinned at two ends, separated by distance  $l$ . When  $l$  is less than the beam length, the beam settles into one of the two symmetric equilibrium configurations. A sinusoidal force is applied at the ends, and the beam oscillates about the equilibrium position. As the excitation increases, however, the rod begins to snap back and forth between the two equilibria. If  $w(x, t)$  is the lateral displacement,

$$w(x, t) = \xi(t) \sin(\pi x). \quad (5)$$

For small forcing amplitudes,  $\xi(t)$  is a periodic function; but as the forcing amplitude increases,  $\xi(t)$  can become quite chaotic. The problem can be properly formulated mathematically, and simplified to a more familiar problem, the Duffing equation. The latter describes a simple nonlinear forced oscillator with frictional damping,

$$\ddot{x} + \alpha \dot{x} + x + \beta x^3 = f \cos(\omega t). \quad (6)$$

This example is sufficient to illustrate much of the phenomenology. When  $\alpha = \beta = f = 0$ , (6) corresponds to the equation of motion of a simple harmonic oscillator of unit mass and frequency. The motion in phase space is extremely simple: a circle in the  $x\dot{x}$  plane, given by the parametric equations,

$$x(t) = A \cos(\omega t + \phi); \quad \dot{x}(t) = -A \sin(\omega t + \phi). \quad (7)$$

The motion is trivially regular. If damping is now introduced, keeping  $\beta = f = 0$ , one has damped harmonic oscillations; the motion now consists of orbits that spiral exponentially into a *sink* at  $\dot{x} = x = 0$ . When forcing is also included, one has a *limit cycle* behaviour, i.e., orbits converge asymptotically onto a limiting structure in the phase plane, and the motion is periodic on this limit cycle.

The sink and the limit cycle are examples of simple *attractors*. When nonlinearity is included in the equation of motion, it is possible to have more complicated attractors—in particular, *strange*, or chaotic, aperiodic attractors. One early example of such an attractor was found by Lorenz in a 3-mode truncation of the Navier-Stokes equation

$$\begin{aligned} \dot{x} &= 10(y - x), \\ \dot{y} &= \mu x - y - xz, \\ \dot{z} &= xy - 8z/3. \end{aligned}$$

The strange attractor (SA) that occurs in this system is shown in perspective in figure 2. The orbit spends random amounts of time on the two distinct portions of the attractor.

SA's are crucial in one picture of the onset of chaos and turbulence, the Ruelle-Takens model. Here chaos is presumed to occur by the creation of SA's, and the mechanism is as follows. Solutions to (1) are studied. For small  $\mu$ , some simple periodic motion is present; as  $\mu$  increases, (Hopf) bifurcations occur; the motion is still regular, but now on  $m$ -dimensional tori, where  $m > 1$ . When two such bifurcations have occurred, then it can be (mathematically) proven that any small perturbation suffices to create a SA, and hence chaos.

Currently, there exist several such scenarios for the onset of chaos and turbulence, each applicable in different circumstances. In the so-called Feigenbaum picture, we consider systems described by (1) or (2). As a function of the parameter  $\mu$ , the following behaviour pattern occurs. For  $\mu < \mu_0$ , there is some kind of a simple sink. At  $\mu_0$ , a bifurcation takes place and an orbit of period  $\tau$  becomes stable and attracting. (Technically, this is through a "pitchfork" bifurcation). As  $\mu$  is increased beyond a certain

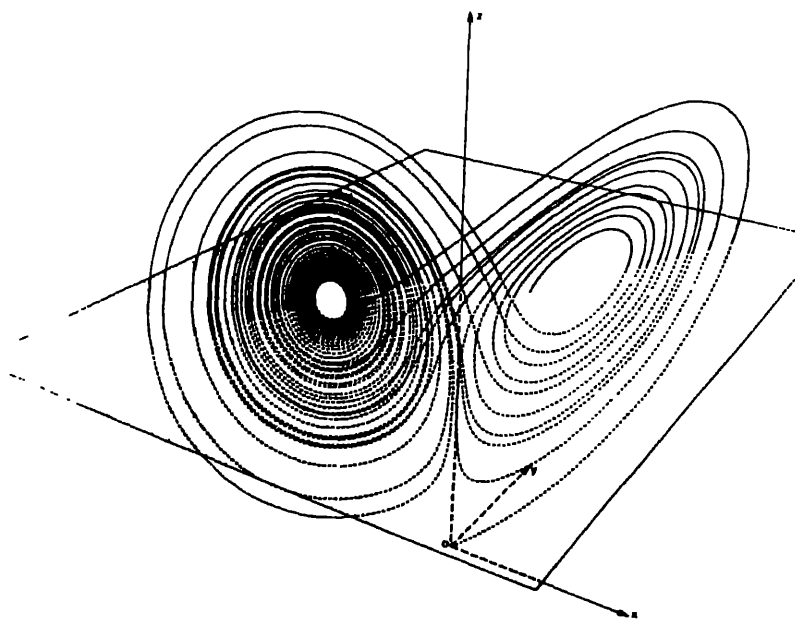


**Figure 2.** The strange attractor in the Lorenz system, equation (8), for  $\mu = 28$ . The attractor consists of two almost planar portions, and the orbit wanders chaotically from one side to the other.

value  $\mu_1$ , the period  $-\tau$  orbit loses stability, but one of period  $2\tau$  is born which is now stable and attracting. At a higher value  $\mu_2$  another bifurcation takes place, with the period- $2\tau$  orbit losing stability while a period- $4\tau$  orbit becomes stable. This process repeats itself: at  $\mu_n$ , a period- $2^n\tau$  orbit becomes stable and attracting while the period- $2^{n-1}\tau$  orbit loses stability. In the limit, one has a  $2^\infty\tau$ -period orbit, i.e., an orbit of infinite period, or chaos. The interesting thing is that  $\mu_\infty$  is finite—the *period-doubling cascade* occurs quite rapidly, and furthermore, the rate of convergence of the bifurcation points,

$$\delta_n = \frac{\mu_n - \mu_{n-1}}{\mu_{n+1} - \mu_n} \quad (9)$$

logarithmically approaches  $\delta = 4.669201609 \dots$  as  $n \rightarrow \infty$ . The most surprising fact is that the number  $\delta$  is universal for a large general class of  $F_\mu$ . The precise form of  $F_\mu$  does not matter (within certain restrictions). Wherever the period-doubling route to chaos is found, the number  $\delta$  that one computes from measurement is identical to that found by Feigenbaum (i.e.,  $4.669 \dots$ ). Historically, this number was discovered in a study of the discrete one-humped map of the unit interval known as the logistic equation, namely,

$$\begin{aligned} x(j+1) &= \mu x(j)[1 - x(j)], \\ 0 \leq x \leq 1, \quad 0 \leq \mu \leq 4. \end{aligned} \quad (10)$$

(In fact, there are several other universal constants that can be found within such a picture.) The period-doubling route to chaos has been seen to occur in a wide variety of cases—in abstract maps such as (10), in differential equations such as (8), in a variety of

theoretical experiments modelling chemical reaction kinetics, in forced oscillator problems, in a seven-mode truncation of the Navier-Stokes equation, and even in the equations that model repeated yielding in mechanical behaviour. Most crucially, though, a number of physical experiments have also confirmed this picture. The Rayleigh-Bénard flow problem mentioned earlier is one such. In this experiment, liquid helium is heated at around 4 K, and the temperature at a point within the cell is monitored as a function of time. The Rayleigh number,  $R$ , plays the role of the parameter  $\mu$ . For low  $R$ , convective rolls are formed in the experimental cell; the motion is periodic. As the temperature is raised, the motion begins to become turbulent. The Fourier transform of the temperature as a function of the time clearly shows the existence of a basic frequency,  $f$ , and the subharmonic bifurcations, which give rise to peaks at  $f/2$ ,  $f/4$ ,  $f/8$ ,  $f/16$ , etc. (see figure 3). The Feigenbaum constant computed from this experiment turns out to be about 4.8, amply confirming the general theory.

It must also be mentioned that the Rayleigh-Bénard experiment prepared differently displays the Ruelle-Takens behaviour as well. There is yet another common mechanism, *intermittency*, through which chaos can occur, via "tangent" bifurcations. Prior to the onset of full-scale chaotic behaviour, there are long periods of time when the motion is perfectly regular, interspersed with short bursts of erraticity. This route too can be observed experimentally.

In dissipative systems, chaos comes about in a manner different from that in conservative systems. Essential ingredients are bifurcations and attractors. One can have either period-doubling bifurcations and a periodic attractor in the Feigenbaum scenario (thus only one independent frequency), or bifurcations from a period orbit to tori, followed by a strange attractor in the Ruelle-Takens picture (thus at most three independent frequencies).

### 3. Summary

This talk has only briefly touched upon the basic phenomenology of irregular motion. Much of the interest in nonlinear dynamics arises from the existence of a large component of the unexpected and the counterintuitive. I have tried to outline the

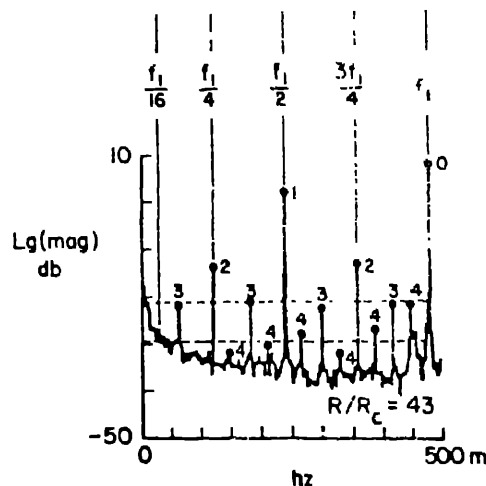


Figure 3. Period doubling subharmonics in the temperature power-spectrum of liquid helium in a Rayleigh-Bénard experiment (from Maurer and Libchaber, *loc. cit.*).

various paths or routes to chaos; unavoidably, there are gaps in this short presentation.

Although much progress has been made, there are still several open questions. For example, there is no minimal (or maximal) degree of complexity necessary to ensure chaos—very nonlinear systems can be integrable, while even the simplest (cubic) nonlinearity can induce chaos. And at the microscopic level, which may or may not be of interest here, quantum effects occur, and there is no clear understanding of how this can modify classical chaos.

When it does occur, chaos can have important consequences. For one thing, it becomes possible to apply statistical methods to advantage, if the behaviour is sufficiently random-like. On the other hand, chaos may be an undesirable feature if one wishes to remain in the region of the precisely predictable—this situation is common, for example, in particle storage rings where particle losses occur via erratic orbits: It is then essential to minimise or totally avoid chaos. The very ubiquity of chaos makes it necessary to examine dynamical processes in greater detail, whatever the context—this can well include mechanical behaviour.

## References

### 1. General references on chaos

- 1980 *Proc. Int. Conf. on Nonlinear Dynamics* (ed) R H G Helleman (Ann. N.Y. Acad. Sci. No. 603)  
 Jorna S (ed) 1978 *Topics in nonlinear dynamics* (Am. Inst. Phys. Conf. Proc., Vol. 46)  
 Helleman R H G 1970 in *Fundamental problems in statistical mechanics* (ed) E D G Cohen (New York: North-Holland Publ) Vol 5, p 165  
 Moser J 1978 *Math. Intell.* **1** 65  
 Ruelle D 1980 *Math. Intell.* **2** 126  
 May R M 1976 *Nature (London)* **261** 459  
 Hofstadter D 1981 *Sci. Am.* **245** 16

### 2. Conservative systems

- Berry M V 1978 in *Topics in nonlinear dynamics* (ed) S Jorna Vol 46 (*Am. Inst. Phys. Conf. Proc.*)  
 Ramaswamy R 1981 *Phys. News* **12** 60

### 3. Dissipative systems

- Eckmann J P 1981 *Rev. Mod. Phys.* **53** 665  
 Kumar D 1982 *Phys. News* **13** 109  
 Tomita K 1982 *Phys. Rep.* **86** 113  
 Crutchfield J, Farmer J and Humberman B 1982 *Fluctuations and simple chaotic dynamics* *Phys. Rep.* **92** 45

### 4. Some experimental references

- Maurer J and Libchaber A 1979 *J. Phys. Lett.* **40** 419  
 Maurer J and Libchaber A 1980 *J. Phys.* **41** C3  
 Feigenbaum M 1979 *Phys. Lett.* **A74** 375  
 Gollub J P, Besons S V and Steinmann J 1980 *Proc. Int. Conf. nonlinear dynamics* (ed) R H G Helleman (Ann. N.Y. Acad. Sci. No. 203)

### 5. Other references

- Lorenz E N 1963 *J. Atmos. Sci.* **20** 130  
 Ruelle D and Takens F 1971 *Commun. Math. Phys.* **20** 167  
 Feigenbaum M 1978 *J. Stat. Phys.* **19** 25  
 Feigenbaum M 1979 *J. Stat. Phys.* **21** 669

**Discussion**

G Ananthakrishna: Why is it often said that Landau's theory does not give a correct description of turbulence?

R Ramaswamy: The trouble with the Landau picture of turbulence is that as you vary a particular parameter, you have a series of bifurcations to the wrong geometrical object. These are in a certain sense bifurcations from a periodic orbit to a toroid, and thence a sequence of toroids. A limiting strange attractor does not appear.

G Ananthakrishna: Which route to the turbulent state is followed in the Rayleigh-Benard case?

Ramaswamy: It has been shown that all 3 routes may be followed.

G Ananthakrishna: Is there any algorithm to get the Poincare map for multi-dimensional systems?

Ramaswamy: It is a difficult process.

S R Shenoy: Can one make a statement about the minimum order of the differential equations and of the nonlinearity in them in order to get chaos?

Ramaswamy: This is difficult. We do not even have a clear way of predicting whether a system is going to be integrable or not. A minimum requirement for chaos is of course nonlinearity, but it is not easy to make a more exact statement of general applicability.

K R Rao: Does the central peak in a second order phase transition have anything to do with chaos?

Ramaswamy: There is no analogy at all between the onset of chaos/turbulence with any kind of phase transition.

M Youssuff: How does one develop a probabilistic description of the chaotic state?

Ramaswamy: One of the reasons for studying chaos is to determine when ergodic theory is valid. Clearly, at the very least, chaos is needed for ergodicity to occur.



\_\_\_\_\_

## Fractals

D DHAR

Tata Institute of Fundamental Research, Bombay 400 005, India

**Abstract.** An elementary introduction to the concept of fractals is given. Some examples of fractals drawn from nature are briefly discussed. It is suggested that fractal geometry may be useful in characterizing the grain size and shape distributions in polycrystalline solids.

**Keywords.** Fractals; non-integral dimensions; grains.

### 1. Introduction

This talk is intended as an elementary introduction to the concept of fractals for non-experts. I shall try to concentrate on some of the qualitative geometrical features, and will not discuss more technical topics such as phase transitions on fractals.

The organization of the talk is as follows: In §2 I shall briefly discuss the motivation for studying these unconventional geometrical objects. The intuitive notion of dimension is generalized in §3 to include non-integral values of the dimension. Some illustrative examples are given in §4. Section 5 contains some concluding remarks.

### 2. Motivation

Fractals are geometrical objects having an effective dimensionality which is non-integral. They are useful in modelling several quite different physical situations. It may not be unreasonable to hope that they would also be useful in describing certain aspects of the mechanical behaviour of matter.

This situation is not entirely like that of a biochemist who tries to sell a 'wonder drug' without quite knowing which ailment it cures. In our case, the drug is acknowledged to be 'neurosensitive'. Whether the effects are desirable or undesirable in a specific proposed application is not known beforehand. In some cases, for example in the understanding of the influence of dimensionality on critical phenomena near phase transitions, fractals have been found to be very useful.

The mechanical specification of a system involves the listing of the variables in terms of which the state of the system is described (kinematics), and of the laws of mutual interaction and time-evolution of these variables (dynamics). The choice of variables in terms of which we characterize the state is important: unnatural choices lead to convoluted descriptions. An example of a bad choice of variables is the Ptolemaic insistence on describing planetary motion in terms of a superposition of uniform circular motions. A comparatively more recent example is the phrase 'temperature-dependence of the Debye temperature' used by some physicists around 1910 to describe the non-agreement of the measured temperature-dependence of the specific heat of materials with Debye's theoretical predictions.

The introduction of fractals to describe the mechanical behaviour of matter has, first, a kinematical aspect. It has not yet been established that our difficulties in understanding the mechanical properties of solids are sufficiently acute to necessitate a substantial change from the conventional picture involving an ideal solid plus defects. However, the general trend of the discussions at this Meeting would seem to indicate that, near the plastic limit, the formalism is under stress. It may be useful to explore the possibility of alternative modes of description.

Most text books on the mechanics of solids start out by classifying the defects in solids as point-, line-, surface-, or volume-defects. It is not surprising that the classification scheme is geometrical, and is almost universally preferred over other possible schemes (alphabetical, historical, mobile/immobile defects, annealed/quenched defects, etc.). The geometrical characterization of defects captures some of their most important features. It cannot be the whole story, but it is a useful place from which to begin.

### 3. A definition of non-integer dimensionality

It is well-known that the strength of solids is a strong function of the grain size and grain shape. Earlier it has been emphasized by Ranganathan that grains in metals are quite irregular in shape (Ranganathan 1984). A schematic representation of possible grain shapes on a two-dimensional lattice is shown in figure 1. Clearly, a material with compact hexagonal grains (as in figure 1a) would be different, mechanically, from a material with very ramified grains (figure 1d). It would be useful to have a numerical characterization of these grain shapes to be able to specify whether the grains are compact objects with a few holes, or are ramified and stringy. Roughly speaking, a compact volume, a disc-like shape, and a string-like shape respectively would behave like three-, two- and one-dimensional objects. A numerical characterization of attributes such as 'stringiness' often gives rise to nonintegral answers, when applied to objects of complex geometrical shapes. Such objects may be said to have a non-integral dimension and are called fractals (Mandelbrot 1977, 1982).

What is meant by saying that an object has dimension 1.5? For that matter, what is meant by saying that an object is three-dimensional? Before giving a definition of dimension, which is generalizable to non-integral values, it is useful to remember that the dimension we assign to an object depends very much on our choice of its representation. A ball of wool may be represented as a point, or a sphere, or as a tangled line (having dimensions 0, 3, and 1 respectively) depending on our scale of description (Mandelbrot 1977). The dimension we assign actually pertains to the mathematical representation of the object, and not to the object itself.

In order to be useful, a definition of dimension must be simple, robust (insensitive to small changes in geometry), and should agree with our intuitive notion of dimension

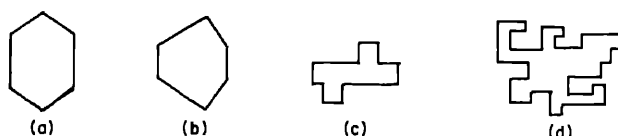


Figure 1. A sequence of increasingly complex grain shapes (schematic).

when applied to conventional spaces (like manifolds). Several such definitions may be found in the literature (Mandelbrot 1977, 1982; Dhar 1977; Engelking 1978). In the following, we consider only the simplest of these.

Consider a space in which the distance between two points, and a volume measure, are defined. Let  $V(R)$  be the volume of the set of points whose distance from an arbitrarily chosen origin is less than  $R$ . If  $V(R)$  varies as  $R^D$  for large  $R$ , for all choices of the origin, we define  $D$  to be the fractal dimensionality of the space. Formally,

$$D = \lim_{R \rightarrow \infty} [\log V(R) / \log R].$$

Clearly, using this definition, a straight line has dimension 1 and a plane has dimension 2. Now consider the triangular gasket shown in figure 2. It consists of an equilateral triangle, the mid-points of the sides of which are joined together and divide the triangle into four smaller, equal triangles (three upright, and the central one inverted). Each of the three upright second-generation triangles is divided similarly into four third-order triangles. The  $3^2$  upright triangles of the third generation are further divided to give  $3^3$  fourth order triangles, and so on, *ad infinitum*. The gasket consists of all the points in the plane which belong to at least one of the line segments used in this division procedure.

It is easy to see that the points belonging to the gasket have zero area, but that the total length of the line segments which constitute the gasket is infinite. It would thus seem reasonable to assign this set of points a dimensionality between 1 and 2. To determine the fractal dimensionality of the gasket we have to define the metric and a volume-measure for this case. The distance between two points is most simply defined as the Euclidean distance between them (alternatively, as the length of the shortest line joining them and lying completely on the gasket). The volume of an  $r$ th generation triangle with all inside points included is defined to be 3. Using these definitions, it is easy to see that

$$V(2R) = 3V(R).$$

Using the definition of  $D$  given earlier, this gives  $D = \log_2 3 \approx 1.54$ . The triangular gasket is thus an example of a fractal.

#### 4. Other examples

In the following we give some additional illustrative examples of fractals. For additional examples, and some very beautiful pictures, see Mandelbrot (1977, 1982).

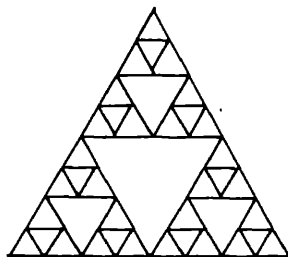


Figure 2. The triangular gasket. Only the edges belonging to the first, second, and third order triangles are shown here for clarity.

### 4.1 Lattice animals

Lattice animals are defined as connected clusters of sites embedded on a lattice (figure 3). The problem of the determination of the mean values of the properties of animals containing a given number of sites, given that all distinct shapes of such animals have equal statistical weights, is called the random animal problem. This assumption is not true for crystal grains, as compact grains have lower surface energy, and are favoured thermodynamically.

If a typical animal on a  $d$ -dimensional hypercubical lattice ( $d$  is an integer here) were compact, its maximum lateral extent  $R$  would vary as  $n^{1/d}$ , where  $n$  is the number of sites in the animal. It is found that random animals are typically stringy, and  $R$  varies as a *larger* power of  $n$ . In 3-dimensions, the dependence is  $r \sim n^{1/2}$ . Thus a random animal in 3-dimensions has a fractal dimension equal to 2 because  $n \sim R^2$ .

### 4.2 Percolation clusters

Consider a  $d$ -dimensional hypercubical lattice ( $d$  integral) in which each nearest-neighbour bond is, independent of others, unbroken (*i.e.*, connects the sites at its ends) with a probability  $p$  (figure 4). For small  $p$  values ( $p$  less than a critical value  $p_c$ ), a site chosen at random is connected to only a finite number of other sites through occupied bonds. In this case, the effective dimension of the clusters may be defined to be zero. For  $p > p_c$ , the mutually connected sites constitute a finite fraction of the total number of sites of the lattice, and form a  $d$ -dimensional network (with some holes). When  $p$  is equal to the critical probability  $p_c$ , the incipient infinite cluster has zero fractional volume, and is very tenuous. However, if we construct a sphere of radius  $R$  about a point, the expected number of sites connected to the origin varies as  $R^D$  where  $D \approx 1.6$  for  $d = 2$ . The infinite cluster at the percolation threshold is an easily-realizable example of a fractal.

### 4.3 Soap powder

If we look at soap powder under a microscope, it is seen to consist of a large number of particles of varying sizes. As in the case of crystallites in metals, the average linear extent

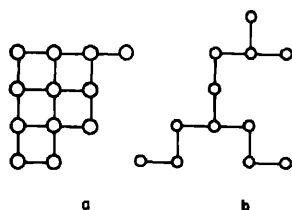


Figure 3. Animals on a square lattice. (a) is a compact cluster, while (b) is stringy.

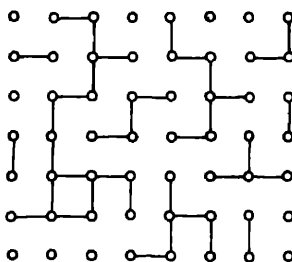


Figure 4. A random configuration of unbroken bonds on a square lattice.

of these powder particles grows faster than the cube root of their mass, and can be used to define an effective dimension of the powder. We should expect the fractal dimension of soap powder to be between 2 and 3. The precise numerical value may perhaps depend upon its chemical structure.

#### 4.4 The distribution of galaxies

The precise nature of the large-scale structure of the distribution of matter in the universe is not very well-known. According to one view, the distribution of galaxies in the universe is essentially uniform. However, a different picture, in which the universe shows clustering at all scales of length, is also consistent with experimental data. According to this picture, galaxies typically reside in clusters of galaxies, which themselves are part of clusters of galaxies and so on. Each cluster contains about 3 subclusters on the average. The size of the cluster is appreciably smaller than inter-cluster distance, which implies that the number of galaxies in a sphere of radius  $R$ , centred at any particular galaxy, grows as  $R^D$  with  $D < 3$ . Thus the distribution of the galaxies in the universe shows a fractal structure.

#### 4.5 Coastlines

The coastline of an island is typically a very zigzag line (figure 5), and its measured length depends very much on the size of the divider spacing (or calliper length) used to measure it (say, from a very detailed map). If we use a smaller divider spacing, we measure more of the small detours and turns that the line makes, and the measured length is larger. If the line is smooth at very short distances, then, as the divider spacing is decreased, the length will tend to a limiting finite value (which is defined to be the 'length of the line'). If, however, the line is rough at all length scales, we may find that  $L(s)$ , the length measured when the divider spacing is  $s$ , varies as  $s^{1-D}$ , where  $D > 1$ . This  $D$  may be called the fractal dimension of the coastline. For several actual coastlines  $D = 1.2$ . For a Brownian motion path  $D = 2$ .

### 5. Concluding remarks

It should be clear from the preceding examples that fractals are not exotic, pathological objects dreamt up by mathematicians, but are very much a part of the world around us. They provide a natural description of the non-classical geometrical forms encountered in nature. It is this common geometrical character, and not the occurrence of fractional powers, which is the characteristic feature of fractals. Fractional power laws are, of course, encountered quite frequently in Nature. For two observables  $X$  and  $Y$ , if  $X$  varies as an integral power of  $Y$  (not equal to  $\pm 1$ ), then  $Y$  varies as a non-integral power of  $X$ . It is preferable not to use the term 'fractal' in the absence of a geometrical structure in the problem (as in, say, of stock-market prices). Fractals may also show up in the discussion of mechanical properties of matter in the context of dynamical response and the onset of chaos. A discussion of these aspects may be found elsewhere (Ramaswamy 1984). Additional references on fractals may be found in Dhar (1981).



Figure 5. A schematic representation of a coastline. The line will show further wrinkles and detours, if observed on an expanded scale.

### References

- Dhar D 1977 *J. Math. Phys.* **18** 577  
Dhar D 1981 in *Current trends in magnetism* (Bombay: Indian Physics Association) p. 207  
Engelking R 1978 *Dimension theory* (Amsterdam: North-Holland)  
Mandelbrot B B 1977 *Fractals: form, chance and dimension* (San Francisco: Freeman)  
Mandelbrot B B 1982 *The fractal geometry of Nature* (San Francisco: Freeman)  
Ramaswamy R 1984 *Bull. Mater. Sci.* **6**  
Ranganathan S 1984 *Bull. Mater. Sci.* **6**

### Discussion

N Kumar: Are fractal dimensions and similar apparently geometrical concepts applicable to *dynamics*?

D Dhar: Yes, there are connections. An example is magnetisation creep.

G Venkataraman: These concepts have also been employed in describing turbulence.

R Ramaswamy: Strange attractors have been shown to have well-defined fractal dimensions.

S Ranganathan: Fractals may have some bearing on the shapes of second phase particles which influence mechanical properties.

## Summary and outlook

V BALAKRISHNAN

As we are running short of time, I will be brief. I would like to begin by repeating the platitude (or self-evident truth!) that, just as approaches to a certain problem can be different, so can the motivations. A person may be motivated to study a problem for purely aesthetic reasons, and not out of any practical considerations at all; but the person should have the freedom to do so. To paraphrase what has been said by many eminent scientists: If a fraction of time spent in a subjective argument over different approaches to a problem was spent in actual computation using any of the techniques under contention, there would perhaps be no need for the argument because the problem would be considerably closer to resolution! Similarly, I feel that there is no need here to debate the respective motivations of physicists and metallurgists, including the question of what constitutes a problem and what is meant by a solution to one. All techniques, however mathematical or however empirical, are acceptable and indeed essential to make any headway in a subject as complicated as the one we have been discussing.

I would now like to make two general comments, one taken from Prof. N Kumar and the other based on Dr K R Rao's talk. In any given subject, theorists generally like to have the broad paradigms brought out so as to have a framework for further development. The general paradigm that is used in the area of mechanical deformation is of course that of dislocations. Given a paradigm, the theoretical physicist then faces the interesting question of the adequacy or otherwise of the paradigm in the light of subsequent experimental information. A well-known example is that of the soliton which is the "paradigm of the 80's" in several branches of physics. When certain regimes of essential nonlinearity are reached, the traditional plane wave-cum-superposition principle is no longer adequate, and new basic entities like solitons (or more generally 'lumps') have to be introduced. So, in this sense, it is very relevant to ask whether, when we look at a practical problem like a large-angle grain boundary, the paradigm of the dislocation is still meaningful—notwithstanding the fact that in the limit of small angles, the boundary is describable in terms of an array of dislocations. Thus, a radical approach which gives up the idea of dislocations altogether would be worth examining further. Equally welcome are other approaches which bring out geometrical coincidences like the dsc lattice together with the idea of dislocations on *this* lattice.

My second general comment concerns the experimental side. A large number of possibilities were catalogued systematically this morning by Dr Rao. Some techniques like acoustic emission, which perhaps have not been emphasized sufficiently for lack of time, should be explored more systematically. Turning to questions for theoreticians arising out of experiment, consider, for example, spinoidal decomposition and the various nonlinear theories of diffusion associated with it. What light does experiment shed on the cut-off and truncation procedures employed in Cahn's theory and its



various modifications to include 'higher order' nonlinearities? What are the experimental inputs needed for a critical discrimination between the various theories—in the manner, for example, critical experimental inputs to the theory of freezing were spelt out by Prof. Ramakrishnan in his lecture? You may recall that he pointed out how the shape of the structure factor really determines how good the approximation is and also serves as a self-consistency check. Something like that would be worth attempting for theories of spinoidal decomposition too. Perhaps this has already been done. I am tempted to recall a remark I came across once—I think it was made by Frauenfelder in the early days when many nuclear physicists were getting into solid state physics *via* the Mössbauer effect—that it is always a big surprise to a person getting into another field to realize that the “natives were not as stupid as they seemed from outside”, and that all the obvious things had been done! I am sure all the physicists here have this realization about metallurgy.

There are some other points of interest which I should like to mention, although my list will surely reflect my personal bias as a theoretical physicist. Consider for example the general question of nucleation and discontinuous transitions. The diversity and richness of the phenomena encountered here were well brought out in the talk by Dr Wadhawan. It seemed to me that considerable work remained to be done to get the 'theory' here to the same stage of development as has been reached for continuous transitions. Another point which struck me relates to describing things in terms of disorder rather than order. For example, when one considers systems with quenched disorder, one starts with simple models, but pretty soon when the defect density becomes high, one introduces things like disorder variables. Starting from the high-temperature phase, one can then use duality properties, for instance, and get information on the ordered phase as well as on the defects in the ordered phase. This is more fruitful than attempting to start at the ground state and work one's way upwards. Perhaps when the dislocation density is very high, this kind of approach may be useful—indeed, I should think that recent ideas on 'solid-state turbulence' are preliminary steps in this direction. But a great deal of work remains to be done to 'quantify' the properties of random tangles of dislocations, etc. Starting from the theory of liquids is of course carrying the idea of coming in from the disordered phase to its ultimate, but this may be *too* basic for the purpose I have in mind here. The theory of *freezing* we heard about was aptly named, for it did not deal with the question of how to go from the solid to the liquid phase, *i.e.*, how to restore the broken symmetry. A complete picture of the transition should of course give us an idea of this obverse side of the coin, too.

I would also like to emphasize a point that Dr Ramaswamy made during his presentation. When one tries to apply ideas like chaos to mechanical behaviour (as has been initiated by Dr Ananthakrishna), it would be good to try and obtain first a *model-independent characterization of the basic variables in the mechanical behaviour problem*. It is very interesting to demonstrate that chaos appears in specific models of dislocation dynamics. Presumably the phenomenon is much more general. So one would like to know what the minimal set of relevant variables is, and so on, in order to extract model-independent information to the extent possible. This is all the more important in an area like chaos because we know that 'neighbouring' dynamical systems can have widely different behaviour. We should at least be able to put various models of dislocation dynamics into their appropriate 'universality' classes. Only then

can one undertake a critical examination of the role of various physical parameters in inducing bifurcations, chaotic behaviour, etc.

Having mentioned chaos, I should also like to make a remark on the slightly older paradigm of solitons, nonlinearities, etc. It may be relevant to ask whether nonlinearities of the kind that arise in the continuum elasticity theory Dr Sahoo talked about, can help to stabilize nondissipative structures like solitons—and if so, what are these? Are they the analogues of dislocations in discrete models? This is no doubt an entirely theoretical kind of question, but I am sure that it would aid progress if we understood the basic reason why these objects get stabilized.

I realize I have essentially been conveying the prejudices of a theorist but that is because I am not really competent to say much about the experimental possibilities. However, I will emphasize that this is a field in which observation is prime. We want facts. However, I should like to heartily endorse a point made by Prof. Kumar. Given the plethora of facts and the very large number of variables involved in the field of mechanical behaviour, physicists generally find the going difficult since they like things to be presented in terms of basic features, or very general arguments and reasons. To snow a physicist with a mass of metallurgical details sounds a bit like French grammar where you list all the irregular verbs and exceptions *ad nauseum*. So, if I may make an appeal—it would be nice for the metallurgists to *intentionally oversimplify* the problems that they face when presenting them to a physicist. *After* he gets interested and starts answering questions, you can 'bring him down to earth', as Prof. Srinivasaraghavan said, by gradually including the complications; otherwise there is a tendency for him to get turned off right in the beginning. This approach will also help sift and place all the facts in order of importance and relevance, in itself a worthwhile and by no means trivial task. Fortunately, in the talks we have had during these three days, this has, by and large, been achieved. Many of us physicists have noted down at least some things that are general features, notwithstanding exceptions, and I am sure some of us will actually explore at least the simplified cases. In that sense, I think, this Meeting has worked out well.

\_\_\_\_\_

100

100

## Panel discussion

Moderator: Prof. S K Joshi, Department of Physics, Roorkee University  
Panelists: Dr R Krishnan, Metallurgy Division, Bhabha Atomic Research Centre  
Dr V C Sahni, Nuclear Physics Division, Bhabha Atomic Research Centre  
Dr S Ray, Metallurgy Department, Roorkee University  
Prof. N Kumar, Department of Physics, Indian Institute of Science

**Prof. Joshi:** We have had a busy and very fruitful Discussion Meeting. This is the last session, and we are gathered to hear the reactions of the panelists, as well as their suggestions. There are no restrictions or guidelines, and the panelists are completely free to express what they feel. I shall alternate between metallurgists and physicists, and will start with Dr Krishnan.

**Dr Krishnan:** During the past three days I have informally talked to many of the participants, and I have come to the conclusion that this Meeting has been a unique experience. I suggest it should continue as an annual feature—if not on the same subject, at least on topics of an allied nature.

A general remark I would like to make is that many of the theoretical papers have shown that it is necessary to take the theoretical aspects more seriously and also utilize mathematical and physical concepts in explaining some of the behaviour of materials. On the other hand, I also felt that perhaps it is not necessary to explain some of the well-accepted observations the metallurgists have made. It would be more useful to complement the metallurgists in a suitable manner.

One topic not fully discussed at this Meeting is fracture. Why are we interested in obtaining a better understanding of the physical basis of mechanical behaviour? Essentially it is so that one can design better materials which will withstand service conditions. For instance, one might be interested in designing a material with good fatigue resistance or good creep resistance. We know that materials can fracture in widely different ways—ductile, brittle, cleavage etc. On the opening day, Prof. Ramaseshan has already pointed out how important it is to know the stress corrosion cracking behaviour of materials under service environments.

Take the nuclear field as an example. The iodine produced as a fission product can interact with the zircaloy clad and make the clad susceptible to stress corrosion cracking. The basic question here is: What does iodine do under stress to the grain boundary? Is there a decohesion caused by a lowering of the cohesive energy of the grain boundary which is locally under stress? Is it possible to predict which atomic species (like iodine) are efficient in lowering the cohesive energy? Theoretical studies of this problem coupled with suitable experiments will go a long way in establishing interplay between physical concepts and metallurgical interests.

Another example, again from the nuclear industry, relates to the irradiation creep

behaviour of zircaloy coolant tubes. While the reactor itself has a life span of about 30 years, one is forced at present to change these tubes once in every 12 yrs or so because of irradiation creep. To develop a material that will be good for the entire life span of the reactor, we must perhaps introduce new ideas. One should examine how the texture (*i.e.* the preferred orientation) and grain shape influence irradiation growth of the material. Perhaps, as Prof. Ranganathan suggested, one could use the concept of fractals to characterize grain shape topology—and thus have a better measure for studying and characterizing irradiation growth.

These are some examples of practical problems where there can be a meaningful dialogue between physicists and metallurgists. They involve finding real-time solutions to real-life problems based on an understanding of the basic behaviour of materials.

**Prof Joshi:** Thank you, Dr Krishnan, for pointing out some problems where physicists and metallurgists could come together. We now turn to Dr Sahni.

**Dr V C Sahni:** I would like to go back to the remark which Dr Venkataraman made on the opening day. He was looking at a certain matrix element and trying to find out whether it would be zero or non-zero at the end of the Meeting. Now metallurgists are essentially practitioners. In fact, you would have noticed this from Dr Krishnan's remarks. On the other hand, physicists are a different kind of people. They tend to look behind a phenomenon, try to understand it from an atomistic basis and so on.

An analogy comes to my mind at this point. Consider the automobile engine. Obviously there are (automobile) engineers who design such objects. But there are also people trying to understand the basics of the combustion process *via* tools like Raman scattering. The hope is that such basic studies can lead to the improvement of the efficiency of the engine.

Physicists cannot from the word go come up with solutions to the practical problems of metallurgists. The important thing is they try to analyze the microscopic basis for a particular type of behaviour. In turn, the metallurgist can build on this instead of relying on a phenomenological understanding of the situation. Of course this is the way science progresses.

So, coming back to the point Dr Venkataraman made about whether there is an overlap matrix element or not, I think we really have to look at the interface between the two disciplines. As Prof. Ranganathan's talk clearly brought out, a topic like the large-angle grain boundary is something which physicists can examine from an atomistic point. If some light is shed, then perhaps it will enable the metallurgists to come up with better materials. In short, physicists can *via* tools of their own (like fluctuation spectroscopy) explore microscopic processes which in turn can form inputs to the metallurgical aspects. So my own view is that the matrix element might not be as large as one would hope for, but it is not zero either. I am in agreement with Dr Krishnan that exercises like this Meeting should continue. Hopefully, if we repeat it a couple of times, we may converge on something significant and improve the matrix element in the future.

**Prof. Joshi:** Thank you, Dr Sahni. I think the value of the matrix element depends on the "frame" of reference just as Deepak Dhar pointed out that the length of a coastline depends on the length scale used for measurement. Locally the matrix element is sometimes positive and sometimes negative. What we must all do is to go to a scale where it becomes *globally* positive! I now request Dr Ray to give his views.

**Dr Ray:** Before we try to explain the mechanical behaviour of a material, we must first define the mechanical *state* of the material. Important in this context is a proper description of the grain boundary concerning which Prof. Ranganathan described a beautiful model. However, from the questions that were raised after that talk, I can see that there are limitations to that model. One wonders what the correct description of the situation at the grain boundary should be. May be something will emerge in the future.

One topic on which we did not focus is vacancies, especially their role in defining the mechanical state of matter. Vacancies play an important role as we know from annealing experiments on cold-worked samples. They are also pertinent to certain aspects of plastic deformation.

Next comes the grain shape. We all know that the grain shape is probably important but we do not yet know how to describe it quantitatively. Probably, the fractal concept might help us.

Let us now consider the transition from the elastic to the plastic regime. We used to think of this in terms of dislocations becoming mobile and multiplying. Now they are being described in terms of fluctuations, bifurcations, chaos and what not! Incidentally, I would like to point out that for bcc metals, there is a temperature below which this transition does not take place; for fcc metals however, this does not hold. All facts taken together, the picture to my mind is a bit puzzling. Is the elastic to plastic changeover really a transition or the emergence of a stable fluctuation of a particular kind?

**Prof. Joshi:** Thank you, Dr Ray. I now invite Prof. Kumar who has all along been making illuminating remarks from the floor, to give us his views as a panelist.

**Prof. Kumar:** I believe it is a part of conventional wisdom (which goes back to the Greek philosopher Lucretius) which says that a thing is explained only if it is done in terms of underlying microscopic objects (which, one presumes, exist). This may be a mental bias but no one seriously questions such an approach now. Certainly it is a part of our training as physicists. The question therefore is: What is the appropriate level of microscopy at which we want to discuss the present problems? Certainly you don't start with quantum mechanics if you want to build a house! There must be an "efficient" relationship between the microscopic world and the phenomenon we wish to understand. Of course all phenomena are not easily reducible to microscopic pictures. That we shall bear in mind. Now I shall get down to something specific.

Physicists often work with paradigms. For instance, if we are talking about a solid, we immediately imagine a perfect crystalline lattice and invoke Bloch's theorem. Everything is fine. Any departure from this idealization is a bit unfortunate but we take care of it in terms of a small perturbation. This is an example of an ideal picture that a physicist uses as a paradigm. On the other hand, a metallurgist, confronted as he is with *actual* metals, has his own paradigms. As I understand it now having come here, they mostly have to do with dislocations (which, I believe, live, multiply, climb, pile up and even die!). This is very nice. It is not necessary that dislocations exist; it is enough if they exist as paradigms! For example, quarks most probably do not exist but it is quite convenient to explain all matter in terms of quarks; it is a good mental picture. On the other hand, if we are going to discuss heavily deformed materials, is this paradigm based on dislocation as an elementary object convenient? True there are pictures showing dislocation—they are real objects and they certainly exist. We can even work

out the mathematics of a single dislocation— no problem. I am told the two-body problem also can be done. But what if we have more than two, say 10, 20 or  $10^{11}$ ? That is where the problem lies. Near a large-angle grain boundary, do they retain their imitable integrity or not? If they don't, then we may have to look for something else in terms of which to describe these structures. Prof. Ranganathan did this by resolving the large deformation at the grain boundaries into a big part (DSC) plus a small part (described in terms of dislocation with Burger's vector taken from the DSC). I am happy with this picture. However, a doubt remains in my mind. In a metal, the large deformations at the grain boundaries must surely be sensed and felt by the electrons. If so, are we justified in ignoring the reactions of the electrons to such a heavy distortion? Even geometrically speaking, one wonders whether the dislocation concept is appropriate at a large angle grain boundary where there is such a pile up. Perhaps things are too amorphous-like in that region, and some alternate description should be tried (if not already done). So, the large-angle grain boundary appears to be a problem which physicists would be interested in because this is a case where one paradigm might give way to another.

Aside from this, there is a nontechnical matter that I raise on behalf of Prof. Ramakrishnan, which is: Where do we go from here? We obviously cannot meet time and again just to review work already available in books and journals. The important question is: Are we sure that there are sufficiently important, interesting, nontrivial open problems which physicists would be interested in? As of now, most of us physicists are *not* working on problems of mechanical behaviour. We are looking for the possibility of Discussion Meeting induced transitions. For something worthwhile to emerge, physicists must be willing to give more than 10% of their time. This is a practical issue if we mean business, and I suppose we do!

**Prof. Joshi:** Thank you Prof. Kumar. I now invite comments from the floor. Comments may please be restricted to broad issues or questions rather than matters of specific detail.

**Dr G Venkataraman:** As mentioned by you Prof. Joshi, I would like to make a few broad suggestions. The first of these arises out of a conversation I had with Prof. Ramaseshan at the time when the idea for the present Meeting took shape. Prof. Ramaseshan pointed out that while holding a meeting of this type was fine, everyone would go back and continue working on the same problems as before, instead of exploring the new grounds revealed at the Meeting. He emphasized that if fresh ground is to be broken, it would essentially have to be by young people who have not yet committed themselves to working in an already established area. I have been discussing this question informally during the last three days with several people, and the consensus appears to be that we must organize a regular, pedagogic school wherein young people can be given a systematic introduction that will orient them for research in this area.

Next I would like to point out that the Department of Science and Technology (DST) has identified this subject as a Thrust Area. If good proposals concerning experimental or theoretical research are made to DST, I am sure funds would be forthcoming.

Lastly, as regards future Meetings of this type, my sampling seemed to reveal that: (i) Future Meetings are necessary, (ii) they should not be large, and (iii) the topic of the Meeting should be more specific say like fracture, physics of large deformations etc.

**Prof. Joshi:** If we look at the growth of the interaction between physicists and metallurgists (in this country), we notice that some of it originated right here at RRC. In this Meeting, we heard on the first day a description of some experiments on serrated yielding performed by Dr Rodriguez's group. A theory of serrated yielding was also presented by a physicist from RRC. Maybe the theory was not explicitly motivated by those experiments but the interactions between the Materials Science group and the Metallurgy group must have had some influence. Some catalytic agent is definitely needed to promote such interdisciplinary interaction, may be in the form of an official directive!

I was having a conversation with Prof. Kumar wherein he remarked that when we return from this Meeting, most of us will go back to doing what we were doing earlier! What we do is, I suppose, decided by many factors but the value system is a key one. If one wants to encourage such interaction, then one must attach a value to it. I suggest that physicists and metallurgists in multidisciplinary Institutes like, for example BARC, should experiment in investing some percentage of their time to interdisciplinary activity of this kind. The outcome of such experiments could perhaps be reported at the next Meeting whenever we have it.

Anyway, as far as this Meeting is concerned, it has been a very fruitful one though, as some comments both from the panel and the floor indicate, a few aspects could have been better. But this Meeting has certainly had its utility, and we shall take advantage of whatever we have learnt to augment this interaction.

**Prof. Kumar:** I just want to add something. When I came here, I had a little misgiving in the sense that the subject obviously is an old one. I was aware that eminent physicists like Sir Charles Frank had worked on the subject. The point is that I had a feeling that around the World there must be many physicists working on metallurgy. Now as a physicist, I am not directly involved in this type of work and therefore I just don't know what has already been done. Unfortunately, no one here explicitly pointed that out, and also what has *not* been done. As someone remarked, the natives are not quite stupid! If we are not properly informed about what has already been done, we might end up reinventing the wheel!! Would someone like to comment?

**Dr R Ramaswamy:** I want to say a few things—probably in repetition, and some of them platitudinous perhaps! When a person like me comes to a Meeting like this, he does not necessarily come looking for problems. One comes, one listens to the problems aired, one says what one can, and one contributes. In that sense, I don't think it is valuable for us to seek where we are going *vis-a-vis* conferences of this type because such a conference serves precisely the purpose for which it was arranged *i.e.* to bring together people of different disciplines and see what each one can get out of it. *Of course* we will go back to doing whatever we were doing before. The hope is that the little one might have heard might make *the* difference. Undoubtedly there will be more conferences of this type in the future but whether they should be held or not are spontaneous questions. When Deepak and I go back to TIFR we might well say, "Why are we doing abstract problems? Let us get together with chemists etc". In that case we are the ones who would have benefited. One cannot induce such things; they happen reasonably spontaneously.

**Prof. C K Majumdar:** When I came here, I certainly did so with the purpose of hearing metallurgists because we physicists do not often hear people of other disciplines. It was



certainly educative. The things learnt should not be viewed in terms of immediate return alone because they also broaden your outlook. Even if you go back to doing what you were doing before, your view point would have changed a little and that is a good thing.

Turning to specific suggestions, I think we should have another such Meeting, perhaps in three years. Time scales are a bit long in this country, and probably, it will be at least three years before we can really talk anything new— by new I mean results obtained in *our* laboratories.

Now there are not many places where interdisciplinary work of this type is being done. I for one do not even know where metallurgical work goes on, apart from organizations like RRC, BARC, HAL and the IIT's. Obviously there must be other organizations using at least some metallurgical skills, the State Transport Corporations for example. Judging from the conditions of the buses they ply, there is clearly scope for some technological improvement (!) which could perhaps be done by metallurgists. At the same time, the wayside auto shops seem to manage alright, and they appear to be having a way of accumulating empirical knowledge that is beneficial to their work. In all the training we talk about, we should not forget such people. Somehow they have to be exposed to modern developments. In other countries this is taken care of, and phenomena like exoemission are actually put to practical use by high-technology companies like Lockheed. Details of such applications are often not discussed in the open literature and we have to learn them on our own. History in fact shows that advanced civilizations often keep technology to themselves and do not allow it to percolate to other civilizations. In such cases therefore, we have to learn the hard way.

Not everything in science should be done just for publication or priority. Certain things, even if it means repetition, *have* to be done to make Society run better. Repetition may not actually be a bad thing for in the process one might actually improve on what is already known. I can give you an example. The Chinese apparently had ice cream long before the Europeans knew about it. Marco Polo brought ice cream knowhow from China to Europe, and later the Americans improved it! In short, there are aspects of technology which we have to develop on our own. In that sense, we should find a way of inducing some technologists also to attend such Meetings in the future.

The other thing I would like to comment on is the School that Dr. Venkataraman mentioned. The School should not just involve lectures alone; the students must also get exposed to some experiments. In that case, I think the School should be organized in places like this (RRC) or at the Indian Institute of Science, where there are appropriate facilities.

**Dr K R Rao:** My comments relate to the remarks made earlier by Prof. Kumar. I think many of us would like to go back and actually do something different instead of continuing to do the same thing we have been doing for the last 25 years or so. In this context, I think the identification of unsolved problems is very important. One example comes to mind and that relates to Atomic Data for Fusion Research prepared by the IAEA about four years ago. A huge report has been written identifying hundreds of problems. IAEA has followed up this effort with some funding, and has also been evaluating the data coming out of the various research Centres. Although we are not trying anything on that scale, I feel that if problems are identified and made known say through the Proceedings of this Meeting, it might lead to various people (including

those not present here) picking up the strands. Particularly in the experimental field, there is no reason why some of us cannot try something new, provided new experiments or problems are identified by specialists.

**Prof. V Balakrishnan:** I wish to comment briefly on a point raised yesterday by Prof. Ramakrishnan. In his characteristic fashion, Prof. Ramakrishnan pointed out that it would be useful for solid state physicists to learn the basics of physical and mechanical metallurgy. This is being done in some places but perhaps the exercise could be made more systematic. It is certainly being done with respect to courses on materials science but not so much in the case of solid state physics. As far as the latter is concerned, if one can spend a lot of time on electronic properties then surely a chapter of mechanical properties is reasonable, especially as it will at least get the jargon straightened out for condensed matter physicists. This chapter need not be very long. I noticed that right here on the first day, many physicists expressed to me their concern about the jargon. They could not understand it, but repeated use of the term dislocation seems to have made it familiar enough to most people (rather like the way theorems are established in high energy physics, namely you repeat it often enough and it becomes a theorem)!

In a slightly more serious vein, I think that some simple experiments on mechanical behaviour should also be introduced in the undergraduate curriculum. And there are very dramatic experiments, like the one on work-hardening demonstrated by Bragg in his Royal Institution lectures. A similar one, perhaps already known to some of you, involves closing one end of an open cylinder with a tissue paper, filling it with sand, after which you put a metal rod and apply enormous load on it. We got this set up at IIT recently and I personally along with several other people put my full weight on the rod and the tissue paper did not break because the stress was distributed by those fine grains of sand. Experiments like this bring out beautifully the effect of interfaces, grain boundaries and so on. Perhaps we should spend some time generating ideas for such elementary but very effective demonstrations which will convey to physicists the basic concepts of metallurgy.

**Dr R Chidambaram:** I think what was unique about this Meeting was that it brought a small group of metallurgists and physicists together. Also, unlike other meetings where people come and either give invited talks or present contributed papers, I got the impression that one was expected in this Meeting to talk about problems one had not completely finished or one did not know enough about. Thus, for example, I did not talk about our work on the equation of state— something we know how to handle. Instead, I talked on something in which we had some doubts and in which some metallurgical concepts were involved. If you look at the matrix element which Dr Sahni was talking about, the value of that matrix element must be obtained, I think, by integrating over the personal responses from all the individual participants, as is being done here during the present Panel Discussion. With this in mind, I will tell you what I personally gained from this Meeting. Honestly, I did not expect that the metallurgists would ask the kind of questions they actually asked after my talk. Of course Dr Majumdar raised a point about the entropy equation which I had not written down. If one knew how to write it down, the problem of the structure of the shock front would be solved substantially, but the current state of the art is such that one does not know how to discuss entropy production in the case of shock propagation in solids. On the other hand, after listening to the large number of talks we had on dislocations and grain

boundaries, I think I now have a better perspective on how to think about these physically, in relation to the propagation of a shock front. That way I think this Meeting has been very successful.

As regards the periodicity of such Meetings, I think a Meeting once in three years as Dr Majumdar suggested would be appropriate. And that should be interspersed with a School in which there are lectures both by physicists (theoretical as well as experimental) and metallurgists.

**Prof. Joshi:** Would a metallurgist from the floor like to react? Yes Dr Rodriguez.

**Dr P Rodriguez:** I would like to make a few observations and the first of these relates to Prof. Ramakrishnan's remark that before physicists deal with the real physical nature of problems in complex materials like alloys, they need to develop a better understanding of the basics of physical and mechanical metallurgy. As history shows, metallurgy has been enriched considerably by the work of the physicists, and in fact many physicists have contributed to the study of plastic deformation and the fracture of metals. For example there is the monumental work of Schmidt and Bose on the deformation behaviour of single crystals of fcc metals. Prof. Ramakrishnan showed a picture of such deformation behaviour, and quoting from Bell's work said that metallurgists ignore it but that is really first-year text book material for metallurgist! We start with the deformation behaviour of a fcc single crystal and then extend it to the polycrystal. That is my first point.

People have quoted many things, the old testaments, their heroes, etc!. I will quote George Santayana who said that those who do not learn history will be condemned to repeat it. So let us be careful about not repeating history! Particularly from some theoretical physicists, I got the impression that they would like to apply some newly discovered mathematical formalisms to explain already explained phenomena. I am not stating this as a criticism but it is important that before going ahead with applying a theory or a model one should take stock of the state of the art. This point was made by Prof. Kumar and it is important. One way of achieving this is to organize a course or even write a text book. We have beautiful books on physics for engineers, physics for metallurgists etc. May be it is time to write a book on metallurgy for physicists!

Another aspect that I would like to point out is that in the important area of deformation and fracture behaviour of materials, we have reached a stage of understanding wherein we can now *a priori* design an alloy. This topic, *i.e.* the relationship between microstructure and mechanical properties of alloys has been completely left out from this Discussion Meeting. By microstructure I mean the substructure for example, the distribution of second phases, their morphology, the dislocation density etc. We find that the total dislocation density *per se* is not always the controlling factor, rather the way the dislocations are arranged, *i.e.* whether they are tangled or have a cell-structure. This topic has been completely overlooked. Of course it is obvious that all topics could not have been covered in a Discussion Meeting like this. But this argument shows that there is enough scope to have more frequent Meetings, focussing attention on such specific topics.

**Prof. Joshi:** Since there is a time restriction, I am afraid I have to interrupt and cut short this interesting Discussion!

I will sum up by saying that there is a need for future Discussion Meetings as well as a tutorial School. The duration, the periodicity, the organization, the themes—all these could be left open at the moment.

Being the last speaker permit me to express our grateful thanks to the Organizers of this unique Meeting. I would also like to express our special thanks to our hosts who have taken such good care of us. Finally, I wish to thank the panelists, those who participated from the floor, and the audience in general for making this discussion lively. Thank you all once again!



## Phase transformations—a physicist's perception

G VENKATARAMAN

Reactor Research Centre, Kalpakkam 603 102, India

**Abstract.** Echoing a recent remark by Prof. Ramaseshan, a perspective review is made of the field of phase transformation, highlighting areas that might appeal to physicists. Prominent in this category are the study of ground state structures, the study of phase diagrams and the study of kinetic phenomena.

Enumeration of ground state structures calls for inputs from group theory as well as reliable potentials, and physicists are therefore well equipped to make significant contributions. The theoretical analysis of phase diagrams (concerning which much experimental information already exists) raises challenging questions in equilibrium statistical mechanics. Since the problems map to Ising models of varying complexity and their generalizations, there are also very interesting connections to magnetism. Lately, computer simulation has added a new dimension, opening up fresh vistas both for theory and experiments. The study of kinetics belongs to the newly emerging area of non-equilibrium statistical mechanics. The focus being on *temporal* phenomena, physicists can play a key role, particularly through the application of various types of relaxation spectroscopy. On the theoretical side too there are challenging problems, especially on account of the dominance of nonlinearities. Indeed if one is bold enough, one could even speculate on possible universalities underlying the complex microstructures invariably seen in late-stage evolution. In short, though the subject of phase transformations has thus far been nursed predominantly by metallurgists, there is enough room for physicists to make an independent entry and to make distinctive contributions.

**Keywords.** Phase transformations; phase diagrams; spinodal decomposition; ordering kinetics.

### 1. Introduction

The theme of this paper relates to a remark made by Prof. Ramaseshan at the Baroda Seminar on Thrust Areas in Physics, and it is perhaps relevant to begin by outlining the background.

Around 1980, the Department of Science and Technology (DST) initiated an intensive exercise to identify Thrust Areas in various scientific disciplines. As a part of this, a Seminar was organized in Baroda during November 1981 to which were invited a cross-section of active physicists in the country. Although the ostensible purpose of the Seminar was to aid the DST in identifying areas which it could fund selectively, Dr. Ramanna who presided made the suggestion that since there was a rare gathering of physicists with diverse interests, the occasion should in fact be utilized to draw up something like a National Plan for Physics. A part of this Plan could then be funded by the DST, and the balance by other appropriate agencies. This suggestion was greeted with enthusiasm, and several exciting proposals were unveiled by those present. Intervening in the discussion, Prof. Ramaseshan remarked that while large projects in areas like gamma-ray astronomy or high-energy physics were no doubt to be commended and also needed, some thought should also be given to researchers in small

---

This paper was originally prepared for the 60th birthday volume of Prof. S Ramaseshan.

universities, most of whom remained outside the orbit of "big science". He went on to emphasize that in drawing up a list of Thrust Areas, consideration must also be given to subjects like phase transformations which not only offered challenge but also did not require massive funding and could therefore be pursued by those with modest resources. I was quite delighted by this suggestion and the specific reference to Phase Transformations since I had just then begun to gravitate towards the subject myself.

Now the subject of phase transformations is well established amongst metallurgists. Physicists, on the other hand, have generally stayed away possibly because it appeared messy to them. However, in the light of many recent developments in physics (*e.g.* advances in the understanding of nonlinear phenomena), some of these so-called messier aspects have acquired an attraction of their own. The main purpose of this article therefore is to draw the attention of physicists to such aspects, and hopefully induce at least some of them to enter this area. The paper is thus essentially a perspective review addressed to physicists, keeping in mind the needs of those who may be totally unfamiliar with the subject. However, in the spirit of Prof. Ramaseshan's remarks, interspersed are several suggestions for further work for those adventurous enough to enter the area.

## 2. Preliminaries

### 2.1 Some elementary facts

To most physicists, a phase transition usually calls to mind a change of state like solid to liquid etc. Metallurgists on the other hand, are interested mainly in transformations *within* the solid state. Of the many variations possible even in this category, we restrict attention to order-disorder transformations associated with compositional fluctuations. In the interest of simplicity, we shall further confine ourselves to binary alloys  $A_{1-x}B_x$   $0 \leq x \leq 1$  (*e.g.* Al-Zn or Cu-Au).

To fix our ideas, let us consider a Cu-Zn alloy ( $\beta$ -brass) with equiatomic composition *i.e.*  $x = 0.5$ . Both at high as well as at low temperatures, there is a well-defined lattice (*viz* bcc) associated with this alloy. However, there is a difference in the way the atoms are distributed amongst the lattice sites. Above  $468^\circ\text{C}$ , the occupancy of the lattice sites by Cu and Zn atoms is statistical whereas below that temperature, there is a well-defined order in the arrangement (see figure 1). One can intuitively see that entropy considerations must dominate at high temperatures leading to disorder. On the other hand, interatomic forces assert themselves at low temperatures leading to an ordered structure as in figure 1b. The temperature  $468^\circ\text{C}$  represents a transition point for the order-disorder process.

In the example just discussed, every atom has an atom of the other species as a nearest neighbour in the ordered state, implying that the potential  $v_{AB}$  dominates over  $v_{AA}$  and  $v_{BB}$ . It could also happen that  $v_{AB}$  is not strong enough to achieve this in which case a different type of ordering ensues wherein, the material organizes itself into large crystalline domains rich in either *A* or *B* type atoms. Essentially, "birds of a feather flock together", and the phenomenon is often called *phase separation* or clustering.

Superficially, phase separation and an order-disorder transition (like the one in  $\beta$ -brass) appear different but if we associate a wavelength scale with the two processes as is schematically done for a 1-D example in figure 2, then we can discuss the two in the same framework, as is done for ferro- and antiferromagnetism. Phase separation being

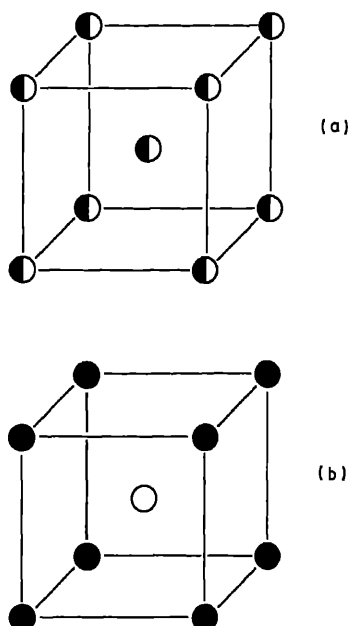


Figure 1. Schematic illustration of order-disorder in  $\beta$ -brass. The structure is bcc in both phases but in the disordered phase, the occupation of the lattice sites by the two species of atoms (shaded and full) is strictly statistical as in (a).

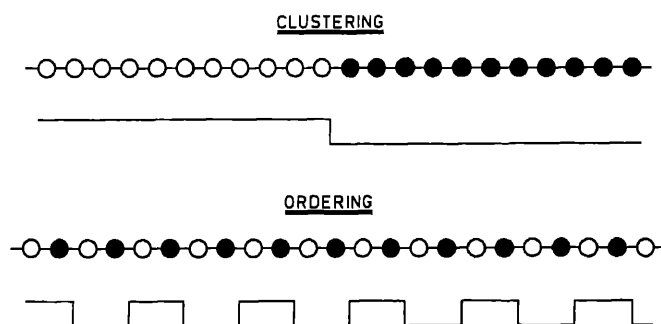


Figure 2. One-dimensional example to illustrate the different wavelength scales for clustering and ordering.

similar to ferromagnetic ordering will be associated with a wavevector  $k \sim 0$  while order-disorder transition being similar to antiferromagnetism will be associated with a wavevector  $k \sim \text{zone boundary}$ .

## 2.2 Phase diagrams—a primer

A study of phase transformations without some knowledge of phase diagrams is hardly possible. Most physicists are no doubt familiar with phase diagrams for monatomic systems but once one enters the world of multicomponent systems, phase diagrams can become quite complex, indeed even for binaries such as we shall be considering. A brief primer on phase diagrams is therefore useful.



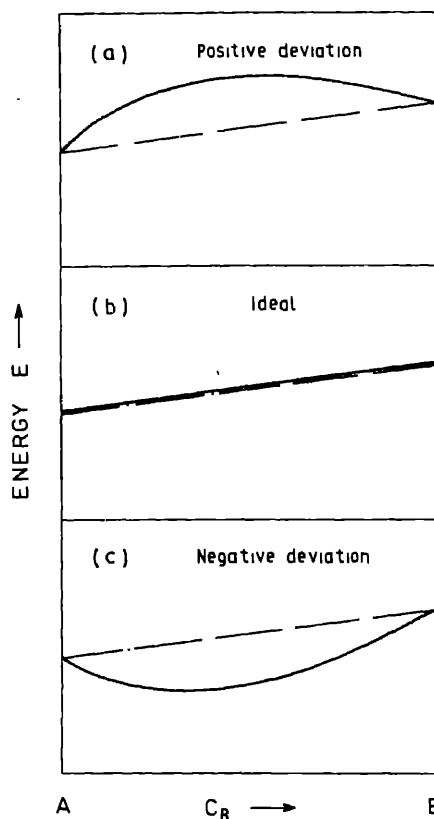


Figure 3. Schematic plot of energy as a function of composition for the three situations discussed in the text.

Broadly speaking, a phase is a state of aggregation. Our interest is in the various phases possible when two atomic species *A* and *B* are mixed together to form a solid at different temperatures and at different compositions. A phase diagram is therefore essentially a map of the various possible states of aggregation in the temperature-composition plane. From thermodynamics we know that the equilibrium state of a system is determined by the minimum of the free energy (*F*) with respect to the appropriate thermodynamic variables. Accordingly, we direct attention now to the minimum of the *F* at various temperatures and compositions. To start with we note that the free energy is given by

$$F = E - TS$$

where *E* is the internal energy\*, *T* the temperature and *S* the entropy. In figure 3, *E* is plotted schematically as a function of composition (Wulff 1971). Here the dashed lines denote the energy before mixing and the solid lines that after the mixing. The 'ideal' situation is that shown in figure 3b where the energy does not change on mixing. More usually, one has either a positive or negative deviation from ideality as in figure 3a or c.

We next consider entropy, for which the situation prior to and after mixing will be as schematically depicted in figure 4. The results of the last two figures may now be

\* Strictly speaking, we should have enthalpy  $H (= E + pV)$  instead of *E*. However, most material processing is done around atmospheric pressure. From a practical point of view therefore *H* is well approximated by *E*.

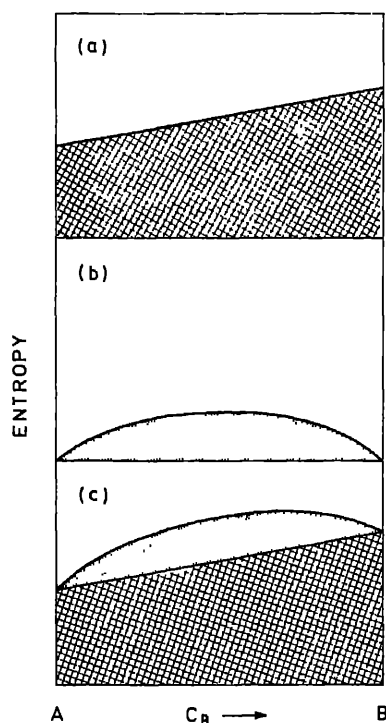


Figure 4. (a). entropy of the  $A_{1-x}B_x$  system before mixing. (b). sketch of entropy of mixing. The total will then be as in (c).

combined to visualize how  $F$  varies with composition at a given  $T$ . Of the several possibilities, that corresponding to negative deviation from ideality is of particular interest to us and the free energy curve for this situation is sketched in figure 5. To find the most stable arrangement that results after mixing at the chosen temperature  $T$  we must obviously look for the minima in  $F$ . Using this criterion, it is clear from the figure that if we prepare a mixture of composition  $c_B$ , then this mixture will be unstable. It will seek stability by splitting into a mixture of two solutions of compositions  $c_B^1$  and  $c_B^2$ . Observe that after such a separation, the  $F$  value diminishes from  $F_u$  to  $F_s$ .

The above scenario applies to all mixtures with composition in the range  $c_B^1$  to  $c_B^2$ , and we conclude that for all compositions in this range, a mixture of two phases is the most stable state. This is the phase separation briefly mentioned earlier. When  $T$  is increased slightly, essentially a similar situation is obtained, with  $c_B^1$  moving slightly away from the  $A$  end and  $c_B^2$  moving slightly away from  $B$ . As  $T$  increases,  $c_B^1$  and  $c_B^2$  approach each other continuously, eventually merging at some temperature  $T_c$ . For  $T > T_c$ , segregation into two phases of different compositions no longer occurs; instead the solid solution itself is stable, and we have a one-phase region. Thus, the locus of  $c_B^1$  and  $c_B^2$  in the temperature-composition plane provides a boundary separating the one-phase and two-phase regions of the solid. Figure 6 shows a portion of the phase diagram of Al-Zn where such a two-phase region exists.

It is of course not necessary that when two atomic species are mixed, one should always get phase separation at low temperatures. Instead one could also obtain ordering, as *e.g.* in Cu-Au systems. We shall have more to say later about these two

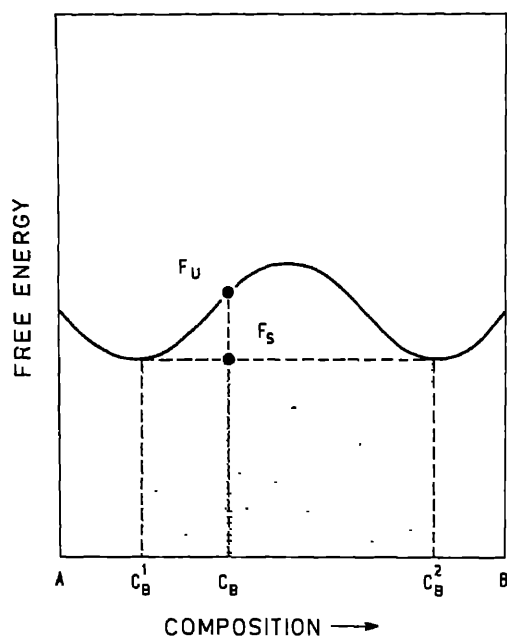


Figure 5. Free energy curve corresponding to a particular temperature for negative deviation from ideality.  $F_u$  is the value corresponding to the unstable state created immediately after mixing, while  $F_s$  is the value corresponding to the stable state. For every composition in the shaded region, the terminal state is a mixture of two phases of compositions  $c_B^1$  and  $c_B^2$ .

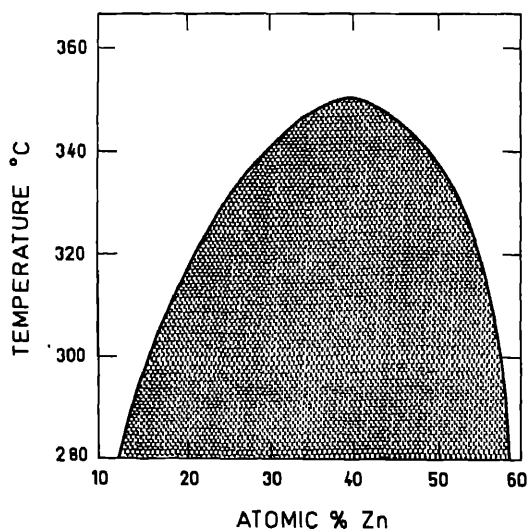


Figure 6. Portion of the Al-Zn phase diagram showing the two-phase region.

representative cases of phase separation and ordering.\* For the nonce let us note that the solid mixtures we are considering are restricted to the substitutional type *i.e.* if we take a perfect *A* type solid and add *B* type atoms, the latter replace *A* at the lattice sites. For this to be possible, the following criteria must be broadly satisfied:

\* Phase separation is *also* a type of ordering! Only the wavelength scale is different.

(i) The atomic radii of the two elements must be within 15% of each other. (ii) The crystal structures of *A* and *B* must be the same. (iii) The valence of *A* and *B* must not differ by more than unity. (iv) The electronegativity must be nearly equal.

While we have sketched the concept of the phase diagram from (elementary) theoretical considerations, we should remember that metallurgists often actually map phase diagrams by doing experiments. Indeed there is a wealth of such data (Hansen 1958), and, as we shall see later, a theoretical analysis of such diagrams is a possible avenue of interest for physicists.

### 2.3 Areas of interest

Given the fact that metallurgists have already contributed much to the subject, especially on the experimental side, it is natural to wonder whether there is any room for physicists (*e.g.* Chen *et al* (1979) point out that prior to the late sixties, there were at least 36 books and reviews on the subject. Also, there have been several major conferences held on the subject during the last decade). However, a careful appraisal does show that there are certain areas in this vast domain where physicists could bring to bear tools that are their specialities. Prominent among these areas are:

(i) The elucidation of ground state structures, (ii) Calculation of phase diagrams, and (iii) The study of kinetic phenomena.

Of the above, the calculation of phase diagrams belongs to the realm of equilibrium statistical mechanics, and, as we shall see in § 3, raises problems in the traditions of Onsager since one mainly deals with Ising models of various complexity. The study of kinetic phenomena on the other hand, takes one to the newly emerging area of nonequilibrium statistical mechanics. The presence of nonlinearities is an added attraction.

In terms of tools, apart from neutron and x-ray scattering which are already familiar, physicists could also exploit various types of relaxation spectroscopy. No doubt the scattering techniques have already been used to some extent in the past but there is considerable scope for enhancing their applications. Particularly in the case of x-rays, the recent availability of synchrotron radiation opens up many new exciting possibilities. Also, there are many technical innovations like position-sensitive detectors that have hardly been used for such studies. As far as relaxation spectroscopic studies are concerned, the field is literally wide open. Complementing all these is the powerful technique of computer simulation, used already to some extent, but admitting of considerably more exploitation. In short, there is plenty of scope for physicists to make a distinctive contribution of their own to the field, although they may be latecomers.

## 3. Equilibrium structures

### 3.1 Ground state structures

Given a disordered structure (say belonging to the fcc lattice), there arises the general question of the type of ordering that will occur at lower temperatures. In a simple situation as in  $\beta$ -brass (see figure 1), one could perhaps have made a good guess of the ordered structure purely from inspection. However, such guesses are not always easy,

requiring, as they do, considerable crystallographic insight. A systematic approach to enumerating the possible ordered structures has been evolved by Soviet scientists, inspired largely by Landau's theory of phase transitions.

Before sketching the work of the Soviet School, we note first that the ground state structure is the atomic arrangement assumed by the solid at absolute zero of temperature. While it is the onus of theory to predict this structure from first principles, a considerable body of information about the structures actually occurring in Nature has already been accumulated through diffraction experiments. Next we remark that ordering is essentially characterized by the appearance of a superlattice. The superlattice structure that emerges depends on (i) the structure of the parent lattice, (ii) the interatomic forces, and (iii) the atomic composition of the system. If, for example, we consider the fcc lattice, then several ordered structures based on it are possible some of which are illustrated in figure 7. The distribution of the various superlattices possible amongst the alloys realizable by combining various elements in the periodic table have been painstakingly compiled by Kozlov *et al* (1974) and the data is worth glancing through.

Returning to the enumeration of possible superlattice structures, the basic idea is the following: Let us first describe the atomic distribution by means of a function  $n(\mathbf{r})$  which gives the probability of finding an atom of some definite kind at site  $\mathbf{r}$  of the lattice. In a disordered alloy  $n(\mathbf{r})$  is a constant  $c$ . On the other hand, when the system orders,  $n(\mathbf{r})$  assumes  $m$  (say) different values  $n_1, n_2, \dots, n_m$  at the  $m$  sublattices associated with the structure. In brass, *e.g.*,  $m = 2$ . Of course,  $n(\mathbf{r})$  corresponding to a particular sublattice position has the same value in all the unit cells. The problem now is to determine the possible distribution  $n(\mathbf{r})$  can have when ordering occurs. Khachaturyan (1974) approaches this by regarding  $n(\mathbf{r})$  as being built up of static composition waves as follows:

$$n(\mathbf{r}) = C + \frac{1}{2} \sum_{\mathbf{k}} \{ Q(\mathbf{k}) \exp(i\mathbf{k} \cdot \mathbf{r}) + C.C. \}. \quad (1)$$

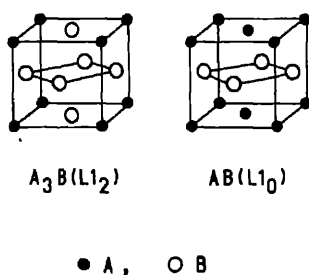
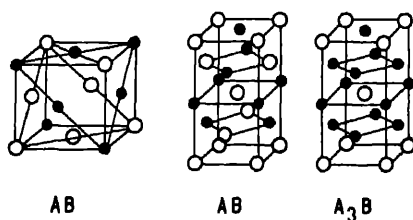


Figure 7. Some of the ordered structures observed in fcc lattices.



Here the summation over  $\mathbf{k}$  runs over the first Brillouin zone of the disordered alloy.  $Q(\mathbf{k})$  is the (complex) amplitude of the concentration wave of wavevector  $\mathbf{k}$ . Following Landau, one now writes the sum over  $\mathbf{k}$  as sums over various possible stars one can form in the Brillouin zone (see figure 8). With this regrouping,

$$n(\mathbf{r}) = C + \sum_s \eta_s \varepsilon_s(\mathbf{r}), \quad (2)$$

where

$$\varepsilon_s(\mathbf{r}) = \frac{1}{2} \sum_i \{ \gamma_s(\mathbf{k}_i(\star s)) \exp i \mathbf{k}_i(\star s) \cdot \mathbf{r} + \text{C.C.} \}. \quad (3)$$

In (3), the summation runs over all the members  $i$  of the star  $s$  whereas in (2) the sum is over all the possible stars. Together, all the wavevectors in the Brillouin zone are accounted for. Comparing with (1)

$$Q(\mathbf{k}_i) = \eta_s \gamma_s(\mathbf{k}_i). \quad (4)$$

The quantities  $\eta_s$  are the long-range parameters which assume the value 0 in the disordered state, and the value 1 at 0°K. Since composition is conserved, the number of order parameters required to describe the ordered structure will be  $(m - 1)$ . Later (in § 3.3) we shall see that the order parameters  $\eta_s$  are essentially the analogues of sublattice magnetizations.

Although formally the summation in (2) ranges over all the stars in the Brillouin zone, in practice (—and this is in the spirit of Landau's theory of phase transition) one

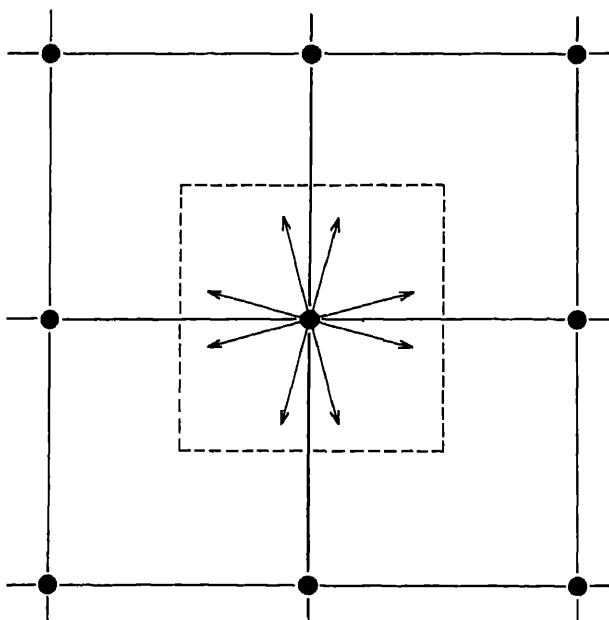


**Figure 8.** Illustration of the concept of star of the wavevector for a square lattice. The dots indicate the reciprocal lattice points, and the dashed line the central Brillouin Zone. The cluster of eight arrows represents a star. Starting from any one of these arrows, one can generate the entire cluster by a systematic application of the point group operations of the lattice.

supposes that a given ordering is associated uniquely with composition waves corresponding to a particular star. For illustration, let us consider ordering in Cu-Au alloys. X-ray experiments have revealed that ordering is linked to the appearance of superlattice  $\{100\}$  reflections (which, of course, are forbidden in the disordered state). It is reasonable therefore to suppose that the ordering is governed by the star of the wavevector  $[100]$  which comprises of the wavevectors  $[100]$ ,  $[010]$  and  $[001]$ . Thus (2) can be written as

$$n(\mathbf{r}) = C + \eta \{ \gamma_1 \exp(i\mathbf{k}_1 \cdot \mathbf{r}) + \gamma_2 \exp(i\mathbf{k}_2 \cdot \mathbf{r}) + \gamma_3 \exp(i\mathbf{k}_3 \cdot \mathbf{r}) \}. \quad (5)$$

where  $\mathbf{k}_1$ ,  $\mathbf{k}_2$  and  $\mathbf{k}_3$  are the three wavevectors of the star. The lattice vector  $\mathbf{r}$  can be expressed in terms of the (cubic) unit cell vectors  $\mathbf{a}_1$ ,  $\mathbf{a}_2$ ,  $\mathbf{a}_3$  as

$$\mathbf{r} = x\mathbf{a}_1 + y\mathbf{a}_2 + z\mathbf{a}_3 \quad (6)$$

with  $(x + y + z) = \text{constant}$ . By letting  $\mathbf{r}$  vary in (5), it is easily seen that  $n(\mathbf{r})$  can take the following values

$$\begin{aligned} n_1 &= C + \eta(\gamma_1 + \gamma_2 + \gamma_3); & n_2 &= C + \eta(\gamma_1 - \gamma_2 - \gamma_3); \\ n_3 &= C + \eta(-\gamma_1 + \gamma_2 - \gamma_3); & n_4 &= C + \eta(-\gamma_1 - \gamma_2 + \gamma_3). \end{aligned} \quad (7)$$

If now we invoke the fact that  $(m - 1)$  equals the number of distinct order parameters and remember that in this case there is only one order parameter, namely  $\eta$ , we are led to the fact that  $m = 2$  for Cu-Au. Hence  $n$  can take only two values at the set of all sites  $(xyz)$  of the fcc lattice, leading to the two possibilities

$$(i) \ n_1 = n_4, \ n_2 = n_3; \quad (ii) \ n_2 = n_3 = (n_1 + n_4). \quad (8)$$

The first alternative arises if  $\gamma_1 = \gamma_2 = 0$  whence

$$n(xyz) = C + \eta\gamma_3 \exp(2\pi iz) = C \pm \eta\gamma \quad (9)$$

in alternate (001) planes. This is the so-called CuAu I structure. On the other hand, if alternative (ii) is to be realized, then we must have all the  $\gamma_i$ 's equal whence

$$\begin{aligned} n(xyz) &= C + \eta\gamma \{ \exp(2\pi ix) + \exp(2\pi iy) + \exp(2\pi iz) \} \\ &= \begin{cases} C + 3\eta\gamma & \text{at the corners of the unit cell cube} \\ C - 3\eta\gamma & \text{at the face centres.} \end{cases} \end{aligned} \quad (10)$$

This is the  $\text{Cu}_3\text{Au}$  structure.

The above example shows how symmetry considerations may be applied a la Landau's theory to obtain some idea of the superlattice structures possible. Merely enumerating possible superlattice structures alone is not enough. This is somewhat similar to the exercise often done for ferroelectrics, where one uses group theory to enumerate the type of ordered structures that can arise. Symmetry thus picks out the various possibilities; which of these is actually favoured depends of course on the interatomic forces. To illustrate, we once again consider the fcc lattice, and direct attention now to the internal energy. The three potentials to be considered are,  $v_{AA}(r)$ ,  $v_{BB}(r)$  and  $v_{AB}(r)$ . In terms of these pair potentials, the internal energy  $E$  may be expressed as

$$\mathcal{E} = \frac{1}{2} \sum_{ij} \sum_{l \neq m} v_{ij}(l-m) \langle \sigma_i(l) \sigma_j(m) \rangle. \quad (11)$$

Here  $i, j$  refer to the species  $A, B$  while  $l$  and  $m$  denote lattice sites. The quantity  $\sigma$  is an occupation operator defined by

$$\begin{aligned}\sigma_A(l) &= 1 && \text{if site } l \text{ is occupied by an A-type atom} \\ &= 0 && \text{if site } l \text{ is not occupied by an A-type atom.}\end{aligned}\quad (12)$$

$\sigma_B(l)$  is defined similarly. The bracket denotes an average (here over the ground state). The lattice energy will evidently be determined by the correlations of the  $\sigma$ 's at the various sites, and the system will choose that atomic configuration for which  $\mathcal{E}$  is a minimum.

It is convenient to introduce an operator  $\gamma_i(l)$  which describes deviations from mean occupation by

$$\gamma_A(l) = \sigma_A(l) - c_A = \begin{cases} 1 - c_A, \\ -c_A, \end{cases}\quad (13)$$

where  $c_A$  is the concentration of  $A$ . Since  $c_A + c_B = 1$ , one has

$$\gamma_B(l) = -\gamma_A(l). \quad (14)$$

Using the  $\gamma$ 's, the part of the internal energy that relates to occupation deviations can be written as

$$E = \frac{1}{2} \sum_{ij} \sum_{l \neq m} v_{ij}(l-m) \langle \gamma_i(l) \gamma_j(m) \rangle. \quad (15)$$

By elementary manipulation, this can be written as

$$E = \frac{1}{2} \sum_{lm} V(l-m) \langle \gamma(l) \gamma(m) \rangle, \quad (16)$$

where we have written  $\gamma$  for  $\gamma_A$ , and  $V$  is an effective potential defined by

$$V(\mathbf{r}) = 2v_{AB}(\mathbf{r}) - v_{AA}(\mathbf{r}) - v_{BB}(\mathbf{r}). \quad (17)$$

In terms of Fourier transforms

$$E = \frac{N}{2} \sum_{\mathbf{k}} V(\mathbf{k}) |\Gamma(\mathbf{k})|^2 \quad (18)$$

where  $\Gamma(\mathbf{k})$  is the transform of  $\gamma(\mathbf{r})$ .

The quantity  $V(\mathbf{k})$  is periodic in reciprocal space reminiscent of, say, phonon dispersion curves, and will therefore have maxima, minima and saddle points (—the well-known van Hove (1953) singularities). The expectation now is that the state of order is governed primarily by where minima in  $V(\mathbf{k})$  occur. One knows that barring unusual circumstances, minima of lattice periodic functions occur at points of high symmetry in the Brillouin zone (van Hove 1953). Thus, ordering is mainly associated with the build up of a compositional wave (also sometimes called concentration wave) with a wavevector corresponding to the special point where  $V(\mathbf{k})$  has a minimum. This therefore is also the wavevector at which a superlattice reflection is seen in the diffraction pattern when ordering occurs. As may be expected, around the transition temperature there are critical fluctuations of the composition in this region of  $\mathbf{k}$ -space and consequently there is an enhancement of the scattering in the superlattice reflection region just prior to ordering. We shall say more about critical scattering later.



The potential  $V(r)$  depends on the details of the electronic structure, and is often not known with sufficient accuracy for present purposes. It is therefore customary to parametrize pair interactions in terms of interactions up to a specified set of neighbours. One now examines minima in  $V(k)$  as the ratio ( $V_2/V_1$ ) is varied (where  $V_1$  and  $V_2$  denote the first and second neighbour interactions). The results can be succinctly paraphrased as in figure 9 due to Clapp and Moss (1968) who followed Villain (1959) who had earlier made such plots for magnetic structures. Incidentally, we see from figure 9 that in a certain range of ratios, ordering occurs for  $k = 0$  leading to clustering of like atoms.

Mention should also be made of the work of Richards and Cahn (1971) and various Japanese workers (Katsura and Narita 1973; Kudo and Katsura 1976; Kanamori and Kakehashi 1977) who have studied ground-state structures using a real-space analysis. Recently some rigorous methods for describing low temperature structures of very general lattice systems have also been developed (Progov and Sinai 1975, 1976; Holsztynski and Slawny 1978; Slawny 1979).

Although some territory has no doubt been covered in the work of the various above mentioned authors, there is considerable scope for further work. One might wonder whether ground-state structures are not encompassed in a study of the phase diagram as a whole (§ 3.2). Indeed they are; however an independent knowledge of ground state structures does help phase diagram calculations and in that sense is a worthwhile, stand-alone activity.

Before leaving the subject, a brief reference must be made to off-stoichiometric structures. Suppose, for instance, we consider an alloy where, say, the concentration of  $A$  species is slightly less than 0.5. The question now is what happens in the ordered state. One's first guess would be that small deviations from stoichiometry would be absorbed as defects. However, when the deviations are substantial, the situation may not be that

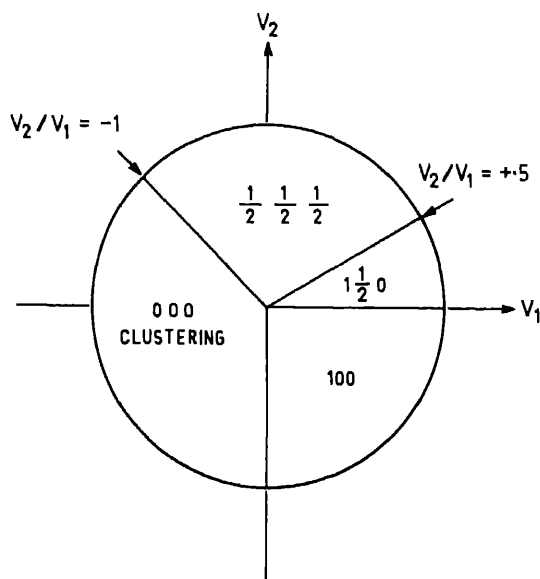


Figure 9. Location of minima of  $V(k)$  as a function of the ratio  $V_2/V_1$  for the fcc lattice. (After Clapp and Moss 1968).

simple. Krivoglaz and Smirnov (1965) suggested that at 0°K, an off-stoichiometric alloy decomposes into alloy of stoichiometric composition and a pure metal. It is not clear whether there is any experimental evidence in support of this suggestion. Kozlov *et al* (1974) have advanced the alternate idea that the excess atoms may undergo further ordering at suitable sites, leading to a new complex structure which they refer to as 'super-superstructure'. The experimental situation if assessed from the literature, can be quite bewildering to a physicist! When an alloy is prepared at high temperatures and cooled below the transition, it not only orders but develops a lot of microstructure; one has therefore to be quite careful in drawing the right conclusions.

One case worth mentioning explicitly is CuAu (nominal equiatomic composition). When this alloy is cooled from high temperatures, it transforms below 385°C into what is called the CuAu II structure illustrated in figure 10 (Ogawa 1974). There is an alternation every five cells, and the overall structure can be thought of as composed of antiphase domains of size  $5b$ . The oscillations are also referred to as long period oscillations (LPO). Such oscillations are reported for many ground state structures, and, in view of the extensive interest amongst physicists on charge density waves etc. are worth a close look (see also § 4.5). Returning to LPO's in Cu-Au alloys, there is evidence that the period  $2M$  is not always an integral number (see figure 11) (Ogawa 1974). Noteworthy here is the fact that  $M$  varies with composition (which effectively alters the electron/atom ratio). There is also a lattice modulation of density related to the LPO. This, as well as the nonintegral values observed for  $M$  are interesting questions (Sato and Toth 1961) but unfortunately we cannot pursue them further here.

Another comment that needs to be made concerns the effective potential  $V(r)$  in (17). Now an implicit assumption underlying (15) is that all ions always exactly occupy the lattice sites. In practice this is not so, and ions could deviate, *e.g.* on account of size. One must therefore allow for such 'positional relaxation', and evaluate the energy of the relaxed system. In effect, it amounts to modifying  $V(k)$  as

$$V(k) \rightarrow V^{(1)}(k) = V(k) - \text{relaxation energy.} \quad (19)$$

Of course if the potential is parametrised, then the parameters refer actually to the effective potential  $V^{(1)}$ . For further details concerning the relaxation energy, a recent article by de Fontaine (1979) may be consulted.

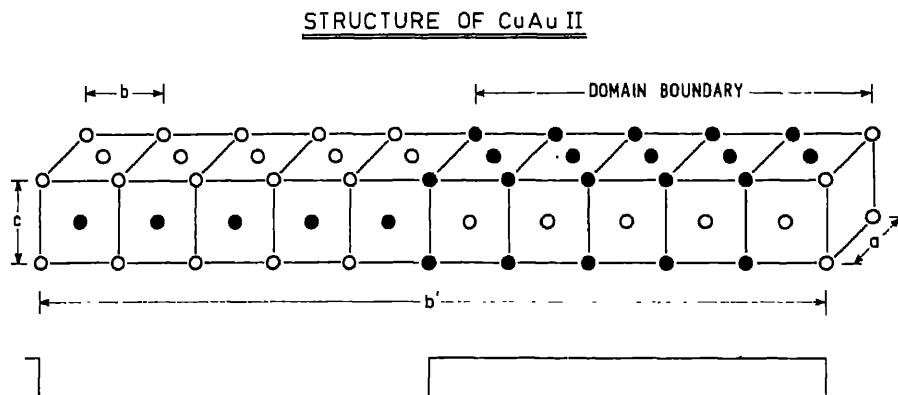


**Figure 10.** Illustration of the long-period oscillation in CuAu II. After every five cells, there is an alternation in the occupancy pattern (after Ogawa 1974).

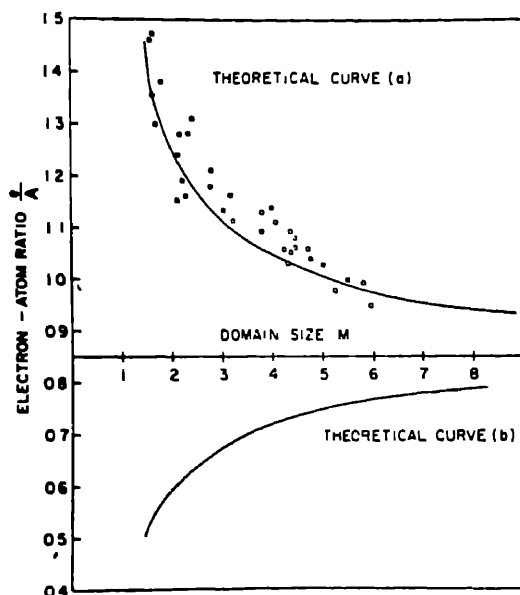


Figure 11. Variation of  $M$  with electron to atom ratio. The solid lines are theoretical curves (due to Sato and Toth 1961) corresponding to two assumptions (after Ogawa 1974).

### 3.2 Calculation of phase diagrams

The phase diagram problem is a logical extension of the ground state problem in that one now studies when order disappears.

It is convenient to discuss the problem in the language of Ising spins rather than in terms of the occupation operators  $\sigma$  introduced earlier. The Ising spin operator  $S_l$  associated to lattice site  $l$  is defined in terms of  $\sigma_B(l)$  as

$$S_l = 1 - 2\sigma_B(l) = \begin{cases} +1 & \text{if site } l \text{ is occupied by an } A \text{ atom} \\ -1 & \text{if site } l \text{ is occupied by a } B \text{ atom.} \end{cases} \quad (20)$$

Observe that in terms of  $\sigma_A(l)$ ,

$$S_l = 1 + 2\sigma_A(l). \quad (21)$$

Using the Ising spins to describe the Hamiltonian, the statistical mechanics of order-disorder can now be mapped into an appropriate Ising problem, establishing links with the rich traditions that already exist in this area.

Now at absolute zero of temperature, the spin system will be perfectly ordered. As the temperature is raised, some spins will flip (meaning  $A$  and  $B$  atoms will exchange places). Such flips no doubt cost energy but the entropy term  $-Ts$  in the expression for free energy provides the required compensation. However, the disorder cannot be increased indefinitely, and at every temperature there is an optimum disorder. If the disorder exceeds the optimum, then  $F$  increases due to increase of  $E$  whereas if it is less, then it again increases but due to inadequate cancellation from the entropy term. Equilibrium is thus dictated by the minimum of the free energy, and in the calculation

of the phase boundaries, the computation of this minimum is an important step.

Given the range of interaction of the Ising spins, the calculation of  $E$  is straightforward (and is discussed further in § 3.3). Far more problematical is the entropy term, and to appreciate the difficulty let us consider a 1-D Ising chain. We assume first that the chain is fully ordered (!) with all spins up (say). The entropy is then zero. At the other extreme where each spin is completely free to flip, there are  $2^N$  configurations possible ( $N$  is the number of spins), and the corresponding entropy is  $S = k_B \log 2^N = Nk_B \log 2$ . The question is how does one calculate the entropy for situations in between where there is intermediate order. If, for example, we *definitely* know two spins alone are down and all the rest up then the number of configurations possible is a simple matter to work out. But unfortunately, we cannot make definitive statements about exactly how many spins are up and how many are down. We can at best have only statistical information about the state of order embodied in the correlation functions

$$\xi_1 = \langle S_i \rangle; \quad \xi_2 = \langle S_i S_m \rangle; \quad \xi_3 = \langle S_i S_m S_n \rangle \dots \quad (22)$$

The set  $\{\xi_i\}$  must first be known and using it the entropy and indeed  $F$  itself must then be computed. Calculation of  $S$  in terms of the  $\xi$ 's is precisely where problems enter, for one must in principle know and use all correlation functions up to  $\xi_N$ . This evidently is also the place for approximations to make their entry!

Before discussing the approximations, we call attention to Onsager's (1944) famous paper on the 2-D square lattice Ising problem where he calculated the partition function exactly. This is not only a *tour de force* but also a touchstone for evaluating various approximation schemes (as we shall soon see).

The approximation schemes alluded to, reduce in effect to using a suitable subset of the full set  $\{\xi_i\}$  of the correlation functions. The subset is so chosen that the group of spins involved form a cluster which is consistent both with the geometry of the lattice and the range of interactions (usually restricted to near neighbours ( $nn$ ) and next nearest neighbours ( $nnn$ )).

Figure 12 gives samples of some clusters used in the study of ordering in fcc Ising lattices. In figure 12a the cluster is a regular tetrahedron made up of  $nn$  spins. In figure 12b one has a  $nn$  regular tetrahedron and an octahedron consisting of  $nn$  and  $nnn$  spins. Within a cluster itself one can identify subclusters *e.g.* the triangle (123) in figure 12b, which is in the overlap of the tetrahedron and the octahedron. Likewise, the triangle (126) in figure 12c is a subcluster shared by two irregular tetrahedra.

The entire computational scheme based on cluster approximation is known as the cluster variation method (cvm). As formally developed by Morita (1972), it is based on the exact variational principle of equilibrium statistical mechanics. In any given implementation of the cvm, one first chooses the largest cluster  $L$  one is going to work with. One then considers all the subclusters  $l$  consistent with  $L$ . Corresponding to each subcluster  $l$ , one now considers the various possible arrangement of spins/atoms. For instance, the arrangement in the triangle (123) could be  $(AAA)$ ,  $(ABA)$ ,  $(BAB)$  etc. If  $J_l$  denotes a configuration such as above, then we next need to know  $x_{J_l}(l)$  the concentration of this configuration in the cluster  $l$ . It is in the calculation of the cluster configuration that the correlation functions enter. To illustrate, we again consider the triangular subcluster (123). Let  $p_1$ ,  $p_2$  and  $p_3$  denote the lattice sites. The correlation functions we then need are the single spin, two spin and three spin functions  $\xi_1$ ,  $\xi_2$ ,  $\xi_3$

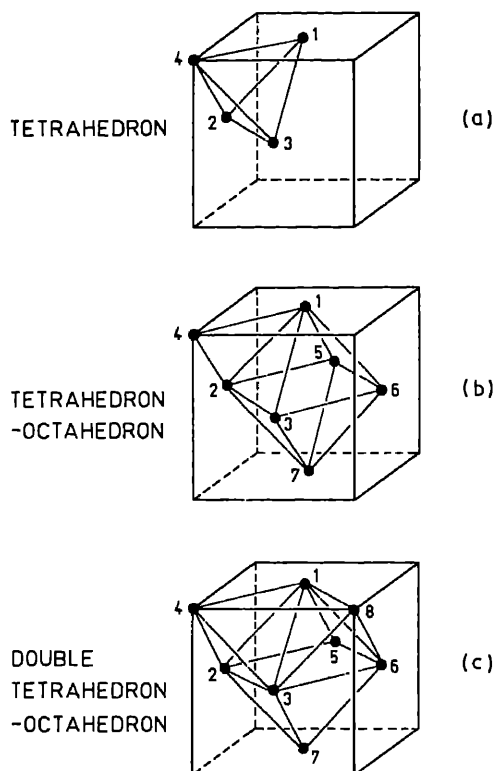


Figure 12. Some of the clusters used in CVM calculations for fcc lattices (a). tetrahedron used by Kikuchi *et al* 1980 (b) and (c) are larger clusters used by Sanchez and de Fontaine (1978, 1980, 1982).

respectively. In terms of these correlation functions,  $x_{AAB}$ , for example will be

$$x_{AAB} = \frac{1}{8} \{ 1 + (+1 + 1 - 1)\xi_1 + [(1 \times 1) + (1 \times -1) + (-1 \times 1)]\xi_2 + (1 \times 1 \times -1)\xi_3 \}. \quad (23)$$

The formal expressions for the cluster probabilities are:

$$\begin{aligned} x_i(p_1) &= \langle \sigma_i(p_1) \rangle = \frac{1}{2} \langle 1 + iS_{p_1} \rangle, \\ x_{ij}(p_1 p_2) &= \langle \sigma_i(p_1) \sigma_j(p_2) \rangle \\ &= \frac{1}{2^2} [1 + i \langle S_{p_1} \rangle + j \langle S_{p_2} \rangle + ij \langle S_{p_1} S_{p_2} \rangle], \\ x_{ijk}(p_1 p_2 p_3) &= \langle \sigma_i(p_1) \sigma_j(p_2) \sigma_k(p_3) \rangle \\ &= \frac{1}{2^3} [1 + i \langle S_{p_1} \rangle + j \langle S_{p_2} \rangle + k \langle S_{p_3} \rangle + ij \langle S_{p_1} S_{p_2} \rangle \\ &\quad + jk \langle S_{p_2} S_{p_3} \rangle \\ &\quad + ki \langle S_{p_3} S_{p_1} \rangle + ijk \langle S_{p_1} S_{p_2} S_{p_3} \rangle] \text{ etc.} \end{aligned} \quad (24)$$

Here  $i, j, k \dots$  take on values  $\pm 1$  for each of the two components in the system. (Result (23) thus readily follows from above).

The entropy can now be expressed as a series in cluster probabilities as

$$S \approx Nk_B \sum_{l=1}^L \gamma_l \sum_{j_l} x_{j_l}(l) \log x_{j_l}(l) \quad (25)$$

where  $\gamma_l$  is an appropriate coefficient (Barker 1953). Once the clusters have been identified and their concentrations or probabilities evaluated, the rest is largely numerical, and will be described shortly.

Historically, one of the early attempts at explaining the order-disorder transformations is due to Bragg and Williams (1934, 1935). Domb (1981) narrates an interesting story concerning these famous papers. Apparently, Bragg gave a seminar in 1933 in Manchester during which he qualitatively described his thoughts on how ordering occurred in binary alloys. Williams, a member of the audience, presented Bragg with a mathematical outline of Bragg's theory at the end of the lecture. (The story of the Rushbrook inequalities is similar! See Stanley 1971). Bragg was impressed but felt that the calculation was so simple, it surely must have been published earlier. However, no such paper had yet appeared and so Bragg and Williams proceeded to publish their ideas!

In the cvm language, the Bragg-Williams theory retains only  $\xi_1$  or point clusters. Next comes the Bethe approximation (1935) which includes pairs *i.e.* also  $\xi_2$ . From these early beginnings, the push has always been towards larger clusters. Modern applications of the cvm have been promoted largely by de Fontaine and coworkers, building upon schemes originally developed by Kikuchi (1951), Barker (1953) and van Baal (1973). Before describing some of these recent results, we refer to figure 13 which gives a feel for the improvements available in going to larger clusters in 2-D square lattice, where Onsager's exact result is available as a bench mark.

Turning now to phase diagrams calculations for real alloys, the main steps in the calculational schemes as implemented at present are as follows (de Fontaine 1982):

- (i) Choose the basic lattice system, the range of interactions and the largest cluster to be used. Form then the  $\xi$ 's.
- (ii) Construct the thermodynamic potential  $\Omega$  (also called the grand potential) defined by

$$\Omega = F - \frac{1}{2}(\mu_A - \mu_B) \sum_l S_l \quad (26)$$

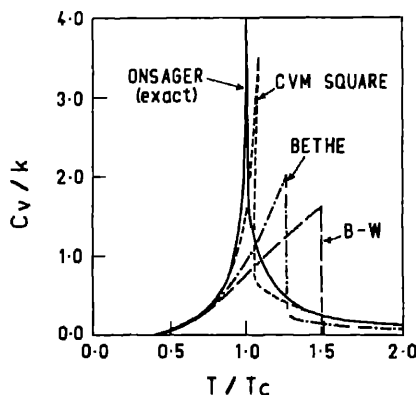


Figure 13. Specific heat variation for the square-Ising lattice. Onsager's result is the exact one. Observe the improvement in going from the Bragg-Williams approximation to the cvm square cluster approximation.

where the  $\mu$ 's are the chemical potentials of the two atomic species. The chemical potential term is required since we would like to permit concentration  $C_B$  to vary (while the total number of atoms is fixed).

(iii) For a fixed  $(T, \mu \equiv 1/2(\mu_A - \mu_B))$ , minimize  $\Omega$  with respect to the  $\xi$ 's considered *i.e.* the set of  $\xi$ 's consistent with the largest cluster  $L$  chosen.

(iv) When  $\Omega$  is minimized, it leads to a set of (nonlinear algebraic) equations for the  $\xi$ 's. Solve these equations.

(v) Use the  $\xi$ 's obtained in step (iv) to compute the equilibrium potential  $\Omega_{\text{eqbr}}$ .

(vi) Plot  $\Omega_{\text{eqbr}}$  vs  $T$  for fixed values of  $\mu$  for the different phases. The point  $(T, \mu)$  at which two curves cross is a point of phase coexistence. An example is given in figure 14.

(vii) Vary  $T$  and  $\mu$  and establish the locus of phase coexistence *i.e.* the phase boundaries.

(viii) Every intersection between the  $\Omega$  curves for two phases,  $\alpha$  and  $\beta$ , say, gives two values of the point correlation function  $\xi_1$ . From these, determine the average concentrations  $c_B^\alpha$  and  $c_B^\beta$ .

(ix) Assemble the results into phase diagrams in the  $(T, \mu)$  and  $(T, c)$  planes.

Following Iliopoulos (1980), one might also add:

(x) Publish your result,

(xi) Choose another alloy system and GO TO (i)!

The cvm has been extensively applied by Kikuchi, de Fontaine and coworkers, from whose contributions we will now cite a few examples. Firstly in table 1 (de Fontaine 1979) we summarize some results obtained for Ising ferromagnets (which, incidentally, are isomorphous to  $AB$  binary solutions; recall earlier remarks about the correspondence between magnetic systems and alloy systems).

Next we consider results for ordering. Kikuchi *et al* (1980) have obtained the phase diagram for the Cu-Au system using  $nn$  interactions for the Ising spins, and a tetrahedron cluster. The calculated phase diagram is shown in figure 15b which is to be

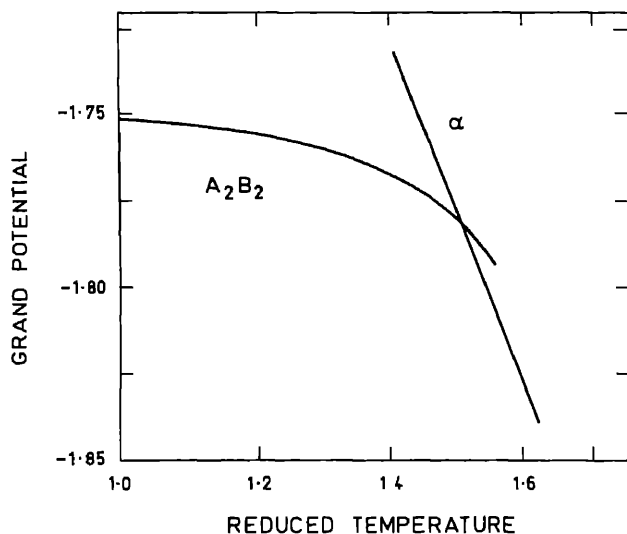


**Figure 14.** Variation of the grand potential with temperature for the  $A_2B_2$  and disordered ( $\alpha$ ) phases, for zero chemical potential ( $c_B = 0.5$ ). The intersection gives the temperature value at which the two phases coexist. (after de Fontaine 1982).

**Table 1.** Calculated normalized transition temperature in units of  $k_B T/zJ$  where  $J$  is the strength of the nearest neighbour interactions and  $z$  the number of nearest neighbours (after de Fontaine 1979).

	2D Square lattice	2D Triangular lattice	3D Simple cubic	Remarks
$z$	4	6	6	
Bragg-Williams (point)	1.0	1.0	1.0	all refer to transition temperatures
cv Bethe (pair)	0.7212	0.8222	0.8222	
cv square or triangle	0.6057	0.62525	0.7683	
cv cube or tetrahedron	—	—	0.7628	
Exact (or best known)	0.567	0.6062	0.7522	

compared with the experimentally determined one (figure 15c) and that calculated by Shockley (1938) using the Bragg-Williams approximation (figure 15a). While those not used to phase diagrams may regard the agreement between cvm and experiment fair, the comparison is actually quite impressive given the approximations involved.

Sanchez and de Fontaine (1978) have gone beyond the tetrahedral approximation to the clusters illustrated in figure 12b and c, and investigated (Sanchez and de Fontaine 1980, 1982) the phase diagram for the  $\langle 1\frac{1}{2}0 \rangle$  family of ordered superstructure *i.e.* lattices where ordering is associated with a  $\langle 1\frac{1}{2}0 \rangle$  compositional wave. In addition to the usually considered  $nn$  interactions, the  $nnn$  interactions were also included. Results have been obtained for a range of values of the ratio of second-to-first-neighbour pair interactions in the range 0 to 0.5. The results are relevant for ordering in diverse systems like Ni-Mo, Ni-V etc. Incidentally, a knowledge of the ground state structure is very helpful in testing out a particular ordered state as in figure 14.

These calculations by de Fontaine and coworkers have shown the distinct superiority of the cvm over earlier models in yielding realistic results. For instance, in Cu-Au systems, the Bragg-Williams approximation predicts a first-order transition for  $\text{Cu}_3\text{Au}$  ( $L1_2$  ordering) and a second-order transition for  $\text{CuAuI}$  ( $L1_0$  ordering), whereas experimentally the transition is of first order for both the stoichiometric compositions. The Bethe approximation is even worse, and predicts no transition at all. The cvm does much better and predicts correctly a first order transition for both. The main advantage of the cvm is that reasonably accurate results are obtained without too much computational effort (—much of this has no doubt been due to the exercise of ingenuity in arriving at the practical computational scheme). In the results reported thus far, about 30 to 70 nonlinear algebraic equations had to be solved but it was not taxing. However, numerical difficulties were found at low temperatures where some of the cluster probabilities tended exponentially to zero. Where transition temperatures are concerned, the cvm does a respectable job, judging from the 3-D cubic Ising ferromagnet for which independent, reliable results are available from high-temperature expansion methods (table 1). But where exponents are concerned, cvm predicts only classical ones for higher-order transitions. This is not unexpected since the method is built around equilibrium correlation functions and does not include fluctuations. It is perhaps not out of place here to mention that Mahan and Claro (1977) have used the real-space renormalization-group approach to calculate a CuAu-type



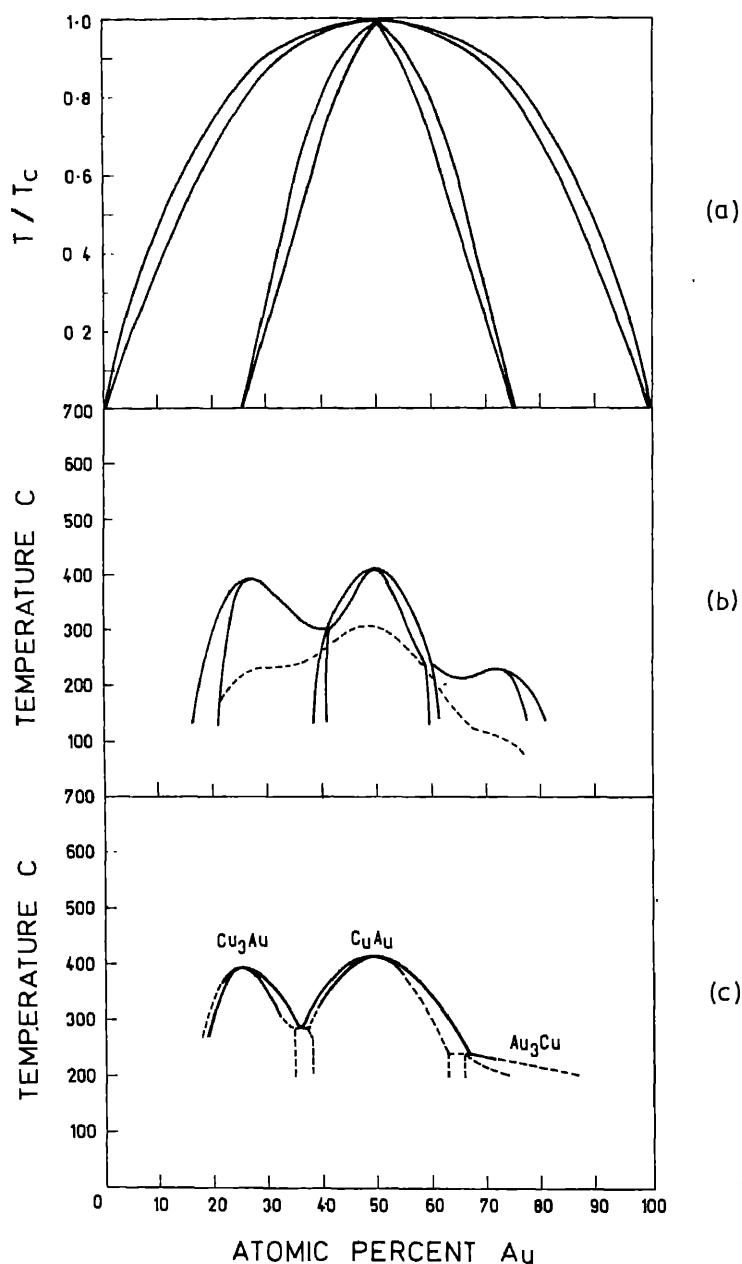


**Figure 15.** Phase diagram for the Cu-Au system (a), results obtained by Shockley (1938). (b), shows the CVM results of Kikuchi *et al* (1980). For comparison, the experimental results are given in (c) (Hansen 1958).

phase diagram. The results are however poor in that the ordering of  $\text{CuAu}$  ( $L1_0$  ordering) is not predicted and the ordering of  $\text{Cu}_3\text{Au}$  ( $L1_2$  ordering) is predicted to be of second order.

The stage is now set to consider a totally different approach to the calculation of phase diagrams *viz.*, that of computer simulation.

### 3.3 Phase diagrams and computer simulation

As in several other branches of physics, computer simulation has proved extremely useful in unveiling various subtle aspects relating to phase transformations. In this subsection, we review the work done in relation to phase diagrams while in a later section, we shall touch upon studies in kinetics.

The basic idea is to start with a representative Hamiltonian that describes configuration interactions, and then use a Monte Carlo technique to deduce the structure appropriate to specific thermodynamic conditions. Since the problem is formulated in the Ising-spin language, there are understandable links with many magnetic problems.

To obtain the desired Hamiltonian, we go back to (11), the expression for internal energy. Adding to it a chemical potential term  $(\mu_A - \mu_B) \sum_l \sigma_B(l)$  as earlier, we have

$$\mathcal{H} = \frac{1}{2} \sum_{ij} \sum_{l \neq m} v_{ij}(l-m) \langle \sigma_i(l) \sigma_j(m) \rangle + (\mu_A - \mu_B) \sum_l \sigma_B(l). \quad (27)$$

Introducing Ising spins as in (20), the Hamiltonian in (27) can now be transformed (barring a constant term) as

$$\mathcal{H} = \sum_{l \neq m} J_{lm} S_l S_m - H \sum_l S_l, \quad (28)$$

where

$$J_{lm} = -\{v_{AA}(l-m) + v_{BB}(l-m) - 2v_{AB}(l-m)\}/4, \quad (29)$$

is the exchange integral for Ising spins, and

$$H = \frac{1}{2} \sum_{m(\neq l)} \{v_{AA}(l-m) - v_{BB}(l-m)\} + \frac{1}{2}(\mu_A - \mu_B), \quad (30)$$

is an 'external' field acting on the Ising spins.

As it stands, the spin at site  $l$  interacts with spins at all other sites  $m$  in the lattice. To make the problem tractable, one restricts, as earlier, the range to the nearest and next nearest neighbours so that  $\mathcal{H}$  now is given by

$$\mathcal{H} = -J \sum_{(nn)} S_i S_j + \alpha J \sum_{(nnn)} S_i S_j - H \sum_i S_i. \quad (31)$$

The parameter  $(-\alpha)$  is a measure of the relative strength of the  $nnn$  interaction.

One now takes a system of  $N = 4L^3$  spins on a fcc lattice with periodic boundary conditions. In the actual simulation,  $N$  was  $\sim 15000$ . Next one specifies an initial configuration  $X_0 = \{S_1, S_2, \dots, S_N\}$ , the choice of which will be discussed shortly. Using pseudo random numbers, one then generates a random change of configuration  $X_0 \rightarrow X_1$ . There are two ways of achieving this, depending on what ensemble one works with. If one is using a canonical ensemble, then the total 'up' spin as well as the total 'down' spin must be individually conserved. Hence  $X_0 \rightarrow X_1$  is achieved by choosing at random a nearest neighbour  $AB$  pair and exchanging spins. This 'Kawasaki dynamics' (Kawasaki 1972) conserves the concentration  $c_B$  of the system. In the case of the grand canonical ensemble, the magnetic field is held constant and  $X_0 \rightarrow X_1$  is implemented via the flip  $S_i \rightarrow -S_i$  of a randomly chosen spin. These spin fluctuations are equivalent to fluctuations of  $c_B$ . As is well-known, both ensembles should yield

results equivalent to each other in the thermodynamic limit  $N \rightarrow \infty$ . Working with finite  $N$  as in simulation experiments, it is important to verify that the results do not depend on the ensemble chosen. Having produced a change  $X_0 \rightarrow X_1$ , one now computes (in both cases) the energy change  $\delta U = \mathcal{H}(X_1) - \mathcal{H}(X_0)$  resulting from the configurational change. The transition probability for such a change is

$$W = \exp(-\delta U/k_B T) / \{1 + \exp(-\delta U/k_B T)\}, \quad (32)$$

which is compared to a random number  $\eta$  chosen uniformly from the interval  $(0, 1)$ . If  $W > \eta$ , the transition is performed; otherwise the old configuration is counted once more for the averaging, the attempted  $X_1$  is rejected, and another transition is tried. The Monte Carlo steps (MCS) are repeated till an equilibrium distribution is obtained. To achieve convergence within a few thousand MCS, it is necessary to choose the initial state  $X_0$  appropriately.

Two groups, namely that of Lebowitz and of Binder have been active in studying phase diagrams by simulation. Recently they merged their efforts to make a detailed study of a system that is a prototype for Cu-Au alloys (Binder *et al* 1981). Since this is the most comprehensive study to date, we shall present some results from it.

In this work, nearest neighbour interactions alone were considered *i.e.*  $\alpha$  was set equal to zero. The initial state was variously chosen as ferromagnetically ordered state, a disordered state or an antiferromagnetic state, as appropriate. Runs using the canonical ensemble were done at various fixed compositions  $c_B$ , and for each composition, runs were taken at several temperatures (actually at several values of  $k_B T/|J|$ ). The grand canonical ensemble runs were done for various fields corresponding to a fixed temperature, and the temperature was subsequently varied. The quantities monitored were, (i) the internal energy, (ii) the net magnetization  $m$  and (iii) the order parameter  $\tilde{m}$ . In terms of the sublattice magnetization  $m_v$  ( $v = 1, 2, 3, 4$ ) defined by

$$m_v = (1/N) \sum_i \langle S_{i,v} \rangle, \quad (33)$$

over  $v$ th sublattice

$m$  is given by

$$m = m_1 + m_2 + m_3 + m_4, \quad (34)$$

while  $\tilde{m}$  is given by

$$\begin{aligned} \tilde{m} &= m_1 + m_2 - m_3 - m_4 && (AB \text{ structure}) \\ &= m_1 + m_2 + m_3 - m_4 && (A_3B \text{ structure}). \end{aligned} \quad (35)$$

Figure 16 shows a plot of magnetization as a function of the applied field. When  $H$  is zero, there is no magnetization. As  $H$  is increased,  $m$  also increases, and the increase would have been linear (dashed line) if the system were disordered. Instead, the  $m$  value stays below the dashed line indicative of order until a field  $H'_C$  is reached when it jumps.  $H'_C$  is thus a critical field required to derive the system to disorder. Order sets in again at  $H''_C$  and disappears at  $H_C$ . The order parameter variations are also shown in figure 16, from which the field-induced transitions (at a fixed temperature) are clearly evident.

Figure 16 is what is termed 'raw data' by Binder *et al* (1981). For several such data, the phase diagram of the Ising antiferromagnet was constructed as in figure 17. Noting that  $\sigma_B(l) = (1 - S_l)/2$ , the average concentration  $C_B$  of  $B$  atoms in the alloy is related to  $m$  by  $C_B = (1 - m)/2$ . Therefore, the diagram of figure 17b which is the phase diagram

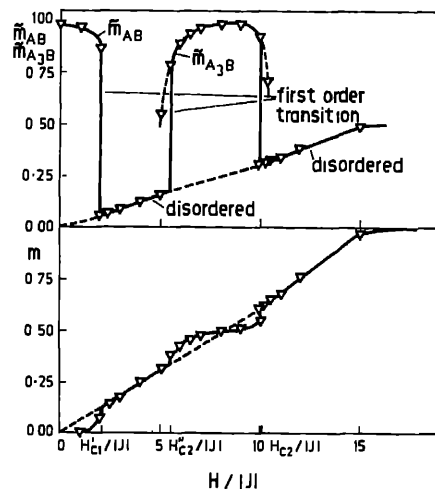
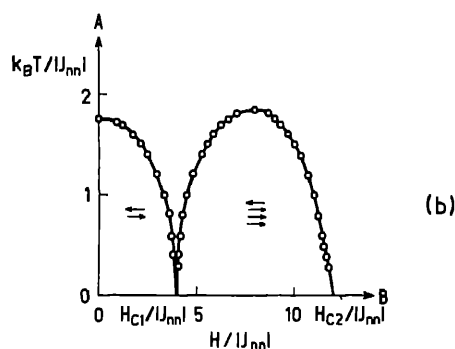
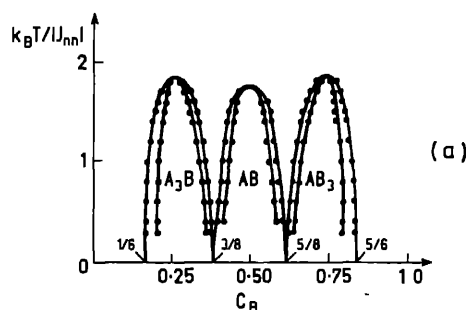


Figure 16. Order parameter (top) and magnetization (bottom) for the nearest neighbour Ising antiferromagnet plotted as a function of the field for the temperature  $T_{k_B}/|J| = 1.5$ . Estimates for the three critical fields  $H_{C1}^*$ ,  $H_{C2}^*$  and  $H_{C2}$  are also indicated. (after Binder *et al* 1981).



(b)

Figure 17. (a) Phase diagram of the nearest neighbour fcc lattice in the temperature-composition plane. Ordered structures are indicated. All transitions are of first order. (b) Phase diagram in the temperature-field plane.



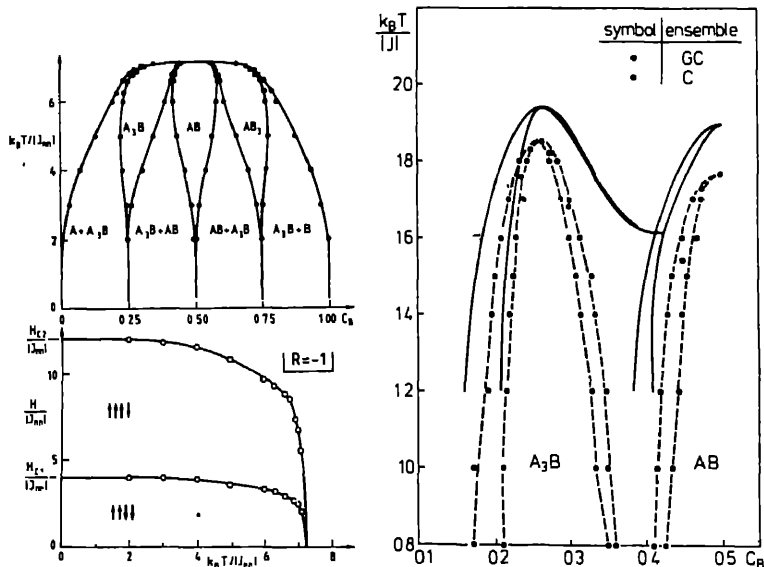
(a)

for an Ising antiferromagnet in a magnetic field can be mapped to the temperature-composition plane as in figure 17a to yield a phase diagram appropriate to the alloy  $AB$ . The two-phase regions shown here arise from the fact that for certain values of the field,  $m$  is multivalued.

Recently, Binder (1981) has extended the above work to include  $nnn$  interactions also. The phase diagram is now considerably altered (see figure 18), a noteworthy feature being the occurrence of a multicritical point at  $H = 0$ . This is an interesting finding in view of a recent theoretical prediction that such a point arises out of a meeting of lines of 3- and 4-state Potts model-like transitions.

Returning to the implications for the alloy problem, the broad finding is that simulation corroborates cvm results as is explicitly brought out in figure 19. At stoichiometric compositions, the two methods come fairly close to each other. This has also been noted from limited simulations done for  $\alpha = 0.25$ . The feeling therefore is that stoichiometric alloys are rather insensitive to the parameters of the model as well as the accuracy of the approximations used. Study of off-stoichiometric systems (both experimentally and theoretically) may be more worthwhile. In this context, Binder (1980a) has proposed that one could, for example, explore short-range order as a function of composition (see figure 20). Measurements of this type would provide a valuable test of whether a model faithfully represents a real system. Another useful hint to emerge from these studies is that the interaction parameters are probably composition dependent. In other words, the same exchange integral  $J(r)$  cannot be used over the entire composition range. The possibility of 'frustration' is yet another interesting finding. To understand this, we refer to figure 21 which shows two neighbouring cells of the  $A_3B$  structure. Focussing attention on the spin at the centre of the common plane, it is found that four of its bonds to  $nm$  are energetically favourable while the other eight are unfavourable. Therefore at the critical field  $H'_C$ , this spin can be overturned at no cost. One has essentially a 'frustration-type' of situation here since the central spin is under conflicting orders. Binder *et al* (1981) therefore advocate improvements to theoretical methods so as to handle frustration.

As of now, the computer simulation method has some limitations. Being time consuming, it cannot be applied for wide ranging explorations as, for example, the cvm. Also the treatment of the configurational entropy is crude. However, there is no doubt that valuable insight has been gained from whatever has been done so far. And it is also



Figures 18-19. 18. (Left) Phase diagram of the next nearest neighbour Ising antiferromagnet in the  $T$ -field and  $T$ -composition planes. Observe that the simulated diagram is still far from experiment. (after Binder 1981). 19. (Right) Comparison of the phase diagram for the fcc binary alloy as obtained by simulation and the cvm results (after Binder *et al* 1981).

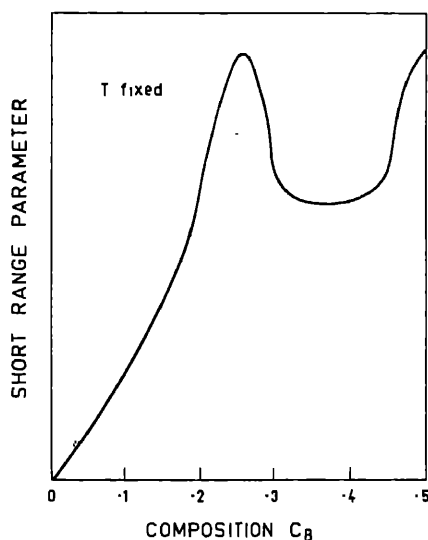


**Figure 20.** Schematic plot of the variation of the (Cowley) short-range order parameter as a function of concentration. The temperature is fixed, and below  $T_c$ . The sharp variations are related to the crossings of the phase boundaries. See also figure 45 (after Binder 1980a).

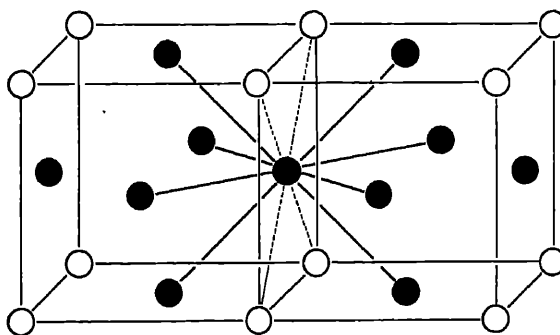


**Figure 21.** Illustration of the concept of a 'spin' under conflicting orders and thereby becoming 'loose' at the critical field. For explanations, see text. According to Binder *et al* (1981) such a 'conflict' leads to a frustration-type of situation as in spin glass (after Binder *et al* 1981).

clear that simulation will always be required both to complement as well as to continually spur experiment and theory.

#### 4. Kinetic phenomena

We turn our attention now to phenomena that occur when one either approaches a phase boundary or crosses it. As is to be expected, there will be manifestations of critical phenomena in the neighbourhood of a transition across the boundary, and such critical effects have indeed been observed even in the twenties. For instance, Johansson and Linde (1928) found that the electrical resistivity of  $\text{Cu}_3\text{Au}$  rose sharply with increasing temperature around  $390^\circ\text{C}$ , the transformation temperature. One could therefore envisage extensive studies on critical exponents related to the vast variety of

transformations possible. It is however unlikely that such studies while *very useful* will reveal anything fundamentally *new* concerning the *basic universalities* under lying critical phenomena since the cream has in a sense already been skimmed off. Far more interesting is the study of dynamic phenomena following a quench as it raises questions in nonequilibrium statistical mechanics, currently an active area.

In systems such as we are interested in, quenching (notionally) causes a step function change of temperature. However, although the phonons have readjusted, the atoms are unable to follow suit and occupy their new equilibrium positions with such rapidity. Positional readjustments involve large scale migration of atoms through diffusive processes, necessarily requiring some time. Thus, immediately after a quench, the system is left in a highly non-equilibrium state. It then coasts down (with the atoms readjusting their positions), eventually attaining equilibrium. Studies made during the coastdown can shed valuable light on the behaviour of systems far from equilibrium. The attendant nonlinearities make such investigations even more interesting.

In this Section, we shall review progress in the understanding of such kinetic phenomena and also indicate questions that still await solutions.

#### 4.1 Linear kinetics

The broad question one faces is: What exactly happens after a quench? There is no simple universal answer to such a question for much depends on whether one is considering the early- or the late-stage behaviour, whether it is a clustering or an ordering system, etc. We shall deal with some of these complications as we go along. For the present we will offer a qualitative picture assuming the system responds linearly to the forces set up following the quench (—a bad assumption!).

Let  $c_B$  be the average concentration of the  $B$  species and  $c(r, t)$  the distribution (of the  $B$  species) in the quenched alloy. It is convenient to consider  $c(k, t)$  the Fourier transform of the composition fluctuation  $[c(r, t) - c_B]$ .  $c(k, t)$  thus represents a compositional wave of wavevector  $k$ . If the system behaves linearly, then each Fourier component has an evolution history that is completely delinked from those of the others. The task now reduces to formulating an equation of motion for  $c(k, t)$  and solving it. Thanks to the linearity assumption, one has (Cahn 1961, 1968)

$$c(k, t) \sim \exp[\alpha(k)t], \quad (36)$$

where  $\alpha(k)$  depends on the forces acting in the quenched system. If  $\alpha$  is negative, the fluctuations decay but if  $\alpha$  is positive the fluctuations grow, in fact indefinitely, indicative of an instability in the system. The question therefore is: How does  $\alpha(k)$  behave as a function of  $k$ , and, in particular, is it positive for certain values of  $k$ ? The latter would depend of course on the instabilities.

Figure 22 shows some schematic plots of  $\alpha$  both above and below the transition temperature for a clustering as well as an ordering system (Cook *et al* 1969). We notice that  $\alpha$  becomes positive only below the transition temperature. Only then do certain fluctuations grow to giant proportions, driving the system to a totally new state altogether. For a clustering system  $\alpha$  becomes positive near the zone centre, whereas for an ordering system it becomes positive in the neighbourhood of the superlattice position associated with the ordering process.

Now fluctuations cannot really grow in an unbounded manner, and such growth is in fact arrested by nonlinearities. Another way of saying this is that the different Fourier

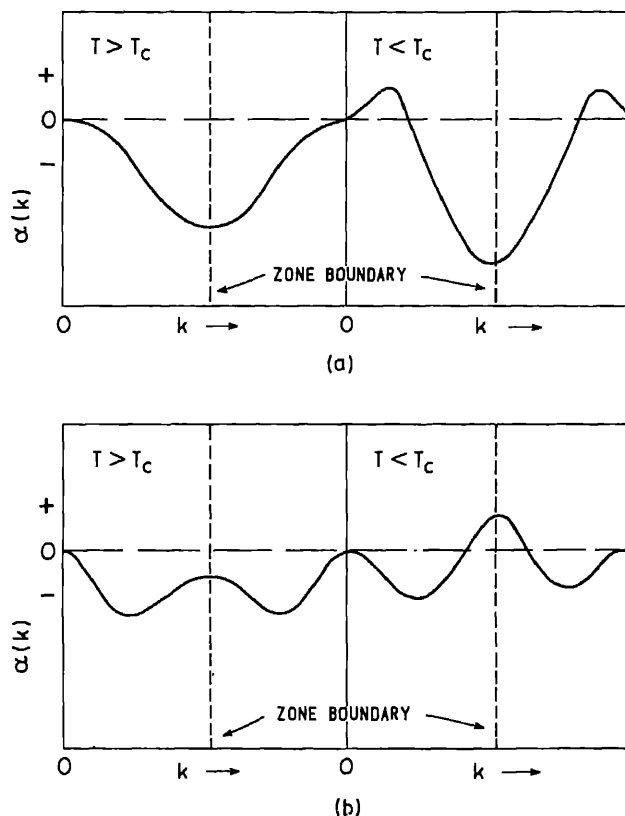


Figure 22. Schematic plot of  $\alpha$  above and below the transition temperature  $T_c$  (a). situation for a clustering reaction, where  $\alpha$  becomes positive below  $T_c$  around  $k=0$ . In an ordering reaction on the other hand,  $\alpha$  becomes positive in the region of the superlattice reflection. The region where  $\alpha$  becomes positive is related to the region where  $V(k)$  has a minimum (after Cook *et al* 1969).

components start interacting with each other, checking runaway growth. While the concept of a 'linear' amplification factor  $\alpha(k)$  does become blurred to some extent in the presence of non-linearities, it certainly is meaningful in the disordered region at least.

Some interesting experiments on 'disordering kinetics' have been performed to obtain plots of  $\alpha(k)$  and they are worth a brief mention (Paulson and Hilliard 1977). In these experiments, a multilayer film several thousand Angstroms thick was prepared by alternately depositing two elements (*e.g.* Cu and Au) in the desired proportions. The as-deposited composition modulation produces satellite peaks in an x-ray diffraction pattern. One now upquenches the specimen, taking it into the one-phase region. The modulation then progressively disappears due to the interdiffusion of the atomic species. By monitoring the time-dependence of the intensity of the satellite peak,  $\alpha(k)$  can be obtained. The wavelength of the modulation can be varied by controlling the deposition, and in this way  $\alpha(k)$  can be studied as a function of  $k$ . A typical plot so obtained is shown in figure 23. We shall return again to the amplification factor for clustering systems in § 4.3.

Linear theories essentially provide first-order answers. They are reasonably adequate



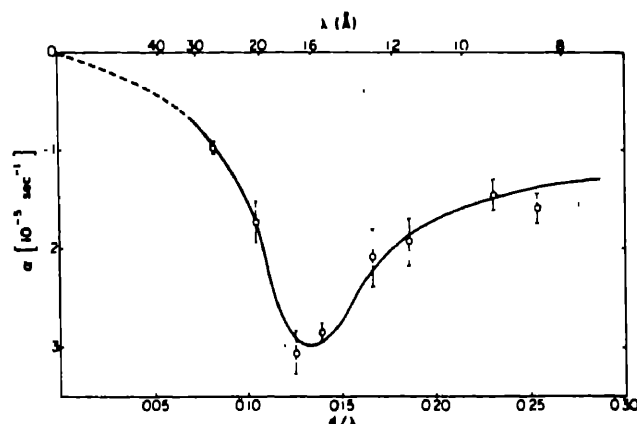


Figure 23. Amplification rates  $\alpha$  vs  $\lambda$  observed at 225°C in thin films of Cu-16 at % Au (after Paulson and Hilliard 1977).

in the disordered region where *all* fluctuations decay, and one does not encounter runaway situations. However, such theories are inadequate as one approaches the critical region; and in the ordered region, they totally fail to describe the kinetics.

#### 4.2 Beyond linear theories

For answers beyond linear theories one should look to nonequilibrium statistical mechanics, and presently we shall consider some general aspects. To provide a framework for the discussion, we shall suppose the free energy density  $f$  to be given by

$$f(x; a, b) = \frac{1}{2} ax^2 + \frac{1}{4} x^4 + bx. \quad (37)$$

This is the Ginzburg-Landau form, together with a magnetic field term  $bx$ . The quantities  $a$  and  $b$  are the control parameters while  $x$  is the order parameter. Our  $f$  here is equivalent to the grand potential discussed in § 3.

Our first interest is in the minima of  $f$ , and the locus traced by them as  $a$  and  $b$  are varied. In the language of catastrophe theory (Gilmore 1981), the minima are the critical points of  $f$ . The various critical points of  $f$  are obtained as follows:

nondegenerate crit. pt.	$(df/dx) = 0$ i.e. $x^3 + ax + b = 0$	
two-fold degenerate		
crit. pt.	$(d^2f/dx^2) = 0$ i.e. $3x^2 + a = 0$	
three-fold degenerate		
crit. pt.	$(d^3f/dx^3) = 0$ i.e. $6x = 0$	(38)

It is easily seen from above that the locus of the doubly degenerate critical points is given by (Gilmore 1981)

$$(a/3)^3 + (b/2)^2 = 0. \quad (39)$$

This 'fold curve' also called the separatrix is sketched in figure 24, and it divides the parameter space into two regions representing functions with one critical point and functions with three critical points. This feature is made explicit with representative

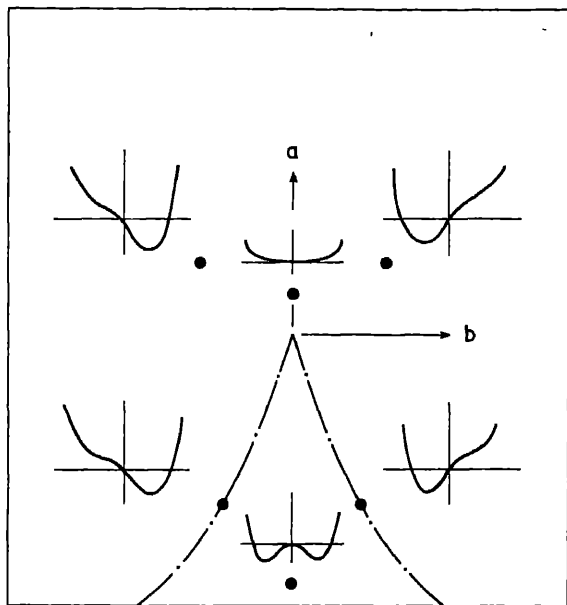


Figure 24. Sketch of the fold curve for  $f$  given by (37). Also shown are representative plots of  $f$  vs  $x$  for the various points in the  $(a, b)$  plane indicated by dots (after Gilmore 1981).

plots for  $f$  corresponding to various points in the  $a$ - $b$  plane. The origin represents the function  $f = (x^4/4)$ , and corresponds to a three-fold degenerate critical point.

It is helpful also to have some idea of certain surfaces associated with  $f$  (Gilmore 1981; Kikuchi and de Fontaine 1976). These are (i) the critical manifold defined by  $(df/dx) = 0$ , (ii) the critical value surface  $f_c$  made up by the values assumed by  $f$  when  $\nabla f = 0$  and (iii) the critical curvature surface defined by  $(d^2f/dx^2) = 0$ . Sketches of these surfaces are given in figure 25, and they aid the analysis of system behaviour following a disturbance to the system. Thus, for instance, the critical curvature surface is useful while discussing the stability of the system.

In nonequilibrium phenomena, the state of the system is governed by  $f$  which often changes for one reason or the other. In this changing situation, the system attempts to find a minimum appropriate to the prevailing conditions but when several minima are available, the question naturally arises regarding which minimum the system jumps to. Two extremes are possible as illustrated in figure 26. In figure 26a the system remains in a stable or metastable equilibrium state until that state disappears whereas in figure 26b the system always chooses the global minimum. Between these two limiting conventions, many other possibilities exist. Which of these conventions operate in a given situation depends on the relative values of the barrier height  $\Delta E$  and the noise level  $N$ . If  $N/\Delta E \ll 1$ , then the delay convention is observed while if  $N/\Delta E \gg 1$  the Maxwell convention operates (figure 27).

Another way of looking at a system evolution is *via* the probability distribution function  $P(x, t)$ . Figure 28a shows a schematic plot of  $f(x)$  at some instant of time while figure 28b depicts  $P(x, t)$  for that same instant. Notice  $P$  peaks away from the minimum, typical of a nonequilibrium situation. As time evolves,  $P(x, t)$  will seek to attain a form appropriate to equilibrium. There are two characteristic times  $T_1$  and  $T_2$  associated with

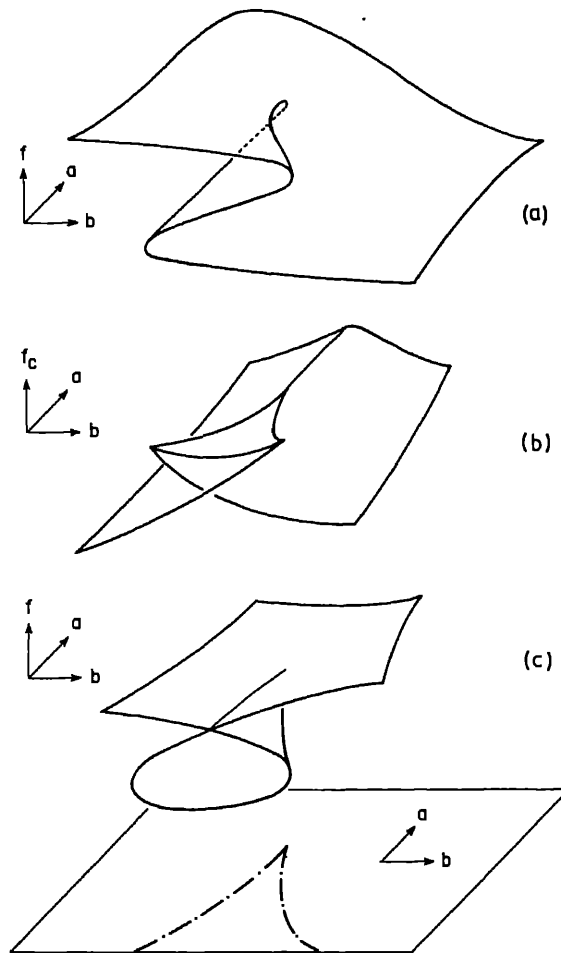


**Figure 25.** Schematic plots of various critical surfaces associated with the  $f$  of (37) (a). surface defined by  $\nabla f = 0$ . (b). critical value surface  $f_c$  which, for a given  $(a, b)$  gives the  $f$  value corresponding to the condition  $\nabla f = 0$ . The critical curvature surface  $f'' = 0$  is sketched in (c). This is useful for discussing instabilities. At the bottom is projected the fold curve. The relationship of the latter to the various surfaces sketched above it should be clear (after Gilmore 1981).

this approach to equilibrium. Of these,  $T_1$  is the time for relaxation to a local minimum and  $T_2$  from a metastable minimum to a global minimum (see figure 28d). In transiting from a local minimum to a global minimum the system essentially drifts (in  $x$  space). Relaxation to a local minimum on the other hand is like a diffusive process.

The regime of the two conventions can also be spelt out in terms of  $T_1$  and  $T_2$ . If  $C = \{a, b, \dots\}$  denotes the set of control parameters, then the delay convention operates if (Gilmore 1981)

$$T_1^{-1} \gg (dC/dt) \gg T_2^{-1}, \quad (40a)$$

while the Maxwell convention operates if

$$T_2^{-1} \gg (dC/dt). \quad (40b)$$

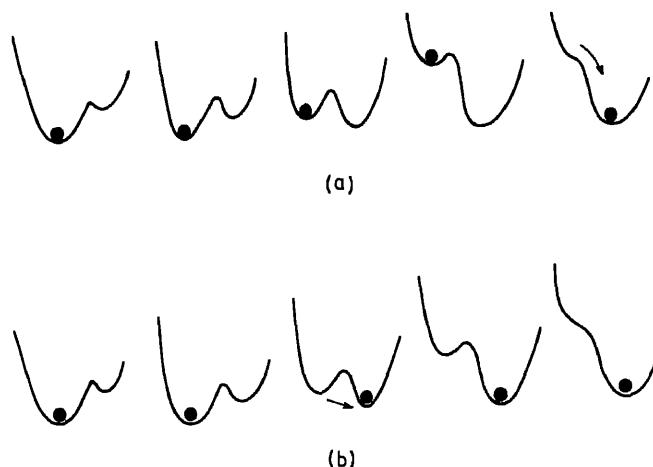


**Figure 26.** Illustration of the two conventions adopted for discussing change of state under nonequilibrium conditions. (a). Delay convention—the system remains in a stable or metastable state until that state disappears, (b). Maxwell convention—the system always chooses the global minimum (after Gilmore 1981).

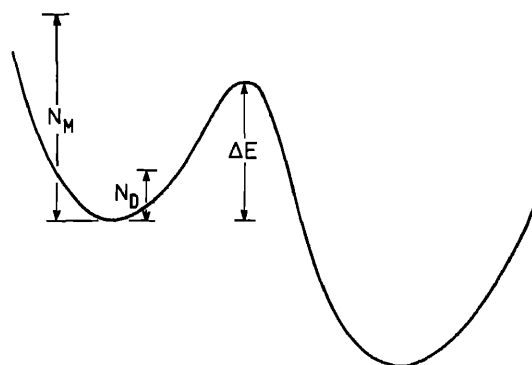


**Figure 27.** Illustration of the conditions under which the delay and Maxwell conventions are applicable.

To see the link between these two conventions and the topography of the critical manifold, we present in figure 29 the projections of the critical manifold on the  $(a, b)$  as well as the  $(a, x)$  plane. When the Maxwell convention is adopted, the critical manifold is a “soldered manifold” because the portions of the manifold  $\nabla f = 0$  describing unstable critical points and metastable minima have been removed and replaced by a flat piece which interpolates between the two minima. Later in § 4.3 when we consider phase separation, we will recognize the projections of the two manifolds on the  $(a, x)$  plane as the coexistence line and the spinodal respectively. The projections on the  $(a, b)$  plane are of special interest in a ferromagnet where one has the practical possibility of varying the magnetic field and inducing a phase transition. It is illuminating to follow the transitions (especially under nonequilibrium conditions), as trajectories on the critical manifold (see Gilmore (1981) for examples and details).

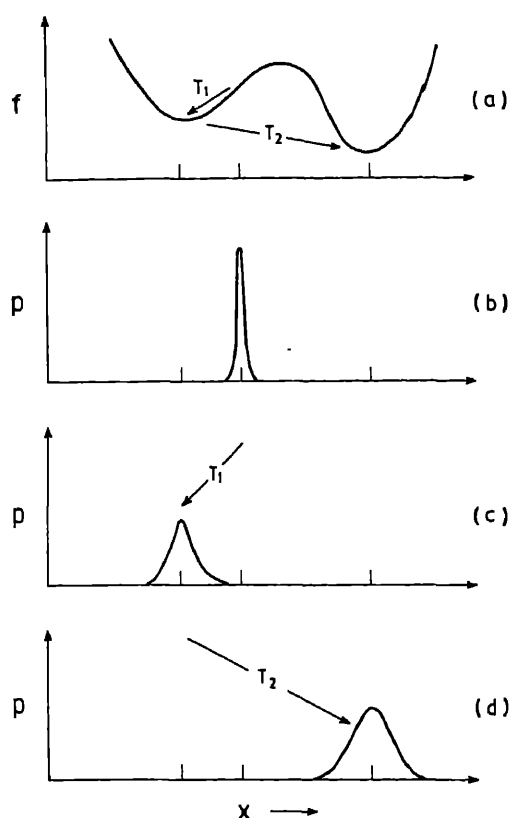


Figure 28. Description of the system evolution in terms of the probability distribution function  $P(x, t)$ . (a) and (b) depict  $f(x)$  and  $P(x, t)$  at some instant  $t$ , say (after Gilmore 1981).

The quantitative aspects of the approach to equilibrium revolve almost entirely around the probability distribution function  $P(x, t)$ . A quench, for example, creates a certain  $P(x, 0)$ . The system not being in equilibrium,  $P$  will naturally evolve approaching that appropriate to equilibrium. The questions in this context are: What is the equation that governs the evolution of  $P$ , how does one solve this question, and how does one use this knowledge of  $P$  to make predictions pertinent to specific experiments?

The evolution of  $P$  is governed by the well-known Fokker-Planck equation

$$\frac{\partial P}{\partial t} = -\frac{d}{dx} [K(x) P] + \frac{1}{2} D \frac{d^2 P}{dx^2}, \quad (41)$$

here  $D$  is the diffusion coefficient and  $K(x)$  a drift force. In many problems, this drift force can be expressed as the gradient of a potential *i.e.*

$$K(x) = -[dV(x)/dx]. \quad (42)$$

In our problems,  $K(x)$  will be related to the free energy.

The derivation of the Fokker-Planck equation from the more fundamental Master equation is too involved a question to be discussed here but fortunately good treatments are available in literature (—see, for example, Haken 1978; for a discussion

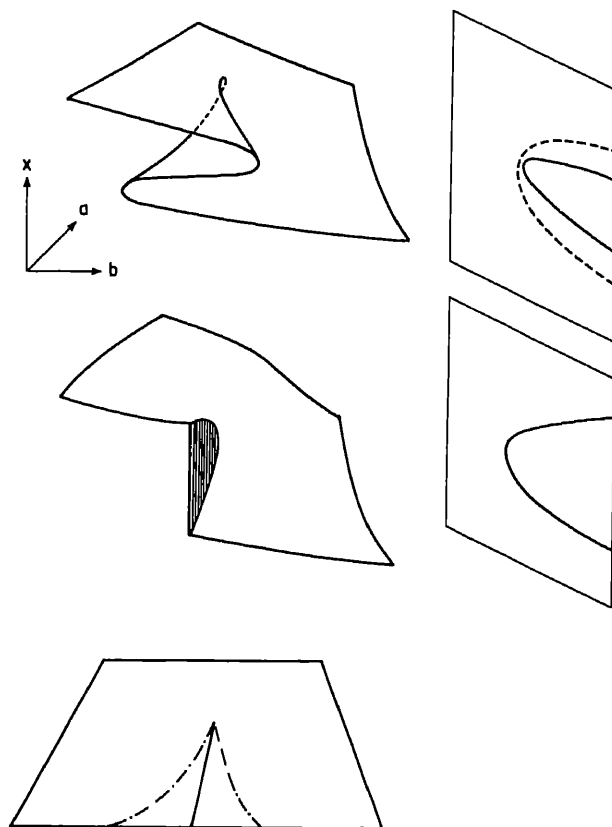


Figure 29. Projections of the critical manifold ( $Vf = 0$ ) on the  $(a, b)$  and  $(a, x)$  planes.

vis-a-vis problems of materials science, see Venkataraman and Balakrishnan 1977; Venkataraman 1982).

The Fokker-Planck equation is sometimes written as a continuity equation i.e. as

$$\dot{P} + \frac{d}{dx} j = 0, \quad (43)$$

where  $j$  the probability current is given by

$$j = \left[ K(x) P - \frac{1}{2} D \frac{dP}{dx} \right]. \quad (44)$$

In equilibrium statistical mechanics, one is interested in the stationary solutions of the Fokker-Planck equation; but in our kind of situations, it is the time-dependent solution that is of interest. In general, finding exact solutions is not possible, and one must resort to a suitable approximation scheme. A very readable account of these problems is available in the book of Haken (1978). Figure 30 shows a schematic plot of the evolution of  $P$  in a typical problem. Starting off as a  $\delta$ -function,  $P$  drifts (which gives rise to the dotted line trajectory) and it also broadens (due to diffusion).

The probability density function we need for discussing clustering etc is somewhat

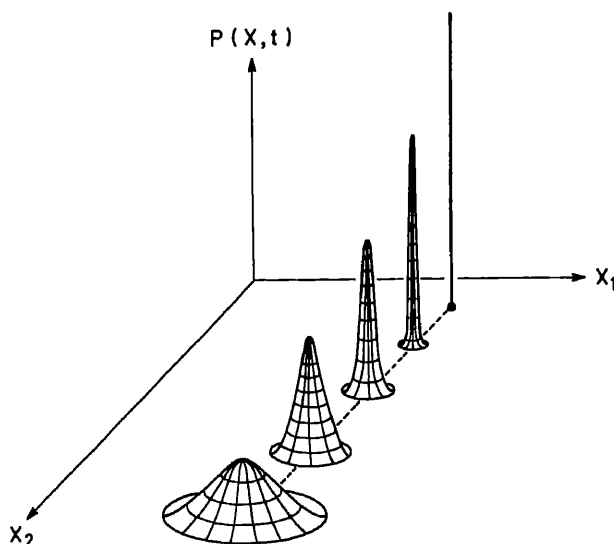


Figure 30. The concept of time evolution of  $P(x, t)$  is discussed in this figure. For convenience  $x$  is assumed to be two dimensional and it is supposed that at  $t = 0$ ,  $P$  starts off as a  $\delta$ -function. With the passage of time, the state of the system *drifts* in  $x$ -space as indicated by the dotted trajectory. Simultaneously, due to fluctuations, the distribution function also broadens.

more general, being a functional of the form  $P(\{\psi\}, t)$ . Here

$$\{\psi\} = (\psi_1, \psi_2, \dots, \psi_n), \quad (45)$$

with  $\psi_r$  being the coarse-grained value of the order parameter  $\psi$  in the  $r$ th cell. *i.e*

$$\psi_r = \frac{1}{n_r} \sum_{l \in \text{cell } r} \psi(l) \quad (46)$$

There are  $n_r$  lattice sites  $l$  in cell  $r$  and there are  $n$  cells in all.  $\{\psi\}$  comprehensively describes the state of the system.

Like  $P(x, t)$  which we considered earlier,  $P(\{\psi\}, t)$  is also conserved. In the continuum limit (where sums over coarse-grained cells are replaced by integrals), the continuity equation is given by

$$\frac{\partial}{\partial t} P(\{\psi\}, t) = - \int dr \frac{\delta J_r}{\delta \psi(r)}, \quad (47)$$

where  $J_r$  is the probability current, and  $\delta$  signifies a functional differentiation.

The expression for  $J_r$  depends on whether the order parameter is conserved or not. The latter quantity is said to be conserved if the change  $\psi_r \rightarrow \psi_r + \varepsilon$  in the cell  $r$  is accompanied by a compensating change  $\psi_s \rightarrow \psi_s - \varepsilon$  in a neighbouring cell  $s$ . In clustering reactions, the order parameter is composition which obviously is conserved. On the other hand, in ordering reactions the order parameter is *not* conserved (—recall the examples of ferro- and antiferro magnets). Bearing these two possibilities in mind, the expression for  $J_r$  can be written as (Billotet and Binder 1979)

$$J_r(\{\psi\}, t) = -C \left[ \frac{\delta F\{\psi\}}{\delta \psi(r)} P(\{\psi\}, t) + k_B T \frac{\delta P(\{\psi\}, t)}{\delta \psi(r)} \right], \quad (48)$$

where  $F\{\psi\}$  is the (coarse-grained) free energy functional. If the order parameter is conserved, then  $C = -M\nabla^2$ , where  $M$  is the mobility\*, whereas if the order parameter is not conserved then  $C$  is simply a rate factor fixing the time scale.

Equations (47) and (48) are too formal and complex for practical use, and watered down versions are necessary. A common practice is to use the above equations to construct equations of motion for various moments of  $P$ . A few illustrative examples follow.

Consider the clustering problem, and let  $c(\mathbf{r})$  denote the local concentration of  $B$  atoms. This is the order parameter, and being conserved

$$J_r(\{c(\mathbf{r})\}, t) = -M\nabla^2 \left[ \frac{\delta F\{c(\mathbf{r})\}}{\delta c(\mathbf{r})} P + k_B T \frac{\delta P(\{c(\mathbf{r})\}, t)}{\delta c(\mathbf{r})} \right]. \quad (49)$$

Multiplying both sides of (47) by  $c(\mathbf{r})$  and integrating we get

$$\int \delta\{c(\mathbf{r})\} c(\mathbf{r}) \frac{\partial}{\partial t} P(\{c(\mathbf{r})\}, t) = - \int \delta\{c(\mathbf{r})\} \int d\mathbf{r}' \times \frac{\delta J}{\delta c(\mathbf{r}')} c(\mathbf{r}). \quad (50)$$

After simplifications, this gives the *average* equation

$$\frac{\partial}{\partial t} \langle c(\mathbf{r}) \rangle = -M\nabla^2 \left\langle \frac{\delta F}{\delta c(\mathbf{r})} \right\rangle. \quad (51)$$

( $M$  is assumed to be a constant *i.e.* independent of  $c(\mathbf{r})$ ). At this stage one makes the convenient assumption that  $P$  is *always* sharply peaked around  $\langle c(\mathbf{r}) \rangle$  *i.e.*

$$P(\{c(\mathbf{r})\}, t) = \pi \delta(c(\mathbf{r}) - \langle c(\mathbf{r}) \rangle) \quad (52)$$

This then leads to

$$\frac{\partial}{\partial t} \langle c(\mathbf{r}) \rangle = -M\nabla^2 \frac{\delta F\{\langle c(\mathbf{r}) \rangle\}}{\delta c(\mathbf{r})}. \quad (53)$$

Being an average equation, the bracket  $\langle \rangle$  can be dropped. The assumption (52) is crucial, for it implies that there are no fluctuations. In terms of figure 30 what it implies is a drift of a  $\delta$ -function with no broadening. In § 4.3 we shall discuss an application of (53).

Our next example relates to ordering where, we must remember, the order parameter is *not* conserved. Binder (1973) has used the same steps as above for this problem. He starts with (47) which, after manipulations, takes the form

$$\frac{\partial P(\{\psi\}, t)}{\partial t} = -C \int d\mathbf{r} \frac{\delta}{\delta \psi(\mathbf{r})} [K(\psi(\mathbf{r}))P] + C \int d\mathbf{r} \frac{\delta^2 P}{\delta \psi(\mathbf{r})^2}, \quad (54)$$

where the drift force  $K(\psi(\mathbf{r}))$  is given by

$$K(\psi(\mathbf{r})) = - \frac{\delta F\{\psi\}}{\delta \psi(\mathbf{r})}. \quad (55)$$

Equation (54) is the Fokker-Planck equation generalized to deal with a situation where  $P$  is a functional rather than a function; compare with equation (41). For  $F$ , Binder assumes the Ginzburg-Landau form. He then calculates the first moment as in (50),

\* The mobility is related to the diffusion coefficient by the Einstein relation  $D = Mk_B T$ .



making an assumption similar to (52). The resulting equation for  $(\partial\psi(r)/\partial t)$  is the time-dependent Ginzburg-Landau equation as applied to the alloy problem. Once again, because of the approximation (52), fluctuations are not included in the treatment.

For comparison with experiment, one needs correlation functions involving the order parameter like

$$\langle \psi(r, t) \psi(r', t) \rangle = \int \delta\{\psi\} \psi(r, t) \psi(r', t) P(\{\psi\}, t). \quad (56)$$

Multiplying both sides of (47) by  $\psi(r, t) \psi(r', t)$  and integrating, one obtains an equation of motion for the correlation function. This was essentially the starting point for Langer's theory (Langer 1969; Langer and Turski 1973; Langer *et al* 1975) of spinodal decomposition. Billotet and Binder (1979) also used a similar approach in their theory of ordering reactions. Suitable approximations were then introduced by the above authors to make the solution of the equation of motion tractable, for subsequent comparison with experiment. As we shall note in the following subsections such theories while including in some measure the nonlinearities (which the time-dependent Ginzburg-Landau equation does) and fluctuations (which the Ginzburg-Landau equation does not) do not yet give perfect agreement, signalling the need for improved approximations.

In brief, the usual starting point for problems involving nonequilibrium systems is the ('generalized') Fokker-Planck equation. From here, one must make one's way through suitable approximations to an equation which can form the basis for comparison with experiments. The latter aspects will be dealt with shortly.

For historical completeness we must mention that, Dienes (1955) and Vineyard (1956) wrote down by analogy with chemical reactions, a *rate* equation for the (long-range) order parameter  $S \equiv \langle \psi \rangle$ . Dienes (1955) calculated  $\dot{S}$  numerically for both first order and second order transitions, and the trends obtained by him are sketched in figure 31. If  $\dot{S}$  is positive for a certain value of  $S$ , then a fluctuation in the system corresponding to that particular  $S$  value will be unstable. Figure 31 will now show that in a second-order phase transition, the system is unstable to infinitesimal fluctuations whereas in a first-order transition, a large fluctuation (in  $S$ ) is necessary. Qualitatively, this is often identified with a nucleation and growth mechanism (Yamauchi and de Fontaine 1974).

The Dienes-Vineyard approach to ordering kinetics has now been superseded by the more formal treatment based on the Fokker-Planck equation.

#### 4.3 Spinodal decomposition

It was at one time believed that phase separation occurred only through a nucleation and growth process *i.e.* small pockets of *A*-rich and *B*-rich regions first formed scattered throughout the specimen which subsequently grew and coalesced, transforming the entire specimen to the ordered state. Experiments however revealed that under certain conditions of quenching, the approach to ordering was quite different being akin to "continuous" ordering that one usually associates with a second-order phase transition. This mode of decomposition is referred to as spinodal decomposition.

One picture being worth a thousand words (!) it is perhaps desirable at this stage to refer to figure 32 (Oki *et al* 1974) which, incidentally, gives some idea of the diversity of microstructure one can observe in such experiments.

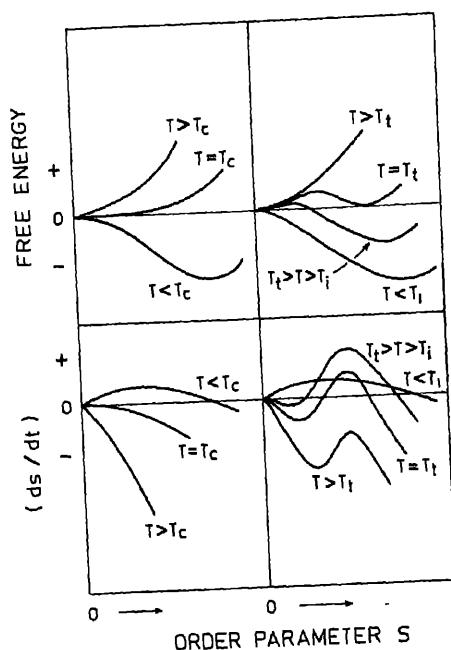


Figure 31. Schematic plots of  $\bar{S}$  vs  $S$  based on the calculations reported by Dienes (1955). The top half of the figure shows sketches of the free energy as a function of the long-range order parameter  $S$  for a first- as well as a second-order phase transition. Sketched below are the variations of  $\bar{S}$  at different temperatures.

The fact that ordering occurred (under certain conditions) simultaneously over large distances indicated that a large scale migration of atoms was involved; and yet when a diffusion model was tried, it failed. The first nontrivial insight into the processes actually occurring came from the work of Cahn (1961, 1962, 1968). To obtain his model, we go back to (53) and put

$$F\{c(r)\} = \int dr \left( \frac{1}{2} K |\nabla c|^2 + f(c) \right), \quad (57)$$

with

$$f(c) = f_0 + \frac{A}{2} (c - c_B^{\text{crit}})^2 + \frac{B}{4} (c - c_B^{\text{crit}})^4, \quad (58)$$

thus obtaining

$$\frac{\partial c(r, t)}{\partial t} = M \nabla^2 [-K \nabla^2 c + (\partial f / \partial c)_T]. \quad (59)$$

Writing  $c(r, t) = c_B + \delta c(r, t)$  and linearizing,

$$\frac{\partial \delta c}{\partial t} = M \nabla^2 [-K \nabla^2 + (\partial^2 f / \partial c^2)_{T, c_B}] \delta c. \quad (60)$$

Solving by Fourier transform,

$$\begin{aligned} c(k, t) &= F \cdot T \text{ of } \delta c(r, t), \\ &= c(k, 0) \exp[\alpha(k)t], \end{aligned}$$

where

$$\begin{aligned} \alpha(k) &= -M k^2 (K k^2 + f''), \\ &= -M K k^2 (k^2 - k_c^2), f'' \equiv (\partial^2 f / \partial c^2)_{c_B T}, k_c^2 = K^{-1} |f''| \text{ for } f'' < 0. \end{aligned} \quad (61)$$

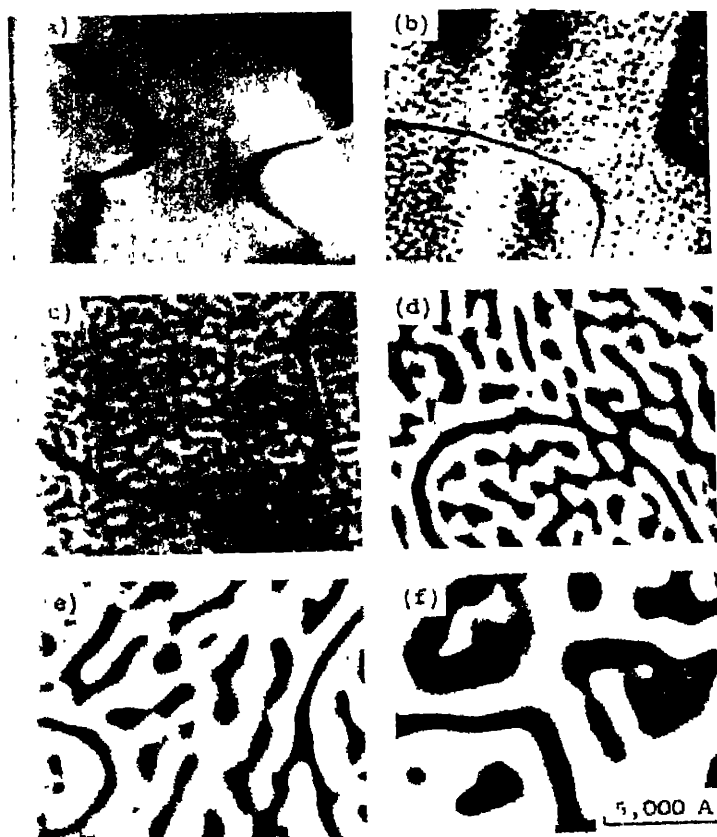


**Figure 32.** Domain structures of Fe-24.7 at % Al alloy quenched from 630°C and annealed at 570°C. Shown here are the dark field micrographs with 200 reflection. (a). quenched. (b). annealed for 10 min (c). (d). (e). (f). annealed for 100, 1000, 3000 and 10000 min respectively (after Oki *et al* 1974).

This is the gift of Cahn's theory.

At this stage, it is worth emphasizing the contributions made by Cahn. Firstly he noted that instead of writing the diffusion current as

$$j(r) = -M \nabla (\partial f / \partial c) \quad (62)$$

as one usually does, one must allow for the possibility of the chemical potential varying from point to point in the medium and rewrite the current as

$$j(r) = -M \nabla \frac{\delta F \{c(r)\}}{\delta c(r)} \quad (63)$$

with  $F$  as in (57) and (58). (It is interesting that Cahn was not aware of the Ginzburg-Landau theory at that time!).

Another question addressed by Cahn is that of coherency strain (figure 33). Sketched in figure 33 are two different scenarios for the coformation of the two phases  $\alpha$  and  $\beta$

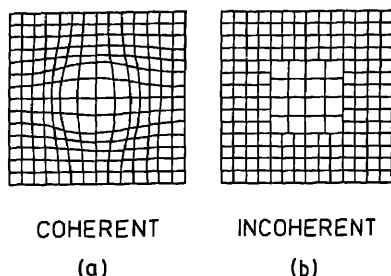


**Figure 33.** Illustration of the concept of the coherency strain. (a). A cluster that is coherent with the matrix. The lattice spacing changes gradually from the grain to the surrounding region through a distortion zone. The strain associated with this distortion is the coherency strain, and makes a contribution to the energy. In the sketch in (b) there is atomic mismatch at the boundary, and no coherency strain. The cluster in this case is said to be incoherent.

(say) after the quench\*. In figure 33b there is complete atomic mismatch at the boundaries separating the  $\alpha$  and  $\beta$  regions. With such a discontinuity, the clusters are said to be *incoherent*. By contrast, in figure 33a there is a gradual accommodation of the lattice parameter change through a distortion zone; the corresponding clusters are called *coherent*. While incoherency is the terminal state, the phases initially formed are coherent whence the free energy has a contribution associated with coherency strain. Assuming the medium to be elastically isotropic, an energy density  $\eta^2 Y (c - c_B^{\text{crit}})^2$  must then be added to  $f(c)$ . Here  $\eta = (d \ln a / da)$ ,  $a$  being the lattice constant, and  $Y$  is given in terms of the Young's modulus  $E$  and Poisson's ratio  $\nu$  as  $Y = E / (1 - \nu)$ . Consequent to this addition,  $\alpha(k)$  gets modified as

$$\alpha(k) = -Mk^2 (Kk^2 + f'' + 2\eta^2 Y). \quad (64)$$

It is now seen from (61) and (64) that the sign of  $\alpha$  depends on a balance of various factors. If coherency strain is absent and if  $f''$  is negative, then  $\alpha$  (in (61)) can assume a positive value in the range  $0 \leq k \leq k_c$  as illustrated in figure 34. Thus compositional fluctuations with wavevectors in this region will grow, the component corresponding to  $k_m$  dominating. All other fluctuations will decay. Simple diffusion theory on the other hand predicts  $\alpha(k) = -Mk^2 f''$  whence *all* fluctuations will grow, the short wavelength ones preferentially.

Referring now to figure 35 we see that  $f''$  is negative only for a certain range of compositions. One could therefore plot within the two-phase region, the locus of points where  $f'' = 0$ . This is the spinodal and, as may be seen from figure 35 it divides the two-phase region into two zones (—see also figure 29).† If a quench is made into the region within the spinodal, an *instability* occurs causing the system to evolve to equilibrium through the growth of long wavelength compositional waves. Ordering thus sets in on a macroscopic scale, and increases gradually in amplitude (—hence the reference to

\*It must be mentioned that spinodal decomposition is also possible in certain binary fluid mixtures. However, there, one does not have coherency strain. For a comprehensive review of both alloys and liquid mixtures, see Gunton (1982).

†The Chamber's dictionary defines spinode as a cusp, the root being the Latin word *spina* meaning thorn. From figure 29 we see the relationship of the cusp to the critical manifold, although one is more used to the projection on the  $(a, x)$  plane rather than the projection on the  $(a, b)$  plane. See also Kikuchi and de Fontaine (1976).

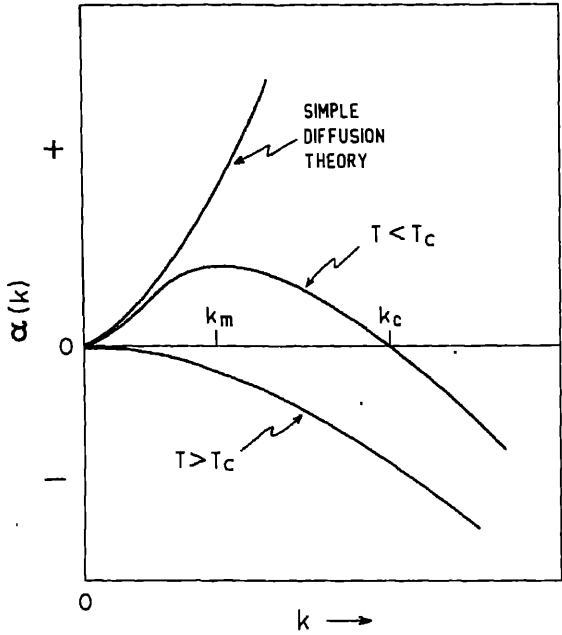


Figure 34. Plots of  $\alpha$  vs  $k$  as given by linear theories.

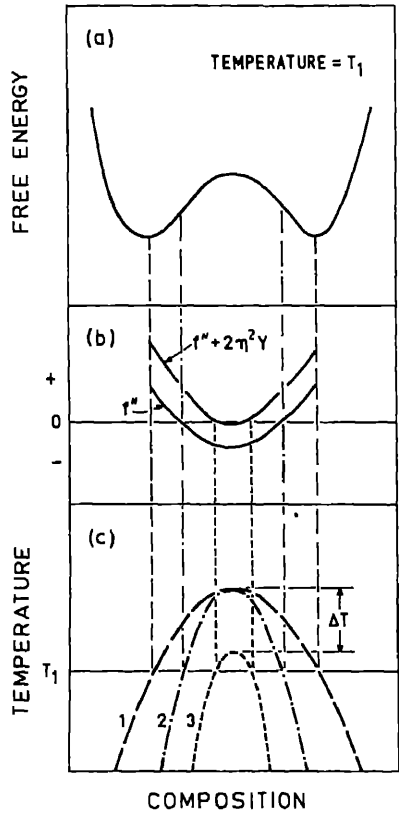


Figure 35. At the top is sketched the usual double well form of the free-energy vs composition. (See also figure 5 and (58)). The second derivative  $f''$  is sketched in the middle. Instability is connected with  $f''$  being negative. If coherency strain is included then  $(f'' + 2\eta^2\gamma)$  must be negative. At the bottom are shown the coexistence curve 1 and the spinodals 2 and 3.

"continuous" ordering). Outside the spinodal but within the coexistence line, there is *metastability* instead of instability. If a quench is made into the metastable region, the system evolves through the nucleation of order in several localized regions. These pockets grow in size and eventually link up so that order percolates everywhere. It appears that after equilibrium is finally reached, it is immaterial what route exactly was taken towards its attainment *i.e.* whether it was quenched into the metastable or the unstable region. However, immediately after nonequilibrium conditions are established, the scenario does depend on whether one is in the region of metastability or of instability. It is in this context one wishes to know where  $f''$  vanishes, and this is precisely where a plot as in figure 25c is useful.

If coherency strain is included, then

$$k_c^2 = K^{-1} |f'' + 2\eta^2 Y|, \quad (65)$$

and for instability one must have  $(f'' + 2\eta^2 Y)$  negative rather than  $f''$ . As a result, the spinodal is depressed with respect to the (incoherent) coexistence curve (see figure 35c). In liquids, such a depression is absent for obvious reasons. In passing, it should also be pointed out that the phase diagrams deduced from theory as in § 3.2 refer to the *coherent* phase diagrams whereas those determined by experiment (Hansen 1958) refer to *incoherent* phase diagrams.

While Cahn's theory gave some clue as to the origin of spinodal decomposition, quantitatively it was inadequate as it assumed linearity. Now one of the stringent tests for a theory is to compare the structure factor  $S(k, t)$  predicted by it in the small  $k$  region with that observed experimentally. In Cahn's theory

$$S(k, t) \equiv \langle c(k, t)c(-k, t) \rangle = S(k, 0) \exp [2\alpha(k)t]. \quad (66)$$

Based on figure 34, one would expect  $S(k, t)$  to peak at  $k_m$  for all  $t$  whereas experiment showed that  $k_m \rightarrow 0$  as  $t \rightarrow \infty$ . Another failing of Cahn's theory is that it predicts the decay of  $S(k, t)$  to zero for  $k > k_c$  whereas it must actually approach that appropriate to the fluctuations at temperature  $T$  (to which the sample has been quenched). Cook (1970) traced this deficiency to the absence of fluctuations in Cahn's theory (recall remarks circa equation (53)) and therefore modified Cahn's diffusion equation into a Langevin equation, *i.e.* he wrote

$$\frac{\partial c}{\partial t} = -\nabla j + \zeta j = -M \nabla (\delta F / \delta c), \quad (67a)$$

with

$$\langle \zeta(r, t) \zeta(r', t') \rangle = 2M \delta(r - r') \delta(t - t'). \quad (67b)$$

Cook's model produced only marginal improvements to that of Cahn's since it too relied on linearity. The real breakthrough came with the work of Langer and coworkers (Langer 1969, 1980; Langer and Turski 1973; Langer *et al* 1975) who not only included fluctuations (as Cook did), but also the nonlinearities (though only approximately).

To understand Langer's work we start with the formal equation of motion for  $S(\mathbf{k}, t)$  which is obtained as described in § 4.2 circa equation (56). Ignoring elastic effects, the equation for  $S(\mathbf{k}, t)$  is:

$$\begin{aligned} \frac{\partial S(k, t)}{\partial t} = & -2Mk^2 [(Kk^2 + f'')S(k, t) + \frac{1}{2}(\partial^3 f / \partial c^3)_{c_s} S_3(k, t) \\ & + \frac{1}{6}(\partial^4 f / \partial c^4)_{c_s} S_4(k, t) + \dots] + 2Mk_B T k^2. \end{aligned} \quad (68)$$

Here

$$S_n(r_1 - r_2, t) = \langle \delta c^{n-1}(r_1, t) \delta c(r_2, t) \rangle \quad (69)$$

and  $S_n(k, t)$  is the Fourier transform of  $S_n(r, t)$ . From (68) we see that Cahn had only the first term of the series and that Cook added the noise term.

A major difficulty with (68) is that it involves the higher-order correlation function  $S_n(k, t)$  to know which we need additional equations of motion! One thus ends up with a hierarchy of coupled equations, a familiar malaise of many-body theory. Langer and coworkers argued that no matter what  $n$  is,  $S_n$  always involves only two spatial positions  $r_1$  and  $r_2$ . It should therefore be possible to compute  $S_n$  for any  $n$  (albeit approximately), given a knowledge of the two-point distribution function  $P_2[c(r_1), c(r_2)]$ . The latter was approximated by

$$P_2[c(r_1), c(r_2)] = P_1[c(r_1)] P_1[c(r_2)] \times \left\{ 1 + \frac{\langle \delta c(r_1) \delta c(r_2) \rangle}{\langle (\delta c)^2 \rangle} \frac{\delta c(r_1) \delta c(r_2)}{\langle (\delta c)^2 \rangle} \right\}. \quad (70)$$

If there were no correlations between the concentrations at  $r_1$  and  $r_2$ , then  $P_2$  would just be a simple product of the one-point probabilities. In Langer's scheme, the correction is proportional to  $\langle \delta c(r_1) \delta c(r_2) \rangle$ . The equation of motion now simplifies to

$$\frac{dS(k, t)}{dt} = -2Mk^2 [Kk^2 + A(t)] + 2Mk_B T k^2, \quad (71)$$

where  $A(t)$  itself depends on  $S(k, t)$  and must therefore be calculated by a self-consistent scheme. For comparison, Cahn's theory gives

$$\frac{dS(k, t)}{dt} = -2Mk^2 [Kk^2 + f''], \quad (72)$$

while Cook's theory gives

$$\frac{dS(k, t)}{dt} = -2Mk^2 [Kk^2 + f''] + 2Mk_B T k^2. \quad (73)$$

The major success of the Langer theory is the prediction that  $k_m$  shifts towards the origin as time increases, in accord with experiment. Another important finding is that the structure factor satisfies dynamic scaling *i.e.*

$$S_T(k, t; c_B) = \varepsilon^{-\gamma} \tilde{S}[k\varepsilon^{-\nu}, t\varepsilon^\gamma, (c - c_B^{\text{crit}})] \quad (74)$$

where  $\varepsilon = (1 - T/T_c)$ , and  $\beta, \nu, \gamma$  have their usual meanings (Stanley 1971). Equation (74) is significant because it shows that dynamic scaling can apply to relaxation *far from equilibrium*.

The theory of Langer also is not without blemishes. One shortcoming is that it exhibits metastable states of infinite life-time. A related defect is the inability to describe properly the late stages of the separation. According to Binder (1977) these failings can be cured by explicitly building in features related to nucleation and growth. The late stage behaviour will be briefly touched upon again in a subsequent section.

To counter the impression one might get that it is all theory (!), we now present some representative but important experimental results. Figure 36 shows small-angle

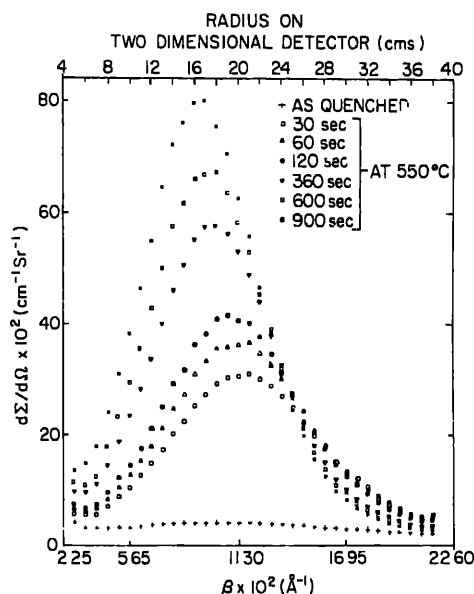


Figure 36. Differential scattering cross-section ( $d\Sigma/d\Omega$ ) vs scattering vector  $\beta$  ( $k$  in our notation) for Au-60 at % Pt alloy quenched from 1270°C and aged at 550°C. In making the measurements, an "arresting technique" as illustrated in figure 44 was used (after Singhal *et al* 1978).

neutron scattering results for a Au-60 at % Pt alloy obtained by Singhal *et al* (1978). The sample was quenched from 1270 ( $\pm 5$ )°C into iced brine and subsequently aged at 550°C. After aging for a certain time, the sample was quenched into water to prepare for measurements (which were done at room temperature). The sample was then successively subjected to additional aging treatment, followed in each case by a measurement to monitor the state of ordering. The data clearly indicates the shift of  $k_m$  towards zero with increasing time.

The next result we discuss is that of Schwahn and Schmatz (1978) for Al-40 at % Zn alloy. This was a clever experiment designed to check the fact that due to coherency strain,  $T_c$  the critical temperature associated with the spinodal is depressed below the (incoherent) phase boundary (see figure 35). Starting from the one-phase region, the sample was quenched to a temperature  $T$  just above  $T_c$ . Holding the sample at  $T$ , small-angle neutron scattering measurements were carried out. In contrast to what one observes in a usual second-order phase transition while approaching  $T_c$  from above, it was noticed that  $S(k)$  changed with time. The reason is that though  $T > T_c$ , the sample was actually below the equilibrium (*i.e.* incoherent) phase boundary. Thus, with passage of time, ordering occurred slowly *via* nucleation and growth and  $S(k)$  probably went over to a form appropriate to that process. Under the circumstances, the spectrum measured just after quench is the one representative of critical scattering *i.e.* the excess scattering arising out of the proximity of  $T$  to  $T_c$  (coherent). A rapid increase of scattered intensity (so isolated) was indeed observed as  $T \rightarrow T_c^+$ , and it was firmly established that  $T_c$  (coherent) was 28°C below the incoherent critical point of 351.5°C (see figure 37). Further,  $S(k)$  immediately after quench had the well-known Ornstein-Zernike (1914) form usually found while approaching a second-order phase transition. Only, in this case the Ornstein-Zernike form was transient, giving way to a fluctuation spectrum appropriate to other processes.

Spinodal decomposition has no doubt been explored by a variety of tools but of these, small-angle neutron scattering is perhaps the most useful for checking out



aspects we are interested in presently. The spectrometers currently available at the various high-flux reactors are quite powerful, being placed in cold-neutron beams and equipped with 2-D detectors and online computers. The possibility of rapid, real-time measurements (as in the Schwahn and Schmatz experiment) is a very attractive feature. At the new DHRUVA reactor at Trombay, a cold neutron source is being planned, and a small-angle measurement facility is also being contemplated. Such a spectrometer would give a great impetus to the above type of experiments in the country. While neutron scattering has an edge at the moment, x-rays have a strong possibility of staging a comeback, especially with the advent of synchrotron-radiation sources.

Computer simulation is another important technique employed to test theoretical predictions. Lebowitz *et al* (1982) for example, have used the Monte Carlo method to study quenching under various conditions (see figure 38). In each case  $S(k, t)$  was determined, with time measured in units of  $\alpha^{-1}$  where  $\alpha^{-1}$  is the average time interval

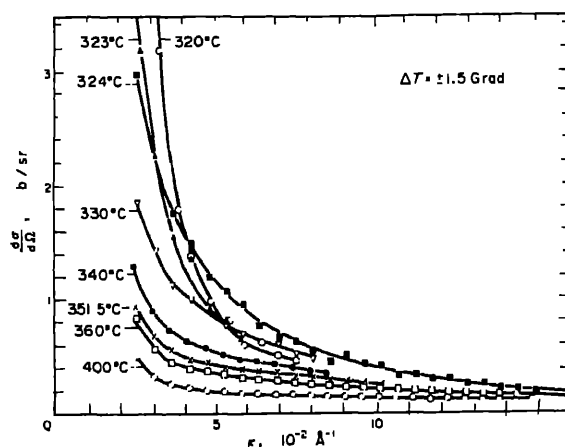


Figure 37. Differential scattering cross-section *vs* wavevector observed at various temperatures in the neighbourhood of the (coherent) critical temperature ( $\sim 324^\circ\text{C}$ ). The sharp rise at small  $k$  is characteristic of critical behaviour. No critical scattering was found at  $351^\circ\text{C}$  the incoherent critical temperature. The  $k$ -dependence near  $324^\circ\text{C}$  follows the Ornstein-Zernike form (after Schwan and Schmatz 1978).

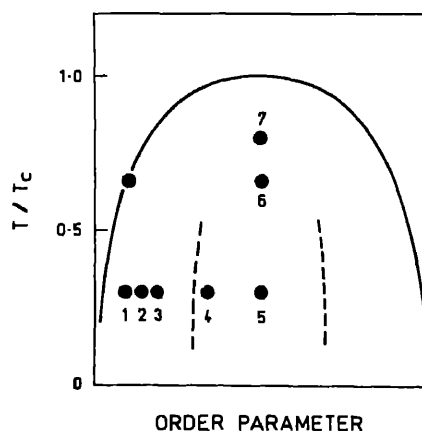


Figure 38. Phase diagram of the Ising model used by Lebowitz *et al* (1982) in their computer simulation studies. The broken lines are spinodals. The dots correspond to the various quenches made. In each case, the system is started from an infinite temperature (after Lebowitz *et al* 1982).

between two attempts at exchanging a specific site. A time range up to  $10^4 \alpha^{-1}$  was scanned, and, as expected, phase separation occurred with varying speeds depending on the nature of the quench. The relaxation was fastest for quench 5 and slowest for quench 1. A problem arises in making comparisons with experimental data since time in the latter is measured in real physical units *i.e.* seconds. However a link is possible since the unit of time in the simulations appropriate to a temperature  $T$  can be taken as  $a^2/6D(T)$  where  $a$  is the lattice constant and  $D$  is the diffusion coefficient of  $A$  atoms in a crystal of  $B$  atoms. Using such a scaling, Lebowitz *et al* (1982) made comparisons with data obtained by Singhal *et al* (1978). The comparison is reproduced in figure 39 and the notable feature is that one could make the data from the actual and computer experiment lie on the same curve by only rescaling the vertical axis. Further comments on the scaling behaviour will be made when we consider long-term behaviour.

#### 4.4 Late stages of phase separation kinetics

Subsequent to quenching, the system will after sometime, segregate locally into regions of  $A$ -rich and  $B$ -rich phases (referred to as grains or droplets or domains). With further passage of time, two things happen. Firstly, within individual grains itself, the atoms continue to approach an organization characteristic of the equilibrium configuration. In addition, the droplets themselves grow, coarsen or ripen, whichever way one wants to describe it. A proper theory for  $S(k, t)$  must reflect both these aspects (see figure 40, Binder 1980b), but such a theory does not exist. Present theories have only one length scale whereas what figure 40 shows is the need for two.

Quantitatively, the above ideas may be expressed as

$$S(k, t) \approx S_{DW}(k, t) + S_{ID}(k, t) \quad (75)$$

where  $DW$  refers to domain wall and  $ID$  to intradomain. As  $t \rightarrow \infty$ ,  $S_{DW} \rightarrow \text{const} \times \delta(k)$  while  $S_{ID} \rightarrow S_{ID}(k, eq)$ . Immediately after quench,  $DW$ 's are not important and  $S \sim S_{ID}$ . However, during late stages, it is  $S_{DW}$  that is more interesting as it gives an insight into the coarsening processes.

One interesting discovery concerning late-stage behaviour is the existence of scaling. Since there is a characteristic length ( $\sim$  domain size), associated with the process, it has

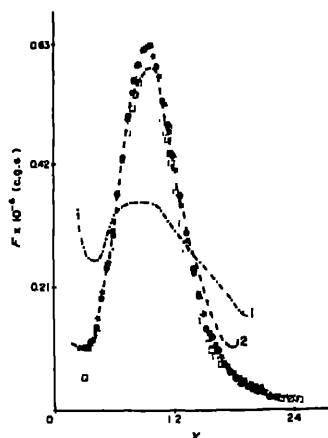


Figure 39. Comparison of the computer simulation results (empty symbols) with experimental data (Singhal *et al* 1978) for Au-60 at % Pt alloy quenched to  $T \sim 0.6 T_c$ . The broken line is for  $t = 0$  (the initial sample was already decomposed to some extent) (after Lebowitz *et al* 1982).

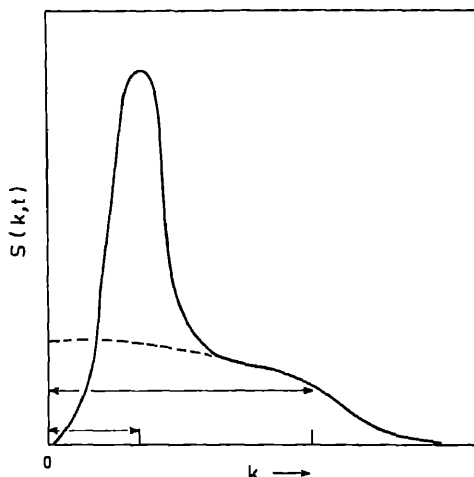


Figure 40. Sketch of  $S(k, t)$  vs  $k$  at long time. The two arrows show the two wavevectors corresponding to the two length scales (intra domain correlations and domain size). (After Binder 1980b).

been conjectured (Binder 1977; Lebowitz *et al* 1982) that

$$S_{DW}(k, t) \sim b(t) \mathcal{F}(k/K(t)) \quad (76)$$

where  $K(t)$  is the characteristic wavevector associated with the characteristic length, and  $b(t)$  is a normalizing function. Lebowitz *et al* (1982) have analyzed the data of Singhal *et al* (1978) for Au-Pt alloy and found good confirmation of this hypothesis (see figure 39).

The question of coarsening has been considered even earlier in the context of nucleation theories. Lifshitz and Slyozov (1961) and independently Wagner (1961) have discussed the growth of droplets of  $B$ -rich phase immersed in an  $A$ -rich matrix. This theory was really derived for small supersaturation such as one obtains in the late stages of a nucleation and growth process (*e.g.* in clouds). It is however often assumed that the LSW theory can also be applied to the late stage coarsening of a spinodally decomposing system. The basic idea is that larger droplets grow at the expense of smaller droplets *via* the diffusion of  $B$  atoms between different droplets. An important conclusion of the theory is that the average droplet size  $\bar{R}(t)$  (which is the characteristic length of the system) satisfies a  $t^{1/3}$  power law. Lebowitz *et al* (1982) found that  $K^{-1}(t)$  derived from simulation studies appeared to show such a behaviour. Attention must here be drawn to the fact that existing studies on grain growth neglect the possible influence of coherency strain, a factor that is pertinent in alloys, though not in liquids (Binder 1977).

There is one aspect of late stage behaviour we now wish to comment on that does not appear to have received attention thus far. It was noticed many years ago by de Fontaine (1967) during a simulation of spinodal decomposition (in one dimension) that whereas a compositional wave of well-defined wavelength develops immediately after instability is established, pretty soon a period doubling occurs. At that time, the possibility of period doubling as a route to chaos was not known (Feigenbaum 1978, 1979, 1980). The question of whether the formation of irregular domains is due to chaos appears worth a fresh examination. It is pertinent here to point out that de Fontaine (1975a) has mapped the problem of concentration evolution into a Hamiltonian problem and examined system evolution in terms of trajectories in a  $(c, dc/dx)$  phase space. More recently, Aubry (1981, 1983) has in the study of certain defect structures, carried out a similar trajectory analysis and, what is more interesting, discovered the

possibility of chaos under certain conditions. One wonders whether it would not be worthwhile to go back to the de Fontaine problem and reexamine it from this new perspective. In support of such a suggestion, we call attention to figure 41 which shows a computer simulated spinodal structure and that for a real binary glass (Hopper 1982). The simulated structure was obtained by superposing twenty 3-D waves of a *single* wavelength but of random orientation and phases. Notwithstanding this, there appears to be a regularity of sorts in the simulated pattern as compared to the real micrograph. Perhaps features related to stochasticity arising out of period doubling do play a role.

#### 4.5 Ordering reactions

The extensive theoretical work on spinodal decomposition reviewed in § 4.3 has been extended to some extent (Binder 1973; Billotet and Binder 1979) to ordering reactions, although there has not been matching experimental work on the kinetic aspects. However, some attention has been paid to critical phenomena one expects near phase boundaries.

We have already called attention to the early work of Johansson and Linde (1928). A more recent example is provided by the work of Hashimoto *et al* (1976) who studied ordering in  $\text{Cu}_3\text{Au}$ . Starting from the one-phase region, the sample was quenched to and held at various temperatures  $T$  below the (first-order) transition temperature  $T_i$  of  $391^\circ\text{C}$ . At each temperature, the electrical resistivity was monitored as a function of time, and the relaxation time  $\tau$  for approach to equilibrium was deduced. A plot of  $\tau$  vs  $T$  showed a sharp increase as  $T \rightarrow T_i^-$ . Other probes have also been used to study critical phenomena *e.g.* Zener relaxation (Radelaar and Ritzen 1969) and isothermal release of energy (d'Heurle and Gordon 1961).

X-rays have always been popular (see, for example the review by Cohen 1970), a recent example being the study of Hashimoto *et al* (1978).  $\text{Cu}_3\text{Au}$  the work horse, was the material investigated. The specimen was first annealed at a temperature  $T > T_i$  and later quenched to a temperature below  $T_i$  and annealed at the latter temperature for various spells. After each spell, the sample was quenched into water and the x-ray intensity in the superlattice region (110) was scanned. Initially, only a broad and diffuse

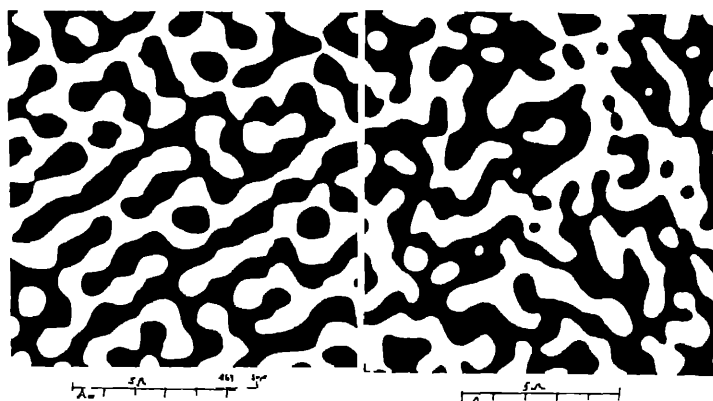


Figure 41. On the right is an electron microscope picture of a real binary glass, showing the phase-separated structure. On the left is the simulated structure obtained using a *single* wavelength (after Hopper 1982).

peak was observed but on increasing annealing time the peak narrowed and intensified, signalling the onset of order. From a plot of linewidth as a function of annealing duration, the relaxation time  $\tau$  could be extracted. A slowing down of relaxation was markedly evident as  $T \rightarrow T_i^-$ . Another investigation meriting particular mention is that of Chen and Cohen (1977). The unique feature was that by employing single crystals, Chen and Cohen were able to study  $\tau$  as a function of  $k$ . Figure 42 shows their results for  $\text{Cu}_{81.5}\text{Au}_{18.5}$  obtained after a temperature change  $355^\circ$  and  $330^\circ\text{C}$ . As expected,  $\tau$  peaks near the superlattice position.

Earlier (in § 4.3) we noted that under certain conditions, phase separation takes on the character of a continuous transition. Is such a scenario possible in *ordering* systems? Indeed it is, as has been emphasized by de Fontaine (1981). The basic concept is easily understood with a reference to figure 43. In figure 43a is shown a family of free energy curves appropriate to a system undergoing a first-order phase transition. If the temperature is gradually lowered from above, order will set in at  $T = T_i$  (figure 43b) *via* a nucleation and growth process. On the other hand, a sudden quench to a temperature below  $T_i$  can produce the situation depicted in figure 43c. The system responds to the instability through the generation of an ordering wave of wavevector corresponding to the minimum of  $V(k)$ . The wave swells in amplitude gradually, spreading order everywhere. Therefore, vis-a-vis nonequilibrium situations, one can think of an instability temperature  $T_{\text{instab}}$  ( $< T_i$ ) below which *continuous ordering* occurs.

While the concept seems possible, there is as yet no direct evidence for the existence of the instability temperature, although in an experiment due to Bardhan *et al* (1977) on  $\text{Cu}_3\text{Au}$  there is a strong suggestion. The analogue of the Schwahn-Schatz experiment (§ 4.3) would be desirable. Incidentally, the dashed line in figure 15b is the variation of  $T_{\text{instab}}$  with composition, as deduced from CVM.

In some situations, continuous ordering is possible with an interesting twist. Following the creation of an instability, the system responds with a compositional wave whose wave vector does *not* coincide with that corresponding to the superlattice reflection.

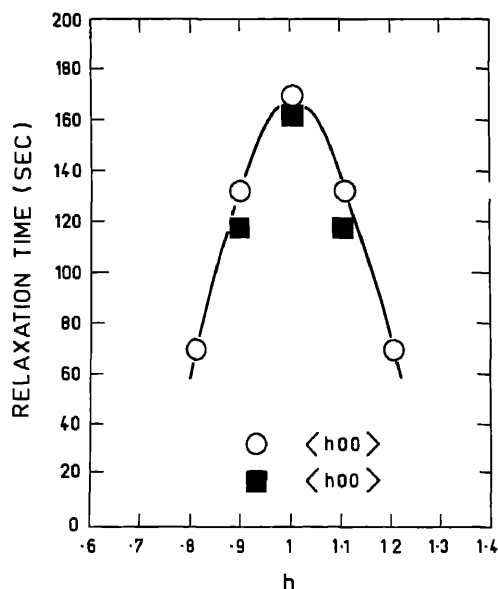
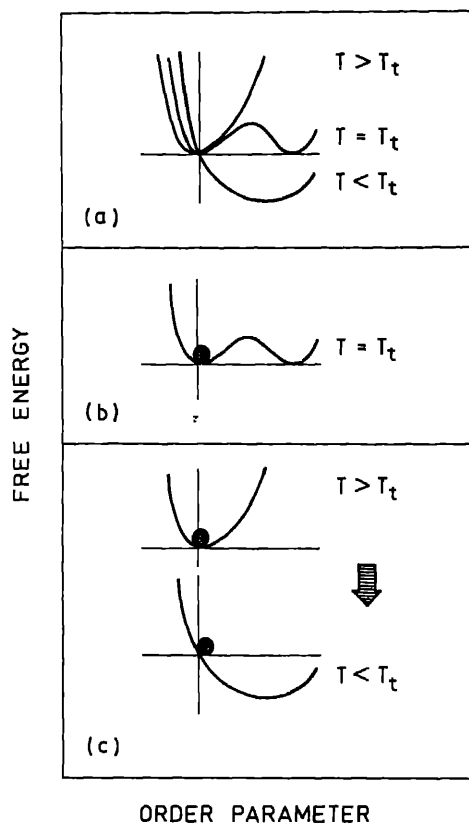


Figure 42. Wavevector-dependent relaxation time  $\tau(k)$ . Shown here are data obtained along  $\langle h00 \rangle$  and  $\langle hh0 \rangle$  lines. The continuous line is a guide to the eye (after Chen and Cohen 1977).



**Figure 43.** System response to different temperature treatments (a). free energy curves for a first order transition, with transition temperature  $T_t$ . When slowly cooled from above, the system experiences metastability on reaching  $T_t$ , and orders by a nucleation and growth process. If suddenly cooled to a temperature well below  $T_t$  as schematically illustrated in (c), it experiences an instability.

However, the system somehow seems to realize this during its evolution, and comes up with a suitable mid-course correction (rooted in nonlinearities?) so that the correct ordered structure results on attainment of equilibrium. Apparently, the point of maximum instability in reciprocal space need not always coincide with the wavevector corresponding to the ordering wave. de Fontaine (1975b) has suggested that Ni-Mo is a good candidate system for exhibiting such a schizophrenic behaviour! Here the instability is associated with a  $\langle 1 \frac{1}{2} 0 \rangle$  wave whereas the ordering is based on a  $\langle 100 \rangle$  wave. There is some evidence from x-ray diffraction (Chakravarti *et al* 1974) and electron microscopy (Das *et al* 1973) in support of the idea but a convincing test would be through a suitably designed real-time experiment.

On the theoretical side, Cook *et al* (1969) extended the Cahn-type analysis (which was essentially applied to a continuum) to discrete lattice systems and demonstrated that under suitable conditions, ordering with the formation of a superlattice was possible. In fact, the curves of figure 22 are the products of such a *linear* theory. In an effort to incorporate nonlinearities, Billotet and Binder (1979) have followed the footsteps of Langer with, however, due allowance for the fact that the order parameter is *not* conserved. (Recall remarks made in § 4.2 regarding conserved and nonconserved order parameters). Earlier, Binder (1973) had tried a time-dependent Ginzburg-Landau type approach, with as much success as may be expected of a mean field theory.

Billotet and Binder (1979) report many numerical calculations but unfortunately, barring some simulation results, they do not have much experimental data to compare

with. In fact Binder and Stauffer (1976) attempted to stimulate experimenters by explicitly calling attention to various aspects of the behaviour of electrical resistivity of binary alloys at phase transitions but the response of the experimental community does not seem to be adequate.

A few remarks now about late stage behaviour in ordering systems. It has been noted (Binder 1980b) that as in clustering reactions, one has to recognize the existence of two length scales (see figure 40), one of which is related to intradomain ordering and the other to domain size. Since one is dealing with an ordering reaction, the intradomain part can be conveniently explored near superlattice positions in a diffraction experiment. The domain-wall effects on the other hand, are best picked up in a small-angle scattering experiment.

There is another aspect of domain walls that has occasionally been mentioned in the literature (*e.g.* Gunton 1982) but does not appear to have been examined in depth. Now the formation of different domains is usually thought of in terms of nucleation of ordering in different regions and the subsequent growth of the latter, leading to the formation of interfaces. In the symmetry-breaking language on the other hand, each ordered region corresponds to a manifestation of one of the possible ground states. The macroscopic physical system is thus trapped in different ground states in different physical regions. The resulting configuration/defect (*i.e.* dw) is therefore a topological entity. The topological aspects of dw's have barely been investigated and are probably worth a closer scrutiny.

Finally, a brief hark back to long-period oscillations (see § 3.1) (Aubry 1981, 1983). One wonders whether some of the considerations in Aubry's analysis of incommensurate structures do not have relevance to LPO seen in some ordered systems. This also appears worth looking into.

We close this section by calling attention to an authoritative review by Freidel (1974) on the electronic aspects of order-disorder transformations (which we have skipped!). Physicists wishing to study order-disorder transformations, should not miss this paper!

## 5. What can experimenters do?

The title of this section is not intended to suggest that experimenters have been slack but merely that there is a dearth of certain types of information *e.g.* relaxation data.

Now each probe has its own characteristic sensitivity, and it is necessary to integrate for a certain time  $\tau_M$  during the experiment to obtain a signal above the background. When exploring nonequilibrium phenomena this poses a problem if the relaxation time  $\tau_R$  is less than  $\tau_M$ . One then has to use an "arresting" technique as illustrated in figure 44, wherein the system is periodically "frozen" in its coast down and then monitored. For example, the data of figure 36 was obtained in this fashion. However, if the signal is strong, one may be able to follow temporal changes directly in realtime. Improvements are therefore necessary for many techniques, if realtime measurements are to become feasible. In some cases like electrical resistivity, the required sensitivities are already there but nevertheless, the capabilities do not appear to have been fully exploited. Where neutron and x-ray scattering are concerned, increase in the primary source strength is an important factor. The availability of synchrotron radiation sources is therefore a welcome development in respect of x-ray scattering. Hardly any results pertaining to phase transformations have been reported using synchrotron sources, and there is much room for innovation and ingenuity.

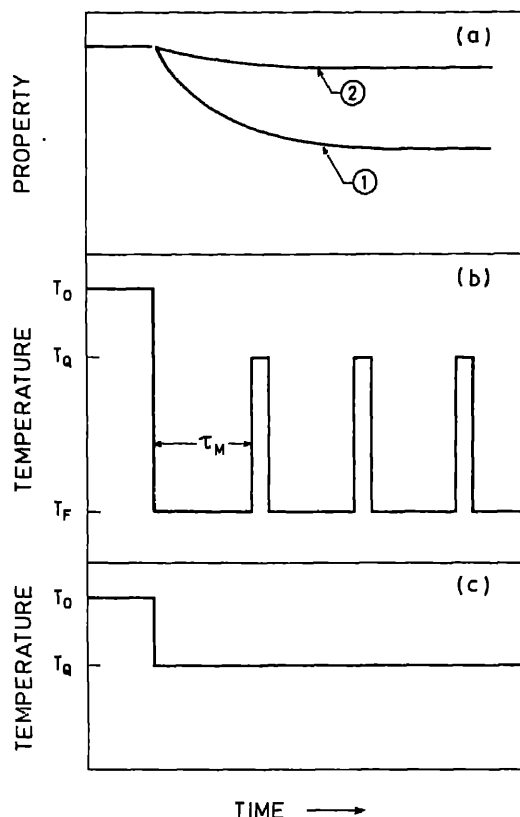


**Figure 44.** (a) Time variations of some property when a system is quenched as in (c). If the decay is rapid as in case (1), then the system must be periodically arrested in its coast down as illustrated in (b). This gives convenient measurement slots whose width  $\tau_M$  can be chosen suitably to optimize (signal/noise) ratio. However, if the measurement time is small, then one can follow the decay in realtime i.e. the time-temperature profile will be as in (c). In the examples shown, this could be applied to case (2).

While discussing realtime measurements, it must be remembered that depending on the temperature, composition etc., the relaxation times can vary over several orders of magnitude. Attention is drawn in this context to the various quenches attempted by Lebowitz *et al* (1982) in their simulation experiments (see figure 38) and the wide spread in relaxation times observed by them. Thus, many techniques can in fact be used on an as-available basis without waiting for improvements, provided one chooses the conditions of experiment properly. In passing, it is worth noting that computer simulation is an expensive way of obtaining relaxation times. It is therefore very desirable to back it up with more extensive studies using a convenient probe (like resistivity).

The types of probes one could think of are many. Some, like resistivity, have already been mentioned. Others include internal friction, ultrasonic attenuation etc. Binder and Stauffer (1976) have discussed in detail how resistivity measurements can be linked to order parameter dynamics. They have also called attention to the need for conventional studies of scaling behaviour as one crosses the phase boundaries. For instance, it would



be very interesting to follow the variation of resistivity with concentration at various temperatures as sketched in figure 45. The sharp rise and fall in the indicated regions are closely related to critical dynamics of the order parameter.

In contrast to "macroscopic" probes like resistivity, the Mössbauer effect provides a probe that is nucleus sensitive. Oki *et al* (1977) have, for example, exploited this method to examine aspects of transformations in Fe-Al alloys. There is clearly more scope for work of this kind. Indeed, one could also consider NMR. With high-power pulsed NMR systems now commercially available, relaxation studies of the type considered here are no longer a mere theoretical possibility. The neutron is yet another nucleus-sensitive probe. In addition, it can also undergo magnetic scattering. Both these factors can be skilfully exploited, particularly where magnetic alloys are concerned. As of now, there appear to be very few examples of ordering kinetics studied using neutrons. One investigation I am aware of is the experiment of Collins and Teh (1973) on  $\text{Ni}_3\text{Mn}$ . These authors upquenched in the ordered state, and for each step change  $\Delta T$  of temperature, they measured the time required for the order parameter to stabilize to its new value. The kinetics of the order parameter were monitored *via* Bragg intensity of an appropriate reflection. Of course, a sophisticated technique like neutron scattering is not always required. Nowick and Weisenberg (1958) for example, simply followed the time variation of the Young's modulus in their upquench experiments on ordered  $\text{Cu}_3\text{Au}$ . In general, there is a paucity of information about system dynamics following a quench. One needs both upquench and downquench experiments, within a given phase (Binder 1977) as well as across a boundary.

While it is natural to think of relaxation time studies in the time domain, we should not forget traditional spectroscopy which also can give information about relaxation time, though of smaller magnitude. An experiment one could think of would be the analogue of the soft-mode studies made in connection with structural phase transitions (—for a review of this area, see Venkataraman 1979). There one has a lattice dynamical

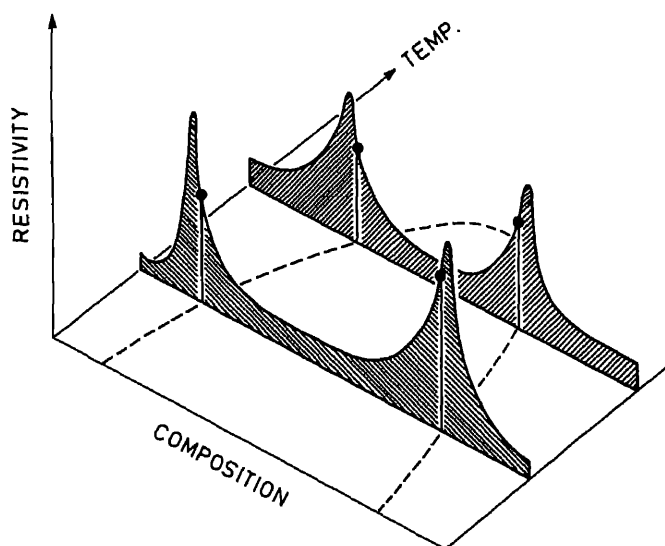


Figure 45. Schematic plot of resistivity vs composition at various temperatures. The dots show the regions where there is a sharp rise or fall. (after Binder and Stauffer 1976).

mode whose frequency diminishes as  $T \rightarrow T_c^+$ . In ordering reactions, we have a compositional wave but of zero frequency. The scattering of radiation from this wave gives rise to intensity in the superlattice region. If an energy scan is made of the scattered intensity (—and this is possible with neutrons), then one will observe a certain frequency spread around  $\omega = 0$ , the spread being related to the relaxation time of the concerned compositional fluctuation. As  $T \rightarrow T_c^+$ , the line width must decrease, indicative of critical slowing down of the compositional fluctuations. A systematic, quasi-elastic scattering investigation of the 'softening' of compositional fluctuations does not appear to have been made so far.

Our preoccupation with long-range order should not blind us to short-range order which too is an important quantity! As the name itself indicates, the focus is on ordering on a localized scale. The key quantity is the (Ising) spin correlation  $\langle S_i S_m \rangle$ . By suitable definitions (de Fontaine 1979), this spin correlation function can be related to the pair correlation function  $g(R = m - i)$  well-known in theory of liquids, and to experimentally measured quantities like the Warren-Cowley parameters. Clearly, short-range order would be of particular interest in the early stages after a quench, and in the disordered phase close to  $T_c$ . With synchrotron sources now available, it may be possible to follow the evolution of short-range order in realtime, at least in select cases. The results can then be linked to models for spin dynamics. Other possible studies concerning short-range order have been mentioned in § 3.3.

At a recent Discussion Meeting on the Physical Basis of Mechanical Behaviour organized under the auspices of the Academy (where, incidentally, Prof. Ramaseshan delivered the keynote address), Dr G Srinivasan raised the interesting question of heat liberated following a quench. In the discussion that followed, Prof. C K Majumdar drew attention to the pioneering work of Bragg and Williams (1935) wherein the approach to order had been discussed in terms of a fictitious temperature. Today, with our knowledge of magnetic resonance etc., we would identify this as the Ising spin temperature and the approach to equilibrium as a spin-lattice relaxation problem. This digression in the Discussion Meeting served to focus attention on the paucity of thermal measurements. Subsequently, I have come across one paper (d'Heurle and Gordon 1961) wherein calorimetry experiments on  $\text{Au}_3\text{Cu}$  during ordering are reported. By and large, studies on the energetics of ordering appear to be rare.

While comparing relaxation times obtained *via* different techniques, we should note that the coupling of the various probes to the order parameter is not the same. Moreover, some like resistivity, integrate the fluctuations of the order parameter over the wavevectors. Two such "integral" probes may not weight the different  $k$ 's in the same manner. In this sense, x-rays and neutrons enjoy the advantage that one can select a specific wavevector for study. All the same, other probes have their own utility in that they are usually faster and also less expensive!

Thus far, we have confined attention to *equal-time* correlation functions of the form  $\langle \psi(r, t) \psi(r', t) \rangle$ . This function continually changes with time till equilibrium is attained at  $t = \infty$ . Probes like x-rays sample equal-time correlation function because they essentially produce an "instantaneous snapshot" of the system. We now extend consideration to *unequal* time correlation functions *i.e.*, functions of the form  $\langle \psi(r, t) \psi(r', t') \rangle$ . The relevance of such functions to experiment will be discussed shortly.

Billotet and Binder (1980) were the first to consider such functions in the context of phase transformations. The kinetics of such functions were modelled closely after Langer's and their own earlier work on equal-time correlation function. They start with

the conditional probability  $P^{\text{cond}}(\{\psi^1\}, t_1; \{\psi^2\}, t_2)$  which is the probability that the system is in the state  $\{\psi^2\}$  at time  $t_2$ , given that it was in state  $\{\psi^1\}$  at  $t_1$ . The continuity equation for  $P^{\text{cond}}$  is:

$$\frac{\partial}{\partial t_2} P^{\text{cond}}(\{\psi^1\}, t_1; \{\psi^2\}, t_2) = - \int d\mathbf{r} \frac{\delta J_r^{\text{cond}}(\{\psi^1\}, t_1; \{\psi^2\}, t_2)}{\delta \psi_r^{(2)}}, \quad (77)$$

the expression for  $J_r^{\text{cond}}$  being an obvious extension of (48). The sequence of steps thereafter is essentially the same as before, and, as earlier, a decoupling approximation is made for  $P(\psi_{r_1}^{(1)}, t_1; \psi_{r_2}^{(2)}, t_2)$  which is the probability that we have a state  $\psi_{r_1}^{(1)}$  at  $\mathbf{r}_1$  at time  $t_1$  and a state  $\psi_{r_2}^{(2)}$  at  $\mathbf{r}_2$  at time  $t_2$ . In this way, they finally arrive at the following expression for  $S(\mathbf{k}, t_2, t_1)$ :

$$S(\mathbf{k}, t_2, t_1) = S(\mathbf{k}, t_1) \exp \left[ -C \int_{t_1}^{t_2} dt \{Kk^2 + A(t)\} \right], \quad t_2 > t_1. \quad (78)$$

with  $C = Mk^2$  if the order parameter is conserved.

The need for unequal-time correlation functions arises from the fact that some techniques probe the system not instantaneously, but over a certain period of time. For example, in an ultrasonic attenuation experiment, a time  $\sim (1/\text{frequency})$  is involved. Similarly, in a neutron inelastic scattering experiment, fluctuations on a time scale  $t \sim (\hbar/\Delta E)$  are explored where  $\Delta E$  is the energy transfer (Brockhouse 1958). Now in a system in thermodynamic equilibrium, one can exploit the fact that the system is stationary and express a correlation function of the form

$$\langle \psi(t) \psi(t') \rangle \text{ as } \langle \psi(0) \psi(t' - t) \rangle.$$

Stationarity however does not obtain in our kind of situations. At best, one can divide the whole time range into suitable slots, and hope for stationarity within each slot (Stratanovich 1963).

Figure 46 offers a schematic comparison of the measurement of equal-time and unequal-time correlation functions. The total time span from  $t = 0$  (instant of quench) to  $t = \infty$  (when terminal equilibrium is attained) is imagined to be divided into convenient (not necessarily equal!) intervals such that there is local stationarity in each time slot in the Stratanovich sense. An experiment like x-ray diffraction if done in real time, would give the "average" structure for each time slot. Fluctuations *within* each slot will not be explored. For that, it is necessary to either use a "frequency sensitive" probe or directly a correlation technique. Owing to the overall nonstationary nature of the process, the correlation function  $C(k, \tau; n)$  will depend on the index  $n$  of the time slot.

As just indicated, one method of exploring fluctuations is to employ a frequency-dependent probe like slow neutron inelastic scattering. Billotet and Binder (1980) have used their model for fluctuations to compute  $S(k, \omega; n)$ . Their spectra show pronounced deviations from the usually expected Lorentzian line shapes; also there are oscillations. However, they obtain negative cross-sections which, as they themselves note, is unphysical. Billotet and Binder attribute this to the inadequacy of their approximations. If earlier experience in the theory of liquids is any guide (de Gennes 1959), then I suspect that the trouble probably lies in the fact that the decoupling approximation for  $P$  has failed to respect the relevant sum rules.

While as of now theory is in a somewhat poor shape, there is nothing to prevent experimenters from studying fluctuations under nonequilibrium conditions using the various probes at their disposal. In particular, slow neutron scattering, ultrasonic

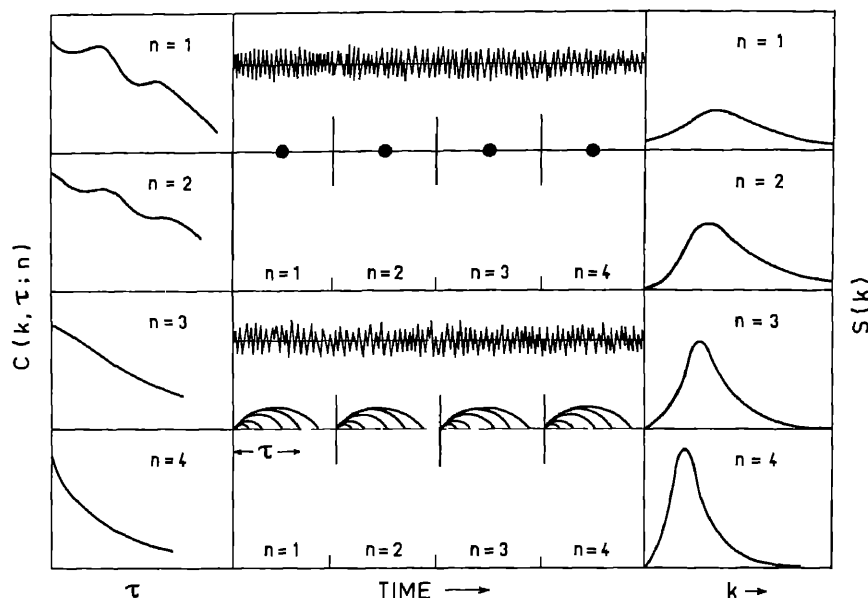
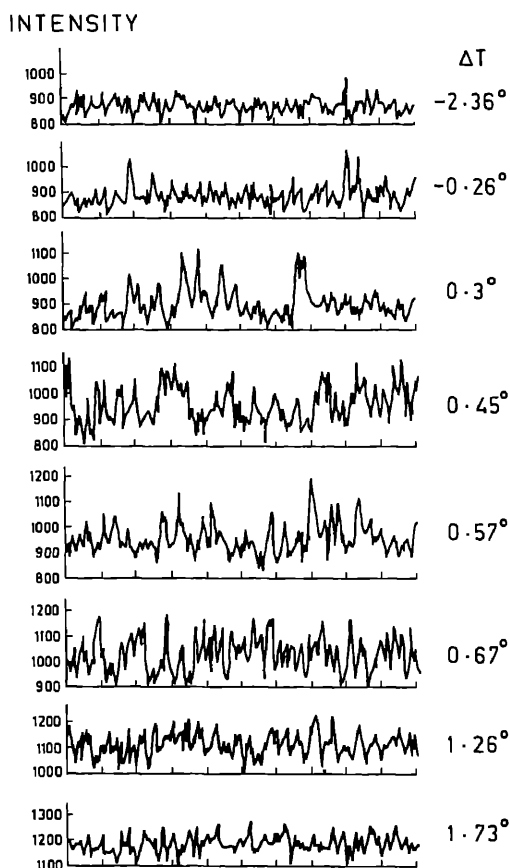


Figure 46. Shown in the middle are signals and their compartmentalization into slots indexed by  $n$ . In each slot, there is assumed to be stationarity. A conventional x-ray experiment measures equal-time correlation function for each slot, and the results finally appear as on the right. By performing an intensity correlation experiment in each slot, one can obtain information related to  $\langle \psi(k, t) \psi(k, t + \tau) \rangle_n$  for each slot. Sketches of  $C(k, \tau; n)$  are given on the left. For each  $n$ , one will have different  $C(\tau)$  plots for the different  $k$ 's.

attenuation, internal friction are some of the tools which could be tried. Vigorous experimentation could in fact act as a spur to theory!

An alternative method of exploring unequal-time correlation functions is to resort to the newly emerging technique of fluctuation spectroscopy (Magde 1977; Venkataraman 1982). Here one observes a suitable quantity  $Q$  (which couples to the order parameter) over a time span corresponding to one of our slots, and records all its fluctuations. One then processes the data to obtain  $\langle Q(t)Q(t') \rangle_n$ . One example of fluctuations observed by neutron scattering is given in figure 47 (Pederson and Riste 1980). Of course in this particular example the system was in a stationary state but that is not necessarily a requirement. In fact, Kim *et al* (1978) have carried out a similar experiment but using light, and have actually studied phase separation kinetics in a fluid binary mixture. Intensity fluctuation spectroscopy (Berne and Pecora 1976) is being regularly used for exploring biophysical problems but its use in condensed matter physics is still rare. Where alloys are concerned light scattering is not possible but one could resort to a study of resistivity fluctuations (*e.g.* Venkataraman and Balakrishnan 1979). No such experiment relating to kinetics of phase separation in solids has been reported so far. However, Kim *et al* (1980) have used precisely this technique to study fluctuations in a binary fluid mixture near its critical point. If sufficient intensity is available, even x-ray and neutron experiments to explore fluctuations in the time domain can be attempted. In brief, the entire subject of fluctuations during decay to equilibrium is largely unexplored both theoretically and experimentally.



**Figure 47.** Fluctuations of the scattered neutron intensity from a liquid crystal with a temperature gradient across. The system is in a stationary but nonequilibrium state. Observe that as the temperature gradient is varied, the fluctuation amplitude becomes large at a certain stage. This is associated with the onset of turbulence in the material (after Pedersen and Riste 1980).

## 6. Lamellar eutectic growth

In addition to the solid-to-solid transformations so far considered, certain liquid-to-solid transformations are also interesting, besides being important technologically. To understand such transformations, we refer to figure 48 which shows a binary phase diagram of the type we are currently interested in. For example, Ag-Cu and Pb-Sn systems exhibit such diagrams. Consider an alloy of composition  $C_0$  and at a temperature such that its state is represented by the point  $a$  in the figure. On cooling and crossing the liquidus curve, one enters the region marked  $(\alpha + L)$  which is a two-phase region where a liquid and a solid both coexist, the solid with composition  $C$  and the liquid with composition  $C_L$ . The relative proportions of the solid and the liquid vary continuously as one moves down the line  $abc$  until at the temperature  $T_E$  called the eutectic temperature, the liquid (of composition  $C_e$ ) freezes. Of course one could come down along  $df$ ; then one would have a pure liquid phase until  $T_E$  at which point freezing occurs. This phase transformation *i.e.*, the freezing of the eutectic liquid is often called a eutectic reaction.

The solid state microstructure of the material having the composition  $C_e$  will be an intimate mixture of two phases  $\alpha$  and  $\beta$  which are often present in the form of thin (around a few microns) platelets or rods. The lamellar microstructure of a typical

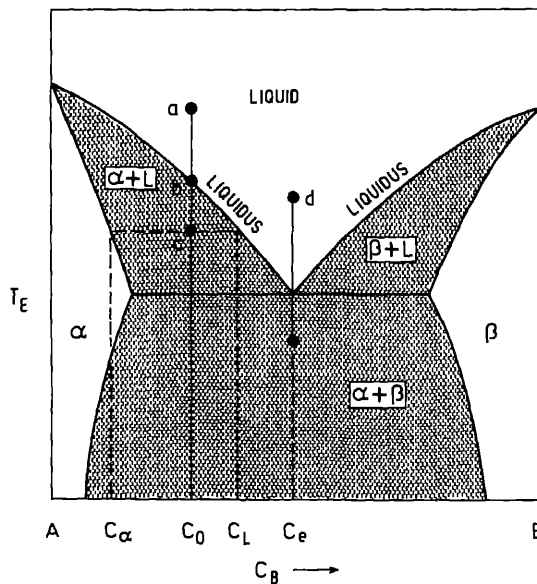


Figure 48. Illustration of the eutectic reaction.

eutectic is shown in figure 49 (Lyman 1972). The pattern is quite striking, undoubtedly reminding physicists of the patterns associated with hydrodynamic instabilities, for example. Indeed Langer has recently noted such similarities and has pointed out that as in the well-known Benard patterns associated with convective instability, the relevant steady state equations are incapable of predicting the unique behaviour observed experimentally. Specifically, the steady state theory of lamellar eutectic permits a wide range of lamellar spacings at any growth velocity whereas experiments seem to indicate a unique spacing. Accordingly, Datye and Langer (1981) have performed (as in hydrodynamics) a stability analysis for a model thinfilm eutectic. A major conclusion to emerge is that for off-eutectic compositions, there occurs a short wavelength instability. Figure 50 taken from the work of these authors shows a sketch of the oscillatory mode at its point of marginal instability. There is apparently some evidence from experiment for the existence of such a mode. As Langer notes, there is scope for much more work in this area both experimental and theoretical (especially in relation to kinetics). It certainly would be interesting to attempt experiments which are the analogue of those discussed in figure 47.

## 7. Summary

In this article, a broad overview of phase transformations has been attempted, essentially from a physicist's angle. While there are many aspects that might appeal to physicists, three areas have been highlighted since overlap with physics is manifestly evident. They are: The study of ground structures, the study of phase diagrams and the study of kinetics. In each area there are no doubt specifics and important details such as metallurgists are usually interested in, but there are also general features amenable to a basic analysis which physicists are likely to be attracted to.

In the area of ground state structures, the emphasis thus far appears to have been mainly on structures derived from bcc and fcc lattices. There is an obvious need to

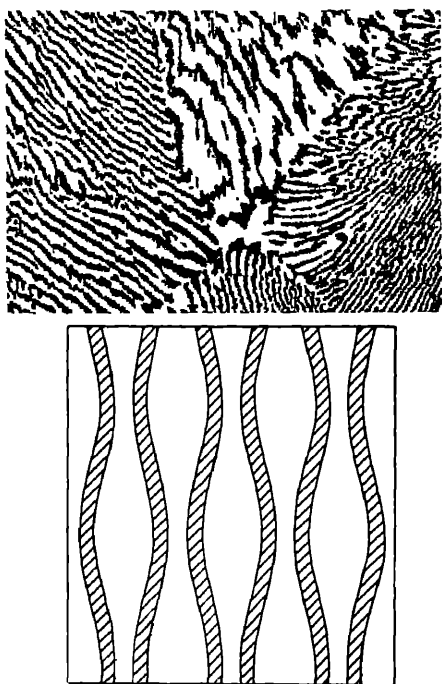


Figure 49-50. 49. Picture of a 63 Sn-37 Pb eutectic (softsolder). The lead-rich solution appears dark in a matrix of tin lamellae (light) (after Lyman 1972). 50. Oscillatory mode at its point of marginal instability (after Datye and Langer 1981).

extend this to other systems like hcp etc. We call attention also to formal papers (Progov and Sinai 1975, 1976; Slawny 1979) on the subject lest such activity be dismissed as pedestrian! Inputting potential derived from first principles has thus far been largely avoided but given the vast progress made in pseudopotentials in recent years and the prospects for bigger and faster computers, one could envisage a new thrust. No doubt there is the additional complication of relaxation energy (see equation (19)) but one now knows how to handle this, at least in principle.

Study of phase diagrams *via* simulation has made impressive progress but there is still a vast territory ahead. The viability of the cvm has been well established although there is room for improvement both in terms of going to larger clusters (which, incidentally, will call for fresh computational ingenuity) as well as allowing the exchange integral to vary with composition. The possibility of frustration is a stimulating discovery and so far, theory has not addressed itself to this question. Given the vigorous study made of this concept in spin glass, one could envisage exciting new vistas in the study of ordered systems also. The mappings that phase diagram investigations have achieved vis-a-vis models popular in the study of magnetism should act as an extra stimulant to physicists. Indeed one could probably now hunt around for suitable systems which are proving grounds for various kinds of Potts model etc.

As regards kinetics, there is a pressing need for real-time measurements. This therefore is an area where physicists can make important contributions, given their vast experience with the study of relaxations. Of course the experiments may not be always easy, and ingenuity may be required in many cases! Correlation techniques have a bright future if one is bold enough to apply them (although theoretical support for interpretation is at present not available). Neutron scattering and x-ray scattering (especially using synchrotron radiation sources) are the preferred tools but others like

Mössbauer spectroscopy, ultrasonic attenuation and even resistivity can provide useful complements, being less expensive and also less time-consuming. Thus, while neutron scattering could be reserved for select measurements, back-up wide ranging scans can come from the other probes mentioned. Where theory is concerned, the area of kinetics is a veritable jackpot in as much as one is faced with fascinating questions about phase changes far from equilibrium.

To keep the discussion relatively simple we have confined ourselves to substitutional systems (usually, metals with metals give such systems). If we extend consideration to systems where the *B* atoms enter interstitially in *A* (e.g. O in Ti), then it opens up a new world altogether. And then there are ternaries. No doubt they complicate matters, but who knows what surprises they have in store? In addition, there are the mixed oxides and mixed glasses which too, under certain circumstances, show phase separation. The interesting point about these systems is that they are amenable to study by light scattering (Schroder 1977), a technique we have barely mentioned. In respect of light scattering, the new wave of interest on colloidal crystals (Pieranski 1983) is also noteworthy. It is quite conceivable that various kinetic studies of colloidal crystals can be performed using laser light the way one usually investigates alloys using x-rays.

We have stayed away from defects, for example vacancies. One knows vacancies affect diffusion and therefore the role of vacancies may require examination. Perhaps for the present, these questions are best left to the metallurgists!

We have also not dwelt much on microstructure. Metallurgists relish them! Certainly the patterns are fascinating but one tends to dismiss any underlying universality on the grounds that microstructure is probably controlled by local factors like dislocation density etc. This may be true to some extent but at the same time it is difficult to believe that Nature has no basic rules governing domain formation etc. Now that some links between defects and symmetry have been established (Mermin 1979), it is worth searching for possible universalities governing microstructure formation and evolution. Such deep insight can come only from physics but it requires a really bold venture!

## 8. Concluding remarks

The story goes that towards the end of the twenties when the Golden Age of quantum mechanics was drawing to a close, Dirac remarked that, 'the rest is all chemistry'. Such an extreme view of physics has continued to prevail, and as late as 1970, van Hove (who has himself made notable contributions to condensed matter physics) observed during an after-dinner address at the Batelle Colloquium on Critical Phenomena that, "We should constantly recall and reassert that the elucidation of the fundamental laws remain the most essential task of physics". Referring to critical phenomena and topics of a similar kind he said, "It seems to me that physics now looks more like chemistry in the sense that in percentage, a much larger portion of the total research activity deals with complex systems, structure and processes, as against a smaller fraction concerned with the fundamental laws of motion and interaction. This Colloquium is a good example. Surely we all believe that the fundamental laws of classical mechanics, of the electromagnetic interaction and of statistical mechanics dominate the multivarious transitions and critical phenomena you discuss this week, and I presume that none of you expects his work on such problems to lead to the modification of these laws. You



know the basic equations better than the phenomena. You are after the missing link between them *i.e.* the intermediate concepts "... which should allow a quantitative understanding and prediction of the phenomena ...". Domb (1981) from whose essay on Critical Phenomena these quotes have been extracted, strongly disputes such a narrow interpretation of the goals of physics and points out that the goal is not restricted to the discovery of fundamental laws alone but encompasses the understanding of natural phenomena in general. Asserting that the giants of the past followed such an approach Domb observes, "Clerk Maxwell tried to construct a mechanical model to illustrate Faraday's laws of induction. He drew heavily on the theory of vortices in a perfect fluid and classical elasticity and was thereby led to introduce his famous displacement current. It was only later that he removed the 'scaffolding' to reveal the beautifully symmetric pattern of Maxwell's equations".

It is ironic that just around the time van Hove expressed his misgivings, Wilson did his celebrated work on critical phenomena which later earned for him the highest accolade of Science—the Nobel Prize. More significant, this paved the way for important feedback from statistical mechanics to particle physics (— *e.g.* there have been Monte Carlo simulations in connection with lattice gauge theories (Callaway and Rahman 1982), not dissimilar to the simulations discussed in §3.3).

In a different context, Anderson (1972) too has taken exception to the excessive importance attached to the study of fundamental laws. He observes, "The ability to reduce everything to simple fundamental laws does not imply the ability to start from those laws and reconstruct the Universe. In fact, the more the elementary particle physicists tell us about the nature of the fundamental laws, the less relevance they seem to have to the very real problems of the rest of science, ...". Illustrating his point with examples from many-body physics, he questions whether a cooperative phenomenon like symmetry breaking (which lies at the heart of a phase transition) can be predicted starting purely from a knowledge of the basic interaction between the constituent elementary objects. As he succinctly puts it, more is different! Incidentally, symmetry breaking is another area where there has been a profitable feedback from condensed matter physics to particle physics.

The purpose of the above remarks and quotes is not merely to reinforce the point that condensed matter physics can as much be a frontier area, as, say, particle physics but also to remind condensed matter physicists that they in turn should avoid a snooty attitude towards materials science. As we have tried to argue in this article, there are many fascinating questions in materials science also, buried in the 'complexities' that traditional physicists shun. For those who dare to delve into these complexities and isolate the basic questions, the rewards could be great.

Beauty, it is said, is in the eyes of the beholder. Where physics is concerned, something similar appears to be true. The physics, turned out, often depends more on the investigator than on the phenomenon (at least the usual perception one has of it). We merely have to remind ourselves of the magical touch that Einstein gave to the observations of the botanist Robert Brown on the dancing pollen grain. What if he had dismissed it as 'not physics'?

In this country, Prof. Ramaseshan was perhaps the first person to establish a bridge between physics and materials science in a big way. Reared in the traditions of the Raman School, where the emphasis always was on natural phenomena in their totality, he was not averse to taking on the problems of materials when the challenge came. On the other hand, he invariably put to use his rich experience in physics and demonstrated

that by doing so, one could introduce novel approaches to familiar problems. Not surprisingly, he made the plea at Baroda for a larger perspective while defining Thrust Areas. It has been a pleasant task for me to amplify and illustrate that theme through this article. I only hope it does full justice to his remarks.

### Acknowledgements

My interest in this area was aroused by the lectures I heard a few years ago at Varenna given by Prof. de Fontaine. I am grateful to him for subsequently sending me several of his reprints and preprints which helped me dig deeper into the subject. I would also like to express my thanks to Dr D Sahoo for several discussions, to Radha Ranganathan for assistance with the preparation of the manuscript, to P Subba Rao for efficient and skilful typing and to P Harikumar and R Kannan for taking care of the graphics. Finally, I would like to acknowledge my indebtedness to the many authors whose work I have freely drawn upon in preparing this review.

### References

- Allen S M and Cahn J W 1972 *Acta Metall.* **20** 423  
 Anderson P W 1972 *Science* **177** 393  
 Aubrey S 1981 in *Physics of defects* (ed) R Balian et al (Amsterdam: North Holland) p 431  
 Aubrey S 1983 *J. Phys.* **44** 147  
 Bardhan P, Chen H and Cohen J B 1977 *Philos. Mag.* **35** 653  
 Barker J A 1953 *Proc. R. Soc. (London)* **A216** 45  
 Berne B J and Pecora R 1976 *Dynamic light scattering* (New York: Wiley)  
 Bethe H A 1935 *Proc. R. Soc. (London)* **A150** 552  
 Billotet C and Binder K 1979 *Z. Phys.* **B32** 195  
 Billotet C and Binder K 1980 *Physica* **A103** 99  
 Binder K 1973 *Phys. Rev.* **B8** 3423  
 Binder K 1977 *Phys. Rev.* **B15** 4425  
 Binder K 1980a *Phys. Rev. Lett.* **45** 811  
 Binder K 1980b in *Systems far from equilibrium*, Lecture Notes in Physics 132 (ed) L. Garrido (Berlin: Springer)  
 Binder K 1981 *Z. Phys.* **B45** 61  
 Binder K, Lebowitz J L, Phani M K and Kalos M H 1981 *Acta Metall.* **29** 1655  
 Binder K and Stauffer D 1976 *Z. Phys.* **B24** 407  
 Bragg W L and Williams E J 1934 *Proc. R. Soc. (London)* **A145** 699  
 Bragg W L and Williams E J 1935 *Proc. R. Soc. (London)* **A151** 540  
 Brockhouse B N 1958 *Nuovo Cimento* **9** (Suppl.) 45  
 Cahn J W 1961 *Acta Metall.* **9** 795  
 Cahn J W 1962 *Acta Metall.* **10** 179  
 Cahn J W 1968 *Trans. AIME* **242** 166  
 Cahn J W and Hilliard J E 1958 *J. Chem. Phys.* **28** 258  
 Callaway D and Rahman A 1982 *Phys. Rev. Lett.* **49** 613  
 Chakravarti B, Starke E A, Sparks C J and Williams R O 1974 *J. Phys. Chem. Solids* **35** 1317  
 Chen H and Cohen J B 1977 *J. Phys.* **C7** 314  
 Chen H, Comstock R J and Cohen J B 1979 *Annu. Rev. Mater. Sci.* **9** 51  
 Cohen J B 1970 in *Phase transformations* (ed) H I Aaronson (Metals Park Ohio: Am. Soc. Metals) p 561  
 Collins M F and Teh H C 1973 *Phys. Rev. Lett.* **30** 781  
 Cook H E 1970 *Acta Metall.* **18** 297  
 Cook H E, de Fontaine D and Hilliard J E 1969 *Acta Metall.* **17** 765  
 Clapp P C and Moss S C 1968 *Phys. Rev.* **171** 751

- Das S K, Okamoto P R, Fisher P M J and Thomas G 1973 *Acta Metall.* **21** 913
- Datye V and Langer J S 1981 *Phys. Rev.* **B24** 4155
- de Fontaine D 1967 Ph.D Thesis (Evanston Ill: Northwestern University)
- de Fontaine D 1975a in *Treatise on solid state chemistry* (ed) N B Hannay (New York: Plenum) p 129
- de Fontaine D 1975b *Acta Metall.* **23** 553
- de Fontaine D 1979 in *Solid state physics* (eds) H Ehrenreich, F Seitz and D Turnbull (New York: Academic) Vol. 34 p 73
- de Fontaine D 1981 *Met. Trans.* **A12** 559
- de Fontaine D 1982 in *Mechanical and thermal behaviour of materials* (eds) C Caglioti and A Ferro Milone (Amsterdam: North Holland) p 449
- de Gennes P G 1959 *Physica* **25** 825
- d'Heurle F M and Gordon P 1961 *Acta Metall.* **9** 304
- Dienes G J 1955 *Acta Metall.* **3** 549
- Domb C 1981 in *Perspectives in statistical physics* (ed) H J Raveche (Amsterdam: North Holland) p 173
- Feigenbaum M J 1978 *J. Stat. Phys.* **19** 25
- Feigenbaum M J 1979 *J. Stat. Phys.* **21** 665
- Feigenbaum M J 1980 *Commun. Math. Phys.* **77** 65
- Freidel J 1974 in *Order-disorder transformations in alloys* (ed) H Warlimont (Berlin: Springer) p 1
- Gilmore R 1981 *Catastrophe theory for scientists and engineers* (New York: Wiley)
- Gunton J D 1982 *First order transitions, metastability and spinodal decomposition* (Temple: University Report)
- Haken H 1978 *Synergetics, An introduction* (Berlin: Springer)
- Hansen M 1958 *Constitution of binary alloys* (New York: McGraw Hill)
- Hashimoto T, Miyoshi T and Ohtsuka T 1976 *Phys. Rev.* **B13** 1119
- Hashimoto T, Nishimura K and Takeuchi Y 1978 *Phys. Lett.* **A65** 250
- Holsztynski W and Slawny J 1978 *Commun. Math. Phys.* **61** 177
- Hopper R W 1982 *J. Non. Crystall. Solids* **49** 263
- Iliopoulos J 1980 *Contemp. Phys.* **21** 159
- Johansson C M and Linde J O 1928 *Ann. Phys.* **86** 291
- Kanamori J and Kakehashi Y 1977 *J. Phys.* **38** C7 274
- Katsura S and Narita A 1973 *Prog. Theor. Phys.* **50** 1426, 1750
- Kawasaki K 1972 in *Phase transitions and critical phenomena* (eds) C Domb and M S Green (New York: Academic) Vol 2 p 443
- Khachaturyan A G 1974 in *Order-disorder transformations in alloys* (ed) H Warlimont (Berlin: Springer)
- Kikuchi R 1951 *Phys. Rev.* **81** 988
- Kikuchi R and de Fontaine D 1976 *Scr. Metall.* **10** 995
- Kikuchi R, Sanchez J M, de Fontaine D and Yamauchi H 1980 *Acta Metall.* **28** 651
- Kim M W, Chou Y C, Goldberg W I and Kumar A 1980 *Phys. Rev.* **A22** 2138
- Kim M W, Schwartz A J and Goldberg W I 1978 *Phys. Rev. Lett.* **41** 651
- Kozlov E V, Demet'ev V M, Emelyanov V N, Kormin N M, Taylashev A S and Stern D'M 1974 in *Order-disorder transformations in alloys* (ed) H Warlimont (Berlin: Springer) p 58
- Krivoglaz M A and Smirnov A A 1965 *Theory of order-disorder in alloys* (Amsterdam: Elsevier)
- Kudo T and Katsura S 1976 *Prog. Theor. Phys.* **56** 435
- Langer J S 1969 *Ann. Phys.* **54** 258
- Langer J S 1980 in *Systems far from equilibrium Lecture notes in Physics* 132 (ed) L Garrido (Berlin: Springer) p 12
- Langer J S, Bar-on and Miller H 1975 *Phys. Rev.* **A11** 1417
- Langer J S and Turski L A 1973 *Phys. Rev.* **A8** 3230
- Lebowitz J L, Marro J and Kalos M H 1982 *Acta Metall.* **30** 297
- Lifshitz I M and Slyozov V V 1961 *J. Phys. Chem. Solids* **19** 35
- Lyman T (ed) 1972 *Atlas of microstructures of industrial alloys* (Metals Park, Ohio: Am. Soc. Metals) Vol 6, p 318 (picture no: 2628)
- Magde D 1977 in *Molecular biology, biochemistry and biophysics* (eds) J Pecht and R Rigler (Berlin: Springer-Verlag) p 43
- Mahan G D and Claro F H 1977 *Phys. Rev.* **B16** 1168
- Mermin N 1979 *Rev. Mod. Phys.* **51** 591
- Morita T 1972 *J. Math. Phys.* **13** 115
- Nowick A S and Weisenberg L R 1958 *Acta Metall.* **6** 260

- Ogawa S 1974 in *Order-disorder transformations in alloys* (ed) H Warlimont (Berlin: Springer) p 240
- Oki K, Sagane H and Eguchi T 1974 *Jpn J. Appl. Phys.* **13** 753
- Oki K, Yamamura A, Masaka M and Eguchi T 1977 *Trans. Jpn Inst. Metals* **18** 520
- Onsager L 1944 *Phys. Rev.* **65** 117
- Ornstein L S and Zernike F 1914 *Proc. Acad. Sci. (Amsterdam)* **17** 793
- Paulson W M and Hilliard J E 1977 *J. Appl. Phys.* **48** 2117
- Pedersen A M and Riste T 1980 *Z. Phys.* **B37** 171
- Pieranski P 1983 *Contemp. Phys.* **24** 25
- Progov S A and Sinai Y 1975 *Theor. Math. Fizika* **25** 358
- Progov S A and Sinai Y 1976 *Theor. Math. Fizika* **26** 61
- Radelaar S and Ritzen J M J 1969 *Phys. Status Solidi* **B31** 277
- Richards M J and Cahn J W 1971 *Acta Metall.* **19** 1263
- Sanchez J M and de Fontaine D 1978 *Phys. Rev.* **B17** 2926
- Sanchez J M and de Fontaine D 1980 *Phys. Rev.* **B21** 216
- Sanchez J M and de Fontaine D 1982 *Phys. Rev.* **B25** 1759
- Sato H and Toth R S 1961 *Phys. Rev.* **124** 1833
- Schwahn D and Schmatz W 1978 *Acta Metall.* **26** 1571
- Shockley W 1938 *J. Chem. Phys.* **6** 130
- Shroder J 1977 in *Treatise on materials science and technology* (eds) M Tomozowa and R H Doremus (New York: Academic Press) Vol 12 p 158
- Singhal S P, Herman H and Koztorz G 1978 *J. Appl. Crystall.* **11** 572
- Slawny J 1979 *J. Stat. Phys.* **20** 711
- Stanley H E 1971 *Introduction to phase transitions and critical phenomena* (Oxford: Clarendon)
- Stratanovich R L 1963 *Topics in the theory of random noise* Vol 1 (New York: Gordon and Breach)
- van Baal C M 1973 *Physica* **64** 571
- van Hove L 1953 *Phys. Rev.* **89** 1189
- Venkataraman G 1979 *Bull. Mater. Sci.* **1** 129
- Venkataraman G 1982 in *Mechanical and thermal behaviour of materials* (eds) C Caglioti and A Ferro Milone (Amsterdam: North Holland) p 278
- Venkataraman G and Balakrishnan V 1977 in *Proceedings of the Indo-German Seminar on Radiation Damage* (Kalpakkam: RRC) p 273
- Venkataraman G and Balakrishnan V 1979 *Mater. Sci. Bull. (India)* **1** 59
- Villain J 1959 *J. Phys. Chem. Solids* **11** 303
- Vineyard G H 1956 *Phys. Rev.* **102** 981
- Wagner C 1961 *Z. Electrochem.* **65** 243
- Wulff J 1971 (ed) *Structure and properties of materials* (Bombay: Wiley-Eastern) Vol II
- Yamauchi H and de Fontaine D 1974 in *Order-disorder transformations in alloys* (ed) H Warlimont (Berlin: Springer) p 148



## Growth of research and development in rare metals extraction in India

C V SUNDARAM and C K GUPTA\*

Reactor Research Centre, Kalpakkam 603 102, India

\* Extractive Metallurgy Section, Bhabha Atomic Research Centre, Trombay, Bombay 400 085, India

**Abstract.** The ushering in of the era of high technology in our country witnessed the emergence and growth of several new technologies which are either totally unconventional or less common in otherwise well known and established areas of industrial practice. A vivid example of the second category of advances is found in the development of extractive processes for obtaining the less common metals particularly required for service in nuclear, aerospace and electronics industries. In this paper, the growth of research and development in rare metals extraction in India is surveyed from its infancy in the fifties to the present stature of a firm footed technology accredited with several directed achievements and well-developed maturity.

**Keywords.** Rare metal extraction; physical beneficiation; chemical beneficiation; breakdown process; separation process; halide metallurgy; electrolytic reduction.

### 1. Introduction

One of the greatest technological upheavals in the history of human civilization was triggered by the second world war. During the post war period a large spectrum of high technology industries flourished. The frontiers of established technologies expanded and new highways opened up in the hitherto unexplored regions. The march of human progress entered into what is variously referred to as the nuclear age, the space age and the electronics age.

If one looks at the mainstream technologies which defined the direction and sustained the momentum of such a total technological advance, achievements in metals and materials development stand out, having played a vital role. The development of appropriate metals and materials has always been crucial to transform scientific ideas into practical realities.

We witness today, in our country, wide-ranging activities in the fields of science and technology. Since independence, we have come a long way in securing such an expansion. It is a matter of pride that we observe in the national scene massive development programmes in a number of advancing technological areas, as for instance, in nuclear energy, aeronautics and aerospace, electronics and oceanography—thanks to the efforts made and the support given to usher in this new era.

Tracing back the sequence of science and technology development, it would seem to have started with the launching of the atomic energy programme in the country. Following the institution of the Atomic Energy Commission (AEC) and the modest beginnings made in the early fifties, many disciplines of science and engineering—of relevance to this programme—have evolved and flourished. The wide variety and scope in these disciplines have enabled the progressive transfer of the experience to other

areas of science and technology. Developments in space, aeronautics and electronics have gradually entered the national scene.

Any discussion on technological growth has to lead a discussion on materials development which constitutes the supporting structure like a back bone. As indicated in figure 1, while many of the ferrous and non-ferrous metals that are in every day use, are also required for peripheral structural applications in modern technology, they are not adequate for the critical core component applications in these technologies. Several members of the rare metals group *viz* beryllium, titanium, zirconium, hafnium, vanadium, niobium, tantalum, thorium, uranium, plutonium and the rare earths, possess the unique combination of physicomachanical, nuclear, electronic, and chemical properties. Taken together, these characteristics have qualified many of the above mentioned metals for core component applications.

The extractive processes to obtain this specific family of metals indigenously at sufficient purity levels and in adequate quantities were not initially available. The development programme of AEC, however, proceeded on the basic assumption that as it progresses, an adequate, dependable and continuing supply of appropriate metals and materials will be assured. To relieve the dependence on overseas sources for the strategic materials and to keep scientific and technological progress from being impeded or slowed down by materials shortages, pursuits on metals and materials development received close attention. It is needless to mention here that without a strong and sound materials base, it is difficult to attain, in the long run, technological self-sufficiency, particularly in the frontier areas.

India is fortunately blessed with significant raw material reserves with respect to many of the strategic metals. Complete and proper utilization of our natural rare metal resources presupposes the availability of a comprehensive body of scientific knowledge and engineering experience in the field of metal processing. An organization with multidisciplinary resources and skill to support a large spectrum of research projects in virtually all phases of metallurgy (figure 2) could accomplish this feat. This responsibility was thus taken over by the various laboratory and industrial units of the Department of Atomic Energy and, in particular, by the Bhabha Atomic Research Centre (BARC). "Growth of R & D in rare metal extraction in India" then predominantly

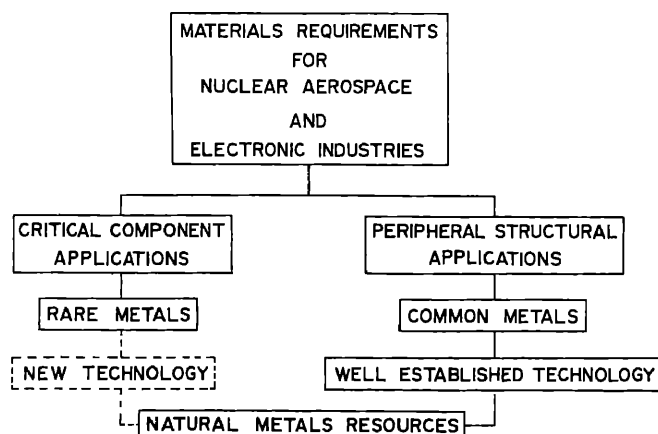


Figure 1. Status of materials requirement in high technologies.

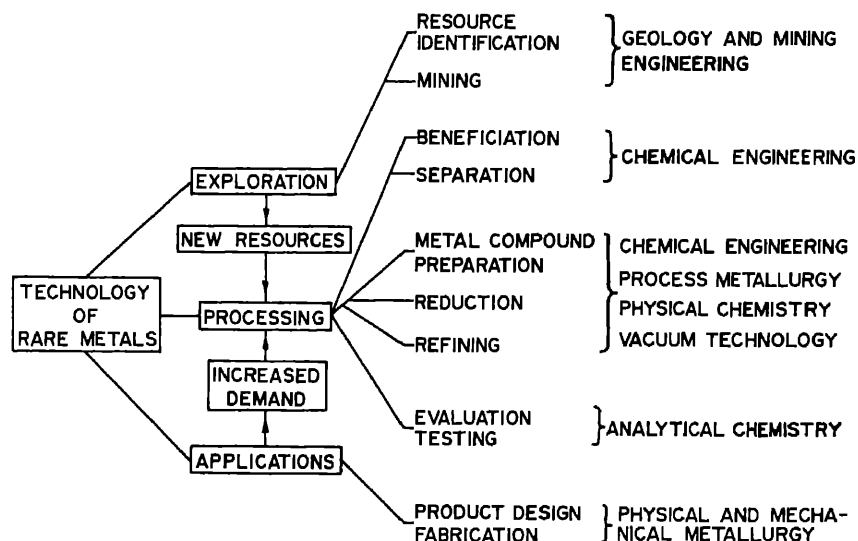


Figure 2. Multidisciplinary content of rare metal extraction.

pertains to tracing the process metallurgy activities of the DAE family during the past three decades.

## 2. Definition of rare metals extraction

Extractive metallurgy consists of the science and art of winning metals from the mined ore. For most common metals, the extractive metallurgy means the sequence of roasting, smelting and refining operations as indicated in figure 3. This scheme has characteristically failed to work in the extraction of many of the rare metals with which this presentation is concerned. Rare metals occur in nature in very complex forms, often in very low concentration. The procedures involved for recovering metal values are very elaborate, complex and require special equipment, processes and skill. Further, these metals show a high degree of sensitivity to impurities, which influence pronouncedly their physical, chemical and metallurgical properties. This dictates that the rare metals be properly protected at every stage of their production and use.

Broadly, the process sequence for rare metals, as indicated in figure 3 consists of the all important separation step followed by specialised reduction and refining operations. As a further elaboration, figure 4 presents a generalised scheme for rare metal extraction. For an appreciation of such a sequence, a brief reference may be drawn to the extractive metallurgy of niobium, the flow sheet for which appears in figure 5.

The joint occurrence of niobium and tantalum in nature conditioned by their close chemical similarities and the difficulties in separating them from each other halted their industrial development. In the past three decades, with substantial growth in demand and also in technology, complete flowsheets have been developed to get the pure metals in sufficient quantities.

The beneficiated columbite-tantalite ore is fed to the separation step. A pyrovacuum method was first attempted to separate the metals by chlorination but a hydro-



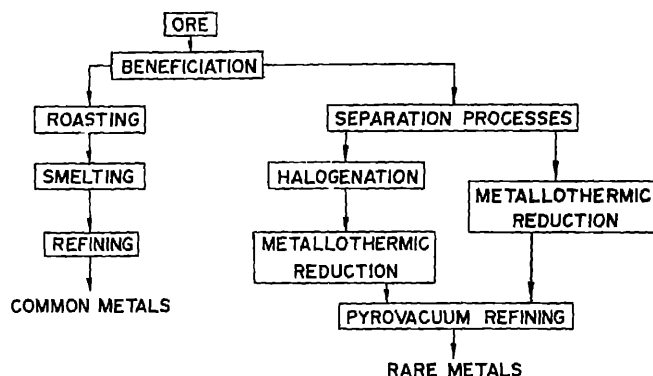


Figure 3. Extraction sequences for common and uncommon metals.

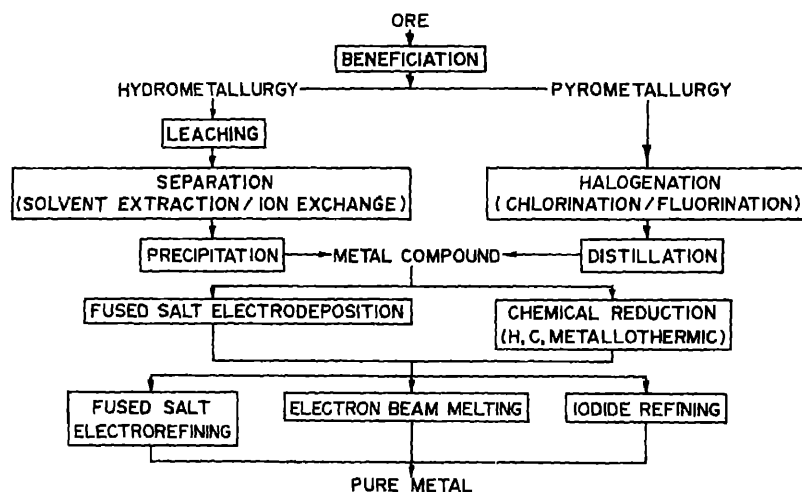


Figure 4. Generalised scheme for rare metal extraction.

metallurgical route involving solvent extraction of the fluoride leach liquor of the beneficiated columbite-tantalite found industrial acceptance sooner. Pure niobium pentoxide obtained after the separation step is converted to the metal by either carbothermic reduction at high temperatures under vacuum or aluminothermic reduction and pyrovacuum refining. Depending on the purity desired, primary niobium is subjected to electron beam melt refining/electron beam floating zone refining to obtain the final product.

Now one can see the path niobium ore travels before it becomes metal. It may be added here that niobium is a well-behaved member of the rare metal family, and in many cases we may have to encounter tougher reactive rare metals.

### 3. Indian experience in rare metal extraction

The Indian experience in rare metal extraction has been founded on a commitment to provide means by which the current and emerging demands for special metals and

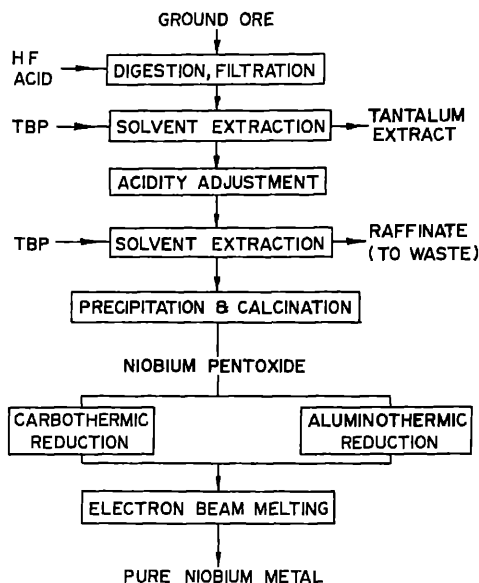


Figure 5. Flow sheet for niobium extraction.

materials in our country could be met. The emphasis has been on developing techniques effective on our indigenous resources. It is needless to say that this development of technology being totally indigenous, we encountered several teething troubles with respect to some processing steps due to scale up which were successfully overcome by persistent efforts. Every effort was made to introduce indigenous equipment which posed considerable problems and cost considerable time. Based on the research and development work at BARC administered mainly under the metallurgy, chemical engineering and chemistry groups, techniques and processes have been successfully evolved and developed to levels conducive to setting up of production plants. By way of some typical examples, mention may be made of:

- uranium oxide and metal production, involving ore leaching, ion exchange, solvent extraction, calcination, hydrofluorination and chemical reduction, induction melting, high temperature sintering and further fabrication;
- zirconium metal production by alkali fusion of zircon, solvent extraction, calcination, chlorination, magnesium reduction and vacuum distillation, vacuum arc melting, extrusion and pilgering;
- tantalum metal production by hydrofluoric acid dissolution of columbite-tantalite, solvent extraction, sodium reduction, powder metallurgy and electron beam melting;
- beryllium metal production by silicofluoride sintering of beryl, leaching, purification, fluoride decomposition, magnesium reduction, vacuum melting and vacuum hot pressing.

The experience has led to the setting up of the Nuclear Fuel Complex (NFC) at Hyderabad which for the past ten years has been engaged in the production of a range of nuclear and special materials. Based on the parallel investigation on titanium sponge production and pilot plant demonstration at NFC, a larger production plant for the

metal is under establishment at the Defence Metallurgical Research Laboratory (DMRL), Hyderabad. The pilot plant for beryllium, set up at Vashi, New Bombay has commenced operation.

Starting off from this introductory indication of the scope and level of directed R & D efforts that have gone into the emergence and rise of India in the rare metals field in the world, it is now appropriate to proceed a coverage of the Indian experience in more representative detail by looking at each of the unit operations in turn.

#### 4. Physical beneficiation

It is a characteristic of all the rare metal resources that they occur as dilute, multicomponent complex minerals widely dispersed and distributed in various geological formations. Development of beneficiating techniques for these ores has, in fact, grown into a technology of lean ore beneficiation. This technology has also aided in many instances in the beneficiation of lean and complex common metal resources also.

In table 1 are listed the main rare metals minerals occurring in our country. Besides there are at least twice as many secondary minerals for each of these metals. There are then the second line reserves to be prospected. The principal beneficiating methods which are at our disposal are indicated in figure 6. One or more of these methods in combination have been employed for beneficiation. It is instructive to briefly review the processes applied to the important resources of many rare metals, beach sands.

Table 1. Important rare metal resources

Metal	Mineral	Composition	Location
Th	Monazite	(Ce, Y, Ca, Th) PO <sub>4</sub>	Beach sands of Kerala, Orissa, Andhra Pradesh, Tamil Nadu
Zr	Zircon	ZrSiO <sub>4</sub>	Beach sands
Ti	Ilmenite Rutile	FeTiO <sub>3</sub> TiO <sub>2</sub>	Beach sands
Nb	Columbite	(Fe, Mn) Nb <sub>2</sub> O <sub>6</sub>	Hazaribagh, Monghyr (Bihar)
	Pyrochlore	(Na, Ca) <sub>2</sub> Nb <sub>2</sub> O <sub>6</sub> (OH, F)	Dharmapuri Dist (TN), Khammam (AP), Gujarat, Bhilwada Dist (Rajasthan)
	Samarskite	(Fe, Y, U) <sub>2</sub> (Nb, Ti, Ta) <sub>2</sub> O <sub>7</sub>	Pegmatites of Hazaribagh, Nellore, Jaipur and Tonk Dist of Rajasthan
Ta	Tantalite	(Fe, Mn) (Ta, Nb) <sub>2</sub> O <sub>6</sub>	Hazaribagh, Monghyr (Bihar)
	Microlite	(Ca, Na) <sub>2</sub> Ta <sub>2</sub> O <sub>6</sub> (O, OH, F)	Hazaribagh, Monghyr (Bihar)
Be	Beryl (aquamarine, emerald, heliodro, morganite)	Al <sub>2</sub> Be <sub>3</sub> (Si <sub>6</sub> O <sub>18</sub> )	Bihar, Rajasthan, AP, MP.,
U	Uraninite	(U <sub>1-x</sub> <sup>4+</sup> U <sub>x</sub> <sup>6+</sup> )O <sub>2+x</sub>	Jaduguda, Singhbhum (Bihar)
	Pitchblende	Variety of uraninite	South Kanara (Karnataka)

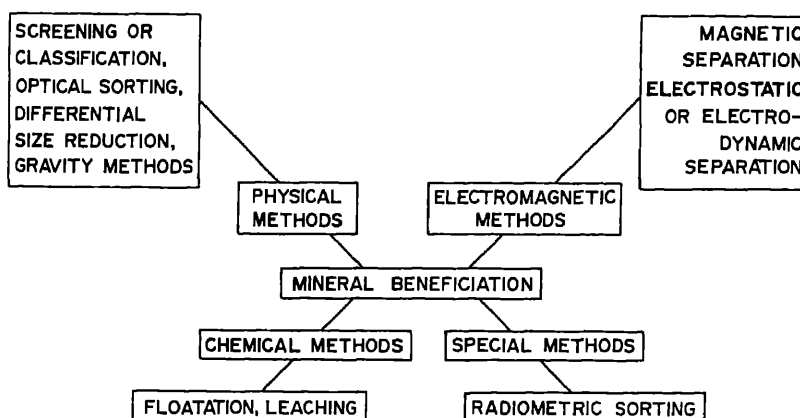


Figure 6. Beneficiation techniques for rare metals resources.

Table 2. Typical mineral composition of monazite sands

Constituent	Percent
Monazite	0.5-1
Ilmenite	65-80
Rutile	3-6
Zircon	4-6
Sillimanite	2-5
Garnet	1-5

The commonly occurring minerals in beach sand deposits are ilmenite, rutile, zircon, monazite, sillimanite and garnet. Table 2 gives the typical mineral composition of the beach sands. The beach sand minerals occur extensively but in small concentrations in the alluvial deposits. The sand is mined by suction dredging and subjected to preconcentration with a view to obtain a bulk gravity concentrate comprising the heavy minerals. The lean sand deposit containing 2-5% heavy minerals is subjected to concentration using pinched sluices, cone concentrators, spirals and wet tables to obtain a concentrate with more than 80% heavy minerals. The separation of individual minerals is carried out by dry methods. Almost all the principal mineral dressing methods *viz* screening, gravity separation, magnetic separation, electrostatic separation, froth flotation etc are employed in the recovery of economic minerals from beach sand deposits.

Monazite, ilmenite, rutile and zircon are classified as scheduled minerals according to the Atomic Energy Act of 1962. Indian Rare Earths Limited operates three beneficiating plants—two at Manavala Kurichi in Tamil Nadu and one at Chavara, Kerala. Another plant is operated by Kerala Minerals and Metals Limited. At present the country's entire need of beach sand minerals is being met by IRE and KMM. Extensive dense sand deposits along the south Orissa coast over a stretch of 150 km has been located by Atomic Minerals Division and unlike the existing dry mill beneficiating operations, the Chatrapur operation would include a wet plant also for exploiting the Orissa deposit.

## 5. Chemical beneficiation and breakdown processes

The tenor of the uranium ores—uraninite, pitch blends, brannerite, uranothorite and carnotite—exploited for metal production assays usually around 0.05–0.2%  $U_3O_8$ . These low grade ores are directly leached to extract the uranium values since most of the physical beneficiation techniques have not been found economically feasible. There are many methods and techniques in leaching. Ore characteristics, material handling problems, methods employed for metal recovery from the pregnant solution, tailings disposal and many other factors determine the leaching technique.

Except in the case of high grade uranium ores or ores with a high concentration of acid consuming minerals which will necessitate alkali leaching with sodium carbonate, acid leaching with sulphuric acid is particularly suited to the dissolution of uranium values from the ore. As only hexavalent uranium is soluble in aqueous solution, the leaching is performed in the presence of an oxidising agent such as  $MnO_2$ ,  $NaClO_3$  and  $Fe_2(SO_4)_3$ . Acid concentration and pH are the two important process parameters. In the case of ores containing uraninite and pitchblende, such as the one at Jaduguda, acid concentration is normally controlled by maintaining pH of 1.5 to 2. This type of leaching, under controlled pH conditions helps in preventing the dissolution of acid consuming minerals like spatite. It has been found that high concentration of phosphate in the solution influences the oxidation potentials and complicates the uranium recovery process.

Besides aqueous leaching, chemical breakdown processes involve digestion with acid or alkali solution or more drastic fusion with alkali and alkali fluorides. The major breakdown processes commonly employed in our country to solubilize the metal values are schematically outlined in figure 7. It is understood that, as broadly presented for uranium, several parameters require control for accomplishing successful breakdown operation. The beryl ore is opened up to yield water soluble  $Na_2BeF_4$  by fusing it with sodium silicofluoride and sodium carbonate at 700°C.

Having seen so far the established and commercially operating breakdown processes, we can briefly digress to see the direction for new developments.

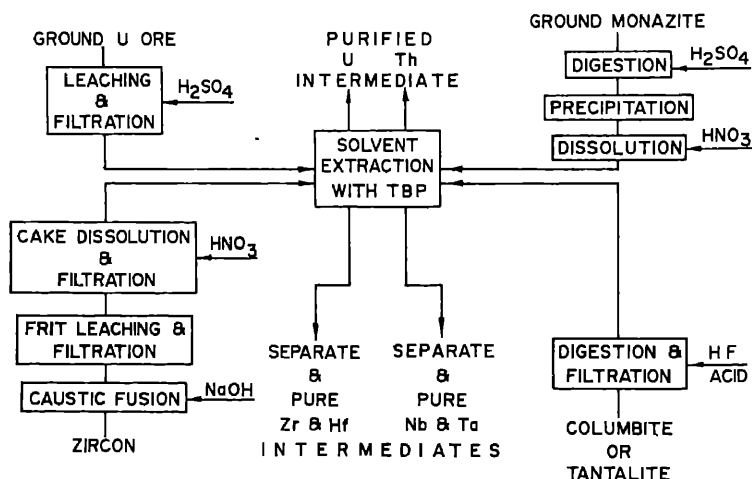


Figure 7. Schematics of ore treatment processes prior to solvent extraction separation.

A powerful new leaching technique is pressure leaching. Complex minerals like ilmenite and pyrochlore can be transformed into relatively pure oxides in a single step by treatment with hydrochloric acid at high temperature and pressure in an autoclave. References abound evidencing application of pressure leaching to many other minerals including those of uranium. A new approach to leaching low grade uranium ores is provided by the so-called bacterial or microbial leaching. Certain types of autotrophic bacteria of the thiobacillus-ferrobacillus group act on the sulphate minerals like pyrite and lead to generation of ferric sulphate and sulphuric acid to leach out uranium.

Other breakdown methods developed to various levels of advancement include soda ash sintering of zircon, electrothermal smelting of ilmenite, beneficiation of ilmenite and zircon in plasma furnaces and chlorination breakdown of ores.

## 6. Separation processes

The leach solution obtained by chemical breakdown of the beneficiated ore is passed through some unique sequence of "purification" operations peculiar to rare metal extraction. This purification of the pregnant rare metal solution is essentially to separate the co-occurring elements from the desired metal before it is put through subsequent reduction and refining operations. It must be emphasised that the elements co-occurring with the rare metals if allowed to proceed through the reduction step normally cannot be removed from the reduced primary metal by any of the common post reduction refining. This situation may be thought of as arising due to the great reactivity of the rare metals in general. A great deal of effort has gone into the development of separation processes for the purification of uranium and thorium to nuclear grades of purity, separation of rare earth metals from one another, niobium from tantalum and zirconium from hafnium. Of the many alternatives explored and studied at Trombay, two major processes have emerged for effective plant level utilization—solvent extraction and ion exchange.

In solvent extraction, the purification is achieved by selective extraction of compounds of a given element or impurities from aqueous solutions into an organic solvent which is immiscible with water. This is possible when the distribution coefficients of the components in the mixture differ from each other sufficiently. The distribution coefficient which is the crucial parameter in solvent extraction depends on the properties of the solvent, the concentration of the extracted species in the aqueous phase, the presence of other species in the solution, the acidity of the aqueous phase and the temperature. The studies conducted at Trombay were directed not only at optimising these conditions but also obtaining the engineering details such as selection of suitable solvent, collection of equilibrium data, determination of stages, mass transfer rates, choice of contacting equipment and scale-up.

A typical extraction flowsheet is given in figure 8. Starting from its application for recovering uranium from ore leach liquors, solvent extraction has grown in diversity and some of the important systems are presented in table 3. Solvent extraction is practised on a plant scale in our department for the extraction of uranium, thorium, plutonium and for the separation of zirconium from hafnium and niobium from tantalum starting from a variety of aqueous feed solutions using TBP as the organic phase and mixer settlers for contacting equipment.

Ion exchange has been the specialist separation process for use with very dilute feed

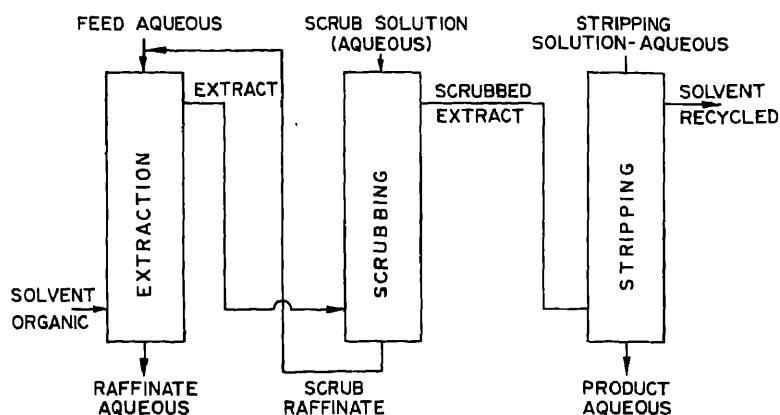


Figure 8. Typical solvent extraction flowsheet.

Table 3. Solvent extraction for separation for purification of rare metals

Metal	Organic phase	Aqueous solution	Remarks
U	TBP	Nitrate	Purification of U to nuclear grade
Th	TBP	Nitrate	Purification of Th to nuclear grade
Zr	TBP	Nitrate	Separation from Hf
Ta	TBP	Fluoride	Separation from Nb
Lanthanides	DEHPA	Chloride	Separation of individual lanthanides

solutions. The most spectacular application of ion exchange has been in the recovery of uranium from low grade ore leach liquors. It is especially better than solvent extraction in such cases.

Ion exchangers are sparingly soluble solids (organic or inorganic) with active functional groups which can be exchanged for ions present in the solution. The schematics of the ion exchange operation is given in figure 9. As the affinity of the ion exchange resin depends on the charge and size of the ionic species involved in the exchange and the distribution coefficient varies with the conditions of the aqueous phase like acidity etc, selective separation and purification can be achieved. Ion exchange separations are generally slow and operate on much less throughputs compared to solvent extraction processes. However as indicated already, for dilute solutions, in cases where separation factors are close and in some cases for processing unclarified solutions ion exchange is particularly sought after. Some important systems processed by ion exchange are given in table 4.

## 7. Halide metallurgy

The separation steps generally give the pure products in the form of either oxides or halides. These metal compound intermediates are converted to the metal by various reduction processes. Here again, peculiar for rare metals, one encounters a unique

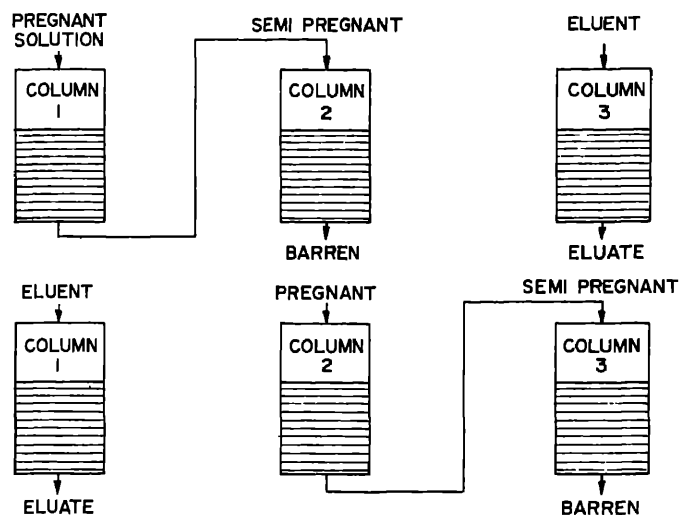


Figure 9. Ion exchange—adsorption, elution flow-sheet.

Table 4. Ion exchange separation for purification of rare metals

Metal	Ion Exchanger	Aqueous feed	Remarks
U	Deacidite FF(530)	Sulphate	Uranium separated from elements co-occurring in the ore
Zr	Cation exchanger ZK-225	Nitrate	Zr is separated from Hf
Ta	Anion exchanger EDE-10P	Fluoride	Ta is separated from Nb
Rare earths	Cation exchanger Dowex 50, ZK 225	Chloride	Rare earth metals are separated from each other

system of metal production. The intermediate which is reduced to obtain the metal is invariably a halide. The involvement of halides in rare metals extraction is certainly not restricted to the reduction step. Its omnipresent close involvement at many other stages of metal extraction also shall be looked into in what follows.

Halogens and halides find application in almost all stages of rare metal extraction from ore beneficiation to metal purification as given in figure 10. The diversity of halide metallurgy can be gauged from the following examples. (i) Ore breakdown: chlorination of zircon, ilmenite, rutile, silicofluoride treatment of beryl, zircon; (ii) Halogenation of crude intermediate: chlorination of zirconium carbide; (iii) Halogenation of pure intermediate: chlorination of zirconium dioxide, titanium dioxide; hydrofluorination of uranium dioxide; (iv) Reduction of metal halides: sodium reduction of  $K_2TaF_7$ , calcium reduction of  $UF_4$ , magnesium reduction of  $TiCl_4$ ,  $ZrCl_4$ ,  $BeF_2$ , electrolysis of RE chlorides; (v) Reclamation of scrap: by chlorination and fused salt electrorefining; (vi) Ultrapurification of commercial grade metal: iodide process for crystal bar titanium, zirconium and hafnium.

Starting with the gas-solid reactions, to carry out the entire range of processes as



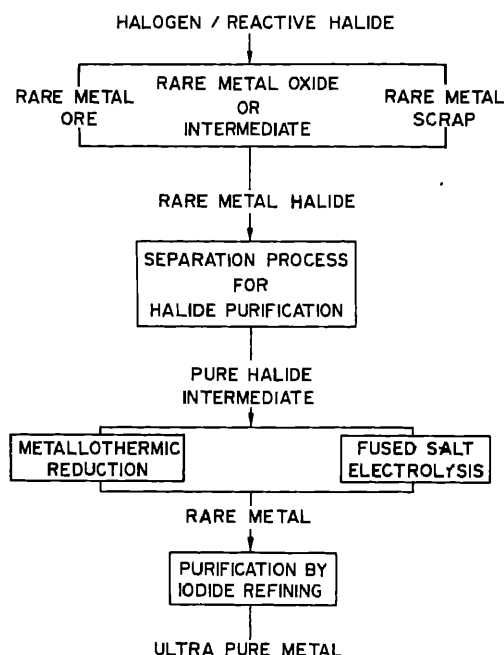


Figure 10. Halogenation in rare metal extraction.

indicated above, a large variety of reactors have been developed and process optimised at Trombay and later transferred to the industrial units of the Department.

The high temperature of these reactions and the corrosive nature of the halogen and the halide vapours, restrict the choice of the material of construction and the type of equipment for large scale operation. While nickel is compatible with fluorine and fluoride vapours upto 800°C, nickel and inconel alloys can withstand chlorine upto 600°C. In the production of  $ZrCl_4$  or  $TiCl_4$  that involves temperatures of 700–900°C, one has to use quartz or silica in the reaction zone.

Further, a halogenation plant will also include provision for safe metering of the corrosive halogens and the safe disposal of the unreacted halogens by neutralising with alkali or otherwise, due to high toxicity.

At Trombay, a rotating magnesium-tube lined reactor is employed for the production of  $UF_4$  by the hydrofluorination of  $UO_2$  powder. A special constructional feature of the reactor is that it has two concentric tubes with the annular space filled with an inert seal gas. The inside tube is made of magnesium to withstand the corrosive action of hydrofluoric acid, while steel is chosen for the outer tube for ease of fabrication and strength. The leak tightness of the seals between the rotating tube and the stationary end parts of the furnace is obtained by adopting the principle of positive gas pressure seal between teflon inner sealing rings and outer rubber sealing rings. The reactor is held in a slightly inclined position to facilitate smooth flow of  $UO_2$  powder fed through a screw conveyor.

As a further example, one can look at the chlorinator used for the production of zirconium and titanium chloride.

The feed for static bed chlorinators consists of a mixture of oxide and carbon

preformed into briquettes. The green briquettes are dried and coked at 800°C in inert nitrogen atmosphere to obtain highly porous briquettes for efficient chlorination. The large scale chlorination is carried out in a high purity silica brick lined furnace. The briquettes are heated by impressing three phase voltage across three graphite electrodes embedded in the charge. The carbonised briquettes possess sufficient electrical conductivity which improves with temperature, and with appropriate voltage and current control, the charge is slowly heated to the reaction temperature of 700–900°C.  $\text{ZrCl}_4$  vapours evolving from the chlorinator furnace are condensed in a double walled inconel condenser at 150–200°C as dense crystals suitable for metal production. Blocking is a common problem in chlorinators. Hence pressure monitoring gauges, pressure release discs, and clearance ports have to be provided at critical locations.

Most of the chlorination reactions are exothermic in nature and require close control of temperature which is better achieved in fluidised bed reactors. These reactors also offer advantages like excellent gas-solid contact, good heat transfer, relatively inexpensive reactors and easier start-up and shutdown operations. Systems for the multistage fluidised bed hydrofluorination of  $\text{UO}_2$  and the fluidised bed chlorination of zircaloy scrap in an inert bed have been developed at this Department.

The volatility of halides, the facility for purifying these by distillation and possibility of reducing these halides with metals like magnesium, sodium, and calcium have provided a powerful means for the production of reactive metals.

### 8. Metal reduction processes

The reduction of rare metal starts either from a halide or an oxide and follows the route as given in figures 11 and 12.

A majority of the rare metals have been produced by reducing their halides. The reason may either be that it is not possible to reduce the oxide directly at all (*e.g.* Ti, U, Be) or that it is more convenient to reduce the halide (*e.g.* Zr, Hf, Ta, Th).

### 9. Reduction of halides

The reduction of halides is accomplished by using the metals, sodium, magnesium or calcium as the reducing agent. Depending upon the physical properties of the reactants

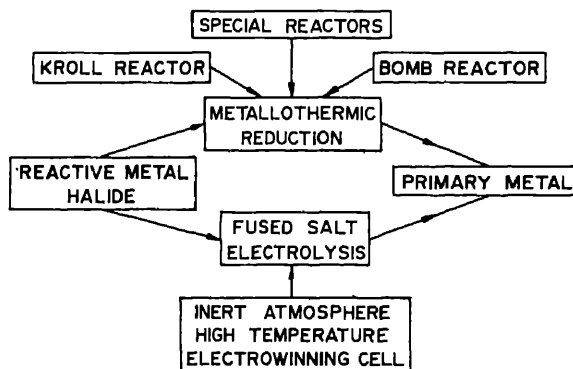


Figure 11. Reduction of rare metals—halide route.

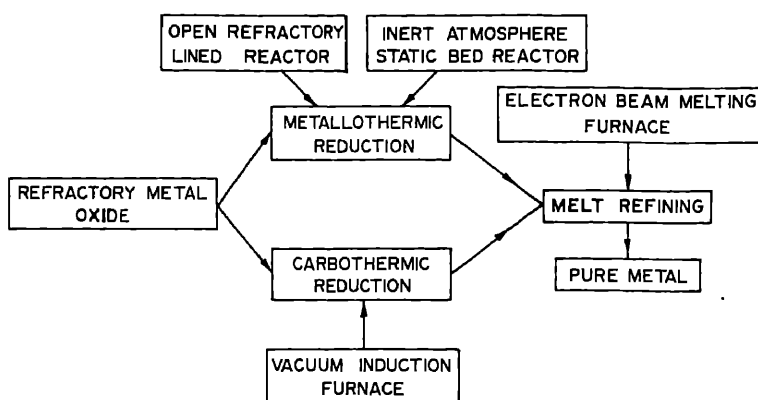


Figure 12. Reduction of rare metals—oxide route.

and products and the heat of reaction, the product metal is recovered as an ingot (U, Th), sponge (Zr, Ti) or powder (Ta). The reduction processes developed for U, Th, Zr, Ti, Ta and Be in fact provide fine examples of process metallurgy of fluorides and chlorides realised on an industrial scale for the production purposes. The exothermic metal reduction processes fall under two major categories—adiabatic (thermit type) and isothermal (Kroll type). Calciothermic reduction of uranium tetrafluoride is a fine example of the thermit type reaction. The uranium metal plant at Trombay has been producing consistently and efficiently uranium metal by the calciothermic reduction route.

In the Trombay practice, high purity  $UF_4$  powder is intimately mixed with calcium granules and the mixture is charged into a leak tight tapered S.S. bomb reactor, which is initially lined with dry  $CaF_2$  powder by vibratory packing. The  $CaF_2$  lining serves for heat insulation and containment of the molten uranium. The calciothermic reduction is triggered—in an argon atmosphere—by electrically igniting a magnesium ribbon embedded at the top of the charge. The reaction is instantaneous, spreads rapidly through the mass, and the resulting liquid uranium droplets coalesce and collect at the bottom, forming a massive solid ingot on cooling.

A reduction route employing indigenous magnesium in place of imported calcium has been developed on a pilot plant scale is due to be adopted in the plant's expansion.

The calciothermic route described for uranium is applicable to the production of thorium and plutonium metals also.

The production of metals by the isothermal Kroll type reduction is exemplified by the magnesium reduction of zirconium tetrachloride. The process that has been tested on pilot plant scale at Trombay and adopted for tonnage production at the Nuclear Fuel Complex, Hyderabad is described below.

The reactor employs a specially designed S.S. retort and a three-zone furnace system for carrying out the reduction reaction. Zirconium tetrachloride and clean magnesium pigs are loaded in separate containers in the retort. After *in situ* purification of the chloride by pumping out the volatiles at  $300^\circ C$ , the magnesium temperature is raised to above its melting point (to  $850^\circ C$ ) and the chloride distilled in a controlled manner to react at the surface of molten magnesium. At the end of the reduction the excess magnesium and  $MgCl_2$  are separated from the resulting zirconium sponge by pyrovacuum distillation in another heavy-walled retort capable of evacuation down to

< 1 micron at 900°C, the inconel retort is heated to 900°C using an evacuated bell-type furnace.

Similar reduction and pyrovacuum distillation equipment are suitable for production of titanium, thorium and hafnium metals.

For the production of tantalum powder from  $K_2TaF_7$ , a liquid-liquid reactor technique was developed at Trombay. Filtered high purity liquid sodium is continuously metered under argon cover on to the stirred mass of molten  $K_2TaF_7$  and NaCl kept at 800–900°C in an inconel alloy 600 reactor. The tantalum metal powder is recovered from the reduced mass after leaching out the by-product fluorides with a series of aqueous reagents. This effort has extended to setting up of a production plant at NFC.

Calcium metal is unsuitable for the reduction of beryllium fluoride due to the formation of highly stable  $CaBe_{13}$ . Beryllium metal is produced in the form of pebbles by the magnesium reduction of  $BeF_2$  in a graphite crucible in an induction furnace at 1100–1400°C. The metal pebbles owing to their lightness float to the surface of the slag. The beryllium pilot plant at Vashi, New Bombay is designed for the production of the metal and its alloys to meet indigenous requirement.

## 10. Reduction of oxides

The area of oxide reduction processes has been extensively investigated for producing a number of rare metals. The oxides are characterised by their good stability, they are easily prepared and are often the economically attractive intermediates in metal production processes. As specific examples of the advances at Trombay, reference may be made of fairly large scale production processes operated for preparation of zirconium, hafnium and thorium metal powders through calciothermic reduction of their respective oxides. Another notable advance has been in the aluminothermic reduction technology applied with great ingenuity in the preparation of niobium, tantalum, vanadium and molybdenum.

A metallothermic reduction process that does not generate excess heat and thereby avoids the growth or sintering of reduced metal particles is highly conducive to metal powder preparation. Calcium reduction of zirconium dioxide at 900°C generates only around 43 kcal per g mole of oxide. Further, the reduction is carried out in the presence of a heat sink like  $CaCl_2$ , very fine metal powder (predominantly 3 micron size) results dispersed in a matrix of CaO and  $CaCl_2$ . The metal powder is recovered from the reduced mass by careful aqueous leaching and drying. This technique has led to the establishment of a production facility for 1 ton Zr powder per annum at NFC.

Calciothermic reduction has also been investigated in detail for the preparation of hafnium, thorium, niobium and tantalum metal powders from their oxides. The process essentially consists of mixing the charge of calcium metal granules, metal oxide and calcium chloride heat sink in proper proportions and soaking it at the reduction temperature (950–1000°C) in flowing argon atmosphere, for sufficient time; the reduced mass is subsequently leached with dilute acids.

Unlike the static bed reduction described above, in a bomb process, highly exothermic reactions are conducted to prepare high melting metals in their consolidated form. To achieve this objective in reactions releasing inadequate heat, there are various means.

These include: (i) preheating to ignition, (ii) additives acting as thermal boosters, and (iii) combination of both.

The best reductant for the purposes just outlined is aluminium. The aluminothermic reduction may be described as combustion of aluminium to its oxide—the oxygen being released from the metal oxide. The reactions are carried out in an open vessel lined with refractory. The reactants at room temperature are mixed and charged and the charge is primed locally by means of an electric fuse embedded in the charge. In preheating to ignition, the entire charge is set to fire and the reaction is under near adiabatic conditions. The aluminothermic reduction, essentially a non-furnace process, proceeds rapidly to completion, but several hours of cooling is allowed before the contents are taken out. The metal if showing some slag adherence is cleaned by manual chipping.

A flowsheet, based on the aluminothermic reduction, for the production of niobium metal has been chosen for setting up of a plant at NFC.

Carbothermic reduction to produce refractory metals has become a reality only with the advancement in the regime of vacuum technology. The reactions are performed in a high temperature-high vacuum induction furnace where the pelletised oxide-carbon or carbide-oxide charge is reacted in the solid state to yield carbide or metal. A precise control of charge composition and the reaction conditions is very essential for obtaining pure metals having low residual carbon and oxygen contents. Adopting this process, complete flowsheets have been developed at the Metallurgy Division, BARC for the production of reactor grade niobium and capacitor grade tantalum metals.

## 11. Electrolytic reduction

For electrowinning of the reactive metals, only fused salt systems operating in an inert atmosphere have been found suitable.

Molten salt electrowinning processes for the preparation of refractory metals, particularly tantalum and titanium and rare earths like misch metal and cesium have been extensively investigated at Trombay. The metal compound (chloride, fluoride or oxide) is dissolved in a low melting eutectic salt mixture composed of two or more alkali or alkaline earth chlorides or fluorides. During electrolysis, the high melting rare metals are obtained as adherent dendrite deposits on the cathode (which is kept suspended in the fused salt) or alternatively if the adherence characteristics are poor, the metal is generated in the form of powder, in which case the cell itself is used as the cathode (and the anode is kept suspended).

Tantalum and titanium have been electrodeposited in the dendritic and sponge form by electrolysis of KCl-NaCl melt containing respectively potassium tantalum fluoride and titanium chloride as functional salt. While for tantalum a centrally suspended metallic rod has been used as cathode, for titanium a perforated metallic basket served as the cathode. Such electrode arrangement for multivalent titanium has been found essential to separate the catholyte and anolyte.

In the pilot plant work on electrowinning of titanium, a 1000 amp internally heated inert atmosphere electrolytic cell has been used to standardise the parameters. The metals belonging to the rare earth group have been electrodeposited from all-chloride electrolytes.

## 12. Consolidation and purification of rare metals

The primary sponge metals and metal powders are required to be consolidated by melting or sintering prior to conversion to mill products. In some cases the melting or sintering operation refines the metal to an extent.

The tolerable limits of impurities in rare metals are quite low. All the properties which make these metals unique in comparison with other common metals are drastically impaired even by low levels of metallic and interstitial impurities. Therefore, great care and special techniques are employed in the refining operation as summarised in figure 13.

Most of the purification methods for rare metals involve high temperature and vacuum. The purification methods available for the rare metals include (i) vacuum melting, (ii) iodide refining, (iii) zone melting, and (iv) molten salt electrorefining.

Except the metals uranium and beryllium which are consolidated and to some extent refined by vacuum induction melting and casting, majority of the rare metals are consolidated and refined by arc and electron beam melting procedures. In both these methods, crucible contamination is eliminated by carrying out the meltings in watercooled copper crucibles.

In vacuum arc melting, the heat is generated on the surface of the molten metal by the application of a low voltage high current electric arc from an electrode which may be either consumable or nonconsumable. While nonconsumable method is suitable for consolidation of metals, no appreciable purification is achievable on account of the low vacuum involved. On the other hand, in the consumable arc melting, the material to be melted is preformed into an electrode which is progressively consumed during melting. The process has the advantage of operating under higher vacuum ( $10^{-2}$  to  $10^{-3}$  torr) without contamination from electrode material and finds widespread use in the consolidation of rare metals. Facilities available at Trombay allow melting of 4 to 6 in. dia ingots of zirconium and titanium and at NFC metal ingots upto 12 in. dia can be cast.

Electron beam melting furnaces operate in high vacuum and provide high degree of super heat in the melt region and thus enable much greater refining than that possible with arc furnaces. In electron beam melting, the specimen is heated by subjecting it to

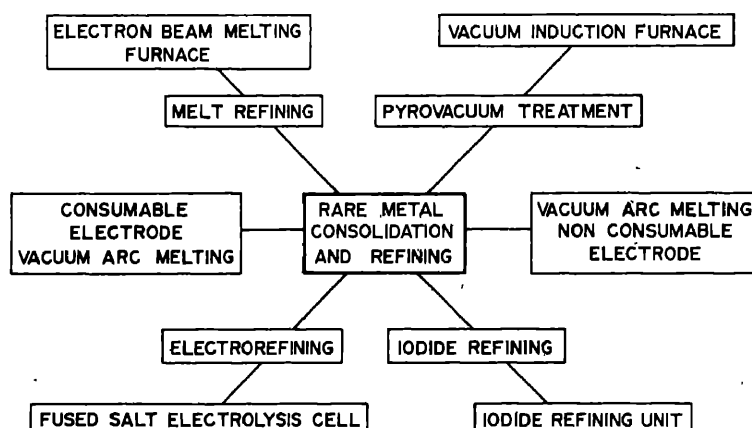


Figure 13. Techniques for consolidation and refining of rare metals.

bombardment by a beam of high energy electrons under a vacuum better than  $10^{-4}$  torr. Electron beam melting has, in fact, played a prominent role in its application to consolidation and purification of primary metals with widely different production history, and to preparation of metals with their finished purities meeting specific application requirements. Electron beam melting is effective and extensively used particularly in the production flowsheets of niobium and tantalum metals.

The reactions and processes that take place during vacuum melting and result in purification include (i) distillation of volatile impurities, (ii) vaporization of suboxides, (iii) carbon deoxidation, and (iv) vacuum degassing.

While vacuum melting is very effective in the purification of refractory metals it is not so with reactive rare metals like titanium, zirconium and hafnium. The so-called iodide refining has been found to be very effective in the refining of these metals.

Iodide refining, also known as the Van Arkel de Boer process, is based on the reversibility of a reaction between a metal and iodine. Purification of zirconium by this process has been studied extensively in the Metallurgy Division, BARC. The process is carried out in an evacuated inconel 600 vessel along the axis of which a high purity zirconium wire is aligned and electrically heated to  $1300^{\circ}\text{C}$ . The crude zirconium sponge is stacked inside the vessel in the annular space between the vessel wall and a concentric screen. Iodine required for the process is sublimed into the evacuated vessel. The vessel is externally heated to  $250\text{--}400^{\circ}\text{C}$  to form volatile  $\text{ZrI}_4$  by reaction between zirconium sponge and iodine. The iodide vapours decompose on the surface of the high temperature zirconium filament resulting in a deposit of pure metal on it. The iodine vapours simultaneously liberated travel back for further reaction with the crude sponge.

A decomposition assembly developed at Metallurgy Division, BARC has been growing kilogram quantities of high purity crystal bars of zirconium, titanium and hafnium.

Zone melting is essentially a purification process by repeated crystallization from the melt. In practice two liquid-solid interfaces are produced for distribution of impurities by causing a relatively small molten zone to transverse the length of the bar of the charge. Many repetitions of the process lead to considerable purification even in cases where the distribution coefficient is close to unity. The impurities more soluble in the solid concentrate in the starting end.

It has been possible to produce kg quantities of metals such as Bi, Sb, Sn and Cd in their ultra-pure form for use in the semiconductor industry with zone refiners designed and fabricated at Trombay. A larger semi-automatic zone refiner is turning out ultrapure materials at NFC.

Zone refining in vacuum combines the benefits of conventional zone refining in a protective atmosphere, vacuum degassing and selective distribution of impurities. For refining of refractory metals an electron beam floating zone melting unit has been fabricated and used at the Metallurgy Division.

Electrorefining, next to electrowinning of metals is the most important aspect of fused salt electrolysis. While in electrowinning graphite has been found to be the most popular and inexpensive anode material, electrorefining cells essentially employ impure metal as the anode. The metal is crushed to suitable size and spread over the crucible bottom or packed in the annular space between the crucible and a perforated graphite screen to expose a large anode area. Molybdenum is the best reported cathode material in electrorefining. Iron has been used for vanadium electrorefining.

Molten salt electrorefining technique has been perfected for the preparation of high

purity metals like niobium, tantalum, vanadium, molybdenum and chromium from their aluminothermally reduced alloy form. More recently electrorefining technique has been proved to be an effective mode for purification of calcium reduced hafnium. It has been possible to apply electrorefining for metal values of zircaloy scrap, and off-grade titanium sponge. Such purification technique has been found suitable not only for clean scrap but also for scraps contaminated with other metals and alloys which cannot be directly re-used in conventional remelting. Thus of all the refining methods applicable to rare metals, electrorefining stands out to be the most powerful technique with a wide range of refining capabilities.

### 13. Thermodynamics in rare metals extraction

In the development of process metallurgy of rare metals, the role of basic research particularly thermodynamic investigations has been very significant. Thermodynamic data have come to the rescue in many situations either during the choice of process parameters or in explaining many of the system behaviours. Though the involvement of thermodynamic analysis is very extensive and pervades almost all stages of rare metals reduction, refining and service, investigations concerning the vapour pressure and vaporization behaviours at elevated temperatures; solid solubility and phase diagram data have particularly been the main thrust areas for data collection and utilization. Investigations on metal-crucible interaction behaviours and decomposition processes can be cited for some of the direct application areas for thermodynamic data.

At the Extractive Metallurgy Section, several actual processes have been developed based solely on the available thermodynamic data of the system concerned. While it is impossible to carbothermally reduce zirconium and hafnium oxides, the important master alloys zirconium-niobium and hafnium-tantalum have been obtained by a carbothermic reduction process consisting of reduction of niobium pentoxide with zirconium carbide or tantalum pentoxide with hafnium carbide respectively. This scheme of reduction was worked out from the theoretical considerations of the thermodynamic stabilities of carbides and oxides and the stabilities and vaporization behaviours of the suboxides of zirconium, hafnium, niobium and tantalum. Another example of major flow sheet development that was visualised from the thermodynamic properties of the concerned compounds, is found in a recently concluded investigation on the preparation of pure niobium and tantalum through their nitride intermediates. The comparative stability of niobium and tantalum nitrides with respect to the niobium and tantalum carbides at moderate temperatures and the complete instability of these nitrides (in contrast to the persistent stability of the carbides) at higher temperatures and vacuum conditions has made it possible to obtain the pure metals starting from the oxides by a single sequential step consisting of (i) carbothermic reduction of niobium or tantalum pentoxide under a nitrogen atmosphere at 1500–1600°C to obtain the corresponding nitride and (ii) pyrovacuum decomposition of the nitride, at 2000–2100°C under  $10^{-4}$  torr, to pure metal.

In addition to the above mentioned types of applications, thermodynamic analyses have extensively been employed in various pyrovacuum refining operations, leading to successful process operation, improved yield, reduction in number of processing steps and similar improvements.



#### 14. Evaluation of rare metals

The development of flow sheets for the extraction of high pure rare metals has depended to a great extent on the parallel development and availability of powerful analytical techniques which enabled the evaluation of products at various stages. Special efforts are required particularly when the impurity concentrations are vanishingly low. The important analysis techniques applied in the rare metals evaluation are diagrammatically presented in figure 14.

#### 15. Concluding remarks

In the evolution and developments of flowsheets for rare metal extraction, the R&D effort has had many facets as summarised in figure 15.

As compared with the historical development of the process metallurgy of common metals, there has been a much more systematic and scientific approach to the chemical metallurgy of rare metals. This has been possible through many advances in analytical chemistry, physical chemistry, instrument and equipment development, physical and chemical engineering which have provided new technologies, and also through entirely

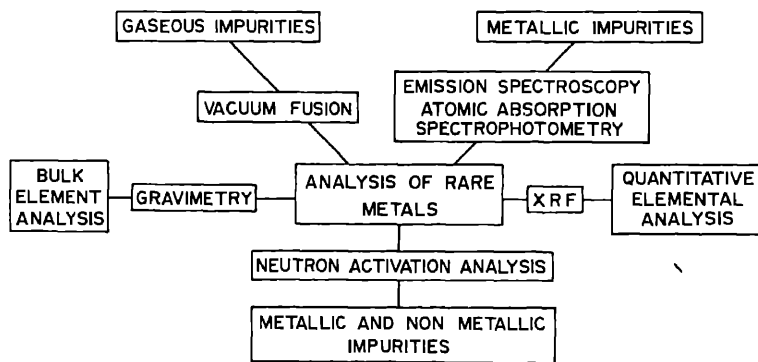


Figure 14. Evaluation of rare metals.

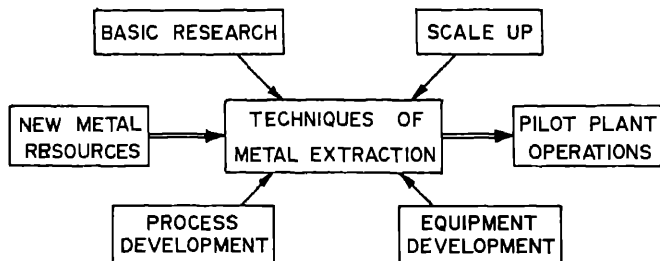


Figure 15. Development of extractive processes for rare metals.

novel metallurgical engineering designs. Our basic understanding of chemical and metallurgical systems, phenomena and reactions has also vastly improved through progress in theory and experiment in rare metals extraction.

Although process metallurgy of rare metals has grown into a powerful, mature and composite discipline, a good deal of scope for further R&D efforts still remains. Specifically one can mention fertile areas like pyrochemical counter current fused salt reactors for achieving separation of zirconium from hafnium, adoption of fluidised bed reactor for gas solid reactions, employment of plasma processing techniques for mineral beneficiation and refractory metal reduction—all of which deserve detailed study.

An interesting aspect of development of processes for rare metals extraction has been that many of these new techniques have important relevance to the common metals processing also. Special mention may be made of the prospects of solvent extraction processes in the copper and nickel industries and ion exchange in certain by-product metal recovery processes from effluent solutions, chlorination processing of complex sulphide ores, and vacuum melt refining.

Growth, development and maturity in operating practice have marked the evolution of various process options taken for investigations at BARC. Whenever possible and desirable, the process development was pursued through the various stages and led to its logical conclusion—setting up of operating production facilities. An important aspect that has marked this style of evolution is that the person or persons who have conceived, tested and developed the idea and the process have also been given the opportunity of setting up the plant and running it. This has made further growth and expansion of the plant feasible and easier. In certain cases, the nature of the project is more suited for effecting a transfer of technology to organizations outside the department. In this context, it is well worth noting that the technology of aluminothermic reduction of ferroalloys viz., ferrovanadium, ferroniobium, ferromolybdenum and ferrotungsten—so well mastered at the Extractive Metallurgy Section has been transferred to industries in Madhya Pradesh. In another instance, based on the flowsheet and technology developed at the Extractive Metallurgy Section, a demonstration plant for the processing of cassiterite concentrates is being set up at Raipur by Metallurgy Division jointly with the Madhya Pradesh State Mining Corporation. One would appreciate that such instances are tantamount to bringing the advanced research facilities and expertise within the reach of a wider section of industries and to the greater service for our country's mainstream industrial activity.

The foresight and imagination in the organisation, of the successive stages of the programme, has paid good dividends; strong and comprehensive base that we now have in rare metals processing industry should inspire confidence for further growth and diversification of this technology in our country.

### **Acknowledgement**

The authors appreciate the manysided help rendered by Shri N Krishnamurthy, Metallurgy Division, BARC in the preparation of this paper. Contributions from the various research groups, particularly from the Metallurgy, Chemistry, Chemical Engineering and Ore Extraction Divisions of BARC, Bombay and the Nuclear Fuel Complex, Hyderabad have actually provided the basic theme of this present article.

**Representative bibliography**

- Damodaran A D, Deshpande S G, Majumdar A A, Sastri M S, Jena P K, Bose D K, Chandra S, Gupta C K and Taneja A K 1970 *Proc. Indian Nat. Sci. Acad.* **A36** 306
- Gupta C K 1972 in *Recent developments in metallurgical science and technology, Proc. IIM Symp. on Process Metallurgy*, New Delhi p. 515
- Gupta C K 1984 Extractive metallurgy of niobium, tantalum and vanadium *Int. Metals Rev.* (Under Publication)
- Gupta C K and Sundaram C V 1973 *The Banaras Metall.* **5** 190
- Krishnamurthy N, Venkataramani R, Garg S P and Sundaram C V 1981 in *Trends in refractory metals, hard metals, and special materials and their technology, Proc. Tenth Plansee Seminar Metallwerk Plansee, Reutte*, Vol. 1, p 263
- Mukherjee T K, Bose D K and Gupta C K 1972 in *DAE Symp. High. Temp. Mat.* Hyderabad, p. 221
- Mukherjee T K and Gupta C K 1976 *Trans. SAEST* **11** 127
- Mukherjee T K, Garg S P, Gupta C K, Sundaram C V, Taneja A K and Damodaran A D 1978 in *Electron beam melting and welding, Proc. Int. Conf., Avignon*
- Proc. INSA-BARC Winter School on Chemistry and Metallurgy of Rare Metal Extraction*, BARC (Jan 1975)
- Saratchandran N and Sundaram C V 1970 in *DAE Materials Science Symp.* NAL, Bangalore, p. 251
- Subramanyam R B, Saratchandran N and Sundaram C V 1973 *J. Sci. Ind. Res.* **32** 672
- Subba Rao K S, Sharma B P, Paul C M and Sundaram C V 1977 *Beryllium development programme in India, Conf. Preprints: Beryllium, Fourth Int. Conf. on Beryllium*, The Metals Society, London
- Sundaram C V, Garg S P and Sehra J C 1979 in *Metal sciences—The emerging frontiers, Proc. Int. Conf.*, The Indian Institute of Metals
- Sundaram C V and Sharma B P 1972 in *Recent developments in metallurgical science and technology, Proc. IIM Symp. on Process Metallurgy*, New Delhi, p. 479
- Sundaram C V and Suri A K 1976 in *High temperature reactions and processes Proc. KREC*, Suratkal p. 27

## Plutonium metallurgy in India

P R ROY and C GANGULY

Radiometallurgy Division, Bhabha Atomic Research Centre, Bombay 400 085, India

**Abstract.** The embryo of plutonium metallurgy in India, as well as in Asia, was formed nearly 25 years back in Trombay. Thereafter, in the intervening 25 years, significant amount of research and development work have been carried out at BARC on this man-made fissile element and indigenisation has been achieved in the fabrication, characterisation and property evaluation of plutonium metal, delta-stabilised alloys, Al-Pu fuels, Pu-Be neutron sources, (UPu)O<sub>2</sub> fuels for thermal and fast reactors and (UPu)C and (UPu)N advanced fuels for liquid metal-cooled fast breeder reactors (LMFBR).

This paper summarises the development of plutonium metallurgy in India highlighting the safety aspects, our achievements and potential of plutonium for generation of nuclear electricity in the coming decades.

**Keywords.** Plutonium; fissile; delta-stabilised alloys; Al-Pu fuels; Pu-Be neutron sources; Mixed oxide and carbide fuels; fast breeder-test reactor; liquid metal-cooled fast breeder reactors; nuclear electricity.

### 1. Introduction

The metallurgy of plutonium, the man-made unique and most unusual metal, was introduced in India in 1960 when a team consisting of a chemist, a chemical engineer and a metallurgist successfully isolated mg quantities of plutonium metal beads in the Trombay laboratory by calciothermic reduction of plutonium tetrafluoride. Thereafter, in the intervening 25 years, there has been an enormous scale-up of production and extensive investigation of plutonium metal, its alloys and compounds. A sophisticated plutonium metallurgy laboratory for safe and secured fabrication and characterisation of plutonium fuels has come up in Trombay and today we are on the threshold of intensive utilisation of plutonium for generation of nuclear electricity and breeding of fissile materials simultaneously.

Plutonium does not occur in nature but is synthetically formed by the transmutation of the naturally occurring  $^{238}_{92}\text{U}$ . Soon after its discovery by Seaborg, Wahl and Kennedy in February 1941, in the Berkeley laboratory in USA, plutonium served as a major ingredient of the Manhattan nuclear weapon project during the second world war (Seaborg 1958). However, today it is most significant because of its peaceful potential as a nuclear reactor fuel offering energy thousand times greater than all available fossil fuels.

From the very inception of nuclear energy programme in India in the mid 1950s, the tremendous potential of plutonium for unlocking the huge energy reserves of our limited uranium (Rao 1982) (~ 60000 tons) and abundant thorium (~ 320000 tons) resources was recognised. Accordingly, laboratory separation and analytical procedures for plutonium started in Trombay in 1958 and by 1964 our spent uranium fuel reprocessing plant for recovery of plutonium was commissioned, for the first time in Asia.

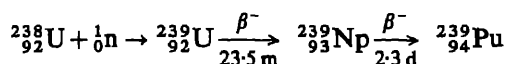
The present dissertation summarises the milestones of plutonium metallurgy in India, highlighting our achievements in development and fabrication of plutonium metal and plutonium bearing metallic and ceramic fuels and our future programme for utilisation of plutonium for generation of nuclear electricity.

## 2. Formation and separation

As is known, uranium occurring in nature contains mainly two isotopes, viz.  $^{238}\text{U}$  (99.3 %) and  $^{235}\text{U}$  (0.7 %). The present generation of nuclear reactors derive energy from the fission of  $^{235}\text{U}$  by slow or thermal neutrons and use natural uranium or 2 to 4 %  $^{235}\text{U}$  enriched uranium in the form of metal or oxide as fuels. The fission reaction is as follows:



One of these released fission neutrons is needed for maintaining the chain reaction and out of the remaining neutrons some are captured by the fertile  $^{238}\text{U}$  to form  $^{239}\text{U}$  which undergoes two successive beta decays, as shown below, leading to the formation of  $^{239}\text{Pu}$ , which is an excellent fissile material:



Thus, the nuclear reactors, apart from generating power also produce fissile  $^{239}\text{Pu}$  as a byproduct, through neutron capture by the fertile  $^{238}\text{U}$ . Other prominent isotopes of plutonium namely  $^{240}\text{Pu}$ ,  $^{241}\text{Pu}$  and  $^{242}\text{Pu}$  are formed from  $^{239}\text{Pu}$  by successive neutron captures. The isotopic content of plutonium in a thermal reactor and the formation of plutonium radionuclides and daughters depend on such factors as discharge burn-up of the fuels, neutron flux and energy spectrum, fuel enrichment, moderator to fuel volume ratio, fuel diameter, cladding materials etc., and are shown in figures 1 and 2 respectively. Typical isotopic composition of plutonium<sup>(3)</sup> from the spent fuel elements of the 40 MW (th) CIRUS test reactor in Trombay, the 200 MW(e) boiling water reactors (BWR) at the Tarapur Atomic Power Station (TAPS) and the pressurised heavy water reactors (PHWR) at the Rajasthan Atomic Power Station (RAPS) are given in table 1.

The irradiated or the spent uranium fuel elements are a mixture of depleted uranium ( $^{238}\text{U} + < 0.7\% ^{235}\text{U}$ ), highly radioactive fission fragments and plutonium. The major

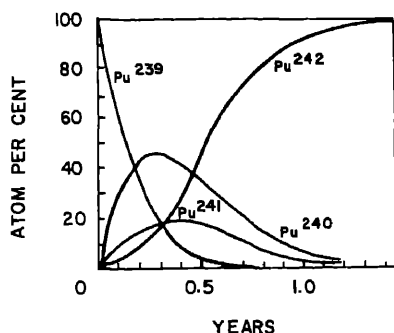


Figure 1. Plutonium isotopic composition as a function of exposure to thermal neutrons.

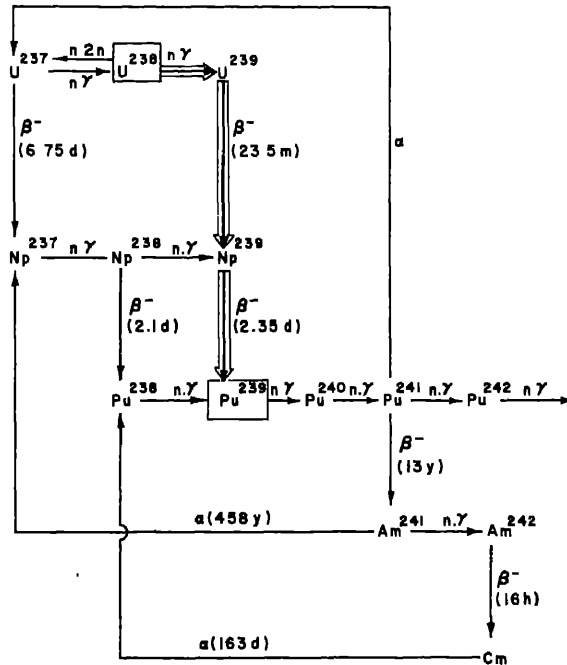


Figure 2. Plutonium radionuclides and daughters.

Table 1. Isotopic composition of plutonium from different reactors.

Reactor	Burn-up (MWD/ton)	$^{238}\text{Pu}$ (w/o)	$^{239}\text{Pu}$ (w/o)	$^{240}\text{Pu}$ (w/o)	$^{241}\text{Pu}$ (w/o)	$^{242}\text{Pu}$ (w/o)
BWR (TAPS)	6100	0.125	82.7	13.94	2.89	0.339
	9500	0.203	73.54	20.31	4.81	1.080
	13750	0.393	65.77	25.17	6.45	2.21
	29000	0.500	53.40	29.60	10.48	6.01
PHWR (RAPS)	2960	0.02	82.52	15.01	2.2	0.22
	5700	0.05	67.7	26.0	4.8	1.2
	6200	0.06	66.07	26.87	5.52	1.48
CIRUS (Trombay)	1000	0.01	93.32	6.27	0.38	0.02

process steps (Roy 1978) in the separation of plutonium from spent fuels are shown in figure 3. After appropriate cooling for the shortlived radioactivity to die down, the spent fuel elements are transferred to a reprocessing plant where the fuel is first mechanically or chemically de jacketed from the cladding material. Next, the fuel is dissolved in nitric acid and the solution is subjected to solvent extraction for removal of fission products in the first stage and uranium in the second stage. The separated plutonium is further purified by ion-exchange process and obtained as plutonium nitrate.

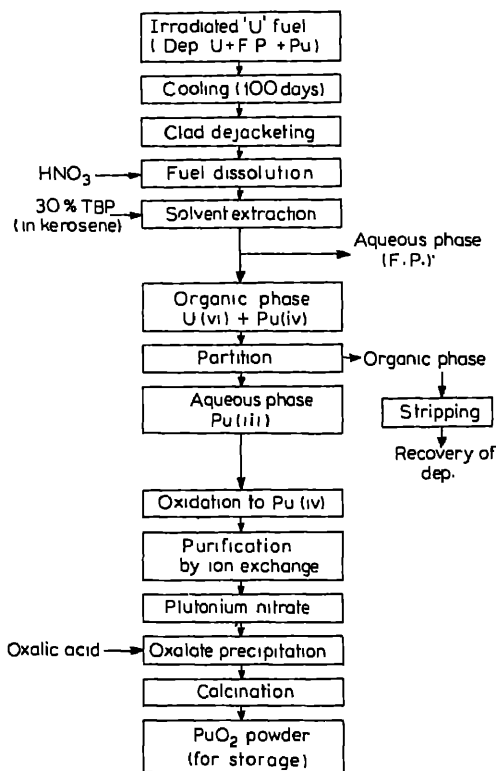


Figure 3. Flowsheet for recovery of plutonium from irradiated fuel.

The nitrate solution is converted to the oxide, mainly by the oxalate precipitation route followed by calcination in air at temperatures ranging from 400–700°C to get  $\text{PuO}_2$  powder suitable for subsequent use. The oxalate process has low filtrate losses, good filterability and relatively high decontamination, particularly for iron. Direct calcination of the nitrate to oxide could dispense with the intermediate precipitation process and thus achieve considerable simplification. The process has been performed satisfactorily on laboratory scale, but suffers from the drawback of complete lack of purification and decontamination which is achieved during precipitation step and thus requires a very pure feed solution.

$\text{PuO}_2$  powder is usually the end product of a spent fuel reprocessing plant because it is most convenient to store plutonium in the form of the oxide from the point of chemical stability and ease of subsequent transportation.

### 3. Safety considerations

The high radiotoxicity, biological behaviour and fissile properties of plutonium present radiological and criticality hazards necessitating special safety considerations in handling of plutonium. In fact, this handling problem makes plutonium metallurgical operations a distinctively different and much more formidable task when compared with that of other conventional metals including uranium. Thus we had to first master

the technique of safe handling of plutonium, either as fine powders or as bulk material, before any significant development of its metallurgy.

The decay characteristics of plutonium isotopes and their daughters are given in table 2 (Janardhanan *et al* 1973).  $^{239}\text{Pu}$ , the major constituent, and other isotopes of plutonium except  $^{241}\text{Pu}$  are predominantly powerful emitters of alpha radiation. Alpha particles emitted by plutonium isotopes do not constitute an external hazard because of its short range in air and body tissue (for  $^{239}\text{Pu}$  alphas the range in air and body tissues

Table 2. Radioactive decay characteristics of plutonium isotopes and daughters.

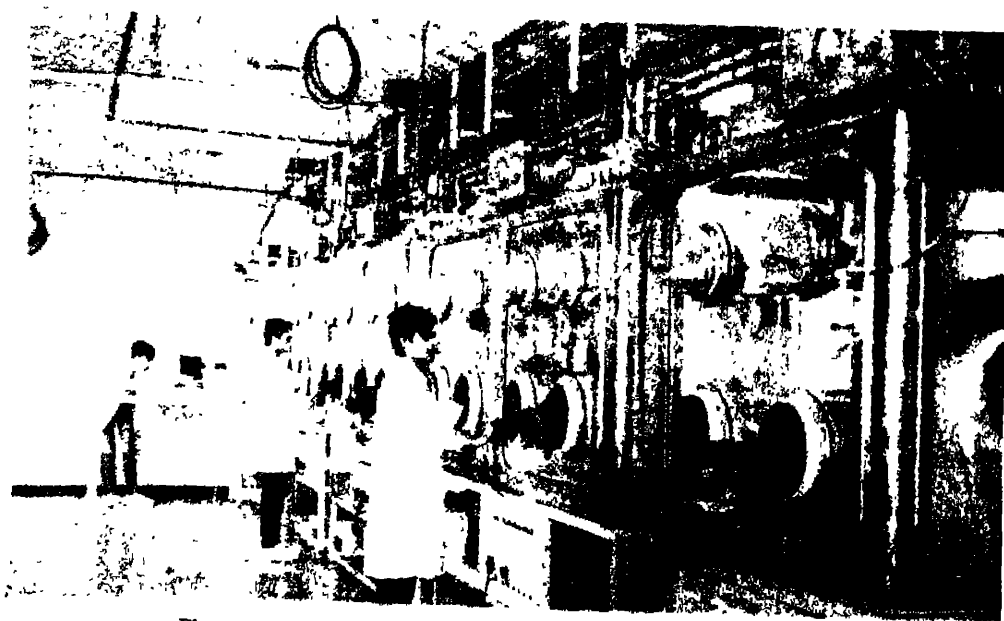
Isotope	Radiation	Yield %	Energy (MeV)	Half-life	Specific activity (Ci/g)
Pu-238	Alpha	100	5.49	86.4 yr	17.4
	Gamma	$10^{-3}$	0.15		
	Gamma	$8 \times 10^{-3}$	0.10		
	Gamma	$3.8 \times 10^{-2}$	0.044		
	L-X-ray	13	0.017		
Pu-239	Alpha	100	5.14	$2.436 \times 10^4$ yr	0.052
	Gamma	$2 \times 10^{-3}$	0.038		
	Gamma	$7 \times 10^{-3}$	0.052		
	Gamma	$2 \times 10^{-3}$	0.12-0.20		
	Gamma	$3 \times 10^{-3}$	0.38		
	L-X-rays	1.4	0.0136		
		2.2	0.0174		
		0.2	0.0205		
Pu-240	Alpha	76	5.162	$6.58 \times 10^3$ yr	0.23
	Alpha	24	5.118		
	Gamma	$10^{-2}$	0.044		
	L-X-rays	10	0.017		
	K-X-rays	40	0.102-0.125		
Pu-241	Alpha	$3 \times 10^{-3}$	4.9	13.0 yr	111.5
	Beta	99.997	0.02		
	Gamma	$2 \times 10^{-4}$	0.145		
	Gamma	$10^{-3}$	0.10		
Pu-242	Alpha	76	4.89	$3.79 \times 10^5$ yr	0.004
	Alpha	24	4.86		
	Gamma	$10^{-2}$	0.045		
	L-X-rays	10	0.017		
U-237	Beta	100	0.245	6.75 day	$6.74 \times 10^{-4}$
	Gamma	61	0.059		
	Gamma	35	0.207		
	Gamma	4	0.334		
Am-241	Alpha	84	5.48	458 yr	3.13
	Alpha	13.6	5.43		
	Gamma	37	0.017		
	Gamma	2.7	0.026		
	Gamma	0.05	0.043		
	Gamma	37	0.059		
	Gamma	0.02	0.099		



**Table 3.** Maximum permissible concentrations for plutonium radionuclides in body, air and water.

Radionuclide	MPBB		MPC (40 hr exposure/week) ( $\mu\text{C}/\text{cc}$ )	
	$\mu\text{C}$	$\mu\text{g}$	Air	Water
Pu-238	0.04	$2.4 \times 10^{-3}$	$2 \times 10^{-12}$	$10^{-4}$
Pu-239	0.04	0.65	$2 \times 10^{-12}$	$10^{-4}$
Pu-240	0.04	0.18	$2 \times 10^{-12}$	$10^{-4}$
Pu-241	0.9	$8.2 \times 10^{-3}$	$9 \times 10^{-11}$	$7 \times 10^{-3}$
Pu-242	0.05	12.8	$2 \times 10^{-12}$	$10^{-4}$
Am-241	0.05	$1.6 \times 10^{-2}$	$6 \times 10^{-12}$	$10^{-4}$
U-237	0.06	89	$4 \times 10^{-12}$	$9 \times 10^{-5}$

are 3.68 cm and 40  $\mu\text{m}$  respectively). The primary concern in plutonium handling is to prevent particulate matter containing plutonium from entering the body of the operator through inhalation, ingestion or injection because plutonium poses the highest biological hazard when taken into the body. The long biological half-life, the high energy of the emitted alpha particles and the body's selective localisation of plutonium in the bone and lung lead to very low maximum permissible body burdens (MPBB) and maximum permissible concentrations (MPC) in air and water (table 3) (ICRP 1955). Any plutonium-bearing material is, therefore, handled in a well-ventilated laboratory within the confines of hermetically-sealed glove boxes through alpha-tight neoprene gloves. The glove box is maintained under a slightly negative pressure ( $-0.2$  to  $-2$ " WG) under a dynamic flow of air or high purity inert gas ( $\text{N}_2$ , A or He) in order to have 3–10 box volume changes per hour. Figure 4 gives the view of a glove box train

**Figure 4.** The 'Metallography train' of glove boxes in RMD, BARC.

set up in the Radiometallurgy Division at Trombay for safe handling of plutonium (Ghosh *et al* 1973). Inert atmosphere glove boxes are used for handling plutonium metal, carbide and nitrides which are highly susceptible to oxidation and hydrolysis and are pyrophoric in powder form.

The external hazard of plutonium is mainly from gamma and neutron radiations emitted by higher isotopes of plutonium which are present in significant amounts in high burnup plutonium. The surface dose rate of plutonium since its purification increases with time because of build up of  $^{241}\text{Am}$  and  $^{237}\text{U}$ , which are the daughter products of the beta emitting  $^{241}\text{Pu}$ . Appreciable neutron dose rates are also associated with plutonium mainly from the spontaneous fission neutrons emitted by the even-numbered plutonium isotopes, e.g.  $^{238}\text{Pu}$ ,  $^{240}\text{Pu}$  etc., and to some extent due to  $(\alpha, n)$  reactions from plutonium in contact with light elements.

In order to keep the radiation exposure of operators below the permissible limits specified by the International Commission of Radiation Protection (ICRP) the following guidelines are usually followed:

- (a) restrictions are imposed on the mass of plutonium that is handled at a time, to minimise mainly the neutron dose;
- (b) great emphasis is given towards automation and remotisation during handling of plutonium;
- (c) close containment of plutonium bearing powder and dust such that radioactive dust does not build up on equipment and glove box surfaces;
- (d) use of external or localised composite lead glass and lucite shield for gamma and neutron radiation and the use of lead-loaded neoprene gauntlets, particularly while handling high burn-up plutonium.

Unlike other metallurgical industries, in a plutonium facility a maximum of a few kg

Table 4. Critical masses of some plutonium compounds.

Compound	Density (g/cc)	Critical mass (kg)	
		Bare	Water reflected
Pu-solution	—	—	0.51
Pu			5.6 $\alpha$ phase 7.6 $\delta$ phase
$\text{PuO}_2$	11.46	24.5	12.2
$\text{PuN}$	14.25	18.4	9.23
$\text{PuC}$	13.6	17.93	9.07
$\text{PuH}_2$	10.4	15.64	7.49
$\text{PuH}_3$	9.61	12.69	6.32
$\text{Pu}_2\text{C}_3$	12.7	19.72	9.96
$\text{Pu}_2\text{O}_3$	11.47	24.95	12.05
$\text{PuCl}_3$	5.7	167.05	61.59
$\text{PuF}_3$	9.32	32.59	16.0
$\text{PuF}_4$	7.0	56.29	25.29
$\text{Pu}(\text{C}_2\text{O}_4)_2$	4.5	152.0	66.87
$\text{Pu}(\text{NO}_3)_4$	6.2	103.96	54.94

of fissile material is handled at a time to avoid spontaneous self-sustaining nuclear chain reaction or what is known as the criticality accident which can be catastrophic to the personnel and its surroundings. The critical mass of plutonium and its compounds depend on the geometry and the environment. Table 4 gives the critical mass of plutonium and some of its important compounds (Hansen and Clayton 1967). The upper safe limit during handling is usually kept at 50% of the critical mass.

In the plutonium metallurgy laboratory at Trombay safety has always been given priority over cost, convenience and even production capacity. As a result, there has not been a single radiation incident till todate.

#### 4. Nuclear parameters

The important nuclear parameters of the three principal fissile nuclides  $^{235}\text{U}$ ,  $^{239}\text{Pu}$  and  $^{233}\text{U}$  are listed in table 5 (Hanna *et al* 1969).  $\eta$ , the average number of neutrons produced per neutron absorbed by the fissile nucleus is the most important parameter as it influences the conversion or breeding ratio (CR), i.e. the average number of fissile atoms produced in a reactor per fissile atom consumed by fission or capture. The conversion ratio is quantitatively expressed as:

$$\text{CR} = \eta - 1 - L$$

where one neutron is needed to continue the chain reaction and  $L$  represents the non-productive absorption and leakage per neutron absorbed by fissile atom.

Since  $^{239}\text{Pu}$  and  $^{233}\text{U}$  have the highest  $\eta$  values in the fast and thermal neutron range respectively, plutonium breeds best in a fast reactor and  $^{233}\text{U}$  is best suited for thermal converter reactors. In fact, in a fast reactor operating on a  $^{238}\text{U}$ - $^{239}\text{Pu}$  fuel cycle, it is possible to have a breeding ratio in the range of 1.2 to 1.4.

The other advantages of plutonium as a fissile material in fast reactors compared to  $^{235}\text{U}$  are the higher fast fission cross-section (Pu: 1.77 barns; U: 1.44 barns), 5% higher

Table 5. Nuclear properties of the principal fissile nuclides.

Property	$^{233}\text{U}$	$^{235}\text{U}$	$^{239}\text{Pu}$
$\sigma_a$ = Neutron absorption cross-section	$578 \pm 2$	$578 \pm 2$	$1013 \pm 4$
$\sigma_f$ = Fission cross-section	$531 \pm 2$	$580 \pm 2$	$742 \pm 3$
$\sigma_c$ = Neutron capture cross-section	$47 \pm 1$	$98 \pm 1$	$271 \pm 3$
$\alpha$ = Ratio of captures to fissions	$0.089 \pm 0.002$	$0.169 \pm 0.002$	$0.366 \pm 0.004$
$\nu$ = The number of neutrons produced per fission	$2.487 \pm 0.007$	$2.423 \pm 0.007$	$2.880 \pm 0.009$
$\eta$ = The number of neutrons created per neutron absorbed by the nuclide			
(a) Thermal neutrons	$2.284 \pm 0.006$	$2.072 \pm 0.006$	$2.109 \pm 0.007$
(b) Fast neutrons	2.31	1.93	2.49

The cross-sections  $\sigma_a$ ,  $\sigma_f$ , and  $\sigma_c$  are in barns and  $\alpha$ ,  $\nu$  and  $\eta$  are ratios.

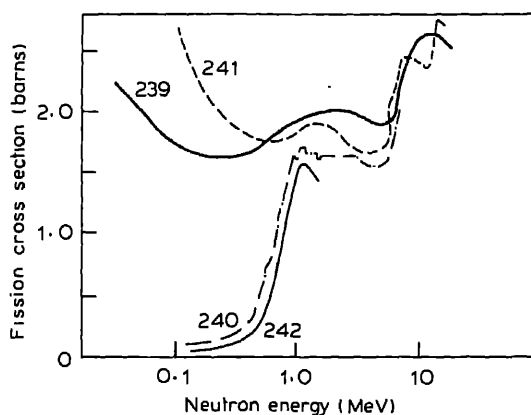


Figure 5. Fast fission cross-section (barns) of Pu isotopes

fission energy release and lower xenon poisoning. Further,  $^{241}\text{Pu}$  is fissile in both thermal and fast neutron range and  $^{240}\text{Pu}$  and  $^{242}\text{Pu}$ , though parasitic, neutron absorber for thermal neutrons, contribute significantly to fast fission. The fission cross-section of important plutonium isotopes in the fast neutron range is shown in figure 5 (Wick 1980).

From reactor physics consideration it may, therefore, be summarised that plutonium is the best fuel for fast reactors but is slightly inferior to  $^{233}\text{U}$  and  $^{235}\text{U}$  in the thermal neutron range.

## 5. Plutonium metal

### 5.1 Preparation

While starting plutonium metallurgical work at Trombay, we had already selected uranium metal as the fuel for our CIRUS Research reactor. It was, therefore, logical for us to first direct all the efforts towards manufacture of high purity nuclear grade plutonium metal.

Much of the metallurgical knowledge for preparation of plutonium metal was acquired during the Manhattan Project in the 1940s. The free energy diagrams of oxide and fluoride of plutonium (Coffinberry and Miner 1961) and other metals are shown in figure 6 and table 6 gives the various thermodynamic data of the reduction reaction (Stoller and Richards 1961). Reduction of plutonium halides, in particular, fluoride and chloride remains the only method by which virtually all the metal is produced till today.

The need to obtain plutonium in massive form with a high yield dictates the choice of a reducing reaction. The reduction reaction should be accompanied by evolution of large quantity of heat which should not only melt the reaction products but also keep them molten long enough for good slag-metal separation. The reducing agent should not dissolve in plutonium or form any intermetallic compound with it. Low melting point of the slag and high boiling point of the reducing agent are additional requirements. Considering all these factors it is found that the reduction of plutonium tetrafluoride with calcium is sufficiently exothermic and the slag in this case melts at a

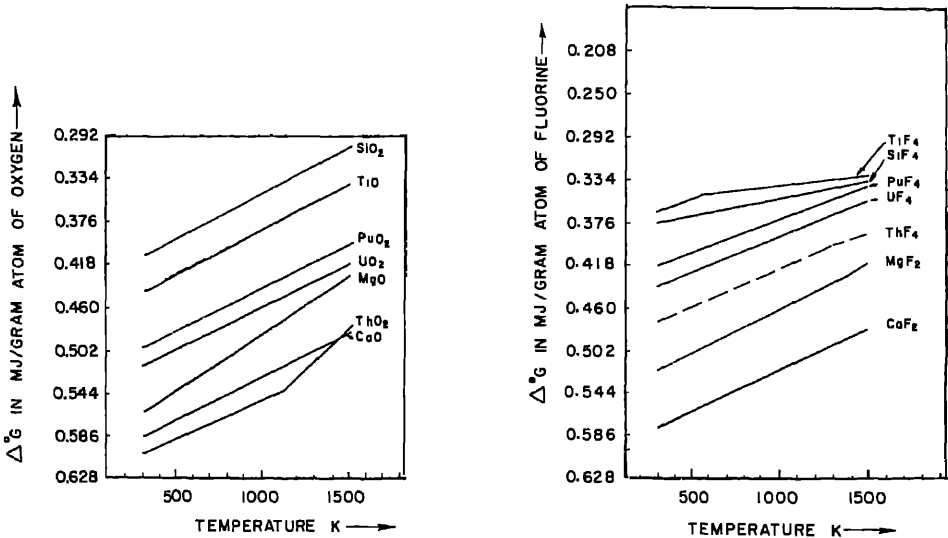


Figure 6. Standard free energy of formation ( $\Delta G^\circ$ ) for important oxides and fluorides of U and Pu.

Table 6. Thermodynamic data of the possible reduction reactions for preparation of plutonium metal

Reaction	$\Delta H$ at 291 K, kcal/mol. plutonium	Melting Point of Slag ( $^\circ\text{C}$ )
$\text{PuO}_2 + \text{Ca} \rightarrow \text{Pu} + 2\text{CaO}$	-52.4	2572
$\text{PuO}_2 + 2\text{Mg} \rightarrow \text{Pu} + 2\text{MgO}$	-40.5	2500-2800
$\text{PuO}_2 + \frac{4}{3}\text{Al} \rightarrow \text{Pu} + \frac{2}{3}\text{Al}_2\text{O}_3$	-9	2050
$\text{PuF}_4 + 2\text{Ca} \rightarrow \text{Pu} + 2\text{CaF}_2$	-149.5	1414
$\text{PuF}_4 + 0.3\text{I}_2 + 2.3\text{Ca} \rightarrow \text{Pu} + 0.3\text{CaI}_2 + 2\text{CaF}_2$	-196	1320
$\text{PuF}_4 + 2\text{Mg} \rightarrow \text{Pu} + 2\text{MgF}_2$	-104.6	1225
$\text{PuF}_4 + \frac{4}{3}\text{Al} \rightarrow \text{Pu} + \frac{2}{3}\text{AlF}_3$	+15	1040
$\text{PuCl}_3 + \frac{3}{2}\text{Ca} \rightarrow \text{Pu} + \frac{3}{2}\text{CaCl}_2$	-56.0	772
$\text{PuCl}_3 + \frac{3}{2}\text{Mg} \rightarrow \text{Pu} + \frac{3}{2}\text{MgCl}_2$	+0.2	708

reasonably low temperature. It can be further seen that the addition of 0.3 mole of iodine makes the reaction more exothermic and also lowers the melting point of the slag by about 100°C.

Figure 7 shows the flowsheet followed at BARC (Roy and Mahajan 1975) for the reduction of tetrafluoride with calcium. Plutonium tetrafluoride and calcium metal in amount equal to stoichiometric plus 30 to 50% excess are mixed thoroughly and charged into a steel bomb which is capable of withstanding pressures of 0.5–3 MPa and temperature upto 1600°C. The bomb is first purged with argon to exclude any air present. The sealed bomb is subjected to resistance or induction heating to about 600°C when the reduction reaction takes place and the products are melted by the heat

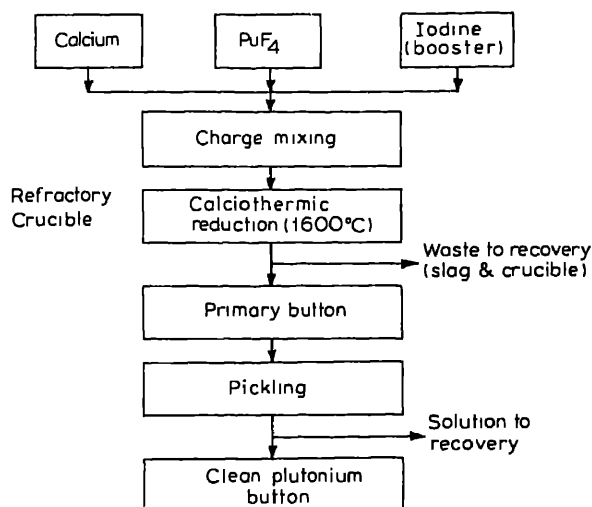


Figure 7. Flowsheet for preparation of plutonium metal.

generated. It is very essential to control the heating rate. If the heating is too rapid, the reaction takes place only at the surface and thus the slag solidifies too rapidly. On the other hand, if preheating period is too long, the calcium particles get coated with  $\text{CaI}_2$  retarding the rate of reaction. The start of the reduction reaction is indicated by a sudden rise in the temperature monitored by a thermocouple or by a drop in the neutron emission from the reaction chamber. The yield in this process is generally 97–99% and the purity normally exceeds 99.8%. Alternatively  $\text{PuF}_4$  and finely divided calcium (50% excess) are mixed and pressed into pellets. The pellets are loaded into a calcium fluoride crucible and then in a quartz tube. On heating a bright flash shows the initiation of the reaction.

Direct reduction of dioxide would overcome the drawbacks of the fluoride and chloride processes namely high neutron emission and hygroscopicity respectively. It would also simplify the process by the elimination of the costly halogenation step. Recent studies (Wade and Wolf 1969) have shown that by proper modification of the reduction apparatus and by using a suitable flux, it is possible to obtain plutonium in massive form by calciothermic reduction of the oxide. Reduction of dioxide by carbon becomes feasible only at temperatures of the order of 3000°C and requires high vacuum system. It also suffers from the formation of plutonium carbide.

## 5.2 Melting and casting

The fabrication of plutonium involves many of the techniques commonly utilised for working of the common metals. However, all operations are directly affected by the extreme toxicity of plutonium in any form, the tendency of the metal to oxidise rapidly, the pyrophoricity and by the obvious necessity of avoiding conditions of criticality.

The low melting point of plutonium offers a considerable amount of freedom in the selection of melting equipment. Although resistance, arc and electron beam furnace have been used for melting plutonium, inductive heating is most advantageous.

Extremely high reactive nature of molten plutonium poses a big problem in the choice of crucible material. Different types of crucible materials have been used. Of the metallic crucibles, tantalum has been extensively used but its use is limited to a maximum temperature of 1000°C after which it is rapidly dissolved by plutonium. Ceramic materials like CaO,  $Y_2O_3$  and  $CaF_2$  are good but not used because of their fragile nature.  $Al_2O_3$ , BeO,  $ThO_2$  lead to contamination of the melt. MgO has been widely used but it also leads to slight contamination of the melt. Graphite has been found to be an excellent crucible material. It is inexpensive, can be easily fabricated and is not subject to thermal shock. However, a suitable coating must be applied to the graphite surface to prevent carbon pick up in the melt. Crucibles may be either tilt-pouring or bottom-pouring type depending upon the type of work to be carried out.

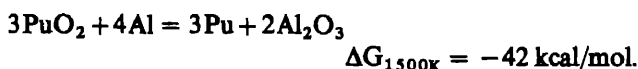
Graphite also serves as the most commonly employed mould material. Metal moulds made of gray cast iron, mild steel, copper and for special purposes tantalum have been used.

Unalloyed plutonium has the general characteristics of a very castable material. The low melting point, high fluidity, high density and extremely small volume change on freezing are all favourable characteristics for casting. Piping and shrinkage porosity observed in most other metals are not encountered when casting plutonium. However, during cooling to room temperature a number of phase transformations take place in pure plutonium metal some of which are accompanied by large volume changes. Accordingly extreme care is exercised in the design of the mould such that the casting does not adhere firmly to the mould and cause cracking. The mould is usually heated to avoid cold shuts in the casting.

## 6. Aluminium-plutonium alloys

As early as in 1961, side by side with the production of plutonium metal, we had also taken up the preparation of Al-Pu alloys by employing similar metallothermic reduction technique (Roy 1962). This technique is particularly advantageous for plutonium alloy preparation because it eliminates costly steps of plutonium metal production, its handling in inert atmosphere and also avoids the problem of gravity segregation which is a common occurrence when a light metal like aluminium is alloyed with plutonium.

Around 500 mg of Al-6.27% Pu were prepared by aluminothermic reduction of  $PuO_2$  in the presence of excess aluminium and cryolite in a graphite crucible around 1100°C. The reaction involved is as follows:



The reduced plutonium immediately alloys with the excess aluminium and the cryolite fluxes the  $Al_2O_3$ . The reaction thus proceeds in the forward direction with proper slag metal separation and high yield. The alloy thus made was recovered by breaking the graphite crucible, remelted for proper homogenisation and cast in another graphite crucible. In the very first preparation itself we could get a yield as high as 96%.

No plutonium metallography facility was available in Trombay at that time. A make-shift arrangement was made for sample preparation, *e.g.* cutting, mounting, grinding, polishing and etching of alloy samples inside a glove box. The microscope, however,

was kept outside the glove box and the sample was examined through a transparent plastic bag attached to the glove box. The as-cast microstructure of the alloy ingot (figure 8) clearly shows lamellar  $\text{PuAl}_4$  particles in an Al matrix.

Al-Pu alloys containing 3–20 w/o plutonium have found widespread application in many research reactors. Aluminium because of its low parasitic thermal neutron absorption cross-section (0.22b) and high thermal conductivity is considered as an excellent inert carrier for the fissile plutonium. Since plutonium has negligible solid solubility (Roy 1964; Ellinger *et al* 1962) with aluminium (figure 9) these alloys essentially comprise of a dispersion of the intermetallic  $\text{PuAl}_4$  in an aluminium matrix.



Figure 8. Microstructure of cast aluminium-plutonium alloy (prepared in 1961,  $\times 100$ ).

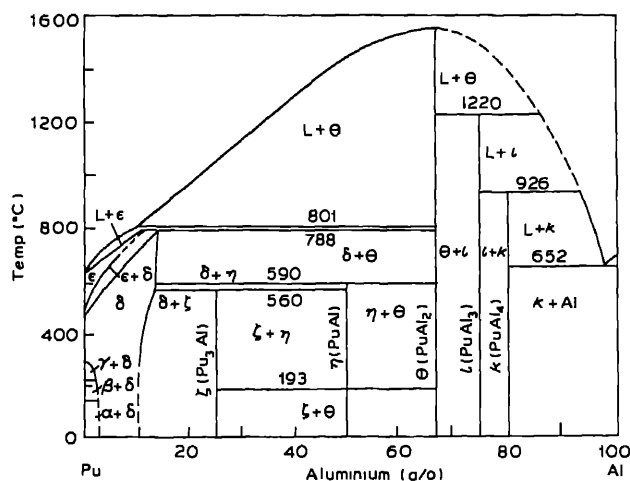


Figure 9. Plutonium aluminium phase diagram.



Such dispersion fuel has the advantage of minimum radiation damage by restricting the fission recoil damage to the area immediately adjacent to the fissile dispersoid particles, namely  $\text{PuAl}_4$ , which are relatively small in size leaving a large area of undamaged non-fissile matrix metal aluminium, which is predominant in volume and in the form of a continuous network surrounding the  $\text{PuAl}_4$  phase.

Towards the end of 1960s, 60 g of Al-13 w/o Pu in the form of sheets ( $40 \times 40 \times 0.5\text{--}2$  mm) was prepared for nuclear physics experiments (Roy *et al* 1969). Experience in cold rolling of Al-Pu alloys was obtained during this campaign.

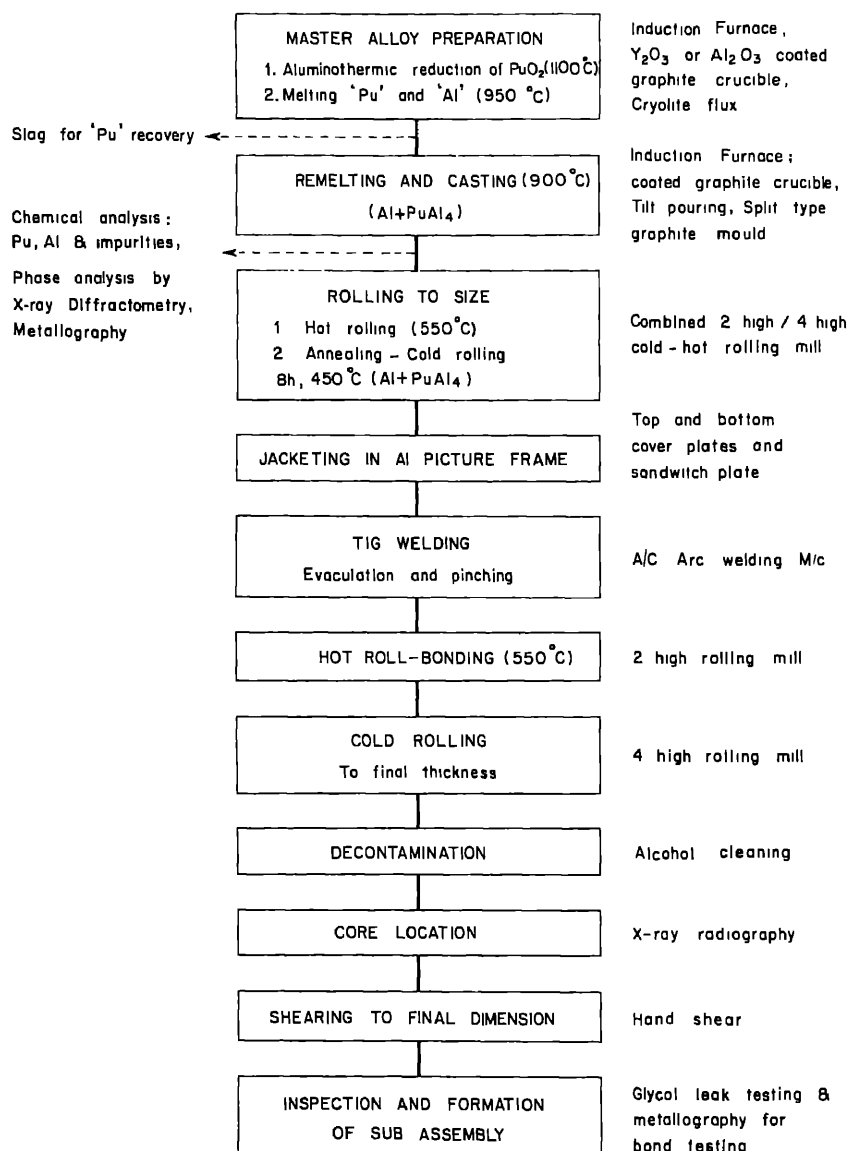
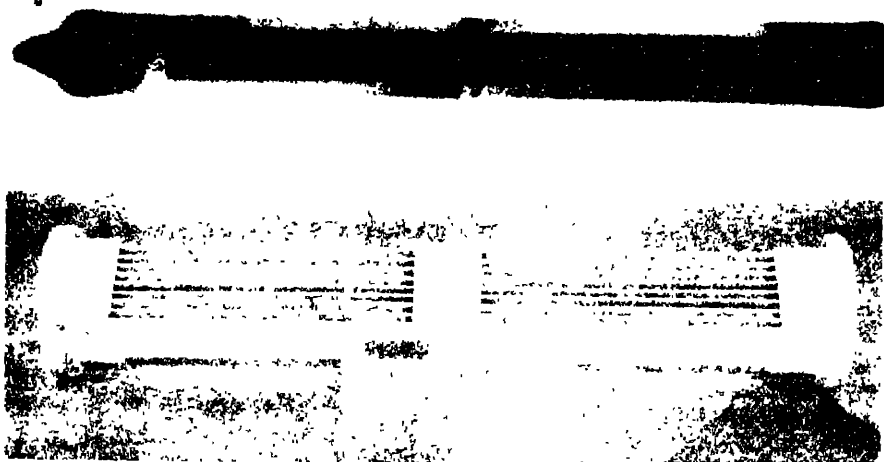


Figure 10. Flow sheet followed in BARC for fabrication of Al clad Al-Pu plate fuel element.



Figures 11, 12. 11. X-ray radiograph of Al clad Al-Pu alloy plate fabricated in radio-metallurgy division, BARC. Dark areas show the alloy meat. 12. 9 plate fuel subassembly of Al clad Al-Pu alloy. After irradiation testing in Zerlina reactor in BARC.

With the commissioning of the new Plutonium Metallurgy Laboratory in 1970, a new pilot scale facility was set up for fabrication of Al-Pu alloy fuel elements at BARC. The main equipment consisted of a high vacuum induction melting-casting unit, a 2 high/4 high cold/hot rolling mill and an annealing furnace.

This facility was utilised in 1973 to fabricate 2 nine plate sub-assemblies of Al-10 w/o Pu and Al-18 w/o Pu plate fuel elements ( $445 \times 51.75 \times 1.78$  mm) by the "picture-frame technique" according to the flowsheet shown in figure 10 (Prasad *et al* 1976) for nuclear physics experiments in the ZERLINA reactor at BARC. The Al-Pu alloy meat was hot roll-bonded to the aluminium cover plates at  $450^\circ\text{C}$ . The radiograph of a roll-bonded Al clad Al-Pu alloy fuel plate and the photograph of a 9-plate sub-assembly fabricated at BARC are shown respectively in figures 11 and 12.

Such Al-Pu plate fuel elements could be utilised as a substitute for the imported aluminium clad Al-13 w/o U(85% enriched  $^{235}\text{U}$ ) plate fuels used in the Apsara Swimming Pool type test reactor at BARC. It also can be used as boosters in our pressurised heavy water reactors (PHWR) to overcome xenon poisoning following post shut-down start-ups.

## 7. Plutonium-beryllium alloys

Pu-Be alloys are used as low flux neutron sources utilising the interaction of alpha particles from plutonium with beryllium atoms to generate neutrons according to the reaction  $\text{Be}^9 (\alpha, n)\text{C}^{12}$ . The principal advantages of Pu-Be alloys over Ra-Be and Po-Be neutron sources is the stability of the neutron yield with respect to time due to the long half-life of  $^{239}\text{Pu}$  (24360 yr) and the relatively small amount of low energy gamma radiation. Moreover, plutonium is relatively non-volatile as compared with radium or polonium and since it readily alloys with beryllium, it is possible to prepare the Pu-Be neutron source as an alloy rather than pressed mechanical mixtures. The alloying further leads

to mechanically strong, non-friable body and reproducibility in neutron yield. The neutron yield of Pu-Be alloys, as shown in figure 13 depends on the beryllium to plutonium atom ratio  $N$  according to the relation:

$$\frac{n}{n_{\max}} = \frac{N \times S_{\text{Be}}}{(N \times S_{\text{Be}} + S_{\text{Pu}})}$$

where,  $n/n_{\max}$  is the fraction of maximum neutron yield,  $S_{\text{Pu}}$  is the stopping power of Pu = 4.5 and  $S_{\text{Be}}$  is the stopping power of Be = 0.63. The neutron yield for a beryllium and plutonium ratio of 13, at which the alloy consists of the intermetallic  $\text{PuBe}_{13}$  (figure 14) is only 36.7 per  $10^6$  alphas compared to 54.9 per  $10^6$  alphas for an atom ratio of 200. An atom ratio of 30 leads to good compromise between the physical size of the source and

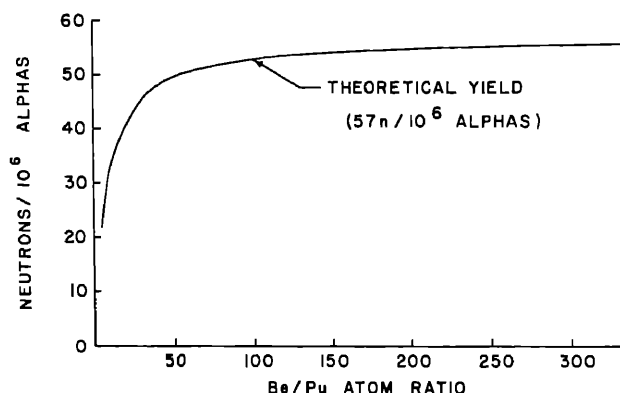


Figure 13. The variation of neutron yield with Be:Pu atom ratio.

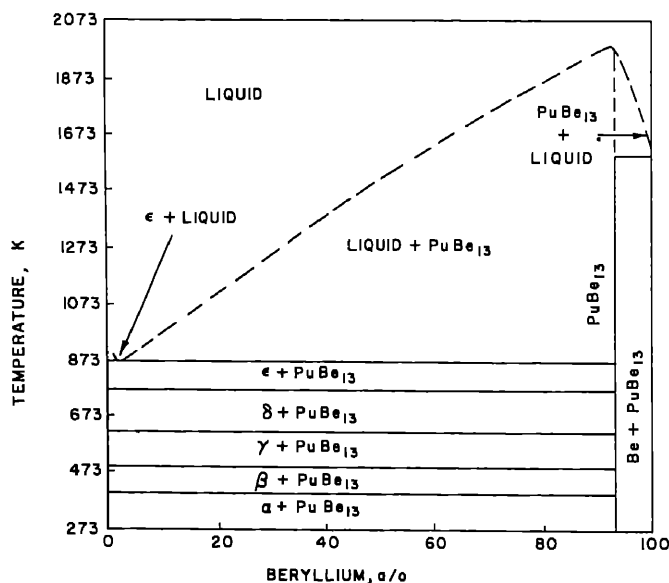


Figure 14. Pu-Be phase diagram.

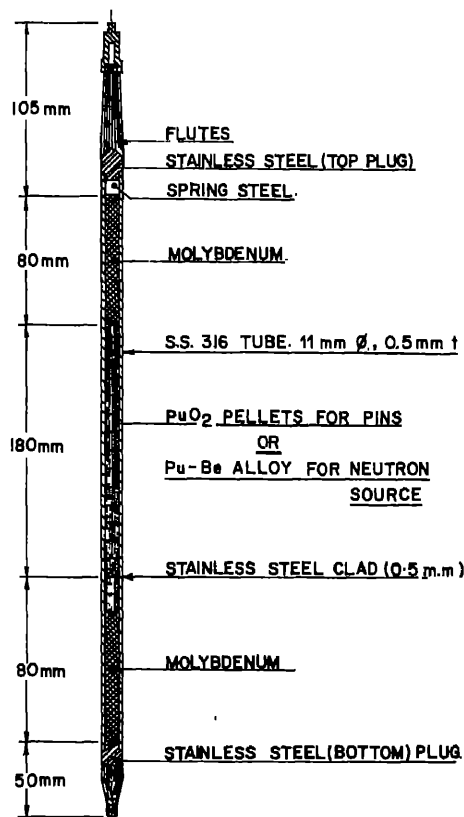
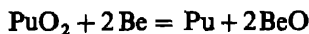


Figure 15. Fuel pin and pencil neutron source for Purnima.

its neutron yield of 46 per  $10^6$  alphas. Further, alloys with  $N \geq 30$  are easily sintered at a relative low temperature of  $1250^\circ\text{C}$  but for  $N$  lower than 30 a minimum sintering temperature of  $1400^\circ\text{C}$  is required.

The first Pu-Be neutron source of nearly 1 Curie strength was prepared at BARC (Roy *et al* 1967) in 1967, by berylothermic reduction of pellets prepared from a powder mixture of around 18 g each of  $\text{PuO}_2$  and Be in vacuum at  $1250^\circ\text{C}$  (Be:Pu atom = 30). The reaction is as follows:



$$\Delta G_{1000\text{K}} = -29.4 \text{ kcal/mol.}$$

The presence of BeO in the reaction product does not alter the neutron emission. The alloys thus prepared undergo reaction sintering and consist of a fine dispersion of  $\text{PuBe}_{13}$  and BeO in a matrix of Be. Subsequently in 1972, the same technique was followed for the preparation of several point and pencil neutron sources of strength between 50 mCi and 5 Ci (Mahajan *et al* 1972).

The Pu-Be neutron sources are encapsulated in metallic cans. For the point source the Pu-Be alloy tablet is first loaded in a one end closed aluminium or stainless steel container with a screwed cap. This sealed inner container is next loaded in an outer container of stainless steel and encapsulated by TIG welding. These point sources have been delivered to several agencies within and outside BARC for calibration of neutron

counters, physics experiments and devices for measuring moisture and hydrocarbons in soil. The 900 mCi pencil sources (figure 15) were used for start-up of the PURNIMA reactor at BARC.

### 8. Delta-stabilised plutonium alloys

Unalloyed plutonium, unlike uranium has never been tried as a nuclear fuel because of its unfavourable metallurgical properties. First, plutonium has a low melting point (640°C). Secondly, there are as many as 6 allotropic transformations of plutonium between 20 and 640°C as shown in table 7 (Zachariasen and Ellinger 1959). No other metal shows as many phase changes within such a narrow temperature range. Particularly undesirable is the large volume change, of the order of 10%, which accompanies the alpha to beta transformation at 122°C. It was, therefore, natural to look for a high temperature phase which could be stabilised down to the room temperature by a proper combination of alloying and heat treatment.

Delta plutonium which is stable between 315 and 456°C has a fcc structure and exhibits the highest ductility and best formability amongst all the plutonium allotropes. The delta phase can be retained at room temperature by small additions of Al, Sn, Zn, Ga, Zr, In, Hf, Ti, Ce, Dy, Er, Tm, La or Th. The delta-stabilised plutonium has many desirable mechanical and metallurgical properties. It is ductile and soft, has a hardness value of 40–45 kg/mm<sup>2</sup> (Vicker's DPH) which is comparable to annealed copper and can be conveniently machined, worked and turned. Further, these alloys have negligible volume change during working, produce good quality casting and are more resistant to oxidation compared to unalloyed plutonium. However, the density of delta-stabilised plutonium is less than unalloyed plutonium.

Delta-stabilised plutonium alloys have been used as fuels in the first fast reactor Clementine of LASL in the late 1940s and subsequently in core IV of EBR I of ANL, ZEPHYR of Harwell and BR-1 and 2 of USSR in the early 1950s.

Delta-stabilised plutonium alloys have been prepared at BARC in the 1970s by vacuum induction melting in coated graphite crucibles and casting in graphite moulds. The principal difficulties faced in melting, and casting these alloys are gravity segregation due to large density difference between plutonium and the alloying elements and adherence of the cast alloy with the mould because of negligible solidification shrinkages of delta plutonium.

Table 7. Allotropes of plutonium and their properties.

Phase	Structure	Stability range (°C)	Density (g/cc)	Coeff. of expansion (micro in./in. °C)	$\Delta V\%$
$\alpha$	Simple monoclinic	Up to 117	19.84	48.4	10.10
$\beta$	Body centred monoclinic	117–213	17.8	38.0	2.58
$\gamma$	Face centred orthorhombic	213–315	17.14	34.7	6.75
$\delta$	fcc	315–456	15.92	–8.8	–0.25
$\delta'$	bct	456–475	16.01	–116.0	–3.0
$\epsilon$	bcc	475–640	16.48	36.5	

## 9. Plutonium dioxide

In the field of ceramic fuel too the trend developed in the uranium system had set the pattern in the plutonium field. In the 1960s uranium dioxide was universally used in most of the commercial thermal power reactors, including ours, and the technology for the production of zircaloy clad  $\text{UO}_2$  fuels by the "pellet-in-tube" process was available in Trombay (Fareeduddin *et al* 1975). This know-how was conveniently extended for the initial development of stainless steel clad  $\text{PuO}_2$  fuels in the new plutonium metallurgy laboratory at Trombay in 1970 (Roy 1975).

Subsequently, the first major plutonium fuel fabrication job was executed in 1972 when the complete core for the zero energy fast reactor PURNIMA in BARC consisting of 186 fuel pins containing around 25 kg, of sintered  $\text{PuO}_2$  fuel pellets was fabricated. The fuel pin (495 mm long  $\times$  11 mm OD) (figure 15) with a cladding thickness of 0.5 mm and consists of a stack of sintered  $\text{PuO}_2$  fuel pellets of average density of 90% theoretical, held tight by a spring between a pair of axial molybdenum reflectors in a 316 stainless steel cladding tube which is sealed leak tight by TiG welded end plugs.

$\text{PuO}_2$  pellets were prepared from oxalate derived sinterable  $\text{PuO}_2$  powder by the powder metallurgy route of cold compaction at around 25 TSI followed by sintering at 1600°C in  $\text{A} + 8\% \text{H}_2$  atmosphere. The finished fuel pins were subjected to rigorous inspections for dimensional checks, x-ray radiographic examinations, mass spectrometric helium leak detection and surface contamination.

## 10. Mixed oxide fuels

Pure  $\text{PuO}_2$  as such is not suitable for use as fuel in power generating reactors as it fails to satisfy the reactor engineering and safety requirements of bigger reactors. Further, for breeding additional fissile material simultaneously with power generation it is essential to dilute  $\text{PuO}_2$  by mixing with fertile materials like  $\text{UO}_2$  or  $\text{ThO}_2$ .

The following mixed oxide fuel compositions have been studied and developed in the last ten years as a part of our fuel development programme for water-cooled thermal and liquid metal cooled fast breeder reactors (LMFBR):

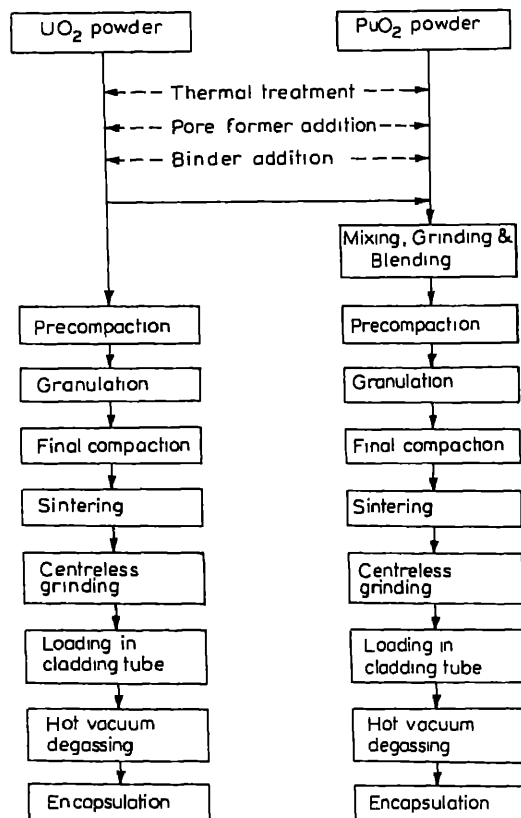
- (a) 76%  $\text{PuO}_2$ –24% natural  $\text{UO}_2$  or 70%  $\text{UO}_2$ –30%  $\text{PuO}_2$  (assuming availability of 85% enriched  $^{235}\text{U}$  for actual use) fuels for our fast breeder test reactor (FBTR).
- (b)  $\text{UO}_2$ – $\text{PuO}_2$  (up to a maximum of 5 w/o  $\text{PuO}_2$ ), popularly known as the MOX fuel, as substitute for the 2–4% enriched  $\text{UO}_2$  fuels for the BWRs at TAPS.

Since  $\text{UO}_2$  and  $\text{PuO}_2$  are isostructural (fcc,  $\text{CaF}_2$  type), mutually solid soluble and have similar physical and chemical properties (table 8), the fabrication flowsheets (figure 16) of the mixed oxides are essentially the same and involves three major steps, namely, (i) simultaneous mixing grinding of the two oxide powders in the desired proportion, (ii) cold compaction of the powder mixture into pellets with or without binder addition, and (iii) sintering the pellets in a controlled atmosphere. The process control steps in pellet fabrication should ensure homogeneous solid solution formation, uniform distribution of plutonium, an oxygen to metal ratio slightly in the hypostoichiometric range and a controlled density.

In addition to the above route, in Trombay we are also working on the "vibrosol" process as an alternative method of preparation of mixed oxide fuel pins (Sood and

Table 8. Selected properties of U, Pu and Th compounds.

Property	Oxide			Carbide		Nitride	
	UO <sub>2</sub>	PuO <sub>2</sub>	ThO <sub>2</sub>	UC	PuC	UN	PuN
Theoretical density (g/cm <sup>3</sup> )	10.96	11.46	10.00	13.63	13.60	14.32	14.25
Metal density (g/cm <sup>3</sup> )	9.66	10.10	8.79	12.97	12.95	13.52	13.46
Metal fraction (w/o)	88.15	88.19	87.89	95.20	95.20	94.44	94.46
Melting point (K)	3000	2675	3640	2780	1875	3125	2840
Thermal conductivity (W/cm K)							
for 100% TD material							
1000 K	0.052	0.034	0.062	0.199	0.108	0.185	0.146
1500 K	0.035	0.023	0.024	0.213	0.142	0.248	0.167
2000 K	0.022	0.018	—	0.225	0.159	0.270	0.184

Figure 16. Process flow sheet for UO<sub>2</sub> and UO<sub>2</sub>-PuO<sub>2</sub> pellet fuel pin.

Vaidya 1979). This method consists of preparing mixed oxide gels by a "wet chemical route" starting from uranyl and plutonium nitrate solutions followed by calcination of the gels to get mixed oxide microspheres of high density ( $\sim 98\%$  TD). By blending microspheres of different size fractions in the range of 10–100  $\mu\text{m}$  and packing them in

the fuel pin by "vibratory compaction", smear density of the fuel pin can be controlled between 60 and 90 % TD. An "internal gelation" (Kanij *et al* 1974) process has been followed for preparing mixed oxide microspheres according to the flowsheet shown in figure 17. The nitrate solutions of the actinides are mixed and cooled. To this, concentrated hexamethylene tetra amine (HMTA) and urea solutions are added which act as internal gelation agents. Droplets of this solution are gelled by contact with hot ( $\sim 90^\circ\text{C}$ ) silicone or paraffin oil.

The vibro-sol method offers the following advantages over the cold pressing sintering process:

- (a) There are less number of fabrication steps and maximum flexibility of operation.
- (b) A high degree of microhomogeneity is obtained in the microsphere since the blending is effected in the liquid stage and steps like prolonged ball milling of oxide powders for achieving good homogenisation are avoided.
- (c) The build-up of radioactive dust on equipment and glove box surfaces which is rather common in the powder metallurgy route is also avoided since no fine powder handling is involved.
- (d) The method is more suitable for remote operation and automation.

The main drawback of the vibro-sol route is that in the event of an accidental breach of the cladding tube, there could be more expulsion of fuel particles to the coolant circuit as compared to pellet fuel, thereby causing a gross contamination of the primary coolant.

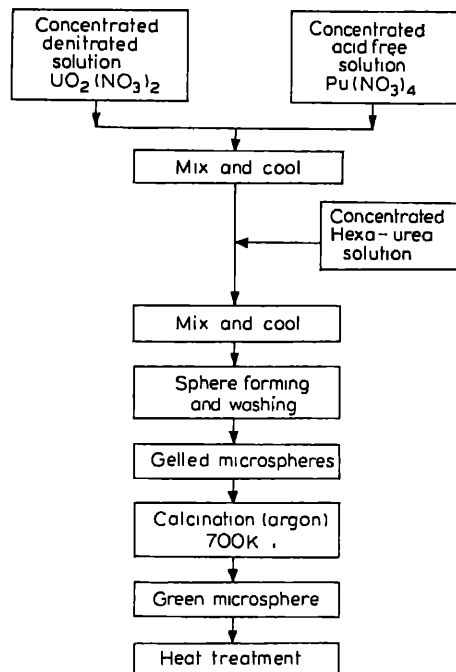


Figure 17. The kema internal gelation process.



10.1  $\text{UO}_2\text{-PuO}_2$  for LMFBRs

As a first step of our venture in the LMFBR technology a decision was taken in the 1970s to set up a small 42.5 MW(th) fast breeder test reactor (FBTR), similar to the Rapsodie-Fortissimo reactor of France, at the Reactor Research Centre, Kalpakkam. It was also decided to fabricate the fuel for this reactor in Trombay from our available natural uranium resources and plutonium. Normally, in such small test reactors the fissile requirement of the core, as shown in figure 18, is met by enriched uranium along with plutonium in order to have a high neutron flux level and to compensate for the neutron leakage loss in the small core. However, we preferred to replace the  $^{235}\text{U}$  completely by plutonium and consequently looked into the possibility of using 76%  $\text{PuO}_2\text{-}24\%$   $\text{UO}_2$  in place of already proven 70%  $\text{UO}_2$  (enriched to 85%  $^{235}\text{U}$ )-30%  $\text{PuO}_2$  fuel of Rapsodie.

Unfortunately, preliminary metallurgical investigations revealed that  $(\text{U}_{0.24}\text{Pu}_{0.76})\text{O}_2$  was not compatible with the sodium coolant and led to the formation of  $\text{Na}_3(\text{U, Pu})\text{O}_4$  with accompanying high swelling as shown in figure 19(a) (Internal Report 1970; Housseau 1974). The sodium-fuel interaction and in turn the swelling could be significantly reduced if the O/M ratio of the fuel was kept around 1.8 (figures 19b, c) but then the already low thermal conductivity of the plutonium rich oxide fuel further reduces by nearly 30% (figure 20) (Internal report 1974). Moreover, the mixed oxide fuel of this composition with an optimum O/M ratio of 1.98 and pellet density of 92% TD always had a two-phase microstructure at room temperature as shown in the x-ray diffraction pattern (figure 21) and photomicrograph (figure 22) (Ramachandran *et al* 1981).

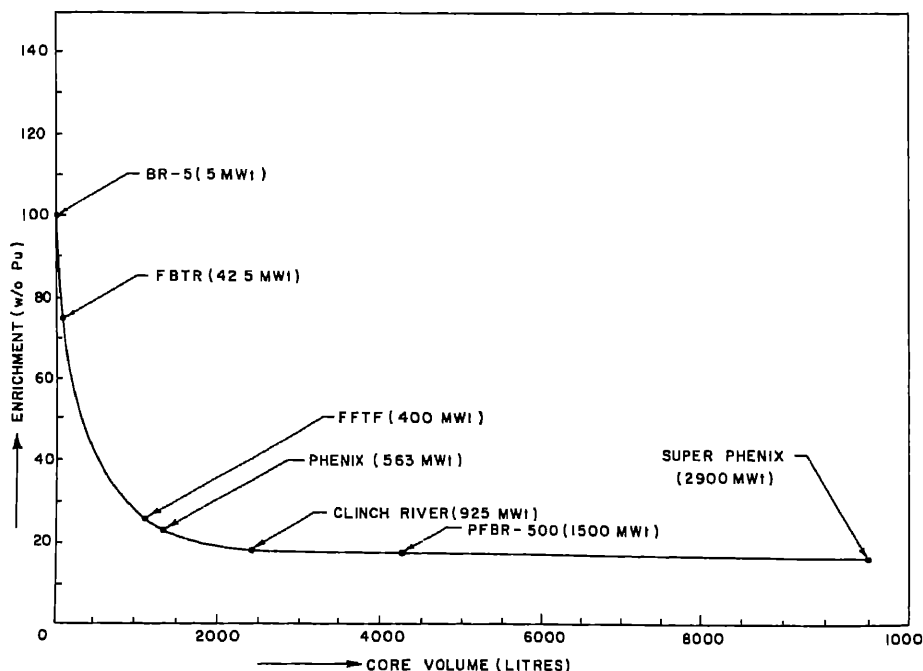


Figure 18. Enrichment—core volume.

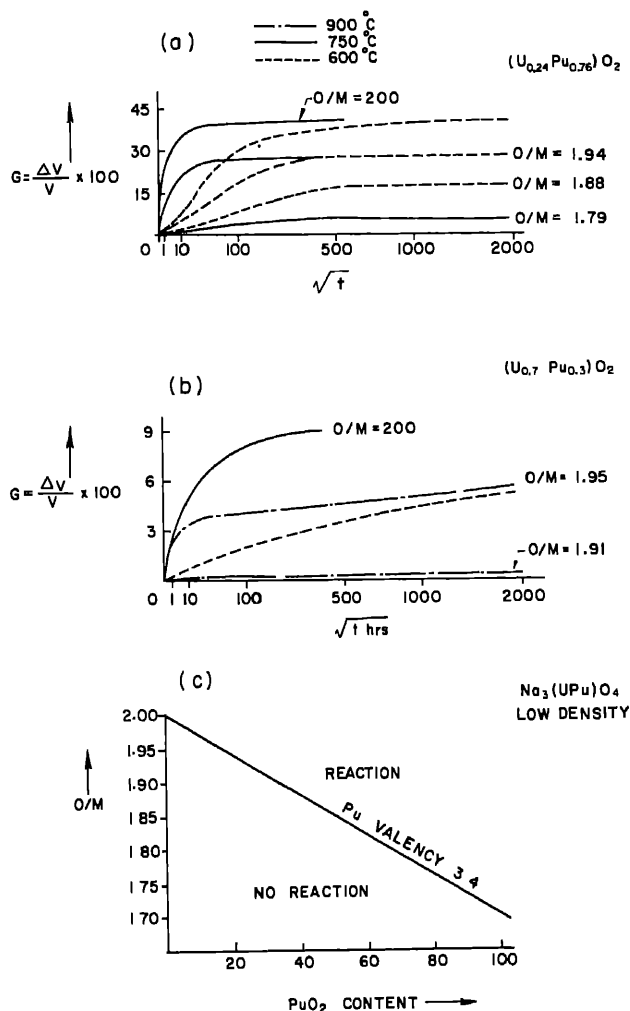


Figure 19. Swelling of uranium and plutonium rich mixed oxide after interaction with sodium.

In view of the above deficiencies, investigation of plutonium rich  $(U, Pu)O_2$  was not pursued further. The next logical step was to revert back to the development of fabrication flowsheet of 70%  $UO_2$ -30%  $PuO_2$ . Single-phase mixed oxide pellets of this composition with density 92% TD and O/M ratio 1.98 could be reproducibly fabricated in our laboratory (Majumdar *et al* 1984). A typical microstructure of single phase mixed oxide pellet is shown in figure 23.

## 10.2 MOX fuel for TAPS

Zircaloy-2 clad 2-4% enriched  $UO_2$  is the fuel for the two BWR at TAPS. The enriched uranium for these reactors was imported ever since the reactors were commissioned in 1967. However, with changing political conditions great difficulties were experienced in

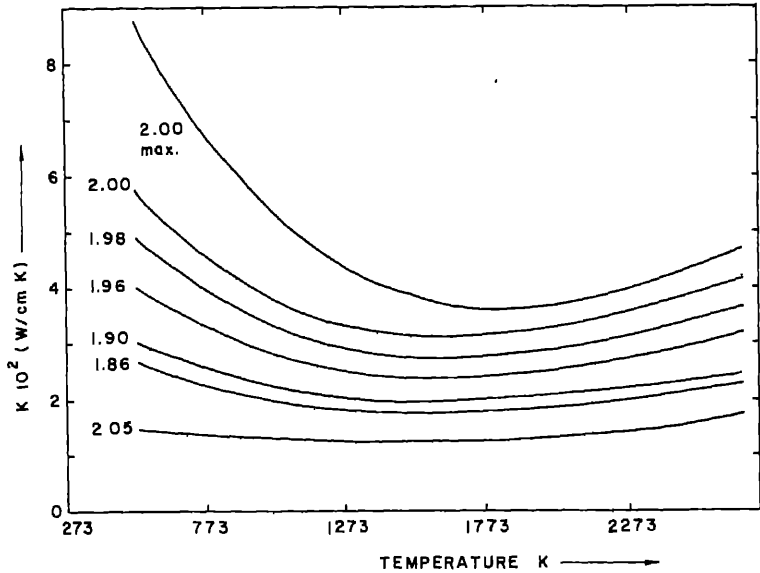


Figure 20. Thermal conductivity vs. temperature of 76% PuO<sub>2</sub>-24%UO<sub>2</sub> pellets of different stoichiometry.

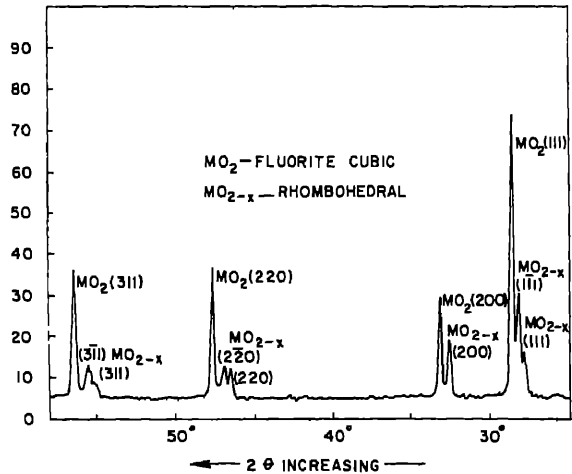
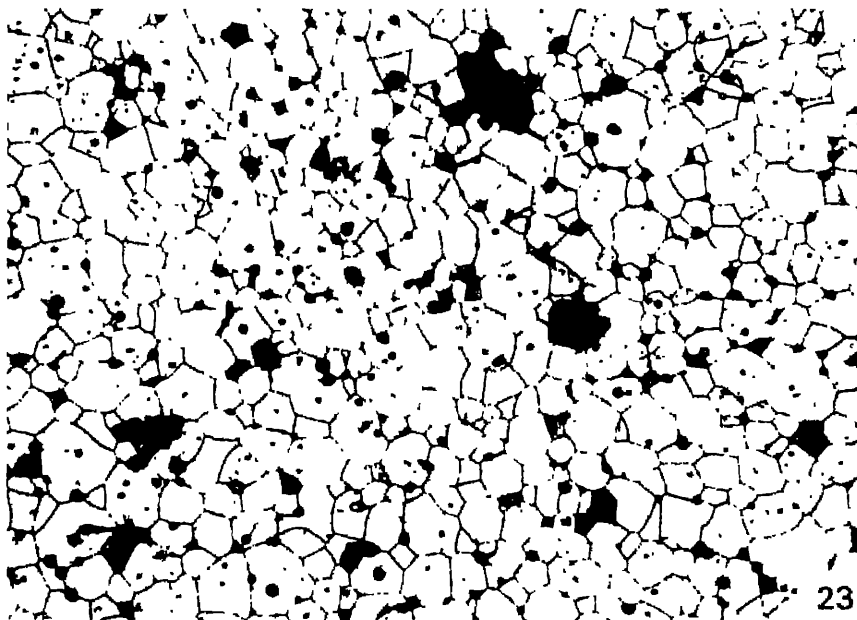
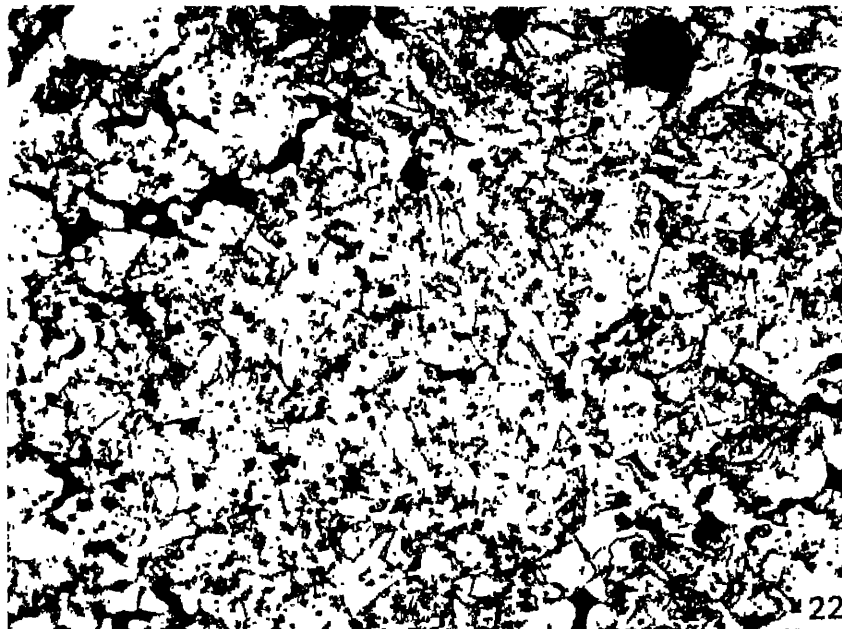


Figure 21. XRD pattern of (U<sub>0.24</sub>Pu<sub>0.76</sub>)O<sub>2-x</sub> sintered pellet.

importing enriched uranium and a decision was taken in 1978 to explore the possibility of fabricating indigenously MOX fuel containing 2–5 w/o PuO<sub>2</sub> as a substitute for the enriched UO<sub>2</sub> fuel. Accordingly, a crash programme was launched to augment the existing plutonium fuel fabrication laboratory with a capacity of 1 kg fuel per day to 50 kg per day to meet the interim requirement of TAPS.



Figures 22, 23. 22. Microstructure of  $(U_{0.24} Pu_{0.76})O_2$  showing two phases ( $\times 400$ ).  
23. Microstructure of single phase  $(U_{0.70} Pu_{0.30})O_2$  ( $\times 320$ ).

Though the first MOX fuel experience (Sah *et al* 1977) was acquired in Trombay in 1972 when a test pin of  $UO_2$ -1.5 w/o  $PuO_2$  of specifications similar to our PHWR fuel element was fabricated for irradiation testing in the pressurised water loop (PWL) of our CIRUS reactor, the MOX substitute fuel for TAPS was a real challenge to the metallurgists as

this was a time bound project involving plant scale handling and fabrication of plutonium fuels in a laboratory originally designed for R and D work only.

After extensive investigation, fabrication flowsheet with optimum process parameters was developed to get MOX fuel pellets according to specification (Roy *et al* 1984). There is a stringent requirement of uniformity of plutonium distribution in the fuel pellets from the view point of in-reactor performance. This has been confirmed from the alpha-autoradiography of the MOX pellets shown in figure 24.

The pilot scale MOX fuel fabrication facility of capacity 50 kg sintered MOX pellets per day has been commissioned in BARC and production trials with a few tons of  $\text{UO}_2$  pellets have been successfully completed. The facility essentially consists of:

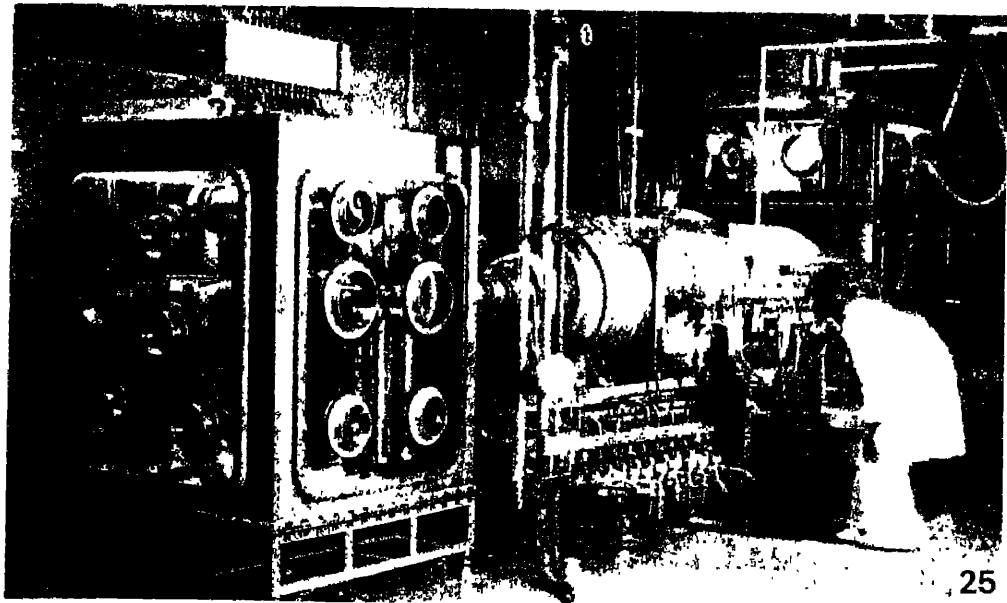
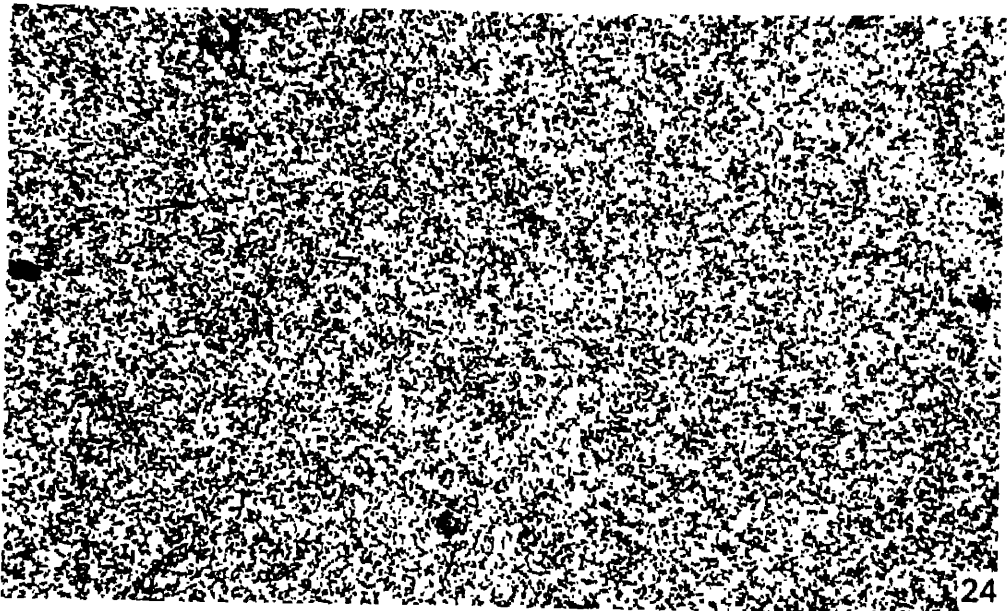
- (a) a train of interconnected glove boxes for preparation of MOX granules starting from  $\text{UO}_2$  and  $\text{PuO}_2$  powders by milling, blending, precompaction and granulation;
- (b) a compaction-sintering train consisting of a 30 ton automatic double action hydraulic press, dewaxing furnaces and a continuous sintering furnace (Sengupta *et al* 1982) (figure 25);
- (c) a centreless grinder for grinding pellet to final diameter;
- (d) a welding train for vacuum degassing of sintered pellets, followed by loading of pellets in a one end welded preautoclaved 4m long zircaloy-2 tubes and encapsulation by TIG welding under a helium pressure of around 0.3 MPa;
- (e) a train of glove boxes for refabrication of sintered MOX pellets from rejected oxide; and
- (f) facilities for nondestructive testing (NDT) of zircaloy hardwares and fuel pins by airgauging, ultrasonic testing, radiography, helium leak detection mass spectrometry and other quality control facilities like metallography, x-ray diffractometry and x-ray fluorescence spectrometry.

The mechanical and thermal properties of  $\text{UO}_2$  are not significantly affected by addition of up to 5 w/o of  $\text{PuO}_2$ . With 5%  $\text{PuO}_2$  addition, the thermal conductivity is reduced by around 5%, the melting point decreases by  $26^\circ\text{C}$ , the thermal expansion and density increase marginally by 1%, the fission gas release and swelling are unaffected and the creep and nuclear self-shielding properties are improved.

Irradiation-testing of a prototype MOX fuel cluster of 6 pins (figure 26) in the PWL, CIRUS was started in December 1979 simulating the operating conditions at TAPS. This MOX fuel cluster has performed very satisfactorily without failure up to the target burn-up of 18000 MWD/ton. A second similar cluster has already been fabricated and is under testing in the reactor.

## 11. Mixed carbide and nitride fuels

The mixed oxide fuels are not, however, the ultimate in the field of development of plutonium fuels for LMFBR. The oxide fuel has the inherent drawback of relatively low heavy atom density, high light atom fraction and poor thermal conductivity. These factors are responsible for its low breeding ratio and low power ratings. On the other hand the potential of (UPu)C and (UPu)N have all along been recognised as better and advanced LMFBR fuels on the basis of their higher breeding ratio and higher linear and specific power ratings which results in much shorter doubling time. An added advantage is the relatively good compatibility of (UPu)C and (UPu)N with sodium (Sengupta *et al* 1982).



Figures 24, 25. 24. Alpha auto radiograph of MOX pellets ( $\times 80$ ). 25. Continuous sintering furnace for MOX pellets.

Since plutonium-rich mixed oxide fuels were not suitable for FBTR, efforts were directed to develop the fabrication flowsheet for plutonium rich (UPu)C and (UPu)N fuels. Towards the end of 1970s  $(U_{0.3}Pu_{0.7})C$  and  $(U_{0.3}Pu_{0.7})N$  pellets of controlled density and phase content were successfully produced in the plutonium metallurgy laboratory at Trombay as per the flowsheet shown in figure 27 (Ganguly 1980).



**Figure 26.** MOX fuel pin cluster for irradiation in PWL, CIRUS (a). MOX cluster (b). Individual MOX pins.

The two main stages in the fabrication are: (a) synthesis of (UPu)C and (UPu)N by carbothermic reduction of mechanically mixed  $\text{UO}_2$ ,  $\text{PuO}_2$  and graphite powders compacted in the form of tablets in vacuum or flowing argon for the carbide and flowing nitrogen or nitrogen + 8% hydrogen mixture for the nitride; (b) crushing and milling of carbide and nitride clinkers followed by cold pressing and sintering in argon, argon + 8% hydrogen or vacuum.

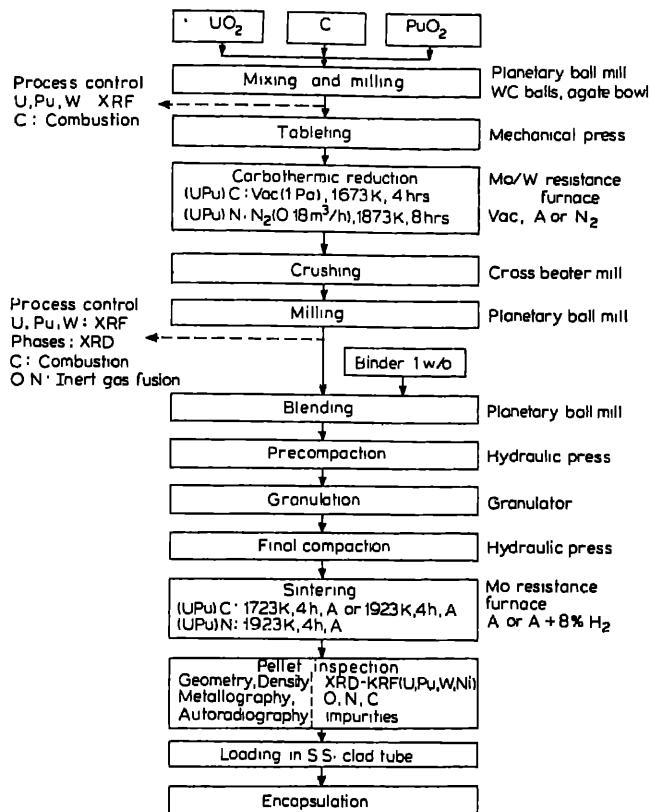


Figure 27. Flow sheet for preparation of  $(\text{U}_{0.3}\text{Pu}_{0.7})\text{C}$  and  $(\text{U}_{0.3}\text{Pu}_{0.7})\text{N}$  fuel pellets for LMFB at BARC.

Equilibrium thermodynamic calculations confirmed by experimental results show that  $(\text{UPu})\text{C}$  prepared by carbothermic reduction of oxides contain substantial amount of oxygen because of the formation of a mixed uranium plutonium monoxycarbide solid solution in the final stage of the carbothermic reduction process which above  $1625^\circ\text{C}$  remove essentially all the oxygen from the monocarbide but might result in the formation of the undesirable liquid phase  $\text{PuC}_{1-x}$  by peritectic decomposition and lead to high plutonium volatilisation losses.

In the synthesis of  $(\text{UPu})\text{N}$  by solid state carbothermic reduction of a powder mixture of  $\text{UO}_2$ ,  $\text{PuO}_2$  and graphite, nitrogen plays the dual role of the reactant and the carrier for the removal of  $\text{CO}$ . The  $(\text{UPu})\text{N}$  produced by this method has high oxygen and carbon contents.

### 11.1 Advantages of plutonium rich $(\text{UPu})\text{C}$ and $(\text{UPu})\text{N}$

Initial theoretical studies on plutonium rich  $(\text{UPu})\text{C}$  and  $(\text{UPu})\text{N}$  unfolded the following advantages of this fuel over the uranium rich composition: (a)  $\text{UC}$  and uranium rich  $(\text{UPu})\text{C}$  have no carbon solubility range but there is a limited carbon homogeneity range in the  $\text{PuC}$  and plutonium rich  $(\text{UPu})\text{C}$  as shown in the  $\text{U-Pu-C}$



phase diagram (figure 28) (Storms and Ackermann 1974). It is, therefore, relatively simple to prepare  $(U_{0.3}Pu_{0.7})C$  as a nearly single phase material.

(b) With nitrogen, plutonium forms only one compound namely PuN whereas uranium has three nitrogen compounds, namely UN,  $U_2N_3$  and  $UN_2$  (Potter 1975). The higher nitrides of uranium, however, are easily decomposed to the mononitride by a high temperature treatment in vacuum or inert gas. Single phase PuN and plutonium rich (UPu)N are therefore relatively easy to prepare.

(c)  $Pu_2C_3$  and  $(U_{0.3}Pu_{0.7})C_{1.02}$  have lower carbon potentials compared to  $U_2C_3$  at all temperatures and a lower carbon potential than stainless steel 316 up to  $725^\circ C$  as shown in figure 29 (Gotzmann and Hofmann 1974; Internal report 1980). The chances of carbon transfer from plutonium rich mixed carbide to stainless steel is therefore lower and there will be no clad carburisation if the temperature inside the clad is kept below  $725^\circ C$ .

(d) The melting points of (Sheth and Leibonitz 1974) of PuC and PuN are less than that of UC and UN respectively for which the optimum carbothermic and sintering temperatures of plutonium rich (UPu)C and (UPu)N are  $150\text{--}200^\circ C$  lower than their uranium rich counterparts (Ganguly *et al* 1980, 1982). Hence, the plutonium volatilisation losses are relatively less (within 1–2%).

### 11.2 Mixed carbide facility for FBTR

The small scale (60 g) laboratory experiments established the overall feasibility of the fabrication of controlled density (UPu)C and (UPu)N pellets as nearly single phase material as shown in the x-ray diffraction patterns (figure 30) and the microstructures (figure 31). On the basis of this experience a production laboratory was set up during 1981–82 for the fabrication and quality control of 1.5 kg/day of finished mixed carbide fuel pellets from  $UO_2$  and  $PuO_2$  feed materials (Ganguly and Roy 1981). This laboratory has two main facilities, namely (a) pellet production facility, and (b) process control facility.

The pellet production facility consists of a train of 12 interconnected glove boxes housing conventional powder metallurgy equipment. In addition, for rapid process control at different stages in the preparation and sintering of MC and MN

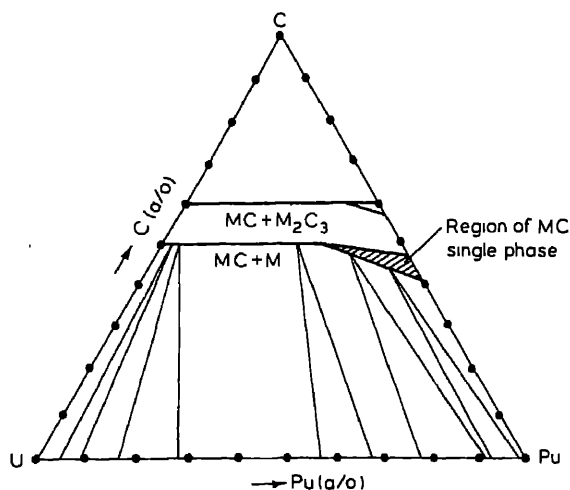


Figure 28. U-Pu-C system at  $600^\circ C$  ( $M = U, Pu$ ).

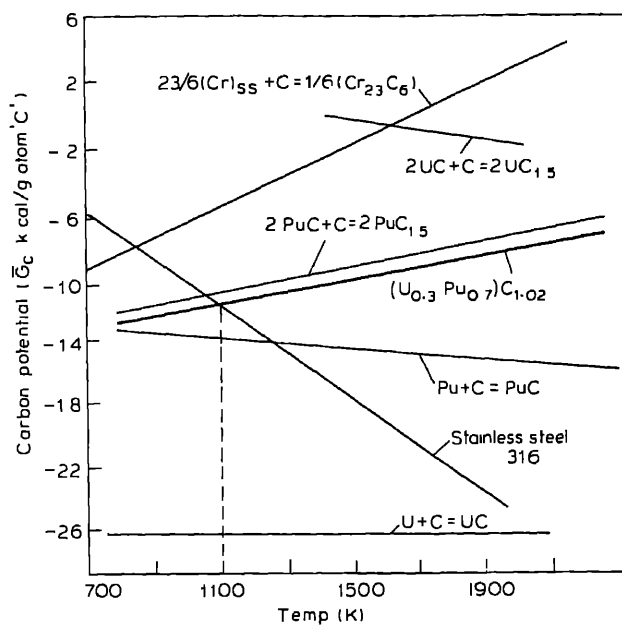
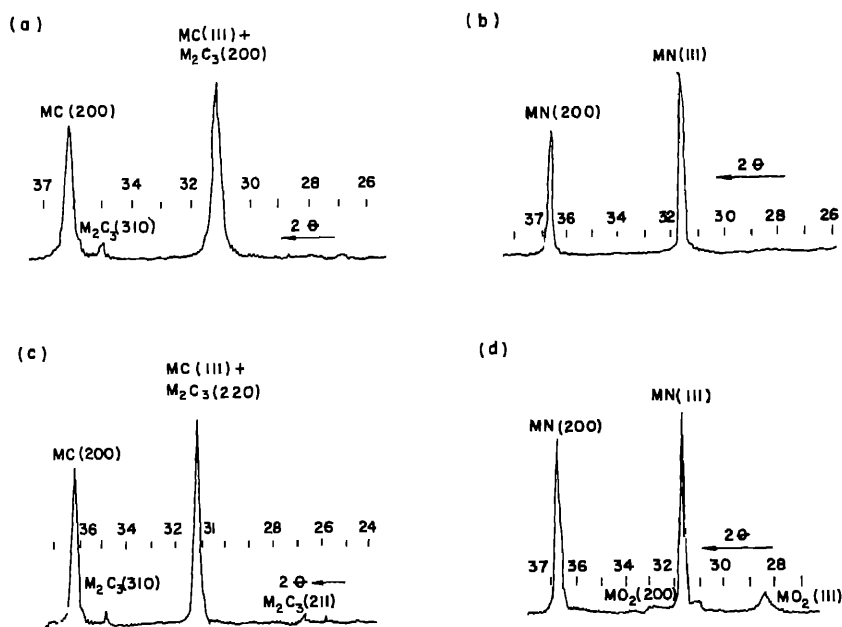
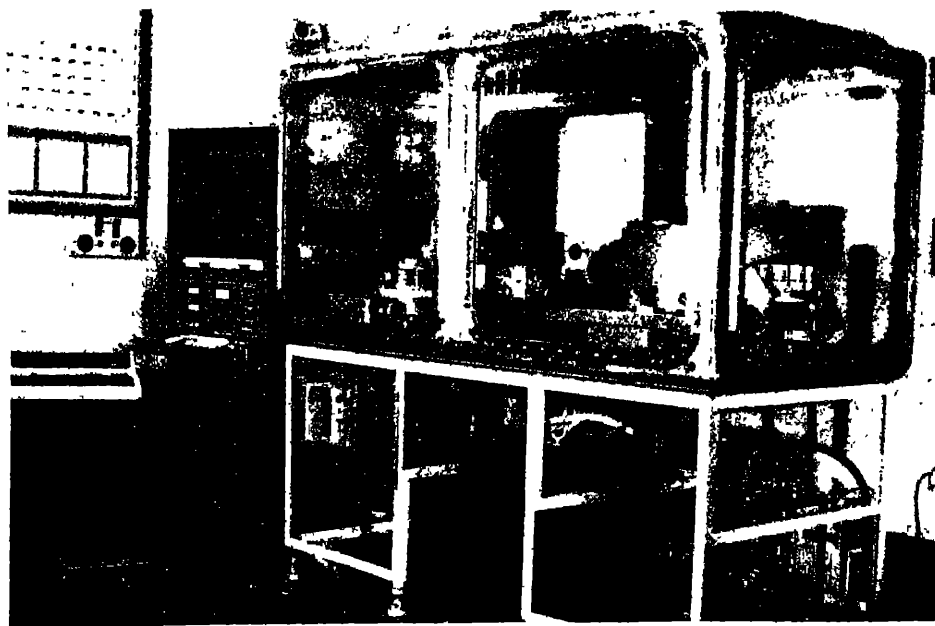
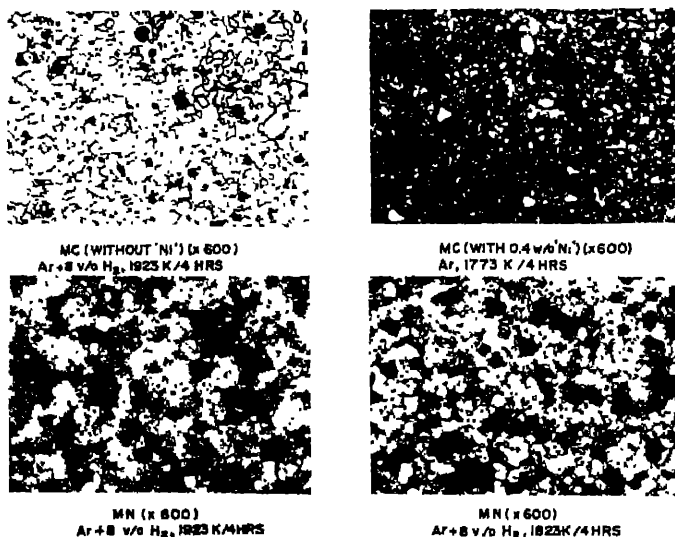


Figure 29. Carbon potentials of carbides.

Figure 30. X-ray diffraction pattern of MC and MN;  $M = (U_{0.3}Pu_{0.7})$  after carbothermic reduction of  $UO_2 + PuO_2 + C$  for (a). carbide (b). nitride; after sintering of (c). carbide (without -Ni) and (d). nitride.

powders the following equipment have also been installed (Ganguly *et al* 1981): (a) a combined and sequential oxygen and nitrogen inert gas fusion analyser for rapid analysis of oxygen and nitrogen in powders and pellets; (b) a rapid carbon analyser for powder and pellet based on the method of combustion and determination by thermal conductivity meter; (c) an automatic, combined and sequential x-ray fluorescence spectrometer and x-ray diffractometer for rapid analysis of U, Pu, tungsten, nickel and different phases present in powder and pellets (figure 32).



Figures 31, 32. 31. Microstructure of plutonium rich (UPu)C and (UPu)N pellets. 32. Combined XRD-XRF unit in RMD, BARC under commissioning inside a glove box.

## 12. Looking forward

In our travels into the plutonium age over the past quarter of a century, we have passed many milestones, meeting new challenges, probing new frontiers, indigenising all aspects of plutonium metallurgy and fuels and have reached today a stage of commercial exploitation of plutonium in nuclear power reactors.

Our well-known three stage nuclear power strategy projects the pivotal role of plutonium in the coming decades for a viable and rapidly expanding electricity generation programme. The first stage based on our operating and forthcoming natural  $\text{UO}_2$  fuelled PHWRs will be limited to only 10–15 GW(e) for 30 yr but will produce between 100–150 tons of fissile plutonium as by-product along with depleted uranium. The second stage, which is likely to start towards the turn of this century, will make most effective utilisation of these large quantities of plutonium by recycling it several times with depleted uranium in LMFBR. Around 350 GW(e) would be possible for 65 yr with  $^{238}\text{U}$ – $^{239}\text{Pu}$  fuel cycle and simultaneously  $^{232}\text{Th}$  could be converted to  $^{233}\text{U}$ . Finally, in the third stage, the self sustaining  $^{232}\text{Th}$ – $^{233}\text{U}$  thermal breeder fuel cycle could be used in PHWR to unlock 1000 GW(e) for 240 yr, thus establishing that nuclear power is the only long term answer to our energy crisis.

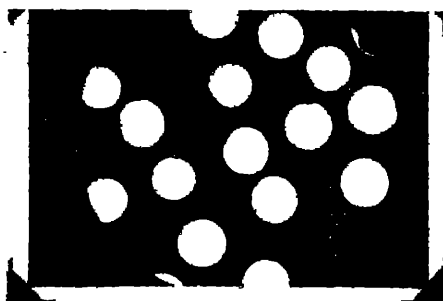
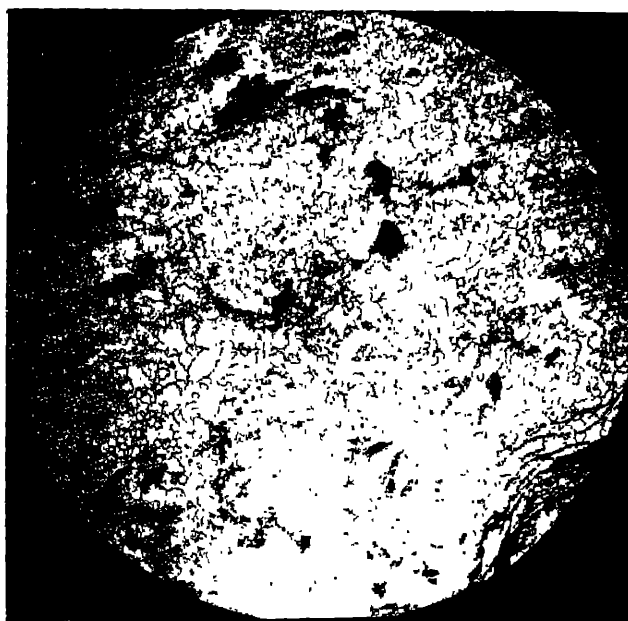
A plutonium-fuelled prototype fast breeder reactor of 500 MW(e) capacity (PFBR-500) has been already planned for the 1990s (Singh *et al* 1981). This reactor will essentially act as a “lead station” to demonstrate the basic safety, reliability and economics of plutonium fuel reprocessing, refabrication and irradiation on a commercial scale and will generate data on which “series ordered LMFBR stations” can be commissioned with confidence after 2010.

A larger capacity plutonium fuel fabrication plant is coming up at Tarapur to meet our future requirement of plutonium fuels in PFBR-500 and thermal reactors. This plant is being designed and constructed in the philosophy of “secured automated fabrication (SAF)” through a carefully staged development from present glove box operations to semi-remote or remote operations placing emphasis on radiotoxic dust reduction and its containment. This development should ultimately result in systems that maximise personnel radiation protection, restrict and control access to plutonium, provide near real time accountability and improve the uniformity and quality of plutonium fuels.

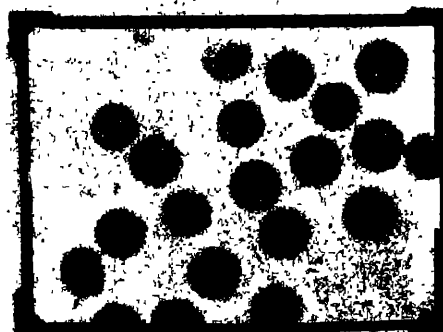
New fabrication flowsheets for plutonium bearing fuels amenable to automation and remotisation are being developed in Trombay. One of the promising process is the ‘gel-pelletisation route’ (Gilissen *et al* 1982) which uses gel derived microspheres rather than powder as feed material for pellet pressing. Because of the free flowing and dust-free nature of microspheres, the gel-pelletisation process is ideally suited for remote fabrication of the fuel pellets. In our preliminary experiments with gelled microspheres of  $(\text{UPu})\text{O}_2$ , high density sintered pellets have been prepared. Figure 33 shows the microstructure of such a pellet and figure 34 shows the alpha autoradiograph.

The  $\text{ThO}_2$ – $\text{PuO}_2$  (up to maximum of 5%  $\text{PuO}_2$ ) is a promising fuel for our thorium based PHWR (Ganguly and Roy 1982). If due to technological or political reasons recycling of plutonium is delayed in our LMFBR, such fuels could be conveniently used in our existing PHWR without involving major resource investment and engineering modifications.

In conclusion it may be stated that plutonium technology is mostly classified in nature and detailed informations are not available in open literature. In spite of that we have succeeded in the harnessing of plutonium entirely with indigenous resources and



PHOTOMICROGRAPH Mag: 20X



AUTORADIOGRAPH Mag: 20X

Figures 33, 34. 33. Microstructure of  $\text{UO}_2$  pellet prepared by the gel pelletisation route ( $\times 90$ ). 34. Microstructure and alpha-autoradiograph of MOX structures.

without any foreign assistance. Only a vertical take off is needed and a few obstacles are to be overcome before this great gift of nature and our control over it bears the fruit of its present promise.

### Acknowledgement

Thanks are due to the Radiometallurgy Division as a whole, including the staff members of Post Irradiation Examination, Engineering Services, Oxide Fuels, Advanced Fuels, Quality Control and Inspection and Cladding and Welding Sections. In addition, the support from Fuel Reprocessing Division and Radiochemistry Division is acknowledged. The continuous encouragement received from the higher authorities is also gratefully acknowledged.

### References

- Coffinberry A S and Miner W N 1961 *The metal plutonium* (Chicago: University Press)
- Ellinger F G, Land C C and Miner W N 1962 *J. Nucl. Mater.* **5** 165
- Fareeduddin S, Garg R K, Gupta U C, Kantan S K, Rajendran R and Rao N K 1964 3rd Int. Conf. Peaceful use of atomic energy, IAEA, Vol. II p 345
- Ganguly C 1980 *Studies on preparation and sintering of mixed uranium plutonium monocarbide, mononitride and monocarbonitride*; Ph.D. Thesis, University of Calcutta.
- Ganguly C, Jain G C and Roy P R 1981 *Proc. of DAE Sym. on Nucl. Chemistry and Radiochemistry*
- Ganguly C and Roy P R 1981 *Proc. BNES Conf. on Fast Reactor Fuel Cycles*, London
- Ganguly C and Roy P R 1982 *Proc. Int. Sym. in Ceramics*, BHEL Bangalore
- Ganguly C, Roy P R and Seal A K 1980 *Trans. PMAI* **7** 40
- Ganguly C, Roy P R and Seal A K 1982 *Trans. IIM* Vol. 35 No. 2 p 148
- Ghosh J K, Roy P R and Moorthy V K 1973 *BARC/I-254*
- Gilissen R, Panwels H, Sleurs J and Smolders A 1982 *Trans. Am. Nucl. Soc.* **40** 26
- Gotzmann O and Hofmann P 1974 *Proc. of Int. Sym. on Fuel and Fuel Elements for Fast Reactor* IAEA p 233
- Hanna G C, Westcott C H, Lemmel H D, Leonard B R Jr., Story J S and Altree P M 1969 *Atomic Energy Rev.* **7** p. 3
- Hansen L P and Clayton R D 1967 *Nucl. Appl.* **3** 484
- Housseau M 1974 *Proc. Sym. on fuel and fuel element for fast reactors*, IAEA p 277
- Internal Report prepared on FBTR mixed oxide fuel by DAE, India and CEA, France (Sept. 1970)
- Internal Report of DAE working group on mixed uranium plutonium carbide fuels for FBTR (1980)
- Janardhanan S, Krishnamurthi T N, Dabhadkar S B and Soman S D 1973 *BARC/I-259*
- Kanij J B W, Noothont A J and Votock I 1974 IAEA-161 p 185, Vienna
- Mahajan V K, Ganguly C, Ramakumar M S, Roy P R and Moorthy V K 1972 *BARC-629*
- Majumdar S, Arunkumar, Kamath H S, Ramachandran R, Purushotham D S C and Roy P R 1984 *BARC-1182*
- Majumdar S, Purushotham D S C and Roy P R 1982 *BARC/I-730*
- Potter P E 1975 *Plutonium and other actinides* p 211
- Prasad G J, Ganguly C and Roy P R 1976 *BARC/I-423*
- Recommendation of the ICRP-Suppl. 6, 1955 *Br. J. Radiol.*
- Ramachandran R, Arunkumar, Purushotham D S C and Roy P R 1981 *Trans. PMAI* **8** 277
- Rao N K 1982 *Proc. Sym. Int. Conf. on Nucl. Power Experience* IAEA, Vienna
- Roy P R 1962 *AEET/Radiochem.* **22**
- Roy P R 1964 *J. Nucl. Mater.* **11** 59
- Roy P R 1975 *Proc. IAEA group meeting on facilities and techniques for (UPu)<sub>2</sub> fuel fabrication*, Mol, Belgium
- Roy P R 1978 *Proc. Seminar on Nucl. Metallurgy*, IIM Bombay
- Roy P R, Deshpande R G and Laxminarayanan T S 1967 *BARC-294*
- Roy P R, Laxminarayanan T S, Singh R K and Haraprakash A 1969 *BARC/I-37*

Roy P R and Mahajan V K 1975 *Proc. IWSA-BARC Winter School*, Bombay

Roy P R, Purushotham D S C, Majumdar S, Ramachandran R, Kamath H S, Ghosh J K and Goswami G L *et al* 1984 BARC-1203

Sah D N, Sahoo K C, Chatterjee S, Majumdar S, Kamath H S, Ramachandran R, Bahl J K, Purushotham D S C, Ramakumar M S, Sivaramakrishnan K S and Roy P R 1977 BARC-918

Seaborg G T 1958 *The transuranium elements* (Massachusetts, USA: Addison-Wesley Publishing Co.)

Sengupta A K, Ganguly C and Roy P R 1982 BARC/I-740

Sheth A and Leibonitz L 1974 ANL-AFP-3

Singh B, Bhoje S B, John T M, Lee S M, Singh R S and Paranjpe S R 1981 *Proc. BNES Conf. on Fast Reactor Fuel Cycles*, London

Sood D D and Vaidya V N 1979 *Proc. Sym. on Sintering and Sintered Products*, BARC, Bombay

Stoller S M and Richards R B 1961 *Reactor Handbook* (New York: Interscience Publishers) 2 454

Storms E K and Ackermann R J 1974 *Proc. of IAEA Panel Meeting on U-Pu-C System*, Grenoble, France

Wade W Z and Wolf T 1969 *J. Nucl. Sci. Technol.* 6 402

Wick O J 1980 *Plutonium handbook* (La-Cränge Park, Illinois: American Nuclear Society)

Zachariasen W H and Ellinger F H 1959 *Acta Crystallogr.* 12 175

## Internal friction in hexagonal metals

M K ASUNDI and C N RAO

Physical Metallurgy Division, Bhabha Atomic Research Centre, Trombay, Bombay 400 085, India

**Abstract.** An overview of the studies of internal friction in hexagonal metals and alloys is presented. An outline of the experimental techniques of measurement and the atomistic mechanisms causing internal friction is also given.

**Keywords.** Anelasticity; internal friction; hexagonal metals.

### 1. Introduction

All materials possess the intrinsic ability to dissipate mechanical energy by some internal atomistic or microscopic processes. This property is called *internal friction* or damping capacity. Internal friction is mainly observed in systems undergoing periodic vibrations and its magnitude can be determined by the decay of free vibrations or of travelling waves in a test piece. In recent times, internal friction has become an important tool for investigating the atomistic processes in solids. One of the best known examples is the internal relaxation due to the diffusion of interstitial solutes in a bcc solid which can be conveniently studied by low cycle torsion pendulum measurements.

This paper gives a brief account of the various measures of internal friction, the experimental techniques of measurement and the mechanisms for internal friction followed by an overview of the studies on hexagonal materials. The results on zirconium and titanium alloys are given in greater detail due to the extensive studies made on these materials.

### 2. Relaxation and internal friction

A measure of the damping capacity is the quantity  $\Delta W/W$  where  $\Delta W$  is the energy loss per cycle and  $W$  is the total vibrational energy. It is given by the integral  $\int \sigma d\epsilon$  over one cycle where  $\sigma$  is the applied stress and  $\epsilon$  is the resulting strain. For an ideal elastic body, there will be no dissipation of energy and the integral vanishes. When there is internal dissipation, stress and strain are no longer in phase with each other and the dissipation can be due to static or dynamic hysteresis (figure 1). For static hysteresis (figure 1a) part of the strain is irreversible and the internal friction will generally be independent of the frequency of vibrations, but will be strongly dependent on the amplitude of vibrations.

For dynamic hysteresis (figure 1b) relaxation occurs over a finite time by internal rearrangements in the material and depends on the rate of change of  $\sigma$  and  $\epsilon$ . Such a behaviour is called *anelastic*, a term introduced by Zener (1948). For small amplitude of



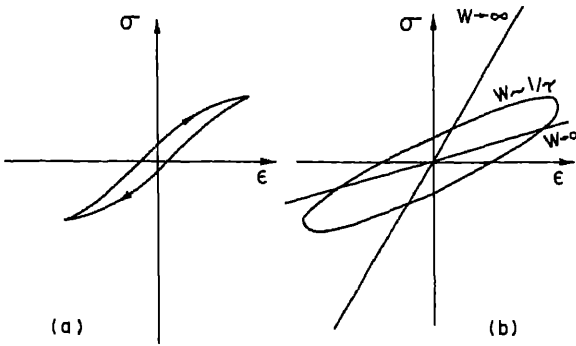


Figure 1. Schematic representation of mechanical hysteresis (a) static hysteresis (b) dynamic hysteresis.

the vibrations, the relation between  $\sigma$ ,  $\epsilon$  and their time derivatives is linear and the damping will be independent of amplitude but strongly dependent on the frequency of vibration. At very high frequencies, there is little time for the relaxations to take place and no energy loss will be obtained. At very low frequencies, complete relaxation occurs and the behaviour of the system is purely elastic with a smaller relaxed value of the elastic modulus. At some intermediate frequency  $\omega$  (of the order of  $1/\tau$  where  $\tau$  is the relaxation time for the internal rearrangement) a maximum in internal friction will occur.

The various parameters used for quantitative specification of damping are dimensionless ratios which are independent of the size of the sample and the nature of the experimental system when the damping is independent of the amplitude of vibration.

2.1 The logarithmic decrement  $\delta$

The damping of a system freely vibrating in a single mode can be expressed in terms of the rate of decay of the vibration amplitude. The logarithmic decrement is given by

$$\delta = \frac{1}{n} \ln (A_0/A_n), \tag{1}$$

where  $A_0$  and  $A_n$  are the amplitudes before and after  $n$  cycles of vibration.

2.2  $Q^{-1}$  value

For a system undergoing forced vibrations, the amplitude magnification factor  $Q$  at resonance and the relative width  $\Delta\omega/\omega_r$  of the resonance (where  $\omega_r$  is the resonance frequency) depend solely on the damping of the system. For the resonance width at half maximum they are related as

$$Q^{-1} = \Delta\omega/\omega_r, \tag{2}$$

and provide a direct measure of the damping.

2.3 Specific damping capacity,  $P$

If  $W$  is the total energy of the oscillating system at the commencement of a cycle and  $\Delta W$  the energy dissipated in the cycle, the specific damping capacity is defined as

$$P = \Delta W/W. \tag{3}$$

### 2.4 Tangent of the phase angle

In the case of linear damping, an applied sinusoidal force  $f_0 \sin \omega t$  produces a displacement  $x_0 \sin(\omega t - \phi)$ , where  $\phi$  is the phase lag between the applied force and displacement. The ratio of the components of strain out-of-phase and in-phase with the stress given by  $\tan \phi$  can be used as a measure of the damping.

For small damping values, the different quantities defined above are approximately related to each other as

$$\delta/\pi = Q^{-1} = P/2\pi = \tan \phi. \quad (4)$$

### 3. Experimental methods of measurement

When considering a relaxation effect, four quantities are of interest; (i) the relaxation strength, which determines the peak height; (ii) the relaxation time which determines the peak position on the temperature scale; (iii) the shape of the peak which can be characterized in terms of the width at half maximum; and (iv) the modulus defect which causes a variation of the resonance frequency of the specimen in the temperature range of the damping peak.

Over the years, a variety of equipment have been built in various laboratories to measure internal friction. According to the method by which stresses are generated in the specimen, the techniques can be divided into resonance methods, pulse-echo methods and mechanical after-effect methods. Whereas the pulse-echo technique is restricted to high frequencies (over 1 MHz) and the after-effect method to very long relaxation times (over 10 sec), the resonance methods are useful in the range of low to medium frequencies (0.01 Hz to 100 kHz). In a given type of experimental system one is usually restricted to a limited number of operating frequencies and hence to observe a relaxation process one has to vary the temperature. Thus, practically all the instruments described in the literature provide for measurements over a range of temperature.

A comprehensive description of the experimental methods can be found in the books by Nowick and Berry (1972) and De Batist (1972).

### 4. Mechanisms of internal friction

A number of atomistic and microscopic mechanisms can contribute to energy dissipation in solids. Some of these are: (a) stress-induced ordering of interstitial and substitutional atoms, commonly known as Snoek and Zener relaxations (Snoek 1941; Zener 1947), (b) grain boundary viscosity (Kê 1949), (c) thermoelastic damping (Waterman 1958), (d) dislocation damping (Read 1940), (e) magnetic damping in ferromagnetic materials (Cochardt 1959) and (f) electronic damping at low temperatures (Bommel 1954).

Covering the various aspects of relaxation processes and experimental results, extensive reviews have been published by Zener (1948), Nowick and Berry (1972), Nowick (1953), Entwistle (1962), De Batist (1972), Berry (1962), Mason (1966), Niblet and Wilks (1960), Wilks (1965), Burdett and Queen (1970), Fantozzi and Ritchie (1981) and Lucke and Granato (1957).

A brief account of the relaxations ascribed to point defects, dislocations and grain boundaries is given below:

#### 4.1 Internal friction due to point defects

Point defects produce anelastic behaviour through a process known as stress-induced ordering, in which the equilibrium configuration of a collection of defects in the crystal changes with time to a new state under applied stress. When the stress is removed, the change is reversed and with time the original state of order is restored. The occurrence of stress-induced ordering for point defects depends mainly on the ability of an applied stress to change the free energy associated with the presence of a defect in the crystal. If defects are present in several crystallographically equivalent positions whose free energies can be split by an external stress, a redistribution of the defects among these states will re-establish equilibrium. Only those defects which produce local strains having a lower symmetry than that of the lattice are capable of producing relaxation under shear. Such defects are called *asymmetric defects* or *elastic dipoles*.

An outstanding example of anelasticity produced by an elementary point defect acting as an elastic dipole is provided by the Snoek relaxation, first observed in  $\alpha$ -Fe containing small amounts of C or N (Snoek 1941, 1942). The Snoek effect has since been observed in a number of other bcc transition metals containing impurity atoms (like C, N, O, H) in interstitial positions of the lattice. The Snoek peaks due to O, C and N in niobium are shown in figure 2 (Hoffman and Wert 1966).

In  $\alpha$ -Fe, the carbon atoms occupy the octahedral sites of the type  $[1/2, 0, 0]$  (figure 3). The interstitial atom is an elastic dipole of  $\langle 100 \rangle$  tetragonal symmetry, which will cause stress induced ordering. The direction of the tetragonal dipole axis may lie along any one of the crystal cube axes X, Y, Z depending on the particular site which the interstitial atom occupies. Sites which produce the tetragonal axis along the X direction have been labelled X in the figure (Similarly Y and Z sites). When an interstitial impurity makes thermally-activated jumps between neighbouring sites, which are  $a/2$  apart, the dipole axis re-orientes by  $90^\circ$  with each jump. Thus, the relaxation rate is related in a simple way to the mean jump rate of the interstitial atoms.

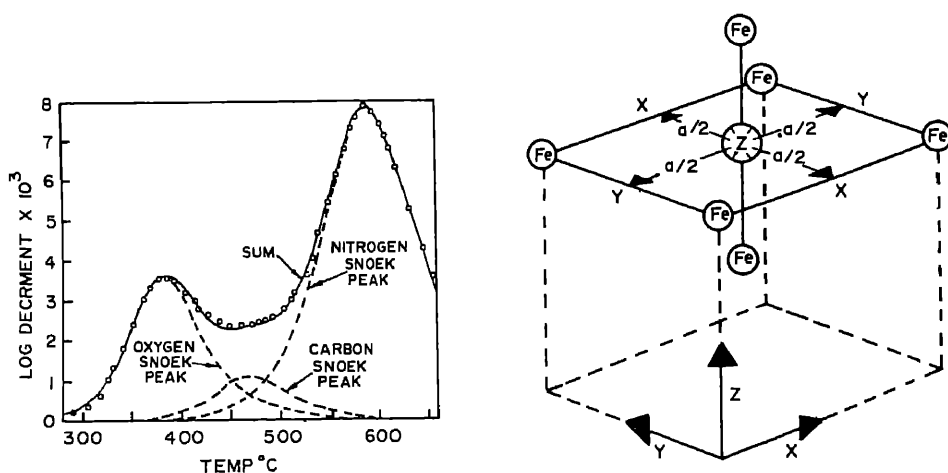


Figure 2. Snoek peaks in a  $\langle 100 \rangle$  crystal of niobium tested in longitudinal vibration at 80 kHz.

Figure 3. Solute atom (shaded) in an interstitial octahedral site of bcc Fe.

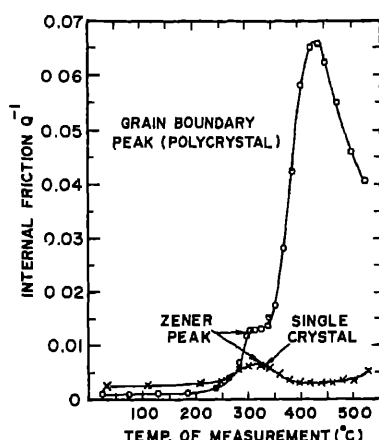


Figure 4. Zener peak in polycrystalline and single crystal specimens of  $\alpha$ -brass (torsional vibration at 0.5 Hz).

Another important kind of point defect process, ascribed to stress-induced reorientation of solute pairs, is the Zener relaxation, first observed by Zener (1943) in a single crystal of 70–30  $\alpha$ -brass. Since then, similar relaxation peaks have been found in a number of binary (and other complex) alloys with fcc, bcc and hcp crystal structures. According to the pair reorientation theory of Zener (1947) asymmetric distortions can be expected around two adjacent solute atoms *i.e.* around a nearest neighbour pair. This enables splitting of free energies of differently oriented pairs by an applied stress. Figure 4 gives the Zener peak observed in  $\alpha$ -brass.

In addition to the solute-solute (*S-S*) defect pair, interaction of substitutional-interstitial (*S-I*) pairs, and *I-I* pairs may lead to internal friction peaks (see for example Nowick and Berry 1972).

#### 4.2 Relaxation involving dislocations

A variety of relaxation peaks occur at temperatures, usually below room temperature, after plastic deformation. They are considered to be caused by the movement and interaction of dislocations with point defects.

In the vibrating-string model (Granato and Lucke 1956) the dislocation line is considered to behave like an elastic string fixed at two points in the lattice, restricted to move in two dimensions in the glide plane. A number of anelastic effects can be deduced from the model. One important result is that the anelastic properties of dislocations should be strongly frequency dependent. Changing the resonance frequency of dislocations by decreasing the free length of the vibrating string (introducing additional pinning centres by irradiation) affords an effective method of checking the results of the dislocation damping theory and to study the production and recovery of defects.

By considering the movement of the dislocation string in a periodic lattice potential—the Peierls potential—additional relaxation effects due to anelastic motion of segments of the dislocation line are predicted.

Dislocation motion described by means of kink diffusion (Brailsford 1961) along dislocation lines can also be used to explain dislocation damping caused by resonance effects as well as relaxation effects.

The trapping of point defects in the stress field of a dislocation will have a profound effect on dislocation damping through variation in free dislocation length. A number of relaxation peaks observed in plastically deformed metals have been attributed to the interaction and motion of point defects and dislocations. The amplitude dependence of dislocation damping can be explained qualitatively in terms of dislocations anchored by point defects.

The Bordoni peak, first observed at low temperatures for deformed copper, has been studied in a number of metals. A second (Niblett-Wilks) peak associated with the Bordoni peak occurs at a lower temperature and is usually much smaller than the main peak (Niblett and Wilks 1956). A series of three peaks has been observed in deformed metals in the range between room temperature and the low temperature Bordoni peaks (Hasiguti *et al* 1962).

### 4.3 Boundary relaxation processes

Grain boundaries, domain boundaries and semi-coherent and incoherent interface boundaries between phases can result in relaxation effects giving an internal friction maximum when the boundary movement corresponds to the frequency of the applied stress field. Such effects will be observed at low frequencies and relatively high temperatures. The grain boundary peak in aluminium is shown in figure 5.

## 5. Internal friction studies in hexagonal metals

### 5.1 Relaxation effects in hcp metals

In the hexagonal close-packed structure, there are two possible locations for an interstitial (figure 6). The volume associated with the octahedral site is larger than that of the tetrahedral site and hence larger atoms like O, C and N are expected to occupy the octahedral sites. Both the sites have trigonal symmetry, the same as that of the host lattice, and hence single interstitials are not expected to cause anelastic effects, unless there is an interaction between the two kinds of interstitials forming an *I-I* pair (Povolo

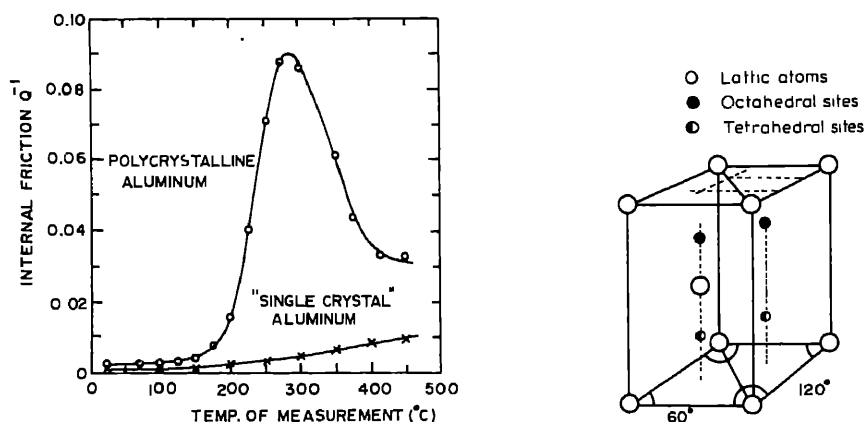


Figure 5. Grain boundary peak in polycrystalline aluminium (Torsional vibration at 0.8 Hz).

Figure 6. Interstitial positions in the hexagonal close packed lattice.

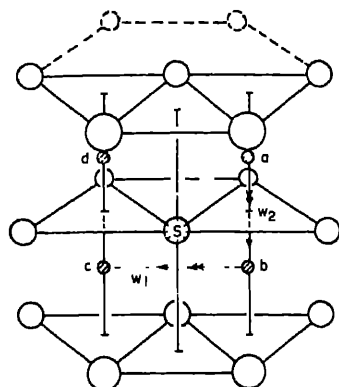


Figure 7. The two types of interstitial jumps producing reorientation of a nearest neighbour *I-S* pair in the hcp structure.  $W_1$  is the jump rate parallel to the basal plane and  $W_2$  is perpendicular to the basal plane.

and Bisogni 1967). This will be possible for small atoms like H which may occupy octahedral as well as tetrahedral sites. In terms of the jump probabilities  $W_1$  for the transition from tetrahedral to octahedral site and  $W_2$  for the reverse jump, the relaxation time  $\tau$  is given by

$$\tau^{-1} = W_1 + W_2. \quad (5)$$

Relaxation due to interstitial-substitutional (*I-S*) pair in hexagonal crystals has been discussed by Nowick (1967). The nearest neighbour pairs lie in (100) type planes and the (*I-S*) defect is of the  $\langle 100 \rangle$  monoclinic type and two kinds of jumps are possible during the relaxation (figure 7). In terms of the probability  $W_1$  for a jump normal to the basal plane and  $W_2$  for a jump within the basal plane, the two relaxation times are given by

$$\begin{aligned} \tau_1^{-1} &= 3W_2 + 2W_1, \\ \tau_2^{-1} &= 3W_2. \end{aligned} \quad (2)$$

In addition to the relaxations due to point defect interactions, relaxation effects can also occur due to dislocations and semi-coherent or incoherent interface boundaries.

## 5.2 Relaxations associated with interstitials

**5.2a *I-I* interactions:** Relaxation peaks due to hydrogen interstitial pair have been observed by Koster *et al* (1956) in Ti, by Bungardt and Preisendanz (1960) in Zr and by Hasiguti *et al* (1965) in zircaloy-2. Miller and Browne (1970) and Browne (1972) reported a relaxation peak due to oxygen interstitial pair in Ti, Zr and Hf. For *I-I* interaction the relaxation strength should be proportional to the number of such pairs and hence to the square of the interstitial content. Miller and Browne (1970) reported such behaviour for both Ti-O and Ti-C alloys. However, investigations by others (Misra and Asundi 1972a, b; Povolito and Bisogni 1967) failed to identify the *I-I* peak in zirconium and titanium. Interstitials were observed to give rise to relaxation only in conjunction with a substitutional atom.

**5.2b *I-S* pair relaxations:** Interstitial relaxation in hcp metals involving *I-S* pairs was first reported by Pratt *et al* (1954) for Ti containing oxygen. Similar results were reported by Gupta and Weinig (1962) and Bratina (1962). The height of the *I-S* peak was a linear function of the oxygen content, and was related to the size of the substitutional atom.

Bisogni *et al* (1964) measured the relaxation of oxygen and nitrogen in polycrystalline hafnium containing zirconium as substitutional element. Miller (1962) reported an oxygen peak in 'iodide pure' titanium, but the result could be due to the presence of traces of substitutional atoms. Misra and Asundi (1970, 1972) made extensive study of the internal friction due to oxygen and nitrogen in Ti and Zr with a variety of substitutional atoms having different size factors. In zirconium for all the alloying elements, oxygen gave two peaks, the relaxation strength depending on the concentration of oxygen. At low oxygen concentrations, the high temperature peak was more prominent and was ascribed due to three oxygen atom jumps. At high oxygen concentrations, the low temperature peak was more prominent and was due to a single oxygen jump. In nitrogen, only those substitutional elements with atomic size larger than that of zirconium gave internal friction peaks similar to those for oxygen. In titanium, *S-I* relaxation peaks were studied for various interstitials like C, O and N.

Using the torsion pendulum technique in the frequency range 0.5 to 1.5 Hz and the temperature range  $-190^{\circ}\text{C}$  to  $800^{\circ}\text{C}$ , Misra (1976) presented extensive results on a series of Zr and Ti base dilute alloys.

**5.2c *I-V* pair interactions:** In materials with low temperature irradiation damage interstitial-vacancy pairs may cause relaxation effects. Moser *et al* (1973) have studied *I-V* pair interaction in neutron irradiated bcc, hcp and fcc metals. The influence of oxygen and  $\gamma$ -irradiation on the elastic modulus and internal friction of iodide pure zirconium has been reported by Federov *et al* (1971). It has been shown that stable oxygen-vacancy aggregates of various complexities may exist even after annealing. Three relaxation processes associated with oxygen-vacancy complexes are reported in quenched or irradiated zirconium samples.

### 5.3 Boundary relaxations

There are a number of results in the literature pertaining to twin boundary and grain boundary relaxations. Reed-Hill and Dahlberg (1966) studied the elastic after-effect in iodide pure zirconium prestrained at  $77^{\circ}\text{K}$ . At a prestrain of less than 1%, the microstructure indicated  $\{11\bar{2}1\}$  twins. It is very likely that the twin boundaries move easily under load. The activation energy obtained in their study (22.7 kcal/mol) has been interpreted as that for slip ahead of the twin interface.

Studies of internal friction associated with grain boundaries in Ti and Zr were reported by Pratt *et al* (1954), Bratina and Winegard (1956), Bungardt *et al* (1962) and Misra and Asundi (1972a). Bungardt *et al* (1962) observed well-developed peaks around  $600^{\circ}\text{C}$  at 1 Hz, whose magnitude changes with grain size.

Bedford *et al* (1972) in their studies on zirconium having different cell structures found an increase in the damping for finer cell structure similar to that observed for grain boundary relaxations for fine grain structure. The high background damping in deformed zirconium is attributed to relaxation of dislocation cell walls. On recovery, dislocation rearrangement results in polygonized sub boundaries and lowering of the damping at higher temperatures.

### 5.4 Dislocation relaxations

The behaviour of dislocations in hexagonal crystals is highly anisotropic because of the limited number of slip systems that can operate in the structure. Consequently, strong

orientation dependence of dislocation damping effects is to be expected in single crystal experiments.

The Bordoni peak in Zr and Ti is generally much smaller than the corresponding peak for fcc metals, probably due to the presence of interstitial impurities. Gruzin and Semenikhin (1963) studied the low temperature damping (Bordoni peak) in high purity zirconium which had been deformed to various amounts using a flexural vibration technique. The effect of alloying as well as fast neutron irradiation on the stability of the peak was studied. Doherty and Gibbons (1971) studied the Bordoni peaks in zirconium using a composite resonator technique in the frequency range of 100 to 150 kHz and found an additional peak towards the low temperature range for a sample cold worked by 38% reduction in cross-section. Under the application of hydrostatic pressure, both the peaks were observed to increase in height. Fonquet *et al* (1970) studied Zr and Zr base alloys at a frequency of 13 kHz.

Hasiguti (1953) found that there exists an internal friction peak above the temperature of the Bordoni peak in cold worked metals. This type of peak known as the Hasiguti peak has been reported in Ti, Zr, Mg (Hasiguti *et al* 1962) and beryllium (Abrams *et al* 1966). The Hasiguti peak is usually small and has higher activation energy than the Bordoni peak and is caused by dislocation relaxation. Yukiti and Hasiguti (1972) reviewed the basic mechanism of thermally-activated unpinning of dislocations resulting in the Hasiguti peak and deduced that the peak temperature shifts with stress amplitude.

The most extensive study on single crystals was carried out by Tusi and Sack (1967). Internal friction studies and electron microscopic observations were carried out on Mg single crystals. Figure 8 shows the results for magnesium single crystals after 0.5% compression. ( $\theta$  is the angle between the crystal axis and the hexagonal axis). A broad peak at around 200°K was observed in 2–40 kHz range. From the orientation dependence, it is inferred that dislocation motion in the basal plane is involved in the relaxation process. The peak height increased with deformation and attained a maximum by 2.5% deformation by compression. The peak height was quite sensitive to the presence of impurities. About 1% Li completely suppress it, whereas Fe and Ni prevent the peak from disappearing even in annealed samples. A small peak at about 20°K was noticed in cold worked polycrystals and highly deformed single crystals, presumably due to grain boundary or twin boundary relaxations.

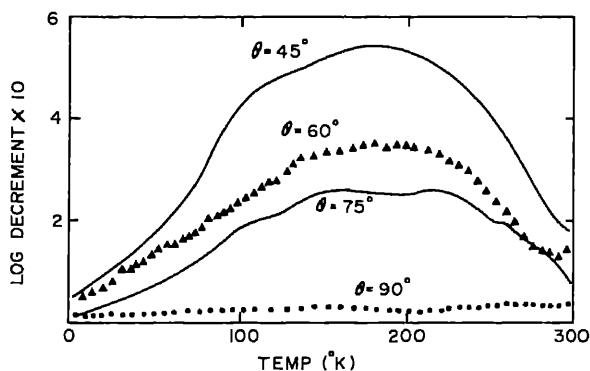


Figure 8. Internal friction of single crystals of magnesium of different orientations after 0.5% compression.



Amplitude-dependent internal friction in Mg single crystals has been studied by Roberts (1968) in the temperature range of 80–320°K at frequencies 0.015 to 0.75 Hz. Very broad peaks were observed indicating the possibility of a large number of relaxation processes occurring together. The results are interpreted in terms of thermally activated dislocation-dislocation interactions. (Roberts and Hartman 1963; Alefeld 1962).

Esnouf and Fantozzi (1981) observed a strong internal friction peak at about half the melting temperature in high purity polycrystalline Mg. The position of the peak was dependent on strain amplitude. The results are explained in terms of dislocation glide controlled by jog climbing and diffusion of vacancies along dislocations. Atrens (1974) studied the interaction of oxygen as pinning points for dislocations in zirconium. In deformed and annealed zirconium, Ritchie and Sprungmann (1981) observed three internal friction peaks in the temperature range of 480 to 600°C and interpreted them in terms of dislocation core diffusion and unpinning of dislocations.

## 6. Conclusion

Compared to bcc and fcc metals, the experimental studies on hexagonal metals are fewer and various aspects are to be investigated in detail for a better understanding of the relaxation processes in hexagonal metals. Many of the results were obtained on polycrystalline materials in the form of wires or rods and hence subject to pronounced texture effects. Single crystal studies are desirable for elucidating the orientation effects on dislocation interactions. Such results would be of considerable value in understanding the point defect and dislocation interactions in hcp metals.

## References

- Abrams E H, Kamber K T and Ang C Y 1966 *Acta. Metall.* **14** 729
- Alefeld G 1962 *Z. Phys.* **170** 249
- Atrens A 1974 *Scr. Metall.* **8** 401
- Bedford A J, Fuller P G and Miller D R 1972 *J. Nucl. Mater.* **43** 164
- Berry B S 1962 *Acta Metall.* **10** 271
- Bisogni E, Mat G and Wert C 1964 *J. Less Common Metals* **7** 197
- Brailsford A D 1961 *Phys. Rev.* **122** 778
- Bratina W J 1962 *Acta Metall.* **10** 332
- Bratina W J and Winegard W C 1956 *Trans. AIME* **206** 186
- Bommel H E 1954 *Phys. Rev.* **96** 220
- Browne K M 1972 *Acta Metall.* **20** 507
- Bungardt K and Preisendanz H 1960 *Z. Metall.* **51** 280
- Bungardt, Preisendanz H and Horn E 1956 *Z. Metall.* **53** 495
- Burdett C F and Queen T J 1970 *Metall. Rev.* **143** 47
- Cochardt A 1959 in *Magnetic properties of metals and alloys* (ed) R M Bozorth, (Cleveland, Ohio: Am., Soc. Metals) 251
- De Batist R 1972 *Internal friction of structural defects in crystalline solids* (Amsterdam: North-Holland Publishing Company)
- De Fouquet J, Boch P, Petit J and Hisu G 1970 *J. Phys. Chem. Solids* **31** 1901
- Doherty J E and Gibbons D F 1971 *J. Appl. Phys.* **42**
- Entwistle K M 1962 *Metall. Rev.* **7** 175
- Esnouf C and Fantozzi G 1981 *J. Phys. Colloq (France)* **42** C-5 445
- Fantozzi G and Ritchie I G 1981 *J. Phys. Colloq. (France)* **42** C-5 3
- Fedorov G B, Kissil A Ye and Festisov G V 1971 *Fiz. Met. Metalloved* **32** 621

- Granato A V and Lucke K 1956 *J. Appl. Phys.* **27** 583, 789
- Gruzin P L and Semenikhin A N 1963 *Fiz. Met. Metalloved* **15** 791
- Gupta D and Weinig S 1962 *Acta Metall.* **10** 292
- Hasiguti R R 1953 *Proc. Int. Conf. Theor. Phys., Kyoto and Tokyo* 577
- Hasiguti R R, Igata N and Kamoshita G 1962 *Acta Metall.* **10** 442
- Hasiguti R R, Igata N, Tonomae R, Nakumara Y, Saso S and Domato K 1965 *Symp. Nondestructive testing in nuclear technology*, Bucharest
- Hoffman R A and Wert C 1966 *J. Appl. Phys.* **37** 237
- Ke T S 1949 *J. Appl. Phys.* **20** 274
- Koster W, Bangert L and Evers M 1956 *Z. Metall.* **47** 567
- Lucke K and Granato A V 1957 in *Dislocations and mechanical properties of metals* (ed) J Fischer, (New York: Wiley)
- Mason W P (ed) 1966 *Physical acoustics* (New York: Academic Press) Vol III
- Miller D 1962 *Trans. Met. Soc. AIME* **224** 275
- Miller D and Browne K M 1970 *The science technology and applications of titanium* (London: Pergamon) 401
- Misra S 1976 *Anelastic and internal friction behaviour of zirconium and titanium and their alloys* Ph.D Thesis, The Banaras Hindu University.
- Misra S and Asundi M K 1970 *Trans. Indian Inst. Metals* **23** 73 1972a *Can. Met. Q.* **11** 69
- Misra S and Asundi M K 1972b *Titanium science and technology* (ed) R I Jaffe and H M Burte (New York: Plenum Press)
- Moser P, Verdore J, Chambron W, Nivert V and Pichon R 1973 *5th Int. Conf. Internal Friction and Ultrasonic Attenuation in Crystalline Solids*, Aachen
- Niblet D H and Wilks J 1956 *Philos Mag* **1** 415
- Niblet D H and Wilks J 1960 *Adv. Phys.* **9** 1
- Nowick A S 1953 *Prog. Metal Phys.* **4** 1
- Nowick A S 1967 *Adv. Phys.* **16** 1
- Nowick A S and Berry B S 1972 *Anelastic relaxation in crystalline solids* (New York: Academic Press)
- Povolo F and Bisogni E A 1967 *Acta Metall.* **15** 701
- Pratt J N, Bratina W J and Chalmers B 1954 *Acta Metall.* **2** 203
- Read T A 1940 *Phys. Rev.* **58** 371
- Reed-Hill R E and Dahlberg K P 1966 *J. Elec. Chem. Technol* **4** 303
- Ritchie I G and Sprungmann K W 1981 *J. Phys. Colloq (France)* **42** C-5 427
- Roberts J M 1968 *Trans. Jpn Inst. Metals* **9** 69
- Roberts J M and Hartmann D E 1963 *J. Phys. Soc. Jpn* **18** 119
- Snoek J L 1941 *Physica* **8** 711
- Snoek J L 1942 *Physica* **9** 862
- Tusi R T C and Sack H S 1967 *Acta Metall.* **15** 1715
- Waterman P C 1958 *J. Appl. Phys.* **29** 1190
- Wilks J 1965 *Brit. J. Appl. Phys.* **16** 587
- Yukuti R and Hasiguti R R 1972 *J. Less Common Metals* **28** 249
- Zener C 1943 *Trans. AIME* **152** 122
- Zener C 1947 *Phys. Rev.* **71** 34
- Zener C 1948 *Elasticity and anelasticity of metals* (Chicago: University Press)

Figure 1 consists of two bar charts. The left chart, titled 'COVID-19 cases in 2020', shows the number of cases for various countries. The USA has the highest number of cases, followed by Spain, Italy, France, Germany, and the UK. The right chart, titled 'Dengue fever cases in 2020', shows the number of cases for various countries. The USA has the highest number of cases, followed by Brazil, India, and Mexico.



The figure consists of two side-by-side scatter plots. Both plots have 'Number of Children' on the x-axis and 'Number of Adults' on the y-axis. The left plot shows a positive linear trend with a regression line starting near the origin and sloping upwards. The right plot shows a negative linear trend with a regression line sloping downwards from the top-left towards the bottom-right.



## A novel method of RF powder sputtering

K SOLOMON HARSHAVARDHAN and K N KRISHNA

Materials Research Laboratory, Indian Institute of Science, Bangalore 560012, India

MS received 12 June 1984

**Abstract.** A new method of RF sputtering by which thin films of metals, semiconductors and insulators can be sputtered from their respective powders, has been successfully demonstrated. The films have been characterized for their surface and crystal structure using conventional methods of SEM and TEM. All the films are amorphous with a relatively smooth surface topography. The relative merits and demerits of the technique have been briefly discussed.

**Keywords.** RF sputtering; target; shield; Crookes dark space; amorphous films; scanning electron microscopy; transmission electron microscopy.

### 1. Introduction

Owing to their remarkable performance RF sputtering techniques have evolved as indispensable tools for vapour deposition of materials (Holland 1956; Chopra 1969; Jackson 1970; Maissel and Glang 1970). The technique offers manifold advantages over the other conventional methods such as thermal (resistive heating) and electron beam evaporation when a precise control over the film composition, thickness and adhesion is desired (Chopra 1969).

By definition, sputtering is the physical removal of the surface atoms of a solid target by the energetic particle bombardment and is caused by the momentum transfer of the incoming particles to the atoms near the surface layers of the solid. The ejected atoms can be deposited onto suitably placed substrates. Sputtering can be categorized into DC and RF sputtering. The former method is used effectively for sputtering of metal targets (Maissel and Glang 1970) but fails in insulating (dielectric) and semiconducting targets because of the build-up of a surface charge of positive ions on the insulator (or semiconductor) which prevents any further ion bombardment (Holland 1956; Chopra 1969). Applications of an RF field, in such cases, removes the inherent problems by providing swarms of secondary electrons from the plasma, which neutralize the positive space charge.

Targets used in conventional or commercial systems are fabricated in the form of discs and are secured to the target holders which are often water cooled. The targets are generally supported or suspended horizontally, fastened to the chamber top plate and electrically insulated from it. The substrates are kept below the target on a plate at a distance of  $\sim 8$  cm and can be maintained either at ground potential or at a negative bias. Fabrication of such targets involves long and cumbersome procedures primarily because of the geometrical constraints of the existing set-up in commercial instruments. Further, the amount of material and the cost involved in making such targets can be enormous, particularly when large area targets are desired. Hence, there is a definite

need to improve the geometrical set-up, so that the efficiency of the technique can be considerably enhanced. We have successfully solved this problem by redesigning the apparatus. The present paper reports this simple and versatile technique by which practically all types of materials can be sputtered as thin films, the material being taken in the form of compressed powders.

## **2. Conventional and redesigned RF sputtering**

Block diagrams of a conventional RF sputtering system with its important accessories and the redesigned (modified) apparatus are shown in figures 1a and b respectively. The sputtering system used (Materials Research Corporation, USA, Model SEM-8622) is provided with a 13.56 MHz RF generator capable of producing a maximum output power level of 1.5 kW. A capacitatively coupled tuning network is used for impedance matching between the generator and the load. Before each sputtering run, the system is evacuated ( $\sim 10^{-7}$  Torr) using standard high speed oil diffusion pumps (Varian Associates, USA). Sputtering was performed in an argon plasma at a constant pressure of  $2 \times 10^{-3}$  Torr. The pressure was controlled using a micrometer leak valve. High purity argon gas (99.999%, Indian Oxygen Limited) was used. During sputtering, liquid nitrogen was circulated in the cryo-trap to reduce contamination either from the backstreaming of vapours of diffusion pump oil or from the adsorbed gases inside the chamber.

Unlike in the conventional system (figure 1a), the cathode in the modified set-up (figure 1b) is at the bottom of the chamber and the substrates are kept on the top at a distance of  $\sim 8$  cm. The powdered form of the material to be sputtered is uniformly spread into a circular trough (0.5 mm depth and 50 mm dia.) machined out from a stainless steel plate. The target and the target holder are thus integrated into one single element. The powder is first compressed into the trough using a hydraulic press at loads of  $\sim 5000$ – $10000$  kg and the holder is then secured to the cathode which is watercooled.

The circular area surrounding the target (usually  $< 6$  mm in thickness) which does not glow during the sputtering process is called the Crookes dark space (Maissel and Glang 1970; Chopra 1969). When electrons leave the target and move under the influence of an RF field, they travel some distance before picking up energy from the field and making ionizing collisions with inert gas atoms. This distance is determined by the pressure of the gas. As a result there is no ionization in this region and hence no discharge in the immediate vicinity of the target. This fact has been exploited by us for placing a shield over the cathode (figure 1b). The shield has a central aperture, the area of the aperture being determined by the area from which sputtering from the target is desired. The crucial feature of the design is that, the shield is at the ground potential and the shield to target distance is less than the Crookes dark space. Further, the annulus in the shield must follow all the contours of the cathode-target combination such that at no point the distance between them exceeds the length of the Crookes dark space, at the working pressure of the sputtering gas. The target-to-shield distance should not be made very small so as to avoid loss of power to the target. The typical distance used was 4 mm at a working pressure of  $\sim 2 \times 10^{-3}$  Torr and the aperture diameter was  $\sim 50$  mm. It may be worthwhile to note that the plasma is confined in space in the shape of a truncated cone, with its smaller end fitting into the annulus in the shield (figure 1b). Further, for a fixed area of the aperture, the cone diameter at the minimum can be made

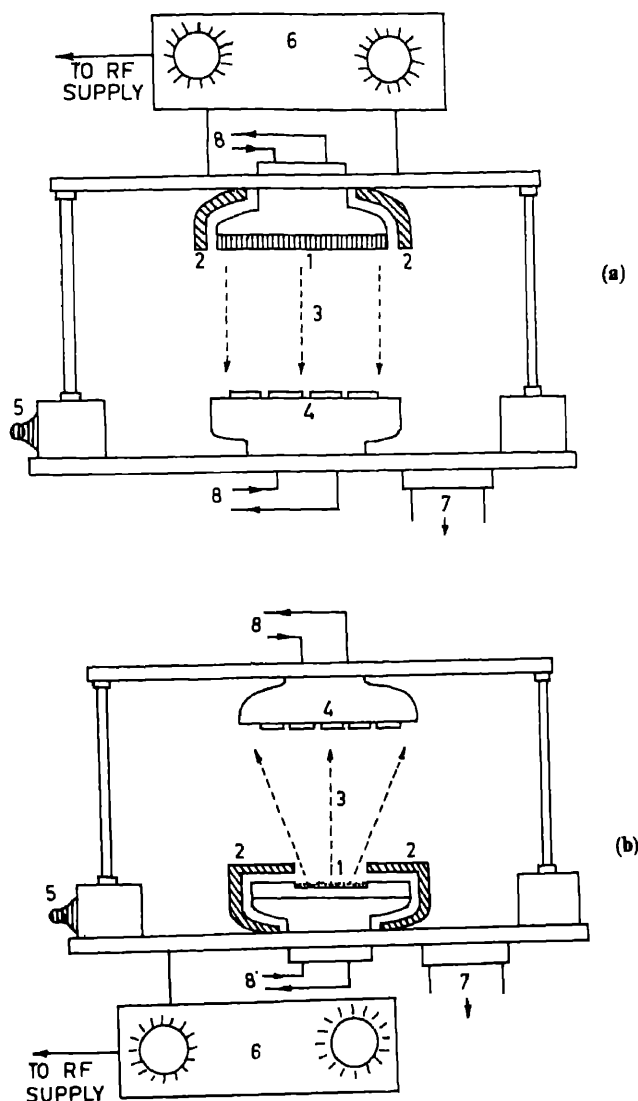


Figure 1. Block diagrams of the RF sputtering system with the important accessories  
 a. Conventional and b. Modified (1-target, 2-cathode shield, 3-plasma region, 4-anode (substrate holder), 5-argon gas inlet, 6-RF tuning network, 7-gasoutlet, 8-coolant water).

smaller by reducing the argon gas pressure. However, this flexibility is limited and beams approximately 20 mm less than the aperture diameter can be obtained.

### 3. Sputtering and characterization of films

This method which is essentially a powder sputtering method has been successfully used by us for depositing thin films of metals such as Cu and Al, semiconductors such as Ge, Se,  $\text{As}_2\text{Se}_3$  and insulators such as SiC. Typical RF power levels and other sputtering parameters used are listed in table 1.

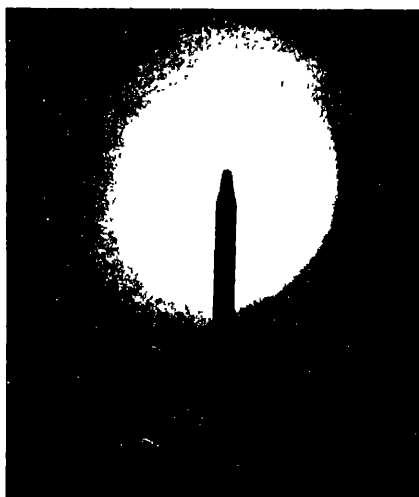
Table 1. Deposition parameters of various materials.

Material sputtered	RF power (W)	Target potential (V)	Sputtering pressure ( $\times 10^{-3}$ ) (Torr)	Nature of the films	
				Present work	Earlier Reports (References)
Cu	200	1000	2	Amorphous	Polycrystalline (Buckel 1959; Patten <i>et al</i> 1971; Segmuller 1973)
Al	325	700	2	Amorphous	Polycrystalline (Barna <i>et al</i> 1970; Bosnel and Thomas 1972; Tellier and Tosser 1977; Sherman 1977)
Ge	175	1200	2	Amorphous	Amorphous (de Neufville 1972; Kolomiets <i>et al</i> 1976; Tauc 1970)
Se	100	1200	2	Amorphous	Amorphous (Grigorovici 1969; Kolomiets <i>et al</i> 1976, Lucovsky 1967)
As <sub>2</sub> Se <sub>3</sub>	75	60	2	Amorphous	Amorphous (de Neufville 1972; Kolomiets <i>et al</i> 1976; Tauc 1970)
SiC	325	1800	10	Amorphous	Amorphous (Fritzsche 1973), Polycrystalline (Nishino <i>et al</i> 1977)

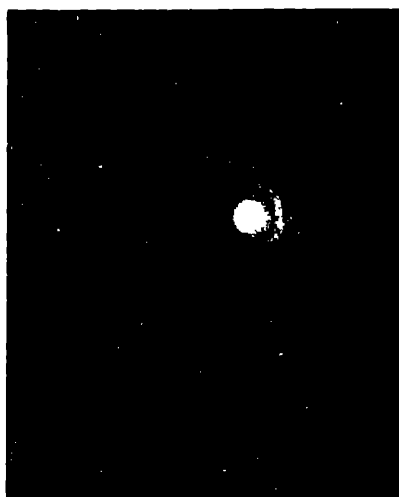
The powder sputtered films of various materials were characterized for their surface morphology and structures. The surface morphology, surface roughness and the topology of the gross microstructure were investigated (Cambridge Stereoscan-150 SEM). Prior to the analysis, the films were coated with a thin layer of sputtered gold (when non-conducting specimens were studied), to reduce the charging and blurring effects which lead to the loss of definition and resolution of the image particularly at higher magnifications. The surface of most of the films had no distinguishing features. The SEM for a typical case of As<sub>2</sub>Se<sub>3</sub> (figure 2) depicts a fairly smooth surface. Since

Figure 2. Scanning electron micrograph of As<sub>2</sub>Se<sub>3</sub> film ( $\times 1200$ ).Figure 3. Laue photographs of amorphous films of a. Al b. Cu c. Ge d. Se e. As<sub>2</sub>Se<sub>3</sub> f. SiC.

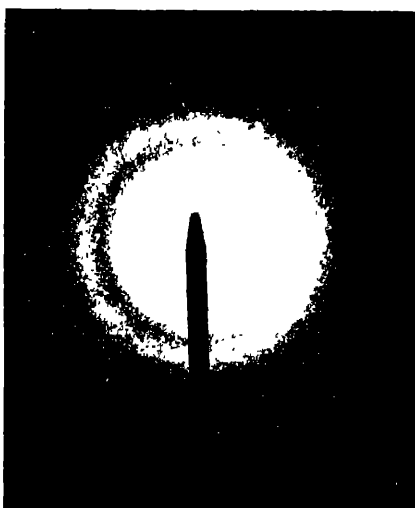
(a)



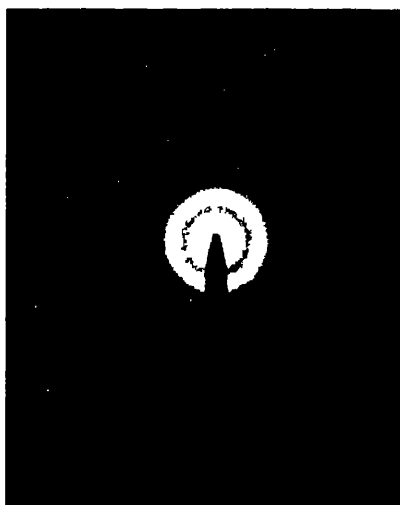
(b)



(c)



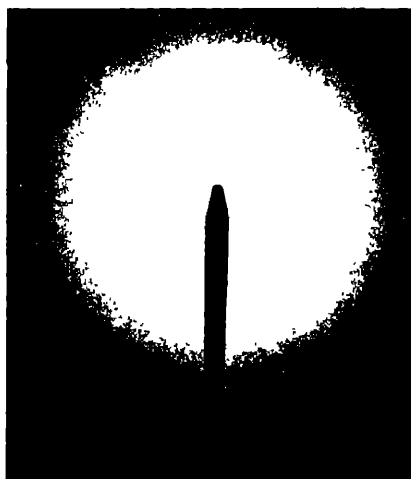
(d)



(e)



(f)





sputtering is a high temperature deposition process, the smooth surface structure can be attributed to high adatom mobility of the sputtered species, which agrees with earlier reports (Holland 1956; Chopra 1969; Maissel and Glang 1970).

Structures of these films were investigated using electron diffraction technique. Films of thickness 500–1000 Å were deposited onto freshly cleaved NaCl single crystals and floated in distilled water. Films were lifted onto 400 mesh copper grids. The grids were then transferred to the specimen holder of a Philips EM 301 electron microscope and examined. The diffraction patterns as well as the micrographs were recorded for all the films studied. Low beam conditions ( $\sim 10^{-6}$  A/cm<sup>2</sup>) were used for the semiconducting films to minimize the heating effects as well as the electron beam-induced structural changes. A striking feature of all the films studied has been that their diffraction patterns were featureless halos indicating that the films were all amorphous. Though our results for semiconducting films agree with similar results (Lucovsky *et al* 1967; Grigorovici 1969; Tauc 1970; de Neufville 1972; Kolomiets *et al* 1976), there are surprising differences in the case of sputtered metal films of Al and Cu, which were reported to give polycrystalline sputtered films (Buckel 1959; Patten *et al* 1971; Segmuller 1973; Barna *et al* 1970; Bosnel and Thomas 1972; Tellier and Tosser 1977; Sherman 1977) but were found to be amorphous in our studies. RF sputtered films of SiC have been reported to be both amorphous (Fritzsche 1973) like in the present case, and polycrystalline (Nishino *et al* 1977) depending on the sputtering conditions. Laue photographs of various films are shown in figures 3(a–f).

#### 4. Limitations and possible improvements of the set-up

We have noted that the present set-up offers several advantages over the conventional sputtering methods. However, there are a few disadvantages associated with the present design. (i) By employing the cathode shield with a central aperture, the area of sputtering has been controlled but the thickness uniformity has been adversely affected. This can be minimized by a proper choice of target to substrate distance and redesigning of the substrate holder. (ii) It may be reasonably argued that undesirable gases and impurities are entrapped in the target in the present design. But such effects have not been well understood and some of these aspects are being presently investigated.

#### 5. Conclusions

In the present study a simple and versatile technique for RF sputtering of thin films of metals, semiconductors and dielectrics has been described and its use has been successfully demonstrated. The method offers a cost effective means of sputtering of various materials particularly when commercial targets are not available.

#### Acknowledgements

The authors would like to thank Prof. C N R Rao for encouragement and Prof. K J Rao for helpful discussions.

## References

- Barna A, Barna P B, Pocza J F and Pozsgai I 1970 *Thin Solid Films* **5** 201
- Bosnell J and Thomas C B 1972 *Solid State Electron.* **15** 1261
- Buckel W 1959 *Proc. Int. Conf. on Structure and Properties of thin films* (eds) C A Neugebauer, J B Newkirk and D A Vermilyea (New York: John Wiley) p. 53
- Chopra K L 1969 *Thin Film Phenomena* (New York: McGraw Hill)
- de Neufville J P 1972 *J. Non-Cryst. Solids* **8-10** 85
- Fritzsche H 1973 *Electronic and structural properties of amorphous semiconductors* (eds) P G LeComber and J Mort (New York: Academic Press) p. 106
- Grigorovici R 1969 *J. Non-Cryst. Solids* **1** 303
- Holland L 1956 *Vacuum deposition of thin films* (Chapman and Hall) Chap. 14
- Jackson G N 1970 *Thin Solid Films* **5** 209
- Kolomiets B T, Lantrotova S S, Lyubin V M, Pukh V P and Tagirdzhanov M A 1976 *Sov. Phys. Solid State* **18** 866
- Lucovsky G, Mooradian A, Taylor W, Wright G B and Keezer R C 1967 *Solid State Commun.* **5** 133
- Maissel L I and Glang R 1970 *Handbook of thin film technology* (New York: McGraw Hill) Chap. 4
- Nishino S, Matsunami H, Odaka M and Tanaka T 1977 *Thin Solid Films* **40** L27
- Patten J W, McClanahan E D and Johnston J W 1971 *J. Appl. Phys.* **42** 4371
- Segmuller A 1973 *Thin Solid Films* **18** 287
- Sherman D 1977 *Thin Solid Films* **45** 537
- Tauc J 1970 *Optical properties of solids* (ed) F Abeles (Amsterdam: North Holland)
- Tellier C R and Tosser A J 1977 *Thin Solid Films* **43** 261



## Preparation and characterisation of $\beta''$ - $\text{Al}_2\text{O}_3$

H S KALSI, R P TANDON, BALBIR SINGH, R C GOEL and B K DAS

National Physical Laboratory, New Delhi 110012, India

MS received 6 August 1983; revised 6 April 1984

**Abstract.** Beta alumina solid electrolyte is a potential candidate in the fabrication of Na-S batteries. In the present study, it has been prepared in the form of discs by uniaxially as well as isostatically pressing and sintering in the temperature range 1585–1630°C, the highest sintered density of 3.25 g/cm<sup>3</sup> has been achieved in the samples isostatically pressed and sintered at 1630°C. X-ray analysis of the samples shows formation of  $\beta''$ -phase. Microstructure of the sintered samples reveals some darker regions which are attributed to low soda content. Resistivity at 300°C measured by the two-probe method at a frequency of 1 MHz on samples having vacuum-deposited silver electrodes is 15 ohm-cm, which is slightly higher than the value of 5–13 ohm-cm reported in literature using molten sodium electrodes. The activation energy of conductivity is 0.24 eV which is comparable to the literature value of 0.24–0.35 eV.

**Keywords.** Conducting ceramic; ionic conductor; sodium beta alumina; solid electrolyte.

### 1. Introduction

Beta-alumina ceramics have potential application in a variety of devices such as (a) electrolyte in the Na-S battery (Kummer and Weber 1968) for automotive propulsion or electric utility load levelling (b) thermoelectric devices (Weber 1974) and electrochemical devices for measuring sodium and oxygen activities. Amongst these, the sodium sulphur battery system based on beta alumina is the most advanced one.

The general formula for beta alumina is  $\text{Na}_2\text{O} \cdot x\text{-Al}_2\text{O}_3$ , where  $x$  varies from 5–11. Two structural forms of beta type alumina exist (Kummer 1972). At  $x = 11$  the composition yields  $\beta$ -alumina which starts converting in  $\beta''$ -alumina as the sodium content increases and at  $x = 5$ , the  $\beta$ -phase is completely converted into the  $\beta''$ -phase.  $\beta''$ -alumina has higher ionic conductivity than  $\beta$ -alumina but is unstable at a temperature greater than 1500°C. As the sintering temperature of  $\beta''$ -alumina is > 1500°C, some stabilizing agent like lithium oxide or magnesium oxide or both are added (Gordon *et al* 1977).

Lithium-stabilised  $\beta''$ -alumina was synthesised from reactive  $\alpha$ -alumina which was prepared at NPL, India (Das *et al* 1982). To compare the results, reactive  $\alpha$ -alumina of M/s Reynolds, USA was also used to synthesise  $\beta''$ -alumina.

### 2. Experimental procedure

$\beta''$ - $\text{Al}_2\text{O}_3$  was synthesised using two varieties of reactive  $\alpha$ - $\text{Al}_2\text{O}_3$  (NPL, India; M/s Reynolds USA (which has particle size  $\leq 0.7 \mu\text{m}$  and purity > 99.6 %)). The other two raw materials, sodium carbonate and lithium carbonate were of AR grade. The material was processed by using zeta process (Youngblood *et al* 1977) in which sodium-alumina

composition and a lithium alumina composition known as zeta alumina were processed and calcined separately and the two were then mixed in proper proportions to yield the desired composition.

The composition chosen for this experiment was 84.09 %  $\text{Al}_2\text{O}_3$ , 13.54 %  $\text{Na}_2\text{O}$  and 2.37 %  $\text{Li}_2\text{O}$  all taken in mole percent.  $\text{Na}_2\text{O} \cdot 5.25 \text{Al}_2\text{O}_3$  and  $\text{Li}_2\text{O} \cdot 5.5 \text{Al}_2\text{O}_3$  prepared for making the above composition were separately calcined at  $1340^\circ\text{C}$  for 2 hr and the compositions dry-ball milled to a particle size of  $< 1 \mu\text{m}$ . The powder was then mixed with polyvinyl butyral and benzene, which acts as a binder for about 2 hr and the slurry dried in air. The material was granulated using a nylon sieve and pressed uniaxially and isostatically into discs (15 mm dia and 2.5 mm thickness). A flow chart of the zeta process is shown in figure 1. To study the effect of particle size on the density, the

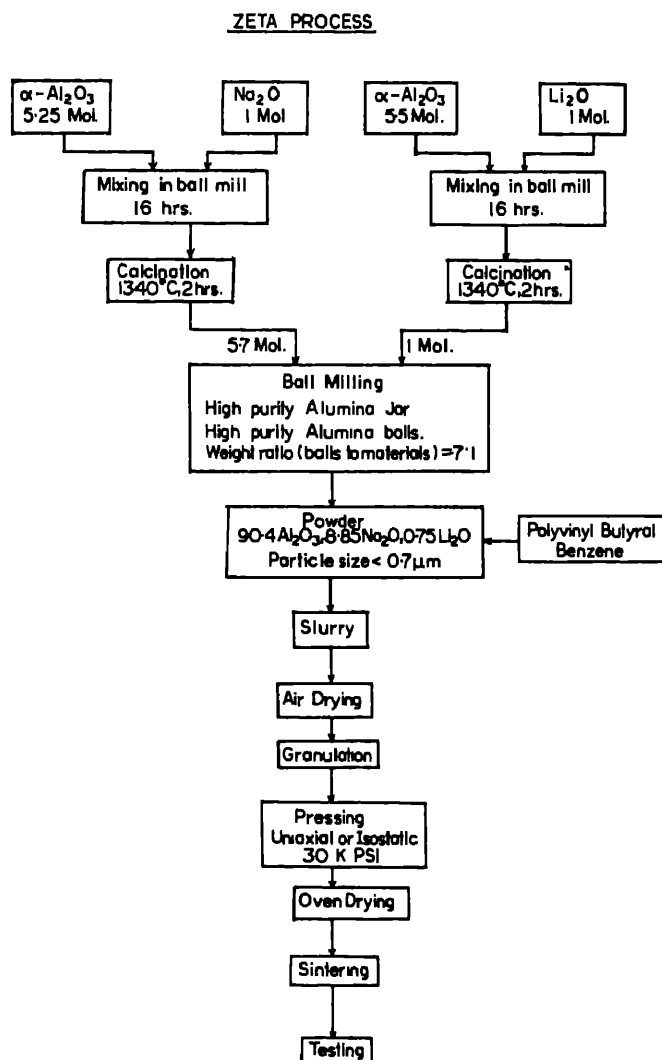


Figure. 1. Flow chart of zeta process for the synthesis of  $\beta'$ - $\text{Al}_2\text{O}_3$ .

Table 1. Particle size analysis of powders A-E.

Particle size ( $\mu\text{m}$ )	Materials (comm %)				
	A	B	C	D	E
+1.8	0.4	0.2	0.1	0	0
+1.15	4.2	3.4	2.3	1.2	1.2
+0.8	14.0	12.1	10.7	9.5	9.2
+0.65	26.3	22.6	21.3	19.9	20.2
+0.57	38.2	33.2	32.5	31.1	31.3
+0.5	49.2	43.2	43.0	42.3	42.3
+0.46	59.0	52.3	52.6	51.3	51.5
+0.43	67.5	60.5	61.0	59.3	59.5
+0.36	86.3	83.2	83.8	77.8	77.4
+0.33	94.0	90.3	89.9	85.6	86.4
+0.30	98.4	95.5	95.9	92.4	92.9
+0.28	100.0	98.8	99.2	97.6	97.5
+0.26	100.0	100.0	100.0	100.0	100.0
Mean Particle size	0.56	0.54	0.52	0.5	0.5

material was ground for various durations of time to yield different particle size distributions. Five such powders (table 1) having different particle size distribution were processed by pressing uniaxially and isostatically at different pressures. The pressed tablets were dried overnight in an oven ( $160^{\circ}\text{C}$ ) and then covered with coarse beta alumina powder and sintered in super kanthal furnace at a temperature ranging from  $1585$ – $1630^{\circ}\text{C}$  for various time intervals (2–32 min). The temperature schedule of the sintering is shown in figure 2. The material was annealed at  $1480^{\circ}\text{C}$  for 4 hr for complete conversion into the  $\beta''$ -phase. An almost similar two-step sintering schedule was adopted by Kvachkov *et al* (1981, 1982).

Rectangular samples ( $33 \times 32.7 \times 2.7$  mm) for x-ray analysis were prepared by uniaxially pressing and sintering at a temperature ranging from  $1585$ – $1630^{\circ}\text{C}$ . Tables 2a and 2b give the x-ray analysis and it is evident that mostly the  $\beta''$ -phase is present (Ray and Subbarao 1975; ASTM 1967). The density of the sintered discs was measured by Archimedes principle by immersion in xylene.

For microstructural evaluation the discs were broken into small pieces and the broken faces examined under a scanning electron microscope (JEOL JSM-35 CF). Energy dispersive spectroscopy (EDS) mode was employed for the elemental analysis of aluminium and sodium.

The electrical resistivity was measured by employing evaporated silver full face electrodes and by using Siemen's Bridge at 1 MHz to avoid interface polarisation (Yao and Kummer 1967) in a temperature range of  $20$ – $300^{\circ}\text{C}$ .

### 3. Results and discussions

#### 3.1 Effect of compacting pressure on green density

Figure 3 depicts the effect of uniaxial as well as isostatic pressure on the green density of the materials (Kalsi *et al* 1983). The green density increases with pressure. The highest

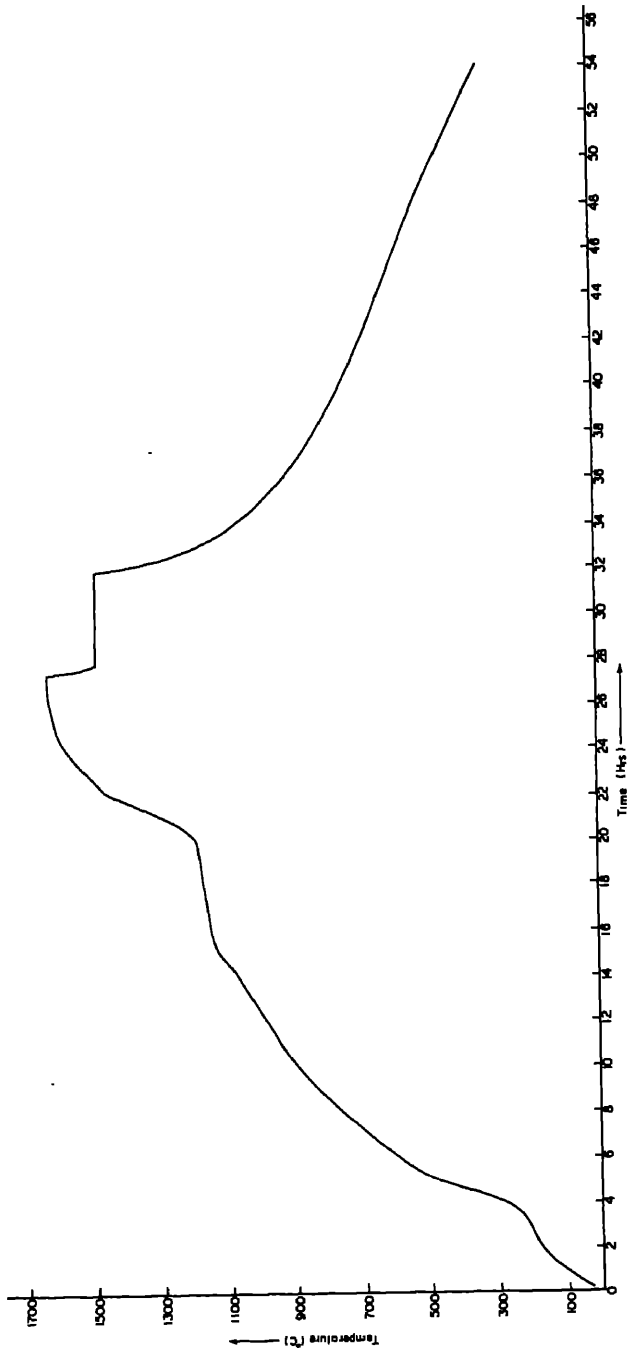


Figure 2. Temperature profile of sintering cycle.

Table 2(a). X-ray diffraction data for  $\beta''$ -Al<sub>2</sub>O<sub>3</sub> prepared from powder D.

dA°	I/I <sub>1</sub>	hkl
11.632	100	003
5.644	47	006
4.495	5	100
4.086	3	001
2.818	12	110
2.683	24	114
2.515	16	116
2.429	9	0014
		200
2.380	3	204
		118
2.254	13	110
2.132	9	1014
		207
2.040	9	209
1.973	5	2010
1.943	7	1016
1.596	6	2014
1.559	6	306
1.406	17	220

Table 2(b). X-ray diffraction data for  $\beta''$ -Al<sub>2</sub>O<sub>3</sub> prepared from powder E.

dA°	I/I <sub>1</sub>	hkl
11.632	100	003
5.717	56	006
4.484	7	100
4.086	6	001
2.818	16	110
2.691	28	114
2.600	5	101
		0013
2.515	22	116
2.417	12	0014
		200
2.383	3	203
2.254	18	110
2.139	12	1014
		207
2.045	16	200
1.973	5	2010
1.943	8	1016
1.596	8	2010
1.559	8	306
1.486	4	309
1.404	25	220

green density of 2.27 g/cm<sup>3</sup> was obtained in powder A (table 1) at a uniaxial compacting pressure of 3600 kg/cm<sup>2</sup> whereas at an isostatic pressure of 2600 kg/cm<sup>2</sup> a highest green density of 2.3 g/cm<sup>3</sup> was obtained for the same powder.

The variation of green density with particle size presented in figure 3 shows that the density decreases with particle size.

### 3.2 Effect of compacting pressure on the sintered density

Variation of the sintered density with uniaxial and isostatic pressure is shown in figure 4. The highest sintered density of 3.22 g/cm<sup>3</sup> was obtained for powder D (table 1) compacted at uniaxial pressure of 1800 kg/cm<sup>2</sup> and sintered at 1630°C, whereas for the isostatically pressed samples sintered at 1630°C, the sintered density is independent of the isostatic pressure in the range of 700–2600 kg/cm<sup>2</sup>. The highest sintered density of 3.25 g/cm<sup>3</sup> for powder D was obtained.

The variation of sintered density with particle size is also shown in figure 4 and it is clear that as the particle size decreases the sintered density increases.

### 3.3 Shrinkage studies

The shrinkage was measured as a function of uniaxial compacting pressure for all the five powders by sintering at 1630°C. The results are shown in figure 5. Shrinkage is higher at lower pressures with no significant change beyond 3000 kg/cm<sup>2</sup>. Powder D exhibits the highest shrinkage followed by powder E (table 1).



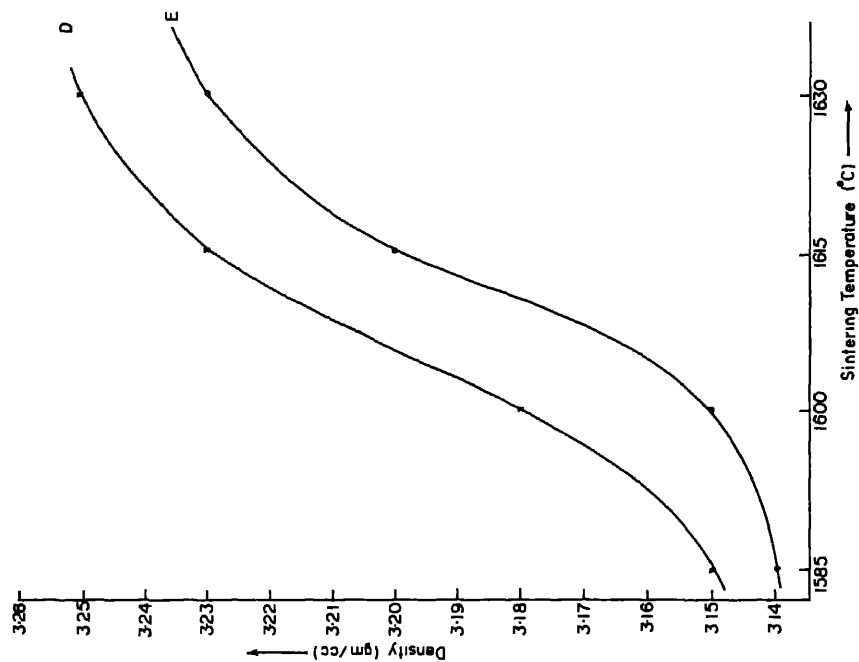


Figure 6. Variation of sintered density of powders D and E as a function of sintering temperature.

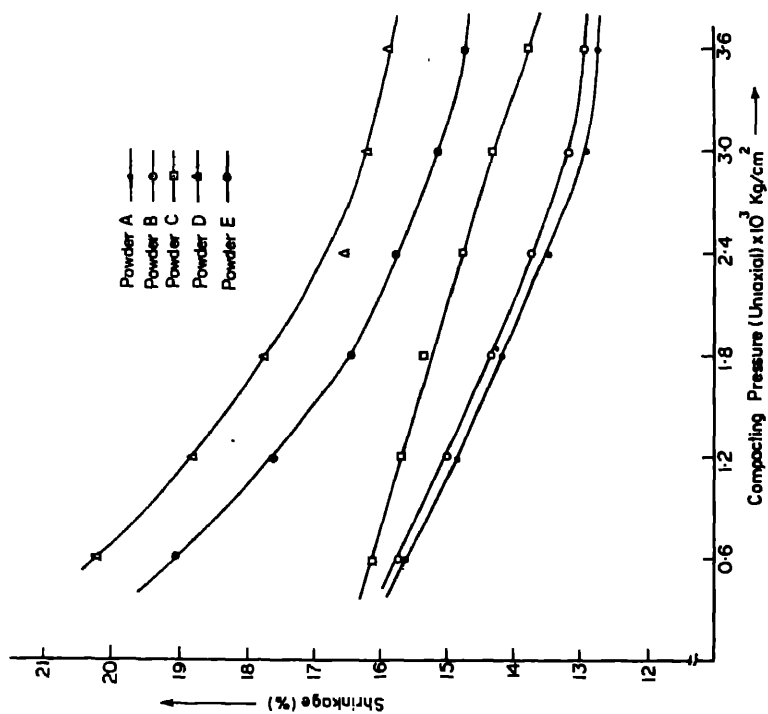


Figure 5. Variation of shrinkage with uniaxial compacting pressure for samples of different initial particle sizes and sintered at 1630 °C for 20 min.

(a)



(b)

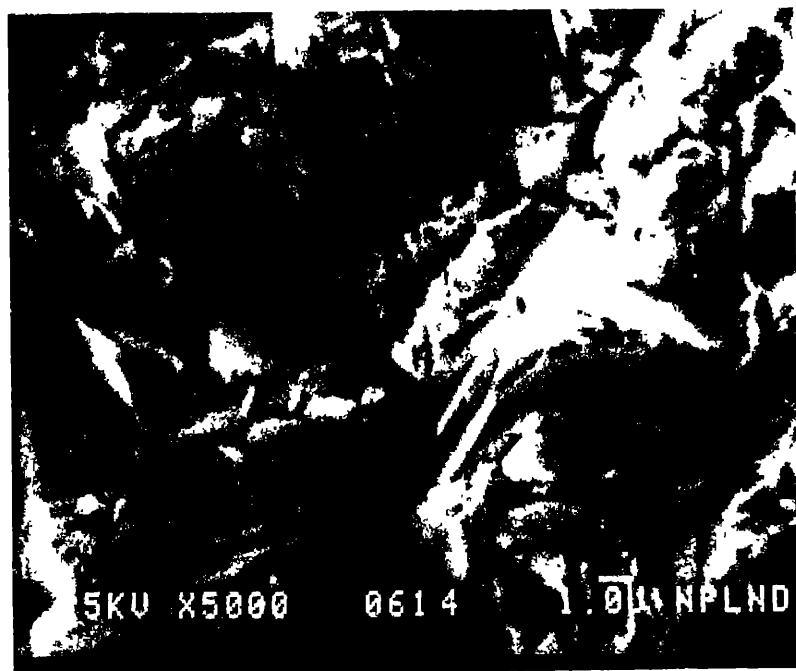


Figure 7. Microstructure of  $\beta''$ - $\text{Al}_2\text{O}_3$  prepared from a. powder D and b. the powder E and sintered at  $1630^\circ\text{C}$  for 20 min.

#### 4. Conductivity measurements

Ionic conductivity of beta alumina type superionic conducting material has been studied by several investigators (Wynn and Miles 1971; Demontt and Hancock 1971; Kummer 1972; Whittingham and Huggins 1971). Such measurements need either reversible electrodes *i.e.* molten sodium (Demontt and Hancock 1971) or  $\text{NaNO}_2/\text{NaNO}_3$  (Sudworth *et al* 1973) eutectic mixture, in which case conductivity is independent of the frequency. For measurements made using platinum or silver blocking electrodes the conductivity becomes frequency dependent below 1 MHz. At 1 MHz and above, it is independent of the frequency. In this study the measurements were made at 1 MHz using evaporated silver blocking electrodes; and resistivity of the order of 15 ohm-cm at 300°C was obtained.

The activation energy of conductivity was 0.24 eV which is close to the value reported (Kalsi *et al* 1983) for  $\text{Li}_2\text{O}$  doped compositions of  $\beta''\text{-Al}_2\text{O}_3$ . It may be pointed out here that this is slightly higher (Kalsi *et al* 1983) than those for the corresponding  $\text{MgO}$ -doped compositions. This difference could be due to the difference in structure or atomic jump mechanism which controls the ionic conductivity.

#### 5. Conclusion

In  $\beta''\text{-Al}_2\text{O}_3$  samples isostatically pressed and sintered at 1630°C a density of 3.25 g/cm<sup>3</sup> has been obtained. A maximum shrinkage of 20% was observed in samples uniaxially pressed at 600 kg/cm<sup>2</sup> and sintered at 1630°C. X-ray analysis reveals the formation of  $\beta''$ -phase. The microstructure reveals randomly oriented elongated crystals of  $\beta''\text{-Al}_2\text{O}_3$  having some darker portions; which are regions of low soda content. The resistivity of the order of 15 ohm-cm at 300°C has been obtained. An activation energy of 0.24 eV was obtained which is close to the value reported in literature.

#### Acknowledgement

The authors thank the Director, NPL, New Delhi for facilities. Thanks are due to Mr S U M Rao and Shri D K Suri for scanning electron microscopy and x-ray diffraction analysis work respectively. This work is supported financially by the Department of Nonconventional Energy Sources, New Delhi.

#### References

- ASTM 1967 19-1173
- Das B K, Kalsi H S, Khullar S M, Kumar Rahul, Goel R C and Misra S C K *Int. Symp. on Ceramics* 27-30 Nov. 1982 Bangalore (India) Vol. I Part II
- Demont D S and Hancock P 1971 *Proc. Br. Ceram. Soc.*
- Fielder W L, Kantz H E, Fordyce J S and Singer J 1975 *J. Electrochem. Soc.* 122 528
- Gordon R S, McEntire B J, Miller M L and Virkar A V 1977 *Mater. Sci. Res.* Vol. 11, p. 1405
- Hodge J D 1983 *J. Am. Ceram. Soc.* 66 166
- Kalsi H S, Tandon R P and Das B K 1983 *Symp. on Adv. in electrochemical Energy Storage and Conversion* 21-1-1983, CECRI, Karaikudi (India)
- Kummer J T 1972 *Prog. Solid State Chem.* 7 141

- Kummer J T 1972 *Prog. Solid State Chem.* (ed.) H Reiss and J O McCaldin (New York: Pergamon Press) Vol. 7
- Kummer J T and Weber N 1968 *Soc. Automotive Eng. Trans.* **76** 1003
- Kvachkov R, Yanakiev A, Poulieff C N, Bakanor I, Yankulov P D and Budevski E 1981 *J. Mater. Sci.* **16** 2710
- Kvachkov R, Yanakiev A, Poulieff C N, Yankulov P D, Rashkov S and Budevski E 1982 *Solid State Ionics* **7** 151
- Ray A K and Subbarao E C 1975 *Mater. Res. Bull.* Vol. **10** 583
- Sudworth J L, Tilley A R and South K D 1973 *Fast ion transport in solids* (ed.) W Van Gool (Amsterdam: North Holland) p. 581
- Weber N 1974 *Energy Convers.* **14** 1
- Whittingham M S and Huggins R A 1971 *J. Electrochem. Soc.* **118** 1
- Wynn Jones I and Miles L T 1971 *Proc. Br. Ceram. Soc.* **16** 1
- Yao Y F V and Kummer J T 1967 *J. Inorg. Nucl. Chem.* **29** 2453
- Youngblood C E, Virkar A V, Canon W R and Gordon R S 1977 *Am. Ceram. Soc. Bull.* **56** 206

15  
16  
17  
18  
19  
20  
21  
22  
23  
24  
25  
26  
27  
28  
29  
30  
31  
32  
33  
34  
35  
36  
37  
38  
39  
40  
41  
42  
43  
44  
45  
46  
47  
48  
49  
50  
51  
52  
53  
54  
55  
56  
57  
58  
59  
60  
61  
62  
63  
64  
65  
66  
67  
68  
69  
70  
71  
72  
73  
74  
75  
76  
77  
78  
79  
80  
81  
82  
83  
84  
85  
86  
87  
88  
89  
90  
91  
92  
93  
94  
95  
96  
97  
98  
99  
100

101  
102  
103  
104  
105  
106  
107  
108  
109  
110  
111  
112  
113  
114  
115  
116  
117  
118  
119  
120  
121  
122  
123  
124  
125  
126  
127  
128  
129  
130  
131  
132  
133  
134  
135  
136  
137  
138  
139  
140  
141  
142  
143  
144  
145  
146  
147  
148  
149  
150  
151  
152  
153  
154  
155  
156  
157  
158  
159  
160  
161  
162  
163  
164  
165  
166  
167  
168  
169  
170  
171  
172  
173  
174  
175  
176  
177  
178  
179  
180  
181  
182  
183  
184  
185  
186  
187  
188  
189  
190  
191  
192  
193  
194  
195  
196  
197  
198  
199  
200

## Evidence of screw dislocations on (002) cleavages of lithium carbonate single crystals

K S RAJU\*, M PALANISWAMY, P RAMASAMY and G S LADDHA

Crystal Growth Centre, AC College of Technology, Anna University, Madras 600 025, India

\*Department of Crystallography and Biophysics, University of Madras, Guindy Campus, Madras 600 025, India

MS received 2 April 1983; revised 8 December 1983

**Abstract.** Well-defined triangular etch pits are produced on etching (002) cleavages of lithium carbonate single crystals with 2 % citric acid. On etching of cleavage face and matched face these pits nucleate at the intersection sites of dislocations with the cleavage face. On successive etching of a cleavage face, shallow irregular arrays of pits do not enlarge in size as compared to other isolated pits on the same face. These irregular arrays of pits have reasonable correspondence on an etched match face, suggesting they form at dislocation sites.

**Keywords.** Chemical etching; tilt boundaries; twist boundaries; spiral etch pits; lithium carbonate single crystal.

### 1. Introduction

Etch methods have been applied to understand the history of growth of crystals and their dislocation content (Gilman and Johnston 1956; Patel and Tolansky 1957; Patel and Goswami 1964; Patel and Raju 1966, 1967; Raju 1981). It was established that the geometric shape of the etch pits on a crystal face is strictly related to the symmetry of the crystal face and the nature of the etchant (Patel and Singh 1968; Hari Babu and Bansigir 1968; Buckley 1958; Borle and Bagai 1976; Connick and May 1969; Wehner 1958 etc). Irregular arrays comprising of edge and screw dislocations on (0001) and (10 $\bar{1}$ 1) faces of hematite (Sunagawa 1968) as well as on (010) faces of gypsum (Raju 1980) have been reported.

In the present paper spiral etch pits observed along the irregular arrays on (002) cleavage faces of  $\text{Li}_2\text{CO}_3$  single crystals are reported.

### 2. Experimental

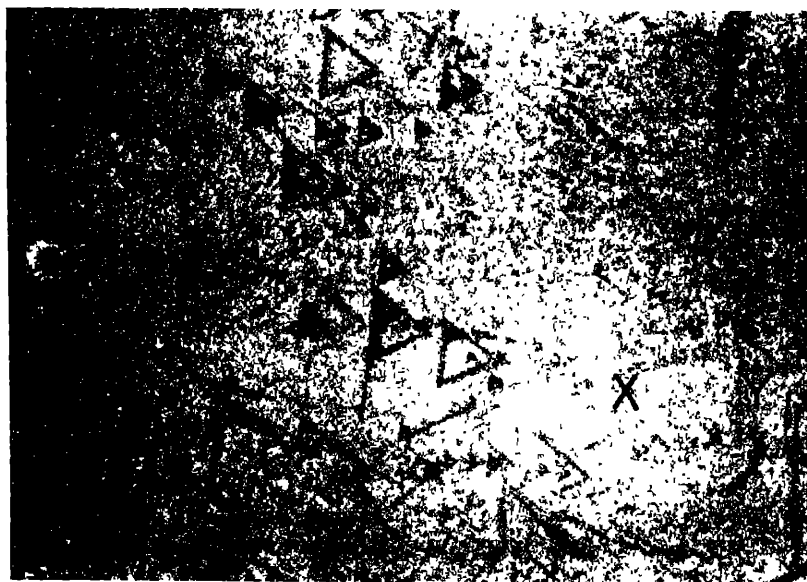
In the present work, transparent single crystals (Palaniswamy *et al* 1982) of lithium carbonate were cleaved parallel to the (002) plane and etched in 2 % citric acid for the required time. The etch patterns were studied by optical methods. Silver coating on the etched cleavages was avoided as it would spoil the surface for further etching. For examining the cleavage surfaces at higher resolution and magnification, scanning electron microscope (Cambridge Stereoscan model S-150 and operating voltage 20 kV) was used after sputtering the crystal surface with gold.

### 3. Observations

#### 3.1 Successive etching of an isolated cleavage

Figures 1 and 2 reveal the etch patterns produced on etching a (002) basal cleavage face of lithium carbonate crystal with 2% citric acid for 2.5 and 4 min respectively. It is clear that on successive etching, some isolated etch pits enlarge in size and shape whereas the array (marked XY in figure 1) remains almost the same (marked X'Y' in figure 2). The

(1)



(2)



Figures 1 and 2. ( $\times 200$ ) Etch pattern 1. on (002) cleavage etched 2% citric acid for 2½ min. 2. of the region of figure 1 etched for a total of 4 min

pit marked Y in figure 1 on successive etching appears like a clockwise spiral as seen in the pit marked Y' in figure 2.

### 3.2 Etching of a matched pair

In order to investigate the irregular arrays of etch pits, a matched face is etched identically for  $2\frac{1}{2}$  min in 2% citric acid. Figures 3 and 4 clearly show a reasonable

(3)



(4)



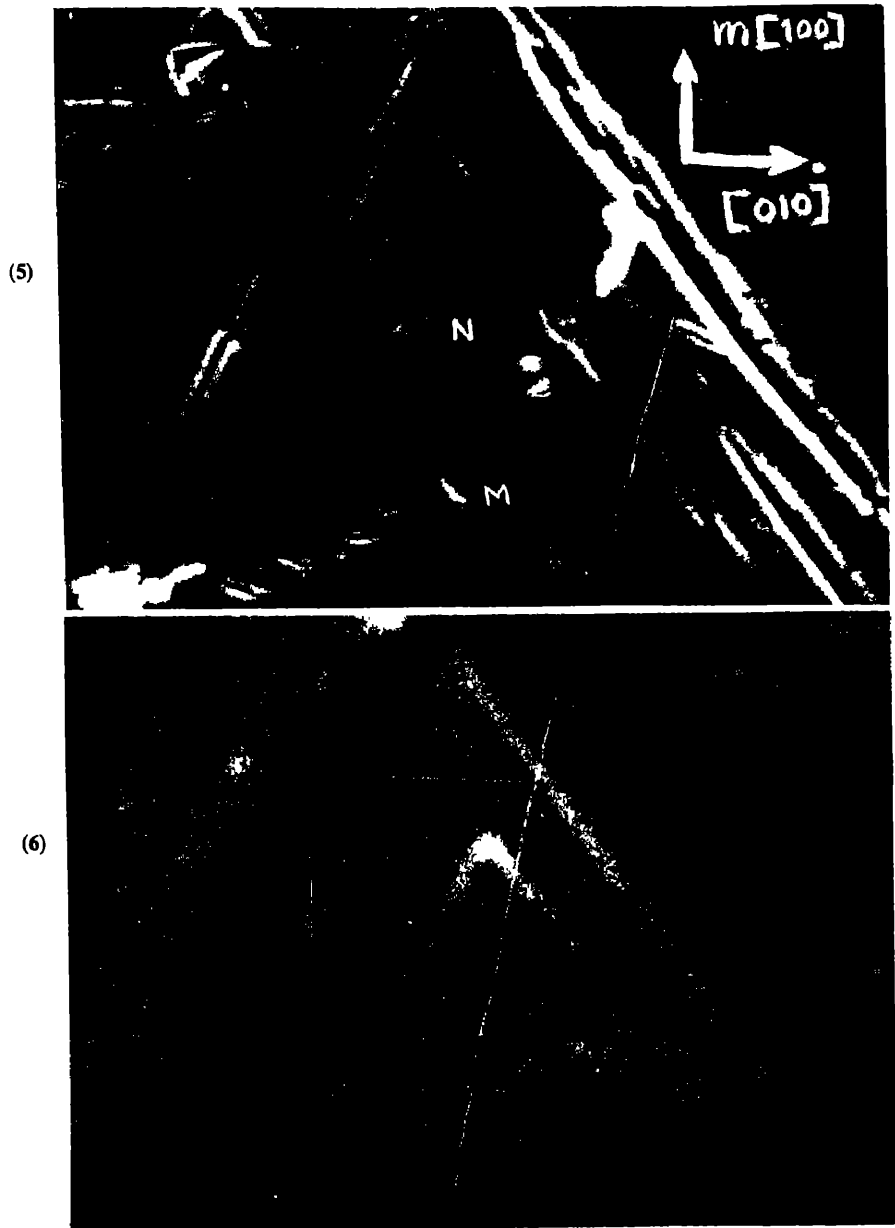
Figures 3 and 4. ( $\times 325$ ) Etch patterns of a matched cleavage etched in 2% citric acid for  $2\frac{1}{2}$  min.



amount of correlation in the three dominant irregular arrays of etch pits. The pit marked Z in the central array of figure 3 resembles an anticlockwise spiral.

### 3.3 SEM studies

One of the arrays in figure 3 is scanned in the electron microscope (figure 5). The pit marked M clearly looks like a clockwise spiral of single turn, while the pit marked N is



Figures 5 and 6. SEM photograph 5. revealing an irregular array of etch pits ( $\times 2000$ ) 6. of the magnified region of figure 5 ( $\times 7500$ ).

not clear. Hence the pit N is observed at higher magnification as shown in figure 6. It is interesting to note that pit N also resembles a clockwise spiral having a white contour.

#### 4. Discussion

The shape of the etch pits on (002) cleavage face of  $\text{Li}_2\text{CO}_3$  single crystal has been observed to be triangular, irrespective of the etchants used (Palaniswamy *et al* 1982).  $\text{Li}_2\text{CO}_3$  is monoclinic and has the space group  $C2/c$  which is a part of class  $2/m$ . The (002) cleavage in  $2/m$  is mono-symmetrical, which means it contains one mirror plane. Etch pits on (002) plane must show mirror symmetry. The mirror symmetry axis  $m[100]$  is perpendicular to the base of the etch pits, which happens to be the two-fold axis  $[010]$  as shown in figure 5.

On successive etching, the isolated pits enlarge in size retaining their shape, suggesting dislocation of etch pits. This has been supported by the exact correspondence of isolated etch pits on matched faces. That the irregular arrays remain shallow without enlarging reasonably in depth on successive etching and reveal correspondence on etched match faces suggest that these are also dislocation arrays of a different nature than those of isolated dislocation pits. One of the pits marked Z in the irregular array in figure 3 indicates that this dislocation may be of screw type, anticlockwise. That the pits forming the irregular array etch differently than those of isolated pits enlarging in size, may be attributed to the association of screw dislocations in the array of pits.

That the pits (marked M and N in figure 5) constituting the irregular array resemble spirals support the conjecture that they reveal screw dislocations in the crystal (Patel and Raju 1966).

These irregular arrays of etch pits may represent general grain boundaries having both edge and screw dislocations, which might have been formed due to the impingement of misoriented guest crystals causing stresses in the growing crystal. This agrees with the findings of Sunagawa (1968) on hematite and Raju (1980) on gypsum.

#### 5. Conclusions

That the spiral etch pits observed are along irregular arrays and these irregular arrays (of etch pits) have correspondence on match faces indicate that they may reveal tilt or twist boundaries consisting of edge and screw dislocations in the crystal. Therefore it is concluded that the spiral etch pits forming the components of irregular arrays represent the sites of screw dislocations on (002) basal cleavages of lithium carbonate single crystal.

#### Acknowledgements

The authors thank Dr N Ramanathan, Director, Central Leather Research Institute, Adyar, Madras for permission to use the scanning electron microscope and to Dr A Rajaram for the assistance in SEM studies. One of the authors (KSR) thanks Dr E Pippel and Dr W Neumann for valuable discussions. MP thanks Anna University for the award of a fellowship.

**References**

- Buckley H E 1958 *Crystal growth* (New York: John Wiley) 4 edn p. 321
- Borle W N and Bagai R K 1976 *J. Cryst. Growth* **36** 259
- Connick W and May F G J 1969 *J. Cryst. Growth* **5** 65
- Gilman J J and Johnston W G 1956 *J. Appl. Phys.* **27** 1018
- Hari Babu V and Bansigir K G 1968 *J. Cryst. Growth* **2** 9
- Patel A R and Tolansky S 1957 *Proc. Roy. Soc. (London)* **A243** 41
- Patel A R and Goswami K N 1964 *Acta Crystallogr.* **17** 569
- Patel A R and Raju K S 1966 *Acta Crystallogr.* **21** 190
- Patel A R and Raju K S 1967 *Acta Crystallogr.* **23** 217
- Patel A R and Singh R P 1968 *J. Cryst. Growth* **2** 373
- Palaniswamy M, Gnanam F D, Ramasamy P and Laddha G S 1982 *Cryst. Res. Technol.* **17** 911
- Raju K S 1980 *Bull. Mater. Sci.* **2** 139
- Raju K S 1981 *J. Mater. Sci.* **16** 2512
- Sunagawa I 1968 *Mineral Mag.* **36** 625
- Wehner G K 1958 *J. Appl. Phys.* **29** 217

## Etch pit observations on the habit faces of gel grown nickel molybdate crystals

K V KURIEN\* and M A ITTYACHEN

Department of Physics, University of Kerala, Kariavattom 695 581, Trivandrum, India

\*Department of Physics, Mar Thoma College, Tiruvalla 689 105, India

MS received 30 April 1983; revised 30 April 1984

**Abstract.** The results obtained from etching experiments on the habit faces of  $\text{NiMoO}_4 \cdot x\text{H}_2\text{O}$  are described. Dilute solutions of chemical reagents such as  $\text{HNO}_3$ ,  $\text{CH}_3\text{COOH}$ ,  $\text{NaOH}$ ,  $\text{KOH}$  are found to be the best etchants for revealing dislocation etch pits. The shape and nature of the etch pits are also described.

**Keywords.** Etch pits; dislocation; habit faces; gel grown;  $\text{NiMoO}_4 \cdot x\text{H}_2\text{O}$  crystals

### 1. Introduction

Etching is a well-known technique for dislocation studies in crystals. It is the result of variation in surface reaction or dissolution rates influenced by crystallographic orientation effects, lattice imperfection and chemical combination. Etch patterns observed on crystal faces play an important role in obtaining information on the history of growth of crystals, as their etch patterns are intimately related to the growth phenomena. The first attempt to provide an explanation for the process of etching is due to Goldschmidt (1904). A satisfactory explanation regarding the origin of etch pits and their development has been given on the concept of lattice defect known as dislocation. A dislocation etch is an attractive means of studying the early stages of deformation in crystalline solids. This has led to the discovery of a number of etchants.

In the present work, an attempt has been made to investigate the nature and shape of etch pits by etching the (001) and (011) surfaces of gel-grown nickel molybdate crystals (Kurien and Ittyachen 1980). Well-shaped square and octagonal platelets (average size  $3 \times 2 \times 0.3 \text{ mm}^3$ ) have been selected for this purpose.

### 2. Experimental and results

As there is no previous study of etching behaviour of these crystals, a number of prospective etchants were tried to reveal the dislocation sites and dislocation density. Water and quite a few acids were found to etch the cleavage faces of their flakes of nickel molybdate crystals. Nitric acid, acetic acid, sodium hydroxide, potassium hydroxide and a mixture of nitric acid and hydrochloric acid are suitable etchants for their action on the (001) face. Water has some polishing action on the surface. Sulphuric and hydrofluoric acids were unsuitable for etching the faces of gel-grown nickel molybdate



**Figures 1-5.** 1. Square type etch pits on the (001) face when etched in nitric acid. 2. Well-defined square and rectangular etch pits with terrace when etched in acetic acid. 3. Square-shaped pits with two sides well developed when etched in sodium hydroxide. 4. Rectangular pits on the (001) face when etched in nitric acid. 5. Square-shaped pits with two sides well-developed when etched in potassium hydroxide.

crystals. Increase in concentration or temperature resulted in the increase of surface dissolution without forming the visible pits tabulated in table 1. A large number of clusters of pits were formed first on the surfaces of thin flake-like crystals in the initial stages of etching. However, on repeated etching most of the pits became flat-bottomed, enlarged and eventually vanished. But some of the pits remained nearly constant during successive etching. A large number of pits were symmetrical pits, composed of closed rectangular and square terraces. Both nitric and acetic acids could yield identical etch

**Table 1.** Experimental conditions for etch pit formation on the (001) and (011) faces of gel grown nickel molybdate crystals

Etchant	Concentration	Time (min)	Observation
HCl	1:100	1	Rapid attack
	1:150		
	1:200	1	Few perfect pits were observed on the (001) and (011) faces
HF	1:150	1	Rapid attack
	1:200		
	1:400		
HNO <sub>3</sub>	1:200	1-2	Well-defined square and rectangular pits were obtained on the (001) (figure 1) and (011) (figure 4) faces
	1:300		
	1:400		
CH <sub>3</sub> COOH	1:200	1	Clustered etch pits of smaller size
	1:100	2	Well-defined square and rectangular pits with terrace (figure 2)
	1:150		
NaOH	0.05-0.1 N	2	Square-shaped pits with two sides well developed (figure 5)
HF + HNO <sub>3</sub>	1:300	1	Destructive reaction: no etch pit formation

The experiment was conducted at room temperature.

pits. But in the case of sodium and potassium hydroxides only two sides of the square pits were well-developed. The sides of the square pits in all cases were parallel to the  $\langle 100 \rangle$  direction. The average etch pit density was of the order of  $10^4$ - $10^5$  cm<sup>-2</sup>. In isolated crystals, the dislocation density was between  $10^2$  and  $10^3$  cm<sup>-2</sup>.

### 3. Discussion

Studies on different types of etch pits and their densities give useful information regarding the nature of the defects, impurity content and the history of growth of crystals. Etch pits may be produced due to several reasons. In the present case, initially a clustering of etch pits is formed. They are well-defined, very small point-bottomed, rectangular square pits. However, on repeated etching most of the pits became flat-bottomed and eventually vanished. The origin of flat-bottomed pits is due to the localised defects such as microprecipitates, vacancies etc. (Michael *et al* 1970). Evidently in this case etch pits are not being formed at the dislocation sites but at the impurity sites. The large flat-bottomed pits were assumed to be due to edge dislocations produced during the later stages of crystal growth (Johnston 1962). The edge and screw dislocations give rise to two distinct types of pits. The etch pits due to edge dislocations were generally small compared to those due to screw dislocation (Amelinckx 1976). The terrace nature of pits is a common phenomenon in the case of calcite, mica, etc. (Patel *et al* 1963). The terrace nature of pits obtained in this study can be explained by postulating the precipitation of some sort of impurities along the dislocation line which

inhibits the action of the etchant depending on the nature, density and location of the impurities. The impurities might be evenly spaced along the dislocation line which result into pits having various types of terraces. The number of times the inhibition action is operated can be judged by the number of terraces—obtained when the inhibition action lasts longer, widely terraced pits are produced.

#### 4. Conclusion

The high density etch pits obtained in the initial stages of etching suggests that the crystals have a high density of impurities adsorbed on the surfaces in the later stages of growth.

#### References

- Amelinckx S and Dekeyser N 1952 *Naturwissenschaften* **39** 448
- Amelinckx S 1976 *J. Appl. Phys.* **31** 1359
- Goldschmidt V 1904 *Z. Kristallogr.* **38** 273
- Gilman J J and Johnston W G 1956 *J. Appl. Phys.* **27** 1018
- Horn F H and Gevers W 1952 *Philos. Mag.* **43** 1210
- Johnston W G 1962 *Progress in ceramic science* (ed.) J E Burke (New York: Pergamon) Vol 2
- Kurien K V and Ittyachen M A 1980 *Krist. Tech.* **15** 7, 763
- Michael F, Ehman G R, Jindal J W, Faust Jr and William B White 1970 *J. Appl. Phys.* **41** 7
- Patel A R and Goswami S 1963 *Physica* **29** 33
- Patel A R and Ramanathan S 1963 *Amer. Miner.* **48** 691

## Elastic properties of As-Sb-Se glasses

A GIRIDHAR, SUDHA MAHADEVAN and A K SINGH

Materials Science Division, National Aeronautical Laboratory, Bangalore 560 017, India

MS received 27 June 1983; revised 23 August 1983

**Abstract.** Results of measurement of elastic moduli on As-Sb-Se glasses are reported and their composition dependence discussed. The Young's and the shear moduli lie in the range of 170–210 and 65–80 kb respectively. These values are typical of chalcogenide glasses. For (As, Sb)<sub>40</sub>Se<sub>60</sub> glasses, the moduli increase monotonically with increasing Sb<sub>2</sub>Se<sub>3</sub> content. The observed composition dependence of the moduli for the As<sub>x</sub>Sb<sub>15</sub>Se<sub>85-x</sub> glasses is examined in terms of the chemically ordered structural units in the glasses.

**Keywords.** As-Sb-Se glasses; elastic properties; CONM model.

### 1. Introduction

The results of measurement of glass transition temperature ( $T_g$ ), electrical conductivity and density ( $d$ ) on glasses of the As-Sb-Se system were reported earlier (Giridhar and Sudha Mahadevan 1982). The study covered two groups of glasses: (i) those whose composition could be represented by (As, Sb)<sub>40</sub>Se<sub>60</sub> and (ii) those whose composition could be represented by As<sub>x</sub>Sb<sub>15</sub>Se<sub>85-x</sub>. The (As, Sb)<sub>40</sub>Se<sub>60</sub> glasses fall along the (As<sub>2</sub>Se<sub>3</sub>) (Sb<sub>2</sub>Se<sub>3</sub>) pseudobinary section and represent the so-called 'stoichiometric' compositions of the As-Sb-Se system. The  $T_g$ , electrical conductivity and  $d$  of these glasses showed a monotonic increase with increasing Sb<sub>2</sub>Se<sub>3</sub> content. In the As<sub>x</sub>Sb<sub>15</sub>Se<sub>85-x</sub> glasses, with the stoichiometric As<sub>25</sub>Sb<sub>15</sub>Se<sub>60</sub> composition as reference, glasses with more than 60 at. % of Se were referred to as Se-rich glasses and those with less than 60 at. % of Se as As-rich glasses of this family. The As<sub>x</sub>Se<sub>100-x</sub> and Ge<sub>x</sub>Sb<sub>15</sub>Se<sub>85-x</sub> glasses show an extremum in  $T_g$  and  $d$  at the respective stoichiometric compositions (Myers and Felty 1967; Mohan *et al* 1981; Narasimham *et al* 1981; Giridhar *et al* 1981). The composition dependence of  $T_g$  and  $d$  of the As<sub>x</sub>Sb<sub>15</sub>Se<sub>85-x</sub> glasses exhibit an interesting feature, namely, that the  $T_g$  and  $d$  of the As-rich glasses of this family are higher than those of the As<sub>25</sub>Sb<sub>15</sub>Se<sub>60</sub> composition (Giridhar and Sudha Mahadevan 1982).

The results of measurements of elastic properties on eight glass compositions are reported in this paper. Four of these compositions can be represented by (As, Sb)<sub>40</sub>Se<sub>60</sub>, while the other four belong to the As<sub>x</sub>Sb<sub>15</sub>Se<sub>85-x</sub> family.

### 2. Experimental

The cylindrical samples (about 12 mm in diameter and 6 mm in length) suitable for ultrasonic sound velocity measurements were obtained by the following procedure.

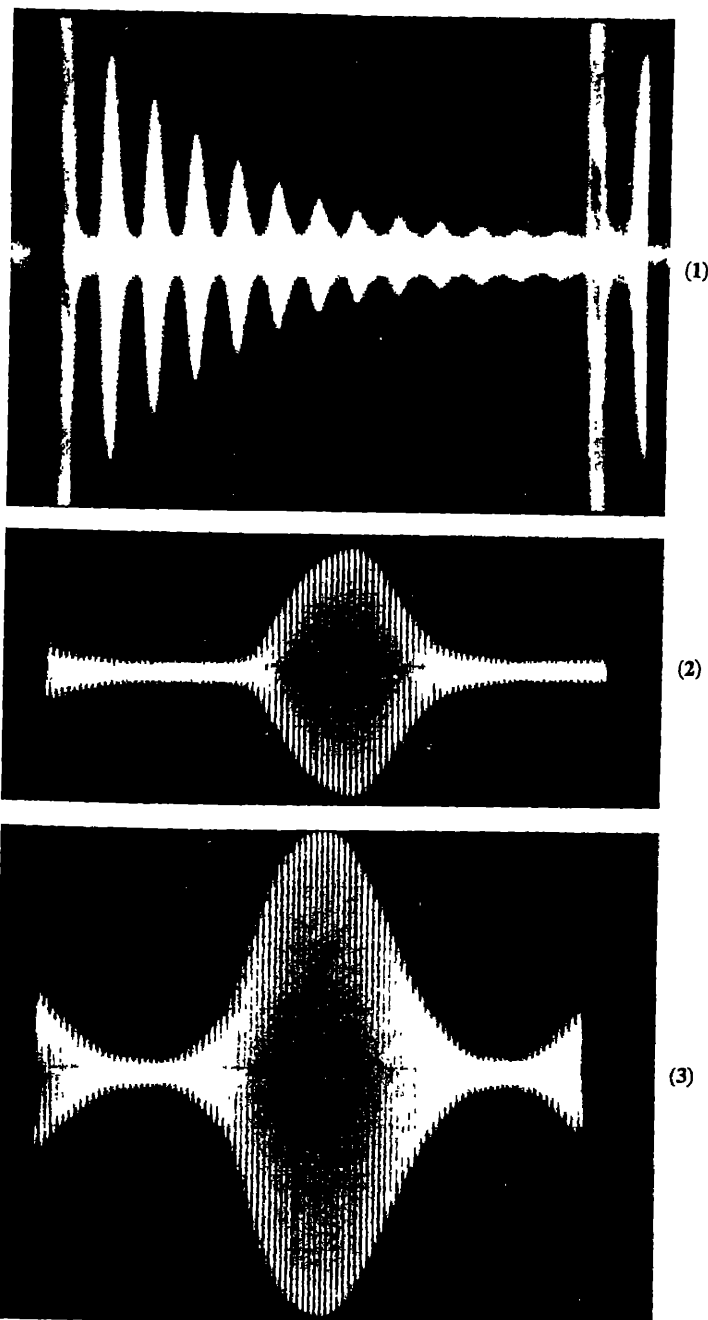


The elemental components (5N purity, from Koch Light Co.) in appropriate proportions were sealed in a quartz ampoule (12 mm in diameter) under a vacuum of  $10^{-3}$  torr. The contents of the ampoule were melted in a rotary furnace at about  $950^{\circ}\text{C}$  for 24 hr. The melt was then cooled to  $800^{\circ}\text{C}$  and quenched in water at  $90^{\circ}\text{C}$ . Care was taken to see that the ampoule stayed in a vertical position during the quenching operation. Quenching in hot water rather than in cold water was found essential to prevent any cracking or shattering of the cylindrical sample during further processing. The ampoule was then introduced into a tubular furnace where the glass was annealed at a temperature of about  $5^{\circ}$  higher than  $T_g$  for 1 hr and then brought to room temperature by slow cooling. Just before breaking open, the ampoule was chilled in an ice bath for 15 min to facilitate retrieval of the specimen from the ampoule. The faces of the cylindrical samples thus obtained were rendered flat and parallel (the wedge angle being better than  $0.2$  sec) using a lapping-polishing jig specially designed and fabricated for this purpose. Using Salol (phenyl salicilate) as the bonding material the longitudinal and transverse velocities in the samples were measured (at  $25^{\circ}\text{C}$ ) by using 10 MHz X-cut and Y-cut transducers, by McSkimin's pulse superposition technique (McSkimin 1961; McSkimin and Andreatch 1962). As already indicated (Sudha Mahadevan *et al* 1983), an ultrasonic pulse echo interferometer (supplied by Systems Dimensions, Bangalore, model SDUI-003) in conjunction with a 50 MHz Philips oscilloscope and frequency/time interval counter (accuracy of one nsec) was used for this purpose. The accuracy of velocity measurements limited mainly by thickness measurements (for which a Mitutoyo height master transfer stand combination was used), was  $0.03\%$ . A spread of about  $1.5\%$  was observed in the velocities in different specimens of the same composition. The typical quality of the echo pattern obtained in our set up is shown in figures 1–3. A train of 10–12 echoes could be obtained in most cases (figure 1); this is because of the high parallelism of the faces. The measurement of the delay time was facilitated by the good resolution obtained in the amplitude of the expanded echoes (figures 2 and 3).

### 3. Results and discussion

#### 3.1 $(\text{As}, \text{Sb})_{40}\text{Se}_{60}$ glasses

The results for these glasses are summarised in figure 4 and table 1. The shear ( $G$ ), the Young's ( $E$ ), the bulk ( $K$ ) moduli and the Poisson's ratio ( $\sigma$ ) of  $(\text{As}, \text{Sb})_{40}\text{Se}_{60}$  glasses increase monotonically with increasing  $\text{Sb}_2\text{Se}_3$  content (figure 4). Extrapolation of  $G$ ,  $E$ ,  $K$  and  $\sigma$  values (figure 4) of these glasses to zero  $\text{Sb}_2\text{Se}_3$  content, which corresponds to  $\text{As}_2\text{Se}_3$ , gives the values of moduli which agree well with one set of reported values for  $\text{As}_2\text{Se}_3$  (Thompson and Bailey 1978). The other values (Hilton and Hayes 1975; Soga and Kunugi 1973) fall slightly away from the extrapolated data. Also shown in figure 4 is the variation of the mean atomic volume with composition. For isostructural crystalline compounds, the bulk modulus increases with decrease in volume (Anderson and Nafe 1965). However, in our discussion (Sudha Mahadevan *et al* 1983) of the variation of  $K$  with mean atomic volume of several chalcogenide glass systems, namely Ge-Sb-Se, Ge-As-Se, Ge-Sb-S and Ge-Se, it was seen that the mean atomic volume is not the only factor determining the bulk modulus of these glasses. Besides volume, other factors such as the nature of the type of bonding could also be effective in



Figures 1-3 1. Typical exponential echo train for a  $\text{As}_{10}\text{Sb}_{15}\text{Se}_{75}$  sample for longitudinal waves. 2. Expanded echo wave form for pulse superposition for  $p = 2$ , minimum amplitude. 3. Expanded echo wave form for pulse superposition for  $p = 2$ , maximum amplitude.

determining the bulk modulus. In  $(\text{As}, \text{Sb})_{40}\text{Se}_{60}$  glasses, (figure 4) the bulk modulus increases with increasing  $\text{Sb}_2\text{Se}_3$  content while the corresponding volume has also increased. Therefore, the type of bonding, rather than the volume has greater influence in determining the bulk modulus of these glasses.

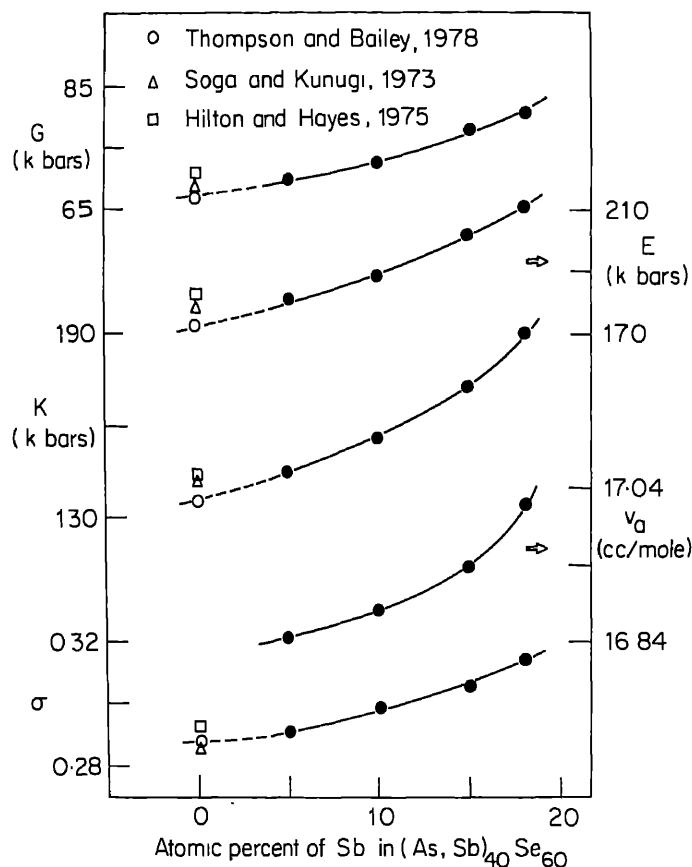


Figure 4. Variation of elastic moduli and mean atomic volume for  $(\text{As}, \text{Sb})_{40}\text{Se}_{60}$  glasses shown as a function of Sb content. Data for  $\text{As}_2\text{Se}_3$  are from literature.

Table 1. Elastic data for As-Sb-Se glasses

Composition (As:Sb:Se)	$d(\text{g/cc})$	Long. vel. $C_1$ (m/sec)	Trans. vel. $C_t$ (m/sec.)	Shear mod. $G$ (kbars)	Young's mod. $E$ (kbars)	Bulk mod. $K$ (kbars)	Poisson's ratio $\sigma$
35:15:50	4.990	2302	1253	78.34	202.05	159.97	0.2895
30:15:55	4.983	2294	1245	77.24	199.46	159.21	0.2912
25:15:60	4.980	2358	1248	77.56	202.30	173.26	0.3054
20:15:65	4.920	2243	1208	71.80	186.05	151.78	0.2957
10:15:75	4.850	2121	1170	66.39	170.14	129.66	0.2813
35: 5:60	4.730	2245	1218	70.17	181.24	144.80	0.2914
30:10:60	4.860	2281	1222	72.57	188.50	156.07	0.2987
22:18:60	5.040	2429	1263	80.40	211.40	190.14	0.3147

### 3.2 $As_xSb_{15}Se_{85-x}$ glasses

The data for  $As_xSb_{15}Se_{85-x}$  glasses are shown in figure 5 and table 1. With the stoichiometric composition  $As_{2.5}Sb_{15}Se_{60}$  as reference, the  $G$  and  $E$  of As-rich glasses are seen to be essentially constant while those of the Se-rich glasses show a decrease with increasing Se-content. The bulk modulus exhibits a maximum for the stoichiometric composition (figure 5). Also shown in figure 5 is the variation of the mean atomic volume with composition. Based on the decrease of the mean atomic volume with increasing As content in the As-rich glasses, an increase of bulk modulus is expected, while it is seen that the bulk moduli of these glasses have decreased (figure 5).

In Ge-Sb-S and Ge-Sb-Se systems (Hayes *et al* 1974; Hilton and Hayes 1975; Sudha Mahadevan *et al* 1983) the Poisson's ratio ( $\sigma$ ) increases with increasing chalcogen content. As  $\sigma$  denotes the ratio of transverse to longitudinal strains which arise from a single tensile stress, its increase with increasing chalcogen content has been attributed to a change in glass structure from an essentially network to a chain-like form (Hilton and Hayes 1975). However, in the  $As_xSb_{15}Se_{85-x}$  glasses studied presently,  $\sigma$  exhibits a maximum for the stoichiometric composition and there is a decrease of  $\sigma$  for the Se-rich glasses in contrast to the expected increase.

The chemically-ordered network model (CONM) wherein the maximum number of

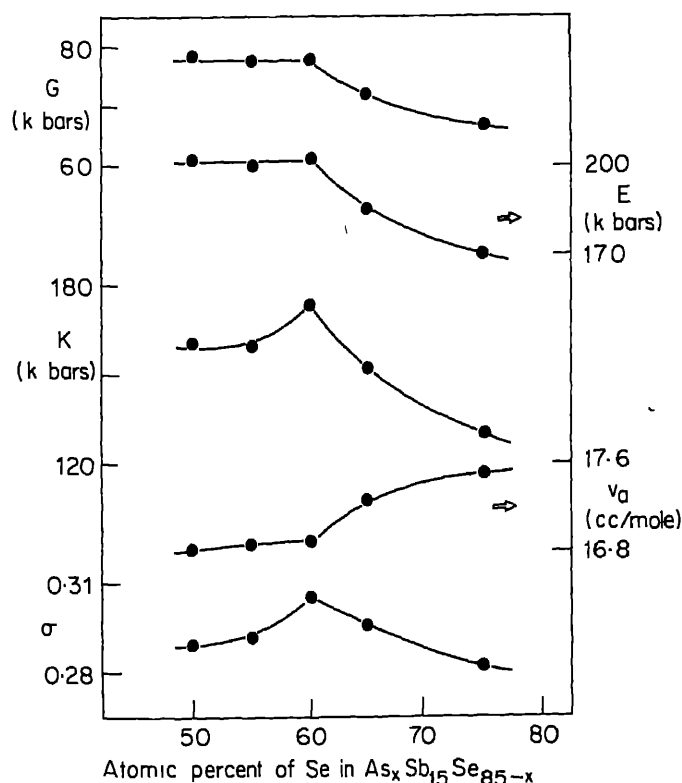


Figure 5. Variation of elastic moduli and mean atomic volume with composition for  $As_xSb_{15}Se_{85-x}$  glasses.

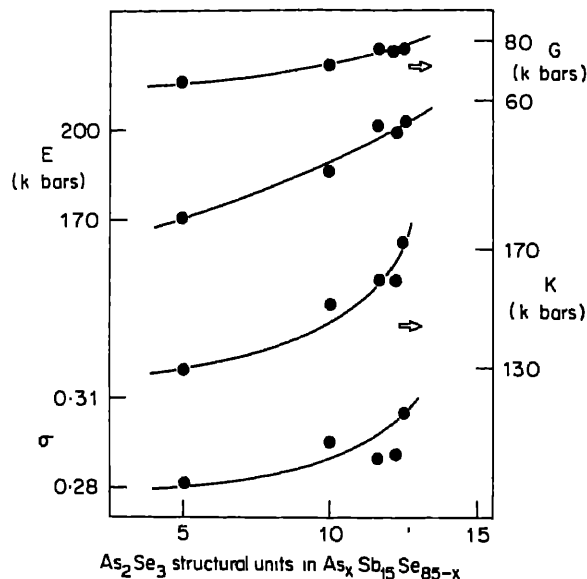


Figure 6. Dependence of elastic moduli on the  $As_2Se_3$  structural units in  $As_xSb_{15}Se_{85-x}$  glasses.

heteropolar bonds are formed first and the remaining part of the valence requirement is met with by homopolar bonding at random accounted satisfactorily for the composition dependence of the density of these glasses (Giridhar and Sudha Mahadevan 1982). For a correlation of the elastic properties with composition, the results were examined using the CONM model. A close study of the glass compositions in view of the results of figure 5 indicates the importance of  $As_2Se_3$  content (*i.e.* As-Se bonds) in determining the elastic properties of these glasses, as the observed features in the composition dependence of  $K$  and  $\sigma$  can be linked to the  $As_2Se_3$  content in these glasses. It can be seen (figure 6) that the moduli do show in general an increase with increasing  $As_2Se_3$  content in the glasses. Though scatter in the points is seen in the dependence of the moduli on the  $As_2Se_3$  content (figure 6), the increase in these quantities is obvious.

#### 4. Conclusions

Elastic moduli of  $(As, Sb)_{40}Se_{60}$  glasses decrease monotonically with decreasing  $As_2Se_3$  content in the glasses.

In the  $As_xSb_{15}Se_{85-x}$  glasses, with the  $As_{25}Sb_{15}Se_{60}$  glass as reference, the shear and Young's modulus of As-rich glasses do not vary much with the composition, while those of the Se-rich glasses decrease with increasing Se content. The bulk modulus and the Poisson's ratio of these glasses exhibit a maximum at the stoichiometric composition. An examination of the results indicates that the elastic properties of these glasses are sensitive to the  $As_2Se_3$  content in these glasses.

## References

- Anderson O L and Nafe J E 1965 *J. Geophys. Res.* **70** 3951  
Giridhar A, Narasimham P S L and Sudha Mahadevan 1981 *J. Non-Cryst. Solids* **43** 29  
Giridhar A and Sudha Mahadevan 1982 *J. Non-Cryst. Solids* **51** 305  
Hayes D J, Rehtin M D and Hilton A R 1974 *Ultrasonics Symp. Proc.* p. 502 (ed.) De Klerk, Institution of Electrical and Electronics Engineers, New York  
Hilton A R and Hayes D J 1975 *J. Non-Cryst. Solids* **17** 339  
McSkimin H J 1961 *J. Acoust. Soc. Am.* **33** 12  
McSkimin H J and Andreatch P 1962 *J. Acoust. Soc. Am.* **34** 609  
Mohan R, Panchapakesan T S and Rao K J 1981 *Bull. Mater. Sci.* **3** 29  
Myers M B and Felty E J 1967 *Mater. Res. Bull.* **2** 535  
Narasimham P S L, Giridhar A and Sudha Mahadevan 1981 *J. Non-Cryst. Solids* **43** 365  
Soga N and Kunugi M 1973 *J. Phys. Chem. Solids* **34** 2143  
Sudha Mahadevan, Giridhar A and Singh A K 1983 *J. Non-Cryst. Solids* **57** 423  
Thompson J C and Bailey K E 1978 *J. Non-Cryst. Solids* **27** 161

11/11/11

11/11/11

11/11/11

11/11/11

11/11/11

11/11/11

11/11/11

11/11/11

11/11/11

11/11/11

11/11/11

11/11/11

11/11/11

11/11/11

11/11/11

11/11/11

11/11/11

11/11/11

11/11/11

11/11/11

11/11/11

11/11/11

11/11/11

11/11/11

11/11/11

11/11/11

11/11/11

11/11/11

11/11/11

11/11/11

11/11/11

11/11/11

11/11/11

11/11/11

11/11/11

11/11/11

11/11/11

11/11/11

11/11/11

11/11/11

11/11/11

11/11/11

11/11/11

11/11/11

11/11/11

11/11/11

11/11/11

11/11/11

11/11/11

11/11/11

11/11/11

11/11/11

11/11/11

11/11/11

11/11/11

11/11/11

11/11/11

11/11/11

11/11/11

11/11/11

11/11/11

11/11/11

11/11/11

11/11/11

## DC electrical conductivity of $\text{Na}_2\text{O-ZnO-B}_2\text{O}_3$ glass system

R V ANAVEKAR, N DEVARAJ and J RAMAKRISHNA\*

Department of Physics, Bangalore University, Bangalore 560 001, India

\*Department of Physics, Indian Institute of Science, Bangalore 560 012, India

MS received 12 December 1983

**Abstract.** The d.c. electrical conductivity of  $\text{Na}_2\text{O-ZnO-B}_2\text{O}_3$  glass system has been measured as a function of temperature in the range of 350–600°K. The conductivity data show that the activation energy of  $\text{Na}^+$  ions is dependent on ZnO concentration. The results have been discussed in the light of the cluster model of glasses.

**Keywords.**  $\text{Na}_2\text{O-ZnO-B}_2\text{O}_3$  glass; electrical conductivity; density; activation energy.

### 1. Introduction

It is well known that glasses containing alkali ions are essentially solid cationic electrolytes, the current being carried by relatively mobile alkali ions. The motion of alkali ions in glasses is important, not only because of its relation to electrical conductivity, but also to chemical durability and to ion exchange kinetics. Similar work has been earlier reported on binary silicate and binary borate glasses. Some studies on borate glasses containing two different alkali oxides and alkali-alkaline earth oxides have also been reported (Israd 1969; Erzukeyan 1969; Day 1976; Sakka *et al* 1979; Mutusita *et al* 1980). In the present work we report the d.c. electrical conductivity of sodium borate glasses with different concentrations of ZnO. The behaviour of activation energy of  $\text{Na}^+$  ions has been discussed on the basis of the cluster model of glasses (Rao and Rao 1982).

### 2. Experimental

Analytical grade chemicals were used to prepare glasses corresponding to their glass-forming region (Rawson 1967). Appropriate quantities of boric acid ( $\text{H}_3\text{BO}_3$ ), sodium carbonate ( $\text{Na}_2\text{CO}_3$ ) and zinc oxide (ZnO) were taken and melted in a crucible at 1100°C for about 2 hr. The melt was then poured on a brass-block and it was quickly pressed with a polished copper-block. The glasses formed were annealed at about 400°C for 2 hr. X-ray studies showed that the glasses were amorphous. Samples of dimensions ( $\sim 20 \times 20 \times 2$  mm) suitable for the measurement of electrical conductivity were prepared by grinding and polishing (using rough powder) the two flat surfaces. Silver paint was applied to these flat surfaces to serve as electrodes.

Measurements were made with glasses of the compositions listed in table 1. To measure the resistance of the samples, a special sample holder was designed following Mahadevan *et al* (1977). The resistance of the samples was determined by measuring the



**Table 1.** Glass composition, density and activation energy ( $E_a$ ).

Mol% composition			Density (gm/cm <sup>3</sup> )	Activation energy (eV)	
Na <sub>2</sub> O	ZnO	B <sub>2</sub> O <sub>3</sub>		(600–500) °K	(500–400) °K
10	5	85	2.04	0.77	—
10	10	80	2.49	0.97	0.15
10	15	75	2.60	0.95	0.17

current through the sample for an applied voltage (25 V); the voltage was briefly applied to avoid polarization. The temperature was measured with a chromel-alumel thermocouple placed very close to the sample. The d.c. electrical conductivity was measured as a function of temperature over the range 350–600°K. Density was also measured by the Archimedes method using benzene and the values are given in table 1.

### 3. Results and discussion

The variation of the d.c. electrical conductivity as a function of  $1/T$  for three different compositions is shown in figure 1. The activation energies are calculated from the Arrhenius equation;

$$\sigma = \sigma_0 \exp\left(\frac{-E_a}{kT}\right)$$

where  $\sigma_0$  is the pre-exponential factor,  $E_a$  is the activation energy for conduction and  $k$  is the Boltzmann constant. The variation of  $E_a$  as a function of ZnO concentration is shown in figure 2. The values of activation energy obtained are shown in table 1. The conductivity behaviour in figure 1 shows that the glass with 5 mol% ZnO has a single activation barrier and also has a higher conductivity, while the glass with 10 and 15 mol% ZnO has two conductivity regions and lower overall conductivity. In order to understand the behaviour of  $\ln \sigma$  in figure 1, we note the following features about borate glasses.

In borate glasses the principal structural elements present are boroxol, tetraborate and diborate groups. The diborate groups get converted into triborate and pentaborate units. In the glasses investigated here the extent of any such borate grouping which consist of tetrahedral borons depends upon the total quantity of added oxides ( $\text{Na}_2\text{O} + \text{ZnO}$ ). In order to investigate the role of  $\text{Zn}^{2+}$  ion in these glasses, we note that the  $e/r^+$  ratio (2.7) is quite high. It is likely that it acts as a network former, particularly in low  $\text{Zn}^{2+}$  concentration. Such  $\text{Zn}^{2+}$  positions in the network also help in cross-linking the borate chains.  $\text{Zn}^{2+}$  ions in such situations can modify the diborate groups into more open rings without affecting the extent of tetrahedral borons (Selvaraj and Rao 1983). However at higher concentrations  $\text{Zn}^{2+}$  ions act as network modifiers and may ultimately lead to phase separation. In glasses containing 5 mol% ZnO, therefore,  $\ln \sigma$  variation as a function of  $1/T$  is linear. Addition of 5 mol% ZnO is unlikely to cause any phase separation. The activation energy of  $\text{Na}^+$  ions (0.77 eV) may be compared with that of (0.60 eV) 10 mol%  $\text{Na}_2\text{O}$ -90 mol%  $\text{B}_2\text{O}_3$  glass (Chakravorty and Chakraborti 1980). This may perhaps reflect the fact that incorporation of  $\text{Zn}^{2+}$

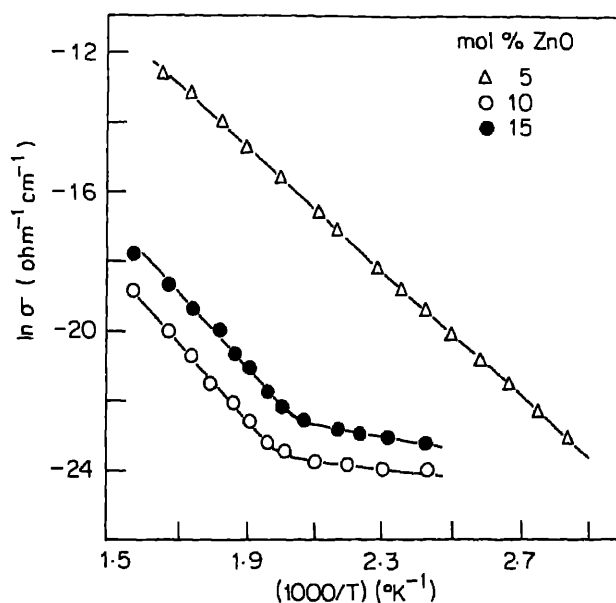


Figure 1. Variation of d.c. conductivity with temperature.

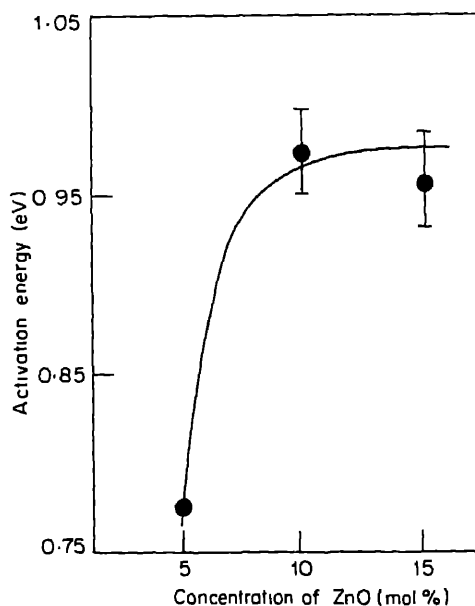


Figure 2. Variation of activation energy with concentration of ZnO.

into cross-linking positions increases the cohesion and density, thereby increasing the activation barrier for migration of  $\text{Na}^+$  ions. In samples with 10 mol % ZnO and 15 mol % ZnO there appears to be two regions of conductivity (figure 1) characterized by two values of activation energy ( $E_a$ ). This possibly indicates the presence of two distinct regions which act as precursors to phase separations. We feel that the two

phases correspond to oxide-poor and oxide-rich regions (oxide representing the total quantity of  $\text{Na}_2\text{O}$  and  $\text{ZnO}$ ). The oxide-poor region can be expected to be less dense with lower  $E_a$  and lower conductivity (low concentration of charge carriers and perhaps even low mobility). The oxide-rich region corresponds to high  $E_a$  and high conductivity. The charge carriers being primarily  $\text{Na}^+$  ions, one can see that the conductivity is slightly lower for lower effective concentration of  $\text{Na}^+$  ions. The activation barriers for both glasses (10 mol% and 15 mol%  $\text{ZnO}$ ) are virtually constant (figure 2) which should be the case if conduction is mainly by the oxide-rich region and hence we find that the results support a two-region model for these glasses.

The two-region model is essentially a cluster model recently described by Rao and Rao (1982). The more ordered cluster region is likely to be an oxide-rich region while the oxide-poor region corresponds to the tissue (less order) region. Indeed  $\text{AgI-Ag}_2\text{O-MoO}_3$  glasses (Senapati *et al*, private communication) also exhibit such two-region conductivity behaviour in accordance with the cluster model of glasses. In 5 mol%  $\text{ZnO}$  glass, the regions are not sufficiently differentiated to exhibit two-region conductivity at high temperatures; it is likely to be seen in low temperature measurements.

### Acknowledgements

The authors (RVA and ND) express their thanks to Prof. P Paramasivaiah for his interest and encouragement and to Prof. K J Rao of IISc., Bangalore for many useful discussions.

### References

- Chakravorty D and Chakraborti S 1980 *J. Non-Cryst. Solids* **38 and 39** 295
- Day D E 1976 *J. Non-Cryst. Solids* **21** 343
- Erzukyran E 1969 *Arm. Khim. Zh.* **22** 109
- Israd J O 1969 *J. Non-Cryst. Solids* **1** 235
- Mahadevan S, Giridhar A and Rao K J 1977 *J. Phys.* **C10** 4499
- Mutusita K, Takayama S and Sakka S 1980 *J. Non-Cryst. Solids* **40** 149
- Rao K J and Rao C N R 1982 *Mater. Res. Bull.* **17** 1337
- Rawson H 1967 *Inorganic glass-forming system* (New York: Academic Press) pp. 97
- Sakka S, Mutusita K and Kimiya K 1979 *Phys. Chem. Glasses* **20** 25
- Selvaraj U and Rao K J 1983 *Spectra. Chim. Acta.* (communicated)
- Senapati H, Parthasarathi G and Rao K J (Private communication)

## Photon, electron and ion beam induced physical and optical densification in chalcogenide films

K L CHOPRA, L K MALHOTRA, K SOLOMON  
HARSHAVARDHAN and S RAJAGOPALAN

Department of Physics, Indian Institute of Technology, New Delhi 110016, India

MS received 10 October 1983

**Abstract.** Irradiation of 80° deposited Se-Ge films with band gap photons, 8 keV electrons and 50 keV He<sup>+</sup> ions produces, primarily irreversible red shift of the absorption edge and major changes in doping and electrochemical adsorption processes. These changes have been attributed predominantly to the radiation-induced thickness and hence volume contraction resulting due to the physical collapse of the low density columnar microstructure of the obliquely deposited films. The far IR and Urbach tail studies reveal an enhanced strength of electron-phonon coupling, in obliquely deposited films having a very porous columnar microstructure, compared to normally deposited films. It has been shown that this enhanced electron phonon coupling is conducive to large thickness contraction and associated changes. These changes have been used in reprographic and lithographic applications. A correlation has been established between the thickness contraction and lithographic parameters. The possibility of generating both positive and negative relief patterns on the same film by controlling the etching time has been demonstrated.

**Keywords.** Chalcogenide films; optical densification.

### 1. Introduction

Thin films of amorphous Se-Ge have been shown to behave as inorganic resists for visible, uv and deep uv light as well as electron beam and ion beam exposures and possess many advantages over the conventional organic resists currently in use (Yoshikawa *et al* 1976, 1977, 1980; Tai *et al* 1979; Balasubramanyam *et al* 1981; Venkatesan 1981). Using the light, electron beam or ion beam induced doping, or the darkening effects, both negative and positive type resists can be realized. Extensive studies carried out in our laboratory have shown that very large thickness and hence volume contraction (physical densification) takes place in Se<sub>75</sub>Ge<sub>25</sub> films deposited at 80° incidence and exposed to photons, electrons or ions (Singh *et al* 1979, 1980a; Chopra *et al* 1981, 1982). The thickness contraction results in a much larger darkening in these films, compared to that obtained on exposure of films deposited at normal incidence. Thickness contraction occurs also when Se<sub>75</sub>Ge<sub>25</sub> films overcoated with a very thin (100–200 Å) layer of a metal, such as Ag, are irradiated. This affects the doping of Ag into the chalcogenide film. Both the positive and negative resist behaviour of the obliquely deposited films are expected to be different from that of the normal incidence films and to be correlated with the thickness contraction resulting in these films on irradiation. In the present study, we have examined this correlation and utilized it to (a) yield a better lithographic sensitivity and contrast, both for the negative and positive resist behaviour, and (b) obtain both positive and negative resist characteristics in the same film.

## 2. Experimental

The experimental details for vacuum deposition of amorphous Se-Ge films are the same as reported earlier (Singh *et al* 1979; Rajagopalan *et al* 1979). The films were masked with a sharp edge and exposed to photons and ions. A 250 W mercury vapour lamp with an intensity of 30 mW/cm<sup>2</sup> was used for band gap photon illumination. Ion (He<sup>+</sup>) irradiation was carried out with a 50 keV ion beam, using an ion accelerator (Sames J-15) in a vacuum of 10<sup>-7</sup> torr, at room temperature. No ion sputtering or deformation of the film occurred during irradiation. The films were irradiated with an 8 keV, 0.2  $\mu$ m diameter electron beam (PHI 590-A Super SAM instrument) for electron beam exposures. The thickness contraction was determined by measuring the thickness difference between the exposed/irradiated and the unexposed/unirradiated regions with the help of Talystep and then normalized against the original starting thickness of the as-deposited film.

For studying the negative resist behaviour, thin layers of Ag and Cu, (about 200 Å thick), were deposited on the as-prepared Se-Ge films by electrochemical adsorption (dipping in 0.025 M AgNO<sub>3</sub> 1 M CuSO<sub>4</sub> respectively) as well as by thermal evaporation. The resulting metal-Se-Ge films were then irradiated with photons, electrons and ions in the same way as described above and the thickness contraction was determined. The chemical dissolution rates of the films, with and without the metal overlayer, were determined by developing the films in 0.25 M NH<sub>4</sub>OH solution.

## 3. Results and discussion

A comparison of the thickness contraction brought about by the irradiation of the 80°-deposited Se<sub>75</sub>Ge<sub>25</sub> films by photons, electrons and ions is shown in figure 1. A

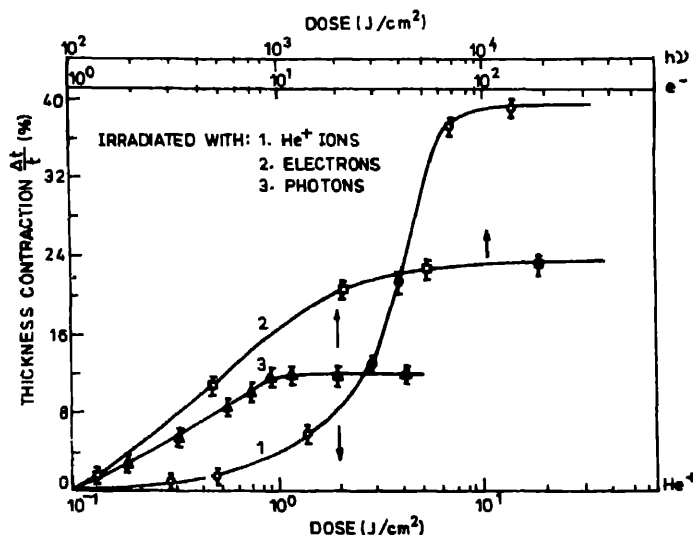


Figure 1. Thickness contraction as a function of incident flux for photon, electron and ion beam-irradiated 80°-Se<sub>75</sub>Ge<sub>25</sub> films.

comparison of the incident energy reveals that ions are more effective in bringing about contraction followed by electrons and then photons. It may be pointed out that calculations of projected range and range straggling for  $\text{He}^+$  ions in  $\text{Se}_{75}\text{Ge}_{25}$  film show that there is no ion implantation in the film since the film thickness is smaller than the projected range.

The as-deposited Se-Ge films dissolve readily in an alkaline solution. The solubility is increased on irradiation. For  $\text{Se}_{75}\text{Ge}_{25}$  films deposited at normal incidence, the increase in the solubility is rather small and hence not a very useful effect. The large thickness contraction occurring in  $80^\circ$  films leads to large microstructural changes which in turn increases the solubility difference between the irradiated (contracted) and unirradiated regions (Singh *et al* 1980b). The dissolution rates can be obtained from figure 2 which shows the normalized remaining thickness *vs* normalized etching time (i.e. the time taken to remove a certain thickness of an irradiated or a virgin film divided by the total time taken for the complete removal of the irradiated or the virgin film) for an as-deposited and irradiated (with ions, electrons and photons)  $\text{Se}_{75}\text{Ge}_{25}$  film. Two kinds of etching selectivity are obtained as a function of the etching time. In the initial stages of etching, the unexposed regions etch faster than the exposed regions, i.e., a negative resist behaviour is obtained even without the use of an overlayer metal. The etching behaviour changes to a positive resist type (exposed portion dissolving faster than the unexposed portion) after a certain etching time which is higher for photons and comparatively much lower for electrons and ions. If the etching is stopped when the exposed or irradiated portion has been completely etched off, the fractional final thickness remaining in the unirradiated or unexposed portion is about 88% for the ion irradiated, 78% for electron irradiated and 33% for photon irradiated films. A comparison of this data with that reported by earlier workers reveals that a much higher remaining thickness is obtained by us (Yoshikawa *et al* 1976, 1977; Tai *et al* 1979;

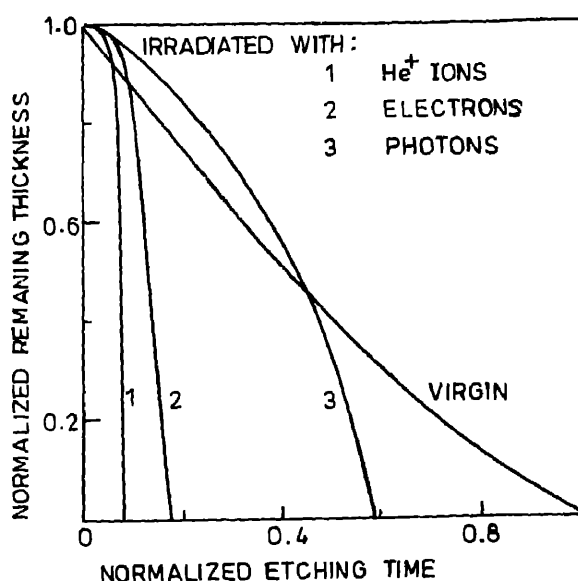


Figure 2. Normalized remaining thickness *vs* normalized etching time for a virgin and irradiated (with ions, electrons and photons)  $80^\circ\text{-Se}_{75}\text{Ge}_{25}$  films.

Balasubramanyam *et al* 1981; Venkatesan 1981). Thus the value of 33% obtained in photon-irradiated films in the present case is much higher than 13% reported by Yoshikawa *et al* (1976), in normal incidence  $\text{Se}_{75}\text{Ge}_{25}$  films obtained by sputtering. The difference can be attributed to the large thickness contraction obtained in the  $80^\circ$  films and absent in normal incidence films. Similarly, the large value of 88% in the ion-irradiated case obtained in the present study is much higher than 58% reported by Balasubramanyam *et al* (1981), on obliquely deposited films of the same material possibly due to the larger thickness contraction in our films resulting from the use of heavier  $\text{He}^+$  ions. Thus, a control of etching time can permit both positive and negative relief patterns to be generated on the same film.

Figure 3 shows the normalized remaining thickness *vs* ion dosage corresponding to an etching time just sufficient for the complete removal of the exposed portion. As mentioned above; a very large selective etching of 88% has been obtained. A contrast ( $\gamma$ ) of 4.5 and sensitivity ( $S$ )  $\sim 10^{-4} \text{ C/cm}^2$  have been obtained. Though the sensitivity is lower than the conventional organic resists, the large selective etching and a reasonably good value of contrast make the films suitable for positive resist applications. Typical values of the lithographic parameters for positive resist applications for different radiations are listed in table 1.

Negative resist characteristics are obtained when the films with an overlayer of Ag or Cu are irradiated with ions, electrons or photons. Figure 3 shows our results on the negative resist characteristics for  $\text{He}^+$  irradiated Se-Ge films with an overlayer of Ag. A sensitivity  $\sim 1.4 \times 10^{-5} \text{ C/cm}^2$  and a contrast of 8.3 have been obtained. The negative resist characteristics for different radiations obtained by this process are also listed in table 1. The high value of contrast should produce a high intrinsic resolution in these films for ion beam lithographic applications. Submicron lithographic patterns have been generated by us and other workers routinely (Balasubramanyam *et al* 1981; Venkatesan 1981; Chopra *et al* 1982).

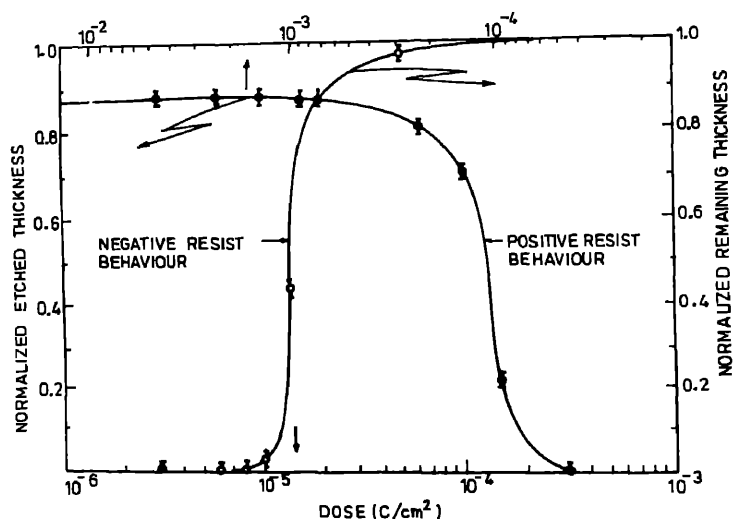
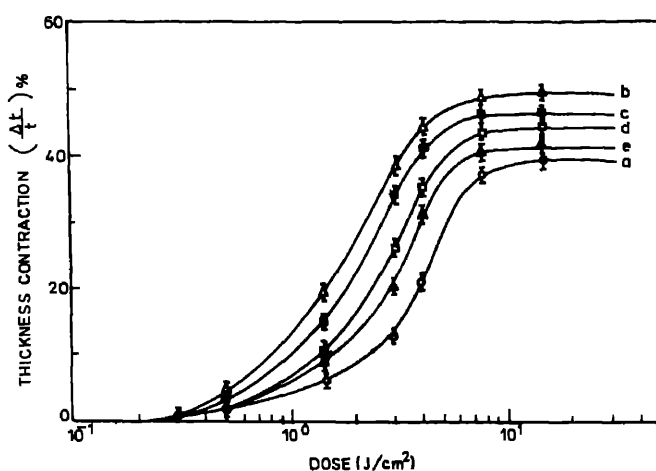


Figure 3. Positive and negative resist characteristics of  $80^\circ$ - $\text{Se}_{75}\text{Ge}_{25}$  films subjected to  $\text{He}^+$  irradiation.

**Table 1.** Lithographic parameters (sensitivity,  $S$ , and contrast,  $\gamma$ ) for different radiations for  $80^\circ\text{-Se}_{7.5}\text{Ge}_{2.5}$  films.

Radiation	As-positive resist		As-negative resist	
	$S$	$\gamma$	$S$	$\gamma$
$\text{He}^+$ ions	$\sim 1.2 \times 10^{-4} \text{ C/cm}^2$	4.5	$\sim 1.6 \times 10^{-5} \text{ C/cm}^2$	8.3
Electrons	$\sim 8 \times 10^{-4} \text{ C/cm}^2$	4	$\sim 1 \times 10^{-4} \text{ C/cm}^2$	7.6
Band gap photons	$\sim 10^{20} \text{ photons/cm}^2$	1.7	$\sim 10^{19} \text{ photons/cm}^2$	3.5

**Figure 4.** Thickness contraction as a function of ion dosage for: a. as-deposited, b. as-deposited with an overlayer of electrochemically adsorbed Ag, c. as-deposited with an overlayer of evaporated Ag, d. as-deposited with an overlayer of electrochemically adsorbed Cu, and e. as-deposited with an overlayer of evaporated Cu.

Our studies show that the thickness contraction plays an important rôle in the negative resist action in the obliquely deposited films. Figure 4 shows the thickness contraction as a function of ion dosage for: (a) as-deposited, (b) as-deposited with an overlayer of electrochemically adsorbed Ag, (c) as-deposited with an overlayer of evaporated Ag, (d) as-deposited with an overlayer of electrochemically adsorbed Cu, and (e) as-deposited with an overlayer of evaporated Cu. It is noteworthy that the thickness contraction is larger in a film having an overlayer of a metal than in one without an overlayer. The improved negative resist characteristics in obliquely deposited films is therefore a direct consequence of enhanced thickness contraction.

### Acknowledgements

The authors are grateful to Mr A K Tyagi of RRC Kalpakkam, for ion irradiation and Miss M Rajeswari for assistance. The financial aid from the Electronics Commission, Government of India, is gratefully acknowledged.



**References**

- Balasubramanyam K, Karapiperis L K, Lee C A and Ruoff A L 1981 *J. Vac. Sci. Technol.* **19** 1
- Chopra K L, Harshavardhan K S, Rajagopalan S and Malhotra L K 1981 *Solid State Commun.* **40** 387
- Chopra K L, Harshavardhan K S, Rajagopalan S and Malhotra L K 1982 *Appl. Phys. Lett.* **40** 428
- Rajagopalan S, Singh B, Bhat P K, Pandya D K and Chopra K L 1979 *J. Appl. Phys.* **50** 1
- Singh B, Rajagopalan S, Bhat P K, Pandya D K and Chopra K L 1979 *Solid State Commun.* **29** 167
- Singh B, Rajagopalan S, Bhat P K, Pandya D K and Chopra K L 1980a *J. Non-Cryst. Solids* **35-36** 1053
- Singh B, Rajagopalan S and Chopra K L 1980b *J. Appl. Phys.* **51** 1768
- Tai K L, Sinclair W R, Vadimsky R G, Moran J M and Rand M J 1979 *J. Vac. Sci. Technol.* **16** 1977
- Venkatesan T 1981 *J. Vac. Sci. Technol.* **19** 1368.
- Yoshikawa A, Ochi O, Nagai H and Mizushima Y 1976 *Appl. Phys. Lett.* **29** 10
- Yoshikawa A, Ochi O, Nagai H and Mizushima Y 1977 *Appl. Phys. Lett.* **31** 3
- Yoshikawa A, Ochi O and Mizushima Y 1980 *Appl. Phys. Lett.* **36** 107

## Oxidation of thin films of tin at room temperature in hydrogen sulphide atmosphere

C I MUNEERA and V UNNIKRISHNAN NAYAR

Department of Physics, University of Kerala, Kariavattom, Trivandrum 695 581, India

**Abstract.** The oxidation of thin films of tin at room temperature in an atmosphere containing 10%  $H_2S$  and 90% air has been studied by measuring the changes in resistance of thin films. Morphological studies have also been carried out using optical and scanning electron microscopes. Reaction kinetics change from logarithmic law at ordinary atmospheres to a power law in the presence of  $H_2S$ . The basis of formation of sulphide along with the oxide is explained, the former growing on a lower layer and the latter on an upper layer.

**Keywords.** Oxidation; tin; hydrogen sulphide; thin films; resistance change.

### 1. Introduction

Hydrogen sulphide is a naturally occurring gas forming part of the sulphur-cycle (Minster 1963). Owing to its highly corrosive nature,  $H_2S$  testing on metals and alloys is of industrial importance. Tin is a metal of widespread use in external atmosphere mainly as a sacrificial coating on metals. Extensive studies on the oxidation of tin have been carried out by Boggs and coworkers (Boggs *et al* 1961a, b, 1963, 1964a; Boggs 1961c, 1964b). Chan duc Thiep *et al* 1977a, b employed the selective Mössbauer spectroscopy method to study the oxidation mechanism of thin films of tin deposited on glass. The formation of sulphur containing mixed films on tin was discussed by Gabe (1977). The present paper contains investigations about the effect of  $H_2S$  on the oxidation of thin films of tin at constant relative humidities ( $\approx 85\%$ ) and at room temperature ( $\approx 303$  K).

### 2. Experimental

The oxidation rate was followed by measuring the rate of increase of resistance of thin films (900 Å) of tin (99.999%) which had been evaporated on to optically plane glass substrates at room temperature. Thick electrode films of tin were previously deposited at the ends of the glass substrates, which were cleaned by chemical and ion-bombardment methods. All evaporations were carried out in a conventional vacuum line at pressures greater than  $10^{-5}$  torr. The films and electrodes were evaporated from a molybdenum boat.

After measuring the resistances, the films coated in the same pump-down were quickly transferred to an enclosed glass chamber (Muneera *et al* 1983) evacuated to a pressure of  $10^{-2}$  Torr. The required amount of air was then admitted into the chamber followed by 10% by volume of dry  $H_2S$  stored in a reservoir. The relative humidity inside the chamber was assessed using a dry and wet thermometer

assembly. Resistances of the films were measured at regular intervals for several hours using a vernier potentiometer of accuracy  $10^{-6}$  v. div $^{-1}$ . After about ten days, the films were taken out and photographed. Both optical and scanning electron microscopes were used to study the structure of the oxide films formed. Resistance could not be measured for longer periods due to the failure of metal contacts used for external connections. Studies with higher percentage of  $H_2S$  were also not possible because of the vigorous attack by the highly corrosive gas on the metal contacts used.

### 3. Results and discussion

The change in resistance of the thin film can be related to the oxide thickness (Hunt and Ritchie 1972). If the evaporated thin film is regarded as a thin isotropic metal sheet which oxidises on one surface only and obeys Ohm's law, then it follows that the film resistance  $R$  and the oxide thickness  $X$  are related by the equation

$$x = \frac{\phi \rho l}{\omega} \left( \frac{1}{R_0} - \frac{1}{R} \right), \quad (1)$$

where  $\phi$  is the thickness of the oxide, derived from unit thickness of metal,  $\rho$  is the resistivity of the metal film,  $l$  is the length of the film between contacts,  $\omega$  is the width of the film and  $R_0$  is the resistance of the film prior to oxidation. In deriving this equation it has been assumed that the resistivity of oxide formed is very much larger than that of the metal. This condition is satisfied in the present studies as the oxide and sulphide formed on the thin film of tin at room temperature are amorphous (Bound and Richards 1939; Hart 1952; Britton and Bright 1957; Boggs *et al* 1961b; Raymond and Donald 1955). From (1) it is clear that the oxide thickness  $x$  is proportional to  $-1/R$ .

The oxidation of tin at room temperature obeys a direct logarithmic rate law (Tamman and Köster 1922; Katz 1956; Britton and Bright 1957; Gabe 1977). With the introduction of 10%  $H_2S$ , the oxidation rate changed from a direct logarithmic law to a power law of the form

$$x^n = kt, \quad (2)$$

where  $x$  is the oxide thickness and  $k$  and  $n$  are constants. This is evident from the plot of  $\log 1/R$  vs  $\log t$  in figure 1.

The surface structures developed on the film after about ten days of exposure to  $H_2S$  + air atmosphere are shown in figures 2–8. There are two types of nucleation centres: the slightly large bright centres and the more distributed form of fine grains or powdery nuclei (figure 2). Some of the former grow into larger growth centres near the edges of the films (figures 3–5). They are different from the wheel-shaped or dendritic growth centres (Boggs *et al* 1961b; Muneera *et al* 1983) observed on films exposed to normal atmospheres (figures 9–10). Figure 6 shows the larger growth centre along with the other nucleation centres. Growth centres under different stages of growth are observed on the same specimen.

The various chemical reactions which can take place when the film is kept in an atmosphere containing 10%  $H_2S$  and 90% air are as given below (Boggs *et al*

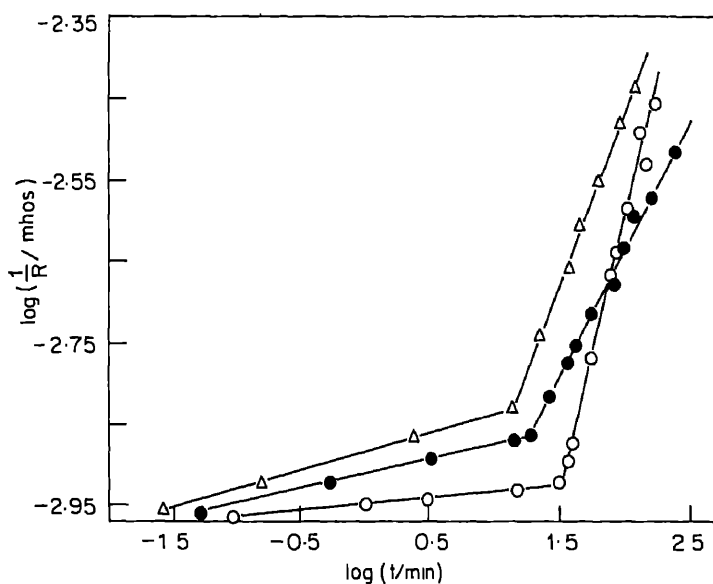


**Figure 1.** Plot of  $\log 1/R$  vs  $\log t$ . The oxidation rate for the initial period is different as observed usually.

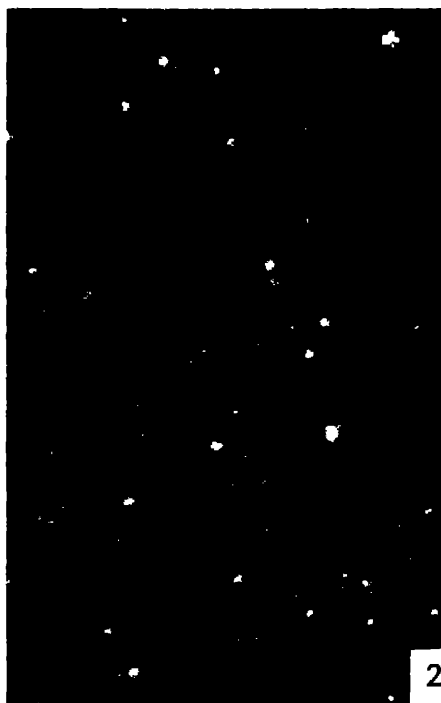


**Figure 2.** The two types of nucleation centres observed on a film kept in 10%  $H_2S$  + air atmosphere for about ten days ( $\times 220$ ).

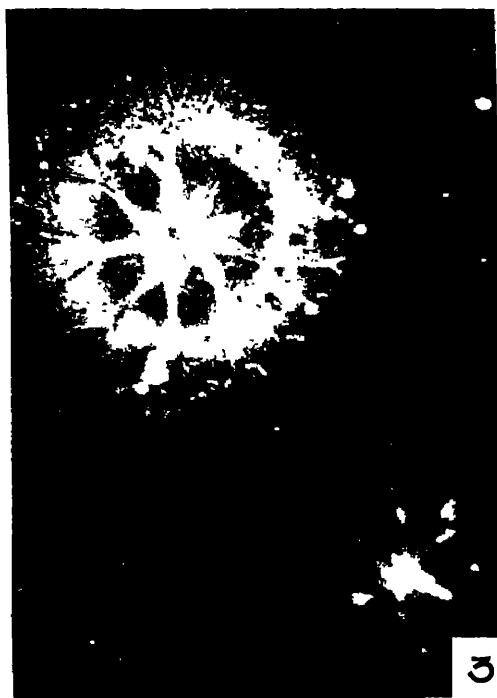
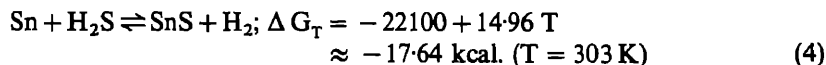
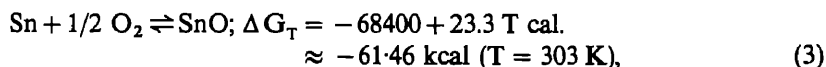


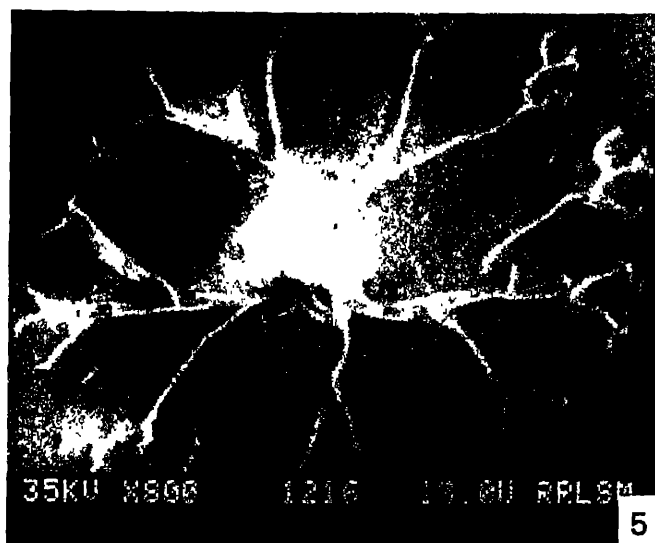
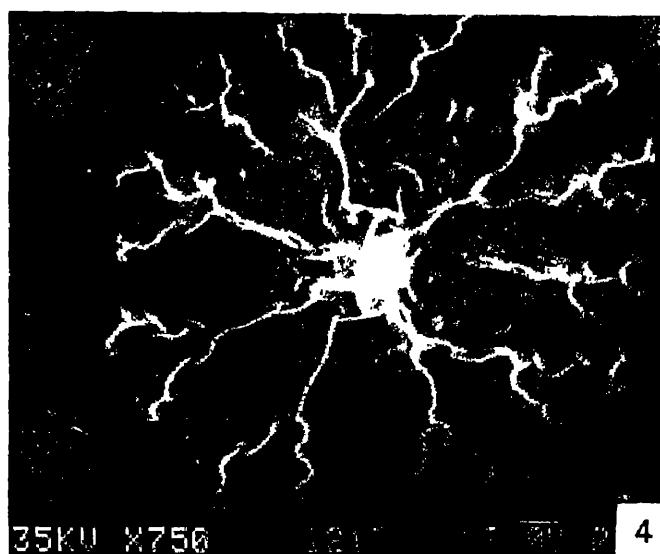
Figure 3. Optical micrograph of the wheel-shaped dendrites seen at the edges of the film ( $\times 480$ ).

1961 a,b,c; Gabe 1977). The relevant thermodynamical data are obtained from Kubaschewski *et al* (1967)



Thermodynamically the greater possibility of reaction is the one in which there is maximum decrease in free energy change. Thermodynamic equilibrium will not be attained for short periods of oxidation and at room temperature, the conditions under which the present studies are made. In such cases the reaction kinetics determine the possibility of occurrence of a particular chemical reaction. It has been reported that the oxide formed on tin at room temperature is SnO (Boggs *et al* 1961 a,b, 1963; Gabe 1977). Therefore considering the higher partial pressure of  $\text{O}_2$  (143.64 mm of Hg) and greater electron affinity of sulphur, both SnO and SnS are expected to form, although the free energy change associated with reaction (4) is less than that with reaction (3).

The oxidation of tin at room temperature takes place by the outward migration of cations (Boggs *et al* 1961). In the presence of 10%  $\text{H}_2\text{S}$  and 90% air, both hydrogen sulphide and oxygen are expected to be adsorbed on the surface. Because of the higher partial pressure of oxygen, it seems reasonable that SnO is formed first and grows by



Figures 4-5. SEM of the rosette-shaped dendrite in which the lower sulphide layer 4, also grows into branches following the upper oxide dendrites and 5, forms a circular bed for the radiating oxide dendrites.

outward migration of cations. From SEM and optical microscopic studies, it can be concluded that at sites where  $\text{SnO}$  grows into 'radially symmetric dendrites', the sulphide forms a layer beneath the oxide layer (figures 3-5). The oxide and sulphide together forms 'wheel-shaped' (figure 3) or 'rosette shaped' (figures 4-5) dendrites at these sites. Even at other sites where  $\text{SnO}$  forms comparatively smaller growth centres the powdery or fine-grain like  $\text{SnS}$  is observed on a lower layer (figures 2, 6). Therefore

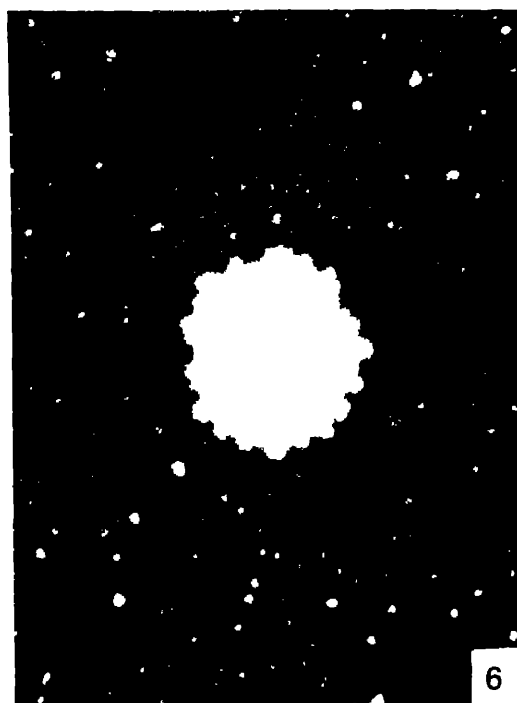


**Figure 6.** The larger growth centre along with the two types of nucleation centres ( $\times 220$ ).

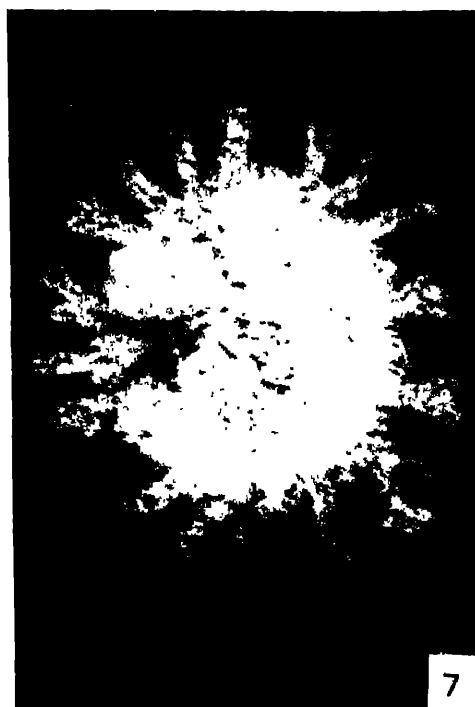


**Figure 7.** Optical micrograph of figure 4 under transmitted light showing podia-like extensions at the boundary ( $\times 540$ ).

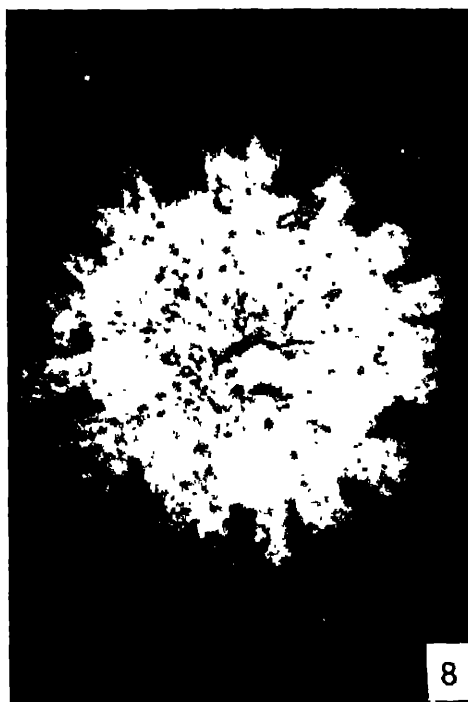


Figure 8. Later growth stage of a pattern similar to that shown in figure 7 ( $\times 500$ ).

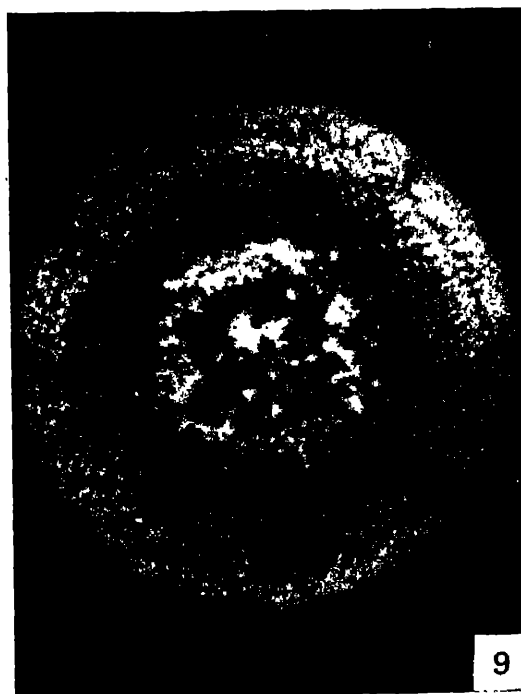
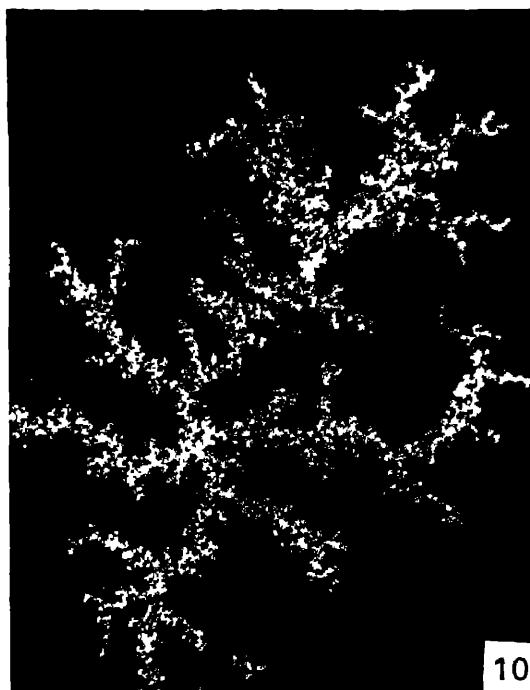


Figure 9. Wheel-shaped growth centre observed on a film kept in normal atmosphere ( $\times 1440$ ).





**Figure 10.** The dendritic growth of oxide observed on the film kept in normal atmosphere ( $\times 200$ ).

SnS is presumed to form between the metal and the oxide layer, *i.e.*, at the oxide-metal interface. It must grow by the inward migration of sulphur through the oxide layer reacting with cations and electrons at the sulphide-oxide interface. The presence of sulphur in the oxide remarkably enhances the cation diffusivity (Wooten and Birks 1972; Lawless 1974). The oxidation rate is therefore increased to that of a power law when 10%  $H_2S$  is introduced.

The radially symmetric dendrites may be formed in a way similar to that of the dendrites found at low oxygen pressures (Boggs *et al* 1961b). These structures are commonly observed near the edges of the films where the chance of finding high density of grain-boundaries is greater. Although the partial pressure of oxygen is considerably high, the presence of  $H_2S$  and the higher electron affinity of sulphur leads to an initial adsorbed layer of variable oxygen concentration. The 'wheel-shaped' or 'rosette shaped' dendrites grow laterally in radial directions (see the small growth centre in figure 3). The areas between adjacent primary branches become depleted in oxygen as oxygen in the adsorbed layer is consumed during the formation of radiating branches. These branches grow outward into areas richer in oxygen uniformly forming secondary and tertiary branches and a well-defined radially symmetric circular pattern is obtained. The sulphide layer also grows laterally forming a circular bed for the radiating dendrites (figure 5). In figure 3 the sulphide layer formed below the radially symmetric dendrite forms a rim at its boundary. In certain cases (figure 4) the sulphide layer also grows into branches following the oxide dendrites. When viewed under transmitted light using an

optical microscope, figure 4 appears as shown in figure 7. The distinction between oxide and sulphide layer is less clear in figure 7. At the boundary of the growth centre, the oxide and sulphide together form 'podia'-like extensions (figures 7, 8). The tips of the branches seem to have thickened. With further oxidation, the area between podia-like extensions get filled up gradually (figure 8).

#### 4. Conclusion

With the presence of 10%  $H_2S$ , the rate equation changes from a logarithmic law to a power law, indicating an increase in oxidation rate. This is explained on the basis of formation of sulphide along with the oxide, the former growing on a lower layer and the latter on the upper layer. The oxide and sulphide together forms 'wheel-shaped' or 'rosette-shaped' dendrites at the edges of the film.

#### References

- Boggs W E, Kachik R H and Pellissier G E 1961a *J. Electrochem. Soc.* **108** 6  
Boggs W E, Trosso P S and Pellissier G E 1961b *J. Electrochem. Soc.* **108** 13  
Boggs W E 1961c *J. Electrochem. Soc.* **108** 124  
Boggs W E, Kachik R H and Pellissier G E 1963 *J. Electrochem. Soc.* **110** 4  
Boggs W E, Kachik R H and Pellissier G E 1964a *J. Electrochem. Soc.* **111** 636  
Boggs W E 1964b *Br. Pat.* **963** 763  
Bound M and Richards D A 1939 *Proc. Phys. Soc. London* **51** 256  
Britton S C and Bright K 1957 *Metallurgia* **56** 163  
Chan duc Thiep, Ts. Bonchev, Mitrikov M, St. Peneva, Topalova K and Zukeva E 1977a *Bulg. J. Phys.* **4** 130  
Chan duc Thiep, Ts. Bonchev, Nguyen Chi Toa and St. Peneva 1977b *Bulg. J. Phys.* **4** 399  
Gabe D R 1977 *Surf. Technol.* **5** 463  
Hart R K 1952 *Proc. R. Soc. (London)* **B65** 955  
Hunt G L and Richie I M 1972 *J. Chem. Soc., Faraday Trans. I*, **68** 1413  
Katz W 1956 *Stahl Eisen* **76** 1672  
Kubaschewski O, LL Evas E and Alock C B (eds) 1967 *Metallurgical thermochemistry* (New York: Pergamon Press)  
Lawless K R 1974 *Rep. Prog. Phys.* **37** 231  
Minster J T 1963 *Nature (London)* **199** 474  
Muncera C I, Varghese S and Unnikrishnan Nayar V 1983 *Oxid. Met.* **19** 187  
Raymond E K and Donald F O (eds) 1955 *Kirk-Othmer encyclopedia of chemical technology* (New York: Interscience) vol. 14  
Tamman G and Köster W 1922 *Z. Anorg. U. Allegm. Chem.* **123** 196  
Wooten M R and Birks N 1972 *Corrosion Sci.* **12** 829

75 1 11

1 1 5

1 1 5

1 1 5

1 1 5

1 1 5

1 1 5

1 1 5

1 1 5

1 1 5

1 1 5

1 1 5

1 1 5

1 1 5

1 1 5

1 1 5

1 1 5

1 1 5

1 1 5

## Annealing behaviour of electron-beam deposited tin dioxide films

ARJEESH GUPTA, POONAM GUPTA and V K SRIVASTAVA

Department of Physics, University of Roorkee, Roorkee 247 672, India

MS received 23 November 1983; revised 31 March 1984

**Abstract.** The sheet resistivity of tin dioxide films deposited by electron-beam evaporation has been studied during annealing, both as a function of time and temperature. The annealing behaviour of  $\text{SnO}_2$  films under the above two different conditions is consistent. A qualitative interpretation has been given for the decrease and the minimum observed in the resistivity. The increase in resistivity has been confirmed by scanning-electron micrographs. The films were also characterized by x-ray diffractometry.

**Keywords.** Tin dioxide films; electron beam evaporation; annealing behaviour; sheet resistivity.

### 1. Introduction

Thin transparent conducting films of  $\text{SnO}_2$ , because of their wide application in solar cells, have currently become a subject of intense investigation. The  $\text{SnO}_2$  film is a transparent conductor which is sometimes known as Nesa glass (Ishiguro *et al* 1958). The optical and electrical properties of  $\text{SnO}_2$  films were studied by Arai (1960) who found them to be polycrystalline *n*-type degenerate semiconductor with a free carrier density of  $7 \times 10^{18}$ – $1.7 \times 10^{19} \text{ cm}^{-3}$  and an energy band gap of about 3.5 eV. The change in the conductivity of the material ( $\text{SnO}_2$ ) in thin films as compared to that in bulk arises due to anion oxygen defects.

It is known (Raccanelli and Madalena 1976; Viscrion and Georgescu 1969; Shanthi *et al* 1980) that post-annealing treatment of  $\text{SnO}_2$  films can result in change of electrical properties. It has recently been reported (Ghosh *et al* 1978; Nagatoma *et al* 1979) that the annealing of  $\text{SnO}_2$  films plays an important role in the improvement of the performance characteristics of  $\text{SnO}_2/\text{Si}$  solar cells. It has been found that on annealing the resistivity of pure  $\text{SnO}_2$  single crystals reduces and that of the  $\text{SnO}_2$  films deposited by hydrolysis of an ether-alcohol solution of  $\text{Sn}(\text{OC}_2\text{H}_5)_4$  first decreases and then increases drastically on annealing at temperatures higher than 500°K (Jarzebeski 1976). But no satisfactory explanation is available for the phenomenon.

As far as the authors are aware, investigations on the annealing behaviour of electron beam deposited  $\text{SnO}_2$  film, which are important in solar cells, have not been reported. The present work was therefore undertaken.

### 2. Experimental

#### 2.1 Sample preparation

$\text{SnO}_2$  films were prepared by electron-beam evaporation at a pressure  $\sim 10^{-6}$  torr. Undoped  $\text{SnO}_2$  (99.90%) was evaporated by an electron-beam gun onto chemically

cleaned glass substrates at room temperature (300°K). An evaporation rate of  $4 \text{ \AA sec}^{-1}$  was maintained to produce films of  $\text{SnO}_2$  with approximately uniform thickness of about 1300 Å. The thickness of the films was measured during evaporation by a quartz crystal thickness monitor and also by the interferometry method.

## 2.2 Resistivity measurement

The resistivity of the films was measured in a furnace during annealing as a function of time. The temperature of the furnace was maintained constant ( $\pm 5^\circ\text{C}$ ). The sheet resistivity of  $\text{SnO}_2$  films was also measured during annealing as a function of temperature in the range (623–808 K). The temperature of the furnace was regulated at approximately  $3^\circ\text{C/min}$ . The temperature was measured with a chromel-alumel thermocouple. X-ray diffraction measurements of the films were made (Philips x-ray diffractometer, model No. PW-1140/90) and scanning electron micrographs taken (SEM-501, Philips make).

## 3. Results and discussion

The sheet resistivity of the as-deposited  $\text{SnO}_2$  films was very high ( $> 20 \text{ M}\Omega$ ) and decreased with annealing in air. The variation of sheet resistivity as a function of time during isothermal annealing at different temperatures is shown in figure 1. The as-deposited or unannealed  $\text{SnO}_2$  films (evaporation temperature above  $1800^\circ\text{C}$ ) are expected to be amorphous in character as shown by its high resistivity. This amorphous character is confirmed by x-ray diffractometric characterisation (figure 2a). The peaks of the x-ray diffraction pattern show crystallization with time during annealing at 717, 701 and 688 K respectively (figure 2) as also indicated by decrease in resistivity. As expected, the general shape of the isothermal annealing curves (figure 1), at different temperatures is very similar.

It was observed that the time at which the films became conducting increases as the annealing temperature decreases. This is expected because the thermally activated process of transformation from the amorphous to the polycrystalline phase will slow down with decrease of annealing temperature. This also explains the broadening of the minima with decreasing annealing temperature. The decrease in sheet resistivity with time (figure 1) may be attributed to the reduction in defect density as shown by the x-ray diffraction results, and in addition chemisorption of oxygen also takes place which further reduces the resistivity of the films (Shanthi *et al* 1980). The sheet resistivity attains a minimum when the defect distribution may be assumed to be in equilibrium (Chopra 1969). The increase in the observed resistivity after the minimum is dominated by the formation of pores and further increase in size of the pores. The SEM photographs (figures 3a, b) corresponding to 37 and 60 min annealing give only pores with their size increasing.

The variation in sheet resistivity with temperature on annealing the  $\text{SnO}_2$  film in air is plotted in figure 4. The film showed irreversible decrease in sheet resistivity, perhaps due to the reduction of defect density with increasing temperature. This mechanism governing the resistivity of films is well known (Maissel and Glang 1970). The minimum nearly corresponds to the Debye temperature of  $\text{SnO}_2$  [ $\sim 500^\circ\text{K}$ ], so that the largest

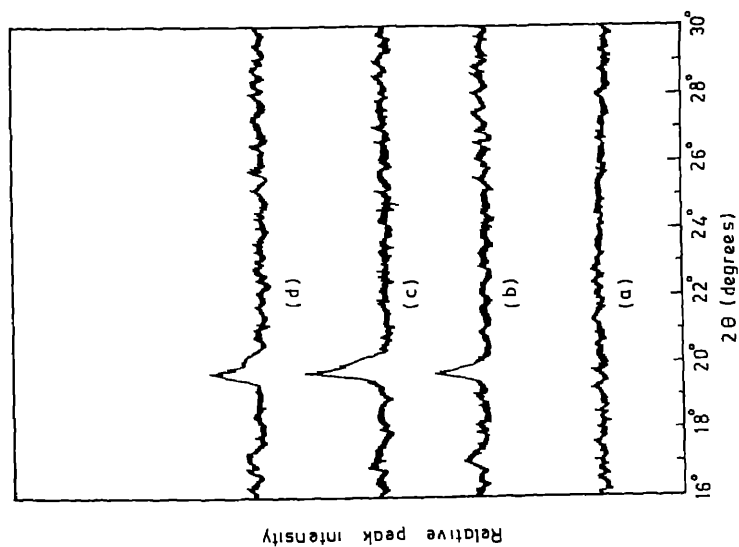


Figure 2. X-ray diffraction pattern for  $\text{SnO}_2$  films deposited on glass substrate. a. Unannealed films, b.  $t = 4$  min annealed at 717 K, c.  $t = 37$  min annealed at 701 K, d.  $t = 1$  hr annealed at 688 K.

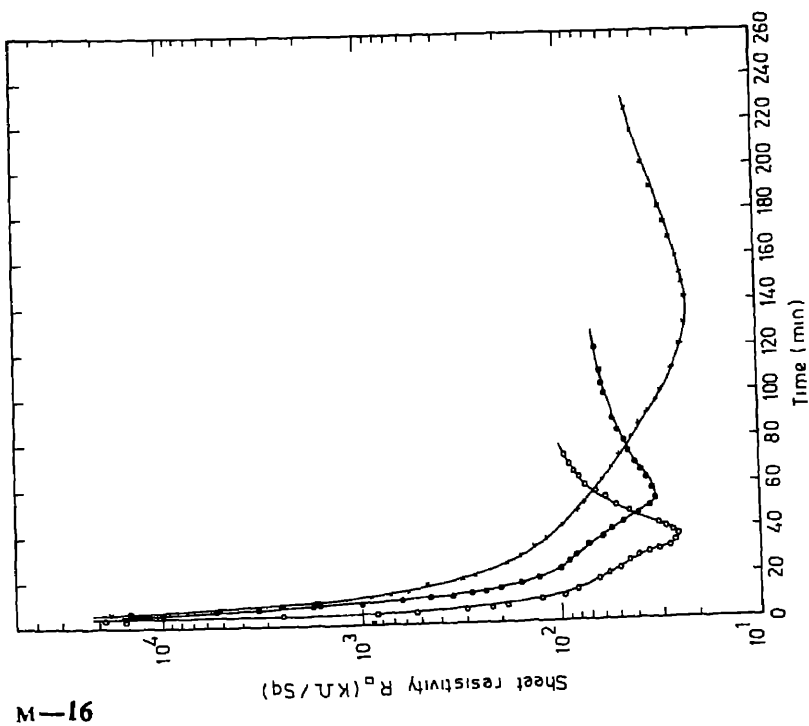


Figure 1. Sheet resistivity vs time for  $\text{SnO}_2$  films deposited on glass substrate during isothermal annealing (o) 701 K; (●) 688 K; (x) 660 K.

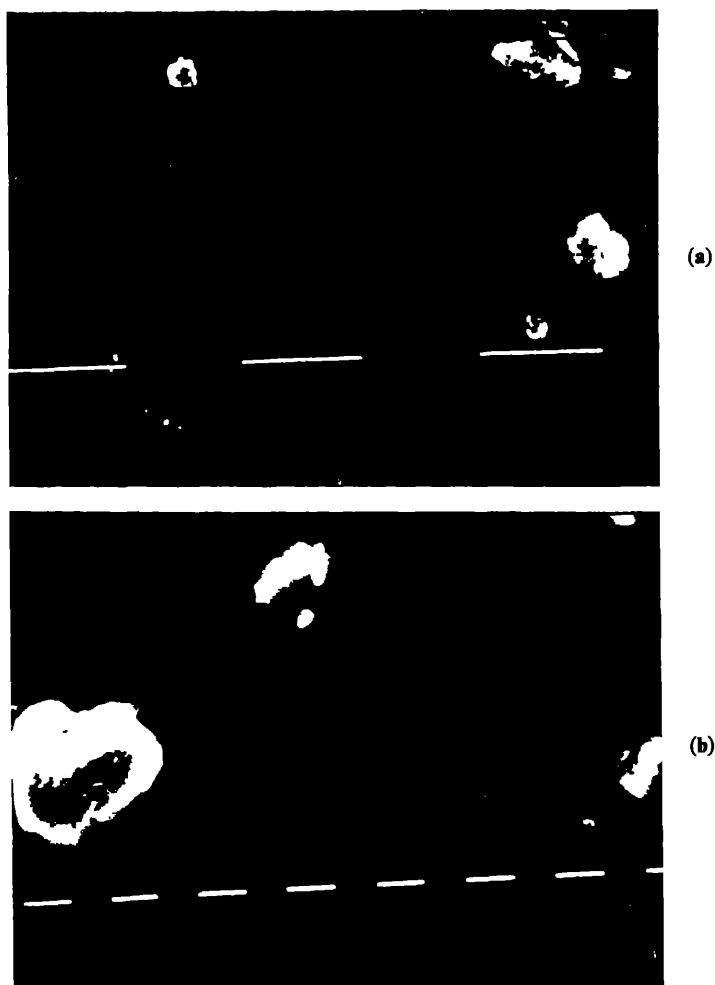


Figure 3. Scanning electron micrograph of  $\text{SnO}_2$  films deposited on a glass substrate annealed at 701 K, a. annealed for 37 min (magnification:  $160 \times 1.1$ ). b. annealed for 1 hr (magnification  $640 \times 1$ ).

part of the lattice defects is removed because of the maximum frequency of the lattice vibrations (Chopra 1969). Therefore, beyond this point the resistivity increases.

We have attempted here to give a qualitative interpretation of the results obtained on the annealing behaviour of tin dioxide films. A quantitative study is in progress.

### Acknowledgement

AG and PG are thankful to CSIR (India) for financial support. The authors express their sincere thanks to Mr N K Saini for help in carrying out SEM experiments.

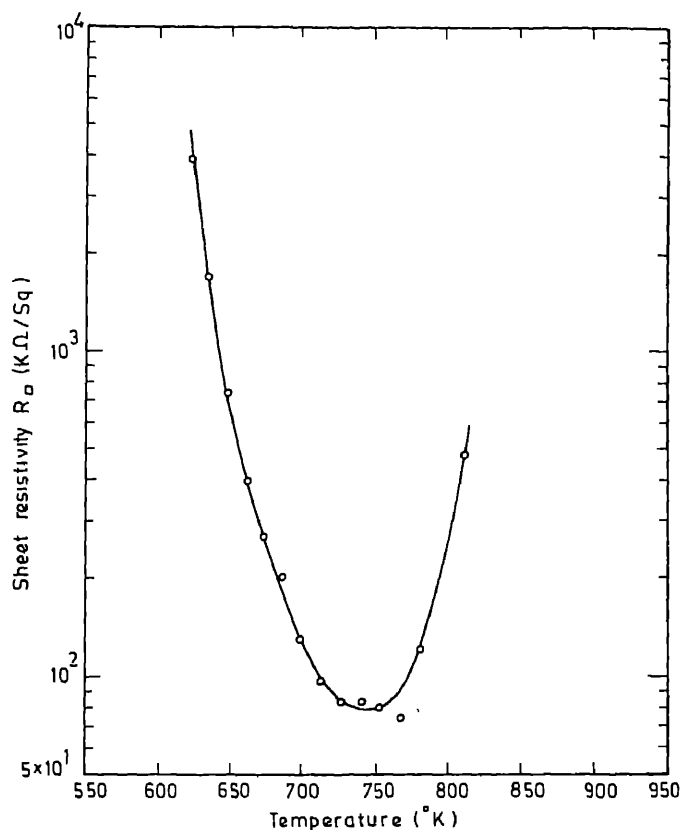


Figure 4. Sheet resistivity vs temperature for  $\text{SnO}_2$  film deposited on a glass substrate.

## References

- Arai T 1960 *J. Phys. Soc. Jpn* **15** 916  
 Chopra K L 1969 *Thin film phenomenon* (New York: McGraw Hill) 381-387  
 Ghosh A K, Fishman C and Feng T 1978 *J. Appl. Phys.* **49** 3490  
 Ishiguro K, Sasaki T, Arai T and Imai I 1958 *J. Phys. Soc. Jpn* **13** 296  
 Jarzebeski Z M 1976 *J. Electrochemical Soc.* **123** 299C  
 Maissel L I and Glang R 1970 *Handbook of thin films technology* (New York: McGraw Hill) 13-26  
 Nagatoma T, Endo M and Omoto O 1979 *Jpn J. Appl. Phys.* **18** 1103  
 Raccanelli A and Madalena A 1976 *J. Am. Ceram. Soc.* **59** 425  
 Shanthi E, Banerjee A, Dutta V and Chopra K L 1980 *Thin Solid Films* **71** 237  
 Viscian I and Georgescu V 1969 *Thin Solid Films* **3** R17



7-11-1919

10-11-1919

11-11-1919

12-11-1919

13-11-1919

14

15

16

17

18

19

20

21

22

23

24

## Temperature dependence of microhardness in mixed crystals

SANKAR P SANYAL and R K SINGH

Department of Physics, Rani Durgawati University, Jabalpur 482 001, India

MS received 7 October 1983

**Abstract.** The temperature dependence of microhardness of mixed KCl-KBr crystals has been studied using the Kataoka and Yamada theory which considers plastic deformation and internal stress field due to elastic interactions in mixed crystals. The microhardness showed systematic variation with temperature in both the components and the mixed crystals and the probable reasons for this variation are indicated.

**Keywords.** Mixed crystals; microhardness; temperature dependence; Kataoka-Yamada theory.

### 1. Introduction

In recent years, considerable attention has been paid to the study of mixed crystal properties as they are useful in many technological applications (*e.g.* mixed crystals of alkali halides are used for laser windows). One well-known property is microhardness, which for mixed crystals always exceeds its value for the component crystals (Armington *et al* 1973; Hari Babu *et al* 1975). A number of theories (Gilman 1973; Shukla and Bansigir 1976; Boser 1972; Ridhagani and Asimow 1968) have been proposed to explain this extra hardness of mixed crystals. Earlier theories of Gilman (1973) and Shukla and Bansigir (1976) could not explain the microhardness of mixed crystals as indicated by Bhimshankaran (1974), and Srivastava (1980). Kataoka and Yamada (1977) have given a theory according to which the random distribution of doped ions can produce an internal stress field interaction that increases the microhardness of the mixed crystals. This theory has been applied to mixed alkali halides (Srivastava 1980) and mixed silver halides (Sanyal and Singh 1982).

Motivated by the success of the theory of Kataoka and Yamada theory, we have applied it to study the temperature dependence of microhardness of  $\text{KCl}_x\text{Br}_{1-x}$  system from 300–1000 K. It is known (Subba Rao and Hari Babu 1978) that the excess of microhardness in mixed crystals results from the increased value of dislocation density. However, this dislocation density in mixed crystals decreases with increase in temperature. Thus, it seems worthwhile to investigate the exact nature of change of microhardness with temperature in mixed crystals. Srivastava (1980) used the Kataoka-Yamada theory to explain the microhardness of  $\text{KCl}_x\text{Br}_{1-x}$  measured by Subba Rao and Hari Babu (1978) at 300 K only. In doing so, he used the measured microhardness values of KCl, KBr and  $\text{KCl}_{0.48}\text{Br}_{0.52}$  as the input data. Thus, the predictions made by Srivastava are more or less borne out. In the present analysis, however, the results of microhardness of  $\text{KCl}_{0.48}\text{Br}_{0.52}$  have only been used at 300 K to determine a parameter. The values of microhardness of component crystals (KCl and KBr) have been obtained in terms of Debye temperatures (Bollmann 1980).

## 2. Theory

The microhardness ( $H_v$ ) of binary ionic solids is related to the Schotky defect formation energy ( $w_s$ ) as (Shukla and Bansigir 1976)

$$H_v = 205.8 W_s / r^3, \quad (1)$$

where  $r$  is the interionic separation. According to Sastry and Mulimani (1969),  $W_s$  is also related to the Debye temperature ( $\Theta_D$ ), such that

$$W_s = (\Theta_D / 32.37)^2 M V^{2/3}. \quad (2)$$

Here,  $M$  and  $V$  are the molar mass and volume. Now,  $H_v$  can be written in terms of the Debye temperature as:

$$H_v = 6.833 (M V^{2/3} / r^3) \Theta_D^2 \times 10^{-5} \text{ (kg/mm}^2\text{)}, \quad (3)$$

from (1) and (2). This equation is, however, valid only for the component crystals and not for mixed crystals, as it fails to account for the extra hardness in them. We have therefore considered the extra hardness using the Kataoka-Yamada theory in which the doped ions are assumed to behave as a source of constriction and expansion in the lattice in order to maintain the crystal symmetry. The random distribution of these ions produces a fluctuating stress in the mixed crystals and is responsible for the increase in their hardness. The mean expectation value of the internal stress,  $\tau_0$ , arising from the random distribution of anions is given by (Kataoka and Yamada 1977)

$$\tau_0 = \frac{4\sqrt{2}}{\pi} \alpha \left( \frac{\alpha}{\alpha'} \right)^{1/2} \frac{\sigma^2 r^2}{\lambda} \left( \frac{\Delta V}{r^3} \right) \beta_1 \beta_2, \quad (4)$$

where  $\alpha$  and  $\alpha'$  are the lattice sums.  $\Delta V$  is the difference in anion volume of the two components and  $\beta_1$  and  $\beta_2$  are fractional molar concentrations of the two components in the mixed crystals. The symbols  $\sigma$  and  $\lambda$  are related to the second order elastic constants by

$$\sigma = \frac{1}{2} (C_{11} - C_{12}) \quad (5)$$

and

$$\lambda = \frac{1}{2} (C_{11} + C_{12}) \left[ \frac{C_{44} (C_{11} - C_{12})}{C_{11} (C_{11} + C_{12} + C_{44})} \right]^{1/2} r^2. \quad (6)$$

In terms of  $\tau_0$  the hardness due to internal stress field can be expressed as

$$H_{\text{isf}} = F \tau_0 \quad (7)$$

with  $F$  as a constant. Thus, the microhardness of mixed crystals is ultimately given by

$$H_m = \beta_1 H_1 + \beta_2 H_2 + H_{\text{isf}}, \quad (8)$$

where  $H_1$  and  $H_2$  are the hardness of the component crystals.

## 3. Results and discussion

The microhardness ( $H_v$ ) values of the component crystals, KCl and KBr at different temperatures (300–1000 K) were calculated from (3) using the values of Debye temperature ( $\Theta_D$ ) and interionic separation ( $r_0$ ) reported by Tolpadi (1977) and

Subramaniam (1979). Their values for KCl and KBr at different temperatures are listed in table 1 and are compared with their measured data at 300 K (Bollman 1980; Subba Rao and Hari Babu 1978). The microhardness ( $H_m$ ) values for the mixed crystals at different temperatures have been calculated from (8) using the required values of elastic constants reported by Subramaniam (1978). The variations of microhardness with temperature for the component crystals and mixed KCl-KBr are presented in figure 1 and those with mole percentage of KBr are presented in figure 2.

Table 1. Microhardness ( $H_v$ ) of KCl and KBr at different temperatures.

Temperature (K)	$H_v$ (kg/mm <sup>2</sup> )	
	KCl	KBr
300	10.306 9.9 <sup>a</sup>	8.468 7.9 <sup>b</sup>
400	9.464	8.231
500	8.906	7.785
600	8.317	7.329
700	7.706	6.847
800	7.020	6.331
900	6.236	5.784
1000	5.293	5.133

<sup>a</sup> Bolmann (1980); <sup>b</sup> Subba Rao and Hari Babu (1978).

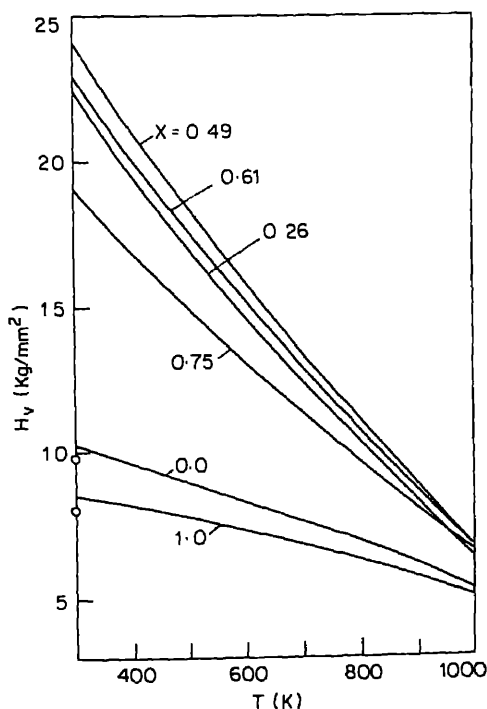


Figure 1. Variation of microhardness of  $\text{KCl}_x\text{Br}_{1-x}$  system with temperature. Experimental points (o) at 300 K have been taken from Subba Rao and Hari Babu (1978).

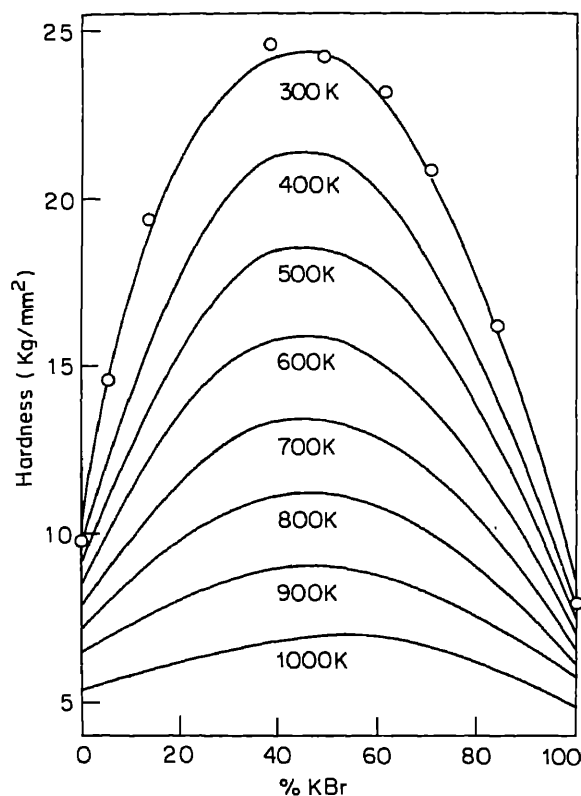


Figure 2. Variation of microhardness of  $\text{KCl}_x\text{Br}_{1-x}$  system with % of KBr in KCl at different temperatures. Experimental points are taken from Subba Rao and Hari Babu (1978).

Table 1 shows that the microhardness of the component crystals can be satisfactorily predicted by using (3). These values decrease almost linearly with temperature as shown in figure 1. This might be so because the microhardness is a measure of the resistance offered by dislocation motion which becomes easier when the temperature is raised. The variation of  $H_v$  with temperature in mixed crystals is, however, not linear, perhaps due to the elastic effects arising from the size misfit of cations.

Figure 2 shows that the extra hardness in mixed crystals (Hari Babu and Subba Rao 1978) at 300 K has been adequately explained even without using the  $H_v$  values of the component crystals. This prediction is better than that achieved by Subba Rao and Hari Babu (1978) where they neglected the effects due to elastic interactions (Kataoka and Yamada 1977). Our results on  $H_v$  at higher temperatures could not be compared due to lack of measured data. Their variation with temperature is, however, systematic and consistent with the measured results in other solids (Bhatt and Desai 1982).

## References

- Armington A F, Posen H and Lipson H 1973 *J. Electron. Mater.* **2** 127  
 Bhatt V P and Desai C F 1982 *Bull. Mater. Sci.* **4** 23

- Bhimasankaran T 1974 Ph.D. Thesis, Osmania University, AP  
Bollman W 1980 *Phys. Status Solidi* **A6** 395  
Boser O 1972 *Metall. Trans.* **3** 843  
Gilman J J 1973 *J. Appl. Phys.* **44** 983  
Hari Babu V, Subba Rao U V and Venkata Ramaiah K 1975 *Phys. Status Solidi* **A28** 269  
Kataoka T and Yamada T 1977 *Jpn J. Appl. Phys.* **16** 1119  
Riddhagni B R and Asimow R M 1968 *J. Appl. Phys.* **39** 4164  
Sanyal S P and Singh R K 1982 *J. Phys.* **D15** 1083  
Sastry P V and Mulimani P G 1969 *Philos. Mag.* **20** 859  
Shukla M and Bansigir K G 1976 *J. Phys.* **D9** L49  
Srivastava U C 1980 *J. Appl. Phys.* **51** 1510  
Subba Rao U V and Hari Babu V 1978 *Pramana* **11** 149  
Subramaniam B 1979 *Indian J. Phys.* **A54** 109  
Tolpadi S 1977 *Indian J. Phys.* **A51** 181



## Some aspects of dislocation-precipitate interaction in under-aged aluminium-germanium alloy

KISHORE

Department of Metallurgy, Indian Institute of Science, Bangalore 560 012, India

MS received 6 September 1982; revised 13 December 1983

**Abstract.** The glide dislocation-precipitate interaction in under-aged alloy is investigated by microscopy and low-temperature deformation techniques. Slip-line features of room temperature deformed samples were observed by optical microscopy. From tensile tests at various temperatures the variation of flow stress with  $T^{2/3}$  was established. Comparing the present results with those obtained on the peak-hardened condition of the same alloy it is concluded that moving dislocation shear through the small rod-shaped germanium precipitates.

**Keywords.** Under-aged; dislocation-precipitate interaction; slip lines; flow stress.

### 1. Introduction

The interaction between glide dislocations and precipitate particles has been studied in detail in many age-hardenable alloy systems (Nicholson and Nutting 1961; Kelly 1963; Lutzer and Weissman 1970; Raynor and Silcock 1970; Nourbakhsh and Nutting 1980). From mechanical property studies coupled with microscopy, it is possible to arrive at the likely interaction between moving dislocations and precipitate particles. While efforts are not wanting in understanding the dislocation precipitate interaction in peak-aged and over-aged states, the partially-aged condition has received hardly any attention. The purpose of the present work is to study the dislocation-precipitate interaction in under-aged aluminium-2% germanium alloy using microscopy and mechanical deformation techniques.

### 2. Experimental

Weighed quantities of super-pure aluminium and germanium were melted together in an argon atmosphere in a resistance furnace and cast in a graphite-lined metal mould. The Ge content was 1.98% by weight. The cast ingot was lightly worked by hammering before annealing at 400°C for 48 hr. The homogenised rod was reduced to a 1 mm thick strip by cold-rolling coupled with intermediate annealing treatment. Tensile and hardness samples were cut from the rolled strip and electropolished after mechanical polishing. They were solutionised at 450°C for 2 hr and quenched into ice-water mixture maintained close to 0°C. Thermostatically-controlled paraffin oil bath, maintained at 165°C, was used for ageing the samples. Hardness variation with ageing time was determined using a Vicker's unit. From such a data it was possible to establish the peak-hardened condition. In the present experiment as the peak hardness occurred



at around 70 hr, the tensile test specimens were aged for 18 hr to have the microstructure corresponding to the under-aged condition.

The partially-aged test specimens with a gauge length of 20 mm were pulled in a modified Hounsfield tensometer (Prasad *et al* 1969) at a strain rate of about  $10^{-3} \text{ sec}^{-1}$  at temperatures varying between 77 and 420°K. From the load-elongation plot, the flow stress was determined. The tensile-deformed samples were viewed under a light microscope for slip-line features. Using the window technique and an electrolyte of 90/10 acetic acid/perchloric acid mixture maintained at  $-15^{\circ}\text{C}$ , electron transparent thin specimen in aged condition was prepared for viewing under a Philips 301 microscope. Electrolytic thinning was achieved by applying a voltage of 18 V between the electrode and the specimen.

### 3. Results and discussion

Figure 1 shows the variation in Vickers hardness number as a function of time of ageing at  $165^{\circ}\text{C}$ . The data points follow the typical trend seen in any age-hardenable alloy system, namely, an increase of hardness as ageing occurs, a peak followed by a decrease. The peak corresponding to an optimum dispersion of precipitates (Mott and Nabarro 1940) occurs around 70 hr as mentioned earlier. Figure 2, a TEM micrograph, depicts the appearance and distribution of precipitates in the under-aged condition. Small and dense rod-shaped Ge precipitates can be clearly seen in the photomicrograph. The inter-particle spacing and the size of the rods in the under-aged sample are smaller (figure 2) compared to the peak-aged condition (figure 3).

The slip-line pattern of partially-aged and room temperature-deformed sample is shown in figure 4. They are straight running, continuous and thin. Slip-line features resemble the pattern obtained for peak-aged state (Kishore and Vasu 1978). It is known that slip bands give reliable information about the mechanism of plastic deformation of the materials (Seeger 1963). The slip-line appearance could change with a change in the type of obstacle present in the matrix. When small coherent particles are present, the dislocation can easily shear the particle aggregates and the appearances of the line in such cases are only slightly different from those obtained for the pure metal or solid

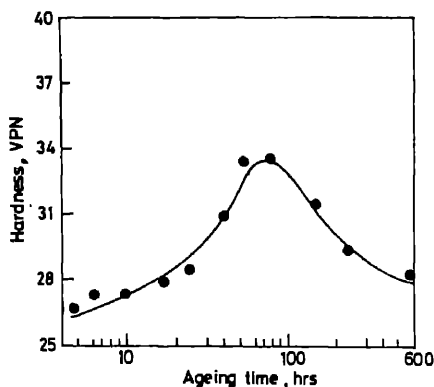


Figure 1. Hardness variation with time during ageing at  $165^{\circ}\text{C}$  ( $T_a = 450^{\circ}\text{C}$ ).

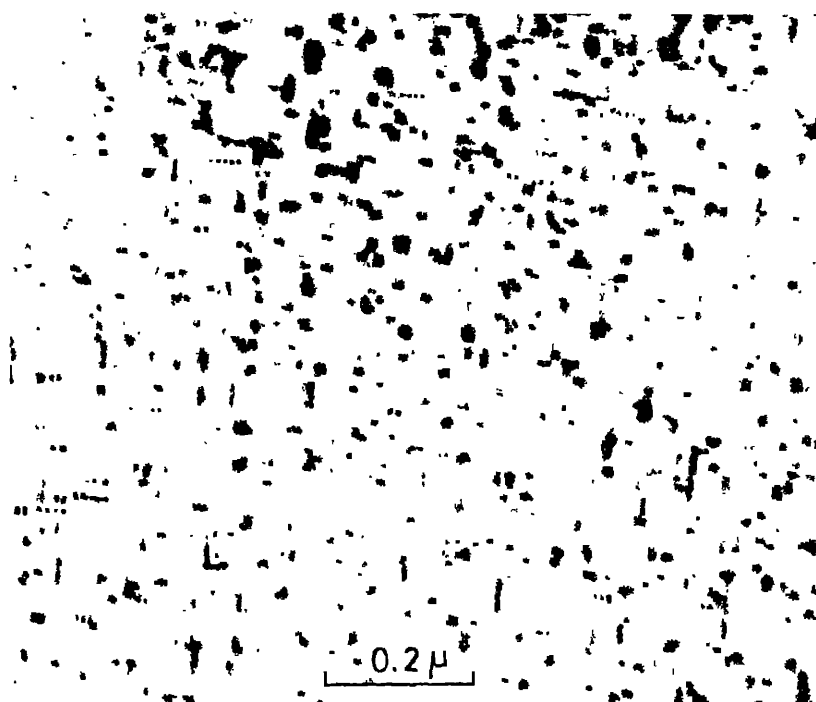
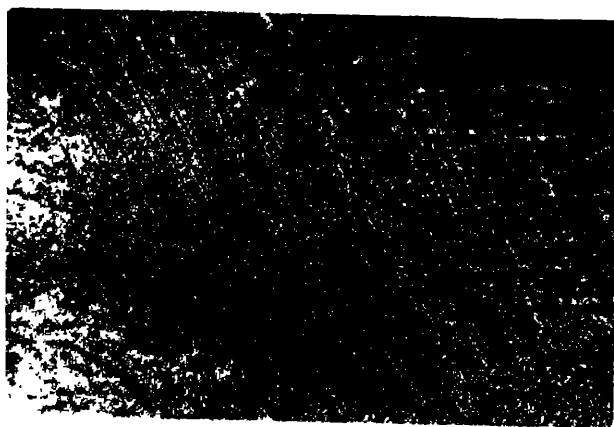


Figure 2. Electron micrograph of partially-aged sample showing small and dense rod-shaped precipitates ( $T_s = 450^\circ\text{C}$ ,  $T_a = 165^\circ\text{C}$ ,  $t_a = 18$  hr).

solution (Greetham and Honeycombe 1960–61; Silcock 1960; Thomas and Nutting 1956–57, 1957–58). Wavy, fragmented slip lines are seen when incoherent, large nondeforming particles are encountered during the movement of glide dislocations (Wilcox and Gilbert 1967; Greetham and Honeycombe 1960–61; Price and Kelly 1962). Starke *et al* (1973) have shown that small germanium clusters can be sheared. As the slip traces in partially-aged condition used in this work are similar to those obtained on peak-hardened condition (Kishore and Vasu 1978) and the longer and somewhat widely spaced rods of peak-aged state have been shown to be sheared by moving dislocation using TEM (Kishore *et al* 1976), it may be inferred that in the present under-aged condition also the precipitate particles are cut through by the glide dislocations. Further evidence to this deduction comes from an examination of  $\tau - T^{2/3}$  relation following the report of Chun and Byrne (1969). They examined the strengthening in a Mg-5% Zn alloy by determining the temperature dependence of CRSS for the as quenched, fully-hardened and overaged conditions. The shearing of the precipitates in the peak aged state, and the linear variation of flow stress,  $\tau$  with  $T^{2/3}$  were noticed by them. Lipsitt (1971) also showed that yield strength in the Al-Zn alloy varies linearly with  $T^{2/3}$ . In figure 5 are plotted the data showing variation of flow stress with  $T^{2/3}$  for the under-aged Al-Ge alloy. For the sake of comparison the results obtained in the peak-aged state are also included. It is noteworthy that the points lie on a straight line in both the cases suggesting the existence of similar interaction between the glide dislocations and the precipitate particles. Hence, it may be inferred that as in the peak-hardened



**Figure 3.** A TEM photograph of the peak-hardened alloy (70 hr at 165°C) showing rod-, triangular-, and rectangular-shaped precipitates.



**Figure 4.** Slip traces in under-aged sample deformed at room temperature ( $\epsilon = 25\%$ ; 200 $\times$ ).

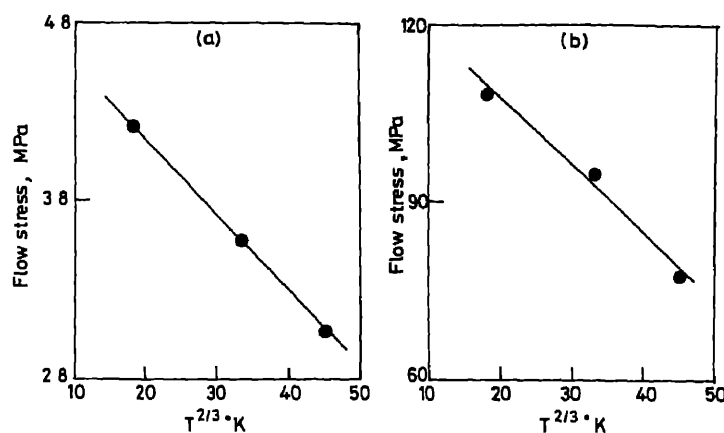


Figure 5. Flow stress-(temperature)<sup>2/3</sup> relation for (a), under-aged (b), peak-aged conditions ( $\dot{\epsilon} = 9.8 \times 10^{-4} \text{ sec}^{-1}$ ).

state, in the under-aged state too, the dislocations penetrate the germanium precipitates.

In view of the similarity of behaviour of flow stress variation with temperature as well as nature of slip traces in the under-aged condition with peak-aged alloy reported earlier (Kishore and Vasu 1978) it can be said that in the partially-aged condition also the Ge precipitates are sheared by the glide dislocations.

#### 4. Conclusions

Partially-aged alloy exhibit straight slip traces. The flow stress of the dilute alloy varies linearly with  $T^{2/3}$  and the moving dislocations cut through the germanium precipitates.

#### Acknowledgements

The author thanks Prof. K I Vasu for his interest in the work. The assistance received from colleagues in the Department is gratefully acknowledged.

#### References

- Chun J C and Byrne J G 1969 *J. Mater. Sci.* **4** 861
- Greetham G and Honeycombe R W K 1960-61 *J. Inst. Metals* **89** 13
- Kelly A 1963 in *Electron microscopy and strength of crystals* (eds) G Thomas and J Washburn (New York: Interscience) p. 947
- Kishore, Sastry D H and Vasu K I 1976 *Proc. Second Int. Conf. on Mechanical Behaviour of Materials*, Boston, USA 1851
- Kishore and Vasu K I 1978 *Metallography* **11** 51
- Lipsitt H A 1971 *Metall. Trans.* **2** 1739
- Lutzing G and Weissman S 1970 *Acta Metall.* **18** 785
- Mott N F and Nabarro F R N 1940 *Proc. Phys. Soc.* **52** 86
- Nicholson R B and Nutting J 1961 *Acta Metall.* **9** 332
- Nourbakhsh S and Nutting J 1980 *Acta Metall.* **28** 357

---

1046      *Kishore*

Prasad Y V R K, Sastry D H and Vasu K I 1969 *J. Indian Inst. Sci.* **51** 377

Price R J and Kelly A 1962 *Acta Metall.* **10** 980

Raynor D and Silcock J M 1970 *Metal Sci.* **J.4** 121

Seeger A 1963a *J. Phys. Soc. Jpn* **18** p. 59

Seeger A 1963b *Proc. at NPL*, Vol I Symp. No. 15 The relation between structure and mechanical properties of metals 4

Silcock J M 1960 *Acta Metall.* **8** 589

Starke E A, Kralik G and Gerold V 1973 *Mater. Sci. Eng.* **11** 319

Thomas G and Nutting J 1956-57 *J. Inst. Metals* **85** 1

Thomas G and Nutting J 1957-58 *J. Inst. Metals* **86** 8

Wilcox B A and Gilbert A 1967 *Acta Metall.* **15** 601

## Evaluation of magnetic hyperfine field distributions from Mössbauer spectra of disordered alloys and metallic glasses

C BANSAL

School of Physics, University of Hyderabad, Hyderabad 500134, India

MS received 15 March 1983

**Abstract.** A simple computer program is described to evaluate magnetic field distributions from complex Mössbauer spectra of magnetic alloys. The use of this program for test cases of Vitrovac 4040 amorphous sample and a simulated spectrum of two gaussian peaks is discussed.

**Keywords.** Mössbauer spectra; metallic glasses; magnetic hyperfine field distributions.

### 1. Introduction

The Mössbauer spectra for disordered magnetic alloys and metallic glasses are generally complex because of the overlap of the component lines due to a wide variety of environments in which the Mössbauer atom is situated. In some cases when the overlap is not too large the average hyperfine field can still be evaluated if the field is distributed around an average value (Bansal *et al* 1975). In other cases when the broadening is large this may not be possible. When two or more types of magnetic behaviour are present *i.e.* magnetic splitting due to magnetically ordered regions and a single line due to a paramagnetic contributions it is again very difficult to extract useful information from Mössbauer spectra (Bansal and Chandra 1979).

Several methods have been proposed to obtain the distribution of magnetic fields which generate the complex spectra (Window 1971; Hesse and Rübartsch 1974; Logan and Sun 1976) and improvements on them also given (LaCaer and Dubois 1979; Wivel and Morup 1981).

### 2. Window's method

Amongst these, the method due to Window is a model-independent field distribution analysis which assumes an arbitrary probability distribution of the magnetic hyperfine fields  $P(H)$  and expands it in a Fourier series of trigonometric functions.

$$P(H) = \sum_{n=1}^N a_n [\cos(n\pi H/H_{\max}) - \cos n\pi]. \quad (1)$$

The field distribution in this form satisfies the boundary conditions: (i)  $P(-H) = P(H)$ , since in the absence of an external field the lines produced due to a field  $H$  are in the same positions as those produced by a field  $-H$ . The series therefore contains

only cosine terms. (ii) There is an upper cut-off point beyond which  $P(H)$  goes to zero smoothly *i.e.*

$$\left. \frac{dP(H)}{dH} \right]_{H=H_{\max}} = 0.$$

If now the coefficients  $a_n$  of the series can be determined so as to fit the experimental spectrum, the required field distribution is known.

The Mössbauer spectrum generated at velocity  $v$  due to this distribution is given by

$$S(v) = \int_0^{H_{\max}} P(H) L_6(v, H) dH, \quad (2)$$

where

$$L_6(v, H) = \sum_{i=1}^6 \frac{1}{\pi} \frac{\Gamma_i/2}{(\Gamma_i/2)^2 + (v - \alpha_i H)^2}, \quad (3)$$

is the normalised Lorentzian shape function of the lines of a component spectrum for field  $H$ .  $\Gamma_i$  are the linewidths of the six lines of the component spectrum and  $\alpha_i H$  are their positions. Equation (2) can be rewritten as

$$\begin{aligned} S(v) &= \sum_n a_n \int_0^{H_{\max}} f_n(H) L_6(v, H) dH, \\ &= \sum_n a_n S_n(v), \end{aligned} \quad (4)$$

$$\text{where } S_n(v) = \int_0^{H_{\max}} f_n(H) L_6(v, H) dH$$

is the spectrum created by the term  $f_n(H)$ . If the experimental spectrum at velocity  $v$  is denoted by  $W(v)$ , the coefficients  $a_n$  of the field distribution can be found by minimizing the function

$$\phi = \sum_v [S(v) - W(v)], \quad (5)$$

with respect to the parameters  $a_n$  or other parameters like isomer shift if necessary. A  $\chi$  nonlinear least square fitting procedure is normally used to obtain the required coefficient  $a_n$ . This procedure is iterative and therefore time-consuming. If the isomer shift is also required to be obtained from a fit to the spectrum this procedure is justified. However in most systems when one is not concerned with relatively small isomer shift values exactly one can safely assume a constant isomer shift for all the elementary field  $H$ . A good guess for this can usually be obtained from the centroid of the spectrum or from a spectrum above the Curie temperature. This then can be given as a fixed parameter.

### 3. Procedure

We get  $N$  simultaneous equations which are linear in  $a_n$  if we differentiate  $\phi$  in (4), with respect to  $a_n$ 's and set them equal to zero.

$$\phi = \sum_v \left[ \sum_n a_n S_n(v) - W(v) \right]^2,$$

$$\frac{1}{2} \frac{\partial \phi}{\partial a_n} = \sum_v [S(v) - W(v)] S_n(v). \quad (6)$$

Differentiating once again w.r.t  $a_m$

$$\frac{1}{2} \frac{\partial^2 \phi}{\partial a_m \partial a_n} = \sum_v S_m(v) S_n(v) = X_{mn} \text{ (say)}. \quad (7)$$

Substituting (7) in (6) and setting  $\partial \phi / \partial a_n = 0$

$$\sum_m a_m X_{mn} - \sum_v W(v) = 0.$$

There are  $n$  such equations for  $n = 1, 2, \dots, N$ .

Defining the matrices

$$\beta_n = \left[ \sum_v W(v) S_n(v) \right],$$

$$X_{mn} = \left[ \sum_v S_m(v) S_n(v) \right],$$

we get the matrix equation

$$aX = \beta.$$

This can be solved to get the matrix of the coefficients  $a_n$

$$a = X^{-1} \beta.$$

A simple computer program can be written to set up the matrices  $X$  and  $\beta$ , finding the inverse of  $X$  and then calculating  $a$ . These coefficients can then be used to generate the field distribution  $P(H)$ .

### 4. Examples of use

A test usage of the program is illustrated in figures 1 and 2. In figure 1, spectrum A is the Mössbauer spectrum simulated for two Gaussian fields of equal intensity as shown in A'. The intensity ratios of the component spectra were constrained in the ratio 3:2:1:1:2:3 and the isomer shift fixed at zero. Using 5 terms in the Fourier series expansion of  $P(H)$  the field distribution obtained using the program outlined above is shown in B'. The two peaks are unresolved. When 10 terms are included in the Fourier series the distribution marked C' is obtained and the simulated and fitted spectrum agree very well as shown in C.

Figure 2 shows the experimental Mössbauer spectrum for an amorphous sample (Vitrovac 4040 from Vacuumschmelze GMBH, Hanau, Germany) together with the



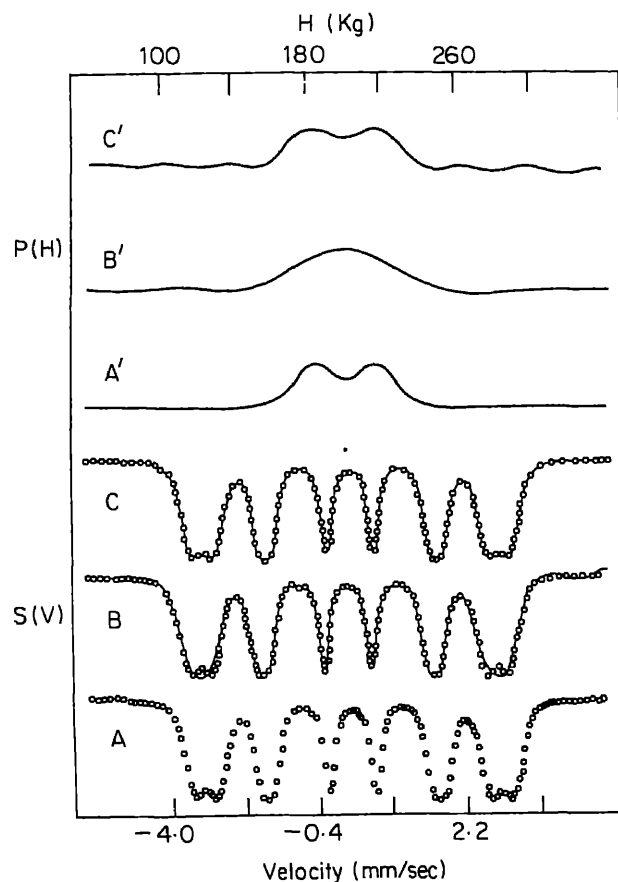
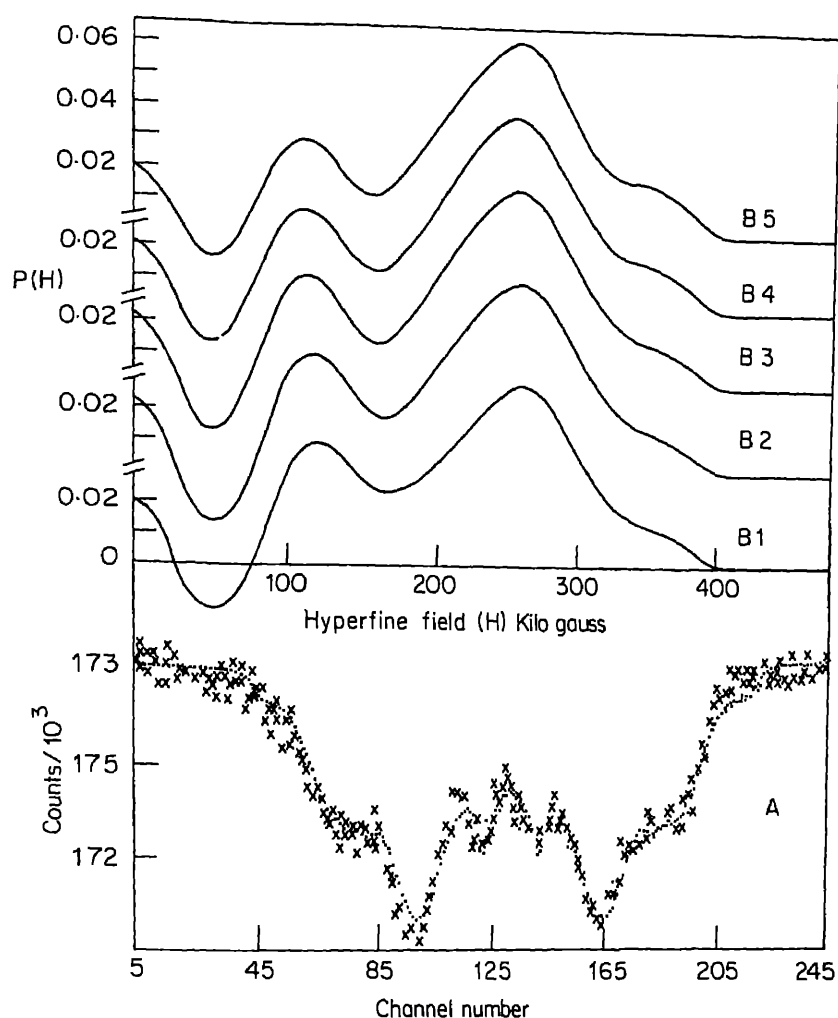


Figure 1. The Mössbauer spectrum A is simulated for two Gaussian peaks shown in A'. The field distribution B' is obtained using the computer program described here when 5 terms are used in the Fourier series expansion of  $P(H)$ . The corresponding Mössbauer spectrum is shown in B. For 10 terms in  $P(H)$  the distribution C' is obtained and the corresponding fit is shown in C.

field distributions obtained using this program. In fitting such spectra there is uncertainty in the value of the intensity ratios to be chosen for the elementary spectra. One of the ways generally used is to vary the intensity ratio in the form  $3:x:1:1:x:3$  and use that value of  $x$  which gives the best fit to the experimental spectrum. The field distributions for various  $x$  values are shown in figure 2. For a value  $x = 2.5$  one gets a good fit to the spectrum.

The number of terms in the Fourier series that should be retained in the expansion for  $P(H)$  also has to be chosen carefully. For a small number of terms the resolution is poor. As seen in figure 1, the two Gaussian peaks are not resolved when only 5 terms are used but are seen separately for 10 terms in the expansion. However if the number of terms is made very large there occurs another difficulty. The distribution tries to fit the statistical fluctuation in data which are unphysical and thereby produces oscillations in the field distribution.



**Figure 2.** The experimental Mössbauer spectrum for Vitrovac 4040 sample (+) and fitted spectrum (·) for the field distribution in B2. The field distributions for various values of  $x$  (intensity ratio of 2nd and 5th lines relative to 3rd and 4th lines) are shown as B1 ( $x = 2$ ), B2 ( $x = 2.5$ ), B3 ( $x = 3$ ), B4 ( $x = 3.5$ ), B5 ( $x = 4$ ).

## 5. Conclusions

The program described above is simple to write and can be simply modified to analyse spectra which have a paramagnetic single line in addition to distributions at higher velocities or for situations in which the baseline is parabolic. A listing of the program is available with us and has about 175 statements in Fortran IV.

## Acknowledgement

The author is grateful to Dr R G Pillay of the TIFR, Bombay, for help in writing the program and testing it.

### References

- Bansal C, Ray J and Chandra G 1975 *J. Phys.* **F5** 1663  
Bansal C and Chandra G 1979 *Phys. Rev.* **B20** 3357  
Hesse J and Rübartsch A 1974 *J. Phys.* **E7** 526  
LaCaer G and Dubois J M (1979) *J. Phys.* **E12** 1083  
Logan J and Sun E 1976 *J. Noncryst. Solids* **20** 285  
Window B 1971 *J. Phys.* **E4** 401  
Wivel C and Morup S 1981 *J. Phys.* **E14** 605

## Spin wave relaxation processes in polycrystalline yttrium iron garnets

S N BHATIA, P B JOSHI and C M SRIVASTAVA

Department of Physics, Indian Institute of Technology, Powai, Bombay 400 076, India

MS received 7 May 1983

**Abstract.** The wavevector and temperature dependence of the spinwave linewidth in yttrium iron garnets has been studied for polycrystalline samples of average grain diameter  $12.8\ \mu\text{m}$  and has been compared with the calculated relaxation times of basic three-magnon confluence and four-magnon scattering processes.

**Keywords.** Relaxation; spin-wave line-widths; yttrium iron garnets

### 1. Introduction

The nature of the intrinsic relaxation processes which determine the dissipative characteristics of magnetically ordered materials is well understood for the crystalline state (Gurevich and Anisimov 1975). The uniform precession mode which is created in the parallel pumping experiment loses its energy into the degenerate magnon modes. The small wavevector ( $k$ ) magnons thus generated relax by the three-magnon confluence process (3c) while the larger  $k$  magnons,  $4 \times 10^5 < k < 9 \times 10^5\ \text{cm}^{-1}$ , attain equilibrium *via* scattering involving four magnons (4sc). The splitting process requiring magnons of high frequencies is therefore restricted to  $k > 10^6\ \text{cm}^{-1}$ . The observed temperature and  $k$  dependences of these processes have been established to be in accord with the theoretical results (Sparks 1967; Vaks *et al* 1968; Gurevich and Anisimov 1975). Such an understanding is lacking for the polycrystalline materials. Vrehan's (1966) transit time model has been used successfully by Patton (1970) and Scotter (1972) to explain the observed relaxation time for the  $k \rightarrow 0$  limit in large grains but the model fails for finite  $k$  and small grain samples. An empirical relation based on the predictions of transit time model for the wavevector dependence of the spin-wave linewidth, obeyed by samples of grain size  $1\text{--}12\ \mu\text{m}$  has been arrived at by Prakash and Srivastava (1980). However no attempt appears to have been made to correlate such measurements with the fundamental processes involving the magnons. We have measured the spin-wave linewidths of polycrystalline YIG as functions of the wavevector and temperature for samples of various grain sizes and analysed them in terms of the basic scattering processes of the magnons.

### 2. Experimental

Polycrystalline YIG samples (densities  $> 99\%$  average grain diameter  $0.9\text{--}12.8\ \mu\text{m}$ ) were prepared using the normal sintering and hot pressing techniques.

A high power microwave bench giving pulses of  $4\ \mu\text{sec}$  duration,  $80\ \text{kW}$  peak power

with a repetition frequency of 50 pulses/sec and operating at microwave frequency 9.391 GHz was used to study the parallel pumping instability threshold ( $h_c$ ) in these samples. A reflection-type rectangular cavity operating in  $TE_{104}$  mode was used and the sample was mounted at its  $3\lambda_g/2$  position in a vacuum-jacketed glass tube. Liquid nitrogen vapour was blown through this tube to regulate the sample temperature between 120 and 300 K.

### 3. Results

The instability threshold field ( $h_c$ ) has been observed as a function of the applied magnetic field  $H_0$ . The spin-wave linewidth ( $\Delta H_k$ ) is calculated from  $h_c$  through the relation

$$h_c = (\omega_k/\omega_m)/(\Delta H_k/\sin^2 \theta_k),$$

where  $\omega_k$  is the operating frequency,  $\omega_m = 4\pi\gamma M$  and  $\theta_k$  is the angle between the direction of propagation of the spin-waves and  $H_0$ . The  $h_c$  vs  $H_0$  curve was used to calculate  $\Delta H_k$  up to  $(h_c)_{\min}$ , the corresponding  $k$  value being obtained from the standard dispersion relations.  $\Delta H_k$  vs  $k$  curves for the grain size  $12.8 \mu\text{m}$  are shown in figure 1. Temperature is displayed as a parameter on these curves.

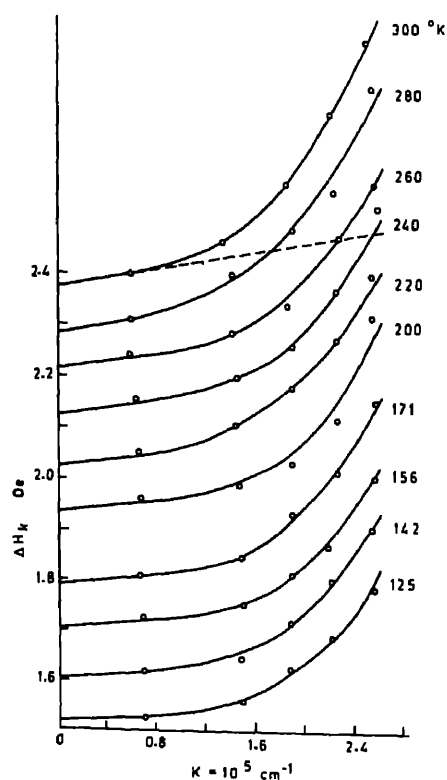


Figure 1. Wavevector dependence of the spin-wave line-width for polycrystalline YIG.

The striking feature of these curves is the nonlinear dependence of  $\Delta H_k$  on  $k$  for all temperatures. This is in contrast to the linear dependence reported earlier (Patton 1970; Prakash and Srivastava 1980) and is attributed to the rather large range of  $k$  used in the present graphs. Over the limited range of  $1.5 \times 10^5 < k < 3 \times 10^5 \text{ cm}^{-1}$  used in earlier studies, the present data also shows an almost linear dependence of  $\Delta H_k$  on  $k$ . A similar linear dependence was also observed by White *et al* (1979) between 88 and 368 K. Their most dense sample appears to have lesser  $4\pi M_s$  and therefore more porosity than ours. Pores could be the dominant scattering centres (Scotter 1972).

The initial portion of each curve however appears to be a straight line up to a certain value of the wavevector  $k_{\min}$ , after which the nonlinearities begin.  $k_{\min}$  appears to decrease with increasing temperature. This initial portion of each graph was fitted to the equation,

$$\Delta H'_k = \Delta H_{k \rightarrow 0}(T) + a(T)k. \quad (1)$$

After subtracting  $\Delta H'_k$  from the observed  $\Delta H_k$  for  $k > k_{\min}$ , the difference  $\Delta H_k - \Delta H'_k$  was fitted to

$$\Delta H_k - \Delta H'_k = b(T)k^2, \quad (2)$$

for each temperature. The observed variations of  $a(T)$  and  $b(T)$  with temperature are shown in figure 2. Also shown in this figure is the number of thermal magnons excited  $n(T)$  which is linear with  $T$  as the energy of these magnons

$$\hbar\omega_k \approx \gamma H_0 + Dk^2 \approx \gamma H_0 \approx 1, \quad k_\beta \ll k_\beta T.$$

The increase in  $a(T)$  and  $b(T)$  with temperature can be attributed to the larger number of magnons present at higher temperatures. Two processes *viz* the three-magnon confluence and the four-magnon scattering brought on by the dipolar forces, show respectively a linear and a quadratic dependence on both  $k$  and  $T$ . Their respective contributions to  $\Delta H_k$  for single crystals are

$$(\Delta H_k)_{3c} = \frac{\pi M \gamma k_B}{2D\omega_k} T k = C_{3c} T k, \quad (3)$$

$$\begin{aligned} (\Delta H_k)_{4sc} &= \frac{1}{3\pi} \frac{\omega_k}{\gamma} \frac{k_\beta^2 T^2}{(4\pi M D)^2} \left( \ln \frac{\hbar\omega_k}{k_\beta T} \right)^2 k^2 \\ &= C_{4sc} T^2 k^2. \end{aligned} \quad (4)$$

These expressions are valid for magnons with predominant Zeeman energy ( $Dk^2 \ll \gamma H_0$ ) and at high temperatures, ( $\hbar\omega_k \ll k_\beta T$ ). As mentioned above both these conditions are valid here.

We notice from figure 2 that the coefficients  $a(T)$  and  $b(T)$  are roughly linearly and quadratically proportional to  $T$  suggesting that (1) and (2) could be representing the 3c and 4sc processes and consequently the proportionalities.

$$a(T) \propto C_{3c},$$

$$\text{and } b(T) \propto C_{4sc}.$$

However (3) and (4) which are valid for single crystals cannot be used directly here for polycrystalline materials as their contributions to  $\Delta H_k$  are an order of magnitude smaller than the experimentally observed values at all temperatures. Thus for

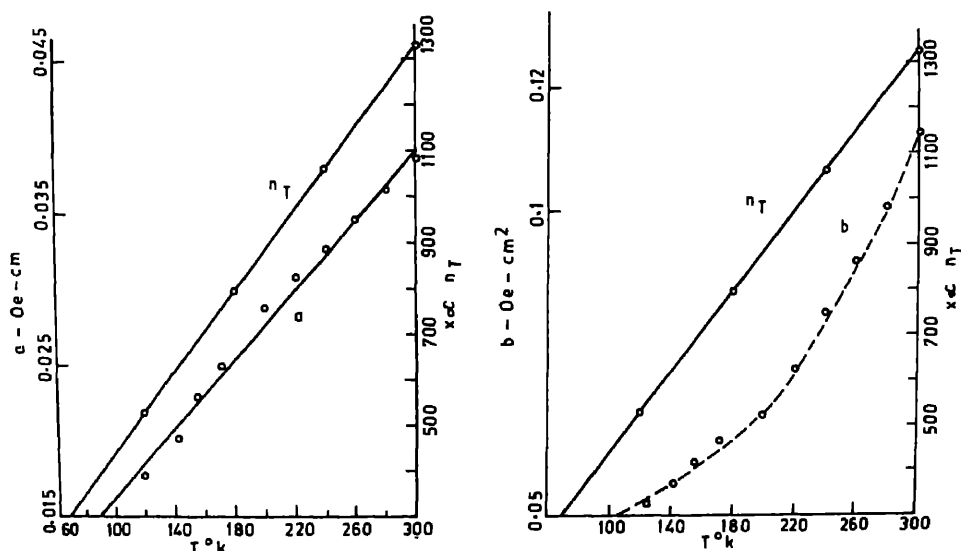


Figure 2. Temperature variation of the coefficients  $a$  and  $b$ .  $n(T)$  is proportional to the number of thermal magnons excited at these temperatures.

$k = 2 \times 10^5 \text{ cm}^{-1}$  experimental  $\Delta H_k$  values are 0.2 and 0.1 Oe at 300 and 120 K respectively as against 0.02 and 0.004 Oe calculated for the 4sc processes. Thus it appears that in changing over from the single crystal to the polycrystalline materials, only the form of these expressions is preserved.

$\Delta H_{k \rightarrow 0}$  obtained from figure 1 is plotted against  $T$  in figure 3. Again a linear dependence on  $T$  is indicated with the data at the lowest temperatures showing some deviations from this line. This is again contrary to the observations of White *et al* (1979) who report an essentially temperature-independent  $\Delta H_k$ , and is also contradictory to the transit time model. This dissipation parameter contains contributions which may depend upon  $k$  but do not vanish as  $k \rightarrow 0$ . In the present case, 3c and 4sc processes do not contribute to  $\Delta H_{k \rightarrow 0}$ . Major contribution to  $\Delta H_{k \rightarrow 0}$  is stipulated to come from the Kasuya-LeCraw magnon-phonon processes (Sparks 1964) which show a similar temperature dependence. Here again magnitude-wise the observed  $\Delta H_{k \rightarrow 0}$  is an order of magnitude larger than that predicted for single crystals (Sparks 1964). However more data at temperatures below 120 K are required to justify this association.

#### 4. Conclusion

For the sample with average grain size  $12.8 \mu\text{m}$  the dissipation processes occurring appear to be identical to those in single crystals with two major differences, (i) the minimum  $k$  value at which the 4sc processes start contribution is significantly smaller here ( $k_{\min} < 1.2 \times 10^5 \text{ cm}^{-1}$  at 300 K) than in single crystals (typically  $2 \times 10^5 \text{ cm}^{-1}$ ) and (ii) the magnitudes of the contributions of the respective processes are an order of magnitude greater here than in single crystals. This increased scattering of magnons could be due to the grain boundaries present in the polycrystalline materials. This

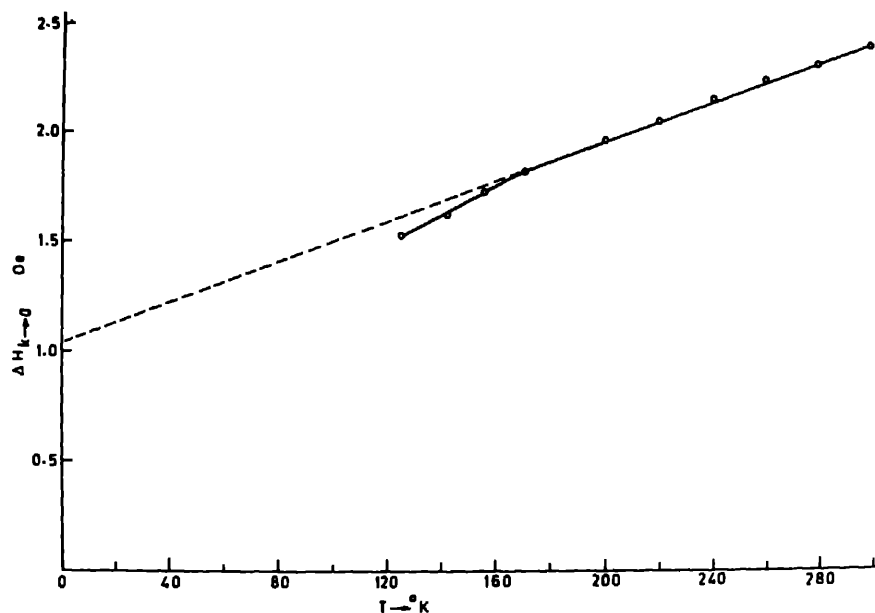


Figure 3. Temperature dependence of the spin-wave linewidth  $\Delta H_k$  for  $k \rightarrow 0$ . Note the deviations from linearity at the lower temperatures.

scattering should be more intense in smaller grain samples where there are more boundaries which is in qualitative agreement with the previous observations of Prakash and Srivastava (1980). The details of this mechanism are being investigated.

### References

- Gurevich A G and Anisimov A N 1975 *Sov. Phys.* **41** 336
- Patton C E 1970 *J. Appl. Phys.* **41** 1637
- Prakash O and Srivastava C M 1980 *Bull. Mater. Sci.* **2** 181
- Scotter D G 1972 *J. Phys.* **D5** L93
- Sparks M 1967 *Phys. Rev.* **160** 364
- Sparks M 1964 *Ferromagnetic relaxation theory* (New York: McGraw-Hill)
- Vaks V G, Larkin A I and Pikin S A 1968 *Sov. Phys. JETP* **26** 647
- Vrehans Q H F 1966 *J. Appl. Phys.* **40** 1849
- White G, Patton C E and Edmondson 1979 *J. Appl. Phys.* **50** 2118



1

1

1

1

• • •

!

1

1

2

1

## Spin-wave excitations in amorphous ferromagnets

ANIL K BHATNAGAR, B BHANU PRASAD, N RAVI and  
R JAGANNATHAN\*

School of Physics, \*School of Chemistry, University of Hyderabad, Hyderabad 500 134, India

MS received 7 May 1983

**Abstract.** Mössbauer measurements have been performed on a number of metallic glasses. The temperature dependence of average hyperfine or internal magnetic field  $H_{\text{eff}}(T)$  arises from long wavelength spin wave excitations in these glasses. Values of  $B_{3/2}$  and  $C_{5/2}$  are in general much higher than those observed for crystalline ferromagnets indicating higher density of states for spin waves in amorphous ferromagnets.

**Keywords.** Spin wave excitations; amorphous ferromagnets; Mössbauer measurements; metallic glasses; temperature dependence.

### 1. Introduction

Amorphous metallic alloys, prepared by rapid quenching of molten alloys, have become an important class of materials from theoretical as well as practical points of view in recent years. There have been extensive studies of magnetic and electrical properties of iron-rich metallic glasses in the past decade. Study of magnetic phenomena in these glasses presents a fascinating field for theorists and experimentalists as magnetism is a structure sensitive property, and therefore, it is expected to be affected in amorphous solids. In this paper we discuss the temperature dependence of hyperfine magnetic field of iron-rich metallic glasses as measured by the  $^{57}\text{Fe}$  Mössbauer spectroscopy. Results are interpreted in terms of excitations of long wavelength spin waves.

### 2. Experimental

Mössbauer spectra of a number of commercially available metallic glasses ( $\text{Fe}_{81}\text{B}_{13.5}\text{Si}_{3.5}\text{C}_2$ ,  $\text{Fe}_{78}\text{B}_{13}\text{Si}_9$ ,  $\text{Fe}_{79}\text{B}_{16}\text{Si}_5$ ,  $\text{Fe}_{40}\text{Ni}_{40}\text{B}_{20}$  and  $\text{Fe}_{67}\text{Co}_{18}\text{B}_{14}\text{Si}_1$ ) were recorded in the temperature range 77–900 K using an Elscint spectrometer coupled with a 256 channel MCA. The spectrometer was used in the constant acceleration mode and the source was  $^{57}\text{Co}$  in rhodium matrix. The Curie temperatures of  $\text{Fe}_{81}\text{B}_{13.5}\text{Si}_{3.5}\text{C}_2$ ,  $\text{Fe}_{78}\text{B}_{13}\text{Si}_9$ ,  $\text{Fe}_{40}\text{Ni}_{40}\text{B}_{20}$  and  $\text{Fe}_{79}\text{B}_{16}\text{Si}_5$  were determined by the constant Doppler velocity thermal-scan method (Bhanu Prasad *et al* 1983), while that of  $\text{Fe}_{67}\text{Co}_{18}\text{B}_{14}\text{Si}_1$  was estimated by plotting hyperfine magnetic field,  $H_{\text{eff}}(T)$  vs temperature since the Curie temperature,  $T_c$ , in this case was larger than the crystallization temperature (Bhanu Prasad *et al* 1980).  $H_{\text{eff}}(T)$  values were determined by fitting each spectrum to the Lorentzian line-shape sextet pattern. The spectrometer was calibrated using a thin iron foil.

### 3. Results and discussion

The decrease in magnetization of a crystalline ferromagnet at low temperatures can be explained if the low lying magnetic excitations are spin waves which obey the following dispersion relation:

$$\hbar\omega(q) = Dq^2 + Eq^4 + \dots \quad (1)$$

where  $\hbar\omega(q)$  is the energy of spin wave with propagation wave number  $q$ , and  $D$  and  $E$  are the stiffness constants. Usually  $E$  is much smaller than  $D$ . This dispersion relation leads to the following temperature dependence of magnetization  $M(T)$ ,

$$M(T) = M(0) (1 - BT^{3/2} - CT^{5/2} - \dots), \quad (2)$$

where  $B$  and  $C$  are constants and are related to  $D$  and  $E$  as given below.

$$B = 2.612 [g\mu_B / M(0)] (k_B/4\pi D)^{3/2} \quad (3)$$

$$C = 1.341 [g\mu_B / M(0)] (k_B/4\pi D)^{5/2} (15\pi E/D) \quad (4)$$

where  $k_B$  is the Boltzmann constant,  $\mu_B$  is the B  hr magneton and  $g$  is the usual  $g$  factor. Equation 2 can be rearranged to give

$$\frac{M(T) - M(0)}{M(0)} = -BT^{3/2} - CT^{5/2} - \dots \quad (5)$$

or

$$\frac{M(T) - M(0)}{M(0)} = -B_{3/2}(T/T_c)^{3/2} - C_{5/2}(T/T_c)^{5/2} - \dots \quad (6)$$

Inelastic neutron scattering measurements on some of amorphous ferromagnets have established the existence of long wavelength spin waves obeying the dispersion relation given by (1) (Lynn *et al* 1976; Rhyne *et al* 1979). Similarly magnetization measurements (Tsuei *et al* 1968; Kaul 1981) and ferromagnetic resonance studies (Spano and Bhagat 1981) have shown that the temperature dependence of  $M(T)$  follows the behaviour predicted by (2).

From M  ssbauer measurements the average internal magnetic field  $H_{\text{eff}}(T)$  is determined. It has been found experimentally that for most iron-rich metallic glasses, the average internal magnetic field is directly proportional to the magnetization to a good approximation and the proportionality constant is approximately 135 kOe/ $\mu_B$  (Chien *et al* 1979). Therefore, (5) and (6) can be expressed in terms of  $H_{\text{eff}}(T)$  as follows:

$$\frac{H_{\text{eff}}(T) - H_{\text{eff}}(0)}{H_{\text{eff}}(0)} = -BT^{3/2} - CT^{5/2} - \dots \quad (7)$$

or

$$\frac{H_{\text{eff}}(T) - H_{\text{eff}}(0)}{H_{\text{eff}}(0)} = -B_{3/2}(T/T_c)^{3/2} - C_{5/2}(T/T_c)^{5/2} - \dots \quad (8)$$

where  $B$ ,  $C$ ,  $B_{3/2}$ , and  $C_{5/2}$  constants remain the same as in (5) and (6). Thus the temperature dependence of  $H_{\text{eff}}(T)$  at low temperatures can also be interpreted in terms of excitations of spin waves. At first it may seem surprising that spin waves can be excited in noncrystalline solids. However, the situation is quite akin to the sound wave

propagation in glasses. This is so because the long wavelength modes are not sensitive to the local order or disorder. In particular Herring and Kittel (1951) have shown that long wavelength spin waves can exist even in a ferromagnetic continuum medium.

Average hyperfine magnetic fields of various metallic glasses were determined as explained in §2. A plot of  $[H_{\text{eff}}(T) - H_{\text{eff}}(0)]/H_{\text{eff}}(0)$  vs  $(T/T_c)^{3/2}$  for various metallic glasses is shown in figure 1. A computer least square fit of (7) and (8) to experimental data yields values of  $B$ ,  $C$ ,  $B_{3/2}$  and  $C_{5/2}$  which are given in table 1. For sake of comparison, the values of these constants for crystalline Fe and Ni, and glassy  $\text{Fe}_{40}\text{Ni}_{40}\text{P}_{14}\text{B}_6$ ,  $\text{Fe}_{80}\text{B}_{20}$  and  $\text{Fe}_{82}\text{B}_{12}\text{Si}_6$  are also listed in the table. It is observed that  $B_{3/2}$  values range from 0.2–0.4 and are much larger than the values for crystalline Fe and Ni. Also  $T^{3/2}$  dependence of relative change in  $H_{\text{eff}}(T)$  extends to much higher temperatures than observed for crystalline ferromagnets.  $T^{3/2}$  plus  $T^{5/2}$  dependence, as given by (7) and (8), can be fitted to experimental data over a large temperature interval. Values of  $B$  ( $B_{3/2}$ ) and  $C$  ( $C_{5/2}$ ) depend upon the temperature interval used to fit the data (Bhatnagar *et al* 1982; Saegusa and Morrish 1982). If data is fitted over a large temperature interval then it has the effect of reducing the  $B$  ( $B_{3/2}$ ) value and increasing the  $C$  ( $C_{5/2}$ ) value which is expected. It has also been observed that  $B$  and  $C$  values

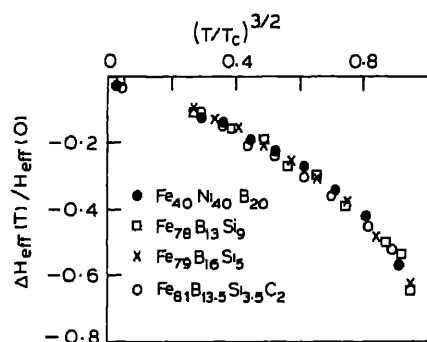


Figure 1. Plot of  $[H_{\text{eff}}(T) - H_{\text{eff}}(0)]/H_{\text{eff}}(0)$  vs  $(T/T_c)^{3/2}$  for various iron-rich metallic glasses.

Table 1. Sample compositions, Curie temperature  $T_c$ , coefficients  $B$ ,  $C$ ,  $B_{3/2}$  and  $C_{5/2}$  for amorphous ferromagnets and crystalline Fe and Ni.

System	$T_c$ (K)	$B$ ( $10^{-6}$ K $^{-3/2}$ )	$C$ ( $10^{-8}$ K $^{-5/2}$ )	$B_{3/2}$	$C_{5/2}$	Reference
$\text{Fe}_{80}\text{B}_{20}$	685	22	1.2	0.40	0.17	Chien (1978)
$\text{Fe}_{40}\text{Ni}_{40}\text{B}_{20}$	695	22	0.4	0.40	0.06	Present work
$\text{Fe}_{40}\text{Ni}_{40}\text{P}_{14}\text{B}_6$	537	38	1.2	0.47	0.08	Chien and Hasegawa (1977)
$\text{Fe}_{78}\text{B}_{13}\text{Si}_9$	733	10	2.4	0.21	0.35	Present work
$\text{Fe}_{79}\text{B}_{16}\text{Si}_5$	730	11	2.3	0.22	0.33	Present work
$\text{Fe}_{82}\text{B}_{12}\text{Si}_6$	658	—	—	0.34	0.21	Ok and Morrish (1980)
$\text{Fe}_{81}\text{B}_{13.5}\text{Si}_{3.5}\text{C}_2$	698	16	2.1	0.30	0.27	Present work
$\text{Fe}_{81}\text{B}_{13.5}\text{Si}_{3.5}\text{C}_2$	668	—	—	0.30	0.29	Saegusa and Morrish (1982)
Crystalline Fe	1042	3.4	0.1	0.114	0.04	Chien and Hasegawa (1977)
Crystalline Ni	637	7.5	1.5	0.117	0.15	Chien and Hasegawa (1977)

become much smaller after the amorphous material crystallizes (Hasegawa and Ray 1979). Hence, the high  $B(B_{3/2})$  and  $C(C_{5/2})$  values seem to be the characteristic of the amorphous state. Higher  $B$  values in glassy ferromagnets also mean lower values of  $D$ , the stiffness constant, for glassy systems as seen from (3). Lower values of  $D$  also mean that the density of states for spin waves are higher in the amorphous state. Theoretical calculations do show higher density of states for spin waves in amorphous materials due to fluctuations in the exchange interaction arising from the random atomic arrangement (Montgomery *et al* 1970; Simpson 1974). Thus the existence of spin wave excitations in amorphous ferromagnets is clearly demonstrated by Mössbauer measurements as well as by magnetization (Kaul 1981) and inelastic neutron scattering measurements (Lynn *et al* 1976; Axe *et al* 1977; Rhyne *et al* 1979).

#### 4. Conclusion

The temperature dependence of the average internal magnetic field of a number of ferromagnetic metallic glasses can be described by the expression  $H_{\text{eff}}(T) = H_{\text{eff}}(0) (1 - BT^{3/2} - CT^{5/2} - \dots)$ , which is indicative of spin wave excitations in these solids. Values of  $B(B_{3/2})$  are much higher than those for crystalline Fe, Ni etc. This observation can be explained if higher density of states for spin waves are assumed in the amorphous ferromagnets. Values of  $B(B_{3/2})$  and  $C(C_{5/2})$  are found to depend upon the temperature interval used to fit experimental data to the  $T^{3/2}$  and  $T^{5/2}$  dependence.

#### Acknowledgements

Authors thank the Science and Engineering Research Council (DST, India) and the Department of Atomic Energy for support.

#### References

- Axe J D, Shirane G, Mizoguchi T and Yamauchi K 1977 *Phys. Rev.* **B15** 2763
- Bhanu Prasad B, Bhatnagar A K and Jagannathan R 1980 *Solid State Commun.* **36** 661
- Bhanu Prasad B, Bhatnagar A K and Jagannathan R 1983 *J. Appl. Phys.* **54** 2019
- Bhatnagar A K, Bhanu Prasad B, Ravi N, Jagannathan R and Anantharaman T R 1982 *Solid State Commun.* **44** 905
- Chien C L 1978 *Phys. Rev.* **B18** 1003
- Chien C L and Hasegawa R 1977 *Phys. Rev.* **B16** 2115
- Chien C L, Musser D, Gyorgy E M, Sherwood R C, Chen H S, Luborsky F E and Walter J L 1979 *Phys. Rev.* **B20** 283
- Hasegawa R and Ray R 1979 *Phys. Rev.* **B20** 211
- Herring C and Kittel C 1951 *Phys. Rev.* **81** 869
- Kaul S N 1981 *Phys. Rev.* **B24** 6550
- Lynn J W, Shirane G, Birgeneau R J and Chen H S 1976 *AIP Conf. Proc.* **34** 313
- Montgomery C G, Krugler J I and Stubbs R M 1970 *Phys. Rev. Lett.* **25** 669
- Ok H N and Morrish A H 1980 *Phys. Rev.* **B22** 4215
- Rhyne J J, Lynn J W, Luborsky F E and Walter J L 1979 *J. Appl. Phys.* **50** 1583
- Saegusa N and Morrish A H 1982 *Phys. Rev.* **B26** 10
- Simpson A W 1974 *Wiss. Z. dTH Dresden* **3** 1020
- Spano M L and Bhagat S M 1981 *J. Magn. Mag. Mater.* **24** 143
- Tsuei C C, Longworth G and Lin S C H 1968 *Phys. Rev.* **170** 603

## Infrared absorption in spinel ferrites

T T SRINIVASAN, C M SRIVASTAVA, N VENKATARAMANI\* and  
M J PATNI\*

Department of Physics, \*Materials Science Centre, Indian Institute of Technology, Powai,  
Bombay 400 076, India

MS received 31 May 1983

**Abstract.** The IR spectra of a number of ferrites,  $MFe_2O_4$ ,  $M$ (Mn, Fe, Co, Ni, Cu and Zn) have been studied at room temperature in the range  $200\text{--}1000\text{ cm}^{-1}$ . In all the cases the spectrum consists of four bands, two of which have strong absorption while the other two have weak absorption and often appear as shoulders on the main band. However up to 20% of the inverse ferrite, the shoulder in the low energy side appears as a band. In this paper we have analysed the origin of the above bands.

**Keywords.** IR spectrum; ferrites; centre frequency; force constants.

### 1. Introduction

Infrared spectrum of ferrites has been studied by Waldron (1955). The effect of a Jahn-Teller ion on the lattice vibrational frequencies of nickel ferrite has also been studied by Srivastava and Srinivasan (1982). Waldron has assumed that the 14 atoms in the primitive unit cell of a spinel lattice can be divided into two  $MO_4$  groups and one  $Fe_4$  group of tetrahedral symmetry. This allows the classification of the vibrations into the point group  $T_d$ . The conclusions reached by him are not very satisfactory. For example, the force constants  $K_t$  for the  $t\text{--}o$  bond for the normal ferrite  $ZnFe_2O_4$  and  $MnFe_2O_4$  are substantially smaller than that for the inverse spinels like Co, Fe and Ni ferrites. The normal ferrites are formed due to the strong tetrahedral site preference of the divalent ions like  $Zn^{2+}$ . As the size of the  $Zn^{2+}$  ( $0.74\text{ \AA}$ ) ion is larger than the  $Fe^{3+}$  ( $0.64\text{ \AA}$ ) ion, the overlap and strength of the  $t\text{--}o$  bond is expected to be greater for  $ZnFe_2O_4$  than say for  $Fe_3O_4$ . We would therefore expect that the increased covalency in the bond would more than compensate for the decrease in the electrostatic energy due to the change for  $3+$  and  $2+$  state of the metal ion. Further each of the two broad bands showed asymmetry in the line shape. Waldron (1955) has also reported the presence of low as well as high frequency shoulders in his observations. We have analysed them as additional vibrational modes of the system. The IR frequencies are given in tables 1 and 2.

### 2. Experimental

The samples were prepared using the normal conventional ceramic technique. All the samples had densities higher than 97% of their x-ray density. The x-ray analysis showed a single phase and a spinel structure.

**Table 1.** IR spectral frequencies of ferrites.

MFe <sub>2</sub> O <sub>4</sub>	Centre frequency (linewidth)cm <sup>-1</sup>			
	T <sub>2</sub> <sup>a</sup>	T <sub>2</sub> <sup>b</sup>	E <sup>a</sup>	E <sup>b</sup>
Mn	330 (88)	400 (100)	545 (78)	640 (90)
Fe*	350 (62)	410 (55)	590 (78)	640 (100)
Co*	340 (67)	390 (50)	570 (75)	650 (78)
Ni	340 (105)	396 (40)	587 (100)	660 (110)
Cu	330 (70)	400 (90)	565 (80)	620 (75)
Zn	338 (105)	415 (120)	550 (85)	660 (160)

\*Waldron's (1955) data.

**Table 2.** IR spectral frequencies of Zn<sub>1-x</sub>Ni<sub>x</sub>Fe<sub>2</sub>O<sub>4</sub> (0 ≤ x ≤ 1).

x	Centre frequency of (cm <sup>-1</sup> )			
	T <sub>2</sub> <sup>a</sup>	T <sub>2</sub> <sup>b</sup>	E <sup>a</sup>	E <sup>b</sup>
0	338	415	550	660
0.02	338	415	555	670
0.04	338	420	553	670
0.06	340	420	555	670
0.08	338	421	555	670
0.15	340	421	559	670
0.2	340	422	562	670
1	340	396	587	660

The ferrite powders were dispersed in KBr and pressed to get a clear disc. The spectra in the range of 200–1000 cm<sup>-1</sup> were recorded at room temperature (SP 2000 IR Spectrometer, TYPE UNICHEM make). In order to examine the effect of the transformation from the normal to the inverse ferrite on the lattice modes of vibration we have studied the IR spectra of Zn<sub>1-x</sub>Ni<sub>x</sub>Fe<sub>2</sub>O<sub>4</sub> [0 ≤ x ≤ 0.2 and x = 1]. These are shown in figure 1. The spectrum has been analysed in terms of four bands, each having a Lorentzian shape.

### 3. Analysis and discussion

Our observations show that the spectrum in all the cases consists of four bands, two of which have strong absorption. The remaining two have weaker absorption, and in some

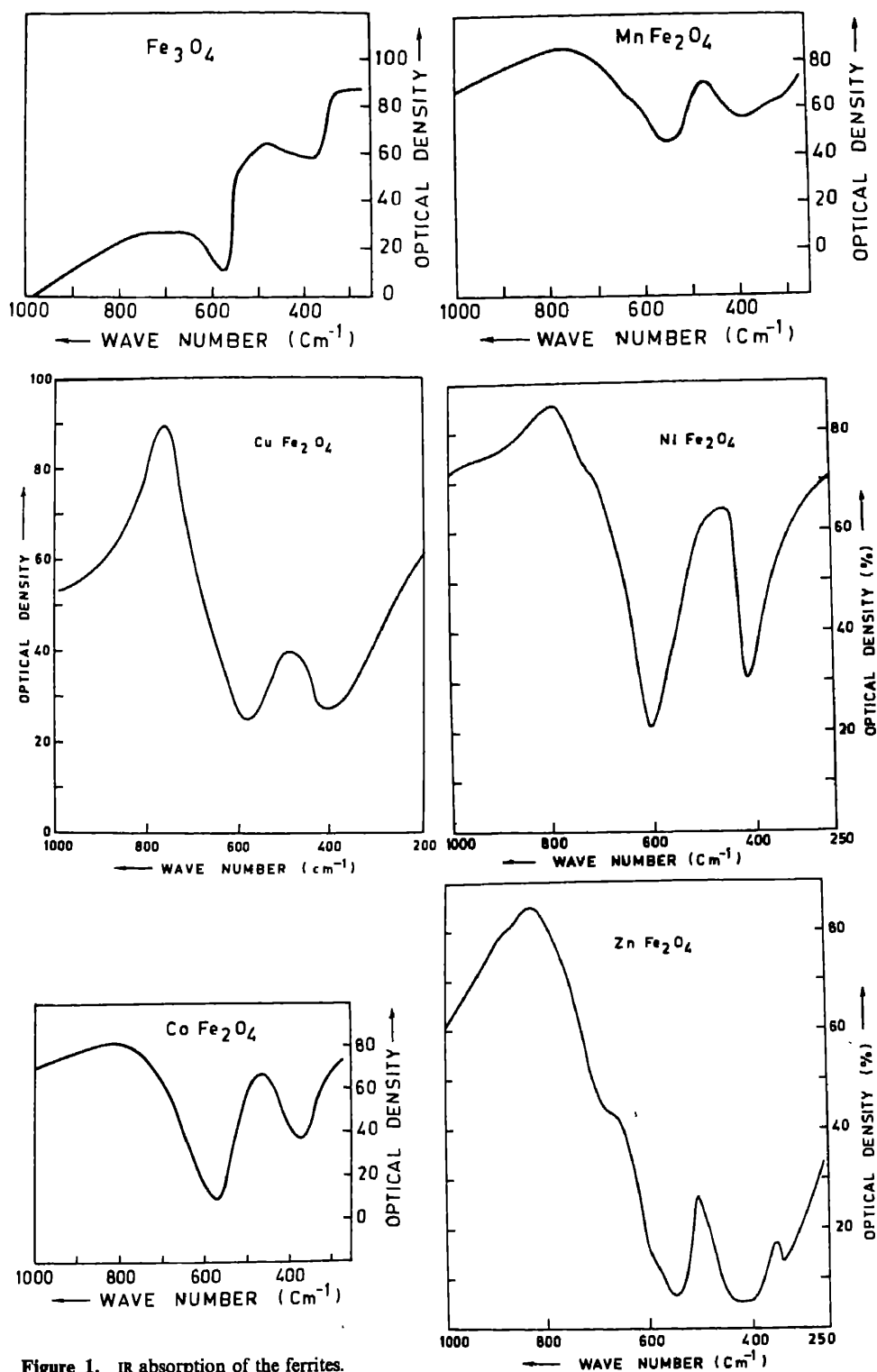


Figure 1. IR absorption of the ferrites.



cases appear as a shoulder to the main bands. We have attributed these to the absorption by lattice vibrations having  $E$  and  $T_2$  symmetries. These type of phonon modes have been assumed by Bates and Steggle (1975) for the analysis of EPR data in  $\text{Fe}^{2+}$  in  $\text{Al}_2\text{O}_3$ . As there are two types of metals in the sites, we have  $E^o$ ,  $E^t$ ,  $T_2^o$  and  $T_2^t$  phonon modes where the superscripts 'o' and 't' indicate the  $E$  and  $T_2$  symmetry of the atomic displacements around the octahedral and tetrahedral metal ions. The bands were identified on the systematics of the observed central frequencies as the metal ion  $M$  was changed from  $d^5$  to  $d^{10}$  configurations. The frequency increases in the following order

$$\nu(T_2^o) < \nu(T_2^t) < \nu(E^o) < \nu(E^t).$$

It is difficult to assign the precise nature of atomic displacements for these modes of vibrations. We assume that those of the  $T_2$  type would be bond-bending while the  $E$  type would be bond-stretching so that in general  $\nu(T_2) < \nu(E)$ . Again we would assume that the bond stretching for tetrahedral site would lead to a higher force constant than that for the octahedral site. On this basis we would be able to assign the bands in the order given in tables 1 and 2. The IR frequencies as a function of the number of  $d$  electrons in  $M^{2+}$  ion are plotted in figure 2. It is seen that with an assignment the stretching mode of the tetrahedral  $t-o$  bond ( $E^t$ ) has a larger value for  $\text{ZnFe}_2\text{O}_4$  as compared to others. This mode however has a relatively weak absorption. The stretching modes ( $E^o$ ) for the normal Mn and Zn ferrites have identical frequencies as these have only  $\text{Fe}^{3+}$  ions on the B-site. The bond stretching modes ( $E^o$ ) on the B-site have a strong absorption. For  $\text{Ni}^{2+}$ , it shows a higher frequency and a narrow band. This seems to be related to the ground singlet state of the ion. Even  $T_2^t$  bands in this ferrite ( $\Delta\nu \approx 40 \text{ cm}^{-1}$ ) is narrower as compared to others. The bond-bending frequencies  $T_2^t$  and  $T_2^o$  are nearly the same as expected. In table 2 the variation of centre frequencies as one goes from normal ferrite ( $\text{ZnFe}_2\text{O}_4$ ) to inverse ferrite ( $\text{NiFe}_2\text{O}_4$ ) is given for all the four bands.

In an inverse ferrite the octahedral site is occupied by  $\text{Fe}^{3+}$  and the divalent ion  $M^{2+}$ . Due to charge imbalance the oxygen ion is likely to shift towards the  $\text{Fe}^{3+}$  ion making

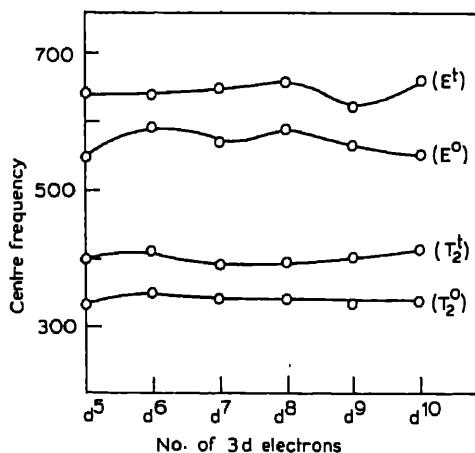


Figure 2. IR frequencies as a function of the number of  $d$  electrons in  $M^{2+}(\text{MFe}_2\text{O}_4)$ .

the force constant between  $\text{Fe}^{3+}$  and  $\text{O}^{2-}$  more. Hence we expect an increase in the bond stretching  $E^o$  phonon mode, frequencies as we go from normal to inverse spinels. This is supported by our results on  $\text{Zn}_{1-x}\text{Ni}_x\text{Fe}_2\text{O}_4$  in which we find that  $\nu(E^o)$  increase as  $x$  is increased and the others  $T_2^o$ ,  $T_2^i$  and  $E^i$  do not change with the type of spinel structure, given in table 2.

#### 4. Conclusions

IR spectrum of spinel ferrites in the range of  $200\text{--}1000\text{ cm}^{-1}$  consists four bands. These bands have been assigned on the basis of  $E$  and  $T_2$  phonon symmetries around the crystallographic metal ion sites,  $A$  and  $B$ . On gradual change from normal to inverse spinel structure only one of the bands is affected as expected.

#### References

- Bates C A and Steggles P 1975 *J. Phys.* **C8** 2283  
Srivastava C M and Srinivasan T T 1982 *J. Appl. Phys.* **53** 8148  
Waldron R D 1955 *Phys. Rev.* **99** 1727



## Influence of spin orbit coupling and lanthanide contraction on the exchange interaction in rare earth garnets

C M SRIVASTAVA, C SRINIVASAN and R AIYAR

Department of Physics, Indian Institute of Technology, Bombay 400 076, India

MS received 7 May 1983

**Abstract.** The exchange constants observed in the rare earth iron garnets, obtained from fitting magnetization and paramagnetic susceptibility as a function of temperature have been analysed in terms of Anderson's theory of superexchange. The transfer integrals and covalency parameters have been obtained for various rare earth ions overlapping with oxygen.

**Keywords.** Exchange constants; superexchange; transfer integrals; covalency parameters; molecular field constants.

### 1. Introduction

In an earlier paper (Srivastava *et al* 1982) we had reported the simultaneous fitting of saturation magnetisation ( $M_s$ ) and paramagnetic susceptibility ( $\chi$ ) for the ferrimagnetic garnets  $R_3Fe_5O_{12}$  where  $R$  is yttrium or a trivalent rare earth ion with configuration  $(Xe) 4f^n$  ( $7 \leq n \leq 13$ ). We had used the molecular field constants to determine the exchange constants by means of the equation

$$J_{ij} = \frac{g_i g_j \mu_B^2 n_j \lambda_{ij}}{2 Z_{ij}}, \quad (1)$$

where  $g_i, g_j$  are the  $g$  factors of the sublattices  $i$  and  $j$ ,  $\lambda_{ij}$  are the molecular field constants,  $n_j$  is the number of  $j$  ions per unit mole and  $Z_{ij}$  is the number of  $n - n_j$  ions to an ion on  $i$ th sublattice. But if one of the ions involved is a rare earth ion then (1) is not the correct expression to convert the molecular field constants to  $J_{ij}$ . This is because for the rare earths the orbital momentum is not quenched and hence the exchange energy is

$$E_i = -2n_j Z_{ij} J_{ij} (g_i - 1) \bar{J}_i \cdot \bar{S}_j. \quad (2)$$

Here, we have assumed that the  $i$ th ion is a rare earth and the factor  $(g_i - 1)$  comes because the rare earth spin has to be projected on  $J_i$  the angular momentum. In terms of  $\lambda_{ij}$ ,  $E_i$  is given by

$$\begin{aligned} E_i &= -\mu_i \cdot \mu_j = -g_i \bar{J}_i \mu_B \cdot \lambda_{ij} \bar{M}_j, \\ &= -n_j g_i g_j \mu_B^2 n_j \lambda_{ij} \bar{J}_i \cdot \bar{S}_j \end{aligned} \quad (3)$$

From (2) and (3) we get

$$J_{ij} = \frac{g_i g_j \mu_B^2 n_j \lambda_{ij}}{2 Z_{ij} (g_i - 1)}. \quad (4)$$

Table 1. Exchange constants ( $^{\circ}\text{K}$ ) in garnets ( $\text{R}_3\text{Fe}_5\text{O}_{12}$ ).

R	Values in $^{\circ}\text{K}$		
	$-J_{ac}$	$-J_{dc}$	$-J_{cc}$
Y	0	0	0
Gd	0.60	1.8	0
Tb	1.12	2.0	0
Dy	2.97	2.97	-0.9
Ho	2.64	2.80	0
Er	2.70	3.40	0
Tm	2.64	3.96	0
Yb	21.00	16.1	-0.2

The  $-J_{aa}$ ,  $-J_{ad}$  and  $-J_{dd}$  values are 6.45, 30.40 and 12.05 respectively in all the cases.

Equation (4) differs from (1) because of the factor  $(g_i - 1)$  in the denominator. Hence the exchange constants have to be corrected by dividing the values reported earlier (Srivastava *et al* 1982) by  $(g_i - 1)$  where  $g_i$  is the  $g$  factor of the rare earth site. These are shown in table 1.

## 2. Exchange constants from Anderson's theory

We give below the calculation of exchange constants from Anderson's theory of superexchange for these garnets. For the exchange between a rare earth and  $\text{Fe}^{3+}$  ions in garnets Levy (1966) has shown that if the  $Z$  axis for the interaction is chosen as the  $\text{RE-O}^{2-}$  bond direction then the only orbital on the RE ion contributing to the exchange is the one with  $m_l = 0$  (i.e.  $f_z$  orbital). Following the same convention we find that the only transfer integral in Anderson's expression for  $180^{\circ}$  superexchange interaction is  $b_{\sigma\sigma}$  arising from the overlaps of  $f_z$  orbital on RE ion and  $e_g(d_z^2)$  on  $\text{Fe}^{3+}$  with a  $p_z$  orbital on the  $\text{O}^{2-}$  ion. Similarly the only transfer integral for the  $90^{\circ}$  exchange is  $b_{\pi\sigma}$  arising from overlaps of  $t_{2g}$  and  $f_z$  orbitals with  $p_x$  orbital on oxygen. Thus we have (ignoring direct overlap of magnetic orbitals)

$$J_{ij} = -\frac{1}{4(g_i - 1)J_i S_j} 2 \frac{b_{\sigma\sigma}^2}{U} \text{ for } 180^{\circ} \text{ superexchange} \quad (5a)$$

$$J_{ij} = -\frac{1}{4(g_i - 1)J_i S_j} 2 \frac{b_{\pi\sigma}^2}{U} \text{ for } 90^{\circ} \text{ superexchange} \quad (5b)$$

In rare earths the spin orbit interaction is very strong compared to the crystal field energy, hence the ground state wavefunction will have admixtures of states with all values of  $m_l$ . However, as explained above only the  $m_l = 0$  state contributes to the superexchange. Hence if we assume that all the  $m_l$  states have equal probability of being occupied then the probability that the state  $m_l = 0$  has unpaired electron is  $1 - (n - 7)/7 = 2 - (n/7)$  where  $n$  is the number of electrons in the  $4f$  shell ( $n \geq 7$ ). Using this in (5) and noting that  $J_{ac}$  is a predominantly  $90^{\circ}$  exchange while  $J_{dc}$  is a  $180^{\circ}$

exchange we get for a  $f^n-d^5$  superexchange interaction

$$J_{dc} = -\frac{1}{4(g_i-1)J_iS_j}2\frac{b_{\sigma\sigma}^2}{U}\left(2-\frac{n}{7}\right), \quad (6a)$$

$$J_{ac} = -\frac{1}{4(g_i-1)J_iS_j}2\frac{b_{\pi\sigma}^2}{U}\left(2-\frac{n}{7}\right). \quad (6b)$$

The values of the coulomb energy can be estimated by a procedure used by Anderson (1959) to evaluate  $U$  for the  $3d$  series transition metal ions. Taking the free ion ionisation potential (IP) for these ions we find that  $I_4 - I_3$  i.e. the difference between the 4th and 3rd IP gives the free ion  $U$ . This has to be corrected in the solid. Firstly the transfer of electrons take place through a finite distance and not to infinity as is the case for calculating IP. Anderson estimated this correction to be 4 eV for  $3d$  electrons. We shall assume the same correction for  $R^{3+}$  ions. The next correction is the dielectric polarisation correction because the coulomb repulsion takes place in a dielectric medium and not in vacuum. This gives another correction of 4 eV. Finally because of covalency another 10% correction is required. Using the IP calculated by Sugar and Reader (1973) and using the above method we get  $U = 10 \text{ eV} \pm 1 \text{ eV}$  for all the rare earth ions except  $\text{Gd}^{3+}$  as shown in table 2. Since the ground state of  $\text{Gd}^{2+}$  is  $5d^2f^7$  and not  $f^8$ , the  $U$  value for Gd will reduce if the correct IP for  $4f^7 \rightarrow f^8$  transition is taken. Hence we can assume  $U = 10 \text{ eV}$  for all the heavy rare earths. Using (4) instead of (1) as was used in our earlier work (Srivastava *et al* 1982) to get the correct values of  $J_{ij}$  we have obtained the values of  $b_{\sigma\sigma}$  and  $b_{\pi\sigma}$  using (7) for all these garnets which are given in table 3. In table 3 we also give the distance of closest approach of the rare earth and oxygen orbitals

$$S^{-1} = \frac{r_{R-O} - (r(R^{3+}) + r(O^{2-}))}{r(R^{3+}) + r(O^{2-})}.$$

The values of  $r_{R-O}$ ,  $r(R^{3+})$ ,  $r(O^{2-})$  are from Tch  ou *et al* (1970), Khattak and Yang (1979) and CRC handbook (1980) respectively. Figure 1 gives a plot of  $b^2$  against  $S^{-1}$  for both  $b_{\sigma\sigma}^2$  and  $b_{\pi\sigma}^2$ . This curve resembles the curve obtained by Slater (1953) for metals. However,  $b_{\sigma\sigma}^2$  does not show the peak in the observed region of overlap. Yb does not fit in the above scheme because as shown by Copland (1970) the  $5p$  shell plays a

Table 2. Coulomb energy  $U$  (eV) for rare earth ions.

Ion	Ionisation potential (eV)		Free ion $U = I_4 - I_3$ (eV)	Corrected $U$ (eV)	Covalency correction (10%)	Corrected $U$ in solid (eV)
	$I_3$	$I_4$				
Gd	20.63	44.01	23.78	15.38	1.54	13.84
Tb	21.91	39.79	12.88	9.88	0.99	8.89
Dy	22.79	41.47	18.68	10.68	1.07	9.61
Ho	22.84	42.48	19.64	11.68	1.17	10.57
Er	22.74	42.65	19.91	11.91	1.19	10.92
Tm	23.68	42.69	19.01	11.01	1.10	9.91
Yb	25.03	43.74	18.71	10.71	1.07	9.64

The correction for  $n-n$  and dielectric polarization was 8 in all the cases.

Table 3. Transfer integrals in garnets  $R_3\text{Fe}_5\text{O}_{12}$ .

$R$	$J_i$	$b_{\sigma\sigma}^2$ (eV) <sup>2</sup>	$b_{\pi\sigma}^2$ (eV) <sup>2</sup>	$S^{-1}$ $r(R-O) - r(R^{3+}) - r(O^{2-})$
				$r(R^{3+}) + r(O^{2-})$
Gd	3.5	0.0271	0.0091	0.016
Tb	6.0	0.0295	0.0168	0.022
Dy	7.5	0.0448	0.0448	0.024
Ho	8.0	0.0419	0.0398	0.026
Er	7.5	0.0513	0.0408	0.032
Tm	6.0	0.0596	0.0398	0.035
Yb	3.5	0.0240	1.15	0.037

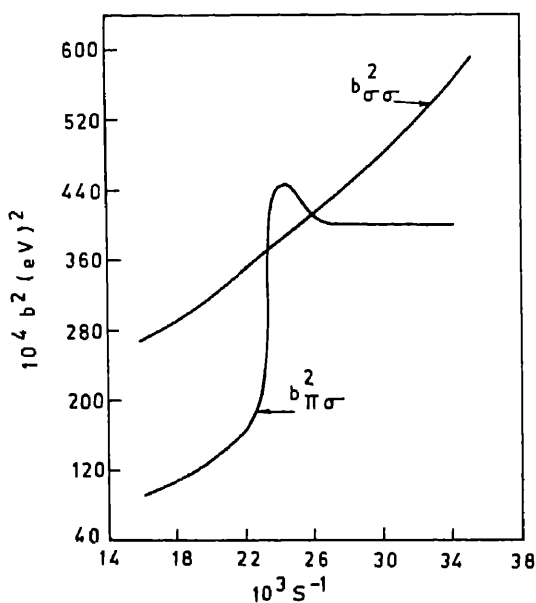


Figure 1. Transfer integrals in garnets.

dominant role in superexchange in YbIG, unlike the other garnets where the 4f shell is the dominant orbital contributing to superexchange.

### 3. Covalency parameters

Zeiger and Pratt (1973) have shown that the transfer integrals  $b_{ij}$  are related to the covalency parameters  $\lambda_{ic}$  and  $\lambda_{jc}$ , where  $c$  refers to the intervening anion by

$$b_{ij} = \lambda_{ic}\lambda_{jc}\Delta E_c$$

where  $\Delta E_c$  is the one electron ionization energy of the anion. For the  $\text{Fe}^{3+}\text{-Fe}^{3+}$

Table 4. Covalency parameters and transfer integrals in garnets.

	Type of exchange	Transfer integral	Value of $b_k$ (eV)	$\lambda_\sigma$ ( $\text{Fe}^{3+}-\text{O}^{2-}$ )	$\lambda_\pi$ ( $\text{Fe}^{3+}-\text{O}^{2-}$ )	$\lambda_\sigma$ ( $\text{R}^{3+}-\text{O}^{2-}$ )
$\text{Fe}^{3+}$	$J_{ad}$	$b_{\sigma\sigma}$	0.48	0.24		
		$b_{\pi\pi}$	0.18		0.14	
	$J_{dd}$	$b_{\sigma\sigma'}$	0.12	0.12		
		$b_{\pi\sigma}$	0.30	0.25	0.14	
$\text{Gd}^{3+}$	$J_{ac}$	$b_{\pi\sigma}$	0.095		0.14	0.078
	$J_{dc}$	$b_{\sigma\sigma}$	0.16	0.25		0.08
$\text{Tb}^{3+}$	$J_{ac}$	$b_{\pi\sigma}$	0.13		0.14	0.107
	$J_{dc}$	$b_{\sigma\sigma}$	0.17	0.25		0.08
$\text{Dy}^{3+}$	$J_{ac}$	$b_{\pi\sigma}$	0.21		0.14	0.17
	$J_{dc}$	$b_{\sigma\sigma}$	0.21	0.25		0.098
$\text{HO}^{3+}$	$J_{ac}$	$b_{\pi\sigma}$	0.20		0.14	0.16
	$J_{dc}$	$b_{\sigma\sigma}$	0.20	0.25		0.094
$\text{Er}^{3+}$	$J_{ac}$	$b_{\pi\sigma}$	0.20		0.14	0.17
	$J_{dc}$	$b_{\sigma\sigma}$	0.22	0.25		0.105
$\text{Tm}^{3+}$	$J_{ac}$	$b_{\pi\sigma}$	0.20		0.14	0.16
	$J_{dc}$	$b_{\sigma\sigma}$	0.24	0.25		0.11
$\text{Yb}^{3+}$	$J_{ac}$	$b_{\pi\sigma}$	1.07		0.14	0.8
	$J_{dc}$	$b_{\sigma\sigma}$	0.15	0.25		0.07

exchange we have

$$\begin{aligned}
 b_{\sigma\sigma} &= \lambda_\sigma(\text{Fe}^{3+})\lambda_\sigma(\text{Fe}^{3+})\Delta E_c \\
 b_{\pi\pi} &= \lambda_\pi(\text{Fe}^{3+})\lambda_\pi(\text{Fe}^{3+})\Delta E_c \\
 b_{\pi\sigma} &= \lambda_\pi(\text{Fe}^{3+})\lambda_\sigma(\text{Fe}^{3+})\Delta E_c \\
 b_{\sigma\sigma'} &= \lambda_\sigma(\text{Fe}^{3+})\lambda_{\sigma'}(\text{Fe}^{3+})\Delta E_c
 \end{aligned}
 \tag{7}$$

For  $\text{Fe}^{3+} - \text{R}^{3+}$  exchange we have

$$\begin{aligned}
 b_{\pi\sigma} &= \lambda_\sigma(\text{R}^{3+})\lambda_\pi(\text{Fe}^{3+})\Delta E_c \\
 b_{\sigma\sigma} &= \lambda_\sigma(\text{R}^{3+})\lambda_\sigma(\text{Fe}^{3+})\Delta E_c
 \end{aligned}
 \tag{8}$$

The electron affinity of oxygen is  $-1.47\text{eV}$  and for  $\text{O}^-$  it is  $7.2\text{eV}$  so that  $\Delta E_c = 8.67\text{eV}$ . Using this in (7) and (8) we obtain the  $\lambda$  values which are listed in table 4.

We observe that  $\lambda_\sigma > \lambda_\pi$  for  $\text{Fe}^{3+}$  exchange as expected from chemical bond theory. Also  $\lambda_\sigma$  values for the rare earth ions are generally lower than that for the  $\text{Fe}^{3+}$  bonds. This also agrees with the chemical theory of covalent bonds where it is known that the covalent bonds involving the  $3d$  orbitals are stronger than those involving the  $4f$  orbitals.

## References

- Anderson P W 1959 *Phys. Rev.* 115 2  
 Copland G M 1970 *Chem. Phys. Lett.* 7 175



- CRC Handbook of Chemistry and Physics 1980–81, 61st (CRC Press Florida) p. F.216
- Khattak C P and Yang F F Y 1979 *Handbook of physics and chemistry of rare earths* (ed.) Schneider Jr and L Eyrings (Amsterdam: North Holland) Vol. 3 p. 565
- Levy P M 1966 *Phys. Rev.* **147** 311
- Slater J C 1953 *Rev. Mod. Phys.* **25** 199
- Srivastava C M, Srinivasan C and Aiyar R 1982, *J. Appl. Phys.* **53** 781
- Sugar J and Reader J 1973 *J. Chem. Phys.* **59** 2083
- Tchéou F, Fuess H and Bertaut H 1970 *Solid State Commun.* **8** 1745
- Zeiger H J and Pratt G W 1973 *Magnetic interactions in solids* (Oxford: Clarendon) p. 242

## Electrical properties of films at microwave frequencies

D C DUBE

Physics Department, Indian Institute of Technology, New Delhi 110 016, India

MS received 1 June 1983

**Abstract.** A technique suitable for the measurement of electrical properties of films/sheets at microwave frequencies has been described. Groups of materials are identified for which the absence of any kind of electrodes in these microwave measurements can be utilised with advantage. Results are presented for a variety of materials such as metal films, superionic conductors, semiconductors and insulating polymers.

**Keywords.** Microwaves; waveguide; dielectric constant; a.c. conductivity.

### 1. Introduction

Knowledge of the electrical properties of films at microwave frequencies is helpful in material study and characterization for device fabrication. Thin metal and insulating films, for example, are extensively used in microwave integrated circuits. There, it is of interest to know the attenuation and phase produced by a particular film and variation of these quantities with parameters such as film thickness, temperature etc. Thin semi-metal and metal films were studied by several workers (Gunn 1967; D'Aiello and Freedman 1969; Duggal and Rup 1969; Ramey *et al* 1970). The microwave applications of thin metallic films have also gained importance as exemplified by the use of films as microwave mirrors and as large size film reflectors (Korolev and Gridnev 1963). Microwave measurements are essential in the above cases. But in many situations advantage can be taken of the fact that at microwave frequencies the measurements basically are electrodeless and therefore these are recommended to study materials which require special type of electrodes. Groups of materials may be identified where contacts do pose problems, such as *e.g.* (i) semi-conductors (ii) fast ion conducting solids (iii) membranes and other biological systems. Such materials can be conveniently studied at microwave frequencies.

Section 2 describes few techniques including the one developed earlier (Dube and Natarajan 1973), for the measurement of dielectric constant, loss and conductivity of films and foils. Finally the results are presented for a variety of films.

### 2. Measurement techniques

The most widely used method for microwave measurements of dielectric parameters of solids is the short-circuited line technique of Von Hippel (Von Hippel 1961). The technique involves the measurement of vswr (voltage standing wave ratio  $= E_{\max}/E_{\min}$ ) on the standing waves set-up when the microwaves are totally reflected from a short circuit. A dielectric specimen in the form of a small block which completely

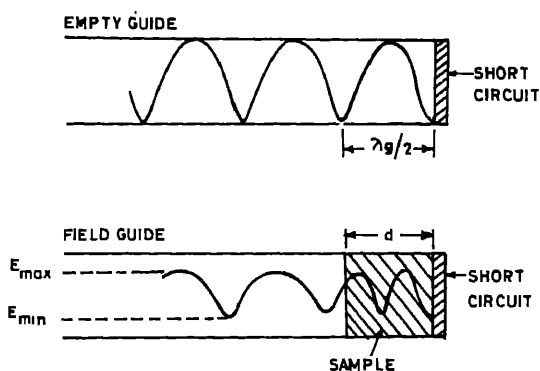


Figure 1. Standing wave pattern in empty and field guide.

fills the section of waveguide is placed next to the short circuit. This alters both the position of standing wave pattern and the size of the voltage ratio by amounts which depend on the dielectric constant and loss of the material and on the length of the 'filled guide' (figure 1).

Von Hippel's method when applied to a very thin specimen does not give accurate results, the reason being the lack of strong interaction between the e.m. wave and the thin specimen. Therefore the presence of the specimen shifts the voltage minima only slightly (often insignificantly) and the change in standing wave ratio is also small (often not measurable accurately).

Recently, Von Hippel's technique has been modified to suit thin samples by measuring impedance not only with short circuit (figure 1) but also using an open circuit and matched terminations (Das Gupta and Pramanic 1982). The method is effective only for high dielectric constant films.

Cavity methods which measure the change in resonance frequency and broadening of resonance response on introduction of the specimen are also not very successful for the same reasons of lack of strong interaction when the specimen is very thin. However, attempts have been made to study thin samples using specific forms of cavities (Conklin 1965; Sobol and Hughes 1967) and other forms of sample holders (Pilipenko *et al* 1970). Cavity perturbation technique has also been used (Rzepecka and Hamid 1972).

### 3. An accurate and convenient technique

In the above techniques such as that of Von Hippel, the accuracy of measurement is poor due to weak interaction of e.m. wave with the specimen. And the reason for the poor interaction is the fact that in normally used  $TE_{10}$  mode of excitation the electric field is maximum at the centre of the waveguide and diminishes to zero at the side walls (figure 2); most of the portion of the specimen lies in the weak field regions. Keeping this in view, a suitable technique was developed (Dube and Natarajan 1973) to study thin film specimens. In this technique the thin specimen is placed longitudinally at the centre of the broad side of a hollow rectangular waveguide excited in the  $TE_{10}$  mode so that the whole specimen remains in maximum electric field as shown in figure 3. In this geometry Maxwell's equations can be solved for the  $TE_{10}$  mode by taking  $Z$  variations of the form  $\exp(-i\beta Z)$  (axis of waveguide is along the  $z$ -direction). Then by usual

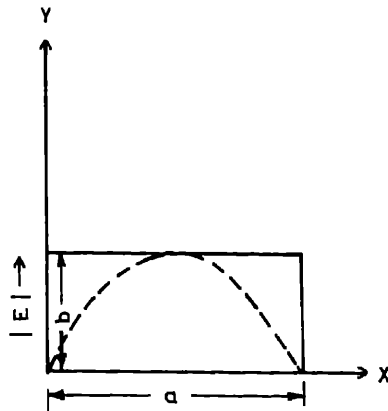


Figure 2. Electric field distribution in a rectangular waveguide in the  $TE_{10}$  mode.

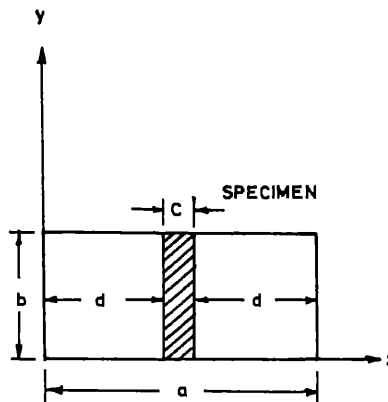


Figure 3. Cross-section of a rectangular waveguide with specimen.

methods (Collin 1960), the following dispersion relation is obtained

$$\tan[d(k^2 - \beta^2)^{1/2}] \tan[\frac{1}{2}c(ek^2 - \beta^2)^{1/2}] = \frac{(k^2 - \beta^2)^{1/2}}{(ek^2 - \beta^2)^{1/2}} \quad (1)$$

where  $k = \omega/C_0$  is the free space propagation vector and  $\omega$  is the angular frequency. Equation 1 is a transcendental equation, and its solution can be obtained only by graphical methods. For complex dielectric constants, the solution of (1) is very difficult even graphically. Therefore, we simplify (1) under the approximation  $\frac{1}{2}c(ek^2 - \beta^2)^{1/2} < 1$ , which holds very well in the case of thin films; hence using  $\epsilon = \epsilon_r - i\epsilon_i$  and  $\beta = \beta_r - i\beta_i$ , we get the following expressions for the real and imaginary parts of the complex dielectric constant:

$$\epsilon_r = \frac{1}{k^2} \left( (\beta_r^2 - \beta_i^2) + \frac{a_1 a_3 + a_2 a_4}{a_3^2 + a_4^2} \cdot \frac{1}{\frac{1}{2}cd} \right), \quad (2)$$

$$\epsilon_i = \frac{1}{k^2} \left( 2\beta_r \beta_i - \frac{a_2 a_3 - a_1 a_4}{a_3^2 + a_4^2} \cdot \frac{1}{\frac{1}{2}cd} \right), \quad (3)$$

where

$$a_1 = d \operatorname{Re} (k^2 - \beta^2)^{1/2},$$

$$a_2 = d \operatorname{Im} (k^2 - \beta^2)^{1/2},$$

$$a_3 = \frac{2 \sin 2a_1}{\exp(2a_2) + \exp(-2a_2) + 2 \cos 2a_1},$$

and

$$a_4 = \frac{\exp(2a_2) - \exp(-2a_2)}{\exp(2a_2) + \exp(-2a_2) + 2 \cos 2a_1},$$

and

$$\beta_i = \text{attenuation introduced by unit length of the specimen (measured in nepers m}^{-1}\text{)}$$

$$\beta_r = \beta_p + \beta_0 \text{ (measured in radians m}^{-1}\text{)}$$

where

$$\beta_p = \text{phase shift produced by the unit length of the specimen}$$

and

$$\beta_0 = 2\pi/\lambda g, \text{ where } \lambda g \text{ is the guide wavelength in the empty guide,}$$

$$c = \text{thickness of specimen, and}$$

$$d = \frac{1}{2}(a - c), a \text{ being the width of the waveguide (figure 3).}$$

Thus, in complex dielectrics, the value of  $\epsilon_r$  and  $\epsilon_i$  can be obtained from (2) and (3). For loss-free dielectrics the solution of (1) can be obtained without any approximations. The two main quantities required to be measured experimentally are the phase and attenuation introduced by the specimen. Two experimental arrangements have been proposed (Dube and Natarajan 1973, 1974). Either may be used for these measurements. Both make use of rectangular waveguide system excited in the TE<sub>10</sub> mode. One arrangement has been shown in figure 4.

Microwave power is obtained from a Klystron source. The power is divided into two arms at the 10-dB directional coupler. The lower arm contains the standard impedance, i.e., a standard variable attenuator and a standard variable phase shifter ( $0^\circ \rightarrow 360^\circ$ ). The upper arm contains the sample holder which is an approximately 10 cm long waveguide having a sharply cut longitudinal slot at the middle. The sample is introduced through this slot. The powers from the upper and the lower arms are again combined at a 3-dB directional coupler. The power output from the directional coupler is fed to the detecting system.

To start with, a null point is obtained in the detector by properly adjusting the variable attenuator and the phase shifter. The introduction of the specimen disturbs the balance. The null conditions are restored by varying the attenuator and phase shifter. Thus the phase shift and attenuation introduced by the sample can be accurately measured. Large sample lengths should be used for producing large phase shifts and attenuations.

Reflections from the edge of the sample are normally extremely small. But these can be detected by a separate experiment and if required, tuner no. 8 in figure 4 may be used for matching purposes.

The minimum detectable phase shift and attenuation in the measuring system were  $0.25^\circ$  and 0.02 dB, respectively.

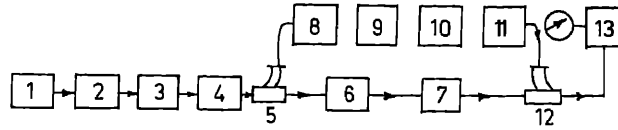


Figure 4. Schematic diagram of the experimental set up: 1. Klystron power source; 2. Frequency meter; 3. Padder attenuator; 4. Ferrite isolator; 5. and 12, Directional couplers; 6. Calibrated variable phase shifter; 8 and 11 tuners; 9. Variable attenuator; 10. sample holder waveguide; 13. Amplifier and meter.

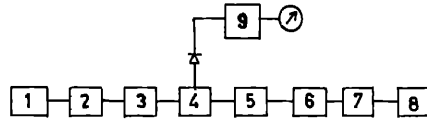


Figure 5. Schematic diagram of the experimental set-up; 1. Klystron power source; 2. Frequency meter; 3. Ferrite isolator; 4. Waveguide travelling detector; 5. variable attenuator; 6. E-H tuner; 7. sample holder waveguide; 8. movable short; 9. Amplifier and meter.

To study dielectric parameters as a function of temperature, the guide section containing the specimen may be cooled by a low temperature bath around the section or may be heated by a cylindrical furnace.

The other experimental set-up (Dube and Natarajan 1974) is shown in figure 5. This is a simpler arrangement and does not require calibrated variable phase shifter and attenuator and is as accurate as the first set-up.

Here the travelling wave detector is used to measure the shift of the voltage minimum when the specimen is introduced. Let the specimen length be  $L$  cm and the phase shift produced be  $X$  cm, then phase introduced by the specimen per unit length is

$$\beta_s = \beta_0 \frac{X}{L}$$

Thus the total phase constant  $\beta_r$  is given by

$$\beta_r = \beta_0 + \beta_s$$

or 
$$\beta_r = \beta_0 \left( 1 + \frac{X}{L} \right)$$

For measuring the dielectric loss, the vswr is taken with and without the specimen. Let these be  $\rho_1$  and  $\rho_2$ ; then

$$r = \frac{\rho_1 - 1}{\rho_1 + 1} = \exp(-\alpha), \quad (4)$$

and

$$r' = \frac{\rho_2 - 1}{\rho_2 + 1} = \exp - (\alpha + 2\beta_i L), \quad (5)$$

where  $r$  and  $r'$  are the reflection coefficients of the system with and without the sample and  $\alpha$  is the attenuation constant. Hence  $\beta_i$  can be calculated from (4) and (5).

#### 4. Results and discussion

The accuracy of the proposed technique for measuring the dielectric parameters of films was checked by studying two materials namely, mylar and teflon whose dielectric properties are well known over a wide frequency range including microwaves. Results are summarised in table 1.

In the recent past the technique has been used to study films/sheets/wafers of varying nature and differing widely in electrical properties. Some of the results are given below.

Complex permittivity and conductivity have been studied for silicon semiconductor (Natarajan *et al* 1978).  $\epsilon_r$  and  $\epsilon_i$  values for one sample of *p*-silicon for various thicknesses are given in table 2. The thickness of the starting sample was reduced by etching and lapping.

The d.c. conductivities measured by the four-probe technique and the microwave conductivities obtained from the relation  $\sigma_{a.c.} = \omega\epsilon_0\epsilon_i$  are compared in table 3 for three samples of *p*-silicon.

The microwave conductivity is slightly less than the d.c. values. This is somewhat

**Table 1.** Dielectric parameters of teflon and mylar films at 9.375 GHz at room temperature (310°K)

Sample	Sample thickness ( $\mu\text{m}$ )	Phase shift per unit length (deg.)	Dielectric constant	
			Present work	Literature
Teflon	90	0.61	2.03	2.08 <sup>a</sup>
	130	0.96	2.03	$2.07 \pm 0.03^b$
	186	1.28	2.02	
Mylar	75	1.15	3.13	3.145 <sup>c</sup>
	130	1.91	3.10	
	250	3.74	3.18	

<sup>a</sup> Von Hippel (1961); <sup>b</sup> Pilipenko *et al* (1970); <sup>c</sup> Conklin (1965).

**Table 2.** Complex permittivity for a *p*-type silicon (5.45  $\Omega$  cm) at room temperature (310°K) and at a frequency of 9.410 GHz

Thickness (microns)	Phase shift per unit length (degrees)	Attenuation per unit length (decibels)	$\epsilon_r$	$\epsilon_i$
272	15.0	8.6	11.61	30.58
226	13.0	7.5	11.65	32.12
200	12.0	6.9	11.81	33.13
180	10.8	6.1	11.58	32.68
140	8.6	5.1	11.62	34.61
94	5.8	3.4	11.41	34.76
70	4.5	2.4	11.63	32.69

Table 3. Comparison of d.c. and a.c. conductivities for three samples of *p*-silicon

d.c. conductivity by four-probe technique $(\Omega \text{ m})^{-1}$	Microwave conductivity from $\sigma_{a.c.} = \omega \epsilon_0 \epsilon_i$ $(\Omega \text{ m})^{-1}$
10.26	9.79
15.63	15.17
18.35	17.97

constant with the usual expressions for a.c. and d.c. conductivities.

$$\sigma_{a.c.} = \frac{ne^2\nu}{m[v^2 + \omega^2]},$$

and

$$\sigma_{d.c.} = \frac{ne^2}{m\nu},$$

where  $m$ ,  $e$ ,  $n$  and  $\nu$  are the mass, charge, concentration and collision frequency of the holes in *p*-silicon.

The microwave data may also be used to determine other transport parameters of silicon. The dielectric constant and conductivity in terms of effective mass  $m^*$  and relaxation time  $\tau$  may be written as

$$\epsilon_r = \epsilon_L - \frac{ne^2\tau^2}{\epsilon_0 m^* [1 + (\omega\tau)^2]},$$

$$\sigma = \frac{ne^2\tau}{m^* [1 + (\omega\tau)^2]} = \omega \epsilon_0 \epsilon_i,$$

where  $\epsilon_L$  is the lattice dielectric constant and  $\epsilon_0$  is the permittivity of free space. From the above two equations, we get

$$\tau = \frac{\epsilon_L - \epsilon_r}{\omega \epsilon_i}.$$

With the present results the relaxation time in silicon comes out to be around  $10^{-13}$  sec, which agrees well with the data ( $\approx 10^{-13}$  sec) produced by Blatt (1968).

The conductivity variations with temperature for *p*-silicon samples (d.c. resistivities 10.5, 40 and 170 ohm cm) in the temperature range 190–525°K are plotted in figure 6. The curves for the three silicon samples exhibit broadly similar characteristics, viz the conductivity initially decreases with increase of temperature and later increases very rapidly with temperature. This is, of course, expected, considering the relative predominance of extrinsic and intrinsic conduction mechanisms. The conductivity of the samples (having resistivities 10.5 and 40 ohm-cm) decreases from room temperature to 440°K. In this temperature region lattice scattering by acoustical phonons plays the dominant role (Blackmore 1969). As the temperature is raised further, the concentration of free electrons and holes increases and the intrinsic conduction predominates thereafter. In the case of the third sample (170 ohm cm, the highest resistivity of all the



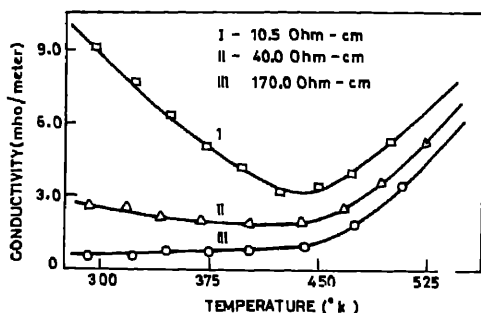


Figure 6. Microwave conductivity variation of silicon wafers in the temperature range 293–523°K.

three) the conductivity rises slowly from room temperature up to 440 K and increases very rapidly subsequently thereby showing its intrinsic behaviour right from room temperature. Bhar (1963) made similar measurements on temperature variations of microwave conductivity for bulk *p*-silicon samples having conductivities 0.7 and 0.1 mho m<sup>-1</sup> in the temperature range 273–480°K. His results also resemble the curves of figure 6.

Electrical parameters have been measured for metal and semimetal films of thicknesses less than the skin depths deposited on glass substrates by vacuum thermal evaporation technique (Dube *et al* 1978).

Figures 7 and 8 show the phase shift and attenuation constants as a function of film thickness for the semimetal bismuth. Table 4 contains the results for  $\epsilon_r$  and  $\epsilon_i$  for bismuth films of different thicknesses. The high values of  $\epsilon_r$  and  $\epsilon_i$  are attributed to the presence of free carriers and are consistent with the results of Rahneberg (1971) for bismuth films measured by a different technique at 14.50 GHz. Gold and aluminium films also show high dielectric parameters of the order of 10<sup>5</sup> (Dube *et al* 1978).

Dielectric behaviour of pure polyvinyl chloride (PVC) and iodine-doped PVC has been studied at microwave frequencies using the proposed technique (Natarajan and Dube 1981). Pure PVC films were obtained by dissolving the polymer powder in tetrahydrofuran and permitting the evaporation of the solvent at room temperature. Iodine-doped PVC samples were prepared from the PVC solution in which a requisite amount of iodine was dissolved. The concentration of iodine in the samples varied from 4–40% by weight.

Figure 9 depicts the variation of  $\epsilon_r$  with temperature for all PVC samples. It is seen that at any fixed temperature, the dielectric constant increases as the iodine content in the sample increases. This effect is more pronounced for iodine concentrations above ~5% (by weight). For temperatures above 90°C the dielectric constant decreases for all samples containing iodine.

The rise in  $\epsilon_r$  with iodine concentration may be attributed to the presence of highly polarizable molecular iodine in the specimen. The presence of free iodine was detected in the absorption spectrum in the visible region.

The volume expansion due to transition from glassy to rubbery state seems to account for the decrease of  $\epsilon_r$  with temperature in the vicinity of 85°C as the glass transition temperature ( $T_g$ ) of PVC falls in the region 70–105°C (Brandrup and Immergut 1975). Variation of loss-tangent ( $\tan \delta$ ) with temperature for different iodine

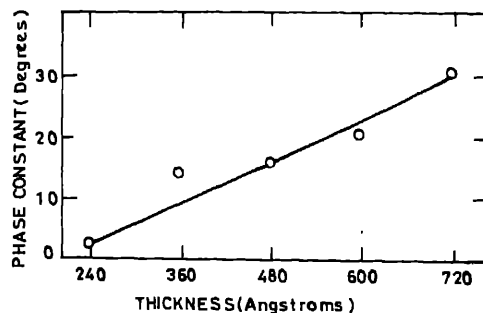


Figure 7. Variation of phase constant as a function of bismuth film thickness.

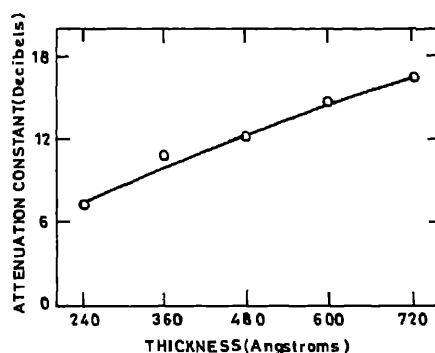


Figure 8. Variation of attenuation constant as a function of bismuth film thickness.

Table 4. Complex permittivity for thin bismuth films for various thicknesses at 310°K and at a frequency of 9.410 GHz.

Thickness (angstroms)	Phase shift/ length (degrees)	Attenuation/ length (decibels)	Dielectric parameters ( $\times 10^5$ )	
			$\epsilon_r$	$\epsilon_i$
240	2.5	7.5	0.36	3.12
360	12.0	10.8	0.91	2.91
480	15.5	12.2	0.89	2.38
600	20.0	13.7	0.83	1.83
720	30.0	16.3	1.05	1.86

dopings has been shown in figure 10. For iodine content of 10% and above, well-defined loss-peak appears at around 90°C in each case. With increasing iodine content, the position of loss peak does not change; however, the peak height changes considerably. The fact that loss tangent maxima does not change in position but only in magnitude with iodine concentration shows that on increasing the doping the number of dipoles participating in the orientation process increases, while the frequency of orientation remains unchanged.

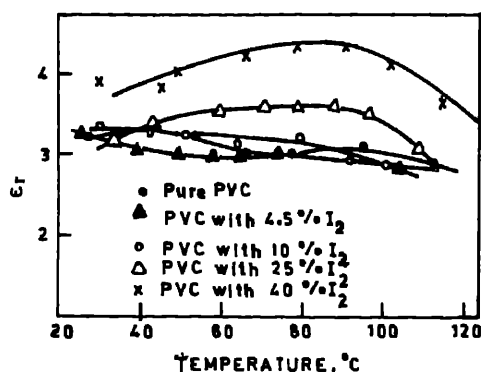


Figure 9. Variation of  $\epsilon'$  with temperature for pure and iodine doped PVC.

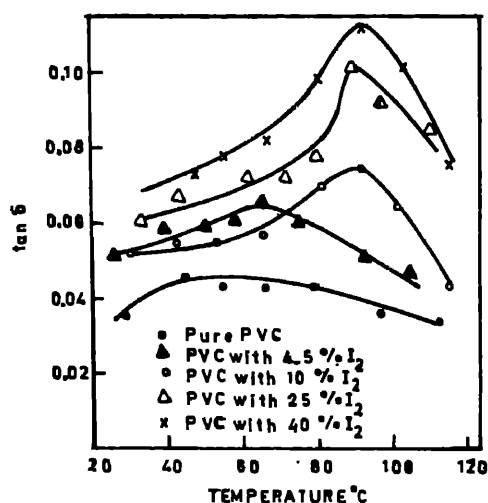


Figure 10. Variation of  $\tan \delta$  with temperature for pure and iodine doped PVC.

Fast ion conducting solids (also called superionic conductors) have become very important in the recent past due to their applications in many electrochemical devices. Electrical measurements on these materials require special attention due to the variety of electrodes (blocking, reversible and their combinations) (Bottelberghs 1978) used making the analysis more complex. The ionic conduction has been studied recently at microwave frequencies (Dube and Saraswat 1982) in silver iodide in the high conductivity  $\alpha$ -phase. Thin pellets of AgI of varying packing density were used and dielectric and conductivity data obtained. This data can be transformed to 100% dense bulk using correlation formulae (Landau and Lifshitz 1960; Leoyenga 1965; Dube 1970).

$$\epsilon_p'^{1/3} - 1 = \delta(\epsilon_b'^{1/3} - 1),$$

$$\epsilon_b'' = \frac{\epsilon_p''}{\delta} (\epsilon_b'/\epsilon_p')^{2/3},$$

Table 5. Conductivity and dielectric constant for  $\alpha$ -AgI ( $T = 160^\circ\text{C}$ ) at 10 kHz

Packing fraction %	Observed parameters for pellets		Values converted to 100% density by correlation formulae		Values reported in literature in microwave region (Gebhardt <i>et al</i> 1980)	
	Dielectric constant	Conductivity ( $\Omega\text{cm}$ ) <sup>-1</sup>	Dielectric constant	Conductivity ( $\Omega\text{cm}$ ) <sup>-1</sup>	Dielectric constant	Conductivity ( $\Omega\text{cm}$ ) <sup>-1</sup>
72	12.0	0.044	21.74	0.092		
82	15.4	0.076	22.30	0.119		
86	16.9	0.084	22.45	0.110	22.00	1.22
92	19.4	0.088	22.75	0.116		

and

$$\sigma_b = \omega \epsilon_0 \epsilon_b'',$$

where  $\epsilon_p'$  and  $\epsilon_p''$  are the dielectric constant and loss factor for the pellet of packing fraction  $\delta$  and  $\epsilon_b'$ ,  $\epsilon_b''$  are the corresponding parameters for the bulk.  $\sigma_b$  is the conductivity at angular frequency  $\omega$ .  $\epsilon_0$  is permittivity of free space ( $= 8.85 \times 10^{-12} \text{ Fm}^{-1}$ ). Various results have been summarised in table 5. It is seen that while the deduced dielectric constant data match with experimentally reported value of 22, the conductivity results are found reduced by an order of magnitude. This reduction in conductivity is attributed to the presence of grain boundaries in the unsintered samples used in the above studies.

In conclusion, it may be said that the microwave technique described is very convenient and accurate and can be used to study electrical transport behaviour of materials differing widely in characteristics.

## References

- Bhar J N 1963 *Proc. IEEE* **51** 1623
- Blakemore J S 1969 *Solid State Physics* (Toronto: Saunders Company)
- Blatt F J 1968 *Physics of electronic conduction in solids* (New York: McGraw-Hill)
- Bottelberghs P H 1978 in *Solid electrolytes: General principles, characterization, materials, applications* (eds Paul Hagenmuller and W Van Gool (New York: Academic Press)
- Brandrup J and Immergut E M (eds) 1975 *Polymer handbook* (New York: John Wiley) 2nd edn p. 44
- Collin R E 1960 *Field theory of guided waves* (New York: McGraw-Hill) Chap. 6
- Conklin G E 1965 *Rev. Sci. Instrum.* **36** 1347
- D'Aiello R V and Freedman S J 1969 *J. Appl. Phys.* **40** 2156
- Das Gupta C and Pramanick P 1982 *Microwave* **76**
- Dube D C 1970 *J. Phys.* **D3** 1648
- Dube D C and Natarajan R 1973 *J. Appl. Phys.* **44** 4927
- Dube D C and Natarajan R 1974 *J. Phys.* **E7** 256
- Dube D C, Natarajan R and Tripathi V K 1978 *Indian J. Phys.* **A52** 405
- Dube D C and Saraswat A K 1982 *J. Appl. Phys.* **53** 7095
- Duggal V P and Rup R 1969 *J. Appl. Phys.* **40** 492
- Gebhardt K F, Soper P D, Merski J, Balle T J and Flygare W H 1980 *J. Chem. Phys.* **72** 272
- Gunn M W 1967 *IEEE Proc.* **114** 207
- Korolev F A and Gridnev V I 1963 *Radiotekh. Electron.* **8** 1480

- Landau L D and Lifshitz F M 1960 *Electrodynamics of continuous media* (London: Pergamon) p. 46
- Looyenga H 1965 *Physica* **31** 401
- Natarajan R, Dube D C and Tripathi V K 1978 *Indian J. Phys.* **52** 567
- Natarajan R and Dube D C 1981 *Indian J. Pure Appl. Phys.* **19** 675
- Pilipenko V V, Polovnikov G G, Sologub V G and Shestopilov V P 1970 *Sov. Phys. Tech. Phys.* **14** 1662
- Rahneberg E W 1971 *Measurement of the Complex Permittivity of Thin Bismuth Films within the Ku-band*  
Ph.D. Thesis, University of Arizona USA
- Ramey R L, Landes H S and Manus E A 1970 *IEEE Trans. Microwave Theory Technol.* **MTT-18** 196
- Rzepecka M A and Hamid M A K 1972 *IEEE Trans. Microwave Technol.* **MTT-20** 30
- Sobol H and Hughes J J 1967 *IEEE Trans. Microwave Technol.* **MTT-15** 377
- Von Hippel A R 1961 *Dielectric materials and applications* (New York: Wiley)

## Surface modification of polyvinyl chloride towards blood compatibility

GEETHA KURIAN and CHANDRA P SHARMA

Department of Biomedical Engineering, Sree Chitra Tirunal Institute for Medical Sciences and Technology, Trivandrum 695 012, India

MS received 29 January 1983; revised 6 September 1983

**Abstract.** The surface modification of medical grade polyvinylchloride (PVC) from various sources with the ionic bonding of polyelectrolyte is investigated by exposing the PVC sheets to 1% zephiran chloride for 10 min and then to 50 mg % solution of polyelectrolyte for 10 min. Surface energy and platelet adhesion studies were carried out to demonstrate the suitability of our improved surface towards blood compatibility. Relative changes due to  $\gamma$ -irradiation are also discussed.

**Keywords.** Polyvinyl chloride; surface modification; blood compatibility

### 1. Introduction

Polyvinylchloride (PVC) with a wide choice of additives and ingredients such as plasticizers, fillers, stabilisers etc (Ownes and Read 1979) is being used for various biomedical applications. However the surface of the PVC may change depending upon the additives used. Since the prosthetic blood interaction is dependent on the nature of the surface, various surfaces may behave differently. Therefore, we have attempted in this paper to mention the modification of the medical grade PVC from different sources using polyelectrolyte towards improved blood compatibility.

Polyelectrolytes from synthetic poly (*cis*-1,4 isoprene) possess anticoagulant activity (van der Does *et al* 1979) and have been used for surface modification of polymers (Sederel *et al* 1983). Therefore we have chosen natural rubber, (Source Hevea Brasiliensis "Para Rubber") to obtain the polyelectrolyte for our studies. It seems the effect of surface modification with this method is independent of the PVC type and therefore appears quite promising for future investigations.

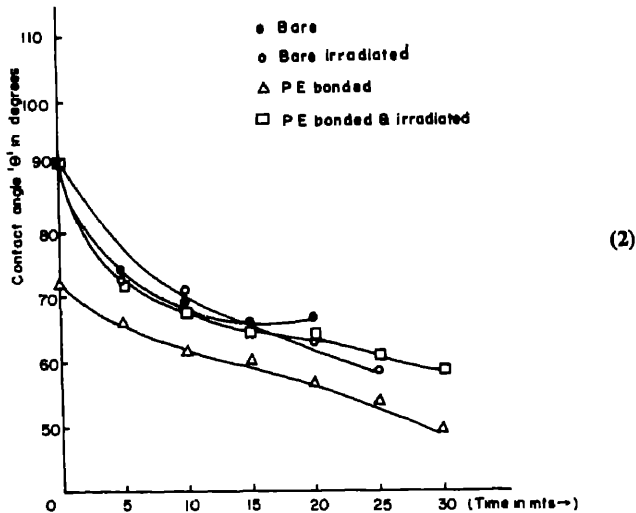
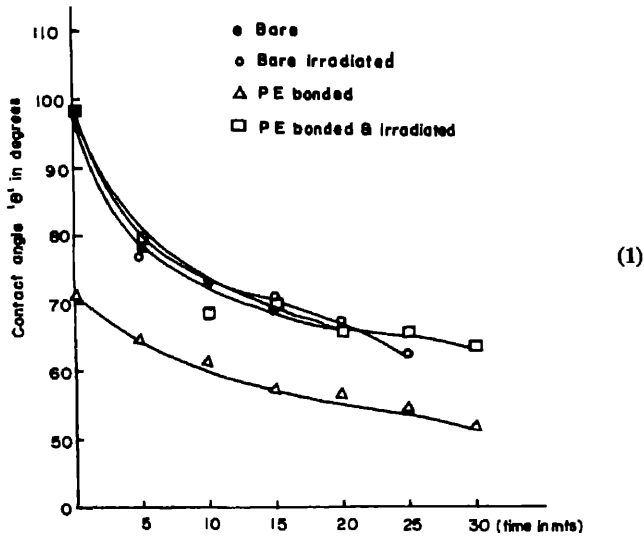
### 2. Experimental work

The PVC sheets of different sources are dipped in 0.1% soap solution. They are thoroughly cleaned with distilled water, finally rinsed with methanol and dried in vacuum oven. Polyelectrolyte (synthesised from natural rubber, van der Does *et al* 1979) is ionically bound on the various PVC sheets by first exposing to 1% Zephiran chloride for 10 min and then to polyelectrolyte (50 mgm % in water) for 10 min. The bare as well as the polyelectrolyte coated PVC sheets were irradiated at room temperature ( $\text{CO}^{60}$  gamma source) with a constant dose rate of 0.25 Mrad (strength 843/Rontgen/hr/m) for 4 hr 30 min.

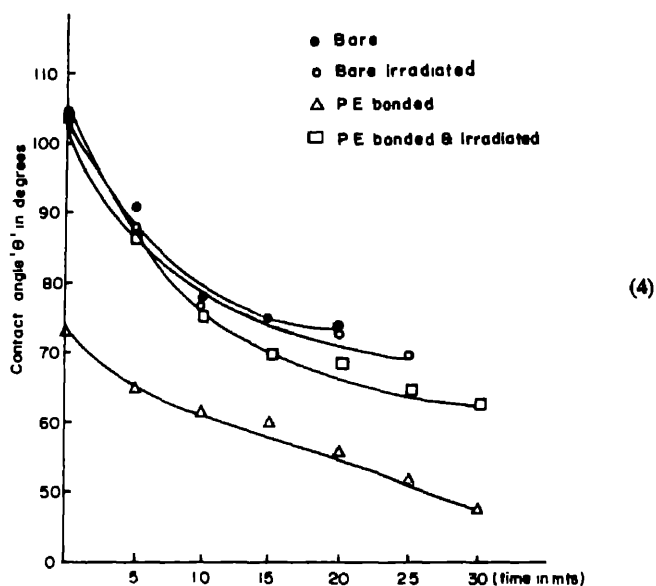
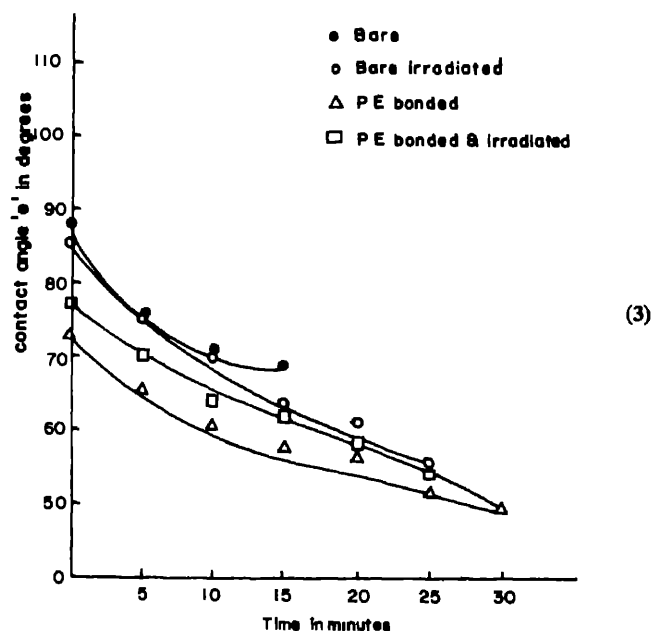
Inherent viscosity of the various bare PVC sheets was compared and the results are given in table 1. Variation of contact angle with time are also studied with a goniometer at room temperature using double distilled water as shown in figures 1–4.

2.1 Blood coagulation studies

Calf blood is used for evaluating the recalcification time under controlled pH and temperature with the PVC coated tubes. Glass tubes of 7.5 cm length and 1 cm diameter are coated with 10 % solution of PVC in tetrahydrofuran. The tubes are dried at 60°C in a



Figures 1–2. Change in contact angle with time on PVC surfaces 1. Bhor 2. SCTIMIST.



Figures 3-4. Change in contact angle with time on PVC surfaces 3. TUTA 4. Fenwal.

vacuum oven. The clotting time for the plasma is determined at 37°C (Austen and Rhymes 1975). The results are tabulated in table 2.

## 2.2 Platelet adhesion on PVC surfaces: Preparation of platelet suspension

Washed calf platelets are prepared and suspended in tyrode solution (Sharma and Chandy 1982) for adhesion studies. The washed PVC sheets are exposed to platelet



**Table 1.** Inherent viscosity data of various PVC sheets.

PVC sheets	Viscosity (dl/g)
I	1.27
II	1.03
III	1.01
IV	1.08

I—Bhor Industry India Product for SCTIMST. II—Polymer Technology Division Product of our Institute for blood bag applications, submitted by S N Pal, SCTIMST. III—Tuta Industry Australia, blood bag. IV—Fenwal, Travenol Inc. (USA), blood bag.

**Table 2.** Plasma recalcification time

Surfaces	Plasma recalcification time (sec) SD (n = 5)
Plain glass	140 ± 2
I	187 ± 5
II	166 ± 11
III	340 ± 3
IV	198 ± 20

I, II, III and IV are as noted in table 1.

**Table 3.** Platelet adhesion on various PVC sheets.

PVC sheets	Bare PVC sheets		Polyelectrolyte coated PVC sheets	
	Before $\gamma$ -irradiation (n = 10)	After $\gamma$ -irradiation (n = 10)	Before $\gamma$ -irradiation (n = 10)	After $\gamma$ -irradiation (n = 10)
I	5.8 ± 0.8	4.9 ± 0.7	3.6 ± 0.5	4.2 ± 0.4
II	5 ± 0.8	4.9 ± 0.7	3.6 ± 1.2	4.2 ± 0.5
III	5 ± 1.0	4.9 ± 0.7	3.6 ± 0.53	3.8 ± 1.0
IV	5.8 ± 0.8	5 ± 0.7	3.6 ± 1.2	4.4 ± 0.6

I, II, III and IV are as noted in table 1.

suspension for 1 hr, rinsed with phosphate buffer of pH 7.4 under uniform flow for about 3 min and the platelets are fixed with Coomassie Blue G. The number of platelets adhered to the PVC sheets are accounted using an optical microscope. Different fields are read randomly and averaged in a similar fashion for all samples. The results are given in table 3.

### 3. Results and discussion

Platelet adhesion and contact angle studies were carried out on bare as well as on polyelectrolyte coated PVC surfaces to investigate the effect of polyelectrolyte coating on PVC towards blood compatibility.

It seems when polyelectrolytes are on the surface the material is improved towards blood compatibility. Platelet adhesion is relatively less as indicated in table 3. Although they are different before modification as indicated by our plasma recalcification time (table 2) and the change in contact angle with time (figures 1–4), the contact angle becomes relatively more stable and the behaviour of the various PVC sheets becomes alike (figures 1–4). After irradiation the effect of polyelectrolyte is no longer obvious as shown in figures 1–4. It becomes a part of the PVC structure such that leaching components do not have any additional resistance as it was before irradiation. Therefore we suggest that PVC surfaces can be improved towards blood compatibility like polyelectrolyte as described above, provided the material is already sterilised by  $\gamma$ -irradiation, since for long term applications ionic bonding of polyelectrolytes with PVC surface may not be stable enough. This modification is suggested for all short term medical applications of PVC coming in contact with blood such as oxygenators and blood bags etc. No adverse change in platelet adherence is observed on modified surfaces if autoclaving sterilization (Sharma and Nirmala 1983) is used instead of  $\text{CO}^{60}$ ,  $\gamma$ -irradiation.

### Acknowledgement

The authors appreciate the help received from Dr V N Krishnamurthy of Vikram Sarabhai Space Centre, Trivandrum for  $^{60}\text{Co}$   $\gamma$ -irradiation of our samples, Dr A V Lal for providing calf blood, Mr S N Pal for the PVC samples and Mr Thomas Chandy and Mrs M K Sheela for help.

### References

- Austen D E G and Rhymes I L 1975 *A laboratory manual of blood coagulation* (Oxford: Blackwell Scientific Publications) p. 35.
- Owen B D and Read R L 1979 *J. Polym. Sci., Polym. Chem. Ed.* 17 2719
- Sederel L C, van der Does E, Evverman B J, Bantjes A, Kluft C and Kempen H J M 1983 *Biomaterials* 4 3
- Sharma C P and Chandy T 1982 *J. Colloid Interface Sci.* 89 479
- Sharma C P and Nirmala N V 1983 *Polyvinyl chloride compatibility* at National Seminar on *Recent developments in Polymer Science*, AC College Campus, Madras, December 22 and 23rd, Proceedings to follow in honour of Prof. M Santappa
- van der Does L, Bengeling T, Frochling P E and Bantjes A J 1979 *Polym. Sym.* 66 337

## Errata

I. "Lithium solid electrolytes and their application" by D N Bose and D Majumdar, *Bull. Mater. Sci* 6 pp. 223–230 May 1984

The paper falls under the subject "Electrical Properties" and not under "Glasses" as printed in the Contents Page of the Journal.

---

II. "Electrical properties of polycrystalline silicon and zinc oxide semiconductors" by S N Singh, S Kumari and B K Das, *Bull. Mater. Sci.* 6 pp 243–258 May 1984

(i) On page 247 the lines following the description of eq (3) should read as

For a discrete energy level, on the other hand,  $\phi_B$  is obtained from the solution of equation (Martinez and Piqueras 1980)

$$(8\epsilon N_D q \phi_B)^{1/2} = q N_{is} \left[ \frac{1}{1 + \exp [(E_T - E_{FG} - q \phi_B)/kT]} - \frac{1}{1 + \exp [(E_T - E_{FB})/kT]} \right], \quad (4)$$

and (ii) On page 250, the first line of last paragraph of section 2.2c should read as

"A comparison of (11) and (17) shows that the activation energies of  $\mu_{\text{eff}}$  and  $\sigma$  are not identical."

---

### SUBJECT INDEX

- A.C. conductivity  
Electrical properties of films at microwave frequencies 1075
- Accelerator irradiation  
High voltage electron microscope irradiation and observations in metallic glasses 595
- Activation energy  
Electron transport in non-crystalline garnet films 53  
DC electrical conductivity of  $\text{Na}_2\text{O-ZnO-B}_2\text{O}_3$  glass system 1009
- Alloy design  
Mechanisms and empirical equations for deformation and some principles of alloy design 677
- Al-Pu fuels  
Plutonium metallurgy in India 923
- Al-rare earth system  
High resolution electron microscopic studies of  $\text{HoAl}_3$ ,  $\text{Er}_{0.5}\text{Gd}_{0.5}\text{Al}_3$  and  $\text{Y}_{0.91}\text{Er}_{0.09}\text{Al}_3$  in thin film form 603
- Aluminium alloy  
Analytical electron microscopy of aluminium alloys 513
- Amorphous character  
Effect of compositional modifications on the piezoelectric properties of spray dried lead zirconate titanate ceramics 83
- Amorphous ferromagnets  
Spin-wave excitations in amorphous ferromagnets 1059
- Amorphous films  
A novel method of RF powder sputtering 971
- Amorphous semiconductors  
Electronic conduction in bulk  $\text{Se}_{1-x}\text{Te}_x$  glasses at high pressures and at low temperatures 231
- Analytical microscopy  
Metallic glasses 579
- Anelasticity  
Internal friction in hexagonal metals 959
- Annealing behaviour  
Annealing behaviour of electron-beam deposited tin dioxide films 1029
- Anodic dissolution  
Electrochemical preparation of potassium gold cyanide 165
- Antimony film  
Electron diffraction analysis of antimony films 611
- Antiphase boundaries  
High resolution electron microscopy of long range ordered alloys 417
- As-Sb-Se glasses  
Elastic properties of As-Sb-Se glasses 1001
- Atomistic behaviour  
Field ion microscopic observations of  $\text{LaB}_6$  on tungsten 573
- Austenite  
Structure and properties of an investment—cast austenitic stainless steel 119
- BCS theory  
On the mechanism of pairing in the BCS theory 273
- Beam broadening  
X-ray microanalysis in the transmission electron microscope 503
- Biological molecules  
Investigation of hydrogenous materials using neutrons 151
- Biquadratic exchange interaction  
A Mössbauer study of hyperfine interactions in the boroferrite  $\text{Fe}_{3-x}\text{Ga}_x\text{BO}_6$  ( $x = 0, 0.12$ ) 33
- Blood compatibility  
Surface modification of polyvinyl chloride towards blood compatibility 1087
- Boroferrite  
A Mössbauer study of hyperfine interactions in the boroferrite  $\text{Fe}_{3-x}\text{Ga}_x\text{BO}_6$  ( $x = 0, 0.12$ ) 33
- Boron  
Structural and magnetic investigations of some new boron containing rare earth intermetallic compounds 263
- Breakdown process  
Growth of research and development in rare metals extraction in India 901
- Burgers vectors  
Grain boundary-dislocation interactions 699

- Carbon-carbon composites  
Use of coal tar pitch for carbon-carbon composites 91
- Carbon matrix  
Use of coal tar pitch for carbon-carbon composites 91
- Catalytic oxide  
MnO<sub>2</sub> catalyzed carbon electrodes for dioxygen reduction in concentrated alkali 259
- Cavity  
Fracture of particulate composites 799
- Centre frequency  
Infrared absorption in spinel ferrites 1063
- Ceramic materials  
Effect of compositional modifications on the piezoelectric properties of spray dried lead zirconate titanate ceramics 83
- Cermet  
Metal-to-ceramic bonding in (Al<sub>2</sub>O<sub>3</sub> + Fe) cermet studied by Mössbauer spectroscopy 13
- Chalcogenide films  
Photon, electron and ion beam induced physical and optical densification in chalcogenide films 1013
- Chalcogenide glasses  
Electronic conduction in bulk Se<sub>1-x</sub>Te<sub>x</sub> glasses at high pressures and at low temperatures 231
- Chaos  
Elementary concepts in chaos and turbulence 807
- Chemical beneficiation  
Growth of research and development in rare metals extraction in India 901
- Chemical etching  
Evidence of screw dislocations on (002) cleavages of lithium carbonate single crystals 991
- Classical statistical mechanics  
Computer simulation of tensile testing 643
- Coal-fired MHD generator  
High temperature materials for magnetohydrodynamic channels 71
- Cohesive energy  
Strength and electronic structure 717
- Composite  
Fracture of particulate composites 799  
Glass-metal particulate composites 193  
Some recent advances in materials technology 405
- Computer simulation  
Computer simulation of tensile testing 643
- Conducting ceramic  
Preparation and characterisation of  $\beta$ -Al<sub>2</sub>O<sub>3</sub> 979
- Conducting polymers  
Some recent advances in materials technology 405
- CONM model  
Elastic properties of As-Sb-Se glasses 1001
- Continual mechanical twinning  
Serrated plastic flow 653
- Convergent beam electron diffraction  
Scanning transmission electron microscopy and microdiffraction techniques 477
- Cooper pairing  
On the mechanism of pairing in the BCS theory 273
- Cooperative behaviour  
Repeated yield drop phenomena as a cooperative effect 665
- Corrosion resistance  
Structure and properties of an investment cast austenitic stainless steel 119
- Covalency parameters  
Influence of spin orbit coupling and lanthanide contraction on the exchange interaction in rare earth garnets 1069
- C-periodicity  
High resolution electron microscopy as a tool for structural investigations 459
- Critical exponent  
Magnetic structure of zinc ferrite 27
- Critical temperature  
On the mechanism of pairing in the BCS theory 273
- Crookes dark space  
A novel method of RF sputtering 971
- Crystal puller  
Sophisticated equipment developed for growth and evaluation of perfection of nearly perfect crystals 129
- Crystalline solids  
Relevance of liquid state to solid state properties 773
- Crystallization behaviour  
Metallic glasses 579
- Crystallization temperature  
High voltage electron microscope irradiation and observations in metallic glasses 595
- Curie temperature  
Curie temperatures and 0°K magnetic moments of zinc-substituted lithium ferrites 39
- Curvature tensor  
Elastic continuum theories of lattice defects: A review 775
- Cycle period  
Elevated temperature low cycle fatigue studies on AISI 304 steel 111
- Defect characteristics  
High voltage electron microscope irradiation and observations in metallic glasses 595
- Defects  
Repeated yield drop phenomena as a cooperative effect 665

- Defects**  
Effects of mechanical deformation: Exoemission 755
- Defect structure**  
High resolution electron microscopy of superconductors 453
- Deformation mechanisms**  
Mechanisms and empirical equations for deformation and some principles of alloy design 677
- Delta ferrite**  
Structure and properties of an investment cast austenitic stainless steel 119
- Delta-stabilised alloys**  
Plutonium metallurgy in India 923
- Densification mechanism**  
Dependence of microstructure on process variables in manganese zinc ferrites 65
- Density**  
ix: electrical conductivity of  $\text{Na}_2\text{O-ZnO-B}_2\text{O}_3$  glass system 1009
- Diametral strain**  
Elevated temperature low cycle fatigue studies on AISI 304 steel 111
- Dielectric constant**  
Electrical properties of films at microwave frequencies 1075
- Dielectric studies**  
Dielectric and pyroelectric studies on triglycine sulphate-polymer composites 105
- Diffusional flow**  
Superplasticity 689
- Dioxygen reduction**  
 $\text{MnO}_2$  catalyzed carbon electrodes for dioxygen reduction in concentrated alkali 259
- Disclinations**  
Elastic continuum theories of lattice defects: A review 775
- Dislocation**  
Etch pit observations on the habit faces of gel grown nickel molybdate crystals 997
- Dislocation creep**  
Superplasticity 689
- Dislocation density correlations**  
Elastic continuum theories of lattice defects: A review 775
- Dislocation density tensor**  
Elastic continuum theories of lattice defects: A review 775
- Dislocation dynamics**  
Mechanisms and empirical equations for deformation and some principles of alloy design 677
- Dislocation interactions**  
Grain boundary-dislocation interactions 699
- Dislocation-precipitate interaction**  
Some aspects of dislocation-precipitate interaction in under-aged aluminium-germanium alloy 1041
- Dislocations**  
Effects of mechanical deformation: Exoemission 755  
Relevance of liquid state to solid state properties 773  
Elastic continuum theories of lattice defects: A review 775
- Disordered materials**  
Investigation of hydrogenous materials using neutrons 151
- Disordered zones**  
Electron microscopy of defect clusters produced by radiation damage 537
- Domain structures**  
High resolution electron microscopy of long range ordered alloys 417
- Dual phase steels**  
Applications of scanning transmission electron microscope microanalysis in the study of materials 491
- Ductility**  
Superplasticity 689
- Ductility minimum**  
Serrated plastic flow 653
- Dynamic strain ageing**  
Serrated plastic flow 653
- Elastic continuum theory**  
Elastic continuum theories of lattice defects: A review 775
- Elastic field equations**  
Elastic continuum theories of lattice defects: A review 775
- Electron emission**  
Effects of mechanical deformation: Exoemission 755
- Electronic energy**  
Strength and electronic structure 717
- Electron-mediated interactions**  
Strength and electronic structure 717
- Electron microscopy**  
High resolution electron microscopy of superconductors 453  
Electron microscopy of defect clusters produced by radiation damage 537  
Electron microscopy of layered single crystals grown by direct vapour transport method 549
- Electrical conductivity**  
Fast ion conducting lithium glasses Review 201  
DC electrical conductivity of  $\text{Na}_2\text{O-ZnO-B}_2\text{O}_3$  glass system 1009
- Electrical properties**  
Glass-metal particulate composites 193  
Electrical properties of polycrystalline silicon and zinc oxide semiconductors 243
- Electrolytic reduction**  
Growth of research and development in rare metals extraction in India 901

- Electro-optic  
Hydrothermal growth of  $A^{II}B^{VI}$  semiconductors 177
- Electron beam evaporation  
Annealing behaviour of electron-beam deposited tin dioxide films 1029
- Electron diffraction  
Electron diffraction analysis of antimony films 611
- Electron exchange  
Influence of the presence of  $Fe^{2+}$  ion in nickel-zinc ferrite 7
- Electron diffraction  
Formation of lamellar  $M_{23}C_6$  on and near twin boundaries in austenitic stainless steels 617
- Electron transport  
Electron transport in non-crystalline garnet films 53
- Electrochemical preparation  
Electrochemical preparation of potassium gold cyanide 165
- Electronic simulation  
Instabilities in yielding 645
- Empirical equations  
Mechanisms and empirical equations for deformation and some principles of alloy design 677
- Epoxy resin  
Amine-cured epoxy/glass fibre composites 99
- Equation of state  
The pressure-volume relation of ytterbium up to 9 GPa 395
- Etch pits  
Etch pit observations on the habit faces of gel grown nickel molybdate crystals 997
- Exchange constants  
Influence of the presence of  $Fe^{2+}$  ion in nickel-zinc ferrite 7  
Influence of spin orbit coupling and lanthanide contraction on the exchange interaction in rare earth garnets 1069
- Exchange parameter  
Curie temperatures and 0°K magnetic moments of zinc-substituted lithium ferrites 39
- Fast breeder-test reactor  
Plutonium metallurgy in India 923
- Ferrimagnetism  
Amorphous state ferroelectricity, magnon scattering and phase stability in microparticle materials 327
- Ferrites  
Curie temperatures and 0°K magnetic moments of zinc-substituted lithium ferrites 39  
Infrared absorption in spinel ferrites 1063
- Ferroelasticity  
Ferroelasticity 733
- Ferroelectric ferroelastics  
Ferroelasticity 733
- Ferroelectricity  
Pyroelectric materials 317  
Amorphous state ferroelectricity, magnon scattering and phase stability in microparticle materials 327
- Ferroelectrics  
Investigation of hydrogenous materials using neutrons 151
- Ferromagnetic resonance  
Ferromagnetic resonance in metallic glasses: study of fracture, stress and thermal stability 1
- Field ion microscope  
Details of an imaging atom probe 569
- Field ion microscopy  
Field ion microscopic observations of  $LaB_6$  on tungsten 573
- First order phase transitions  
Instabilities in first order phase transitions 701
- Fissile  
Plutonium metallurgy in India 923
- Flow stress  
Serrated plastic flow 653  
Some aspects of dislocation-precipitate interaction in under-aged aluminium-germanium alloy 1041
- Fluctuations in materials  
Experimental study of fluctuations in materials 805
- Fluorescence and absorption corrections  
X-ray microanalysis in the transmission electron microscope 503
- Force constants  
Infrared absorption in spinel ferrites 1063
- Fractals  
Fractals 817
- Fracture  
Ferromagnetic resonance in metallic glasses: study of fracture, stress and thermal stability 1  
Fracture of particulate composites 799
- Frequency-modified life  
Elevated temperature low cycle fatigue studies on AISI 304 steel 111
- Gamma  $Fe_2O_3$   
Amorphous state ferroelectricity, magnon scattering and phase stability in microparticle materials 327
- Gamma ferric oxide  
Development of pure and doped gamma ferric oxide 59
- Garnet  
Mössbauer spectroscopy of titanium-substituted iron garnets 17
- Gel grown  
Etch pit observations on the habit faces of gel grown nickel molybdate crystals 997
- Glass-forming ability  
Metallic glasses 579

- Glass-metal composites  
 Glass-metal particulate composites 193
- Glass structure  
 Fast ion conducting lithium glasses—Review 201
- Glassy electrolytes  
 Fast ion conducting lithium glasses—Review 201
- Gold plating salt  
 Electrochemical preparation of potassium gold cyanide 165
- Grain boundary  
 Superplasticity 689  
 Grain boundary—dislocation interactions 699
- Grain boundary effects  
 Electrical properties of polycrystalline silicon and zinc oxide semiconductors 243
- Grains  
 Fractals 817
- Growth technique  
 Electron microscopy of layered single crystals grown by direct vapour transport method 549
- Growth temperature  
 Preparation of single crystal films of magnetic bubble materials—Rare earth yttrium iron gallium garnets by liquid phase epitaxy and their physical properties 47
- Habit faces  
 Etch pit observations on the habit faces of gel grown nickel molybdate crystals 997
- Hallide metallurgy  
 Growth of research and development in rare metals extraction in India 901
- Hardness pendulum  
 Observations on the physical basis of mechanical behaviour 627
- Heat bath  
 Experimental study of fluctuations in materials 805
- Helium embrittlement  
 Radiation effects in nuclear reactor materials—Correlation with structure 339
- Hexagonal metals  
 Internal friction in hexagonal metals 959
- High pressure  
 Lithium solid electrolytes and their applications 223  
 The pressure-volume relation of ytterbium up to 9 GPa 395
- High resolution analysis  
 Analytical electron microscopy of aluminium alloys 513
- High resolution electron microscopy  
 High resolution electron microscopy of long range ordered alloys 417  
 High resolution electron microscopy as a tool for structural investigations 459
- High resolution electron microscopy  
 High resolution electron microscopic studies of  $\text{HoAl}_3$ ,  $\text{Er}_{0.5}\text{Gd}_{0.5}\text{Al}_3$  and  $\text{Y}_{0.91}\text{Er}_{0.09}\text{Al}_3$  in thin film form 603
- High resolution microscopy  
 Metallic glasses 579
- High strength and low alloy steels  
 Applications of scanning transmission electron microscope microanalysis in the study of materials 491
- High temperature electrode  
 High temperature materials for magnetohydrodynamic channels 71
- High voltage electron microscopy  
 High voltage electron microscope irradiation and observations in metallic glasses 595
- High voltage pulser  
 Details of an imaging atom probe 569
- Hot pressing  
 Dependence of microstructure on process variables in manganese zinc ferrites 65
- Hydrogen sulphide  
 Oxidation of thin films of tin at room temperature in hydrogen sulphide atmosphere 1019
- Hydrogenous materials  
 Investigation of hydrogenous materials using neutrons 151
- Hydrothermal growth  
 Hydrothermal growth of  $\text{A}^{\text{II}}\text{B}^{\text{VI}}$  semiconductors 177
- Hyperfine field  
 Mössbauer spectroscopy of titanium-substituted iron garnets 17  
 Magnetic structure of zinc ferrite 27
- Hyperfine interactions  
 A Mössbauer study of hyperfine interactions in the boroferrite  $\text{Fe}_{3-x}\text{Ga}_x\text{Bo}_6$  ( $x = 0, 0.12$ ) 33
- Imaging atom probe  
 Details of an imaging atom probe 569
- Imide-amine hardness  
 Amine-cured epoxy/glass fibre composites 99
- Impact resistance  
 Mechanisms and empirical equations for deformation and some principles of alloy design 677
- Inhomogeneities  
 Elastic continuum theories of lattice defects: A review 775
- Instabilities  
 Instabilities in yielding 645  
 Instabilities in first order phase transitions 701
- Insulator materials  
 High temperature materials for magnetohydrodynamic channels 71
- Intensity ratio  
 X-ray microanalysis in the transmission electron microscope 503
- Internal friction  
 Internal friction in hexagonal metals 959



- Investment casting  
Structure and properties of an investment—cast austenitic stainless steel 119
- Ionic conductivity studies  
Lithium solid electrolytes and their applications 223
- Ionic conductor  
Preparation and characterisation of  $\beta''$ - $\text{Al}_2\text{O}_3$  979
- Iron garnet  
Mössbauer spectroscopy of titanium-substituted iron garnets 17
- Irradiation creep  
Radiation effects in nuclear reactor materials—Correlation with structure 339
- Irradiation effects  
Radiation effects in nuclear reactor materials—Correlation with structure 339
- Irradiation embrittlement  
Radiation effects in nuclear reactor materials—Correlation with structure 339
- Irradiation growth  
Radiation effects in nuclear reactor materials—Correlation with structure 339
- Irradiation hardening  
Radiation effects in nuclear reactor materials—Correlation with structure 339
- IR spectrum  
Infrared absorption in spinel ferrites 1063
- Jahn-Teller ion spinels  
Influence of the presence of  $\text{Fe}^{2+}$  ion in nickel-zinc ferrite 7
- Kataoka-Yamada theory  
Temperature dependence of microhardness in mixed crystals 1035
- Lamellar  $\text{M}_{23}\text{C}_6$   
Formation of lamellar  $\text{M}_{23}\text{C}_6$  on and near twin boundaries in austenitic stainless steels 617
- Lanthanum hexaboride  
Field ion microscopic observations of  $\text{LaB}_6$  on tungsten 573
- Laser devices  
Hydrothermal growth of  $\text{Al}^{\text{III}}\text{B}^{\text{VI}}$  semiconductors 177
- Lattice defects  
Elastic continuum theories of lattice defects: A review 775
- Lattice imaging  
High resolution electron microscopy as a tool for structural investigations 459  
High resolution electron microscopic studies of  $\text{HoAl}_3$ ,  $\text{Er}_{0.5}\text{Gd}_{0.5}\text{Al}_3$  and  $\text{Y}_{0.91}\text{Er}_{0.09}\text{Al}_3$  in thin film form 603
- Lead zirconate titanate  
Effect of compositional modifications on the piezoelectric properties of spray dried lead zirconate titanate ceramics 83
- Lead zirconate titanate  
Amorphous state ferroelectricity, magnon scattering and phase stability in microparticle materials 327
- Limit cycle solutions  
Repeated yield drop phenomena as a cooperative effect 665
- Liquid metal-cooled fast breeder reactors  
Plutonium metallurgy in India 923
- Liquid phase epitaxy  
Preparation of single crystal films of magnetic bubble materials—Rare earth yttrium iron gallium garnets by liquid phase epitaxy and their physical properties 47
- Liquid state properties  
Relevance of liquid state to solid state properties 773
- Lithium carbonate single crystals  
Evidence of screw dislocations on (002) cleavages of lithium carbonate single crystals 991
- Lithium ion conductors  
Lithium solid electrolytes and their applications 223
- Localised spin canting  
Curie temperatures and 0°K magnetic moments of zinc-substituted lithium ferrites 39
- Long range order  
High resolution electron microscopy of long range ordered alloys 417
- Low cycle fatigue  
Elevated temperature low cycle fatigue studies on AISI 304 steel 111
- Macroscopically defect free cement  
Some recent advances in materials technology 405
- Magnetisation  
Curie temperatures and 0°K magnetic moments of zinc-substituted lithium ferrites 39
- Magnetic bubble materials  
Preparation of single crystal films of magnetic bubble materials—Rare earth yttrium iron gallium garnets by liquid phase epitaxy and their physical properties 47
- Magnetic properties  
Magnetic properties of metallic glass  $\text{Fe}_{39}\text{Ni}_{39}\text{Mo}_4\text{Si}_6\text{B}_{12}$  21  
Glass-metal particulate composites 193
- Magnetic recording materials  
Development of pure and doped gamma ferric oxide 59
- Magnetic structure  
Magnetic structure of zinc ferrite 27
- Magnetic susceptibility  
Structural and magnetic investigations of some new boron containing rare earth intermetallic compounds 263

- Magnetic hyperfine field distributions**  
 Evaluation of magnetic hyperfine field distributions from Mössbauer spectra of disordered alloys and metallic glasses 1047
- Magnon scattering**  
 Amorphous state ferroelectricity, magnon scattering and phase stability in microparticle materials 327
- Martensitic transformation**  
 Deformation and martensitic transformation 703
- Manganese zinc ferrites**  
 Dependence of microstructure on process variables in manganese zinc ferrites 65
- Mechanical behaviour**  
 Observations on the physical basis of mechanical behaviour 627  
 Experimental study of fluctuations in materials 805
- Mechanical deformation**  
 Effects of mechanical deformation: Exoemission 755
- Mechanical properties**  
 Structure and properties of an investment—cast austenitic stainless steel 119  
 Glass-metal particulate composites 193
- Melt-quenching**  
 Metallic glasses 579
- Metglasses**  
 Some recent advances in materials technology 405
- Metal-ceramic joint**  
 High temperature materials for magnetohydrodynamic channels 71
- Metal excess systems**  
 Structure and superconductivity in ternary systems of compounds 283
- Metal-hydrogen systems**  
 Investigation of hydrogenous materials using neutrons 151
- Metastable crystalline states**  
 Electron diffraction analysis of antimony films 611
- Metastable phases**  
 Analytical electron microscopy of aluminium alloys 513
- Metallic glasses**  
 Ferromagnetic resonance in metallic glasses: study of fracture, stress and thermal stability 1  
 Magnetic properties of metallic glass  $\text{Fe}_{39}\text{Ni}_{39}\text{Mo}_4\text{Si}_6\text{B}_{12}$  21  
 Metallic glasses 579  
 High voltage electron microscope irradiation and observations in metallic glasses 595  
 Spin-wave excitations in amorphous ferromagnets 1059  
 Evaluation of magnetic hyperfine field distributions from Mössbauer spectra of disordered alloys and metallic glasses 1047
- Microanalysis**  
 Applications of scanning transmission electron microscope microanalysis in the study of materials 491
- Microdiffraction**  
 Scanning transmission electron microscopy and microdiffraction techniques 477
- Microemulsion**  
 Amorphous state ferroelectricity, magnon scattering and phase stability in microparticle materials 327
- Microfocus x-ray generator**  
 Sophisticated equipment developed for growth and evaluation of perfection of nearly perfect crystals 129
- Microhardness**  
 Temperature dependence of microhardness in mixed crystals 1035
- Microparticle**  
 Amorphous state ferroelectricity, magnon scattering and phase stability in microparticle materials 327
- Microstructure**  
 Structure and properties of an investment—cast austenitic stainless steel 119
- Microwaves**  
 Electrical properties of films at microwave frequencies 1075
- Mixed crystals**  
 Temperature dependence of microhardness in mixed crystals 1035
- Mixed oxide and carbide fuels**  
 Plutonium metallurgy in India 923
- MnO<sub>2</sub>**  
 MnO<sub>2</sub> catalyzed carbon electrodes for dioxygen reduction in concentrated alkali 259
- Modulated phases**  
 High resolution electron microscopic studies of  $\text{HoAl}_3$ ,  $\text{Er}_{0.5}\text{Gd}_{0.5}\text{Al}_3$  and  $\text{Y}_{0.91}\text{Er}_{0.09}\text{Al}_3$  in thin film form 603
- Modulated structure**  
 High resolution electron microscopy of long range ordered alloys 417
- Molecular field constants**  
 Influence of spin orbit coupling and lanthanide contraction on the exchange interaction in rare earth garnets 1069
- Morphotropic phase boundary**  
 Effect of compositional modifications on the piezoelectric properties of spray dried lead zirconate titanate ceramics 83
- Mössbauer measurements**  
 Spin-wave excitations in amorphous ferromagnets 1059
- Mössbauer spectra**  
 Mössbauer spectroscopy of titanium-substituted iron garnets 17

- Mössbauer spectra  
Evaluation of magnetic hyperfine field distributions from Mössbauer spectra of disordered alloys and metallic glasses 1047
- Mössbauer spectroscopy  
Metal-to-ceramic bonding in ( $\text{Al}_2\text{O}_3 + \text{Fe}$ ) cermet studied by Mössbauer spectroscopy 13  
Magnetic properties of metallic glass  $\text{Fe}_{39}\text{Ni}_{39}\text{Mo}_4\text{Si}_6\text{B}_{12}$  21  
Amorphous state ferroelectricity, magnon scattering and phase stability in microparticle materials 327
- Mössbauer study  
A Mössbauer study of hyperfine interactions in the boroferrite  $\text{Fe}_{3-x}\text{Ga}_x\text{BO}_6$  ( $x = 0, 0.12$ ) 33
- $\text{Na}_2\text{-ZnO-B}_2\text{O}_3$  glass  
DC electrical conductivity of  $\text{Na}_2\text{O-ZnO-B}_2\text{O}_3$  glass system 1009
- Neutrons  
Investigation of hydrogenous materials using neutrons 151
- Nickel alloys  
Radiation effects in nuclear reactor materials—Correlation with structure 339
- Nickel-zinc ferrite  
Influence of the presence of  $\text{Fe}^{2+}$  ion in nickel-zinc ferrite 7
- $\text{NiMoO}_4 \cdot x\text{H}_2\text{O}$  crystals  
Etch pit observations on the habit faces of gel grown nickel molybdate crystals 997
- NMR  
Lithium solid electrolytes and their applications 223
- Non-crystalline garnet  
Electron transport in non-crystalline garnet films 53
- Non-integral dimensions  
Fractals 817
- Nonlinear dynamics  
Elementary concepts in chaos and turbulence 807
- Nonlinear Langevin equations  
Repeated yield drop phenomena as a cooperative effect 665
- Non-local elasticity  
Elastic continuum theories of lattice defects: A review 775
- Nuclear electricity  
Plutonium metallurgy in India 923
- Nuclear reactor materials  
Radiation effects in nuclear reactor materials—Correlation with structure 339
- Optical densification  
Photon, electron and ion beam induced physical and optical densification in chalcogenide films 1013
- Optical properties  
Glass-metal particulate composites 193
- Ordering kinetics  
Phase transformations—a physicist's perception 837
- Overlap integrals  
Magnetic structure of zinc ferrite 27
- Oxidation  
Oxidation of thin films of tin at room temperature in hydrogen sulphide atmosphere 1019
- Oxide glasses  
Glass-metal particulate composites 193
- Pairing interaction  
On the mechanism of pairing in the bcs theory 273
- Phase changes  
Electron diffraction analysis of antimony films 611
- Phase diagrams  
Phase transformations—a physicist's perception 837
- Phase identification  
Analytical electron microscopy of aluminium alloys 513
- Phase transformations  
Electron microscopy of layered single crystals grown by direct vapour transport method 549  
Phase transformations—a physicist's perception 837
- Phase transitions  
Ferroelasticity 733
- Physical beneficiation  
Growth of research and development in rare metals extraction in India 901
- Piezoelectric  
Hydrothermal growth of  $\text{Al}^{\text{III}}\text{B}^{\text{VI}}$  semiconductors 177
- Piezoelectricity  
Effect of compositional modifications on the piezoelectric properties of spray dried lead zirconate titanate ceramics 83  
Pyroelectric materials 317
- Plastic deformation  
Deformation and martensitic transformation 703
- Plastic properties  
Elastic properties of As-Sb-Se glasses 1001
- Plating  
Electrochemical preparation of potassium gold cyanide 165
- Plutonium  
Plutonium metallurgy in India 923
- Point defect clusters  
Electron microscopy of defect clusters produced by radiation damage 537
- Polycrystalline semiconductors  
Electrical properties of polycrystalline silicon and zinc oxide semiconductors 243

- Polymers**  
Investigation of hydrogenous materials using neutrons 151
- Polysilicon**  
Electrical properties of polycrystalline silicon and zinc oxide semiconductors 243
- Polytype in SiC**  
High resolution electron microscopy as a tool for structural investigations 459
- Polytype structures**  
Structural disorder and solid state transformations in single crystals of  $\text{Zn}_x\text{Cd}_{1-x}\text{S}$  and  $\text{Zn}_x\text{Mn}_{1-x}\text{S}$  369
- Polyvinyl chloride**  
Surface modification of polyvinyl chloride towards blood compatibility 1087
- Potassium gold cyanide**  
Electrochemical preparation of potassium gold cyanide 165
- Precipitation morphology**  
Formation of lamellar  $\text{M}_{23}\text{C}_6$  on and near twin boundaries in austenitic stainless steels 617
- Pressure-induced semiconductor-to-metal transitions**  
Electronic conduction in bulk  $\text{Se}_{1-x}\text{Te}_x$  glasses at high pressures and at low temperatures 231
- Pseudoelasticity**  
Deformation and martensitic transformation 703
- Pu-Be neutron sources**  
Plutonium metallurgy in India 923
- Pyroelectricity**  
Pyroelectric materials 317
- Pyroelectric studies**  
Dielectric and pyroelectric studies on triglycine sulphate-polymer composites 105
- Quantitative model**  
X-ray microanalysis in the transmission electron microscope 503
- Quadrupole splitting**  
Mössbauer spectroscopy of titanium-substituted iron garnets 17
- Radiation damage**  
Radiation effects in nuclear reactor materials—  
Correlation with structure 339  
High resolution electron microscopy of superconductors 453  
Electron microscopy of defect clusters produced by radiation damage 537
- Random distribution model**  
A Mössbauer study of hyperfine interactions in the boroferrite  $\text{Fe}_{3-x}\text{Ga}_x\text{BO}_6$  ( $x = 0, 0.12$ ) 33
- Rapid solidification techniques**  
Metallic glasses 579
- Rare earths**  
Structural and magnetic investigations of some new boron containing rare earth intermetallic compounds 263
- Rare metal extraction**  
Growth of research and development in rare metals extraction in India 901
- Relaxation**  
Spin wave relaxation processes in polycrystalline yttrium iron garnets 1053
- Repeated yield drop**  
Repeated yield drop phenomena as a cooperative effect 665
- Resistance change**  
Oxidation of thin films of tin at room temperature in hydrogen sulphide atmosphere 1019
- RF sputtering**  
A novel method of RF powder sputtering 971
- Saturation temperature**  
Preparation of single crystal films of magnetic bubble materials—Rare earth yttrium iron gallium garnets by liquid phase epitaxy and their physical properties 47
- Scanning electron microscopy**  
A novel method of RF powder sputtering 971
- Selective surfaces**  
Some recent advances in materials technology 405
- Semiconductors**  
Hydrothermal growth of  $\text{AlB}^{\text{VI}}$  semiconductors 177
- Separation process**  
Growth of research and development in rare metals extraction in India 901
- Serrated flow**  
Serrated plastic flow 653
- Shape memory effect**  
Deformation and martensitic transformation 703
- Sheet resistivity**  
Annealing behaviour of electron-beam deposited tin dioxide films 1029
- Shield**  
A novel method of RF powder sputtering 971
- Shock deformation**  
Shocks and high velocity deformation 633
- Shock front**  
Mechanisms and empirical equations for deformation and some principles of alloy design 677
- Shock melting**  
Shocks and high velocity deformation 633
- Shock propagation**  
Shocks and high velocity deformation 633
- Single crystals**  
Structural disorder and solid state transformations in single crystals of  $\text{Zn}_x\text{Cd}_{1-x}\text{S}$  and  $\text{Zn}_x\text{Mn}_{1-x}\text{S}$  369
- Silicon carbide**  
High resolution electron microscopy as a tool for structural investigations 459

- Sintering**  
 Dependence of microstructure on process variables in manganese zinc ferrites 65  
 Effect of compositional modifications on the piezoelectric properties of spray dried lead zirconate titanate ceramics 83
- Slag ceramic interaction**  
 High temperature materials for magnetohydrodynamic channels 71
- Slip lines**  
 Some aspects of dislocation-precipitate interaction in under-aged aluminium-germanium alloy 1041
- Sodium beta alumina**  
 Preparation and characterisation of  $\beta''$ -Al<sub>2</sub>O<sub>3</sub> 979
- Solid electrolyte**  
 Preparation and characterisation of  $\beta''$ -Al<sub>2</sub>O<sub>3</sub> 979
- Solid state batteries**  
 Fast ion conducting lithium glasses—Review 201
- Solid state properties**  
 Relevance of liquid state to solid state properties 773
- Spinel**  
 Metal-to-ceramic bonding in (Al<sub>2</sub>O<sub>3</sub> + Fe) cermet studied by Mössbauer spectroscopy 13
- Spinodal decomposition**  
 Phase transformations—a physicist's perception 837
- Spin-reorientation**  
 A Mössbauer study of hyperfine interactions in the boroferrite Fe<sub>3-x</sub>Ga<sub>x</sub>BO<sub>6</sub> (x = 0, 0.12) 33
- Spin wave excitations**  
 Spin-wave excitations in amorphous ferromagnets 1059
- Spin-wave line-widths**  
 Spin wave relaxation processes in polycrystalline yttrium iron garnets 1053
- Spiral etch pits**  
 Evidence of screw dislocations on (002) cleavages of lithium carbonate single crystals 991
- Spray drying**  
 Effect of compositional modifications on the piezoelectric properties of spray dried lead zirconate titanate ceramics 83
- Stacking fault energy**  
 Electron microscopy of layered single crystals grown by direct vapour transport method 549
- Stacking sequence**  
 High resolution electron microscopy as a tool for structural investigations 459
- Stainless steel**  
 Structure and properties of an investment—cast austenitic stainless steel 119  
 Radiation effects in nuclear reactor materials—Correlation with structure 339
- STEM**  
 Applications of scanning transmission electron microscope microanalysis in the study of materials 491
- Strain rates**  
 Elevated temperature low cycle fatigue studies on AISI 304 steel 111
- Strength**  
 Strength and electronic structure 717
- Strengthening mechanisms**  
 Strength and electronic structure 717
- Stress**  
 Ferromagnetic resonance in metallic glasses: study of fracture, stress and thermal stability 1  
 Effects of mechanical deformation: Exoemission 755
- Stress and strain rate**  
 Superplasticity 689
- Structural characterization**  
 High resolution electron microscopic studies of HoAl<sub>3</sub>, Er<sub>0.5</sub>Gd<sub>0.5</sub>Al<sub>3</sub> and Y<sub>0.91</sub>Er<sub>0.09</sub>Al<sub>3</sub> in thin film form 603
- Structural disorder**  
 Structural disorder and solid state transformations in single crystals of Zn<sub>x</sub>Cd<sub>1-x</sub>S and Zn<sub>x</sub>Mn<sub>1-x</sub>S 369
- Structural investigation**  
 High resolution electron microscopy as a tool for structural investigations 459
- Sublattices**  
 Influence of the presence of Fe<sup>2+</sup> ion in nickel-zinc ferrite 7
- Superconducting compounds**  
 Structure and superconductivity in ternary systems of compounds 283
- Superconducting materials**  
 High resolution electron microscopy of superconductors 453
- Superconductivity**  
 On the mechanism of pairing in the BCS theory 273
- Superconductors**  
 Investigation of hydrogenous materials using neutrons 151
- Superexchange**  
 Influence of spin orbit coupling and lanthanide contraction on the exchange interaction in rare earth garnets 1069
- Superplasticity**  
 Superplasticity 689
- Superstructure**  
 High resolution electron microscopy of long range ordered alloys 417
- Surface modification**  
 Surface modification of polyvinyl chloride towards blood compatibility 1087

- Surface states  
Observations on the physical basis of mechanical behaviour 627
- Surface studies  
Scanning transmission electron microscopy and microdiffraction techniques 477
- Structural investigations  
Structural and magnetic investigations of some new boron containing rare earth intermetallic compounds 263
- Surface roughness  
Observations on the physical basis of mechanical behaviour 627
- Symmetry  
Ferroelasticity 733
- Target  
A novel method of RF powder sputtering 971
- Temperature dependence  
Spin-wave excitations in amorphous ferromagnets 1059  
Temperature dependence of microhardness in mixed crystals 1035
- Tensile testing  
Computer simulation of tensile testing 643  
Instabilities in yielding 645
- Ternary systems  
Structure and superconductivity in ternary systems of compounds 283
- Theoretical models  
Structural disorder and solid state transformations in single crystals of  $\text{Zn}_x\text{Cd}_{1-x}\text{S}$  and  $\text{Zn}_x\text{Mn}_{1-x}\text{S}$  369
- Thermal decomposition  
Development of pure and doped gamma ferric oxide 59
- Thermal hysteresis  
A Mössbauer study of hyperfine interactions in the boroferrite  $\text{Fe}_{3-x}\text{Ga}_x\text{BO}_6$  ( $x = 0, 0.12$ ) 33
- Thermal stability  
Ferromagnetic resonance in metallic glasses: study of fracture, stress and thermal stability 1
- Thermo-compression bonds  
Metal-to-ceramic bonding in  $(\text{Al}_2\text{O}_3 + \text{Fe})$  cermet studied by Mössbauer spectroscopy 13
- Thermoplastic  
Use of coal tar pitch for carbon-carbon composites 91
- Thermopower  
Lithium solid electrolytes and their applications 223
- Thin films  
Electron transport in non-crystalline garnet films 53  
Oxidation of thin films of tin at room temperature in hydrogen sulphide atmosphere 1019
- Tilt boundaries  
Evidence of screw dislocations on (002) cleavages of lithium carbonate single crystals 991
- Tin  
Oxidation of thin films of tin at room temperature in hydrogen sulphide atmosphere 1019
- Tin dioxide films  
Annealing behaviour of electron-beam deposited tin dioxide films 1029
- Torsion tensor  
Elastic continuum theories of lattice defects: A review 775
- Transfer integrals  
Influence of spin orbit coupling and lanthanide contraction on the exchange interaction in rare earth garnets 1069
- Transition metal dichalcogenides  
Electron microscopy of layered single crystals grown by direct vapour transport method 549
- Transmission electron microscopy  
X-ray microanalysis in the transmission electron microscope 503  
A novel method of RF powder sputtering 971
- Transport number  
Fast ion conducting lithium glasses—Review 201
- Triglycine sulphate polymers  
Dielectric and pyroelectric studies on triglycine sulphate-polymer composites 105
- Tungsten field evaporation  
Field ion microscopic observations of  $\text{LaB}_6$  on tungsten 573
- Turbulence  
Elementary concepts in chaos and turbulence 807
- Twin boundaries  
Formation of lamellar  $\text{M}_{23}\text{C}_6$  on and near twin boundaries in austenitic stainless steels 617
- Twinning  
Ferroelasticity 733
- Twist boundaries  
Evidence of screw dislocations on (002) cleavages of lithium carbonate single crystals 991
- Under-aged  
Some aspects of dislocation-precipitate interaction in under-aged aluminium-germanium alloy 1041
- Uranium  
Radiation effects in nuclear reactor materials—Correlation with structure 339
- Vacuum casting  
Structure and properties of an investment—cast austenitic stainless steel 119
- Void growth  
Fracture of particulate composites 799
- Void nucleation  
Fracture of particulate composites 799

- Void swelling  
 Radiation effects in nuclear reactor materials—  
 Correlation with structure 339
- Waveguide  
 Electrical properties of films at microwave  
 frequencies 1075
- Work hardening peaks  
 Serrated plastic flow 653
- X-ray diffraction  
 The pressure-volume relation of ytterbium up to 9  
 GPa 395  
 Electron microscopy of layered single crystals  
 grown by direct vapour transport method 549
- X-ray diffraction topography camera  
 Sophisticated equipment developed for growth  
 and evaluation of perfection of nearly perfect  
 crystals 129
- X-ray diffractometer  
 Sophisticated equipment developed for growth  
 and evaluation of perfection of nearly perfect  
 crystals 129
- X-ray microanalysis  
 X-ray microanalysis in the transmission electron  
 microscope 503  
 Analytical electron microscopy of aluminium  
 alloys 513
- Yielding  
 Instabilities in yielding 645
- Ytterbium  
 The pressure-volume relation of ytterbium up to 9  
 GPa 395
- Yttrium iron garnet  
 Amorphous state ferroelectricity, magnon scatter-  
 ing and phase stability in microparticle materials  
 327  
 Spin wave relaxation processes in polycrystalline  
 yttrium iron garnets 1053
- Zinc ferrite  
 Magnetic structure of zinc ferrite 27
- Zirconium alloys  
 Radiation effects in nuclear reactor materials—  
 Correlation with structure 339
- ZnO varistors  
 Electrical properties of polycrystalline silicon and  
 zinc oxide semiconductors 243

# AUTHOR INDEX

- Agarwal M K  
Electron microscopy of layered single crystals  
grown by direct vapour transport method 549
- Aiyar R  
*see* Venkataramani N 65  
*see* Srivastava C M 1069
- Amelinckx S  
High resolution electron microscopy of long  
range ordered alloys 417
- Ananthakrishna G  
Repeated yield drop phenomena as a cooperative  
effect 665
- Anantharaman M R  
Development of pure and doped gamma ferric  
oxide 59
- Anavekar R V  
DC electrical conductivity of  $\text{Na}_2\text{O-ZnO-B}_2\text{O}_3$   
glass system 1009
- Asundi M K  
Internal friction in hexagonal metals 959
- Ayyub P  
*see* Multani M S 327
- Bahadur D  
*see* Srivastava C M 17  
Electron transport in non-crystalline garnet films  
53
- Balakrishnan V  
Summary and outlook 823
- Balasubramanian N  
*see* Ramaseshan S 405
- Banerjee S  
Electron microscopy of defect clusters produced  
by radiation damage 537  
Instabilities in first order phase transitions 701
- Bansal C  
Metal-to-ceramic bonding in ( $\text{Al}_2\text{O}_3 + \text{Fe}$ ) cermet  
studied by Mössbauer spectroscopy 13  
Evaluation of magnetic hyperfine field distri-  
butions from Mössbauer spectra of disordered  
alloys and metallic glasses 1047
- Bhatia S N  
Spin wave relaxation processes in polycrystalline  
yttrium iron garnets 1053
- Bhatnagar Anil K  
*see* Parashar R S 1  
*see* Prasad B Bhanu 21  
Spin-wave excitations in amorphous ferro-  
magnets 1059
- Bhat T Balakrishna  
Mechanisms and empirical equations for deform-  
ation and some principles of alloy design 677
- Bose D N  
Lithium solid electrolytes and their applications  
223
- Chakravorty D  
Glass-metal particulate composites 193
- Chandrasekharaiiah M N  
*see* Prasad B Bhanu 21
- Chatterjee S N  
*see* Kishan Pran 39
- Chidambaram R  
Shocks and high velocity deformation 633
- Chopra K L  
Photon, electron and ion beam induced physical  
and optical densification in chalcogenide films  
1013
- Cowley J M  
Scanning transmission electron microscopy and  
microdiffraction techniques 477
- Dasannacharya B A  
Investigation of hydrogenous materials using  
neutrons 151
- Das B K  
*see* Singh S N 243  
*see* Kalsi H S 979
- Datta K K  
*see* Seth R L 91
- Devaraj N  
*see* Anavekar R V 1009
- Dhar Ajay  
*see* Sreenivas K 105
- Dhar D  
Fractals 817
- Dhar S K  
*see* Malik S K 263
- Dube D C  
Electrical properties of films at microwave  
frequencies 1075
- Embury J D  
*see* Ramachandran T R 513
- Ganguly C  
*see* Roy P R 923
- Geetha Balakrishnan  
*see* Rao G V Subba 283
- Geetha Kurian  
Surface modification of polyvinyl chloride to-  
wards blood compatibility 1087
- Giridhar A  
Elastic properties of As-Sb-Se glasses 1001
- Goel R C  
*see* Kalsi H S 979



- Gopal E S R  
see Parthasarathy G 231
- Goyal P S  
see Dasannacharya B A 151
- Gupta Arjeesh  
Annealing behaviour of electron-beam deposited tin dioxide films 1029
- Gupta C K  
see Sundaram C V 901
- Gupta M S  
see Singh Anand Kumar 603  
Harshavardhan K Solomon 1013  
see Chopra K L 971  
A novel method of RF powder sputtering
- Houghton D C  
see Ramachandran T R 513
- Indira Rajagopal  
Electrochemical preparation of potassium gold cyanide 165
- Ittyachen M A  
see Kurien K V 997
- Jagannathan R  
see Vithal M 33  
see Bhatnagar Anil K 1059
- Jebbaraj P M  
Structure and properties of an investment—cast austenitic stainless steel 119
- Joag D B  
Field ion microscopic observations of  $\text{LaB}_6$  on tungsten 573
- Joglekar S M  
see Srivastava C M 7
- Joshi P B  
see Bhatia S N 1053
- Kalsi H S  
Preparation and characterisation of  $\beta''\text{-Al}_2\text{O}_3$  979
- Kanitkar M M  
see Joag D B 573
- Kanitkar P L  
see Joag D B 573
- Keer H V  
see Anantharaman M R 59
- Kishan Pran  
Curie temperatures and 0°K magnetic moments of zinc-substituted lithium ferrites 39
- Kishore  
Some aspects of dislocation-precipitate interaction in under-aged aluminium-germanium alloy 1041
- Krishna K N  
see Harshavardhan K Solomon 971
- Krishan Lal  
Sophisticated equipment developed for growth and evaluation of perfection of nearly perfect crystals 129
- Krishnan R  
see Rodriguez P 339
- Krishna P  
see Sebastian M T 369
- Kshatriya J D  
see Agarwal M K 549
- Kulkarni A R  
Fast ion conducting lithium glasses—Review 201
- Kumari S  
see Singh S N 243
- Kurien K V  
Etch pit observations on the habit faces of gel grown nickel molybdate crystals 997
- Kuzmina I P  
see Kuznetsov V A 177
- Kuznetsov V A  
Hydrothermal growth of  $\text{A}^{\text{II}}\text{B}^{\text{VI}}$  semiconductors 177
- Laddha G S  
see Raju K S 991
- Lal C  
see Seth R L 91
- Lal Ramji  
Effect of compositional modifications on the piezoelectric properties of spray dried lead zirconate titanate ceramics 83
- Landuyt J Van  
see Amelinckx S 417
- Laroia K K  
see Kishan Pran 39
- Lorimer G W  
X-ray microanalysis in the transmission electron microscope 503
- Maiti H S  
see Kulkarni A R 201
- Majumdar D  
see Bose D N 223
- Malhotra L K  
see Chopra K L 1013
- Malik S K  
Structural and magnetic investigations of some new boron containing rare earth intermetallic compounds 263
- Manoharan R  
 $\text{MnO}_2$  catalyzed carbon electrodes for dioxygen reduction in concentrated alkali 259
- Mansingh Abhai  
see Sreenivas K 105
- Mittal V P  
see Seth R L 91
- Mohandas E  
see Seshadri V R 569
- Mukhopadhyay G  
Effects of mechanical deformation: Exoemission 755

- Multani M S  
Amorphous state ferroelectricity, magnon scattering and phase stability in microparticle materials 327
- Muneera C I  
Oxidation of thin films of tin at room temperature in hydrogen sulphide atmosphere 1019
- Murthy H R Krishna  
Relevance of liquid state to solid state properties 773
- Nagpaul L K  
see Kishan Pran 39
- Nandedkar R V  
High voltage electron microscope irradiation and observations in metallic glasses 595
- Nayar V Unnikrishnan  
see Muneera C I 1019
- Neelakantan K  
see Seshadri V R 569
- Om Prakash  
see Srivastava C M 17
- Palaniswamy M  
see Raju K S 991
- Palkar V R  
see Multani M S 327
- Pande C S  
High resolution electron microscopy of superconductors 453
- Parashar R S  
Ferromagnetic resonance in metallic glasses: study of fracture, stress and thermal stability 1
- Parthasarathy G  
Electronic conduction in bulk  $\text{Se}_{1-x}\text{Te}_x$  glasses at high pressures and at low temperatures 231
- Patel J V  
see Agarwal M K 549
- Patel P D  
see Agarwal M K 549
- Patni M J  
see Srivastava C M 7  
see Srinivasan T T 1063
- Paul A  
see Kulkarni A R 201
- Poonam Gupta  
see Gupta Arjeesh 1029
- Prabhawalker P D  
Electron diffraction analysis of antimony films 611
- Pragati Mukhopadhyay  
Preparation of single crystal films of magnetic bubble materials—Rare earth yttrium iron gallium garnets by liquid phase epitaxy and their physical properties 47
- Prasad B Bhanu  
Magnetic properties of metallic glass  $\text{Fe}_{35}\text{Ni}_{39}\text{Mo}_4\text{Si}_6\text{B}_{12}$  21  
see Bhatnagar Anil K 1059
- Purdy Gary R  
Applications of scanning transmission electron microscope microanalysis in the study of materials 491
- Raghavan K Srinivasa  
Superplasticity 689
- Raghunathan V S  
see Seshadri V R 569
- Rai R S  
see Singh G 459
- Raj R G  
see Varma D S 99
- Rajagopalan S  
see Chopra K L 1013
- Rajagopalan S R  
see Indira Rajagopal 165
- Rajan K Govinda  
Strength and electronic structure 717
- Raju K S  
Evidence of screw dislocations on (002) cleavages of lithium carbonate single crystals 991
- Ramachandran T R  
Analytical electron microscopy of aluminium alloys 513
- Ramakrishna J  
see Anavekar R V 1009
- Ramakrishnan P  
see Lal Ramji 83
- Ramakrishnan T V  
see Murthy H R Krishna 773
- Ramasamy P  
see Raju K S 991
- Ramaswamy Ramakrishna  
Elementary concepts in chaos and turbulence 807
- Ramaseshan S  
Some recent advances in materials technology 405  
Observations on the physical basis of mechanical behaviour 627
- Ranganathan S  
Grain boundary-dislocation interactions 699
- Rao C N  
see Asundi M K 959
- Rao K R  
Experimental study of fluctuations in materials 805
- Rao T Sudersena  
see Sreenivas K 105
- Rao G V Subba  
Structure and superconductivity in ternary systems of compounds 283
- Rao B Uma Maheshwar  
see Srivastava C M 17  
see Pragati Mukhopadhyay 47